DESY–PROC–2007–02

arXiv:0712.3633v2 [hep-ph] 5 Jun 2008

12th International Conference on Elastic and Diffractive Scattering (Blois Workshop)

Forward Physics and QCD

21 – 25 May 2007

DESY - Hamburg



Proceedings of the

12th International Conference on Elastic and Diffractive Scattering Forward Physics and QCD

EDS 2007

May 21-25, 2007
DESY, Hamburg, Germany

Editors: J. Bartels, K. Borras, M. Diehl and H. Jung

Verlag Deutsches Elektronen - Synchrotron

Impressum

Proceedings of the 12th International Conference on Elastic and Diffractive Scattering Forward Physics and QCD 2007

Conference homepage
`http://www.desy.de/~eds07/`

Slides at
`https://indico.desy.de/conferenceDisplay.py?confId=372`

The copyright is governed by the Creative Commons agreement, which allows for free use and distribution of the articles for non-commertial activity, as long as the title, the authors' names and the place of the original are referenced.

Editors: J. Bartels, K. Borras, M. Diehl and H. Jung
Cover Photo: ©Rainer Mankel, DESY
Photo of Participants: Marta Mayer (DESY, Hamburg)
December 2007
DESY-PROC-2007-02
ISBN 978-3-935702-24-9
ISSN 1435-8077

Published by
Deutsches Elektronen - Synchrotron, DESY
Notkestraße 85
22607 Hamburg
Germany

Organizing Committee:

J. Bartels, K. Borras, M. Diehl and H. Jung

Conveners:

lepton-proton collisions: X. Janssen (Universite Libre de Bruxelles) and L. Motyka (DESY)
pp **and** $p\bar{p}$ **collisions:** S. Gieseke (Karlsruhe), M. Grothe (Wisconsin and Torino) and C. Royon (Saclay)
heavy-ion collisions: K. Tuchin (Iowa State and RIKEN/BNL) and S. White (BNL)
opportunities at future colliders: U. Klein (Liverpool)
cosmic rays and astroparticle physics: R. Engel (Karlsruhe)
theoretical developments in high-energy QCD: V. Khoze (Durham) and A. Sabio Vera (CERN)

Advisory Committee:

M. Albrow (Fermilab), S. J. Brodsky (SLAC), J. Dainton (Liverpool), A. De Roeck (CERN),
Yu. Dokshitzer (Paris), A. Donnachie (Manchester), K. Goulianos (New York), M. Haguenauer (Palaiseau),
E. Levin (Tel Aviv), A. Levy (Tel Aviv), L. Lipatov (St. Petersburg/Hamburg), A. D. Martin (Durham),
L. McLerran (Brookhaven), J. Mnich (DESY), O. Nachtmann (Heidelberg), B. Nicolescu (Paris),
R. Peschanski (Saclay), A. Santoro (Rio de Janeiro), M. Strikman (PennState), J. Trân Thanh Vân (Orsay),
M. Rijssenbeek (Stony Brook), A. Vorobiev (St. Petersburg), A. White (Argonne), G. Wolf (DESY)

Permanent Committee of the EDS Conferences:

B. Aubert (Annecy), G. Belletini (Pisa), D. Denegri (Saclay), G. Giacomelli (Bologna), A. Krisch (Michigan),
V. Kundrat (Prague), N. N. Khuri (New York), A. Martin (CERN), G. Matthiae (Rome), B. Nicolescu (Paris),
R. Orava (Helsinki), J. Orear (Cornell), J. Peoples (Fermilab), E. Predazzi (Torino), C.-I. Tan (Providence),
J. Trân Thanh Vân (Orsay), C. N. Yang (Stony Brook)

Supported by:

Deutsches Elektronen-Synchroton DESY
Deutsche Forschungsgemeinschaft
SFB 676 (Particles, Strings and the Early Universe)

Preface

The *12th International Conference on Elastic and Diffractive Scattering*, held on 21 – 25 May 2007 at DESY in Hamburg, had the subtitle *Forward Physics and QCD*. Besides discussing in detail elastic and diffractive scattering in ep and pp collisions, emphasis was put on the QCD description of diffractive processes, which becomes more and more important in the preparation for the start of the highest-energy proton-proton collider ever build, the LHC. Especially the issue of the underlying event and multi-parton interaction, which is relevant not only for QCD processes but also for all searches for new phenomena, was discussed in detail.

With more than 100 participants this workshop showed the increasing interest and importance of this area in high energy physics. Many young researchers participated in this conference, showing that this is an active, challenging and exciting field.

Unfortunately, not all presentations during the workshop appear as a writeup in these proceedings: K. Below and G. Marchesini were not able to deliver a written version of their contribution. All the talks with transparcenies are available at: `https://indico.desy.de/conferenceDisplay.py?confId=372`

We thank all the participants for making this conference so interesting and lively. We also thank A. Grabowksy, S. Platz and L. Seskute for their continuous help and support during all the meeting weeks. We are grateful to the DESY directorate for financial support of this workshop and for the hospitality which they extended to all the participants of the workshop.

The Organizing Committee:
J. Bartels, K. Borras, M. Diehl and H. Jung



Contents

I Lepton-Proton Collisions **1**

Exclusive vector meson electroproduction at HERA **2**

A Levy

Exclusive Processes at HERMES **10**

R Fabbri

Fitting DVCS at NLO and beyond **17**

K Kumerički, D Müller, K Passek-Kumerički

Exclusive vector meson electroproduction **26**

D Ivanov

Photo and electroproduction of vector mesons: a unified nonperturbative treatment **33**

E Ferreira, H. G Dosch

Vector meson electroproduction within GPD approach **39**

S Goloskokov

On the limitations of the color dipole picture **45**

C Ewerz, A von Manteuffel, O Nachtmann

What is measured in hard exclusive processes? **51**

J Londergan, A.P Szczepaniak

A Regge-pole model for DVCS **57**

L Jenkovsky

Glue drops inside hadrons **63**

B.Z Kopeliovich, B Povh, I Schmidt

Studying QCD factorizations in exclusive $\gamma^*\gamma^* \to \rho_L^0\rho_L^0$ **69**

S Wallon, B Pire, M Segond, L Szymanowski

Low Q^2 and High y Inclusive Cross Section Measurements from the HERA Experiments ZEUS and H1 **75**

J Kretzschmar

Status of Deeply Inealstic Parton Distributions **81**

J Blümlein

Diffractive PDFs **90**

P Laycock

Factorisation breaking in diffraction **96**

A Bonato

Diffractive structure function F_L^D from fits with higher twist **102**

K Golec-Biernat, A Łuszczak

Diffractive parton distributions: the role of the perturbative Pomeron **110**

G Watt, A.D Martin, M Ryskin

Multiple interactions in H1 and ZEUS **118**

T Namsoo

Diffractive neutral pion production, chiral symmetry and the odderon **124**

C Ewerz, O Nachtmann

II pp and $p\bar{p}$ Collisions **129**

Central production of new physics **130**

J Forshaw, A Pilkington

Diffraction at CDF **137**

K Goulianos

Prospects for proton tagging at high luminosities at the LHC **145**

M Tasevsky

Total cross section measurement and diffractive physics with Totem **153**

M Deile

Prospects of forward energy flow and low-x physics at the LHC **160**

A Hamilton

Diffractive physics in ALICE **168**

R Schicker

The odderon at RHIC and LHC **173**

B Nicolescu

Prospects for diffraction at the LHC **181**

A De Roeck

Multiple scattering, underlying event, and minimum bias **192**

G Gustafson

Multiple interactions and AGK rules in pQCD **200**

M Salvadore, J Bartels, G. P Vacca

Multiple parton interactions, underlying event and forward physics at LHC **207**

L Fanò

Elastic scattering, total cross section and luminosity measurements at ATLAS **215**

C Sbarra

Diffraction at HERA and implications for Tevatron and LHC **221**

L Schoeffel

Search for exclusive events using the dijet mass fraction **226**

O Kepka, C Royon

Diffractive production of quarkonia **231**

A Szczurek

Rapidity gap survival in the black-disk regime **239**

L Frankfurt, C.E Hyde, M. Strikman, C. Weiss

Pomeron intercept and slope: the QCD connection **248**

K Goulianos

Exclusive J/ψ and Υ hadroproduction as a probe of the QCD Odderon **254**

L Szymanowski

The soft and the hard pomerons: elastic scattering and unitarisation **260**

J-R Cudell, A Lengyel, E Martynov, O.V Selyugin

pp elastic ecattering at LHC in a nucleon-structure model **267**

M Islam, J Kašpar R. J Luddy

To the theory of high-energy nucleon collisions **273**

V Kundrat, Jan Kašpar, Miloš Lokajíček

Saturation effects in elastic scattering at the LHC **279**

O Selyugin, J.-R Cudell

Elastic pp and $\bar{p}p$ scattering in the models of unitarized pomeron **285**

E Martynov

III Heavy-Ion Collisions 291

Forward Physics with BRAHMS in pp and dAu collisions at RHIC **292**

D Röhrich

Manifestations of gluon saturation at RHIC **300**

J Albacete

Measurement of the cross section and the single transverse spin asymmetry in very forward neutron production from polarized pp collisions at RHIC **308**

M Togawa

Gluon saturation: from pp to AA **316**

A Kovner

Photoproduction in ultra-peripheral heavy-ion collisions **321**

J Nystrand

Fractional energy losses in the black disk regime and BRAHMS effect **327**

L Frankfurt, M Strikman

The coherent inelastic processes on nuclei at ultrarelativistic energies **336**

V.L Lyuboshitz , V V Lyuboshitz

IV Opportunities at future colliders **343**

Low x and diffractive physics at future electron-proton/ion colliders **344**

H Kowalski

Low-x physics at a future electron-proton/ion (EIC) collider facility **352**

B Surrow

The LHeC and its low x Physics Potential **356**

J Dainton, M Klein, P Newman

Perturbative QCD in the Regge limit: prospects at ILC **360**

S Wallon

V Cosmic Rays and Astroparticle Physics **371**

On the measurement of the proton-air cross section using cosmic ray data **372**

R Ulrich, J Blümer, R Engel, F Schüssler, M Unger

EAS-TOP:The proton-air inelastic cross-section at $\sqrt{s} \approx$ 2 TeV **380**

G. C Trinchero

UHE Cosmic Rays above 10^{17} eV: the role of percolation **386**

J Alvarez-Muñiz, P Brogueira, R Conceição, J Dias de Deus, M.C Espírito Santo, M Pimenta

Extended air shower simulations based on EPOS **392**

K Werner, T Pierog

LHCf: a LHC Detector for Cosmic Ray Physics **398**

A Tricomi

VI Theoretical Developments in High-Energy QCD **405**

RHIC physics: short overview **406**

A Stasto

Nuclear shadowing and collisions of heavy ions **414**

A Kaidalov

NLO jet production in k_T factorization **421**

J Bartels, A Sabio Vera, F Schwennsen

Connections between high-energy QCD and statistical physics **428**

S Munier

High energy QCD beyond the mean field approximation **436**

A Shoshi

High-energy scattering and Euclidean-Minkowskian duality **444**

E Meggiolaro

Insight into new physics with tagged forward protons at the LHC **452**

V Khoze, A.D Martin, M.G Ryskin

BFKL at NNLO **459**

S Marzani, R.D Ball, P Falgari, S Forte

Unintegrated parton distributions and correlation functions **465**

A Stasto

Nonlinear QCD at high energies **471**

E Levin

Small x QCD and multigluon states: a color toy model **476**

G P Vacca, P. L Iafelice

The Reggeon $\rightarrow$ 2 Reggeons + particle vertex in the Lipatov effective action formalism **482**

M Braun, M.I Vyazovsky

On the behaviour of R_{pA} at high energy **488**

M Kozlov, A Shoshi, B.W Xiao

The coordinate representation of NLO BFKL and the dipole picture **495**

V Fadin

Angular decorrelations in Mueller-Navelet jets and DIS **501**

A Sabio Vera, F Schwennsen

Breakdown of coherence? **507**

M Seymour

BFKL equation and anomalous dimensions in $N = 4$ SUSY **515**

L Lipatov

Gluon saturation and black hole criticality **523**

L Álvarez-Gaumé, C Gómez, A Sabio Vera, A Tavanfar, M. A Vázquez-Mozo

VII Summary **529**

Experimental summary **530**

H Abramowicz

Theoretical summary **538**

K Golec-Biernat

Part I

Lepton-Proton Collisions

Exclusive vector meson electroproduction at HERA

Aharon Levy
Tel Aviv University and DESY

Abstract
The latest results on exclusive vector meson electroproduction from HERA are reviewed. In particular, the new high-statistics measurements of the ρ^0 electroproduction are presented and compared to several models.

1 Introduction

Exclusive electroproduction of light vector mesons is a particularly good process for studying the transition from the soft to the hard regime of strong interactions, the former being well described within the Regge phenomenology while the latter - by perturbative QCD (pQCD). Among the most striking expectations [1] in this transition is the change of the logarithmic derivative δ of the cross section σ with respect to the $\gamma^* p$ center-of-mass energy W, from a value of about 0.2 in the soft regime (represented by a soft Pomeron [2] exchange diagram in Fig. 1) to 0.8 in the hard one (represented by a two-gluon exchange diagram in Fig. 2), and the decrease of the exponential slope b of the differential cross section with respect to the squared-four-momentum transfer t, from a value of about 10 GeV^{-2} to an asymptotic value of about 5 GeV^{-2} when the virtuality Q^2 of the photon increases.

When calculating the cross section of exclusive electroproduction of vector mesons (V), one needs information on the wave function of the initial virtual photon, the wave function of the produced vector meson, the $q\bar{q}p$ scattering amplitude, which requires the gluon density and the p elastic form factor (see Fig. 2). In the following we present the available data on exclusive vector

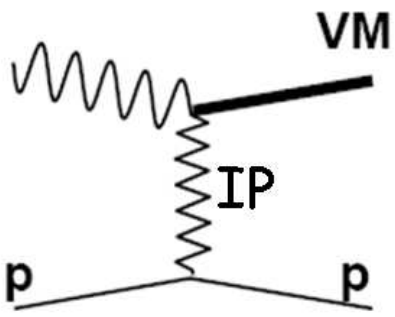


Fig. 1: *A diagram describing exclusive vector meson electroproduction in terms of a Pomeron exchange.*

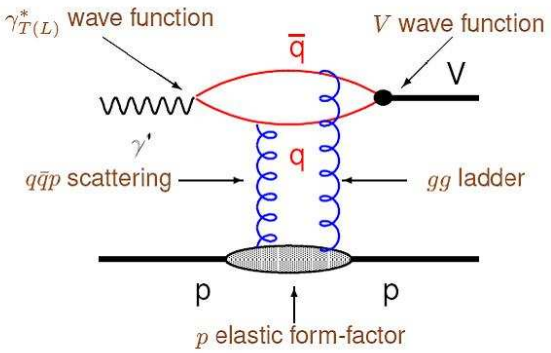


Fig. 2: *A diagram describing exclusive vector meson electroproduction in terms of a two-gluon exchange.*

meson electroproduction and then use the recent precision measurements by ZEUS [3] of the ρ^0 vector meson to discuss what one can learn about the produced vector meson wave function and about the gluon density in the proton.

2 W dependence of the cross section

The soft to hard transition can be seen by studying the W dependence of the cross section for exclusive vector meson photoproduction, from the lightest one, ρ^0, to the heavier ones, up to the Υ. The scale in this case is the mass of the vector meson, as in photoproduction $Q^2 = 0$. Figure 3 shows $\sigma(\gamma p \to Vp)$ as function of W for light and heavy vector mesons. For comparison, the total photoproduction cross section, $\sigma_{tot}(\gamma p)$, is also shown. The data at high W can be parameterised as W^δ, and the value of δ is displayed in the figure for each reaction. One sees clearly the transition from a shallow W dependence for low scales to a steeper one as the scale increases.

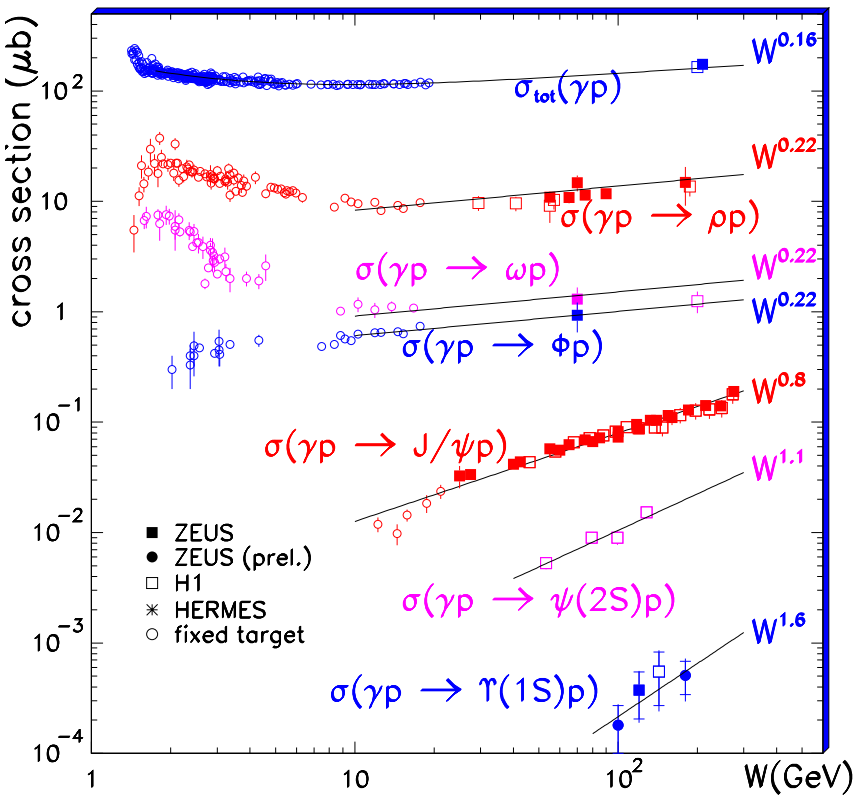


Fig. 3: *The W dependence of the cross section for exclusive vector meson photoproduction, $\sigma(\gamma p \to Vp)$. The total photoproduction cross section is also shown. The lines are the result of a fit of the form W^δ to the high energy part of the data.*

One can also check this transition by varying Q^2 for a given vector meson. The cross section $\sigma(\gamma^* p \to \rho^0 p)$ is presented in Fig. 4 as a function of W, for different values of Q^2. The cross section rises with W in all Q^2 bins. In order to quantify this rise, the logarithmic derivative δ of σ with respect to W is obtained by fitting the data to the expression $\sigma \sim W^\delta$ in each of the Q^2 intervals. The resulting values of δ from the recent ZEUS measurement are compiled

in Fig 5. Also included in this figure are values of δ from other measurements [4] for the ρ^0 as well as those for ϕ [5], J/ψ [6] and γ [7] (Deeply Virtual Compton Scattering (DVCS)). In this case the results are plotted as a function of $Q^2 + M^2$, where M is the mass of the vector meson. One sees a universal behaviour, showing an increase of δ as the scale becomes larger, in agreement with the expectations mentioned in the introduction. The value of δ at low scale is the one expected from the soft Pomeron intercept [2], while the one at large scale is in accordance with twice the logarithmic derivative of the gluon density with respect to W.

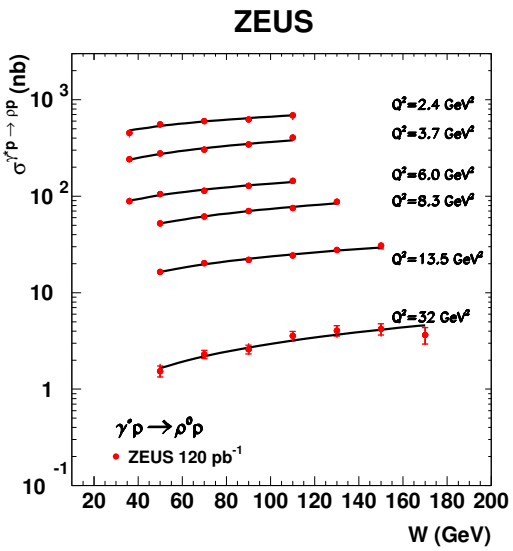


Fig. 4: *The W dependence of the cross section for exclusive ρ^0 electroproduction, for different Q^2 values, as indicated in the figure. The lines are the result of a fit of the form W^δ to the data.*

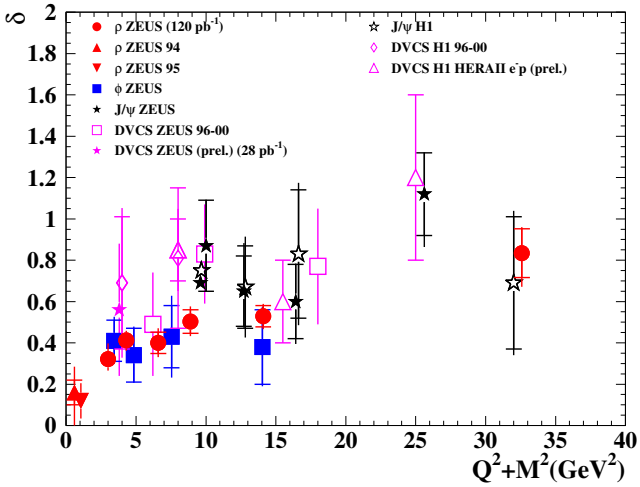


Fig. 5: *A compilation of the value of δ from a fit of the form W^δ for exclusive vector-meson electroproduction, as a function of $Q^2 + M^2$. It includes also the DVCS results.*

3 t dependence of the cross section

The differential cross section, dσ/dt, has been parameterised by an exponential function $e^{-b|t|}$ and fitted to the data of exclusive vector meson electroproduction and also to DVCS. The resulting values of b as a function of the scale $Q^2 + M^2$ are plotted in Fig. 6. As expected, b decreases to a universal value of about 5 GeV^{-2} as the scale increases.

The value of b can be related via a Fourier transform to the impact parameter. Assuming that the process of exclusive electroproduction of vector mesons is hard and dominated by gluons, one can use the relation $< r^2 >= b(\hbar c)^2$ to obtain the radius of the gluon density in the proton. The value of about 5 GeV^{-2} corresponds to a value of $< r >_g \sim 0.6$ fm, smaller than the value of the charge density of the proton ($< r >_p \sim 0.8$ fm), indicating that the gluons are well-contained within the charge-radius of the proton.

One can study the W dependence of dσ/dt for fixed t values and extract the effective Pomeron trajectory $\alpha_{IP}(t)$. This was done in case of the ρ^0 for two Q^2 values and the trajectory was fitted to a linear form to obtain the intercept $\alpha_{IP}(0)$ and the slope α'_{IP}. These values are

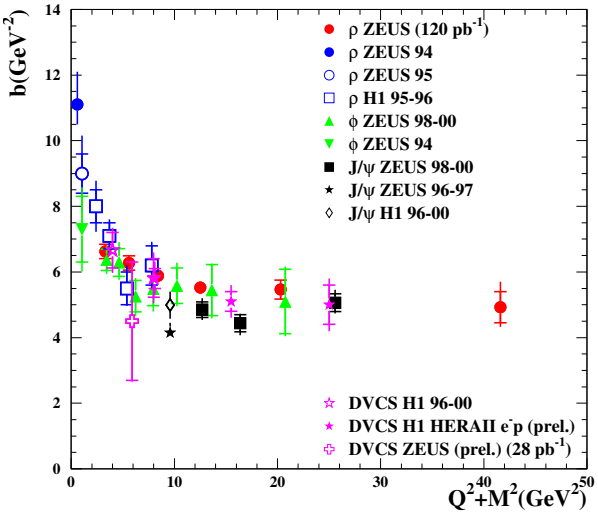


Fig. 6: *A compilation of the value of the slope b from a fit of the form $d\sigma/d|t| \propto e^{-b|t|}$ for exclusive vector-meson electroproduction, as a function of Q^2+M^2. Also included is the DVCS result.*

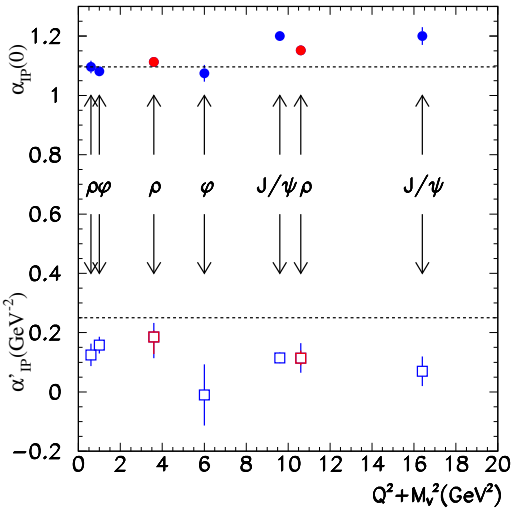


Fig. 7: *Values of the intercept and slope of the effective Pomeron trajectory as a function of Q^2+M^2, as obtained from measurements of exclusive electroproduction of ρ^0, ϕ, and J/ψ vector mesons.*

presented in a compilation of the effective Pomeron intercept and slope, from this and from similar studies for other vector mesons, in Fig. 7. As in the other compilations, the values are plotted as a function of Q^2+M^2. The value of $\alpha_{IP}(0)$ increases with Q^2 while the value of α'_{IP} tends to decrease with Q^2.

4 Q^2, W and t dependence of $r_{00}^{04} = \sigma_L/\sigma_{tot}$ for $\gamma^* p \to \rho^0 p$

The helicity analysis of the decay-matrix element r_{00}^{04} of the ρ^0 was used to extract the ratio $R = \sigma_L/\sigma_T$ of longitudinal (σ_L) to transverse (σ_T) $\gamma^* p$ cross sections. When the value of r_{00}^{04} is close to one, as is the case for this analysis, the error on R becomes large and highly asymmetric. It is then advantageous to study the properties of r_{00}^{04} itself which carries the same information ($= \sigma_L/\sigma_{tot}$), rather than R. While r_{00}^{04} is an increasing function of Q^2, as shown in Fig. 8, it is independent of W in all Q^2 intervals (Fig. 9). This implies that the W behaviour of σ_L is the same as that of σ_T, a result which is somewhat surprising. The $q\bar{q}$ configurations in the wave function of γ_L^* have typically a small transverse size, while the configurations contributing to γ_T^* may have large transverse sizes. The contribution to σ_T of large-size $q\bar{q}$ configurations, which are more hadron-like, is expected to lead to a shallower W dependence than in case of σ_L. Thus, the result presented in Fig. 9 suggests that the large-size configurations of the transversely polarised photon are suppressed.

The above conclusion can also explain the behaviour of r_{00}^{04} as a function of t, shown in Fig. 10 for two Q^2 values. Different sizes of interacting objects imply different t distributions, in particular a steeper $d\sigma_T/dt$ compared to $d\sigma_L/dt$. This turns out not to be the case. In both Q^2

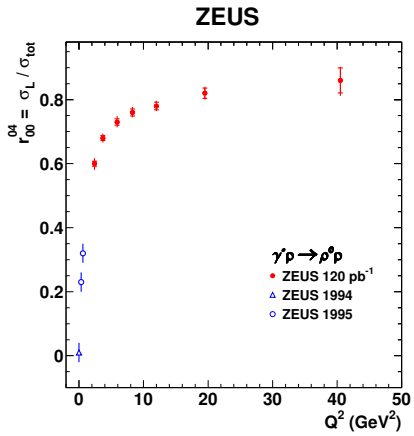


Fig. 8: *The ratio r_{00}^{04} as a function of Q^2 for $W = 90$ GeV.*

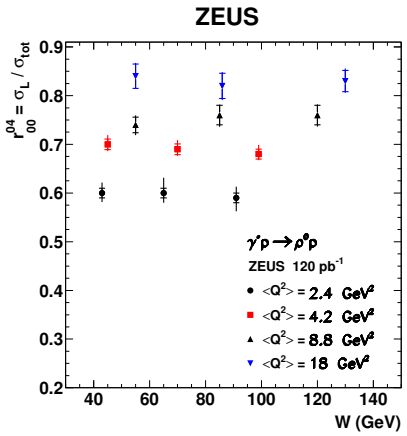


Fig. 9: *The ratio r_{00}^{04} as a function of W for different values of Q^2, as indicated in the figure.*

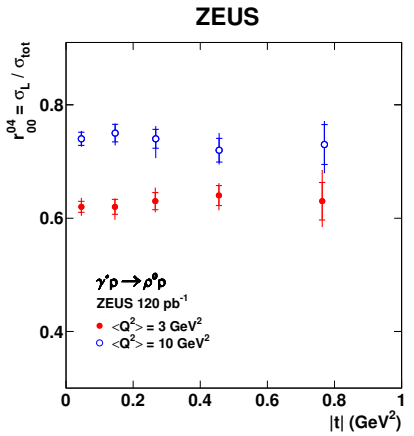


Fig. 10: *The ratio r_{00}^{04} as a function of $|t|$ for different values of Q^2, as indicated in the figure.*

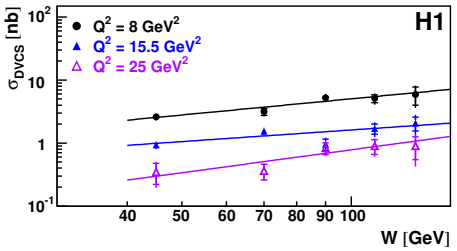


Fig. 11: *The DVCS cross section as a function of W at three values of Q^2. The solid lines represent the results of fits of the form W^δ.*

ranges, r_{00}^{04} is independent of t, reinforcing the earlier conclusion about the suppression of the large-size configurations in the transversely polarised photon.

This suppression is also seen in DVCS, $\gamma^* p \to \gamma p$. The final state photon is real and therefore transversely polarised. Using s-channel helicity conservation, also the initial virtual photon would be transversely polarised. Looking at the new H1 measurement of the DVCS cross section [8], shown in Fig. 11, which has a steep W dependence ($\delta \sim 0.8$), one concludes that the large-size configurations in the transversely polarised photon are suppressed.

5 Comparison of the data of $\gamma^* p \to \rho^0 p$ to models

The precision measurements of the reaction $\gamma^* p \to \rho^0 p$ were used to compare to some selected pQCD-inspired models.

All models are based on the dipole representation of the virtual photon, in which the photon first fluctuates into a $q\bar{q}$ pair (colour dipole), which then interacts with the proton to produce the ρ^0. The ingredients necessary in such calculations are the virtual-photon wave-function, the

dipole-proton cross section and the ρ^0 wave-function. The photon wave-function is known from QED. The models differ in the treatment of the dipole-proton cross section and the assumed ρ^0 wave-function.

The models of Frankfurt, Koepf and Strikman (FKS) [9] and of Martin, Ryskin and Teubner (MRT) [10] are based on two-gluon exchange as the dominant mechanism for the dipole-proton interaction. The gluon distributions are derived from inclusive measurements of the proton structure function. In the FKS model, a three-dimensional Gaussian is assumed for the ρ^0 wave-function, while MRT use parton-hadron duality and normalise the calculations to the data. For the comparison with the present measurements the MRST99 [11] and CTEQ6.5M [12] parameterisations for the gluon density were used.

Kowalski, Motyka and Watt (KMW) [13] use an improved version of the saturation model [14], with an explicit dependence on the impact parameter and DGLAP evolution in Q^2, introduced through the unintegrated gluon distribution [15]. Forshaw, Sandapen and Shaw (FSS) [16] model the dipole-proton interaction through the exchange of a soft [2] and a hard [17] Pomeron, with (Sat) and without (Nosat) saturation, and use the DGKP and Gaussian ρ^0 wave-functions. In the model of Dosch and Ferreira (DF) [18], the dipole cross section is calculated using Wilson loops, making use of the stochastic vacuum model for the non-perturbative QCD contribution.

While the calculations based on two-gluon exchange are limited to relatively high-Q^2 values (typically ~ 4 GeV^2), those based on modelling the dipole cross section incorporate both the perturbative and non-perturbative aspects of ρ^0 production.

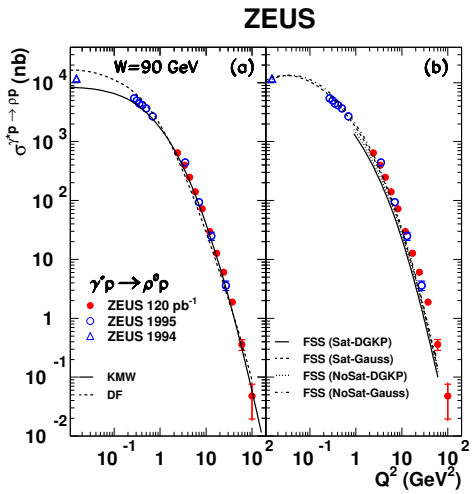


Fig. 12: *The Q^2 dependence of the $\gamma^* p \to \rho^0 p$ cross section at W=90 GeV. The same data are plotted in (a) and (b), compared to different models, as described in the text.*

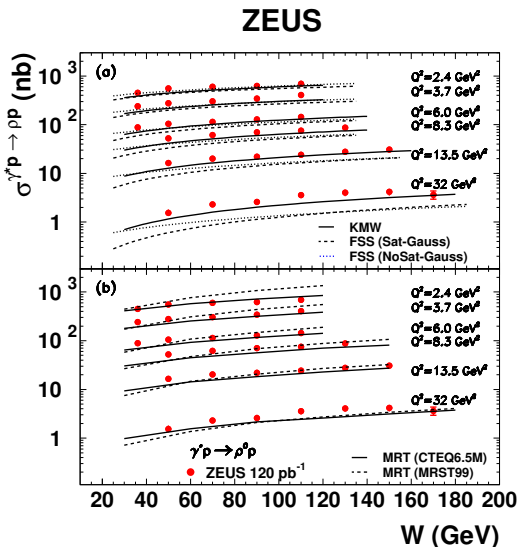


Fig. 13: *The W dependence of the $\gamma^* p \to \rho^0 p$ cross section for different values of Q^2, as indicated in the figure. The same data are plotted in (a) and (b), compared to different models, as described in the text.*

The different predictions discussed above are compared to the Q^2 dependence of the cross section in Fig. 12. None of the models gives a good description of the data over the full kine-

matic range of the measurement. The FSS model with the three-dimensional Gaussian ρ^0 wave-function describes the low-Q^2 data very well, while the KMW and DF models describe the $Q^2 > 1$ GeV^2 region well.

The various predictions are also compared with the W dependence of the cross section, for different Q^2 values, in Fig. 13. Here again, none of the models reproduces the magnitude of the cross section measurements. The closest to the data, in shape and magnitude, are the MRT model with the CTEQ6.5M parametrisation of the gluon distribution in the proton and the KMW model.

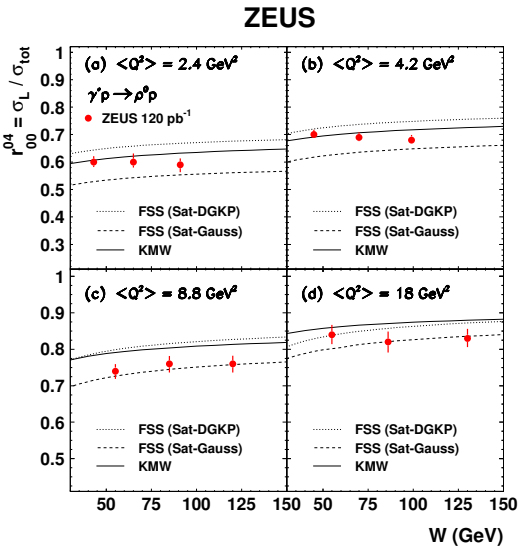


Fig. 14: *The ratio r_{00}^{04} as a function of W for different values of Q^2 compared to the predictions of models as indicated in the figure (see text).*

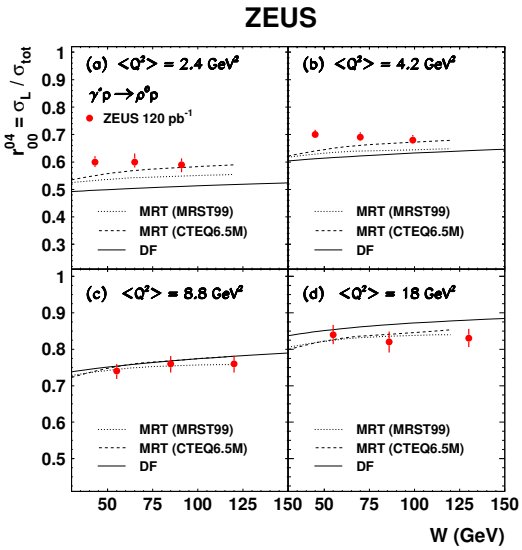


Fig. 15: *The ratio r_{00}^{04} as a function of W for different values of Q^2 compared to the predictions of models as indicated in the figure (see text).*

While all the models exhibit a mild dependence of r_{00}^{04} on W, consistent with the data as shown in Figs. 14 and 15, none of them reproduces correctly the magnitude of r_{00}^{04} in all the Q^2 bins.

In summary, none of the models considered above is able to describe all the features of the data. The high precision of the measurements can be used to refine models for exclusive ρ^0 electroproduction and contribute to a better understanding of the ρ^0 wave function and of the gluon density in the proton.

References

[1] H. Abramowicz, L. Frankfurt and M. Strikman, *Interplay of hard and soft physics in small x deep inelastic processes*, Surveys High Energy Phys. **11**, 51 (1997).

[2] A. Donnachie and P.V. Landshoff, *Total cross-sections*, Phys. Lett. **B 296**, 227 (1992).

[3] ZEUS Coll., S. Chekanov et al., *Exclusive ρ^0 production in deep inelastic scattering at HERA*, DESY07-118 (2007).

[4] ZEUS Coll., J. Breitweg et al., *Elastic and Proton-Dissociative ρ^0 Photoproduction at HERA*, Eur. Phys. J. **C 2**, 2 (1998); ZEUS Coll., M. Derrick et al., *Exclusive Electroproduction of ρ^0 and J/ψ Mesons at HERA*, Eur. Phys. J. **C 6**, 603 (1999); H1 Coll., C. Adloff et al., *Elastic electroproduction of ρ mesons at HERA*, Eur. Phys. J. **C 13**, 371 (2000).

[5] H1 Coll., C. Adloff et al., *Measurement of elastic electroproduction of ϕ mesons at HERA*, Phys. Lett. **B 483**, 360 (2000); ZEUS Coll., S. Chekanov et al., *Exclusive Electroproduction of ϕ Mesons at HERA*, Nucl. Phys. **B 718**, 3 (2005).

[6] ZEUS Coll., S. Chekanov et al. *Exclusive electroproduction of J/ψ mesons at HERA*, Nucl. Phys. **B 695**, 3 (2004); H1 Coll., A. Aktas et al., *Elastic J/ψ production at HERA*, Eur. Phys. J. **C 46**, 585 (2006).

[7] ZEUS Coll., S. Chekanov et al., *Measurement of deeply virtual Compton scattering at HERA*, Phys. Lett. **B 573**, 46 (2003); H1 Coll., A. Aktas et al., *Measurement of Deeply Virtual Compton scattering at HERA*, Eur. Phys. J. **C 44**, 1 (2005).

[8] H1 Coll., A. Aktas et al., *Measurement of Deeply Virtual Compton scattering and its t-dependence at HERA*, DESY-07-142 (2007).

[9] L. Frankfurt, W. Koepf and M. Strikman, *Diffractive heavy quarkonium photoproduction and electroproduction in QCD*, Phys. Rev. **D 57**, 512 (1998); L. Frankfurt, W. Koepf and M. Strikman, *Hard diffractive electroproduction of vector mesons in QCD*, Phys. Rev. **D 54**, 3194 (1996).

[10] A.D. Martin, M.G. Ryskin and T. Teubner, *Q^2 dependence of diffractive vector meson electroproduction*, Phys. Rev. **D 62**, 014022 (2000).

[11] A.D. Martin, R.G. Roberts, W.J. Stirling and R.S. Thorne, *Parton distributions: A New global analysis*, Eur. Phys. J. **C 4**, 463 (1998).

[12] W.K. Tung, H.L. Lai, A. Belyaev, J. Pumplin, D. Stump and C.-P. Yuan, *Heavy Quark Mass Effects in Deep Inelastic Scattering and Global QCD Analysis*, JHEP **0702**, 053 (2007),

[13] H. Kowalski, L. Motyka and G. Watt, *Exclusive diffractive processes at HERA within the dipole picture*, Phys. Rev. **D 74**, 074016 (2006).

[14] K. Golec-Biernat and M. Wuesthoff, *Saturation effects in deep inelastic scattering at low Q^2 and its implications on diffraction*, Phys. Rev. **D 59**, 014017 (1999); K. Golec-Biernat and M. Wuesthoff, *Saturation in diffractive deep inelastic scattering*, Phys. Rev. **D 60**, 114023 (1999).

[15] See e.g. M.A. Kimber, A.D. Martin and M.G. Ryskin, *Unintegrated parton distributions*, Phys. Rev. **D63**, 114027 (2001).

[16] J.R. Forshaw, R. Sandapen and G. Shaw, *Color dipoles and ρ, ϕ electroproduction*, Phys. Rev **D 69**, 094013 (2004).

[17] A. Donnachie and P.V. Landshoff, *New data and the hard Pomeron*, Phys. Lett. **B 518**, 63 (2001).

[18] H.G. Dosch and E. Ferreira, *Nonperturbative and perturbative aspects of photo- and electroproduction of vector mesons*, hep-ph/0610311 (2006).

Exclusive Processes at HERMES

Riccardo Fabbri (on behalf of the HERMES Collaboration)
DESY, Notkestrasse 85, D-22607 Hamburg, Germany, E-mail: Riccardo.Fabbri@desy.de

Abstract
Hard exclusive production in deep inelastic lepton scattering provides new access to the poorly known Generalized Parton Distributions of the nucleon. Different observables for hard exclusive production of photons and mesons have been measured by the HERMES experiment. Emphasis is given to recent results which help to determine the total angular momentum of quarks in the proton.

1 Introduction

The analysis of hard exclusive processes can be used to investigate the generalized parton distributions (GPDs) [1]. From a formal point of view, GPDs show a continuity in describing both inclusive and exclusive processes, the usual parton distributions being a kinematic limit of GPDs. Also, the elastic form factors are specific moments of GPDs. Strong interest in the formalism of GPDs has emerged after GPDs were found to offer the first possibility to reveal the total angular momentum carried by the quarks and gluons in the nucleon.

In this paper, the latest results obtained by the HERMES experiment on Deeply Virtual Compton Scattering (DVCS) and exclusive meson production are reviewed [2]. The data presented here were collected using internal, longitudinally or transversely polarized or unpolarized hydrogen and deuterium targets with longitudinally polarised 27.6 GeV positrons (electrons) in the HERA storage ring at DESY.

2 Deeply Virtual Compton Scattering

The basic mechanism for DVCS (in electroproduction) is a quark absorbing a virtual photon and radiating a real photon. At large photon virtuality, the process amplitude is a convolution of a hard scattering term exactly calculable in perturbative QCD, and a soft (non perturbative) term [3]. The soft term describes the nucleon transition in the process, and is parameterized by the four leading-twist GPDs which conserve quark helicity, H, E, $\tilde{H}$, and $\tilde{E}$. In hard exclusive processes like DVCS, a direct extraction of the GPDs from experimentally measured observables can in general not be performed because at the amplitude level, GPDS are convolved with the hard scattering term, and cannot be disentangled. As a consequence, models of GPDs have to be used to calculate observables that can be compared to corresponding experimental results. The convolved H, E, $\tilde{H}$, and $\tilde{E}$ terms are traditionally represented with the symbols $\mathcal{H}, \mathcal{E}$, $\tilde{\mathcal{H}}$, and $\tilde{\mathcal{E}}$, respectively.

Experimentally, for electroproduction of photons, one cannot disentangle the DVCS from the Bethe-Heitler (BH) process, where the virtual photon is absorbed by the nucleon target and a real photon is emitted by either the incoming or the outgoing lepton. Within the HERMES kinematical acceptance, the DVCS cross section is at least one order of magnitude smaller than

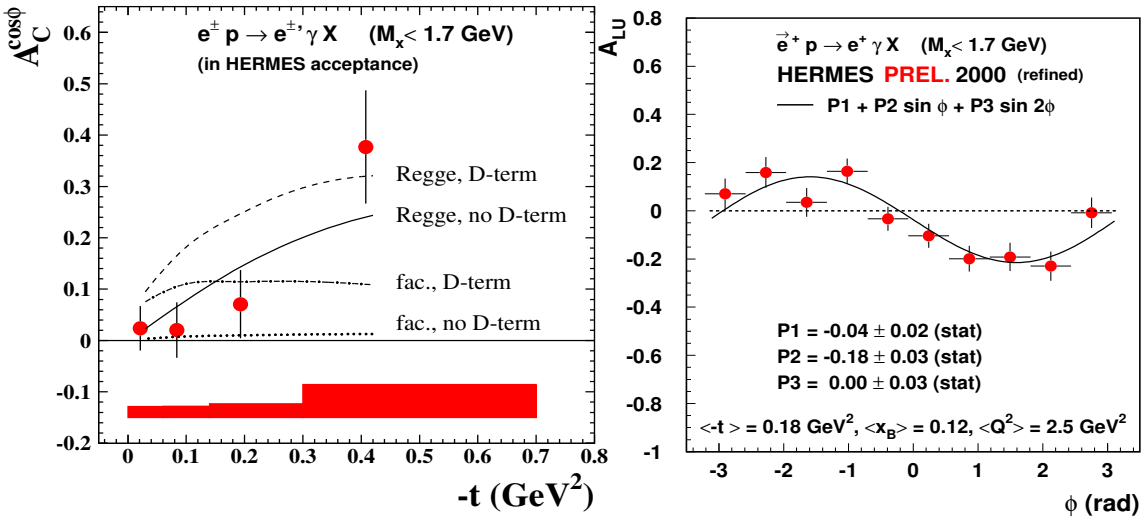


Fig. 1: Left panel: t-dependence of $\cos\phi$ moment of beam-charge asymmetry A_C. Different predictions [5] in the GPD framework are also shown. Right panel: ϕ-dependence of the beam-spin asymmetry A_{LU}. Superimposed to the data are the fit results which show the $\sin\phi$ modulation of A_{LU}.

the BH cross section [4]. Nevertheless, the DVCS amplitude can still be accessed through the BH-DVCS interference term, which can be projected out by considering specific cross section asymmetries in the azimuthal angle ϕ. The latter is defined as the angle between the incoming and outgoing lepton trajectories and the plane correspondingly defined by the virtual and the real photon.

The event selection at HERMES requires events with exactly one photon and one charged track, identified as the scattered lepton, with $Q^2 > 1$ GeV^2, where $-Q^2$ is the squared four-momentum of the initial virtual photon. The recoiling proton is not detected, and exclusive events are identified by requiring the missing mass M_X of the reaction $ep \to e\gamma X$ to correspond to the proton mass. Due to the finite energy resolution, the exclusive sample is selected in the region $-1.5 < M_X < 1.7$ GeV, based on signal-to-background studies using Monte Carlo simulations.

For an unpolarized target, the beam-charge cross section asymmetry $A_C(\phi)$ with unpolarized lepton of either charge, and the beam-spin cross section asymmetry $A_{LU}(\phi)$ using a longitudinally polarized positron beam, at leading-twist in the HERMES kinematics reduce to [4]

$$A_C(\phi) \stackrel{\text{def}}{=} \frac{d\sigma(e^+p,\phi) - d\sigma(e^-p,\phi)}{d\sigma(e^+p,\phi) + d\sigma(e^-p,\phi)} \quad \propto \quad \cos\phi \cdot Re(F_1\mathcal{H}), \tag{1}$$

$$A_{LU}(\phi) \stackrel{\text{def}}{=} \frac{d\sigma(\overrightarrow{e^+}\,p,\phi) - d\sigma(\overleftarrow{e^+}\,p,\phi)}{d\sigma(\overrightarrow{e^+}\,p,\phi) + d\sigma(\overleftarrow{e^+}p,\phi)} \quad \propto \quad \sin\phi \cdot Im(F_1\mathcal{H}), \tag{2}$$

where F_1 is the Dirac form factor of the proton. The first measurement of the asymmetry A_C was performed by HERMES using a hydrogen target. The dependence of the $\cos\phi$ moment on the squared four-momentum transfer t to the target is shown in the left panel of Fig. 1, and compared with predictions in the GPD framework based on [5] (VGG) with different assumptions on the

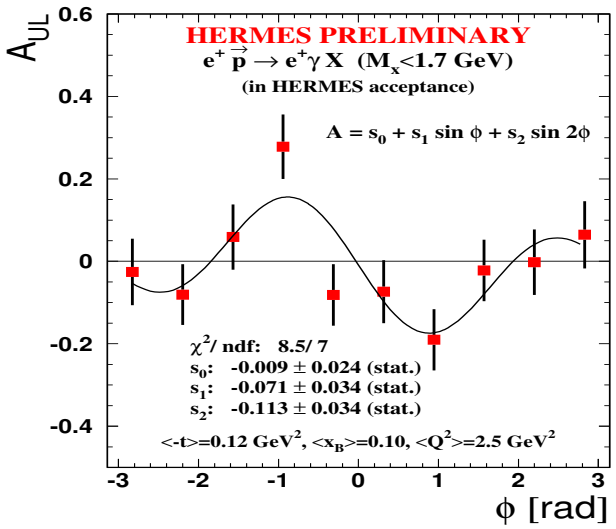


Fig. 2: ϕ-dependence of the asymmetry A_{UL} on a hydrogen target.

GPDs. The data seem to disfavor the model with the non-factorized t-dependence (Regge) for the GPDs with the contribution of the so-called D-term [6]. The ϕ-dependence of the asymmetry A_{LU} is shown in the right panel of Fig. 1. Also displayed are the fit results which show the expected leading-twist $\sin\phi$ modulation of the asymmetry.

The longitudinal target-spin cross section asymmetry $A_{UL}(\phi)$ for an unpolarized positron beam, at leading-twist is expected to reduce [7], in the HERMES kinematics, to

$$\begin{aligned} A_{UL}(\phi) &\stackrel{\text{def}}{=} \frac{d\sigma(e^+ \overrightarrow{p}, \phi) - d\sigma(e^+ \overleftarrow{p}, \phi)}{d\sigma(e^+ \overrightarrow{p}, \phi) + d\sigma(e^+ \overleftarrow{p}, \phi)} \\ &\propto \sin\phi \cdot Im\left(F_1\tilde{\mathcal{H}} + \frac{x_B}{2-x_B}(F_1+F_2)\mathcal{H}\right), \end{aligned} \tag{3}$$

where F_2 is the Pauli form factor of the proton. The ϕ-dependence of the longitudinal target-spin asymmetry on a hydrogen target is shown in Fig. 2, where the fit results show the expected non-zero leading-twist $\sin\phi$ modulation of the asymmetry. The $\sin 2\phi$ moment is 3σ different from zero, an indication that higher-twist effects might contribute to A_{UL} in the HERMES kinematics.

A useful observable to access the convolved GPDs $\mathcal{E}$ and $\tilde{\mathcal{E}}$ is the transverse target-spin asymmetry with unpolarized beam A_{UT}, which in the HERMES kinematics reads

$$\begin{aligned} A_{UT}(\phi-\phi_S) &\stackrel{\text{def}}{=} \frac{d\sigma(\phi-\phi_S) - d\sigma(\phi-\phi_S+\pi)}{d\sigma(\phi-\phi_S) + d\sigma(\phi-\phi_S+\pi)} \\ &\propto Im\left[F_2\mathcal{H} - F_1\mathcal{E}\right]\cdot\sin(\phi-\phi_S)\cos\phi + \\ &\quad Im\left[F_2\tilde{\mathcal{H}} - F_1\frac{x_B}{2-x_B}\tilde{\mathcal{E}}\right]\cdot\cos(\phi-\phi_S)\sin\phi, \end{aligned} \tag{4}$$

where ϕ_S denotes the azimuthal angle between the target polarization plane with respect to the lepton plane. The kinematical dependences of the moments $A_{UT}^{\sin(\phi-\phi_S)\cos\phi}$ and $A_{UT}^{\cos(\phi-\phi_S)\sin\phi}$ on transversely polarized hydrogen target are shown in Fig. 3. Also shown are the predictions [8] based on the VGG code [5] with different ansaetze for the parameterizations of GPDs [9]. The

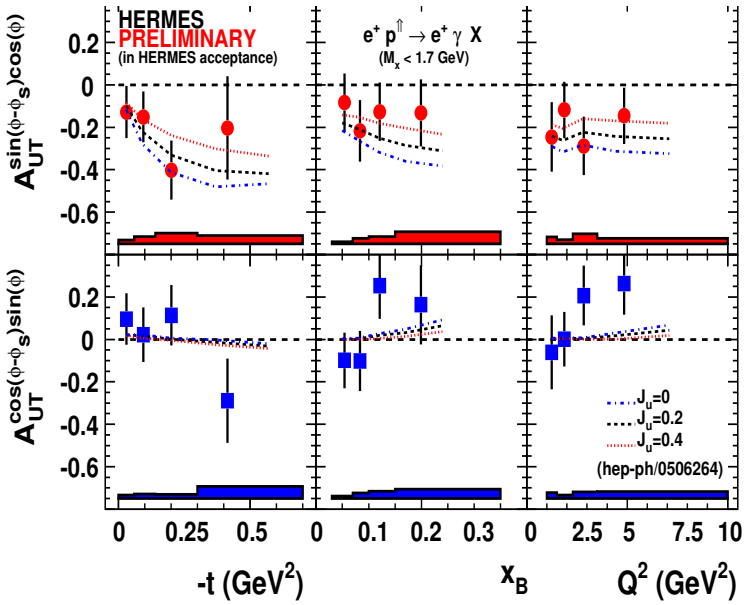


Fig. 3: t-, Bjorken x_B-, and Q^2-dependences of the moments $A_{UT}^{\sin(\phi-\phi_S)\cos\phi}$ (upper panels) and $A_{UT}^{\cos(\phi-\phi_S)\sin\phi}$ (bottom panels) on hydrogen target. Also shown are different predictions based on GPDs. The systematic uncertainty is given by the error band.

displayed curves represent the moments evaluated for a set of u-quark total angular momentum values J_u, as a model parameter for E, and for a fixed value of the d-quark total angular momentum $J_d = 0$, as inspired by the results of recent lattice calculations [10].

By comparing the measured moment and the moment predicted for different J_u and J_d assumptions (relaxing the condition $J_d = 0$) using the VGG code, the quantity $\Delta\chi^2 = \chi^2 - \chi^2_{min}$ is calculated from

$$\chi^2(J_u, J_d) = \sum_{i}^{kin\ bins} \frac{\left[A_{UT,i}^{\sin(\phi-\phi_S)\cdot\cos(\phi)}\ |_{exp} - A_{UT,i}^{\sin(\phi-\phi_S)\cdot\cos(\phi)}\ |_{VGG(J_u,J_d)}\right]^2}{\delta A^2_{stat,i} + \delta A^2_{syst,i} + \delta A^2_{accept,i}}. \quad (5)$$

The area in the (J_u, J_d)-plane, in which the $\Delta\chi^2$ value is not larger than unity is defined as the one-standard-deviation constraint on J_u versus J_d, and is shown in Fig. 4. This HERMES result, described by the relation $J_u + J_d/2.9 = 0.42 \pm 0.21 \pm 0.06$, provides the first GPD model-dependent constraint on the total angular momenta J_u and J_d.

3 Exclusive Meson Production

Another process to access GPDs is the exclusive production of mesons by hard longitudinal virtual photons. In the Bjorken limit the process amplitude can be factorized similarly to the DVCS case, with one additional soft part describing the hadronization of virtual partons into the final meson state [11]. Validity of factorization has been demonstrated only for longitudinal photons. Nevertheless, compared to the longitudinal cross section, the cross section for transversely polarized photons was shown to be suppressed by a factor $1/Q^2$.

While the leading order amplitude factorization holds, interesting selection rules among produced mesons and probed GPDs in the target nucleon arise, due to quantum numbers conservation in the QED and QCD processes involved [11]. As an example, longitudinally polarized

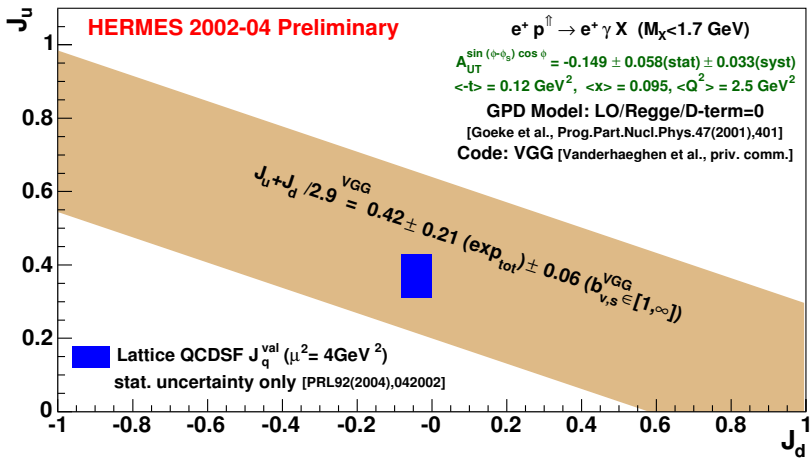


Fig. 4: Model-dependent constraint on the total angular momentum J_u vs J_d, obtained by comparing the data and theoretical predictions on the moment $A_{UT}^{\sin(\phi-\phi_S)\cos\phi}$, as described in the text. The t-dependence of the GPDs is modeled using the Regge ansatz. The impact of this choice, compared to its alternatives, was found to be negligible. The D-term contribution to the GPDs is set to zero, as suggested by the results on the beam-spin asymmetry.

vector meson channels are sensitive only to the unpolarized GPDs (H and E). Additionally, flavor singlet and non-singlet combinations of unpolarized GPDs can be separately accessed by measuring either vector mesons or meson states with quantum numbers of the f-meson family [12]. In contrast, DVCS depends at the same time on both unpolarized and polarized GPDs.

3.1 Hard Exclusive ρ^0_L Meson Production

Exclusive longitudinal ρ^o events, generated from scattering positrons or electrons off transversely polarized proton target, were identified by detecting the scattered leptons and the produced h^+h^- hadron pairs. The invariant mass of the two-hadron system $m_{2\pi}$ was determined assuming both hadrons to be pions. The requirement $0.6 < m_{2\pi} < 1.0$ GeV was used to select exclusive resonant pion pairs produced in the decay $\rho^o \to \pi^+\pi^-$. In addition, the missing energy ΔE of the events was required to be lower than 0.6 GeV, assuming the undetected recoiling target to be a proton. The non-resonant exclusive pion background was estimated to be a few percent, and the data were not corrected for it. Due to the limited experimental missing mass resolution, the analyzed exclusive reaction $ep \to ep\rho^o \to ep\pi^+\pi^-$ cannot be separated unambiguously from semi-inclusive background which can be smeared into the exclusive region. This contribution was estimated using a PYTHIA simulation, and the data were corrected for it.

From the exclusive events, the transverse target spin asymmetry for longitudinal ρ^0 production was determined by using the unbinned maximum likelihood method. The x- and t-dependence of the extracted asymmetry moment $A_{UT}^{\sin(\phi-\phi_S)}$ are shown in Fig. 5.

3.2 Hard Exclusive $\pi^+\pi^-$ Production

Hard exclusive pion pair production may involve both resonant and non-resonant channels mainly through the quark exchange mechanism which is dominant at HERMES kinematics. The pion pairs can be generated with the values of the strong isospin I, total angular momentum J, and

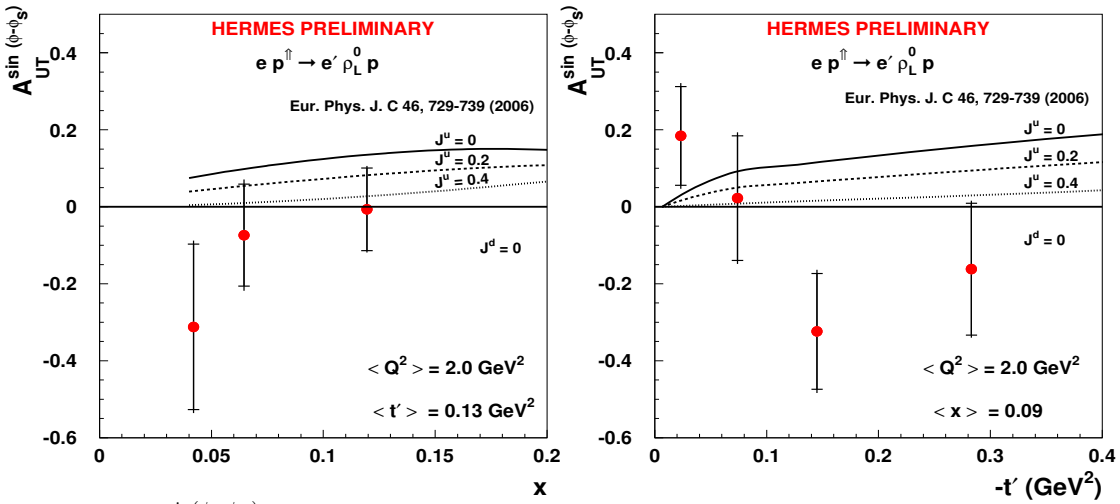


Fig. 5: Moment $A_{UT}^{\sin(\phi-\phi_S)}$ for exclusive production of longitudinally-polarized ρ^0 off transversely polarized protons. The x- (left panel) and $t-$dependence (right panel) are compared with predictions based on a GPD model [8] which show the potential analysis sensitivity to the quark angular momentum J, entering the parameterization of GPD E.

C-parity of either a ρ-meson ($I = 1$, $J = 1, 3..., C = -1$), or an f-meson ($I = 0$, $J = 0, 2...$, $C = +1$). The quark exchange with $C = +1$ and $C = -1$ is described by flavor singlet and non-singlet $\mathcal{H}$ and $\mathcal{E}$ combinations [12], respectively. The latter cannot be accessed by analyzing ρ^0 decay. The interference between the two isospin channels provide information on the weaker isoscalar channel at the amplitude level.

For the purpose of studying the interference between $\pi^+\pi^-$ production in P-wave ($I = 1$) and S, D-wave states ($I = 0$), the Legendre moment $\langle P_1(\cos\theta)\rangle$ [13] is particularly useful because it is only sensitive to such interference. Here θ is the polar angle of the π^+ meson with respect to the direction of the $\pi^+\pi^-$ pair in the pions rest-frame, and P_1 is the first-order Legendre polynomial.

The first experimental data for hard exclusive $\pi^+\pi^-$ pair production on hydrogen and deuterium targets have been reported by HERMES. The Bjorken x-dependence of $\langle P_1\rangle$ is shown

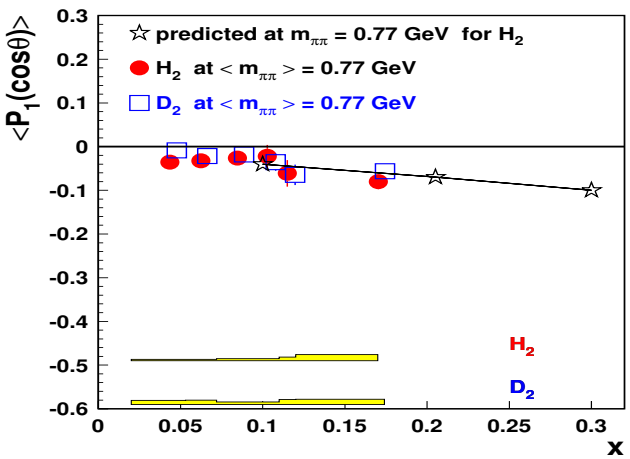


Fig. 6: The x-dependence of the Legendre moment $\langle P_1\rangle$ for both hydrogen and deuterium targets, in the regions $0.60 < m_{\pi\pi} < 0.95$ GeV, at $\langle Q^2\rangle \sim 2$ GeV^2. The systematic uncertainty is given by the error band. Theoretical predictions (stars) [13] for hydrogen, which neglect two-gluon exchange mechanism, are compared with the data, and are found to be in fair agreement with them.

in Fig. 6 in the $\pi^+\pi^-$ invariant mass $m_{\pi\pi}$ region around the ρ^0 meson resonance. For both targets $\langle P_1 \rangle$ is non-zero, which we interpret as originating from the interference of the resonant ρ^0 P-wave with non-resonant S-wave $\pi^+\pi^-$ production. The moment increases in magnitude with x, suggesting that the exchange of flavor non-singlet quark GPD combinations ($C = -1$) becomes competitive with the dominant singlet exchange ($C = +1$).

4 Conclusions

Several observables in DVCS, hard exclusive ρ^0_L and $\pi^+\pi^-$ production have been measured, and compared with GPD-based predictions in order to provide constraints on GPDs. The first GPD model-dependent constraint on the total angular momenta J_u and J_d has been obtained.

References

[1] D. Müller et al., Fortsch. Phys. **42** (1994) 101; A. V. Radyushkin, Phys. Rev. D **56** (1997) 5524. X. Ji, J. Phys. G **24** (1998) 1181.

[2] HERMES Collaboration, K. Ackerstaff et al., Nucl. Inst. and Methods **A 417** (1998) 230; HERMES Collaboration, A. Airapetian et al., hep-ex/0605108; submitted to Phys. Rev. Lett; Z. Ye; (for the HERMES Collaboration), Proc. of the International Europhysics Conference on High Energy Physics, Lisboa, Portugal, July 2005; hep-ex/0512010; Z. Ye (for the HERMES Collaboration), Proc. of the 14th International Workshop on Deep Inelastic Scattering, Tokyo, Japan, April 2006; hep-ex/0606061; A. Rostomyan (for the HERMES Collaboration), Proc. of the 15th International Workshop on Deep Inelastic Scattering and QCD, Munich, Germany, April 2007; HERMES Collaboration, A. Airapetian et al., Phys. Lett. **B** 599 (2004) 212.

[3] A. V. Radyushkin, Phys. Lett. B **380** (1996) 417.; X. Ji, Phys. Rev. D **55** (1997) 7114.

[4] V. A. Korotkov and W.-D. Novak, Eur. Phys. J. C **23** (2002) 455.

[5] M. Vanderhaeghen et al., Code for the calculation of DVCS and BH process, private communication, 2001.

[6] M. V. Polyakov and C. Weiss, Phys. Rev. D **60** (1999) 114017.

[7] W.-D. Novak, Proc. of HadronPhysics I3 Topical Workshop, 2004; hep-ex/0503010.

[8] F. Ellinghaus et al., Eur. Phys. J. C **46** (2006) 729.

[9] K. Göeke et al., Prog. Part. Nucl. Phys. **47** (2001) 401.

[10] M. Göckeler et al., Phys. Rev. Lett. **92** (2004) 042002.

[11] J. Collins et al., Phys. Rev. D **56** (1997) 2982; A. Freund, Phys. Rev. D **61** (2000) 074010.

[12] M. Diehl, Phys. Rept. **388** (2003) 41.

[13] B. Lehmann-Dronke et al., Phys. Lett. **B475** (2000) 147.

Fitting DVCS at NLO and beyond

K. Kumerički[1]*, D. Müller*[2]*, K. Passek-Kumerički*[3]†
[1]Department of Physics, Faculty of Science, University of Zagreb, Croatia
[2]Institut für Theoretische Physik II, Ruhr-Universität Bochum, Germany
[3]Theoretical Physics Division, Rudjer Bošković Institute, Croatia

Abstract
We outline the twist-two analysis of deeply virtual Compton scattering within the $SO(2,1)$ partial wave expansion of the amplitude, represented as a Mellin–Barnes integral. The complete next-to-leading order results, including evolution, are obtained in the $\overline{\rm MS}$ and a conformal factorization scheme. Within the latter, exploiting conformal symmetry, the radiative corrections are evaluated up to next-to-next-to-leading order. Using a new proposed parameterization for GPDs, we study the convergence of perturbation theory and demonstrate that our formalism is suitable for a fitting procedure of DVCS observables.

1 Introduction

The proton structure has been widely explored in inclusive measurements, mainly, in deeply inelastic lepton-proton scattering (DIS). Here the scattering essentially occurs due to the exchange of a virtual boson (photon) on a single parton, and so one can access *parton distribution functions* (PDFs). This universal, however, convention-dependent functions $q_a(x)$ are interpreted as probabilities that partons of certain flavour a will be found with given longitudinal momentum fraction x. Since the PDFs are naturally defined in a translation invariant manner, they do not carry information about the transversal distribution of partons. Some information about transversal degrees of freedom can be obtained from elastic lepton-proton scattering. The electromagnetic form factors $F_{1,2}(t)$ are Fourier transforms of the electric and magnetic charge distribution in nucleon, and can be, e.g., in the infinite momentum frame, interpreted as probability that partons are found at some transversal distance $\mathbf{b}$ from the center-of-mass. However, one can not assume that a realistic probability distribution of partons, given by a two-variable function $q(x,\mathbf{b})$ is simply a direct product, i.e., $q(x)\otimes q(\mathbf{b})$, of two probability functions. Rather it is anticipated that longitudinal and transversal degrees of freedom have a cross talk, e.g., as x gets bigger partons carry more of the nucleon longitudinal momentum and are expected to be closer to the proton center, and thus the $\mathbf{b}$ dependence in $q(x,\mathbf{b})$ should become narrower with increasing x.

The three dimensional distribution of partons in the nucleon can be addressed within more general objects, called *generalized parton distributions* (GPDs) [1, 2]. Such distributions can be revealed by analyzing hard exclusive leptoproduction of mesons or photon. The former processes are perhaps theoretically more problematic to describe but offer a direct view into individual flavour GPDs. To the latter one the *deeply virtual Compton scattering* (DVCS) process

† speaker

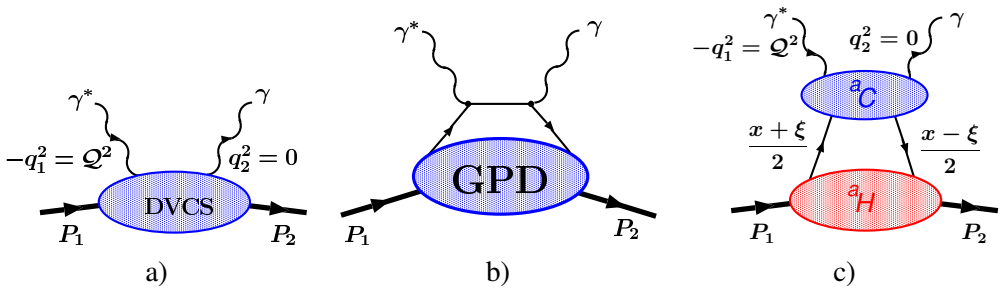


Fig. 1: a) DVCS. b) Leading-order perturbative contribution to DVCS. c) Factorization (to all orders in α_s) on an example of special parity-even, helicity conserving contribution ${}^a\mathcal{H}$ (5).

contributes, where one photon has a large virtuality. DVCS is theoretically considered as the cleanest probe of GPDs, however, here only certain flavour combinations of GPDs appear.

The non-forward Compton scattering process is described by the Compton tensor

$$T_{\mu\nu}(q,P,\Delta) = \frac{i}{e^2}\int d^4x\, e^{ix\cdot q}\langle P_2,S_2|Tj_\mu(x/2)j_\nu(-x/2)|P_1,S_1\rangle, \tag{1}$$

where $q = (q_1+q_2)/2$, $P = P_1+P_2$ and $\Delta = P_2-P_1$. The generalized Bjorken limit corresponds to $Q^2 = -q^2 \to \infty$ with the scaling variables

$$\xi = \frac{Q^2}{P\cdot q}, \qquad \eta = -\frac{\Delta\cdot q}{P\cdot q}, \tag{2}$$

and the momentum transfer squared Δ^2 being fixed. Note that in the forward case, i.e., $\Delta \to 0$, the hadronic DIS tensor $W_{\mu\nu}$ is related to the *forward* Compton scattering tensor by the optical theorem $W_{\mu\nu} = \Im\mathrm{m}T_{\mu\nu}(q,P=2p,\Delta=0)/(2\pi)$, where $p = P_1 = P_2$ and $\xi \to x_{Bj}$.

In DVCS – Fig.1a – the virtuality of the incoming photon $\mathcal{Q}^2 = -q_1^2$ is large while the final photon is on-shell. The skewness parameter η and the Bjorken-like scaling parameter ξ are then equal to twist-two accuracy, i.e., $\eta = \xi + \mathcal{O}(1/\mathcal{Q}^2)$. In the generalized Bjorken limit, similarly as for DIS structure functions, the amplitude factorizes into long- and short-distance contributions (Fig.1b and c): short-distance physics is perturbatively calculable Compton scattering on a parton, while long-distance physics is encoded in an non-perturbative amplitude for a parton being emitted and later reabsorbed by the nucleon. The latter *amplitude* is called GPD.

The GPDs with even parity, we are considering here, are defined as

$$\begin{aligned}
{}^qF(x,\eta,\Delta^2) &= \int\frac{dz^-}{2\pi}\, e^{ixP^+z^-}\langle P_2|\bar q(-z)\gamma^+ q(z)|P_1\rangle\Big|_{z^+=0,\,\mathbf{z}_\perp=\mathbf{0}}\\
{}^GF(x,\eta,\Delta^2) &= \frac{4}{P^+}\int\frac{dz^-}{2\pi}\, e^{ixP^+z^-}\langle P_2|G_a^{+\mu}(-z)G_{a\mu}{}^+(z)|P_1\rangle\Big|_{z^+=0,\,\mathbf{z}_\perp=\mathbf{0}},
\end{aligned} \tag{3}$$

and similar for odd parity. Furthermore, it is convenient to decompose GPDs,

$${}^aF = \frac{\bar u(P_2)\gamma^+u(P_1)}{P^+}\,{}^aH + \frac{\bar u(P_2)i\sigma^{+\nu}u(P_1)\Delta_\nu}{2MP^+}\,{}^aE, \qquad a = q,G. \tag{4}$$

into helicity conserving and non-conserving generalized form factors. The Compton tensor (1) is analogously decomposed into Compton form factors with corresponding parity and helicity properties. In the forward limit ($\Delta \to 0$) GPDs reduce to PDFs. Together with sum rules, e.g., relating GPDs to electromagnetic form factors, this provides constraints that are important for GPD modelling. But as they do not constrain much the skewness (η) dependence, modelling is still a difficult problem. One guiding feature is a polynomiality property of GPDs: n-th (Mellin) moment of GPD is even polynomial in η of order n or $n \pm 1$. Similar polynomiality will be obeyed also for conformal moments which are just linear combination of Mellin moments. The usefulness of the GPDs has also been widely realized in connection with the spin problem, since they encode the angular momentum carried by the individual parton species, as explicated by the Ji's sum rule [2]. For recent detailed account of GPDs and their properties, we refer to [3].

In the following we outline the perturbative QCD approach to DVCS that is based on the conformal partial wave expansion, represented as Mellin-Barnes integral, as described in Ref. [4, 5]. Here, as in Refs. [5–7], we concentrate on the dominant Compton form factor $\mathcal{H}$ corresponding to parity-even helicity-conserving GPD H. For simplicity, we present only the results for the singlet part which is dominant for the kinematics of collider experiments.

2 Deeply virtual Compton scattering

Besides DVCS the Bethe-Heitler brehmstrahlung process contributes to the measured hard photon leptoproduction off a proton. The Bethe-Heitler amplitude, known in leading order of the QED fine structure constant, is expressed in terms of the known electromagnetic form-factors. Generally, there are two types of DVCS experiments: collider experiments and fixed target experiments. The former usually provide information in the phase space $10^{-4} \lesssim \xi \lesssim 10^{-1}$ and $1\,\mathrm{GeV}^2 \lesssim \mathcal{Q}^2 \lesssim 100\,\mathrm{GeV}^2$, and such are H1 and ZEUS experiments at HERA. The main observables here are total and differential DVCS cross sections, however, also the beam charge asymmetry is feasible. For the fixed target experiments, such as Hall A, Hall B (CLAS) at JLAB, and HERMES at DESY, the interference term can be more easily accessed via single beam, target spin and beam charge (HERMES) asymmetries, while the investigated phase space covers the so-called valence quark region, i.e., $0.05 \lesssim \xi \lesssim 0.3$ within $1\,\mathrm{GeV}^2 \lesssim \mathcal{Q}^2 \lesssim 10\,\mathrm{GeV}^2$.

One can express $\mathcal{H}$ as a convolution (Fig.1c) over the longitudinal momentum fraction x

$$ {}^a\mathcal{H}(\xi, \Delta^2, \mathcal{Q}^2) = \int \mathrm{d}x\; {}^aC(x, \xi, \mathcal{Q}^2/\mu^2)\; {}^aH(x, \eta = \xi, \Delta^2, \mu^2)\,, \tag{5} $$

where μ^2 is a factorization scale that separates short- and long-distance dynamics often taken $\mu^2 = \mathcal{Q}^2$. Here the index $a \in \{\mathrm{NS}, \mathrm{S}(\Sigma, G)\}$ denotes either non-singlet or singlet parts, where to latter both quarks (Σ) and gluons (G) contribute.

The coefficient function C^a is a perturbative quantity which describes $q\gamma^* \to q\gamma$ and $g\gamma^* \to g\gamma$ subprocesses. The well known leading-order (LO) contribution to C^a is actually a pure QED process (Fig. 1b). The next-to-leading order (NLO) contribution – the first order in α_s – has been calculated by various groups [8]. Obviously, to stabilize the perturbation series and investigate its convergence one needs the second order in α_s, i.e., next-to-next-to-leading order (NNLO) contributions. The importance of NNLO in singlet case is amplified by the fact that at LO photons scatter only off charged partons, whereas gluons start contributing at NLO.

The GPDs are intrinsically non-perturbative quantities whose form at some initial scale has to be deduced by some non-perturbative methods (lattice calculation, fit to data etc.). The evolution to the factorization scale of interest is governed by perturbation theory, cf. [5,7] for LO examples. The anomalous dimensions of non-diagonal operators were calculated up to NLO [9]. Still, NLO evolution is numerically not easy to implement and has been investigated beyond NLO only recently, using the below explained procedure [5].

Instead of using the convolution form (5) one can equivalently use the sum over the conformal moments, and the singlet contribution takes then the form

$$^{\mathrm{S}}\mathcal{H}(\xi,\Delta^2,\mathcal{Q}^2) = 2\sum_{j=0}^{\infty}\xi^{-j-1}\boldsymbol{C}_j(\mathcal{Q}^2/\mu^2,\alpha_s(\mu))\;\boldsymbol{H}_j(\eta=\xi,\Delta^2,\mu^2)\,, \tag{6}$$

where $\boldsymbol{C}_j = \left({}^{\Sigma}C_j, {}^{G}C_j\right)$ and $\boldsymbol{H}_j = \left({}^{\Sigma}H_j, {}^{G}H_j\right)$ are conformal moments. They are analogous to common Mellin moments used in DIS but the integral kernel x^j is replaced by Gegenbauer polynomials $C_j^{3/2}(x)$ and $C_j^{5/2}(x)$, which are solutions of LO evolutional equations for quarks and gluons, respectively. Unfortunately, the series (6) only converges in the unphysical region. Hence, it is necessary to resum this series, e.g., by means of the Mellin-Barnes integral [5]

$$^{\mathrm{S}}\mathcal{H}(\xi,\Delta^2,\mathcal{Q}^2) = \frac{1}{2i}\int_{c-i\infty}^{c+i\infty} dj\,\xi^{-j-1}\left[i+\tan\left(\frac{\pi j}{2}\right)\right]\boldsymbol{C}_j(\mathcal{Q}^2/\mu^2,\alpha_s(\mu))\boldsymbol{H}_j(\xi,\Delta^2,\mu^2)\,. \tag{7}$$

The advantages of using conformal moments, i.e., Mellin-Barnes representation, are manifold. It allows for an efficient and stable numerical treatment, it enables a simple inclusion of evolution, and it opens a new door for interesting modelling of GPDs. Finally, by making use of conformal operator product expansion (OPE) and known NNLO DIS results, it enables the assessment of NNLO contributions.

3 Conformal approach to DVCS beyond NLO

Neither Wilson coefficients nor anomalous dimensions are calculated (only so-called quark bubble insertions were partly evaluated) in non-forward kinematics at NNLO. To access the NNLO of non-forward Compton scattering, we use the conformal approach, making it possible to calculate relevant objects using only diagonal results of forward Compton scattering, i.e., DIS.

DVCS belongs to a class of two-photon processes (DIS, DVCS, two-photon production of hadronic states ...) calculable by means of the OPE, $T_{\mu\nu}(q,P,\Delta) \to C_j\,O_j$, for which the use of generalized Bjorken kinematics and conformal symmetry enables a unified description. While massless QCD is conformally invariant at tree level, this invariance is broken at the loop level since renormalization introduces a mass scale, leading to the running of the coupling constant ($\beta \neq 0$). Assuming the existence of a non-trivial fixed point α_s^*, i.e., $\beta(\alpha_s^*) = 0$, the conformal OPE (COPE) prediction for Wilson coefficients in general kinematics reads [10]

$$C_j(\alpha_s^*) \;=\; c_j(\alpha_s^*)\,{}_2F_1\left(\begin{matrix}(2+2j+\gamma_j(\alpha_s^*))/4,\,(4+2j+\gamma_j(\alpha_s^*))/4\\ (5+2j+\gamma_j(\alpha_s^*))/2\end{matrix}\middle|\frac{\eta^2}{\xi^2}\right)\left(\frac{\mu^2}{Q^2}\right)^{\gamma_j(\alpha_s^*)/2}\,. \tag{8}$$

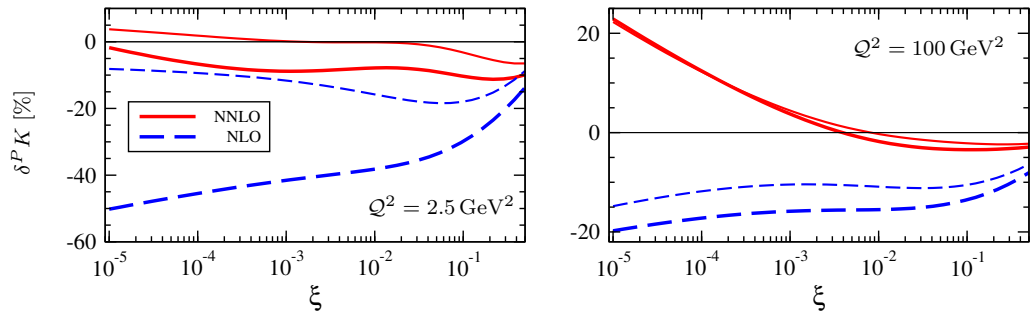


Fig. 2: Relative NLO and NNLO corrections (12) in the $\overline{\rm CS}$ scheme ($\Delta^2 = 0.25\mathrm{GeV}^2$, input scale $\mathcal{Q}_0^2 = 2.5\mathrm{GeV}^2$). Thick [thin] lines – "hard" ["soft"] gluon: $N_G = 0.4$, $\alpha_G(0) = \alpha_\Sigma(0) + 0.05$ [$N_G = 0.3$, $\alpha_G(0) = \alpha_\Sigma(0) - 0.02$].

For $\eta = 0$ equation (8) reduces to the DIS Wilson coefficients $C_j \to c_j$ and thus fixes the normalization c_j. The choice $\eta = \xi$ corresponds to DVCS in the conformal limit. The anomalous dimensions governing the evolution are diagonal and the same as in DIS.

For a general factorization scheme, e.g., the $\overline{\rm MS}$ scheme, the conformal symmetry breaking occurs also due to the renormalization of the composite operators and causes the appearance of non-diagonal anomalous dimensions $\gamma_{jk} = \delta_{jk}\gamma_j + \gamma_{jk}^{\rm ND}$. This induces a mixing of of both operators, i.e., GPDs, and Wilson coefficients under evolution. In the kinematical forward limit ($\eta = 0$) the diagonal evolution equations are again obtained, i.e., the DIS case corresponds to the COPE result. For DVCS, e.g., evaluated in the $\overline{\rm MS}$ scheme, there appear also conformal symmetry breaking terms which are not proportional to β, i.e., the non-diagonal terms survive.

The non-diagonal terms of anomalous dimensions encountered in $\overline{\rm MS}$ scheme can be removed by a finite renormalization [10], i.e, by a specific choice of the factorization scheme $C^{\overline{\rm MS}}\, O^{\overline{\rm MS}} = C^{\overline{\rm MS}}\, B\, B^{-1}\, O^{\overline{\rm MS}} = C^{\overline{\rm CS}} O^{\overline{\rm CS}}$. In this new scheme, called conformal subtraction ($\overline{\rm CS}$) scheme, all non-diagonal terms are "pushed" to the β proportional part. $\gamma_{jk}^{\overline{\rm CS}} = \delta_{jk}\gamma_k + \beta/g\Delta_{jk}$, Furthermore, since there is an ambiguity in $\overline{\rm MS} \to \overline{\rm CS}$ rotation matrix, by judicious choice one can "push" mixing under evolution to NNLO. Hence, in $\overline{\rm CS}$ scheme, we are using, the unknown correction Δ_{jk} starts at NNLO and it can be additionally suppressed by the choice of an appropriate initial condition. Finally, we express our result in $\overline{\rm CS}$ scheme as

$$C_j^{\overline{\rm CS}} = \sum_{k=j}^{\infty} C_k(\alpha_s(\mathcal{Q}))\; \mathcal{P} \exp\left\{ \int_{\mathcal{Q}}^{\mu} \frac{d\mu'}{\mu'} \left[\gamma_j(\alpha_s(\mu'))\delta_{kj} + \frac{\beta}{g}\Delta_{kj}(\alpha_s(\mu')) \right] \right\}, \qquad (9)$$

with $C_k(\alpha_s(\mathcal{Q}))$ obtained from the $\eta = \xi$ limit of Eq. (8) and using $c_j(\alpha_s)$. As stated above the Δ_{kj} mixing term appears at NNLO and is neglected. We take c_j and γ_j calculated to NNLO order from Refs. [11], and obtain the DVCS prediction to NNLO in the $\overline{\rm CS}$ scheme.

4 Results

We have used the formalism described in the preceding sections to investigate the size of NNLO corrections to non-singlet [6] and singlet Compton form factors [7], to obtain complete (non-

diagonal evolution included) $\overline{\rm MS}$ NLO predictions [5], and to perform fits, in both $\overline{\rm MS}$ and $\overline{\rm CS}$ schemes, to DVCS and DIS data and extract information about GPDs [5].

One can use a simple Regge-inspired ansatz for GPDs

$$\boldsymbol{H}_j(\eta,\Delta^2,\mathcal{Q}_0^2)=\begin{pmatrix} N'_\Sigma\, F_\Sigma(\Delta^2)\, B\big(1+j-\alpha_\Sigma(0),8\big) \\ N'_G\, F_G(\Delta^2)\, B\big(1+j-\alpha_G(0),6\big)\end{pmatrix}+\mathcal{O}(\eta^2)\,, \tag{10}$$

with (p_a is a flavour dependent integer)

$$\alpha_a(\Delta^2)=\alpha_a(0)+0.15\Delta^2\,,\qquad F_a(\Delta^2)=\frac{j+1-\alpha_a(0)}{j+1-\alpha_a(\Delta^2)}\left(1-\frac{\Delta^2}{M_0^{a\,2}}\right)^{-p_a}\,. \tag{11}$$

In the forward case ($\Delta=0$) this ansatz is equivalent to the standard building blocks for PDFs: $\Sigma(x)=N'_\Sigma\, x^{-\alpha_\Sigma(0)}\,(1-x)^7$, $G(x)=N'_G\, x^{-\alpha_G(0)}\,(1-x)^5$. We have performed the analysis of radiative corrections with generic parameters and made fits of parameters N_Σ, $\alpha_\Sigma(0)$, M_0^Σ, N_G, $\alpha_G(0)$, M_0^G. The work on a more realistic η-dependent ansatz is in progress.

We introduce now the quantities that we utilize as a measures of the scheme dependence and, foremostly, as indicators for the convergence of the perturbation series. It is natural to employ for this purpose the ratios of Compton form factors, i.e., the corresponding modulus and phase difference, at order $\mathrm{N}^P\mathrm{LO}$ to the one at order $\mathrm{N}^{P-1}\mathrm{LO}$, where $P=\{0,1,2\}$ stands for LO, NLO, and NNLO order, respectively:

$$\delta^P K=\frac{\left|\mathcal{H}^{\mathrm{N}^P\mathrm{LO}}\right|}{\left|\mathcal{H}^{\mathrm{N}^{P-1}\mathrm{LO}}\right|}-1\,,\qquad \delta^P\varphi=\arg\left(\frac{\mathcal{H}^{\mathrm{N}^P\mathrm{LO}}}{\mathcal{H}^{\mathrm{N}^{P-1}\mathrm{LO}}}\right)\,. \tag{12}$$

The phase differences are small, and we will not comment on them here further. The NLO corrections to the moduli in $\overline{\rm MS}$ and $\overline{\rm CS}$ schemes have a similar ξ-shape, where $\overline{\rm MS}$ corrections are generally larger. The relative NLO and NNLO corrections in $\overline{\rm CS}$ scheme are depicted in Fig. 2. From the left panel, showing corrections at the input scale, we realize that the large negative NLO corrections to the modulus (thick dashed) in the 'hard' gluon scenario are shrunk at NNLO to less than 10% (thick solid), in particular in the small ξ region. In the 'soft' gluon case the NNLO corrections (thin solid) are $\pm5\%$. For $\xi\sim0.5$, the corrections are reduced only unessentially and are around 5% and 10% at both NLO and NNLO level. If evolution is switched on (right panel), our findings drastically change. For $\xi\gtrsim5\cdot10^{-2}$ NNLO corrections are stabilized on the level of about 3% at $\mathcal{Q}^2=100$ GeV^2. But they start to grow with decreasing ξ and reach at $\xi\approx10^{-5}$ the 20% level. As in DIS, this breakdown of perturbation theory at small ξ obviously stems from evolution and is thus universal, i.e., process independent. The large change of the scaling prediction within the considered order does not influence the quality of fits, and, in particular, the possibility of relating DVCS and DIS data. Hence, the problem of treatment or resummation of these large corrections is relevant primarily to our partonic interpretation of the nucleon content. As long as we precisely define the treatment of the evolution operator, perturbative QCD can be employed as a tool for analyzing data also in the small ξ region.

The Mellin-Barnes integral approach offers the possibility for a fast and numerically stable analysis. Our numerical routine is designed for the purpose of fitting DVCS (and DIS) observables [12] and testing various GPD ansaetze; an example is presented in Fig. 3.

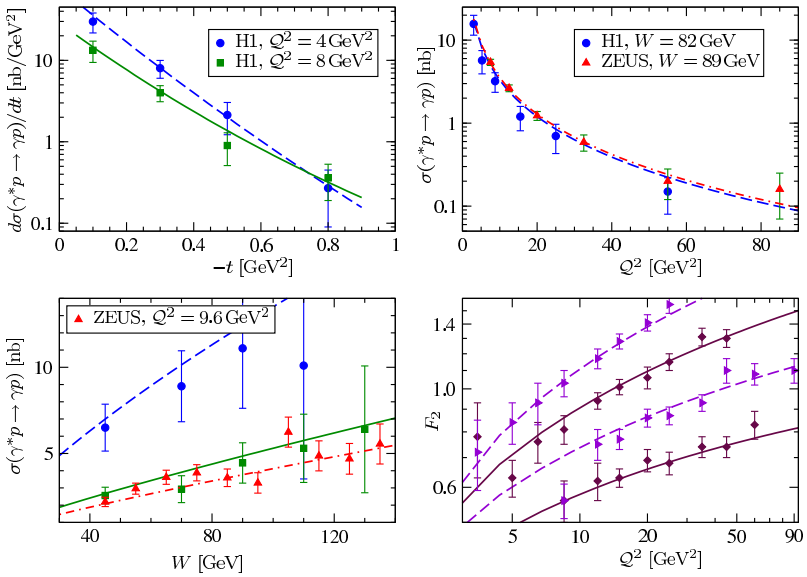
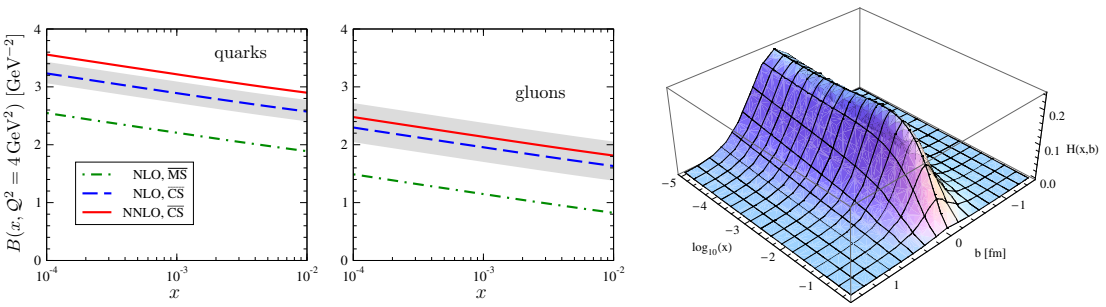


Fig. 3: Fit example: differential DVCS cross section versus Δ^2 (up,left), Δ^2-integrated cross section versus $\mathcal{Q}^2$ (up,right) and W (down,left) as well as the DIS structure function F_2 at $x_b = 8\times10^{-3}, 3.2\times10^{-3}, 1.3\times10^{-3}, 4\times10^{-4}$ (down,right).

Fourier transform of resulting GPDs for $\eta = 0$,

$$H(x,\mathbf{b}) = \int \frac{d^2\mathbf{\Delta}}{(2\pi)^2}\, e^{-i\mathbf{b}\cdot\mathbf{\Delta}} H(x,\eta=0,\Delta^2=-\mathbf{\Delta}^2)\,, \tag{13}$$

can be interpreted in the infinite momentum frame as probability density [13], see Fig. 4b. The average transversal parton distance squared $\langle\mathbf{b}^2\rangle$ is given by the GPD slope $B = \langle\mathbf{b}^2\rangle/4$, shown in Fig. 4a. The results confirm the picture, mentioned in the introduction, about the correlation of transversal and longitudinal degrees of freedom: harder partons are closer to the center.



a) b)

Fig. 4: a) Resulting GPD slope $B = \langle\mathbf{b}^2\rangle/4$ at the input scale $\mathcal{Q}^2 = 4\,\mathrm{GeV}^2$ and b) 3D picture of gluon GPD (13).

5 Summary

GPDs encode a unified description of the proton structure and they are experimentally accessible via the hard leptoproduction of photon or mesons. We have shown that the representation of Compton form factors as Mellin-Barnes integrals offers a useful tool in analyzing DVCS: the inclusion of evolution is simple, numerical treatment is stable and fast. Although the motivation for this representation originated from manifest conformal symmetry at LO, we have shown here that this Mellin–Barnes integral representation can be used within the standard $\overline{\rm MS}$ scheme beyond LO. Such a representation can straightforwardly be obtained from the momentum fraction representation and, therefore, also other GPD related processes, e.g., the hard electroproduction of mesons, can be given in terms of Mellin–Barnes integrals. This opens a new road for the 'global' analysis of experimental data within the perturbative GPD formalism to NLO accuracy. Furthermore, the use of conformal symmetry enables elegant approach to higher-order radiative corrections to the DVCS amplitude. We have shown that although NLO corrections can be sizable, and are strongly dependent on the gluonic input, the NNLO corrections are small to moderate, supporting perturbative framework of DVCS. The observed change in the scale dependence is not so conclusive: similarly as in DIS we encounter large NNLO effects for $\xi < 10^{-3}$, which signal a breakdown of naive perturbation series in the evolution operator. Nevertheless, this breakdown is universal and if we precisely define the treatment of this operator, perturbative QCD can be employed as a tool for analyzing data even in the small ξ region. Finally, fits to available DVCS and DIS data work well and give access to transversal distribution of partons.

References

[1] D. Müller, D. Robaschik, B. Geyer, F.-M. Dittes, and J. Hořejši, Fortschr. Phys. **42**, 101 (1994); A. Radyushkin, Phys. Lett. **B380**, 417 (1996). hep-ph/9604317.

[2] X.-D. Ji, Phys. Rev. Lett. **78**, 610 (1997). hep-ph/9603249.

[3] M. Diehl, Phys. Rept. **388**, 41 (2003). hep-ph/0307382; A. V. Belitsky and A. V. Radyushkin, Phys. Rept. **418**, 1 (2005). hep-ph/0504030.

[4] D. Müller and A. Schäfer, Nucl. Phys. **B739**, 1 (2006). hep-ph/0509204.

[5] K. Kumerički, D. Müller, and K. Passek-Kumerički (2007). hep-ph/0703179.

[6] D. Müller, Phys. Lett. **B634**, 227 (2006). hep-ph/0510109.

[7] K. Kumerički, D. Müller, K. Passek-Kumerički, and A. Schäfer, Phys. Lett. **B648**, 186 (2007). hep-ph/0605237.

[8] X.-D. Ji and J. Osborne, Phys. Rev. **D57**, 1337 (1998). hep-ph/9707254; A. V. Belitsky and D. Müller, Phys. Lett. **B417**, 129 (1998). hep-ph/9709379; L. Mankiewicz, G. Piller, E. Stein, M. Vanttinen, and T. Weigl, Phys. Lett. **B425**, 186 (1998). hep-ph/9712251.

[9] D. Müller, Phys. Rev. **D49**, 2525 (1994); A. V. Belitsky and D. Müller, Nucl. Phys. **B527**, 207 (1998). hep-ph/9802411; A. V. Belitsky and D. Müller, Nucl. Phys. **B537**, 397 (1999). hep-ph/9804379.

[10] D. Müller, Phys. Rev. **D58**, 054005 (1998). hep-ph/9704406; D. Müller, Phys. Rev. **D59**, 116003 (1999). hep-ph/9812490; B. Melić, D. Müller, and K. Passek-Kumerički, Phys. Rev. **D68**, 014013 (2003). hep-ph/0212346.

[11] E. B. Zijlstra and W. L. van Neerven, Nucl. Phys. **B383**, 525 (1992); A. Vogt, S. Moch, and J. A. M. Vermaseren, Nucl. Phys. **B691**, 129 (2004). hep-ph/0404111.

[12] H1 Collaboration, C. Adloff *et al.*, Phys. Lett. **B517**, 47 (2001). hep-ex/0107005;
ZEUS Collaboration, S. Chekanov *et al.*, Phys. Lett. **B573**, 46 (2003). hep-ex/0305028;
H1 Collaboration, A. Aktas *et al.*, Eur. Phys. J. **C44**, 1 (2005). hep-ex/0505061.

[13] M. Burkardt, Phys. Rev. **D62**, 071503 (2000). hep-ph/0005108;
M. Burkardt, Int. J. Mod. Phys. **A18**, 173 (2003). hep-ph/0207047.

Exclusive vector meson electroproduction

D.Yu. Ivanov
Sobolev Institute of Mathematics, 630090 Novosibirsk, Russia

Abstract
We discuss exclusive vector meson electroproduction within the QCD collinear factorization framework. In Bjorken kinematics the amplitude factorizes in a convolution of the nonperturbative meson distribution amplitude and the generalized parton densities with the perturbatively calculable hard-scattering amplitudes, which are presently known to next-to-leading order (NLO). At small $x_{\rm B}$ NLO corrections are very large. It is related to appearance of BFKL type logarithms in the hard-scattering amplitudes, that calls for a resummation of these effects at higher orders. Here we report the first results of such resummation.

1 Introcuction

The process of elastic vector meson electroproduction on a nucleon,

$$\gamma^*(q)\, N(p) \to V(q')\, N(p')\,, \tag{1}$$

where $V = \rho^0,\, \omega,\, \phi$, was studied in many fixed target and in HERA collider experiments. On the theoretical side, the large negative virtuality of the photon, $q^2 = -Q^2$, provides a hard scale for the process which justifies the application of QCD factorization methods that allow to separate the contributions to the amplitude coming from different scales. The factorization theorem [1] states that in a scaling limit, $Q^2 \to \infty$ and $x_B = Q^2/2(p\cdot q)$ fixed, a vector meson is produced in the longitudinally polarized state by the longitudinally polarized photon and that the amplitude of the process (1) is given by a convolution of the perturbatively calculable hard-scattering amplitudes C^i, the nonperturbative meson distribution amplitude (DA) ϕ_V, and the generalized parton densities (GPDs) H^i.

$$A = \sum_{i=q,g} \int\int dx\, dz\, H^i(x,\xi,t,\mu_F)\, C^i(x,z,\mu_F)\, \phi_V(z,\mu_F)\,, \tag{2}$$

where $\xi = x_B/(2-x_B)$ is the skewness variable, $t = (p-p')^2$ and μ_F is a factorization scale. GPDs encode important information on hadron structure, including aspects that cannot be deduced directly from experiment, like the transverse spatial distribution of partons and their orbital angular momentum, for more details see [2].

Deeply virtual Compton process (DVCS) provides the theoretically cleanest access to GPDs. Recently two-loop effects were incorporated into the analysis of DVCS [3]. A theoretical description of exclusive meson production is more involved since it includes an additional nonperturbative quantity, a meson DA. The primary motivation for the strong interest in this process (and in the similar process of heavy quarkonium production) is that it can serve to constrain

the gluon density in a nucleon. Indeed, in vector meson production case the gluon GPD enters the description already at the leading order (LO) in the strong coupling α_s, whereas in DVCS it appears first at NLO, and, like in inclusive DIS, is accessible only through scaling violation.

2 NLO corrections

The hard-scattering amplitudes for process (1) were calculated at NLO in [4], and for exclusive heavy quarkonium photoproduction in [5]. The analysis of NLO effects showed that in kinematics typical for the HERA collider experiments, $x_B \sim 10^{-3}$, the NLO corrections are huge even for really large values of hard scales $\sim 30\,\mathrm{GeV}^2$. If the factorization scale is chosen close to the value of a hard scale, $\mu_F \sim Q$, the corrections have opposite signs in comparison to the Born term. Which may lead to the change of signs of the imaginary and the real parts of the amplitude within phenomenologically relevant interval of x_B. Besides, the factorization and renormalization scale uncertainties were found being very large.

Recently these findings were confirmed in [6], where very detailed analysis of the cross sections and the transverse target polarization asymmetries in exclusive meson production was performed both for small and larger values of x_B, typical for fixed-target experiments. For the fixed target kinematics it seems that NLO corrections start to be under control, though their values are still large at presently available values of Q^2. For the transverse target polarization asymmetries the situation is better, in some cases.

Going back to small x_B, why NLO corrections are large in this case? The inspection of NLO hard-scattering amplitudes shows that the imaginary part of the amplitude dominates and that the leading contribution to the NLO correction originates from the broad integration region $\xi \ll x \ll 1$, where the gluonic part approximates ($N_c = 3$ is the number of colors)

$$ImA^g \sim \int\limits_0^1 \frac{dz\,\phi_V(z)}{z(1-z)} \left[H^g(\xi,\xi,t) + \frac{\alpha_s N_c}{\pi} \ln\left(\frac{Q^2 z(1-z)}{\mu_F^2}\right) \int\limits_{2\xi}^1 \frac{dx}{x} H^g(x,\xi,t) \right]. \qquad (3)$$

Given the behavior of the gluon GPD at small x, $H^g(x,\xi) \sim xg(x) \sim const$, we see that NLO correction is parametrically large, $\sim \ln(1/\xi)$, and negative unless one chooses the value of the factorization scale sufficiently lower than the kinematic scale. For the asymptotic form of meson DA, $\phi_V^{as}(z) = 6z(1-z)$, the last term in (3) changes the sign at $\mu_F = \frac{Q}{e}$, for the DA with a more broad shape this happens at even lower values of μ_F. Similar, $\ln(1/\xi)$ enhanced, contribution appears also in the quark singlet channel.

The partonic momentum fraction x is related to the Mandelstam energy variable $\hat{s}$ of the partonic subprocess $x/\xi \sim \hat{s}/Q^2$. The leading part of NLO partonic amplitude (proper normalized) grows as the first power of energy, $x \sim \hat{s}$, whereas at LO partonic amplitude behaves like a constant at large $\hat{s}$. The reason for this difference is the appearance, starting from NLO, of partonic diagrams with the gluon exchange in the $t-$ channel, see Fig. 1. At LO one has only diagrams with the quark exchange, both for the gluon and quark channels.

At higher orders the diagrams with gluon $t-$ channel exchange give contributions to the amplitudes of partonic subprocesses enhanced, for n loops, by $\alpha_s^n \log^{n-1} x$. In its turn, these terms inserted in the factorization formula will produce large contributions $\sim \alpha_s^n \log^n(1/\xi)$ to

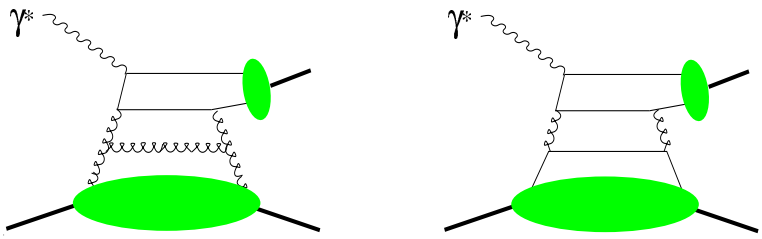


Fig. 1: NLO diagrams with $t-$ channel gluon exchange; the gluon and the quark GPD contributions.

the process amplitude, where each power of the strong coupling is compensated by the same power of a large logarithm of energy. It is a natural idea to resum these enhanced at small x_B contributions using the BFKL approach [7].

3 High energy resummation

The central point in this high energy resummation is to perform it consistently, without spoiling the all-order factorization of collinear singularities. Care should be taken of the factorization scheme used at the factorization of the process amplitude (2) in terms of GPDs and hard-scattering amplitudes. The higher order terms of the hard-scattering amplitudes derived within the high energy approximation (BFKL approach) can be supplemented by the knowledge of hard-scattering amplitudes calculated exactly at fixed order. Then, one can use them together in factorization formula (2) without double counting.

For inclusive hard processes, heavy quark production and DIS, the method of such high energy resummation was elaborated in [8]. It is based on Curci, Furmanski and Petronzio approach [9] to separation of collinear singularities. The amplitudes on a parton (quark, gluon) target are considered in $D = 4 + 2\epsilon$ non-integer dimensions. That separates automatically the leading twist. Collinear singularities appear in this approach as $1/\epsilon^n$ poles, these poles are absorbed into a definition of parton densities. Another essential ingredients of [8] method is an analysis of Mellin moments, high-energy terms in Mellin moment space N look like singularities $(\alpha_s/N)^n$ at $N \to 0$, and a consideration of BFKL equation in $D = 4 + 2\epsilon$ dimensions.

We found[1] that this technique may be directly generalized on the analysis of exclusive non-forward reactions. Below we present the first results of this study.

Like in DIS the imaginary part of the amplitude is given by the sum of quark singlet and gluon contributions

$$\mathcal{I}mA(\xi,t) = \frac{1}{\xi}\int\limits_{\xi}^{1} dx \left[D^{(+)}\left(\frac{\xi}{x}\right) H^{(+)}(x,\xi,t) + \frac{1}{\xi} D^{g}\left(\frac{\xi}{x}\right) H^{g}(x,\xi,t)\right] . \qquad (4)$$

$D^{(+)}$ and D^g are the imaginary parts of the quark and gluon hard-scattering amplitudes. In difference to forward DIS case the parton densities in (4) depend on both longitudinal momentum

[1] D.Yu.Ivanov, R. Kirschner and A.Papa, in preparation

fractions. Due to that the Mellin moments of the amplitude do not factorize into the product of the moments

$$D_N(t) = \int\limits_0^1 d\xi\, \xi^N \mathcal{I}mA(\xi,t) = \tag{5}$$

$$\int\limits_0^1 \int\limits_0^1 du\, dx\, u^{N-1} x^N \left[D^{(+)}(u)\, \mathcal{H}^{(+)}(x, u\,x, t) + \tfrac{1}{u\,x} D^g(u)\, \mathcal{H}^g(x, u\,x, t) \right] .$$

Using polynomiality property of GPDs, in particular for the gluon case

$$\int_0^1 dx\, x^n H^g(x,\eta,t) = \sum_{j=0,\mathrm{even}}^{n} (2\eta)^j A^g_{n+2,j}(t) + (2\eta)^{n+2}\, C^g_{n+2}(t)\,, \tag{6}$$

one can show that for the integer odd N

$$D_N(t) = \sum_{k=0}^{\infty} 2^k \left[D^{(+)}_{N+k-1} A^q_{N+k+1,k}(t) + D^g_{N+k-2} A^g_{N+k+1,k}(t) \right] \tag{7}$$

which is a sum of moment products (not just a product, as in DIS case).

One can analytically continue (7) from the integer odd N into entire complex N plane. The high energy asymptotic of the amplitude is related with the behavior of $D_N(t)$ near unphysical point $N \to 0$. One can split (7) into a sum of the singular and the regular at $N \to 0$ parts

$$D_N(t) = C^{(+)}_N q^{(+)}_N(t) + C^g_N g_N(t) + D^{\mathrm{reg}}_N(t) \tag{8}$$

The singularities of the sum (7) at $N \to 0$ are due to the $k = 0$ term only. Therefore

$$C^{(+)}_N = D^{(+)}_{N-1}, \quad q^{(+)}_N(t) = A^q_{N+1,0}(t), \quad C^g_N = D^g_{N-2}, \quad g_N(t) = A^g_{N+1,0}(t)\,. \tag{9}$$

Note that at $t \to 0$, $q^{(+)}_N(t)$ and $g_N(t)$ reduce to the moments of usual parton densities

$$q^{(+)}_N(t) \to q^{(+)}_N = \int\limits_0^1 dx\, x^N q^{(+)}(x)\,, \quad g_N(t) \to g_N = \int\limits_0^1 dx\, x^N\, g(x)\,. \tag{10}$$

This consideration shows that the non-forward nature of hard exclusive reactions does not complicate much their analysis in the high energy limit. Therefore the method used in DIS [8] may be applied here. The difference between DIS and our case is in the different form of k_t dependent amplitudes for corresponding partonic subprocesses.

Below I will concentrate on the dominant at high energy gluon contribution. The results will be presented for the process (1) (assuming for simplicity the asymptotic form of meson DA) and for the process of heavy quarkonium electroproduction (where the formation of quarkonium is treated in NRQCD). The amplitude is presented as follows

$$\mathcal{I}mA^g \sim H^g(\xi,\xi) + \int\limits_{2\xi}^1 \frac{dx}{x} H^g(x,\xi) \sum_{n=1} C_n(L) \frac{\bar{\alpha}_s^n}{(n-1)!} \log^{n-1} \frac{x}{\xi}\,, \tag{11}$$

where $\bar{\alpha}_s = N_c\alpha_s/\pi$, we omitted normalization factors irrelevant for the subsequent discussion, in the r.h.s $H^g(\xi,\xi)$ represents the Born contribution and the sum stands for the high energy terms. $C_n(L)$ are polynomials of variable $L = \log\frac{Q^2}{\mu_F^2}$ which we need to calculate.

Note that the Born term belongs to the regular part (in terms of (7)), whereas the high energy terms behave as $(\bar{\alpha}_s/N)^n$ at $N \to 0$. Therefore in the high energy terms one can replace gluon GPD in (11) by its forward limit, $H^g(x,\xi) \to xg(x)$, but in the Born contribution $H^g(\xi,\xi)$ should be kept different from $xg(x)$.

Omitting all details of the derivation we just present the results. We work in $\overline{\rm MS}$ scheme. We define (properly normalized) k_t dependent amplitude of the gluon subprocess

$$h_V(k_t^2) = \int\limits_0^1 dz\,\frac{Q^2}{{k_t}^2 + z(1-z)Q^2}\phi_V(z)\Big/\int\limits_0^1 dz\,\frac{\phi_V(z)}{z(1-z)}\,, \tag{12}$$

then we calculate its Mellin transform

$$h_V(\gamma) = \gamma\int\limits_0^\infty \frac{d{k_t}^2}{{k_t}^2}\left(\frac{{k_t}^2}{Q^2}\right)^\gamma h_V(k_t^2) = \frac{\Gamma^3[1+\gamma]\Gamma[1-\gamma]}{\Gamma[2+2\gamma]}\,. \tag{13}$$

The high energy terms are defined from the expression

$$C_N^g \sim h_V(\gamma)R\left(\frac{Q^2}{\mu_F^2}\right)^\gamma\,. \tag{14}$$

The gluon anomalous dimension is determined by the solution of equation $1 = (\bar{\alpha}_s/N)\chi(\gamma)$, where $\chi(\gamma)$ is the BFKL eigenfunction, the function R depends on $\bar{\alpha}_s/N$ and is defined in [8]. Expanding C_N^g in a series of the variable $y = \bar{\alpha}_s/N$ one can obtain analytical expressions for the polynomials $C_n(L)$.

Below we illustrate the values of these polynomials for the case $\mu_F = Q$

$$\begin{aligned} V: &\quad 1 - 2\,y + 4\,y^2 - 2.39\,y^3 - 4.09\,y^4 + \ldots \\ \text{onium}: &\quad 1 - 1.39\,y + 2.61\,y^2 + 0.481\,y^3 - 4.96\,y^4 + \ldots \\ F_L: &\quad 1 - 0.33\,y + 2.13\,y^2 + 2.27\,y^3 + 0.434\,y^4 + \ldots \end{aligned}$$

here the first two lines represent results for the exclusive light vector meson and quarkonium production respectively, in the third line we show for comparison the results for longitudinal DIS structure function [8]. We see that the numerical values of $C_1(0)$ are negative in all cases, but for the exclusive reactions its absolute values are about $4 \div 6$ times larger then in the case of F_L, explaining very large negative NLO corrections found for exclusive meson production. On the other hand, the values of the second polynomial are positive and large, $C_2(0) = 4$ for the light vector meson production. This gives a hope that inclusion of these high energy terms in the analysis may stabilize predictions for exclusive meson production.

To investigate this possibility we perform the following numerical study. We calculate the amplitude of light vector meson production with (11), where in the high energy terms we use a

very simple input for the gluon density $H^g(x,\xi) \sim xg(x) \sim x^{-0.2}$, for the Born term we take $H^g(\xi,\xi) = 1.2\,\xi\, g(\xi)$. Definitely, more realistic input for gluon GPD should be used (especially for $H^g(\xi,\xi)$), but at the present stage we just want to clarify the qualitative role of the high energy terms. In Fig. 2 we present the energy dependence of the amplitude (in arbitrary units) calculated for two values of photon virtuality $Q^2 = 10$ and $20\,\mathrm{GeV}^2$, for the running coupling we use $\alpha_s(10) = 0.25$ and $\alpha_s(20) = 0.16$, and for the factorization scale $\mu_F^2 = Q^2/2$. The solid line on Fig. 2 represents the Born contribution, the dashed line – the Born + the first high energy term, the dotted line – the Born + 2 first high energy terms, the dashed-dotted – the Born + 6 first high energy terms. We see that high energy resummation is convergent fast, the difference

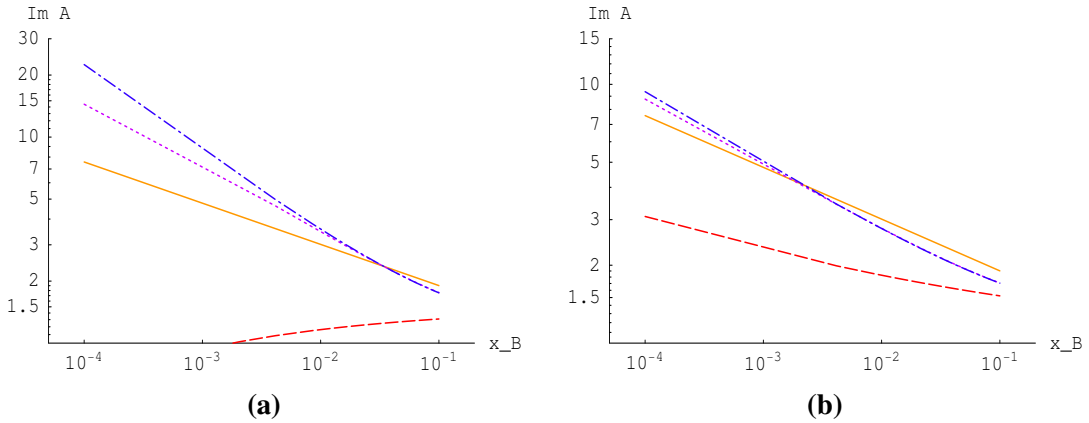


Fig. 2: The convergence of the high energy resummation: **(a)** $Q^2 = 10\mathrm{GeV}^2$, **(b)** $Q^2 = 20\mathrm{GeV}^2$.

between the dashed and the dashed-dotted lines is not big for $Q^2 = 10\,\mathrm{GeV}^2$ and is really small for $20\,\mathrm{GeV}^2$ cases. The other observation is that the inclusion of only first high energy term (dashed line) seems to be a bad approximation. Even for $20\,\mathrm{GeV}^2$ case, where the Born and the resummed results are close to each other, the dashed line is about factor of 3 below.

The dependence of the amplitude on the choice of factorization scale is shown in Fig. 3. Again, the dashed lines correspond to the Born + the first high energy term, the dashed-dotted lines – the Born + 6 first high energy terms. The upper dashed and dashed-dotted lines are for $\mu_F^2 = Q^2/4$, the lower dashed and dashed-dotted lines are for $\mu_F^2 = Q^2/2$. We observe a sizeable reduction of the factorization scale dependence if the high energy terms are resummed in comparison to the case when only the first of these terms is taken into account.

4 Summary

Large NLO corrections are found for hard exclusive vector meson production. At intermediate to larger values of x_B, typical for fixed-target experiments, it seems that NLO corrections start to be under control for large values of Q^2, say above $10\,\mathrm{GeV}^2$. However, the situation is much worse for the region of small x_B, typical for the HERA collider experiments. Here NLO corrections are not under control even for such large values of hard scales as $30\,\mathrm{GeV}^2$, which prevents the interpretation of the precise HERA data in terms of GPDs. The problem is related to appearance

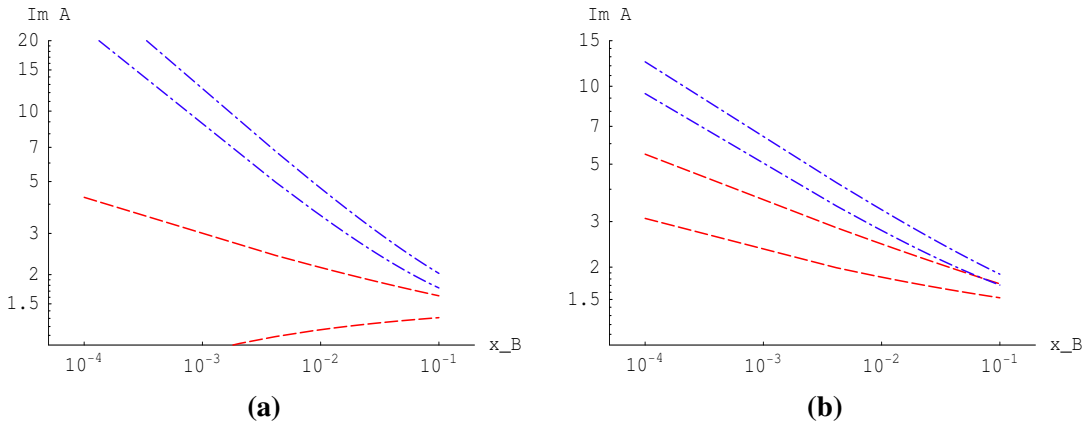


Fig. 3: **(a)** $Q^2 = 10\mathrm{GeV}^2$, **(b)** $Q^2 = 20\mathrm{GeV}^2$

of BFKL type logarithms in the hard-scattering amplitudes, that calls for a resummation of these effects at higher orders. Here we present the first results for such a study. The methods used earlier for forward DIS process may be generalized to the case of nonforward hard exclusive reactions. We obtained analytical results for the corresponding high energy terms in (11). The first numerical calculation incorporating the high energy resummation is encouraging.

I am very grateful to the organizers and to Alexander von Humboldt Foundation for the support of my participation in EDS07 conference. This work is also sponsored in part by grants RFBR-06-02-16064 and NSh 5362.2006.2.

References

[1] J. C. Collins, L. Frankfurt, and M. Strikman, Phys. Rev. **D56**, 2982 (1997).

[2] D. Mueller, D. Robaschik, B. Geyer, F. M. Dittes, and J. Horejsi, Fortschr. Phys. **42**, 101 (1994);
X.-D. Ji, Phys. Rev. Lett. **78**, 610 (1997);
A. V. Radyushkin, Phys. Lett. **B380**, 417 (1996);
M. Burkardt, Phys. Rev. **D62**, 071503 (2000).

[3] K. Kumericki, D. Muller, and K. Passek-Kumericki (2007).

[4] D. Y. Ivanov, L. Szymanowski, and G. Krasnikov, JETP Lett. **80**, 226 (2004).

[5] D. Y. Ivanov, A. Schafer, L. Szymanowski, and G. Krasnikov, Eur. Phys. J. **C34**, 297 (2004).

[6] M. Diehl and W. Kugler (2007). arXiv:0708.1121 [hep-ph].

[7] E. A. Kuraev, L. N. Lipatov, and V. S. Fadin, Sov. Phys. JETP **45**, 199 (1977);
I. I. Balitsky and L. N. Lipatov, Sov. J. Nucl. Phys. **28**, 822 (1978).

[8] S. Catani, M. Ciafaloni, and F. Hautmann, Phys. Lett. **B242**, 97 (1990);
S. Catani and F. Hautmann, Nucl. Phys. **B427**, 475 (1994).

[9] G. Curci, W. Furmanski, and R. Petronzio, Nucl. Phys. **B175**, 27 (1980).

Photo and electroproduction of vector mesons: a unified nonperturbative treatment

Erasmo Ferreira [1†], *H. G. Dosch*[2]
[1]Instituto de Fisica, Universidade Federal do Rio de Janeiro,
C.P. 68528, Rio de Janeiro 21945-970, RJ, Brazil
[2]Institut für Theoretische Physik, Universität Heidelberg,
Philosophenweg 16, D-69120 Heidelberg, Germany

Abstract
We have made a calculation of elastic photo- and electroproduction of ρ, ω, ϕ, J/ψ and Υ vector mesons based on a framework in which the photon and vector meson wave functions and properties of the QCD vacuum field play prominent roles. No free parameters enter, and a successful description is made of all available data, with emphasis put in their general and universal features.

1 Introduction and some results

Our calculation of photo and electroproduction [1] uses a general method for high energy scattering based on the functional integral approach [2] to QCD and on the WKB method, which is capable of incorporating both the perturbative and nonperturbative aspects. The nonperturbative input is given by a special model of nonperturbative QCD, called stochastic vacuum model [3,4], that has been successfully applied in many fields, from hadron spectroscopy to high energy scattering. The energy dependence is based on the two-pomeron model of Donnachie and Landshoff [5].

The original approach for the implementation of the dipole treatment of vector meson production, which provides the framework for the present work, was developed by the Heidelberg group [6–8]. This approach calculates the basic loop-loop interaction using the stochastic vacuum model [3, 4, 9], which is a genuine nonperturbative treatment that allows connections with other branches of nonperturbative QCD, especially with the fundamental and striking feature of confinement. The same approach using the loop-loop amplitude and the stochastic vacuum model was used consistently by A. Donnachie and H.G. Dosch for calculations of DVCS and structure functions.

Details of our calculations are given in our recent article [1] and in references given there. Photon and vector mesons wave functions are written in light cone coordinates and play a fundamental role. The vector meson wave functions, written by analogy with the transverse and longitudinal virtual photon wave functions, have extension parameters determined by their values at the origin, fixed through the $q\bar{q}$ electromagnetic coupling f_V responsible for their ee^+ and $\mu^-\mu^+$ decays.

Our scheme has a structure similar to other approaches, of mainly nonperturbative nature, based on the color dipole dynamics, with the assumption that the photon fluctuates into a $q\bar{q}$ pair,

[†] speaker

which then scatters with the proton, according to a properly built dipole cross section $\sigma_{\rm dipole}$. The $q\bar{q}$ dipole then recombines to form again a photon, or eventually a vector meson, in the final state. Photons, either real or virtual, enter in a well defined way through their QED wave functions, and the dipole cross section is built with the necessary ingredients to describe the observed phenomenology and, as much as posible, to follow QCD prescriptions. The proton structure gives an impact parameter dependence that allows description of t dependence.

As a whole, these nonperturbative models for γ^* induced processes, all based in the dipole picture, are phenomenologically satisfactory. This is not surprising, since it has already been shown [10] that many features of these processes, particularly the Q^2 dependence, are reproduced by the overlap of the light cone wave functions of photons and mesons folded with the basic r^2 behavior of the dipole cross sections.

Our unified quantitative predictions for different kinds of vector mesons cover several scales of magnitudes in cross sections. This global coverage is exhibited in Fig. 1 showing the integrated elastic cross sections of electroproduction of all vector mesons, for varied virtuality Q^2 of the incident photon. When plotted against $Q^2+M_V^2$, the curves have very regular behavior, which is solely determined by the overlap of photon and vector meson wave functions.

In Fig. 2 the charge factors squared $\hat{e}_V^2$ for each kind of meson are extracted, making the quantities almost universal in a $Q^2 + M_V^2$ plot. The effective meson charges $\hat{e}_V$ are $1/\sqrt{2}$ for the ρ and $1/3\sqrt{2}$ for the ω meson, while for the ϕ, ψ and Υ mesons they are the same as the s, c and b quark charges. However, the universality is only approximate, and our calculation predicts correctly the observed displacements. The universality is still more interesting when the factors given by the squared electromagnetic couplings f_V^2 are extracted. The residual displacements may be due to radiative corrections in the electromagnetic decays, which modify the f_V couplings. The wave functions a the origin should be evaluated without these corrections in the decay rates. With appropriate factors $f_V^{(0)2}$ extracted from the cross section values, the universality should become exact.

Our calculation is free of external parameters, and covers the wide meson spectrum. Fig. 3 shows our prediction for the upsilon case, which is fulfilled accurately by the recent Zeus (preliminary) measurements. In the other side of the scale, we look at ρ meson electroproduction, where we also have a good description of the data.

In our work [1], the data on the energy dependence of the integrated cross sections for ρ, ϕ and ψ mesons have been presented and compared to the theoretical predictions for each case. The parameter $\delta(Q^2)$ of the suggested simple energy dependence

$$\sigma(Q^2) = \text{Const.} \times W^{\delta(Q^2)}$$

has also been given in each case. This parametrization is an approximation valid in a limited energy range, since the true energy dependence in our calculation is already determined by the two-pomeron scheme, but it is considered useful in practice.

We then evaluate δ using the energy range W=20 - 100 GeV, for all values of Q^2. The results are put together in Fig. 4. All curves start at the minimum value 4×0.08 at the same unphysical point $Q^2 + M_V^2 = 0$ and all are asymptotic to $\delta = 4 \times 0.42$ as Q^2 increases. We then

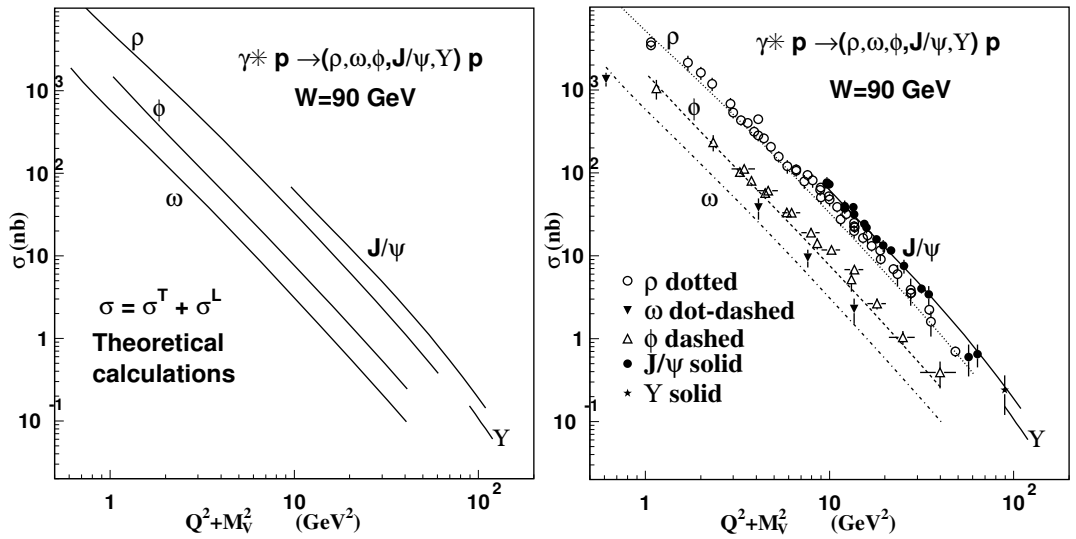


Fig. 1: Integrated elastic cross sections for all vector mesons at W=90 GeV, as functions of $Q^2 + M_V^2$. Our theoretical calculations with the stochastic vacuum model represent well the data, covering several orders of magnitude, without free parameters. The lines can be parametrized as sum of two terms of form $a/(Q^2 + M_V^2)^n$.

have the convenient form of parametrization

$$\delta(Q^2) = 0.32 + 1.36 \frac{(1 + Q^2/M_V^2)^n}{A + (1 + Q^2/M_V^2)^n} \ . \tag{1}$$

Our model has definite predictions for the t dependence of differential cross sections, with a curvature in the log plot, shown in Fig. 4 and described by the form

$$\frac{d\sigma}{d|t|} = \left[\frac{d\sigma}{d|t|}\right]_{t=0} \times F(|t|) = \left[\frac{d\sigma}{d|t|}\right]_{t=0} \times \frac{e^{-b|t|}}{(1 + a|t|)^2} \ . \tag{2}$$

As the virtuality Q^2 grows, the ranges of the overlap functions decrease, and the electroproduction cross sections of all mesons become flatter, all tending together to the shape characteristic of the Υ meson, with same limiting values $a = 4.02$ GeV^2 and $b = 1.60$ GeV^2 for the parameters. The limiting shape of the distribution for very large Q^2 is illustrated in Fig. 5, where we see all vector mesons superposed. In the figure we draw the bit of straight line representing the slope considered as the average for the interval from $|t| = 0$ to $|t| = 0.2$ GeV^2. As indicated inside the plots, the calculations of form factors presented in the figures are made for $W = 90$ GeV. In the second plot presented in Fig. 5 we show the (absence of) dependence of the form factor on the energy W. Thus we predict that there is no shrinking of the forward peak in $d\sigma/d|t|$ as the energy increases. The experimental data are not yet sufficient to test all these predictions.

2 Final remarks

We have shown the predictions for elastic electroproduction processes using two basic ingredients:

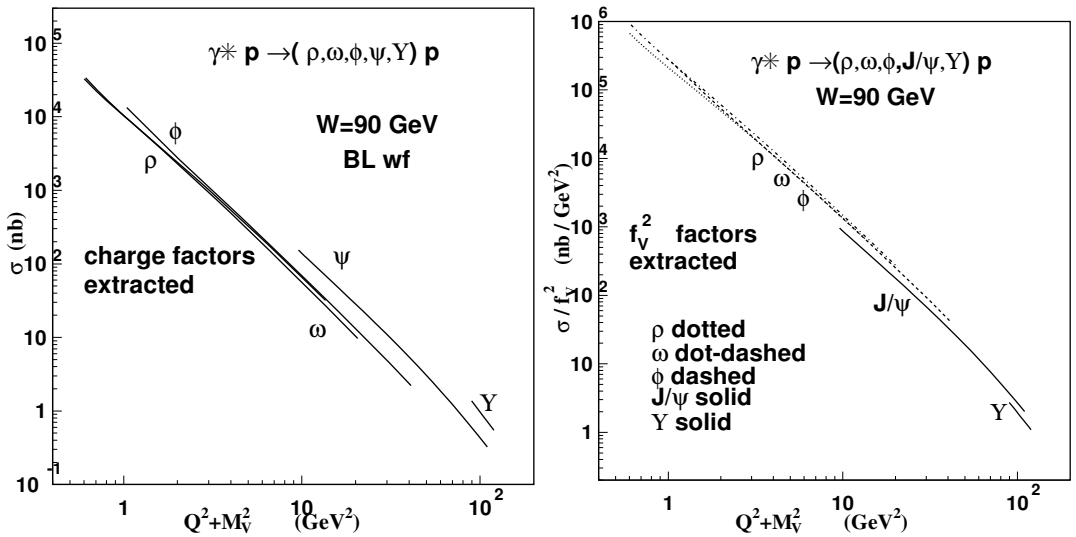


Fig. 2: Extraction of factors given by the squares of the electric charges of the quarks reduce the cross sections of the vector mesons nearly to a single quantity, exhibiting an interesting universality. As shown in the right hand side, the universality is still neater when the extracted factor is the electromagnetic coupling f_V of the $q\bar{q}$ pair to the electromagnetic current. This coupling is used to fix the value of the vector meson wave function at the origin.

1) the overlaps of photon and meson wave functions, written as packets of quark-antiquark dipoles, with protons described also as packets of dipoles (in a convenient diquark model for the nucleon),
2) the interaction of two dipoles described in terms of geometric variables in an impact parameter representation of the amplitudes based on nonperturbative properties of the QCD gluon field.

These quantities put together and integrated over the distribution of dipoles in initial and final states lead to a correct description of the data concerning all vector mesons.

In all cases the variations with energy are very well described by the Regge picture, with soft and hard pomerons coupled to large and small dipoles, respectively.

Each of the different mesons enter in the calculation characterized only by the masses and charges of its quark contents, and with their normalized wave function individualized only by the corresponding electromagnetic decay rate (related to the value of the wave function at the origin).

The specific nonperturbative input is the stochastic vacuum model, which has been successfully applied in many fields, from hadron spectroscopy to high energy scattering. The basic interaction of two dipoles depends only on universal features of the QCD field, which are the numerical values of the gluon condensate and of the correlation length of the finite range correlations. These two quantities have been determined by lattice investigations and tested independently in several instances of phenomenological use of the dipole-dipole interaction.

As has already been pointed out [10], the main features of the Q^2 dependence of electroproduction of vector mesons are contained in the overlap integral of photon and meson wave

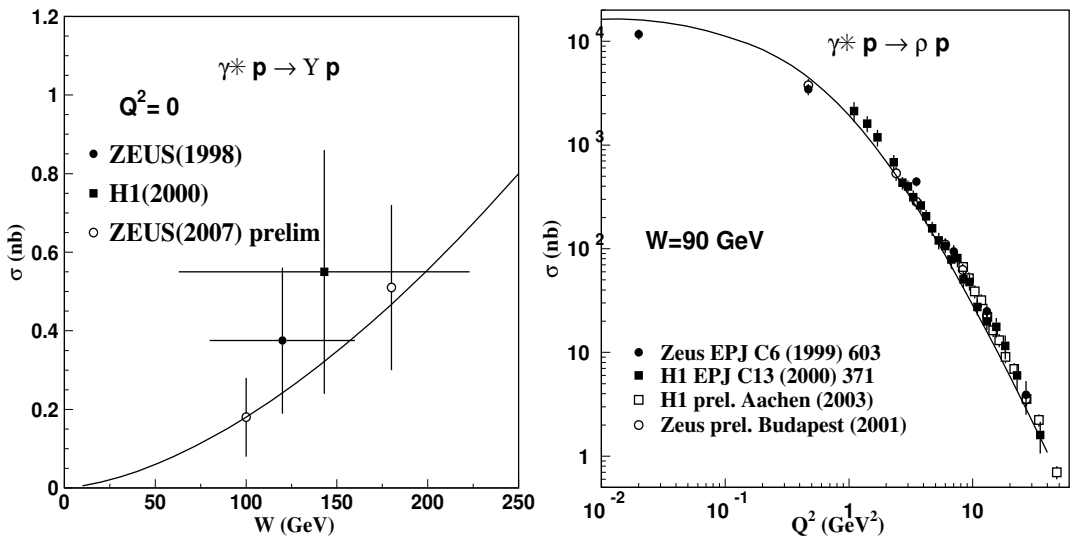


Fig. 3: Our calculation of the cross section of upsilon photoproduction is made without free parameters, with energy dependence described by the two-pomeron model of Donnachie and Landshoff. The new Zeus data (still preliminary) confirms our predicions [1] with perfection. In the right-hand-side, our calculation of the cross section of rho electroproduction is shown, compared with the data.

functions.

Our calculation gives a fair overall description of all observables of vector meson production: the energy dependence, the Q^2 dependence, the ratio of longitudinal to transverse mesons and the angular distribution. All results were compared to the large amount of HERA data for $\rho, \omega, \phi, \mathrm{J}/\psi$ and Υ mesons.

References

[1] H. G. Dosch and E. Ferreira, Eur. Phys. J. C **51**, 83 (2007).

[2] O. Nachtmann, Annals Phys. **209**, 436 (1991).

[3] H. G. Dosch, Phys. Lett. B **190**, 177 (1987).

[4] H. G. Dosch and Y. A. Simonov, Phys. Lett. B **205**, 339 (1988).

[5] A. Donnachie and P. V. Landshoff, Phys. Lett. B **437**, 408 (1998).

[6] H. G. Dosch, T. Gousset, G. Kulzinger, and H. J. Pirner, Phys. Rev. D **55**, 2602 (1997).

[7] H. G. Dosch, T. Gousset, and H. J. Pirner, Phys. Rev. D **57**, 1666 (1998).

[8] G. Kulzinger, H. G. Dosch, and H. J. Pirner, Eur. Phys. J. C **7**, 73 (1999).

[9] H. G. Dosch, E. Ferreira, and A. Kramer, Phys. Rev. D **50**, 1992 (1994).

[10] E. Ferreira and V. L. Baltar, Nucl. Phys. A **748**, 608 (2005).

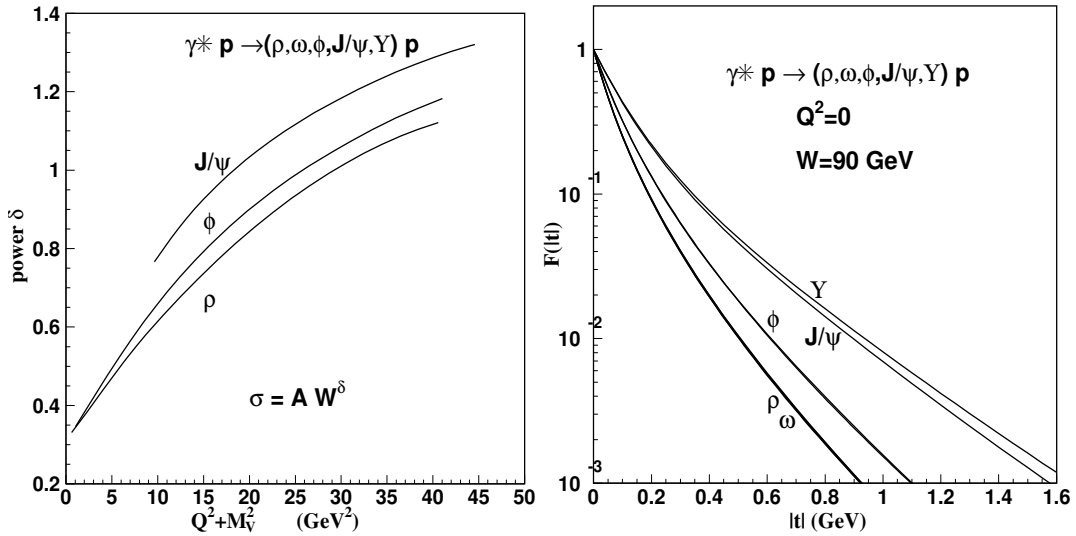


Fig. 4: In the LRH, parameter $\delta(Q^2)$ of the energy dependence of the cross sections. In the RHS, the form factor $F(|t|)$ of the $|t|$ distribution in the elastic differential cross sections, with the characteristic curvatures in the log plot predicted in our calculations. The curves follow the shapes given by Eq.(2). The values of the parameters in the limit of very large Q^2 are $a = 4.02\ \mathrm{GeV}^{-2}$ and $b = 1.60\ \mathrm{GeV}^{-2}$.

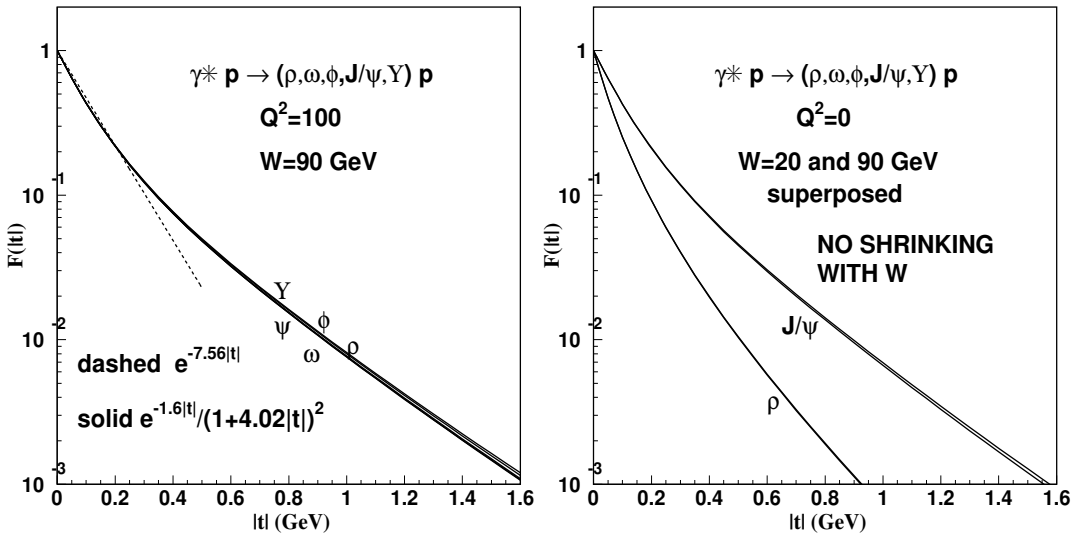


Fig. 5: The plot in the left hand side shows the shape of the $|t|$ distribution in the differential cross section for electroproduction common to all vector mesons for very large Q^2. The straight line passes through the points $|t|$ equal to zero and 0.2 GeV^2, indicating the average slope that would be measured in this limit. The plot in the right hand side shows that $F(|t|)$ does not depend significantly on the energy, and thus measurement of slopes at fixed Q^2 would give a constant value for each vector meson.

Vector meson electroproduction within GPD approach

S.V. Goloskokov
Bogoliubov Laboratory of Theoretical Physics, Joint Institute for Nuclear Research,
Dubna 141980, Moscow region, Russia

Abstract
We analyze electroproduction of light vector meson at small Bjorken x within the generalized parton distribution (GPD) approach. Calculation is based on the modified perturbative approach, where the quark transverse degrees of freedom in the hard subprocess are considered. Our results on the cross section are in fair agreement with experiment from HERMES to HERA energies.

1 Introduction

In this report, we investigate vector mesons electroproduction at small Bjorken x on the basis of the GPD approach [1, 2]. At large Q^2 the leading order amplitude with longitudinal photon and vector meson polarization (LL amplitude) dominates and factorizes [3] into a hard meson leptoproduction off partons and GPDs, Fig.1. Other transition amplitudes are suppressed by

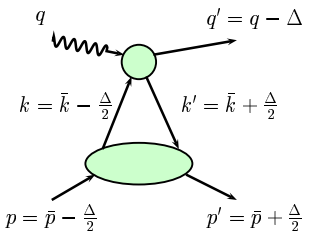


Fig. 1: The handbag diagram for the meson electroproduction off proton.

powers of $1/Q$ and have singularities [4] in the collinear approximation. This leads to problems with factorization of these amplitudes.

In this report, we analyse LL amplitude of vector meson electroproduction at large Q^2. In contrast to [1], where the gluon dominated region $x \leq 0.01$ was considered, we extend here our analysis to $x \leq 0.2$ [2]. This range covers the energy region from HERMES to HERA energies. Our model is based on the modified perturbative approach (MPA) [5] which includes the quark transverse degrees of freedom accompanied by Sudakov suppression. The transverse quark momentum regularizes the end-point region of the amplitudes. The $x \sim 0.2$ range study requires inclusion of the sea and valence quark GPDs in our analysis. It is shown that in our model we obtain a fair description of HERMES, H1 and ZEUS data [6–8] for electroproduced ρ and ϕ mesons at small x [2].

2 Leptoproduction of Vector Mesons in the GPD approach

The parton contribution to the photoproduction amplitudes $\gamma^* p \to V p$ with positive proton helicity reads as a convolution of the hard subprocess amplitude $\mathcal{H}^V$ and unpolarized H^i and polarized $\tilde{H}^i$ GPDs :

$$\mathcal{M}^V_{\mu'+,\mu+} \;=\; \frac{e}{2}\,\mathcal{C}^V \sum_\lambda \int d\overline{x}\,\mathcal{H}^{Vi}_{\mu'\lambda,\mu\lambda} H^i(\overline{x},\xi,t), \tag{1}$$

where i denotes the gluon and quark contribution, μ (μ') is the helicity of the photon (meson), $\overline{x}$ is the momentum fraction of the parton with helicity λ, and the skewness ξ is related to Bjorken-x by $\xi \simeq x/2$. The flavor factors are $C_\rho = 1/\sqrt{2}$ and $C_\phi = -1/3$. The polarized GPDs $\tilde{H}^i$ at small x are much smaller than the unpolarized GPDs H^i and they are unimportant in the analysis of the cross section.

The subprocess amplitude $\mathcal{H}^V$ is represented as the contraction of the hard part F which is calculated perturbatively and the non-perturbative meson wave function ϕ_V which depends on the transverse quark momenta $k_\perp$ in the vector meson

$$\mathcal{H}^V_{\mu'\lambda,\mu\lambda} = \frac{2\pi\alpha_s(\mu_R)}{\sqrt{2N_c}} \int_0^1 d\tau \int \frac{d^2\mathbf{k}_\perp}{16\pi^3}\phi_V(\tau,k_\perp^2)\; F^\pm_{\mu'\mu}. \tag{2}$$

The wave function is chosen in the simple Gaussian form

$$\phi_V(\mathbf{k}_\perp,\tau) \;=\; 8\pi^2\sqrt{2N_c}\,f_V a_V^2\;\exp\left[-a_V^2\,\frac{\mathbf{k}_\perp^2}{\tau\bar{\tau}}\right], \tag{3}$$

which leads after integration over $k_\perp$ to the asymptotic wave function. Here $\bar{\tau} = 1-\tau$, f_V is the decay coupling constant and the a_V parameter determines the value of average transverse momentum of the quark.

In calculation of the subprocess within the MPA [5] we keep the $k_\perp^2$ terms in the denominators of the hard amplitudes. The gluonic corrections in hard subprocess are treated in the form of the Sudakov factors which additionally suppress the end-point integration regions.

The GPD is a complicated function which depends on three variables. We use the double distribution form [9]

$$H_i(\overline{x},\xi,t) = \int_{-1}^1 d\beta \int_{-1+|\beta|}^{1-|\beta|} d\alpha\delta(\beta+\xi\,\alpha-\overline{x})\,f_i(\beta,\alpha,t), \tag{4}$$

with the distribution function

$$f_i(\beta,\alpha,t) = h_i(\beta,t)\,\frac{\Gamma(2n_i+2)}{2^{2n_i+1}\,\Gamma^2(n_i+1)}\,\frac{[(1-|\beta|)^2-\alpha^2]^{n_i}}{(1-|\beta|)^{2n_i+1}}\,. \tag{5}$$

Here

$$\begin{aligned} h_g(\beta,0) &= |\beta| g(|\beta|) && n_g = 2 \\ h^q_{sea}(\beta,0) &= q_{sea}(|\beta|)\mathrm{sign}(\beta) && n_{sea} = 2 \\ h^q_{val}(\beta,0) &= q_{val}(\beta)\Theta(\beta) && n_{val} = 1, \end{aligned} \tag{6}$$

where g and q are ordinary gluon and quark PDFs.

For the parton distribution the simple Regge ansatz is used

$$h_i(\beta,t) = e^{b_0 t}\beta^{-(\delta_i(Q^2)+\alpha' t)}\,(1-\beta)^{2n_i+1}\sum_{j=0}^{3} c_i^j\,\beta^{j/2}. \tag{7}$$

The parameter $\delta_i(Q^2)$ is connected with the corresponding Regge trajectory. For example, for gluon we have

$$\delta_g(Q^2) = \alpha_P(0) - 1 = 0.1 + 0.06\ln\left(Q^2/Q_0^2\right),\ Q_0^2 = 4\text{GeV}^2, \tag{8}$$

which determines the behavior of the gluon distribution at low x and the energy dependence of the cross section at high energies. The parameter α' in (7) is a slope of the Regge trajectory $\alpha_i(t) = \alpha_i(0) + \alpha_i' t$. The other parameters in (7) are taken from comparison with the CTEQ6M parameterization [10].

The valence quark sea differs from the strange sea. The simple model is used

$$H^u_{sea} = H^d_{sea} = \kappa_s H^s_{sea}, \tag{9}$$

which is in correspondence with the CTEQ6 results. The flavor symmetry breaking factor is chosen in the form

$$\kappa_s = 1 + 0.68/(1 + 0.52\ln\left(Q^2/Q_0^2\right) \tag{10}$$

which fits well CTEQ6M PDFs.

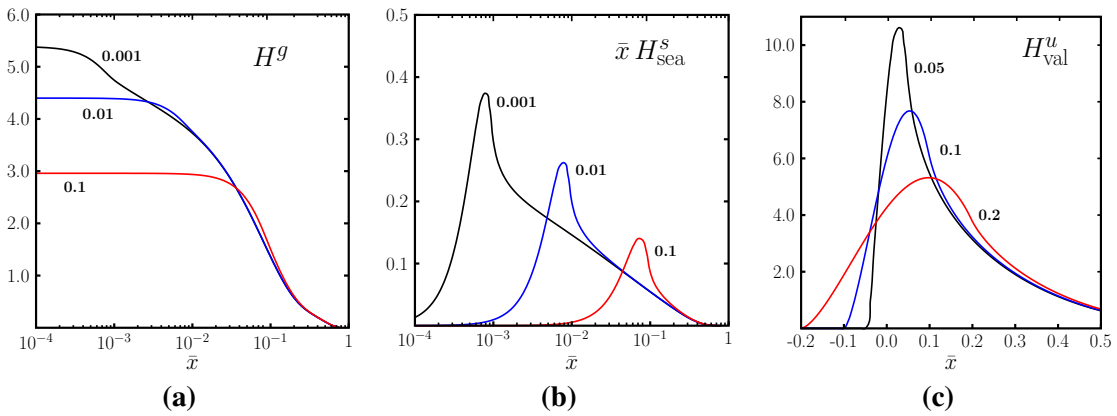


Fig. 2: GPDs **(a)** H^g, **(b)** xH^s_{sea}, **(c)** H^u_{val} vs. x for some values of skewness. GPDs are shown at $t = 0$ and scale $Q^2 = 4\text{GeV}^2$

The model results for gluon and quark GPDs for different values of skewness are shown in Fig. 1.

3 Longitudinal cross section

Now we have all ingredients to calculate cross sections. Estimations for the vector meson production are obtained using $f_{\rho L} = 0.209\,\mathrm{GeV}$, $a_{\rho L} = 0.75\,\mathrm{GeV}^{-1}$; $f_{\phi L} = 0.221\,\mathrm{GeV}$; $a_{\phi L} = 0.7\,\mathrm{GeV}^{-1}$. The value of the diffractive peak slope can be found in [2]. The longitudinal cross section for the ρ and ϕ production integrated over t is shown in Fig. 3 at HERA energies. In this energy range the valence quark effects are unimportant. In Fig. 3a, the cross section of ρ production is shown together with the individual contributions to the cross section: gluon contribution, the gluon-sea-quark interference, and quark contribution. It can be seen that a typical contribution of the interference to σ_L does not exceed 50% with respect to the gluon one. Thus, the gluon term really gives the predominant contribution to the cross section [11] and we find good agreement of our results with the H1 and ZEUS experiments [7, 8] at HERA.

The model results for the ϕ production cross section shown in Fig. 3b are consistent with the H1 and ZEUS data [7, 8]. In ϕ production the gluon-sea quark interference contribution to the cross section does not exceed 25%. Note that the uncertainties in the GPDs provide errors in the cross section about $25-35\%$ which are shown in Fig. 3b for ϕ production. The ρ production cross section in Fig. 3a has the similar uncertainties. They are of the same order of magnitude as the gluon-sea interference. The leading twist results which do not consider effects of transverse quark motion, are presented in Fig. 3b too. One can see that the $k_\perp^2/Q^2$ corrections in the hard amplitude denominators are extremely important at low Q^2. They decrease the cross section by a factor of about 10 at $Q^2 \sim 3\mathrm{GeV}^2$. The role of these corrections at $Q^2 \sim 40\mathrm{GeV}^2$ is not so essential-about 40%.

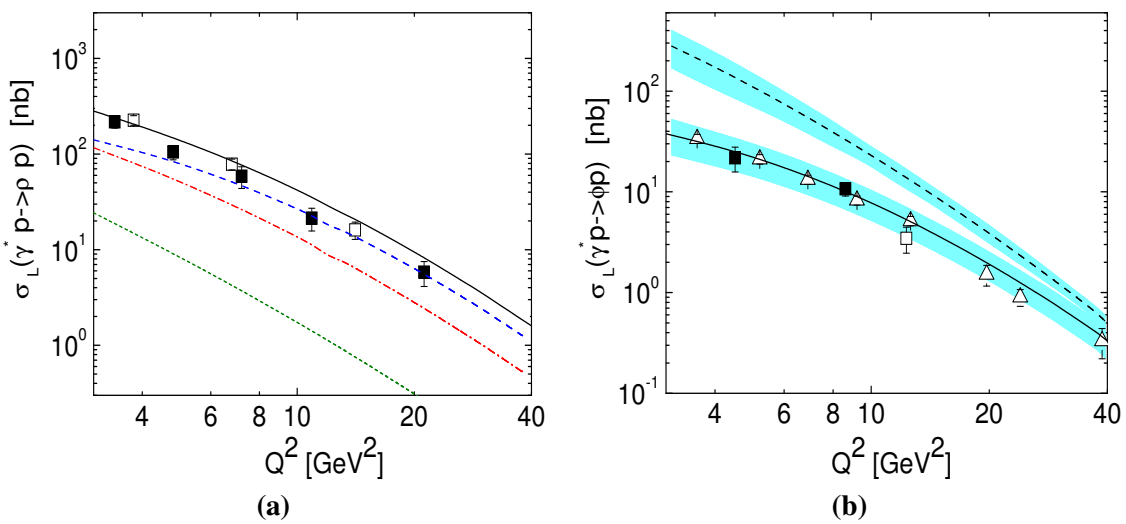


Fig. 3: **(a)** Longitudinal cross sections of ρ production at $W = 75\mathrm{GeV}$. Full line cross section, dashed- gluon contribution, dashed-dot - gluon-sea interference, dotted line -sea contribution. **(b)** Full line- longitudinal cross sections of ϕ production at $W = 75\mathrm{GeV}$ with error band from CTEQ PDF uncertainties. Dashed line -leading twist results. Data are from H1 and ZEUS.

Let us discuss the energy dependence of the cross section. At small x where only gluon

and sea contribute it behaves as

$$\sigma_L \propto W^{4\delta(Q^2)}, \tag{11}$$

where the power δ is determined in (8). At larger x the valence quark contribution should play an important role. In Fig. 4a, we show our results for the ρ- production cross section at $Q^2 = 4\text{GeV}^2$ in a wide energy range. Together with the gluon contribution, the gluon + sea and interference of valence quark with gluon + sea plus valence quark contribution to the cross section are shown. It can be seen that for energies above $W \geq 10\text{GeV}$ the gluon and sea effects well reproduce the cross section. At HERMES energies $W \sim 5\text{GeV}$ the valence quarks contribution is important.

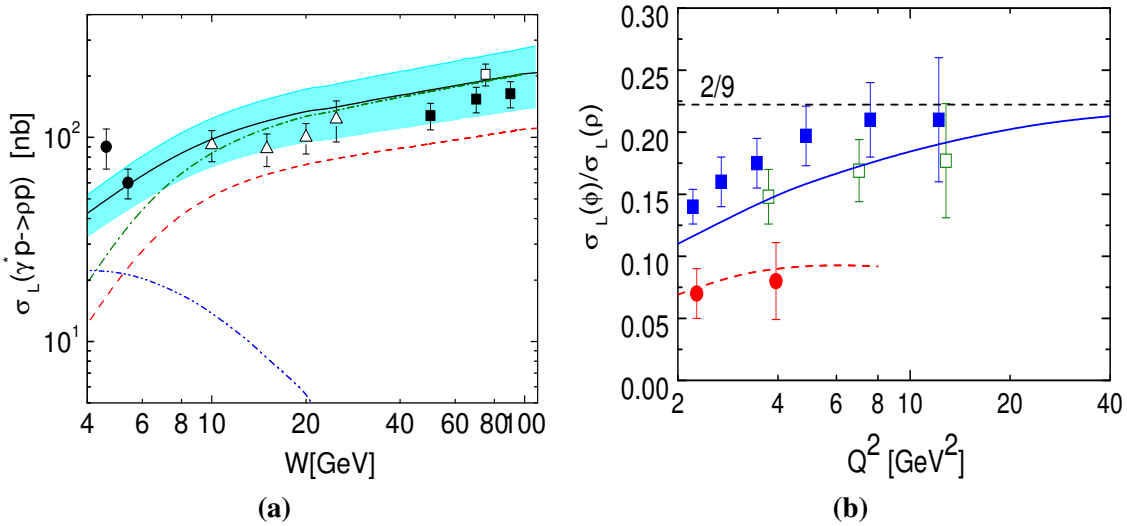


Fig. 4: **(a)** Longitudinal cross sections of ρ production at $Q^2 = 4\text{GeV}^2$ as a function of W. Full line cross section, dashed- gluon contribution, dashed-dot - gluon+sea, dashed dot dotted- (gluon+sea)-valence interference plus valence contribution. **(b)** The ratio of ϕ/ρ cross sections via Q^2. Full line- $W = 75\text{GeV}$, dashed line -$W = 5\text{GeV}$. Data are from H1 and ZEUS and HERMES.

For ρ production the interference of valence quarks with gluons and sea contribution give of about 40% contribution to the cross section at $W \sim 5\text{GeV}$. At COMPASS energies $W \sim 10\text{GeV}$ the valence quarks give only about 10% contribution to the cross section. Thus, COMPASS physics is very close to asymptotic HERA energies.

The ratio of the ϕ/ρ cross sections at HERA energies $W = 75\text{GeV}$ is shown in Fig. 4b. It is obvious that if the quark sea does not contribute (or sea is symmetric), this ratio is determined by the flavor factors in (1) and should be equal to $\sigma(\phi)/\sigma(\rho) = 2/9$. The HERA data show a strong deviation of this ratio from $2/9$ value. In our model, this violation at HERA energies and low Q^2 finds a natural explanation by the flavor symmetry breaking factor (10) effect. At high Q^2 the κ_s factor goes to 1 and the ratio of the cross section is close to the $\sigma(\phi)/\sigma(\rho) = 2/9$ limit. Thus, we can conclude that the Q^2 dependence of the $\sigma(\phi)/\sigma(\rho)$ ratio is completely determined by the flavor symmetry breaking factor κ_s. It cannot be explained if one does not consider the quark sea contribution. At HERMES energies the valence quarks contribution in ρ production gives an additional suppression the of $\sigma(\phi)/\sigma(\rho)$ ratio -see Fig. 4b.

4 Conclusion or Summary

We have analyzed electroproduction of light mesons at small Bjorken-x in the handbag model where the process amplitudes are factorized into the GPDs and a partonic subprocess. The subprocess was calculated [2] within the modified perturbative approach where the transverse momenta of the quark and antiquark as well as Sudakov corrections were taken into account. These effects suppress the contributions from the end-point regions where one of the partons entering into the meson wave function becomes soft and factorization breaks down in the collinear approximation. It is found that the GPD approach gives a fine description of the longitudinal cross section for light meson production. The power corrections $\sim k_\perp^2/Q^2$ in propagators of the hard amplitude play an extremely important role at low Q^2. Inclusion of these corrections gives a possibility to describe experimental data properly.

The gluonic contribution plays an essential role for all energies $W > 5$GeV in vector meson electroproduction. The gluon-sea interference is about 30(50)% for ϕ (ρ) production. Valence quarks contribute only for $W < 10$GeV. For the ρ production at HERMES energies $W \sim 5$GeV, valence quarks give about 40% effect in the cross section. At COMPASS $W \sim 10$GeV their contribution is about 10% only. The flavor symmetry breaking of the sea naturally explain the deviation of the $\sigma(\phi)/\sigma(\rho)$ ratio from the asymptotic limit equal to 2/9 at HERA energies at low Q^2.

Thus, we can conclude that in different energy ranges, information about quark and gluon GPDs can be extracted from the cross section of the vector meson electroproduction. This reaction at small x and large Q^2 is an excellent tool to study the gluon and quark GPDs.

This work is supported in part by the Russian Foundation for Basic Research, Grant 06-02-16215 and by the Heisenberg-Landau program.

References

[1] S. Goloskokov and P. Kroll, Euro. Phys. J. **C42**, 281 (2005).

[2] S. Goloskokov and P. Kroll, Euro. Phys. J. **C50**, 829 (2007).

[3] X. Ji, Phys. Rev. **D55**, 7114 (1997);
A. Radyushkin, Phys. Lett. **B380**, 417 (1996).

[4] L. Mankiewicz and G. Piller, Phys. Rev. **D61**, 074013 (2000);
I. Anikin and O. Teryaev, Phys. Lett. **B554**, 51 (2003).

[5] J. Botts and G. Sterman, Nucl. Phys. **B325**, 62 (1989).

[6] HERMES Collaboration, A. Airapetian *et al.*, Eur. Phys. J. **C17**, 389 (2000);
HERMES Collaboration, A. Borissov, Proceedings of Diffraction 06 **PoS (DIFF2006)**, 014 (2006).

[7] H1 Collaboration, C. Adloff *et al.*, Eur. Phys. J. **C13**, 371 (2000);
H1 Collaboration, C. Adloff *et al.*, Phys.Lett. **B483**, 360 (2000).

[8] ZEUS Collaboration, J. Breitweg *et al.*, Eur. Phys. J. **C6**, 603 (1999);
ZEUS Collaboration, S. Chekanov *et al.*, Nucl.Phys. **B718**, 3 (2005).

[9] I. V. Musatov and A. V. Radyushkin, Nucl. Phys. **B467**, 443 (1996).

[10] CTEQ Collaboration, J. Pumplin *et al.*, JHEP **0207**, 012 (2002).

[11] M. Diehl and A. Vinnikov, Phys. Lett. **B609**, 286 (2005).

On the Limitations of the Color Dipole Picture

Carlo Ewerz [a]†*, Andreas von Manteuffel* [b]*, Otto Nachtmann* [b]
[a] ECT*, Strada delle Tabarelle 286, I-38050 Villazzano (Trento), Italy
[b] Institut für Theoretische Physik, Universität Heidelberg, Philosophenweg 16, D-69120 Heidelberg, Germany

Abstract
We discuss two aspects of the color dipole picture of high energy photon-proton scattering. First we present bounds on various ratios of deep inelastic structure functions resulting from the dipole picture that, together with the measured data, can be used to restrict the kinematical range of its applicability. The second issue that we address is the choice of energy variable in the dipole-proton cross section.

1 The dipole picture of high energy photon-proton scattering

The color dipole picture of high energy photon-proton scattering (or more generally photon-hadron scattering) [1, 2] has been a very popular and successful framework for the analysis of structure function data measured at HERA. In the dipole picture the photon-proton scattering is viewed as a two-step process. In the first step the real or virtual photon splits into a quark-antiquark pair – a color dipole – of size $r = |\boldsymbol{r}|$ in the two-dimensional transverse plane of the reaction. The probability for this splitting to happen is encoded in the so-called photon wave function $\psi^{(q)}_{T,L}(\alpha, \boldsymbol{r}, Q)$, where Q^2 is the photon virtuality, α denotes the fraction of the longitudinal momentum of the photon that is carried by the quark, and q indicates the quark flavor. In leading order in the electromagnetic and strong coupling constants $\alpha_{\rm em}$ and α_s the squared photon wave functions for transversely (T) and longitudinally (L) polarized photons are given by

$$\left|\psi^{(q)}_{T}(\alpha, \boldsymbol{r}, Q)\right|^2 = \frac{3}{2\pi^2}\,\alpha_{\rm em} Q_q^2 \left\{\left[\alpha^2 + (1-\alpha)^2\right]\epsilon_q^2 [K_1(\epsilon_q r)]^2 + m_q^2 [K_0(\epsilon_q r)]^2\right\} \tag{1}$$

and

$$\left|\psi^{(q)}_{L}(\alpha, \boldsymbol{r}, Q)\right|^2 = \frac{6}{\pi^2}\,\alpha_{\rm em} Q_q^2 Q^2 [\alpha(1-\alpha)]^2 [K_0(\epsilon_q r)]^2\,, \tag{2}$$

respectively. Here m_q is the quark mass for flavor q, Q_q the corresponding electric charge, and $\epsilon_q = \sqrt{\alpha(1-\alpha)Q^2 + m_q^2}$. $K_{0,1}$ denote modfied Bessel functions, and we have summed over the polarizations of the quark and antiquark. Integrating over the longitudinal momentum fraction α we obtain a density for the photon wave function,

$$w^{(q)}_{T,L}(r, Q^2) = \int_0^1 d\alpha\, \left|\psi^{(q)}_{T,L}(\alpha, \boldsymbol{r}, Q)\right|^2 . \tag{3}$$

† speaker

It gives the probability that a highly energetic, transversely or longitudinally polarized photon of virtuality Q^2 splits into a quark-antiquark dipole of flavor q and size r.

In the second step of the reaction, the color dipole of size r scatters off the proton. Here the dipole is assumed to consist of an on-shell quark and antiquark and is treated as a hadron-like state. The second step is expressed in terms of the dipole-proton cross section $\hat{\sigma}^{(q)}(r, W^2)$ which naturally depends on the quark flavor, the size of the dipole, and on the c.m.s. energy W of this subprocess. The two steps of the photon-proton reaction are then connected by integrating over the size and orientation of the intermediate dipole state and by summing over quark flavors to obtain the total $\gamma^{(*)}p$ cross section,

$$\sigma_{T,L}(W^2, Q^2) = \sum_q \int d^2r \, w_{T,L}^{(q)}(r, Q^2) \, \hat{\sigma}^{(q)}(r, W^2) \,. \tag{4}$$

In general, the dipole cross section $\hat{\sigma}$ cannot be calculated from first principles. Instead, one uses models for $\hat{\sigma}$ that implement certain features like saturation etc., and then fits the parameters of these models to measured data for the total structure function F_2, given for $W^2 \gg Q^2$ and $W^2 \gg m_p^2$ by $F_2(W, Q^2) = Q^2[\sigma_T(W^2, Q^2) + \sigma_L(W^2, Q^2)]/(4\pi^2\alpha_{\rm em})$.

The dipole picture is not exact. Its derivation from a genuinely nonperturbative formulation of photon-proton scattering – or, in other words, its foundations in quantum field theory – have been studied in [3, 4]. As a key result of those papers the assumptions and approximations are spelled out in detail which are necessary to arrive at the usual dipole picture outlined above. In particular it was possible to identify correction terms which are potentially large in certain kinematical regions. As with any approximate formula it is important to determine as precisely as possible its range of applicability – in the case of the dipole picture the kinematical range in which potential corrections to the formulae given above are small. We will address this issue in the next two sections.

Note that the energy variable in the dipole-proton cross section $\hat{\sigma}$ is W^2. However, many popular models for $\hat{\sigma}$ use Bjorken-x, $x = Q^2/(W^2 + Q^2)$, instead. We will discuss the choice of energy variable in section 4 below.

2 Bound on $R = \sigma_L/\sigma_T$

The densities $w_{T,L}$ are obviously non-negative (see (3)), and the same holds for the dipole cross sections $\hat{\sigma}^{(q)}$, since they are supposed to describe the physical scattering process of a dipole on a proton. We notice that in the formula (4) for the cross sections σ_L and σ_T the corresponding densities $w_L^{(q)}$ and $w_T^{(q)}$ are convoluted with the same dipole cross section $\hat{\sigma}^{(q)}$. Based on these observations one can derive bounds on the ratio $R = \sigma_L/\sigma_T$ [4, 5] from the dipole picture. The ratio of two integrals with non-negative integrands cannot be smaller (larger) than the minimum (maximum) of the ratio of the integrands. Applied to the cross sections σ_L and σ_T of (4) this implies

$$\min_{q,r} \frac{w_L^{(q)}(r, Q^2)}{w_T^{(q)}(r, Q^2)} \;\le\; R(W^2, Q^2) \;\le\; \max_{q,r} \frac{w_L^{(q)}(r, Q^2)}{w_T^{(q)}(r, Q^2)} \,. \tag{5}$$

Note that here the dipole cross sections $\hat{\sigma}^{(q)}$ drop out. Consequently, these bounds depend only on the well-known wave functions for longitudinally and transversely polarized photons. Let us

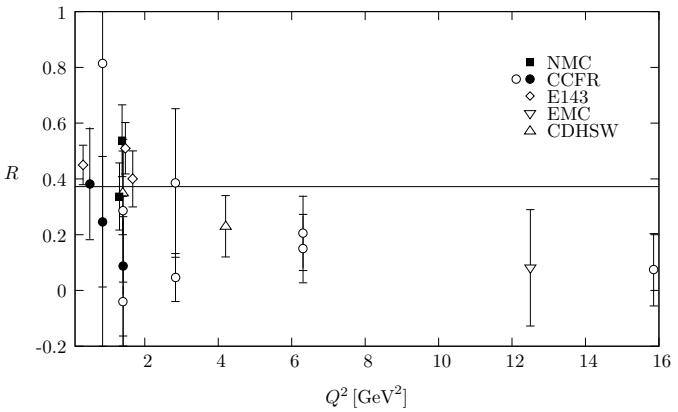


Fig. 1: Comparison of experimental data for $R = \sigma_L/\sigma_T$ in the region $x < 0.05$ with the bound (6) resulting from the dipole picture. Full points correspond to data with $x < 0.01$, open points are data with $0.01 < x \leq 0.05$.

point out that these bounds on R are independent of the choice of energy variable (W^2 or x) in the dipole cross section $\hat{\sigma}$. Evaluating the bounds (4) we find that the lower bound is trivial ($R \geq 0$), and the upper bound has the numerical value

$$R(W^2, Q^2) \leq 0.37248\,. \tag{6}$$

This bound has to be satisfied in the kinematical region in which the dipole picture is applicable. A violation of the bound in some kinematical region, on the other hand, would indicate that the dipole picture cannot be used there.

The bound (6) is confronted with the experimental measurements of R in Fig. 1, where only data points with $x < 0.05$ are included. The data have rather large error bars and seem to respect the bound. However, in the kinematical region of $Q^2 < 2\,\mathrm{GeV}^2$ the data appear to come very close to the bound – a situation that could hardly be accomodated with a realistic dipole cross section $\hat{\sigma}$. The application of the dipole picture in this interesting region (in which possible saturation effects are expected to become manifest) might therefore be questionable. Unfortunately, there are no HERA data on R available which could clarify this important point. For a detailed discussion and references to the corresponding experimental publications see [4,5].

3 Bounds on ratios of F_2 at different Q^2

In analogy to the derivation of the bound on R discussed above one can also obtain bounds on other ratios of deep inelastic structure functions. We can for example consider the ratio of structure functions F_2 taken at the same energy W but at different photon virtualities Q^2. In [5,6] it was shown that for such a ratio one can derive the inequalities

$$\frac{Q_1^2}{Q_2^2}\,\min_{q,r}\frac{w_T^{(q)}(r,Q_1^2)+w_L^{(q)}(r,Q_1^2)}{w_T^{(q)}(r,Q_2^2)+w_L^{(q)}(r,Q_2^2)} \leq \frac{F_2(W,Q_1^2)}{F_2(W,Q_2^2)} \leq \frac{Q_1^2}{Q_2^2}\,\max_{q,r}\frac{w_T^{(q)}(r,Q_1^2)+w_L^{(q)}(r,Q_1^2)}{w_T^{(q)}(r,Q_2^2)+w_L^{(q)}(r,Q_2^2)}\,. \tag{7}$$

Note that for these bounds to be valid it is essential that the energy variable in the dipole cross section $\hat{\sigma}$ is indeed W^2, in particular, $\hat{\sigma}$ must not depend on Q^2. These bounds are independent

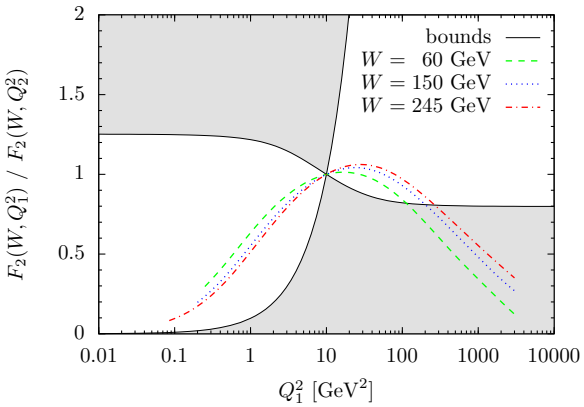


Fig. 2: The bounds (7) on $F_2(W,Q_1^2)/F_2(W,Q_2^2)$ for $Q_2^2 = 10\,\mathrm{GeV}^2$ and the corresponding fit to HERA data for three different values of W. Data in the shaded region cannot be described in the usual dipole picture.

of any other assumptions about the dipole cross section $\hat{\sigma}$, and are in fact given in terms of the photon wave functions only. They also do not depend on the energy W.

In this case both the upper and the lower bound are non-trivial. Both bounds are shown in Fig. 2 for the choice $Q_2^2 = 10\,\mathrm{GeV}^2$. In the dipole picture the shaded area is excluded. Also in that Figure we show the corresponding HERA data for three different energies W. More precisely, we show the ratios resulting from the ALLM97 fit [7] to the data. Within the experimental errors this fit can be regarded as a substitute of the data and is more convenient to use for a comparison with our bounds. (Note that we use this fit only within the kinematical range of the actual data.) As can be seen in the Figure the data violate the bound (7) at large Q^2 while the bound is respected at low Q^2. We can therefore obtain a maximal photon virtuality $Q^2_{\max}$ beyond which the dipole picture breaks down. (In order to obtain an optimal value we have also varied the reference scale Q_2^2.) The W-dependence of this maximal Q^2 is shown as the dashed line in Fig. 3. As expected, the dipole picture can be used up to higher Q^2 for larger values of W.

In [6] we have considered correlated ratios of F_2-structure functions taken at the same energy W but at three different photon virtualities Q_i^2. It turns out that we can derive bounds on these correlated ratios from the dipole picture which are stronger than the bound discussed above. These bounds can be obtained from elementary geometrical considerations, but space limitations prevent us from presenting them here. We refer the interested reader to [6] for a detailed description. Using those methods we can show, for instance, that $F_2(W,Q_1^2)/F_2(W,Q_3^2)$ is restricted to a certain range that in turn depends on the value of $F_2(W,Q_2^2)/F_2(W,Q_3^2)$. Also these correlated bounds do not involve any model assumptions about the dipole cross section $\hat{\sigma}$ and are entirely given in terms of the photon wave functions. By confronting the correlated bounds with the ALLM97 fit to HERA data we have been able to restrict even further the range in Q^2 allowed by the dipole picture. More precisely, we have obtained a $Q^2_{\max}$ up to which the three values Q_i^2 can be chosen arbitrarily without giving rise to a violation of the bound by the corresponding data. In Fig. 3 the W-dependence of this $Q^2_{\max}$ is shown as the solid line. The correlated bounds give a stronger restriction on the kinematical range in which the dipole picture can be used as compared to the bound on the plain ratios (7).

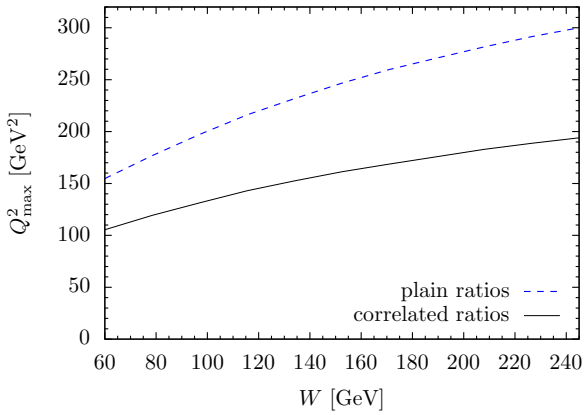


Fig. 3: W-dependence of the upper limit $Q^2_{\rm max}$ of the Q^2-range in which the HERA data are consistent with the bounds obtained from the dipole picture. The dashed line results from the bound (7) while the solid line results from correlated bounds involving three different values of Q^2.

4 The energy variable in the dipole cross section

Let us finally turn to the choice of energy variable in the dipole cross section $\hat{\sigma}$. Recall that the photon wave function describes the probability that a photon of virtuality Q^2 splits into a dipole of size r. Clearly, for a given Q^2 dipoles of all possible sizes r can emerge, with probabilities given by (1), (2) and (3). It is therefore not possible to extract Q^2 from the dipole size r. Let us further recall that the second step of the scattering process in the dipole picture is the scattering of the dipole of size r on the proton. This dipole is fully characterized by r (and – less relevant here – its longitudinal momentum, α and the spin orientations). The dipole-proton cross section $\hat{\sigma}$, understood as an actual scattering process of its own, can only depend on the properties of the initial state, namely the dipole and the proton. In particular, it cannot depend on the photon virtuality Q^2. Hence $\hat{\sigma}$ cannot be a function of Bjorken-x which can only be calculated with the knowledge of Q^2. For a more formal presentation of this argument see [4].

It is an interesting observation, on the other hand, that in the recent past almost all phenomenologically successful models for the dipole cross section use x as its energy variable. The most prominent example is the Golec-Biernat-Wüsthoff (GBW) model [8], for further references see [3, 4]. It is often argued that the probability distribution of dipole sizes has a maximum at $r \simeq C/Q$ (where $C \simeq 2.4$), and that therefore one can effectively replace the dipole size r in $\hat{\sigma}$ by its most likely value. The value Q^2 in x is then interpreted as corresponding to this most likely dipole size r, $Q = C/r$. In Fig. 4 we have inverted this procedure for the case of the GBW model, that is we have reconstructed a W- but not Q^2-dependent $\hat{\sigma}$ from its x-dependence. Here we plot again the ratio $F_2(W, Q_1^2)/F_2(W, Q_2^2)$, with the choice $W = 60\,\text{GeV}$ and $Q_2^2 = 10\,\text{GeV}^2$, in order to compare with the bound (7). The effect of replacing $Q \to C/r$ turns out to be sizable, especially at large Q^2. The modified model by construction respects the bound (7), while the original GBW model strongly violates it at large Q^2. The considerable difference between the two arises because the peak of the distribution of dipole sizes is actually rather broad, such that using only its maximum value is in fact not a good approximation.

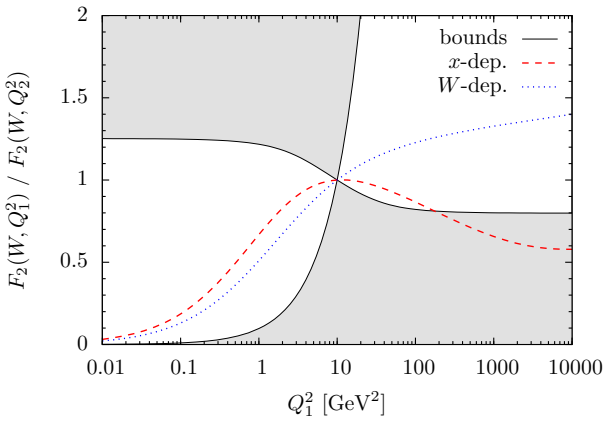


Fig. 4: Ratios of structure functions for the GBW model [8] (x-dependent dipole cross section, dashed line) and for a modification of the model with a W-dependent dipole cross section (dotted line) in comparison with the bounds (7).

Strictly speaking, the use of x instead of W in the dipole cross section is incorrect in the dipole picture. Phrased positively, it is actually a step *beyond* the dipole picture to use an x-dependent dipole cross section $\hat{\sigma}$. The better agreement of the x-dependent models of the dipole cross section with the data seems to indicate that some important corrections to the dipole picture are effectively taken into account by using x as the energy variable. In our opinion it would be very interesting to identify and to understand these additional contributions.

5 Conclusions

The dipole picture of high energy photon-proton scattering is only an approximation. We have derived various bounds on ratios of structure functions from the dipole picture, and have used these bounds to restrict the kinematical range of applicability of the dipole picture. One should analyse the data in the framework of the dipole picture only within this allowed range if one wants to arrive at firm conclusions. Further, we have discussed the choice of energy variable in models of the dipole cross section. We have pointed out that this issue is more delicate than has previously been assumed and certainly deserves to be studied in more detail.

References

[1] N. N. Nikolaev and B. G. Zakharov, Z. Phys. **C49**, 607 (1991).

[2] A. H. Mueller, Nucl. Phys. **B415**, 373 (1994).

[3] C. Ewerz and O. Nachtmann, Annals Phys. **322**, 1635 (2007). hep-ph/0404254.

[4] C. Ewerz and O. Nachtmann, Annals Phys. **322**, 1670 (2007). hep-ph/0604087.

[5] C. Ewerz and O. Nachtmann, Phys. Lett. **B648**, 279 (2007). hep-ph/0611076.

[6] C. Ewerz, A. von Manteuffel, and O. Nachtmann (2007). arXiv:0708.3455 [hep-ph].

[7] H. Abramowicz, E. M. Levin, A. Levy, and U. Maor, Phys. Lett. **B269**, 465 (1991);
H. Abramowicz and A. Levy (1997). hep-ph/9712415.

[8] K. Golec-Biernat and M. Wüsthoff, Phys. Rev. **D59**, 014017 (1999). hep-ph/9807513.

What is Measured in Hard Exclusive Electroproduction?

J.T. Londergan[†]*and A.P. Szczepaniak*
Department of Physics and Nuclear Theory Center
Indiana University, Bloomington, IN 47405, USA

Abstract
We examine the relation between amplitudes measured in exclusive lepto-production and the quark content of the nucleon. We show that in the limit of high energy and small t, the natural interpretation of amplitudes measured in these hard exclusive processes is in terms of the quark content of the meson cloud and not the target itself. In this regime, Regge amplitudes will make a significant contribution to these exclusive amplitudes. This leads to violation of QCD scaling.

1 Theoretical Analysis of Exclusive Electroproduction

Recently there has been much interest in hard exclusive reactions. This followed from the proof of factorization by Collins *et al.* [1] for exclusive lepto-production. The proof guarantees that under certain conditions, the exclusive amplitude can be factorized into a hard term calculable from QCD and a soft term that ideally should be universal. This latter contribution has typically been parameterized by generalized parton distributions or GPDs [2–4]. This is analogous to the case of deep inelastic scattering (DIS), where inclusive cross sections can be parameterized in terms of universal parton distribution functions (PDFs) that are related to quark probabilities in the nucleon. The only difference is that in hard exclusive processes the amplitude typically requires an integral over the GPDs.

From duality we know that it is in principle possible to use any channel to describe the scattering amplitude. In DIS it is known that the s-channel representation is generally the most efficient way to characterize these reactions. The only exception to this occurs at very small Bjorken $x_{BJ} \to 0$. Except in this small-x regime, DIS amplitudes can be related to the intrinsic quark structure of the nucleon. At very small x, amplitudes associated with t-channel processes will become important; as $x_{BJ} \to 0$ the structure function evolves to represent ladders of partons originating from t-channel meson exchanges, and Regge exchange makes an important contribution in this regime.

Once it was realized that Regge exchange may play a significant role in exclusive electroproduction, attempts have been made to incorporate Regge effects using analogies with DIS, *i.e* to restrict Regge contributions in exclusive electroproduction reactions to low-x_{BJ} so that scaling is not otherwise modified [5–8]. It had not been proven that Regge contributions should only contribute to exclusive amplitudes in this domain. We will investigate the question of whether Regge effects should be substantial in hard exclusive processes and if so, in what kinematic regime they will be important. Rather surprisingly, we find that, at high energies when Q^2 is large and t small, Regge effects will be significant. This implies that in this region, hard exclusive processes

[†] speaker

will be more sensitive to the structure of exchanged mesons than they are to the intrinsic quark structure of the nucleon.

We first investigated this question by examining hard exclusive processes in a t-channel formalism, as was reported in a recent paper [9]. Consider a general hard exclusive amplitude

$$a^*(q) + N(p) \to b(q') + N(p') \ . \tag{1}$$

In exclusive electroproduction $a^*(q)$ is a virtual photon with momentum q, where $-q^2 = Q^2$. In Eq. (1), $N(p), N(p')$ represent the initial and final nucleons with momenta p and p', respectively. In the Bjorken limit we have $p^2 = p'^2 = m_N^2 \ll Q^2$, and $b(q')$ denotes a final photon or meson with momentum q' satisfying $0 \leq q'^2 \sim m_N^2 \ll Q^2$. As is well known, DIS cross sections are proportional to the imaginary part of the forward virtual Compton amplitude; this is a special case of Eq. (1) when $p' = p$ and $q' = q$.

In Ref. [9] we examined the contribution to this exclusive amplitude arising from exchange of a particle of spin J in the t-channel. For simplicity we ignored spin and other internal degrees of freedom and assumed only scalar currents. The hadronic contribution to the cross section is determined from the hadronic tensor,

$$T(Q^2, \nu, t, q'^2) = \int d^4z e^{i\frac{q+q'}{2}z} \langle p'|T\left[j(\frac{z}{2})j(-\frac{z}{2})\right]|p\rangle. \tag{2}$$

In Eq. (2) T is a function of four independent Lorentz scalars with $\nu = p{\cdot}q/m_N = Q^2/(2x_{BJ}m_N)$, $t = (p'-p)^2 = (q-q')^2$, and $j(z) = \phi^\dagger(z)\phi(z)$ represents a (scalar) quark current in the Heisenberg picture which couples to the external fields representing the a and b particles in Eq. (1).

In the limit of high energy the contribution to the hadronic tensor from t-channel exchange of a spin-J meson is proportional to

$$T_J = \frac{\beta_J^l(t)\beta_J^u(q^2, q'^2, t)}{t - M_J^2} \sum_{\lambda=-J}^{J} \left[\frac{(p'+p)^{\mu_1}}{2} \cdots \frac{(p'+p)^{\mu_J}}{2} \epsilon^{\lambda}_{\mu_1\cdots\mu_J}(p'-p)\right] \times \left[\frac{(q'+q)^{\nu_1}}{2} \cdots \frac{(q'+q)^{\nu_J}}{2} \epsilon^{*\lambda}_{\nu_1\cdots\nu_J}(p'-p)\right]. \tag{3}$$

In Eq. (3), ϵ is the spin-J polarization vector, and β_J^l and β_J^u are the residue functions at the *lower* and *upper* vertex, respectively. This is shown schematically in Fig. 1. In the Bjorken limit, $s \to Q^2(1 - x_{BJ})/x_{BJ}$ and the amplitude reduces to

$$T_J = \frac{\beta_J^l(t)\beta_J^u(q^2, q'^2, t)}{t - M_J^2} \left(\frac{Q^2}{2x_{BJ}}\right)^J. \tag{4}$$

The key question is how the upper residue function depends on the large variables (Q^2 and $-q'^2 = Q^2$ in the case of inclusive processes, and Q^2 for the exclusive amplitudes). It is well known that for kinematics relevant to inclusive scattering, the upper residue function behaves as $(1/Q^2)^{J+1}$, *modulo* logarithmic corrections, so that the amplitude scales, $Q^2 T_J \propto (1/x_{BJ})^J$,

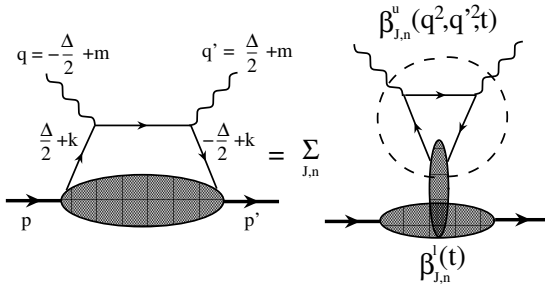


Fig. 1: t-channel meson contribution to the hadronic tensor for exclusive lepto-production. The amplitude is summed over all spins J that can contribute, and depends on the product of the residue functions β at the upper and lower vertices.

as expected [10–13]. Summing over all spins leads to the Regge behavior, $Q^2T = \sum_J T_J \propto (1/x_{BJ})^{\alpha(0)}$. In the small $x_{BJ} \to 0$ limit in DIS, the leading Regge trajectory with $\alpha(0) > 0$ will dominate the behavior of the hadronic tensor, while all daughter trajectories with $\alpha_n(0) < \alpha(0)$ are subleading at very small x. For finite x_{BJ}, however, daughter Regge trajectories are no longer suppressed, and as a result the Regge description becomes ineffective while the s-channel parton model description becomes natural.

The situation is quite different for exclusive electroproduction. This can be shown by writing the contribution of a t-channel spin J exchange in terms of the two-current correlation in the exchanged meson. This can be expanded in terms of a covariant Bethe-Salpeter amplitude for the exchanged meson, represented in terms of the spectral density g_{Jn}. The spectral density is related to the parton distribution amplitude in a meson and can in principle be constrained from electromagnetic data [14] and QCD asymptotics [15]. In the Bjorken limit, using the Feynman parametrization for the quark propagators and ignoring small terms we showed that the upper vertex function could be written [9]

$$\beta^u_{Jn} \;=\; \int_{-1}^{1} dx \int d\mu^2 g_{Jn}(x,\mu^2) \int_0^1 d\alpha \frac{\alpha^J}{\left[-\alpha\left(\frac{q'^2+q^2}{2} + x\frac{q'^2-q^2}{2}\right) + \mu^2\right]^{n+J-1}} \,. \tag{5}$$

For inclusive amplitudes when $q'^2 = q^2 = -Q^2$, the x disappears from the denominator and the integration over α is dominated by $\alpha \sim \mu^2/Q^2$. As a result, the entire integral is of order $(\mu^2/Q^2)^{J+1}$, as we argued earlier.

For exclusive amplitudes however where $q'^2 \sim 0$, the integrand of Eq. (5) is dominated by the region $1-x = \mathcal{O}(\mu^2/Q^2)$, and finite α. The endpoint behavior of the distribution amplitudes g_{nJ} is spin independent, and for leading-twist amplitudes $g_{Jn}(x \to 1) \sim (1-x)$. This leads to a J-independent suppression of the upper vertex with Q^2, $\beta^u_{Jn} \sim \mathcal{O}(\mu^4/Q^4)$ *independent of the spin of the exchanged meson*. Upon summing over all spins from a single trajectory one finds

that for small t the hadronic tensor is proportional to $(Q^2/x_{BJ})^{\alpha(t)}$. Thus, in the Bjorken limit exclusive lepto-production should be dominated by a single leading Regge trajectory for all x_{BJ}, and not just for $x_{BJ} \to 0$. In this regime hard exclusive processes probe the nucleon's meson cloud rather than its intrinsic quark properties.

Since this result was rather surprising, we repeated the derivation of hard exclusive amplitudes in an s-channel framework [16], where we analyzed the "handbag" diagrams used in extracting GPDs. We obtained the same results, namely that in the region of high energy and small t, Regge effects will make sizeable contributions to hard exclusive amplitudes. We showed that the DVCS formalism is ill-defined in the presence of Regge behavior in the parton-nucleon amplitude. This has the following consequences for hard exclusive processes.

1. The breakdown of collinear factorization in these processes means that the soft amplitudes are not universal, but are process-dependent amplitudes that we call Regge Exclusive Amplitudes.
2. The validity of QCD factorization for exclusive lepto-production will require, in addition to a hard scale Q^2, a sizeable value of t.
3. In the region of small t Regge effects will make substantial contributions to DVCS and exclusive meson lepto-production.
4. Exclusive lepto-production processes will show violation of QCD scaling arguments. These scaling violations will persist regardless of the magnitude of Q^2, in contradiction to expectations of QCD scaling.
5. In the region of small t hard exclusive amplitudes will exhibit a Q^2 behavior $(Q^2/x_{BJ})^{\alpha(t)}$ characteristic of hadronic Regge amplitudes. These amplitudes should be well approximated by the contribution from the leading Regge trajectory.

2 Experimental Support for Regge Exchange

Recently a Hall A Collaboration at Jefferson Laboratory has carried out a test of scaling in DVCS reactions [17]. The data appear to be in very good agreement with the Q^2-independent DVCS amplitude predicted by QCD [18], however the available Q^2 window is quite small, from $1.5 - 2.5\,\mathrm{GeV}^2$ and within the published experimental errors one cannot rule out a power-like dependence of the amplitude, $A \propto (Q^2)^{\alpha}$, with α as large as 0.25. Even more surprising, "standard" Regge-exchange models have proved successful in describing a variety of differential cross sections [19, 20], in the kinematic range where scaling would be expected based on comparisons with DIS. Our calculations show that the success of the Regge picture is to be expected, and is not accidental.

A recent experimental analysis of ω electroproduction at Jefferson Laboratory [19] showed that their data was in good agreement with predictions from standard Regge phenomenology, while showing large uncertainties with analyses based on models of GPDs [21]. Though our results were derived in the Bjorken limit with $s/|t| \gg 1$, the JLab data corresponds to energies of a few GeV and values up to $|t| \sim 2.7$. In Fig. 2 we compare our predictions with exclusive meson electroproduction data. QCD scaling arguments predict that the reduced π^+ cross section should fall off at fixed x_{BJ} as $1/Q^2$. We predict a behavior $(Q^2)^{2\alpha-1}$ with $0 < \alpha < 1$. Fitting π^+ data from HERMES [22] in the range $0.26 < x_{BJ} < 0.8$ gives $\alpha = 0.31 \pm 0.2$. Similarly

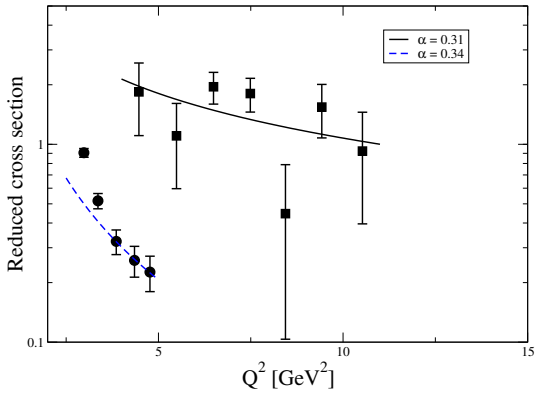


Fig. 2: A simple fit to some meson electroproduction data; π^+ results from HERMES (squares, [22]), and ω (circles, [19]) results from the CLAS Collaboration at Jefferson Lab. In the case of π^+ production the cross section reduced by the photon flux is plotted in arbitrary units.

for ω electroproduction cross section from the CLAS collaboration [19] we find $\alpha = 0.34 \pm 0.24$ for the range $0.52 < x_{BJ} < 0.58$.

We see that for both DVCS and exclusive meson electroproduction, not only are scaling violations observed, but the additional Q^2 dependence is softer than predicted by scaling, and is in agreement with our predicted factor of $(Q^2)^\alpha$ where $0 < \alpha < 1$. At this point it is difficult to compare the Regge exponents α obtained from the fit with total cross-section data, since the electroproduction data corresponds to different values of t. This issue warrants further phenomenological study.

In conclusion, we have shown that the Regge nature of parton-nucleon amplitudes generates divergences in GPDs at low t. In this region we predict sizeable effects due to scattering from the meson cloud in the nucleon, while at sufficiently large t the dominant effect will come from scattering of quarks in the nucleon. An important remaining question is how one can disentangle scattering off the meson cloud from effects of nucleon tomography.

Some of the work here was done in collaboration with F. Llanes-Estrada. The authors would like to thank S. Brodsky, J-M. Laget, W. Melnitchouk, D. Mueller, A. Radyushkin, M. Strikman and C. Weiss for useful comments and discussions. JTL was supported by NSF contract PHY-0555232 and APS by DOE contract DE-FG0287ER40365.

References

[1] J. Collins, L. Frankfurt, and M. Strikman, Phys. Rev. D **56**, 2982 (1997).

[2] X. D. Ji, J. Phys. G **24**, 1181 (1998).

[3] A. V. Radyushkin, Phys. Rev. D **56**, 5524 (1997).

[4] F. M. Dittes, D. Mueller, D. Robaschik, B. Geyer, and J. Horejsi, Phys. Lett. B **209**, 325 (1998).

[5] S. Ahmad, H. Honkanen, S. Liuti, and S. K. Taneja, Phys. Rev. D **75**, 094003 (2007).

[6] V. Guzey and M. V. Polyakov, Eur. Phys. J. C **46**, 151 (2006).

[7] K. Kumericki, D. Muller, and K. Passek-Kumericki. (unpublished), arXiv:hep-ph/0703179.

[8] L. Jenkovszky, Phys. Rev. D **74**, 114026 (2006).

[9] A. P. Szczepaniak and J. T. Londergan, Phys. Lett. B **643**, 17 (2006).

[10] B. Ioffe, V. Khoze, and L. Lipatov, *Hard Processes*. North-Holland, Amsterdam, 1984.

[11] S. Brodsky, F. Close, and J. Gunion, Phys. Rev. D **5**, 1384 (1972).

[12] S. Brodsky, F. Close, and J. Gunion, Phys. Rev. D **6**, 177 (1972).

[13] S. Brodsky, F. Close, and J. Gunion, Phys. Rev. D **8**, 3678 (1973).

[14] A. Szczepaniak and A. Williams, Phys. Lett. B **302**, 87 (1993).

[15] G. Lepage and S. Brodsky, Phys. Rev. D **22**, 2157 (1980).

[16] A. Szczepaniak, J. Londergan, and F. Llanes-Estrada. (unpublished), arXiv:0707.1239.

[17] Jefferson Lab Hall A Collaboration, C. M. Camacho *et al.*, Phys. Rev. Lett. **97**, 262002 (2006).

[18] M. Vanderhaeghen, P. A. M. Guichon, and M. Guidal, Phys. Rev. Lett. **80**, 5064 (1998).

[19] CLAS Collaboration, L. Morand *et al.*, Eur. Phys. J. A **24**, 445 (2005).

[20] V.Kubarovsky, *Deep virtual meson production*. Exclusive Reactions at High Momentum Transfer, JLab, Newport News, VA May, 2007. Http://conferences.jlab.org/exclusive/program.html.

[21] M. Diehl, W. Kugler, A. Schaefer, and C. Weiss, Phys. Rev. D **72**, 034034 (2005).

[22] R. Fabbri, *Exclusive photon and meson production at hermes*. 12th International Conference on Elastic and Diffractive Scattering, DESY, May 2007. Http://www.desy.de/∼eds07/program.html.

A Regge-pole model for DVCS

L.L. Jenkovszky[1]
[1]Bogolyubov Institute for Theoretical Physics,
National Academy of Sciences of Ukraine, Kiev-143, Ukraine

Abstract
A simple, calculable Regge-pole model for deeply virtual Compton scattering (DVCS) is presented and confronted with the experimental data from HERA.

1 Introduction

Interest in deeply virtual Compton scattering (DVCS) $ep \to e\gamma p$ to large extent is triggered by the prospects to use it as a tool in studies of Generalized Parton Distributions (GPD) [1, 2].

At HERA the DVCS cross-section has been measured [3, 4], in diffractive ep interactions, as a function of Q^2, W and t that are respectively the photon virtuality, the invariant mass of the $\gamma^* p$ system and the squared 4-momentum transferred at the proton vertex; the diagram in Fig. 1a shows the production of a real photon at HERA.

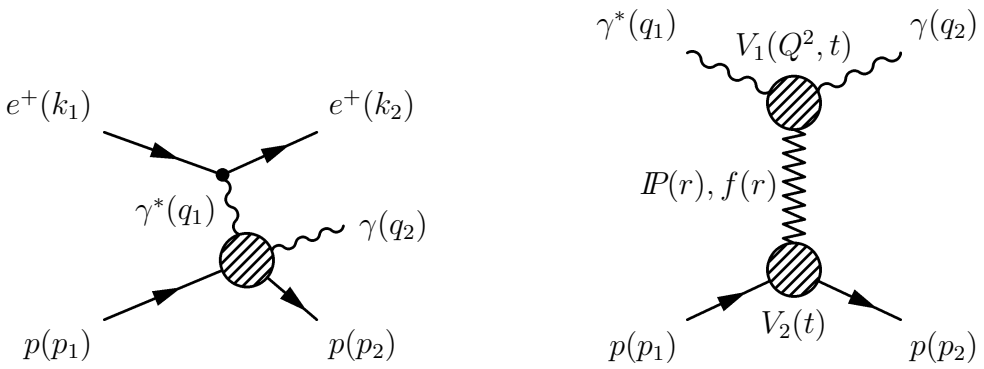


Fig. 1: *a) Diagram of a DVCS event at HERA; b) DVCS amplitude in a Regge-factorized form.*

The vertex can be considered as a function of the invariants $[Q^2, q_1 \cdot r]$ or $[t, q_1 \cdot r]$. This does not mean that the variables cannot appear separately but it could also happen that $q_1 \cdot r$ become a scaling variable, and consequently the vertex will finally depend on $q_1 \cdot r$ only. It depends on the dynamics of the process and, for the moment, we prefer to keep t, apart from Q^2, as the second independent variable.

The interplay of the Q^2- and t-dependences in the DVCS amplitude was recently discussed in Ref. [5, 6], where the existence of a new, universal variable z was suggested. The basic idea is that Q^2 and t, both having the meaning of the squared mass of a virtual particle (photon or Reggeon), should be treated by means of a variable, defined as

$$z = q_1^2 + t = -Q^2 + t, \tag{1}$$

in the same way as the vector meson mass squared is added to the squared photon virtuality, giving $\tilde{Q}^2 = Q^2 + M_V^2$ in the case of vector meson electroproduction.

In this talk, based on our recent publication [6], we examine an explicit model for DVCS with Q^2- and t-dependences determined by the $\gamma^* P\gamma$ vertex. We suggest the use of the new variable defined in Eq. 1 with its possible generalization to vector meson electroproduction,

$$z = t - (Q^2 + M_V^2) = t - \tilde{Q}^2 \tag{2}$$

or virtual photon (lepton pair) electroproduction,

$$z = t - (Q_1^2 + Q_2^2), \tag{3}$$

where $Q_2^2 = -q_2^2$. However, contrary to Ref. [5], here we introduce the new variable only in the upper, $\gamma^* P\gamma$ vertex, to which the photons couple.

In the next Section we introduce the model. Its viability is supported by the correct photoproduction- ($Q^2 = 0$) and DIS- ($Q^2 > 0$ and $t \to 0$) limits and by the fits to the data.

2 The model

According to Fig. 1b, this DVCS amplitude can be written as

$$A(s, t, Q^2)_{\gamma^* p \to \gamma p} = -A_0 V_1(t, Q^2) V_2(t) (-is/s_0)^{\alpha(t)}, \tag{4}$$

where A_0 is a normalization factor, $V_1(t, Q^2)$ is the $\gamma^* P\gamma$ vertex, $V_2(t)$ is the pPp vertex and $\alpha(t)$ is the exchanged Pomeron trajectory, which we assume to be logarithmic:

$$\alpha(t) = \alpha(0) - \alpha_1 \ln(1 - \alpha_2 t). \tag{5}$$

(Here we consider only the helicity conserving amplitude.)

Such a trajectory is nearly linear for small $|t|$, thus reproducing the forward cone of the differential cross section, while its logarithmic asymptotics provides for the large-angle scaling behavior, typical of hard collisions at small distances, with power-law fall-off in $|t|$, obeying quark counting rules. We are referring to the dominant Pomeron contribution plus a secondary trajectory, e.g. the f-Reggeon. Although we are aware of the importance of this subleading contribution at HERA energies, nevertheless we cannot afford the duplication of the number of free parameters, therefore we include it effectively by rescaling the parameters. Ultimately, the Pomeron and the f-Reggeon have the same functional form, differing only by the values of their parameters.

For convenience, and following the arguments based on duality (see Ref. [8] and references therein), the t dependence of the pPp vertex is introduced via the $\alpha(t)$ trajectory: $V_2(t) = e^{b\alpha(t)}$ where b is a parameter. A generalization of this concept will be applied also to the upper, $\gamma^* P\gamma$ vertex by introducing the trajectory

$$\beta(z) = \alpha(0) - \alpha_1 \ln(1 - \alpha_2 z), \tag{6}$$

where the value of the parameter α_2 may be different in $\alpha(t)$ and $\beta(z)$ (a relevant check will be possible when more data will be available). Hence the scattering amplitude (6), with the correct signature, becomes

$$A(s,t,Q^2)_{\gamma^* p\to\gamma p} = -A_0 e^{b\alpha(t)} e^{b\beta(z)} (-is/s_0)^{\alpha(t)} = -A_0 e^{(b+L)\alpha(t)+b\beta(z)}, \tag{7}$$

where $L \equiv \ln(-is/s_0)$.

From Eq. (7) the slope of the forward cone is

$$B(s,Q^2,t) = \frac{d}{dt}\ln|A|^2 = 2\left[b + \ln\left(\frac{s}{s_0}\right)\right]\frac{\alpha'}{1-\alpha_2 t} + 2b\,\frac{\alpha'}{1-\alpha_2 z}, \tag{8}$$

which, in the forward limit, $t = 0$ reduces to

$$B(s,Q^2) = 2\left[b + \ln\left(\frac{s}{s_0}\right)\right]\alpha' + 2b\,\frac{\alpha'}{1+\alpha_2 Q^2}. \tag{9}$$

Thus, the slope shows shrinkage in s and antishrinkage in Q^2.

3 Photoproduction- and DIS limits

In the $Q^2 \to 0$ limit the Eq. (7) becomes

$$A(s,t) = -A_0 e^{2b\alpha(t)} (-is/s_0)^{\alpha(t)}, \tag{10}$$

where we recognize a typical Regge-behaved photoproduction (or, for $Q^2 \to m_H^2$, on-shell hadronic (H)) amplitude. The related deep inelastic scattering structure function is recovered by setting $Q_2^2 = Q_1^2 = Q^2$ and $t = 0$, to get a typical elastic virtual forward Compton scattering amplitude:

$$A(s,Q^2) = -A_0 e^{b(\alpha(0)-\alpha_1\ln(1+\alpha_2 Q^2))} e^{(b+\ln(-is/s_0))\alpha(0)} \propto -(1+\alpha_2 Q^2)^{-\alpha_1}(-is/s_0)^{\alpha(0)}. \tag{11}$$

For not too large Q^2 the contribution from longitudinal photons is small (it vanishes for $Q^2 = 0$). Moreover, at high energies, typical of the HERA collider, the amplitude is dominated by the helicity conserving Pomeron exchange and, since the final photon is real and transverse, the initial one is also transverse - to the extent that helicity is conserved. Hence the relevant structure function is F_1 that, at leading order, is related to F_2 by the Callan-Gross relation.

For $t = 0$ (with $x \approx Q^2/s$, valid for large s), the structure function assumes the form:

$$F_2(s, Q^2) \approx \frac{(1-x)Q^2}{\pi\alpha_e} \Im A(s, Q^2)/s, \tag{12}$$

where α_e is the electromagnetic coupling constant and the normalization is $\sigma_t(s) = \frac{4\pi}{s}\Im A(s, Q^2)$. It has the correct (required by gauge invariance) $Q^2 \to 0$ limit and obeys Bjorken scaling at large enough s and Q^2.

The model fails at large Q^2, where Bjorken scaling is known to be badly violated, and Regge behavior should be replaced by (or appended with) the DGLAP evolution, as shown, for example, in Ref. [10]. An explicit model interpolating between Regge behavior at small- and intermediate Q^2 and the approximate solution of the DGLAP equation at large Q^2 was developed in Ref. [11]. In any case, a "global fit" to DVCS and DIS data would require also the inclusion of both the longitudinal and transverse photons.

4 Fits to the $ep \to e\gamma p$ data; DIS

A standard procedure for the fit to the HERA data on DVCS [3, 4] based on Eq. (7) has been performed in [6].

To avoid the introduction of too many parameters, given the limited number of experimental data points, we used a single Reggeon term, as already discussed in Sec. 2, which can be treated as an effective Reggeon. The parameters $\alpha(0)$, α_1 and α' have been fixed to 1.25, 1.0 and 0.38 GeV^{-2}, respectively and the values of the fitted parameters A_0 and b, described in Eq. (7) are listed in Table 1. The value of α' has been determined in an exploratory fit with this parameter left free to vary between 0.2 and 0.4 GeV^{-2}.

The ZEUS measurements have been rescaled to the W and Q^2 values of the H1 measurements. The mean value of $|t|$ has been fixed to 0.17 GeV^2 according with the H1 measurements of the differential cross-section in the range (0.1-0.8)GeV^2 for H1 [3] taking into account the value 6.02GeV^{-2} for the slope B as determined by the experiment.

parameter	σ_{DVCS} vs Q^2	σ_{DVCS} vs t	σ_{DVCS} vs W
$\|A_0\|^2$	0.08 ± 0.01	0.11 ± 0.24	0.06 ± 0.01
b	0.93 ± 0.05	1.04 ± 0.91	1.08 ± 0.10
$\chi^2/ndof$	0.57	0.15	1.15

Table 1: *The values of the fitted parameters quoted in Eq. (7).*

The results of the fits to the HERA data on DVCS are shown in Fig. 2. The cross-section $\sigma(\gamma^* p \to \gamma p)$ as a function of Q^2 and $W = \sqrt{s}$ are presented respectively in Fig. 2a and Fig. 2b. The differential cross-section $d\sigma(\gamma^* p \to \gamma p)/dt$, given by

$$\frac{d\sigma}{dt}(s, t, Q^2) = \frac{\pi}{s^2}|A(s, t, Q^2)|^2, \tag{13}$$

is presented in Fig. 2c.

The quality of the fits is satisfactory; in particular our model fits rather well the cross-sections as a function of Q^2 and the cross-section differential in t. Although the present HERA

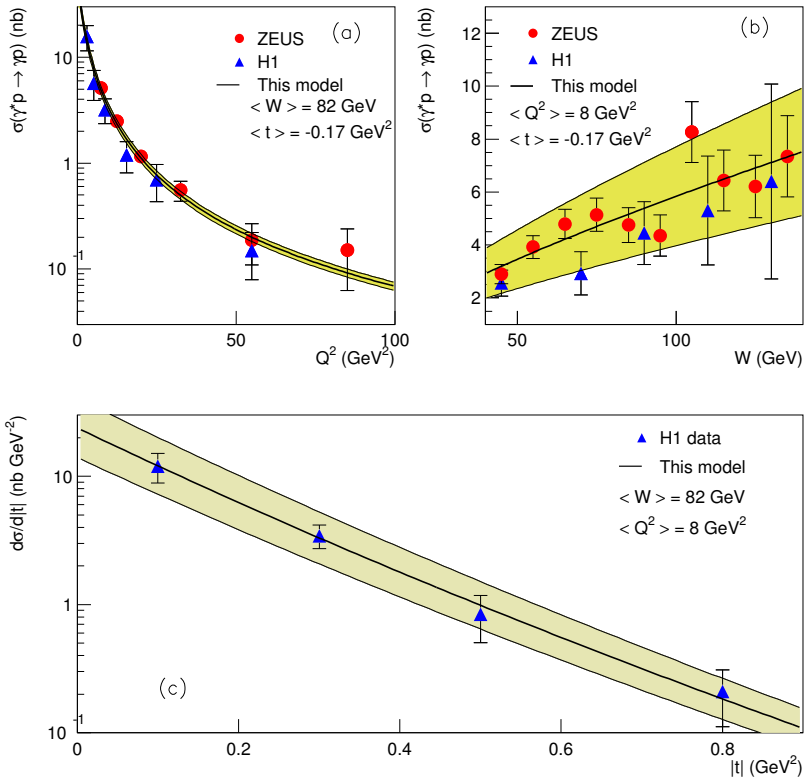


Fig. 2: *The $\gamma^* p \to \gamma p$ cross section as a function of Q^2 (a), of W (b) and the cross section differential in t (c) measured by the H1 and ZEUS experiments [3, 4].*

data on DVCS are well within the "soft" region, the model potentially is applicable for much higher values of $|t|$, dominated by hard scattering.

5 Conclusions and discussion

The model may have two-fold applications. On one hand, it can be used by experimentalists as a guide. The fits to the data could be improved, when more data are available, by accounting for the Pomeron and f-Reggeon contributions separately as well as by using expressions for Regge trajectories which take into account analyticity and unitarity. On the other hand, it can be used to study various extreme regimes of the scattering amplitude in all the three variables it depends on. For that purpose, however, the transition from Regge behavior to QCD evolution at large Q^2 should be accounted for. A formula interpolating between the two regimes (Regge pole

and asymptotic QCD evolution) was proposed in Ref. [11] for $t = 0$ only. Its generalization to non zero t values is possible by applying the ideas and the model presented in this paper. The applicability of the model in both soft and hard domains can be used to learn about the transition between perturbative (QCD) and non-perturbative (Regge poles) dynamics.

Independently of the pragmatic use of this model as a instrument to guide experimentalists, given its explicit form, it can be regarded also as an explicit realization of the corresponding principle of exclusive-inclusive connection in various kinematical limits.

Last but not least, the simple and feasible model of DVCS presented in this paper can be used to study general parton distributions (GPD). The presence of the Regge phase in our model can be used for restoring the correct phase of the amplitude, for which the interference experiments (with Bethe-Heitler radiation) are designed.

References

[1] F.M. Dittes, D. Mueller, D. Robaschik, B. Geyer and J. Horejsi, Phys. Lett. B 1988, **209**, 325;
D. Mueller, D. Robaschik, B. Geyer, F. M. Dittes and J. Horejsi, Fortsch. Phys. 1994, **42**, 101.

[2] X. Ji, Phys. Rev. Lett. 1997, **78**, 610; A.V. Radyushkin, Phys. Lett. B 1996, **380**, 417; M.Diehl, Phys. Rept. 2003 **388**, 41.

[3] H1 Coll.: A. Aktas et al., Eur. Phys. J. C, 2005, **44**, 1.

[4] ZEUS Coll.: S. Chekanov et al., Phys. Lett. B, 2003, **573**, 46.

[5] R. Fiore, L. Jenkovszky, V. Magas, and A. Prokudin, Interplay between Q^2- and $t-$ dependences in deeply virtual Compton scattering, In the Proceedings of the Crimean conference *New Trends in High-Energy Physics*, Yalta, 10-17 September 2005.

[6] M. Capua *et al.*, Phys. Lett. B 2007, **645**, 161.

[7] R. Fiore, L.L. Jenkovszky, V.K. Magas, and F. Paccanoni, Phys. Rev. D 1999, **60**, 116003.

[8] L.L. Jenkovszky, Rivista Nuovo Cim. 1987, **10**, 1; M. Bertini et al. *ibid* **19** (1996) 1.

[9] R. Fiore, L.L. Jenkovszky, F. Paccanoni and A. Prokudin, Phys. Rev. D 2003, **68**, 014005.

[10] L. Csernai et. al. Eur. Phys. J. C 2002, **24**, 205.

[11] P. Desgrolard, L.L. Jenkovszky, E. Paccanoni, Eur. Phys. J. C 1999, **7**, 263.

Glue drops inside hadrons

B.Z. Kopeliovich[1]*, B. Povh*[2]*,*[†] *Ivan Schmidt*[1]
[1]Universidad Tecnica Federico Santa Maria, Valparaiso, Chile, and
Institut für Theoretische Physik der Universität, Heidelberg, Germany
[2]Max-Planck-Institut für Kernphysik, 69029 Heidelberg, Germany

Abstract

We present experimental evidences for the existence of a semi-hard scale in light hadrons. This includes the suppression of gluon radiation that is seen in high mass hadron diffraction; the weak energy dependence of hadronic total cross sections; the small value of the Pomeron trajectory slope measured in photoproduction of J/Ψ; shortage of gluons in the proton revealed by an unusual behavior of the proton structure function in the soft limit. All these observations suggest that gluons in hadrons are located within spots of a small size relative to the confinement radius.

1 Introduction

There is growing theoretical and experimental support leading towards the existence of a non-perturbative scale smaller than the usual $1/\Lambda_{QCD} \sim 1\,$fm, and which is related to the gluonic degrees of freedom. First, an analysis of hadronic matrix elements of the gluonic contribution to the energy momentum tensor, using the QCD sum rules approach, gives a value of 0.3 fm for the radius of the corresponding form factor [1]. From the lattice side, numerical simulations of the gluon two point correlation function turn out a value of also $0.2 - 0.3\,$fm for the correlation length [2], and the energy of the QCD string appears concentrated in a tube of radius $0.3\,$fm in the transverse direction [3]. On the other side, it has been shown that the instanton radius peaks approximately at 1/3 fm [4]. Furthermore, high statistics data for diffractive gluon bremsstrahlung in hadronic collisions is difficult to explain unless gluons in the proton have transverse momenta as high as about 0.7 GeV [5]. This has been confirmed by studies of diffractive parton distributions, which concluded that they have a rather small transverse size [6]. What actually happens is that the smallness of the gluon clouds slows down Gribov diffusion of the gluons in transverse plane, and this results in a small slope of the Pomeron trajectory in hard reactions [7], in agreement with data. More arguments in favor of small gluonic spots coming from DIS can be found in [8]. Some of these results have been corroborated by recent studies of the spatial distribution of gluons in the transverse direction at small x [9]. Here we overview the available experimental evidences for the presence of a semihard scale in hadronic structure.

[†] speaker

2 Gluon radiation is suppressed

If gluons in hadrons are located within small spots of radius r_0, they have enlarged transverse momenta $q_T \sim 1/r_0$. Such gluons cannot be resolved by soft interactions and be shaken off, which means that the bremsstrahlung cross section should be suppressed compared to perturbative estimates.

However, in the case of soft inelastic collisions followed by multiparticle production the events with or without gluon radiation look alike. In both cases the produced particles build a plateau in rapidity, and then it is difficult to find any definite signature of the radiated gluons.

Diffraction offers an exclusive possibility to identify gluon radiation. A high-energy hadron can dissociate diffractively either via excitation of the valence quark skeleton, or by radiating gluons. These two mechanisms are characterized by different dependence on the effective mass, M_X, of the excitation,

$$\frac{d\sigma(hp \to Xp)}{dM_X^2} = \begin{cases} \frac{1}{M_X^3} & \text{excitation of the quark skeleton} \\ \frac{1}{M_X^2} & \text{diffractive gluon bremsstrahlung} \end{cases} \tag{1}$$

The M_X-dependence at large M_X correlates with the spin of the slowest particle produced in the excitation. Only a vector particle, i.e. a gluon, can provide the $1/M_X^2$ dependence.

Thus, one can single out the cross section of diffractive gluon radiation from the large mass tail of the M_X-distribution. An analysis [10] of diffractive data shows that gluon radiation is amazingly weak. In order to understand that one can interpret diffraction in terms of the Pomeron-proton total cross section, as is shown in Fig. 1. If we treat the Pomeron like a gluonic

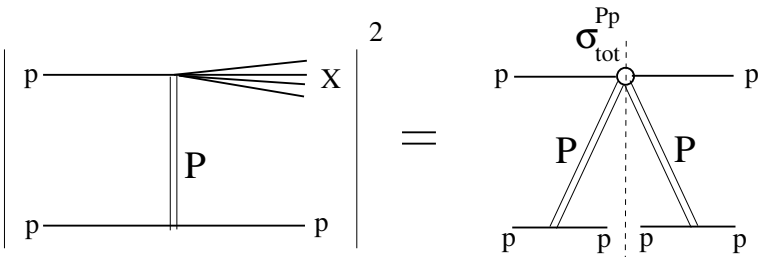


Fig. 1: The cross section of diffractive excitation of a proton expressed in terms of the total Pomeron-proton cross section.

dipole, one may expect a cross section $9/4$ times larger than for a $\bar{q}q$ dipole. Comparing with the pion-proton cross section, say $25\,$mb, one arrives at the estimate of about $50\,$mb. However, data suggest quite a smaller value, about $2\,$mb. A straightforward explanation for such a dramatic disagreement would be a much smaller size of the gluonic dipole (Pomeron) compared to the quark-antiquark dipole (pion). Thus, one concludes that gluons should be located within small spots in the proton.

Although it is not quite rigorous, one might try to estimate the diffractive radiation cross section perturbatively, and in this case the result exceeds data by more than an order of magnitude. To reduce the cross section down to the observed value one should assume that the mean quark-gluon separation is as small as $r_0 = 0.3\,$fm [5]. With such a modified quark-gluon light-cone

distribution function, the effective triple-Pomeron coupling has the form [5],

$$G_{3\mathbb{P}}(0) \equiv (1-x_F)^{\alpha_{\mathbb{P}}(0)} \left.\frac{d\sigma_{sd}(pp\to pX)}{dx_F\, dp_T^2}\right|_{p_T=0} = \frac{81\alpha_s\sigma_0}{(16\pi)^2}\,\ln\left[\frac{2(r_0^2+R_0^2)^2}{R_0^2(2r_0^2+R_0^2)}\right]. \qquad (2)$$

Here we assume that $1 \gg 1-x_F \gg s_0/s$, where $s_0 \sim 1$ GeV^2. The energy dependent parameters $\sigma_0(s)$ and $R_0(s)$ controlling the shape of the universal dipole cross section [11] are defined in [5]. With $r_0 = 0.3$ fm, the triple-Pomeron coupling eq. (2) agrees with the result of the triple-Regge analysis [10] of single diffractive data.

3 Energy dependence of hadronic cross sections is weak

It is well known that hadronic cross sections rise with energy approximately as s^ϵ, where the exponent is quite small, $\epsilon \approx 0.1$. What is the origin of this small number? We do not expect any small parameters in the soft regime of strong interactions.

This problem is closely related to the topic of the previous section. In fact, the energy dependence is driven by gluon radiation which turns out to be suppressed. Before we saw a manifestation of this effect in diffraction, now in the total inelastic cross section.

Without gluon radiation the geometric cross section of two hadrons would be constant, since their transverse size is Lorentz invariant, i.e. is energy independent. The phase space for one gluon radiation is proportional to $\ln(s)$, so multigluon radiation leads to powers of $\ln(s)$ in the cross section. The calculations performed in [12] confirm this. The hadronic cross section was found to have the following structure,

$$\sigma_{tot} = \sigma_0 + \sigma_1 \left(\frac{s}{s_0}\right)^\Delta, \qquad (3)$$

where σ_0 is the energy independent term related to hadronic collisions without gluon radiation. The second term in (3) is the contribution of gluon bremsstrahlung to the total cross section. Here the parameter σ_1 is expected to be small due to the smallness of the gluonic spots. Indeed, it was found in [12] that $\sigma_1 = 27\,C\,r_0^2/4$, where factor $C \approx 2.4$ is related to the behavior of the dipole-proton cross section, calculated in Born approximation at small separations, $\sigma(r_T) = Cr_T^2$ at $r_T \to 0$.

The energy dependence of the second term in (3) was found to be rather steep, $\Delta = 4\alpha_s/3\pi = 0.17$. This exponent seems to be too large compared to the experimentally measured $\epsilon \approx 0.1$. There is, however, no contradiction due to the presence of the large energy independent term in (3). Approximating the cross section (3) by a simple power dependence on energy, the effective exponent reads,

$$\epsilon = \frac{\Delta}{1+\sigma_0/\sigma_1\,(s/s_0)^{-\Delta}} \qquad (4)$$

So, one should expect a growing steepness of the energy dependence for the total cross section. One can estimate the value of r_0 demanding the effective exponent to be $\epsilon \approx 0.1$ in the energy range of fixed target experiments, say at $s \sim 1000$ GeV^2. With $\sigma_0 = 40$ mb found in [12] one gets $r_0 = 0.3$ fm.

Thus, the observed slow rise of the total hadronic cross sections provides another evidence for the existence of small gluonic spots with transverse size $r_0 \sim 0.3\,\mathrm{fm}$.

One may expect a steeper energy dependence for heavier flavors. Indeed, for J/Ψ-proton scattering σ_0 is so small, that $\epsilon \approx \Delta$. Indeed, data for J/Ψ photoproduction from HERA [13] show that $\epsilon \approx 0.2$. One should be careful, however, interpreting the data within the vector dominance model [14], and remember that Eq. (3) was derived assuming that r_0 is much smaller than the hadronic size, otherwise interferences should be included.

4 Diffractive cone shrinks with energy slowly

The prediction of a shrinkage of the diffraction cone has been one of the first achievements of the Regge theory. Indeed, data show that the elastic slope in hadronic collisions rises with energy as, $B_{el}(s) = B_0 + 2\alpha'_{I\!P}\,\ln(s/s_0)$, where $\alpha'_{I\!P} \approx 0.25\ \mathrm{GeV}^{-2}$. This is about four times smaller than in binary processes mediated by other Reggeons, $\alpha'_{I\!R} \approx 1\,\mathrm{GeV}^{-2}$. Why?

The diffractive cone shrinkage is usually related to Gribov diffusion of gluons in the transverse plane. If each "step" in impact parameters, $\Delta b^2 = r_0^2$, is small, the diffusion should proceed slowly. Indeed, a rather small value of the Pomeron trajectory slope was predicted in [12],

$$\alpha'_{I\!P} = \frac{1}{2}\,\frac{dB_{el}}{d\ln(s/s_0)} = \frac{\alpha_s}{3\pi}\,r_0^2 = 0.1\,\mathrm{GeV}^{-2}\ . \tag{5}$$

This seems to be too small, in strong contradiction with value $0.25\,\mathrm{GeV}^{-2}$ known from data for the elastic slope. One may wonder, why the same model [12] which predicts (5) describes well data for elastic slope, as is demonstrated in Fig. 2. The relatively large value of $\alpha'_{I\!P}$, turns out to result from unitarity saturation. Indeed, the elastic differential cross section (actually the amplitude) Fourier transformed to impact parameter representation (see details in [12]) demonstrate unitarity saturation at small impact parameters. In spite of the observed rise of the total cross section with energy, there is no room for further growth at small impact parameters, only the amplitudes of peripheral collisions rise with energy. This leads to a rising with energy radius of interaction directly related to the elastic slope. Thus, a substantial part of the observed energy dependence of the elastic slope and of the effective $\alpha'_{eff} = 0.25\,\mathrm{GeV}^{-2}$ is related to saturation of the unitarity bound. How to disentangle the two effects?

To get rid of unitarity corrections one can consider the interaction of a small dipole with a proton. For example photoproduction of a heavy quarkonium [7], or high Q^2 electroproduction of ρ. Then, the elastic amplitude is too small to be affected by unitarity (absorptive) corrections, and the energy dependence of the slope must be solely due to the rise of the gluon clouds, i.e. Gribov diffusion. This expectation of [12] was nicely confirmed in elastic photoproduction $\gamma + p \to J/\Psi + p$ measured by the ZEUS experiment [13] which found $\alpha'_{I\!P} = 0.115 \pm 0.018\,\mathrm{GeV}^{-2}$. The data and fit are depicted in Fig. 3

5 There is a shortage of gluons at low scale

As far as gluons are located within small spots, it is difficult to resolve them at low scale, $Q^2 < 4/r_0^2$. With poor resolution the proton looks like a 3-quark system containing no gluons. At the same time, no changes happen at higher Q^2 which resolve distances much smaller than the

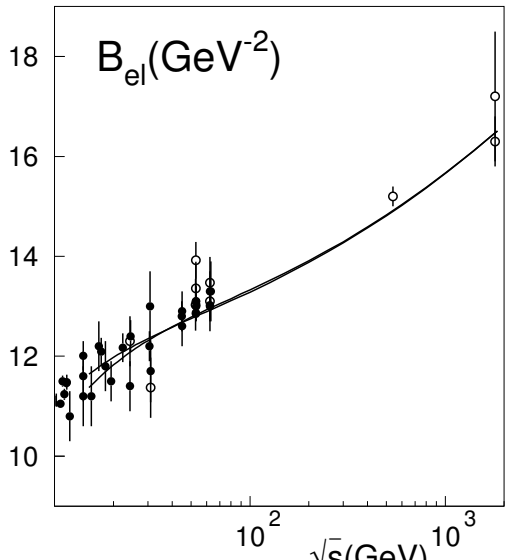


Fig. 2: Elastic slope for $pp/\bar{p}p$ (bottom/upper curves) collisions, calculated in [12] with the small Pomeron slope according to (5). The references to the data can be found in [12].

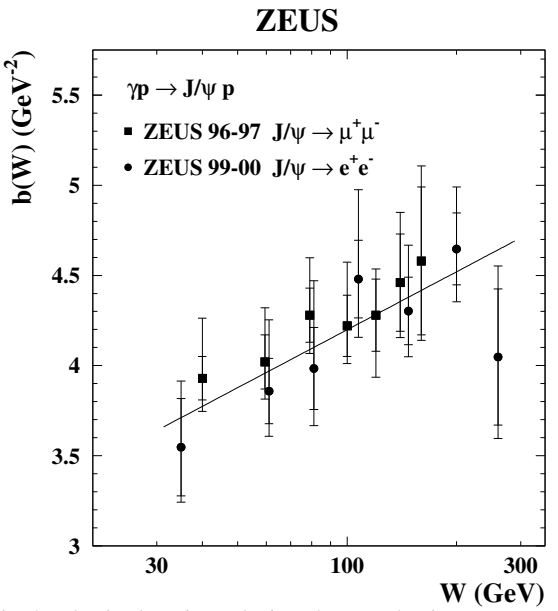


Fig. 3: Elastic slope in exclusive photoproduction $\gamma + p \to J/\Psi + p$. Data are from the ZEUS experiment [13]. The solid curve is a fit with $\alpha'_{\mathbf{I\!P}} = 0.115 \pm 0.018\,\mathrm{GeV}^{-2}$, in good agreement with (5).

size of gluonic spots. In this regime the gluon density is rising toward smaller x unless related values of Q^2 become too low to resolve the spots. This explains the ZEUS data [15] depicted in Fig. 4 for logarithmic Q^2 derivative of the structure function. This derivative suddenly drops at Q^2 below few GeV^2 showing that parton distributions are frozen below this scale, no evolution happens due to lack of gluons.

Summarizing, a comprehensive list of experimental evidences for existence of two scales in the hadronic structure is currently available. Many of them directly indicate a small gluonic spot structure of light hadrons.

The full size paper on the "Two Scales of Hadron Structure" is to be found in arXiv.org/abs/0708.3636.

Acknowledgments: We are thankful to Hans-Jürgen Pirner for helpful discussions. This work was supported in part by Fondecyt (Chile) grants numbers 1030355 and 1050519, and by DFG (Germany) grant PI182/3-1.

References

[1] V.M. Braun, P. Górnicki, L. Mankiewicz, Phys. Lett. B302 (1993) 291.

[2] M. D'Elia, A. Di Giacomo, Phys. Lett. B408 (1997) 315.

[3] G.S. Bali, Int. Conference in Quark Confinement and Hadorn Spectrum, Newport News (Virginia, USA), June 1998.

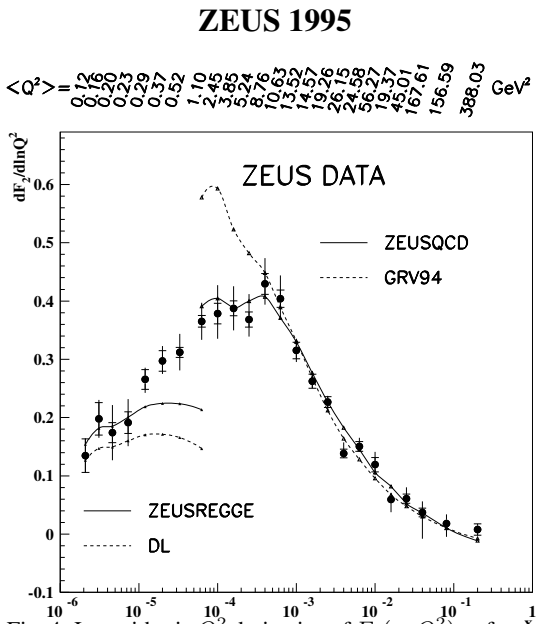


Fig. 4: Logarithmic Q^2 derivative of $F_2(x, Q^2)$ as function of x and Q^2 [15]. The observed turn over and fall at small Q^2 indicates at shortage of gluons.

[4] E.V. Shuryak, Phys. Lett. B486 (2000) 378.

[5] B.Z. Kopeliovich, A. Schäfer, and A.V. Tarasov Phys. Rev. D62 (2000) 054022.

[6] F. Hautmann, D.E. Soper, Phys. Rev. D63 (2000) 011501.

[7] B.Z. Kopeliovich and B. Povh, J. Phys. G30 (2004) S999.

[8] E. Shuryak and I. Zahed, Phys. Rev. D69 (2004) 014011.

[9] M.I. Strikman and C. Weiss, Phys. Rev. D69 (2004) 054012.

[10] Yu.M. Kazarinov, B.Z. Kopeliovich, L.I. Lapidus, and I.K. Potashnikova, Sov. Phys. JETP **70** (1976) 1152.

[11] B.Z. Kopeliovich, L.I. Lapidus, and A.B. Zamolodchikov, Sov. Phys. JETP Lett. **33**, 595 (1981); Pisma v Zh. Exper. Teor. Fiz. **33**, 612 (1981).

[12] B.Z. Kopeliovich, I.K. Potashnikova, B. Povh, and E. Predazzi, Phys. Rev. Lett. 85 (2000) 507; Phys. Rev. D63 (2001) 054001.

[13] ZEUS Collaboration, S. Chekanov et al., Eur. Phys. J. C24 (2002) 345.

[14] J. Hüfner and B.Z. Kopeliovich, Phys. Lett. B426 (1998) 154.

[15] ZEUS Collaboration, J. Breitweg et al., Eur. Phys. J. C7 (1999) 609.

Studying QCD factorizations in exclusive $\gamma^*\gamma^* \to \rho_L^0\rho_L^0$

S. Wallon[1]†, *B. Pire*[2], *M. Segond*[1], *L. Szymanowski*[3]
[1] LPT, Université Paris-Sud, CNRS, Orsay, France,
[2] CPHT, École Polytechnique, CNRS, Palaiseau, France,
[3] IFPA, Université de Liège, Belgium and SINS, Warsaw, Poland

Abstract
The exclusive process $e^+\,e^-\to e^+\,e^-\,\rho_L^0\,\rho_L^0$ allows to study various dynamics and factorization properties of perturbative QCD. At moderate energy, we demonstrate how collinear QCD factorization emerges, involving generalized distribution amplitudes (GDA) and transition distribution amplitudes (TDA). At higher energies, in the Regge limit of QCD, we show that it offers a promising probe of the BFKL resummation effects to be studied at the International Linear Collider (ILC).

1 Introduction: Exclusive processes at high energy QCD

1.1 Motivation

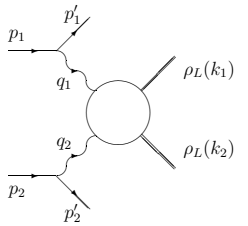


Figure 1: Amplitude for $e^+\,e^-\to e^+\,e^-\,\rho_L^0\,\rho_L^0$.

Since a decade, there has been much progress in experimental and theoretical understanding of hard exclusive processes, including Deeply Virtual Compton Scattering (involving Generalized Parton Distributions) and $\gamma\gamma$ scattering in fixed target $e^\pm p$ (HERMES, JLab, ...) experiments and at colliders, such as $e^\pm p$ (H1, ZEUS) or e^+e^- (LEP, Belle, BaBar, BEPC). Meanwhile, the hard Pomeron [1] concept has been developped and tested at inclusive (total cross-section), semi-inclusive (diffraction, forward jets, ...) and exclusive (meson production) level, for colliders at very large energy: $e^\pm p$ (HERA), $p\bar{p}$ (Tevatron) and e^+e^- (LEP, ILC). Here we focus on

$$\gamma^*\gamma^* \to \rho_L^0\rho_L^0 \tag{1}$$

with both γ^* *hard*, through $e^+e^-\to e^+e^-\rho_L^0\rho_L^0$ with double tagged outoing leptons (Fig.1). It is a beautiful theoretical laboratory for investigating different *dynamics* (collinear, multiregge) and *factorization* properties of high energy QCD: it allows a perturbative study of GPD-like objects at moderate s and of the hard Pomeron at asymptotic s.

1.2 From DIS to GDA and TDA in collinear factorization

Deep Inelastic Scattering, as an inclusive process, gives access to the forward amplitude through the optical theorem. Structure functions can be written as convolution of (hard) Coefficient Functions with (soft) Parton Distributions. Deeply Virtual Compton Scattering and meson electroproduction on a hadron $\gamma^* h \to \gamma\, h,\, h'\, h$, as exclusive processes, give access to the full amplitude,which is a convolution, for $-t \ll s$, of a (hard) CF with a (soft) Generalized Parton Distribution [2,3]. Extensions were made from GPDs. First [2,4], the crossed process $\gamma^*\,\gamma \to h\,h'$ can be factorized, for $s \ll -t$, as a convolution of a (hard) CF with a (soft) Generalized Distribution

† speaker

Amplitude describing the correlator between two quark fields and a two hadron state. Second [5], starting from meson electroproduction and performing $t \leftrightarrow u$ crossing, and then allowing the initial and the final hadron to differ, we write the amplitude for the process $\gamma^* h \to h"\, h'$ as a convolution of a (hard) CF with a (soft) Transition Distribution Amplitude describing the $h \to h'$ transition and with a (soft) Distribution Amplitude (describing $q\bar{q}h"$ vertex).

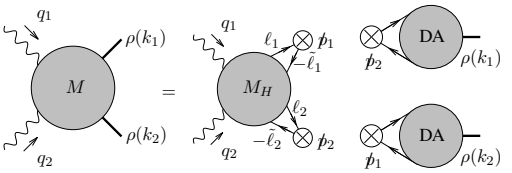


Figure 2: $\gamma^*(Q_1)\gamma^*(Q_2) \to \rho_L^0(k_1)\rho_L^0(k_2)$ with collinear factorization in $q\bar{q}\rho$ vertices.

We will rely on collinear factorization for our process (1) at each $q\bar{q}\rho$ vertex only. At high Q_i^2, each of the two quarks making the ρ mesons are almost collinear, flying in the light cone directions p_1 and p_2 (used as Sudakov vectors), and their momentum read $\ell_i \sim z_i\, k_i$ and $\tilde{\ell}_i \sim \bar{z}_i\, k_i$. The amplitude M is factorized as a convolution of a hard part M_H with two ρ_L^0 DAs (see Fig.2), defined as matrix elements of non local quarks fields correlator on the light cone[1] [2]

$$\langle \rho_L^0(k)|\bar{q}(x)\gamma^\mu q(0)|0\rangle = \frac{f_\rho}{\sqrt{2}}\, k^\mu \int_0^1 dz\, e^{iz(kx)}\phi(z)\ , \qquad \text{for } \ q = u, d\ .$$

2 Computation at fixed W^2

2.1 Direct calculation

We compute [6] the amplitude M following the Brodsky, Lepage approach [7]. At Born order (quark exchange) and in the forward case for simplicity, the amplitude M reads[3],

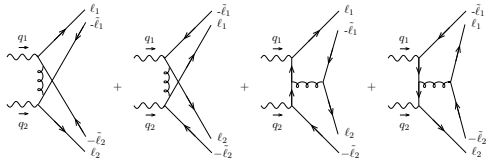


Figure 3: Diagrams contributing to M_H for γ_L^*.

$$M = T^{\mu\,\nu}\epsilon_\mu(q_1)\epsilon_\nu(q_2)\ ,\ T^{\mu\,\nu} = \frac{1}{2} g_T^{\mu\,\nu}\ T^{\alpha\,\beta} g_{T\,\alpha\,\beta} + \left(p_1^\mu + \frac{Q_1^2}{s} p_2^\mu\right)\left(p_2^\nu + \frac{Q_2^2}{s} p_1^\nu\right)\frac{4}{s^2} T^{\alpha\,\beta} p_{2\,\alpha}\, p_{1\,\beta}\ .$$

In the case of longitudinally polarized photons, their polarization vectors read, with $s \equiv 2\, p_1 \cdot p_2$,

$$\epsilon_\parallel(q_1) = \frac{1}{Q_1} q_1 + \frac{2Q_1}{s} p_2 \quad \text{and} \quad \epsilon_\parallel(q_2) = \frac{1}{Q_2} q_2 + \frac{2Q_2}{s} p_1\ . \tag{2}$$

Due to QED gauge invariance, the first terms in RHS of (2) do not contribute. In the forward case discussed here, the number of diagrams then reduces to 4, as illustrated in Fig.3. They result into

$$T^{\alpha\,\beta} p_{2\,\alpha}\, p_{1\,\beta} = -\frac{s^2 f_\rho^2 C_F e^2 g^2 (Q_u^2 + Q_d^2)}{8 N_c Q_1^2 Q_2^2} \int_0^1 dz_1\, dz_2\, \phi(z_1)\, \phi(z_2)$$

$$\times \left\{ \frac{(1 - \frac{Q_1^2}{s})(1 - \frac{Q_2^2}{s})}{(z_1 + \bar{z}_1 \frac{Q_2^2}{s})(z_2 + \bar{z}_2 \frac{Q_1^2}{s})} + \frac{(1 - \frac{Q_1^2}{s})(1 - \frac{Q_2^2}{s})}{(\bar{z}_1 + z_1 \frac{Q_2^2}{s})(\bar{z}_2 + z_2 \frac{Q_1^2}{s})} + \frac{1}{z_2 \bar{z}_1} + \frac{1}{z_1 \bar{z}_2} \right\}. \tag{3}$$

[1] We limit ourselves to longitudinally polarized mesons to avoid potential end-point singularities.

[2] $\phi(z) = 6z(1-z)\,(1 + \sum_{n=1}^{\infty} a_{2n} C_{2\,n}^{3/2}(2z-1))\,.$

[3] $g_T^{\mu\,\nu} = g^{\mu\nu} - \frac{p_1^\mu p_2^\nu + p_1^\nu p_2^\mu}{p_1 \cdot p_2}\,.$

For transversally polarized photons, no simplification occurs and the 12 diagrams give

$$T^{\alpha\,\beta} g_{T\,\alpha\,\beta} = -\frac{e^2(Q_u^2+Q_d^2)\,g^2\,C_F\,f_\rho^2}{4\,N_c\,s}\int_0^1 dz_1\,dz_2\,\phi(z_1)\,\phi(z_2)\left\{2\left(1-\frac{Q_2^2}{s}\right)\left(1-\frac{Q_1^2}{s}\right)\right.$$
$$\times\left[\frac{1}{(z_2+\bar z_2\frac{Q_1^2}{s})^2(z_1+\bar z_1\frac{Q_2^2}{s})^2}+\frac{1}{(\bar z_2+z_2\frac{Q_1^2}{s})^2(\bar z_1+z_1\frac{Q_2^2}{s})^2}\right]+\left(\frac{1}{\bar z_2\,z_1}-\frac{1}{\bar z_1\,z_2}\right)$$
$$\left.\times\left[\frac{1}{1-\frac{Q_2^2}{s}}\left(\frac{1}{\bar z_2+z_2\frac{Q_1^2}{s}}-\frac{1}{z_2+\bar z_2\frac{Q_1^2}{s}}\right)-\frac{1}{1-\frac{Q_1^2}{s}}\left(\frac{1}{\bar z_1+z_1\frac{Q_2^2}{s}}-\frac{1}{z_1+\bar z_1\frac{Q_2^2}{s}}\right)\right]\right\}. \quad (4)$$

The z_i integrations have no end-point singularity (Q_i^2 are non-zero and DAs vanishes at $z_i=0$).

2.2 Interpretation in terms of QCD Factorization

2.2.1 GDA for a transverse photon in the limit $\Lambda_{QCD}^2 \ll W^2 \ll Max(Q_1^2,Q_2^2)$

When W^2 is smaller than the highest photon virtuality, the direct calculation (4) simplifies in[4]

$$T^{\alpha\,\beta} g_{T\,\alpha\,\beta} \approx \frac{C}{W^2}\int_0^1 dz_1\,dz_2\left(\frac{1}{\bar z_1+z_1\frac{Q_2^2}{s}}-\frac{1}{z_1+\bar z_1\frac{Q_2^2}{s}}\right)\left(\frac{1}{\bar z_2\,z_1}-\frac{1}{\bar z_1\,z_2}\right)\phi(z_1)\,\phi(z_2)$$

showing that the hard amplitude M_H can be factorized as a convolution between a hard coefficient function T_H and a GDA_H, itself *perturbatively* computable (Fig.4), extending the results of [8]. This is proven at Born order by computing perturbatively the GDA from its definition

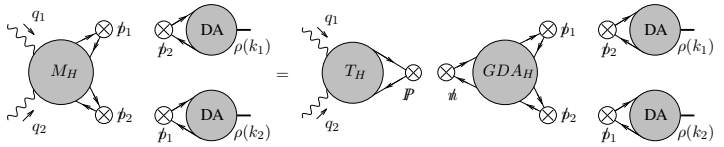


Figure 4: Factorisation of the amplitude in terms of a GDA.

$$\langle\rho_L^0(k_1)\,\rho_L^0(k_2)|\bar q(-\alpha\,n/2)\not n\,\exp\left[ig\int_{-\frac{\alpha}{2}}^{\frac{\alpha}{2}} dy\,n_\nu\,A^\nu(y)\right]q(\alpha\,n/2)|0\rangle$$
$$=\int_0^1 dz\,e^{-i(2z-1)\alpha(nP)/2}\Phi^{\rho_L^0\rho_L^0}(z,\zeta,W^2) \quad (\text{for } Q_1>Q_2,\ P\sim p_1 \text{ and } n\sim p_2)$$

with the kinematics fixed according to Fig.5. W^2 being hard, the GDA can be factorized into Hard part $\otimes$ DA DA (see Fig.6), as

$$\Phi^{\rho_L\rho_L}(z,\zeta\approx 1,W^2) = -\frac{f_\rho^2\,g^2\,C_F}{2\,N_c\,W^2}\int_0^1 dz_2\,\phi(z)\,\phi(z_2)\left[\frac{1}{z\bar z_2}-\frac{1}{\bar z z_2}\right]. \quad (5)$$

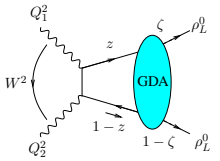


Figure 5: GDA Kinematics.

[4] In this example $\frac{W^2}{Q_1^2}=\frac{s}{Q_1^2}\left(1-\frac{Q_1^2}{s}\right)\left(1-\frac{Q_2^2}{s}\right)\approx 1-\frac{Q_1^2}{s}\ll 1$; we denote $C=\frac{e^2(Q_u^2+Q_d^2)\,g^2\,C_F\,f_\rho^2}{4\,N_c}$

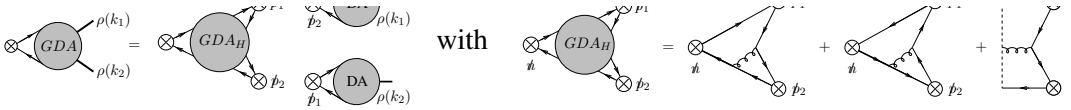


Figure 6: Perturbative GDA factorization.

In forward kinematics, the QCD Wilson line (last term in Fig.6) vanishes. The Born order hard part is (see Fig.7)

$$T_H(z) = -4\,e^2\,N_c\,Q_q^2\,\left(\frac{1}{\bar{z}+z\,\frac{Q_2^2}{s}}-\frac{1}{z+\bar{z}\,\frac{Q_2^2}{s}}\right).$$

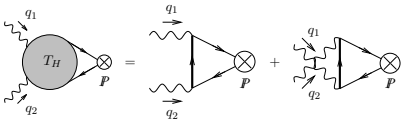


Figure 7: Hard part T_H at lowest order.

2.2.2 TDA for longitudinal photon in the limit $Q_1^2 \gg Q_2^2$ (or $Q_1^2 \ll Q_2^2$)

The amplitude $M = T^{\alpha\,\beta} p_{2\,\alpha}\,p_{1\,\beta}$ (3) can be interpreted in this limit as a convolution $M = TDA \otimes CF \otimes DA$, according to

$$T^{\alpha\,\beta} p_{2\,\alpha} p_{1\,\beta} = -i\frac{C}{2}\int_{-1}^{1} dx \int_{0}^{1} dz_1\,\left[\frac{1}{\bar{z}_1(x-\xi)}+\frac{1}{z_1(x+\xi)}\right]\phi(z_1)$$

$$\times N_c\left[\Theta(1\geq x\geq\xi)\,\phi\left(\frac{x-\xi}{1-\xi}\right)-\Theta(-\xi\geq x\geq -1)\,\phi\left(\frac{1+x}{1-\xi}\right)\right],$$

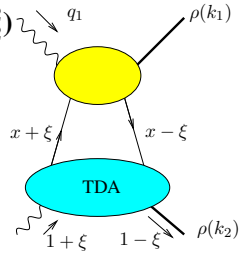


Figure 8: TDA kinematics.

the TDA being defined through the usual GPD kinematics (see Fig.8), with $n_1 = (1+\xi)p_1$ and $n_2 = \frac{p_2}{1+\xi}$, defining x, ξ as momentum fraction along n_2. This factorisation (see Fig.9a) is proven at Born order by computing perturbatively the TDA $\gamma^* \to \rho_L^0$ defined as

$$\int \frac{dz^-}{2\pi s}\,e^{ix(n_2.z)}\,\langle\rho_L^q(k_2)|\bar{q}(-z/2)\,\not{n}_1\,\exp\{-ieQ_q\int_{z/2}^{-z/2} dy_\mu\,A^\mu(y)\}q(z/2)|\gamma^*(q_2)\rangle$$

$$= \frac{e\,Q_q\,f_\rho}{n_2^+}\,\frac{1}{Q_2^2}\,\epsilon_\nu(q_2)\left((1+\xi)n_2^\nu+\frac{Q_2^2}{s(1+\xi)}n_1^\nu\right)\,T(x,\xi,t_{min})\,,$$

where the QED Wilson line is explicitly indicated (QCD Wilson line gives no contribution). Since Q_2^2 hard, the TDA can be factorized (see Fig.9b) as

$$T(x,\xi,t_{min}) \equiv N_c\left[\Theta(1\geq x\geq\xi)\,\phi\left(\frac{x-\xi}{1-\xi}\right)-\Theta(-\xi\geq x\geq -1)\,\phi\left(\frac{1+x}{1-\xi}\right)\right].$$

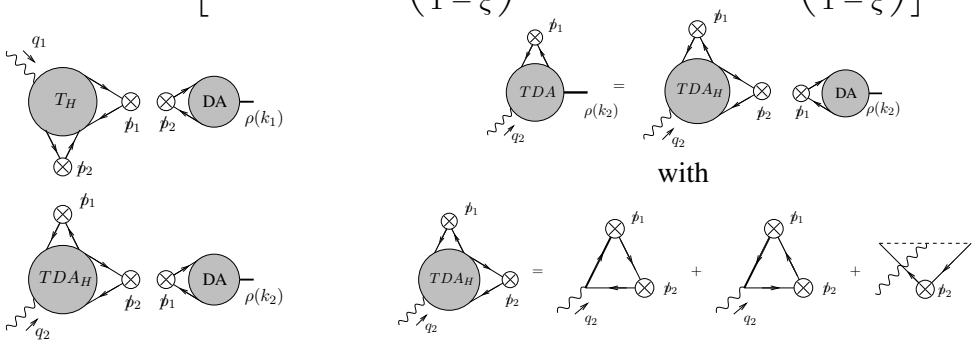


Figure 9: a: Factorization of the amplitude in terms of a TDA. b: Perturbative TDA factorization.

The Hard term reads, at Born order (see Fig.10),

$$T_H(z_1,x) = -i\, f_\rho\, g^2\, e\, Q_q\, \frac{C_F\, \phi(z_1)}{2\, N_c\, Q_1^2} \epsilon^\mu(q_1)$$
$$\times \left(2\xi\, n_{2\,\mu} + \frac{1}{1+\xi} n_{1\,\mu}\right)\left[\frac{1}{z_1(x+\xi-i\epsilon)} + \frac{1}{\bar{z}_1(x-\xi+i\epsilon)}\right],$$

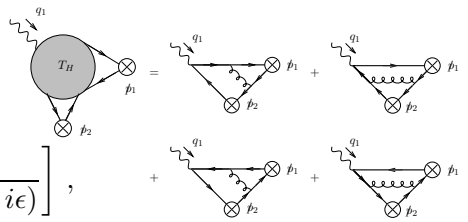


Figure 10: Hard part T_H at lowest order.

3 Computation at large W^2

The dynamics of QCD in the perturbative Regge limit [9] is governed by gluons. BFKL enhancement effects are expected to be important at large rapidity. The exclusive process (1) tests this limit [10–12], for both Q_i^2 *hard* and of the *same order* (to suppress collinear dynamics à la DGLAP [13] and ERBL [14]), giving access to the full non-forward Pomeron structure, in relation with saturation studies, where a full impact parameter picture is needed. Increasing $s_{\gamma^*\gamma^*}$ for fixed values Q_1^2 and Q_2^2 causes transition from the linear to non-linear (saturated) regime.

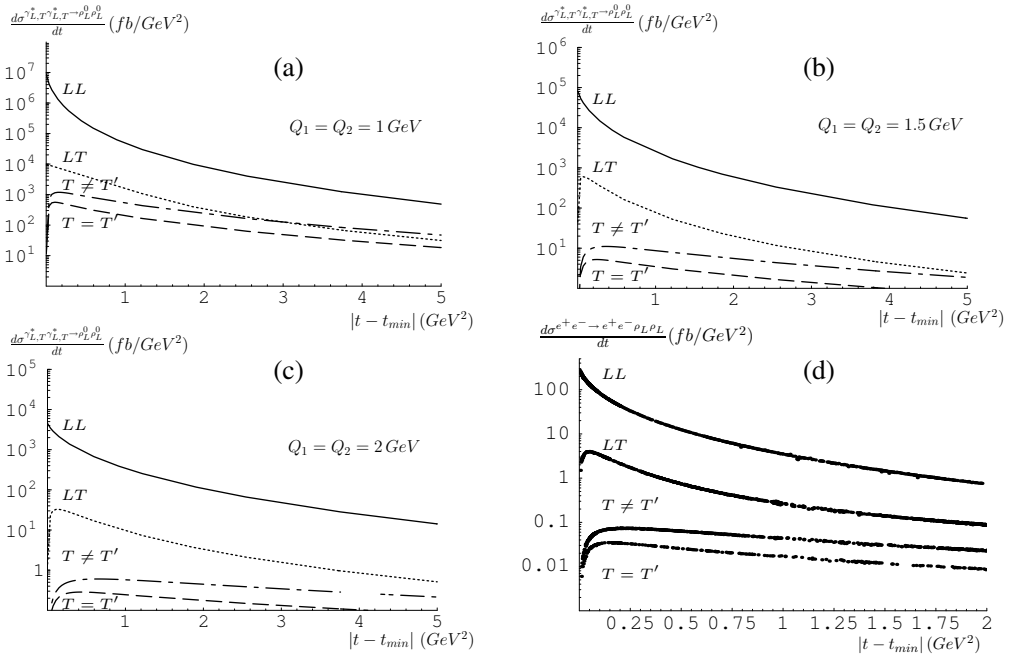


Figure 11: $\gamma^*_{L,T}\gamma^*_{L,T} \to \rho_L^0\ \rho_L^0$ (a,b,c) and $e^+e^- \to e^+e^-\rho_L^0\ \rho_L^0$ (d) differential cross-sections.

When $s_{\gamma^*\gamma^*} \gg -t, Q_1^2, Q_2^2$, we rely on the impact representation which reads, at Born order,

$$\mathcal{M} = is \int \frac{d^2\,\underline{k}}{(2\pi)^4 \underline{k}^2\,(\underline{r}-\underline{k})^2} \mathcal{J}^{\gamma^*_{L,T}(q_1)\to\rho^0_L(k_1)}(\underline{k}, \underline{r}-\underline{k})\ \mathcal{J}^{\gamma^*_{L,T}(q_2)\to\rho^0_L(k_2)}(-\underline{k}, -\underline{r}+\underline{k})$$

where the impact factors $\mathcal{J}^{\gamma^*_{L,T}}$ are rational functions of the transverse momenta $(\underline{k}, \underline{r})$. The 2-d integration is treated analytically, relying on conformal transformations in the transverse momentum plane. The integrations over momentum fractions z_1 and z_2 (hidden in $\mathcal{J}$) are performed numerically. We use $Q_1 Q_2$ as a scale for α_S. As displayed in Fig.11a,b,c, cross-sections are strongly peaked at small Q^2 and small t, and longitudinally polarized photons dominates. The

non-forward Born order cross-section for $e^+e^- \to e^+e^-\rho_L^0\ \rho_L^0$ is obtained with the help of the equivalent photon approximation. Defining y_i as the longitudinal momentum fractions of the bremsstrahlung photons, one finds that $\sigma^{e^+e^-\to e^+e^-\rho_L\rho_L}$ gets its main contribution from the low y and Q^2 region, which is the very forward region. At ILC, $\sqrt{s}_{e^+e^-} = 500\,\mathrm{GeV}$, with $125\,\mathrm{fb}^{-1}$ per year. The measurement seems feasible since each detector design includes a very forward electromagnetic calorimeter for luminosity measurement, with tagging angle for outgoing leptons down to 5 mrad. In Fig.11d, we display our results within the Large Detector Concept. We obtain $\sigma^{tot} = 34.1\,\mathrm{fb}$ and $4.3\,10^3$ events per year. The LL BFKL enhancement is enormous but not trustable, since it is well known that NLL BFKL is far below LL. Work to implement *resummed* LL BFKL effects [15] is in progress, with results in accordance with the NLL based one [16]. The obtained enhancement is less dramatic (~ 5) than with LL BFKL, but *still visible*.

Aknowledgements

L.Sz. is supported by the Polish Grant 1 P03B 028 28. He is a Visiting Fellow of FNRS (Belgium).

References

[1] E.A. Kuraev, L.N. Lipatov and V.S. Fadin, Phys. Lett. B **60**, 50-52 (1975); Sov. Phys. JETP **44**, 443-451 (1976) ; Sov. Phys. JETP **45**, 199-204 (1977) ; Ya.Ya. Balitskii and L.N. Lipatov, Sov. J. Nucl. Phys. **28**, 822-829 (1978).

[2] D. Müller, D. Robaschik, B. Geyer, F. M. Dittes, J. Hořejši, Fortsch. Phys. **42**, 101 (1994);

[3] X. Ji, Phys. Rev. Lett. **78**, 610 (1997); Phys. Rev. D **55**, 7114 (1997); A. V. Radyushkin, Phys. Rev. D **56**, 5524 (1997); For a review, see M. Diehl, Phys. Rept. **388**, 41 (2003) and A. V. Belitsky and A. V. Radyushkin, Phys. Rept. **418**, 1 (2005).

[4] M. Diehl, T. Gousset, B. Pire and O. Teryaev, Phys. Rev. Lett. **81**, 1782 (1998); M. Diehl, T. Gousset and B. Pire, Phys. Rev. D **62**, 073014 (2000); I. V. Anikin, B. Pire and O. V. Teryaev, Phys. Rev. D **69**, 014018 (2004).

[5] B. Pire and L. Szymanowski, Phys. Rev. D **71**, 111501 (2005); Phys. Lett. B **622**, 83 (2005); J. P. Lansberg, B. Pire and L. Szymanowski, Phys. Rev. D **73**, 074014 (2006); Phys. Rev. D **75**, 074004 (2006) and arXiv:0709.2567 [hep-ph].

[6] B. Pire, M. Segond, L. Szymanowski and S. Wallon, Phys. Lett. B **39**, 642-651 (2006); PoS D **IFF2006**, 034 (2006).

[7] S. J. Brodsky and G. P. Lepage, Phys. Rev. D **24**, 1808 (1981).

[8] M. Diehl, T. Feldmann, P. Kroll and C. Vogt, Phys. Rev. D **61**, 074029 (2000).

[9] See talk "Perturbative QCD in the Regge limit: Prospects at ILC", arXiv:0710.0833 [hep-ph], slides: https://indico.desy.de/conferenceDisplay.py?confId=372

[10] M. Segond, L. Szymanowski and S. Wallon, Eur. Phys. J. C **52**, 93 (2007) [arXiv:hep-ph/0703166].

[11] B. Pire, L. Szymanowski and S. Wallon, Eur. Phys. J. C **44**, 545 (2005); LCWS 04, Paris, France, 19-24 Apr 2004, Published in "Paris 2004, Linear colliders, vol. 1," 335-340; Nucl. Phys. A **755** (2005) 626-629; EDS05, Blois, France, 15-20 May 2005, "Towards High Energy Frontiers", eds. M. Haguenauer et al., 373-376.

[12] R. Enberg, B. Pire, L. Szymanowski and S. Wallon, Eur. Phys. J. C **45**, 759 (2006) [Erratum-ibid. C **51**, 1015 (2007)]; Acta Phys. Polon. B **37**, 847 (2006).

[13] V. N. Gribov and L. N. Lipatov, Yad. Fiz. **15**, (1972) 781 [Sov. J. Nucl. Phys. **15**, 438 (1972)]; G. Altarelli and G. Parisi, Nucl. Phys. B **126**, 298 (1977); Y. L. Dokshitzer, Sov. Phys. JETP **46**, 641 (1977) [Zh. Eksp. Teor. Fiz. **73**, 1216 (1977)].

[14] G.P. Lepage and S.J. Brodsky, Phys. Lett. B **87**, 359 (1979); A.V. Efremov and A.V. Radyushkin, Phys. Lett. B **94**, 245 (1980).

[15] V. A. Khoze, A. D. Martin, M. G. Ryskin and W. J. Stirling, Phys. Rev. D **70**, 074013 (2004).

[16] D. Y. Ivanov and A. Papa, Nucl. Phys. B **732**, 183 (2006) and Eur. Phys. J. C **49** 947 (2007).

[17] slides: https://indico.desy.de/conferenceDisplay.py?confId=372#9

Low Q^2 and High y Inclusive Cross Section Measurements from the HERA Experiments ZEUS and H1

Jan Kretzschmar[1]†
[1] DESY Zeuthen, Plantanenallee 6, 15738 Zeuthen, Germany

Abstract
An overview of inclusive cross section measurements from the HERA experiments covering the low Q^2 domain, $0.2\,\mathrm{GeV}^2 < Q^2 < 150\,\mathrm{GeV}^2$, is presented. The emphasis is put on new experimental results obtained at lowest values of $Q^2 < 10\,\mathrm{GeV}^2$ and high $y > 0.6$. Furthermore future prospects for measurements of the structure functions F_2 and F_L are shortly discussed.

1 Introduction

The HERA collider facility in Hamburg, Germany, is a unique tool for lepton-proton scattering at highest energies. It consists of two accelerators: one for protons, which are accelerated up to 920 GeV beam energy, and one for electrons or positrons, which are accelerated to 27.6 GeV. For the two colliding beam experiments H1 and ZEUS this is equivalent to a maximal centre of mass energy of $\sqrt{s} = 320$ GeV. At the end of June 2007 the data taking has finished after a final period of running at lowered proton beam energies of $E_p = 460$ GeV and $E_p = 575$ GeV.

In Deep Inelastic Scattering (DIS) of leptons off nucleons the substructure of the nucleons was discovered and DIS continues to be the tool for exploring the substructure of the nucleons with high precision. The kinematics of the scattering are described in terms of the Lorentz invariant quantities: the Bjorken scaling variable x, the inelasticity y, and the virtuality Q^2, which are related by $Q^2 = xys$. Figure 1 shows the kinematic (x, Q^2)-plane, where the HERA experiments and the fixed target experiments have made measurements of the proton structure. Q^2 values of up to 50000 GeV^2 and x values down to 10^{-6} are reached at HERA.

One of the most fundamental measurements to be performed is that of the inclusive cross section for the reaction $ep \to e'X$, which can be expressed at low Q^2 in the form

$$\frac{\mathrm{d}^2\sigma_{NC}^{e^\pm p}}{\mathrm{d}x\mathrm{d}Q^2} = \frac{2\pi\alpha^2 Y_+}{xQ^4}\left(F_2(x,Q^2) - \frac{y^2}{Y_+}F_L(x,Q^2)\right) = \frac{2\pi\alpha^2 Y_+}{xQ^4}\cdot\sigma_r\ , \tag{1}$$

with $Y_+ = 1 + (1-y)^2$ and the structure functions F_2 and F_L. Usually the data are presented in the form of the reduced cross section σ_r, which is defined to exclude the kinematic factor.

In the following, three parts of the phase space are discussed in more detail, which are as well marked in figure 1

- In the *Bulk Low Q^2 domain*, defined as $10\,\mathrm{GeV}^2 < Q^2 < 150\,\mathrm{GeV}^2$, the cross section is dominated by the contribution of the structure function F_2. Here also the highest precision

† talk presented at EDS07 on behalf of the H1 and ZEUS Collaborations

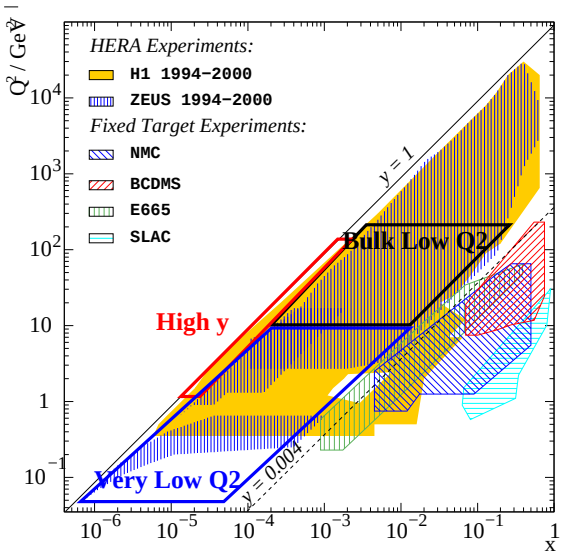


Fig. 1: Kinematic plane in (x, Q^2), where measurements of the proton structure function F_2 have been performed by the HERA collider and fixed target experiments, respectively.

is reached. In QCD fits, also including data at larger Q^2 and x, the Parton Distribution functions (PDFs) and the strong coupling constant α_s can be determined. The evolution of the PDFs with Q^2 can be described using the DGLAP equations.

- In the *very low* Q^2 *domain*, $0.2\,\mathrm{GeV}^2 < Q^2 < 10\,\mathrm{GeV}^2$, the transition to the non-perturbative regime is covered. Here the strong coupling α_s becomes large and perturbative QCD calculations are not applicable.
- The *high* $y > 0.6$ *domain* is sensitive to the influence of the longitudinal structure function F_L, which provides an independent access to the gluon density.

For data taken at different centre of mass energies the kinematic plane is shifted allowing the direct measurement of F_L.

2 The Low Q^2 Bulk Domain

The domain $10\,\mathrm{GeV}^2 < Q^2 < 150\,\mathrm{GeV}^2$ is interesting because the experimental precision is high and a hard scale is present, so perturbative QCD calculations are applicable. The structure function $F_2(x, Q^2)$ has been measured with very high accuracy by both H1 [1] and ZEUS [2]. Figure 2 gives an example of the progress made with the HERA collider: from the very first data and the discovery of the strong rise of F_2 towards low x to the currently reached $2-3\%$ precision. QCD fits using this data have been performed by the HERA collaborations [3] as well as other authors to exploit this data.

For the future a new measurement by H1 is expected with reduced systematic uncertainties. A further improvement may be achieved by combining data from ZEUS and H1 to obtain a final word of the HERA experiments on the structure function F_2 with best precision. First preliminary results have been presented [4].

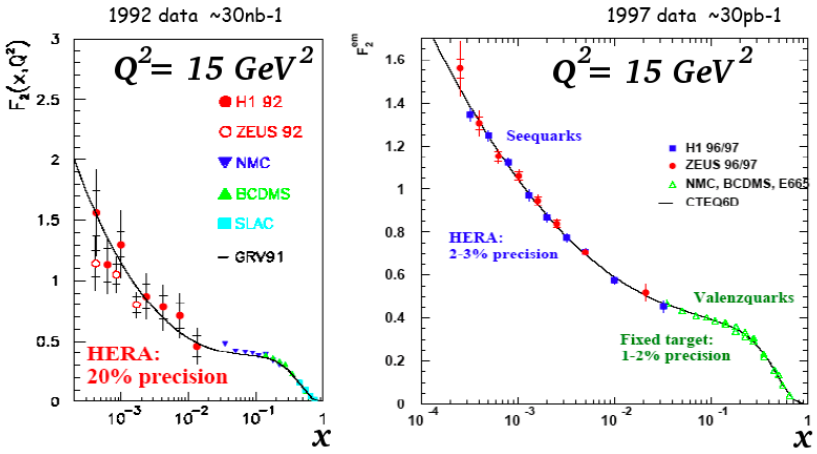


Fig. 2: Measurement of the proton structure function F_2 at $Q^2 = 15$ GeV^2 with the very first HERA data (left) and with much improved precision (right).

3 The Lowest Q^2 Region

As the virtuality of the exchanged photon becomes smaller, $Q^2 \to 0$, the transition is made to the non-perturbative QCD regime. From a theoretical and experimental point of view this is both interesting and challenging. Experimentally specialised techniques have to be employed to detect scattered leptons at very small angles:

- Both H1 and ZEUS have used events with tagged Initial State Radiation [5], which extends the accessible phase space to lower Q^2. Recent H1 measurements are using untagged ISR events for the same purpose [6].
- The lowest values of Q^2, down to $0.045\,\mathrm{GeV}^2$, were reached by ZEUS using a special low angle calorimeter and tracker called BPT [7].
- Recently H1 has presented new results which are based on data using a minimum bias trigger setup and an improved tracking of the scattered lepton using the Backward Silicon Tracker (BST). A part of the data was taken with a shifted vertex position to enhance the acceptance for lower Q^2 values down to $0.2\,\mathrm{GeV}^2$ [6].

The new H1 analysis achieves a very good control of the energy of the scattered lepton. The reconstruction of the event kinematics is done mostly independent of the hadronic final state using the BST. The precision is further improved by combining three data sets.

Including these new results, the HERA measurement in this kinematic domain is completed with very good precision of typically a few %. The results, expressed as the effective photon-proton cross section $\sigma^{eff}_{\gamma^* p} = 4\pi^2\alpha/(Q^2(1-x)) \cdot \sigma_r$, are given in figure 3.

4 The High y Region

The analysis in the high $y > 0.6$ region is experimentally especially difficult, as the energy of the scattered lepton E'_e is small. Therefore the scattered lepton is difficult to identify and the background posed by photoproduction (γp) events is high. On the other hand, the results are

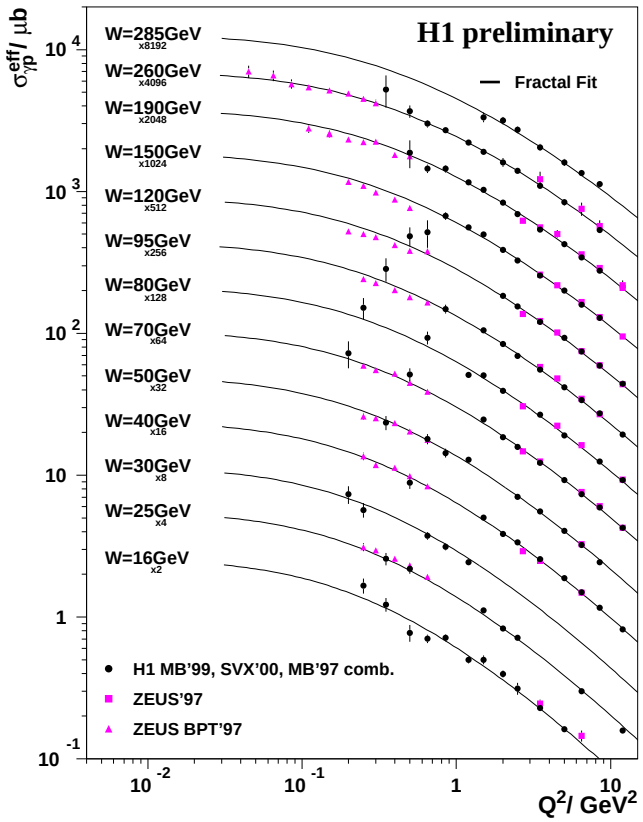


Fig. 3: ZEUS and H1 measurements in the transition region $Q^2 \sim 1\,\mathrm{GeV}^2$.

particularly interesting, as the cross section at high y is influenced by both structure functions F_2 and F_L. The experimental problems are similar to the ones posed by a direct measurement of F_L.

Both ZEUS and H1 have released new preliminary cross section measurements at high y. The techniques used to cope with the large background are different:

- ZEUS can study the γp background in detail using events with the scattered lepton tagged in a special calorimeter. The measurement uses a Monte Carlo model for the subtraction. The preliminary analysis reaches down to $E'_e = 5$ GeV and up to $y = 0.8$ [8].
- In the H1 analysis the background is determined directly from data using the charge of the scattered lepton track. This enables a cross section measurement without the use of γp Monte Carlo models. The analysis can go to very low energies of $E'_e = 3.3$ GeV, which corresponds to $y = 0.9$ [9].

The H1 measurement makes use of a large data set of $96\,\mathrm{pb}^{-1}$ and improves the uncertainty by a factor of 2 w.r.t the previous publication. The cross section together with measurements at lower y is shown in figure 4. The results of the ZEUS measurements are shown there as well. For ZEUS it represents the first measurement at high y and the full accessible Q^2 range is covered. An extension to higher values of Q^2 was meanwhile presented by H1 [10].

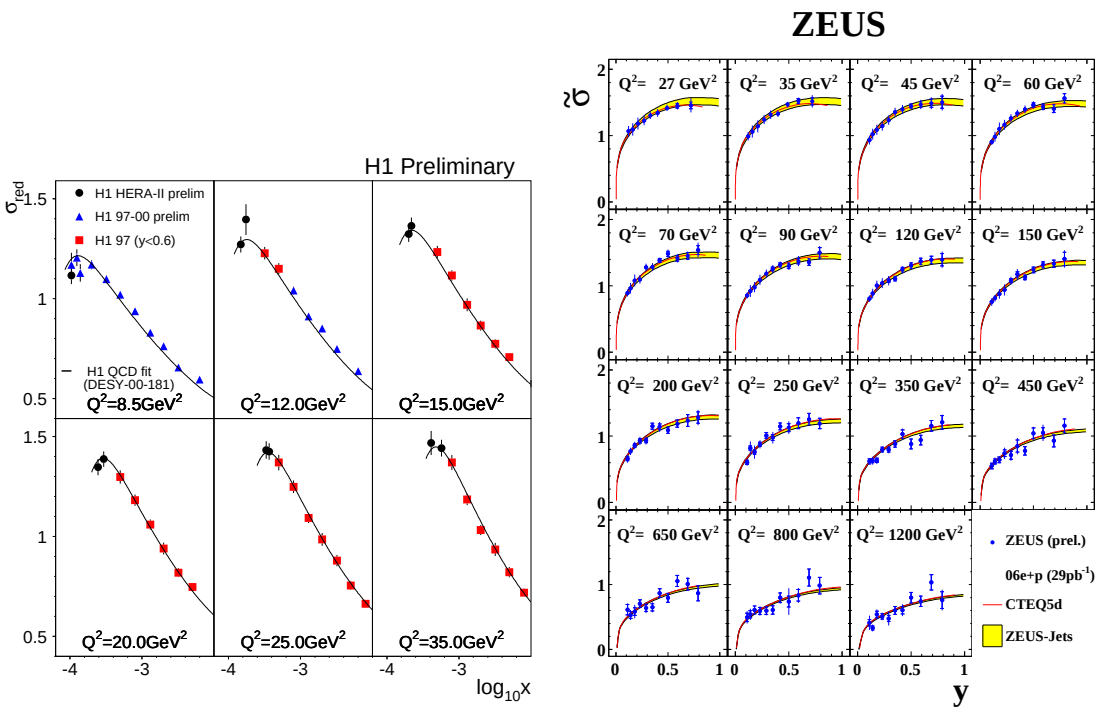


Fig. 4: New measurements of the inclusive DIS cross section at high y by H1 and ZEUS

5 The Direct F_L Measurement

The program of HERA structure function measurements would not be complete without a direct measurement of the longitudinal structure function F_L. To disentangle the contributions to the inclusive cross section, measurements at different centre of mass energies $\sqrt{s}$ are needed. Therefore, for the last 3 months of its operation time HERA was operated at reduced proton beam energies $E_p = 460$ GeV and $E_p = 575$ GeV. The luminosity accumulated was approximately $\mathcal{L}_{460} \approx 13$ pb^{-1} and $\mathcal{L}_{575} \approx 7$ pb^{-1}, respectively, see also figure 5.

The measurement principle with the systematical and statistical uncertainties, as expected for the H1 measurement, is also illustrated in figure 5. It is performed using the inclusive cross sections at a fixed set of (x, Q^2) for all three centre of mass energies, which lie according to equation 1 on a straight line as a function of y^2/Y_+. The extrapolation to $y \to 0$ gives F_2, while the slope determines F_L.

6 Conclusion

While the experimental phase of the HERA experiments is over, the data still has a lot of potential for precise inclusive cross section measurements at low Q^2. Recently new and improved results were presented for lowest Q^2 and in the high y domain.

For the future, improved determinations of the structure function F_2 can expected due to new analyses and the combination of available H1 and ZEUS data. The longitudinal structure

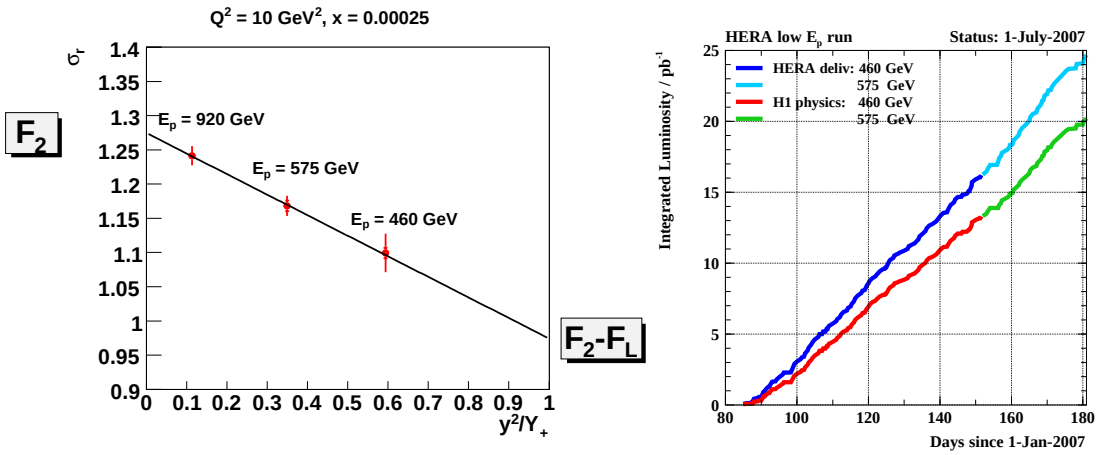


Fig. 5: On the left: illustration of the F_L measurements using cross section measurements from three centre of mass energies. On the right: Luminosities of the data sample collected during the low and medium E_p runs in 2007.

function will be measured for the first time directly using the data from the successful HERA running at lowered centre of mass energy.

With extended and more precise measurements at hand, we will be able to test the theory of strong interaction QCD and improve our knowledge about the structure of the proton. Eventually this also will lead to precise input for measurements at the upcoming Large Hadron Collider.

References

[1] H1 Collaboration, C. Adloff *et al.*, Eur. Phys. J. C **21**, 33 (2001). `hep-ex/0012053`.

[2] ZEUS Collaboration, S. Chekanov *et al.*, Eur. Phys. J. C **21**, 443 (2001). `hep-ex/0105090`.

[3] ZEUS Collaboration, S. Chekanov *et al.*, Phys. Rev. D **70**, 052001 (2004). `hep-ex/0401003`;
ZEUS Collaboration, S. Chekanov *et al.* (2005). `hep-ph/0503274`;
H1 Collaboration, C. Adloff *et al.*, Eur. Phys. J. **C30**, 1 (2003). `hep-ex/0304003`.

[4] H1 and ZEUS Collaborations, *Combination of H1 and ZEUS Deep Inelastic $e^{\pm}p$ Scattering Cross Sections*, 2007. H1prelim-07-007, presented at LP 2007, Daegu, Republic of Korea.

[5] H1 Collaboration, T. Ahmed *et al.*, Z. Phys. **C66**, 529 (1995);
ZEUS Collaboration, M. Derrick *et al.*, Z. Phys. **C69**, 607 (1996). `hep-ex/9510009`;
ZEUS Collaboration, *Measurement of the Proton Structure Functions F_2 and F_L Using Initial State Radiative Events at HERA*. Contributed Paper to EPS 2003, Aachen, Abstract 502, 2003.

[6] H1 Collaboration, *Measurement of the Inclusive ep Scattering Cross Section at low Q^2 and x at HERA*, 2007. H1prelim-07-045, presented at DIS 2007, Munich, Germany.

[7] ZEUS Collaboration, J. Breitweg *et al.*, Phys. Lett. B **487**, 53 (2000). `hep-ex/0005018`.

[8] ZEUS Collaboration, *Measurement of neutral-current DIS cross sections at large y*, 2007. ZEUS-prel-07-002, presented at DIS 2007, Munich, Germany.

[9] H1 Collaboration, *Inclusive ep Scattering Cross Section at low Q^2 and high y*, 2007. H1prelim-07-042, presented at DIS 2007, Munich, Germany.

[10] H1 Collaboration, *Inclusive ep Scattering Cross Section at high Q^2 and high y*, 2007. H1prelim-07-144, presented at EPS 2007, Manchester, United Kingdom.

Status of Deeply Inelastic Parton Distributions

Johannes Blümlein
DESY, Platanenallee 6, D-15738 Zeuthen, Germany

Abstract
A brief review on the status of unpolarized parton densities and the determination of the QCD scale $\Lambda_{\rm QCD}$ from deep-inelastic scattering data is presented.

1 Introduction

Deeply inelastic lepton–nucleon scattering provides a clean way to extract the parton densities of the nucleons together with the QCD scale $\Lambda_{\rm QCD}$. The exact determination of the parton densities is decisive for the understanding of the scattering cross sections at hadron colliders as LHC [1]. The main goal of the investigation is the measurement of the leading twist distributions. In the large x region higher twist effects are measurable as well [2,3]. [1] During the last years the determination of moments of parton distribution functions [5] and the QCD scale [6,7] within lattice-QCD calculations became more and more precise. A comparison of these results and the measurement of the corresponding quantities from precision data using higher order perturbation theory will provide highly non-trivial tests of Quantum Chromodynamics. On the perturbative side, the running of $\alpha_s(Q^2)$ is known to 4–loop orders [8] while the anomalous dimensions and the massless Wilson coefficients were calculated to 3–loop order [9, 10]. The heavy flavor Wilson coefficients are known to 2–loop order only [11–13]. A first coefficient contributing at 3–loop order was calculated recently [14]. Due to this the QCD analysis of deeply inelastic structure functions in $l^{\pm}N$ scattering may be performed for flavor non–singlet combinations to $O(\alpha_s^3)$ and to a very good approximation even to $O(\alpha_s^4)$, cf. [3]. In the flavor singlet case, strictly speaking, the analysis cannot be performed to 3-loop order, since the corresponding heavy flavor Wilson coefficients are not known yet. It can be performed in an approximation to 3–loop order, describing the heavy flavor contributions to 2–loop order, which induces a remaining theoretical error. In the present paper we concentrate on the case of unpolarized deep-inelastic scattering. A recent overview on the status of polarized parton densities was given in [15]. The paper is organized as follows. In section 2 we summarize main aspects of QCD analyses and discuss recent progress in measuring unpolarized parton distribution functions. Section 3 summarizes determinations of $\Lambda_{\rm QCD}$ in deeply inelastic scattering and in Section 4 we discuss future perspectives.

[1] Similarly, one may hope to find higher twist effects in the region of small x in the future [4].

2 QCD Analysis of Unpolarized Structure Functions

In case of light–cone dominance the deeply inelastic structure functions at twist–2 are described by a Mellin convolution of the bare parton densities and the hard scattering cross sections, which are both infinite, but are renormalized to finite parton densities and Wilson coefficients by absorbing the ultraviolet singularities of the latter into the former :

$$\begin{aligned} F_j(x,Q^2) &= \hat{f}_i(x,\mu^2) \otimes \sigma_j^i \left(\alpha_s, \frac{Q^2}{\mu^2}, x\right) \qquad (1)\\ &\qquad \uparrow \text{bare pdf} \qquad \uparrow \text{sub} - \text{system cross} - \text{sect.} \\ &= \underbrace{\hat{f}_i(x,\mu^2) \otimes \Gamma_k^i \left(\alpha_s(R^2), \frac{M^2}{\mu^2}, \frac{M^2}{R^2}\right)}_{\text{finite pdf}\equiv f_k} \otimes \underbrace{C_j^k \left(\alpha_s(R^2), \frac{Q^2}{\mu^2}, \frac{M^2}{R^2}, x\right)}_{\text{finite Wilson coefficient}} \end{aligned}$$

The scale evolution of the structure functions is described by the Symanzik-Callan equations for the ultraviolet singularities [16], and likewise for the renormalized parton densities and Wilson coefficients,

$$\left[M\frac{\partial}{\partial M} + \beta(g)\frac{\partial}{\partial g} - 2\gamma_\psi(g)\right] F_i(N) = 0 \qquad (2)$$

$$\left[M\frac{\partial}{\partial M} + \beta(g)\frac{\partial}{\partial g} + \gamma_\kappa^N(g) - 2\gamma_\psi(g)\right] f_k(N) = 0 \qquad (3)$$

$$\left[M\frac{\partial}{\partial M} + \beta(g)\frac{\partial}{\partial g} - \gamma_\kappa^N(g)\right] C_j^k(N) = 0\,. \qquad (4)$$

Here the Wilson coefficients contain as well the heavy quark degrees of freedom, while the parton distributions can only be defined for strictly massless partons in the respective kinematic region, i.e. for collinear particles. Clearly for $Q^2 \lessapprox m_H^2$ heavy quarks cannot be treated as partons. It is known for long [17] that the heavy quark contributions have quite different scaling violations if compared to light partons for a very large range in Q^2.

The solution of the evolution equations is easiest being performed in Mellin space. Here the corresponding evolution equations can be solved to all orders in the coupling constant analytically, cf. e.g. [18]. The solution has to be continued analytically from even values of the Mellin moment $N \to N \in \mathbf{C}$. This requires the continuation of harmonic sums [19] representing the higher order anomalous dimensions and light flavor Wilson coefficients [20] and that of heavy flavor Wilson coefficients [12]. At every loop order and expansion depth in the dimensional regularization parameter ε a uniform maximal number of basis elements is needed to construct the respective single–scale quantities. To 3–loop orders 14 basic Mellin transforms are sufficient [21]. The structure of this representation is characterized by meromorphic functions in the complex N plane, the perturbative part of it obeys nested recursions $z \to z-1$ and can be

constructed analytically starting from the respective asymptotic representation in the region $|z| \to \infty$, cf. [22]. The expression for the structure functions used in the χ^2-minimization can be easily obtained by a single fast numeric contour integral around the singularities of the problem. To keep the evolution code fast all relations expressing the evolution kernels can be stored in large arrays during the initialization of the code, while in the minimization procedure only the parameters of the parton distribution functions are varied along with $\Lambda_{\rm QCD}$. The procedure can be systematically generalized including resummations, e.g. in the small–x region [18]. These effects, however, were found to be non-dominant in the region of HERA data. Initially large effects are likely canceled by sub-leading terms almost completely, as being the case for all quantities calculated in fixed orders up to $O(\alpha_s^3)$. Usually three sub-leading terms (series) are required to obtain the correct result, cf. [18]. We will therefore not include effects of this kind in the present analysis, see [23] for a survey. Other recent analyses also find only small small x effects [24] in the evolution of $F_2(x, Q^2)$ in the region $x \gtrapprox 10^{-4}$ currently probed at HERA.

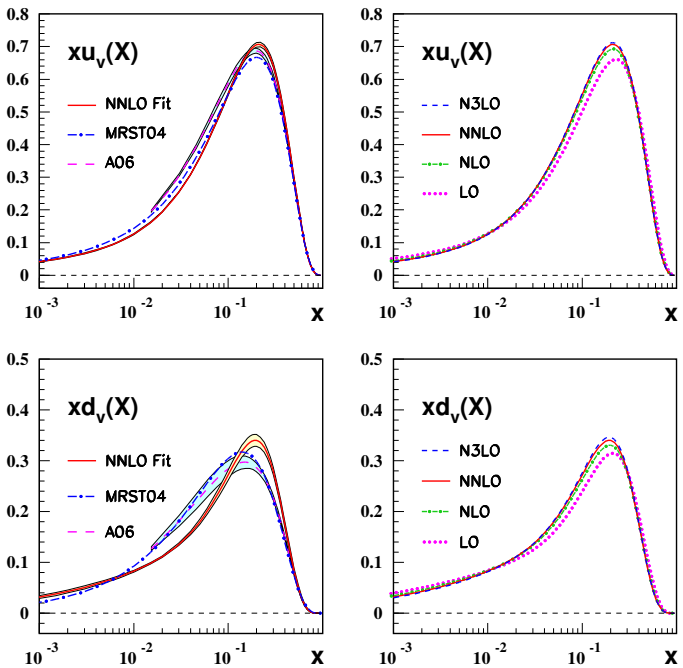


Figure 1: The NNLO valence quark distributions, [3], compared to other analyses and perturbative stability of the fit comparing different higher order corrections.

A flavor non–singlet analysis of the deep-inelastic world data was carried out recently in [3]. This analysis primarily aimed on measuring $\alpha_s(M_Z^2)$ widely free of gluonic effects. Due to the fact that the $O(\alpha_s^3)$ Wilson coefficients dominate the scaling violations at the 4–loop level and the effect of the splitting function is rather minor only, as estimated by a Padé-approximation, the analysis is effectively of 4–loop order. We accounted for a $\pm$ 100% error in the estimated 4-loop anomalous dimension. Comparison

with the second moment of the non-singlet 4–loop anomalous dimension [25] showed agreement within better than 20 % well confirming our error treatment. In Figure 1 the fit results are shown for the valence quarks and compared to other analyses [26, 27] (left figures). The right figures show the convergence of the analysis from leading order (LO) to 4-loop order (NNNLO).

In Ref. [3] also a model-independent extraction of higher twist-contributions in the large x region was performed. Here it is essential to describe the leading twist contributions as accurately as possible, since the leading twist Wilson coefficients are large in the large x region.

The light sea quark densities are known at lower precision if compared to that of the valence quarks. Here still more data are required. The distribution $x(\overline{u} - \overline{d})(x, Q^2)$ can be obtained from Drell–Yan data. In a recent analysis [27] improved sea quark distributions $x(\overline{u} \pm \overline{d})$ were obtained, see Figure 2a. The 3–loop corrections lower the theory error to the level of the experimental accuracy. A recent determination of the strange quark density was performed by the CTEQ collaboration [28], see Figure 2b. This distribution is about half the value of that of the up and down sea quarks.

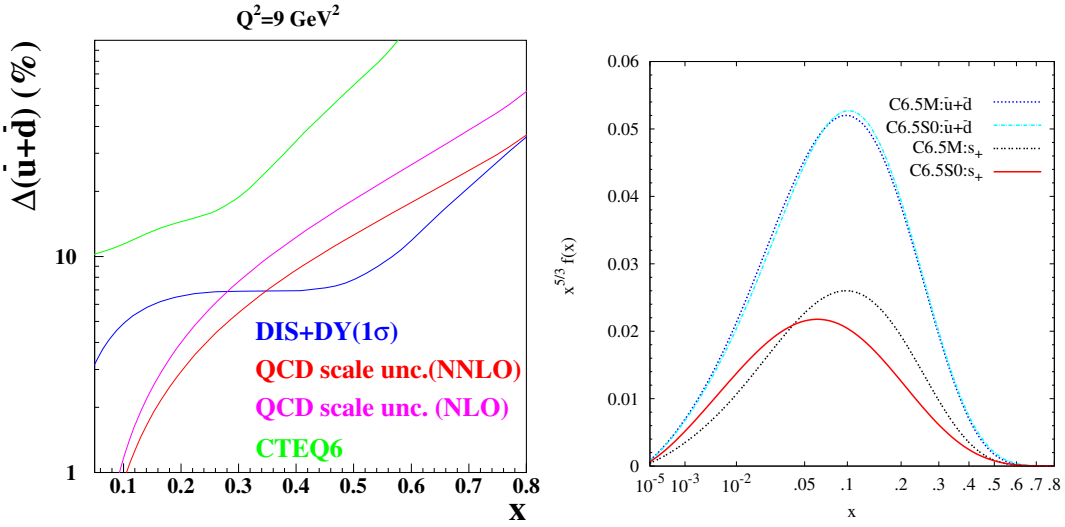


Figure 2: Uncertainty of $x(\overline{u} + \overline{d})$ distribution [27] (left). The light flavor distributions for $Q^2 = 1.69\text{GeV}^2$, Ref. [28].

The correct determination of the gluon density is of central importance since many scattering processes at LHC are gluon induced. The gluon distribution is rapidly growing as $x \to 0$ with rising values of Q^2. This expectation is confirmed by different analyses [27, 29, 30]. As an example we show the results of the recent analysis [29] in Figure 3a, where a rising behaviour is found down to scales of $Q^2 = 2$ GeV^2. In contrast to this MSTW [31] find a gluon distribution which is turning to lower values in the region $x \approx 10^{-3}$ for scales $Q^2 = 5$ GeV^2 and lower, contrary to the results found in [27, 29, 30]. The value of $\alpha_s(M_Z^2)$ in [31] $0.1191 \pm 0.002 \pm 0.003$ comes out larger than that in

[3,27,29], $\alpha_s(M_Z^2) = 0.1142 \pm 0.0021; 0.1128 \pm 0.0015; 0.112$. In [30] a determination of α_s is not undertaken, since the different data sets used in the fit bear too different systematics to allow this, which was outlined in [32] in detail. The analysis in [26] differs from that in [27] due to the inclusion of jet data from Tevatron, which are known to require a larger value of $\alpha_s(M_Z^2)$.

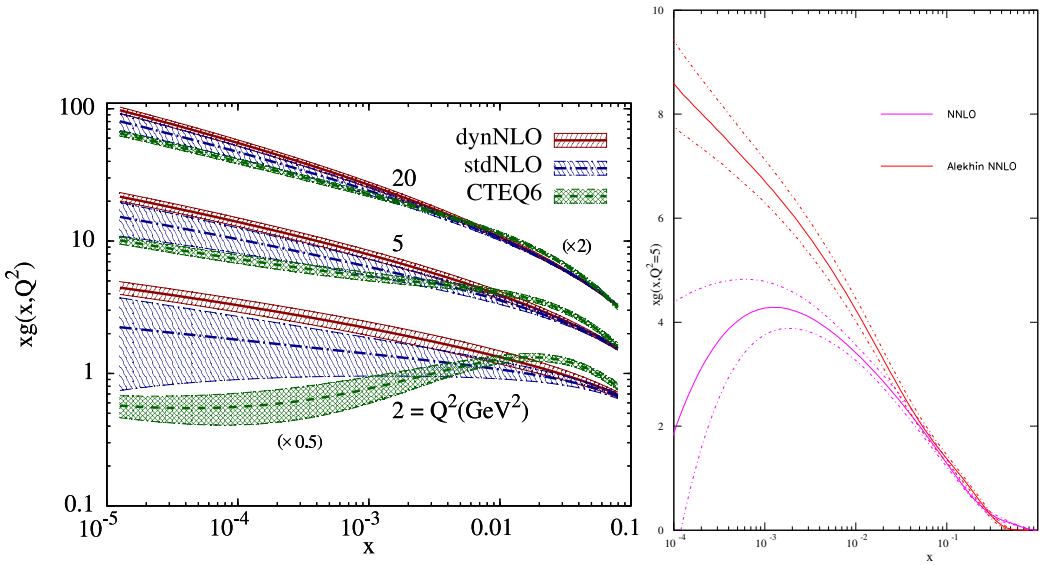


Figure 3 : Gluon momentum distribution at NLO [29, 30] (left) and at NNLO [26, 27] (right).

The measurement of $F_L(x, Q^2)$ can help to clarify this question. A recent analysis [33] shows very good agreement with the current measurements [34], which are partly still preliminary. The question of the correct value of the gluon distribution function should be clarified soon.

3 $\Lambda_{\rm QCD}$ and $\alpha_s(M_Z^2)$

A summary on different measurements of $\alpha_s(M_Z^2)$ from $l^{\pm}N$ scattering data in NLO, NNLO, and NNNLO is given in Figure 4, see also [35]. Present analyses are carried out at the 3-loop level based on the anomalous dimensions [9] and Wilson coefficients [36]. If the analysis is restricted to deeply inelastic data the values of $\alpha_s(M_Z^2)$ come out somewhat lower as the world average [37]. The convergence of the perturbative extraction of $\alpha_s(M_Z^2)$ out of the deeply–inelastic world data [3] is illustrated comparing the central values from NLO to NNNLO :

$$\alpha_s(M_Z^2) = 0.1148 \rightarrow 0.1134 \rightarrow 0.1142 \pm 0.0021. \tag{5}$$

The change from the N^{2}LO to the N^{3}LO value is found deeply inside the current experimental error. The N^{3}LO value corresponds to

$$\Lambda_{\rm QCD}^{\overline{\rm MS},{\rm N_f}=4} = 234 \ \pm 26 \ {\rm MeV}. \tag{6}$$

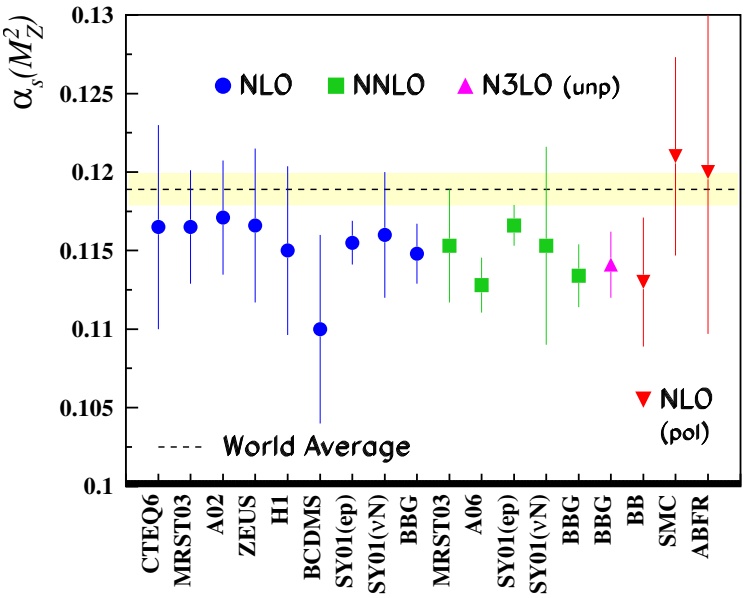


Figure 4: Summary of $\alpha_s(M_Z^2)$ measurements in deep-inelastic unpolarized and polarized $l^{\pm}N$ scattering: from NLO to NNNLO, Ref. [3].

$\Lambda_{\rm QCD}^{\overline{\rm MS}}$ was measured also in two recent lattice simulations based on two active flavors ($N_f = 2$). These investigations paid special attention to non-perturbative renormalization and kept the systematic errors as small as possible.

$$\Lambda_{N_f=2}^{\rm latt} = 245 \pm 16 \pm 16 \text{ MeV} \;\; [6], \qquad \Lambda_{N_f=2}^{\rm latt} = 261 \pm 17 \pm 26 \text{ MeV} \;\; [7] \; . \tag{7}$$

A direct comparison with the case $N_f = 4$ in the above data analyses is not yet possible. However, the difference between the earlier $N_f = 0$ and the present result in $\Lambda_{\rm QCD}$ amounts to $O(10 \text{ MeV})$ only. We have to wait and see what is obtained for $N_f = 4$ in coming analyses.

4 Future Perspectives

Most of the data taken at HERA still have to be analyzed to extract the final data of $F_{2,L}(x,Q^2)$, $F_2^{Q\overline{Q}}(x,Q^2)$, and other structure functions. The analysis of these measurements will be mandatory for the final precision determination of the parton distribution functions in the small x region, in particular for the gluon and sea quark distribution functions. Important information on the large x behaviour of the valence quark densities will be obtained from JLAB [38]. Currently our knowledge of the individual light flavor sea quark distributions is still rather limited. Here, the measurement of the Drell-Yan process and $W^{\pm}$ and Z–production at LHC will add in significant further information. That far signs of non-linear gluon evolution were not found in deeply inelastic scattering, unlike suggested by earlier theoretical expectations [4]. As the scale at which these effects come into operation cannot be determined pertubatively one has to search for

those effects at still smaller values of x using suitable scattering cross sections at LHC in the near future. After the completion of the HERA programme still inclusive measurements at much higher luminosity are required to determine some of the parton densities at higher precision. For a more detailed measurement of the sea quark distributions deuteron targets are required at high luminosity [39]. Here a programme like foreseen for the EIC [40] can contribute essentially. The flavor contents of the sea-distribution can be analysed in great detail at high luminosity neutrino factories operating at higher energies [41]. The results of both these facilities will be instrumental to explore distributions, which are more difficult to access, such as the polarized distribution functions, the transversity distribution, as well as the twist–3 and higher twist correlation functions to perform further rather non-trivial tests of QCD also in this area. Various of these observables can be accessed at high precision in lattice calculations in the near future. In this way ab-initio predictions at the one side can be compared to precision data analyzed within perturbation theory to higher orders on the other side. It is therefore highly desirable, that these facilities [40, 41] are built in the future.

References

[1] S. Alekhin *et al.*, arXiv:hep-ph/0601013; arXiv:hep-ph/0601012;
M. Dittmar *et al.*, arXiv:hep-ph/0511119.

[2] M. Virchaux and A. Milsztajn, Phys. Lett. B **274** (1992) 221;
S. I. Alekhin and A. L. Kataev, Phys. Lett. B **452** (1999) 402 [arXiv:hep-ph/9812348].

[3] J. Blümlein, H. Böttcher and A. Guffanti, Nucl. Phys. B **774** (2007) 182 [arXiv:hep-ph/0607200]l
Nucl. Phys. Proc. Suppl. **135** (2004) 152 [arXiv:hep-ph/0407089].

[4] L. V. Gribov, E. M. Levin and M. G. Ryskin, Nucl. Phys. B **188** (1981) 555;
A. H. Mueller and J. W. Qiu, Nucl. Phys. B **268** (1986) 427;
J. C. Collins and J. Kwiecinski, Nucl. Phys. B **335** (1990) 89;
J. Bartels, G. A. Schuler and J. Blümlein, Z. Phys. C **50** (1991) 91.

[5] D. Dolgov *et al.* [LHPC collaboration], Phys. Rev. D **66** (2002) 034506, [arXiv:hep-lat/0201021];
M. Göckeler, R. Horsley, D. Pleiter, P. E. L. Rakow and G. Schierholz [QCDSF Collaboration],
Phys. Rev. D **71** (2005) 114511 [arXiv:hep-ph/0410187];
K. Jansen et al., in preparation.

[6] M. Della Morte, R. Frezzotti, J. Heitger, J. Rolf, R. Sommer and U. Wolff [ALPHA Collaboration],
Nucl. Phys. B **713** (2005) 378, [arXiv:hep-lat/0411025];

[7] M. Göckeler, R. Horsley, A. C. Irving, D. Pleiter, P. E. L. Rakow, G. Schierholz and H. Stuben,
Phys. Rev. D **73** (2006) 014513, [arXiv:hep-ph/0502212].

[8] T. van Ritbergen, J. A. M. Vermaseren and S. A. Larin, Phys. Lett. B **400** (1997) 379;
M. Czakon, Nucl. Phys. B **710** (2005) 485.

[9] S. Moch, J. A. M. Vermaseren and A. Vogt, Nucl. Phys. B **688** (2004) 101 [arXiv:hep-ph/0403192];
691 (2004) 129 [arXiv:hep-ph/0404111].

[10] J. A. M. Vermaseren, A. Vogt and S. Moch, Nucl. Phys. B **724** (2005) 3 [arXiv:hep-ph/0504242].

[11] E. Laenen, S. Riemersma, J. Smith and W. L. van Neerven, Nucl. Phys. B **392** (1993) 162;
S. Riemersma, J. Smith and W. L. van Neerven, Phys. Lett. B **347** (1995) 143
[arXiv:hep-ph/9411431];

[12] S. I. Alekhin and J. Blümlein, Phys. Lett. B **594** (2004) 299 [arXiv:hep-ph/0404034];

[13] M. Buza, Y. Matiounine, J. Smith, R. Migneron and W. L. van Neerven, Nucl. Phys. B **472** (1996) 611 [arXiv:hep-ph/9601302];
I. Bierenbaum, J. Blümlein and S. Klein, Nucl. Phys. B **780** (2007) 40 [arXiv:hep-ph/0703285].

[14] I. Bierenbaum, J. Blümlein and S. Klein, arXiv:0710.3348 [hep-ph], Acta Phys. Pol. **B** in print; and in preparation.

[15] J. Blümlein, arXiv:0708.1474 [hep-ph].

[16] K. Symanzik, Commun. Math. Phys. **18** (1970) 227;
C. G. Callan, Phys. Rev. D **2** (1970) 1541.

[17] E. Eichten, I. Hinchliffe, K. D. Lane and C. Quigg, Rev. Mod. Phys. **56** (1984) 579 [Addendum-ibid. **58** (1986) 1065].

[18] J. Blümlein and A. Vogt, Phys. Rev. D **58** (1998) 014020 [arXiv:hep-ph/9712546].

[19] J. A. M. Vermaseren, Int. J. Mod. Phys. A **14**, 2037 (1999) [arXiv:hep-ph/9806280];
J. Blümlein and S. Kurth, Phys. Rev. D **60** (1999) 014018 [arXiv:hep-ph/9810241].

[20] J. Blümlein, Comput. Phys. Commun. **133** (2000) 76 [arXiv:hep-ph/0003100];
J. Blümlein and S. O. Moch, Phys. Lett. B **614** (2005) 53 [arXiv:hep-ph/0503188].

[21] J. Blümlein and V. Ravindran, Nucl. Phys. B **749** (2006) 1, [arXiv:hep-ph/0604019]; Nucl. Phys. B **716** (2005) 128, [arXiv:hep-ph/0501178];
J. Blümlein and S. Klein, arXiv:0706.2426 [hep-ph]; J. Blümlein and S. Moch, in preparation.

[22] J. Blümlein, DESY 07–042.

[23] J. Blümlein, QCD evolution of structure functions at small x, arXiv:hep-ph/9909449.

[24] G. Altarelli, R. D. Ball and S. Forte, Nucl. Phys. B **742** (2006) 1 [arXiv:hep-ph/0512237];
M. Ciafaloni, D. Colferai, G. P. Salam and A. M. Stasto, JHEP **0708** (2007) 046 [arXiv:0707.1453 [hep-ph]].

[25] P. A. Baikov and K. G. Chetyrkin, Nucl. Phys. Proc. Suppl. **160** (2006) 76.

[26] A. D. Martin, R. G. Roberts, W. J. Stirling and R. S. Thorne, Phys. Lett. B **604** (2004) 61 [arXiv:hep-ph/0410230].

[27] S. Alekhin, K. Melnikov and F. Petriello, Phys. Rev. D **74** (2006) 054033 [arXiv:hep-ph/0606237].

[28] H. L. Lai, P. Nadolsky, J. Pumplin, D. Stump, W. K. Tung and C. P. Yuan, JHEP **0704** (2007) 089 [arXiv:hep-ph/0702268].

[29] M. Glück, P. Jimenez-Delgado and E. Reya, arXiv:0709.0614 [hep-ph].

[30] J. Pumplin et al., CTEQ Collab., JHEP **07** (2002) 012.

[31] A. D. Martin, W. J. Stirling, R. S. Thorne and G. Watt, arXiv:0706.0459v3 and Phys. Lett. B **652** (2007) 292.

[32] J. Pumplin, A. Belyaev, J. Huston, D. Stump and W. K. Tung, JHEP **0602** (2006) 032, [arXiv:hep-ph/0512167].

[33] M. Glück, P. Jimenez-Delgado, and E. Reya, DO–TH 07/08, October 2007.

[34] H1 collaboration, C. Adloff et al. , hep-ex/9611017,
Phys. Lett. **B393** (1997) 452, [hep-ex/9611017];
E.M. Lobodzinska, hep-ph/0311180;
T. Lastovicka, H1 Collab., Eur. Phys. J. **C33** (2004) s388.

[35] J. Blümlein, arXiv:0706.2430 [hep-ph].

[36] E. B. Zijlstra and W. L. van Neerven, Nucl. Phys. B **383** (1992) 525.

[37] S. Bethke, Prog. Part. Nucl. Phys. **58** (2007) 351.

[38] The Science and Experimental Equipment for the 12 GeV Upgrade of CEBAF, JLAB White Paper, Jan. 10, 2005.

[39] J. Blümlein, M. Klein, T. Naumann and T. Riemann, Structure Functions, Quark Distributions and $\Lambda_{\rm QCD}$ at Hera, PHE 88-01, Contribution to Proc. of DESY Theory Workshop on Physics at HERA, Hamburg, West Germany, Oct 12-14, 1987. Published in DESY HERA Workshop 1987:0067.

[40] C. Aidala et al. [EIC Working Group], A White Paper Prepared for the NSAC LPR 2007, A High Luminosity, High Enery Electron-Ion-Collider.

[41] M. L. Mangano *et al.*, arXiv:hep-ph/0105155.

Diffractive PDFs

Paul Laycock on behalf of the H1 and ZEUS collaborations
Institute University of Liverpool

Abstract
Results are presented of the inclusive diffractive DIS cross-section and the data are used to test the proton vertex factorisation hypothesis. This hypothesis having been shown to be a good approximation to the data, the diffractive PDFs resulting from a NLO QCD fit to the inclusive data, which uses this approximation, are shown. The diffractive dijet cross-section in DIS is measured and compared to the predictions based on these DPDFs and reasonable agreement is found, further supporting the factorisation ansatz. Finally, the diffractive dijet and inclusive data are fit simultaneously resulting in diffractive PDFs that have similar precision in both the quark-singlet and gluon components.

1 Inclusive Diffractive DIS at HERA

A schematic diagram for the inclusive diffractive DIS process $ep \to eXp$ at HERA is shown in figure 1. It has been shown by Collins [1] that the diffractive DIS process factorises; shown in figure 1 is an additional assumption that the proton vertex dynamics factorise from the vertex of the hard scatter - proton vertex factorisation. The kinematic variables used to describe inclusive DIS are:

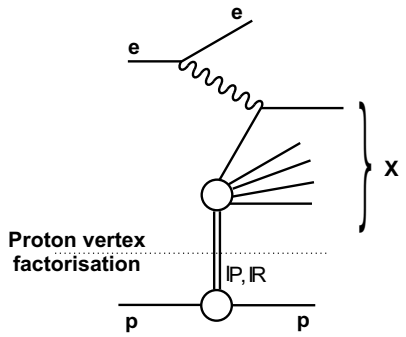
$$Q^2 = -q^2 = -(k - k')^2,\ x = \frac{Q^2}{2p \cdot q},\ y = \frac{p \cdot q}{p \cdot k}. \tag{1}$$

Here Q^2 is the virtuality of the exchange boson, x is the Bjorken scaling variable and y is the inelasticity. They are defined in terms of k and k', the four-momenta of the incoming and outgoing electrons, respectively, and the four-momentum of the incoming proton p. In addition to these standard DIS variables and the Mandelstam variables (t, s) the kinematic variables x_{IP} and β are useful in describing the diffractive DIS interaction. They are defined as:

$$\beta = \frac{Q^2}{Q^2 + M_X^2 - t},\ x_{IP} = \frac{Q^2 + M_X^2 - t}{Q^2 + W^2 - M_p^2} = \frac{x}{\beta} \tag{2}$$

where M_X is the invariant mass of the hadronic system X, M_p is the mass of the proton and $W^2 = (q + p)^2$ is the square of the centre of mass of the photon-proton system. x_{IP} is the fractional momentum of the proton carried by the diffractive exchange and β is the fractional momentum of the struck parton with respect to the diffractive exchange. The data are then discussed in terms of a reduced cross-section, $\sigma_r^{D(3)}(\beta, Q^2, x_{IP})$, defined as:

$$\frac{d^3\sigma_{ep\to eXp}}{d\beta dQ^2 dx_{IP}} = \frac{4\pi\alpha_{em}^2}{\beta Q^4}\left(1 - y + \frac{y^2}{2}\right)\sigma_r^{D(3)}(\beta, Q^2, x_{IP}). \tag{3}$$



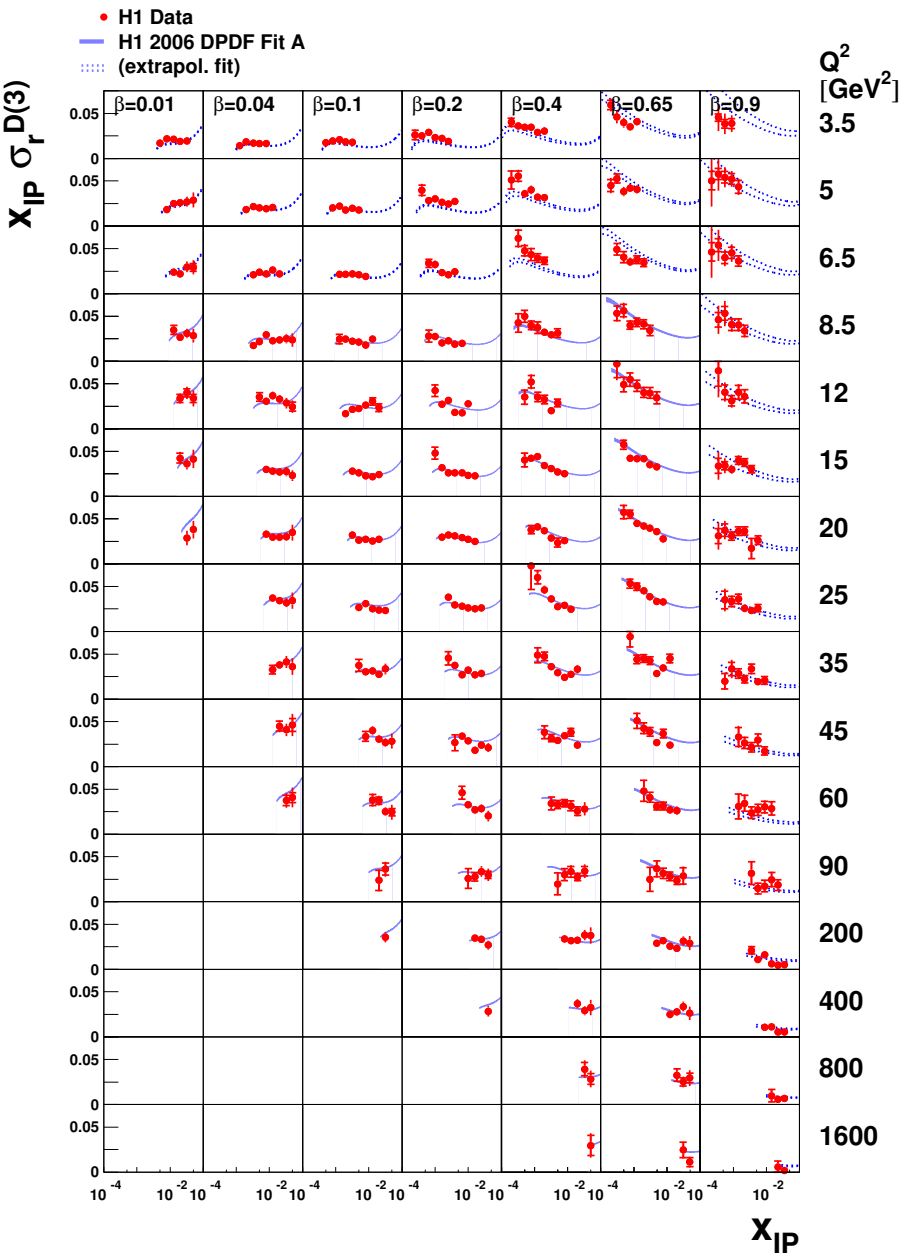


Fig. 1: (top) A schematic illustration of the NC diffractive DIS process $ep \to eXp$ at HERA. The dotted line indicates where the diagram can be divided under the assumption of proton vertex factorisation. The inclusive diffractive DIS cross section as measured by the H1 collaboration (bottom).

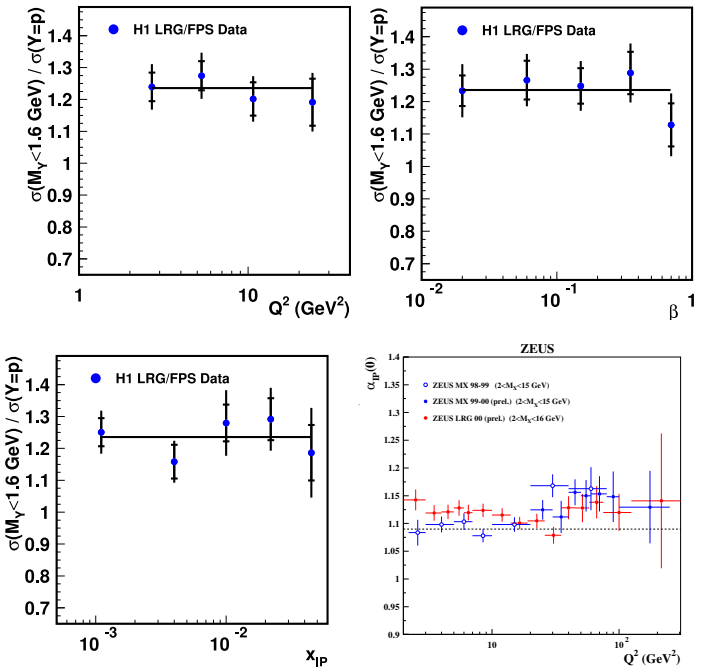


Fig. 2: The ratio of the tagged to untagged cross sections as a function of kinematic variables and (bottom right) the Q^2 dependence of the x_{IP} dependence of the data. The proton vertex factorisation hypothesis is a valid approximation within the precision of the data.

1.1 Experimental Methods

The inclusive diffractive DIS process is ideally measured by tagging the final state proton, e.g. [2], but such an experimental method suffers from low detector acceptance. In addition to this proton tagging method, both the H1 and ZEUS experiments use the topology of the hadronic final state to select diffractive events [3–5]; shown in figure 1 are the high statistics results of H1 using the large rapidity gap method.

If, as shown in figure 2, the ratio of the two methods, tagged to non-tagged, is taken as a function of the kinematic variables and if the Q^2 dependence of $\alpha_{IP}(0)$ (the x_{IP} dependence of the data) is studied it can be seen that, within the current experimental precision, the proton vertex factorisation hypothesis is a valid approximation of the data.

1.2 Inclusive diffractive DIS PDFs

Given the validity of the proton vertex factorisation ansatz, a NLO QCD fit using the proton vertex factorisation approximation is performed to the inclusive data [3], producing the diffractive PDFs shown in figure 3. Also shown in figure 3 are the individual contributions of both the quark and gluon driven terms to the logarithmic Q^2 derivative of the inclusive cross section. At high β, sensitivity to the gluon is all but lost. The result is an ambiguous gluon at high momentum fractions z, as seen by the comparison of Fits A and B, which give a similar χ^2 fit probability.

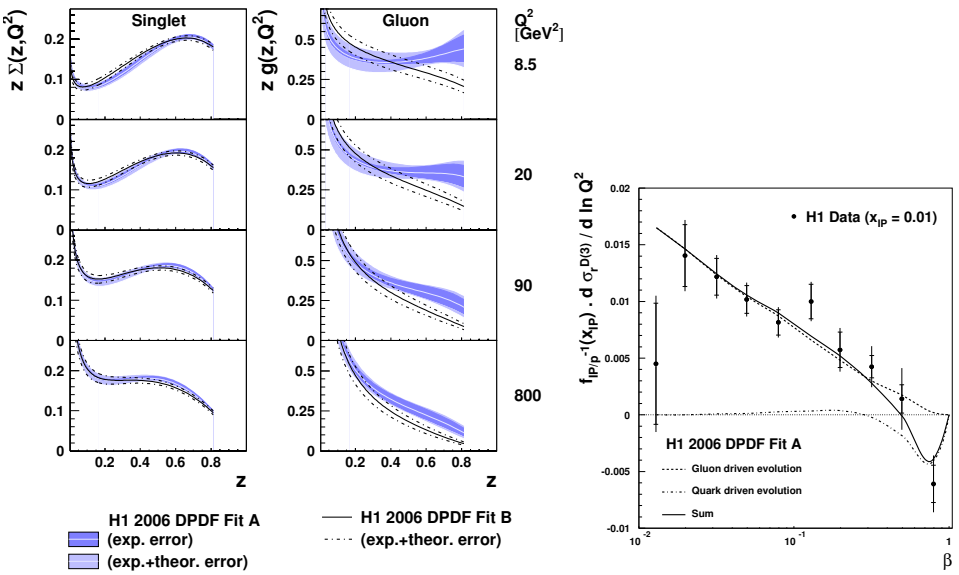


Fig. 3: The diffractive PDFs resulting from two NLO QCD fits to the inclusive data (left) and (right) the $\ln Q^2$ dependence of the data showing the quark and gluon driven terms separately.

2 Diffractive Dijets in DIS

Shown in figure 4 is a schematic diagram for the diffractive dijets in DIS process at HERA. Assuming that this diagram dominates the production mechanism, this process should provide a sensitive tool with which to probe the diffractive gluon and test the predictions obtained from fits to inclusive diffractive data. Figure 4 shows a comparison of a measurement made by ZEUS of the diffractive dijet cross section in DIS [6] compared to the predictions of both fits to the H1 inclusive data. The prediction of Fit B is favoured. For more comparisons, see the talk on "Factorisation breaking in diffraction, including leading baryons" by A. Bonato in these proceedings.

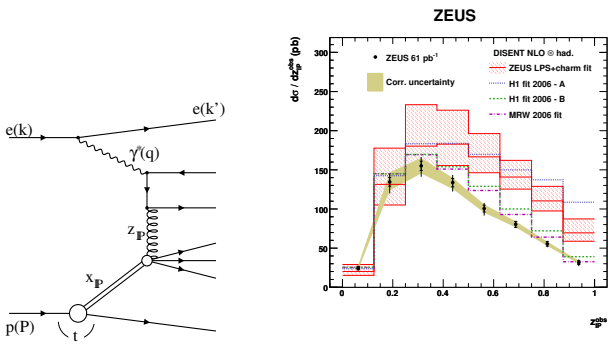


Fig. 4: A schematic diagram for the diffractive dijets in DIS process (left). The diffractive dijets in DIS data compared to the results of both fits to the inclusive data (right).

2.1 Combined fit of inclusive and dijet data

The diffractive dijet data has been used in combination with the inclusive data to fully constrain both the quark-singlet and gluon terms in a combined NLO QCD fit [7]. The resulting fit is shown compared to the diffractive dijet data in figure 5; it is worth noting that the difference in the description of the inclusive data, when compared to the inclusive-only fit, is negligible. Finally, the diffractive PDFs resulting from the combined fit are shown in figure 6. The gluon and quark components have similar good precision across the whole phase space and in particular the gluon is well constrained at large momentum fractions z.

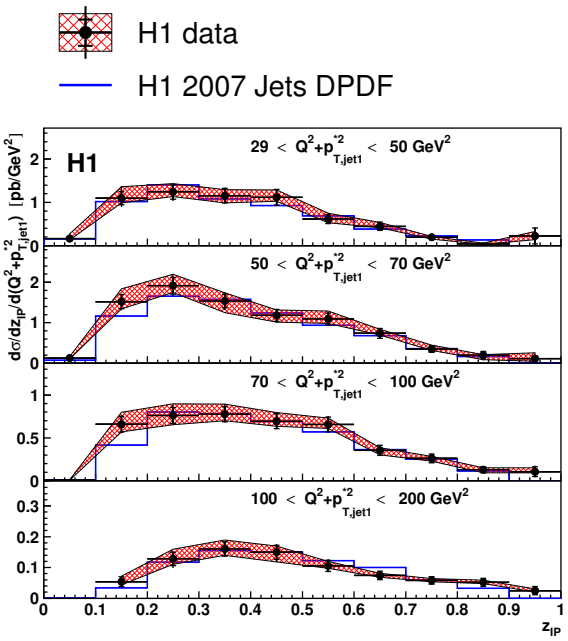


Fig. 5: The diffractive dijet data compared to a combined NLO QCD fit of the same diffractive dijet data and the inclusive data.

3 Conclusion

Results have been presented of the inclusive diffractive DIS cross-section and the data were used to test the proton vertex factorisation hypothesis. Within the current limit of experimental precision, the proton vertex factorisation hypothesis is seen to be a good approximation of the data. Following this, NLO QCD fits of the inclusive data were shown, with the observation that the gluon is not well constrained by the inclusive data alone at large momentum fractions. This was seen to be a direct consequence of the dominance of the quark-driven contributions to the logarithmic Q^2 derivative of the cross section at large momentum fractions.

The diffractive dijet cross-section in DIS has been measured and compared to the predictions based on these inclusive DPDFs and reasonable agreement was found, further supporting the factorisation ansatz. Finally, the result of a simultaneous fit to both the diffractive dijet and inclusive data produced diffractive PDFs that have similar precision in both the quark-singlet and gluon components. In particular, the gluon resulting from this combined fit is well constrained at large momentum fractions.

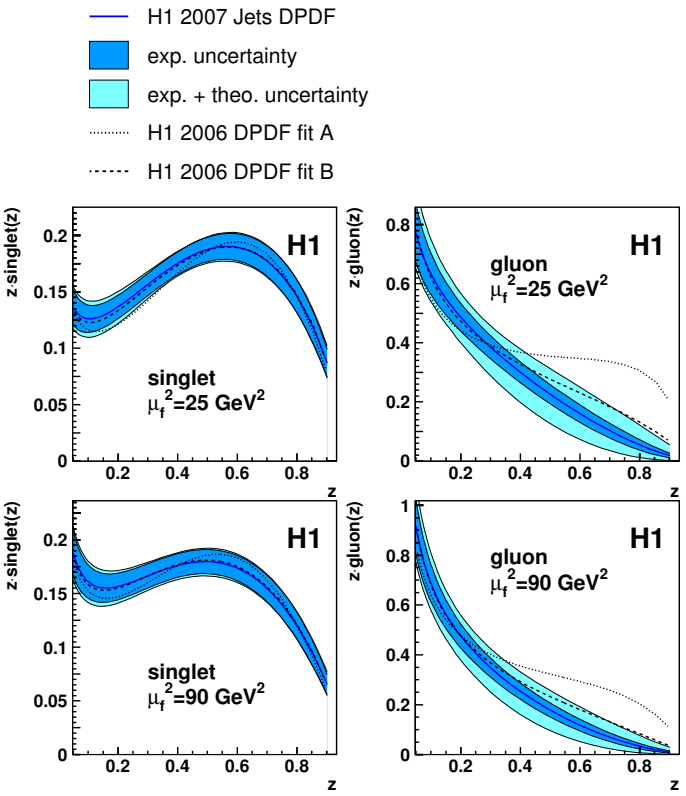


Fig. 6: The DPDFs resulting from the combined fit to the inclusive and dijet diffractive DIS data.

References

[1] J. C. Collins, Phys. Rev. **D57**, 3051 (1998). hep-ph/9709499.

[2] H1 Collaboration, A. Aktas *et al.*, Eur. Phys. J. **C48**, 749 (2006). hep-ex/0606003.

[3] H1 Collaboration, A. Aktas *et al.*, Eur. Phys. J. **C48**, 715 (2006). hep-ex/0606004.

[4] ZEUS Collaboration, S. Chekanov *et al.* (2006). ZEUS-prel-06-024.

[5] ZEUS Collaboration, S. Chekanov *et al.* (2006). ZEUS-prel-06-025.

[6] ZEUS Collaboration, S. Chekanov *et al.* (2007). arXiv:0708.1415 [hep-ex].

[7] H1 Collaboration, A. Aktas *et al.* (2007). arXiv:0708.3217 [hep-ex].

Factorisation breaking in diffraction

A. Bonato, on behalf of the H1 and ZEUS collaborations
DESY / Universität Hamburg

Abstract
Diffractive and leading neutron production contribute to a significative part of the ep interaction at the HERA collider. In the theoretical models that describe these set of events some factorisation properties of the cross sections are either expected or postulated. The test of such factorisations from the H1 and ZEUS collaborations is presented here.

1 Introduction

At the ep collider HERA the internal structure of the proton can be probed by the photon, γ^*, emitted by the electron. In diffractive interactions the outgoing proton stays intact or in a low-mass resonant state [1]. These specific events contribute significantly to the total cross section and can be modelled via the emission from the proton of a diffractive colour-singlet exchange that subsequently is probed by the γ. The outgoing protons are accompanied by the presence of a Large Rapidity Gap (LRG), a large angular region in the direction of the scattered proton without hadronic activity [2, 3]. In recent years, perturbative QCD (pQCD) was shown to be a valuable tool to describe this subset of events, given the presence of a hard scale that allows the use of perturbative analysis [1, 3, 4]. In the case of deep inelastic scattering (DIS), high values of the virtuality of the photon, Q^2, emitted by the electron that probes the proton internal structure provide such a hard scale. When the photon exchanged is almost real (i.e. for the kinematic regime $Q^2 \sim 0\ GeV^2$ known as photoproduction, γp) a hard scale can still be obtained by producing jets with a high transverse energy, E_T, or quarks with a heavy mass.

It has been proven for diffractive DIS that the cross section can be factorised into two parts, universal parton distribution functions (dPDFs) and process-dependent coefficients that can be calculated in pQCD [5]. In spite of its theoretical proof in DIS, QCD factorisation in diffraction has been shown to fail in $p\bar{p}$ collisions at the TeVatron accelerator [6]. The Next-To-Leading (NLO) order pQCD calculations using dPDFs extracted at HERA overestimated the data by roughly a factor of ten. Such a data suppression is due to soft rescatterings between spectator partons present in the protons that may spoil the LRG used for tagging the event as diffractive (Rapidity Gap Survival probability). Phenomenological models are able to describe this suppression and predict that a similar effect should be seen at HERA in diffractive γp when the low-virtuality photon exhibits a hadronic behaviour (resolved photon) [7, 8]. No suppression is expected in DIS nor in the subset of γp events where the photon couples directly to a quark in the hard subprocess (direct photon).

The test of this theorem is important for proving that diffractive processes can be described by means of pQCD. Furthermore the study of diffractive final states is useful for constraining the dPDFs that are extracted from inclusive diffractive data and have large uncertainties, especially the gluon densities. Such a combined fit has been published recently by the H1 collaboration [9].

2 QCD Factorisation in diffraction

The most suited final states for testing the QCD factorisation in diffraction are the production of dijets and heavy quarks. The appealing features of these processes are

- presence of a hard scale that allows the use of pQCD;
- sensitivity to the gluon content of the diffractive exchange via the boson-gluon fusion (BGF) production process.

The NLO prediction can be compared to the measurement of the cross section in order to observe any suppression of the data relative to the theory. The relevant variables in these analyses are the virtuality of the γ, Q^2, the energy of the $\gamma - p$ centre-of-mass, W and the fractional longitudinal momentum lost by the proton, $x_{I\!P}$. In the dijets analyses the variable $z_{I\!P}^{\rm obs}$ is defined as the fraction of the diffractive exchange momentum carried by the parton entering the hard subprocess and is therefore the variable most sensitive to the dPDFs. In the γp case the variable x_γ is introduced; it describes the fraction of photon momentum entering in the hard subprocess and is therefore a good discriminant between direct- (i.e. $x_\gamma \simeq 1$) and resolved-photon (i.e. x_γ significantly lower than 1).

New results in diffractive dijet production in DIS have become available from the ZEUS and H1 collaboration at the time of writing [9–11]. The measurement performed by the H1 collaboration of the $z_{I\!P}^{\rm obs}$ dependence of the differential cross section can be seen in Fig. 1. The experimental data are compared to NLO predictions using two different available dPDFs. The data favour in particular the H1 2006 fit B even tough the theoretical uncertainties are large. ZEUS observes similar agreement between measured data and theoretical prediction. Additionally, the calculation using the MRW2006 fit [4] provides a good description of the data, very similar to the one using the H1 2006 fit B. This agreement supports the QCD factorisation statement in the DIS regime.

In Fig. 2, the differential cross section as a function of x_γ is presented for dijets in diffractive photoproduction for H1 and ZEUS respectively [12, 13]. The interpretation of the $p\bar{p}$ data suggests a suppression in the low x_γ region where the photon behaves like a hadron. The H1 measurement sees a global suppression of a factor 2, independently of x_γ while ZEUS doesn't see any significant overestimation of the NLO compared to the data. The differences in these results can be partially addressed in the uncertainties on the theoretical calculations. The different kinematic regions covered by the two analyses can also be due to the different outcome of the analyses. For instance, in the ZEUS case, the higher cut on the jet transverse energy suppresses the resolved photon contribution.

Results from the H1 Collaboration for diffractive D^* production in DIS are shown in Fig. 3 [14]. The cross section is presented as a function of the variable β, that here plays the role of $z_{I\!P}^{\rm obs}$ in the dijet case. The measurement is compared to both the central values of a NLO calculation using different dPDFs and to previous measurements. A consistent picture can be observed where measurements and theoretical predictions agree, again supporting QCD factorisation in diffractive DIS.

The production of D^* in γp was measured recently by both H1 and ZEUS [14, 15]. The ZEUS measurement of the differential cross section for such a process as a function of $x_{I\!P}$ is presented in Fig. 4. The NLO predictions based on different dPDFs are compared to the data

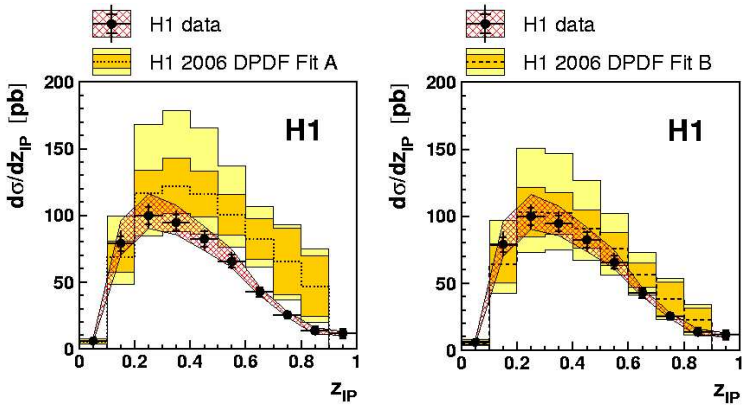


Fig. 1: H1 measurement of the single differential cross section as a function of $z_{I\!P}^{\rm obs}$. The data are shown as dots. The internal error bars represent the statistical uncertainty, the outer error bars the sum in quadrature of the statistical and uncorrelated systematic uncertainties. The hatched area shows the correlated systematic uncertainty. The measured points are compared to the NLO prediction using the (left) "H1 2006 fit A" and (right) "H1 2006 fit B" dPDFs. The dark shaded band surrounding the theoretical curve represents the uncertainty coming from the dPDFs and the hadronisation corrections. The lighter shaded band is the sum in quadrature of the dPDFs uncertainty and the scale uncertainty.

and exhibit a good agreement. Such a consistency can be explained by the fact that the charm content in the resolved photon is limited and therefore D^* can be produced only via BGF, i.e. direct-photon processes where QCD factorisation is expected to hold.

3 Vertex factorisation in leading neutron production

The production of leading baryons is a significant fraction of the events observed at HERA. A recent ZEUS publication presented measurements where an outgoing neutron carrying a fraction $x_{\rm L} = \frac{E_n}{E_p}$ of the initial p energy was detected by means of a dedicated forward instrumentation [16]. The models for the production of leading neutron at HERA largely use the One-Pion Exchange (OPE) approximation for describing such a process. The relevance of this production mechanism is more important at high values of $x_{\rm L}$. The limiting fragmentation hypothesis is commonly used in this context. It states that, in the high energy limit, the production of particles in the proton-target fragmentation region is independent of the nature of the incident particle, i.e. the lepton variables Q^2 and W. Factorisation tests involve comparing semi-inclusive rates, normalised to their total cross sections, to study whether particle production from a given target is independent of the lepton variables.

The vertex factorisation can be broken by rescattering effects that occur between the leading neutron and the γ. In that case the neutron kinematics may change towards lower $x_{\rm L}$ and higher $p_{\rm T}$, migrating consequently outside the detector acceptance. In Fig. 5 the ratio ρ is shown as a function of $x_{\rm L}$. This variable is defined as the ratio of two normalised differential cross section measured in two distinct Q^2 regions. If the vertex factorisation holds, ρ is equal to

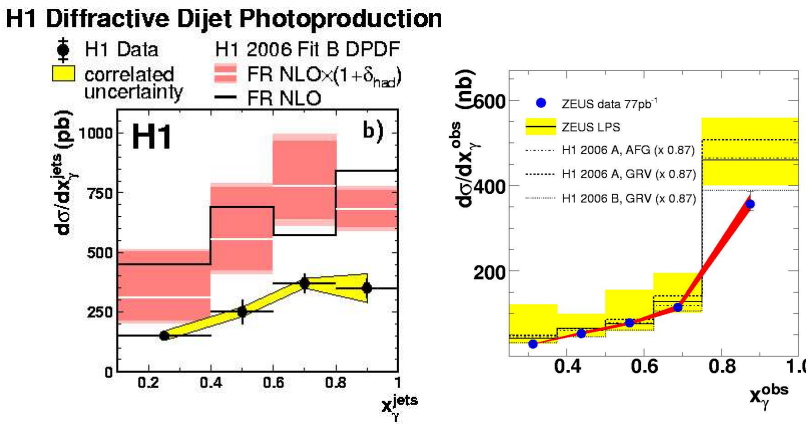


Fig. 2: Differential cross section for dijet production in diffractive γp as a function of x_γ measured by (left) H1 and (right) ZEUS. In both plots the data are shown as dots, the statistical uncertainty as the internal error bars, the sum in quadrature of the statistical and uncorrelated systematic uncertainties as outer error bars and the shaded band shows the correlated systematic uncertainty.

unity. Otherwise the enhanced rescattering in the low Q^2 region would lower this ratio. As seen in the plot this ratio is significantly lower than 1, meaning that vertex factorisation is violated. Two different models for this absorption process are compared to the data. The D'Alesio-Pirner model [17] implements absorption effects via rescattering between the leading neutron and the γ, in a fashion similar to the QCD factorisation breaking described in Sect. 2. When the γ has a low virtuality its transverse size is larger and the probability that the leading neutron scatters over it is increased. The NSZ model [18] describes absorption employing the optical theorem together with multi-Pomeron exchanges . The two predictions are also presented after correcting for the different W dependence of the pion cross section in DIS and γp cross sections. The D'Alesio-Pirner model describes well both normalisation and shape of the measurement while the NSZ one does not have a steep enough rise as a function of x_{L}.

4 Conclusions

Many factorisation mechanisms are used in describing the production of leading baryons. The experimental test of them is an important step in order to build a robust theory for explaining these processes. A key tool for a QCD-motivated description of diffraction is the QCD factorisation theorem. Analyses performed by the H1 and the ZEUS collaborations show that this ansatz is valid in the DIS regime, although large theoretical uncertainties affect the power of the test. In the γp regime, the situation is still unclear and some discrepancies between the conclusions of the two experiments are observed. The vertex factorisation used in many phenomenological models for describing the leading neutron production has been shown by ZEUS to be broken in γp processes. It is interesting to notice that the model that best describes this vertex factorisation breaking implements the same rescattering effects that affects the QCD factorisation in diffraction.

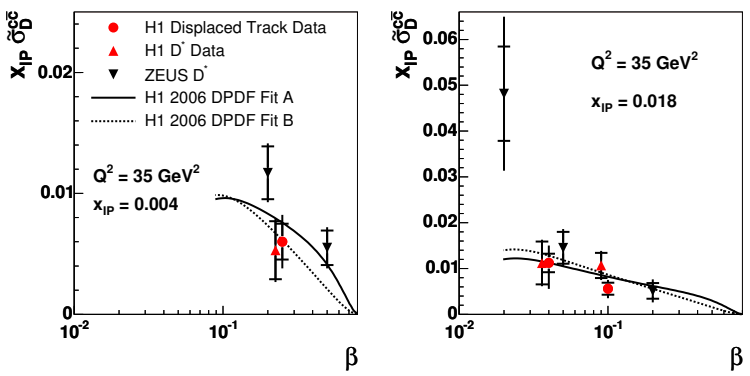


Fig. 3: Differential cross section for D^* meson production in diffractive DIS as a function of β, measured for two different values of $x_{I\!P}$. The data are shown as dots, the statistical uncertainty as the internal error bars, the sum in quadrature of the statistical and uncorrelated systematic uncertainties as outer error bars. The two curves represent the central values of NLO predictions using two different sets of dPDFs.

References

[1] ZEUS Coll., S. Chekanov et al., Eur. Phys. J. **C 38**, 43 (2004).

[2] ZEUS Coll., J. Breitweg et al., Eur. Phys. J. **C 6**, 43 (1999).

[3] H1 Coll., A. Aktas et al., Eur. Phys. J. **C 48**, 715 (2006).

[4] A.D. Martin, M.G. Ryskin and G. Watt, Phys. Lett. **B 644**, 131 (2006).

[5] J.C. Collins, Phys. Rev. **D 57**, 3051 (1998);
J.C. Collins, J. Phys. **G 28**, 1069 (2002).

[6] CDF Coll., T. Affolder et al., Phys. Rev. Lett. **84**, 5043 (2000).

[7] A.B. Kaidalov, V.A. Khoze, A.D. Martin and M.G. Ryskin, Eur. Phys. J. **C 21**, 521 (2001);
E. Gotsman, E. Levin and U. Maor, Phys. Lett. **B 438**, 229 (1998);
B. Cox, J. Forshaw and L. Lönnblad, JHEP 9910:023 (1999).

[8] A.B. Kaidalov, V.A. Khoze, A.D. Martin and M.G. Ryskin, Phys. Lett. **B 567**, 61 (2003).

[9] H1 Coll., A. Aktas et al., *Subm. to JHEP*, arXiv:0708.3217v1 (2007).

[10] ZEUS Coll., S. Chekanov et al., *Accepted by Eur Phys. J. C*, arXiv:0708.1415 (2007).

[11] P. Laycock for the H1 and ZEUS collaborations, *these proceedings*.

[12] H1 Coll., A. Aktas et al., Eur. Phys. J. **C 51**, 549 (2007).

[13] ZEUS Coll., S. Chekanov et al., *Subm. to Eur Phys. J. C*, arXiv:0710.1498 (2007).

[14] H1 Coll., A. Aktas et al., Eur. Phys. J. **C 50**, 1 (2007).

[15] ZEUS Coll., S. Chekanov et al., Eur. Phys. J. **C 51**, 301 (2007).

[16] ZEUS Coll., S. Chekanov et al., Nucl. Phys. **B 776**, 1 (2007).

[17] U. D'Alesio and H.J. Pirner, Eur. Phys. J. **A 7**, 109 (2000).

[18] N.N. Nikolaev, J. Speth and B.G. Zakharov, Preprint KFA-IKP(TH)-1997-17 (hep-ph/9708290), KFA-IKP (1997).

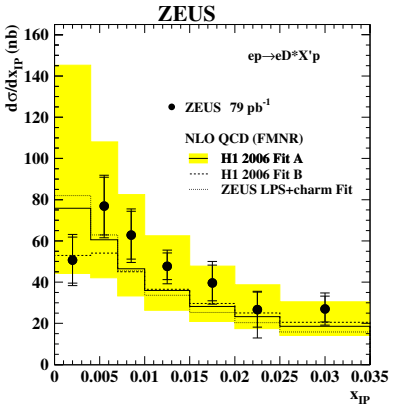


Fig. 4: Differential cross section for D^* meson production in diffractive γp as a function of $x_{I\!P}$. The data are shown as dots, the statistical uncertainty as the internal error bars, the sum in quadrature of the statistical and uncorrelated systematic uncertainties as outer error bars. The curves represent the central values of NLO predictions using different sets of dPDFs. The theoretical uncertainty on the NLO prediction due to the scale choice is displayed as a shaded band only for the calculation using the H1 2006 fit A.

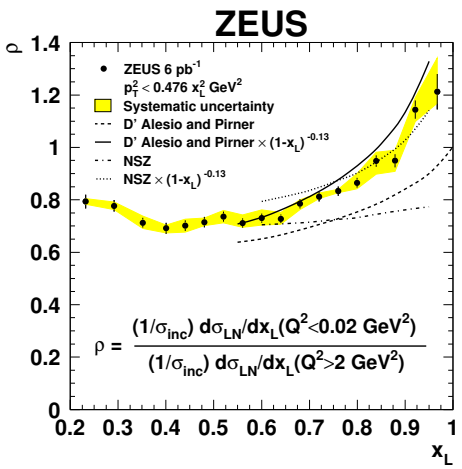


Fig. 5: The value of ρ, the ratio of the x_{L} distributions for γp and DIS, as a function of x_{L}. The error bars show the statistical uncertainty; the shaded band show the systematic uncertainties. The theoretical predictions from two models are shown as a dashed and a dashed-dotted curve. The same predicitons corrected for the W dependence of the pion cross section in γp and DIS are shown as a solid and a dotted curve.

Diffractive structure function F_L^D from fits with higher twist

Krzysztof Golec-Biernat[1,2†], *Agnieszka Łuszczak*[1]
[1]Institute of Nuclear Physics Polish Academy of Sciences, Cracow, Poland
[2]Institute of Physics, University of Rzeszów, Rzeszów, Poland

Abstract
We make predictions for the diffractive longitudinal structure function F_L^D to be measured at HERA, based on the DGLAP fits of diffractive parton distributions with an additional twist–4 term. This term describes the diffractive $q\bar{q}$ production from longitudinal photons and significantly changes predictions for F_L^D obtained in the pure DGLAP analysis.

1 Introduction

We are interested in diffractive deep inelastic scattering (DDIS) at HERA which provides a very interesting example of processes with a clear interplay between hard and soft aspects of QCD interactions. In addition to the scattered electron and proton a diffractive system forms, which is well separated in rapidity from the scattered proton. The most important observation made at HERA is that diffractive processes in DIS are not rare, they constitute up to 15% of all deep inelastic events [1–4].

After the integration over the proton azimuthal angle, the DDIS cross section depends on two diffractive structure functions, F_2^D and F_L^D. They depend on four variables: Bjorken-x, photon virtuality Q^2 and two additional variables

$$x_{I\!P} = \frac{Q^2 + M^2 - t}{Q^2 + W^2}\,, \qquad\qquad t = (p - p')^2\,, \tag{1}$$

where M is mass of the diffractive system, W is center-of-mass energy of the gamma-proton system and p, p' are incident and scattered proton momenta.

In our analysis the diffractive structure functions are given by the decomposition into the leading and higher twist contributions

$$F_{2,L}^D \;=\; F_{2,L}^{D(tw2)} \;+\; F_L^{D(tw4)} \;+\; \ldots\,. \tag{2}$$

In the Bjorken limit, the leading twist–2 part depends logarithmically on Q^2 while the twist–4 part is suppressed by an additional power of $1/Q^2$. However, this contribution plays an especially important role in DDIS since it dominates over the twist–2 for small diffractive masses $M^2 \ll Q^2$. Thus, it cannot be neglected. Physically, the twist–4 contribution is given by the diffractively produced $q\bar{q}$ pair from *longitudinally* polarized virtual photons. The effect of this contribution, is particularly important for the longitudinal diffractive structure function F_L^D which is supposed to be measured in the last runs of HERA.

[†] speaker

2 Twist–2 contribution

The leading twist–2 part of the diffractive structure functions is given in terms of diffractive parton distributions (DPD) through the standard collinear factorization formulae [5–8]. In the next-to-leading logarithmic approximation we have

$$F_2^{D(tw2)}(x,Q^2,x_{I\!P},t) \;=\; S_D + \frac{\alpha_s}{2\pi}\left\{C_2^S \otimes S_D + C_2^G \otimes G_D\right\} \tag{3}$$

$$F_L^{D(tw2)}(x,Q^2,x_{I\!P},t) \;=\; \frac{\alpha_s}{2\pi}\left\{C_L^S \otimes S_D + C_L^G \otimes G_D\right\} \tag{4}$$

where α_s is the strong coupling constant and $C_{2,L}^{S,G}$ are coefficients functions known from inclusive DIS [9, 10]. The integral convolution is performed for the longitudinal momentum fraction and reads

$$(C \otimes F)(\beta) = \int_\beta^1 dz\, C\left(\beta/z\right) F(z)\,. \tag{5}$$

Notice that in the leading order, when terms proportional to α_s are neglected, $F_L^{D(tw2)} = 0$. The functions S_D and G_D are built from diffractive quark and gluon distributions, q_D^f and g_D:

$$S_D(x,Q^2,x_{I\!P},t) \;=\; \sum_{f=1}^{N_f} e_f^2\, \beta\left\{q_D^f(\beta,Q^2,x_{I\!P},t) + \overline{q}_D^f(\beta,Q^2,x_{I\!P},t)\right\} \tag{6}$$

and

$$G_D(x,Q^2,x_{I\!P},t) = \beta g_D(\beta,Q^2,x_{I\!P},t)\,. \tag{7}$$

From these equations we see that the new variable β, given by the formula

$$\beta = \frac{x}{x_{I\!P}} = \frac{Q^2}{M^2+Q^2}\,, \tag{8}$$

plays the role of the Bjorken variable in DDIS.

The DPD evolve with Q^2 with the DGALP evolution equations [11] for which $(x_{I\!P},t)$ are external parameters. In this analysis we assume *Regge factorization* for these variables:

$$q_D^f(\beta,Q^2,x_{I\!P},t) \;=\; f_{I\!P}(x_{I\!P},t)\; q_{I\!P}^f(\beta,Q^2) \tag{9}$$

$$g_D(\beta,Q^2,x_{I\!P},t) \;=\; f_{I\!P}(x_{I\!P},t)\; g_{I\!P}(\beta,Q^2)\,. \tag{10}$$

The motivation for such a factorization is a model of diffractive interactions with pomeron exchange [12]. In this model $f_{I\!P}$ is the pomeron flux

$$f_{I\!P}(x_{I\!P},t) \;=\; N\,\frac{F_{I\!P}^2(t)}{8\pi^2}\, x_{I\!P}^{\,1-2\,\alpha_{I\!P}(t)}\,, \tag{11}$$

where $\alpha_{I\!P}(t) = \alpha_{I\!P}(0) + \alpha'_{I\!P} t$ is the pomeron Regge trajectory and

$$F_{I\!P}^2(t) \;=\; F_{I\!P}^2(0)\,\mathrm{e}^{-B_D|t|} \tag{12}$$

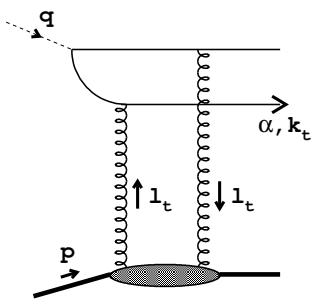


Fig. 1: Twist-4 contribution from longitudinally polarized photons. Two gluons here model the pomeron exchange which is later unitarized and effectively described by the dipole cross section, see the text below.

is a formfactor which describes the pomeron coupling to the proton. Following [7] we set $F_{I\!P}^2(0) = 54.4$ GeV^{-2} and $B_D = 5.5$ GeV^{-2} from HERA data. In addition, $\alpha'_{I\!P} = 0.25$ GeV^{-2} and $\alpha_{I\!P}(0)$ is fitted to data. The quark distributions are flavour independent and are given by a singlet quark distribution $\Sigma_{I\!P}(\beta, Q^2)$:

$$q^f_{I\!P}(\beta, Q^2) \,=\, \overline{q}^f_{I\!P}(\beta, Q^2) \,\equiv\, \frac{1}{2N_f}\,\Sigma_{I\!P}(\beta, Q^2)\,, \tag{13}$$

where N_f is the number of active flavours. We fit the distributions $\Sigma_{I\!P}(\beta)$ and $G_{I\!P}(\beta)$ at an initial scale $Q_0^2 = 1.5$ GeV^2 to diffractive data from HERA, using the DGLAP evolution equations in the next-to-leading order approximation. We also include the charm quark contribution into the analysis [13].

3 Twist–4 contribution

This contribution describes the $q\overline{q}$ diffractive production from the longitudinally polarized virtual photons, see Fig. 1. Although formally suppressed by $1/Q^2$, it dominates over the vanishing twist–2 contribution for small diffractive masses $M^2 \ll Q^2$ ($\beta \to 1$) [14–16]. This is why it cannot be neglected in the analysis of diffractive data in DIS.

We used the following form of the twist–4 contribution which has to be added to $F_2^{D(tw2)}$ and $F_L^{D(tw2)}$ [17]:

$$F_{Lq\bar{q}}^{D(tw4)} = \frac{3\,\sum_f e_f^2}{16\pi^4 x_{I\!P}}\,\mathrm{e}^{-B_D|t|}\,\frac{\beta^3}{(1-\beta)^4}\int\limits_0^{\frac{Q^2(1-\beta)}{4\beta}} dk^2\,\frac{k^2/Q^2}{\sqrt{1-\dfrac{4\beta}{1-\beta}\dfrac{k^2}{Q^2}}}\,\phi_0^2 \tag{14}$$

with

$$\phi_0 \;=\; k^2 \int\limits_0^\infty dr\, r\, K_0\left(\sqrt{\frac{\beta}{1-\beta}}kr\right) J_0(kr)\, \hat{\sigma}(x_{I\!P}, r)\,, \tag{15}$$

where K_0 and J_0 are Bessel functions. Strictly speaking, formula (14) contains all powers of $1/Q^2$ but the twist–4 part proportional to $1/Q^2$ dominates. The function $\hat{\sigma}(x_{I\!P}, r)$ in eq. (15) is the dipole-proton cross section which describes the diffractive interaction of the quark or gluon dipole with the proton. Following [18] we choose

$$\hat{\sigma}(x_{I\!P}, r) \;=\; \sigma_0 \left\{1 - \exp\left(-r^2 Q_s^2(x_{I\!P})\right)\right\} \tag{16}$$

where $Q_s^2(x_{I\!P}) \;=\; Q_0^2\, x_{I\!P}^{-\lambda}$ is the saturation scale which brings the energy dependence of the twist–4 contribution. The three parameters of the dipole cross section: σ_0, Q_0^2 and λ, are taken from [18]. This form of the dipole cross section provides a successful description of the inclusive and diffractive data from HERA. We also consider a reggeon contribution, described in detail in [13], which improves a fit quality through a better $x_{I\!P}-$dependence.

4 Fit results

In our analysis we use diffractive data on F_2^D (or the reduced cross section σ_r^D) from H1 [3, 4] and ZEUS [1, 2]. These data were obtained in different kinematical regions and using different methods of their analysis, thus we decided to analyse them separately. In all cases we find a good fit quality. A full discussion of the fit details is given in [13].

For each data set we performed two fits: without twist–4 (pure DGLAP fits) and with twist–4 added. Thus we obtained two sets of diffractive paton distributions which allow us to make predictions for the longitudinal structure function F_L^D. The diffractive parton distributions (DPD) from the analysis of H1 data are shown in Fig. 2. They are given in terms of the pomeron parton distributions which can be multiplied by the pomeron flux $f(x_{I\!P}, t)$ to obtain the DPD.

We see that the singlet quark distributions from the two fits are practically the same while the gluon distributions are different. The gluon from the fit with twist–4 is stronger peaked near $\beta \approx 1$ than in the twist–2 fit. This rather surprising result can be understood by looking at the logarithmic slope $\partial F_2^D / \partial \ln Q^2$ for fixed β. In the leading logarithmic approximation we have from the DGLAP equations

$$\frac{\partial F_2^D}{\partial \ln Q^2} \sim \frac{\partial \Sigma_{I\!P}}{\partial \ln Q^2} = P_{qq} \otimes \Sigma_{I\!P} \;+\; P_{qG} \otimes G_{I\!P} \;-\; \Sigma_{I\!P} \int P_{qq} \tag{17}$$

where the negative term sums virtual corrections. For large β, the measured slope is negative which means that the virtual term must dominate over the positive ones. The addition of the twist–4 contribution to F_2^D contributes a negative value to the slope which has to be compensated by a larger gluon distribution.

In Fig. 3, we show the diffractive structure functions resulting from the determined parton distributions. As expected, F_2^D is practically the same in both fits. However, the F_L^D curves are significantly different due to the twist–4 contribution (shown as the dotted lines), present in the twist–(2+4) fit. Let us emphasise that both sets of curves were found in fits which well describe

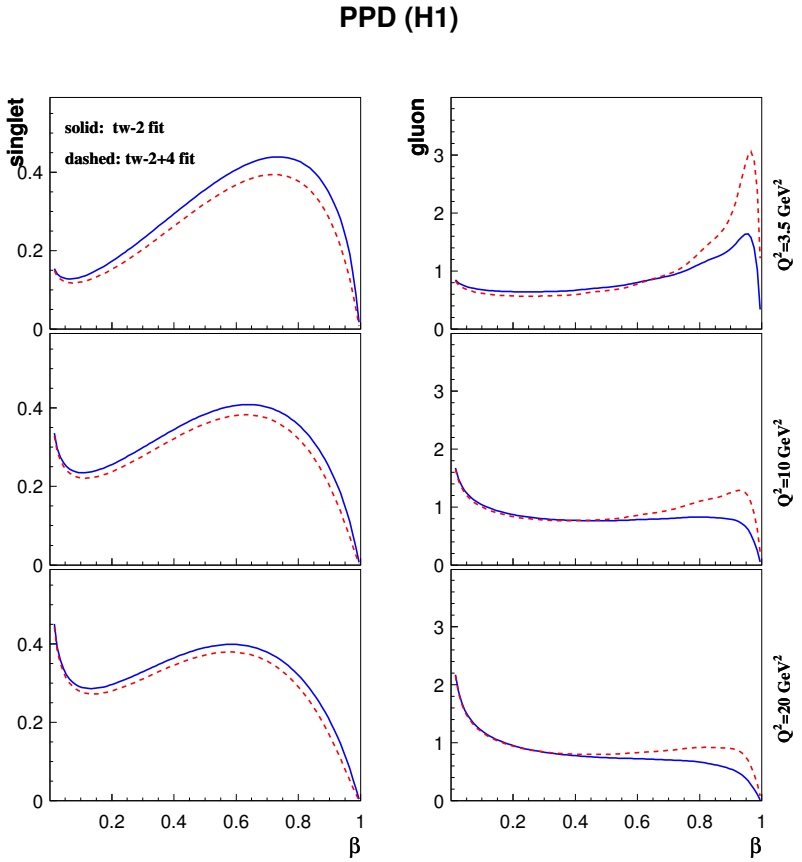


Fig. 2: Pomeron parton distributions: quark singlet (left) and gluon (right) from the H1 data. Solid lines: twist–2 fit; dashed lines: fit with twist–4.

the existing data, especially in the region of β where twist–4 is important. Thus, an independent *measurement* of F_L^D in this region would be an important confirmation of the QCD approach to diffraction.

The importance of the twist–4 contribution for F_L^D at large β is also shown in Fig. 4 where we present our predictions based on the analysis of the H1 data. The solid curve gives F_L^D from the pure DGLAP fit while the dashed curves are predictions of the fits with the twist–4 contribution from [16]. The upper curve corresponds to the fit with the original normalization of twist-4 while for the lower curve twist–4 was multiplied by 0.5. Thus, the band reflects the scale of our uncertainty. Let us emphasise that in all three cases shown in this figure, we found a good description of the data. Giving the size of the effect, we conclude that the planned measurements at HERA will have a chance to directly confirm the QCD mechanism of DIS diffraction. A similar analysis performed for the diffractive ZEUS data leads to the same conclusion, see [16] for details.

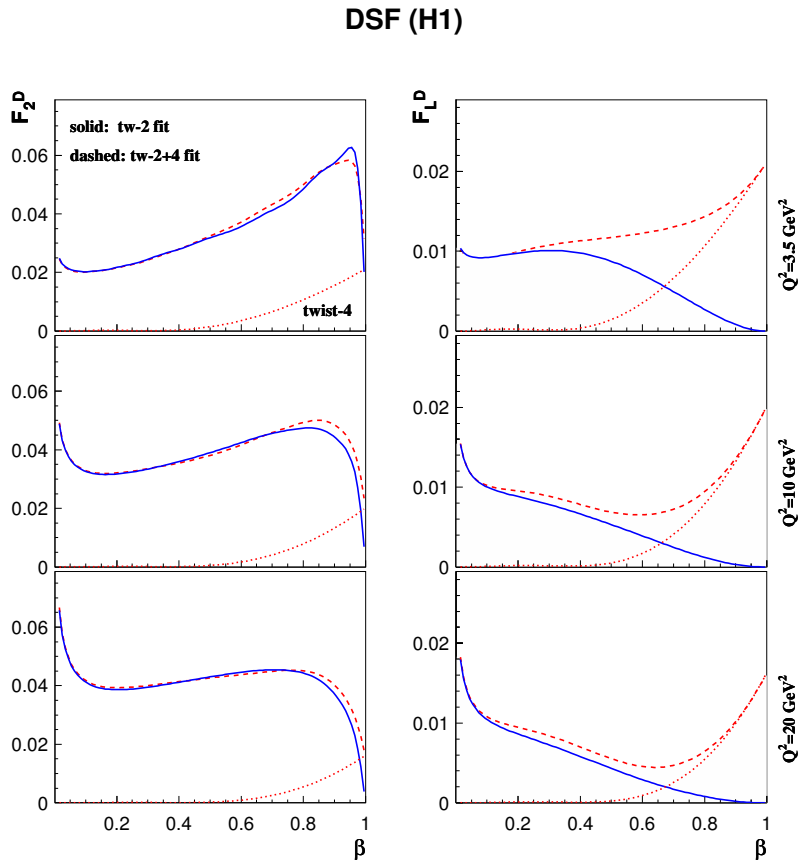


Fig. 3: Diffractive structure functions F_2^D (left) and F_L^D (right) from fits to the H1 data for $x_{I\!P} = 10^{-3}$. Solid lines: twist–2 fit; dashed lines: twist–(2+4) fit; dotted lines: twist–4 contribution.

5 Summary

We performed an analysis of the diffractive data from HERA determining diffractive parton distributions. In addition to the standard twist–2 formulae, we also considered a twist–4 contribution, suppressed by an additional power of $1/Q^2$ but dominating in the region of large β. This contribution comes from the $q\overline{q}$ diffractive production from longitudinally polarized virtual photons and dominates for $M^2 \ll Q^2$.

The twist–4 contribution leads to the diffractive gluon distribution which is more strongly peaked at $\beta \approx 1$ than the gluon distribution from the pure twist–2 fits. The main impact of this contribution is on the longitudinal diffractive structure function, which is significantly bigger than F_L^D from the twist–2 analysis in the region of $\beta > 0.6$. Thus, an independent measurement of F_L^D in this region at HERA could provide an additional confirmation of the QCD mechanism of diffractive interactions in DIS.

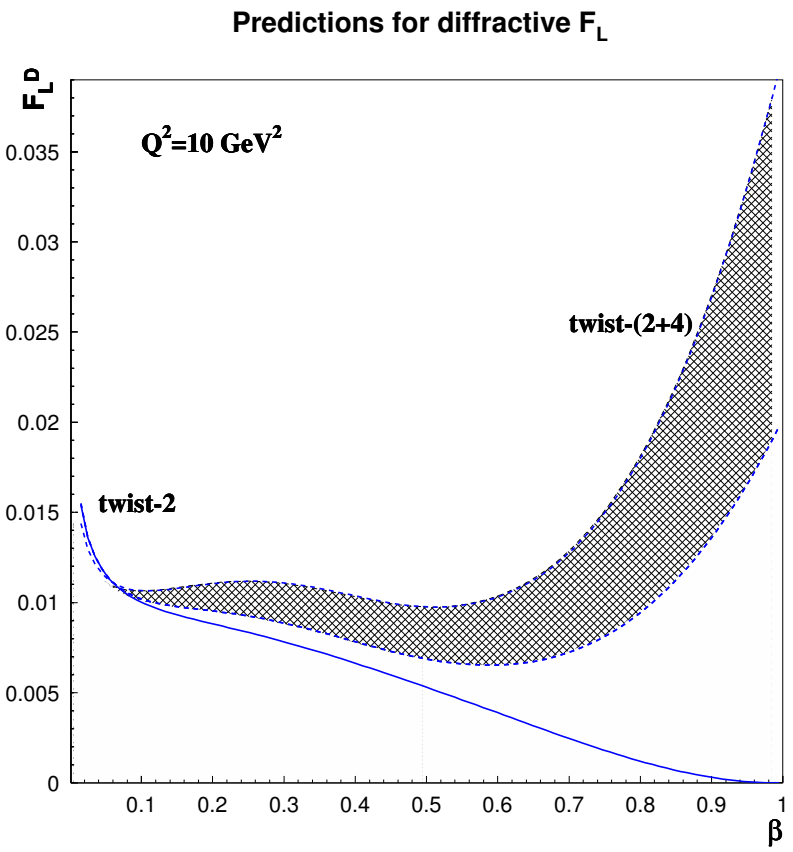


Fig. 4: Predictions for F_L^D for $x_{I\!P} = 10^{-3}$ from fits to H1 data. The solid line: F_L^D from twist–2 fit; dashed lines: F_L^D from fit with twist–4 from [16] – original curve (upper) and multiplied by 0.5 (lower).

ACKNOWLEDGEMENTS

A partial support by the MEiN research grant 1 P03B 028 28 (2005-08) and by the Polish-German Joint Project "Hadronic final states and parton distribution functions" is acknowledged.

References

[1] ZEUS Collaboration, S. Chekanov *et al.*, Eur. Phys. J. **C38**, 43 (2004). hep-ex/0408009.

[2] ZEUS Collaboration, S. Chekanov *et al.*, Nucl. Phys. **B713**, 3 (2005). hep-ex/0501060.

[3] H1 Collaboration, A. Aktas *et al.*, Eur. Phys. J. **C48**, 749 (2006). hep-ex/0606003.

[4] H1 Collaboration, A. Aktas *et al.*, Eur. Phys. J. **C48**, 715 (2006). hep-ex/0606004.

[5] L. Trentadue and G. Veneziano, Phys. Lett. **B323**, 201 (1994).

[6] A. Berera and D. E. Soper, Phys. Rev. **D50**, 4328 (1994). hep-ph/9403276.

[7] J. C. Collins, J. Huston, J. Pumplin, H. Weerts, and J. J. Whitmore, Phys. Rev. **D51**, 3182 (1995). hep-ph/9406255.

[8] A. Berera and D. E. Soper, Phys. Rev. **D53**, 6162 (1996). hep-ph/9509239.

[9] W. Furmanski and R. Petronzio, Phys. Lett. **B97**, 437 (1980).

[10] W. Furmanski and R. Petronzio, Zeit. Phys. **C11**, 293 (1982).

[11] J. C. Collins, Phys. Rev. **D58**, 094002 (1998). hep-ph/9806259.

[12] G. Ingelman and P. E. Schlein, Phys. Lett. **B152**, 256 (1985).

[13] K. Golec-Biernat and A. Luszczak (2007). hep-ph/0704.1608v2.

[14] M. Wusthoff, Phys. Rev. **D56**, 4311 (1997). hep-ph/9702201.

[15] J. Bartels, J. R. Ellis, H. Kowalski, and M. Wusthoff, Eur. Phys. J. **C7**, 443 (1999). hep-ph/9803497.

[16] K. Golec-Biernat and M. Wusthoff, Phys. Rev. **D60**, 114023 (1999). hep-ph/9903358.

[17] K. Golec-Biernat and M. Wusthoff, Eur. Phys. J. **C20**, 313 (2001). hep-ph/0102093.

[18] K. Golec-Biernat and M. Wusthoff, Phys. Rev. **D59**, 014017 (1999). hep-ph/9807513.

Diffractive parton distributions: the role of the perturbative Pomeron

G. Watt[1]*, A.D. Martin*[2] *and M.G. Ryskin*[3] †
[1] Department of Physics & Astronomy, University College London, WC1E 6BT, UK
[2] Institute for Particle Physics Phenomenology, University of Durham, DH1 3LE, UK
[3] Petersburg Nuclear Physics Institute, Gatchina, St. Petersburg, 188300, Russia

Abstract
We consider the role of the perturbative Pomeron-to-parton splitting in the formation of the diffractive parton distributions.

Diffractive deep-inelastic scattering (DDIS), $\gamma^* p \to X + p$, is characterised by a large rapidity gap (LRG) between the cluster X of outgoing hadrons and the slightly deflected proton, understood to be due to 'Pomeron' exchange. Let the momenta of the incoming proton, the outgoing proton, and the photon be labelled p, p' and q respectively; see Fig. 1(a). Then the basic kinematic variables in DDIS are the photon virtuality, $Q^2 = -q^2$, the Bjorken-x variable, $x_B = Q^2/(2p \cdot q)$, the squared momentum transfer, $t = (p - p')^2$, the fraction of the proton's light-cone momentum transferred through the LRG, $x_{\mathbb{P}} = 1 - p'^{+}/p^{+}$, and $\beta \equiv x_B/x_{\mathbb{P}}$.

It is common to perform analyses of DDIS data based on two levels of factorisation. First the t-integrated diffractive structure function $F_2^{\mathrm{D}(3)}$ may be written as the convolution of the usual coefficient functions $C_{2,a}$ as in DIS with diffractive parton distribution functions (DPDFs) a^{D} [1]:

$$F_2^{\mathrm{D}(3)}(x_{\mathbb{P}}, \beta, Q^2) \;=\; \sum_{a=q,g} \beta \int_\beta^1 \frac{\mathrm{d}z}{z^2}\, C_{2,a}\left(\frac{\beta}{z}\right)\, a^{\mathrm{D}}(x_{\mathbb{P}}, z, \mu_F^2), \tag{1}$$

with the factorisation scale μ_F usually taken to be Q. The DPDFs $a^{\mathrm{D}} = zq^{\mathrm{D}}$ or zg^{D} satisfy DGLAP evolution in μ_F. The convolution variable $z \in [\beta, 1]$ is the fraction of the Pomeron's light-cone momentum carried by the parton entering the hard subprocess. At leading-order (LO) the coefficient functions are $C_{2,q}(x) = e_q^2\, \delta(1-x)$ and $C_{2,g}(x) = 0$. The collinear factorisation theorem (1) applies when μ_F is made very large; it is correct up to power-suppressed corrections. In the second stage, Regge factorisation is usually assumed, such that the diffractive parton densities a^{D} are written as the product of the Pomeron flux factor $f_{\mathbb{P}} = \int \mathrm{d}t\ \exp(B_{\mathbb{P}}\, t)\ x_{\mathbb{P}}^{1-2\alpha_{\mathbb{P}}(t)}$ and the Pomeron parton densities $a^{\mathbb{P}} = zq^{\mathbb{P}}$ or $zg^{\mathbb{P}}$, that is,

$$a^{\mathrm{D}}(x_{\mathbb{P}}, z, \mu_F^2) = f_{\mathbb{P}}(x_{\mathbb{P}})\, a^{\mathbb{P}}(z, \mu_F^2). \tag{2}$$

The Pomeron trajectory is $\alpha_{\mathbb{P}}(t) = \alpha_{\mathbb{P}}(0) + \alpha'_{\mathbb{P}}\, t$. For simplicity, we omit the contribution of secondary Reggeons to the right-hand side of (2). Such an approach says nothing about the mechanism for diffraction: information about the diffractive exchange ('Pomeron') needs to be parameterised at the input scale μ_0 and fitted to the data.

† speaker

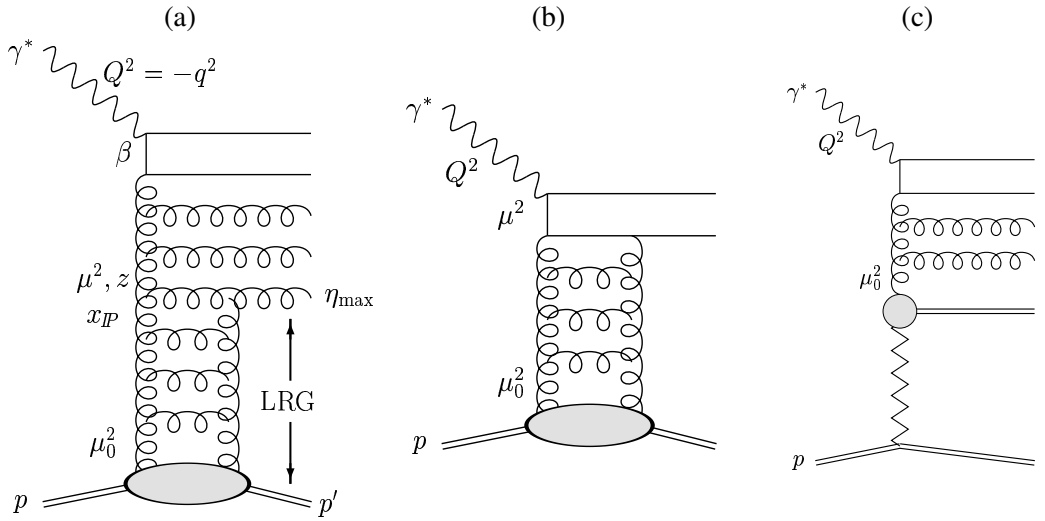


Fig. 1: (a) The perturbative *resolved* Pomeron contribution, which is the basis of the perturbative QCD approach, (b) the perturbative *direct* Pomeron contribution, and (c) the non-perturbative *resolved* Pomeron diagram, which accounts for the contribution from low scales, $\mu < \mu_0$.

An alternative way to describe DDIS is to consider the heavy photon transition to $q\bar{q}$ or effective $(q\bar{q})g$ dipoles, which then interact with the target proton via two-gluon exchange [2, 3]; the case of the $q\bar{q}$ dipole is shown in Fig. 1(b). Here the Pomeron is modelled by the t-channel colour-singlet pair of gluons and we have an explicit form of the Pomeron parton distributions $a^{\mathbb{P}}(z, \mu^2)$ given at the initial virtuality $\mu^2 = k_t^2/(1-z)$ fixed by the transverse momentum k_t of the outgoing components of the dipole. Such an approach relies on the existence of a large saturation scale $Q_S^2 \gtrsim 1$ GeV^2 [4] to act as an infrared cutoff and suppress the contribution from large dipole sizes, thereby justifying the use of perturbative QCD for the whole $F_2^{\mathrm{D}(3)}$. However, more sophisticated dipole models [5] now give a lower $Q_S^2 \lesssim 0.5$ GeV^2 in the HERA kinematic regime, therefore significant non-perturbative contributions to inclusive DDIS are to be expected.

The two theoretical frameworks are essentially contradictory: the Regge factorisation approach is motivated by 'soft' Pomeron exchange, whereas the two-gluon exchange approach is motivated by perturbative QCD. Nevertheless, a 'doublethink' mentality exists whereby the two approaches are both commonly applied separately in the description of data, often within the same paper, with few attempts made to reconcile them.

The two approaches can be combined [6–8] by generalising the $\gamma^* \to q\bar{q}$ and $\gamma^* \to q\bar{q}g$ transitions to an arbitrary number of parton emissions in the final state, as shown in the upper half of Fig. 1(a). The perturbative Pomeron is described by a parton ladder ending in a pair of t-channel gluons or sea-quarks; the former is shown in the lower half of Fig. 1(a). The virtualities of the t-channel partons are strongly ordered as required by DGLAP evolution: $\mu_0^2 \ll \ldots \ll \mu^2 \ll \ldots \ll \mu_F^2$. The scale μ^2 at which the Pomeron-to-parton splitting occurs can vary between $\mu_0^2 \sim 1$ GeV^2 and μ_F^2. For $\mu < \mu_0$, the representation of the Pomeron as a perturbative parton ladder is no longer valid, and instead, in the lack of a precise theory of non-perturbative QCD, we appeal to Regge theory where the 'soft' Pomeron is treated as an effective Regge pole with

intercept $\alpha_{\mathbb{P}}(0) \simeq 1.08$; see Fig. 1(c).

The probability to find an appropriate pair of t-channel gluons with transverse momentum l_t, integrated over l_t, is given by the usual gluon distribution of the proton obtained from the global parton analyses, $x_{\mathbb{P}}g(x_{\mathbb{P}}, \mu^2)$, where $\mu^2 = k_t^2/(1-z)$ is the virtuality of the first t-channel parton in the upper part of the diagram. The emitted parton at the edge of the LRG in Fig. 1(a) has rapidity $\eta_{\max}$ and transverse momentum k_t and carries a fraction $(1-z)$ of the Pomeron's light-cone momentum. For inclusive DDIS we must integrate over k_t, accounting for the components of the Pomeron wave function of different sizes $\sim 1/k_t$, which translates to an integral over μ of the form

$$a^{\rm D}(x_{\mathbb{P}}, z, \mu_F^2) \;=\; \int\limits_{\mu_0^2}^{\mu_F^2} \frac{{\rm d}\mu^2}{\mu^2}\,\frac{1}{x_{\mathbb{P}}}\left[R_g \frac{\alpha_S(\mu^2)}{\mu} x_{\mathbb{P}} g(x_{\mathbb{P}}, \mu^2)\right]^2 \; a^{\mathbb{P}}(z, \mu_F^2; \mu^2). \tag{3}$$

The term $f_{\mathbb{P}}(x_{\mathbb{P}}; \mu^2) \equiv [\ldots]^2/x_{\mathbb{P}}$ plays the role of the Pomeron flux in (2). R_g is the skewed factor which accounts for the fact that in the lower parts of Fig. 1(a,b) we deal not with the diagonal but with the skewed (or generalised) parton distributions. For low values of $x_{\mathbb{P}} \ll 1$ this skewed factor is given by the Shuvaev prescription [9]. The notation $a^{\mathbb{P}}(z, \mu_F^2; \mu^2)$ for the Pomeron parton densities means that they are DGLAP-evolved from an initial scale μ^2 up to the factorisation scale μ_F^2.

At first sight, the integral (3) appears to be concentrated in the infrared region of low μ. However, for DDIS we consider very small $x_{\mathbb{P}}$ values. In this domain, the gluon distribution of the proton has a large anomalous dimension. Asymptotically, as $x_{\mathbb{P}} \to 0$, BFKL predicts $x_{\mathbb{P}}g(x_{\mathbb{P}}, \mu^2) \sim (\mu^2)^{0.5}$ for fixed α_S [10]. In this case the integral (3) takes the logarithmic form, and we cannot neglect the contribution from large scales μ.

By differentiating (3) with respect to $\ln(\mu_F^2)$, the evolution equation now reads [7]

$$\frac{\partial a^{\rm D}(x_{\mathbb{P}}, z, \mu^2)}{\partial \ln \mu^2} \;=\; \sum_{a'=q,g} P_{a,a'} \otimes a'^{\rm D} \;+\; \sum_{\mathbb{P}=G,S,GS} P_{a,\mathbb{P}}(z) f_{\mathbb{P}}(x_{\mathbb{P}}; \mu^2)\,. \tag{4}$$

Here the first term, involving the usual parton-to-parton splitting functions, $P_{a,a'}$, arises from DGLAP evolution in the upper parts of Fig. 1(a,c). The second (inhomogeneous) term, involving the Pomeron-to-parton splitting functions, $P_{a,\mathbb{P}}(z) \equiv a^{\mathbb{P}}(z, \mu^2; \mu^2)$, arises from the transition from the two t-channel partons (that is, the Pomeron) to a single t-channel parton in Fig. 1(a). The notation $\mathbb{P} = G, S, GS$ denotes whether the uppermost two t-channel partons are gluons ($\mathbb{P} = G$) or sea-quarks ($\mathbb{P} = S$)[1] , while the interference term is denoted by $\mathbb{P} = GS$. The LO Pomeron-to-parton splitting functions, $P_{a,\mathbb{P}}$, were calculated in [7], where the perturbative Pomeron flux factors, $f_{\mathbb{P}}(x_{\mathbb{P}}; \mu^2)$, are also given.

Simultaneously, we need to add in (1) the direct Pomeron–photon interaction described by the coefficient function $C_{2,\mathbb{P}} = C_{T,\mathbb{P}} + C_{L,\mathbb{P}}$ corresponding to the hard subprocess shown in

[1]Note that besides the two-gluon exchange we also account for the $q\bar{q}$ t-channel colour-singlet state, since even at very small $x_{\mathbb{P}}$ the sea-quark contribution does not die out. Moreover, the skewed factor R_q for the $q\bar{q}$ t-channel state is more than three times larger than that for the gluons [9].

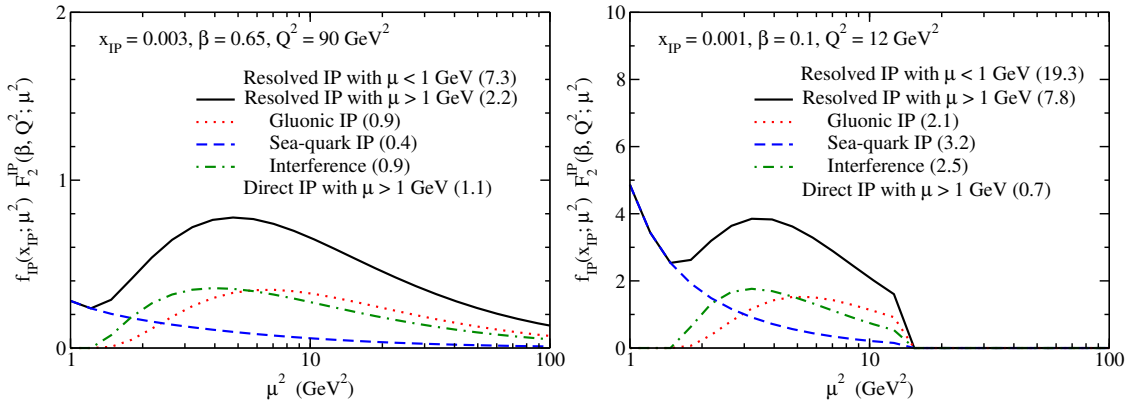


Fig. 2: The breakdown of the resolved Pomeron contribution for $\mu > 1$ GeV to the total $F_2^{\mathrm{D}(3)}$ as a function of μ^2 for two representative values of $(x_{\mathbb{P}}, \beta, Q^2)$. The integral over $\ln(\mu^2)$ is shown by the numbers in parentheses in the legend. Also shown are the integrated contributions from the the resolved Pomeron with $\mu < 1$ GeV and the direct Pomeron with $\mu > 1$ GeV. The secondary Reggeon contributions are negligible for the values of $x_{\mathbb{P}}$ chosen here.

Fig. 1(b):

$$F_2^{\mathrm{D}(3)} = \sum_{a=q,g} C_{2,a} \otimes a^{\mathrm{D}} + \sum_{\mathbb{P}=G,S,GS} C_{2,\mathbb{P}}. \tag{5}$$

For the LO $C_{T,\mathbb{P}}$ the light-quark contributions in the limit $\mu^2 \ll Q^2$ are subtracted since they are already included in the first term of (5) via the inhomogeneous evolution of the DPDFs. This subtraction defines a choice of factorisation scheme. There is no such subtraction for the LO $C_{L,\mathbb{P}}$, which are purely higher-twist, or for the heavy quark contributions since we work in the fixed flavour-number scheme (FFNS).

Thus, we see from (4) and (5) that the diffractive structure function is analogous to the photon structure function, where there are both resolved and direct components and where the photon PDFs also satisfy an inhomogeneous evolution equation.

As usual the evolution starts from some not-too-small scale μ_0 and all the contributions, both perturbative and non-perturbative, coming from $\mu \leq \mu_0$ are parameterised in terms of the Regge factorisation as some input which should be fitted to the data. Note that inclusion of the inhomogeneous term in (4) and the direct Pomeron coefficient function in (5) does not add any new free parameters to the description of the DPDFs. The LO Pomeron-to-parton splitting functions are known [7] and at next-to-leading order (NLO) they can be calculated unambiguously. The numerical results [8] presented below were obtained by fitting the H1 LRG data [11] with $M_X > 2$ GeV and $Q^2 \geq 8.5$ GeV^2, adding statistical and systematic experimental errors in quadrature, and taking the input distributions at $\mu_0^2 = 2$ GeV^2, which gave a $\chi^2/\mathrm{d.o.f.}$ of 0.84.

From Fig. 2 we see that integrating the perturbative contributions to $F_2^{\mathrm{D}(3)}$ starting from $\mu = 1$ GeV we collect up to a third of the whole diffractive structure function $F_2^{\mathrm{D}(3)}$. Of course, the numerous corrections (higher order α_S corrections, power corrections, etc.) are not negligible at such low scales as $\mu \sim 1$ GeV. Nevertheless, this fact indicates that an important part of the diffractive parton densities comes from the relatively small size components of the 'Pomeron'.

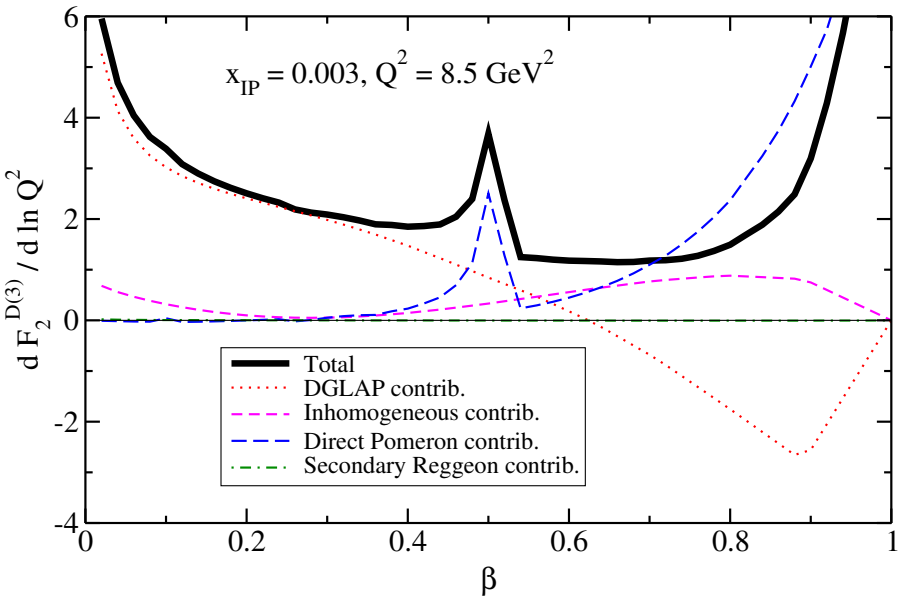


Fig. 3: The breakdown of the contributions to the slope $\partial F_2^{\mathrm{D}(3)}/\partial \ln Q^2$ as a function of β. Contributions apart from the usual DGLAP terms start becoming important for $\beta \gtrsim 0.4$. The peak at $\beta = Q^2/(Q^2 + 4m_c^2) \simeq 0.51$ is due to the threshold for charm production from the direct Pomeron–photon interaction.

That is why fitting the DDIS data in terms of the Regge factorisation one needs the effective Pomeron intercept $\alpha_{\mathbb{P}}(0) \simeq 1.12$ larger than that ($\alpha_{\mathbb{P}}(0) \simeq 1.08$) measured in the purely soft hadron–hadron scattering.

In Fig. 3 we show the breakdown of the different contributions to the slope $\partial F_2^{\mathrm{D}(3)}/\partial \ln Q^2$. As it is seen, the inhomogeneous term in the evolution equation is fairly large and starts becoming important for $\beta \gtrsim 0.4$. Note that the direct Pomeron contribution at large β, mostly the twist-four $F_L^{\mathrm{D}(3)}$, only gives an important contribution to the total $F_2^{\mathrm{D}(3)}$ for $\beta \gtrsim 0.9$, but the contribution to the Q^2 slope starts becoming important at moderate β. Therefore, it is not possible to avoid the presence of this contribution by simply excluding data points with $\beta > 0.8$ from the fit, as is done in the H1 2006 analysis [11]. In the analysis of inclusive DDIS data, the diffractive gluon density is mainly determined by the derivative $\partial F_2^{\mathrm{D}(3)}/\partial \ln Q^2$. The presence of these additional positive contributions to the Q^2 slope at large β apart from the usual DGLAP contribution means that a smaller gluon density is required for $z \gtrsim 0.4$ compared to the H1 2006 Fit A performed in the usual Regge factorisation framework [11]; see Fig. 4.

In our analysis we account for the twist-four $F_L^{\mathrm{D}(3)}$ contribution coming from the direct Pomeron–photon fusion, that is, from the last term in (5) corresponding to Fig. 1(b). This contribution, which goes to a constant value as $\beta \to 1$, was calculated in [2, 3] and turns out to be numerically appreciable. For the coupling to massless quarks, this contribution to (5) takes the form [7]

$$C_{L,\mathbb{P}} = \int_{\mu_0^2}^{\frac{Q^2}{4\beta}} \mathrm{d}\mu^2 \, \frac{1/Q^2}{\sqrt{1 - 4\beta\mu^2/Q^2}} \, f_{\mathbb{P}}(x_{\mathbb{P}}; \mu^2) \, F_L^{\mathbb{P}}(\beta). \tag{6}$$

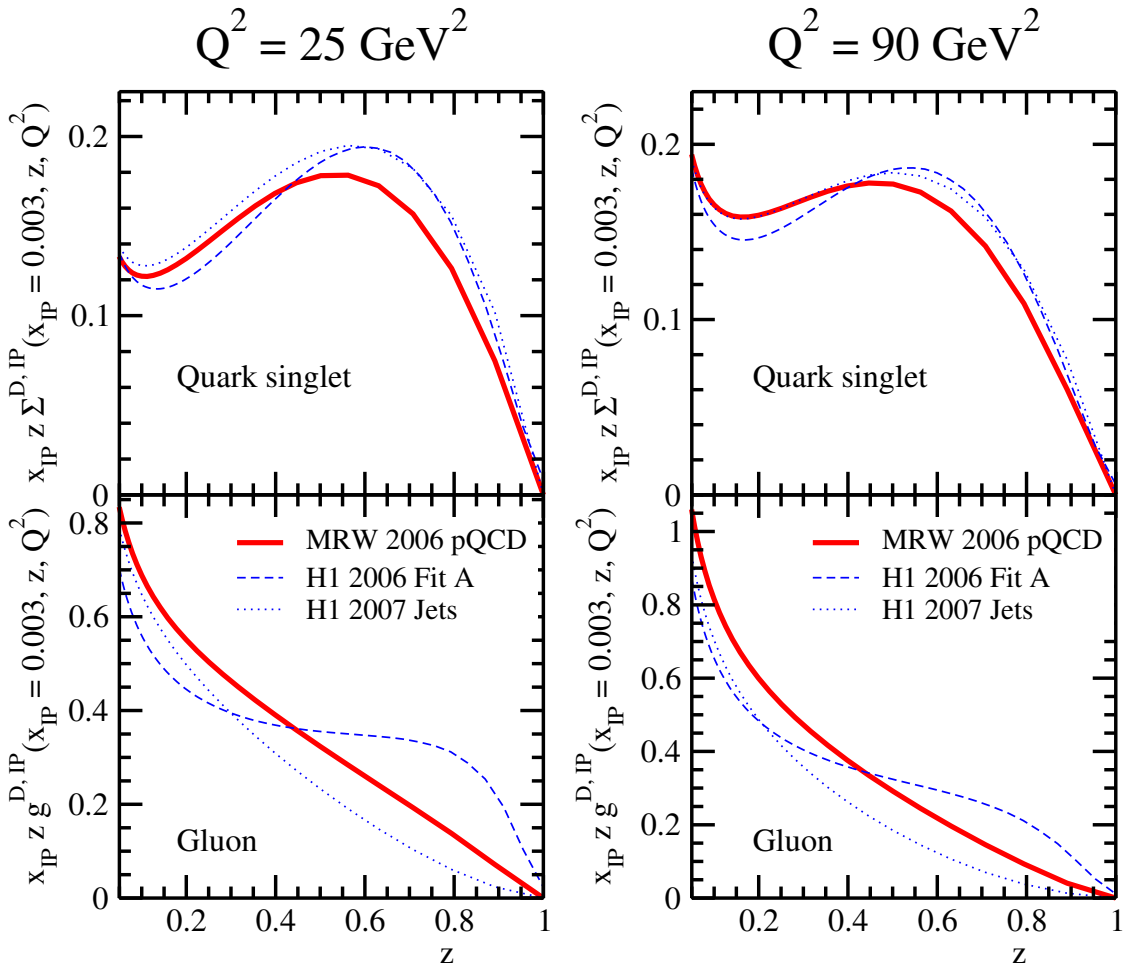


Fig. 4: The MRW 2006 pQCD DPDFs compared to those from the H1 2006 Fit A and the H1 2007 Jets fit. All the DPDFs shown here are normalised to $M_Y < 1.6$ GeV by multiplying by a factor 1.23 relative to $M_Y = m_p$, where M_Y is the mass of the proton dissociative system.

Differentiating with respect to $\ln(Q^2)$ gives a positive term from the integrand evaluated at $\mu^2 = Q^2/(4\beta)$, analogous to the inhomogeneous term in the evolution equation, in addition to the negative term proportional to $-1/Q^2$ obtained from taking the derivative of the integrand.

A recent analysis [12] includes the twist-four $F_L^{\mathrm{D}(3)}$ contribution from all k_t in addition to the usual Regge factorisation formulae of (1) and (2). It is found that the twist-four $F_L^{\mathrm{D}(3)}$ term gives a negative contribution to the Q^2 slope, such that a larger gluon distribution at high z is needed than in the usual Regge factorisation approach. However, the contribution from $\mu^2 = k_t^2/(1-\beta) < \mu_0^2$ is already included in the input Pomeron PDFs taken at a scale $\mu_0^2 = 1.5$ GeV^2, so some double-counting is involved. Moreover, the DGLAP evolution is not accounted for in the dipole cross section, and the inhomogeneous term in the evolution equation of the DPDFs is neglected. The future measurement of $F_L^{\mathrm{D}(3)}$ [13] will provide an important check of

the calculations of the twist-four component.

The smaller diffractive gluon density at high z found in our analysis, compared to the H1 2006 Fit A, is preferred by the data on inclusive diffractive dijet production, $\gamma^* p \to \text{dijet}\, X' + p$, where at LO the dijet system originates from the outgoing $q\bar{q}$ pair in Fig. 1(a,c) and the rest of the hadronic system X' originates from the other outgoing partons in Fig. 1(a,c). However, the data still tend to be slightly overestimated [14]. This can also be seen in Fig. 4 where the 'MRW 2006' gluon at high z is smaller than the 'H1 2006 Fit A' gluon, but larger than the 'H1 2007 Jets' gluon obtained from a combined fit, within the Regge factorisation framework, to inclusive DDIS and inclusive diffractive dijet data [15]. The χ^2 for the 190 inclusive DDIS points increases from 158 (H1 2006 Fit A) to 169 (H1 2007 Jets fit) on inclusion of the dijet data. Therefore, the gluon density determined indirectly from the inclusive DDIS data, under the assumption of pure DGLAP evolution, is different from the gluon density preferred by the dijet data. The apparent tension between the inclusive DDIS and dijet data in the Regge factorisation approach is partly alleviated by the inclusion of the perturbative Pomeron terms.

Note that in the 'MRW 2006' analysis [8] the parton distributions of the proton, representing the lower parton ladders in Fig. 1(a,b), were taken from a NLO global fit. However, since the Pomeron-to-parton splitting is only calculated at LO, it may be more appropriate to take the inclusive parton distributions from a LO fit, where the gluon density is much larger at small x and does not take a valence-like form at low scales. In this case, the inhomogeneous term in the evolution equation, and the other direct Pomeron contributions, would be enhanced, leading to an even smaller diffractive gluon density at high z. Note that even if LO DGLAP evolution is used in the lower parton ladders of Fig. 1(a,b), NLO DGLAP evolution may still be used for the evolution of the Pomeron PDFs in the upper parts of Fig. 1(a,c).

A more direct way to observe the perturbative Pomeron contribution to DDIS is to study the transverse momenta of secondaries in the 'Pomeron fragmentation' region, at the edge of the LRG, as in Ref. [16]. In contrast with the Regge factorisation of Fig. 1(c), where the transverse momentum distribution of the partons inside a Reggeon is assumed to have an exponential form with a rather low mean value of intrinsic k_t, in the perturbative case of Fig. 1(a) the k_t-distribution of the lowest jet in Fig.1(a) obeys a power law, given by the integrand of (3). Therefore we expect a larger k_t of the secondaries with the long power-like tail.

So far, measurements of inclusive diffractive dijets at HERA have primarily been made in the kinematic region of small $\beta \equiv x_B/x_{\mathbb{P}}$ where the resolved Pomeron mechanism of Fig. 1(a,c) gives the dominant contribution, and the contribution from exclusive diffractive dijets, Fig. 1(b), is negligible. However, a first measurement has been made of dijets in DDIS with a cut on $\beta > 0.45$ in order to enhance the contribution from exclusive diffractive dijets, $\gamma^* p \to \text{dijet} + p$ [17]. Within the HERA kinematic domain the sea-quark component of the Pomeron is quite important (see Fig. 2). This statement can be checked by observing the diffractive high-E_T dijet distributions in the exclusive $\gamma^{(*)} p \to \text{dijet} + p$ process. At LO we expect the ratio of cross sections for high-E_T dijets produced via the two-gluon (gg) and $q\bar{q}$ t-channel exchange to be [7]

$$\frac{(\mathrm{d}\sigma_T^{\gamma^* p}/\mathrm{d}E_T)\Big|_{\mathbb{P}=G}}{(\mathrm{d}\sigma_T^{\gamma^* p}/\mathrm{d}E_T)\Big|_{\mathbb{P}=S}} = \frac{81}{4}\left[\frac{\alpha(1-\alpha)Q^2}{E_T^2+\alpha(1-\alpha)Q^2}\,\frac{R_g\, x_{\mathbb{P}} g(x_{\mathbb{P}},\mu^2)}{R_q\, x_{\mathbb{P}} S(x_{\mathbb{P}},\mu^2)}\right]^2, \tag{7}$$

where α is the photon's light-cone momentum fraction carried by the high-E_T jet, and the scale $\mu^2 = \alpha(1-\alpha)Q^2 + E_T^2$. Therefore, measurements of exclusive diffractive dijets at large E_T in photoproduction would probe the presence of the $q\bar{q}$ t-channel exchange. However, it remains to be seen whether a measurement of exclusive diffractive dijets is feasible without imposing a cut on β.

In summary, we have shown how to obtain *universal* diffractive parton densities $a^{\rm D}$ which can be used in the description of different diffractive processes. We emphasise that the perturbative QCD contribution originated by the inhomogeneous (last) term in (4) is not small and, starting from a relatively low scale $\mu_0 = 1\,\text{GeV}$, may generate up to a third of the diffractive parton densities. Simultaneously, an account of this inhomogeneous term, and the twist-four $F_L^{\rm D(3)}$ contribution, leads to a lower diffractive gluon density at high z in comparison to that obtained using the Regge factorisation hypothesis. The presence of the perturbative (large scale) contributions reveals itself in larger transverse momenta (with a power-like tail) of the secondaries observed in the 'Pomeron fragmentation' region. The colour singlet sea-quark pair exchange is an important component of the perturbative Pomeron, which plays the dominant role in exclusive diffractive dijet production with $E_T^2 \gg Q^2$. Parameterisations for the DPDFs and the diffractive structure functions are made publically available.[2]

Acknowledgments

M.G.R. gratefully acknowledges the financial support of DESY and the II Institute of Theoretical Physics, University of Hamburg. G.W. acknowledges the UK Science and Technology Facilities Council for the award of a Responsive Research Associate position.

References

[1] J. C. Collins, Phys. Rev. **D57**, 3051 (1998). hep-ph/9709499.
[2] M. Wusthoff, Phys. Rev. **D56**, 4311 (1997). hep-ph/9702201.
[3] K. J. Golec-Biernat and M. Wusthoff, Phys. Rev. **D60**, 114023 (1999). hep-ph/9903358.
[4] K. J. Golec-Biernat and M. Wusthoff, Phys. Rev. **D59**, 014017 (1999). hep-ph/9807513.
[5] H. Kowalski, L. Motyka, and G. Watt, Phys. Rev. **D74**, 074016 (2006). hep-ph/0606272.
[6] A. D. Martin, M. G. Ryskin, and G. Watt, Eur. Phys. J. **C37**, 285 (2004). hep-ph/0406224.
[7] A. D. Martin, M. G. Ryskin, and G. Watt, Eur. Phys. J. **C44**, 69 (2005). hep-ph/0504132.
[8] A. D. Martin, M. G. Ryskin, and G. Watt, Phys. Lett. **B644**, 131 (2007). hep-ph/0609273.
[9] A. G. Shuvaev, K. J. Golec-Biernat, A. D. Martin, and M. G. Ryskin, Phys. Rev. **D60**, 014015 (1999). hep-ph/9902410.
[10] L. N. Lipatov, Phys. Rept. **286**, 131 (1997). hep-ph/9610276.
[11] H1 Collaboration, A. Aktas *et al.*, Eur. Phys. J. **C48**, 715 (2006). hep-ex/0606004.
[12] K. J. Golec-Biernat and A. Luszczak. arXiv:0704.1608 [hep-ph].
[13] P. Newman. hep-ex/0511047.
[14] ZEUS Collaboration, S. Chekanov *et al.* arXiv:0708.1415 [hep-ex].
[15] H1 Collaboration, A. Aktas *et al.* arXiv:0708.3217 [hep-ex].
[16] H1 Collaboration, C. Adloff *et al.*, Eur. Phys. J. **C20**, 29 (2001). hep-ex/0012051.
[17] ZEUS Collaboration, J. Szuba, Ph.D. thesis, Akademia Górniczo-Hutnicza (Cracow), June 2005.

[2] http://durpdg.dur.ac.uk/hepdata/mrw.html

Multiple Interactions in H1 and ZEUS

Tim Namsoo[1] *on behalf of the H1 and ZEUS collaborations*
[1]DESY

Abstract
Multi-parton interactions (MPIs) and the underlying event are believed to contribute to the hadronic energy flow in hadron-hadron collisions and possibly even lepton-hadron collisions. Two measurements are presented here, each of which may be sensitive to MPIs. Both were conducted at the HERA electron-proton collider: a three- and four-jet analysis in photoproduction and a mini-jet analysis in deep-inelastic scattering (DIS) made by the ZEUS and H1 collaborations, respectively.

1 Introduction

The underlying event is a generic term for all energy flow not associated with the primary process, however, defining what constitutes the primary process is non-trivial. As a working definition, the primary process may be thought of as the idealised parton-parton interactions that would occur if the beams were simply sources of quasi-free partons. The primary interactions would be completely insensitive to the incoming particles (beyond their PDFs) and beam remnants. The underlying event, then, is everything else that can affect the primary process and contributes to the event. Thus, effects like secondary remnant-remnant interactions and multiple-scattering, as a primary parton re-scatters off the remnants, may contribute to the underlying event. Both contributions will be referred to as multi-parton interactions (MPIs).

Remnant-remnant interactions are only possible following a hadron-hadron-like collision since it is the composite nature of hadrons that leads to there being remnants. Multiple-scattering, however, only requires one of the incoming particles to be a hadron so may also be present in lepton-hadron interactions. Remnant-remnant interactions, in particular, may occur at a scale hard enough to generate additional jets and so constitute a potential source of multi-jets in the final state.

The electron-proton (ep) collisions at HERA [1], with a centre-of-mass energy, $\sqrt{s} = 318$ GeV, may be mediated by either direct or resolved photons. In a direct collision, the photon interacts as a point-like particle whereas in a resolved event, the photon fluctuates into a partonic system prior to interacting. The four-vector of the exchanged photon is denoted by q. In events with a virtuality, $Q^2 \leq 1$ GeV^2, where $Q^2 = -q^2$, which is a positive quantity at HERA, the photon is long-lived with respect to the characteristic interaction time. Such events are referred to as photoproduction events and the exchanged photon may fluctuate into a partonic system. In higher Q^2, deep-inelastic scattering (DIS) collisions, the resolved behaviour of the photon is suppressed and direct interactions dominate. Thus, both remnant-remnant and multiple-scattering may be present in a photoproduction sample, whereas the former is expected to be suppressed with increasing Q^2. The underlying event has been studied before at HERA in photoproduction collisions [2] but not in DIS.

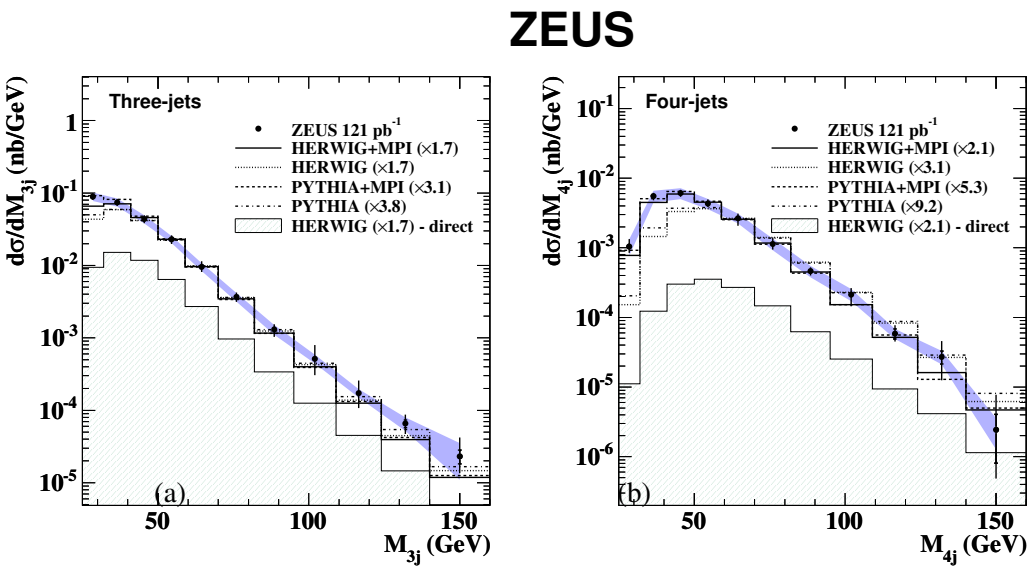


Fig. 1: Measured cross section as a function of (a) M_{3j} and (b) M_{4j} (solid circles). The inner and outer error bars and the shaded band represent the statistical, the statistical plus systematic and the calorimeter energy scale uncertainties, respectively.

2 Three- and four-jet events in photoproduction

2.1 Introduction

Multi-jet events may be produced by primary processes beyond leading order (LO) in the strong coupling constant, α_s, or, as described above, by the overlay of a hard remnant-remnant interaction onto a LO primary process. Moreover, even soft MPIs may affect the distribution of multi-jet events by adding to or redistributing the energy flow generated by a beyond-LO primary process. More specifically, the lowest order primary process capable of generating an n-jet direct photoproduction event, in the absence of a hard MPI, is $\mathcal{O}(\alpha\alpha_s^{n-1})$, where α is the fine structure constant.

The multi-jet analysis by the ZEUS collaboration looked at photoproduction events ($Q^2 < 1$ GeV^2) that contained at least three (or four) jets with transverse energies, $E_T^{\rm jet} \geq 6$ GeV, in the pseudorapidity range, $|\eta^{\rm jet}| \leq 2.4$, and in the kinematic region $0.2 \leq y \leq 0.85$, where y is the inelasticity. These events were studied in two regions defined in terms of invariant n-jet mass, M_{nj}, as $25 \leq M_{nj} < 50$ GeV and $M_{nj} \geq 50$ GeV, and the cross sections were measured differentially.

To assess the influence of MPIs in each of the four samples, that will be referred to as the three- or four-jet, high- or low-mass samples, the data were compared to predictions from two Monte Carlo (MC) programs, HERWIG 6.505 [3] and PYTHIA 6.206 [4] both with and without simulated MPIs. The MPIs in HERWIG were simulated using a separate program called JIMMY 4.0 [5], which is an impact parameter model. The MPIs in PYTHIA were generated according to the so-called "simple model" [4], available via an internal PYTHIA routine.

In addition, the three-jet cross sections were compared to the $\mathcal{O}(\alpha\alpha_s^2)$ perturbative quantum chromodynamics (pQCD) prediction by Klasen, Kleinwort and Kramer [6]. This was, at the time, the highest order prediction available in photoproduction. It is only LO for the three-jet process and so could not be compared with the four-jet data.

2.2 Results

The three- and four-jet cross sections are given as a function of M_{nj} in Fig. 1. In general, both cross sections decrease exponentially with increasing M_{nj}. Also shown in Fig. 1 are the HERWIG and PYTHIA predictions with and without MPIs, normalised to the high-mass region ($M_{nj} \geq 50$ GeV). Both models without MPIs fail to describe the M_{nj} dependence of the cross section and significantly underestimate the low mass data. The discrepancy is larger in the four-jet case. With the inclusion of MPIs, both scaled MC predictions give a reasonably good description of the data over the full M_{nj} ranges.

It is noted that the predicted influence of MPIs in the samples is highly sensitive to the tunable parameters within the models. The PYTHIA model was run using its default setting whereas the JIMMY model was tuned to the data shown [7].

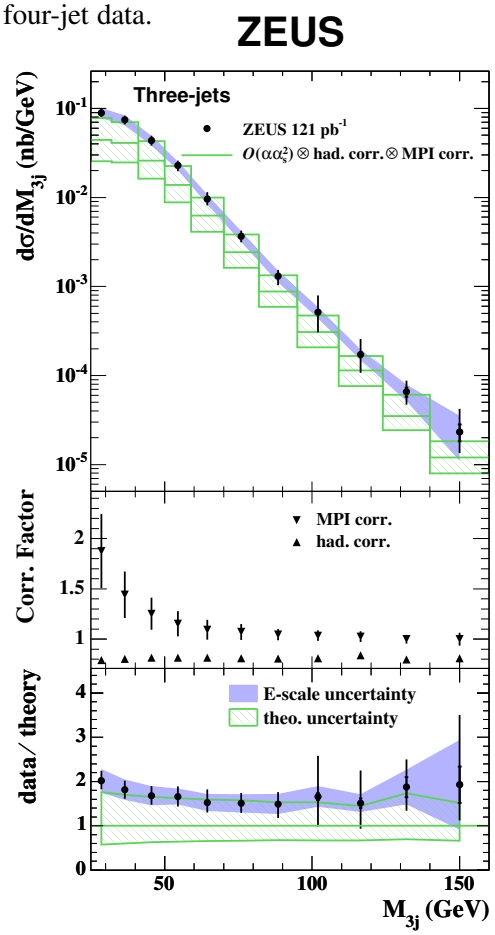


Fig. 2: (a) Measured three-jet cross section as a function of M_{3j} in compared with an $\mathcal{O}(\alpha\alpha_s^2)$ prediction, corrected for hadronisation and MPI effects. (b) The hadronisation and MPI corrections as a function of M_{3j}. (c) The ratio of the M_{3j} cross section divided by theory. The theoretical uncertainty is represented by the dashed bands.

Figure 2 shows an $\mathcal{O}(\alpha\alpha_s^2)$ prediction, corrected for hadronisation effects and MPIs, compared to the measured $\mathrm{d}\sigma/\mathrm{d}M_{3j}$ cross section. The hadronisation and MPI corrections, including their estimated uncertainties, are given in Fig. 2b. The hadronisation corrections are constant in M_{3j}, while the MPI corrections increase significantly towards low M_{3j}. The theoretical uncertainties on both the MPI corrections and the pQCD predictions are large. The magnitude and shape of the calculation is consistent with the data within the large theoretical uncertainties. This is best seen in the data over theory ratio shown in Fig. 2c. The level of consistency between data and theory would be far worse at low M_{3j} if it were not for the large MPI corrections.

3 Mini-jets in DIS

3.1 Introduction

Although the presence of MPIs in photoproduction is far from universally accepted, their presence in DIS is even less so.

Investigation at HERA into low-x hard scattering, where x is the Björken scaling variable, identifies the large contribution from diffractive events. Such events are described, in part, by the exchange of pomerons. In a pQCD framework, the pomerons may be described by sums of gluon ladders. With this description, applying the AKG cutting rules [8] (slicing through multiple ladders, i.e. pomerons) highlights the potential importance of MPIs in DIS [9]. It is, therefore, interesting to see if evidence of such a phenomenon can be identified within the data.

The H1 collaboration looked at DIS events with $5 \leq Q^2 \leq 100$ GeV^2 and $0.1 \leq y \leq 0.7$, that contained at least one jet, defined using the k_T clustering algorithm [10] in the hadronic centre-of-mass (HCM) frame, with $E_T^{\rm jet} \geq 5$ GeV in both the HCM and laboratory frames. Four regions in azimuthal angle, ϕ, were then defined with respect to the highest $E_{T,}^{\rm jet}$ jet in the HCM frame, as depicted in Fig. 3. This "leading-jet" was required to have $-1.7 \leq \eta^{\rm jet} \leq 2.79$ in the laboratory frame and the hadronic system was required to have an invariant mass, $W \geq 200$ GeV. Finally, the average multiplicity, $\langle N_{\rm minijet} \rangle$, of so-called mini-jets, with $E_T^{\rm mini} \geq 3$ GeV, was measured in each of the four ϕ regions. A possible signature of MPIs would be an inflated value of $\langle N_{\rm minijet} \rangle$, most noticeably, in the less populated, high- and low-activity transverse regions.

3.2 Results

To ascertain whether the measured values of $\langle N_{\rm minijet} \rangle$ were indeed large, the results were compared to the predictions of three MC models, RAPGAP [11], ARIADNE, based on the colour dipole model (CDM) [12], and PYTHIA. The latter model was ran with and without simulated MPIs, whereas the previous two did not include MPIs. These data can be seen in Fig. 4 as a function of the transverse momentum of the leading-jet in the HCM frame, labelled $P^*_{T,1j}$ on the figure, and in three Q^2 bins.

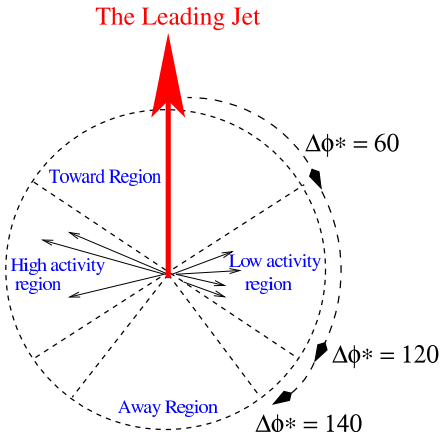


Fig. 3: Definition of the four azimuthal regions used in the mini-jet analysis in DIS.

The toward-region data are reasonably well described by all four MC models. The RAPGAP and PYTHIA models marginally underestimate $\langle N_{\rm minijet} \rangle$ at low-$P^*_{T,1j}$ in the lowest Q^2 bin. The PYTHIA description is improved by the introduction of MPIs.

The away-region is well described by CDM and RAPGAP models but PYTHIA significantly over-estimates $\langle N_{\rm minijet} \rangle$ at low-$P^*_{T,1j}$ in all three Q^2 bins, although more so at high-Q^2. The PYTHIA model predicts the away-region to be the least sensitive to MPIs.

The $\langle N_{\rm minijet} \rangle$ values, in the low- and high-activity regions, tend to be underestimated by all of the models that do not include MPIs, in all $P^*_{T,1j}$ and Q^2 bins. The underestimation

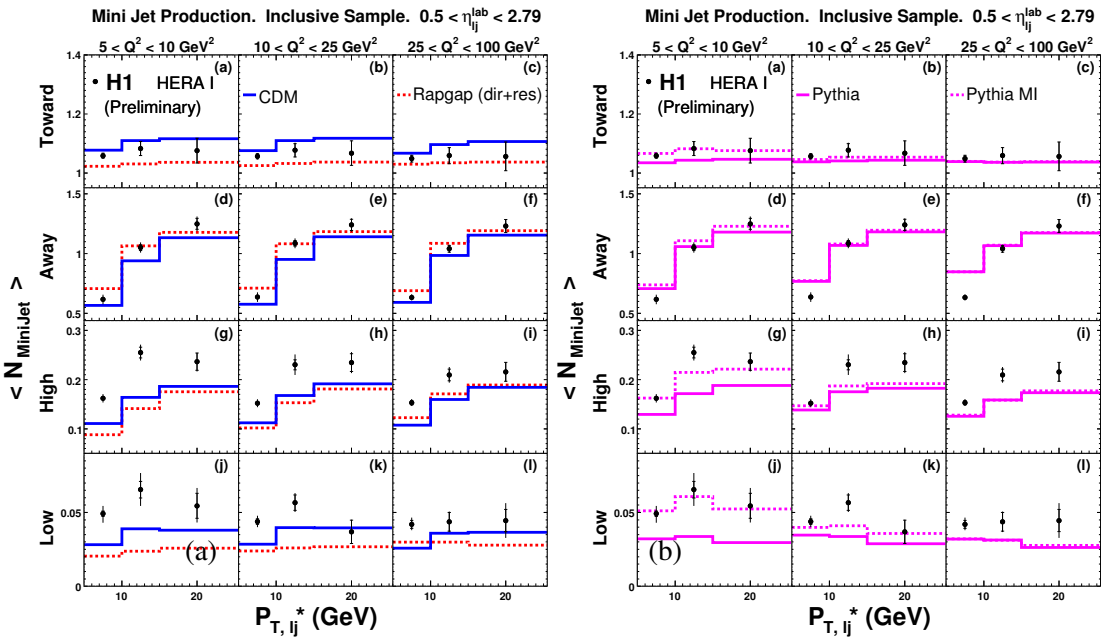


Fig. 4: The $\langle N_{\mathrm{minijet}} \rangle$ data, in all four azimuthal regions, as a function of $P^*_{T,1j}$ in three Q^2 bins. Also shown are the predictions from four MC models.

of the data is more pronounced at low-Q^2 and low-$P^*_{T,1j}$. The introduction of MPIs into the PYTHIA model certainly aids the description of the low-Q^2 data, however, the affect of the MPIs diminishes rapidly with Q^2 and the high-Q^2 data is still underestimated.

Conclusions, similar to those made using the PYTHIA model, were drawn from comparisons with the HERWIG model (not shown). The analysis was also performed on a subsample of the data in which a second jet, with $P^*_{T,1j} \geq 5$ GeV, was observed in the away-region. Again, the results were similar and not shown.

4 Conclusions

Effects have been observed in both photoproduction and DIS ep data that are suggestive of an MPI contribution. More specifically, the ZEUS collaboration observed that the three- and four-jet photoproduction cross sections are larger at low $M_{3j(4j)}$ than is predicted by two parton shower MC models, and in the three-jet case, a LO pQCD calculation. This behavior is expected if MPIs contribute to the data and two independent MPI models correctly account for the differences between the MC without MPIs and the data. However, the prediction of MPI models are highly tunable and the accuracy of the description of multi-jet final states by LO matrix element plus parton shower MC models is not assured.

The H1 collaboration have observed a larger average mini-jet multiplicity in DIS events than was predicted by both parton shower and colour dipole model MC models. In this case, MPIs, as predicted by the PYTHIA model, improved the description of the data at low-Q^2, although were not predicted to influence the data at higher virtualities.

References

[1] G. Voss and B. Wiik, Ann. Rev. Nucl. Part. Sci. **44**, 413 (1994).

[2] ZEUS Collaboration, M. Derrick *et al.*, Phys. Lett. **B348**, 665 (1995);
H1 Collaboration, S. Aid *et al.*, Z. Phys. **C70**, 17 (1996).

[3] G. Corcella *et al.*, HERWIG 6.5 Manual, hep-ph/0011363 (2000);
G. Corcella *et al.*, HERWIG 6.5 Release Note, hep-ph/0210213 (2001);
G. Marchesini *et al.*, Comput. Phys. Commun. **67**, 465 (1992).

[4] T. Sjöstrand *et al.*, PYTHIA 6.206 Manual, hep-ph/0108264 (2002);
T. Sjöstrand *et al.*, Comput. Phys. Commun. **135**, 238 (2001).

[5] J. Butterworth, J. Forshaw, and M. Seymour, Z. Phys. **C72**, 673 (1996).

[6] M. Klasen, T. Kleinwort, and G. Kramer, Z. Phys. Rev.-e **C1** (1998);
M. Klasen, Eur. Phys. J. **C7**, 225 (1999).

[7] T. Namsoo, PhD. Thesis, University of Bristol, UK. (unpublished) (2006).

[8] V. Abramovski, V. Gribov, and O. Kancheli, Yad. Fiz. **18**, 595 (1973).

[9] J. Bartels, M. Salvadore, and G. Vacca, Eur. Phys. J. **C42**, 53 (2005).

[10] S. Catani *et al.*, Nucl. Phys. **C406**, 187 (1993).

[11] H. Jung, Comput. Phys. Commun. **86**, 147 (1995).

[12] L. Lönnblad, Comput. Phys. Commun. **71**, 15 (1992).

Diffractive Neutral Pion Production, Chiral Symmetry and the Odderon

Carlo Ewerz [a], *Otto Nachtmann* [b†]
[a] ECT*, Strada delle Tabarelle 286, I-38050 Villazzano (Trento), Italy
[b] Institut für Theoretische Physik, Universität Heidelberg, Philosophenweg 16, D-69120 Heidelberg, Germany

Abstract
We discuss the diffractive photo- and electroproduction of a single neutral pion at high energies where it can occur due to odderon exchange. We show that this process is dynamically suppressed as a consequence of chiral symmetry. Our result reconciles earlier theoretical expectations with the non-observation of this reaction at HERA.

1 Diffractive neutral pion production as a probe of the odderon

In this talk we want to present the main results of our study [1] of diffractive production of a single neutral pion in photon-proton scattering at high energy,

$$\gamma^{(*)}(q) + p(p) \longrightarrow \pi^0(q') + X(p') \,, \tag{1}$$

where the photon can be real or virtual, and X can be any diffractively produced hadronic system. For simplicity we will in the following assume that X is a proton, but our considerations can also be applied to other states X, for example for $X = N^*$ or $X = n + \pi^+$ [1]. Since the photon and the neutral pion have opposite C-parity the object exchanged in this reaction must be odd under charge conjugation, and hence at high energy must be an odderon ($\mathbb{O}$), see Figure 1. (Note that we draw the incoming particles to the right.)

The odderon, the $C = -1$ partner of the pomeron, was introduced in [2], for a general review see [3]. It has since been studied in great detail especially from a theoretical point of view. But experimentally the odderon remains an elusive object. Some weak evidence for its existence has only been seen in elastic scattering at the ISR where the pp and $p\bar{p}$ differential cross sections show a difference at around $|t| \sim 1.3\,\mathrm{GeV}^2$ [4], for a recent discussion see [5]. There, however, the odderon is only one among many contributions and hence difficult to pin down. In recent years it has been realized that the chances to observe the odderon are better in exclusive processes in which the odderon essentially gives the only contribution. As an important example of this strategy the reaction (1) has been proposed and discussed in [6].

A detailed analysis based on a nonperturbative model of QCD dynamics performed in [7] led to the prediction

$$\sigma(\gamma p \to \pi^0 N^*) \approx 300\,\mathrm{nb} \,, \tag{2}$$

while the subsequent experimental search at HERA [8] did not find a signal and resulted in the upper bound

$$\sigma(\gamma p \to \pi^0 N^*) < 49\,\mathrm{nb} \,. \tag{3}$$

[†] speaker

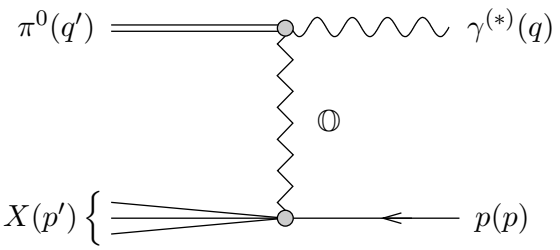


Fig. 1: Diffractive photo- or electroproduction of a π^0 due to odderon exchange.

Possible causes for the failure of the prediction of [7] were discussed in [9]. Since the reaction (1) has the largest phase space of all processes in which hadrons are diffractively produced a strong dynamical suppression appeared necessary in order to provide a likely reason. In [1] we have found that the approximate chiral symmetry of QCD indeed induces a strong suppression.

2 PCAC

Let us define a quark field operator describing up and down type quarks, $\psi(x) = (u(x), d(x))^{\mathrm{T}}$, and the associated triplet of axial vector currents ($a = 1, 2, 3$)

$$A^a_\mu(x) = \bar{\psi}(x)\gamma_\mu\gamma_5\frac{\tau^a}{2}\psi(x). \tag{4}$$

The well-known PCAC relation states that the divergence of this axial vector current is related to a correctly normalised pion field operator ϕ^a by

$$\partial_\lambda A^{a\lambda}(x) = \frac{f_\pi m_\pi^2}{\sqrt{2}}\,\phi^a(x)\,, \tag{5}$$

where $f_\pi \approx 130\,\mathrm{MeV}$ is the pion decay constant, see for example [10]. Let us now consider along with diffractive pion production the corresponding production of an axial vector current A^3,

$$\gamma^{(*)}(q,\nu) + p(p,s) \quad\longrightarrow\quad \pi^0(q') + p(p',s')\,, \tag{6}$$
$$\gamma^{(*)}(q,\nu) + p(p,s) \quad\longrightarrow\quad A^3(q',\mu) + p(p',s')\,, \tag{7}$$

and let us denote the corresponding amplitudes by $\mathcal{M}^\nu(\pi^0; q', p, q)$ and $\mathcal{M}^{\mu\nu}(A^3; q', p, q)$, respectively, which we consider for $q^2 \le 0$ and $q'^2 \le m_\pi^2$. Using the PCAC relation (5) we can then express the former amplitude in terms of the latter via

$$\mathcal{M}^\nu(\pi^0; q', p, q) = \frac{2\pi m_p\sqrt{2}}{f_\pi m_\pi^2}\,(-q'^2 + m_\pi^2)\,iq'_\mu\mathcal{M}^{\mu\nu}(A^3; q', p, q)\,. \tag{8}$$

3 Axial vector current production

The amplitude $\mathcal{M}^{\mu\nu}(A^3; q', p, q)$ for axial vector current production (7) can be treated with the same general nonperturbative methods that were developed for Compton scattering in [11]. We

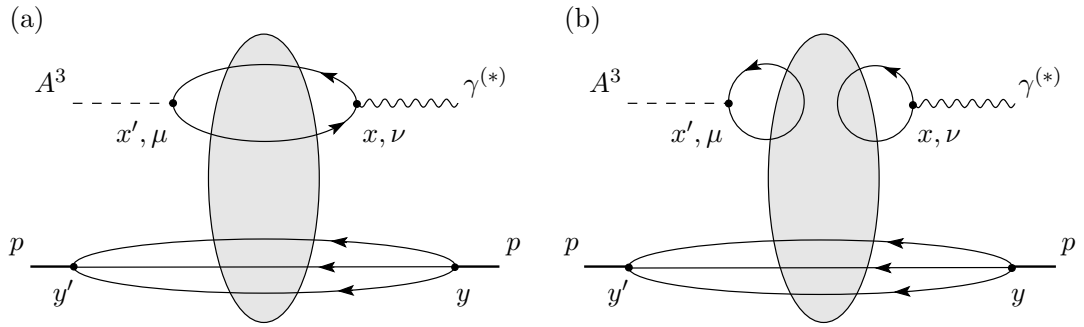


Fig. 2: Leading diagrams at high energies for the reaction (7).

use the LSZ formula to relate the amplitude to Green's functions, and the latter can then be written as functional integrals over quark and gluon fields. Integrating out the quark degrees of freedom leads us to diagram classes characterised by their quark line skeleton. Those diagrams which contain the leading terms at high energies are shown in Figure 2, and they are exactly the odderon exchange diagrams on which we want to concentrate here. The solid lines represent full quark propagators in a given gluon field configuration, and the shaded blobs indicate the functional integral over the gluon fields.

4 From axial vector current to pion production

We now consider the divergence of the amplitudes of Figure 2, that is we contract them with q'^μ or take a derivative ∂^μ. For the axial vector current this gives at the quark level

$$\partial^\mu A^3_\mu(x) = i[m_u \bar{u}(x)\gamma_5 u(x) - m_d \bar{d}(x)\gamma_5 d(x)]\,, \tag{9}$$

and hence there is a factor m_q of the light quark masses in the divergence amplitude. Note that the gluon anomaly does not contribute here. Such anomalous pieces are contained in the individual contribution of the quark flavours to the divergence of A^3_μ and would have the quark line topology of diagram (b) in Figure 2, but they cancel in $\partial^\mu A^3_\mu$.

The quark loops in the diagrams of Figure 2 which couple to the axial vector current contain a factor γ_5. As a consequence, these loops give rise to an additional factor m_q of the light quark mass. This can be shown in a more detailed analysis which makes use of Lippmann-Schwinger equations for the quark propagator, for details see [1]. Hence we find that the divergence amplitude $q'_\mu \mathcal{M}^{\mu\nu}(A^3; q', p, q)$ is proportional to the square of the light quark masses. More precisely,

$$q'_\mu \mathcal{M}^{\mu\nu}(A^3; q', p, q) = m_u^2\, \mathcal{C}^{(u)\nu}(q', p, q) - m_d^2\, \mathcal{C}^{(d)\nu}(q', p, q)\,, \tag{10}$$

where the functions $\mathcal{C}^{(q)\nu}$ have pion poles but are otherwise finite. (These poles are cancelled by the explicit factor $(-q'^2 + m_\pi^2)$ in (8) when we insert (10) there.) We know from the theory of chiral symmetry that the squared pion mass is linear in the light quark masses,

$$m_\pi^2 = B(m_u + m_d) \tag{11}$$

with

$$B = -\frac{2}{f_\pi^2}\langle 0|\bar{u}(x)u(x)|0\rangle \approx 1800\,\text{MeV}\,. \tag{12}$$

Therefore we can conclude from (8) and (10) that the odderon exchange amplitude for pion production is proportional to the square of the pion mass,

$$\mathcal{M}^\nu(\pi^0;q',p,q) \;\sim\; \frac{1}{m_\pi^2}\,\mathcal{M}^{\mu\nu}(A^3;q',p,q) \;\sim\; \frac{1}{m_\pi^2}\,m_q^2 \;\sim\; m_\pi^2\,. \tag{13}$$

We thus find that the odderon exchange amplitude for π^0-production vanishes in the chiral limit $m_\pi^2 \to 0$. This result can be generalised to the reaction (1) with an arbitrary hadronic final state X.

5 Conclusion

We have considered the diffractive process $\gamma^{(*)}p \to \pi^0 X$ at high energies where it should be dominated by odderon exchange. As a consequence of chiral symmetry the odderon exchange amplitude for this process vanishes in the chiral limit $m_\pi^2 \to 0$. We still expect a strong dynamical suppression in the case of approximate chiral symmetry as it is realised in Nature. The cross section should be suppressed by a factor m_π^4/M^4, where M is a mass scale characterising the scattering process. In the calculation of the process $\gamma p \to \pi^0 N^*$ in [7] that effect had not been properly taken into account. A numerical estimate suggests that due to chiral symmetry the cross section found there is reduced by a factor of at least about 50 [9], changing the prediction (2) to less than about 6 nb. That reconciles the theoretical expectation with the experimental upper bound (3) of [8].

The considerations that we have outlined here can also be applied to pion production in other diffractive processes. An example that is relevant at the LHC and a future ILC is the quasidiffractive reaction $\gamma\gamma \to \pi^0\pi^0$ at high energies. Also this reaction is at high energies mediated by odderon exchange. Here an even stronger suppression due to approximate chiral symmetry is expected.

References

[1] C. Ewerz and O. Nachtmann, Eur. Phys. J. **C49**, 685 (2007). hep-ph/0608082.

[2] L. Lukaszuk and B. Nicolescu, Nuovo Cim. Lett. **8**, 405 (1973);
D. Joynson, E. Leader, B. Nicolescu, and C. Lopez, Nuovo Cim. **A30**, 345 (1975).

[3] C. Ewerz (2003). hep-ph/0306137.

[4] A. Breakstone *et al.*, Phys. Rev. Lett. **54**, 2180 (1985).

[5] H. G. Dosch, C. Ewerz, and V. Schatz, Eur. Phys. J. **C24**, 561 (2002). hep-ph/0201294.

[6] A. Schäfer, L. Mankiewicz, and O. Nachtmann. In Proc. of the Workshop *Physics at HERA*, DESY Hamburg 1991, vol. 1, p. 243;
V. V. Barakhovsky, I. R. Zhitnitsky, and A. N. Shelkovenko, Phys. Lett. **B267**, 532 (1991);
W. Kilian and O. Nachtmann, Eur. Phys. J. **C5**, 317 (1998). hep-ph/9712371.

[7] E. R. Berger *et al.*, Eur. Phys. J. **C9**, 491 (1999). hep-ph/9901376.

[8] H1 Collaboration, C. Adloff *et al.*, Phys. Lett. **B544**, 35 (2002). hep-ex/0206073.

[9] A. Donnachie, H. G. Dosch, and O. Nachtmann, Eur. Phys. J. **C45**, 771 (2006). hep-ph/0508196.

[10] S. L. Adler and R. F. Dashen, *Current Algebras and Applications to Particle Physics*. Benjamin, New York, 1968.

[11] C. Ewerz and O. Nachtmann, Annals Phys. **322**, 1635 (2007). hep-ph/0404254;
C. Ewerz and O. Nachtmann, Annals Phys. **322**, 1670 (2007). hep-ph/0604087.

Part II

pp and $p\bar{p}$ Collisions

Central Production of New Physics

Jeff Forshaw[†]*, Andy Pilkington*
University of Manchester, Manchester M13 9PL UK.

Abstract
We discuss some of the physics which can be explored through a study of the Central Exclusive Process (CEP), $pp \to p + X + p$, where X is some system of particles produced centrally in pseudo-rapidity. In particular, we talk about the case where X is a single Higgs boson, with properties determined either by the SM, the MSSM or the NMSSM. The possibility that X could be a pair of long-lived gluinos is also discussed.

1 Introduction

The interest in measuring the CEP process $pp \to p + X + p$ at the LHC is very substantial, for example see the contributions to the proceedings of this conference from de Roeck [1], Khoze et al [2] and Tasevsky [3]. The FP420 collaboration aims to install suitable proton detectors at 420m from the interaction point (IP), which is the ideal place to guarantee acceptance for central systems in the 70-150 GeV range [4]. This reach can be increased to higher masses upon using also detectors stationed at 220m from the IP. In addition, the theoretical modelling [5] (for an introduction see [6]) has recently received a reassuring degree of validation with the recent CDF measurements of CEP dijet production, as presented in the talk by Goulianos [7]. Most recently, there have been two studies of SM and MSSM Higgs production which deal with the relevant physics to a high level of detail [8, 9]. In this short review I'd like, in the next section, to discuss these recent developments before moving on in the remaining sections to discuss a potentially very interesting scenario in the NMSSM and then the possibility to measure the gluino mass through CEP in models where the gluino is stable. Particular attention is paid to the possibility of making measurements at high luminosities, i.e. $\sim 10^{34}$ cm^{-2}s^{-1}.

2 SM & MSSM Higgs

CEP of a SM Higgs and its decay to WW has been explored in [10] where it was shown that triggering is not a problem and the backgrounds can safely be eliminated. The bottom line is that it is possible to measure the SM Higgs this way, with a handful of events per 30 fb^{-1} of data collected at modest luminosities (i.e. $\sim 2 \times 10^{33}$ cm^{-2}s^{-1}) for Higgs masses in the range 140-200 GeV. It is pretty clear that these are conservative estimates and that improvements in efficiency could readily be achieved through lowering the trigger threshold for the leptons.

More of a challenge is the detection of Higgs bosons via their decay to bottom quarks. Of course this channel is swamped by background in inclusive production and it would be of immense value if it could be observed using CEP. The challenge of establishing whether $H \to b\bar{b}$

[†] speaker

can be observed in CEP was taken up in the recent papers of Cox, Loebinger & Pilkington [8] and Heinemeyer et al [9] with the latter focussing on the case of MSSM Higgses (and other decay channels). We'll discuss the Heinemeyer et al paper first (briefly since more details can be found in [2, 3]).

It is expected that the LHC will be able to discover the lightest MSSM Higgs boson without too much trouble. However, the challenge is to distinguish it from a SM Higgs and to observe the heavier Higgses predicted by supersymmetry. It is in the pursuit of this goal that problems emerge. There is a region of MSSM parameter space (the lower portion of the $\tan\beta - M_A$ plane called the 'wedge region') where it could be very difficult to detect the heavier neutral Higgs bosons. Moreover, the existence of this wedge region is rather robust against variations in the MSSM input parameters. The conclusion of [9] is that CEP offers the unique possibility to observe a previously discovered CP even[1] heavier Higgs, H, directly through its decay to b quarks and with excellent resolution on its mass. It also has the feature that the discovery contours extend slightly into the previously excluded wedge region, making it the discovery channel in that region provided measurements can be made at high luminosities ($\sim 10^{34}$ cm^{-2}s^{-1}).

These conclusions are in line with those drawn in [8]. In that paper, special attention was paid to the challenge of running at high luminosity and in particular the effect of pileup. Pileup refers to the fact that at high enough luminosities there are many proton-proton interactions per collision with typically 35 interactions per collision at 10^{34}cm^{-2}s^{-1}. Clearly these extra collisions produce ambient activity in the detector which contaminates signal events. Moreover it can generate fake signal events as a result of the co-incidence of two or more separate interactions, e.g. for a $p + (H \to b\bar{b}) + p$ signal the dominant background comes from the threefold coincidence of two single diffractive events ($pp \to p + X$) with a third inclusive $pp \to X$ event. It is this overlap background which renders a measurement of the SM Higgs through its decay to $b\bar{b}$ extremely challenging. With its $\tan\beta$ enhanced cross-section, the situation is more favourable for a MSSM Higgs. In that context, one of the major results of [8] is the establishment of the fact that pileup can be brought under control even at 10^{34}cm^{-2}s^{-1} as a result primarily of time-of-flight vertexing (the primary pp vertex can be located very accurately as a result of the 10ps timing resolution of the base FP420 design) and cuts on the number of charged tracks. Various triggering options have also been explored and shown to be viable. That said, it should also be noted that if the Higgs sector were in fact to correspond to something like the m_h^{max} scenario considered in [8] then one would almost certainly be keen to make every effort to put the 420m detectors into the L1 trigger. Additionally, further improvements may be made on the fast-timing rejection of the overlap background. In such a setup, it is claimed that a 10σ observation could be made with a measurement of the Higgs mass to much better than 1 GeV with 300 fb^{-1} of data.

3 NMSSM Higgs

The unsettling possibility that the only light scalar Higgs boson could decay predominantly to four taus arises in the NMSSM. It occurs as a result of the decay chain $h \to aa \to \tau^+\tau^-\tau^+\tau^-$ where a represents a light pseudo-scalar Higgs.

[1] The CP odd Higgs would be filtered out.

The NMSSM extends the MSSM by the introduction of a singlet superfield, $\hat{S}$. To do so provides the possibility to solve the fine tuning and little heirarchy problems present in the MSSM and it provides a natural solution to the μ-problem [11]. The Higgs sector of the NMSSM contains three CP-even and two CP-odd neutral Higgs bosons, and a charged Higgs boson.

In [12], a partial 'no-lose' theorem for NMSSM Higgs discovery was established. The theorem states that the LHC would be able to detect at least one of the NMSSM Higgs bosons, utilizing Higgs decay modes other than Higgs-to-Higgs decays. However, in [13] it was shown that there exists a small part of the NMSSM parameter space where Higgs-to-Higgs decays are in fact dominant. Benchmark points were presented for which the primary decaying neutral Higgs boson has strong coupling to gauge bosons and has mass in the range [90 GeV, 150 GeV] but decays almost entirely to a pair of lighter higgses. Both of these Higgs bosons could have escaped the LEP searches and would quite possibly also evade the standard LHC search modes [13].

Fortunately the troublesome region can be covered using CEP. In [14] attention is focussed on scenario 1 of [13], for which the scalar Higgs, h, has mass 92.9 GeV and the pseudo-scalar Higgs, a, has mass 9.73 GeV.[2] The $h \to aa$ decay occurs with a branching ratio of 92% and is troublesome since each a decays to $\tau^+\tau^-$ with a branching ratio of 81% [15, 16]. The signal process has been incorporated into the ExHuME v.1.3.4 Monte Carlo [17] and the backgrounds were generated using ExHuME for $pp \to p + gg + p$ and $pp \to p + b\bar{b} + p$. We do not need to simulate light quark production because these backgrounds are suppressed relative to $b\bar{b}$ by a factor of m_q^2/m_b^2. POMWIG [18] is used to simulate this source of background and the version used incorporates the latest diffractive parton distribution functions from the H1 experiment at HERA [19]. In addition to these direct backgrounds, at sufficiently high luminosity it becomes necessary to consider the OLAP background. Specifically, the possibility of a threefold coincidence of two single diffractive $pp \to p + X$ events with a generic $pp \to X$ inelastic process was considered. The inclusive QCD events $pp \to X$ were generated using PYTHIA, with the 'ATLAS tune' to Tevatron data. The forward protons (from single diffraction) were then added to the event using the prescription presented in [8], which also allows one to estimate the probability of the threefold coincidence as a function of instantaneous luminosity. The two protons detected by the 420m detectors do not originate from the same vertex as the primary scatter which produces the muon and this can be exploited to reduce the OLAP background. According to the results presented in [8], a rejection factor of 18 (15) should be obtained at low (high) luminosity running. Overlap backgrounds from twofold coincidences are not considered since it was shown in [8] that the largest twofold background is a factor of ~ 5 smaller than that for threefold coincidences. Finally, the pure QED backgrounds: $pp \to p + \tau^+\tau^- l^+ l^- + p$ (where l is any charged lepton) were also considered and simulated using MADGRAPH [20]. All final state particle four-momenta were smeared according to the relevant detector component resolution [21] with the outgoing proton momenta smeared by the amount given in [22] and the effects of pileup were accounted for by superimposing additional inelastic pp collisions simulated using PYTHIA on top of both signal and background events. The above numbers are quoted assuming that triggering requires a single muon with $p_T > 6$ GeV, although increasing this threshold to 20 GeV may be more appropriate at high luminosity (see [14] for details).

The final results are encouraging: after all cuts, the signal cross-section is around 0.08 fb

[2] These values are not exactly those quoted in [13].

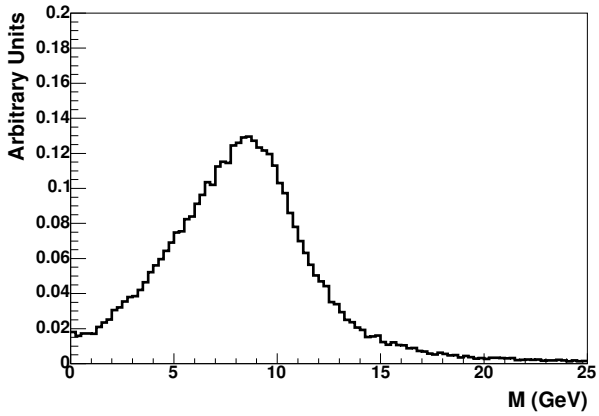


Fig. 1: The reconstructed a mass for the signal events.

with a total background of less than 0.02 fb excluding the OLAP background. By far the largest source of background is the DPE production of $pp \to p + jjX + p$ and the QED background is entirely negligible. The OLAP background is luminosity dependent, and estimated to be 0.1 fb at 10^{34} and 100 times smaller at 10^{33}. It should be noted that the results correspond to a wide central mass window from 70-110 GeV, which would be desirable if one is operating in search mode. Once a signal has been identified, a much tighter mass cut would lead to a further reduction in backgrounds. It is striking that even at high luminosities the effects of pileup are under control. The principal reason for the smallness of the backgrounds arises because the analysis strategy is very much oriented upon the use only of charged tracks, the muon detectors and the proton detectors, i.e. the calorimeter is barely needed (there is a muon isolation cut which is not critical for the analysis). In fact the principal cuts used to eliminate the backgrounds are cuts to insist on exactly 4 or 6 charged tracks and a series of cuts to ensure that the charged tracks have the right topology (i.e. they should cluster and form back-to-back pairs). It remains to be seen how much of this charged track philosophy can be exported to other CEP processes.

Another advantage of studying NMSSM Higgs production via CEP is that not only can the mass of the scalar Higgs be determined on an event by event basis, so too can the mass the the pseudo-scalar a. Knowledge of the mean rapidity and invariant mass of the central system (from the 420m detectors) in conjunction with the assumption that the a's are highly boosted (so that their decay products are roughly collinear with the original a direction) allows four a mass measurements per event. Fig.1 illustrates the a mass distribution: it is clearly peaked around the correct mass and the width is determined mainly by the collinearity approximation (not detector resolution).

4 Gluinos

The possibility that the gluino may be long-lived is a hallmark of the 'Split Supersymmetry' scenario [23, 24], though long lived gluinos have been studied before, in the context of models in which the gluino is the Lightest Supersymmetric Particle (LSP) [25–27]. In Split Supersymmetry

$m_{\tilde{g}}$ (GeV)	$\sigma_{m_{\tilde{g}}}$ (GeV)	$\frac{\sigma_{m_{\tilde{g}}}}{\sqrt{N-1}}$ (GeV)	N
200	2.31	0.19	145
250	2.97	0.50	35.0
300	3.50	1.10	10.2
320	3.61	1.54	6.5
350	3.87	2.45	3.5

Table 1: The gluino mass resolution as a function of the gluino mass.

the SUSY breaking scale, m_S, is large ($m_S \gg$1 TeV) and the scalar particles acquire masses at this scale. The sfermions of the theory are protected by chiral symmetries and so can have masses at the TeV scale as can one neutral Higgs boson whose mass is allowed to be finely tuned. As a result the gluino can be long-lived on collider timescales since it can only decay via the massive scalar particles.

Data from the Tevatron have been used to place the limit $m_{\tilde{g}} > 170$ GeV on the mass of a long lived gluino [28], for the case in which the gluino forms only neutral hadrons which remain neutral as they pass through the detector. This limit is expected to rise to $\simeq 210$ GeV using Run II data [28]. We should stress that this is a conservative limit, since it is anticipated that these hadrons will undergo charge conversion reactions as they pass through the detector [29]. In the most optimistic case, the Tevatron may reach gluino masses of up to $\simeq 430$ GeV if no signal is observed [28].

In [22], the possibility of CEP gluino pair production was considered in the case where the gluinos are sufficiently long-lived that they do not decay within the detector.[3] According to that paper, there could be sufficient rate (with negligible backgrounds) for detection provided the gluinos have mass below $\simeq 350$ GeV and the gluino mass could be measured to an accuracy at the 1% level after 3 years of high luminosity running.

For CEP, triggering is on the fastest R-hadron[4] in the event (it looks like a delayed muon), in conjunction with a cross-check that the forward detector readout contains hits in either the same event or the previous one. Due to the relatively large masses that are of interest, good acceptance for central masses in the range $300 - 1500$ GeV requires use of at least one pot at 220m. Even in the most conservative scenario with 420m pots at 5mm from the beam and 220m pots at 3mm from the beam, the acceptance is more than 40% up to central masses of 950 GeV.

The resulting gluino mass resolution, given 3 years of high luminosity running, is shown in Table 1. In particular the final error on the gluino mass measurement is shown for N events. In conclusion, it should be possible to measure the gluino mass to an accuracy below 1% up to gluino masses of $\simeq 350$ GeV.

[3] It means we do not consider the case where the gluinos stop and subsequently decay within the calorimeter.

[4] The colour singlet bound state containing a gluino.

5 Conclusions

Central exclusive production is able to explore a wide range of interesting physics[5] and the experimental programme is already well developed [1]. In this short note we focussed upon Higgs boson and gluino production. The key points to note are as follows.

- The prospects for SM Higgs production are good for m_H in the range 140-200 GeV via the WW decay channel.
- The prospects for MSSM Higgs production are good, especially in regions of MSSM parameter space where there is a $\tan\beta$ enhancement of the rate. CEP offers the possibility to measure the scalar Higgses, h and H, through the decay to $b\bar{b}$.
- CEP is able to close the loop-hole in the NMSSM whereby the lightest scalar Higgs could be invisible at the LHC as a result of its decay to four taus. It offers the opportunity to measure the pseudo-scalar mass on an event-by-event basis. This analysis is very robust against pileup by virtue of the fact that it makes very little use of the calorimeters.
- Should there exist light, stable, gluinos, CEP could pair produce them if they have masses below 350 GeV and their mass could be measured.

Acknowledegments

We thank Peter Bussey, Tim Coughlin, Brian Cox, Jack Gunion, Lee Hodgkinson, Fred Loebinger and Andreas Papaefstathiou for their collaboration. This research was supported by the UK's STFC.

References

[1] A. de Roeck, *Prospects for diffraction at the LHC*, in *these proceedings*.

[2] V. Khoze, A. Martin, and M. Ryskin, *Insight into New Physics with Tagged Protons at the LHC*, in *these proceedings*.

[3] M. Tasevsky, *Proton tagging at high luminosities at LHC*, in *these proceedings*.

[4] M. G. Albrow *et al.* CERN-LHCC-2005-025.

[5] V. A. Khoze, A. D. Martin, and M. G. Ryskin, Eur. Phys. J. **C23**, 311 (2002). hep-ph/0111078.

[6] J. Forshaw, *Diffractive Higgs production: Theory*, in *proceedings of HERA and the LHC: A Workshop on the implications of HERA for LHC physics*. 2005. Also in preprint hep-ph/0508274.

[7] K. Goulianos, *Diffraction at CDF*, in *these proceedings*.

[8] B. E. Cox, F. K. Loebinger, and A. D. Pilkington (2007). arXiv:0709.3035 [hep-ph].

[9] S. Heinemeyer *et al.* (2007). arXiv:0708.3052 [hep-ph].

[10] B. E. Cox *et al.*, Eur. Phys. J. **C45**, 401 (2006). hep-ph/0505240.

[11] R. Dermisek and J. Gunion, Phys. Rev. Lett. **95**, 041801 (2005). hep-ph/0502105.

[12] U. Ellwanger, J. F. Gunion, and C. Hugonie (2001). hep-ph/0111179.

[13] U. Ellwanger, J. F. Gunion, and C. Hugonie, JHEP **07**, 041 (2005). hep-ph/0503203.

[14] J. R. Forshaw, J. F. Gunion, L. Hodgkinson, A. Papaefstathiou, and A. D. Pilkington, *Reinstating the no-lose theorem for NMSSM Higgs discovery at the LHC*. In preparation.

[15] U. Ellwanger and C. Hugonie, Comput. Phys. Commun. **175**, 290 (2006). hep-ph/0508022.

[5] We have not discussed the menu of standard physics processes.

[16] U. Ellwanger, J. F. Gunion, and C. Hugonie, JHEP **02**, 066 (2005). hep-ph/0406215.

[17] J. Monk and A. Pilkington, Comput. Phys. Commun. **175**, 232 (2006). hep-ph/0502077.

[18] B. E. Cox and J. R. Forshaw, Comput. Phys. Commun. **144**, 104 (2002). hep-ph/0010303.

[19] H1 Collaboration, A. Aktas *et al.* (2007). arXiv:0708.3217 [hep-ex].

[20] F. Maltoni and T. Stelzer, JHEP **02**, 027 (2003). hep-ph/0208156.

[21] CERN-LHCC-99-14.

[22] P. J. Bussey, T. D. Coughlin, J. R. Forshaw, and A. D. Pilkington, JHEP **11**, 027 (2006). hep-ph/0607264.

[23] N. Arkani-Hamed and S. Dimopoulos, JHEP **06**, 073 (2005). hep-th/0405159.

[24] G. F. Giudice and A. Romanino, Nucl. Phys. **B699**, 65 (2004). hep-ph/0406088.

[25] G. R. Farrar and P. Fayet, Phys. Lett. **B76**, 575 (1978).

[26] S. Raby and K. Tobe, Nucl. Phys. **B539**, 3 (1999). hep-ph/9807281.

[27] H. Baer, K.-m. Cheung, and J. F. Gunion, Phys. Rev. **D59**, 075002 (1999). hep-ph/9806361.

[28] J. L. Hewett, B. Lillie, M. Masip, and T. G. Rizzo, JHEP **09**, 070 (2004). hep-ph/0408248.

[29] A. C. Kraan, Eur. Phys. J. **C37**, 91 (2004). hep-ex/0404001.

Diffraction at CDF

Konstantin Goulianos, on behalf of the CDF Collaboration
The Rockefeller University, 1230 York Avenue, New York, NY 10065-6399, USA

Abstract
The diffractive program of the CDF collaboration at the Fermilab Tevatron $p\bar{p}$ Collider is reviewed with emphasis on measurements of the diffractive structure function and on exclusive production from Run II at $\sqrt{s}$ =1.96 TeV. Results on cross sections for exclusive dijet production are used to calibrate theoretical estimates for exclusive Higgs production at the Large Hadron Collider.

1 Introduction

The CDF collaboration has been conducting studies of diffractive interactions at the Fermilab Tevatron $p\bar{p}$ collider since 1989, aiming at elucidating the QCD nature of hadronic diffraction [1]. Diffractive interactions are characterized by one or more large rapidity gaps [2], presumed to occur via the exchange of a *Pomeron*, generically defined as a quark/gluon combination carrying the quantum numbers of the vacuum [3]. The diffractive process directly analogous to classical diffraction is elastic scattering. The total cross section is also of interest in testing theoretical models of diffraction, since it is related to the imaginary part of the forward elastic scattering amplitude through the optical theorem. However, the most stringent tests for QCD inspired models of diffraction are provided by inelastic diffraction. In this paper, we review the results on diffraction reported by CDF and discuss their physics significance. These results have been obtained from a comprehensive program spanning two decades, as outlined in the table below.

Run	Sub-Run	Date	$\int$Lum (pb^{-1})	Process
Run I	IØ	1988-1989	5	σ_{el}, σ_{tot}, σ_{el}
	Ia	1992-1993	20	see Fig. 1 (b)
	Ib	1993-1995	100	”
	Ic	1995-1996	10	”
Run II	IIa	2003-2006	1000	see text
	IIb	in progress		

2 Run IØ Results

In Run IØ, CDF measured the elastic, soft single diffractive, and total $p\bar{p}$ cross sections at $\sqrt{s}$ =630 and 1800 GeV. The measurement was performed with the CDF I detector, which during run IØ had tracking coverage out to $|\eta| \sim 7$ and Roman Pot Spectrometers on both sides of the Interaction Point (IP). The normalization was obtained by the luminosity independent method, which is based on simultaneously measuring the total interaction rate, which depends on σ_{tot}, and the elastic scattering differential rate at $t = 0$, which depends on σ_{tot}^2 (optical theorem):

$$\sigma_{tot} \propto \frac{1}{L}\left(N_{el} + N_{inel}\right) \;\&\; \sigma_{tot}^2 \sim \frac{1}{1+\rho^2}\frac{dN_{el}}{dt}|_{t=0} \;\Rightarrow\; \sigma_{tot} = \frac{16\pi}{1+\rho^2}\frac{1}{N_{el}+N_{inel}}\frac{dN_{el}}{dt}|_{t=0}$$

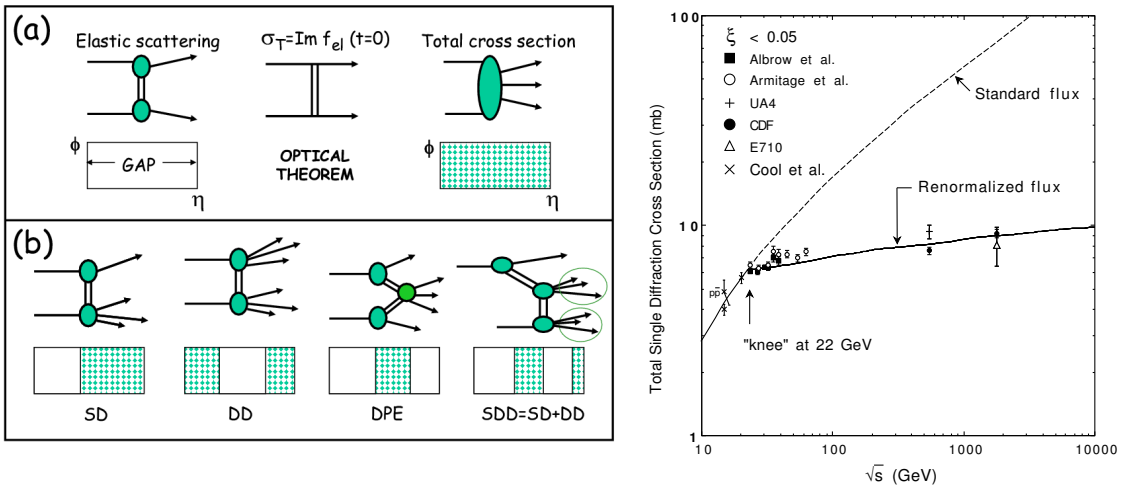


Fig. 1: *(left)* Schematic diagrams and event topologies in azimuthal angle ϕ versus pseudorapidity η for (a) elastic and total cross sections, and (b) single diffraction (SD), double diffraction (DD), double Pomeron exchange (DPE), and double plus single diffraction cross sections (SDD=SD+DD). The hatched areas represent regions in which there is particle production. *(Right)* The total $pp/p\bar{p}$ single diffraction dissociation cross section data (sum of $\bar{p}$ and p dissociation) for $\xi < 0.05$ compared with Regge predictions based on standard and renormalized Pomeron flux [5].

A global Regge fit to total and elastic $p\bar{p}/pp$, $\pi^{\pm}p$, and $K^{\pm}p$ cross sections using the eikonal approach to ensure unitarity yields results consistent with the CDF cross sections even when the CDF results are not used in the fit [4]. In contrast, the standard Regge fit to total single diffractive cross sections, shown in Fig. 1 (*right*), overestimates the Tevatron cross sections by a factor of ~ 10. This discrepancy represents a breakdown of factorization, which is restored by the renormalization procedure proposed in Ref. [5] (see also Ref. [6]).

3 Run Ia,b,c Results

The diffractive processes studied by CDF in Tevatron Runs Ia,b,c are schematically shown in Fig. 1b. Both soft and hard processes were studied. A discussion of the results obtained and of their significance in deciphering the QCD nature of the diffractive exchange can be found in Ref. [7]. The most interesting discoveries are the beakdown of factorization and the restoration of factorization in events with multiple rapidity gaps.

Breakdown of factorization. At $\sqrt{s}$ =1800 GeV, the SD/ND ratios (gap fractions) for dijet, W, b-quark, and J/ψ production, as well the ratio of DD/ND dijet production, are all $\approx 1\%$. This represents a suppression of a factor of $\sim$10 relative to predictions based on diffractive parton densities measured from DDIS at HERA, indicating a breakdown of QCD factorization comparable to that observed in soft diffraction processes relative to Regge theory expectations. However, factorization approximately holds among the four different diffractive processes at fixed $\sqrt{s}$, which indicates that the suppression comes from the formation of the rapidity gap, as predicted by the generalized gap renormalization model (see Ref. [7]).

Restoration of factorization in multi-gap diffraction. Another interesting aspect of the data is that ratios of two-gap to one-gap cross sections for both soft and hard processes obey factorization. This provides both a clue to understanding diffraction in terms of a composite Pomeron and an experimental tool for diffractive studies using processes with multiple rapidity gaps (see Ref. [7]).

4 The Run II Diffractive Program

In Run II, CDF has been conducting the following studies of diffraction:

– structure function in dijet production,

– t distributions,

– exclusive dijet, diphoton [8], and e^+e^- [9] production,

– structure function in W production,

– gap between jets: dependence of the cross section on gap size for fixed $\Delta\eta^{jet}$.

In this paper, we present preliminary results on the diffractive structure function, on diffractive t-distributions, and on exclusive dijet production. The diffractive W and 'gap between jets' analyses are in progress.

4.1 Run II forward detectors

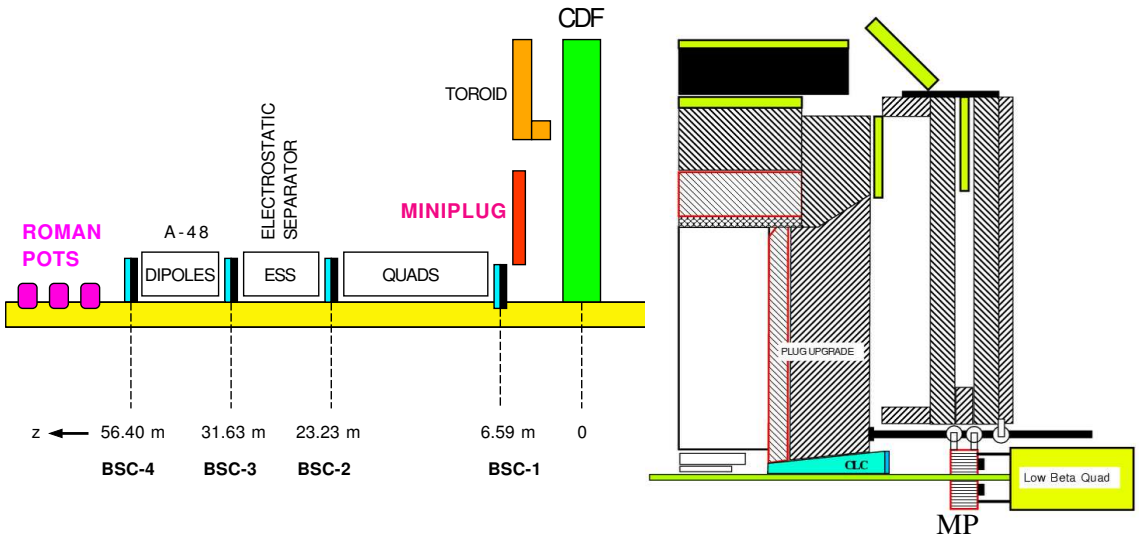


Fig. 2: The CDF detector in Run II: *(left)* location of forward detectors along the $\bar{p}$ direction; *(right)* position of the Cerenkov Luminosity Monitor (CLC) and MiniPlug calorimeters (MP) in the central detector.

The Run II diffractive program was made possible by an upgraded CDF detector [10], which includes the following special forward components (see Fig. 2):

– Roman Pot Spectrometer (RPS) to detect leading antiprotons,

– MiniPlug (MP) forward calorimeters covering the region of $\sim 3.5 < |\eta| < 5.5$,

– Beam Shower Counters (BSC) surrounding the beam pipe within $\sim 5.5 < |\eta| < 7.5$.

The Roman Pot Spectrometer is the same one that was used in Run Ic. It consists of X-Y scintillation fiber detectors placed in three Roman Pot Stations located at an average distance of 57 m downstream in the $\bar{p}$ direction. The detectors have a position resolution of $\pm 100\,\mu m$, which makes possible a $\sim 0.1\%$ measurement of the $\bar{p}$ momentum. In Run Ic, the $\bar{p}$-beam was behind the proton beam, as viewed from the RPS side. An inverted polarity (with respect to Run I) of the electrostatic beam separators enabled moving the RPS detectors closer to the $\bar{p}$-beam and thereby gain acceptance for small $|t|$ down to $\xi \equiv 1 - x_F(\bar{p}) = 0.03$ (for larger $|t|$, lower ξ values can be reached).

The MiniPlug calorimeters are placed within the holes of the muon toroids. They consist of layers of lead plates immersed in liquid scintillator. The scintillation light is picked up by wavelength shifting fibers strung through holes in the lead plates and read out by multi-channel PMT's. The calorimeter "tower" structure is defined by arranging fibers in groups to be read out by individual PMT pixels. There are 84 towers in each MiniPlug measuring energy and position for both electromagnetic and hadron initiated showers [11].

The Beam Shower counters are rings of scintillation counters "hugging" the beam pipe. The BSC-1 rings are segmented into four quadrants, while the other BSCs are segmented into two halves. The BSC-1 are also used to provide rapidity gap triggers and for measuring beam losses.

4.2 Diffractive structure function from dijet production

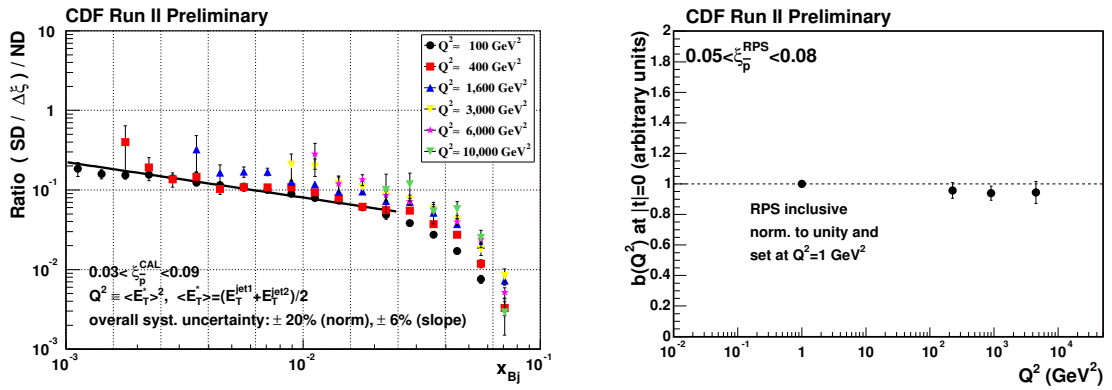


Fig. 3: *(left)* Ratio of diffractive to non-diffractive dijet event rates as a function of x_{Bj} (momentum fraction of parton in antiproton) for different values of $E_T^2 = Q^2$; *(right)* $b|_{t=0}$ slope vs Q^2.

In Run II, CDF has obtained preliminary results for the x_{Bj}, Q^2, and t dependence of the diffractive structure function from dijet production at $\sqrt{s} = 1960$ GeV. The measured x_{Bj} rates confirm the factorization breakdown observed in Run I (see review in Ref. [12]). The Q^2 and t dependence results are shown in Fig 3.

Q^2 dependence. In the range 10^2 GeV$^2 < Q^2 < 10^4$ GeV^2, where the inclusive E_T distribution falls by a factor of $\sim 10^4$, the ratio of the SD/ND distribution increases by only a factor of ~ 2. The above results indicate that the Q^2 evolution in diffractive interactions is similar to that in ND interactions.

t-dependence. The slope parameter $b(Q^2)|_{t=0}$ of an exponential fit to t distributions near $t = 0$ shows no Q^2 dependence in the range 1 GeV$^2 < Q^2 < 10^4$ GeV^2.

These results support the picture of a composite Pomeron formed from color singlet combinations of the underlying parton densities of the nucleon (see Ref. [7]).

4.3 Exclusive Dijet Production

Exclusive production in $p\bar{p}$ collisions is of interest not only for testing QCD inspired models of diffraction, but also as a tool for discovering new physics. The process that has attracted the most attention is exclusive Higgs boson production. The search for Higgs bosons is among the top priorities in the research plans of the LHC experiments. While the main effort is directed toward searches for inclusively produced Higgs bosons, an intense interest has developed toward exclusive Higgs production, $\bar{p}/p + p \rightarrow \bar{p}/p + H + p$. This Higgs production channel presents several advantages: it can provide clean events in an environment of suppressed QCD background, in which the Higgs mass can accurately be measured using the missing mass technique by detecting and measuring the momentum of the outgoing proton and (anti)proton. However, exclusive production is hampered by expected low production rates [13]. As rate calculations are model dependent and generally involve non-perturbative suppression factor(s), it is prudent to calibrate them against processes involving the same suppression factors(s), but have higher production rates that can be measured at the Tevatron. One such processes is exclusive dijet production, which proceeds through the same mechanism as Higgs production, as shown in Fig. 4.

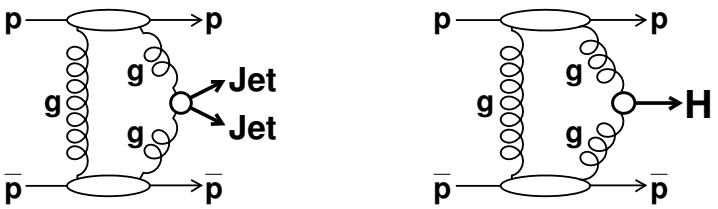


Fig. 4: Lowest order diagrams for exclusive dijet (left) and Higgs (right) production in $\bar{p}p$ collisions.

The search for exclusive dijets is based on measuring the dijet mass fraction, R_{jj}, defined as the mass of the two leading jets in an event, M_{jj}, divided by the total mass reconstructed from the energy deposited in all calorimeter towers, M_X. The signal from exclusive diets is expected to appear at high values of R_{jj}, smeared by resolution and radiation effects. Events from inclusive DPE production, $\bar{p}p \rightarrow \bar{p} + gap + jj + X + gap$, are expected to contribute to the entire M_{jj} region. Any such events within the exclusive M_{jj} range contribute to background and must be subtracted when evaluating exclusive production rates.

The exclusive signal is extracted from the inclusive R_{jj} distribution by fitting the data with MC simulations [14]. Two methods have been used. In the first one, the POMWIG and ExHuME generators are used for simulating inclusive and exclusive events, respectively, while in the second, inclusive (exclusive) distributions are simulated using the POMWIG (DPEMC) program. Experimentally, the MC non-exclusive dijet background shape is checked by a study of high E_T b-tagged dijet events, as quark jet production through $gg \to \bar{q}q$ is suppressed in LO QCD by the $J_z = 0$ selection rule as $m_q/M^{jet} \to 0$.

Figure 5 shows measured R_{jj} distributions plotted versus dijet mass fraction. On the left, the number of events within the specified kinematic region the data are compared with fits based on POMWIG plus ExHuME distribution shapes, and on the right with fits based on POMWIG⊕DPEMC predictions. Both approaches yield good fits to the data. The suppression factor expected for exclusive b-tagged dijet events is checked with CDF data in Fig. 6. Within the quoted errors, this result validates the MC based method for extracting the exclusive signal. In

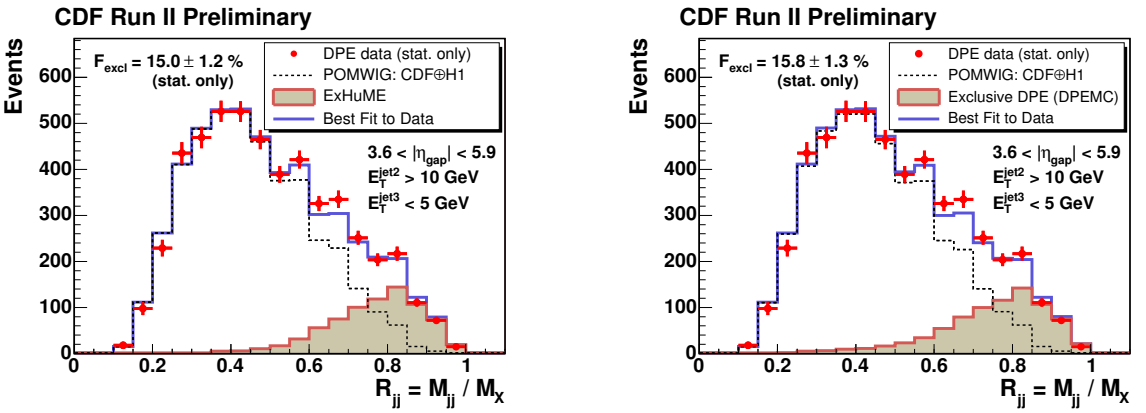


Fig. 5: Extraction of exclusive dijet production signal using Monte Carlo techniques to subtract the inclusive dijet background: *(left)* dijet mass fraction in data (points) and best fit (solid line) obtained from MC events generated using the POMWIG (dashed) and ExHuME (filled) MC generators for inclusive and exclusive events, respectively; *(right)* the same data fitted with POMWIG and exclusive DPEMC generators.

Fig. 7 *(left)*, integrated cross sections above a minimum $E_T^{jet1,2}$ are compared with ExHuME and DPEMC predictions. The data favor the ExHuME prediction. ExHuME hadron level differential cross sections $d\sigma^{excl}/dM_{jj}$, normalized to the measured data points of Fig. 7 *(left)*, are shown in Fig. 7 *(right)* with errors propagated from the uncertainties in the data. Within the errors, the good agreement with the default ExHuME prediction up to masses in the region of the standard model Higgs mass predicted from global fits to electroweak data confirms the calculation of Ref. [13] for exclusive Higgs boson production at the LHC.

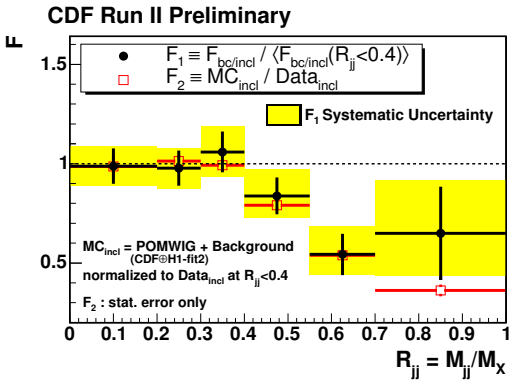


Fig. 6: *(circles)* Fraction of heavy flavor (b, c) to all dijet events in data, F_1, as a function of dijet mass fraction showing the expected suppression at high M_{jj}; *(squares)* fraction, F_2, of inclusive MC to data from Fig. 5 (left). The agreement between the measured suppression levels in F_1 and F_2 serves to validate the MC based technique for extracting the exclusive production rate from the data.

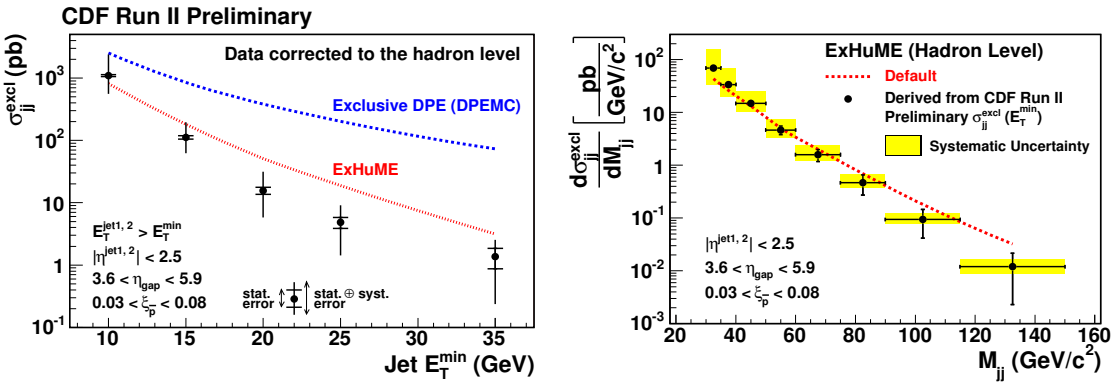


Fig. 7: *(left)* Measured exclusive dijet cross sections versus the minimum E_T of the two leading jets compared with ExHuME and DPEMC predictions; *(right)* ExHuME hadron level differential exclusive dijet cross section vsersus dijet mass normalized to the CDF cross sections at *left*. The systematic errors shown are propagated from those in the data; the ExHuME predictions have comparable systematic uncertainties.

5 Summary

Diffractive processes studied by CDF in Run I include elastic and total cross sections, soft diffractive cross sections with single and multiple rapidity gaps, and hard single diffractive production of dijet, W, b-quark, and J/ψ production, as well as central dijet production in events with two forward rapidity gaps (double Pomeron exchange). The results obtained support a picture of universality of diffractive rapidity gap formation across soft and hard diffractive processes, which favors a composite over a particle-like Pomeron made up from color singlet quark and/or gluon combinations with vacuum quantum numbers.

Run II preliminary results on the x_{Bj} and Q^2 dependence of the diffractive structure function obtained from dijet production are also presented, as well as results on the slope parameter of the t-distribution of diffractive events as a function of Q^2. In the range 10^2 GeV^2 $< Q^2 <$ 10^4 GeV^2, where the inclusive E_T distribution falls by a factor of $\sim 10^4$, the ratio of SD/ND

distributions varies by at most a factor of ~ 2, indicating that the Q^2 evolution in diffractive interactions is similar to that in ND ones. The slope parameter $b(Q^2)|_{t=0}$ of an exponential fit to t distributions near $t = 0$ in the range $1\ \mathrm{GeV}^2 < Q^2 < 10^4\ \mathrm{GeV}^2$ shows no Q^2 dependence. These results support a picture of a composite diffractive exchange (Pomeron) made up from the underlying parton densities of the nucleon [7].

References

[1] See e. g. K. Goulianos, *Diffractive and Total Cross Sections at Tevatron and LHC*, in *Hadron Collider Physics Symposium 2006*, May 22-26, Duke University, Durham, NC, USA.

[2] Rapidity gaps are regions of rapidity devoid of particles; rapidity, $y = \frac{1}{2}\frac{E+p_L}{E-p_L}$, and pseudorapidity, $\eta = -\ln\tan\frac{\theta}{2}$, are used interchangeably in this paper, as in the kinematic region of interest the values of these two variables are approximately equal.

[3] P. D. B. Collins, *An Introduction to Regge Theory and High Energy Physics*, Cambridge University Press (1977); V. Barone and E. Predazzi, *High-Energy Particle Diffraction*, Springer Press (2001); S. Donnachie, G. Dosch, O. Nachtmann, and P. Landshoff, *Pomeron Physics and QCD*, Cambridge University Press (2002).

[4] R. J. M. Covolan, J. Montanha, and K. Goulianos, *A New Determination of the Soft Pomeron Intercept*, Phys. Lett. B **389**, 176 (1996).

[5] K. Goulianos, *Renormalization of Hadronic Diffraction and the Structure of the Pomeron*, Phys. Lett. B **358**, 379 (1995); Erratum-*ib.* **363**, 268 (1995).

[6] K. Goulianos, *Pomeron Intercept and Slope: the QCD Connection*, in these proceedings.

[7] K. Goulianos, *Hadronic Diffraction: Where do we Stand?*, in *La Thuile 2004, Results and Perspectives in Particle Physics*, edited by M. Greco, Proc. of Les Rencontres de Physique de la Vallé d'Aoste, La Thuile, Aosta Valley, Italy, February 29 - March 6, 2004, pp. 251-274; e-Print Archive: hep-ph/0407035.

[8] T. Aaltonen *et al.* (CDF Collaboration), *Search for Exclusive $\gamma\gamma$ Production in Hadron-Hadron Collisions*, FERMILAB-PUB-07-384-E, Jul 2007, e-Print: arXiv:0707.2374 [hep-ex], Submitted to Phys. Rev. Lett.

[9] A. Abulencia *et al.* (CDF Collaboration), *Observation of Exclusive Electron-Positron Production in Hadron-Hadron Collisions*, Phys.Rev.Lett.98:112001,2007, FERMILAB-PUB-06-436-E, Nov 2006, e-Print: hep-ex/0611040.

[10] R. Blair *et al.* (CDF Collaboration), *The CDF II Detector: Technical Design Report*, FERMILAB-Pub-96/390-E.

[11] K. Goulianos and S. Lami, *Performance of a Prototype Position Sensitive Towerless Calorimeter*, *Nucl. Instrum. Meth. A* **430**, 34-47 (1999); K. Goulianos *et al.*, *The CDF MiniPlug calorimeters*, *Nucl. Instrum. Meth. A* **496**, 333-346 (2003).

[12] M. Gallinaro (for the CDF collaboration), *Diffractive and exclusive measurements at CDF*, Presented at 14th International Workshop on Deep Inelastic Scattering (DIS 2006), Tsukuba, Japan, 20-24 Apr 2006; e-Print Archive: hep-ex/0606024.

[13] V. Khoze, A. Kaidalov, A. Martin, M. Ryskin, and W. Stirling, *Diffractive processes as a tool for searching for new physics*, e-Print Archive:hep-ph/0507040, and references therein.

[14] Monte Carlo programs used in the CDF analysis: **POMWIG** (implements diffraction into the HERWIG Monte Carlo Generator) B. Cox and J. Forshaw, *Comput. Phys. Commun.* **144**, 104 (2002); **DPEMC** (extends POMWIG to include inclusive and exclusive DPE) M. Boonekamp and T. Kucs, *Comput. Phys. Commun.* **167**, 217 (2005); **ExHuME** (implements the exclusive dijet production calculation of Ref. [13]), J. Monk and A. Pilkington, e-Print Archive: hep-ph/0502077.

Proton tagging at high luminosities at LHC

Marek Taševský
Institute of Physics, Na Slovance 2, 18221 Prague 8, Czech Republic

Abstract
We show that forward proton taggers at the LHC installed at 220 and 420 m from ATLAS and / or CMS give access to a very rich forward physics program including possibilities to study the diffractive structure of proton or Higgs boson production in central exclusive diffraction processes, and also the photon-photon and photon-proton physics. The focus is put on projects aiming at tagging scattered protons at high luminosities at the LHC.

1 Introduction

There has been a great attention recently being devoted to the possibility of complementing the standard LHC physics menu by adding forward proton detectors to the ATLAS [1] and CMS [2] detectors. As a general and well-known feature of the hadronic production at LHC, the particle multiplicity is peaked in the central region, while most of the energy flows very forward and undetected by the main detector. In order to have a chance to explore the very rich forward physics it is necessary to instrument the forward region of the main detectors. The forward detector projects around the interaction point (IP) of ATLAS (IP1) and CMS (IP5) outside the main detectors are summarized as follows:

- 14 m:
  T2 GEM trackers of the Totem experiment [3] at CMS. Each of them contains 10 aligned detector half-planes with 512 strips. The acceptance is $5.2 < |\eta| < 6.5$ and resolution is $\Delta\phi \times \Delta\eta = 0.06 \times 0.017\pi$. Installation is foreseen in 2007.
- 16 m:
  CASTOR (Centauros and Strange Object Research) [4] calorimeter at the CMS side is composed of tungsten/quartz planes with Cerenkov radiation as a measuring principle and with separate electromagnetic (20.1 X_0) and hadronic (9.5 λ_I) sections. It is an octagonal cylinder (length of 1.5 m, diameter of 36 cm) with 16-fold segmentation in ϕ and 14-fold segmentation in z. The acceptance is $5.2 < |\eta| < 6.6$. The construction is two-staged: the first CASTOR will be installed in 2008, the second one in 2009.

  Two LUCID (Luminosity measurement using Cerenkov Integrating Detector) [5] detectors at the ATLAS side consist each of 168 gasfilled (C4F10 gas) aluminum tubes with Cerenkov radiation as a measuring principle. It is a cylinder (length of 1.5 m, diameter of 13.7 cm) with 168 tubes and 1176 fibers. The acceptance is $5.5 < |\eta| < 6.2$. The construction is also staged: a partial detector is being build in 2007, the full detector later.
- 140 m:
  ZDC (Zero Degree Calorimeter) at the CMS side [6] is a tungsten/quartz Cerenkov calorimeter with separate electromagnetic (19 X_0) and hadronic (5.6 λ_I) sections. The acceptance

for neutral particles (γ, π^0, n) is $\eta > 8.1$ (100% for $\eta > 9.3$). The installation is planned for 2007.

ZDC at the ATLAS side [7] is a tungsten/quartz Cerenkov calorimeter with separate electromagnetic (29 X_0) and hadronic (3.4 λ_I) section. It has 3-fold segmentation in z for the the hadronic section; quartz rods in the electromagnetic and the first hadronic module provide transverse coordinate measurement. The acceptance for neutral particles is $\eta > 8$. The installation of one side is planned for 2007/2008 and the completion should be phased with the LHCf detector.

The LHCf [8] tungsten-scintillator/silicon calorimeters share the location with the ATLAS ZDC in the 140 m region.

- 220 m:
  Roman Pots from the Totem experiment at the CMS side are formed by two units separated by 4 m and each consisting of 2 vertical and one horizontal pot approaching the beam down to 10σ+250 μm = 1.5 mm. Each pot has 5+5 planes of edgeless silicon detectors. It reaches a spatial resolution of 20 μm per plane. The overall proton acceptance for central exclusive production (CEP) processes varies with beam optics: it is almost 90% in the range $10^{-3} < -t < 0.3$ GeV^2 and $10^{-4} < \xi < 0.2$ for $\beta^* = 1540$ m, while for $\beta^* = 0.5$ m (the highest instantaneous luminosity) it is around 40% in the range $10^{-3} < -t < 10$ GeV^2 and almost 100% in the range $0.02 < \xi < 0.2$, where ξ is the fractional proton momentum loss. The installation should be completed in 2007.

  Roman Pots of the RP220 project at the ATLAS side [9] should contain just horizontal pots with silicon strip or 3D silicon detectors with foreseen spatial resolution of 10–15 μm and active edge of 30–60 μm in the case of the silicon strip option. The installation is foreseen to happen in 2010.
- 240 m:
  ALFA (Absolute Luminosity For ATLAS) [10] contains two vertical stations approaching the beam down to 1.5 mm. It is composed of 10+10 planes of scintillating fiber detectors with spatial resolution of 30 μm and the insensitive region smaller than 100 μm. The ALFA system is foreseen to be installed in the 2008/2009 shutdown.
- 420 m:
  FP420 [11] is an R&D collaboration formed to study the possibility to adapt 15 m long cryostat using moving a beam pipe at both sides, ATLAS and CMS. It is designed to operate at the highest luminosity optics for which the 3D silicon detectors is the best solution to stand high radiation levels. The detectors yield $\Delta p/p = 10^{-4}$ and hence a mass resolution of about 1%. The overall proton acceptance for CEP processes is almost 100% in the range $0.002 < \xi < 0.02$ giving the exclusive central system in a mass range $30 < M < 200$ GeV. The acceptance is around 40% in the range $10^{-3} < -t < 10$ GeV^2. A timing detector with at least 10 ps is necessary to be installed to suppress the pile-up background. The installation is foreseen in 2010.

In the following, an emphasis is put on the two projects aiming at installing forward proton taggers for high luminosities, namely the FP420 and RP220. In the sections 2–5, common aspects for both projects are discussed, followed then by sections about the status of both projects.

2 Physics motivation for forward proton taggers at high luminosities

The use of forward proton tagging will provide an exceptionally clean environment to search for new phenomena at the LHC and to identify their nature. Of particular interest in this context is Central Exclusive Production (CEP), $pp \to p \oplus \phi \oplus p$ (where $\oplus$ denotes a rapidity gap), which gives access to the generalized (or skewed) PDFs. At the highest available luminosities, CEP may become a discovery channel for particles with appropriate quantum numbers that couple to gluons. The CEP of a SM (or MSSM) Higgs boson is an attractive and at the same time a challenging process. It is attractive for two reasons: firstly, if the outgoing protons remain intact and scatter through small angles then, to a good approximation, the central system ϕ must be produced in a spin 0, CP even state, therefore allowing a clean determination of the quantum numbers of any observed resonance. Secondly, from precise measurements of proton momentum losses, ξ_1 and ξ_2, the mass of the central system can be measured much more precisely than from the dijet method, by the so-called missing mass method, $M^2 = \xi_1 \xi_2 s$, which is independent of the decay mode. The simplest decay mode from an experimental perspective is the WW decay mode, in which one (or both) of the W bosons decay leptonically. With standard single and double lepton trigger thresholds at ATLAS or CMS, approximately 6 events are expected for Higgs boson mass around 160 GeV with luminosity of 30 fb^{-1} [12]. In the $\mathrm{b\bar{b}}$ decay mode, the quantum number selection rules in CEP strongly suppress the QCD b-jet background, nevertheless severe requirements, necessary to get rid of the pile-up background, make the event yield rather modest. In certain regions of the MSSM parameter space the cross section for the CEP of the lightest Higgs boson is significantly enhanced and possibly making the $\mathrm{b\bar{b}}$ decay mode the discovery channel [13]. Another interesting feature coming from the MSSM studies is that the Higgs boson mass spectrum gets broader with increasing $\tan\beta$, which from a certain value of $\tan\beta$ may serve as a distinguishing criterion between the SM and MSSM signals [13].

Forward proton tagging at high luminosities will also give access to a rich QCD program. The proton structure can be investigated via the diffractive process $pp \to pX$ and $pp \to pXp$ where X includes a dijet system, vector bosons or heavy quarks. These reactions give access to the diffractive PDFs as well as to the so-called rapidity gap survival probability. The latter is closely linked to soft rescattering and the features of the underlying event at LHC.

As the LHC beams act also as a source of high-energy photons a rich program of photon-photon and photon-proton physics can be pursued. The LHC will open up a new kinematic regime for the photoproduction of jets, providing information on the low-x and low-Q^2 structure of the proton. Top-quark pairs will also be produced in this mode. In photon-photon collisions, one may expect lepton pairs (theoretically very well-known: this kind of process is a candidate for the luminosity measurement) as well as W-pairs.

3 Acceptance

In general, the position of a proton hit in detectors at 220 or 420 m depends (for a given beam optics) on the energy and the scattering angle of the outgoing proton and the z-vertex position of the collision. The energy and scattering angle are directly related to the kinematic variables ξ and $-t$. Fig.1 shows the acceptance in the (x, y) plane for the 220 m and 420 m detectors for beam 1 and beam 2, respectively, around IP1 (ATLAS). The scattered protons were tracked with

the MAD-X package [14] with LHC optics version 6.5. The distribution of diffractively scattered protons explains why only horizontal stations are needed for both, the FP420 and RP220 projects. The two projects however differ in where these stations are necessary to be put: as protons in the 220 m region are deflected away from the ring, they can be detected by pots approaching the beam from outside the ring. In contrast to that, protons in the 420 m region are deflected inward the ring and this poses greater demands on the engineering work related to the adaptation of the connection cryostat as described in Section 6.

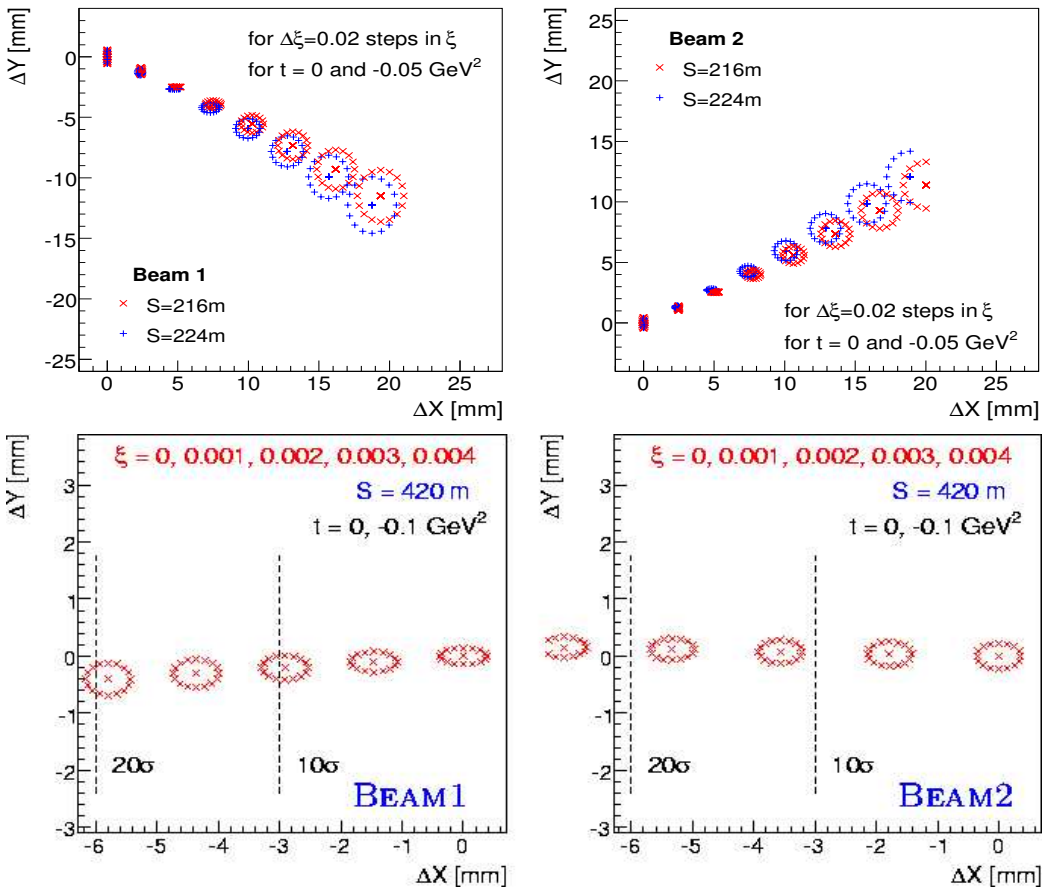


Fig. 1: The acceptance for diffractively scattered protons in the (x, y) plane determined by MAD-X at 220 m for beam 1 (upper left), beam 2 (upper right) and at 420 m for beam 1 (lower left) and beam 2 (lower right).

The low-ξ (and therefore low mass) acceptance depends critically on the distance of approach of the active area of the sensitive detectors from the beam. This is shown in Fig.2 on left hand plot. While the acceptance for the 420+420 configuration in the 120 GeV mass range is not too sensitive to the distance of approach (not shown), the acceptance of the 220+420 configuration is quite sensitive. This is because the 220 m detectors have acceptance only for relatively high ξ forcing the proton detected at 420 m to have lower ξ and therefore to be closer to the

beam. The final distance of approach will depend on the beam conditions, machine-induced backgrounds and collimator positions, and the RF impact of the detector on the beams. For FP420, the nominal operating position is assumed to be between 5 and 7.5 mm, depending on the beam conditions, for RP220, it is between 1.5 and 2 mm. For masses above about 120 GeV, the 220 m detector adds to the acceptance with power increasing as mass increases. While the difference between the IP1 and IP5 acceptances and beam 1 and 2, for the 420 detectors is negligible, the situation is more complicated at 220 m where the crossing angle is in the vertical plane for IP1 and the horizontal plane for IP5. This results in a significantly higher acceptance at IP1 (ATLAS) than IP5 (CMS) for 420+220 configuration, as shown in Fig.2 on right side [11].

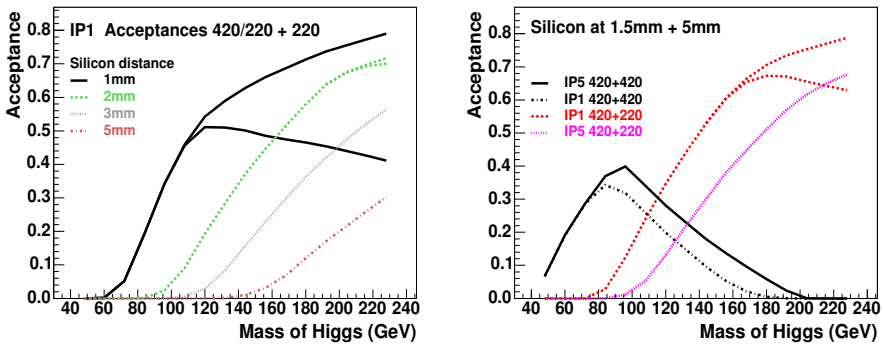


Fig. 2: Mass acceptance for various detector configurations. Left: 420+220 configuration for various combinations of distance of approach to the beam (with 5 mm as the nominal value for the 420 detector). Right: 420+420 and 420+220 configurations for one combination of the distance of approach to the beam (5 mm for 420 m and 1.5 mm for 220 m detectors) for IP1 and IP5. In the case of splitted curves, the lower one corresponds to the 420+220 configuration, while the higher one to the sum of acceptances for the 420+220 and 220+220 configurations.

4 Timing detectors

The necessity of equipping the forward detectors operating at the highest luminosities by timing detectors emerged from studies estimating the effect of pile-up background on diffractive processes at LHC [15]. At an instantaneous luminosity of $2 \times 10^{33}\mathrm{cm}^{-2}\mathrm{s}^{-1}$, the average number is 7 events per bunch crossing, at $1 \times 10^{34}\mathrm{cm}^{-2}\mathrm{s}^{-1}$, it is 35. Of these pile-up events, 3% (1%) contain a proton within the acceptance of forward detector at 220 m (420 m). If we consider e.g. the case of CEP of a Higgs boson with 120 GeV mass that decays into a pair of b-jets, an overlay of three events, namely two single diffractive ones each with a proton within the acceptance of forward detectors on opposite sides and one hard-scale dijet event, mimics the signal almost perfectly. Given the much larger cross section of inclusive dijet events compared to the signal, this is the most important source of background. This background can be reduced by exploiting the correlations between quantities measured in the central detector and those measured by the forward detectors. One possibility is to compare ξ or pseudorapidity, η, another possibility is to use fast timing detectors placed close to the forward detectors. Fast timing detectors with an

expected sub-10 ps time resolution corresponding to a vertex resolution of better than 2.1 mm should be able to assign a vertex to the proton detected in the forward detector and as preliminary studies indicate, to reject about 97% of cases that appear to be CEP events but where the protons in reality originated from coincidences with pile-up events. Currently the development of fast timing detectors proceeds on several fronts, the interest comes also from other fields of physics as well as from medical applications. Presently two detector options are studied, namely Quartz and Gas Cerenkov which may be read out with a Constant Fraction Discriminator which allows the time resolution to be significantly improved compared to usual electronics.

5 Trigger

The detectors at 420 m are too far away from the central detectors to be included in the L1 trigger in normal running conditions. The events with protons detected in the 420 m detectors can however be retained by other means. In the case of no pile-up, it is possible to lower the L1 trigger jet thresholds by a sufficient value to retain the Higgs boson events by vetoing on energy in the forward region at L1 [16]. Another way is to collect the events with protons tagged by a 420 m detector on one side and by a 220 m detector on the other side (this point is elaborated below). A further 10% of b-jet events can be saved irrespective of pile-up conditions by triggering on muons from B-hadron decays in the jets [15].

A big advantage of Roman Pots at 220 m is that they can be directly included in the L1 trigger. Various strategies to trigger on diffractive physics have been studied in [15]. As anticipated in Section 1 and 4, the big issue for any diffractive channel at high LHC luminosities is the fact that diffractive protons from pile-up events may fake the signal diffractive protons. For example, at the highest luminosity the rate of fake pile-up protons per bunch crossing seen in both Roman Pots at 220 m on CMS side is about 50%. The rates for the 420+420 and 420+220 configurations are 10% and about 60%, respectively [15]. The numbers for the ATLAS case are similar. These rates are of course enormous and need to be brought down to an acceptable L1 level. The trigger strategy depends on the mass of the diffractively produced object. Triggering on heavy mass objects (e.g. masses above 200 GeV) should not be a problem since the expected L1 rate of a two jet trigger with $E_T > 100$ GeV is about 6 kHz at the highest luminosity and it can be reduced to about 2 kHz if we require in addition the double proton tag at 220 m. Triggering on low mass objects is more difficult but in principle feasible as documented in the detailed study [17] where a diffractive L1 trigger for 120 GeV Higgs boson decaying in two b-jets has been proposed. The trigger consists of the following conditions:

- 2 jets with $E_T > 40$ GeV (an expected L1 trigger rate is 2.6 kHz and 260 kHz at $\mathcal{L} = 10^{32}\text{cm}^{-2}\text{s}^{-1}$ and $\mathcal{L} = 10^{34}\text{cm}^{-2}\text{s}^{-1}$, respectively).
- Requirement of exclusiveness, $(E_{T1} + E_{T2})/H_T > 0.9$, where H_T is the scalar sum of all L1 jet transverse momenta, reduces the rate by a factor of 2 independently of luminosity
- One proton detected in the detector at 220 m on at least one side from the IP.
- Momentum conservation along the beam axis, $(\eta_1 + \eta_2) \cdot \eta_{220} > 0$ where $\eta_{1,2}$ are pseudorapidities of two L1 jets and η_{220} is the pseudorapidity of the proton detected in the detector at 220 m, reduces the rate by a factor of 2
- Requirement of $\xi_{1(2)} < 0.05$ following from the missing mass formula.

The output rate of this trigger was estimated to be within 1 kHz up to luminosities of $\mathcal{L} = 2 \times 10^{33}\text{cm}^{-2}\text{s}^{-1}$ corresponding to 7 pile-up events per bunch crossing. Other reductions might be achieved from the knowledge of the precise Higgs boson mass after it has been measured and from a possible use of timing detectors at L1. The single-sided 220 m condition opens up space for the protons caught in detectors at 420 m thereby enabling to collect also asymmetric 220+420 and partly even 420+420 configurations. This enlarges the missing mass spectrum towards lower values. On top of that, a hit in 420 m detector may help to reduce the output rate of high level triggers - similarly to comparing pseudorapidities or masses of the central object calculated from the dijet system and from both protons seen in detectors on opposite sides from the IP.

A natural proposal for another diffractive L1 trigger would be based on a double-sided proton presence in 220 m detectors. This trigger would only enable us to retain events with higher mass objects (masses above roughly 160 GeV) by requiring in addition standard L1 triggers such as high mass Higgs boson decaying into WW or ZZ, inclusive high p_T dijets and inclusive high p_T jets (or low p_T jets highly prescaled).

6 FP420

The FP420 R&D collaboration, with members from ATLAS, CMS and LHC aims at installing high precision tracking and timing detectors close to the beam at 420 m from the IP. At LHC start-up, the beam pipes in the 420 m region are contained in a 15 m long interconnection cryostat that connects the superconducting arcs and dispersion suppressor regions of the LHC. The cryostat provides continuity not only of cold (2 K) beam pipes, but also of the insulation vacuum, electrical power, cryogenics circuits and thermal and radiation shielding. The engineering challenge of integrating detectors operated at room temperatures into the cryogenic section has been solved by replacing the existing interconnection cryostat with a warm beam-pipe section and a cryogenic bypass. A new connection cryostat with approximately 8 m of room temperature beam pipes has been designed using a modified Arc Termination Module (which includes cold to warm transitions for the beam-pipes) at each end. A solution has also been found for a mechanism which would bring the detectors close to the beam. It is a movable beam-pipe section to which the detector stations would be attached. Detection of the protons will be achieved by two 3D silicon detector stations at each end of the FP420 region. This novel technique uses electrodes processed inside the silicon bulk instead of being implanted on its surface which makes it very radiation-resistive and which may provide the insensitive area as small as 5 μm close to the beam. The current prototypes utilize radiation-hard ATLAS pixel readout chip and were tested in several beam tests. With a silicon detector electrode pitch of 50 μm a resolution in the two spatial dimensions of about 15 μm can be reached. Monte Carlo studies indicate that for CEP of a Higgs boson with mass between 120 and 200 GeV this translates into a mass resolution of around 1.5 GeV, when the two protons are detected at 420 m on opposite sides.

7 RP220

The RP220 project is aiming at installing Roman Pots at 216 and 224 m on both sides of the ATLAS detector. In a natural way, it follows up the ALFA project which is to measure the total cross section of proton-proton interaction, by concentrating on measurements of hard diffractive

physics accessible at high luminosities.

The Roman Pot design closely follows that used by the Totem collaboration and by the ALFA project in ATLAS. As discussed in Section 3, a sensitive detector of a 2×2 cm^2 size placed in a horizontal pot approaching the beam from outside should be sufficient to detect all diffractive protons.

There will be two kind of detectors to be put inside the pots, one for precise position measurements, the other one for precise time measurements. For both cases, the experience of FP420 with their development is closely followed. There are two options for the position detectors: either five layers of silicon strips of 50 μm and two additional layers for triggering purposes, or 3D silicon design as chosen for the FP420 project. In both cases, the precision of the position measurement is foreseen to be 10–15 μm which translates in a mass resolution of the order of 3% over a wide range of masses. The dead zone up to the active edge will be of the order of 50 μm for the strip detector, while it is of the order of 5 μm for the 3D option. Assuming a thin window of 200 μm and the distance of approach to the beam 10σ (15σ), the minimum value of ξ is about 0.01 for beam 1 and 0.012 for beam 2 (0.014 and 0.016), respectively. The detectors will be read out by standard ABCNext chip being developed for the silicon detectors in ATLAS. The latency time of this chip is of the order of 3.5 μs, time long enough to send back the local L1 decision from pots to ATLAS and to receive the L1 decision from ATLAS Central DAQ.

References

[1] ATLAS Collaboration (1999). CERN-LHCC-99-15.

[2] CMS Collaboration (2006). CERN-LHCC-2006-021.

[3] TOTEM Collaboration, V. Berardi *et al.* (2004). CERN-LHCC-2004-002.

[4] A. L. S. Angelis *et al.*, Nuovo Cim. **24C**, 755 (2001).

[5] ATLAS Collaboration (2004). CERN-LHCC-2004-010.

[6] CMS Collaboration, O. A. Grachov *et al.*, AIP Conf. Proc. **867**, 258 (2006). nucl-ex/0608052.

[7] ATLAS Collaboration (2007). CERN-LHCC-2007-001.

[8] LHCf Collaboration (2006). CERN-LHCC-2006-004.

[9] RP220 Collaboration (2007). Http://cern.ch/project-rp220.

[10] ATLAS Collaboration (2007). ATLAS Forward Detectors for Measurement of Elastic Scattering and Luminosity Determination, in preparation.

[11] FP420 Collaboration (2007). FP420 TDR, in preparation.

[12] B. E. Cox *et al.*, Eur. Phys. J. **C45**, 401 (2006). hep-ph/0505240.

[13] S. Heinemeyer *et al.* (2007). arXiv:0708.3052 [hep-ph].

[14] F. C. Iselin *et al.* (2000). CERN-SL-2000-026 AP.

[15] M. Albrow *et al.* (2006). CERN-LHCC-2006-039.

[16] S. Alekhin *et al.* (2005). hep-ph/0601013.

[17] M. Grothe *et al.* (2006). CERN-CMS-NOTE-2006-054.

Total Cross-Section Measurement and Diffractive Physics with TOTEM

M. Deile on behalf of the TOTEM Collaboration
CERN, Genève, Switzerland

Abstract

The TOTEM Experiment will measure the total pp cross-section and study elastic and diffractive scattering at the LHC. For the initial LHC running period, TOTEM has requested a beam optics with $\beta^* = 90\,\mathrm{m}$ which fits well into the standard LHC start-up scenario and whose commissioning is expected to be less complex than the one of TOTEM's baseline optics with $\beta^* = 1540\,\mathrm{m}$. The early running conditions will allow a measurement of the total pp cross-section and – independently – of the luminosity at the 5% level. In addition, the cross-sections and topologies of soft diffractive events can be studied. At a later stage, the precision of the total and elastic cross-section measurements will be improved to the 1% level by using the final TOTEM optics, and the diffraction studies will be extended by collaborating with CMS.

1 Introduction

The TOTEM apparatus [1] with its unique coverage of high rapidities ($3.1 \leq |\eta| \leq 6.5$) and with its unprecedented acceptance for surviving protons is the ideal tool for studying forward phenomena, including elastic and diffractive scattering. Since the particle multiplicity of inelastic events (both non-diffractive and diffractive) peaks in the forward region (Figure 1), TOTEM accepts about 95 % of all inelastic events in its trigger. This is crucial for achieving TOTEM's main objective for the first years of LHC operation, the luminosity-independent measurement of the total cross-section based on the Optical Theorem.

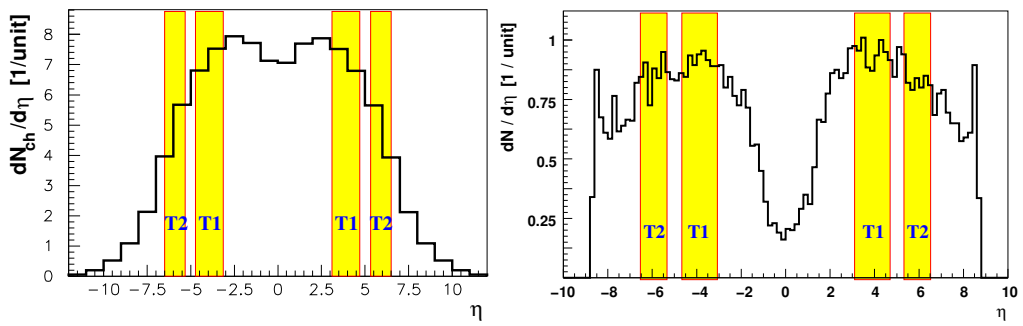


Fig. 1: Pseudorapidity distributions of the charged particle multiplicity for non-diffractive (left) and single diffractive, SD, (right) inelastic collisions at 14 TeV.

2 Measurement of the Total pp Cross-Section

2.1 Motivation and Technique

A precise measurement of the total pp cross-section σ_{tot} and of the elastic scattering over a large t-range is of primary importance for distinguishing between different models of soft proton interactions.

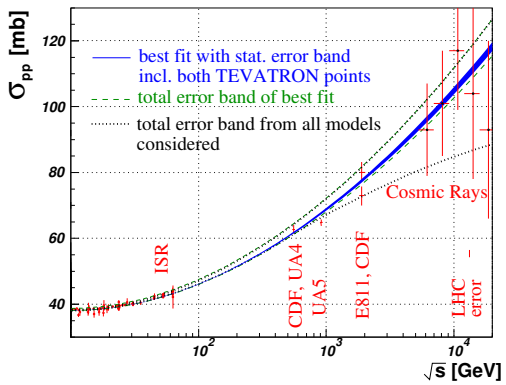


Fig. 2: COMPETE fits [2] to all available pp and $p\bar{p}$ scattering data with statistical (blue solid) and total (green dashed) error bands, the latter taking into account the Tevatron ambiguity. The outermost curves (dotted) give the total error band from all parameterisations considered.

Figure 2 summarises the existing measurements of σ_{tot} from low energies up to collider and cosmic-ray energies. Taking into account all available data, the COMPETE collaboration [2] has performed fits of the energy dependence of the total cross-section and the ratio ρ of the real to imaginary parts of the elastic scattering amplitude, based on different models. The model leading to the best fit predicts for the LHC at $\sqrt{s} = 14\,\mathrm{TeV}$:

$$\sigma_{tot} = 111.5 \pm 1.2^{+4.1}_{-2.1}\,\mathrm{mb}\,, \quad \rho = 0.1361 \pm 0.0015^{+0.0058}_{-0.0025}\,, \tag{1}$$

where the second error is due to the 2.6 standard-deviations discrepancy between the two final results from TEVATRON [3,4]. The cosmic-ray data with their large uncertainties do not provide strong constraints on the model choice. Inclusion of the full set of COMPETE's models leaves a wide range for the expected value of σ_{tot} at 14 TeV, typically from 90 to 130 mb.

The total **pp** cross-section is related to nuclear elastic forward scattering via the two relations

$$\mathcal{L}\,\sigma_{tot}^2 = \frac{16\pi}{1+\rho^2}\cdot\left.\frac{dN_{el}}{dt}\right|_{t=0} \quad \text{and} \quad \mathcal{L}\,\sigma_{tot} = N_{el} + N_{inel}\,, \tag{2}$$

the first of which is known as the Optical Theorem. This equation system can be resolved for σ_{tot} or $\mathcal{L}$ independently of each other:

$$\sigma_{tot} = \frac{16\pi}{1+\rho^2}\cdot\frac{dN_{el}/dt|_{t=0}}{N_{el}+N_{inel}}\,, \tag{3}$$

$$\mathcal{L} = \frac{1+\rho^2}{16\pi}\cdot\frac{(N_{el}+N_{inel})^2}{dN_{el}/dt|_{t=0}}\,. \tag{4}$$

Hence the quantities to be measured are the following:

- $dN_{el}/dt|_{t=0}$: The nuclear part of the elastic cross-section extrapolated to $t = 0$ (see Section 2.3). The expected uncertainty of the extrapolation depends on the acceptance for elastically scattered protons and hence on the beam optics.
- The total nuclear elastic rate N_{el} measured by the Roman Pot system and completed by the extrapolation of the nuclear part dN_{el}^{nuc}/dt to $t = 0$.
- The inelastic rate N_{inel} consisting of diffractive ($\sim$18 mb at LHC) and minimum bias ($\sim$65 mb at LHC) events. It will be measured by the tracking stations T1 and T2.

For the rate measurements it is important that all TOTEM detector systems have level-1 trigger capability. The parameter $\rho = \frac{\mathcal{R}[f_{el}(0)]}{\mathcal{I}[f_{el}(0)]}$, where $f_{el}(0)$ is the forward nuclear elastic amplitude, has to be taken from external theoretical predictions, e.g. [2]. Since $\rho \sim 0.14$ enters only in a $1+\rho^2$ term, its impact is small. At a later stage of TOTEM operation, a measurement of ρ via the interference between Coulomb and nuclear contributions to the elastic scattering cross-section might be attempted at a reduced centre-of-mass energy of about 8 TeV [5].

2.2 Inelastic Rate

The measurement of the inelastic rate is based on inclusive triggers with the forward trackers T1 and T2 and the Roman Pots. To maximise the event detection efficiency on one hand and to optimise the separation of physics signals from machine background on the other hand, an interplay of various trigger strategies will be adopted:

- The inelastic single-arm trigger (requiring activity in T1 or T2 on one side of the IP) has the best efficiency, missing only events with very low diffractive masses (< 10 GeV for SD). However, it suffers from beam-gas background.
- The inelastic double-arm trigger (requiring activity in T1 or T2 on both sides of the IP) suppresses beam-gas background by its coincidence requirement. However, it cannot be used for single diffraction and suffers from reduced efficiency in low-mass double diffraction.
- The purity of the inelastic triggers can be enhanced by reconstructing the interaction vertex from the tracks in T1 or T2.
- Triggering on "non-colliding bunch crossings", where the bunch position in one beam is empty, gives access to a direct measurement of the beam-gas background rate which can then be statistically subtracted from the data obtained with normal triggers.
- Single Diffractive and Double Pomeron Exchange events can be tagged by supplementing the inelastic trigger with a proton trigger on one or both sides of the Roman Pot spectrometer. However, proton inefficiencies in a small kinematic region with low values of $|t|$ have to be extrapolated in this trigger scheme.
- The rates of low-mass single or double diffractive events which are missed in all trigger schemes can be statistically recovered by extrapolating the measured cross-section under theoretical assumptions on $\frac{d\sigma}{dM^2}$. However, one has to keep in mind that low-mass resonances typically escape such extrapolations.

The result of the trigger loss estimate (see [1,5]) is 0.8 mb or 1% of the predicted inelastic cross-section of 80 mb.

2.3 Elastic Scattering

The determination of total cross-section and luminosity according to Eqns. (3) and (4) requires two aspects of elastic scattering to be measured: the total elastic rate and the extrapolation of the differential cross-section $d\sigma/dt$ to the Optical point $t = 0$. Obviously, to be complete, the measured elastic rate has to be complemented by the extrapolated part, so that this extrapolation enters twice in the procedure.

With the $\beta^* = 90$ m optics [5], protons with $|t| > 0.03\,\mathrm{GeV}^2$ are observed in the RP detector at 220 m. This acceptance starting point lies well above the region where the delicate effects from the interference between nuclear and Coulomb scattering play a role. Hence no such perturbation needs to be included in the extrapolation procedure, in contrast to the final $\beta^* = 1540$ m optics with $|t|_{min} = 10^{-3}\,\mathrm{GeV}^2$.

Most theoretical models [6] predict an almost exponential behaviour of the cross-section up to $|t| \approx 0.25\ \mathrm{GeV}^2$, as shown in Figure 3. The deviations from a purely exponential shape are quantified by the exponential slope $B(t) = \frac{d}{dt} \ln \frac{d\sigma}{dt}$ in Figure 3 (right). For all the models considered – except for the one by Islam et al. – the deviations are small. In the t-range mentioned, the slope $B(t)$ can be well described by a parabola which is therefore used for the fitting function and the extrapolation. Since this quadratic behaviour of the slope characterises all the models, the extrapolation method is valid in a model-independent way.

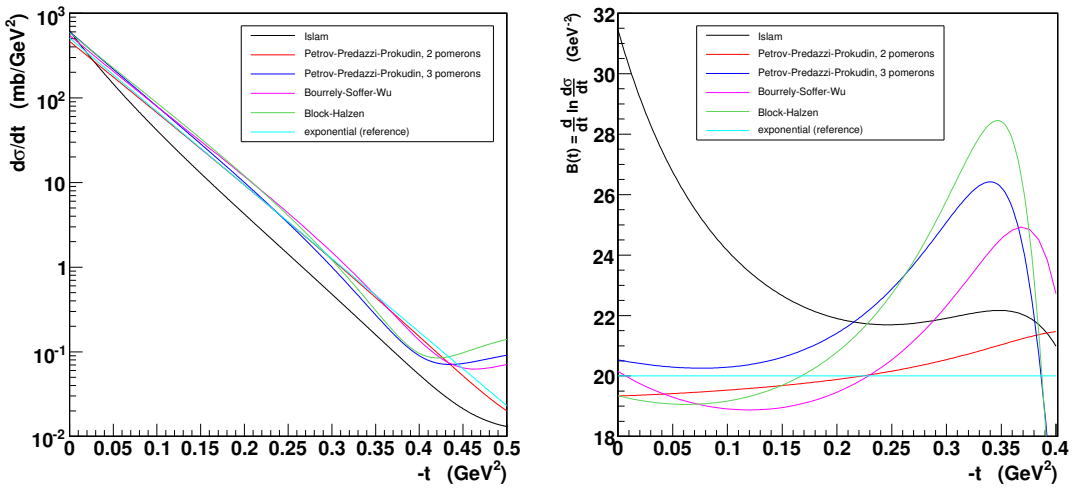


Fig. 3: Left: Differential cross-section of elastic scattering at 14 TeV as predicted by various models. Right: Exponential slope of the differential cross-section.

With the $\beta^* = 90$ m optics – on which we will focus in all the following considerations – the effective length $L_x(220\,\mathrm{m})$ at the Roman Pot at 220m is 0. Hence in this station only the y-component of the scattering angle is measured and only the $t_y \equiv t\,\sin^2\varphi \approx (p\,\Theta_y^*)^2$ component reconstructed. Using the azimuthal symmetry of the elastic scattering process and hence the equality of the distributions of t_y and t_x, the distribution $\mathrm{d}\sigma/\mathrm{d}t$ can be calculated from $\mathrm{d}\sigma/\mathrm{d}t_y$ distribution.

The accuracy of the simulated extrapolation is shown in Figure 4. The key contributions

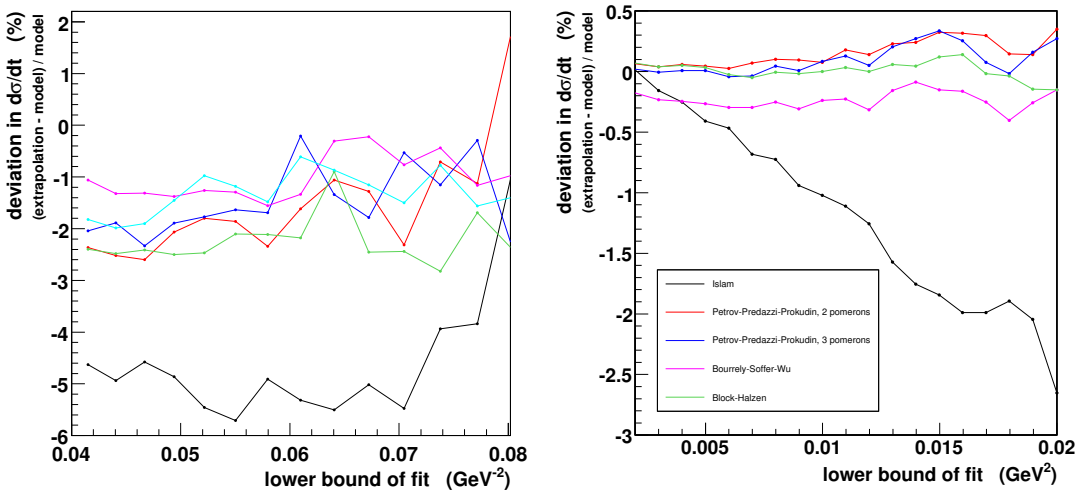


Fig. 4: Extrapolation results based on a MC simulation (not including the L_{eff} error). Left: $\beta^* = 90\,\mathrm{m}$, right: $\beta^* = 1540\,\mathrm{m}$ for comparison. The t_y- (t-) distributions were fitted from the indicated lower bound to $0.25\,\mathrm{GeV}^2$ ($0.025\,\mathrm{GeV}^2$) respectively.

are the following:

- Smearing effects of the t-measurement which are dominated by the beam divergence ($\sigma_{beam} = 2.3\ \mu\mathrm{rad}$). Based on our preliminary MC simulations this contribution leads to a shift of $-2\,\%$ in the extrapolation result (Figure 4 left).
- The statistical error of the extrapolation for an integrated luminosity of $2\,\mathrm{nb}^{-1}$ corresponding to 2×10^4 s (about 5 hours) of running at a luminosity of $10^{29}\ \mathrm{cm}^{-2}\,\mathrm{s}^{-1}$.
- Systematic uncertainty of the t-measurement: the dominant contribution comes from the uncertainty of the effective length L_{eff}. The expected precision of $2\,\%$ would lead to an extrapolation offset of about $3\,\%$.
  Due to the thick beam at $\beta^* = 90\,\mathrm{m}$ ($\sigma_{y_{beam}} = 625\,\mu\mathrm{m}$ at RP220) compared to $\beta^* = 1540\,\mathrm{m}$ ($\sigma_{y_{beam}} = 80\,\mu\mathrm{m}$), detector or beam position inaccuracies have a much smaller impact on the t measurement.
- Model-dependent deviations of the nuclear elastic pp cross-section from an exponential shape lead to a bias in the extrapolation (left-hand plot in Figure 4). Besides the Islam model which can be excluded or confirmed by the measured t-distribution at large t-values, the models stay within $\pm 1\,\%$.

2.4 Combined Measurement Uncertainty

For the early TOTEM optics with $\beta^* = 90\,\mathrm{m}$, the total uncertainty of σ_{tot} in Eqn. (3) has the following contributions:

- Inelastic rate: $\frac{\delta(N_{inel})}{N_{inel}} \approx 1\,\%$. This contribution is almost independent from the beam optics, exceptions being SD and DPE where for some trigger strategies leading protons are parts of the signature.
- Extrapolation of the elastic cross-section: For the early TOTEM optics with $\beta^* = 90\,\mathrm{m}$, $\frac{\delta(dN_{el}/dt|_{t=0})}{dN_{el}/dt|_{t=0}} \leq 4\,\%$.

- Elastic rate: For $\beta^* = 90\,\mathrm{m}$, $\frac{\delta(N_{el})}{N_{el}} \leq 2\,\%$. The high correlation between N_{el} and $\frac{\delta(dN_{el}/dt|_{t=0})}{dN_{el}/dt|_{t=0}}$ leads to a partial cancellation of errors, which is taken into account in the error combination below.
- The ρ parameter, estimated to be about 0.14 by extrapolating measurements at lower energies [2], enters σ_{tot} in the factor $\frac{1}{1+\rho^2} \sim 0.98$, and hence gives only a relative contribution of about 2 %. Assuming a relative uncertainty of 33 % on ρ, determined by the error of the measurements at TEVATRON [4] and extrapolation to LHC energies, we expect an uncertainty contribution of $\frac{\delta(1+\rho^2)}{1+\rho^2} = ^{+1.4\,\%}_{-1.2\,\%}$.

Combination of all these uncertainties by error propagation taking into account the correlations yields a relative error of 4 % in σ_{tot}. The uncertainty of the luminosity calculated from Eqn. (4) is slightly worse (7%) because the total rate enters squared.

At a later stage, the final baseline optics with $\beta^* = 1540\,\mathrm{m}$ will allow a precision improvement to the 1% level. However, to achieve this ambitious goal, an improved knowledge of the optical functions and a RP alignment precision better than 50 μm will be needed.

3 Soft Diffraction

Fig. 5 (left) shows the (t, ξ) acceptances integrated over φ for the special TOTEM optics ($\beta^* =$ 90 m and 1540 m) and for the low-β^* optics (2 m is shown, 0.5 m and 11 m are similar). While for $\beta^* = 0.5\,\mathrm{m}$ only protons with $\xi > 2\,\%$ – corresponding to rather high diffractive masses – are observed, the TOTEM optics give access to all ξ-values down to 10^{-8}, except for very low $|t|$-values. Consequently, a large fraction of the diffractive protons is observed: 65 % for $\beta^* =$90 m and 95 % for 1540 m, allowing first measurements of SD and DPE at LHC. Due to the vanishing effective length L_x at RP220 for the $\beta^* =$90 m optics, the dependence of the x-position on the emission angle Θ_x^* is eliminated, which leads to a ξ-resolution of 6×10^{-3}, mainly due to the vertex uncertainty. For $\xi < 6 \times 10^{-3}$ where $\sigma(\xi)/\xi > 100\%$, events will rather be reconstructed via their rapidity gap (Fig. 5, right). In the regions $0.0017 < \xi < 0.045$ and $1 \times 10^{-7} < \xi < 3 \times 10^{-6}$, the gap edge lies within the acceptance of one arm of T1 or T2, resulting in a resolution of $\sigma_{\Delta\eta}(\xi)/\xi = 0.8 \div 1$. At a later stage, joint data taking together with CMS [7] will benefit from a complete rapidity gap acceptance in the range $3.1 < \Delta\eta < 16.1$. Furthermore, vertex reconstruction by CMS with an accuracy of 30 μm will improve the ξ-resolution to 1.6×10^{-3}.

References

[1] TOTEM: Technical Design Report, CERN-LHCC-2004-002; addendum CERN-LHCC-2004-020.

[2] J.R. Cudell et al.; Benchmarks for the Forward Observables at RHIC, the Tevatron-Run II, and the LHC; PRL **89**, (2002) 201801.

[3] CDF Collaboration (F. Abe et al.), Phys. Rev. **D 50**, (1994) 5550.

[4] E710 Collaboration (N.A. Amos et al.), PRL **63**, (1989) 2784; Phys. Lett. **B 243**, (1990) 158.
E811 Collaboration (C. Avila et al.), Phys. Lett. **B 445**, (1999) 419; Phys. Lett. **B 537**, (2002) 41.

[5] TOTEM collaboration: TOTEM Physics, Proceedings of 17th Rencontre de Blois: 11th International Conference on Elastic and Diffractive Scattering. Château de Blois, France, 2005. arXiv: hep-ex/0602025.

[6] M. M. Islam, R. J. Luddy and A. V. Prokudin: Near forward pp elastic scattering at LHC and nucleon structure, Int. J. Mod. Phys. A21 (2006) pp. 1–42.

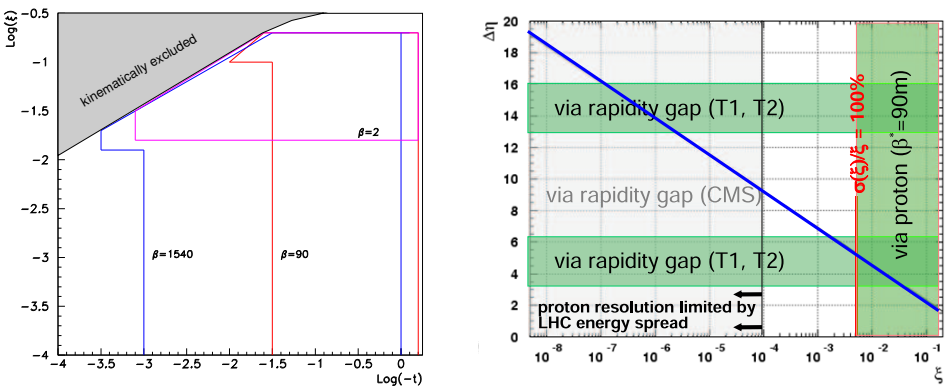


Fig. 5: Left: Acceptance in $\log_{10} t$ and $\log_{10} \xi$ for diffractive protons at RP220 for different optics. The contour lines represent the 10 % level. Right: Rapidity gap as a function of ξ (diagonal line). In the shaded regions TOTEM can reconstruct events via protons (vertical band) or via the rapidity gap in T1 or T2 (horizontal bands).

Claude Bourrely, Jacques Soffer, and Tai Tsun Wu: Impact-picture phenomenology for pi+- p, K+- p and p p, anti-p p elastic scattering at high energies, Eur. Phys. J. C28 (2003), pp. 97–105.
V. A. Petrov, E. Predazzi and A. Prokudin: Coulomb interference in high-energy p p and anti-p p scattering, Eur. Phys. J. C28 (2003) pp. 525–533.
M. M. Block, E. M. Gregores, F. Halzen and G. Pancheri: Photon proton and photon photon scattering from nucleon nucleon forward amplitudes, Phys. Rev. D60 (1999) 054024.

[7] The CMS and TOTEM diffractive and forward working group: Prospects for Diffractive and Forward Physics at the LHC, CERN/LHCC 2006-039/G-124, 2006.

Prospects of Forward Energy Flow and Low-x Physics at the LHC

Andrew Hamilton
Départment de physique nucléaire et corpusculaire (DPNC), Université de Genève
e-mail: Andrew.Hamilton@cern.ch

Abstract
The LHC will soon provide proton-proton collisions at the unprecedented center of mass energy, $\sqrt{s}$ =14 TeV. This not only allows us to probe new regions of high-p_T physics, but also low-x and forward physics. A selection of potential measurements are described to outline the prospects for low-x and forward physics in the ATLAS, CMS, TOTEM, and LHCf experiments.

1 Introduction

In pp collisions, forward scatterings occur when $x_1 \ll x_2$, where x_i is the fraction of the proton's total momentum carried by parton i (the Bjorken-x). Since one of the partons in a forward collision must have a low-x, there is an inherent connection between forward energy flow and low-x physics. After a discussion on the current status of the forward detectors in the ATLAS, CMS, TOTEM, and LHCf experiments, some examples of the forward energy flow and low-x physics potential of these experiments are given.

The gluon density of the parton distribution functions (PDF) of the proton were discovered to grow as $xG(x,Q^2) \propto x^{-\lambda(Q^2)}$, where $\lambda \simeq 0.1 - 0.3$ rises logarithmically with Q^2, in deep-inelastic scattering (DIS) ep collisions at HERA [1]. The 'saturation' region, where the non-linear effects of gluon-gluon fusion due to high gluon density become important, is expected to be accessible at the LHC. Figure 1 shows the coverage of the LHC in x and Q^2 [2], as well as a schematic representation of BFLK [3–5] evolution into the saturation region [6].

Forward physics is also very interesting for the measurement of the high energy ($10^{16} - 10^{20}$ eV) cosmic ray energy and composition spectrum. Above $E_{lab} \sim 10^{14}$ eV only indirect measurements of extensive air showers are possible. These indirect measurements depend on simulations of the air shower high in the atmosphere. Since there is no accelerator data above Tevatron ($\sim 10^{15}$ eV), the simulations have to extrapolate over several orders of magnitude to reach the highest energy cosmic rays at $\sim 10^{20}$ eV. The dominant contribution to the uncertainty of these models is the soft QCD forward energy flow, which can be studied at the LHC.

2 LHC Forward Detectors

The Large Hadron Collider (LHC) will provide pp collisions with $\sqrt{s} = 14$ TeV to four interaction points (IP) instrumented with detectors. This is a summary of the forward detectors instrumented at IP1 and IP5. The ATLAS and LHCf experiments are located at IP1, the CMS and TOTEM experiments are located at IP5. The ALICE and LHCb experiments will not be discussed here.

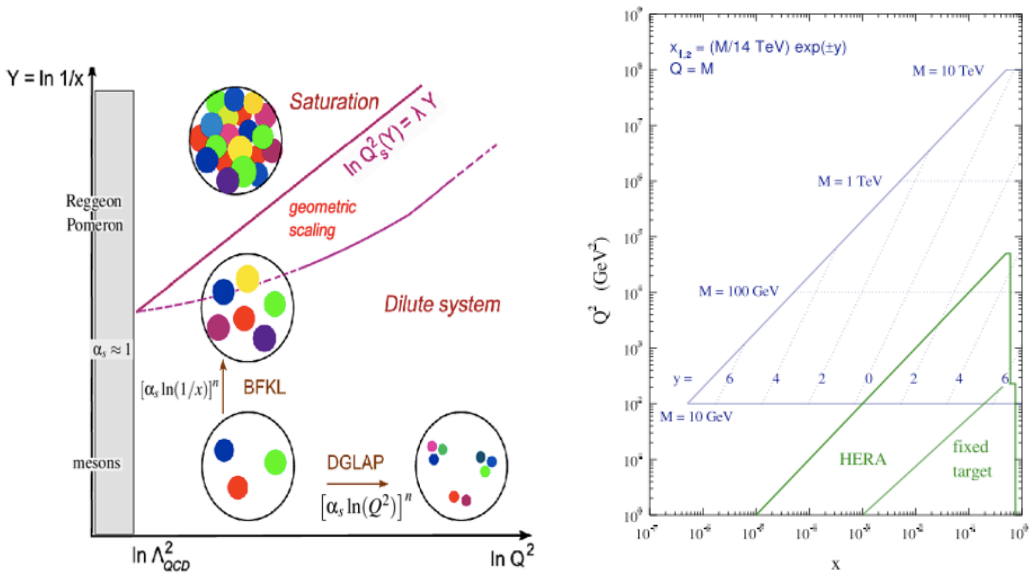


Fig. 1: Schematic of saturation region (left), LHC coverage in x vs Q^2 compared to HERA and fixed target experiments (right).

The ATLAS detector [7] is the general purpose detector at IP1. The ATLAS forward detectors include LUCID, ALFA, and ATLAS-ZDC. The LUCID and ALFA detector's [8] primary objective is luminosity measurement, but they will also be useful for forward physics studies. The LUCID (*LUminosity measurement using Cerenkov Integrating Detector*) detector is located at ± 17 m from the ATLAS IP ($5.4 < |\eta| < 6.1$) and consists of aluminium tubes filled with C_4F_{10} gas surrounding the beam-pipe and pointing towards the ATLAS IP. The Cerenkov light emitted by a traversing particle from the ATLAS IP is reflected down the tube and read out by photo-multipliers. Particles not coming from the ATLAS IP will not traverse an entire tube and thus leave a much smaller signal, thereby reducing backgrounds. The LUCID detector is also expected to be of use in diffractive physics studies (using rapidity gap signatures) and forward multiplicity studies.

The ALFA (*Absolute Luminosity For ATLAS*) detectors are scintillating fibre trackers located inside Roman Pots at ± 240 m from the ATLAS IP. The main purpose of ALFA is to measure elastic proton scattering at low angles to determine absolute luminosity in ATLAS. To achieve an optimal precision in the luminosity measurement, the LHC will have dedicated runs with the so-called high-β^* optics. This will provide the absolute calibration of the luminosity for the LUCID detector. Potential for other physics using ALFA, such as, measuring the total pp cross-section, measuring elastic scattering parameters, and using the tagged protons for diffractive studies are also being explored.

The ATLAS-ZDC (*Zero Degree Calorimeter*) [9] is a tungsten/quartz calorimeter located between the two LHC beam-pipes at ± 140 m from the ATLAS IP. By measuring neutral particles at a 0° polar angle it will have a central role in the ATLAS heavy-ion physics program, where it

will be used to measure the centrality of the collisions, the luminosity, as well as be used in some physics triggers. In the pp physics program, it will be used to study forward particle production and energy flow.

The other experiment at IP1 is LHCf [10]. The primary objective of the LHCf collaboration is to measure the forward production spectra of photons and π°'s in high-energy pp collisions to constrain the models of high energy cosmic ray air shower development. The LHCf detectors are tungsten/scintillator calorimeters with silicon microstrip and scintillating fibre trackers located at ± 140 m from the interaction point.

The CMS [11] experiment is the general purpose detector at IP5. The TOTEM [12] experiment shares IP5 with CMS. The CMS forward detectors include HF, CASTOR, and CMS-ZDC, while the TOTEM detectors, T1/T2 and RP, are all in the forward region. While TOTEM and CMS are independent collaborations, the experiments will have integrated read-out, allowing TOTEM to benefit from the CMS central coverage, and CMS to benefit from the TOTEM forward coverage.

The CMS HF is a steel/quartz calorimeter located 11 m from the CMS IP ($3 < |\eta| < 5$). The primary motivation for the HF is forward jet tagging for the vector-boson-fusion Higgs production channel, but it will play an important role in low-x and forward physics as well. CASTOR is a tungsten/quartz calorimeter with electromagnetic ($5.3 < |\eta| < 6.5$) and hadronic ($5.2 < |\eta| < 6.4$) components located at ± 14 m from the CMS IP. The primary objective of the CASTOR calorimeter in pp collisions is the study of the proton PDFs at very low x ($\sim 10^{-6}$) using Drell-Yan measurements. The CMS-ZDC is a tungsten/quartz calorimeter at ± 140 m from the CMS IP. Like the ATLAS-ZDC, the CMS-ZDC's primary physics objective is to measure the centrality in heavy-ion collisions. In the pp program it can be used to study charge exchange events with a leading neutron as well as forward energy flow.

The primary objectives of the TOTEM experiment are to measure; the pp elastic cross section as a function of the square of the exchanged four-momentum (t), the pp total cross section with a precision of approximately 1%, and diffractive dissociation in pp collisions at $\sqrt{s} = 14$ TeV. The TOTEM experiment consists of 2 tracking telescopes T1 and T2, as well as Roman Pot (RP) stations. The T1 ($3.2 < |\eta| < 5$) and T2 ($5 < |\eta| < 6.6$) telescopes consist of cathode strip chambers and gas electron multiplier chambers, respectively. The TOTEM RP stations containing silicon strip detectors will be placed at a distance of ± 147 m and ± 220 m from IP5. The stations can measure protons with a momentum loss $\xi = \Delta p/p$ in the range $0.02 < \xi < 0.2$ for the nominal collision optics. For other optics with larger β^*, and hence lower luminosity, much smaller values of ξ can be reached.

The FP420 (*Forward Protons at 420m*) [13] research and development project is aiming to instrument both IP1 and IP5 with 3D silicon trackers and fast timing proton taggers to detect the leading proton from high mass exclusive diffractive pp interactions.

3 Physics Prospects

The high cross section of forward jet production makes it a favourable channel to study the low-x behaviour of the proton PDF at 14 TeV. Figure 2 (based on PYTHIA 6.403 [14]) shows that x as low as $10^{-4} - 10^{-5}$ will be accessible in the CMS HF. So far, measurements at the Tevatron

have probed the proton PDF down to $x \simeq 10^{-3}$. The CMS analysis of forward jets has two primary objectives; the single inclusive jet cross-section in HF with $E_T \simeq 20-100$ GeV, and the "Muller-Navelet" (MN) dijet cross-section with a jet in each of the $+\eta$ and $-\eta$ HF detectors [6].

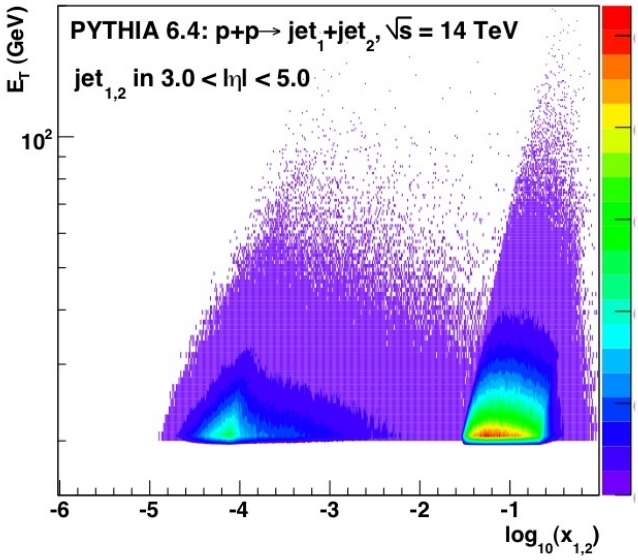


Fig. 2: Generator level $\log(x_{1,2})$ distribution accessible at CMS given that one of the partons falls within the HF acceptance ($3 < |\eta| < 5$ and $E_T > 20$ GeV).

The primary objective of the single inclusive jet cross-section measurement is to constrain the low-x proton PDF by including the data into the global PDF fits. This initial analysis considers only 1 pb^{-1} of low luminosity data, since pile-up (a potentially significant contribution to the systematic error) is negligible at low luminosity. Figure 3 shows that the statistics available in just 1 pb^{-1} are very large, but a full calculation of the systematic uncertainties (primarily from detector response, underlying event, hadronization, and luminosity) needs to be completed before a definitive statement on the possible constrains on the PDF are possible.

The MN dijet measurement is particularly sensitive to the BFKL [15] and small-x [16] evolution of the proton. The colliding partons in the MN kinematics are both large-x valence quarks ($x_{1,2} \approx 0.1$) which produce a large rapidity interval between the two jets. The large rapidity separation enhances the available phase space in longitudinal momentum for BFKL radiation. Recent work [16] indicates that the presence of low-x saturation effects will suppress the forward-backward MN dijet production cross section compared to the BFKL prediction, as seen in Figure 4. By using the $+\eta$ and $-\eta$ HF calorimeters, $\Delta\eta \sim 9$ (where the suppression is $\sim$2 at low Q) can be achieved in the CMS detector. A full study of the rate and jet reconstruction efficiency in the HF must be performed before a conclusion can be drawn regarding the feasibility of this measurement.

Another physics process that could provide information on saturation effects are forward Drell-Yan pairs [6]. With a large imbalance between the x of the q and $\bar{q}$, the Drell-Yan pair is

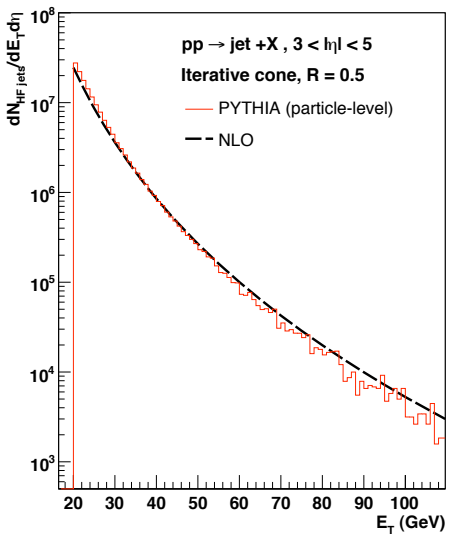


Fig. 3: Number of single inclusive jet events within the CMS HF acceptance expected in 1 pb^{-1} of data using particle-level jets (cone R=0.5) from PYTHIA 6.403 with no detector response, underlying event, or hadronization corrections applied.

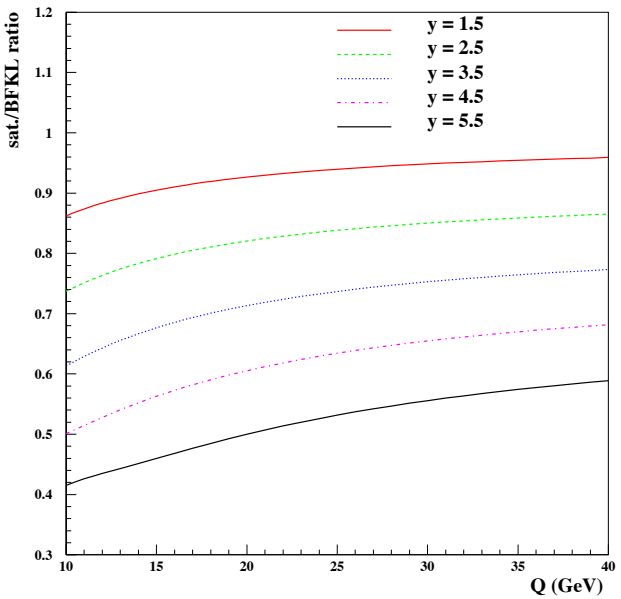


Fig. 4: Suppression of the MN forward dijet cross-section with low-x saturation compared to BFKL as a function of $Q \equiv Q_1 = Q_2$.

boosted to large rapidities, and the low-x q and $\bar{q}$ distributions become accessible. The effect of saturation on the cross section is shown in Figure 5, where a standard parameterisation of the parton density function (CTEQ 5M1) is compared to a saturated parameterisation (EHKQS) [17]. In the kinematic range accessible by the CMS CASTOR calorimeter, a 30% decrease in the cross section is observed. Again, more study is required to make a definitive statement on the feasibility of this measurement, but initial studies are very promising.

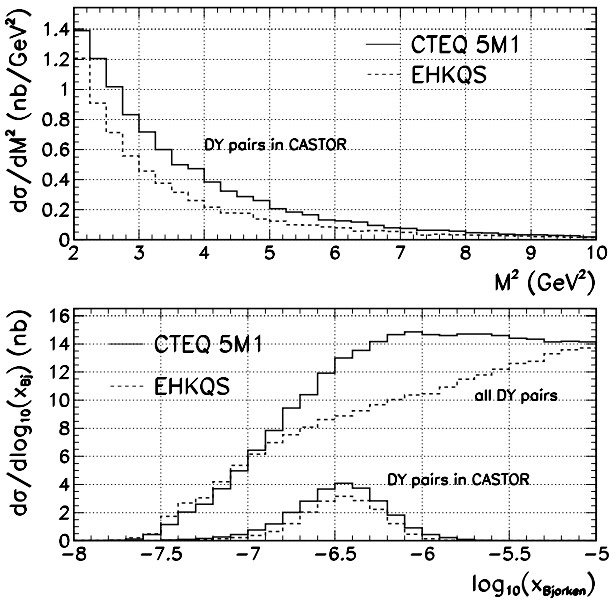


Fig. 5: Comparison Drell-Yan pairs of non-saturation (CTEQ) and saturation (EHKQS) models using the CMS CASTOR detector.

While the ATLAS and CMS ZDC's primary focus is in the heavy ion program, they have significant potential for measuring forward particle production in the pp program as well. The ability to tag a forward neutron allows for the possibility to look for processes like $p+\gamma \rightarrow W+n$, where the forward neutron is used to identify the charge exchange process. The potential for this process to be used to study trilinear gauge boson couplings has not yet been studied with detector acceptances and efficiencies, but theoretical work is underway [18]. Measuring very forward neutral scalar particle production is also possible with the ATLAS and CMS ZDC's. The reconstruction of $\pi^\circ \rightarrow \gamma\gamma$, $\eta \rightarrow \gamma\gamma$, and $\eta' \rightarrow \gamma\gamma$ is shown using the ATLAS ZDC in Figure 6.

The LHCf experiment will also reconstruct very forward $\pi^\circ \rightarrow \gamma\gamma$ events and measure their energy spectrum as well as providing information about forward energy flow for constraining high energy cosmic ray air shower simulations. The modeling of high energy cosmic ray air showers is important to help resolve the apparent conflict in the results of the HiRes [19] and AGASA [20] experiments regarding the GZK cutoff. The predictions of various models are shown in Figure 7 [6]. The LHCf experiment will measure the forward production spectra of π°'s and photon's to constrain these models to improve the shower simulation precision and help

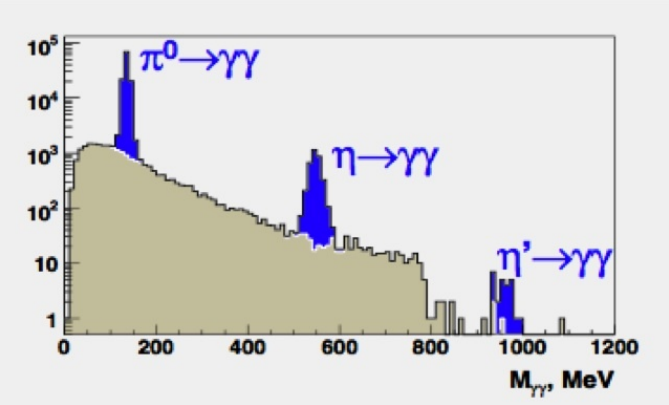


Fig. 6: Potential for forward neutral scalar boson reconstruction in the ATLAS ZDC.

resolve the GZK cutoff question.

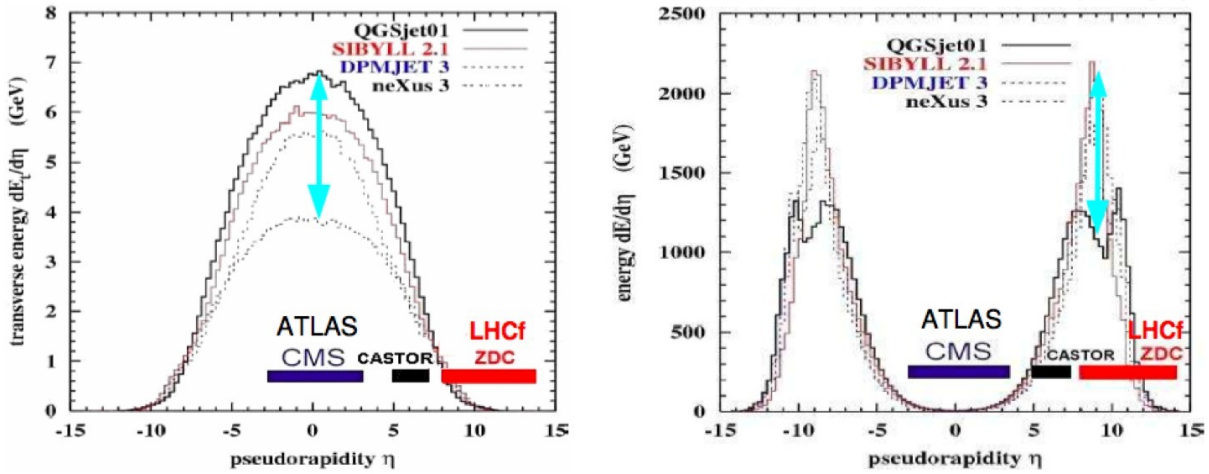


Fig. 7: Comparison of various high energy cosmic ray air shower simulations with an overlay of the acceptance of the ATLAS, CMS, and LHCf experiments.

Conclusions

The ATLAS, CMS, TOTEM, and LHCf experiments are well prepared to explore the low-x and forward energy flow physics that will become accessible in the $\sqrt{s}$=14 TeV pp collisions of the LHC. Using a variety of detector systems and event signatures, the experiments will cover a broad spectrum of exciting forward physics measurements.

Acknowledgments

This talk is on behalf of the ATLAS, CMS, TOTEM, and LHCf collaborations. I would firstly like to thank the members of all four collaborations for the huge effort putting these complex detectors together and developing their physics programs. Specifically, I would like to thank David d'Enterria, Pierre Van Mechelen, Oscar Adriani, James Pinfold, Stephan Ask, Monika Grothe, and Per Grafstrom for their contributions to these proceedings.

References

[1] H1 Collaboration, Phys. Lett **B520**, 183 (2001).

[2] J. Campell, J. Huston, and W. Stirling, Rept.Prog.Phys. **70**, 89 (2007).

[3] L. N. Lipatov, Sov. J. Nucl. Phys. **23**, 338 (1976).

[4] E. A. Kuraev, L. N. Lipatov, and V. S. Fadin, Sov. Phys. JETP **45**, 199 (1977).

[5] I. I. Balitsky and L. N. Lipatov, Sov. J. Nucl. Phys. **28**, 822 (1978).

[6] CMS Collaboration, CERN-LHCC-2006-039 (2006).

[7] ATLAS Collaboration, ATLAS TDR-15, CERN/LHCC/99-15 (1999).

[8] ATLAS Collaboration, CERN-LHCC/04-10, LHCC I-014 (2004).

[9] ATLAS Collaboration, CERN-LHCC/07-01, LHCC I-016 (2006).

[10] LHCf Collaboration, CERN-LHCC-2006-004, LHCF-TDR-001 (2006).

[11] CMS Collaboration, CERN-LHCC-2006-001, CMS-TDR-8.1 (2006).

[12] TOTEM Collaboration, CERN-LHCC-2004-002 , TOTEM-TDR-001 (2004).

[13] FP420 Collaboration, CERN-LHCC-2005-025, LHCC-I-015 (2005).

[14] T. Sjostrand, S. Mrenna, and P. Skands, JHEP **05**, 26 (2006).

[15] A. Mueller and H. Navelet, Nucl. Phys. **B282**, 727 (1987).

[16] C. Marquet and C. Royon, Nucl. Phys. **B739**, 131 (2006).

[17] A. Dainese *et al.*, hep-ph/0601012.

[18] U. Dreyer *et al.*, hep-ph/0702212.

[19] T. Abu-Zayyard *et al.*, astro-ph/0208243.

[20] M. Takeda *et al.*, Phys. Rev. Lett. **81**, 1163 (1988).

Diffractive physics in ALICE

Rainer Schicker, on behalf of the ALICE Collaboration
Phys. Inst., Philosophenweg 12, 69120 Heidelberg

Abstract

The ALICE detector presently being built at CERN consists of a central barrel covering the pseudorapidity range of $-0.9 < \eta < 0.9$ and a muon spectrometer in the pseudorapidity range $-4.0 < \eta < -2.5$. Additional detectors used for trigger purposes and for event classification cover adjacent pseudorapidity intervals of approximately 3 and 4 units on the two sides of the central barrel. Such a geometry is suited for defining a double gap trigger by requiring no activity in the event classification detectors. The centrally produced diffractive state is measured by the detectors in the ALICE central barrel. A few selected physics channels are discussed in order to illustrate the variety of physics topics which becomes accessible by implementing such a rapidity gap trigger.

1 The ALICE detector

The ALICE experiment at the LHC is designed as a general purpose experiment with a central barrel covering the pseudorapidity range $-0.9 < \eta < 0.9$ and a muon spectrometer covering the range $-4.0 < \eta < -2.5$ [1,2]. The ALICE experimental program foresees data taking in pp and PbPb collisions at luminosities of $\mathcal{L}$ = 5x10^{30}cm^{-2}s^{-1} and $\mathcal{L}$ = 10^{27}cm^{-2}s^{-1}, respectively. An asymmetric system pPb will be measured at a luminosity of $\mathcal{L}$ = 10^{29}cm^{-2}s^{-1}.

The central detectors track and identify particles from $\sim$ 100 MeVc^{-1} to $\sim$ 100 GeVc^{-1} transverse momenta. Short-lived particles such as hyperons, D and B mesons are identified by their reconstructed secondary decay vertex. The detector granularity is chosen such that these tasks can be performed in a high multiplicity environment of up to 8000 charged particles per unit of rapidity. Tracking of particles is achieved by the inner tracking system (ITS) of two layers of silicon pixel (SPD), two layers of silicon strip (SSD) and two layers of silicon drift detectors (SDD). The global reconstruction of particle momentum uses the ITS information together with the information from a large Time-Projection-Chamber (TPC) and a high granularity Transition-Radiation Detector (TRD). Particle identification in the central barrel is performed by measuring energy loss in the tracking detectors, transition radiation in the TRD and time-of-flight in a high-resolution TOF array. A single arm High-Momentum Particle Identification Detector (HMPID) with limited solid angle coverage extends the momentum range of identified hadrons. Photons will be measured by a crystal $PbWO_4$ PHOton Spectrometer (PHOS) and an electromagnetic sampling calorimeter (EMCAL).

Additional detectors for trigger purposes and for event classification are placed on both sides of the central barrel such that the pseudorapidity range $-3.7 < \eta < 5$ is covered. Fig. 1

shows the pseudorapidity acceptance of ALICE resulting from the ALICE detectors as explained above. The event characterization detectors shown in this figure are quartz scintillation detectors (T0A,T0C) used for timing, plastic scintillator detectors (V0A,V0C) and silicon detectors (FMD) for multiplicity characterization.

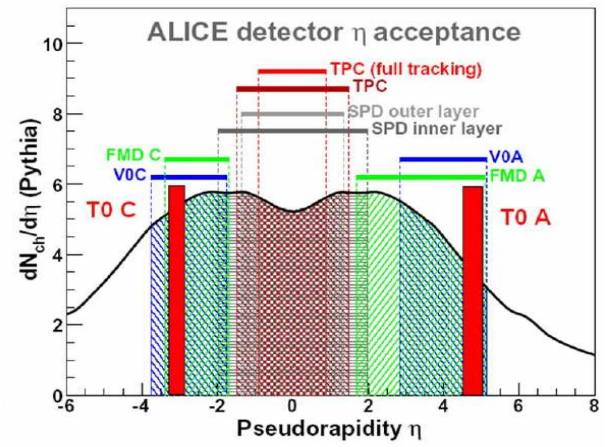


Fig. 1: Pseudorapidity coverage of the different detector systems of ALICE

1.1 The diffractive gap trigger in ALICE

The ALICE trigger is designed as a system with three levels L0,L1,L2 and a high-level software trigger (HLT). A diffractive L0 trigger can be defined by requiring little or no activity in the V0A and V0C detectors explained above. These two detectors are designed with an eight and four-fold segmentation in azimuth and pseudorapidity, respectively. The segmentation in pseudorapidity allows to select a gap width in steps of half a unit up to the maximum pseudorapidity interval of two covered by the detectors.

The high-level trigger has access to the information of all the detectors shown in Fig. 1 and hence can increase the rapidity gap to $-3.7 < \eta < -0.9$ and $0.9 < \eta < 5.0$, respectively.

Due to the absence of a V0A and V0C signal in a diffractive trigger, the L0 signal for this trigger has to be defined within the central barrel. In defining a L0 diffractive trigger, the transition radiation detector needs special consideration. This detector system is put in sleep mode after readout of an event in order to reduce power consumption. A wakeup signal is necessary to activate the onboard readout electronics. The V0A and V0C signals are transfered to the TRD pretrigger system where such a wakeup signal is generated.

A L0 diffractive trigger can, for example, be defined by the silicon pixel detector of the inner tracking system. This signal is, however, not in time for the wakeup call of the transition radiation detector. A TRD diffractive wakeup call can be defined by the information of the time-of-flight array. The information from this array is bundled into 576 segments covering the full central barrel. Each of these segments covers an area of approximately 30x50 cm^2 and delivers one bit per beam bunch crossing depending on whether a track has been seen within the segment. A logic trigger unit collects the 576 bits and can set multiplicity conditions and topological

constraints. In addition, the information of the V0A and V0C detectors is available at this level hence the required gap width can be defined. The output of this trigger unit is fast enough to reach the ALICE central trigger processor well before the time limit for L0 decision.

2 Signatures of the soft and hard Pomeron

The hadron-hadron cross section at high energies is increasing as function of energy. Regge inspired models parameterize such an energy dependence in the form

$\sigma = X_1 s^{\varepsilon_1} + Y_1 s^{\varepsilon_2}$

where the first term arises from soft Pomeron exchange and the second is associated with ρ, ω, f_2, a_2 exchange. Numerical fits to data yield $\varepsilon_1 \sim 0.08$ and $\varepsilon_2 \sim -0.5$ [3]. This parameterization correctly predicted the γp cross section which was subsequently measured at HERA. Extending the formalism to γ^*p collisions predicts the structure function $F_2(x, Q^2)$ at small x

$F_2(x, Q^2) \sim A_1(Q^2) x^{-\varepsilon_1} + A_2(Q^2) x^{-\varepsilon_2}$

It was found, however, that the fit to HERA data requires an additional term $A_0(Q^2) x^{\varepsilon_0}$ with $\varepsilon_0 \sim 0.4$ [4]. Such an additional term is called "hard-Pomeron" exchange.

The ALICE rapidity gap trigger is able to select diffractive events produced by double Pomeron fusion. Soft/hard Pomeron exchanges will be reflected in a soft/hard scale inherent in the system. In the absence of ALICE proton tagging and hence missing t-information, we represent the inherent scale by the transverse momentum p_T of secondaries. A soft/hard scale can be defined according to whether the p_T value is smaller or larger than some threshold value p_{thr}. The invariant mass differential cross section is thought to follow a power law

$\frac{d\sigma}{dM^2} \sim \frac{1}{M^\lambda}$

A representation of the exponent λ as function of the threshold value p_{thr}: $\lambda = \lambda(p_{thr})$ will reveal the contribution from soft/hard exchanges.

In addition, due to the variable gap width described above, all of this analysis can be carried out as function of rapidity gap width.

3 Signatures of the Odderon

The Odderon was first postulated in 1973 and is represented by color singlet exchange with negative C-parity [5]. Due to its negative C-parity, Odderon exchange can lead to differences between particle-particle and particle-antiparticle scattering. In QCD, the Odderon can be a three gluon object in a symmetric color state. Due to the third gluon involved in the exchange, a suppression by the coupling α_s is expected as compared to the two gluon Pomeron exchange. However, finding experimental signatures of the Odderon exchange has so far turned out to be extremely difficult [6]. A continued non-observation of Odderon signatures would put considerable doubt on the formulation of high energy scattering by gluon exchange [7]. The best evidence so far for Odderon exchange was established as a difference between the differential cross sections for elastic pp and $p\bar{p}$ scattering at $\sqrt{s}$ = 53 GeV at the CERN ISR. The pp cross section displays a dip at t = -1.3 GeV^2 whereas the $p\bar{p}$ cross section levels off. Such a behaviour is typical for negative C-exchange and cannot be due to mesonic Reggeons only.

Signatures of Odderon exchanges can be looked for in exclusive reactions where the Odderon (besides the Photon) is the only possible exchange. Diffractively produced C-even states such as pseudoscalar or tensor mesons can result from Photon-Photon, Photon-Odderon and Odderon-Odderon exchange. Any excess measured beyond the well understood Photon-Photon contribution would indicate an Odderon contribution.

Diffractively produced C-odd states such as vector mesons $\phi, J/\psi, \Upsilon$ can result from Photon-Pomeron or Odderon-Pomeron exchange. Any excess beyond the Photon contribution would be indication of Odderon exchange.

Estimates of cross section for diffractively produced J/ψ in pp collisions at LHC energies were first given by Schäfer et al [8]. More refined calculations by Bzdak et al result in a t-integrated photon contribution of $\frac{d\sigma}{dy} \mid_{y=0} \sim 15$ nb and a t-integrated Odderon contribution of $\frac{d\sigma}{dy} \mid_{y=0} \sim 1$ nb [9]. These two numbers carry large uncertainties, the upper and lower limit of these numbers vary by about an order of magnitude. This cross section is, however, at a level where in 10^6 s of ALICE data taking the J/ψ can be measured in its e^+e^- decay channel at a level of 4% statistical uncertainty. Due to the different t-dependence, the Photon and Odderon contribution result in different transverse momentum distribution p_T of the J/ψ. A careful transverse momentum analysis of the J/ψ might therefore allow to disentangle the Odderon contribution.

If the diffractively produced final state is not an eigenstate of C-parity, then interference effects between Photon-Pomeron and Photon-Odderon amplitudes can be analyzed [10]. Charge asymmetry in pion or kaon pairs is thought to be sizable [11, 12]. From the transverse momenta of the two particles in the pairs, the vectors of sum and difference can be calculated. The sum is C-even whereas the difference is C-odd. The opening angle α between sum and difference vector behaves as $\alpha \rightarrow \alpha + \pi$ under C-parity, hence a Fourier analysis of the α-distribution will allow to quantify the C-odd contribution.

4 Photoproduction of heavy quarks

Diffractive reactions involve scattering on small-x gluons in the proton. The number density of gluons at given x increases with Q^2, as described by the DGLAP evolution. Here, Q^2 and x denote the kinematical parameters used in deep inelastic ep scattering. The transverse gluon density at a given Q^2 increases with decreasing x as described by the BFKL evolution equation. At some density, gluons will overlap and hence reinteract. In this regime, the gluon density saturates and the linear DGLAP and BFKL equation reach their range of applicability. A saturation scale $Q_s(x)$ is defined which represents the breakdown of the linear regime. Nonlinear effects become visible for $Q < Q_s(x)$.

Diffractive heavy quark photoproduction represents an interesting probe to look for gluon saturation effects at LHC. The inclusive cross section for $Q\bar{Q}$ photoproduction can be calculated within the dipole formalism. In this approach, the photon fluctuates into a $Q\bar{Q}$ excitation which interacts with the proton as a color dipole. The dipole cross section $\sigma(x,r)$ depends on x as well as on the transverse distance r of the $Q\bar{Q}$ pair. A study of inclusive heavy quark photoproduction in pp collisions at LHC energy has been carried out [13]. These studies arrive at differential cross sections for open charm photoproduction of $\frac{d\sigma}{dy} \mid_{y=0} \sim 1.3$ μb within the collinear pQCD approach as compared to $\frac{d\sigma}{dy} \mid_{y=0} \sim 0.4$ μb within the color glass condensate (CGC). The

cross sections are such that open charm photoproduction seems measurable with good statistical significance. The corresponding numbers for the cross section for bottom photoproduction are $\frac{d\sigma}{dy}\mid_{y=0} \sim 20$ nb and 10 nb, respectively.

Diffractive photoproduction is characterized by two rapidity gaps in the final state. In the dipole formalism described above, the two gluons of the color dipole interaction are in color singlet state. Diffractive heavy quark photoproduction cross sections in pp, pPb and PbPb collisions at LHC have been studied [14]. The cross sections for diffractive charm photoproduction are $\frac{d\sigma}{dy}\mid_{y=0} \sim 6$ nb in pp, $\frac{d\sigma}{dy}\mid_{y=0} \sim 9$ μb in pPb and $\frac{d\sigma}{dy}\mid_{y=0} \sim 11$ mb in PbPb collisions. The corresponding numbers for diffractive bottom photoproduction are $\frac{d\sigma}{dy}\mid_{y=0} \sim 0.014$ nb in pp, $\frac{d\sigma}{dy}\mid_{y=0} \sim 0.016$ μb in pPb and $\frac{d\sigma}{dy}\mid_{y=0} \sim 0.02$ mb in PbPb collisions.

Heavy quarks with two rapidity gaps in the final state can, however, also be produced by central exclusive production, i.e. two Pomeron fusion. The two production mechanisms have a different t-dependence. A careful analysis of the transverse momentum p_T of the $Q\bar{Q}$ pair might therefore allow to disentangle the two contributions.

Acknowledgments

This work was supported in part by German BMBF under project 06HD197D.

References

[1] ALICE Collaboration et al 2004, J.Phys. G: Nucl. Part. Phys. 30 1517-1763

[2] ALICE Collaboration et al 2006, J.Phys. G: Nucl. Part. Phys. 32 1295-2040

[3] A.Donnachie, P.V.Landshoff, Phys.Letters B **296** (1992) 227

[4] P.V. Landshoff, Proceedings XVII Rencontres de Blois (2005) 97

[5] L.Lukaszuk, B.Nicolescu, Lett. Nuovo Cim. **8** (1973) 406

[6] C.Ewerz, Proceedings XVII Rencontres de Blois (2005) 377

[7] S.Donnachie, G.Dosch, P.V.Landshoff, O.Nachtmann, Pomeron physics and QCD, Cambridge University Press (2002) 297

[8] A.Schäfer, L.Mankiewicz, O.Nachtmann, Phys.Lett. B **272** (1991) 419

[9] A.Bzdak, L.Motyka, L.Szymanowski, J.R.Cudell, Phys.Rev. D **75** (2007) 094023

[10] S.J.Brodsky, J.Rathsman, C.Merino, Phys.Lett. B **461** (1999) 114

[11] P.Hägler, B.Pire, L.Szymanowski, O.V.Teryaev, Phys.Lett. B **535** (2002) 117

[12] I.F.Ginzburg, I.P.Ivanov, N.N.Nikolaev, Eur.Phys.J. C**5** (2003) 02

[13] V.P.Goncalves, M.V.Machado, Phys.Rev.D **71** (2005) 014025

[14] V.P.Goncalves, M.V.Machado, Phys.Rev.D **75** (2007) 031502

The Odderon at RHIC and LHC

Basarab Nicolescu[1†]
[1] Theory Group, Laboratoire de Physique Nucléaire et des Hautes Énergies (LPNHE), CNRS and Université Pierre et Marie Curie, Paris

To the memory of Leszek Lukaszuk (1938 - 2007)

Abstract
The Odderon remains an elusive object, 33 years after its invention. The Odderon is now a fundamental object in QCD and CGC and it has to be found experimentally if QCD and CGC are right. In the present talk, we show how to find it at RHIC and LHC. The most spectacular signature of the Odderon is the predicted difference between the differential cross-sections for proton-proton and antiproton-proton at high s and moderate t. This experiment can be done by using the STAR detector at RHIC and by combining these future data with the already present UA4/2 data. The Odderon could also be found by ATLAS experiment at LHC by performing a high-precision measurement of the real part of the hadron elastic scattering amplitude at small t.

1 Introduction

This contribution to EDS07 is based upon work done in collaboration with Regina F. Avila and Pierre Gauron [1].

The Odderon is defined as a singularity in the complex J-plane, located at $J = 1$ when $t = 0$ and which contributes to the odd-under-crossing amplitude F_-. The concept of Odderon first emerged in 1973 in the context of asymptotic theorems [2]. 7 years later, it was possibly connected with 3-gluon exchanges in perturbative QCD [3–5], but it took 27 years to firmly rediscover it in the context of pQCD [6]. The Odderon was also rediscovered recently in the Color Glass Condensate (CGC) approach [7, 8] and in the dipole picture [9]. One can therefore assert that the Odderon is a crucial test of QCD.

On experimental level, there is a strong evidence for the non-perturbative Odderon: the discovery, in 1985, of a difference between $(d\sigma/dt)_{\bar{p}p}$ and $(d\sigma/dt)_{pp}$ in the dip-shoulder region $1.1 < |t| < 1.5$ GeV^2 at $\sqrt{s} = 52.8$ GeV [10, 11]. Unfortunately, these data were obtained in one week, just before ISR was closed and therefore the evidence, even if it is strong (99,9 % confidence level), is not totally convincing.

The maximal Odderon [2, 12], is a special case (tripole) corresponding to the maximal asymptotic $(s \to \infty)$ behavior allowed by the general principles of strong interactions:

$$\sigma_T(s) \propto \ln^2 s, \quad \text{as } s \to \infty \tag{1}$$

[†] Unité de Recherche des Universités Paris 6 et Paris 7, Associée au CNRS

and

$$\Delta\sigma(s) \equiv \sigma_T^{\bar{p}p}(s) - \sigma_T^{pp}(s) \propto \ln s, \quad \text{as } s \to \infty \, . \tag{2}$$

Interestingly enough, an important stream of theoretical papers concern precisely the maximal behavior [2], which was first discovered by Heisenberg in 1952 [13] and later proved, in a more rigorous way by Froissart and Martin [14, 15]. Half a century after the discovery of Heisenberg, this maximal behavior (1) was also proved in the context of the AdS/CFT dual string-gravity theory [16] and of the Color Glass Condensate approach [17]. It was also shown to provide the best description of the present experimental data on total cross-sections [18, 19].

The maximal behavior of $ImF_+(s, t = 0) \propto \ln^2 s$ is naturally associated with the maximal behavior $ImF_-(s, t = 0) \propto \ln s$. In other words, strong interactions should be as strong as possible.

2 Strategy

In the present paper we will consider a very general form of the hadron amplitudes compatible with both the maximal behavior of strong interaction at asymptotic energies and with the well established Regge behavior at moderate energies, i.e. at pre-ISR and ISR energies [20, 21].

Our strategy is the following:

1. We will consider two cases: one in which the Odderon is absent and one in which the Odderon is present.
2. We will use the two respective forms in order to describe the 832 experimental points for pp and $\bar{p}p$ scattering, from PDG Tables, for $\sigma_T(s)$, $\rho(s)$ and $d\sigma/dt(s, t)$, in the s-range

$$4.539 \text{ GeV} \leqslant \sqrt{s} \leqslant 1800 \text{ GeV} \tag{3}$$

and in the t-range

$$0 \leqslant |t| \leqslant 2.6 \text{ GeV}^2 \, . \tag{4}$$

The best form will be chosen.
3. In order to make predictions at RHIC and LHC energies, we will insist on the best possible *quantitative* description of the data.
4. From the study of the interference between $F_+(s, t)$ and $F_-(s, t)$ amplitudes we will conclude which are the best experiments to be done in order to detect in a clear way the Odderon.

3 The form of the amplitudes

$F_\pm$ are defined to be

$$F_\pm(s, t) = \frac{1}{2} \left(F_{pp}(s, t) \pm F_{\bar{p}p}(s, t) \right) \tag{5}$$

and are normalized so that

$$\sigma_T(s) = \frac{1}{s} \mathrm{Im} F(s, 0) \, , \quad \rho(s) = \frac{\mathrm{Re} F(s, t = 0)}{\mathrm{Im} F(s, t = 0)} \tag{6}$$

$$\frac{d\sigma}{dt}(s,t) = \frac{1}{16\pi s^2}|F(s,t)|^2 \ . \tag{7}$$

The $F_+(s,t)$ amplitude is written as a sum of the Regge poles and cuts in standard form [1] and the Heisenberg component $F_+^H(s,t)$ representing the contribution of a 3/2 - cut collapsing, at $t=0$, to a triple pole located at $J=1$ and which satisfies the Auberson-Kinoshita-Martin asymptotic theorem [22]:

$$\begin{aligned} \frac{1}{is}F_+^H(s,t) &= H_1 \ln^2 \bar{s}\, \tfrac{2J_1(K_+\bar{\tau})}{K_+\bar{\tau}} \exp(b_1^+ t) \\ &+ H_2 \ln \bar{s} J_0(K_+\bar{\tau}) \exp(b_2^+ t) \\ &+ H_3[J_0(K_+\bar{\tau}) - K_+\bar{\tau}J_1(K_+\bar{\tau})] \exp(b_3^+ t) \ , \end{aligned} \tag{8}$$

where J_n are Bessel functions, $H_k,\ b_k^+ (k=1,2,3)$ and K_+ are constants,

$$\bar{s} = \left(\frac{s}{s_0}\right) \exp\left(-\frac{1}{2}i\pi\right), \text{ with } s_0 = 1 \text{ GeV}^2 \tag{9}$$

and

$$\bar{\tau} = \left(-\frac{t}{t_0}\right)^{1/2} \ln \bar{s}, \quad \text{with } t_0 = 1 \text{ GeV}^2 \ . \tag{10}$$

In its turn, the $F_-(s,t)$ amplitude is written as a sum of the Regge poles and cuts in standard form [1] and $F_-^{MO}(s,t)$ representing the maximal Odderon contribution, resulting from two complex conjugate poles collapsing, at $t=0$, to a dipole located at $J=1$ and which satisfies the Auberson-Kinoshita-Martin asymptotic theorem:

$$\frac{1}{s}F_-^{MO}(s,t) = O_1 \ln^2 \bar{s} \frac{\sin(K_-\bar{\tau})}{K_-\bar{\tau}} \exp(b_1^- t) + O_2 \ln \bar{s} \cos(K_-\bar{\tau}) \exp(b_2^- t) + O_3 \exp(b_3^- t) \ , \tag{11}$$

where $O_k,\ b_k^- (k=1,2,3)$ and K_- are constants.

4 Numerical results

Let us first consider the case *without the Odderon*. In this case, one has 23 free parameters.

In spite of the quite impressive number of free parameters, the χ^2-value is inacceptably bad:

$$\chi^2/dof = 14.2 \ . \tag{12}$$

A closer examination of the results reveals however an interesting fact: the no-Odderon case describes nicely the data in the t-region $0 \leqslant |t| \leqslant 0.6$ GeV^2 but totally fails to describe the data for higher t-values.

This failure does not mean the failure of the Regge model, which is a basic ingredient of the approach presented in this paper. It simply means the need for the Odderon.

In the case with the Odderon, we have 12 supplementary free parameters.

The total of 35 free parameters of our approach could be considered, at a superficial glance, as too big. However, one has to realize that the 23 free parameters associated with the dominant

$F_+(s,t)$ amplitude and with the component of $F_-(s,t)$ responsible for describing the data for $\Delta\sigma(s)$ (see eq. (2)) and $\Delta\rho(s,t=0)$, where

$$\Delta\rho(s,t=0) \equiv \rho^{\bar{p}p}(s,t=0) - \rho^{pp}(s,t=0) \tag{13}$$

are, almost all of them, well constrained.

Moreover, the discrepancy between the no-Odderon model and the experimental data in the moderate-t region (especially at $\sqrt{s} = 52.8$ GeV and $\sqrt{s} = 541$ GeV) is so big that, in their turn, the supplementary 12 free parameters (at least, most of them) are also well constrained.

Let us also note that the above - mentioned discrepancy in the region of t defined by

$$0.6 < |t| \leqslant 2.6 \text{ GeV}^2 \tag{14}$$

cannot come, as one could thing, from the contributions induced by perturbative QCD. The region (14) is fully in the domain of validity of the non-perturbative Regge pole model and the respective values of t are too small in order to make pQCD calculations.

The resulting value of χ^2 is

$$\chi^2_{dof} = 2.46 \ , \tag{15}$$

an excellent value if we consider the fact that we did not take into account the systematic errors of the experimental data.

The partial value of χ^2, corresponding only to $t = 0$ (σ_T and ρ) data is

$$\chi^2_{dof}\big|_{t=0} = 1.42 \ , \tag{16}$$

an acceptable value (276 experimental forward points taken into account). Of course, better χ^2 values can be obtained in fitting *only* the $t = 0$ data, as it is in often made in phenomenological papers. However, it is obvious that, in a global fit including non-forward data, the corresponding $t = 0$ parameters will be modified and therefore a higher χ^2 value will be obtained. The $t = 0$ and $t \neq 0$ data are certainly independent but the parameter values are obviously correlated in a global fit.

5 Predictions

We plot in Fig. 1 our fit and predictions for $d\sigma/dt$ data at $\sqrt{s} = 52.8$ GeV, at the RHIC energy values $\sqrt{s} = 500$ GeV, at the commissioning run energy value $\sqrt{s} = 900$ GeV and at the LHC energy value $\sqrt{s} = 14$ TeV. The description of the data at $\sqrt{s} = 52.8$ GeV as offered by our approach is the best one existing in literature. It has to be noted that the structure (dip) region moves slowly, with increasing energy, from $|t| \approx 1.35$ GeV^2 at $\sqrt{s} = 52.8$ GeV towards $|t| \simeq 0.35$ GeV^2 at $\sqrt{s} = 14$ TeV.

There is an interesting phenomenon of oscillations present in $\Delta(\frac{d\sigma}{dt})$ (see Fig. 2), which

$$\Delta\left(\frac{d\sigma}{dt}\right)(s,t) \equiv \left|\left(\frac{d\sigma}{dt}\right)^{\bar{p}p}(s,t) - \left(\frac{d\sigma}{dt}\right)^{pp}(s,t)\right| \ , \tag{17}$$

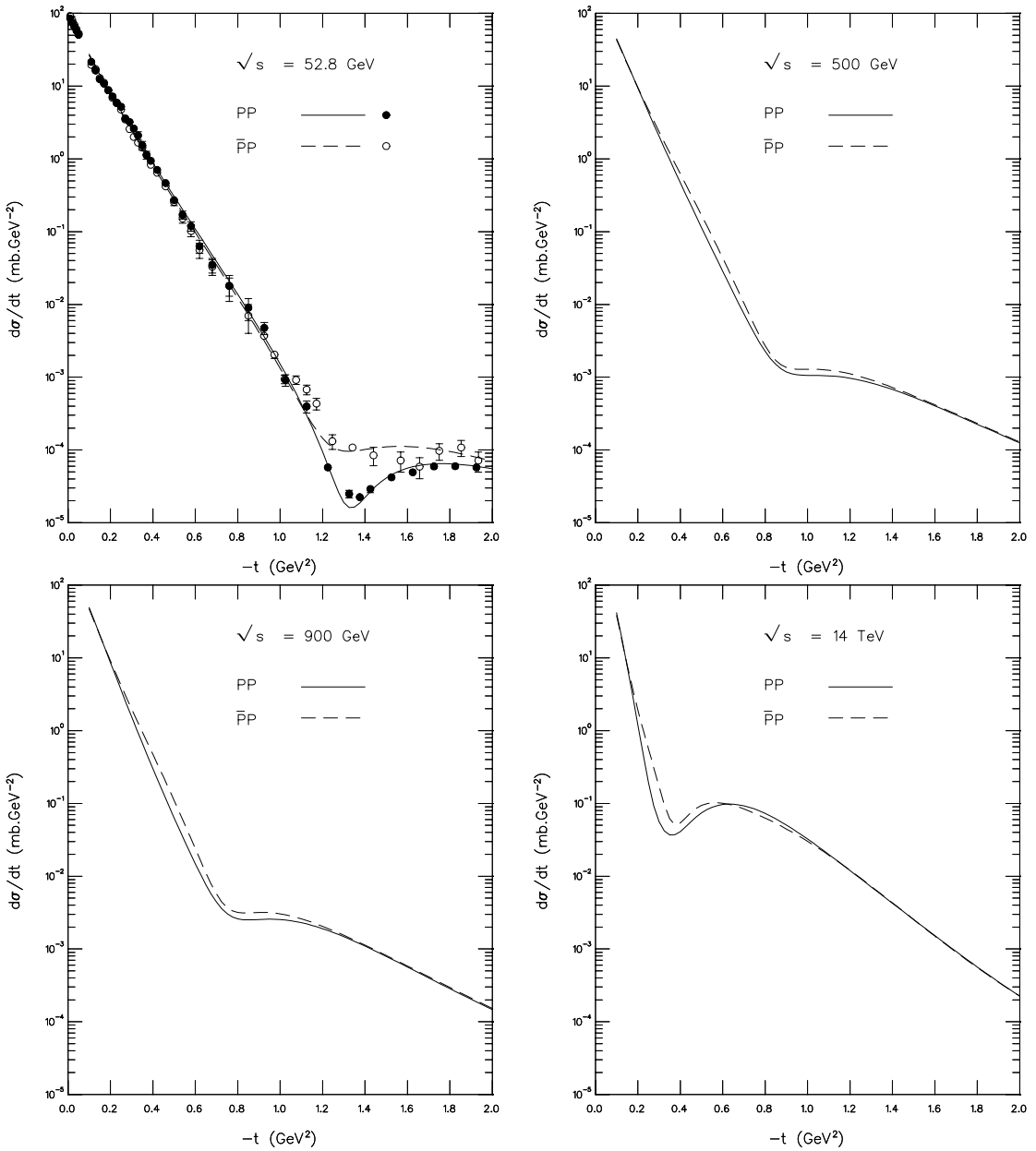


Fig. 1: The structure (dip) region moves slowly, with increasing energy, from $|t| \approx 1.35$ GeV^2 at $\sqrt{s} = 52.8$ GeV towards $|t| \simeq 0.35$ GeV^2 at $\sqrt{s} = 14$ TeV.

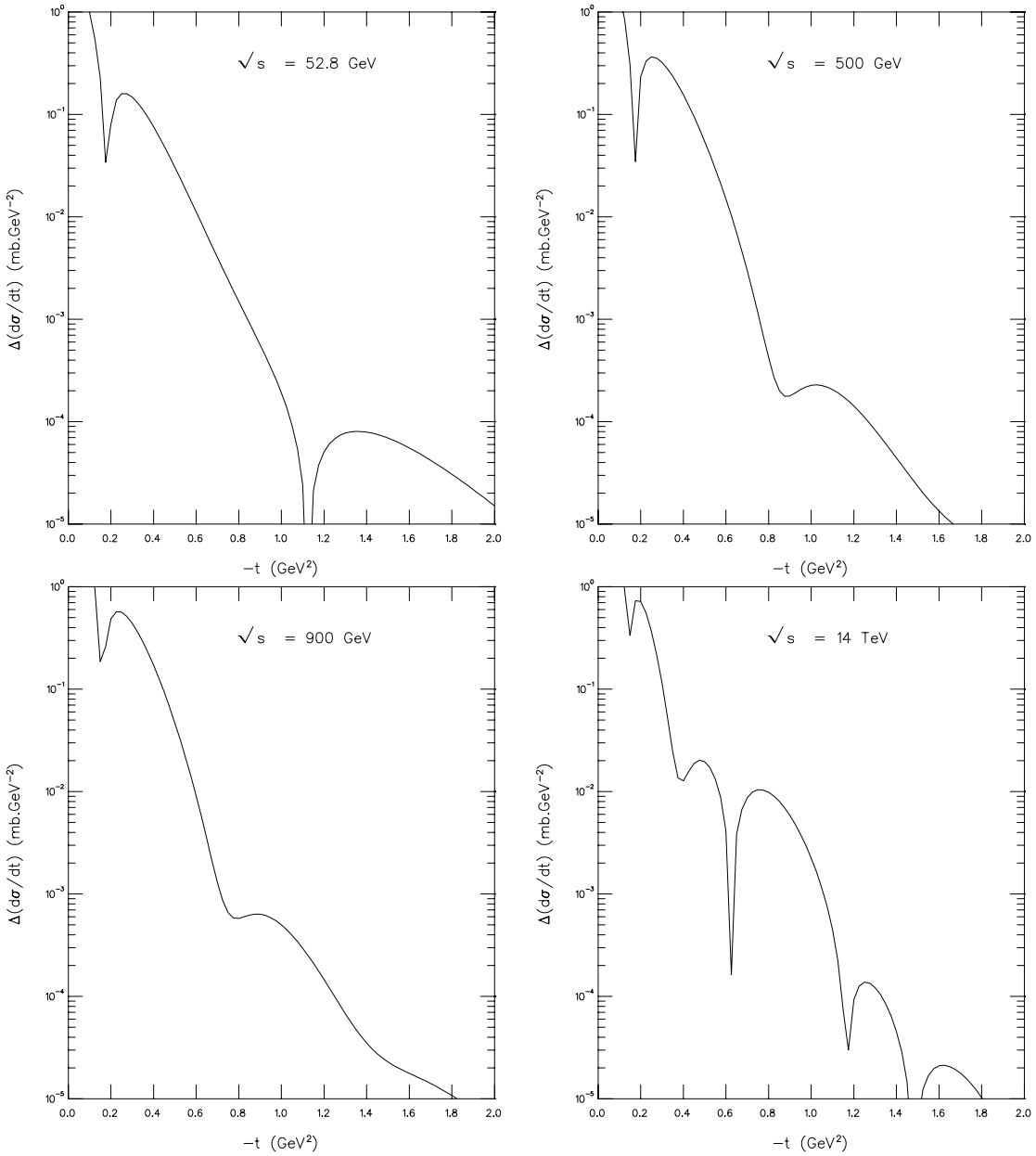


Fig. 2: Oscillations in the difference between the pp and $\bar{p}p$ differential cross-sections $\Delta\left(\frac{d\sigma}{dt}\right)(s,t) \equiv \left|\left(\frac{d\sigma}{dt}\right)^{\bar{p}p}(s,t) - \left(\frac{d\sigma}{dt}\right)^{pp}(s,t)\right|$

due to the oscillations present in the Heisenberg-type amplitude $F_+^H(s,t)$ and in the maximal Odderon amplitude $F_-^{MO}(s,t)$. Unfortunately, we can not directly test the existence of these oscillations at RHIC and LHC energies, simply because we will not have both pp and $\bar{p}p$ accelerators at these energies. However a chance to detect these oscillations at the RHIC energy $\sqrt{s} = 500$ GeV still exists, simply because the UA4/2 Collaboration already performed a high-precision $\bar{p}p$ experiment at a very close energy - 541 GeV [23]. By performing a very precise experiment at the RHIC energy $\sqrt{s} = 500$ GeV and by combining the corresponding pp data with the UA4/2 $\bar{p}p$ high-precision data one has a non-negligible chance to detect an oscillation centered around $|t| \simeq 0.9$ GeV^2 and therefore to detect the Odderon. It is precisely the oscillation centered around $|t| \simeq 0.9$ GeV^2 which is the reminder of the already seen oscillation centered around $|t| \simeq 1.35$ GeV^2 at the ISR energy $\sqrt{s} = 52.8$ GeV.

The participants at the workshop "Odderon Searches at RHIC", held at BNL in September 2005, concluded that the best available setup for the experimental search for the Odderon is the proposed combination of STAR experiment and Roman pots at $pp2pp$ experiment, described in the proposal "Physics with Tagged Forward Protons with the STAR detector at RHIC". They also concluded that the most unambiguous signature of the Odderon is to detect a non-zero difference between pp and $\bar{p}p$ differential cross-sections at $\sqrt{s} = 500$ GeV, as described above. RHIC is an ideal place for discovering the Odderon and therefore testing QCD and CGC [24].

LHC is also a good place to discover the Odderon. We predict

$$\sigma_T^{pp}(\sqrt{s} = 14 \text{ TeV}) = 123.32 \text{ mb} , \tag{18}$$

$$\Delta\sigma(\sqrt{s} = 14 \text{ TeV}) = -3.92 \text{ mb} , \tag{19}$$

$$\rho_{pp}(\sqrt{s} = 14 \text{ TeV},\ t = 0) = 0.103 , \tag{20}$$

and

$$\Delta\rho(\sqrt{s} = 14 \text{ TeV},\ t = 0) = 0.094 . \tag{21}$$

A ρ^{pp}-measurement at LHC would be certainly a very important test of the maximal Odderon, given the fact that our prediction is sufficiently lower than what dispersion relations without Odderon contributions could predict ($\rho \simeq 0.12 - 0.14$).

There are several other proposals for detecting the Odderon, summarized in the nice review written by Ewerz [25].

6 Conclusions

There are very rare cases in the history of physics that a scientific and testable idea is neither proved nor disproved 33 years after its invention. The Odderon remains an elusive object in spite of intensive research for its experimental evidence.

The main reason for this apparent puzzle is that most of the efforts were concentrated in the study of pp and $\bar{p}p$ scattering, where the $F_-(s,t)$ amplitude is hidden by the overwhelming $F_+(s,t)$ amplitude. The most spectacular signature of the Odderon is the predicted difference between pp and $\bar{p}p$ scattering at high s and relatively small t. However, it happens that, after the closure of ISR, which offered the first strong hint for the existence of the Odderon, there is no place in the world where pp and $\bar{p}p$ scattering are or will be measured at the same time. This is the main reason of the non-observation till now of the Odderon.

We show that we can escape from this unpleasant situation by performing a high-precision measurement of $d\sigma/dt$ at RHIC, at $\sqrt{s} = 500$ GeV, and by combining these future data with the already present high-precision UA4/2 data at $\sqrt{s} = 541$ GeV.

There is no doubt about the theoretical evidence for the Odderon both in QCD and CGC. The Odderon is a fundamental object of these two approaches and it has to be found at RHIC and LHC if QCD and CGC are right.

Acknowledgments

I am grateful to Professors Claude Bourrely and Evgenij Martynov who kindly repeated our calculations. This crosscheck proved to be very useful.

I dedicate this talk to the memory of Leszek Lukaszuk (1938-2007), who was not only a brilliant physicist but also an extraordinary human being and an incomparable friend.

References

[1] R. Avila, P. Gauron and B. Nicolescu, Eur. Phys. J. C **49**, 581 (2007).

[2] L. Lukaszuk and B. Nicolescu, Nuovo Cim. Lett. **8**, 405 (1973).

[3] J. Bartels, Nucl. Phys. **B175**, 365 (1980).

[4] T. Jaroszewicz, Acta Phys. Polon. **B11**, 965 (1980).

[5] J. Kwiecinski and M. Praszalowicz, Phys. Lett. **B94**, 413 (1980).

[6] J. Bartels, L. N. Lipatov, and G. P. Vacca, Phys. Lett. **B477**, 178 (2000), hep-ph/9912423.

[7] Y. Hatta, E. Iancu, K. Itakura, and L. McLerran, Nucl. Phys. **A760**, 172 (2005), hep-ph/0501171.

[8] S. Jeon and R. Venugopalan, Phys. Rev. **D71**, 125003 (2005), hep-ph/0503219.

[9] Y. V. Kovchegov, L. Szymanowski, and S. Wallon, Phys. Lett. **B586**, 267 (2004), hep-ph/0309281.

[10] A. Breakstone *et al.*, Phys. Rev. Lett. **54**, 2180 (1985).

[11] S. Erhan *et al.*, Phys. Lett. **B152**, 131 (1985).

[12] B. Nicolescu, 'The present Situation of the Odderon Intercept - Experiment, Theory and Phenomenology', in Proceedings of RIKEN BNL Research Center Workshop 'Odderon Searches at RHIC', BNL-75092-2005 Report, edited by Wlodek Guryn, Yuri Kovchegov, Werner Vogelsang, and Larry Trueman, p.1-6.

[13] W. Heisenberg, Z. Phys. **133**, 65 (1952).

[14] M. Froissart, Phys. Rev. **123**, 1053 (1961).

[15] A. Martin, Nuovo Cim. **A42**, 930 (1965).

[16] S. B. Giddings, Phys. Rev. **D67**, 126001 (2003), hep-th/0203004.

[17] E. Ferreiro, E. Iancu, K. Itakura, and L. McLerran, Nucl. Phys. **A710**, 373 (2002), hep-ph/0206241.

[18] J. R. Cudell *et al.*, Phys. Rev. **D65**, 074024 (2002), hep-ph/0107219.

[19] Review of Particle Physics, Phys. Lett. **B592**, 313 (2004).

[20] P. Gauron, B. Nicolescu, and E. Leader, Nucl. Phys. **B299**, 640 (1988).

[21] P. Gauron, B. Nicolescu, and E. Leader, Phys. Lett. **B238**, 406 (1990).

[22] G. Auberson, T. Kinoshita, and A. Martin, Phys. Rev. **D3**, 3185 (1971).

[23] UA4/2, C. Augier *et al.*, Phys. Lett. **B316**, 448 (1993).

[24] W. Guryn, Y. Kovchegov, L. Trueman, and W. Vogelsang, 'Introduction', in Proceedings of the RIKEN BNL Research Center Workshop 'Odderon Searches at RHIC', op. cit., p. i-iii.

[25] C. Ewerz, hep-ph/0306137.

Prospects for Diffraction at the LHC

Albert De Roeck
CERN, 1211 Geneva 23 Switzerland and University of Antwerp

Abstract
A short review is given on the opportunities for diffractive and forward physics measurements at the LHC.

1 Introduction

The Large Hadron Collider (LHC) [1], is a proton-proton collider being installed in the Large Electron Positron (LEP) tunnel at the CERN Laboratory (the European Laboratory for Particle Physics near Geneva, Switzerland). It will be a unique tool for fundamental physics research and the highest energy accelerator in the world for many years following its completion. The LHC will provide two proton beams, circulating in opposite directions, at an energy of 7 TeV each (center-of-mass $\sqrt{s} = 14$ TeV). These beams upon collision will produce an event rate about 100 times higher than that presently achieved at the Tevatron $p\bar{p}$ collider. The first collisions at 14 TeV are expected for early summer 2008.

The physics potential of the LHC is unprecedented: it will allow to study directly and in detail the TeV energy scale region. The LHC is expected to elucidate the electroweak symmetry breaking mechanism (EWSB) and provide evidence of physics beyond the Standard Model (SM) [2]. The LHC will be also a pivotal instrument to study QCD at the highest energies. Diffraction is an important component in hadronic collisions, and the LHC will shed new light on these still relatively poorly understood interactions. The type of diffractive collisions, or collisions with rapidity gaps expected at the LHC, is shown in Fig. 1 (left).

Diffractive collisions are usually pictured as the result of a diffractive exchange (aka pomeron). In this language the high energy of the LHC beams effectively leads to "pomeron beams" with an energy close to a TeV, allowing to study partonic collisions with fractional momenta of the partons in the "pomeron" of 10^{-3}, and p_T^2 transfers of more than 1 $(\mathrm{TeV}/c)^2$. The gap dynamics is presently not fully understood and events with multi-gaps (Fig. 1) will allow new insights.

Historically diffractive measurements have been made at the $Sp\bar{p}S$, Tevatron and HERA Colliders. An example is given in Fig.1 (right) which shows one of the pioneering measurements for diffractive hard scattering from the UA8 experiment [3], with evidence for a very hard component in the diffractive structure. Beautiful measurements of the diffractive structure became available from HERA, and impressive diffractive di-jets, $W, J/\psi$ and more measurements came from the Tevatron.

2 Diffraction and forward physics at the LHC

Diffractive measurements at present colliders have been made through the detection of rapidity gaps, as is obvious from Fig. 1 (left). This technique has been used extensively at HERA and the

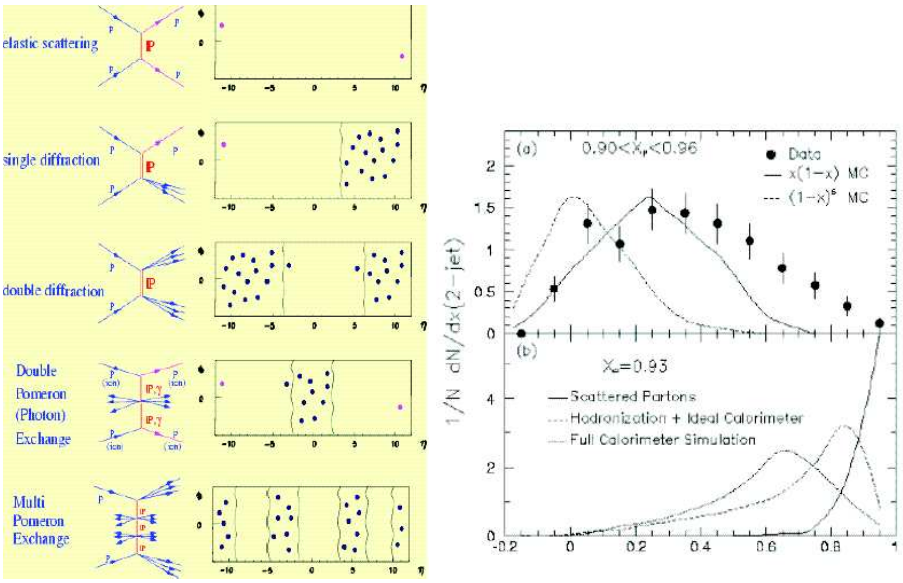


Fig. 1: (Left) Rapidity gap configurations for diffractive events at the LHC; (Right) x(2jet) distribution compared to simulations assuming a soft(dashed) and hard (solid) diffractive structure.

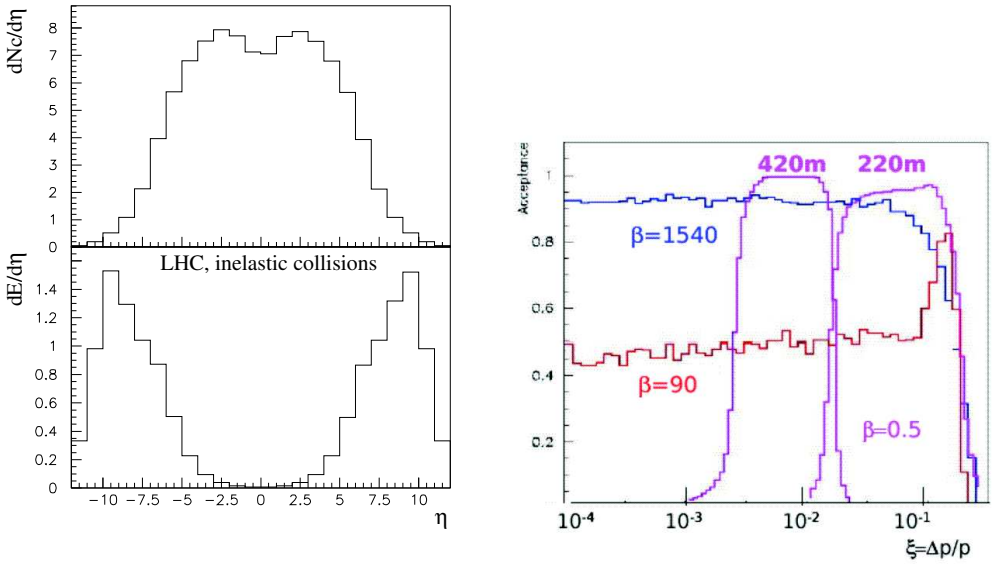


Fig. 2: (Left) Pseudorapidity distribution of the charged particles and of the energy flow at the LHC. The energy is in units of TeV; (Right) ξ acceptance of the Roman Pots of TOTEM and detectors at 420m.

Tevatron. It uses the correlation between the maximum value at which activity (charged tracks or energy) has been measured, η_{max}, and the diffractive variable ξ, the energy lost by the proton in the collision. Obviously this can be used only at low luminosity (perhaps up to 10^{33} cm^{-2} s^{-1} where about 20% of the bunch crossings still contain only one collision), and Monte Carlo corrections are essential. Hence it is important that the detectors have an as large coverage in η as possible.

On the other hand a more direct method is to detect the protons in those collisions where they remain intact (i.e. don't dissociate). This allows to constrain the full kinematics of the scattering. Hence near-beam detectors have been developed and used, the most well known one being the so called Roman Pots. These type of detectors will also be deployed at the LHC.

3 Forward detectors

The central detector of the CMS and ATLAS experiments have an acceptance in pseudorapidity η, of roughly $|\eta| < 2.5$ for tracking information and $|\eta| < 5$ for calorimeter information. Figure 2(left) [4, 5] shows the expected pseudorapidity distribution of the charged particles and of the energy flow at the LHC, demonstrating that with an acceptance limited to $|\eta| < 5$ most of the energy in the collision will not be detected.

Several of the LHC experiments will have so called Zero Degree Calorimeters (ZDCs). These detectors are located at 140m from the interaction point, where the proton beams are separated in their own beampipe. The prime goal of the ZDC is to measure the centrality in AA collisions. So-called ultra-peripheral events can also be tagged. In pp interactions it will allow the study of events with charge exchange and consequently a forward high energy neutron. Its ability to see low energy ($\approx$ 50 GeV) photons is important for exclusive diffractive studies. For cosmic ray physics also the measurement of the high energy π^0 component in pp and pA collisions at the LHC will be very important to tune the air shower models.

The different experiments and their forward detector capabilities are discussed next.

3.1 TOTEM

The TOTEM experiment [6, 7] will measure the pp elastic cross section as a function of t, –the square of the exchanged four-momentum–, the total cross section with a precision of approximately 1%, and diffractive dissociation at $\sqrt{s}$ = 14 TeV. The TOTEM experimental set-up consists of 2 tracking telescopes T1 and T2, as well as Roman Pot (RP) stations, on both sides of interaction point IP5. The T1 and T2 telescopes consist of CSC (Cathode Strip Chambers) and GEM (Gas Electron Multipliers) chambers respectively, and will detect charged particles in the η regions $3.2 < |\eta| < 5$ and $5 < |\eta| < 6.6$. The latter overlaps in acceptance with CASTOR of CMS.

The TOTEM RP stations will be placed at a distance of $\pm$147m and $\pm$220m from IP5. These stations can measure protons with a momentum loss $\xi = \Delta p/p$ in the range $0.02 < \xi < 0.2$ for the nominal collision optics. For other optics with larger β^*, and hence lower luminosity, much smaller values of ξ can be reached.

3.2 CMS

Presently there are two planned additions to extend the coverage in the forward region of CMS:

- Add two calorimeters on either side of the interaction region which will cover higher $|\eta|$ values, called CASTOR ($5.1 < |\eta| < 6.5$) and the Zero Degree Calorimeter (ZDC). Both have an electromagnetic and hadronic section. These calorimeters are of interest for measurements in pp, pA and AA collisions.
- Capitalize on the opportunity to have common runs with the TOTEM experiment, which uses the same interaction region as CMS (IP5). This common physics programme has recently been reported in a document, released by the CMS/TOTEM working group [8].

CASTOR is an electromagnetic/hadronic calorimeter, azimuthally symmetric around the beam and divided into 16 sectors. It is situated in the collar shielding at the very forward region of CMS, starting at 1437 cm from the interaction point, as shown in Figure 3. The pseudorapidity

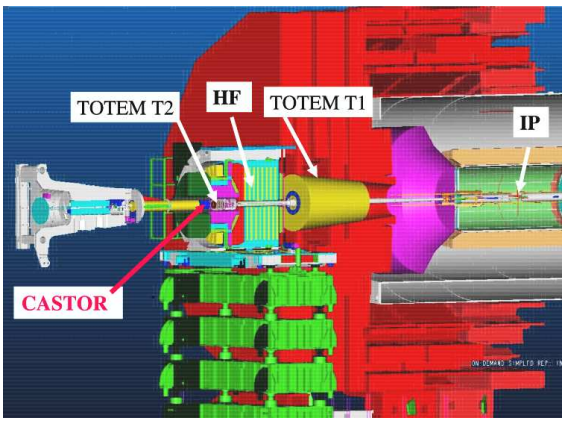


Fig. 3: Schematics of the CMS forward region.

range covered is $5.3 < |\eta| < 6.5$ for the EM-section and $5.1 < |\eta| < 6.4$ for the hadronic section. This η-coverage closes hermetically the CMS pseudorapidity range over almost 13 units. The ZDCs consist of tungsten absorber/quartz fibers.

The Roman Pot detectors of TOTEM aim to detect the protons in diffractive interactions of the type $pp \to p + X$ and $pp \to p + X + p$. When used in conjunction with the central CMS detector interesting phenomena such as hard diffractive scattering can be studied, where the system X can consist of jets, W, Z bosons, high E_T photons, top quark pairs or even the Higgs particle, as discussed recently in [9, 10].

The combination of T2 and CASTOR will allow the study of phenomena at lower Bjorken-x than otherwise reachable. Drell-Yan measurements will enable the parton distributions to be probed down to $x \approx 10^{-6} - 10^{-7}$. The energy and particle flows in the forward region are also of prime interest for tuning Monte Carlo simulation programs used in cosmic ray studies. CASTOR is designed especially to hunt for "strangelets" in AA collisions, which are characterized by very atypical fluctuations in hadronic showers.

It is expected that one CASTOR and two ZDC's will be available for the LHC data taking run in 2008.

3.3 ATLAS

ATLAS plans for its own Roman Pots for luminosity measurements, the ALFA project. Detectors, consisting of scintillating fibres will be placed at 240m in Roman pots. These detectors, in the present design, are not suited for diffractive physics studies at the nominal high luminosity. Instead the option is studied to put radiation hard detectors in Roman Pots or other near beam detector mechanics at 220m, the so called RP220 project.

ATLAS also plans a Cerenkov detector for relative luminosity measurements (LUCID with an acceptance of $5.4 < \eta < 6.1$) and ZDCs at a position of 140m. The ZDCs are made of tungsten absorber and quartz fibres. LUCID could be used to help to define a rapidity gap in the event, at low luminosity.

LUCID and the ZDC should be operational for the 2008 run but ALFA and RP220 (still to be approved) will be installed only after 2009.

3.4 ALICE

The ALICE detector has (on one side) a muon spectrometer that covers the region $2.4 < \eta < 4$ and a ZDC. Thus the forward muon acceptance of ALICE is larger than for the ATLAS and CMS experiments, allowing for a more forward acceptance for the detection of heavy flavors.

Since some time ALICE has a program for the study of minimum bias pp collisions (see e.g [11]). Recently [12] ALICE also studies specific diffractive channels.

3.5 LHCb

LHCb is a collider experiment but with the set-up of a fixed target experiment, namely a single side forward spectrometer covering the range $1.9 < \eta < 4.9$. In particular very forward heavy flavour production can be studied in LHCb. So far LHCb has no specific diffractive program.

3.6 LHCf

The LHCf has recently been approved for forward physics, consisting only of two forward electromagnetic calorimeters at zero degrees, hence positioned at 140m. The aim is to measure the very forward π^0 and γ energy spectrum for pp collisions with an equivalent E_{lab} of 10^{17} eV. LHCf also plans to take data during heavy ion runs. These measurements will help calibrating high energy cosmic ray spectra.

The detectors used will be based on a Tungsten absorber with scintillating fibres (one side) or silicon μstrips (the other side) as active elements. The detectors should measure energy and position of the γ's from the π^0 decays.

3.7 FP420

The FP420 project proposes to complement the experiments CMS and ATLAS by installing additional near-beam detectors at 420m away from the interaction region [13]. The presence of these detectors will allow to measure exclusive production of massive particles, such as the Higgs particle, as discussed in the next section.

The aims of the FP420 R&D study are

- Redesign the area of the machine around 420m. Right now this area contains a connecting cryostat, but no magnet elements.
- Study the mechanics, stability and services for detectors at 420m
- Design and test tracking detectors to operate close to the beam
- Design fast timing detectors (with O(10) psec resolution)
- Study RF pickup, integration, precision alignment, radiation and resolution issues for the FP420 setup.
- Study trigger, event selection, and pile-up issues.
- Study the operation of FP420 detectors at the highest LHC luminosity.

The FP420 collaboration has members from ATLAS, CMS, and "independent" physicists, with excellent contacts with the LHC machine group. In the emerging design the principle of FP420 is based on moving "pockets" which contain tracking and timing detectors. The tracking detectors that are developed are 3D silicon pixel detectors, which are radiation hard and can detect particles close to the edge. Timing detectors include both gas and crystal radiators. The first test beam results of all these detector types are very encouraging and a full pocket beam-test is foreseen for October 2007. Discussions on the implementation of FP420 in the ATLAS and CMS experiments have started. More technical details on FP420 will become available in [14].

4 Forward physics

The forward physics program is very diverse. Examples are:

Soft and Hard diffraction

- Total cross section and elastic scattering, single diffraction (SD).
- Gap survival dynamics, multi-gap events; proton light cone studies ($pp \rightarrow 3jets + p$), Odderon studies.
- Diffractive structure: Production of jets, $W, J/\psi, b$, top quarks, hard photons; Generalized Parton Distributions.
- Double Pomeron exchange (DPE) events as a gluon factory (anomalous W, Z production?).

Exclusive production of new mass states

- Exclusive Higgs production, Exclusive Radion production...
- SUSY and other (low mass) exotics, long lived gluinos.

Low-x dynamics

- Parton saturation, BFKL/CCFM dynamics, proton structure, multi-parton scattering.

New forward physics phenomena

- New phenomena such as DCCs, incoherent pion emission, Centauros.

Strong interest from cosmic rays community, and heavy ions

- Forward energy and particle flows/minimum bias event structure.
- Two-photon interactions and peripheral collisions.
- Forward physics in pA and AA collisions.
- Use QED processes to determine the luminosity to O(1%) ($pp \to ppee, pp\mu\mu$).

Many of these topics can be best studied at start-up luminosities. As mentioned, the forward detectors are of special interest for cosmic ray studies since these measure the production of high energy particles, an important component in the air shower simulations. To better tune such simulations collider data at the highest energies and over an as large acceptance range as possible, are critical.

4.1 Diffraction and QCD

The acceptance for diffractive physics with tagged protons is given in Fig. 2, for TOTEM and for detectors at 420m. Similar numbers hold for the ATLAS RPs. It shows that special runs with high β^* optics allow to detect protons over essentially the whole ξ range, but this corresponds essentially to luminosities below 10^{31} cm^{-1} s^{-1}. At the nominal high luminosity β^* detectors at 220m (TOTEM or RP220) and detectors at 420m are complementary on the region they cover. Physics topics include QCD and diffraction. Detectors at 220/420m can tag and measure protons which have lost 10% to 0.1% of there initial momentum, and study in detail diffractive reactions in that range.

With special optics and rather short running time (perhaps a week) processes with cross sections of μbarns are accessible, while with high luminosity processes with nbarn and pbarn cross sections can be studied. As an example for jet events, generator studies show that with about 300 nb^{-1} about 60000 SD events and 2000 DPE events are produced with jets having an E_T larger than 20 GeV. With 100 pb^{-1} we have 500000 and 30000 events with jets with an E_T larger than 50 GeV. Low luminosities will allow initial studies while high luminosity samples will allow for detailed t, M_x, p_T dependence studies.

A measurement of particular interest for this conference is the total and elastic pp cross section. The total cross section can be measured via the luminosity independent measurement as detailed in [15, 16]. TOTEM opts to use a β^* of 1500m in order to achieve a precision of 1% on the total cross section. While TOTEM may be ready from the start in 2008, this special optics is not expected to come very early on in the LHC running. As a compromise and easier achievable β^* of 90m would allow this measurement as well, but with a precision of O(5%). ATLAS opts for a β^* optics of 2625 m, which would allow to reach smaller $|t|$ values and allow to measure the ρ parameter as well. It has been often emphasized that ρ is an important quantity to measure as it is sensitive to new strong physics at higher energies, beyond the c.m.s. energy of the collisions.

An extensive program of two photon physics and photon-proton physics becomes accessible as well. In particular the study of the processes $\gamma\gamma \to WW$ and ZZ is of interest and can give precise measurements of the anomalous couplings. The QED processes $\gamma\gamma \to \mu\mu, ee$ can be precise monitors of the luminosity. Two photon processes can also be used to search for chargino pair production.

Other processes where forward detectors play a significant role are eg. in the study of low-x processes and the access to the gluon distribtution in the proton via Drell-Yan, jet or heavy flavor production. Values in Bjorken-x down to $10^{-6} - 10^{-7}$ in the perturbative regime can be reached. Adding forward detectors such as CASTOR to CMS will also allow to study forward-central correlations between particles, which are measurements that are very sensitive to for example multiple interactions and the way they are modeled.

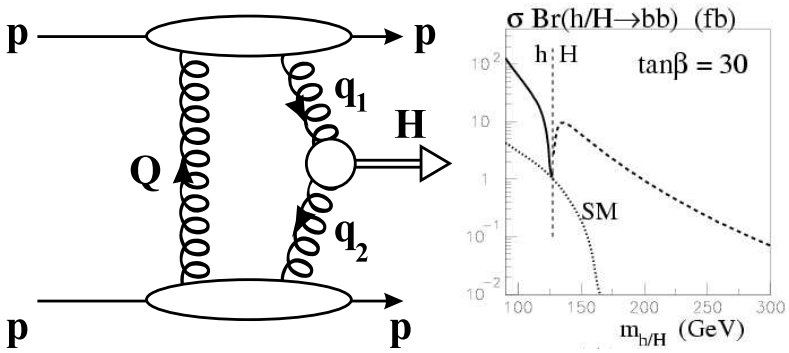


Fig. 4: (Left) Diagram for the CEP process; (Right) Cross section for SM and MSSM exclusive Higgs production.

4.2 Central exclusive Higgs production

Central exclusive Higgs (CEP) production $pp \to p + H + p$ is of special interest. The diagram is shown in Fig. 4 (left). One of the key advantages of CEP is that the $gg \to b\bar{b}$ process is strongly suppressed in LO, hence the decay $H \to b\bar{b}$ has less background and becomes potentially observable. The Higgs to b-quark Yukawa coupling is otherwhise very difficult to access at the LHC. The inclusive $H \to bb$ channel is not accessible due to the too large QCD backgrounds. Recently, the ttH channel was analysed with detailed simulation in [17] and found not to be accessible even with 60 fb^{-1}. Also the WH associated channel was found to be marginally observable in the bb decay mode.

The cross section for CEP of Higgs bosons has been subject of many discussions over the last years, in particular during the HERA/LHC workshops [18], but now generally the calculations of [19] are taken as a reference. Note that there are still some issues and concerns on the CEP soft survival probability at the LHC and the uncertainties in the PDFs. The cross section for the production of a Standard Model CEP Higgs and for a MSSM CEP Higgs (for $\tan\beta = 30$) is shown in Fig. 4. Generator level calculations, including detector and trigger cuts, and estimates of selection efficiencies, show that the decay channels $H \to bb$ and $H \to WW$ are accessable. Eg. $M_H = 120$ GeV/c^2 gives about 11 events with O(10) events background for 30 fb^{-1} in the bb decay mode. For M_H above 140 GeV/c^2 about 5-6 events with no appreciable background for 30 fb^{-1} in the WW decay mode [10] will be observed, using channels with at least one leptonic decay. There are however challenges: the signals from detectors at 420m cannot be used to trigger the events at the first trigger level in neither ATLAS nor CMS. Hence the event will have to be triggered at the first level with the information of the central detector. At the next trigger

level the signals of FP420 can be used. While this is no problem for the WW decay channel, it is a challenge for the bb channel. Several additional selection cuts for a low mass Higgs-like object decaying into jets can be used, but generally, with di-jet thresholds of O(40) GeV and these additional cuts, the rate at the first level for this trigger is very high: O(10) kHz. The usage of the FP420 information can however strongly reduce that rate at the next level, so this is not necessarily a show stopper. But in any case, studies both using detailed [8] and fast [20] simulations show that the measurement of the SM Higgs decay into bb will be very challenging, even with the highest luminosities.

The rate is much larger for MSSM Higgs production as shown in Fig. 4 (right), thus leading to a much more favourable signal to background ratio than for the SM Higgs. The cross section can be a factor 10 or more larger than the SM model one. This has recently been explored in a systematic way in [21]. A typical result is shown in Fig. 5 (left), for a Higgs decaying in bb. The lines in the plot show the relative cross section increase w.r.t. the SM cross section. In some regions of the phase space the CEP process could be a discovery channel. Fig. 5 (right) shows an example of a signal for 60 fb^{-1} after acceptance cuts, trigger efficiencies etc., for a MSSM Higgs with a cross section that is a factor 8 enhanced w.r.t the the SM Higgs, based on the so called m_h^{max} scenario [22], with $m_A = 120$ GeV and $\tan\beta = 40$. A clear signal over background is observable.

A detailed study of the backgrounds to this diffractive process was presented in [8]. At high luminosity, ie. 10^{33} cm^{-2}s^{-1} and higher, the pile-up is considerable, coming mainly from soft single diffractive interactions. Several techniques such as correlations between the detectors at 420/220m, vertices, event multiplicities and especially fast timing are essential to reduce the pile-up background. Rapidity gaps can obviously not be used due to the many interactions per bunch crossing.

Furthermore, to a very good approximation the central system in CEP is constrained to be a colour singlet, $J_Z = 0$ state, and, due to the strongly constrained three particle final state, the measurement of azimuthal correlations between the two scattered protons will allow to determine the CP quantum numbers of the produced central system [23]. Hence this is a way to get information on the spin of the Higgs, and is added value to the LHC measurements.

It was pointed out recently [24] that in case of CPV models the h, A, H may mix into states h_1, h_2, h_3 which may be quasi-degenerated in mass, with mass differences of the order of a few GeV or less. Due to the interference these will show up as one broad mass distribution, with a structure that is sensitive to the underlying parameters. Analyzing the three-way mixing scenario [24] it was found that the different peaks can be detected with a 1 GeV mass resolution, but would need a few hundred fb^{-1} of accumulated luminosity. Other CP violating benchmark scenarios may lead to larger differences between the Higgs peaks and may be easier to detect.

Other searches for new physics in the channel are possible as well. It has been pointed out that the mass of long lived gluinos, as predicted in split SUSY models, can be determined with CEP events to better than 1%, with 300 fb^{-1} for masses up to 350 GeV [25]. More spectacular are the predictions presented in [26], where a very high cross section of CEP WW and ZZ events is expected, in a color sextet quark model.

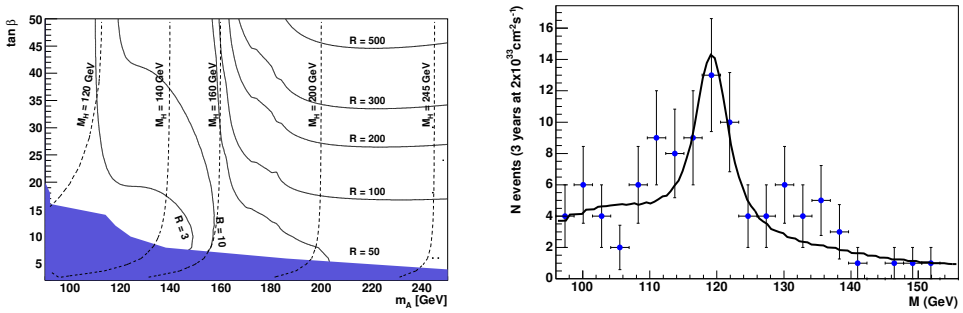


Fig. 5: (Left) Contours for the ratio of signal events in the MSSM to those in the SM in the $H \to bb$ channel in CEP production in the M_A–$\tan\beta$ plane. The ratio is shown in the no-mixing scenario with $\mu = +200$ GeV. The values of the mass of the heavier CP-even Higgs boson, m_H, are indicated by dashed contour lines. (Right) A typical mass fit for 3 years of data taking at 2×10^{33} cm^{-2} s^{-1} (60 fb^{-1}). The significance of the fit is 3.5σ and uses only events with both protons tagged at 420m.

5 Conclusion

The LHC is coming on line, with the first 14 TeV collisions to be expected in summer 2008.

Forward physics at the LHC came a long way during the last years. Two forward physics experiments got approved (TOTEM, LHCf). ATLAS and CMS plan to extend the detector coverage in the forward direction, with ZDCs, CASTOR (CMS) and LUCID (ATLAS). ATLAS also plans to add RPs at 240m and studies additional near beam detectors at 220m. CMS and TOTEM have common physics program on diffraction.

The R&D for FP420 is nearing its completion. Discussions with the ATLAS and CMS managment have started. The earliest date for data taking with these detectors is 2010.

In all, forward physics is now well in the blood of the LHC experiments.

References

[1] The LHC Study Group: *The Large Hadron Collider Conceptual Design*, CERN-AC-95-05 (1995).

[2] J.G. Branson et al., *High Transverse Momentum Physics at the Large Hadron Collider*, Eur. Phys. J Direct **C4** (2002) N1, hep-ph/0110021.

[3] A. Brandt et al. Phys. Lett. B **297** (1992) 417.

[4] E. Lippmaa et al., Felix Collaboration, *FELIX: A full acceptance detector at the LHC*,CERN-LHCC, http://www.cern.ch/FELIX/Loi/letofin.html, 97 (1997).

[5] A. Ageev et al., J. Phys **G28**, (2002), R117.

[6] TOTEM Collaboration, TOTEM Technical Design Report, CERN/LHCC 2004-002 (2004).

[7] TOTEM Collaboration, Addendum to the TOTEM-TDR, CERN/LHCC 2004-020, (2004).

[8] M. Albrow et al. (CMS& TOTEM) *Prospects for diffractive and forward physics at the LHC*. CERN-LHCC-2006-039, CERN-LHCC-G-124, CERN-CMS-NOTE-2007-002, Dec 2006. 156pp.

[9] A. De Roeck, V. A. Khoze, A.D. Martin, R. Orava, and M.G. Ryskin, Eur. Phys. J. C **25** (2002) 391.

[10] B. E. Cox et al. Eur.Phys.J. C **45** (2006) 401, hep-ph/0505240.

[11] J.P. Revol, talk at the TeV4LHC workshop at CERN 28-30 April 2005.

[12] R. Schicker, this conference

[13] M.G. Albrow et al. *FP420: An R& D proposal to investigate the feasibility of installing proton tagging detectors in the 420-m region at LHC*, CERN-LHCC-2005-025, Jun 2005.

[14] M.G. Albrow et al., *FP420 R&D report*, to appear.

[15] M. Deile, this conference

[16] C. Sbarra, this conference

[17] CMS Collaboration *CMS physics : Technical Design Report v.2 : Physics performance* CERN-LHCC-2006-021 (2006); J. Phys. G: Nucl. Part. Phys. **34** (2007) 995, doi:10.1088/0954-3899/34/6/S01.

[18] S. Alekhin et al., *Proceedings of the HERA-LHC workshop*, CERN-2005-014, DESY-PROC-2005-01 (2005), hep-ph/0601013 and hep-ph/0601012.

[19] V.A Khoze, A.D. Martin and M.G. Ryskin, Eur. Phys. J. C. **23** (2002) 311.

[20] B.E. Cox, F.K. Loebinger, A.D. Pilkington, MAN-HEP-2007-15, Sep 2007, arXiv:0709.3035 [hep-ph]

[21] S. Heinemeyer et al., DCPT-07-80, IPPP-07-40, Aug 2007, arXiv:0708.3052

[22] M.S. Carena, S. Heinemeyer, C.E.M. Wagner and G. Weiglein, Eur. Phys. J. C **26** (2003) 601.

[23] V.A Khoze, A.D. Martin and M.G. Ryskin, Eur. Phys. J. C **34** (2004) 327, hep-ph/0401078.

[24] J. Ellis, J. S. Lee and A. Pilaftsis, Phys. Rev. D **71** (2005) 075007, hep-ph/0502251.

[25] P.J. Bussey, T.D. Coughlin, J. R. Forshaw, A.D. Pilkington, JHEP **0611** (2006) 027.

[26] A.R. White, Phys. Rev. D **72** (2005) 036007.

[27] K. Terashi for the CDf collaboration. FERMILAB-CONF-07-148-E, Proceedings of 42nd Rencontres de Moriond on QCD Hadronic Interactions, La Thuile, Italy, 17-24 Mar 2007, arXiv:0705.3804.

Multiple Scattering, Underlying Event, and Minimum Bias

Gösta Gustafson
Dept. of Theoretical Physics, Lund Univ.
Sölveg. 14A, S-22362 Lund, Sweden
e-mail: Gosta.Gustafson@thep.lu.se

Abstract

In this talk I first discuss the experimental evidence for multiple scattering and the properties of the underlying event. The extensive analyses by Rick Field of data from CDF cannot be reconciled with traditional wisdom concerning multiple collisions and the AGK cutting rules. Data seem to imply some kind of color recombination or unexpectedly strong effects from pomeron vertices.

I then discuss theoretical ideas concerning the relation between multiple collisions and unitarity: the AGK rules, pomeron loops, dipole cascade models and diffraction.

1 Experimental overview

1.1 Minijet cross section

In *collinear factorization* the cross section for a parton-parton subcollision is given by

$$\frac{d\sigma^{subcoll}}{dp_\perp^2} \sim \int dx_1 dx_2 f(x_1, p_\perp^2) f(x_2, p_\perp^2) \frac{d\hat{\sigma}}{dp_\perp^2}(\hat{s} = x_1 x_2 s, p_\perp^2). \tag{1}$$

(Note that one hard subcollision corresponds to 2 jets.) The partonic cross section $d\hat{\sigma}/dp_\perp^2$ behaves like $1/p_\perp^4$ for small $p_\perp$, which means that a lower cutoff, $p_{\perp min}$, is needed. The total subcollision cross section is then proportional to $1/p_{\perp min}^2$, and for pp-collisions the subcollision cross section becomes equal to the total cross section for $p_{\perp min} \approx 2.5$ GeV at the Tevatron and ≈ 5 GeV at LHC [1]. Fits to data give $p_{\perp min} \sim 2$ GeV at the Tevatron and slowly growing with energy [2].

In $k_\perp$*-factorization* there is a dynamic cutoff when the momentum exchange $k_\perp$ is smaller than the virtuality of the two colliding partons, given by $k_{\perp 1}$ and $k_{\perp 2}$ [3]. This approach gives a very similar effect. Thus we conclude that at high energies the subcollision cross section is much larger than the total inelastic cross section, which means that on average there must be several hard subcollisions in one event. It was also early suggested that the increase in σ_{tot} is driven by hard parton-parton subcollisions [4].

1.2 Experimental evidence for multiple collisions

1.2.1 Multijet events

Besides from independent multiple subcollisions, multijet events can also originate from multiple bremsstrahlung from two colliding partons. If we study four-jet events the difference between

these two types of events is that in a double parton scattering the four jets balance each other pairwise in the transverse momentum plane, while such a pairwise balance is not present in the multiple bremsstrahlung events. The Axial Field Spectrometer at the ISR proton-proton collider [5] studied an "imbalance parameter"

$$J = \frac{1}{2}[(\mathbf{p}_{\perp 1} + \mathbf{p}_{\perp 2})^2 + (\mathbf{p}_{\perp 3} + \mathbf{p}_{\perp 4})^2], \tag{2}$$

and found that there is a significant enhancement of events with small values of J, which thus showed a clear evidence for multiple subcollisions.

Similar, but less clear, results for four-jet events have been observed by the CDF [6] and D0 [7] experiments at the Tevatron. A more clear signal for multiple collisions at the Tevatron has instead been seen in events with three jets + γ [8]. Evidence for multiple collisions has also been observed in photoproduction by the ZEUS collaboration at HERA [9].

1.2.2 Underlying event

An important question is whether the hard subcollisions are correlated, or if a high $p_\perp$ event just corresponds to two jets on top of a minimum bias event. If the subcollisions are uncorrelated the probability, $P(n)$, for having n subcollisions should be described by a Poisson distribution. This implies that

$$P(2) = \frac{1}{2}P(1)^2. \tag{3}$$

Here the factor 1/2 is compensating for double counting. Expressed in the cross sections $\sigma_n = P(n)\sigma_{nd}$ (where σ_{nd} is the inelastic non-diffractive cross section) this gives the relation $\sigma_2 = \frac{1}{2}\sigma_1^2/\sigma_{nd}$. The experimental groups have used the notation

$$\sigma_2 = \frac{1}{2}\frac{\sigma_1^2}{\sigma_{eff}}, \tag{4}$$

which means that $\sigma_{eff} = \sigma_{nd}$ corresponds to uncorrelated subcollisions. The experimental results on four-jet events referred to above find, however, that σ_{eff} is much smaller than σ_{nd}. Thus at ISR one finds (for jets with $p_\perp > 4$ GeV) $\sigma_{eff} \sim 5$ mb compared to $\sigma_{nd} \sim 30$ mb, CDF finds for four-jet events ($p_\perp > 25$ GeV) and 3 jets+γ the results $\sigma_{eff} \sim 12$ mb and ~ 14 mb respectively, to be compared with $\sigma_{nd} \sim 50$ mb. This means that if there is one subcollision there is an enhanced probability to have also another one. A possible interpretation is that in central collisions there are many hard subcollisions, while there are fewer subcollisions in a peripheral collison.

Another sign of correlations is the observation that in events with a high $p_\perp$ jet the underlying event is enhanced, the so called *pedestal effect*. The UA1 collaboration at the Sp$\bar{\text{p}}$S collider studied the $E_\perp$-distribution in η around a jet [10]. To avoid the recoiling jet they looked in 180° in azimuth on the same side as the jet. The result is that for jets with $E_\perp > 5$ GeV the background level away from the jet is roughly a factor two above the level in minimum bias events. Similar results have been observed in resolved photoproduction by the H1 collaboration [11].

1.3 CDF analysis and the PYTHIA model

Rick Field has made very extensive studies of the underlying event at the Tevatron (see e.g. ref. [12]). He has here tuned the PYTHIA MC to fit CDF data, and found tunes (e.g. tune A and tune DW) which give very good fits to essentially all data. In particular he has looked at the $E_\perp$-flow, the charged particle density, and $p_\perp$-spectra in angular regions perpendicular to a high-$p_\perp$ jet. One noticeable result is that the charged multiplicity in this "transverse" region grows rapidly with the $p_\perp$ of the trigger jet up to $p_\perp(\mathrm{charged\ jet}) \approx 6\,\mathrm{GeV}$, and then levels off for higher jet energies at twice the density in minimum bias events. Also the charged particle spectrum has a much higher tail out to large $p_\perp$ in events with a high $p_\perp$ jet, compared to the distribution in minimum bias events. The multiple collisions have a very important effect in the MC simulations, and the data cannot be reproduced if they are not included.

The version of the PYTHIA MC used by Field is an implementation of an early model by Sjöstrand and van Zijl [2]. In this model it is assumed that high energy collisions are dominated by hard parton-parton subcollisions, and also minimum bias events are assumed to have at least one such subcollision. To be able to reproduce the observed pedestal effect, the parton distribution is assumed to have a more dense central region, and is described by a sum of two (three-dimensional) Gaussians. For fixed impact parameter, b, the number of subcollisions is assumed to be given by a Poisson distribution, with an average proportional to the overlap between the parton distributions in the two colliding protons. Integrated over the impact parameter this gives a distribution which actually can be well approximated by a geometric distribution, that is a distribution with much larger fluctuations than a Poisson.

The PYTHIA model does not include diffraction, and describes only non-diffractive inelastic collisions. Diffraction is related to the fluctuations via the AGK cutting rules [13]. In QCD a single pomeron exchange can be represented by a gluon ladder. The diagram for double pomeron exchange can be cut through zero, one and two of the exchanged pomerons, with relative weights 1, -4, and 2. If we add the contributions to k cut pomerons from diagrams with an arbitrary number of exchanged pomerons, then we get for $k > 1$ with the weights in ref [13] a Poisson distribution. For fixed impact parameter the assumptions in the PYTHIA model are thus in agreement with the AGK rules.

1.4 Relation $E_\perp - n_{ch}$

Although Field's tunes of the PYTHIA model give good fits to data, there are still problems. The relation between transverse energy and hadron multiplicity is not what has been expected. In the AGK paper a cut pomeron was expected to give a chain of hadrons between the remnants of the two colliding hadrons, and two cut pomerons should give two such chains and therefore doubled particle density. This is in contrast to the CDF data, where $E_\perp$ grows more than the multiplicity in multiple collision events.

The original AGK paper was published before QCD, and based on a multiperipheral model. However, also in QCD the DGLAP or BFKL dynamics gives color-connected chains of gluons. In the hadronization process the gluon exchange ought to give two triplet strings (or cluster chains) stretching between the projectile remnants, and in the spirit of AGK two cut pomerons should give four such triplet strings. Field's tunes seem instead to indicate some kind

of color recombination which reduces the effective string length. (Similar recombinations have been studied by Ingelman and coworkers [14].)

In the PYTHIA model used by Field different possibilities for the color connection between the partons involved are studied. The most common parton subcollisions are $gg \to gg$, and as mentioned above this is expected to give two strings between the projectile remnants. Initial state radiation gives extra gluons, for which the color ordering agrees with the ordering in rapidity. Therefore these emissions do not increase the total string length very much, and as a consequence they increase $E_\perp$ more than they increase the hadron multiplicity.

From the experimental data it was noted already in ref. [2] that two subcollisions could not give doubled multiplicity, as expected from four strings as discussed above. It was therefore assumed that the second subcollision could give a just single double string connecting the two outgoing gluons. Another option was replacing the gluons by a $q\bar{q}$ pair, connected by a single triplet string. This reduces the multiplicity even further. A third possibility was to assume that color rearrangement caused the scattered gluons to fit in the color chains of the first collision, in such a way that the total string length was increased as little as possible. This gives a minimal additional multiplicity, and in this case the multiple collisions have an effect on the total $E_\perp$ and multiplicity similar to the bremsstrahlung gluons (but the jets are balanced pairwise in transverse momentum). The default assumption in ref. [2] was to give each of these possibilities the same probability, 1/3. In Field's successful tunes these ratios are changed, such that the last option with color reconnection is chosen in 90% of the cases.

In a more recent study by Sjöstrand and Skands [1] a number of improvements have been added to the old PYTHIA model. The hope was that with these modifications it would be possible to describe data without the extreme color reconnections which have no real theoretical motivation in QCD. Their result is, however, discouraging, as they were not able to tune the new model to give the relation between $p_\perp$ and multiplicity observed in the data.

2 Theoretical ideas

2.1 Pomeron interactions

We have to conclude that something important is missing in our understanding of high energy collisions. Although, in the AGK paper, pomeron interactions are assumed to give small contributions, pomeron vertices (see e.g. [15]) and pomeron loops may be very important. As indicated in fig. 1a, a pomeron loop can give a bump in the particle density if both branches of the loop are cut, and a gap if the cut passes between the two branches. It is also conceivable that such gaps and bumps have to be included in a "renormalized" pomeron [16].

In QCD a pomeron is formed by two gluons in a color singlet. Two pomeron exchange thus corresponds to four gluons in two singlet pairs. If the pairs (1,2) and (3,4) form singlets, then gluon exchange can change the system so that instead the pairs (1,3) and (2,4) form color singlets. This corresponds to an effective $2I\!P \to 2I\!P$ coupling (cf. ref. [17]). A cut with gluons 1 and 2 on one side and 3 and 4 on the other can then give an isolated bump in the particle density, as illustrated in fig. 1b. This type of pomeron interactions can also give a bound state [18], which gives a pole in the angular momentum plane and an essential correction to the normal cut from the exchange of two uncorrelated pomerons.

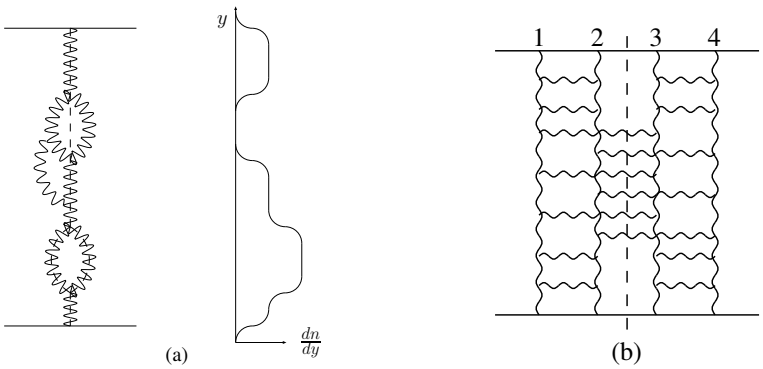


Fig. 1: **(a)** A pomeron loop can be cut through 0, 1, or 2 of its two branches. This can give gaps and bumps in the particle distribution. **(b)** Two pomerons can be represented by four gluons in two color singlet pairs. Gluon exchange can switch the pairs (1,2) (3,4) into the singlet pairs (1,3) (2,4). A cut as indicated in the figure gives a localized bump in the rapidity distribution.

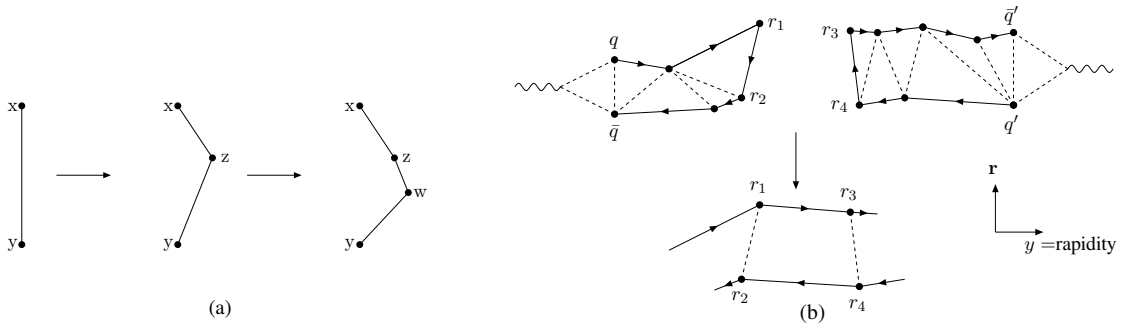


Fig. 2: **(a)** The evolution of the dipole cascade. At each step, a dipole can split into two new dipoles. **(b)** A symbolic picture of a $\gamma^*\gamma^*$ collision in $y - \mathbf{r}_\perp$-space. When two colliding dipoles interact via gluon exchange the color connection between the gluons is modified. The result is dipole chains stretched between the remnants of the colliding systems.

We conclude that there are still many open questions. More experimental information is needed, and to gain insight into the dynamics it is important to go beyond inclusive observables, and study observables related to correlations and fluctuations.

2.2 Dipole cascade models, saturation and pomeron loops

Multiple scattering and rescattering is more easily treated in transverse coordinate space. In Mueller's dipole cascade model [19] a color dipole formed by a $q\bar{q}$ pair in a color singlet is split into two dipoles by gluon emission. Each of these dipoles can split repeatedly into a cascade, see fig. 2a. The probability per unit rapidity for a split is proportional to $\bar{\alpha} = N_c\alpha_s/\pi$. When two dipole chains collide, gluon exchange between two dipoles implies exchange of color and a recoupling of the chains, as shown in fig. 2b. The probability for an interaction between two dipoles i and j, f_{ij}, is proportional to $\alpha_s^2 = \pi^2\bar{\alpha}^2/N_c^2$, and is thus formally color suppressed

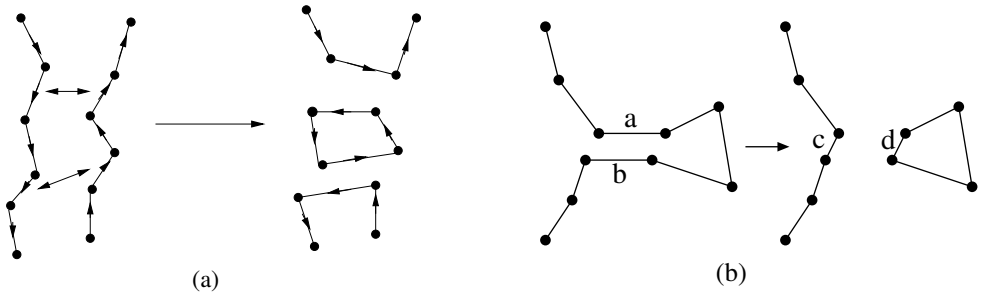


Fig. 3: **(a)** If more than one pair of dipoles interact it can result in dipole loops, which correspond to pomeron loops. **(b)** Schematic picture of a dipole swing. If the two dipoles a and b have the same color, they can be replaced by the dipoles c and d. The result is a closed loop formed within an individual dipole cascade.

compared to the dipole splitting process.

In the eikonal approximation the total scattering probability is determined by the expression $1 - \prod_{ij}(1 - f_{ij})$, which is always smaller than 1 and thus satisfies the constraints from unitarity. As seen in fig. 3a, multiple dipole-dipole interactions can imply that the color dipoles form closed loops, which correspond to the pomeron loops in fig. 1a.

Mueller's model includes those pomeron loops, which correspond to cuts in the particular Lorentz frame used for the calculation, but not loops which are fully inside one of the colliding cascades. This implies that the formalism is not Lorentz frame independent, and different ways have been suggested to achieve a frame independent formulation (see e.g. refs. [20, 21]). However, so far no explicitely frame independent formalism has been presented.

In one approach the evolution is expressed in terms of *interacting* dipoles. This implies that the number of dipoles can be reduced, and the evolution of the projectile cascade depends on the target. Besides the $1 \to 2$ dipole vertex there should here also be a $2 \to 1$ vertex. In another approach the evolution of the projectile is independent of the target, and the non-interacting dipoles are eliminated afterwards. In this approach there is no need to reduce the number of dipoles in the evolution.

Dipole swing

A model based on the latter approach is presented in ref. [22]. In this model pomeron loops can be formed with the help of a recoupling of the dipole chains, a "dipole swing". Just as the dipole-dipole scattering, the pomeron loops in the cascades should be color suppressed. With a finite number of colors we can have not only dipoles but also higher color multipoles. Two charges and two anticharges with the same color may be better approximated by two dipoles formed by nearby charge-anticharge pairs. These pairs may be different from the initially generated dipoles, and the result is a recoupling of the dipole chain, as seen in fig. 3b. The same effect can also be obtained from gluon exchange, which is proportional to α_s and thus also color suppressed cf. to the dipole splitting proportional to $\bar{\alpha}$.

The swing does not result in a reduction of the number of dipoles, but the saturation effect is obtained as the recoupled dipoles are smaller and therefore have smaller cross sections.

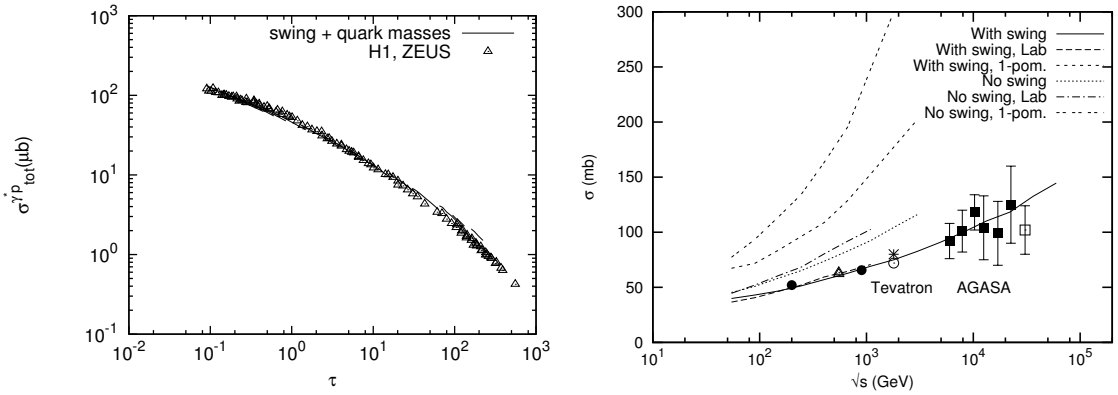


Fig. 4: *Left*: The γp total cross section obtained from the model in The result is plotted as a function of the scaling variable $\tau = Q^2/Q_s^2$, where $Q_s^2 = Q_0^2(x_0/x)^\lambda$ with $Q_0 = 1\text{GeV}$, $x_0 = 3 \cdot 10^{-4}$, $\lambda = 0.29$. *Right*: The total pp scattering cross section. Results are presented for evolution with and without the dipole swing mechanism. The one pomeron result and the result obtained in a frame where one of the protons is almost at rest are also shown.

Inserted in a MC the result is approximately frame independent, and the model describes well both the F_2 structure function in DIS and the pp scattering cross section [22, 23], as shown in fig. 4. (For these results also energy conservation and a running α_s are very important [24].) We see here that the $\gamma^* p$ cross section satisfies geometric scaling. The pp cross section is reduced by about a factor 4 cf. to the one pomeron exchange at the Tevatron, and we also see that the result of the model is the same when calculated in the cms as in the rest frame of the target proton, if pomeron loops are included also in the evolution via the dipole swing.

Besides the total cross sections it is also possible to calculate the probability to have pomeron loops formed by multiple collisions in a given frame, or loops formed within the cascades. As examples we find at the Tevatron in the cms on average 2.2 loops from multiple collisions and 0.65 loops in each of the two cascades. In an asymmetric frame, where the total rapidity range is divided in 4.5 + 10.5 units, we find instead 2 loops from multiple collisions, and 0.15 and 1.35 in the two cascades respectively. In both cases this gives in total 3.5 loops. At LHC we obtain in the same way in total an average of 5 loops.

Using the eikonal approximation it is besides total cross sections also possible to calculate elastic scattering and diffractive excitation [25], but so far it has not been possible to calculate exclusive final states. The aim for the future is to bridge the gap between dipole cascades, AGK, and traditional MC generators, and construct an event generator fully compatible with unitarity and the AGK cutting rules.

3 Conclusions

- Multiple collisions are present in data.
- Hard subcollisions are correlated. The underlying event is different from a minimum bias event.
- Rick Field's tunes of the PYTHIA MC fit Tevatron data well, but the relation between transverse energy and multiplicity is not understood. This may indicate some kind of color

rearrangement, or a "renormalized pomeron".

- Multiple collisions and unitarity constraints are easier treated in transverse coordinate space. The dipole formalism can describe $I\!P$ loops and diffraction. The application of AGK cutting rules then implies the presence of rapidity gaps.
- For the future we hope to be able to combine the dipole formalism and traditional MC generators to obtain event generators which include diffraction and are compatible with unitarity and AGK.

References

[1] T. Sjöstrand and P. Z. Skands, JHEP **03**, 053 (2004). hep-ph/0402078.

[2] T. Sjöstrand and M. van Zijl, Phys. Rev. **D36**, 2019 (1987).

[3] G. Gustafson and G. Miu, Phys. Rev. **D63**, 034004 (2001). hep-ph/0002278;
G. Gustafson, L. Lönnblad, and G. Miu, Phys. Rev. **D67**, 034020 (2003). hep-ph/0209186.

[4] D. Cline, F. Halzen, and J. Luthe, Phys. Rev. Lett. **31**, 491 (1973);
S. D. Ellis and M. B. Kislinger, Phys. Rev. **D9**, 2027 (1974);
L. Durand and P. Hong, Phys. Rev. Lett. **58**, 303 (1987).

[5] Axial Field Spectrometer Collaboration, T. Akesson *et al.*, Z. Phys. **C34**, 163 (1987).

[6] CDF Collaboration, F. Abe *et al.*, Phys. Rev. **D47**, 4857 (1993).

[7] D0 Collaboration, V. M. Abazov *et al.*, Phys. Rev. **D67**, 052001 (2003). hep-ex/0207046.

[8] CDF Collaboration, F. Abe *et al.*, Phys. Rev. **D56**, 3811 (1997).

[9] ZEUS Collaboration, C. Gwenlan, Acta Phys. Polon. **B33**, 3123 (2002).

[10] UA1 Collaboration, C. Albajar *et al.*, Nucl. Phys. **B309**, 405 (1988).

[11] H1 Collaboration, S. Aid *et al.*, Z. Phys. **C70**, 17 (1996). hep-ex/9511012.

[12] CDF Collaboration, R. D. Field. Presented at 33rd International Conference on High Energy Physics (ICHEP 06), Moscow, Russia, 26 Jul - 2 Aug 2006;
CDF Collaboration, R. Field. Presented at 34th International Meeting on Fundamental Physics: From HERA and the Tevatron to the LHC, El Escorial, Madrid, Spain, 2-7 Apr 2006.

[13] V. A. Abramovsky, V. N. Gribov, and O. V. Kancheli, Yad. Fiz. **18**, 595 (1973).

[14] R. Enberg, G. Ingelman, and N. Timneanu, Phys. Rev. **D64**, 114015 (2001). hep-ph/0106246.

[15] J. Bartels, Z. Phys. **C60**, 471 (1993);
J. Bartels and M. Wusthoff, Z. Phys. **C66**, 157 (1995).

[16] S. Ostapchenko, Phys. Lett. **B636**, 40 (2006). hep-ph/0602139.

[17] J. Bartels, M. Salvadore, and G. P. Vacca, Eur. Phys. J. **C42**, 53 (2005). hep-ph/0503049.

[18] J. Bartels and M. G. Ryskin, Z. Phys. **C60**, 751 (1993);
J. Bartels and M. G. Ryskin, Z. Phys. **C62**, 425 (1994).

[19] A. H. Mueller, Nucl. Phys. **B415**, 373 (1994);
A. H. Mueller and B. Patel, Nucl. Phys. **B425**, 471 (1994). hep-ph/9403256;
A. H. Mueller, Nucl. Phys. **B437**, 107 (1995). hep-ph/9408245.

[20] E. Iancu, G. Soyez, and D. N. Triantafyllopoulos, Nucl. Phys. **A768**, 194 (2006). hep-ph/0510094.

[21] M. Kozlov, E. Levin, and A. Prygarin, Nucl. Phys. **A792**, 122 (2007). arXiv:0704.2124 [hep-ph].

[22] E. Avsar, G. Gustafson, and L. Lönnblad, JHEP **01**, 012 (2007). hep-ph/0610157.

[23] E. Avsar and G. Gustafson, JHEP **04**, 067 (2007). hep-ph/0702087.

[24] E. Avsar, G. Gustafson, and L. Lönnblad, JHEP **07**, 062 (2005). hep-ph/0503181.

[25] E. Avsar, G. Gustafson, and L. Lönnblad. Preprint in preparation.

Multiple interactions and AGK rules in pQCD

M. Salvadore[1†], *J. Bartels*[1], *G. P. Vacca*[2]
[1]II. Institut für Theoretische Physik, Universität Hamburg, Luruper Chaussee 149, 22761 Hamburg, Germany,
[2]Dipartimento di Fisica - Università di Bologna and INFN - Sezione di Bologna, via Irnerio 46, 40126 Bologna, Italy

Abstract
We review some aspects of multiple interactions in High Energy QCD; we discuss in particular AGK rules and present some results concerning multiple interactions in the context of jet production.

1 Introduction

Many years ago Abramovsky, Gribov and Kancheli in their pioneering paper [1] have pointed out that, for high energy hadron-hadron scattering, multiple exchange of pomerons leads to observable effects in multiparticle final states. Multi pomeron exchange induces indeed fluctuations in the rapidity densities of the produced particles; concerning the multiple inclusive production of jets, they cause long range rapidity correlations. Nowdays it has become evident that multiple interactions play a substantial role in determining the behaviour of high energy scattering. As in-depth studies of DIS at HERA in the small x region and jet physics at Tevatron have shown, diffractive events represent a substantial fraction of the total cross section.

The advent of LHC will open up a much wider kinematical window with respect to any other hadron collider which as been available so far. Needless to say, the challenging measurements aimed at the discovery of physics beyond the Standard Model require an extremely precise understanding of the background physics. In particular, it is needed to assess the effects introduced by multiple interactions. There are kinematical regions where the power suppression due to the "higher twist" nature of these effect is expected to be compensated. If a jet is produced close to the forward direction for example, one of the colliding hadrons PDF is probed in the region of very small longitudinal fraction, where the dominant gluon density undergo a step rise of the type $\propto (1/x)^{\lambda}$, $x \to 0$, $\lambda > 0$. Here is where the mellow concepts developed in the pre QCD era becomes topical again.

As far as the theoretical motivations for considering multiple interactions are concerned, it is well known that they are expected to unitarize cross sections. The resummation of Leading Logarithms (LL) $\log(1/x)$ in pQCD results in the perturbative BFKL pomeron [2–4], which violated the unitarity constraint expressed by the Froissart bound, $\sigma_{\text{tot}} \leq \log^2(s)$, $s \to \infty$. Finding a systematic way of including a minimal subset of subleading corrections in order to restore unitarity has been subject to intensive research in the past decade.

In this talk we discuss AGK rules in the context of pQCD and some recent results regarding multiple interaction effects in inclusive jet production. The relevant papers are [5, 6].

[†] speaker

2 Review of AGK rules in Regge theory

In their simplest version, AGK cutting rules are nothing but a statement about how the s-channel unitarity is encoded in reggeon diagrams. In standard perturbation theory the corresponding tool is the set of Cutkosky rules [7], which tells us how to build up the discontinuity of an amplitude at a particular order in the coupling, summing up all the possible cut diagrams contributing to the amplitude. Symbolically, we could write

$$2\mathrm{Im}\mathcal{A} = \sum_{\text{cuts}} \not{\mathcal{A}}, \tag{1}$$

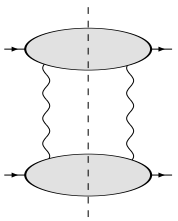
where $\not{\mathcal{A}}$ indicates generically any cut version of the amplitude $\mathcal{A}$. Such an approach is clearly unfeasible when considering reggeon diagrams, since their being already the sum of a full series in the coupling implies that we should consider an infinite set of cut amplitudes already at the simplest level beyond a single ladder. Each term in the sum of multi-ladder diagrams contains a number of possible cuts quickly growing with the number of the rungs in each ladder.

The fundamental observation of AGK was that cut reggeon diagrams where the cut cross a side line of the ladder are strongly suppressed compared to diagrams where the reggeons are cut or uncut completely. The natural question arising from this observation is whether the latter set of diagrams is alone sufficient to reconstruct the full discontinuity; the striking result pointed out in the AGK papers is the affirmative answer to this question. Let us then review their arguments.

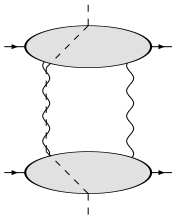
The starting point of the AGK analysis is the Sommerfeld-Watson representation of the elastic scattering amplitude $\mathcal{A}$:

$$\mathcal{A}(s,t) = \int \frac{d\omega}{2i} \xi(\omega) s^{1+\omega} \mathcal{F}(\omega,t), \qquad \xi(\omega) = \frac{\tau - e^{-i\pi\omega}}{\sin \pi\omega}\,. \tag{2}$$

The signature function can be found in [5]. The (real-valued) partial wave $\mathcal{F}(\omega,t)$ has singularities in the complex ω-plane, and the multi-Regge exchange corresponds to a particular branch cut. As we have already pointed out, the central goal of the AGK analysis is the decomposition of the contribution of the n-reggeon cut in terms of s-channel intermediate states. The absorptive part of the amplitude will consist of several different contributions: each piece belongs to a particular energy cut line, and there are several different ways of drawing such energy-cutting lines. Each of them belongs to a particular set of s-channel intermediate states. For example, a cutting line between reggeons,



belongs to double diffractive production on both sides of the cut: there is a rapidity gap between what is inside the upper blob and the lower blob. When relating this contribution with the full diagram, one requires a 'cut version' of the reggeon particle couplings N_n (represented as grey blobs in the figures). Similarly, the cut through a reggeon,



corresponds to a so-called multiperipheral intermediate state, and another cut version of the particle-reggeon coupling appears. The basis of the AGK analysis is the observation that, under very general assumptions for the underlying dynamical theory, these couplings are fully symmetric under the exchange of reggeons, and all their cut versions are identical. This property then allows to find simple relations between the different cut contributions, and to derive a set of counting rules.

Due to the analytic structure of the partial wave $\mathcal{F}(\omega, t)$ in the s-channel physical region, which is given by a set of cuts and poles on the real axis on the right side of a fixed point $\omega = \omega_0$, the amplitude $\mathcal{A}$ can be decomposed into the sum of the different contributions due to the various singularities,

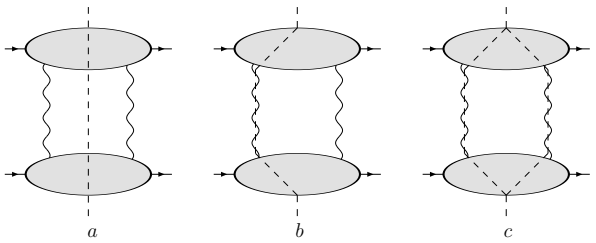
$$\mathcal{A}(s,t) = \sum_{n=1}^{\infty} \mathcal{A}_n(s,t), \tag{3}$$

where $\mathcal{A}_n(s,t)$ is the contribution due to the n-reggeon branch point. A further decomposition of Im$\mathcal{A}_n$ was found by AGK by observing that *the complete result is obtained by summing up just the diagrams where the reggeons are cut or uncut completely*, therefore neglecting all the (multitude of) diagrams where the cutting line breaks up at least one of the reggeons. For the n-reggeon cut there are $n+1$ of such contributions (any number of cut reggeon from 0 to n), and one ends up with

$$\boxed{2\text{Im}\mathcal{A}(s,t) = \sum_{n=1}^{\infty} \sum_{k=0}^{n} \not{A}_{nk}(s,t).} \tag{4}$$

Comparing this last equation with (1), it is immediately clear that we have struck a big deal: in building up the imaginary part of the amplitude, we have got rid of most of the cuts on the r.h.s. of (1), only those in (4) being left.

The simplest case, the two-Pomeron exchange, has the three contributions:



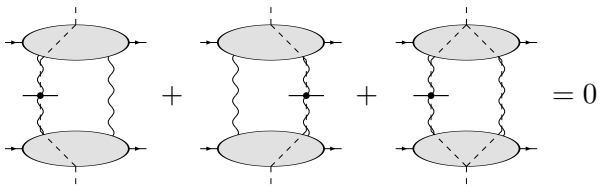
(a) in the diffractive cut all the pomerons are left uncut, and there is a rapidity gap between the fragmentation regions of the two particles; (b) in the single multiplicity cut only one pomeron

has been cut; (c) when both pomerons are cut the multiplicity of particles is doubled with respect to the previous case. In this case one obtains the well known result that the different contributions are in the proportion

$$\mathcal{A}_{20} : \mathcal{A}_{21} : \mathcal{A}_{22} = 1 : -4 : 2. \tag{5}$$

Unfortunately AGK constraints can be formulated only for a very restricted class of interaction vertices (in particular, for the $1 \to n$ Pomeron vertex). For the general case (for example, for the $2 \to 2$ vertex) this is not the case; only explicit models, e.g. calculations in pQCD as the one discussed in section 4, can provide further information.

Another remarkable result stems from the AGK analysis: for the n-particle inclusive cross section, large classes of multi-pomeron corrections cancel. For the single inclusive case all multi-Pomeron exchanges across the produced particle cancel,



(6)

We are now ready to discuss the novel features arising in QCD.

3 AGK rules in pQCD

From this brief review it follows that the central task of performing the AGK analysis in pQCD requires the computation and study of the coupling functions N_n. The simplest task is the study of the two-Pomeron exchange. Since the BFKL Pomeron is a composite state of two reggeized gluons, we have to start from the exchange of four reggeized gluons.

In the simple perturbative situation where the external particles are photons, the computation of these couplings (which are denote D_n) was performed in [8]. The two pomerons exchange contribution is encoded in the amplitude D_4. The most peculiar fact about D_4 is its decomposition into two pieces:

$$D_4 = {D_4}^I + {D_4}^R. \tag{7}$$

The first term, ${D_4}^I$, is completely symmetric under the exchange of any two gluons, whereas the second one, ${D_4}^R$, is a sum of antisymmetric terms which, as a result of bootstrap properties, can be expressed in terms of two-gluon amplitudes, D_2. Under the exchange of the two reggeized gluons, D_2 is symmetric. It is only after this decomposition has been performed, and we have arrived at reggeon particle couplings with 'good' properties, that we can start with the AGK analysis.

Starting from these functions ${D_4}^I$ and ${D_4}^R$, the investigation in [9] has shown in some detail how the AGK counting rules work in pQCD: the analysis has to be done seperately for ${D_4}^I$ and ${D_4}^R$. For the former piece, we obtain the counting arguments for the Pomerons (which is even-signatured) given by AGK; here the essential ingredient is the complete symmetry of ${D_4}^I$ under the permutation of reggeized gluons. In the latter piece, the odd-signature reggeizing gluons lead to counting rules which are slightly different from those of the even signature Pomeron:

once the bootstrap properties have been invoked and ${D_4}^R$ is expressed in terms of D_2 functions, cutting lines through the reggeized gluon appear. Since it carries negative signature, the relative weight between cut and uncut reggeon is different from the Pomeron.

In the light of these facts, we will now attempt to use of the pQCD cutting rules in a nonperturbative environment (e.g.multi-ladder exchanges in pp scattering). Basic ingredients are the nonperturbative couplings of n reggeized gluons to the proton. In order to justify the use of pQCD we need a hard scattering subprocess: we will assume that all reggeized gluons are connected to some hard scattering subprocess; consequently, each gluon line will have its transverse momentum in the kinematic region where the use of pQCD can be justified. Since AGK applies to the high energy limit (i.e. the small-x region), all t-channel gluons are reggeized. Based upon the analysis in pQCD, we now formulate a few general conditions which the nonperturbative couplings N_n have to satisfy in order to get the usual AGK counting rules:

(i) they are symmetric under the simultaneous exchange of momenta and color;
(ii) cut and uncut vertices are identical, independently where the cut line enters.

Whenever these two properties are satisfied, it can be proved that the n-reggeized gluon cut satisfies a similar set of counting rules as the original ones found by AGK, but note that, in contrast to the discussion above, in the case of reggeized gluons we do not need to consider cutting lines inside the reggeized gluons: compared to an uncut gluon, a cut gluon line is suppressed in order α_s. The multiplicity of the final state arises due to the s-channel gluons mediating the interactions between the reggeized ones.

A simple (oversimplified) model for the coupling N_n correspond to eikonal couplings:

$$N_{2n} = \Phi(1,2)\Phi(3,4)\ldots\Phi(2n-1,2n) + \text{permutations} \tag{8}$$

Squaring two of these couplings and taking the large N_c limit one obtains that the multiplicity-k contribution to the total cross section is

$$\sigma_k = \int d^2\boldsymbol{k}\; e^{i\boldsymbol{b}\cdot\boldsymbol{q}} P_k(s,\boldsymbol{b})\,, \tag{9}$$

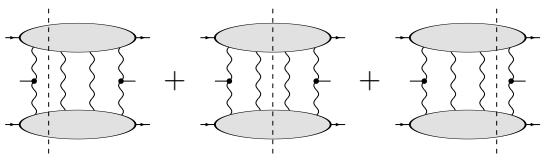
where P_k is a Poissonian distribution,

$$P_k(s,\boldsymbol{b}) = \frac{\Omega(s,\boldsymbol{b})^k}{k!} e^{-\Omega(s,\boldsymbol{b})}\,, \tag{10}$$

which is interpreted as the probability to have k cut pomerons at fixed impact parameter $\boldsymbol{b}$ and total energy $\sqrt{s}$.

4 Multiple interactions in jet production

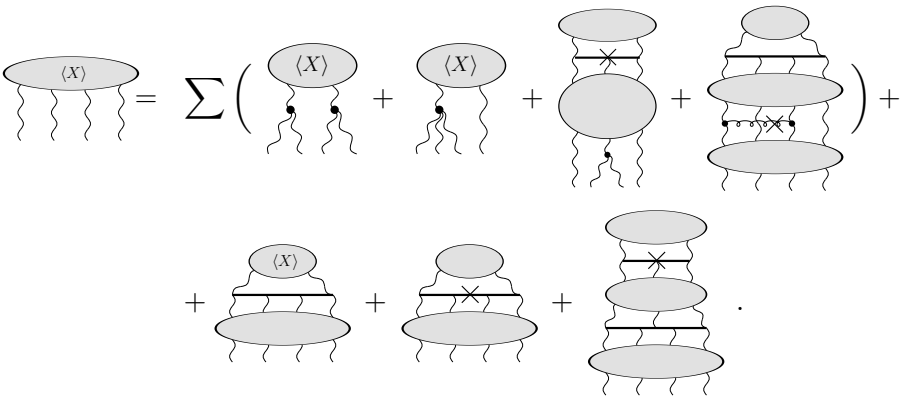
The other remarkable result of AGK, the destructive interference leading to the cancellations of diagrams for jet production as the one represented in eq. (6), has also a counterpart in QCD. The analogous result in QCD reads

$\sum$  $= 0\,,$ (11)

where the sum is over all the possible ways to attach the jet (gluon) on each side of the cut. Such interference take place only due to the summation over all possible final states and integration over the phase space. Any given final state (underlying event), would provide by itself a non-vanishing contribution. The result expressed by eq. (11) is quite general; it holds indeed for an arbitrary number of reggeized gluons and jets (see [5]).

What is left after these cancellation have been exploited are production vertices for the reggeized gluon interactions. Such vertices are model dependent, and must be computed from the underlying theory. The first step in this direction has been taken in [6], where the three cuts of the two-to-four reggeized gluon vertex have been computed. The techniques used are similar to those exploited in [8] for the computation of the two-to-four inclusive vertex (triple pomeron vertex). One writes down a set of coupled evolution equations for the particle-reggeized gluon couplings, where the evolution is given by the exchange of s-channel gluons, and the virtual corrections are taken into account by properly including the gluon Regge trajectories. In the case of single jet production, the kinematics of a gluon is kept fixed. Reshuffling such equation and using the bootstrap property, one obtains the factorization expressed by eq. (7) for the inclusive case.

In the single jet production, the coherence leading to the simple factorization (7) is partially broken by the missing integration over the phase space of the produced jet. In [6] was observed that is possible to obtain gauge invariant objects by identifying antipodal jets: one gives up the distinction between jets emitted in opposite directions in the transverse plane. If doing so, it is possible to factorize the amplitude as a sum of gauge invariant pieces. Explicitely one gets in a pictorial form



(12)

The grey blob on the l.h.s. represents the full particle-reggeized gluons coupling with a gluon fixed. On the r.h.s. one observes the various gauge invariant terms contributing to such coupling. The first three represent "reggeized" terms: they describe the exchange of less then four gluons, some of which are "composite" (they contain corrections beyond the LL reggeized gluon). The fourth term does not contribute to the cross section thanks to the AGK argument expressed by equation (11). The first term in the last line is very simple: the jet is emitted inside the pomeron attached to the external particles, and subsequently the pomeron decays into a four reggeized gluon state via the standard two-to-four vertex. The last two pieces contain new ingredients. In the first appear for the first time the production vertices for the two-to-four transition with the

emission of one jet. There are three variants of such a vertex, depending where the s-channel cut passes. In the last piece the new objects are a universal two-to-three production vertex, and three versions of a three-to-four inclusive vertex. More details and explicit expression can be found in [6].

5 Concluding remarks

We have reviewed some aspects of multiple interactions in pQCD, in the context of the total cross section and associated multiplicity distributions (AGK), and of inclusive jet production. We have shown that similar cutting rules as those first obtained in the framework of soft pomeron Regge theory emerge in pQCD as well. We have also presented new vertices for the inclusive production of a jet across the transition between two and three or four reggeized gluons. The full particle-four-gluons coupling has been decomposed in a sum of gauge invariant pieces, and each of them has been computed explicitely. Explicit expressions for all the new vertices are computed and presented in [6].

References

[1] V. A. Abramovsky, V. N. Gribov, and O. V. Kancheli, Sov. J. Nucl. Phys. **18**, 308 (1974).

[2] E. A. Kuraev, L. N. Lipatov, and V. S. Fadin, Sov. Phys. JETP **44**, 443 (1976).

[3] E. A. Kuraev, L. N. Lipatov, and V. S. Fadin, Sov. Phys. JETP **1977**, 199 (45).

[4] I. I. Balitsky and L. N. Lipatov, Sov. J. Nucl. Phys. **28**, 1597 (1978).

[5] J. Bartels, M. Salvadore, and G. P. Vacca, Eur. Phys. J. **C42**, 53 (2005).

[6] J. Bartels, M. Salvadore, and G. P. Vacca, In preparation.

[7] R. E. Cutkosky, J. Math. Phys. **1**, 429 (1960).

[8] J. Bartels and M. Wusthoff, Z. Phys. **C66**, 157 (1995).

[9] J. Bartels and M. G. Ryskin, Z. Phys. **C76**, 241 (1996).

Multiple Parton Interactions, Underlying Event and Forward Physics at LHC

Livio Fanò[†] *on behalf of ATLAS, CMS and TOTEM collaborations*
INFN and Università degli Studi di Perugia

Abstract
A variety of physics measurements in the low and high P_T regimes will be performed by the LHC experiments in proton-proton collisions at $\sqrt{S}$ =14 TeV to study the Multiple Parton Interactions (MPI) processes . The amount of activity in Minimum Bias and high P_T events will be quantified studying charged tracks and calorimetric clusters. The contribution of MPI to the Underlying Event (UE) will be studied by examining the production of charged particles in the region transverse to jets and in the central region of Drell-Yan muon pairs production. The effective double parton scattering cross section is expected to be measured in different topologies. The study of the activity in diffractive topologies will allow disentangling the MPI component of the Underlying Event from the Beam Remnant and Radiative components.

1 Introduction

Evidence for Multiple Interaction phenomena is strongly supported by both the high-P_T [AFS, CDF] and low-P_T [CDF, UA5] [1] [2] [3] phenomenology at hadron colliders. Such processes have been implemented in the most popular QCD models since the '80 [4]. The deep understanding of the softer component of the collision recently achieved by the CDF collaboration allowed even more sophisticated implementations accounting for flavour and color correlations between different partonic interactions [5]. This paper is subdivided into three sections: in the first section will be discussed the Underlying Event universality and the measurement plan for LHC, the second section is dedicated to the interplay with the forward region and in the third section is briefly discussed the double parton scattering measurements foreseen at LHC.

2 The Underlying Event universality: the measurement plan for LHC

2.1 Underlying Event in the central region

One can use the topological structure of hadron-hadron collisions to study the UE by looking only at the outgoing charged particles [6]. Jets are constructed from the charged particles using a simple clustering algorithm and then the direction of the leading charged particle jet is used to isolate regions of ϕ space that are sensitive to the UE. The transverse region to the charged particle jet direction is almost perpendicular to the plane of the hard, back to back, scattering and is therefore very sensitive to the UE (left Figure 1).

[†] speaker

The charged jet P_T ranging from 900 MeV/c (or 500 MeV/c depending on the lowest threshold for tracking) to 200 GeV/c shown in right figure 1 is quite interesting: due to the MPI, the PYTHIA tunes rise quickly and then reach an approximately flat plateau region at $P_T \sim 20$ GeV/c. Then at $P_T \sim 50$ GeV/c they begin to rise again due to initial and final state radiation which increases as the scale of the hard scattering. The two versions of PYTHIA, with Multiple Parton Interactions model, behave much differently than HERWIG without MPI.

The charged density distributions in jet topologies are studied by ATLAS and CMS with full simulation (Figures 2 and 3). In the ATLAS studies (Figure 2) the leading calorimetric jet is used as reference for the energy scale of the process and the investigated region is extended up to 1 TeV. Results are sumamrized in terms of the average number of reconstructed tracks in the transverse region and the p_T sum average of those tracks [7].

In the CMS studies (Figure 3) the energy scale is defined by the leading charged jet of the event and the observables in the transverse region are the average charged and energy density (left and right Figure 3). Reconstructed and simulated quantities agrees considering charged jet calibration [8] and the lower track reconstruction efficiency in the transverse region (where the spectrum is softer). The ability to lower down the p_T threshold for track reconstruction, allows to reach a higher discriminating power between different MC tunes (as shown in the right Figure 1) with a more inclusive measurement and a better control of the systematic errors related to efficency, purity and p_T estimation. Both ATLAS and CMS experiments have developed several techniques to lower down as much as possible the p_T threshold, the most promising relies on tracking with the pixel detector [9].

Drell Yan muon pair production has been used by CMS to study the UE in an alternative and cleaner topology [8]. In these events the scale of the hard scattering is given by the muon pair invariant mass while all the other charged tracks are attributed to the UE. Figure 4 shows the prediction for the charged density and energy density in the whole ϕ region.

2.2 Underlying Event in the forward region

In diffractive events at least one of the colliding protons survives in the final state. The beam remnant contribution is then reduced and also MPI are reduced. These topologies are studied exploiting the forward region of the detector.

Hard diffractive events, such as $pp \rightarrow p + X + Jet$ are used to study the underlying event activity in a similar way as in not-diffractive topology (eg: $pp \rightarrow X + Jet$), in example using the jet to define the energy scale and studying the UE activity in the transverse region. A comparison between the diffractive and not diffractive processes helps to disentangle the different UE components.

The CMS collaboration is pursuing a program on forward and diffractive physics also with the CASTOR [10] forward cherenkov calorimeter and the near-beam detectors at $\pm$ 220 m from the interaction point (IP) that are part of the TOTEM experiment [11]. The goal is to carry out this program as part of the routine CMS data taking with nominal LHC optics and up to the highest luminosities.

Triggering on the forward and very forward regions, using the CMS Hadron Forward (HF) and CASTOR calorimeters, may give rise to biases depending on the UE model.

The forward CASTOR detector covers the region $5.32 < |\eta| < 6.86$ and permits to investigate the forward activity using central/forward correlations at large rapidity range taking into account the effect of the long-range correlation for model with MPI. It is possible with an ad hoc forward trigger, to enhance the discriminative power in the central region. Figure 6 shows that a little difference in multiplicity in the central region for realistic models as Tune A (itune=303) [12] and new showering model (itune=304) [13] is enhanced in the forward region. For example, depending on the parameterization used for MPI model, more or less energy is taken from the beam remnant as shown in right Figure 7.

3 MPI in High-PT

The final goal is to achieve a uniform and coherent description of multiple parton processes in both High and Low-P_T case. To quantify the High-P_T contribution CMS proposes a program based on double parton scattering [14] [15]. In the simplest model a double high-P_T scattering can be interpreted as 2 different independent hard scatters superimposed. The corresponding cross section is parameterized as:

$$\sigma_{DP} = m\frac{\sigma_A\sigma_B}{2\sigma_{eff}}, \text{ where } \sigma_{eff} = (\frac{N_{DI}}{N_{DP}})(\frac{N_c(1)}{2N_c(2)})\sigma_{NSD}$$

where A and B are 2 different hard scatters, $m = 1, 2$ for indistinguishable or distinguishable scattering and σ_{eff} contains the information about the spatial distribution of the partons. In this formalism $\sigma_B/2\sigma_{eff}$ is the probability that an hard scatter B occurs given a process A and this will be larger or smaller depending on the parton spatial density. The CMS experiment foresees to accomplish this kind of studies using (as CDF [16]) 3jet+γ topology, same sign W production (that is greatly enhanced at the LHC energies as shown in figure 8) and minijet pairs production [17].

4 Conclusions

MPI can be studied using several processes:

- In the central region, studies are advanced for both CMS and ATLAS experiment using Jets and Drell-Yan topologies
- The possibility to use the forward region seems to be in a most advanced state for CMS and TOTEM experiments than for the ATLAS one, studies are ongoing exploiting the possibility to combine different detectors (TOTEM/CMS) and using a dedicated forward subdetector (CASTOR)
- Studies are also ongoing exploring the possibility to measure the double parton scattering, finalized to provide a description of the High-P_T multiple parton interaction

Final goal for LHC will be to identify as best as possible observables and regions where the sensitivity to UE, and in particular the MPI contribution, is maximized. In this way, LHC experiments can be able to properly calculate and understand the underlying event contribution to the measurement and go back to the parton level with an uncertainty as small as possible. The UE, finally, will be process dependent and needs a careful modelling. In particular, for what concern

the MPI, its contribution to the measured cross section has to be carefully understood, again a good modeling is needed to be able to subtract the contribution with only a small uncertainty.

5 Acknowledgments

Many people have contributed to the preparation of this talk with very high quality material and fruitful discussions: the CMS QCD group, Monika Grothe, Paolo Bartalini, Rick Field, Filippo Ambroglini, Klaus Rabbertz, Ferenc Sikler, Fabiola Gianotti, Craig Buttar, Arthur Moraes, Hannes Jung, Kerstin Borras and Mario Deile

References

.

References

[1] "Scaling of Pseudorapidity Distributions at c.m. Energies Up to 0.9-TeV", UA5 Collaboration, Z. Phys. C33 (1986) 1

[2] Tuning of multiple interactions generated by Pythia, CERN 2000-004, 293-300

[3] Pseudorapidity distributions of charged particles produced in $\bar{p}p$ interactions at sqrt[s]=630 and 1800 GeV, F. Abe et al., Phys. Rev. D 41(1989) 2330

[4] A multiple-interaction model for the event structure in hadron collisions, T. Sjostrand, M. van Zijl, Phys. Rev. D 36 (1987) 2019

[5] PYTHIA 6.4 Physics and Manual, T. Sjostrand et al. JHEP 0605:026,2006

[6] Charged jet evolution and the underlying event in proton anti-proton collisions at 1.8 TeV, A. A. Affolder et al. [CDF Collaboration], Phys. Rev. D 65 (2002) 092002.

[7] Les Houches 'Physics at Tev Colliders 2003' QCD/SM Working Group: Summary Report, A. M. Moraes et al. hep-ph/0403100, pgg 8-16

[8] The Underlying Event at the LHC, D. Acosta et al., CMS-NOTE 2006/067

[9] CMS TDR 8.2-Add1, CERN/LHCC 2007-009

[10] Simulation of Energy Response Linearity, Resolution and e/π Ratio for the CASTOR Calorimeter at CMS, P. Katsas A.D. Panagiotou A. Zhokin, CMS-NOTE 2006/147

[11] Prospects for Diffractive and Forward Physics at the LHC, The CMS and TOTEM diffractive and forward physics working group, CERN/LHCC 2006-039/G-124

[12] R. Field and R. C. Group (CDF Collaboration), hep-ph/0510198

[13] Transverse-Momentum-Ordered Showers and Interleaved Multiple Interactions, T. Sjstrand and P. Skands, Eur. Phys. J. C39 (2005) 129

[14] Heavy-quark production in proton-nucleus collisions at the LHC, D. Treleani et al., Int. J. Mod. Phys. A20: 4462-4468 (2005)

[15] Measurement of Double Parton Scattering in $p\bar{p}$ Collisions at sqrt(s) = 1.8 TeV, F. Abe et al., Phys. Rev. Lett. 79, 584 (1997)

[16] Measurement of Double Parton Scattering in $p\bar{p}$ Collisions at sqrt(s) = 1.8 TeV, F. Abe et al., Phys. Rev. D 56, 3811 (1997)

[17] QCD minijet cross sections, I. Sarcevic et al., Phys. Rev. D 40, 1446 - 1452 (1989)

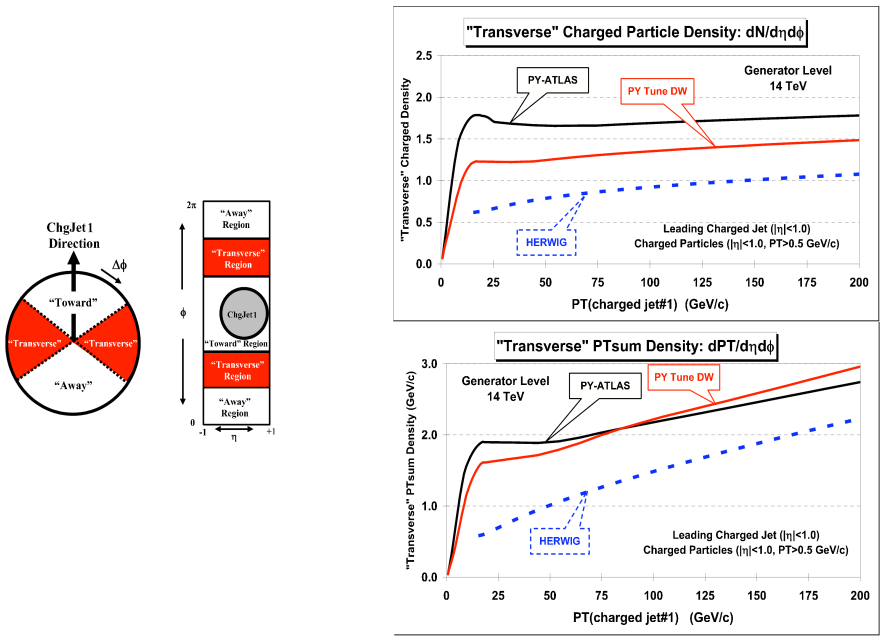


Fig. 1: Left: sketch of the proton-proton interaction in the transverse plane. Right: QCD Monte Carlo models predictions for charged particle jet production at the LHC. Average density of charged particles, $dN_{chg}/d\eta d\phi$, with $|\eta| < 1$ in the Transverse region versus the transverse momentum of the leading charged particle jet with two different cuts on the minimum p_T of the charged particle: p_T >0.5 (top) and p_T >0.9 (bottom)

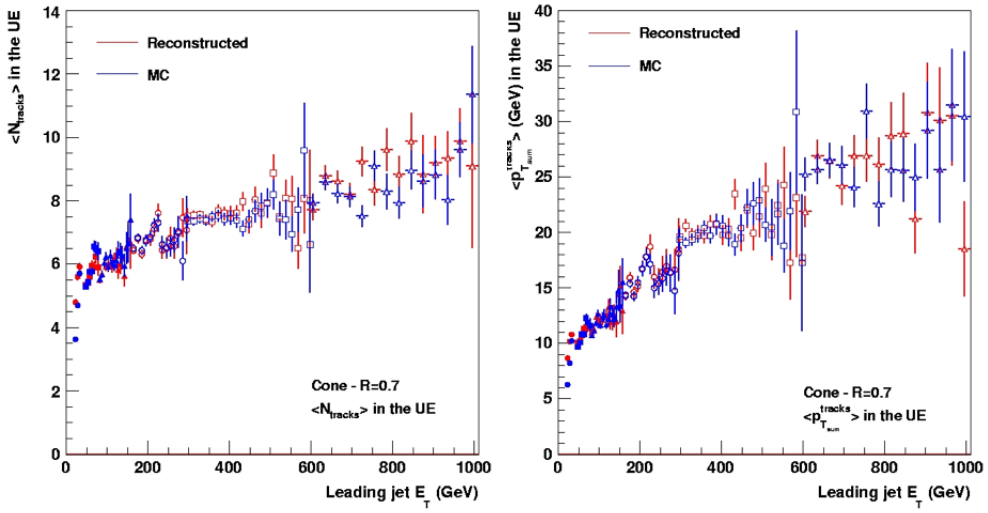


Fig. 2: ATLAS. Mean number of tracks (left) and track p_T sum (right) in the transverse region for both reconstructed (red) and MC (blue) versus the transverse energy of the leading calorimetric jet.

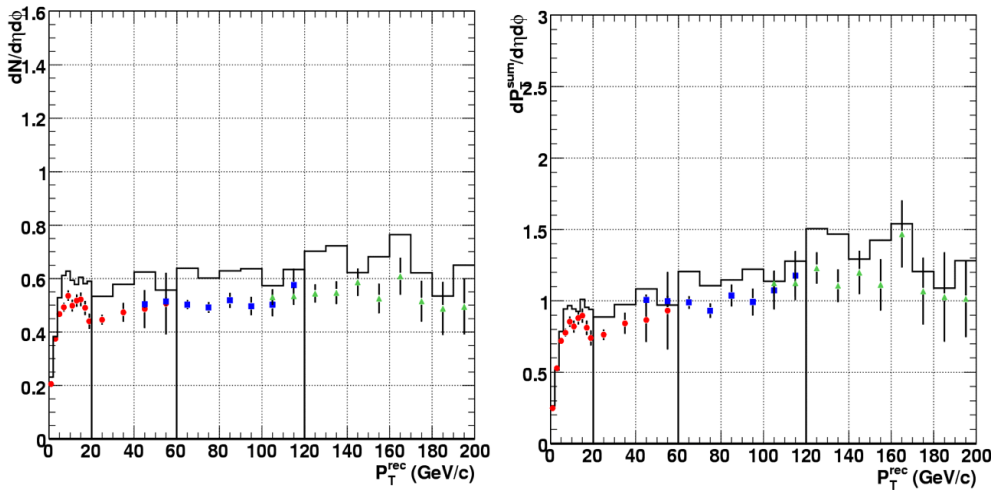


Fig. 3: CMS. Density of charged particles, $dN_{chg}/d\eta d\phi$ (left) and average charged p_T sum density, $pT^{sum}_{chg}/d\eta d\phi$ (right), with $p_T > 0.9$ GeV/c and $|\eta| < 1$ in the transverse region versus the transverse momentum of the leading charged particle jet.

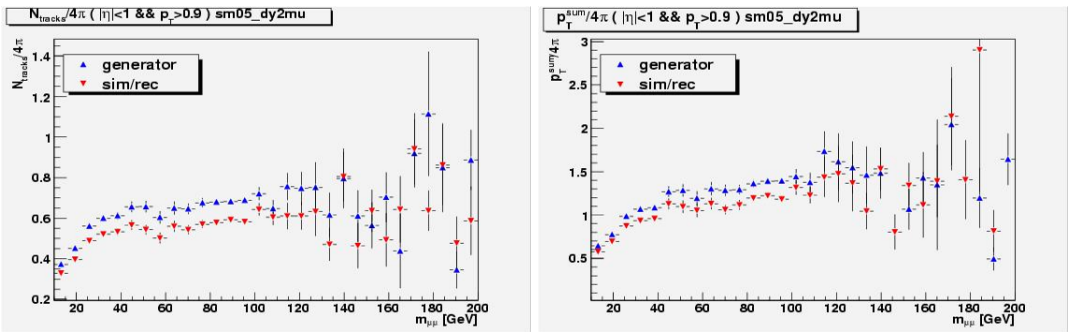


Fig. 4: CMS. Density of charged particles, $dN_{chg}/d\eta d\phi$ and average charged p_T sum density, $pT^{sum}_{chg}/d\eta d\phi$ (right), with $p_T >$0.9 GeV/c and $|\eta| <$1versus the muon-pair invariant mass. Blue triangles are referred to generator-level quantity while the red ones to the full simulated and reconstructed.



Fig. 5: Sketch in the z-y plane of the TOTEM telescopes (T1 and T2). It is also indicated the CASTOR calorimeter.

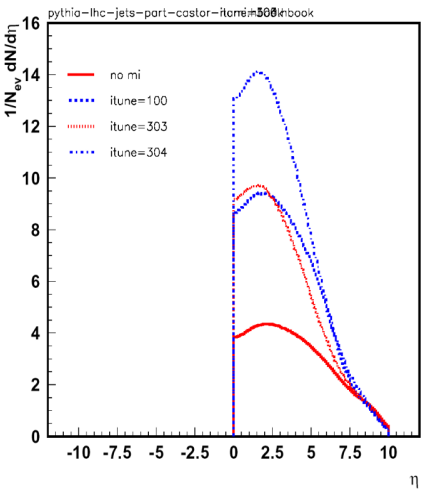


Fig. 6: Charged particles multiplicity: different activity in the central region corresponding to different MC model (itune = 303 and 304) could be enhanced triggering with CASTOR in the forward region.

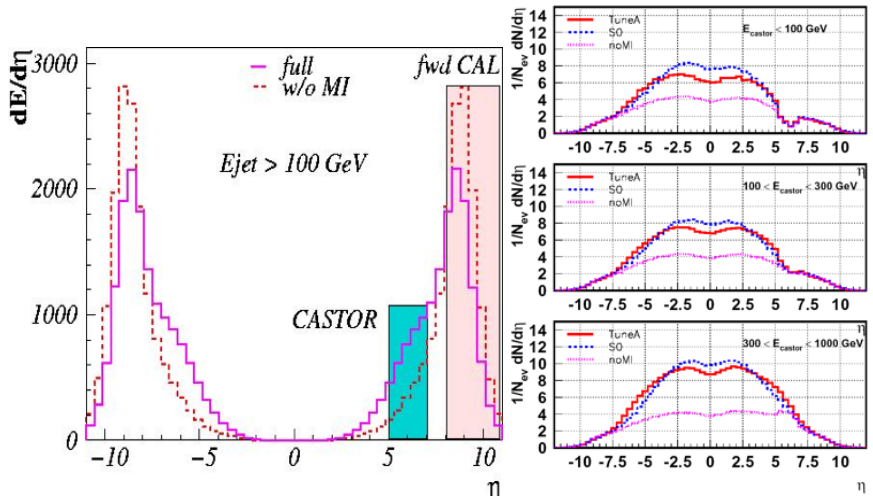


Fig. 7: The energy flow measured by CASTOR (left plot) will help to model the beam remnants contribution and long range correlations (right plot) measuring the central/forward activity using different CASTOR trigger thresholds.

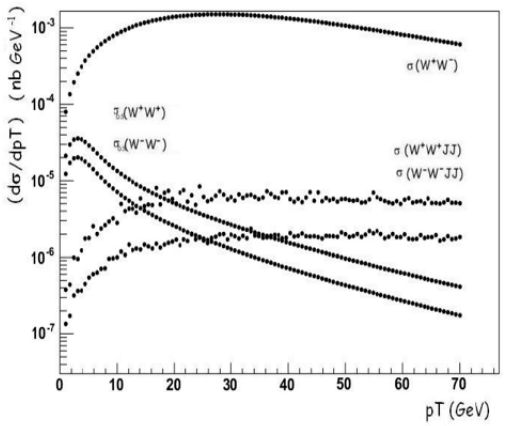


Fig. 8: differential cross section for the same sign W production. Contribution from double parton interaction are superimposed to the single parton interaction production. W^+W^- cross section is also drawn as reference.

Elastic Scattering, Total Cross-Section and Luminosity Measurements at ATLAS

C. Sbarra (on behalf of the ATLAS Luminosity and Forward Physics Working Group)
University of Bologna and INFN, Bologna, Italy

Abstract
The ATLAS strategy to monitor and measure the absolute value of the LHC luminosity at the ATLAS Interaction Point is reviewed. The absolute luminosity will be extracted from the measurement of the t-distribution of the elastic pp-scattering in the Coulomb–Nuclear interference region, as performed during dedicated low luminosity runs using specific beam optics. A luminosity monitor, LUCID, to be precisely calibrated during the elastic scattering parametrization, will also be working in standard physics conditions to provide luminosity values both for bunch by bunch beam monitoring and data analysis. The design, installation plans and expected performances of luminosity–dedicated detectors are presented as well.

1 Introduction

A precise determination of the luminosity L will be a crucial experimental issue at the LHC, as it is necessary to relate the cross section of any physical process to its event rate. Previous experiences at hadron colliders suggest that a 5–10% precision on L may be reached from the measurement of the machine parameters:

$$L = \frac{f \sum_{i=1}^{k_b} N_{1i} N_{2i}}{4\pi \sigma_x^* \sigma_y^*} \tag{1}$$

where f is the revolution frequency, k_b is the number of bunches, N_{ji} is the number of protons in bunch i of beam j and σ_x^* and σ_y^* are the transverse beam dimentions at the Interaction Point (IP). However, at the LHC such a precision would already dominate the systematic error on the determination of fundamental quantities, like the Higgs-boson coupling and the $\tan\beta$ parameter of the MSSM [1].
Besides the machine parameters, the luminosity can also be obtained by measuring the rate of a clean and well–known process. In case of non–negligible background contamination, the background cross–section must be known as well. Both QED and QCD processes will be available at LHC for this task, namely $pp \to pp\mu^+\mu^-$ and $W^\pm \to \ell^\pm\nu$, $Z \to \ell^+\ell^-$. The former will be limited in recorded statistics, whereas the latter requires a good control of the proton PDF, which makes it unclear if the achievable precision on L through this event counting will exceed the level of 5% [2].
Elastic pp-scattering at very small angles together with the total pp cross–section provide a further handle on the determination of the luminosity. In fact, by measuring the total interaction rate

(R_{tot}) and the elastic rate in the forward direction ($dR_{el}/dt|_{t=0}$) both the luminosity and the total cross section (σ_{tot}) can be determined [3]:

$$L = \frac{1}{16\pi}\frac{R_{tot}^2(1+\rho^2)}{dR_{el}/dt|_{t=0}} \tag{2}$$

$$\sigma_{tot} = \frac{16\pi}{(1+\rho^2)}\frac{dR_{el}/dt|_{t=0}}{R_{tot}^2} \tag{3}$$

where ρ represents the real–to–imaginary part ratio of the elastic amplitude in the forward direction. In order to keep extrapolation errors small, this method requires the measurement of very small proton scattering angles (down to about 10μrad at LHC) or, equivalently, very small momentum trasfer $|t| \simeq (p\theta)^2$, where p represents the proton momentum and θ its scattering angle ($t_{min} \simeq 10^{-3}$ GeV^2 at LHC). Dedicated detectors close to the beam–line and specific beam optics are therefore needed for this measurement togheter with a precise determination of the inelastic rate, in turn requiring a good coverage in pseudorapidity. The ATLAS coverage in η is somewhat limited in this context.

A further approach is to measure the elastic pp scattering down to even smaller angles so as to reach the Coulomb region where the interference between the nuclear (f_N) and the Coulomb (f_C) scattering amplitudes is maximum. In particular, both the luminosity and the total cross section can be extracted from the elastic rate dependence on the momentum transfer t in the Coulomb–Nuclear Interference (CNI) region without the need of any inelastic detector [3]. In addition, fundamental soft physics parameters like the nuclear slope and ρ can be measured. This technique was used in the past by the UA4 experiment at the CERN SPS [4], although with a somewhat simplified theoretical description of the elastic cross section. In any case, to implement it at the LHC, proton scattering angles of few μrad ($t_{min} \simeq 6.5 \times 10^{-4}$ GeV^2) need to be detected. As a comparison, the instrinsic LHC beam divergence in high–luminosity runs will be larger than 30μrad, which makes this measurement impossible during standard physics running.

2 ATLAS strategy

The strategy chosen by ATLAS will fulfil two complementary goals: to measure the absolute value of L at the ATLAS IP with $2-3\%$ precision on the one hand, and to monitor the istantaneous luminosity bunch by bunch in physics running conditions on the other hand, so as to provide online–luminosity information useful for fast control and efficient use of the beams as well as data analysis.

The program will be accomplished in various steps: the first estimate of the absolute luminosity will certainly come from the machine parameters, although with limited accuracy, and will be used to first–calibrate the ATLAS dedicated luminosity monitor, the LUCID Cherenkov counter, that will also be operational from the first beams. Then, on a longer time scale, we aim at extracting the absolute luminosity from the t-distribution of the elastic pp–scattering in the CNI region. This will be measured by another dedicated detector, the ALFA scintillating–fiber tracker, housed in Roman Pots [5] at 240 m on both sides of the ATLAS IP. Dedicated runs with specific beam optics will be needed to perform this measurement. Should not the CNI region be reached, the measurement of the forward elastic rate will still provide a measurement of the absolute Luminosity with twice the precision on the measurement of σ_{tot}, once complemented with the total

cross section as measured by the TOTEM experiment [6]. In addition, the rate of events from well known processes will be measured and used to cross–check the calibration of the luminosity monitor. In any case, the best available estimate of the absolute luminosity will be used for the calibration of LUCID, which was designed to be operational over a wide dynamic range and in different beam optics conditions.

2.1 Experimetal aspects of absolute L measurement

In order to measure the t distribution of the elastic pp–scattering in the CNI region various ingredients are needed:

- *Large β^* optics*: a beam with an intrinsic divergence at the ATLAS IP smaller than the minimum scattering angle to be measured is mandatory. This traslates into a large β^* optics, in turn implying large transverse dimensions of the beams at the ATLAS IP, and thus low luminosity. A solution has been found ($\beta^* = 2625$ m, $L \simeq 10^{27}$ cm^{-2}s^{-1}) that is compatible with the one prepared by the TOTEM collaboration for the measurement of the total cross section [6], so as to allow TOTEM and ATLAS to run high–β optics at the same time.
- *Parallel–to–point focusing*: due to the non–negligible beam size implied by the aforementioned large β^* optics ($\sigma^* \simeq 600\mu$m) the measurement of the momentum transfer $|t|$ needs to be independent of the actual vertex position. This is realized by a 90° betatron phase advance in the vertical plane between the IP and the detector, which makes the detector–level vertical displacement of the scattered proton to depend only on its scattering angle.
- *Edgeless detector in Roman Pots*: the ALFA tracking detector (scintillating–fiber based) will approach the circulating beams at $10 - 15\sigma$ (i.e. 1–2 mm) inside Roman Pots placed at 240 m on both sides of the IP. This will allow to measure t with the needed acceptance and precision. The goal spatial resolution is 30μm. Two test beam campagnes have shown that both the detector concept and the readout electronics design are valid. A further test beam is scheduled in October 2007 to test the full system, including Roman Pots. Then, eight vertical Roman Pots housed in four stations will be installed and instrumented during the 2008-2009 shutdown and become fully operational. Meanwhile, based on previous test beam results, the performance of the system has been estimated [7] by reconstructing and analysing 10M of simulated data corresponding to about one week of running at $L \simeq 10^{27}$ cm^{-2}s^{-1}. The measured t distribution has been used to extract both L and σ_{tot}, as well as ρ and the nuclear slope parameter B. Although the standard West–Yennie pp elastic cross–section formula was used (where ρ is independent of t), this study indicates that a measurement of L with about 3% precision is reachable, including systematics from both the beams and the background, as well as the detector acceptance, resolution and alignment. The statistical precision on σ_{tot} is expected to be better than 1%. Further details on the detectors and their associated electronics can be found in [3], and results of prototype–detectors can be consulted in [8].

2.2 Experimetal aspects of relative L measurement

Any detector able to count the number μ of interactions occurring in a bunch crossing (BX) can be used as a luminosity monitor, since $\mu = \sigma \cdot L$ by definition. The LUCID Cherenkov counter

will monitor μ by counting the mean number of charged particles produced in each BX within its acceptance. In order to estimate the absolute value of μ, and thus the luminosity, a proper calibration is needed. The idea is to perform it while measuring the absolute luminosity L in large β^* runs, when the probability to have more than one interaction per BX is negligible and a number $\langle N \rangle$ of charged particles is counted per interaction. Then, if ϵ is the efficiency to detect one interaction and $\langle M \rangle$ is the average number of particles counted by the LUCID at any time:

$$\mu = \frac{\langle M \rangle}{\langle N \rangle \cdot \epsilon} = L \cdot \sigma \tag{4}$$

from which

$$L = \frac{\langle M \rangle}{\langle N \rangle \cdot \sigma \cdot \epsilon} \tag{5}$$

where the product $\sigma \cdot \epsilon$ is a "luminosity independent" calibration constant obtained by comparison to the measured value of L and known with the same precision as L [9].
The LUCID detector consists of two arrays of aluminum tubes filled with C4F10 Cherenkov radiator at about 1.2 bar pressure. The arrays will be placed around the beam pipe at 17 m of the ATLAS IP, on both sides. The Cherenkov light is emitted at about 3° with respect to the impinging charged track direction and is collected at each tube end by either a PMT or an optical fiber–bundle leading to a PMT, after few reflections on the tube internal surface. The key characteristics of the detector are:

- *the Cherenkov threshold*, amounting to 10 MeV for electrons and 2.8 GeV for pions, to limit the background;
- *the pointing geometry* allowing particles coming from the IP to produce more light than background particles coming from the LUCID sides;
- *the aluminum reflectivity*, at the level of 80 to 95% in the 320–700 nm wavelength range after mechanical polishing, as measured in dedicated bench tests;
- *the radiation hardness* needed to survive in a high radiation environment.

In addition, the lack of Landau fluctuations in the number of Cherenkov photons makes the particle counting robust, while a good time resolution (2–3 ns) allows bunch by bunch measurements. Two test beam campagnes in 2006 showed that 80 p.e. are produced on average per aluminum tube traversed by a high momentum collinear track, out of wich 60 are produced in the gas and 20 in the PMT quartz window. Subsequent simulation studies including the background expected in the LUCID area in physics run conditions showed that the single PMT signal can be safely separated from the background by requiring a threshold of 50 p.e. at both low and medium luminosity ($L \leq 10^{33}$ cm^{-2}s^{-1}). Furthermore, radiation hardness tests for the PMTs with both gammas and neutrons proved that these devices are suitable for the first years of LHC running.
The LUCID implementation will therefore be performed in two phases: at low–to–medium luminosity, e.g. up to $L \simeq 10^{33}$ cm^{-2}s^{-1}, 16 tubes with direct PMT readout plus 4 tubes with optical fibers will be installed on each side, corresponding to a pseudorapidity coverage $5.6 \leq |\eta| \leq 6.0$. At higher luminosity, when the PMTs might not survive the intense radiation, 168 tubes coupled to far–away PMTs by optical fibers should replace the previous 20 on each side, covering the pseudorapidity range $5.4 \leq |\eta| \leq 6.1$.
Various methods for particle counting exist, each having both *pro* and *cons*. They range from

the counting of BX with no interactions (*zero counting*), statistically unfit at high luminosity, to *hit–counting*, subject to saturation at high luminosity when more than one charged particle is likely to hit the same tube, and *particle counting*, which is an intrinsically linear method but is sensitive to PMT gain fluctuations. Monte Carlo studies have shown that *hit–counting* is a good option for LUCID phase I, although all methods will be investigated. In particular, no saturation effects and subsequent loss of linearity are expected when the number of interactions per BX is up to 7. Should the background level be substantially worse than expected, side coincidence will be required.
A detailed study of the systematics is currently under study. The one due to differences in optics conditions between calibration and physics has been estimated to be below 1%. Based on the experience of the CDF collaboration with the CLC luminometer [10], conceptually very similar to the LUCID, we hope to keep the systematics at the level of 2%, the ones related to uncertainties in acceptance and inelastic cross–section being included in the error on the calibration constant.

3 The Zero Degree Calorimeters

A letter of Intent [11] has been presented last January to complement the ATLAS detector with Zero Degree Calorimeters (ZDC) to be inserted in the transverse aperture of the ATLAS neutral particle absorbers, at about 140 m from the IP on each side. They consists of Tungsten-quartz fiber calorimeters suited to study both heavy ions and pp physics. In particular, ZDC have shown to be very effective devices for pp beam tuning, and therefore for luminosity monitoring: at RHIC the ZDC coincidence rate versus the relative beam position has been used during Van der Meer scans to measure both the beam crossing angle and the longitudinal position of the IP. ZDC are thus expected to be useful tools to tune the accelerator parameters in the early LHC days. The installation of the hadronic module of the ATLAS ZDC is scheduled for the fall of 2007. Due to the high radiation environment, the devices are expected to survive at most three years in pp collisions at $L \simeq 10^{33}$ cm^{-2}s^{-1}.

4 Conclusions

In the last years new ideas and concerns on the matter of luminosity measurements at the LHC have led to proposals to complement the ATLAS detector with new devices in the forward region. In particular, a luminosity monitor (LUCID) will be installed around the beam pipe at about 17 m from the IP in the 2007–2008 winter, together with a pair of Zero Degree Calorimeters at about 140 m from the IP. Then, in the 2008–2009 shutdown, Roman Pot stations equipped with scintillating fiber trackers (ALFA) will be installed at 240 m from the ATLAS IP to provide elastic scattering and absolute luminosity measurements, the latter with a precision of 2–3%. The luminosity monitor will be calibrated with 5–10% accuracy at the LHC startup based on information from the accelerator. Then, a 5% accuracy on the LUCID calibration is expected at mid–term based on the rate of QED and QCD processes, to reach the goal accuracy of few percent after 2009.

References

[1] ATLAS Collaboration, *The ATLAS Physics TDR (Vol.1)*. CERN/LHCC/99-14.

[2] A. M. Cooper-Sarkar, *Precision PDF measurements at the LHC*. Talk presented at DIS 2007.

[3] ATLAS Collaboration, *ATLAS Forward Detectors for Luminosity Measurement and Monitoring*. CERN/LHCC/2004-010.

[4] UA4 Collaboration, D. Bernard *et al.*, Phys. Lett. **B198**, 583 (1987).

[5] CERN–Rome Collaboration, Phys. Lett. **66B**, 390 (1977).

[6] V. Berardi *et al.*, *TOTEM: Technical Design Report. Total cross section, elastic scattering and diffraction dissociation at the LHC at CERN*. CERN/LHCC/2004-002.

[7] H. Stenzel, *Luminosity calibration from elastic scattering*. ATL-LUM-PUB-2007-2001.

[8] S. Ask *et al.*, Nucl. Instrum. Methods Phys. Res. **A 568**, 588 (2006).

[9] S. Ask *et al.*, *Simulation of Luminosity Monitoring in ATLAS*. ATL-LUM-PUB-2006-2001.

[10] S. Jindariani *et al.*, *Luminosity Uncertainty for Run 2 up until August 2004*. CDF/ANA/7446.

[11] ATLAS Collaboration, *Zero Degree Calorimeters for ATLAS*. CERN/LHCC/2007-001.

Diffraction at HERA and implications for Tevatron and LHC

Laurent Schoeffel
CEA Saclay, DAPNIA-SPP,
91191 Gif-sur-Yvette Cedex, France

Abstract
We describe new QCD fits to diffractive cross sections measured at HERA and we use the parton densities derived from these fits to predict the shape of the dijet mass fraction in double Pomeron exchange at the Tevatron. We discuss the existence of exclusive events in this dijet channel and some prospects are given for the LHC.

1 Diffraction at HERA

One of the most important experimental results from the DESY ep collider HERA is the observation of a significant fraction (around 15%) of diffractive events in deep inelastic scattering (DIS) with large rapidity gap between the scattered proton, which remains intact, and the rest of the final system [1]. In the standard QCD description of DIS, such events are not expected in such an abundance since large gaps are exponentially suppressed due to color strings formed between the proton remnant and scattered partons. For diffractive events, however, a color neutral cluster of partons fragments independently of the scattered proton. The theoretical description of diffractive events is a real challenge since it must combine perturbative QCD effect of hard scattering with nonperturbative phenomenon of rapidity gap formation.

There are various interpretations of this phenomenon, but a very appealing one relies upon a partonic interpretation of the structure of the Pomeron [2]. It is defined in the presence of a hard scale, the photon virtuality Q^2 or jet transverse momentum, which allows to apply perturbative QCD. Soft diffraction, when such a scale is missing, is outside the scope of the model but can be described in the context of Regge pole phenomenology. This phenomenology, however, turns out to be quite useful in the description of a soft part of hard diffraction, responsible for the rapidity gap formation. In fact, it is possible to nicely describe the diffractive cross-section data from HERA by a QCD DGLAP evolution of parton distributions in the Pomeron combined with a Regge parametrisation of flux factors describing the probability of finding a Pomeron state in the proton [1]. It follows exactly the same procedure than for standard DIS except that the diffractive distributions are related to the Pomeron, whose flux factor is factorised and parametrised as a function of $x_{\mathbb{P}}$, the momentum fraction lost by the proton.

Sets of diffractive parton distribution functions (dPDFs) are shown in figure 1. In the infinite momentum frame, the dPDFs have an interpretation of conditional probabilities to find a parton in the proton with the momentum fraction $x = \beta x_{\mathbb{P}}$, where β denotes the fraction of the particular parton in the Pomeron. The gluons dominate the diffractive exchange and carry approximately 70 % of the momentum. While the quark densities are found to be relatively close for H1 and ZEUS experiments, the gluon density differs by more than a factor 2. New preliminary data from ZEUS reduce this discrepancy.

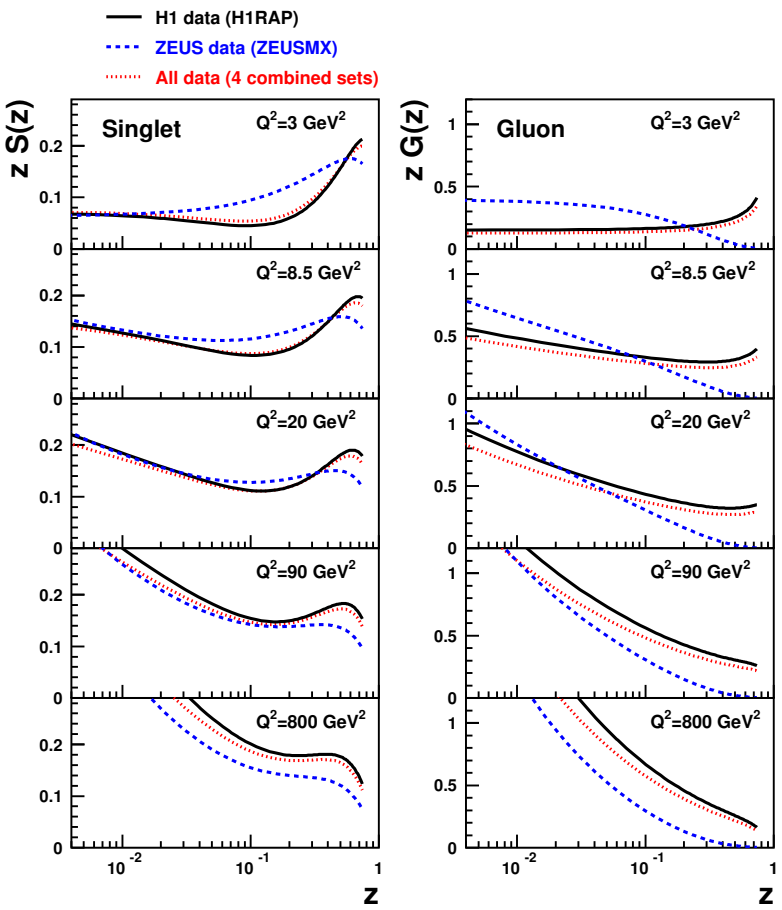


Fig. 1: Singlet and gluon distributions of the Pomeron as a function of z, the fractional momentum of the Pomeron carried by the struck parton, derived from QCD fits on H1RAP data alone, ZEUSMX data alone or the four data sets together. The parton densities are normalised to represent $x_{\mathbb{P}}$ times the true parton densities multiplied by the flux factor at $x_{\mathbb{P}} = 0.003$.

In the following, we will use the QCD fits to the H1 data to compare with the dijet mass fractions measured by the CDF collaboration in double Pomeron exchange and we discuss the possible evidence for exclusive events in this context.

2 Diffraction at Tevatron and LHC

The difference between diffraction at HERA and at the Tevatron is that diffraction can occur not only on either p or $\bar{p}$ side as at HERA, but also on both sides. The former case is called single diffraction whereas the other one double Pomeron exchange. In the same way as we defined the kinematical variables $x_{\mathbb{P}}$ and β at HERA, we define $\xi_{1,2}$ as the proton fractional momentum loss (or as the p or $\bar{p}$ momentum fraction carried by the Pomeron), and $\beta_{1,2}$, the fraction of the Pomeron momentum carried by the interacting parton. The produced diffractive mass is equal to $M^2 = s\xi_1$ for single diffractive events and to $M^2 = s\xi_1\xi_2$ for double Pomeron exchange, where

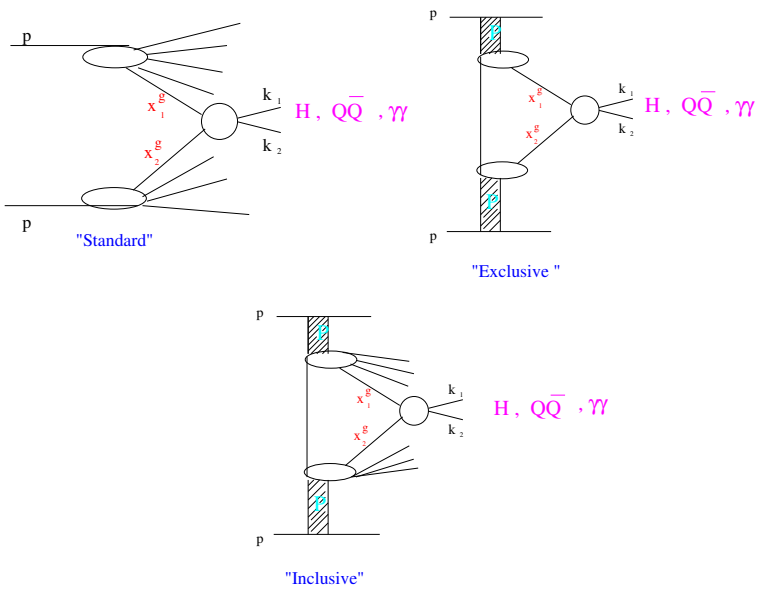


Fig. 2: *Scheme of non diffractive, inclusive double Pomeron exchange and exclusive events at the Tevatron or LHC*

$\sqrt{s}$ is the energy of the reaction in the center of mass frame. The size of the rapidity gap is of the order of $\Delta\eta \sim \log 1/\xi_{1,2}$.

It has been shown that the dPDFs of HERA can not be used directly to make predictions at the Tevatron. Indeed, factorisation does not hold and a gap survival probability of a few % has to be considered. It corresponds to the probability that there is no soft additional interaction or in other words that the event remains diffractive. Knowing the presence of this essential factor, we can discuss the case of the double Pomeron exchange at the Tevatron. A schematic view of non diffractive, inclusive double Pomeron exchange and exclusive diffractive events at the Tevatron or the LHC is displayed in figure 2. The upper left plot shows the "standard" non diffractive events where the Higgs boson, the dijet or diphotons are produced directly by a coupling to the proton associated with proton remnants. The bottom plot displays the standard diffractive double Pomeron exchange (DPE) where the protons remain intact after interaction and the total available energy is used to produce the heavy object and the Pomeron remnants. There may be a third class of processes displayed in the upper right figure, namely the exclusive diffractive production. Exclusive events allow a precise reconstruction of the mass and kinematical properties of the central object using the central detector or even more precisely using very forward detectors installed far downstream from the interaction point [3]. As mentioned above, the mass of the produced object can be computed using roman pot detectors and tagged protons, $M = \sqrt{s\xi_1\xi_2}$, where $\xi_{1,2}$ represent the fractions of energy losses for both protons. We see immediately the advantage of those processes : we can benefit from the good roman pot resolution on $\xi_{1,2}$ to get a good resolution on mass. Therefore, it is possible to measure the mass and the kinematical properties of the produced object and use this information to increase the signal over background ratio by reducing the mass window of measurement [3].

If such exclusive processes exist in DPE, the most appealing is certainly the Higgs boson production through this channel at the LHC [3]. It cannot be observed at the Tevatron due to the low production cross section, but one can use present measurements at the Tevatron to investigate any evidence for the existence of exclusive production in DPE.

3 Dijet mass fraction at the Tevatron

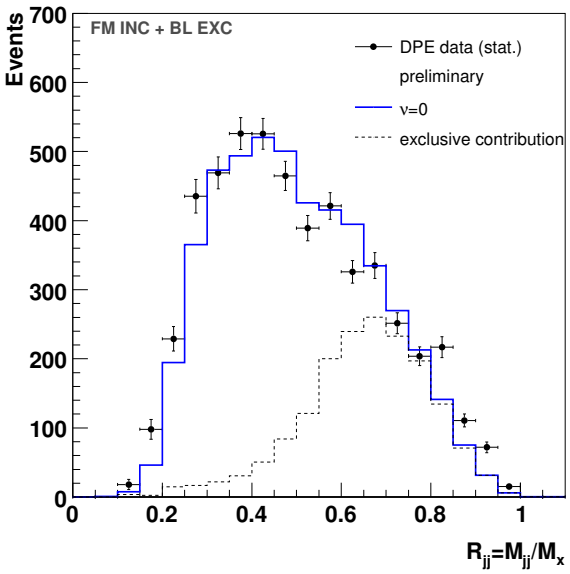


Fig. 3: Dijet mass fraction for jets $p_T > 10\,\mathrm{GeV}$. The data are compared to the sum of inclusive and exclusive predictions. The dPDFs derived from H1 data have been used together with the survival gap probability measured with single diffractive events at Tevatron.

The CDF collaboration measured the so-called dijet mass fraction (DMF) in dijet events when the antiproton is tagged in the roman pot detectors and when there is a rapidity gap on the proton side to ensure that the event corresponds to a double Pomeron exchange [3]. The measured observable R_{JJ} is defined as the ratio of the mass carried by the two jets divided by the total diffractive mass. The DMF turns out to be a very appropriate observable for identifying the exclusive production, which would manifest itself as an excess of the events towards $R_{JJ} \sim 1$. Indeed, for exclusive events, the dijet mass is essentially equal to the mass of the central system because no Pomeron remnant is present. Then, for exclusive events, the DMF is 1 at generator level and can be smeared out towards lower values taking into account the detector resolutions. The advantage of DMF is that one can focus on the shape of the distribution. The observation of exclusive events does not rely on the overall normalization which might be strongly dependent on the detector simulation and acceptance of the roman pot detector. Results are shown in figure 3 with Monte-Carlo expectations calculated using DPEMC [4]. Indeed, we see a clear deficit of events towards high values of the DMF, where exclusive events are supposed to occur. In figure 3,

a specific model describing exclusive events [5] is also added to the inclusive prediction and we obtain a good agreement between data and the sum of MC expectations [4]. It is a first evidence that exclusive events could contribute at the Tevatron [3, 6].

4 Conclusions

We have discussed a first evidence for the existence of exlusive events in double Pomeron exchange at the Tevatron. If such events can be also observed at the LHC, it would be possible to produce a Higgs boson as well as of a dijet system regarding the cross section values accessible at the LHC. First, a direct precise determination of the gluon density in the Pomeron through the measurement of the diffractive dijet cross section at the Tevatron and the LHC would be necessary if one wants to prove the existence of exclusive events in the dijet channel. In particular, a Tevatron or LHC diffractive gluon density could be extracted including *de facto* the survival gap probability. Then, the great benefit of exclusive events concerns the precise reconstruction of the mass of the central object, using roman pot detectors installed far downstream from the interaction point [3]. It gives the opportunity to work with a favorable signal/background ratio compared to standard Higgs searches with a mass below 150 GeV.

References

[1] C. Royon, L. Schoeffel, R. Peschanski and E. Sauvan, Nucl. Phys. B **746** (2006) 15 ; C. Royon, L. Schoeffel, S. Sapeta, R. Peschanski and E. Sauvan, arXiv:hep-ph/0609291.

[2] G. Ingelman, P.E.Schlein, *Phys.Lett.* **B152** (1985) 256.

[3] C. Royon, Acta Phys. Polon. B **37** (2006) 3571 [arXiv:hep-ph/0612153].

[4] M. Boonekamp and T. Kucs, Comput. Phys. Commun. **167** (2005) 217.

[5] A. Bialas, P. V. Landshoff, *Phys. Lett.* **B256** (1990) 540;
A. Bialas, R. Janik, *Zeit. für. Phys.* **C62** (1994) 487.

[6] O. Kepka and C. Royon, arXiv:0704.1956 [hep-ph].

Search for exclusive events using the dijet mass fraction

O. Kepka[1†], *C. Royon*[2]
[1]DAPNIA/Service de physique des particules, CEA/Saclay, 91191 Gif-sur-Yvette, France,
IPNP, Faculty of Mathematics and Physics, Charles University, Prague,
Center for Particle Physics, Institute of Physics, Academy of Science, Prague
[2]DAPNIA/Service de physique des particules, CEA/Saclay, 91191 Gif-sur-Yvette, France

Abstract
We use new HERA QCD fits to predict the shape of a dijet mass fraction R_{JJ} at the Tevatron, investigate the presence of exclusive signal in CDF dijet mass fraction measurement, and look for its appearance in the dijet channel at the LHC.

Exclusive diffractive production of heavy mass objects is an interesting part of the physics program at the LHC. The fact that all energy lost by scattered protons is used to create a desired object (Higgs boson, dijets, diphotons, etc.) in the central rapidity region, yields highly accurate reconstruction of its mass (e.g. Higgs mass precision can reach $\sigma(M) \sim 1\,\text{GeV}$ [1]). The energy flowing into diffractive system can be precisely computed using missing momenta of scattered protons measured by proton taggers placed in the LHC tunnel.

But the exclusive production rate is so far not confidently known. The CDF collaboration advocated a presence of exclusive signal in the dijet production, analyzing the dijet mass fraction R_{jj} distribution [2]. It was an indirect measurement since the exclusive contribution was obtained by subtracting the inclusive diffractive contribution (where the energy lost by protons is used not only for producing the heavy object but also for pomeron remnants) from the measured signal. The inclusive contribution was calculated with the knowledge of diffractive PDFs as measured at HERA.

However, looking at newer QCD fits of HERA data presented in Ref. [3] one notices significant differences from the PDFs used in CDF analysis, mainly in the gluon distribution function. Its normalization has changed by a factor of 2 plus it turned out that the QCD fits poorly constrain the gluon density at large β, where β denotes the momentum fraction of a pomeron carried into the hard interaction by an interacting parton. This is quantitatively expressed as follows: multiplying the gluon density by a factor $(1-\beta)^{\nu}$, the uncertainty on the gluon translates to the uncertainty on the parameter ν as $\nu = 0.0 \pm 0.6$. It is important to see whether this uncertainty on the gluon distribution function cannot imitate the exclusive signal in the dijet mass fraction measurement.

1 Search for the exclusive signal at the Tevatron

In the CDF measurement [2], one requests two jets with p_T greater than certain threshold $p_T^{min} = 10, 25\,\text{GeV}$ and defines the dijet mass fraction distribution R_{jj} as a ratio of the invariant dijet mass to the total diffractive energy in the event. We compared the data with two models for

[†] speaker

inclusive diffraction, namely Factorized (FM) [4] and BPR [5] model. In the first case, diffractive cross section almost exactly factorizes to the flux factor and the parton distribution function; the only factorization breaking comes through the survival probability factor which is about 0.1 for the Tevatron energies and is predicted to be 0.03 for the LHC. Pomeron parameters are obtained from the fits at HERA. BPR model, on the other hand, is viewed as an exchange of two non-perturbative pomerons with soft pomeron parameters as extracted by the Donnachie and Landshoff [6].

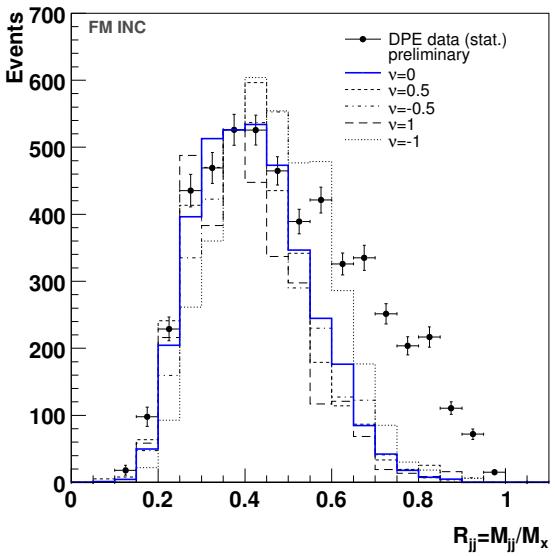


Fig. 1: Dijet mass fraction for jets $p_T > 10\,\mathrm{GeV}$ predicted by Factorized model for inclusive diffraction. The uncertainty of the gluon density at high β is obtained by multiplying the gluon distribution by $(1-\beta)^\nu$ for different values of $\nu = -1, -0.5, 0, 0.5, 1$ (non-solid lines).

In Fig. 1, one can see the comparison of the CDF dijet mass fraction data with $p_T^{min} = 10\,\mathrm{GeV}$ with the Factorized model for inclusive diffraction using the new parton densities [3]. The blue curve denotes the calculation performed with official PDFs whereas the other distributions correspond to gluon density variations at high β for $\nu = -1, -0.5, 0, 0.5, 1$. We note that even taking into account the gluon uncertainties, one is unable to explain the tail of the R_{jj} distribution and even though the data statistics is limited for a dijets with p_T above 25 GeV, the conclusion holds also. BPR model gives similar results; inclusive contribution by itself is insufficient to describe the data.

Therefore, the exclusive R_{jj} distribution predicted by Khoze-Martin-Ryskin (KMR) [7] exclusive model was added on top of the inclusive one, performing a fit of the two contributions to the data. The model is based on the direct coupling of perturbative gluons to the protons. As seen in Fig. 2, one can describe the measured CDF data well by superimposing FM and KMR model. It is worth mentioning that the relative normalizations between the inclusive and the exclusive contributions obtained from the fit for $p_T^{min} = 10\,\mathrm{GeV}$ and $p_T^{min} = 25\,\mathrm{GeV}$ jets

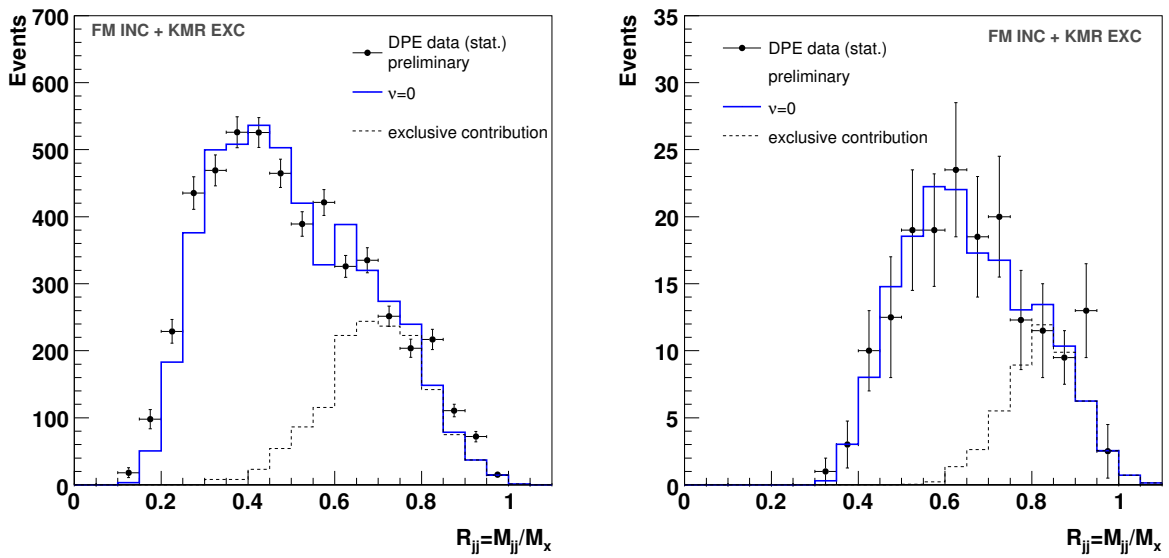


Fig. 2: Dijet mass fraction for jets $p_T > 10\,\text{GeV}$ (left) and $p_T > 25\,\text{GeV}$ (left). Inclusive contribution (FM) and exclusive contribution (KMR) are superimposed. We notice that the exclusive contribution allows to describe the tails at high R_{jj}.

where consistent with each other. This allowed us to determine the relative normalization from the Tevatron measurement and to apply it when making predictions of R_{jj} for the LHC. Let us note that the other existing model for exclusive diffraction, the Bialas-Landshoff model (BL), is disfavoured by the CDF data because it predicts to slow decrease of an exclusive dijet production cross section as a function of the jet p_T [8].

Beside the pomeron inspired models, we also investigated a prediction of the Soft color interaction model (SCI) [9] which succesfully described number of HERA and Tevatron measurements [10]. The model interprets diffraction as a consequence of a special color rearrangement in the final state controlled by just one probabilistic parameter. For low $p_T^{min} = 10\,\text{GeV}$ jet threshold, one needs to add exclusive production to describe the data similarly as in the case of pomeron inspired models, whereas for $p_T^{min} = 25\,\text{GeV}$ the need of an additional contribution to reproduce the data is not so evident. However, it is important to stress that the SCI signal comes from the single diffraction events mainly and thus producing two protons in the final state within this framework is almost impossible. Consequently, the SCI model fails to describe other characteristics of the measurement like jet rapidity distributions and is therefore in disagreement with CDF dijet data [8].

2 Dijet mass fraction at the LHC

Having fixed the relative normalization between the inclusive and exclusive production, we made a prediction of dijet mass fraction at the LHC environment. The prediction of R_{jj} for jets with p_T above 400 GeV is shown in Fig. 3 (left). The exclusive contribution manifests itself as a

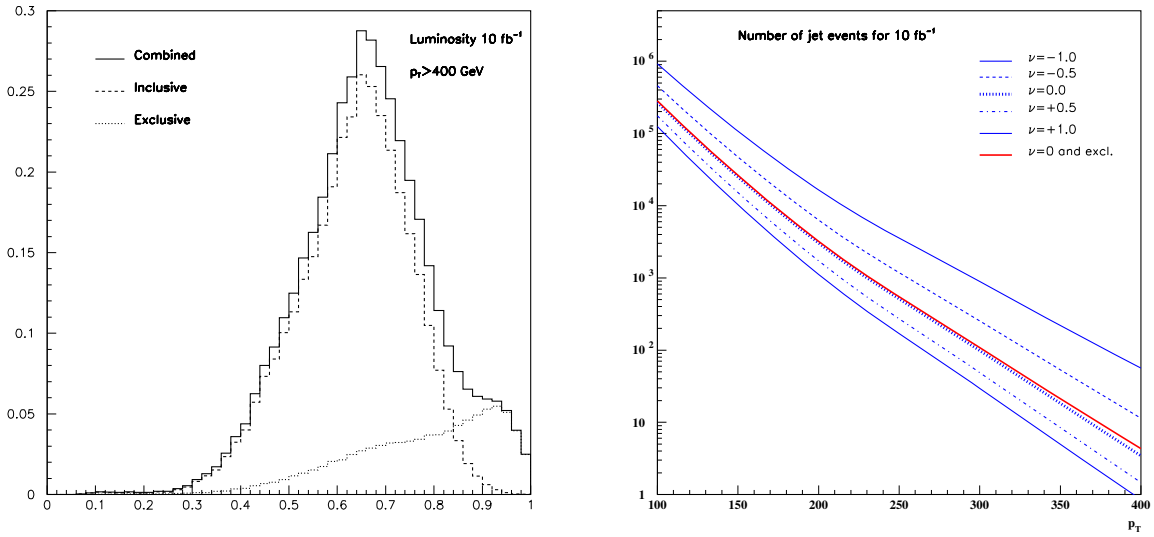


Fig. 3: Left:dijet mass fraction at the LHC for jets $p_T > 400$ GeV. Inclusive contribution (FM) and exclusive contribution (KMR) are superimposed. The exclusive signal appears at high R_{jj}. Right: number of jet events as a function of a jet threshold. The gluon uncertainty in the calculation can overshadow the signal due to the exclusive events.

peak toward high R_{jj}. Precise prediction of the dijet mass fraction distribution depends on many peculiarities, e.g. parameters of the pomeron flux, pomeron structure function, or survival probability factor. One of the important factors is the gluon density in the pomeron. Its tail at high β can significantly influence the number of dijet diffractive events as demonstrated in Fig. 3 (right). The signal due to the exclusive production could be mimicked by the uncertainty on the gluon. It is therefore desirable to perform QCD fits at the LHC to extract the pomeron parton densities precisely in order to be able to distinguish the exclusive exclusive signal.

References

[1] C. Royon, Mod. Phys. Lett. **A18**, 2169 (2003). hep-ph/0308283.

[2] C. Collaboration, *Observation Of Exclusive Dijet Production at Fermilab Tevatron, CDF note 8493* (unpublished).

[3] C. Royon, L. Schoeffel, S. Sapeta, R. Peschanski, and E. Sauvan (2006). hep-ph/0609291.

[4] G. Ingelman and P. E. Schlein, Phys. Lett. **B152**, 256 (1985).

[5] M. Boonekamp, R. Peschanski, and C. Royon, Phys. Rev. Lett. **87**, 251806 (2001). hep-ph/0107113; M. Boonekamp, R. Peschanski, and C. Royon, Nucl. Phys. **B669**, 277 (2003). hep-ph/0301244.

[6] A. Donnachie and P. V. Landshoff, Phys. Lett. **B296**, 227 (1992). hep-ph/9209205.

[7] V. A. Khoze, A. D. Martin, and M. G. Ryskin, Eur. Phys. J. **C19**, 477 (2001). Erratum-ibid.C20:599,2001; V. A. Khoze, A. D. Martin, and M. G. Ryskin, Eur. Phys. J. **C23**, 311 (2002). hep-ph/0111078; V. A. Khoze, A. D. Martin, and M. G. Ryskin, Eur. Phys. J. **C24**, 581 (2002). hep-ph/0203122.

[8] O. Kepka and C. Royon (2007). arXiv:0704.1956 [hep-ph].

[9] A. Edin, G. Ingelman, and J. Rathsman, Z. Phys. **C75**, 57 (1997). hep-ph/9605281;
R. Enberg, G. Ingelman, A. Kissavos, and N. Timneanu, Phys. Rev. Lett. **89**, 081801 (2002).
hep-ph/0203267.

[10] R. Enberg, G. Ingelman, and N. Timneanu, Phys. Rev. **D64**, 114015 (2001). hep-ph/0106246.

Diffractive production of quarkonia

Antoni Szczurek[1,2]
[1]Institute of Nuclear Physics Polish Academy of Sciences, Cracow, Poland
[2]Institute of Physics, University of Rzeszów, Rzeszów, Poland

Abstract
I discuss two selected examples of diffractive production of quarkonia: $pp \to p\eta' p$ and $pp \to pJ/\psi p$. In the first case I consider diffractive pQCD approach and $\gamma\gamma$ fusion, in the second case the amplitude is linked to the amplitude of the process for J/ψ photoproduction at HERA. Absorption effects are discussed briefly for the second reaction.

1 Introduction

Exclusive production of mesons was studied in details only at fixed target collisons at CERN. At present, there is ongoing investigations at Tevatron aiming to measure the exclusive production of both vector and scalar quarkonia, but no result is yet publicly available. Only an upper limit for χ_c was given up to now [1].

There is a long standing debate about the nature of the pomeron. The approximate $\sin^2(\Phi)$ (Φ is the azimuthal angle between outgoing protons) dependence observed experimentally for $pp \to pp\eta'$ [2] was interpreted in Ref. [3] as due to (vector pomeron)-(vector pomeron)-(pseudoscalar meson) coupling. The QCD-inspired calculation for diffractive production of pseudoscalar mesons was presented only recently in Ref. [4]. Here I shall present some results from that analysis obtained within the pQCD approach of Khoze-Martin-Ryskin (KMR) [5].

Recently the J/ψ exclusive production in proton-proton and proton-antiproton collisions was suggested as a candidate in searches for odderon exchange [6]. In order to identify the odderon exchange one has to consider all other possible processes leading to the same final channel. One of such processes, probably dominant, is pomeron-photon or photon-pomeron fusion [7].

The diffractive photoproduction of J/ψ–mesons has been recently a subject of thorough studies at HERA [8, 9], and serves to elucidate the physics of the QCD pomeron and/or the small–x gluon density in the proton (for a recent review and references, see [10]). Being charged particles, protons/antiprotons available at RHIC, Tevatron and LHC are a source of high energy Weizsäcker–Williams photons. Those photons interact with the other nucleon. In some cases such an interaction leads to elastical (ground state proton) production of J/ψ. In the approach presented here the amplitude for the $pp \to ppJ/\psi$ reaction is related to the amplitude of the photoproduction $\gamma p \to J/\psi p$ [7]. Such a method of calculating cross section is expected to be much more precise than any QCD approach which does not refer to the ep HERA data.

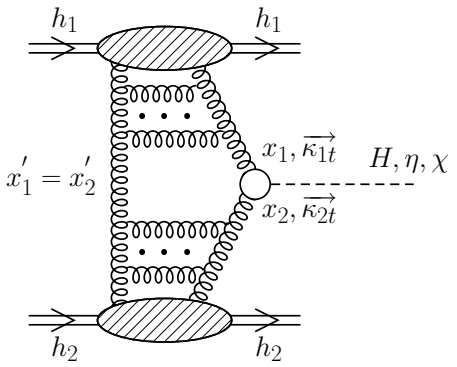


Fig. 1: The sketch of the bare QCD mechanism. The kinematical variables are shown in addition.

2 Diffractive production of η'

Following the formalism for the diffractive double-elastic production of the Higgs boson one can write the amplitude from Fig.1 as

$$\mathcal{M}^{g^*g^*\to\eta'}_{pp\to p\eta' p} = i\,\pi^2 \int d^2k_{0,t} V(k_1,k_2,P_M) \frac{f^{off}_{g,1}(x_1,x_1',k^2_{0,t},k^2_{1,t},t_1) f^{off}_{g,2}(x_2,x_2',k^2_{0,t},k^2_{2,t},t_2)}{k^2_{0,t}\,k^2_{1,t}\,k^2_{2,t}}\,, \quad (1)$$

where $f's$ are skewed unintegrated gluon distributions. For more details see [4].

As an example in Fig. 2 I show the results of calculations obtained with several models of UGDF (for details see [4]) for relatively low energy W = 29.1 GeV. For comparison I show also the contribution of the $\gamma^*\gamma^*$ fusion mechanism. The contribution of the last mechanism is much smaller than the contribution of the diffractive QCD mechanism.

The diffractive and $\gamma^*\gamma^*$ contributions have very different dependence on four-momentum transfers. In Fig.3 I present two-dimensional maps $t_1 \times t_2$ of the cross section for the QCD mechanism (KL UGDF) and the QED mechanism (Dirac terms only) for the Tevatron energy W = 1960 GeV. If $|t_1|, |t_2| > 0.5$ GeV^2 the QED mechanism is clearly negligible. However, at $|t_1|, |t_2| < 0.2$ GeV^2 the QED mechanism may become equally important or even dominant. However, the details depend strongly on UGDFs.

Finally in Fig.4 I show energy dependence of the total cross section for the $pp \to p\eta' p$ reaction for different UGDFs. Quite different results are obtained for different UGDFs. The cross section with the Kharzeev-Levin type distribution (based on the idea of gluon saturation) gives the cross section which is relatively small and almost idependent of beam energy. In contrast, the BFKL distribution leads to strong energy dependence. The sensitivity to the transverse momenta of initial gluons can be seen by comparison of the two solid lines calculated with the Gaussian UGDF with different smearing parameter σ_0 = 0.2 and 0.5 GeV. The contribution of the $\gamma^*\gamma^*$ fusion mechanism (red dash-dotted line) is fairly small and only slowly energy dependent.

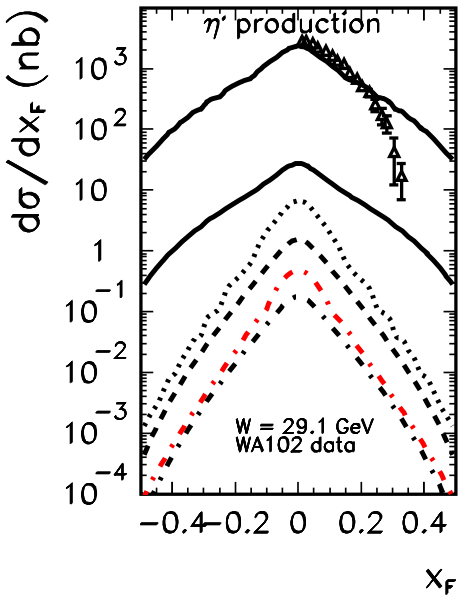


Fig. 2: $d\sigma/dx_F$ as a function of Feynman x_F for W = 29.1 GeV and for different UGDFs. The $\gamma^*\gamma^*$ fusion contribution is shown by the dash-dotted (red) line (second from the bottom). The experimental data of the WA102 collaboration are shown for comparison. The dashed line corresponds to the KL distribution, dotted line to the GBW distribution and the dash-dotted to the BFKL distribution. The two solid lines correspond to the Gaussian distribution with details explained in the original paper. No absorption corrections were included here.

3 Photoproduction of J/ψ

The basic mechanisms leading to the exclusive production of J/ψ are shown in Fig.5. The amplitude for the corresponding $2 \to 3$ process can be written as

$$\begin{aligned}\mathcal{M}^{\lambda_1\lambda_2\to\lambda_1'\lambda_2'\lambda_V}_{h_1h_2\to h_1h_2V}(s,s_1,s_2,t_1,t_2) &= \mathcal{M}_{\gamma I\!P}+\mathcal{M}_{I\!P\gamma}\\ &= \langle p_1',\lambda_1'|J_\mu|p_1,\lambda_1\rangle\epsilon^*_\mu(q_1,\lambda_V)\frac{\sqrt{4\pi\alpha_{em}}}{t_1}\mathcal{M}^{\lambda_{\gamma^*}\lambda_2\to\lambda_V\lambda_2}_{\gamma^*h_2\to Vh_2}(s_2,t_2,Q_1^2)\\ &+\langle p_2',\lambda_2'|J_\mu|p_2,\lambda_2\rangle\epsilon^*_\mu(q_2,\lambda_V)\frac{\sqrt{4\pi\alpha_{em}}}{t_2}\mathcal{M}^{\lambda_{\gamma^*}\lambda_1\to\lambda_V\lambda_1}_{\gamma^*h_1\to Vh_1}(s_1,t_1,Q_2^2)\,.\end{aligned} \tag{2}$$

After some algebra it can be written in the compact form:

$$\begin{aligned}\boldsymbol{M}(\boldsymbol{p}_1,\boldsymbol{p}_2) &= e_1\frac{2}{z_1}\frac{\boldsymbol{p}_1}{t_1}\mathcal{F}_{\lambda_1'\lambda_1}(\boldsymbol{p}_1,t_1)\mathcal{M}_{\gamma^*h_2\to Vh_2}(s_2,t_2,Q_1^2)\\ &+e_2\frac{2}{z_2}\frac{\boldsymbol{p}_2}{t_2}\mathcal{F}_{\lambda_2'\lambda_2}(\boldsymbol{p}_2,t_2)\mathcal{M}_{\gamma^*h_1\to Vh_1}(s_1,t_1,Q_2^2)\,.\end{aligned} \tag{3}$$

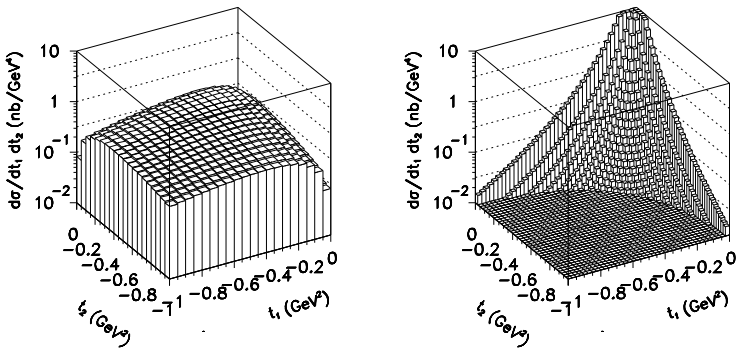


Fig. 3: Two-dimensional distribution in $t_1 \times t_2$ for the diffractive QCD mechanism (left panel), calculated with the KL UGDF, and the $\gamma^*\gamma^*$ fusion (right panel) at the Tevatron energy W = 1960 GeV. No absorption corrections were included here.

The differential cross section is given in terms of $\boldsymbol{M}$ as

$$d\sigma = \frac{1}{512\pi^4 s^2} |\boldsymbol{M}|^2 \, dy dt_1 dt_2 d\phi \,, \tag{4}$$

where y is the rapidity of the vector meson, and ϕ is the angle between $\boldsymbol{p}_1$ and $\boldsymbol{p}_2$. Notice that the interference between the two mechanisms $\gamma\mathbb{P}$ and $\mathbb{P}\gamma$ is proportional to $e_1 e_2 (\boldsymbol{p}_1 \cdot \boldsymbol{p}_2)$ and introduces a charge asymmetry as well as an angular correlation between the outgoing protons.

In Fig.6 I collect rapidity distributions for different energies relevant at RHIC, Tevatron and LHC. One observes an occurence of a small dip in the distribution at midrapidities at LHC energy. One should remember, however, that the distribution for the LHC energy is long-distance extrapolation of the $\gamma^* p \to J/\psi p$ amplitude (or cross section) to unexplored yet experimentally energies $W_{\gamma p}$. Therefore a real experiment at Tevatron and LHC would help to constrain cross sections for $\gamma p \to J/\psi p$ process.

In Fig.7 I show two-dimensional distributions in rapidity and the azimuthal angle. Surprisingly, the interference effect between both diagrams is significant over broad range of J/ψ rapidity. One can see that even at large J/ψ rapidities one observes ansisotropic distributions in the azimuthal angle. This means that interference between photon-pomeron and pomeron-photon mechanisms survives up to large rapidities.

The parametrization of the $\gamma^* p \to Vp$ amplitude which describes corresponding experimental data (see [7]) includes effectively absorption effects due to final state Vp interactions. In the $pp \to ppJ/\psi$ ($p\bar{p} \to p\bar{p}J/\psi$) reaction the situation is more complicated as here pp (or $p\bar{p}$) strong rescatterings occur in addition. In Ref. [7] we have included only elastic rescatterings shown schematically in Fig.8.

In order to demonstrate the effect of the absorption in Fig.9 I show the ratio of the cross section with absorption to that without absorption as a function of t_1 and t_2, for $p\bar{p}$ (left) and pp (right). Generally, the bigger t_1 and/or t_2 the bigger the absorption. On average, the absorption for the $p\bar{p}$ reaction is smaller than the absorption for the pp reactions.

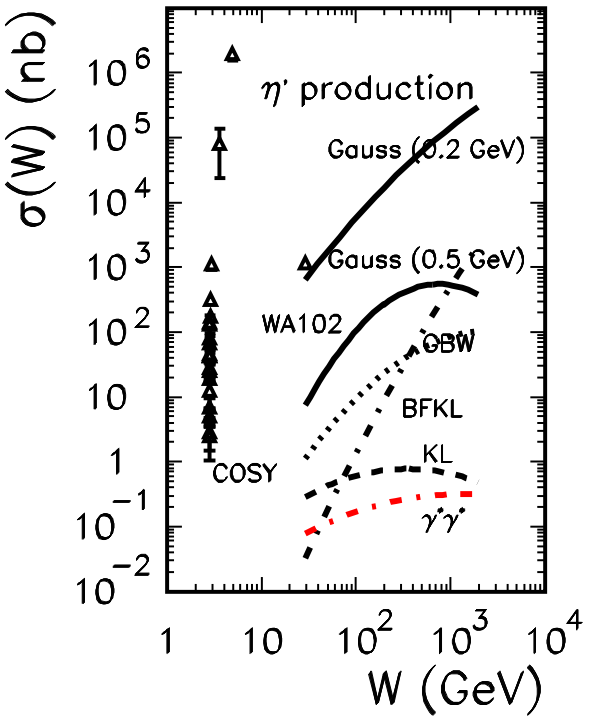


Fig. 4: σ_{tot} as a function of center of mass energy for different UGDFs. The $\gamma^*\gamma^*$ fusion contribution is shown by the dash-dotted (red) line. The world experimental data are shown for reference. No absorption corrections were included here.

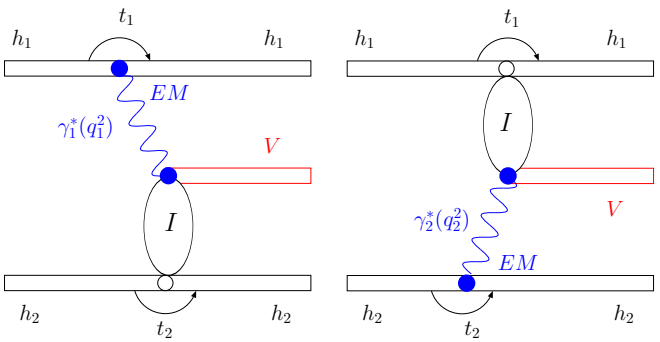


Fig. 5: The sketch of the two mechanisms considered in the present paper: photon-pomeron (left) and pomeron-photon (right). Some kinematical variables are shown in addition.

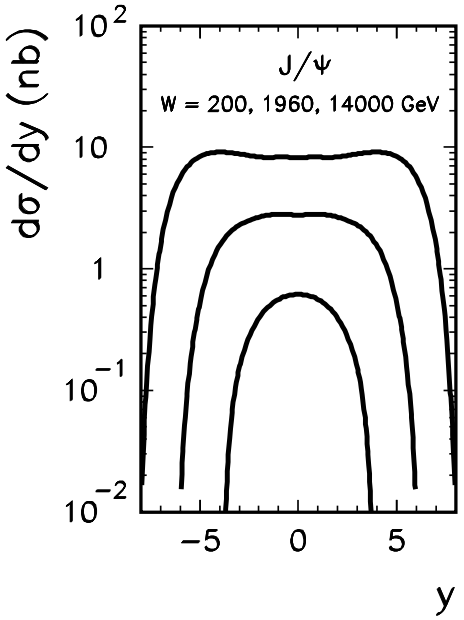


Fig. 6: $d\sigma/dy$ for exclusive J/ψ production as a function of y for RHIC, Tevatron and LHC energies. No absorption corrections were included here.

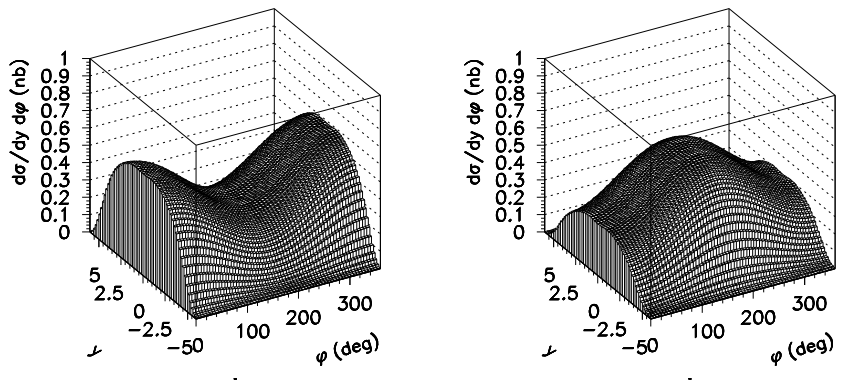


Fig. 7: $d\sigma/dyd\Phi$ for W = 1960 GeV and for $p\bar{p}$ (left panel) and pp (right panel) collisions. No absorption corrections were included here.

4 Summary

In contrast to diffractive Higgs production, in the case of ligh meson production the main contribution to the diffractive amplitude comes from the region of very small gluon transverse momenta and very small longitudinal momentum fractions. In this case application of Khoze-Martin-

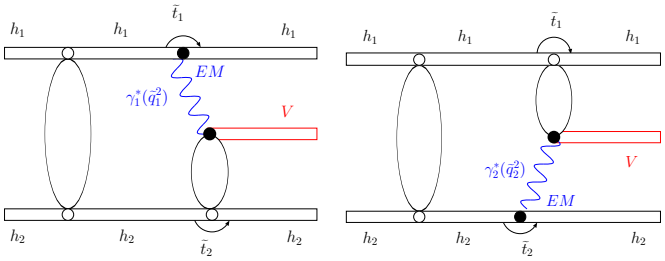


Fig. 8: The sketch of the elastic rescattering amplitudes. Some kinematical variables are shown in addition.

Ryskin UGDFs seems not justified and we have to rely on UGDFs constructed for this region.

The existing models of UGDFs predict cross section much smaller than the one obtained by the WA102 collaboration at the center-of-mass energy W = 29.1 GeV. This may signal presence of subleading reggeons at the energy of the WA102 experiment or suggest a modificaction of UGDFs in the nonperturbative region of very small transverse momenta.

Due to a nonlocality of the loop integral our model leads to sizeable deviations from the $\sin^2\Phi$ dependence (predicted in the models of one-step fusion of two vector objects). The $\gamma^*\gamma^*$ fusion may be of some importance only at extremely small four-momentum transfers squared.

It was shown in [7] that at the Tevatron energy one can study the exclusive production of J/ψ at the photon-proton center-of-mass energies 70 GeV $< W_{\gamma p} <$ 1500 GeV, i.e. in the unmeasured region of energies, much larger than at HERA. At LHC this would be correspondingly 200 GeV $< W_{\gamma p} <$ 8000 GeV. At very forward/backward rapidities this is an order of magnitude more than possible with presently available machines.

An interesting azimuthal-angle correlation pattern has been obtained due to the interference of photon-pomeron and pomeron-photon helicity-preserving terms.

We have estimated also absorption effects. In some selected configurations the absorption effects may lead to the occurence of diffractive minima. The exact occurence of diffractive minima depends on the values of the model parameters. Such minima are washed out when integrated over the phase space or even its part. We have found that on average the rescattering effects in proton-antiproton reactions are much bigger than in proton-proton reactions. In this case the obvious isospin violation is of electromagnetic origin due to the interference of diagrams with photon exchange.

ACKNOWLEDGEMENTS

I thank Hannes Jung and his colleagues for very efficient organization of the conference and hospitality. The collaboration with Roman Pasechnik, Oleg Teryaev and Wolfgang Schäfer on the issues presented here is acknowledged. A partial support by the MEiN research grant 1 P03B 028 28 (2005-08).

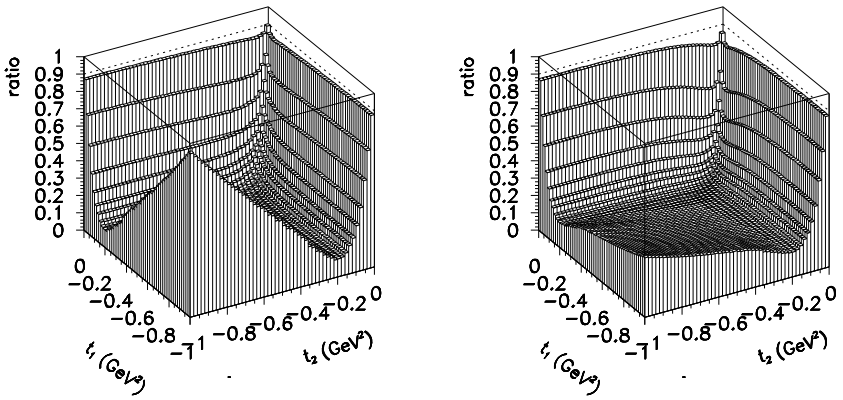


Fig. 9: The ratio of the cross sections with absorption to that without absorption for $p\bar{p}$ (left panel) and pp (right panel) scattering. Here the integration over -1 GeV^2 $< t_1, t_2 <$ 0.0 and -1 $< y <$ 1 is performed.

References

[1] M. Gallinaro [On behalf of the CDF Collaboration], Acta Phys. Polon. B **35**, 465 (2004) [arXiv:hep-ph/0311192].

[2] D. Barberis et al. (WA102 collaboration), Phys. Lett. **B422**, 399 (1998).

[3] F.E. Close and G.A. Schuler, hep-ph/9905305, Phys. Lett. **B464**, 279 (1999).

[4] A. Szczurek, R. S. Pasechnik and O. V. Teryaev, Phys. Rev. D **75**, 054021 (2007) [arXiv:hep-ph/0608302].

[5] V.A. Khoze, A.D. Martin and M.G. Ryskin, Phys. Lett. B **401**, 330 (1997);
V.A. Khoze, A.D. Martin and M.G. Ryskin, Eur. Phys. J. C **23**, 311 (2002);
A.B. Kaidalov, V.A. Khoze, A.D. Martin and M.G. Ryskin, Eur. Phys. J. C **31**, 387 (2003) [arXiv:hep-ph/0307064];
A.B. Kaidalov, V.A. Khoze, A.D. Martin and M.G. Ryskin, Eur. Phys. J. C **33**, 261 (2004);
V.A. Khoze, A.D. Martin, M.G. Ryskin and W.J. Stirling, Eur. Phys. J. C **35**, 211 (2004).

[6] A. Bzdak, L. Motyka, L. Szymanowski and J.-R. Cudell, arXiv: hep-ph/0702134.

[7] W. Schäfer and A. Szczurek, arXiv:0705.2887.

[8] S. Chekanov *et al.* [ZEUS Collaboration], Eur. Phys. J. C **24**, 345 (2002).

[9] A. Aktas *et al.* [H1 Collaboration], Eur. Phys. J. C **46**, 585 (2006).

[10] I. Ivanov, N.N. Nikolaev and A.A. Savin, Phys. Part. Nucl. **37**, 1 (2006).

Rapidity gap survival in the black-disk regime[†‡]

L. Frankfurt[1]*, C.E. Hyde*[2]*, M. Strikman*[3§]*, C. Weiss*[4]
[1] School of Physics and Astronomy, Tel Aviv University, Tel Aviv, Israel
[2] Old Dominion University, Norfolk, VA 23529, USA, and
Laboratoire de Physique Corpusculaire, Université Blaise Pascal, 63177 Aubière, France
[3] Department of Physics, Pennsylvania State University, University Park, PA 16802, USA
[4] Theory Center, Jefferson Lab, Newport News, VA 23606, USA

Abstract

We summarize how the approach to the black–disk regime (BDR) of strong interactions at TeV energies influences rapidity gap survival in exclusive hard diffraction $pp \to p + H + p$ ($H = \text{dijet}, \bar{Q}Q, \text{Higgs}$). Employing a recently developed partonic description of such processes, we discuss (a) the suppression of diffraction at small impact parameters by soft spectator interactions in the BDR; (b) further suppression by inelastic interactions of hard spectator partons in the BDR; (c) effects of correlations between hard and soft interactions, as suggested by various models of proton structure (color fluctuations, spatial correlations of partons). Hard spectator interactions in the BDR substantially reduce the rapidity gap survival probability at LHC energies compared to previously reported estimates.

1 Introduction

At high energies strong interactions enter a regime in which cross sections are comparable to the "geometric size" of the hadrons, and unitarity becomes an essential feature of the dynamics. By analogy with quantum–mechanical scattering from a black disk, in which particles with impact parameters $b < R_{\text{disk}}$ experience inelastic interactions with unit probability, this is known as the black–disk regime (BDR). The approach to the BDR is well–known in soft interactions, where it generally can be attributed to the "complexity" of the hadronic wave functions. It is seen *e.g.* in phenomenological parametrizations of the pp elastic scattering amplitude, whose profile function $\Gamma(b)$ approaches unity at $b = 0$ for energies $\sqrt{s} \gtrsim 2\,\text{TeV}$. More recently it was realized that the BDR is attained also in hard processes described by QCD, due to the increase of the gluon density in the proton at small x. Theoretically, this phenomenon can be studied in the scattering of a small–size color dipole ($d \sim 1/Q$) from the proton. Numerical studies show that at $\sqrt{s} \sim$ few TeV the dipole–proton interaction is close to "black" up to $Q^2 \sim$ several 10 GeV^2 [1]. This fact has numerous implications for the dynamics of pp collisions at the LHC, where multiple hard

[†] A preliminary version of this report was published in the proceedings of DIS07, Munich, 16–20 Apr. 2007, arXiv:0708.3106 [hep-ph].

[‡] Notice: Authored by Jefferson Science Associates, LLC under U.S. DOE Contract No. DE-AC05-06OR23177. The U.S. Government retains a non-exclusive, paid-up, irrevocable, world-wide license to publish or reproduce this manuscript for U.S. Government purposes.

[§] speaker

interactions are commonplace. For example, it predicts dramatic changes in the multiplicities and p_T spectra of forward particles in central pp collisions compared to extrapolations of the Tevatron data [2]. Absorption and energy loss of leading partons by inelastic interactions in the BDR can also account for the pattern of forward pion production in d–Au collisions at STAR [3].

Particularly interesting is the question what the approach to the BDR implies for exclusive hard diffractive scattering, $pp \to p + H + p$. In such processes a high–mass system ($H = \text{dijet}, \bar{Q}Q, \text{Higgs}$) is produced in a hard process involving exchange of two gluons between the protons. At the same time, the spectator systems must interact in a way such as not to produce additional particles. This restricts the set of possible trajectories in configuration space and results in a suppression of the cross section compared to non-diffractive events. For soft spectator interactions this suppression is measured by the so–called rapidity gap survival (RGS) probability. Important questions are (a) what role the BDR plays in traditional soft–interaction RGS; (b) how the physical picture of RGS is modified by hard spectator interactions in the BDR at LHC energies; (c) how fluctuations of the strength of the pp interaction related to inelastic diffraction influence RGS in hard diffractive processes; (d) how possible correlations between hard and soft interactions affect RGS.

These questions can be addressed in a recently proposed partonic description of exclusive diffraction [4], based on Gribov's parton picture of high–energy hadron–hadron scattering. Questions (a) and (b) can be studied within this framework in a practically model–independent way. They require only basic information about the strength of hard and soft interactions and their impact parameter dependence, which is either known experimentally or can be obtained from reasonably safe extrapolations of existing data to higher energies. Questions (c) and (d) require more detailed assumptions about correlations in the partonic wavefunction of the proton, which relate to less understood features of the pp interaction at high energies. We can address them by implementing within the approach of Ref. [4] specific dynamical models of nucleon structure (color fluctuations, transverse correlations between partons). Our studies of these questions are of exploratory nature.

2 Black–disk regime in soft spectator interactions

A simple "geometric" picture of RGS is obtained in the approximation where hard and soft interactions are considered to be independent [4]. The hard two–gluon exchange process can be regarded as happening locally in space–time on the typical scale of soft interactions. In the impact parameter representation (see Fig. 1a) the RGS probability can be expressed as

$$S^2 \;=\; \int d^2b\; P_{\text{hard}}(\boldsymbol{b})\; |1 - \Gamma(\boldsymbol{b})|^2. \tag{1}$$

Here $P_{\text{hard}}(\boldsymbol{b})$ is the probability for two hard gluons from the protons to collide in the same space–time point, given by the overlap integral of the squared transverse spatial distributions of gluons in the colliding protons, normalized to $\int d^2b\; P_{\text{hard}}(\boldsymbol{b}) = 1$ (see Fig. 1b). The function $|1 - \Gamma(\boldsymbol{b})|^2$ is the probability for the two protons not to interact inelastically in a collision with impact parameter b. The approach to the BDR in pp scattering at energies $\sqrt{s} \gtrsim 2\,\text{TeV}$ implies that this probability is practically zero at small impact parameters, and becomes significant only for $b \gtrsim 1\,\text{fm}$ (see Fig. 1b). This eliminates the contribution from small impact parameters in the

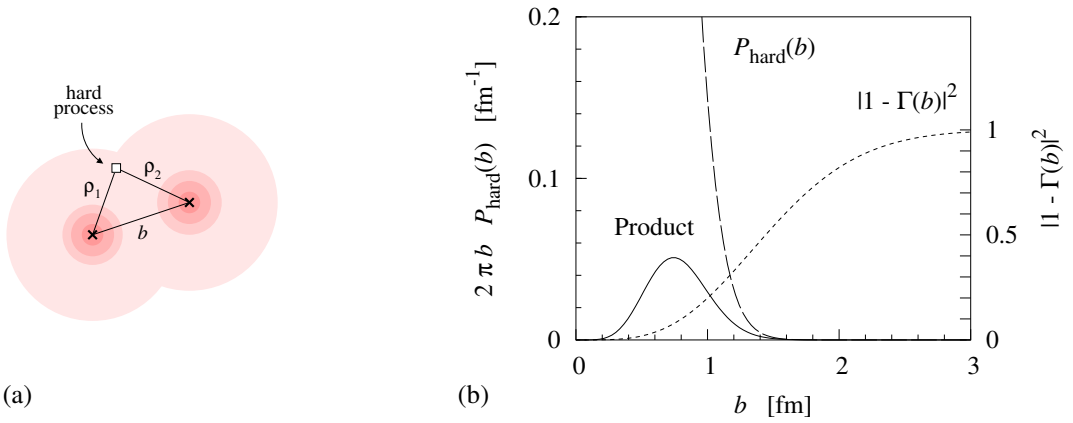


Fig. 1: (a) Transverse geometry of hard diffractive pp scattering. (b) Dashed line: Probability for hard scattering process $P_{\rm hard}(\boldsymbol{b})$ as function of the pp impact parameter, b. Dotted line: Probability for no inelastic interactions between the protons, $|1-\Gamma(\boldsymbol{b})|^2$. Solid line: Product $P_{\rm hard}(\boldsymbol{b})|1-\Gamma(\boldsymbol{b})|^2$. The RGS probability (1) is given by the area under this curve. The results shown are for Higgs production at the LHC ($\sqrt{s} = 14\,\text{TeV}, M_H \sim 100\,\text{GeV}$). (We point out that the distributions shown in Fig. 8 of Ref. [4] correspond to a gluon t–slope $B_g = 4\,\text{GeV}^{-2}$, not $B_g = 3.24\,\text{GeV}^{-2}$ as stated in the caption. The plot here shows the correct distributions for $B_g = 3.24\,\text{GeV}^{-2}$.)

integral (1) (see Fig. 1b) and determines the value of the RGS probability to be $S^2 \ll 1$. One sees that the approach to the BDR in soft interactions plays an essential role in RGS at high energies.

3 Black–disk regime in hard spectator interactions

At LHC energies even highly virtual partons ($k^2 \sim$ few GeV^2) with $x \gtrsim 10^{-2}$ experience "black" interactions with the small–x gluons in the other proton. This new effect causes an additional suppression of diffractive scattering which is not included in the traditional RGS probability [4]. One mechanism by which this happens is the absorption of "parent" partons in the QCD evolution leading up to the hard scattering process (see Fig. 2a). Specifically, in Higgs production at the LHC the gluons producing the Higgs have momentum fractions $x_{1,2} \sim M_H/\sqrt{s} \sim 10^{-2}$; their "parent" partons in the evolution (quarks and gluons) typically have momentum fractions of the order $x \sim 10^{-1}$ and transverse momenta $k_T^2 \sim$ few GeV^2. Quantitative studies of the BDR in the dipole picture show that at the LHC energy such partons are absorbed with near–unit probability if their impact parameters with the other proton are $\rho_{1,2} \lesssim 1\,\text{fm}$ (see Fig. 2b). For proton–proton impact parameters $b < 1\,\text{fm}$ about 90% of the strength in $P_{\rm hard}(b)$ comes from parton–proton impact parameters $\rho_{1,2} < 1\,\text{fm}$ (*cf.* Fig. 1a), so that this effect practically eliminates diffraction at $b < 1\,\text{fm}$. Since $b < 1\,\text{fm}$ accounts for 2/3 of the cross section [see Eq. (1) and Fig. 1b)], and the remaining contributions at $b > 1\,\text{fm}$ are also reduced by absorption, we estimate that inelastic interactions of hard spectators in the BDR reduce the RGS probability at LHC energies to about 20% of its soft–interaction value.

In the above argument one must also allow for the possibility of trajectories with no gluon emission. Mathematically, they correspond to the Sudakov form factor–suppressed $\delta(1-x)$–term in the evolution kernel. While such trajectories are not affected by absorption, their contributions

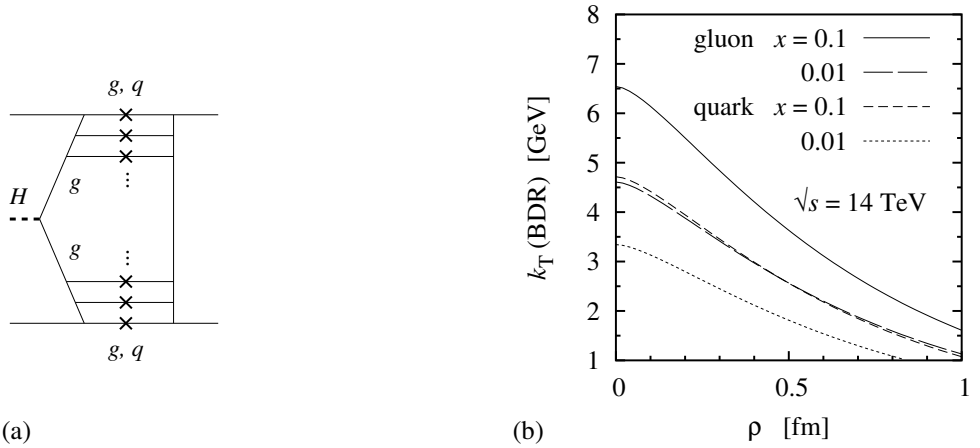


Fig. 2: (a) Absorption of parent partons by interactions in the BDR. The crosses denote absorptive interactions with small-x gluons in the other proton. (b) The critical transverse momentum, $k_T(\mathrm{BDR})$, below which partons are absorbed with high probability ($|\Gamma^{\text{parton-proton}}| > 0.5$), as a function of the parton–proton impact parameter, $\rho = \rho_{1,2}$.

are small both because of the Sudakov suppression, and because they effectively probe the gluon density at the soft input scale, $Q_0^2 \sim 1\,\mathrm{GeV}^2$. The probability for a gluon not to emit a gluon when evolving from virtuality Q_0^2 to Q^2, is given by the square of the Sudakov form factor,

$$C \;=\; \left[S_G(Q^2/Q_0^2)\right]^2 \;=\; \exp\left(-\frac{3\alpha_s}{\pi}\ln^2\frac{Q^2}{Q_0^2}\right). \tag{2}$$

At the same time, each of the parton densities in the trajectory without emissions is suppressed compared to those with emissions by a factor $g(x,Q^2)/g(x,Q_0^2)$, where $Q^2 \sim 4\,\mathrm{GeV}^2$. The overall relative suppression of trajectories without emission is thus by a factor

$$R \;=\; C^2\left[\frac{g(x,Q^2)}{g(x,Q_0^2)}\right]^2 \;\sim\; \frac{1}{10}. \tag{3}$$

Although this contribution is suppressed, it is comparable to that of average trajectories with emissions because the latter are strongly suppressed by the absorption effect described above. Combining the two, we find an overall suppression factor of the order ~ 0.3. In order to make more accurate estimates one obviously would need to take into account fluctuations in the number of emissions more carefully. In particular, trajectories on which only one of the partons did not emit gluons, which come with a suppression factor of $\sqrt{R}$, may give significant contributions.

The approach to the BDR in hard spectator interactions described here "pushes" diffractive pp scattering to even larger impact parameters than are allowed by soft–interaction RGS (except for the Sudakov–suppressed contribution discussed in the previous paragraph). This should manifest itself in a shift of the final–state proton transverse momentum distribution to smaller values, which could be observed in p_T–dependent measurements of diffraction at the LHC.

The estimates reported here are based on the assumption that DGLAP evolution reasonably well describes the gluon density down to $x \sim 10^{-6}$; the quantitative details (but not the basic

picture) may change if small–x resummation corrections were to significantly modify the gluon density at such values of x (see Ref. [5] and references therein). The effect of hard spectator interactions described here is substantially weaker at the Tevatron energy.

4 Color fluctuations in the colliding protons

In the approximation where hard and soft interactions in the diffractive process are considered to be independent, the RGS probability can be expressed through the pp elastic scattering amplitude, and effects of inelastic diffraction do not enter into consideration, see Ref. [4] and the discussion above. It is important to investigate how accurate this approximation is in practice, and how correlations between hard and soft interactions modify the picture. Such correlations generally arise from correlations between partons in the wave functions of the colliding protons, which can be caused by several physical mechanisms, see Ref. [4] for a discussion. Here we focus on one mechanism which is closely related to the presence of inelastic diffraction channels, namely fluctuations of the size of the interacting configurations (color fluctuations). Our study of this effect here is of exploratory nature; details will be reported in a forthcoming publication.

The basic idea is that in diffractive high–energy scattering the colliding hadrons can be regarded as a superposition of configurations of different size, which are "frozen" during the time of the interaction. In the well–known approach of Good and Walker [6] this is implemented by expanding the incident hadron state in eigenstates of the T–matrix of the same quantum numbers. A more general formulation uses the concept of the cross section distribution, $P(\sigma)$, which can be interpreted as the probability for the hadron to scatter in a configuration with given cross section, with $\int d\sigma\, P(\sigma) = 1$ [7]. It is defined such that its average reproduces the total cross section,

$$\langle \sigma \rangle \;\equiv\; \int d\sigma\; \sigma\; P(\sigma) \;=\; \sigma_{\rm tot}, \tag{4}$$

while its dispersion coincides with the ratio of the differential cross sections for inelastic ($pp \to p + X$) and elastic ($pp \to p + p$) diffraction at $t = 0$ [8],

$$\omega_\sigma \;\equiv\; \frac{\langle \sigma^2 \rangle - \langle \sigma \rangle^2}{\langle \sigma \rangle^2} \;=\; \frac{d\sigma_{\rm inel}}{dt} \Big/ \left. \frac{d\sigma_{\rm el}}{dt} \right|_{t=0}. \tag{5}$$

The dispersion and the third moment of $P(\sigma)$ have been extracted from analysis of the pp and pd data up to $s \approx 8 \times 10^2$ GeV^2; at higher energies the shape of the distribution is not well known. Extrapolation of a parametrization of the Tevatron data [9] suggests that between the Tevatron and LHC energy ω_σ should drop by a factor ~ 2, while at the same time the total cross section is expected to grow, indicating that the relative magnitude of fluctuations decreases with increasing energy (see Figs. 3a and b). Generally, one should expect that the different configurations in diffractive scattering are characterized by a different parton density. In hard diffractive processes $pp \to p + H + p$ this effect would then lead to a modification of the "independent interaction" result for the RGS probability, Eq. (1).

The theoretical description of the role of cross section fluctuations in hard diffraction is a complex problem, which requires detailed assumptions about the proton's partonic wave function. Here we aim only for a simple phenomenological estimate, which illustrates the sign and

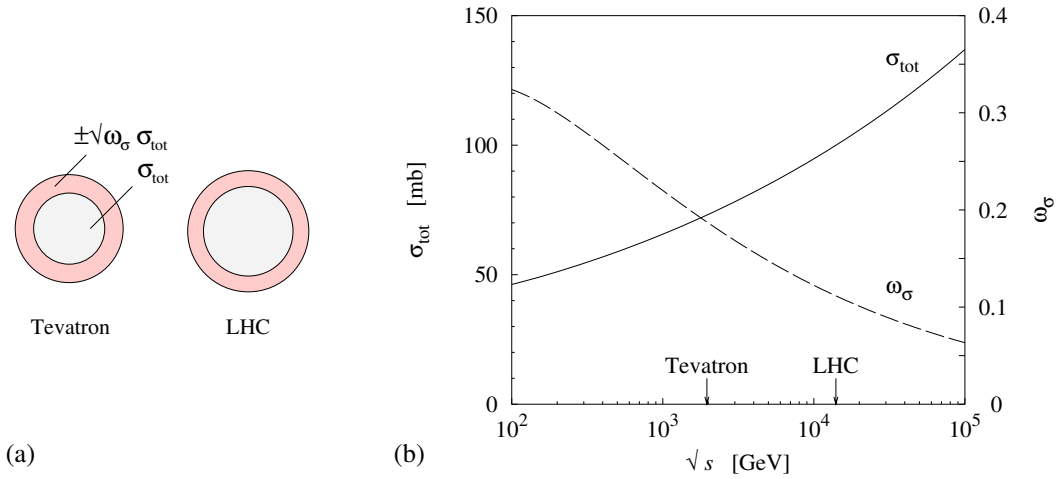


Fig. 3: (a) Graphical representation of the cross section distributions in diffraction at the Tevatron and LHC energy. The area of the inner and outer disk at given energy is proportional to $(1 \pm \sqrt{\omega}_\sigma)\langle\sigma\rangle$, *i.e.*, the average area represents the average cross section $\langle\sigma\rangle = \sigma_{\rm tot}$, the difference (ring) the range of the fluctuations $\pm\sqrt{\omega}_\sigma\langle\sigma\rangle$. (b) The s–dependence of the total cross section $\sigma_{\rm tot}$ (left y–axis) and the dispersion ω_σ (right y–axis), as predicted by a Regge–based parametrization of $\sigma_{\rm tot}$ [10] and a parametrization of the inelastic diffractive cross section $d\sigma_{\rm inel}/dt|_{t=0}$, measured up to the Tevatron energy [9]. The weak energy dependence of the width of the ring in figure (a) reflects the slow variation of the diffractive cross section with energy.

order–of–magnitude of the effect, as well as its energy dependence. Our basic assumption is that the strength of interaction in a given configuration is proportional to the transverse area occupied by color charges. To implement this idea, we start from the cross section distribution $P(\sigma)$ at fixed–target energies ($s \lesssim 8 \times 10^2\,{\rm GeV}^2$), which can be related to the fluctuations of the size of the basic "valence quark" configuration in the proton wave function and is known well from the available data [7]. We then assume that

(a) The parton density is correlated with the parameter σ characterizing the size of the interacting configuration. One simple scenario is to assume that the parton density changes with the size of the configuration only through its dependence on the normalization scale, $\mu^2 \propto R_{\rm config}^{-2} \propto \sigma$. This is analogous to the model of the EMC effect of Ref. [11], and leads to a simple scaling relation for the σ–dependent gluon density,

$$g(x, Q^2\,|\sigma) \;=\; g(x, \xi Q^2), \qquad \xi(Q^2) \;\equiv\; (\sigma/\langle\sigma\rangle)^{\alpha_s(Q_0^2)/\alpha_s(Q^2)}\,, \tag{6}$$

where $Q_0^2 \sim 1\,{\rm GeV}^2$. In Higgs boson production one expects $Q^2 \approx 4\,{\rm GeV}^2$, and $x = M_H/\sqrt{s} = 0.007\,({\rm LHC}), 0.05\,({\rm Tevatron})$ with $M_H = 100\,{\rm GeV}$. An alternative scenario — the constituent quark picture — will be discussed below.

(b) The size distribution in soft high–energy interactions is correlated with the parameter σ characterizing the valence quark configuration. As a minimal model we assume that soft interactions in a configuration with given σ are described by a profile function of the form

$$\Gamma(\boldsymbol{b}, s\,|\sigma) \;=\; \exp\left[-\frac{2\pi b^2}{\sigma_{\rm tot}(s,\sigma)}\right], \qquad \text{with} \quad \sigma_{\rm tot}(s,\sigma) \;=\; \alpha(s) + \beta(s)\frac{\sigma}{\langle\sigma\rangle}, \tag{7}$$

in which the parameters $\alpha(s)$ and $\beta(s)$ are chosen such as to reproduce the average cross section and dispersion of the high–energy cross section distribution (see Fig. 3a and b) when averaging over the (given) σ distribution $P(\sigma)$. Note that the profile in Eq. (7) approaches the black–disk limit at $b \to 0$, and that the average elastic profile $\langle \Gamma(\boldsymbol{b}, s\,|\sigma)\rangle$ obtained in this way is very close to that found in the standard phenomenological parametrizations of the pp elastic and total cross section data. More sophisticated parametrizations could easily be constructed but would not change our qualitative conclusions.

With assumptions (a) and (b) we can estimate the effect of color fluctuations in the protons in hard diffraction in a simple way. In the presence of correlations between the parton density and the strength of soft interactions, the RGS probability is now given by

$$S^2_{\text{corr}} \;=\; \int d^2b \,\left\langle P_{\text{hard}}(\boldsymbol{b}\,|\sigma)\;\; |1-\Gamma(\boldsymbol{b}, s\,|\sigma)|^2 \right\rangle, \tag{8}$$

where $P_{\text{hard}}(\boldsymbol{b}\,|\sigma)$ is the normalized impact parameter distribution for the hard process obtained with the σ–dependent gluon density Eq. (6), and $\langle \ldots \rangle$ denotes the average over the σ distribution. This should be compared to the RGS probability without correlations,

$$S^2_{\text{uncorr}} \;=\; \int d^2b \,\left\langle P_{\text{hard}}(\boldsymbol{b}\,|\sigma) \right\rangle \left\langle |1-\Gamma(\boldsymbol{b}, s\,|\sigma)|^2 \right\rangle, \tag{9}$$

which corresponds to the expression obtained previously in the approximation of independent hard and soft interactions, Eq. (1), if we identify the functions there with the average distributions.[1] For a quantitative estimate, we first consider fluctuations of the interacting configurations in only one of the colliding protons, leaving the other protons unchanged. In this case we obtain

$$\frac{S^2_{\text{corr}} - S^2_{\text{uncorr}}}{S^2_{\text{uncorr}}} \;=\; -0.15 \qquad \text{at} \quad \sqrt{s} = 2\,\text{TeV} \quad \text{(Tevatron)}. \tag{10}$$

If one could consider the fluctuation effect as a small correction, the total effect would be additive and thus proportional to the number of protons, *i.e.*, Eq. (10) would have to be multiplied by 4, corresponding to the two protons in both the amplitude and the complex-conjugate amplitude in the cross section. While the magnitude of the correction Eq. (10) does not really justify such additive treatment, we can at least to conclude that the overall effect from correlations in this model should be a reduction of the RGS probability by $\sim 1/2$. Note that the sign of the correlation effect simply reflects the fact that smaller configurations, which have higher transparency and thus larger survival probability, have a lower density of small–x partons in model adopted here.

Our treatment of color fluctuations here assumes that the basic picture of independent hard and soft interactions in RGS is still valid, and that the fluctuations can be incorporated by way of an "external" parameter controlling the size of the interacting configurations. As explained above (Sec. 3) and in Ref. [4], this assumption breaks down at the LHC energy, where hard spectator interactions approach the BDR. The correction described here thus should be valid at

[1] Note that there are small differences between the functional forms of the σ–averaged distributions in Eq. (9) and the original (σ–independent) distributions used previously in evaluating Eq. (1). This is only the result of imperfect modeling of the σ–dependent distributions and immaterial for the physical correlation effect discussed here.

RHIC and Tevatron energies but not at the LHC. In particular, this can be seen in the fact that the correlation effect of Eq. (10) is obtained from modification of the impact parameter distribution of hard diffraction at $b \lesssim 1$ fm, where we expect hard spectator interactions to be "black" at the LHC, see Sec. 3. Thus, corrections from inelastic diffractive channels of the kind discussed here play a minor role at the LHC energy. This is a welcome conclusion, as it means that our predictions for the RGS probability at the LHC are not substantially modified by such corrections.

The numerical estimate of correlation effects reported here was obtained with the assumption that the gluon density in the interacting configurations scales with the size of the configuration as in Eq. (6). Physically, this corresponds to the assumption that the valence quark configuration in the proton acts coherently as source of the gluon field, and that there are no other physical scales in the proton besides the size of that configuration. This is clearly an extreme scenario and does not take into account the physical scales generated by the non-perturbative vacuum structure of QCD. An alternative scenario would be a constituent quark picture, in which the normalization scale of the gluon density is determined by the "size" of the constituent quark (related to the spontaneous breaking of chiral symmetry) and not related to the size of the multi–quark configuration in the nucleon. For this picture the relation between the gluon density and the size of the interacting configuration would be very different from Eq. (6). It leads to a different kind of correlation between hard and soft interactions, see Ref. [4] and Section 5 below.

5 Transverse spatial correlations between partons

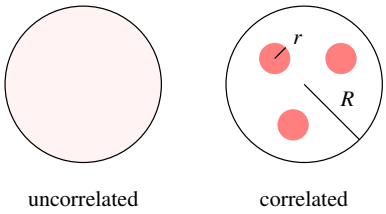


Fig. 4: Transverse parton correlations.

The partonic approach to RGS of Ref. [4] also allows one to incorporate effects of correlations in the partonic wavefunction of the protons. They can lead to correlations between hard and soft interactions in diffraction, which substantially modify the picture of RGS compared to the independent interaction approximation. The analysis of the CDF data on $p\bar{p}$ collisions with multiple hard processes indicate the presence of substantial transverse correlations between partons with $x \gtrsim 0.1$ [1]. Such correlations naturally arise in a constituent quark picture of the nucleon with $r_q \ll R$ (see Fig. 4). It is interesting that the observed enhancement of the cross section due to correlations seems to require $r_q/R \sim 1/3$, which is the ratio suggested by the instanton vacuum model of chiral symmetry breaking (see Ref. [12] for a review). Such correlations modify the picture of RGS in hard diffractive pp scattering compared to the independent interaction approximation in two ways [4]. On one hand, with correlations inelastic interactions between spectators are much more likely in configurations in which two large–x partons collide in a hard process than in average configurations, reducing the RGS probability compared to the uncorrelated case. On the other hand, the "lumpiness" implies that there is generally a higher chance for the remaining spectator system not to interact inelastically compared to the mean–field approximation. A quantitative treatment of correlations in RGS, incorporating both effects, remains an outstanding problem.

6 Summary

The approach to the BDR at high energies profoundly influences the physics of RGS in exclusive diffractive scattering. The onset of the BDR in soft spectator interactions at $\sqrt{s} \gtrsim 2\,\mathrm{TeV}$ eliminates diffractive scattering at small impact parameters and determines the basic order–of–magnitude of the RGS probability at the Tevatron and LHC. At LHC energies, the BDR in hard spectator interactions pushes diffractive scattering to even larger impact parameters and further reduces the RGS probability by a factor of 3 (likely more, 4–5), implying that $S^2 < 0.01$, much smaller than initial estimates reported in the literature, see Ref. [4] and references therein. At the same time, this effect reduces the relative importance of color fluctuations related to inelastic diffraction, making our theoretical predictions of the RGS probability more robust. At the Tevatron energy, we have seen that color fluctuations lower the RGS probability compared to the approximation of independent hard and soft interactions. The simple model estimate presented in Sec. 5 suggests reduction by a factor of the order 1/2; however, more refined estimates are certainly needed. Finally, spatial correlations between partons are likely to modify the picture of RGS both at the Tevatron and the LHC energy; a detailed study of this effect would be of principal as well as of considerable practical interest.

The total RGS probability is an "integral" quantity, which combines contributions from very different trajectories of the interacting pp system. It is also difficult to determine experimentally, as its extraction requires precise knowledge of the cross section of the hard scattering process (gluon GPD, effective virtualities, etc.). Much more detailed tests of the diffractive reaction mechanism can be performed by studying the transverse momentum dependence of the diffractive cross section, which can be interpreted without knowledge of the hard scattering process. In particular, the predicted onset of the BDR in hard interactions between the Tevatron and LHC energy (Sec. 3) should cause substantial narrowing of the p_T distribution, which could be observed experimentally. At RHIC and Tevatron energies, the correlation effects described in Sec. 5 imply that the p_T distribution is narrower than predicted by the independent interaction approximation, allowing one to test this picture experimentally. This underscores the importance of planned transverse momentum–dependent measurements of diffraction at RHIC and LHC.

References

[1] For a review, see: L. Frankfurt, M. Strikman and C. Weiss, Ann. Rev. Nucl. Part. Sci. **55**, 403 (2005).

[2] L. Frankfurt, M. Strikman and C. Weiss, Phys. Rev. D **69**, 114010 (2004).

[3] L. Frankfurt and M. Strikman, Phys. Lett. B **645**, 412 (2007).

[4] L. Frankfurt, C. E. Hyde, M. Strikman and C. Weiss, Phys. Rev. D **75**, 054009 (2007).

[5] M. Ciafaloni, D. Colferai, G. P. Salam and A. M. Stasto, arXiv:0707.1453 [hep-ph].

[6] M. L. Good and W. D. Walker, Phys. Rev. **120**, 1857 (1960).

[7] B. Blaettel, G. Baym, L. L. Frankfurt, H. Heiselberg and M. Strikman, Phys. Rev. D **47**, 2761 (1993).

[8] H. I. Miettinen and J. Pumplin, Phys. Rev. D **18**, 1696 (1978).

[9] K. Goulianos, private communication.

[10] A. Donnachie and P. V. Landshoff, *Phys. Lett.* **B296**, 227 (1992).

[11] F. E. Close, R. G. Roberts and G. G. Ross, Phys. Lett. B **129**, 346 (1983).

[12] D. Diakonov, Prog. Part. Nucl. Phys. **51**, 173 (2003) [arXiv:hep-ph/0212026].

Pomeron intercept and slope: the QCD connection

Konstantin Goulianos
The Rockefeller University, 1230 York Avenue, New York, NY 10065-6399, USA

Abstract
We present a model for the ratio of intercept to slope of the Pomeron trajectory as measured from elastic, diffractive and total cross sections.

1 Regge approach to diffraction

Hadronic diffraction has traditionally been treated in the framework of Regge theory [1–3]. In this approach, the key player mediating diffractive processes is the *Regge trajectory* of the Pomeron, presumed to be formed by a *family* of particles carrying the quantum numbers of the vacuum. Although no particles were known (and have yet to be found!) to belong to this family, the Pomeron trajectory was introduced in the 1970s to account for the observations that the K^+p cross section was found to be increasing with energy at the Serpukov 70 GeV ($\sqrt{s} = 11.5$ GeV for pp collisions) proton synchrontron, and the elastic and total pp cross sections, which at low energies were falling with increasing energy, started to flatten out and then rose with energy as collision energies up to $\sqrt{s}$=60 GeV became available at the Intersecting Storage Rings (ISR) at CERN.

In the Regge approach, high energy cross sections are dominated by Pomeron exchange. For pp interactions, the Pomeron exchange contribution to total, elastic, and single diffractive cross sections is given by

$$\sigma^{tot}(s) = \beta^2_{I\!Ppp}(0) \left(\frac{s}{s_0}\right)^{\alpha_{I\!P}(0)-1} \tag{1}$$

$$\frac{d\sigma^{el}(s,t)}{dt} = \frac{\beta^4_{I\!Ppp}(t)}{16\pi} \left(\frac{s}{s_0}\right)^{2[\alpha_{I\!P}(t)-1]} \tag{2}$$

$$\frac{d^2\sigma_{sd}(s,\xi,t)}{d\xi dt} = \underbrace{\frac{\beta^2_{I\!Ppp}(t)}{16\pi}\, \xi^{1-2\alpha_{I\!P}(t)}}_{f_{I\!P/p}(\xi,t)} \underbrace{\beta_{I\!Ppp}(0)\, g(t)\, (\frac{s}{s_\circ})^{\alpha_{I\!P}(0)-1}}_{\sigma^{I\!Pp}(s\xi,t)}, \tag{3}$$

where $\alpha_{I\!P}(t) = \alpha_{I\!P}(0) + \alpha' t = (1+\epsilon) + \alpha' t$ is the Pomeron trajectory, $\beta_{I\!Ppp}(t)$ the coupling of the Pomeron to the proton, $g(t)$ the $I\!PI\!PI\!P$ coupling, $s' = M^2$ the $I\!P$-p center of mass energy squared, $\xi = 1 - x_F = s'/s \approx M^2/s$ the fraction of the momentum of the proton carried by the Pomeron, and s_0 an energy scale parameter traditionally set to the hadron mass scale of 1 GeV^2. The single diffractive cross section, Eq. (3), factorizes into two terms, the one on the right which can be viewed as the $I\!P$-p total cross section, and the other labeled $f_{I\!P/p}(\xi,t)$, which may be interpreted as the Pomeron flux emitted by the diffracted proton [4].

Regge theory worked reasonably well in describing elastic, diffractive and total hadronic cross sections at energies of up to $\sqrt{s} \sim 60$ GeV, with all processes accommodated in a simple

Pomeron pole approach, as documented in Ref. [5]. Results from a Rockefeller University experiment on photon dissociation on hydrogen published in 1985 [6] were also well described by this approach.

The early success of Regge theory, however, was precarious. The theory was known to asymptotically violate unitarity, as the $\sim s^{\epsilon}$ power law increase of total cross sections would eventually exceed the Froissart bound of $\sigma_T < \frac{\pi}{m_\pi^2} \cdot \ln^2 s$ based on analyticity and unitarity. But the confrontation with unitarity came at much lower energies than what would be considered asymptopia by Froissart bound considerations. As collision energies climbed upwards in the 1980s to reach $\sqrt{s} = 630$ GeV at the CERN S$\bar{p}p$S collider and $\sqrt{s} = 1800$ GeV at the Fermilab Tevatron $\bar{p}p$ collider, diffraction dissociation could no longer be described by Eq. (3), signaling a breakdown of factorization.

The first clear experimental evidence for a breakdown of factorization in Regge theory was reported by the CDF Collaboration in 1994 [7]. In a measurement of the single diffractive cross section in $\bar{p}p$ collisions at $\sqrt{s}$ =546 and 1800 GeV CDF found a suppression factor of ~ 5 (~ 10) at $\sqrt{s}$ =546 GeV (1800 GeV) relative to predictions based on extrapolations from $\sqrt{s}$ ∼20 GeV.

2 Scaling properties and renormalization of diffraction

The breakdown of factorization in Regge theory was traced back to the expected energy dependence of the single diffractive cross section, $\sigma_{sd}^{tot}(s) \sim s^{2\epsilon}$, which is faster than that of the total cross section, $\sigma^{tot}(s) \sim s^{\epsilon}$, so that as s increased unitarity would have to be violated if factorization held. This is reflected in the $s^{2\epsilon}$ dependence of $d\sigma_{sd}(M^2,t)/dM^2|_{t=0}$:

$$\text{Regge theory: } d\sigma_{sd}(M^2,t)/dM|^2_{t=0} \sim s^{2\epsilon}/(M^2)^{1+\epsilon}. \tag{4}$$

In a paper first presented by this author in 1995 at the La Thuile [8] and Blois [9] winter conferences and later published in Phys. Lett. B [10], it was shown that unitarization could be achieved, and the factorization breakdown in single diffraction fully accounted for, by interpreting the Pomeron flux of Eq. (3) as a probability density and *renormalizing* its integral over ξ and t to unity,

$$f_{I\!P/p}(\xi,t) \Rightarrow N_s^{-1} \cdot f_{I\!P/p}(\xi,t), \quad N_s \equiv \int_{\xi(min)}^{\xi(max)} d\xi \int_{t=0}^{-\infty} dt\, f_{I\!P/p}(\xi,t) \sim s^{2\epsilon}/\ln s, \tag{5}$$

where $\xi(min) = M_0^2/s$, with $M_0^2 = 1.4$ GeV^2 being the effective threshold for diffraction dissociation, and $\xi(max) = 0.1$. The s-dependence introduced into the Pomeron flux through the renormalization factor N_s^{-1} replaces the power law factor $s^{2\epsilon}$ in Eq. (4) with $\ln s$ ensuring unitarization. In Fig. 1, $\sigma_{sd}^{tot}(s)$ is compared with Regge predictions using the standard or renormalized Pomeron flux. The renormalized prediction is in excellent agreement with the data.

The elastic and total cross sections are not affected by this procedure. Unitarization may be achieved in these cases by using the eikonal approach, e.g. as reported in Ref. [11], where

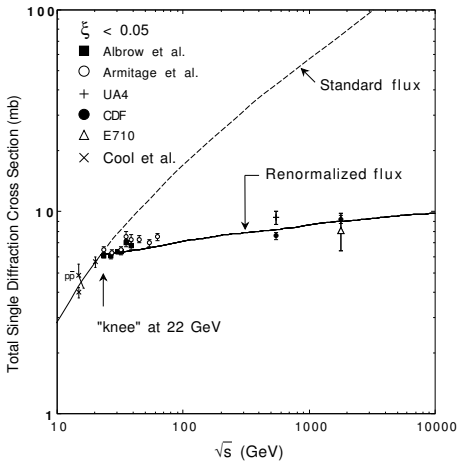


Fig. 1: *Total $pp/\bar{p}p$ single diffraction dissociation cross section data (* both $\bar{p}$ *and* p *sides) for* $\xi < 0.05$ *compared with predictions based on the standard and the renormalized Pomeron flux [10].*

excellent agreement is obtained between elastic and total cross section data and predictions based on Regge theory and eikonalization.

An important aspect of renormalization is that it leads to an approximate scaling behavior, whereby $d\sigma_{sd}(M^2)/dM^2$ has no power law dependence on s. This 'scaling law' holds for the differential soft single diffractive cross section as well, as shown in Fig. 2 [12].

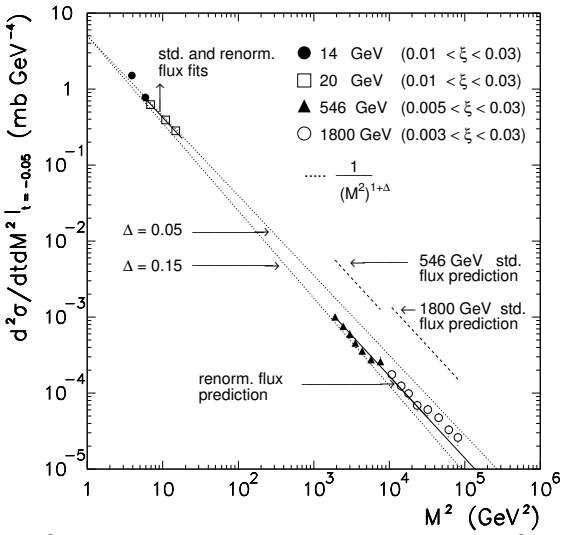


Fig. 2: *Cross sections $d^2\sigma_{sd}/dM^2dt$ for $p + p(\bar{p}) \to p(\bar{p}) + X$ at $t = -0.05$ GeV^2 and $\sqrt{s} = 14$, 20, 546 and 1800 GeV. Standard (renormalized) flux predictions are shown as dashed (solid) lines. At $\sqrt{s}$=14 and 20 GeV, the fits using the standard and renormalized fluxes coincide [12].*

3 Parton model approach to diffraction

The Regge theory form of the rise of the total $pp/\bar{p}p$ cross section at high energies, $\sigma^{tot}_{pp/\bar{p}p}(s) = \sigma_0 \cdot s^{\epsilon}$, which requires a Pomeron trajectory with intercept $\alpha(0) = 1 + \epsilon$, is precisely the form expected in a parton model approach, where cross sections are proportional to the number of available "wee" (lowest energy) partons: $\sigma^{tot}_{pp/\bar{p}p} = N \times \sigma_0$, where N is the flux of wee partons and σ_0 the cross section of one wee parton with the target proton (see Ref. [13]). The wee partons originate from emissions of single partons cascading down to lower energy partons in tree-like chains. The average spacing in (pseudo)rapidity[1] between two successive parton emissions is $\sim 1/\alpha_s$. This spacing governs the wee parton density in the region of particle production, $\Delta\eta' = \ln s$, leading to a total pp cross section of the form

$$\sigma^{tot}_{pp/\bar{p}p} = \sigma_0 \cdot e^{\epsilon \Delta\eta'}. \tag{6}$$

Since from the optical theorem $\sigma^{tot}_{pp/\bar{p}p}$ is proportional to the imaginary part of the forward ($t = 0$) elastic scattering amplitude, the full parton model amplitude may be written as

$$\mathrm{Im\, f^{el}_{pp/\bar{p}p}}(t, \Delta\eta) \sim e^{(\epsilon + \alpha' t)\Delta\eta}, \tag{7}$$

where $\alpha'(t)$ is added as a simple parameterization of the t-dependence.

The parameter α' reflects the transverse size of the cluster of wee partons in a chain, which is governed by the $\Delta\eta$ spacing between successive chains, and therefore must be related to the parameter ϵ. For the relationship between α' and ϵ, we turn to single diffraction, which through the coherence requirement isolates the cross section from one wee parton interacting with the proton, since all possible interaction of other wee partons are shielded by the formation of the diffractive rapidity gap.

Based on the above amplitude, the single diffractive cross section is expected to have the form

$$\frac{d^2\sigma_{sd}(s, \Delta\eta, t)}{dt\, d\Delta\eta} = \frac{1}{N_{gap}(s)} \cdot \underbrace{C_{gap} \cdot F_p^2(t) \left\{ e^{(\epsilon + \alpha' t)\Delta\eta} \right\}^2}_{P_{gap}(\Delta\eta, t)} \cdot \kappa \cdot \left[\sigma_0\, e^{\epsilon \Delta\eta'} \right], \tag{8}$$

where, from right to left, the factor in square brackets represents the cross section due to the partons in the region of particle production, $\Delta\eta' = \ln s$-$\Delta\eta$, κ is a QCD color factor selecting color singlet di-gluon or $q\bar{q}$ exchanges to form the rapidity gap, $P_{gap}(\Delta\eta, t)$ is a gap probability factor representing the scattering between the cluster of dissociation particles and the surviving proton - with $F_p(t)$ being the proton form factor and C_{gap} a constant, and $N_{gap}(s)$ is the integral of the gap probability over all phase space in t and $\Delta\eta$. As $\Delta\eta = -\ln \xi$, the form of Eq. (8) is identical to the Regge form of Eq. (3).

3.1 The ratio $r = \alpha'/\epsilon$

In terms of M^2, Eq. (8) takes the form

$$\frac{d^2\sigma(s, M^2, t)}{dM^2 dt} = \left[\frac{\sigma_0^{pp}}{16\pi} \sigma_0^{I\!P p} \right] \frac{s^{2\epsilon}}{N(s)} \frac{1}{(M^2)^{1+\epsilon}}\, e^{bt} \quad \overset{s\to\infty}{\to} \quad \left[2\alpha' e^{\frac{\epsilon b_0}{\alpha'}} \sigma_0^{I\!P p} \right] \underbrace{\frac{\ln s^{2\epsilon}}{(M^2)^{1+\epsilon}}\, e^{bt}}_{b = b_0 + 2\alpha' \ln \frac{s}{M^2}}. \tag{9}$$

[1] We assume $p_T = 1$ GeV, so that $\Delta y' = \Delta\eta'$.

Integrating this expression over M^2 and t yields the total single diffractive cross section,

$$\sigma_{sd} \stackrel{s\to\infty}{\to} 2\sigma_0^{I\!Pp}\, e^{\frac{\epsilon\, b_0}{2\alpha'}} = \sigma_{sd}^{\infty} = \text{constant}. \tag{10}$$

The remarkable property that the total single diffractive cross section becomes constant as $s \to \infty$ is a direct consequence of the coherence required for the recoil proton to escape intact, which results in selecting one out of the many possible wee partons available for interaction, while another parton provides the color shield to form the diffractive rapidity gap. Since diffraction selects the interaction of one of the partons of the outgoing proton, the constant σ_{sd}^{∞} is identified as the σ_0 of Eq. (6), which is specific to the dissociating particle, in this case the proton, and therefore equals σ_0^{pp}. We thus have

$$2\sigma_0^{I\!Pp}\, e^{\frac{\epsilon\, b_0}{2\alpha'}} = \sigma_0^{pp}, \tag{11}$$

which is the sought after relationship between ϵ and α' in terms of constants which can be deduced from fundamental QCD parameters through the relationships

$$\sigma_0^{I\!Pp} = \beta_{I\!Ppp}(0) \cdot g(t) = \kappa\sigma_0^{pp} \tag{12}$$

$$\kappa = \frac{f_g^{\infty}}{N_c^2-1} + \frac{f_q^{\infty}}{N_c} \tag{13}$$

$$b_0 = R_p^2/2 = 1/(2m_\pi^2), \tag{14}$$

where the color factor κ is expressed in terms of the gg and $q\bar{q}$ color factors weighted by the corresponding gluon and quark fractions, and R_p is the radius of the proton expressed in terms of the pion mass, m_π. Inserting these parameters in Eq. (10) yields

$$r = \frac{\alpha'}{\epsilon} = -[16\, m_\pi^2 \ln(2k)]^{-1}. \tag{15}$$

Numerically, using $m_\pi = 0.14$ GeV and $\kappa = 0.18$, as respectively obtained for gluon and quark fractions of $f_g^{\infty} = 0.75$ and $f_q^{\infty} = 0.25$ (see Ref. [14]), yields $r = 3.14$ - which coincidentally is equal to π! This result is in excellent agreement with the ratio calculated from the values of $\epsilon = 0.08$ and $\alpha' = 0.25$ GeV^{-2} for the soft Pomeron trajectory obtained from fits to experimental data of total and elastic pp and $\bar{p}p$ cross sections for collision energies up to $\sqrt{s}$ =540 GeV, $r_{exp} = 0.25/0.08 = 3.13$ [15]. The smaller value of r obtained from the global fit of Ref. [11] to pp, $\bar{p}p$, $\pi^{\pm}p$, and $K^{\pm}p$ cross sections, $r = 0.26/0.104 = 2.5$, could be attributed to the increase of the intercept due to the additional radiation from hard partonic exchanges at higher energies, as for example in the two-Pomeron model of Ref. [16].

4 Summary

In a QCD based parton model approach to elastic, diffractive, and total cross sections, interactions occur through the emission of partons, which cascade down to wee partons in chains of tree-like configurations. As the spacing between successive emissions is controlled by the strong coupling constant, the total cross section, which is proportional to the number of wee partons produced, assumes a power law behavior similar to that of Regge theory, thereby relating the Pomeron

intercept to the underlying parton distribution function. The transverse size of the cluster of wee partons in a chain originating from one emission, which is the source of the parameter α', depends on the distance in rapidity of the next emission and thereby on the parameter ϵ. Exploiting single diffraction, which through the coherence requirement isolates a chain from a single parton emission, a relationship between ϵ and α' is obtained, which is in excellent agreement with experimental values.

References

[1] P. D. B. Collins, An Introduction to Regge Theory and High Energy Physics, Cambridge University Press (1977).

[2] V. Barone and E. Predazzi, High-Energy Particle Diffraction, Springer Press (2001).

[3] S. Donnachie, G. Dosch, O. Nachtmann, and P. Landshoff, Pomeron Physics and QCD, Cambridge University Press (2002).

[4] G. Ingelman and P.E. Schlein, Jet Structure in High Mass Diffractive Scattering, Phys. Lett. B **152**, 256 (1985).

[5] K. Goulianos, Diffractive Interactions of Hadrons at High Energies, Phys. Reports **101**, 171 (1983).

[6] T. J. Chapin et al., Diffraction Dissociation of Photons on Hydrogen, Phys. Rev. D **31**, 17 (1985).

[7] F. Abe et al. (CDF Collaboration), Measurement of $\bar{p}p$ Single Diffraction Dissociation at $\sqrt{s} = 546$ and 1800 GeV, Phys. Rev D **50**, 5535 (1994).

[8] K. Goulianos, Probing the Structure of the Pomeron at Hadron Colliders and at HERA, in: Proc. Les Rencontres de Physique de la Vallé d'Aoste, La Thuile, Aosta Valley, Italy, 5-11 Mar 1995.

[9] K. Goulianos, Renormalized Diffractive Cross Sections at HERA and the Structure of the Pomeron, in: Proc. 7th Rencontres de Blois, Frontiers in Strong Interactions - 6th International Conference on Elastic and Diffractive Scattering, Blois, France, 20-24 Jun 1995; e-Print Archive: hep-ph/9512291.

[10] K. Goulianos, Renormalization of Hadronic Diffraction and the Structure of the Pomeron, Phys. Lett. B **358**, 379 (1995); Erratum-*ib.* **363**, 268 (1995).

[11] R. J. M. Covolan, J. Montanha, and K. Goulianos, A New Determination of the Soft Pomeron Intercept, Phys. Lett. B **389** (1996) 176.

[12] K. Goulianos and J. Montanha, Factorization and Scaling in Hadronic Diffraction, Phys. Rev. D **59**, 114017 (1999).

[13] E. Levin, An Introduction to Pomerons, Preprint DESY 98-120, arXiv:hep-ph/9808486.

[14] K. Goulianos, *Hadronic Diffraction: Where do we Stand?*, in *La Thuile 2004, Results and Perspectives in Particle Physics*, edited by M. Greco, Proc. of Les Rencontres de Physique de la Vallé d'Aoste, La Thuile, Aosta Valley, Italy, February 29 - March 6, 2004, pp. 251-274; arXiv:hep-ph/0407035.

[15] A. Donnachie and P. Landshoff, Nucl. Phys. **B244** (1984) 322; Nucl. Phys. **B267** (1985) 690; Phys. Lett. **b296** (1992) 227.

[16] A. Donnachie and P. Landshoff, New data and the hard Pomeron, Phys. Lett. B **518** (2001) 63, hep-ph/0105088.

Exclusive J/ψ and Υ hadroproduction as a probe of the QCD Odderon*

Lech Szymanowski
LPT, Université Paris XI, CNRS, Orsay, France, Universite de Liège, Belgium
and SINS Warsaw, Poland

Abstract
We study the exclusive production of J/ψ or Υ in pp and $\bar{p}p$ collisions, where the meson emerges from the pomeron–odderon and the pomeron–photon fusion. We estimate the cross sections for these processes for the kinematical conditions of the Tevatron and of the LHC.

1 Introduction

The new analysis of exprimental data on the exclusive hadroproduction processes by the CDF collaboration [1] shows that these types of processes can be objects of detailed study at the Tevatron and in the near future at the LHC. Up to now, the most intensively studied exclusive hadroproduction processes include the dijet or the $\gamma\gamma$ production in the central rapidity region and the Higgs meson production [2], see Fig. 1. Here, we discuss the exclusive hadroproduction of J/Ψ and Υ mesons, i.e.

$$pp\,(\bar{p}) \;\to\; p'\,V\,p''\,(\bar{p}''\,)\;, \qquad \text{where} \qquad V = J/\psi,\,\Upsilon\;. \tag{1}$$

The main motivation of our recent study [3] of the process (1) is that the production of a charmonium V, with the quantum numbers $J^{PC} = 1^{-\,-}$, occurs as the result of a pomeron-odderon or pomeron-photon fusion. Such studies can thus probe the dynamics of the odderon [4], i.e. the counterpart with negative charge parity of the pomeron. Odderon escapes experimental verification and until now has remained a mystery, although various ways to detect it through its interference with a pomeron mediated amplitude [5] have been recently proposed (for a review see [6]).

2 The scattering amplitude

In the lowest order of perturbative QCD, the pomeron and the odderon are described by the exchange of two and three non-interacting gluons, respectively. The lowest order contribution to the hadroproduction

$$h(p_A) + h(p_B) \to h(p_{A'}) + V(p) + h(p_{B'}) \tag{2}$$

is illustrated by diagrams of Fig. 2, from which the diagrams (a,b) describe the pomeron-odderon fusion and (c,d) the photon-pomeron fusion. The momenta of particles are parametrized by the Sudakov decompositions

$$p_{A'} = (1-x_A)p_A + \frac{\boldsymbol{l}^2}{s(1-x_A)}p_B - l_\perp\;, \quad p_{B'} = \frac{\boldsymbol{k}^2}{s(1-x_B)}p_A + (1-x_B)p_B - k_\perp\;, \tag{3}$$

* Dedicated to the memory of Leszek Łukaszuk, co-father of the odderon, who recently passed away.

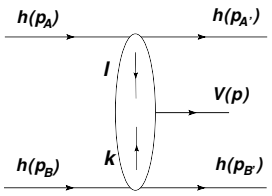


Fig. 1: *Kinematics of the exclusive meson production in pp ($p\bar{p}$) scattering.*

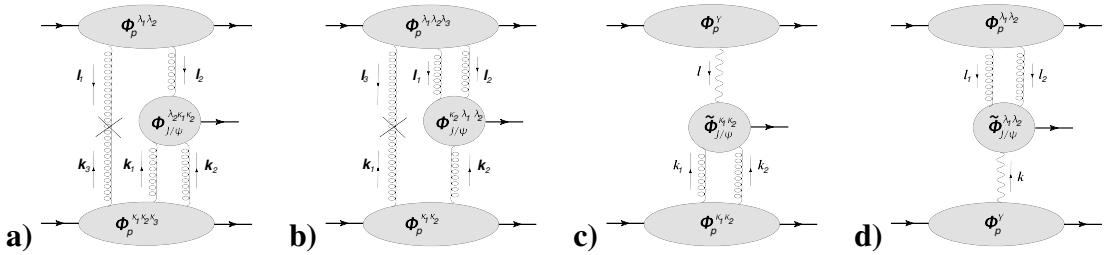


Fig. 2: *The lowest order diagrams contributiong to the pomeron-odderon fusion (a,b) and the pomeron–photon fusion (c,d) for vector meson production.*

with $\boldsymbol{l}^2 = -l_\perp \cdot l_\perp \approx -(p_A - p_{A'})^2 \equiv -t_A, \quad \boldsymbol{k}^2 = -k_\perp \cdot k_\perp \approx (p_B - p_{B'})^2 \equiv -t_B$ and

$$p = \alpha_p p_A + \beta_p p_B + p_\perp$$
$$\alpha_p = x_A - \frac{\boldsymbol{k}^2}{s(1-x_B)} \approx x_A \ , \ \ \beta_p = x_B - \frac{\boldsymbol{l}^2}{s(1-x_A)} \approx x_B \ , \quad p_\perp = l_\perp + k_\perp \ , \qquad (4)$$

which lead to the mass-shell condition for the vector meson, $V = J/\psi, \Upsilon$,
$m_V^2 = s x_A x_B - (\boldsymbol{l} + \boldsymbol{k})^2$.

The scattering amplitude written within the $k_\perp$-factorization approach is a convolution in transverse momenta of $t-$channel fields. For instance, the contribution of Fig. 2a reads:

$$\mathcal{M}_{P\,O} = \qquad (5)$$
$$-is\,\frac{2\cdot 3}{2!\,3!}\,\frac{4}{(2\pi)^8}\int \frac{d^2\boldsymbol{l}_1}{\boldsymbol{l}_1^2}\,\frac{d^2\boldsymbol{l}_2}{\boldsymbol{l}_2^2}\,\delta^2(\boldsymbol{l}_1+\boldsymbol{l}_2-\boldsymbol{l})\,\frac{d^2\boldsymbol{k}_1}{\boldsymbol{k}_1^2}\,\frac{d^2\boldsymbol{k}_2}{\boldsymbol{k}_2^2}\,\frac{d^2\boldsymbol{k}_3}{\boldsymbol{k}_3^2}\,\delta^2(\boldsymbol{k}_1+\boldsymbol{k}_2+\boldsymbol{k}_3-\boldsymbol{k})$$
$$\times\delta^2(\boldsymbol{k}_3+\boldsymbol{l}_1)\,\boldsymbol{k}_3^2\;\delta^{\lambda_1\kappa_3}\cdot\Phi_P^{\lambda_1\lambda_2}(\boldsymbol{l}_1,\boldsymbol{l}_2)\cdot\Phi_P^{\kappa_1\kappa_2\kappa_3}(\boldsymbol{k}_1,\boldsymbol{k}_2,\boldsymbol{k}_3)\cdot\Phi_{J/\psi}^{\lambda_2\kappa_1\kappa_2}(\boldsymbol{l}_2,\boldsymbol{k}_1,\boldsymbol{k}_2)\ ,$$

where $\Phi_P^{\lambda_1\lambda_2}(\boldsymbol{l}_1,\boldsymbol{l}_2)$ and $\Phi_P^{\kappa_1\kappa_2\kappa_3}(\boldsymbol{k}_1,\boldsymbol{k}_2,\boldsymbol{k}_3)$ are the impact factors describing the coupling of the pomeron and the odderon to scattered hadrons, respectively, whereas $\Phi_{J/\psi}^{\lambda_2\kappa_1\kappa_2}(\boldsymbol{l}_2,\boldsymbol{k}_1,\boldsymbol{k}_2)$ is the effective J/ψ-meson production vertex.

The proton impact factors are non-perturbative objects and we describe them within the Fukugita-Kwieciński eikonal model [7]. For the pomeron exchange the impact factor of the proton is the product

$$\Phi_P^{\lambda_1\lambda_2}(\boldsymbol{l}_1,\boldsymbol{l}_2) = 3\,\Phi_q^{\lambda_1\lambda_2}(\boldsymbol{l}_1,\boldsymbol{l}_2)\,\mathcal{F}_P(\boldsymbol{l}_1,\boldsymbol{l}_2)\ , \qquad (6)$$

of the impact factor of a quark

$$\Phi_q^{\lambda_1\lambda_2}(\boldsymbol{l}_1,\boldsymbol{l}_2) = -\bar{\alpha}_s \cdot 8\pi^2 \cdot \frac{\delta^{\lambda_1\lambda_2}}{2\,N_c}\ , \tag{7}$$

and the phenomenological form-factor $\mathcal{F}_P$ describing the proton internal structure

$$\mathcal{F}_P(\boldsymbol{l}_1,\boldsymbol{l}_2) = F(\boldsymbol{l}_1+\boldsymbol{l}_2,0,0) - F(\boldsymbol{l}_1,\boldsymbol{l}_2,0)\ , \tag{8}$$

which vanishes when any of $\boldsymbol{l}_i \to 0$, as required by colour gauge invariance. The function $F(\boldsymbol{k}_1,\boldsymbol{k}_2,\boldsymbol{k}_3)$ is chosen in the form

$$F(\boldsymbol{k}_1,\boldsymbol{k}_2,\boldsymbol{k}_3) = \frac{A^2}{A^2 + \frac{1}{2}\left((\boldsymbol{k}_1-\boldsymbol{k}_2)^2 + (\boldsymbol{k}_2-\boldsymbol{k}_3)^2 + (\boldsymbol{k}_3-\boldsymbol{k}_1)^2\right)}, \tag{9}$$

with A a phenomenological constant chosen to be half of the ρ meson mass, $A = m_\rho/2 \approx 384\,\mathrm{MeV}$. The analogous impact-factor for the odderon exchange reads

$$\Phi_P^{\kappa_1\kappa_2\kappa_3}(\boldsymbol{k}_1,\boldsymbol{k}_2,\boldsymbol{k}_3) = 3\ \Phi_q^{\kappa_1\kappa_2\kappa_3}(\boldsymbol{k}_1,\boldsymbol{k}_2,\boldsymbol{k}_3)\mathcal{F}_O(\boldsymbol{k}_1,\boldsymbol{k}_2,\boldsymbol{k}_3)\ , \tag{10}$$

where

$$\Phi_q^{\kappa_1\kappa_2\kappa_3}(\boldsymbol{k}_1,\boldsymbol{k}_2,\boldsymbol{k}_3) = i\ \bar{\alpha}_s^{\frac{3}{2}}\ 2^5\ \pi^{\frac{7}{2}}\ \frac{d^{\kappa_3\kappa_2\kappa_1}}{4N_c}\ , \tag{11}$$

and the form-factor $\mathcal{F}_O$ has a form

$$\mathcal{F}_O(\boldsymbol{k}_1,\boldsymbol{k}_2,\boldsymbol{k}_3) = F(\boldsymbol{k}=\boldsymbol{k}_1+\boldsymbol{k}_2+\boldsymbol{k}_3,0,0) - \sum_{i=1}^{3} F(\boldsymbol{k}_i,\boldsymbol{k}-\boldsymbol{k}_i,0) + 2\,F(\boldsymbol{k}_1,\boldsymbol{k}_2,\boldsymbol{k}_3)\ . \tag{12}$$

The derivation of the effective production vertex of J/ψ, $\Phi_{J/\psi}^{\lambda_2\kappa_1\kappa_2}(\boldsymbol{l}_2,\boldsymbol{k}_1,\boldsymbol{k}_2)$, in Eq. (5) is one of the main results of our study. The charmonium is treated in the non-relativistic approximation and it is described by the $\bar{c}c \to J/\psi$ vertex

$$\langle \bar{c}\,c|J/\psi\rangle = \frac{g_{J/\psi}}{2}\ \hat{\varepsilon}^{\,*}(p)\left(p\cdot\gamma + m_{J/\psi}\right)\ ,\quad m_{J/\psi} = 2m_c\ , \tag{13}$$

with the coupling constant $g_{J/\psi}$ related to the electronic width $\Gamma_{e^+e^-}^{J/\psi}$ of the $J/\psi \to e^+\,e^-$ decay

$$g_{J/\psi} = \sqrt{\frac{3m_{J/\psi}\Gamma_{e^+e^-}^{J/\psi}}{16\pi\alpha_{em}^2 Q_c^2}}\ ,\quad Q_c = \frac{2}{3}\ . \tag{14}$$

The effective vertex $g + 2g \to J/\psi$ is described by the sum of the contributions of the diagrams in Fig. 3 which has the form

$$\begin{aligned}
&\Phi_{J/\psi}^{\lambda_2\kappa_1\kappa_2}(\boldsymbol{l}_2,\boldsymbol{k}_1,\boldsymbol{k}_2) = \alpha_s^{\frac{3}{2}}\ 8\pi^{\frac{3}{2}}\ \frac{d^{\kappa_1\kappa_2\lambda_2}}{N_c}\ V_{J/\psi}(\boldsymbol{l}_2,\boldsymbol{k}_1,\boldsymbol{k}_2),\\
&V_{J/\psi}(\boldsymbol{l}_2,\boldsymbol{k}_1,\boldsymbol{k}_2) = \\
&\quad 4\pi m_c g_{J/\psi}\left[-\frac{x_B\varepsilon^*\cdot p_B + \varepsilon^*\cdot l_{2\perp}}{\boldsymbol{l}_2^2 + (\boldsymbol{k}_1+\boldsymbol{k}_2)^2 + 4m_c^2} + \frac{\varepsilon^*\cdot l_{2\perp} + \varepsilon^*\cdot p_B\left(x_B - \frac{4\boldsymbol{k}_1\cdot\boldsymbol{k}_2}{sx_A}\right)}{\boldsymbol{l}_2^2 + (\boldsymbol{k}_1-\boldsymbol{k}_2)^2 + 4m_c^2}\right]\ .
\end{aligned} \tag{15}$$

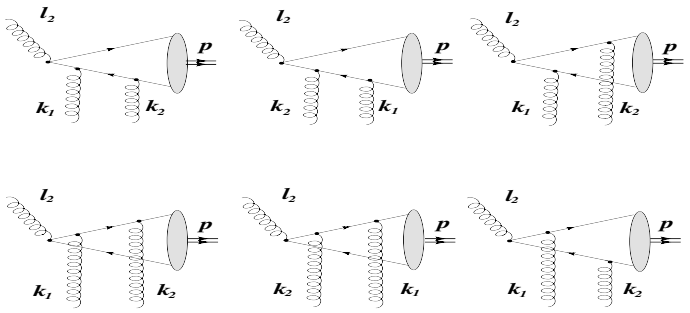


Fig. 3: *The six diagrams defining the effective vertex $g + 2g \to J/\psi$.*

In the numerical analysis we set $\alpha_s(m_c) = 0.38$ and $\alpha_s(m_b) = 0.21$.

The analogous formula which describes the photon-pomeron fusion in Fig. 2c has the form

$$\mathcal{M}_{\gamma P} = \tag{16}$$
$$-\frac{1}{2!}\cdot s\cdot\frac{4}{(2\pi)^4\,\boldsymbol{l}^2}\,\Phi_P^{\gamma}(\boldsymbol{l})\int\frac{d^2\boldsymbol{k}_1}{\boldsymbol{k}_1^2}\frac{d^2\boldsymbol{k}_2}{\boldsymbol{k}_2^2}\,\delta^2(\boldsymbol{k}_1+\boldsymbol{k}_2-\boldsymbol{k})\,\Phi_P^{\kappa_1\kappa_2}(\boldsymbol{k}_1,\boldsymbol{k}_2)\,\tilde{\Phi}_{J/\psi}^{\kappa_1\kappa_2}(\boldsymbol{l},\boldsymbol{k}_1,\boldsymbol{k}_2)\,,$$

where $\Phi_P^{\gamma}(\boldsymbol{l})$ is the phenomenological form-factor of the photon coupling to the proton chosen as $\Phi_P^{\gamma}(\boldsymbol{l}) = -ie\cdot F(\boldsymbol{l},0,0)$. The pomeron impact factor $\Phi_P^{\kappa_1\kappa_2}(\boldsymbol{k}_1,\boldsymbol{k}_2)$ is given by Eq. (6) and $\tilde{\Phi}_{J/\psi}^{\kappa_1\kappa_2}(\boldsymbol{l},\boldsymbol{k}_1,\boldsymbol{k}_2)$ is the corresponding effective vertex expressed through $V_{J/\psi}(\boldsymbol{l},\boldsymbol{k}_1,\boldsymbol{k}_2)$ in Eq. (15)

$$\tilde{\Phi}_{J/\psi}^{\kappa_1\kappa_2}(\boldsymbol{l},\boldsymbol{k}_1,\boldsymbol{k}_2) = \alpha_s\, eQ_c\, 8\pi\,\frac{\delta^{\kappa_1\kappa_2}}{N_c}\,V_{J/\psi}(\boldsymbol{l},\boldsymbol{k}_1,\boldsymbol{k}_2)\,. \tag{17}$$

The phases of the scattering amplitudes describing the two mechanisms of J/ψ-meson production differ by the factor $i = e^{i\pi/2}$. Consequently, they do not interfere and they contribute to the cross section as a sum of two independent contributions.

3 Estimates for the cross sections

We analyse the contributions of pomeron-odderon fusion and the photon-pomeron fusion separately. Denoting $\mathcal{M}_{PO}^{\rm tot} = \mathcal{M}_{PO} + \mathcal{M}_{OP}$ and $\mathcal{M}_{\gamma P}^{\rm tot} = \mathcal{M}_{\gamma P} + \mathcal{M}_{P\gamma}$ we calculate the differential cross sections with respect to the rapidity $y \approx \frac{1}{2}\log(x_A/x_B)$, the squared momentum transfers in the two t-channels, $t_A,\ t_B$, and the azimuthal angle ϕ between $\boldsymbol{k}$ and $\boldsymbol{l}$

$$\frac{d\sigma_i^{(\varepsilon)}}{dy\,dt_A\,dt_B\,d\phi} = \frac{1}{512\pi^4 s^2}\,|\mathcal{M}_i^{\rm tot}|^2 \qquad i = PO,\ \gamma P\,, \tag{18}$$

and the partially integrated cross sections

$$\frac{d\sigma_i}{dy} = \sum_{\varepsilon}\int_{t_{\rm min}^A}^{t_{\rm max}} dt_A \int_{t_{\rm min}^B}^{t_{\rm max}} dt_B \int_0^{2\pi} d\phi\,\frac{d\sigma_i^{(\varepsilon)}}{dy\,dt_A\,dt_B\,d\phi}\,, \tag{19}$$

with $t_{min}^A = 0 = t_{min}^B$ for the PO-fusion and $t_{min}^A = m_p^2 x_A^2$, $t_{min}^B = m_p^2 x_B^2$ for the γP-fusion, and we set $t_{max} = 1.44$ GeV^2. This leads to the naive predictions shown in the Table 1. More

$d\sigma/dy$	J/ψ		Υ	
	odderon	photon	odderon	photon
$p\bar{p}$	20 nb	1.6 nb	36 pb	1.1 pb
pp	11 nb	2.3 nb	21 pb	1.7 pb

Table 1: Naïve cross sections $d\sigma/dy$ given by (19) for the exclusive J/ψ and Υ production in pp and $p\bar{p}$ collisions by the odderon-pomeron fusion, assuming $\bar{\alpha}_s = 1$ and analogous cross sections $d\sigma_\gamma/dy$ for the photon contribution.

realistic cross-sections are obtained by taking into account phenomenological improvements, such as related to the BFKL evolution (which is very important for the pomeron exchange and which may be omitted for the odderon exchange [3]), the effects of soft rescatterings of hadrons, and the precise determination of the value of the model parameter $\bar{\alpha}_s$ in the impact factors. For that we write the corrected cross-sections in the form

$$\left.\frac{d\sigma_{PO}^{\rm corr}}{dy}\right|_{y=0} = \bar{\alpha}_s^5\, S^2_{\rm gap}\, E(s,m_V)\, \frac{d\sigma_{PO}}{dy}, \qquad \left.\frac{d\sigma_{\gamma P}^{\rm corr}}{dy}\right|_{y=0} = \bar{\alpha}_s^2\, E(s,m_V)\, \frac{d\sigma_{\gamma P}}{dy}, \tag{20}$$

where $d\sigma_{PO/\gamma P}/dy$ are the cross sections given by (19) at $\bar{\alpha}_s = 1$. The BFKL evolution for pomeron exchange is taken into account by inclusion of the enhancement factor, which for the central production (i.e. for the rapidity $y = 0$) has the form

$$E(s,m_V) = (x_0\sqrt{s}/m_V)^{2\lambda}. \tag{21}$$

Here, x_0 is the maximal fraction of incoming hadron momenta exchanged in the $t-$channels (or the initial condition for the BFKL evolution) and it is set $x_0 = 0.1$. The effective pomeron intercept λ is determined by HERA data and it equals $\lambda = 0.2$ ($\lambda = 0.35$) for the J/ψ (Υ) production [8].

The gap surviving factor $S^2_{\rm gap}$ for the exclusive production via the pomeron-odderon fusion is fixed by the results of Durham two channel eikonal model [9]: $S^2_{\rm gap} = 0.05$ for the exclusive production at the Tevatron and $S^2_{\rm gap} = 0.03$ for LHC. In the case of production from the photon-pomeron fusion, $S^2_{\rm gap} = 1$ [10].

The available estimates of the effective strong coupling constant $\bar{\alpha}_s$ in the Fukugita–Kwieciński model yield results with rather large spread: from $\bar{\alpha}_s \approx 1$ [7], through $\bar{\alpha}_s \approx 0.6-0.7$ determined from the HERA data [3] to $\bar{\alpha}_s \approx 0.3$ determined from data on elastic pp and $p\bar{p}$ scattering [11]. This led us to introduce three scenarios which differ by the values of $\bar{\alpha}_s$ and of $S^2_{\rm gap}$. In the *optimistic scenario* we use a large value of the coupling, $\bar{\alpha}_s = 1$, combined with the gap survival factors obtained in the Durham two-channel eikonal model. We believe that the best estimates should follow from the *central scenario* defined by $\bar{\alpha}_s = 0.75$, and Durham group estimates $S^2_{\rm gap} = 0.05$ ($S^2_{\rm gap} = 0.03$) at the Tevatron (LHC). The *pessimistic scenario* is defined by $\bar{\alpha}_s = 0.3$ and $S^2_{\rm gap} = 1$.

Table 2 shows our predictions for the phenomenologically improved cross sections in all three scenarios. Their magnitudes justify our hope that the process (1) is a subject of experimental study in the near future at the Tevatron and at the LHC [12]. The encouraging feature of our

$d\sigma^{\rm corr}/dy$	J/ψ		Υ	
	odderon	photon	odderon	photon
Tevatron	0.3–1.3–5 nb	0.8–5–9 nb	0.7–4–15 pb	0.8–5–9 pb
LHC	0.3–0.9–4 nb	2.4–15–27 nb	1.7–5–21 pb	5–31–55 pb

Table 2: The phenomenologically corrected cross sections $d\sigma^{\rm corr}/dy|_{y=0}$ for the exclusive J/ψ and Υ production in pp and $p\bar{p}$ collisions by the pomeron–odderon fusion, and analogous cross sections $d\sigma^{\rm corr}_{\gamma}/dy|_{y=0}$ for the photon contribution for the pessimistic–central–optimistic scenarios.

results is due to the fact, that the measurement of the t_i dependence of the cross section partially permits filtering out the $\gamma\, P$ contributions and to uncover the PO ones.

Acknowledgments

I acknowledge common research and discussions with A. Bzdak, J-R. Cudell and L.Motyka. This work is partly supported by the Polish (MEiN) research grant 1 P03B 028 28 and by the Fonds National de la Recherche Scientifique (FNRS, Belgium). I acknowledge a warm hospitality at Ecole Polytechnique and at LPT-Orsay.

References

[1] K. Goulianos, see talk at this conference.

[2] V. Khose, see talk at this conference.

[3] A. Bzdak, L. Motyka, L. Szymanowski and J. R. Cudell, Phys. Rev. D **75**, 094023 (2007) [arXiv:hep-ph/0702134].

[4] L. Lukaszuk and B. Nicolescu, Nuovo Cimento Letters **8**, 405 (1973).

[5] S. J. Brodsky et al., Phys. Lett. B **461**, 114 (1999) ; Ph. Hagler et al., Phys. Lett. B **535**, 117 (2002), Eur. Phys. J. C **26**, 261 (2002); I. F. Ginzburg et al., Eur. Phys. J. C **30**, 002 (2003).

[6] C. Ewerz, hep-ph/0306137.

[7] M. Fukugita and J. Kwieciński, Phys. Lett. B **83** (1979) 119; see also J. F. Gunion and D. E. Soper, Phys. Rev. D **15** (1977) 2617 and J. R. Cudell and B. U. Nguyen, Nucl. Phys. B **420** (1994) 669.

[8] H1 Collaboration: S. Aid *et al.*, Nucl. Phys. B **472** (1996) 3; H1 Collaboration: C. Adloff *et al.*, Phys. Lett. B **483** (2000) 23; H1 Collaboration: A. Aktas *et al.*, Eur. Phys. J. C **46** (2006) 585. ZEUS Collaboration: J. Breitweg *et al.*, Z. Phys. C **75** (1997) 215; Phys. Lett. B **437** (1998) 432; ZEUS Collaboration: S. Chekanov *et al.*, Eur. Phys. J. C **24** (2002) 345.

[9] V. A. Khoze, A. D. Martin and M. G. Ryskin, Eur. Phys. J. C **18** (2000) 167; V. A. Khoze, A. D. Martin, M. G. Ryskin and W. J. Stirling, Eur. Phys. J. C **35** (2004) 211.

[10] V. A. Khoze, A. D. Martin and M. G. Ryskin, Eur. Phys. J. C **24** (2002) 459.

[11] H. G. Dosch, C. Ewerz and V. Schatz, Eur. Phys. J. C **24** (2002) 561.

[12] R. Schicker, see talk at this conference.

The soft and the hard pomerons: elastic scattering and unitarisation

J.R. Cudell[1]†*, A. Lengyel*[2]*, E. Martynov*[3]*, O.V. Selyugin*[4]
[1]JR.Cudell@ulg.ac.be, AGO dept., Université de Liège, 4000 Liège, Belgium
[2]sasha@len.uzhgorod.ua, Inst. of Electron Physics, 88000 Uzhgorod, Ukraine,
[3]martynov@bitp.kiev.ua, Bogolyubov Institute for Theoretical Physics, 03143 Kiev, Ukraine,
[4]selugin@theor.jinr.ru, Bogoliubov Theoretical Laboratory, 141980 Dubna, Russia

Abstract
The hard pomeron component needed to reproduce small-x data seems to be present in elastic scattering at moderate energy. If this is the case, it is likely that the total cross section at the LHC will be appreciably larger than previously expected.

1 The effective trajectory

Historically, hadronic exchanges have been remarkably well described by the simple-pole model of Donnachie and Landshoff [1], which assumes that, at high energy, the hadronic amplitude is dominated by a simple-pole pomeron:

$$A(s,t) = C(t)s^{1.08+0.25t} \tag{1}$$

The first question is whether this simple model extends to other processes, and in particular to those measured at HERA.

H1 and ZEUS have done amazingly good and useful measurements, and extracted very precise information on F_2, as well as on pomeron-dominated processes such as quasi-elastic vector-meson production, or DVCS. This means that we have a very precise picture of the pomeron, and of the dependence of its properties on Q^2 and t. If we represent pomeron exchange by a simple pole corresponding to a trajectory $\alpha(t) = \alpha(0) + \alpha' t$, its contribution to F_2 would be proportional to $x^{\alpha(0)-1}$ while its contribution to quasi-elastic scattering would go as $\sigma \sim W^{4(\alpha(t)-1)}$. All the data lead to the following effective properties (see e.g. [2]):

- the intercept varies with Q^2 and with the mass M of the produced meson. Its value is always constrained by $1.08 < \alpha(0) < 1.45$, and increases with Q^2 and M^2.
- The slope α' of the trajectory is not universal: it is lower in processes containing a hard scale, such as J/ψ production, and is constrained by 0.16 GeV$^{-2} > \alpha' > 0.08$ GeV^{-2}.

Unfortunately, because the masses and Q^2 are external variables, it is not possible that the trajectory associated with a simple pole depends on them. One may get such a behaviour via more complicated singularities in the complex j plane. Nevertheless, it is striking to observe that different processes lead to the same bounds on the effective intercept, and that both intercept and slope join smoothly with the original Donnachie-Landshoff soft pomeron.

† speaker

2 Regge theory and the two-pomeron picture

This observation prompted Donnachie and Landshoff to extend their original model by adding a new contribution to it [3]: the hard pomeron. The hadronic elastic amplitude thus becomes

$$A_{2\to 2}(s,t) = \sum_i C_i(Q^2, M^2, t) s^{\alpha_i(t)}$$

In general, several trajectories are needed to reproduce all the data, but the two dominant ones at high energy are the hard and the soft pomerons. Both are supposed to have universal trajectories. The effective intercept thus comes from mixing these two pomerons with coefficients that depend on Q^2 and M. Following these ideas, Donnachie and Landshoff were able to reproduce all the data from HERA. The hard pomeron intercept was fitted to $\alpha_H(0) = 1.4372$, so that the small-x measurements of F_2 were reproduced [4]. The fit was then extended to higher values of x [5], and was made compatible with DGLAP evolution [6], so that partonic distributions could be obtained from it [7]. These ideas were also applied to vector-meson quasielastic photoproduction [8], which are also well reproduced in a 2-pomeron model, when the couplings of the pomerons depend on the mass of the produced meson. The fits to these processes, which now involve an interference between the hard and the soft pomeron, lead to compatible values for the hard-pomeron intercept, and to an estimate for its slope: $\alpha'_H \approx 0.1$ GeV^{-2}, while the soft pomeron trajectory remains as in Eq. (1).

So the addition of a hard pomeron leads to a good description of the data at HERA. But if the hard pomeron is a universal exchange, then one would expect it to be present even in soft data. It is indeed unlikely that the couplings become exactly zero for all on-shell light hadrons, especially if we remember that they vary in photoproduction with the mass of the produced mesons. This prompted us to reconsider the fits to total cross sections and to the real part of the elastic amplitude.

3 The hard component of soft data

The main motivation of [9] was in fact to understand why the soft pomeron model of Eq. (1) could provide a good fit to total cross sections for $\sqrt{s} \geq 5$ GeV, while it failed to reproduce the data for $\rho(0)$ [10]. Hence the paper used integral dispersion relations in a rather careful way, and tried to check whether lifting totally the degeneracy of the dominant meson trajectories would help. It was then found that if one added a new crossing-even trajectory, its intercept would automatically go to a value around 1.4, and the quality of the fit would become comparable to that of the best parameterisations of [10]. A careful analysis of the results shows that the main improvement comes from the fit to πp and Kp data, while the pp and $\bar{p}p$ fit is not affected. In fact the coefficient of the hard pomeron is essentially zero in this case, which explains why this contribution was not considered before [11]. The reason for this decoupling is clear: the inclusion of a hard pomeron makes the cross sections rise very fast, so that unitarity corrections must be considered between the ISR and the Sp$\bar{\text{p}}$S energies[1].

So our strategy was to fit data below 100 GeV, which gave us the following results:

- the hard pomeron intercept is

$$\alpha_H = 1.45 \pm 0.01;$$

[1] See O.V. Selyugin's contribution to these proceedings.

- if we write the coefficients of the amplitude for $ab \to ab$ elastic scattering as $g_a g_b$, we obtain an inverse hierarchy:
$$g_K \approx 1.1 g_\pi \approx 3.2 g_p.$$
The hard pomeron seems to couple more to smaller objects.
- As the amplitude is described by simple-pole singularities, its terms should obey Regge factorisation, which can be tested by deriving the amplitude for $\gamma\gamma$ scattering from the amplitudes for pp and γp scattering. The resulting cross section does reproduce the LEP measurement, favouring the deconvolution with PHOJET. The hard pomeron singularity must then be rather close to a simple pole.

After this study, three of us considered the off-forward case [12]. We limited ourselves to the first cone $|t| < 0.5$ GeV^2, so that we would not have to deal with multiple exchanges, or with the question of the odderon, and found that many data sets had problems at small $|t|$, so that we also used $|t| > 0.1$ GeV^2. The elastic ap amplitude is then given by

$$A^{ap}_{2\to 2} = C^{ap}_H F^p_H(t) F^a_H(t) s^{\alpha_H} + C^{ap}_S F^p_S(t) F^a_S(t) + \text{meson contributions},$$

with $F_i(0) = 1$. The dataset we fitted to includes all the available data for pp, $\bar{p}p$, Kp and πp elastic scattering, which we extracted from the HEPDATA system [13], checked, and compiled in a unique format. The resulting database[2], contains about 10000 points, more than 2000 of which fall in the t interval considered here, and at $\sqrt{s} \leq 100$ GeV. Because of this large number of points, we were able to extract the form factors $F_i(t)$ directly from the data, by fitting small intervals $t_j \pm \Delta t_j$ to constant $F_i(t_j)$, and by later fitting smooth curves to these values. The resulting form factors are shown in Fig. 1. There is enough data in the proton case to distinguish between the hard pomeron and the soft pomeron, but we had to assume they were degenerate in the πp and Kp cases. For the meson exchanges, we assumed that $C = +1$ and $C = -1$ trajectories were not degenerate, and found that both form factors had zeroes, which we took into account by multiplying standard form factors by a function $Z(t)$ which is asymptotically 1 but changes sign at $t \approx -0.15$ GeV^2 for the $C = -1$ trajectory and at $t \approx -0.47$ GeV^2 for the $C = +1$ trajectory.

Using direct extraction of the form factors from data produces a remarkably good fit, with a $\chi^2/dof = 0.95$, partially shown in Fig. 2. Note that we had to exclude a few datasets which had gross disagreements with the others (about 100 points). Besides the form factors, it also produces trajectories for the pomerons. We find that

$$\alpha_S = 1.07 + 0.3t \quad (2)$$
$$\alpha_H(t) = 1.45 + 0.1t \quad (3)$$

Although the central value of the hard pomeron slope is in perfect agreement with [8], one must mention that it has a large error, as it is correlated with the choice of form factor for the hard pomeron.

[2] available at `http://www.theo.phys.ulg.ac.be/~cudell/data/`

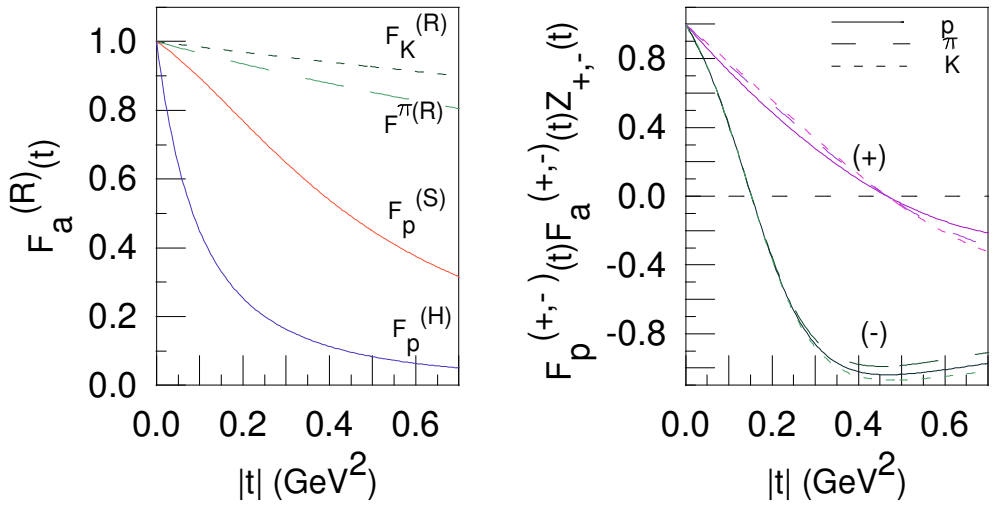


Fig. 1: Form factors for the various exchange terms, for $|t| \leq 0.5$ GeV^2. The left figure gives the form factors of the two pomeron, which are different in the proton case, but taken as identical for mesons ($F^{(R)}$ is the pomeron form factor for both soft and hard pomerons in that case). The right figure shows the form factor of the dominant meson exchanges.

4 Unitarisation and high energies

As explained above, we have had to consider the hard pomeron at low energy $\sqrt{s} \leq 100$ GeV. In order to make contact with higher-energy data, and with LHC physics, it is clear that multiple exchanges have to be considered. The problem of their inclusion is however far from solved. Considerable progress has been made recently in addressing the unitarisation of the BFKL pomeron in a perturbative setting, based on the idea of the saturation of the gluon density. Although there seems to be some relation between the equations describing parton saturation and conventional unitarisation schemes [14], it is far from clear whether one can extend these perturbative methods to a soft regime.

In [10], it was shown that a variety of analytic parameterisations leads to a total LHC cross section between 85 and 117 mb. We showed in [9] that a model including a hard pomeron could lead to a cross section compatible with these limits, provided one used an extended eikonal scheme.

However, two of us have considered in [15] more traditional schemes, i.e. the saturation of the profile function when it reaches the black-disk limit, or the standard one-channel eikonal. The former has the advantage to keep the simple-pole nature of the hard pomeron, so that the low-energy fit is not affected, whereas the latter implies a refitting, which however does not change the parameters significantly. Interestingly, both schemes predict a large cross section at the LHC, of the order of 150 mb, as show in Fig. 2. It thus seems possible to evade the bound presented in [10], provided a universal hard pomeron trajectory is present even in soft scattering. Note that such a trajectory would have consequences not only for the total cross section, but also for the value of the ρ parameter and for the slope of the differential cross section $B(t)$, hence it is very important that all these be measured at the LHC.

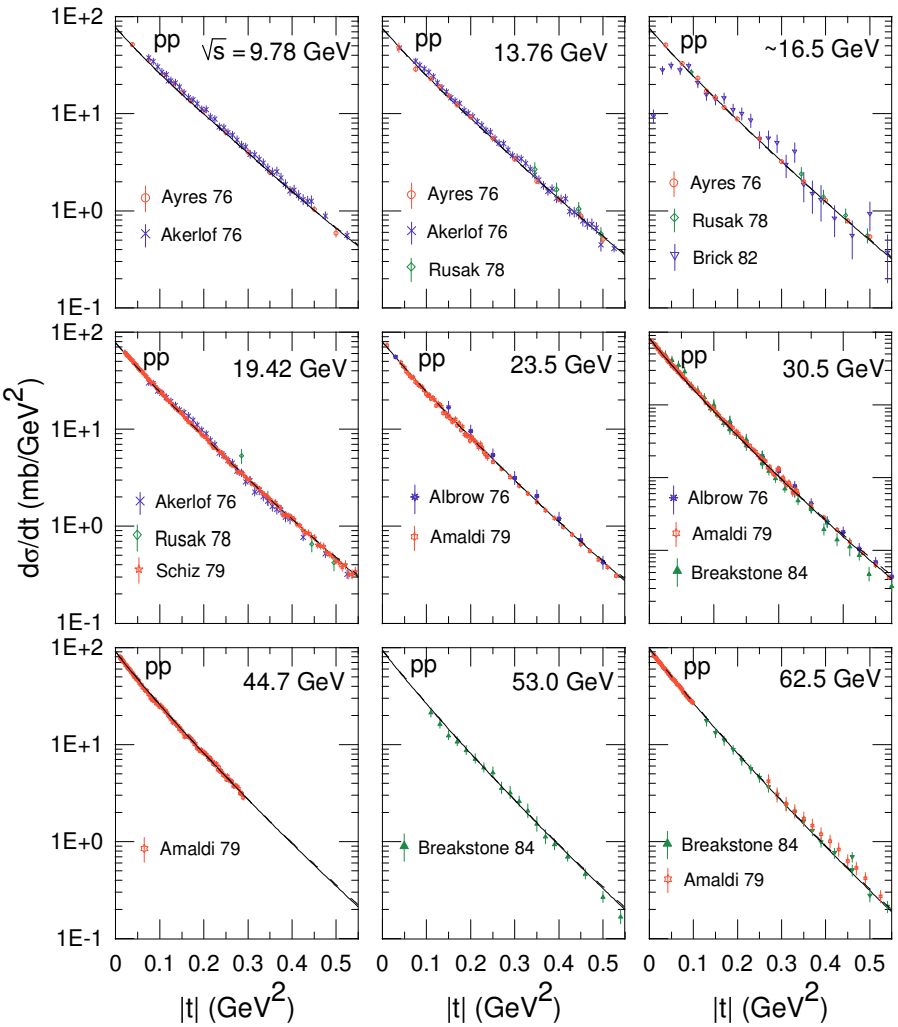


Fig. 2: Fit to elastic differential cross sections in the *pp* case.

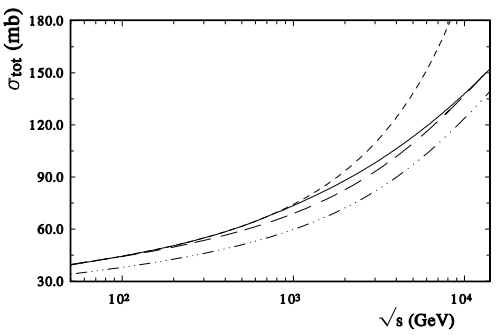


Fig. 3: The total cross section as a function of $\sqrt{s}$, for the bare amplitude (short dashes), a saturated amplitude (plain curve), an eikonalised amplitude (dash-dot-dot), and for a refitted eikonal (long dashes).

5 Conclusion

The idea of universal exchanges of Regge trajectories is an old one, which has been very fruitful in describing hadronic scattering data. It may in fact be the only way to get a grasp on these processes, which escape perturbation theory. The data of HERA have taught us that a hard singularity is present in $\gamma^{(*)}p$ scattering for large Q^2 and for large masses. It is natural to assume that such a singularity is also present in other hadronic processes, even at small Q^2 or for small masses. We have found that the inclusion of a hard pomeron in fits to soft data appreciably improves the description of the data at energies below 100 GeV. The coupling of the hard pomeron is then only a few percents of that of the soft pomeron, but this is enough to reach the black disk limit around 1 TeV. One then needs to worry about multiple exchanges, and this makes predictions for the LHC quite uncertain.

One can say that the observation of a cross section lower than 117 mb would disfavour the ideas presented here, as the unitarisation scheme needed would have to use strong rescatterings, which have no reason to disappear at low energy. On the other hand, the observation of a cross section higher than 117 mb would be a strong indication that a hard singularity is there in soft data. If this is the case, rescattering/saturation effects will modify not only σ_{tot} but also ρ and $B(t)$. It thus seems a good idea to devise a strategy to measure these quantities in an independent way at the LHC.

Acknowledgements: The authors would like to thank for helpful discussions P.V. Landshoff. O.S. gratefully acknowledges financial support from FRNS and would like to thank the University of Liège where part of this work was done.

References

[1] A. Donnachie and P. V. Landshoff, Phys. Lett. **B296**, 227 (1992). hep-ph/9209205.

[2] ZEUS Collaboration, A. Levy, Acta Phys. Polon. **B33**, 3547 (2002). hep-ex/0206048; H1 Collaboration, R. Devenish (2002). hep-ex/0208043.

[3] A. Donnachie and P. V. Landshoff, Phys. Lett. **B437**, 408 (1998). hep-ph/9806344.

[4] A. Donnachie and P. V. Landshoff, Phys. Lett. **B518**, 63 (2001). hep-ph/0105088.

[5] A. Donnachie and P. V. Landshoff, Phys. Lett. **B533**, 277 (2002). hep-ph/0111427.

[6] J. R. Cudell, A. Donnachie, and P. V. Landshoff, Phys. Lett. **B448**, 281 (1999). hep-ph/9901222.

[7] A. Donnachie and P. V. Landshoff, Phys. Lett. **B550**, 160 (2002). hep-ph/0204165.

[8] A. Donnachie and P. V. Landshoff, Phys. Lett. **B478**, 146 (2000). hep-ph/9912312.

[9] J. R. Cudell, E. Martynov, O. V. Selyugin, and A. Lengyel, Phys. Lett. **B587**, 78 (2004). hep-ph/0310198.

[10] COMPETE Collaboration, J. R. Cudell *et al.*, Phys. Rev. Lett. **89**, 201801 (2002). hep-ph/0206172.

[11] J. R. Cudell *et al.*, Phys. Rev. **D65**, 074024 (2002). hep-ph/0107219.

[12] J. R. Cudell, A. Lengyel, and E. Martynov, Phys. Rev. **D73**, 034008 (2006). hep-ph/0511073.

[13] M. R. Whalley, Comput. Phys. Commun. **57**, 536 (1989);
M. Whalley. DPDG-97-02.

[14] O. V. Selyugin and J. R. Cudell, PoS **DIFF2006**, 057 (2006). hep-ph/0611077.

[15] J. R. Cudell and O. V. Selyugin (2006). hep-ph/0612046.

pp Elastic Scattering at LHC in a Nucleon–Structure Model

M. M. Islam[a]*, J. Kašpar*[b] *and R. J. Luddy*[c]
[a] Department of Physics, University of Connecticut, Storrs, CT 06269, USA, (islam@phys.uconn.edu)
[b] TOTEM Collaboration, CERN, Geneva, Switzerland (Jan.Kaspar@cern.ch)
Institute of Physics, Academy of Sciences of the Czech Republic, Prague
[c] Department of Physics, University of Connecticut, Storrs, CT 06269, USA, (RJLuddy@phys.uconn.edu)

Abstract
We predict pp elastic differential cross sections at LHC at c.m. energy 14 TeV and momentum transfer range $|t|$ = 0 – 10 GeV^2 in a nucleon-structure model. In this model, the nucleon has an outer cloud of quark-antiquark condensed ground state, an inner shell of topological baryonic charge ($r \simeq 0.44F$) probed by the vector meson ω, and a central quark-bag ($r \simeq 0.2F$) containing valence quarks. We also predict $\mathrm{d}\sigma/\mathrm{d}t$ in the Coulomb-hadronic interference region. Large $|t|$ elastic scattering in this model arises from valence quark-quark scattering, which is taken to be due to the hard-pomeron (BFKL pomeron with next to leading order corrections). We present results of taking into account multiple hard-pomeron exchanges, i.e. unitarity corrections. Finally, we compare our prediction of pp elastic $\mathrm{d}\sigma/\mathrm{d}t$ at LHC with the predictions of various other models. Precise measurement of pp $\mathrm{d}\sigma/\mathrm{d}t$ at LHC by the TOTEM group in the $|t|$ region 0 – 5 GeV^2 will be able to distinguish between these models.

High energy pp and $\bar{\mathrm{p}}\mathrm{p}$ elastic scattering have been at the forefront of accelerator research since the early seventies with the advent of CERN Intersecting Storage Rings (ISR) and measurement of pp elastic differential cross section in the c.m. energy range $\sqrt{s}$ = 23 – 62 GeV and momentum transfer range $|t|$ = 0.8 – 10 GeV^2 [1]. This was followed by the Fermilab accelerator where pp elastic scattering was measured at c.m. energy $\sqrt{s}$ = 27.4 GeV in a fixed target experiment at large momentum transfers: $|t|$ = 5.5 – 14 GeV^2 [2]. Next came the CERN SPS Collider, where $\bar{\mathrm{p}}\mathrm{p}$ elastic scattering was measured at c.m. energies 546 GeV and 630 GeV – a jump of one order of magnitude in c.m. energy from ISR [3–5]. The Fermilab Tevatron followed next where $\bar{\mathrm{p}}\mathrm{p}$ elastic scattering was measured at c.m. energy 1.8 TeV, but in a rather small momentum transfer range: $|t|$ = 0 – 0.5 GeV^2 [6, 7]. We are now at the threshold of a new period of accelerator research with the LHC starting up soon and with the planned measurement of pp elastic scattering by the TOTEM group at c.m. energy 14 TeV and momentum transfer range $|t| \simeq 0$ – 10 GeV^2 [8, 9].

My collaborators and I have been studying pp and $\bar{\mathrm{p}}\mathrm{p}$ elastic scattering since late seventies. From our phenomenological investigation, we have arrived at two results: 1) a physical picture of the nucleon, 2) an effective field theory model underlying the physical picture [10]. The physical picture shows that the nucleon has an outer cloud, an inner shell of baryonic charge,

* speaker

and a central quark-bag containing the valence quarks (Fig. 1). The radius of the shell is about 0.44 F and that of the quark-bag is 0.2 F. The underlying field theory model turns out to be a gauged Gell–Mann–Levy linear σ-model with spontaneous breakdown of chiral symmetry and with a Wess–Zumino–Witten (WZW) anomalous action. The model attributes the outer nucleon cloud to a quark–antiquark condensed ground state analogous to the BCS ground state in superconductivity– an idea that was first proposed by Nambu and Jona-Lasinio. The WZW action indicates that the baryonic charge is geometrical or topological in nature, which is the basis of the Skyrmion model. The action further shows that the vector meson ω couples to this topological charge like a gauge boson, i.e. like an elementary vector meson. As a consequence, one nucleon probes the baryonic charge of the other via ω-exchange. In pp elastic scattering, in the small momentum transfer region, the outer cloud of one nucleon interacts with that of the other giving rise to diffraction scattering. As the momentum transfer increases, one nucleon probes the other at intermediate distances and the ω-exchange becomes dominant. At momentun transfers even larger, one nucleon scatters off the other via valence quark-quark scattering.

Our calculated pp elastic $\mathrm{d}\sigma/\mathrm{d}t$ at c.m. energy 14 TeV is shown in Fig. 2 by the solid line that includes all three processes: diffraction, ω-exchange, and qq scattering. The dotted curve shows $\mathrm{d}\sigma/\mathrm{d}t$ due to diffraction only. We see that diffraction dominates in the small $|t|$ region, but falls off rapidly. The dot-dashed curve shows $\mathrm{d}\sigma/\mathrm{d}t$ due to ω-exchange only and indicates that ω-exchange dominates in the $|t|$ region 1.5 – 3.5 GeV^2. Beyond that, the valence quark-quark scattering takes over. The dashed curve for $|t| > 3.5$ GeV^2 represents $\mathrm{d}\sigma/\mathrm{d}t$ with single valence quark-quark scattering, whereas the solid curve represents $\mathrm{d}\sigma/\mathrm{d}t$ with all multiple valence quark-quark scattering.

Let us next examine how the three processes are described in our calculations [10]. Diffraction is described by using the impact parameter representation and a phenomenological profile function:

$$T_D(s,t) = i\,p\,W\,\textstyle\int_0^\infty b\,\mathrm{d}b\;J_0(b\,q)\Gamma_D(s,b); \qquad (1)$$

q is the momentum transfer ($q = \sqrt{|t|}$) and $\Gamma_D(s,b)$ is the diffraction profile function, which is related to the eikonal function $\chi_D(s,b)$: $\Gamma_D(s,b) = 1 - \exp(i\chi_D(s,b))$. We take $\Gamma_D(s,b)$ to be an even Fermi profile function:

$$\Gamma_D(s,b) = g(s)[\tfrac{1}{1+e^{(b-R)/a)}} + \tfrac{1}{1+e^{-(b+R)/a}} - 1]. \qquad (2)$$

The parameters R and a are energy dependent: $R = R_0 + R_1(\ln s - i\frac{\pi}{2})$, $a = a_0 + a_1(\ln s - i\frac{\pi}{2})$; $g(s)$ is a complex crossing even energy-dependent coupling strength.

The diffraction amplitude we obtain has the following asymptotic properties:

1. $\sigma_{\mathrm{tot}}(s) \sim (a_0 + a_1 \ln s)^2$ (Froissart-Martin bound)
2. $\rho(s) \simeq \frac{\pi a_1}{a_0 + a_1 \ln s}$ (derivative dispersion relation)
3. $T_D(s,t) \sim i\ s\ \ln^2 s\ f(|t|\ \ln^2 s)$ (Auberson-Kinoshita-Martin scaling)
4. $T_D^{\bar{\mathrm{p}}\mathrm{p}}(s,t) = T_D^{\mathrm{pp}}(s,t)$ (crossing even)

Incidentally, the profile function (2) has been used by Frankfurt et al. to estimate the absorptive effect of soft hadronic interactions (gap survival probability) in the central production of Higgs at LHC [11].

The ω-exchange amplitude in our model has the form

$$T_\omega(s,t) \ \sim \ \exp[i\ \chi_D(s,0)]\ s\ \frac{F^2(t)}{m_\omega^2 - t}. \tag{3}$$

where the factor s shows that ω is behaving like an elementary spin-1 boson. The two form factors indicate that ω is probing two baryonic charge distributions – one for each nucleon. The factor $\exp[i\ \chi_D(s,0)]$ represents the absorptive effect due to soft hadronic interactions.

We view large $|t|$ elastic scattering as a hard collision of a valence quark from one proton with a valence quark from the other proton (Fig. 3). Since this process involves high energy quark-quark scattering at large momentum transfer, one would expect that it should be described by perturbative QCD. In fact, in perturbative QCD, the two quarks would interact via BFKL pomeron, that is, reggeized gluon ladders with rungs of gluons that lead to a fixed branch point in the angular momentum plane at $\alpha_{\rm BFKL}$ = 1 + ω. The value of ω in next to leading order lies in the range 0.13 – 0.18 as argued by Brodsky et al. [12]. We refer to the BFKL pomeron with next to leading order corrections included as the "hard-pomeron". In our calculations, we approximate the hard-pomeron by a fixed pole and take the corresponding qq amplitude as [13]

$$\hat{T}_1(\hat{s},t) = i\ \gamma_{\rm qq}\ \hat{s}\ \left(\hat{s}\ e^{-i\frac{\pi}{2}}\right)^\omega \frac{1}{|t| + r_0^{-2}}, \tag{4}$$

where $\hat{s}$ is the square of the c.m. energy of qq scattering.

Our pp elastic $\mathrm{d}\sigma/\mathrm{d}t$ calculation at 14 TeV reported earlier [10, 13] included only a single hard-pomeron exchange in qq scattering. However, Eq. (4) shows that the hard-pomeron predicts a qq asymptotic total cross section $\hat{\sigma}_{\rm tot}(\hat{s}) \propto \hat{s}^\omega$, i.e. $\hat{\sigma}_{\rm tot}(\hat{s})$ grows like a power of $\hat{s}$ and therefore violates unitarity and the Froissart-Martin bound. To restore unitarity in the qq channel, we use the eikonal representation and write the full qq scattering amplitude as

$$\hat{T}(\hat{s},t) = i\hat{p}\hat{W} \int_0^\infty b\ \mathrm{d}b\ J_0(bq)\left[1 - e^{i\hat{\chi}(\hat{s},b)}\right]. \tag{5}$$

Taking $\hat{T}_1(\hat{s},t)$ in Eq. (4) as the Born or single-scattering amplitude, we obtain by inverting it

$$\hat{\chi}(\hat{s},b) = 2\ i\ \gamma_{\rm qq}\ \left(\hat{s}\ e^{-i\frac{\pi}{2}}\right)^\omega\ K_0(\tfrac{b}{r_0}). \tag{6}$$

Expanding the exponential in (5), we get

$$\hat{T}(\hat{s},t) = -i\ \hat{p}\ \hat{W}\ \int_0^\infty b\ \mathrm{d}b\ J_0(bq)\left[i\ \hat{\chi} - \tfrac{\hat{\chi}^2}{2!} - i\ \tfrac{\hat{\chi}^3}{3!} + \ \tfrac{\hat{\chi}^4}{4!} + ...\right]. \tag{7}$$

The nth term in the series is

$$\hat{T}_n(\hat{s},t) = -i\ \tfrac{(-1)^n\ 2^{n-1}}{n!}\ \gamma_{\rm qq}^n\ \hat{s}\left(\hat{s}\ e^{-i\frac{\pi}{2}}\right)^{n\omega} \int_0^\infty b\ \mathrm{d}b\ J_0(bq)\ K_0^n\left(\tfrac{b}{r_0}\right). \tag{8}$$

Now, $\hat{s} \simeq xx's$, where x and x' are the longitudinal momentum fractions of the protons carried by the valence quarks (Fig. 3). This leads to the following pp elastic amplitude due to qq scattering:

$$T_{\rm qq}(s,t) = \hat{T}_1(s,t)\ \mathcal{F}_1^2(q_\perp) + \hat{T}_2(s,t)\ \mathcal{F}_2^2(q_\perp) + ... + \hat{T}_n(s,t)\ \mathcal{F}_n^2(q_\perp); \tag{9}$$

$\mathcal{F}_1,\ \mathcal{F}_2\ ,...\ \mathcal{F}_n$ are the structure factors that take into account momentum distributions of the valence quarks inside the proton. Our earlier calculation kept only the first term in Eq. (9). Fig. 2 shows that the effect of multiple hard-pomeron exchange in pp scattering is to decrease $\mathrm{d}\sigma/\mathrm{d}t$ at large $|t|$ compared to $\mathrm{d}\sigma/\mathrm{d}t$ due to single hard-pomeron exchange (dashed line in Fig. 2). For $|t| < 3.5$ GeV^2, there is little effect due to multiple scattering, i.e. unitarization.

Results of some of our quantitative calculations are shown in Figs. 4–7. The solid curve in Fig. 4 represents our calculated total cross section as a function of $\sqrt{s}$. Dotted curves represent the error band given by Cudell et al. [14]. In Fig. 5, solid and dashed curves represent our calculated $\rho_{\rm \bar{p}p}$ and $\rho_{\rm pp}$ respectively ($\rho = \mathrm{Re}\ T(s,0)/\ \mathrm{Im}\ T(s,0)$). Dotted curves, as before, represent the error band given by Cudell et al. At $\sqrt{s}$=14 TeV, our values of $\sigma_{\rm tot}$ and $\rho_{\rm pp}$ are

109.4 mb and 0.12 respectively. Fig. 6 shows our calculated $\mathrm{d}\sigma/\mathrm{d}t$ for $\bar{\mathrm{p}}\mathrm{p}$ elastic scattering at $\sqrt{s}$ = 541 GeV in the Coulomb–hadronic interference region using the Kundrát–Lokajíček formulation (upper curve) and West–Yennie formulation (lower curve). Experimental data are from Augier et al. [15]. Fig. 7 shows our predicted $\mathrm{d}\sigma/\mathrm{d}t$ for pp elastic scattering at $\sqrt{s}$ = 14 TeV in the Coulomb–hadronic interference region. Finally, in Fig. 8, we compare our predicted pp elastic $\mathrm{d}\sigma/\mathrm{d}t$ at LHC with the predictions of other models proposed by various groups: Avila et al. [16], Block et al. [17], Bourrely et al. [18], Desgrolard et al. [19], and Petrov et al. (three pomeron) [20].

Conclusions

1. Precision measurement of pp elastic $\mathrm{d}\sigma/\mathrm{d}t$ at LHC by the TOTEM group in the region $|t|$ = 0 – 5 GeV^2 will be able to distinguish between various proposed models (see Fig. 8).
2. In our nucleon-structure model, the qualitative saturation of the Froissart-Martin bound is due to soft hadronic interactions.
3. Large $|t|$ elastic scattering in our model is due to valence quark-quark scattering. This has been described by us as due to the exchange of a hard-pomeron (BFKL pomeron plus next to leading order corrections).
4. Unitarization of the hard-pomeron exchange leads to a decrease of $\mathrm{d}\sigma/\mathrm{d}t$ at large $|t|$, but has little effect on forward $\mathrm{d}\sigma/\mathrm{d}t$.
5. The nucleon structure that we find embodies salient features of many leading models– such as Nambu-Jona-Lasinio model, Skyrmion model, nonlinear σ-model, chiral-bag model– but, at the end, it presents a unique description of the nucleon.

References

[1] E. Nagy *et al.*, Nucl. Phys. B **150**, 221 (1979).
[2] W. Faissler *et al.*, Phys. Rev. D **23**, 33 (1981).
[3] UA4 Collaboration, M. Bozzo *et al.*, Phys. Lett. B **147**, 385 (1984).
[4] UA4 Collaboration, M. Bozzo *et al.*, Phys. Lett. B **155**, 197 (1985).
[5] D. Bernard *et al.*, Phys. Lett. B **171**, 142 (1986).
[6] N. Amos *et al.*, Phys. Lett. B **247**, 127 (1990).
[7] F. Abe *et al.*, Phys. Rev. D **50**, 5518 (1994).
[8] TOTEM Collaboration, Technical Design Report CERN-LHCC-2004-002.
[9] TOTEM Collaboration, CERN-LHCC-2007-013/G130.
[10] M. M. Islam, R. J. Luddy, and A. V. Prokudin, Int. J. Mod. Phys. A **21**, 1 (2006).
[11] L. Frankfurt, M. Strickman, C. Weiss, and M. Zhalov, Czech. J. Phys. **55**, B675 (2005).
[12] S. Brodsky, V. S. Fadin, V. T. Kim, L. N. Lipatov, and G. B. Pivovarov, JETP Lett. **70**, 155 (1999).
[13] M. M. Islam, R. J. Luddy, and A. V. Prokudin, Phys. Lett. B **605**, 115 (2005).
[14] J. R. Cudell *et al.*, Phys. Rev. Lett. **89**, 201801 (2002).
[15] C. Augier *et al.*, Phys. Lett. B **316**, 498 (1993).
[16] R. F. Avila, S. D. Campos, M. J. Menon, and J. Montanha, Eur.Phys.J. C **47**, 171 (2006).
[17] M. M. Block, E. M. Gregores, F. Halzen, and G. Pancheri, Phys. Rev. D **60**, 054024 (1999).
[18] C. Bourrely, J. Soffer, and T. T. Wu, Eur. Phys. J. C **28**, 97 (2003).
[19] P. Desgrolard, M. Giffon, E. Martynov, and E. Predazzi, Eur. Phys. J. C **16**, 499 (2000).
[20] V. Petrov, E. Predazzi, and A. V. Prokudin, Eur. Phys. J. C **28**, 525 (2003).

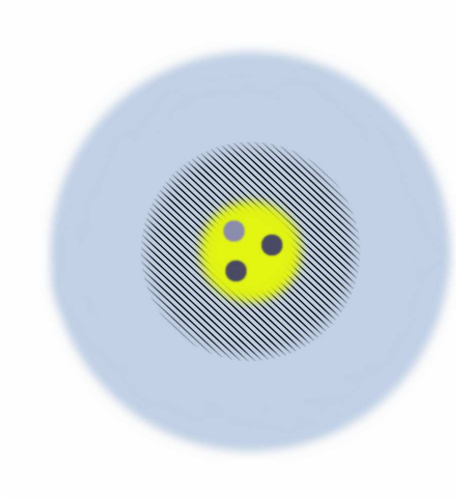


Fig. 1

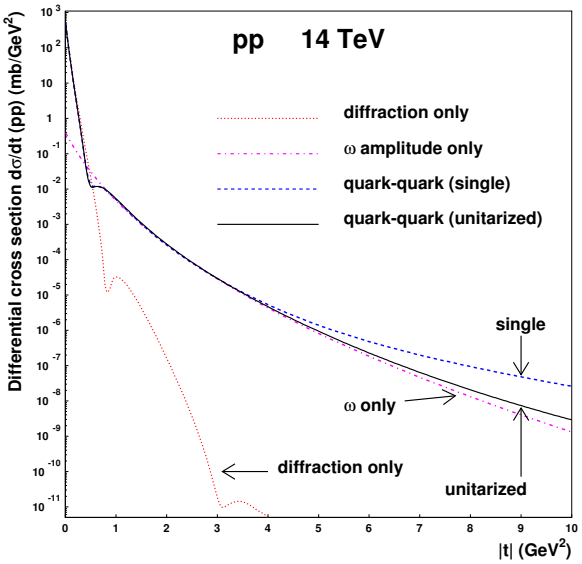


Fig. 2

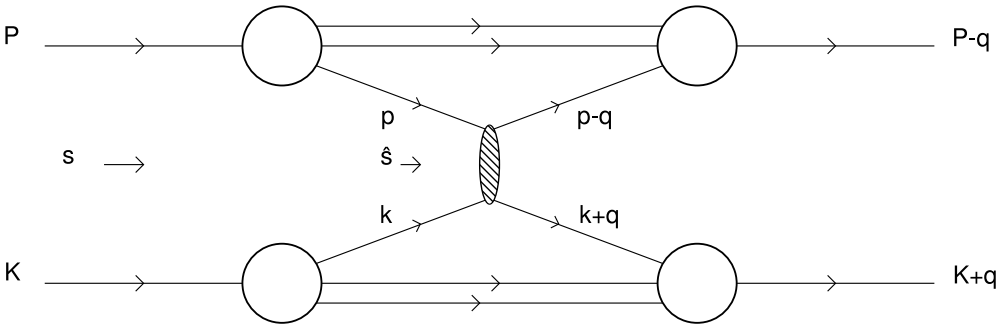


Fig. 3

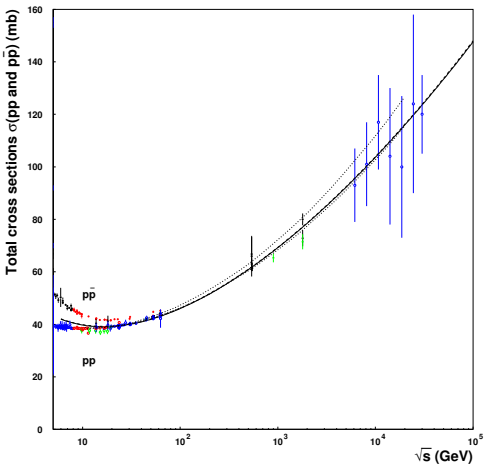


Fig. 4

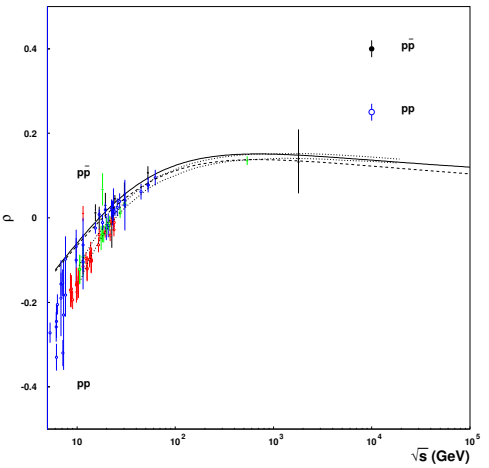


Fig. 5

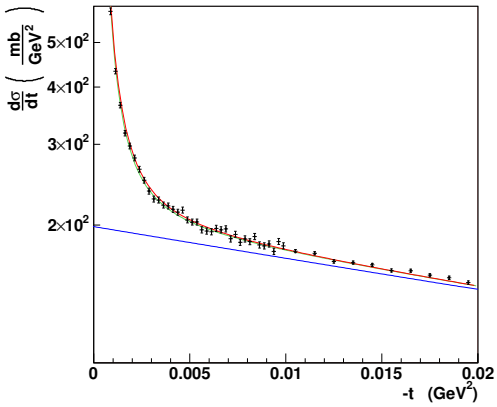


Fig. 6

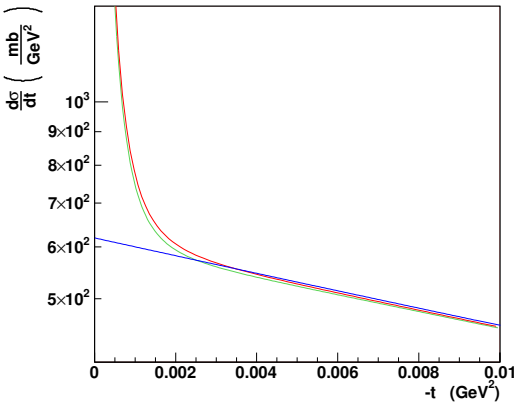


Fig. 7

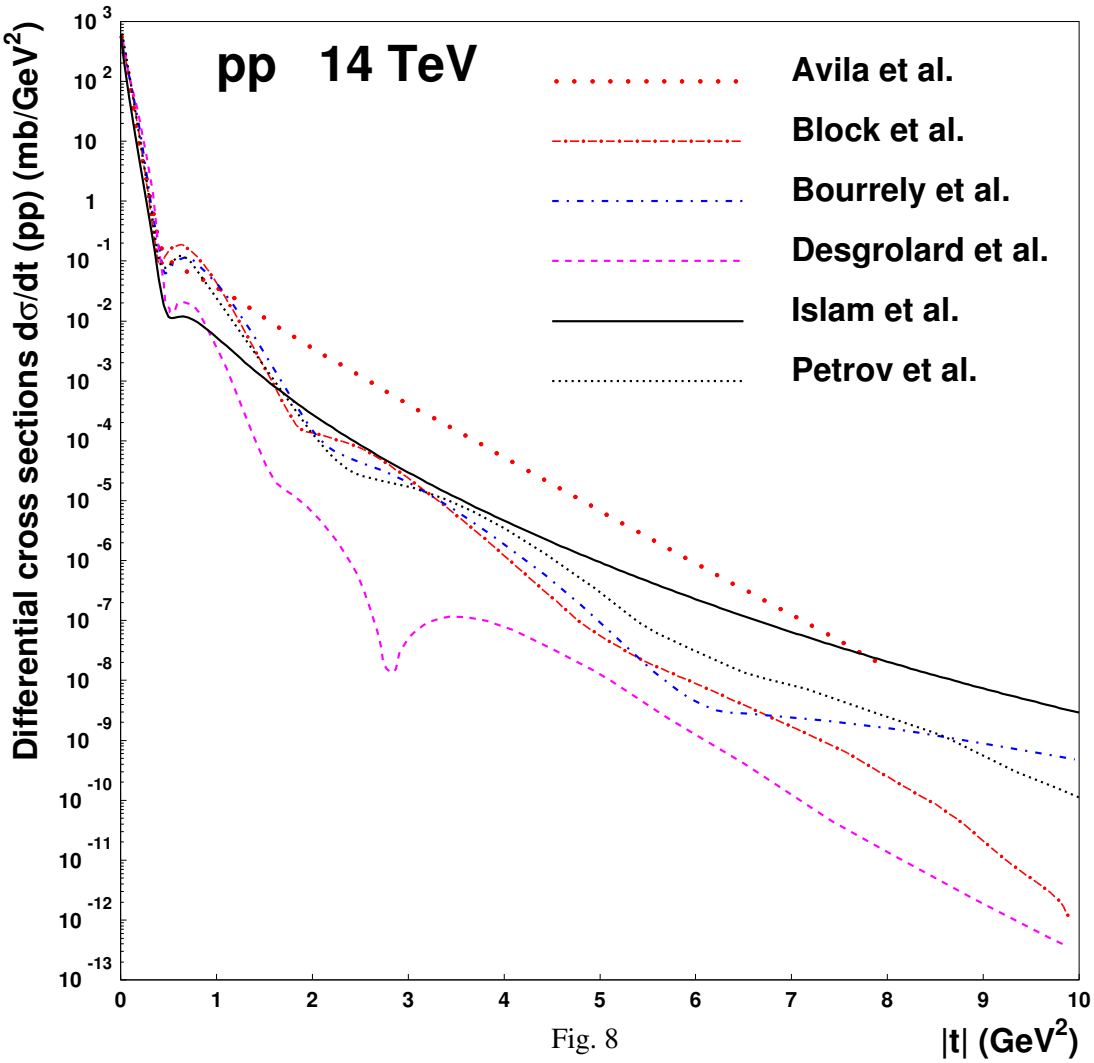


Fig. 8

To the theory of high-energy elastic nucleon collisions

Vojtěch Kundrát, Jan Kašpar, Miloš Lokajíček*
Institute of Physics of the AS CR, v. v. i., 182 21 Prague 8, Czech Republic

Abstract
The commonly used West and Yennie integral formula for the relative phase between the Coulomb and elastic hadronic amplitudes requires for the phase of the elastic hadronic amplitude to be constant at all kinematically allowed values of t. More general interference formula based on the eikonal model approach does not exhibit such limitation. The corresponding differences will be demonstrated and some predictions of different phenomenological models for elastic pp scattering at energy of 14 TeV at the LHC will be given. Special attention will be devoted to determination of luminosity from elastic scattering data; it will be shown that the systematic error might reach till 5 % if the luminosity is derived from the values in the center of the interference region with the help of West and Yennie formula.

1 Limited validity of West and Yennie integral formula

It has been shown in our earlier papers (see [1] and [2]) that the integral formula of West and Yennie [3] for the real relative phase between Coulomb and hadronic amplitudes

$$\alpha\Phi(s,t) = \mp\alpha\left[\ln\left(\frac{-t}{s}\right) - \int_{-4p^2}^{0}\frac{d\tau}{|t-\tau|}\left(1-\frac{F^N(s,\tau)}{F^N(s,t)}\right)\right] \tag{1}$$

requires for the hadronic amplitude $F^N(s,t)$ to have the constant phase at any kinematically allowed value of t; s being the value of the total CMS energy, t the four momentum transfer squared, p the value of the CMS momentum and $\alpha = 1/137.036$ the fine structure constant. The upper (lower) sign corresponds to the pp ($\bar{\mathrm{p}}$p) scattering. It follows in such a case

$$\int_{-4p^2}^{0}\frac{d\tau}{|t-\tau|}\Im\left(\frac{F^N(s,\tau)}{F^N(s,t)}\right) \;\equiv\; 0 \tag{2}$$

and further

$$\int\limits_{-4p^2}^{0}\frac{d\tau}{|t-\tau|}[\Re F^N(s,t)\Im F^N(s,\tau) - \Re F^N(s,\tau)\Im F^N(s,t)] \;\equiv\; 0. \tag{3}$$

Introducing then

$$F^N(s,t) \;=\; i|F^N(s,t)|e^{-i\zeta^N(s,t)}, \tag{4}$$

* speaker

it is possible to write further

$$\int\limits_{-4p^2}^{t} d\tau \; \frac{\sin[\zeta^N(s,t)-\zeta^N(s,\tau)]}{t-\tau} \; |F^N(s,\tau)| - \int\limits_{t}^{0} d\tau \; \frac{\sin[\zeta^N(s,t)-\zeta^N(s,\tau)]}{t-\tau} \; |F^N(s,\tau)| \; \equiv \; 0 \tag{5}$$

for any $t \in [-4p^2, 0]$. Both the integrals in Eq. (5) are proper integrals provided the first derivative of the hadronic phase $[\zeta^N(s,t)]'$ according to t variable is finite. It is evident that Eq. (5) is fulfilled if the phase is t independent, i.e., if

$$\zeta^N(s,t) \; = \; \zeta^N(s,\tau) \; \equiv \; \zeta^N(s). \tag{6}$$

It has been shown in Ref. [2] that Eq. (6) represents the unique solution of Eq. (5), if the relative phase between the Coul. and hadr. amplitudes is to be a real quantity as commonly assumed.

The problem of the t independence of hadronic phase was mentioned for the first time in Ref. [4]. However, this independence was used as an assumption only. Adding the other important assumption concerning purely exponential t dependence of the modulus of hadronic amplitude *in the whole kinematically allowed region of* t it was possible to perform analytically the integration in Eq. (1) (accepting also other approximations valid at asymptotic energies only - for detail see Ref. [1]). For the total elastic scattering amplitude the simplified West and Yennie formula

$$F^{C+N}(s,t) = \pm\frac{\alpha s}{t} f_1(t) f_2(t) e^{i\alpha\Phi} + \frac{\sigma_{tot}}{4\pi} p\sqrt{s}(\rho+i) e^{Bt/2} \tag{7}$$

was then obtained. Here $f_1(t)$ and $f_2(t)$ are the dipole form factors (added by hand only), B is the constant diffractive slope, σ_{tot} the value of the total cross section and the constant $\rho = \Re F^N(s,0)/\Im F^N(s,0)$. These three quantities may depend on s only. The relative phase $\alpha\Phi(s,t)$ exhibits then logarithmic t dependence

$$\alpha\Phi(s,t) = \mp\alpha\left[\ln\left(\frac{-Bt}{2}\right) + \gamma\right], \tag{8}$$

where $\gamma = 0.577215$ is Euler's constant.

2 General eikonal model approach

The contemporary experimental data as well as the phenomenological models of high-energy elastic nucleon scattering show, however, convincingly that the quantity ρ cannot be t independent. Consequently, the West and Yennie approach [3] is not a convenient tool for description of interference between the Coulomb and elastic hadronic interactions of charged nucleons. However, the approach based on the eikonal model removes such troubles. The general formula for the total elastic scattering amplitude proposed in Ref. [5] may be valid at any s and t; it may be written as

$$F^{C+N}(s,t) = \pm\frac{\alpha s}{t} f_1(t) f_2(t) + F^N(s,t)\left[1 \mp i\alpha G(s,t)\right], \tag{9}$$

where

$$G(s,t) = \int\limits_{-4p^2}^{0} dt' \left\{ \ln\left(\frac{t'}{t}\right) \frac{d}{dt'}\left[f_1(t') f_2(t')\right] + \frac{1}{2\pi}\left[\frac{F^N(s,t')}{F^N(s,t)} - 1\right] I(t,t') \right\}, \tag{10}$$

and

$$I(t,t') = \int_0^{2\pi} d\Phi'' \frac{f_1(t'')f_2(t'')}{t''}, \quad t'' = t + t' + 2\sqrt{tt'}\cos\Phi''. \tag{11}$$

Instead of the t independent quantities B and ρ, it is now necessary to consider t dependent quantities being defined as

$$B(s,t) = \frac{d}{dt}\left[\ln\frac{d\sigma^N}{dt}\right] = \frac{2}{|F^N(s,t)|}\frac{d}{dt}|F^N(s,t)|, \qquad \rho(s,t) = \frac{\Re F^N(s,t)}{\Im F^N(s,t)}. \tag{12}$$

The total cross section is then given with the help of the optical theorem as

$$\sigma_{tot}(s) = \frac{4\pi}{p\sqrt{s}}\Im F^N(s,t=0). \tag{13}$$

3 Experimental data and West and Yennie formula

It is the differential cross section that is determined in corresponding experiments. In our normalization it equals

$$\frac{d\sigma(s,t)}{dt} = \frac{\pi}{sp^2}|F^{C+N}(s,t)|^2. \tag{14}$$

In the past practically in all actual experiments the simplified West and Yennie elastic amplitude defined by Eqs. (7) - (8) has been used for the analysis of data at $|t| \leq 0.01$ GeV^2, in spite of the fact that the theoretical assumptions under which the amplitude was derived are not fulfilled at all kinematically allowed values of t but only in its narrow region in forward direction. Generally, some important discrepancies exist. The analysis of corresponding behavior has been performed in Ref. [6] where the general formula (Eqs. (9) - (11)) has been applied to data for pp scattering at energy of 53 GeV under different limitations of some free parameters specifying the modulus and the phase of the hadronic amplitude (as used in Ref. [5] - Eqs. (40) and (42)). The corresponding results were derived in Ref. [6]) and are represented in Fig. 1. First, only the phase has been fixed by putting $\tan\zeta^N(t) = \rho = 0.077$ according to the earlier fit [7] (based on West and Yennie formula), while the modulus parameters have been fitted. This fit has been compared to the case when only ρ has been assumed to be constant, but free; the optimum in such a case has been obtained with $\rho = 0.065$. In both the cases the experimental data have been represented by the square of the modulus fitted in the whole measured interval; see the solid line in Fig. 1. In addition to, in the other case the modulus formula has been limited to a simple exponential form (with two free parameters). Fundamental differences from experimental data exist now; only unsubstantial difference being obtained when ρ has been fixed ($\rho = 0.077$) and when it has been left free and fitted to $\rho = 0.021$; see dotted and dashed lines in Fig. 1. It is evident that the assumption of constant diffractive slope B is in strong contradiction to the experimental data. The curves corresponding to the fits with constant and t dependent quantities ρ are nearly the same, if the modulus is fitted and only weak dependence of ρ on t is allowed. Better χ^2 quantity is obtained if strong dependence on t is allowed.

model	σ_{tot} [mb]	σ_{el} [mb]	$B(0)$ [GeV^{-2}]	ρ	$\sqrt{< b_{tot}^2 >}$ [fm]	$\sqrt{< b_{el}^2 >}$ [fm]	$\sqrt{< b_{inel}^2 >}$ [fm]
Islam	109.17	21.99	31.43	0.123	1.552	1.048	1.659
Petrov et al.2P	94.97	23.94	19.34	0.097	1.227	0.875	1.324
Petrov et al.3P	108.22	29.70	20.53	0.111	1.263	0.901	1.375
Bourrely et al.	103.64	28.51	20.19	0.121	1.249	0.876	1.399
Block et al.	106.74	30.66	19.35	0.114	1.223	0.883	1.336

Table 1: The values of basic parameters predicted by different models

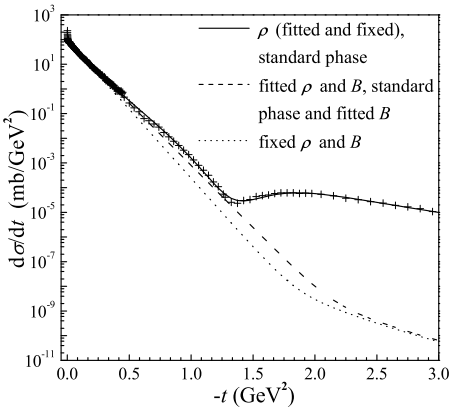


Fig. 1: $\frac{d\sigma}{dt}$ for pp scattering at 53 GeV; all graphs correspond to constant ρ.

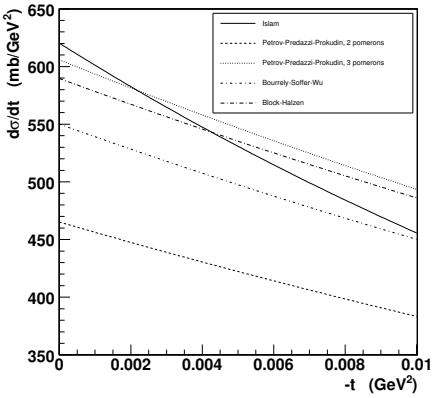


Fig. 2: $\frac{d\sigma}{dt}$ predictions at low $|t|$ for pp scattering at 14 TeV corresponding to different models

4 Model predictions for pp elastic scattering at the LHC

In connection with the TOTEM experiment that will investigate the elastic pp scattering at energy of 14 TeV [8] we have studied the predictions of four models proposed by the following authors: Islam, Luddy and Prokhudin [9], Petrov, Predazzi and Prokhudin (with hadronic amplitude corresponding to the exchange of two, resp. three pomerons - labelled as 2P, resp. 3P) [10], Bourrely, Soffer and Wu [11] and Block, Gregores, Halzen and Pancheri [12]. All the given models have contained some free s dependent parameters that have been established in these papers by fitting the experimental data on pp differential cross sections at several lower energies. Using these fitted values we have established the dynamical quantities: the total cross section, momentum transfer distribution $\frac{d\sigma}{dt}$, the t dependent diffractive slope $B(t)$ and the t dependent quantity $\rho(t)$ at higher energy values. The values of σ_{tot}, σ_{el}, $B(0)$ and $\rho(0)$ for 14 TeV can be found in Table 1. The corresponding model predictions are shown in Figs. 2 - 5. It is evident that the predictions of all the models differ rather significantly. Fig. 2 shows different predictions for values of the differential cross sections at small $|t|$ values. Great differences concern the values for total cross sections that are in direct relation to the values of differential cross section at $t = 0$; they run from 95 mb to 110 mb and differ rather significantly from the value predicted by COMPETE collaboration [13] $\sigma_{tot} = 111.5 \pm 1.2\ ^{+4.1}_{-2.1}$ mb which has been determined by extrapolation of the fitted lower energy data with the help of dispersion relations technique. The predictions of $\frac{d\sigma}{dt}$ values for higher values of $|t|$ are shown in Fig. 3. Let us point out especially the second diffrac-

tive dip demonstrated by Bourrely, Soffer and Wu momentum transfer distribution. The different predictions for t dependence of the diffractive slopes $B(t)$ are shown in Fig. 4. Fig. 5 exhibits the t dependence of the quantity $\rho(t)$. Table 1 contains also the values of the root-mean-squares calculated for each of the analyzed models with the formulas published in Ref. [14].

5 Luminosity estimation on the basis of pp elastic scattering at the LHC

The accurate determination of the elastic amplitude is very important in the case when the luminosity $\mathcal{L}$ is to be calibrated on the basis of elastic process; it holds that [15]

$$\frac{1}{\mathcal{L}}\frac{dN_{el}}{dt} = \frac{\pi}{sp^2}|F^{C+N}(s,t)|^2, \tag{15}$$

where $\frac{dN_{el}}{dt}$ is the counting rate established experimentally at the given t. The so called Coulomb calibration in the region of smallest $|t|$ where the Coulomb amplitude is dominant (reaching nearly 100 $\%$) can be hardly realized due to technical limitations. The approach allowing to avoid corresponding difficulties may be based on Eq. (15), when the elastic counting rate can be, in principle, measured at any t which can be reached, and the total elastic scattering amplitude $F^{C+N}(s,t)$ may be determined with required accuracy at any $|t|$, too. Then the luminosity $\mathcal{L}$ could be determined using Eq. (15). However, in this case it is very important which formula

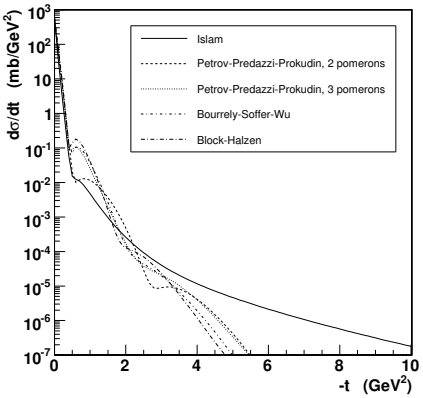


Fig. 3: $\frac{d\sigma}{dt}$ predictions for pp scattering at 14 TeV corresponding to different models

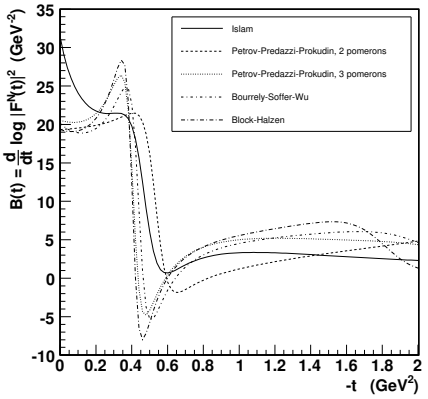


Fig. 4: t dependence of the slope predictions for pp scattering at 14 TeV for different models

for the total elastic amplitude $F^{C+N}(s,t)$ is made use of. In the following we will demonstrate possible differences which can be obtained at different t values in comparison with the commonly used West and Yennie approach. For this reason let us calculate the quantity

$$R(t) = \frac{|F^{C+N}_{eik}(s,t)|^2 - |F^{C+N}_{WY}(s,t)|^2}{|F^{C+N}_{eik}(s,t)|^2}, \tag{16}$$

where $F^{C+N}_{eik}(s,t)$ is the total elastic scattering eikonal model amplitude calculated for an investigated hadronic amplitude $F^{N}(s,t)$ while $F^{C+N}_{WY}(s,t)$ is the West and Yennie total elastic scattering amplitude calculated for the same hadronic amplitude. The calculation was performed

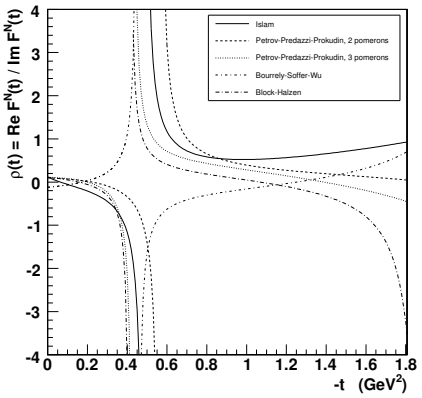


Fig. 5: $\rho(t)$ predictions for pp scattering at 14 TeV corresponding to different models

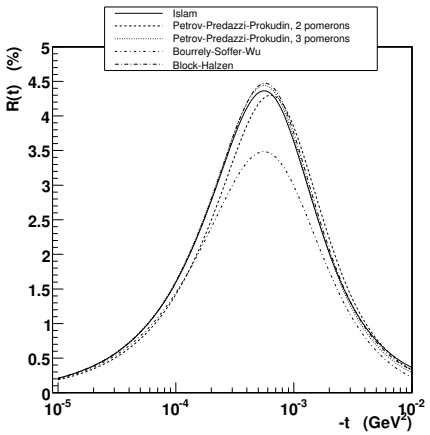


Fig. 6: $R(t)$ quantity predictions for pp scattering at 14 TeV corresponding to different models

for pp elastic scattering at the LHC energy of 14 TeV; in the former case Eqs. (9) - (11) were used, in the latter one Eqs. (7) - (8). The t dependence of $R(t)$ for different models is shown in Fig. 6. The maximum values lie approximately at $t = -0.006$ GeV^2, showing that the differences of physically consistent eikonal models from West and Yennie formula may be almost 5 $\%$. In the preceding case only the models with a weak dependence of $\rho(t)$ on t have been considered. Yet larger difference may be obtained when the cases with weak and strong dependences will be compared; i.e., the cases for central and peripheral distribution of elastic hadron scattering - see the analysis of pp scattering at ISR energies [14]. It means that the luminosity determined for the central and peripheral distributions of elastic pp scattering at LHC energy of 14 TeV may be burdened by a non-negligible mutual systematic error.

References

[1] V. Kundrát and M. Lokajíček, Phys. Lett. B 611 (2005) 102
[2] V. Kundrát, M. Lokajíček and Ivo Vrkoč, hep-ph/07060827
[3] G. B. West and D. Yennie, Phys. Rev. 172 (1968) 1413
[4] U. Amaldi et al., Phys. Lett. 43B (1973) 231
[5] V. Kundrát and M. Lokajíček, Z. Phys. C 63 (1994) 619
[6] J. Procházka, Bachelor Thesis, Charles University, Prague, May 2007
[7] N. Amos et al., Nucl. Phys. B 262 (1985) 689
[8] V. Berardi et al, TOTEM Technical Design Report, CERN-LHCC-2004-002
[9] M. M. Islam, R. J. Luddy and A. V. Prokhudin, Phys. Lett. B 605 (2005) 115
[10] V. A. Petrov, E. Predazzi and A. V. Prokhudin, Eur. Phys. J. C28 (2003) 525
[11] C. Bourrely, J. Soffer and T. T. Wu, Eur. Phys. J. C28 (2003) 97
[12] M. M. Block, E. M. Gregores, F. Halzen and G. Pancheri, Phys. Rev. D60 (1999) 0504024
[13] J. R. Cudell et al., Phys. Rev. Lett. 89 (2002) 201801
[14] V. Kundrát and M. Lokajíček, Phys. Lett. B 544 (2003) 132
[15] M. M. Block and R. N. Cahn, Rev. Mod. Phys. 57 (1985) 221

Saturation effects in elastic scattering at the LHC

O.V. Selyugin[1]†, *J.-R. Cudell*[2]
[1]selugin@theor.jinr.ru, BLTPh, JINR, Dubna
[2]JR.Cudell@ulg.ac.be, IFPA, AGO Dept., Université de Liège

Abstract

The problems linked to the extraction of the basic parameters of the hadron elastic scattering amplitude at the LHC are explored. The impact of the Black Disk Limit (BDL)− which constitutes a new regime of the scattering processes − on the determination of these values is examined.

1 Introduction

The diffraction processes will occupy an important place in the experimental program at the LHC. Firstly, we will need to know the luminosity and the total cross section with a high precision. Secondly, the diffraction processes will be directly explored at the LHC and will contribute to many different observable reactions. The planned analyses very clearly have problems from the theoretical view point. For example, the definition of the differential cross sections of the elastic proton-proton scattering, as presented in [1]

$$\frac{dN}{dt} = \mathcal{L}[\frac{4\pi\alpha^2}{|t|^2} - \frac{\alpha\rho\sigma_{tot}e^{-b|t|/2}}{|t|} + \frac{\sigma_{tot}^2(1+\rho^2)e^{-b|t|}}{16\pi}] \tag{1}$$

does not contain the electromagnetic form factor and the Coulomb-hadron interference phase Φ_{CH}. Such terms have to be included: all the corrections to ϕ_{CH} were calculated in [2]. More importantly, Eq. (1) is based on the assumption of an exponential behavior of the imaginary and real parts of the hadron scattering amplitude, which is at best an approximation.

Furthermore, the TOTEM experiment has announced the extraction of σ_{tot} from the experimental data, assuming a fixed value of $\rho(s, t = 0) = 0.15$. Indeed, the impact of ρ on σ_{tot} is connected with the term $(1 + \rho^2)$, and is very small when ρ is small. However the most important correlation between ρ and σ_{tot} enters the analysis through the Coulomb-hadron interference term, the size of which remains unknown if we do not know the normalization of dN/dt and the size and t-dependence of $\rho(s, t)$ and ϕ_{CH}.

In [1], it was shown that there would be large correlations between the value of ρ and that of σ_{tot}. However, these correlations and the error estimates were obtained using an exponential behavior of the imaginary and real part of the hadron scattering amplitude. Several models predict an increase in the slope $B(t)$ as $t \to 0$, which effectively leads to an additional term in the description of the hadron scattering amplitude. We shall return to this question later.

† speaker

Collaboration	σ_{tot} (mb)	σ_{el}/σ_{tot}	$\rho(t=0)$	$B(t=0)$
[3]	103	0.28	0.12	19
[4]	110.5	0.229		20.5
[5]	111		0.11	
[6]	123.3		0.103	
[7]	128	0.33	0.19	21
[8]	150	0.29	0.24	21.4
[9]	230	0.67		

Table 1: Predictions of different models at $(\sqrt{s} = 14$ TeV, $t = 0)$

$\bar{\rho}$ ($\sqrt{s} = 540$ GeV, $0.000875 \leq \lvert t \rvert \leq 0.12$ GeV^2)			
experiment	experimental analysis	global analysis I [10]	global analysis II [11]
UA4	0.24 ± 0.02	0.19 ± 0.03	-
UA4/2	0.135 ± 0.015	-	0.17 ± 0.02

Table 2: Average values of ρ, derived with fixed total cross section (first two columns), and from a global analysis (last two columns).

One should realise that the theoretical predictions are somewhat uncertain. We show in Table 1 recent estimates of the cross section at the LHC. This is partially due to the fact that the dispersion of the experimental data for σ_{tot} at high energy above the ISR energies is very wide. We must note that, except for the UA4 and UA4/2 collaborations, the other experiments have not published the actual numbers for dN/dt. We can only hope that the new results from the LHC experiments will not continue this practice. In this context, we must remember the eventual problems that may arise if one fixes σ_{tot} or ρ to decrease the size of the errors: indeed, this is what the UA4/2 Collaboration did when they extracted $\rho(0)$, fixing σ_{tot} from the UA4 Collaboration ($\sigma_{tot} = 61.9$ mb), or from their own measurement ($\sigma_{tot} = 63.0$ mb). As shown in Table 2, the resulting values for $\rho(0)$ appear inconsistent. A more careful analysis [10, 11] shows that there is no contradiction between the measurements of UA4 and UA4/2.

2 Fitting procedure for $\sigma_{tot}(s)$ and Black Disk Limit (BDL)

The situation is complicated by the possible transition to the saturation regime, as the Black Disk Limit (BDL) will be reached at the LHC [8, 12]. The effect of saturation will be a change in the t-dependence of B and ρ, which will begin for $\sqrt{s} = 2$ to 6 TeV, and which may drastically change $B(t)$ and $\rho(t)$ at $\sqrt{s} = 14$ TeV [8]. As we are about to explain, such a feature can be obtained in very different models.

The first model is based on a fit to soft data which includes a hard pomeron component [13] of intercept 1.4, which is linked to the growth of the gluon density at small x in inelastic processes [14]. This growth leads to non-linear effects, which saturate the BDL. Such effects

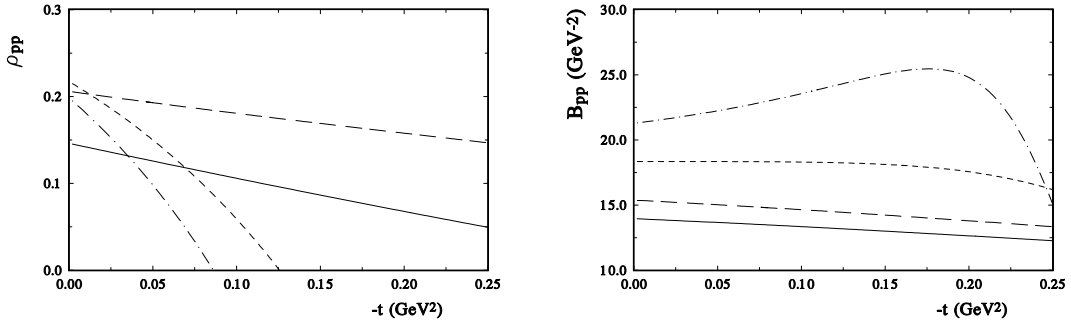


Fig. 1: Results of the ESHPM. Left panel: The ratio of the real to the imaginary part of the amplitude as a function of t, for the bare and the saturated amplitudes at various energies: 100 GeV (plain curve), 500 GeV (long dashes), 5 TeV (short dashes) and 14 TeV (dash-dotted curve). Right panel: The slope of the elastic differential cross section as a function of t, for the bare and saturated amplitudes at various energies: 100 GeV (plain curve), 500 GeV (long dashes), 5 TeV (short dashes) and 14 TeV (dash-dotted curve).

$t = 0$		$t = -0.1$ GeV ^{2}	
DDM	ESHPM	DDM	ESHPM
0.19	0.24	0.08	0.05

Table 3: Results of the DDM and of the ESHPM for ρ at $\sqrt{s} = 14$ TeV

were obtained in [8, 12] and predict that $B(t)$ will increase with t at small t for LHC energies (see Fig. 1). We also show that the saturation of the BDL will heavily change the t-dependence of $\rho(t)$, as shown in Fig. 1. The hard pomeron component will lead to a decrease of the energy at which the BDL regime appears, and the effect on the growth of the total cross section in uncertain. We show in Fig. 1 and Table 3 the results coming from an eikonal unitarisation of the amplitude, and we shall refer to this model [8] as the Eikonalized Soft+Hard Pomeron Model (ESHPM).

The second model in which such effects appear is the Dubna Dynamical model (DDM) of hadron-hadron scattering at high energies [15]. It is based on the general principles of quantum field theory (analyticity, unitarity and so on) and takes into account basic information on the structure of a hadron as a compound system with a central region in which the valence quarks are concentrated, and a long-distance region filled with a color-singlet quark-gluon field. As a result, the hadron amplitude can be represented as a sum of a central and a peripheral part. The DDM predicts that the interaction of the Pomeron with the meson cloud of the hadrons will give an additional term growing like $\sqrt{s}$. This term will become important for energies $\sqrt{s} \geq 500$ GeV. This peripheric effect will lead to a saturation of the overlapping function $G(b)$, see Fig. 2. At small momentum transfer, the DDM predictions agree with the experimental data at $\sqrt{s} = 1.8$ TeV. Interestingly, as shown in Fig. 2, the DDM predicts that the differential cross sections at

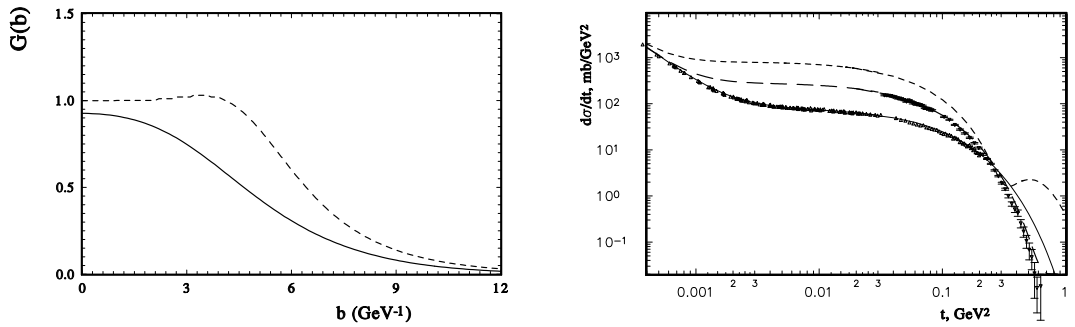


Fig. 2: Predictions of the DDM. Left panel: Overlapping function at $\sqrt{s} = 2$ TeV (solid line) and at $\sqrt{s} = 14$ TeV (dashed line). Right panel: Differential cross sections at $\sqrt{s} = 23.4$ GeV (solid thin line) and at $\sqrt{s} = 1.8$ TeV (dashed line) and at $\sqrt{s} = 14$ TeV (solid thick line).

$\sum \chi_i^2$	$\sigma_{tot}(mb)$	$\rho(t=0)$	B(0) (GeV^{-2})	normalization coefficient
91.2	82.3 ± 0.3	0.15_{fixed}	18.1 ± 0.2	1_{fixed}
88.3	$85. \pm 1.7$	0.15_{fixed}	18.16 ± 0.2	0.94 ± 0.04
89.3	82.3 ± 0.3	0.18 ± 0.02	18.3 ± 0.2	1_{fixed}
88.1	$85.2 \pm 3.$	0.147 ± 0.04	18.1 ± 0.25	0.93 ± 0.07

Table 4: Fits at $\sqrt{s} = 2$ TeV [Input $\rho(0) = 0.23$; $\sigma_{tot} = 82.7$ mb; $B(0) = 18.3$ GeV^{-2})].

$-t \approx 0.3$ GeV^2 will coincide for all high energies. Here again, the t-dependence of the slope-$B(s,t)$ will change its behavior at LHC energies because of saturation effects.

Let us now examine what the standard fitting procedure might give at the LHC in the case of saturation of the BDL, which leads to a behaviour of the scattering amplitude very far from an exponential. As an input, we shall use the predictions for the differential cross sections in the framework of the DDM for two energies $\sqrt{s} = 2$ TeV and $\sqrt{s} = 14$ TeV. For the first energy, the deviation from an exponential is small, whereas it becomes essential at the LHC. We can simulate the future experimental data from this theoretical differential cross sections and assume that 90 points will be measured in a t interval identical to that of the UA4/2 experiment. We then randomize the theoretical curve assuming Gaussian errors similar to those of UA4/2. After that, we can fit the simulated data with an exponential amplitude. The results of this exercise are shown in Tables 4 and 5. It is clear that at $\sqrt{s} = 14$ TeV, the simulated data differ significantly from the results of the fit, especially if one allows for a refitting of their normalisation.

Saturation of the profile function will surely control the behaviour of σ_{tot} at higher energies and will result in a significant decrease of the LHC cross section. However, it is clear that the simple saturation considered here is not enough, as the total cross section at the Tevatron will be 85 mb, which is 2 standard deviations from the CDF result. However, the increase of the slope

$\sum \chi_i^2$	σ_{tot} (mb)	$\rho(t=0)$	B(0) (GeV^{-2})	normalization coefficient
133	155.3 ± 0.5	0.15_{fixed}	23.1 ± 0.2	1_{fixed}
120	$180. \pm 8.6$	0.15_{fixed}	23.2 ± 0.15	0.74 ± 0.07
109	153.4 ± 0.7	0.26 ± 0.03	23.5 ± 0.17	1_{fixed}
108	142.3 ± 2.8	0.29 ± 0.05	23.6 ± 0.2	1.15 ± 0.05

Table 5: Fits at $\sqrt{s} = 14$ TeV [Input $\rho(0) = 0.24$; $\sigma_{tot} = 152.5$ mb; $B(0) = 21.4$ GeV^{-2}].

with t at small t is a generic feature of all saturating models.

3 Oscillations and additional method

As the standard fitting procedure can give misleading results, we need to find an additional method to define or check the basic parameters of the hadron scattering amplitude. Especially as there can be additional specific features in the t-dependence of the different parts of the amplitude. For example, there can be some oscillations in the differential cross sections which can come from different sources. It was shown [16] that if the Pomeranchuk theorem is broken and the scattering amplitude grows to a maximal possible extent, the elastic scattering cross section would exhibit a periodic structure in $q = \sqrt{|t|}$ at small $-t$. It was shown [17] that the oscilations in the UA4/2 data over $\sqrt{|t|}$ can be connected with a rigid-string potential or with residual long-range forces between nucleons. These small oscillations in the differential cross section are difficult to detect by the standard fitting method. Another method was proposed, which consists in the comparison of two statistically independent samples built by binning the whole t-interval in small intervals, proportional to $\sqrt{|t|}$, and by keeping one interval out of two. The deviations of the experimental values from theoretical expectations, weighted by the experimental error, are then summed for each sample k: [18].

$$\Delta R^k(t) = \sum_{|t_i|<|t|} \Delta R_i^k = \sum_{|t_i|<|t|} [(d\sigma^k/dt_i)^{exp} - (d\sigma/dt_i)^{th}]/\delta_i^{exp}, \qquad (2)$$

where δ_i^{exp} is the experimental error. This method gives two curves which statistically coincide if oscillations are absent and which grow apart with t if the oscillations are present.

If the theoretical curve does not precisely describe the experimental data, (for example, if the physical hadron amplitude does not have an exactly exponential behavior with momentum transfer), the sum $\Delta R^k(t)$ will differ from zero, going beyond the size of a statistical error. This method thus gives the possibility to check the validity of the model assumptions and of the parameters which describe the hadron scattering amplitude. Note that another specific method was proposed in [19, 20].

4 Conclusion

As the cross section of proton elastic scattering will be measured at the LHC, we need to know more about the behaviour of the hadron scattering amplitude at small t. The analysis of soft data, taking into account the integral dispersion relations, shows a contribution of the hard pomeron

in elastic scattering. In this case, it is very likely that at the LHC we shall reach the saturation regime called the BDL It will manifest itself in the behavior of $B(t)$ and of $\rho(t)$ and lead to a non-exponential behavior of the hadron scattering amplitude at small t, which will depend on the form of the unitarization procedure. In other words, different impact parameter dependences of the scattering amplitude will lead to different energy dependences of the ratio of the elastic to the total cross sections.

The regime of the BDL may correspond to parton saturation in the interacting hadrons, which is described by a non-linear equation. Indeed, there is a one-to-one correspondance between non-linear equations and the different forms of the unitarization schemes.

The possibility of a new behaviour of $\rho(s,t)$ and $B(s,t)$ at LHC energies has to be taken into account in the procedure extracting the value of the total cross sections by the standard fitting method. It is needed to use additional specific methods for the determination of the size of the total cross section and of $\rho(s,t)$, such as calculating ΔR and comparing independent choices.

The authors would like to thank for helpful discussions E. Martynov and P.V. Landshoff. O.S. gratefully acknowledges financial support from FRNS and would like to thank the University of Liège where part of this work was done.

References

[1] C. Royon, Proceedings , ed. R. Fiore, 15-20 June 2006, Milos, Greece.

[2] O. Selyugin, Mod. Phys. Lett. **A11**, 2317 (1996).

[3] C. Bourrely, J. Soffer, T.T. Wu, Nucl. Phys. **B 247**, 15 (1984).

[4] E. Gotsman,E. Levin, and U. Maor, [hep-ph 0708.1506] (2007).

[5] J.-R. Cudell et al., Phys. Rev. **D 65**, 074024 (2002).

[6] B. Nicolescu, [hep-ph 0707.2923] (2007).

[7] S.V. Goloskokov, and S.P. Kuleshov, and O.V. Selyugin, Fiz. Elem. Chastits At. Yadra[Sov. J. Part. Nucl.] **18**, 14 (1987).

[8] O.V. Selyugin, J.-R. Cudell, [hep-ph 0612046] (2006).

[9] V.A. Petrov, A.V. Prokudin, S.M. Troshin, N.E. Tyurin, J. Phys. G **27**, 2225 (2001).

[10] O. Selyugin, Sov. J. Nucl. Phys. **55**, 466 (1992).

[11] O. Selyugin, Phys. Lett. **B333**, 245 (1994).

[12] O.V. Selyugin, and J.-R. Cudell, Czech. J. of Phys. **54**, A441 (2004).

[13] J.-R. Cudell, E. Martynov, O. Selyugin, A. Lengyel, Phys. Lett. **587**, 78 (2004).

[14] A. Donnachie and P. Landshoff, Phys. Lett. **B 550**, 160 (2002).

[15] S.V. Goloskokov, S.P. Kuleshov, O.V. Selyugin, Z. Phys. **C 50**, 455 (1991).

[16] G. Auberson, T. Kinoshita, A. Martin, Phys. Rev. **D3**, 3185 (1971).

[17] O. Selyugin, Ukr. J. Phys. **41**, 296 (1996).

[18] P. Gauron, B. Nicolescu, O.V. Selyugin, Phys. Lett. **B397**, 305 (1997).

[19] O. Selyugin, Proceedings of VIIth Blois Workshop on Elastic and Diffractive Scattering, ed. P. Chapetta, M. Haguenauer, L.T. Thanh Van, 20-24 June, Blois, France, p. 87 (1995).

[20] P. Gauron, B. Nicolescu, O.V. Selyugin, Phys. Lett. **B629**, 83 (2005).

Elastic pp and $\bar{p}p$ scattering in the models of unitarized pomeron

E. Martynov
Bogolyubov Institute for Theoretical Physics, 03143 Kiev, Ukraine
e-mail: martynov@bitp.kiev.ua

Abstract
Elastic scattering amplitudes dominated by the Pomeron singularity which obey the principal unitarity bounds at high energies are constructed and analyzed. Actually the good agreement with the data is received for both models. The predictions made for the LHC energy values display, however, the quite noticeable difference between the predictions of models at $t \approx -0.4$ GeV^2. Apparently the future results of TOTEM will be more conclusive to make a true choice.

1 Unitarized pomeron models

The purpose of the talk is to demonstrate the description of the data on elastic pp and $\bar{p}p$ scattering at low and middle t in the dipole ($\sigma_t(s) \sim \sigma_{el}(s) \sim \ln s$) and tripole ($\sigma_t(s) \sim \sigma_{el}(s) \sim \ln^2 s$) pomeron models. They are constructed taking into account unitarity and analytical requirements from the beginning as well experimental information on the cross sections, therefore they can be named as models of unitarized pomeron.

As it was shown [1–3] the total cross sections of meson and nucleon interactions are described with the minimal χ^2 in the dipole and tripole models. Without entering the details we note here these models describe also the small-$|t|$ differential cross sections with the same level of precision ($\chi^2/dof \lesssim 1.05$, *dof* $\equiv$ degrees of freedom) as the model of the soft+hard pomerons [4,5] did.

We would like to note the important fact (see more details in [6]). If the partial wave amplitude develops the form

$$\varphi(j,t) = \eta(j)\frac{\beta(j,t)}{[(j-1)^m - kt]^n}, \quad \eta(j) = \frac{1+e^{-i\pi j}}{-\sin \pi j},$$

then $\sigma_{el} \propto \ln^{2mn-2-m} s, \quad \sigma_t \propto \ln^{mn-1} s$, and one can derive from the obvious inequality $\sigma^{el}(s) \leq \sigma^{tot}(s)$

$$\begin{cases} mn & \leq m+1, \\ mn & \leq 3. \end{cases} \tag{1}$$

If $m = 1$ then $n \leq 2$. It means that linear at $t \approx 0$ trajectory is incompatible with $\sigma_{tot} \propto \ln^2 s$. In another words the unitarity limit for a linear trajectory is $\sigma_{tot} \propto \ln s$.

If $\sigma_{el} \propto \sigma_t$ then $n = 1 + \frac{1}{m}$. Furthermore, if $\sigma_t \propto \ln s$ then $m = 1$ and $n = 2$ what corresponds just to the dipole pomeron model. In the tripole pomeron model $m = 2$ and $n = 3/2$ what means $\sigma_t \propto \ln^2 s$.

2 Dipole Pomeron Model

The dominating and subleading terms at high energy in this model are double and simple poles with $\alpha(0) = 1$ and possibly different slopes $\alpha_d{}'$ and $\alpha_s{}'$

$$\varphi(j,t) = \eta(j)\frac{\beta_d(t)}{(j-1-\alpha'_d t)^2} + \eta(j)\frac{\beta_s(t)}{j-1-\alpha'_s t}.$$

We consider the simplest, exponential form factors (or residues). Then the pomeron terms in (s,t) representation has the form

$$a(s,t) = g_d ln(-iz)(-iz)^{1+\alpha'_d t}\exp(b_d t) + g_s(-iz)^{1+\alpha'_s t}\exp(b_s t),$$

where the variable z is proportional to cosine of scattering angle in t-channel

$$z = (t + 2(s - 2m_p^2))/z_0, \qquad z_0 = 1\mathrm{GeV}^2.$$

Let us consider two effective reggeons: crossing-even, $R_+(s,t)$, and crossing-odd, $R_-(s,t)$) instead of f, ω and ρ, a_2 (the latter two reggeons are of less importance at high energy). We take into account their contribution in the standard form. However, we insert additional factor $Z_R(t)$ that changes a sign at some t [1].

$$R(s,t) = \eta_R g_R Z_R(t)(-iz)^{\alpha_R(t)}\exp(b_R t), \quad Z_R(t) = \frac{\tanh(1+t/t_R)}{\tanh(1)},$$

where $\eta_R = -1/\sin(0.5\pi\alpha_+(0))$ for R_+-reggeon and $\eta_R = i/\cos(0.5\pi\alpha_-(0))$ for R_--reggeon. Obviously these terms should be close to f- and ω-reggeons, respectively.

Going to extend wide regions of s ($\sqrt{s} \geq 5$ GeV) and t ($0.1 \leq |t| \leq 6$ GeV^2) [2] we certainly need a few extra terms in amplitude to reach a good fit to the data. First of all it concerns the odderon contribution. The existing data on total cross section and parameters $\rho = \Re ea(s,0)/\Im ma(s,0)$, as well known, do not show any visible odderon contribution. However, it appears definitely to provide the difference of pp and $\bar{p}p$ differential cross sections at $\sqrt{s} = 53$ GeV and t around the dip. So, we add the odderon contribution vanishing at $t = 0$

$$\mathcal{O}(s,t) = t^2 z Z_{R_-}(t)\Big\{o_1 ln^2(-iz)\exp(b_{o1}t) + o_2 ln(-iz)\exp(b_{o2}t) + o_3\exp(b_{o3}t)\Big\}(-iz)^{1+\alpha'_o t}.$$

At high energy and at $t = 0$ two main rescattering terms (or cut terms) in dipole model have the same form as the input amplitude - double pole plus simple pole. It means that comparing the model to experimental data we are not able to distinguish unambiguously input terms and cuts. Then as result, at $t = 0$ one can use the input amplitude only. At $t \neq 0$ the situation occurs more complicated because the slopes of trajectories in the cut terms are different from the input one. These terms are important at large $|t|$ but, in fact, they are already taken into account at $t = 0$.

[1] For crossing-odd term of amplitude such a factor is well known and describes crossover effect, i.e. intersection of the ab and $\bar{a}b$ differential cross sections at $t \approx -0.15$ GeV^2. Our analysis [5] has shown that similar factor is visible in crossing-even reggeon term.

[2] A more sophisticated form for residues should be considered for larger $|t|$.

Keeping in mind the above arguments and willing a good description of the data at $t = 0$ we take pomeron, pomeron-pomeron and pomeron-reggeons cuts vanishing at $t = 0$. Certainly they are not "genuine" rescatterings but mimic them quite efficiently. Thus we write down the pomeron contribution

$$P(s,t) = -g_P(-iz)^{1+\alpha'_P t}\left[\exp(b_{P1}t) - \exp(b_{P2}t)\right],$$

the pomeron-pomeron cut

$$C_P(s,t) = -\frac{t}{\ln(-iz)} g_{PP}(-iz)^{1+\alpha'_P t/2}\exp(b_{PP}t), \tag{2}$$

the pomeron-even reggeon cut

$$C_{R_+}(s,t) = -\frac{tZ_{R_+}(t)}{\ln(-iz)}\eta_{R_+} g_{P+}(t)(-iz)^{\alpha_+(0)+\alpha'_{P+}t}\exp(b_{P+}t), \quad \alpha'_{P+} = \frac{\alpha'_P\alpha'_{R_+}}{\alpha'_P + \alpha'_{R_+}}, \tag{3}$$

and the pomeron-odd reggeon cut

$$C_{R_-}(s,t) = -i\frac{tZ_{R_-}(t)}{\ln(-iz)}\eta_{R_-} g_{P-}(-iz)^{\alpha_-(0)+\alpha'_{P-}t}\exp(b_{P-}t), \quad \alpha'_{P-} = \frac{\alpha'_P\alpha'_{R_-}}{\alpha'_P + \alpha'_{R_-}}. \tag{4}$$

3 Tripole Pomeron Model

The partial wave amplitude in the Tripole pomeron model ($n = 2$, $m = 3/2$ in Eq.(1) we take as

$$\varphi_{tr}(j,t) = \eta(j)\left\{\frac{\beta_1(j,t)}{[(j-1)^2 - kt]^{3/2}} + \frac{\beta_2(j,t)}{[(j-1)^2 - kt]} + \frac{\beta_3(j,t)}{[(j-1)^2 - kt]^{1/2}}\right\}$$

where the second and the third terms are subleading contributions. The amplitude in (s,t)-representation has the form

$$\begin{aligned} a_{tr}(s,t) &= iz\Big\{g_{+1}\exp(b_{+1}t)ln(-iz)^{\frac{2J_1(\xi_+\tau_+)}{\tau_+}} + g_{+2}\tfrac{\sin(\xi_+\tau_+)}{\tau_+}\exp(b_{+2}t) \\ &\quad + g_{+3}J_0(\xi_+\tau_+)\exp(b_{+3}t)\Big\} \end{aligned}$$

where $\xi_+ = ln(-iz) + \lambda_+$, z is defined by Eq.(2), $\tau_+ = r_+\sqrt{-t/t_0}$, $t_0 = 1$ GeV^2, λ_+, r_+ are constants.

Similar expression for odderon contribution (but introducing the factors t and $Z_{R_-}(t)$) is given by

$$\begin{aligned} \mathcal{O}(s,t) &= ztZ_{R_-}(t)\Big\{g_{-1}ln(-iz)^{\frac{2J_1(\xi_-\tau_-)}{\tau_-}}\exp(b_{-1}t) \\ &\quad + g_{-2}\tfrac{\sin(\xi_-\tau_-)}{\tau_-}\exp(b_{-2}t) + g_{-3}J_0(\xi_-\tau_-)\exp(b_{-3}t)\Big\}. \end{aligned}$$

where $\xi_- = ln(-iz) + \lambda_-$ and $\tau_- = r_-\sqrt{-t/t_0}$.

Again, as in the dipole model, we add the "soft" pomeron

$$P(s,t) = -g_P(-iz)^{1+\alpha'_P t}\exp(b_P t),$$

the reggeon and cut contributions which are of the same form as Eqs. (2,3,4) in Dipole pomeron model.

Another version of tripole pomeron model with the different subleading and odderon terms was presented in the papers [7, 8]. Because of the chosen form of signature factors and residues the amplitude in this model (AGLN model) has poles in physical region of t, that limits the region of t, namely $|t| \leq 2.6$ GeV^2 [8], where the model can be considered. Besides, it leads to the intercept value for the crossing-odd reggeon, $\alpha_-(0) = 0.34$. It is in a contradiction with the value known from meson resonance spectroscopy data on ω-trajectory, $\alpha_\omega(0) \approx 0.43 - 0.46$ [9]. In the next Section we demonstrate the curves for differential cross sections obtained in the AGLN model in comparison with the results of our Dipole and Tripole models at energies available and future LHC.

4 Comparison with experimental data

The fitting pp and $\bar{p}p$ data on σ_t and ρ gives the parameters which are different from those derived from the fit all ($p, \bar{p}, \pi$- and K-meson) the data. Therefore at the first stage we fit the data on all hadronic cross sections. We use the standard data set for the $\pi^{\pm}p$ and $K \pm p$ total cross sections and the ratios ρ (at 5 GeV$\leq \sqrt{s} <$2000 GeV) [10] to find intercepts of $C_{\pm}$-reggeons and couplings of the reggeon and pomeron exchanges. There are 542 experimental points in the region under consideration. They are described with $\chi^2_{tot}/dof = 0.994$ in the Dipole Pomeron model and 0.993 in the Tripole Pomeron model.

At the second stage of the fitting procedure we fix all the intercept and coupling values obtained at the first stage. The other parameters are determined by fitting the $d\sigma/dt$ data (2532 points, [11]) in the region $0.1 \leq |t| \leq 6\mathrm{GeV}^2$, $\sqrt{s} \geq 5\mathrm{GeV}$. As to the AGLN-model, it was fitted in [8] to differential cross sections at $\sqrt{s} > 9.7$ GeV and $|t| < 2.6$ GeV^2. Therefore a disagreement between curves and data behaviours at lowest energies is not surprising in the given model.

Results for the quality of fitting are given in Table 1. In the Figs. 1 - 5 we show experimental data at some energies and theoretical curves obtained in three models: AGLN [8], Dipole and Tripole.

Table 1: Quality of the fit to $d\sigma/dt$

	Number of points, N_p	χ^2_{tot}/N_p	
		Dipole	Tripole
$d\sigma^{pp}/dt$	1857	1.512	1.815
$d\sigma^{\bar{p}p}/dt$	675	1.418	1.67

5 Conclusion

We compare three unitarized models of elastic scattering amplitude fitting the Dipole and Tripole models to all existing data. We emphasize that the amplitude leading to the behaviour of $\sigma_t \propto \ln^2 s$ should be parameterized with a special care of the unitarity and analyticity restrictions on properties of the leading partial wave singularity.

The Figures demonstrate good description of the data within the considered models. However, the obtained χ^2 hints that the Dipole pomeron model looks like more preferable.

We believe the most interesting and instructive result for further search of more realistic model is shown in Fig. 5. Our predictions of the compared models (together with AGLN model) for pp cross section at LHC energy are crucially different at $|t|$ around 0.3 - 0.5 GeV^2. Certainly the future TOTEM measurement will allow to distinguish between three considered models.

I would like to thank Prof. B. Nicolescu and Dr. J.R. Cudell for many useful discussions.

References

[1] J. R. Cudell *et al.*, Phys. Rev. **D65**, 074024 (2002). hep-ph/0107219.

[2] COMPETE Collaboration, J. R. Cudell *et al.*, Phys. Rev. Lett. **89**, 201801 (2002). hep-ph/0206172.

[3] E. Martynov, J. R. Cudell, and O. V. Selyugin, Eur. Phys. J. **C33**, s533 (2004). hep-ph/0311019.

[4] J. R. Cudell, E. Martynov, O. V. Selyugin, and A. Lengyel, Phys. Lett. **B587**, 78 (2004). hep-ph/0310198.

[5] J. R. Cudell, A. Lengyel, and E. Martynov, Phys. Rev. **D73**, 034008 (2006). hep-ph/0511073.

[6] E. Martynov (2007). hep-ph/0703248.

[7] L. Lukaszuk and B. Nicolescu, Nuovo Cim. Lett. **8**, 405 (1973);
P. Gauron, B. Nicolescu, and E. Leader, Nucl. Phys. **B299**, 640 (1988);
P. Gauron, B. Nicolescu, and E. Leader, Phys. Lett. **B238**, 406 (1990).

[8] R. Avila, P. Gauron, and B. Nicolescu, Eur. Phys. J. **C49**, 581 (2007). hep-ph/0607089.

[9] P. Desgrolard, M. Giffon, E. Martynov, and E. Predazzi, Eur. Phys. J. **C18**, 555 (2001). hep-ph/0006244.

[10] S. Review of Particle Physics and Eidelman *et al.*, Phys. Lett. **B592** (2004). Encoded data files are available at http://pdg.lbl.gov/2005/hadronic-xsections/hadron.html.

[11] M. Whalley *et al.* Durham Data Base, http://durpdg.dur.ac.uk/hepdata.

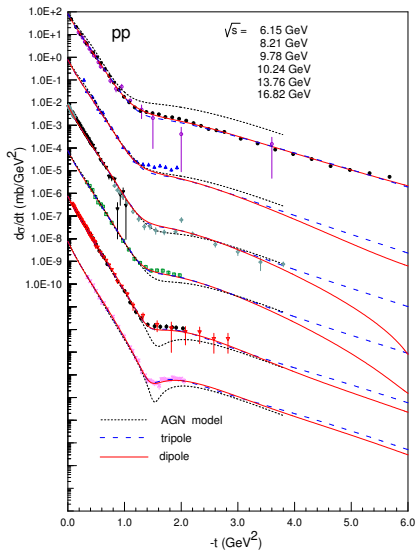


Fig. 1: pp at low energies

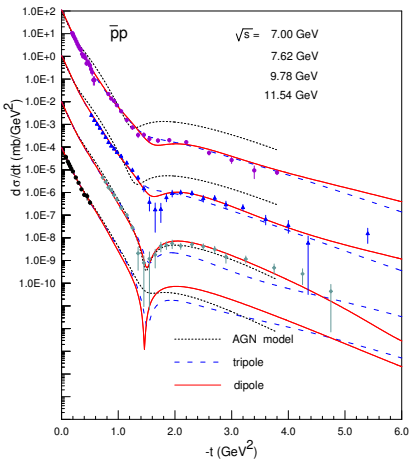


Fig. 2: $\bar{p}p$ at low energies

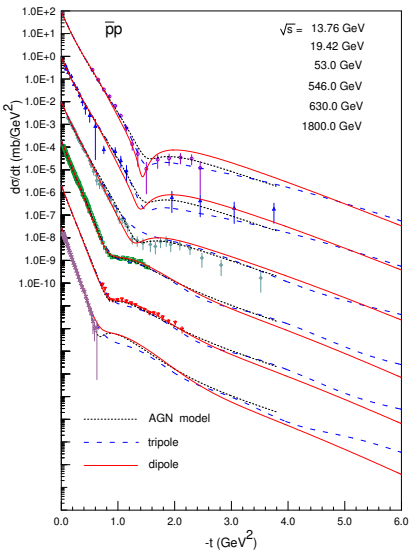


Fig. 3: $\bar{p}p$ at high energies

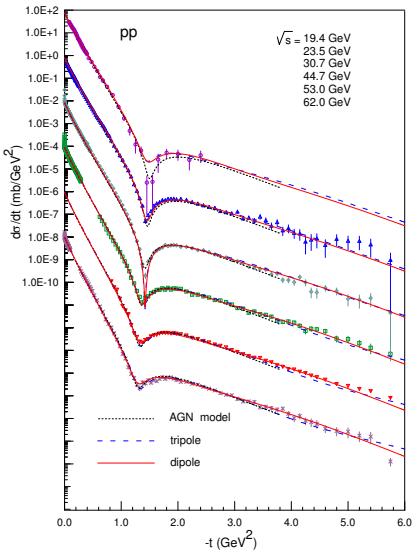


Fig. 4: pp at high energies

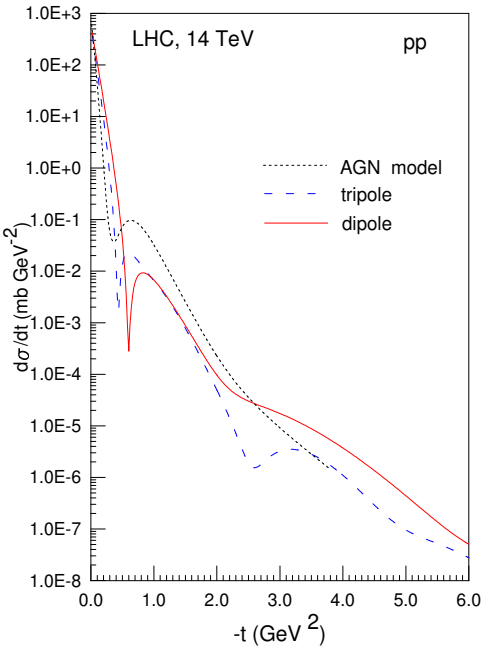


Fig. 5: Predictions for LHC energy

Part III

Heavy-Ion Collisions

Forward Physics with BRAHMS in pp annd dAu collisions at RHIC

Dieter Röhrich for the BRAHMS collaboration
[1]Department of Physics and Technology, University of Bergen, Norway

Abstract
Measurements of elementary pp collisions are an integral component to understand heavy ion collisions. Results for pp collisions at 200 and 62.4 GeV are presented. At both energies NLO pQCD describes pion production well. The nuclear modification factor for d+Au collisions at $\sqrt{s_{NN}}$ = 200 GeV changes from a Cronin-like enhancement of pions (and charged hadrons) at midrapidity to an increasing suppression at forward rapidities. In central Au+Au collisions at 200 GeV a strong pion suppression is observed in R_{AuAu} at all rapidities, while protons are enhanced at all rapidities; the nuclear modification factor does not depend on rapidity.

1 Nuclear Modification factors

One of the goals of the relativistic heavy ion program is to study the properties of matter at high temperature and high density. The explorations at the Relativistic Heavy Ion Collider (RHIC) indicate that that at c.m. energies of 200 GeV per nucleon pair indeed such system is formed with novel properties [1–4]. Part of these conclusions rely on comparison to elementary pp collisions, where effects of a deconfined matter should not be present.

The high-p_{T} spectra of particles produced in nuclear collisions are subject to various initial and final state effects. Initial state effects like the Cronin effect enhance the yield in p+A and A+A collisions as compared to nucleon-nucleon reactions at intermediate transverse momenta, nuclear shadowing and gluon saturation suppress the yield. Parton energy loss due to gluon bremsstrahlung during their passage through a dense medium with free color charges - created in central Au+Au collisions - suppresses the hadron yield at high-p_{T}. This final state effect is also called jet-quenching. The degree of suppression/enhancement is quantified by means of the nuclear modification factor R_{AA} using p+p reference spectra scaled up with the average number N_{coll} of binary nucleonic collisions in the heavy-ion system (or by R_{CP} where peripheral collisions are used as a reference):

$$R_{AA} = \left(d^2N_{AA}/dydp_{\mathrm{T}}\right) / \left(N_{coll} \cdot d^2N_{pp}/dydp_{\mathrm{T}}\right). \quad (1)$$

2 The BRAHMS experiment

The data used for this analysis were collected with the BRAHMS detector system. The BRAHMS detector consists of two movable magnetic spectrometers, the Forward Spectrometer (FS) that can be rotated from 2.3°to 15°, and the Mid-Rapidity Spectrometer (MRS) that can be rotated from 34°to 90°relative to the beam line, and several global detectors for measuring multiplicities

and luminosity, and determining the interaction vertex, and providing a start time (T0) for time-of-flight measurement. The MRS is a single-dipole-magnet spectrometer with a solid angle of 6 msr and a magnetic bending power up to 1.2 Tm. Most of the pp data presented here were recorded at magnetic field settings of 0.4 and 0.6 Tm. The MRS contains two time projection chambers, TPM1 and TPM2 sitting in field free regions in front of and behind the dipole (D5). This assembly is followed by two highly segmented scintillator time-of-flight walls, one (TOFW) at 4.51 m and a second (TFW2) at either 5.58 m (90°setting) or 6.13 m (other angle settings). The FS consists of 4 dipole magnets D1, D2, D3 and D4 with a bending power of up to 9.2 Tm. The spectrometer has 5 tracking stations T1 through T5, and particle identifying detectors: H2, a segmented time-of-flight wall, and a Ring Imaging Cherenkov Detector (RICH) [5].

3 Inclusive pp measurements

The minimum bias trigger used to normalize these measurements is defined with a set of Cherenkov radiators (CC) placed symmetrically with respect to the nominal interaction point and covering pseudo-rapidities that range in absolute value from 3.26 to 5.25. This trigger required that at least one hit is detected in both sides of the array.

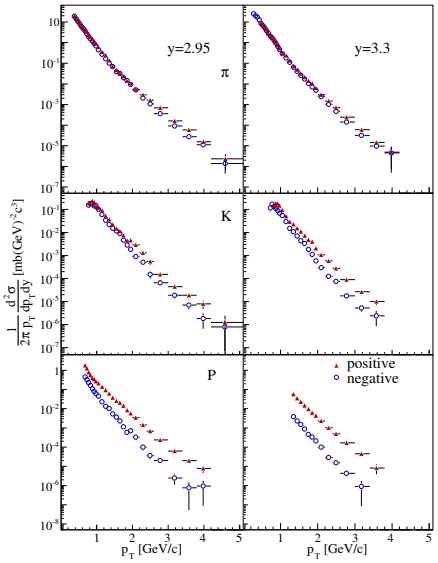


Fig. 1: Invariant cross section distributions for pion, kaons protons and anti-protons produced in p+p collisions at $\sqrt{s} = 200$ GeV at rapidities y=2.95 (left panels) and y = 3.3 (right panels). In all panels, positive charged particles are shown with filled triangles and negative ones with open circles. The errors displayed in these plots are statistical.

The present analysis was done with charged particles that originated from collisions of polarized protons with interaction vertices in the range of ± 40 cm. For the 200 GeV data invariant cross sections were extracted in narrow ($\Delta y = 0.1$) rapidity bins centered at y=2.95 and y = 3.3, respectively. Narrow rapidity bins are required to reduce the effects of rapidly changing cross sections in particular at higher p_T. Each distribution is obtained from the merging of up to five magnetic field settings. The data are corrected for the spectrometer geometrical acceptance,

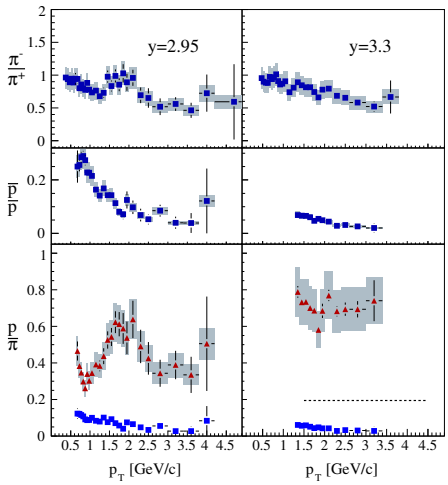


Fig. 2: (Top) Particle ratios versus p_T at y=2.95 and 3.3, (Top) π^-/π^+, (middle) /K^- /K^+ and (bottom) proton/π^+ (red circles) and antiproton/π^- (blue squares). The shaded rectangles indicate an overall systematic error (17%) estimated for these ratios. The dashed line shows an upper limit for the (proton + antiproton)/ $\pi^- + \pi^+$ ratio from e^+e^- collisions.

multiple scattering, weak decays and absorption in the material along the path of the detected particles. The overall tracking and track matching efficiency is about 80-90% and is included in the extraction of the cross sections. Particles are identified by the RICH. The low momentum part of the proton spectra is measured using the RICH in veto mode.

Data for y=2.95 and y=3.3 are presented for pions, kaons and protons in Fig.1. The pions exhibit a power law behavior. The upper panels of Fig. 2 show the ratio π^-/π^+ at y=2.95 and 3.3 respectively. Within systematic errors both ratios display a falling trend as a function of p_T. This may be an indication of the dominance of valence quark fragmentation at these rapidities and reflects the ratio of d to u quarks in the proton. The antiproton to proton ratios shown in the middle panels are much smaller than unity. This is a clear indication that the fragmententation of gluons cannot dominate the production of protons and anti-protons at these high rapidities. The difference between proton/π^+ (red circles) and antiproton/π^- at both rapidities is remarkable and caused by an unexpectedly large proton yield at these rapidities. Such large yield may be related to the mechanism that transfers a conserved quantity, the baryon number, from beam to intermediate rapidities i.e. baryon number transport. What remains as an open question is how a mechanism that is thought to be mainly restricted to the longitudinal component of the momentum, gives these protons such high transverse momenta.

The measured differential cross-sections are compared with NLO pQCD calculations [6] evaluated at equal factorization and renormalization scales, $\mu \equiv \mu_F = \mu_R = p_T$. These calculations use the CTEQ6 parton distribution functions [7] and a modified version of the "Kniehl-Kramer-Potter" (KKP) set of fragmentation functions (FFs) [8] referred to here as mKKP, as well as the "Kretzer" (K) set [9]. The KKP set includes functions that fragment into the sums $\pi^+ + \pi^-$, $K^+ + K^-$ and proton + antiproton. Modifications were necessary to obtain functions producing the separate charges for both π and K. Figure 3 shows that the agreement between the NLO calculations that include the mKKP FFs and the measured pion cross section is remarkable (within

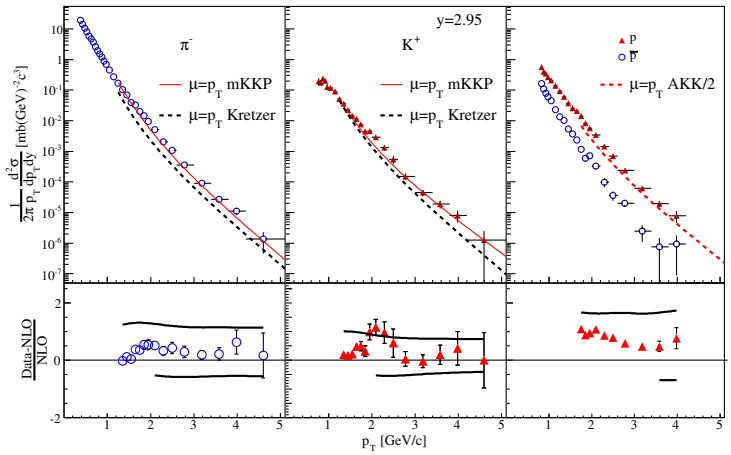


Fig. 3: (Top) Comparison of π^- and K^+ invariant spectra at rapidity 2.95 to NLO pQCD calculations at 200 GeV. The mKKP set of fragmentation functions (solid red line on-line) produce the best agreement with the pion and kaon data. The protons and antiprotons are compared with the calculation using the AKK set divided by 2 (dashed red line), see text for details. (Bottom) Relative differences between data and calculations. The top smooth curves show the effect of setting $\mu = 2p_T$ and the bottom curves $\mu = 1/2p_T$. For the baryons the (red) filled triangles show proton data vs the AKK/2 set.

20% above 1.5 GeV/c). Similar good agreement was obtained for neutral pions at y=0 [11] and at y=3.8 [12] at RHIC. The agreement between the calculated and the measured kaon cross-sections is equally good. The difference between the mKKP and Kretzer parametrizations is driven by higher contributions from gluons fragmenting into pions. This difference has been identified as an indication that the gg and gq processes dominate the interactions at mid-rapidity [11]. The present results indicate that such continues to be the case at high rapidity. The calculation that uses the Kretzer set underestimates the pion yields by a factor of $\sim$ 2 at all values of p_T while for positive kaons the agreement is good at low momentum but deteriorates at higher momenta. An updated version of FFs that we refer to as the "Albino, Kniehl and Kramer" (AKK) set has been extracted from more data made available recently [10]. It reproduces well the proton + antiproton distributions measured at midrapidity by the STAR collaboration [12]. At high rapidity, the contribution from gluons fragmenting into proton or antiproton is dominant in this new set of FFs (80% for p_T less than 5 GeV/c [6]), and the calculated cross sections for both particles consequently have nearly the same magnitude. We thus compare the measured cross sections for proton and antiproton to the NLO calculation using the AKK FFs divided by 2 in the right-most panel of Fig. 3. The calculation is close to the measured proton cross section but it is almost an order of magnitude higher than the measured antiproton distribution. We conclude that the AKK FFs cannot be used to describe baryon yields at high rapidity because they fail to reproduce the measured abundance of antiprotons with respect to protons. Additional details can be found in Ref. [13].

At 62.4 GeV, where the beam rapidity is 4.2, the spectrometer at forward angle samples produced particle that carries a significant fraction of the available momenta (31.2 GeV/c). Thus particle production is influenced by the kinematic limit. Data for identified charged hadrons were

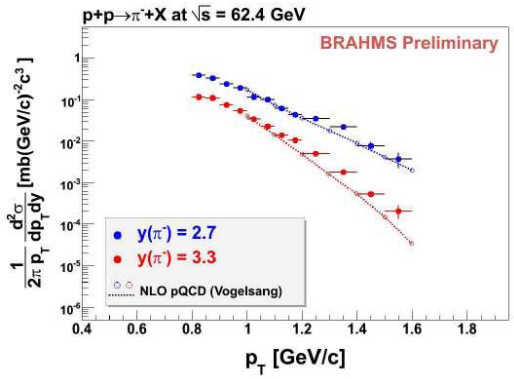


Fig. 4: Invariant cross section for π^- at rapidity 2.7 and 3.3 at 62.4 GeV. The curves are NLO pQCD calculations as described in the text.

collected at 2.3°,3°, 4°, and 6°. Figure 4 shows differential cross sections for π^- for rapidities 2.7 and 3.3 [14]. The cross sections changes rapidily with rapidity at high p_T where x_F values up to 0.5 are probed. The data are compared to NLO pQCD in the same figure. The calculation are done in the same manner as for the 200 GeV using the KPP fragmentation function evalauted at $\mu = p_T$ scale. The calculation describe the overall magnitude and shape quite well, though at the highest rapidity there is a tendency for the calculation to fall below the data at the highest p_T. This may be in agreement with the analysis [15] of 53 GeV π^0 data from the ISR at a fixed angle of 5° , comparable to the conditions for present measurements (2.3°and 4°), but at larger x_F where NLO pQCD is considerably below the data and with increasing discrepancy with x_F. In contrast to the aforementioned paper we do though conclude that NLO pQCD gives a satisfactory description of the charged pion data at high rapidity.

4 Nuclear modification factors for cold nuclear matter

Particle production at forward rapidities probes partons at smaller x scales. Suppression effects due to nuclear shadowing and/or gluon saturation are expected in d+Au collisions at large y. Fig. 5 shows the nuclear modification factor R_{dAu} for minimum bias d+Au events as a function of p_T and η [16]. R_{dAu} rises with p_T and falls with η. At midrapidity, R_{dAu} goes above 1. The so-called Cronin enhancement at $\eta = 0$ has been attributed to multiple scattering of the incoming partons during the collision. At more forward rapidities the data show a suppression of the hadron yields.

The suppression at forward rapidities is already visible at SPS energies, R_{pPb} exhibits a similar suppression trend, the suppression increases with increasing x_F [17, 18].

4.1 CGC saturation models

Saturation effects should increase with the thickness of nuclear material traversed by the incoming probe and indeed we see a greater suppression for more central collisions [16]. Both, R_{dAu} and R_{CP}, as well as the pseudorapidity distribution of charged hadrons and the invariant cross section of π^0 production in d+Au collisions at RHIC can be quantitatively described by gluon saturation within the framework of a Color Glass Condensate [19, 20].

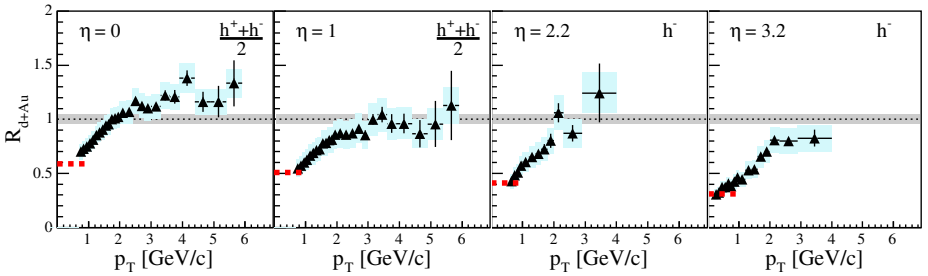


Fig. 5: Nuclear modification factor for charged hadrons at pseudorapidities = 0, 1.0, 2.2, 3.2. One standard deviation statistical errors are indicated by error bars. Systematic errors are shown with shaded boxes. The shaded band around unity indicates the estimated error on the normalization to the number of collisons.

4.2 pQCD models

At higher p_T pQCD based models which implement a Glauber-type collision geometry and include the standard nuclear shadowing and initial state incoherent multiple scattering agree reasonably well with the measured R_{dAu} and cannot be ruled out [21] (see also [22]). However, the centrality dependence of R_{CP} is underestimated [23] and there are doubts that nuclear shadowing is strong enough to describe the data [24]. On the other hand, coherent multiple scattering of a parton with the remnants of the nucleus in the final state can create an additional suppression at low and intermediate p_T which grows with rapidity and centrality [25].

4.3 Phenomenological models

R_{dAu} has been studied in the framework of Gribov-Regge field theory [26], where shadowing in dAu collisions is linked to diffraction. A parametrized gluonic parton distribution function (data from H1 and ZEUS) can describe the suppression at forward rapidities at RHIC. Applying this model to SPS data, gluonic shadowing, although present at SPS, cannot explain the observed suppression effect at large x_F. At SPS energies, shadowing due to valence quarks will dominate in this kinematical region. In general, the large x_F region is dominated by the fragmentation of valence quarks, which may suffer from an induced energy loss via increased gluon bremsstrahlung in cold nuclear matter [27]. In addition, momentum conservation at $x_F \rightarrow 1$ and final state multiple scattering might modify R_{dAu} and R_{CP} (Fig. 6) [27, 28].

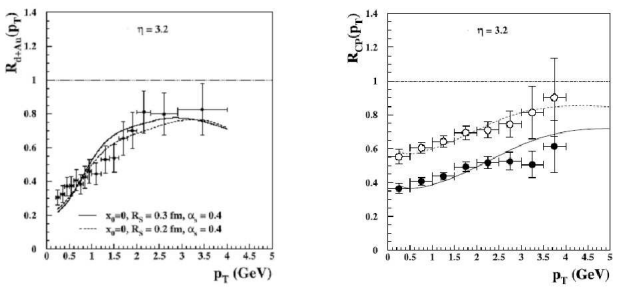


Fig. 6: Suppression due to large x_F effects [27]: R_{dAu} and R_{CP} together with BRAHMS data.

5 Final state effects in central nucleus-nucleus collisions

Pion (and charged hadron) transverse momentum spectra at midrapidity in central Au+Au collisions at 200 GeV show a strong suppression at intermediate and high p_T as compared to properly scaled p+p interactions. This effect is attributed to the energy loss partons suffer while traversing the hot and dense medium produced in these collisions.

Fig. 7 compares the (preliminary) nuclear modification factor for pions (left) and protons (right) at midrapidity to the one at forward rapidities [29, 30] (central Au+Au collisions). The pions are clearly suppressed, protons are enhanced and there is no dependence on rapidity.

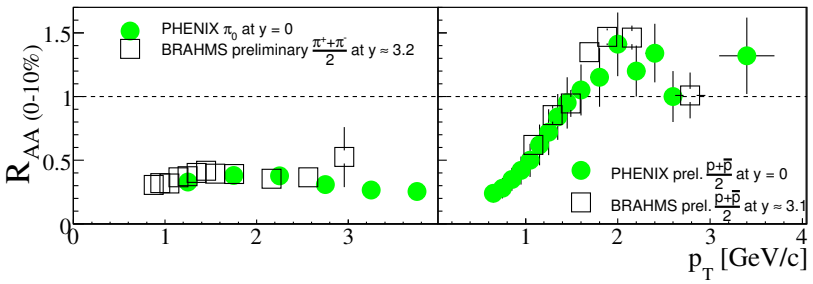


Fig. 7: Preliminary R_{AuAu} for pions (left) and protons (right) at y=0 and y=3 (central Au+Au collisions).

The lack of the rapidity dependence is somewhat surprising since the bulk properties of matter change considerably when going to forward rapidity: the rapidity density of pions drops by a factor of three [31], the radial flow velocity decreases by 30% and the hadron chemistry becomes "SPS-like" [32]. However, a 3D-hydrodynamical simulation starting from a CGC initial condition and including jets [33] can describe both the bulk properties as well as R_{AuAu}. The drop of the CGC initial parton distribution by a factor of two and the different time evolution of the thermalized parton density - resulting in less jet energy loss at $\eta = 3.2$ -, is compensated by a steeper p_T-slope of the pQCD components at forward rapidities.

An alternative explanation for the constant R_{AuAu} could be that the medium at RHIC is so dense that only particles produced close to the surface can escape and that therefore the corona effect masks the lower parton density at $\eta = 3.2$ [34].

6 Conclusion

Unbiased invariant cross sections of identified charged particles as function of p_T were measured at high rapidity in p+p collisions at $\sqrt{s} = 200$ GeV and $\sqrt{s} = 62.4$ GeV. NLO pQCD calculations reproduce reasonably well the produced particle (pions and kaons) distributions.

Suppression phenomena at forward rapidities in d+Au collisions have been seen at RHIC (and SPS); a variety of processes can result in suppression. A strong pion suppression is observed at all rapidities in central Au+Au collisions at 200 GeV, while protons are enhanced at all rapidities (R_{AuAu}); the nuclear modification factor does not depend on rapidity.

References

[1] I. Arsene *et al.*, (BRAHMS collaboration), Nucl. Phys. **A757** 1 (2005).

[2] B. Back *et al.*, (PHOBOS collaboration), Nucl. Phys. **A757** 28 (2005).

[3] J. Adams *et al.*, (STAR collaboration), Nucl. Phys. **A757** 102 (2005).

[4] J. Acox *et al.*, (PHENIX collaboration), Nucl. Phys. **A757** 184 (2005).

[5] M. Adamczyk *et al.*, (BRAHMS collaboration), Nucl. Instrum. Meth. **A499** 437 (2003).

[6] W. Vogelsang, private communication.

[7] J. Pumplin *et al.*, JHEP 0207, 012 (2002); arXiv:hep-ph/0201195.

[8] B.A. Kniehl *et al.*, Nucl. Phys. **B597** 337 (2001).

[9] S. Kretzer *et al*, Eur. Phys. J. **C22** 269 (2001).

[10] S. Albino *et al*, Nucl. Phys. **B725** 181 (2005).

[11] S.S. Adler *et al.*, Phys. Rev. Lett. **91** 241803 (2003).

[12] J. Adams *et al.*, Phys. Rev. Lett. **92** 171801 (2004).

[13] I. Arsene *et al.*, BRAHMS Collaboration. accepted for publication in PRL, arXiv:hep-ex/0701041

[14] F.Videbæk (BRAHMS Collaboration), Proceedings of the 23rd Winter Workshop on Nuclear Dynamics, Bigsky, Montana, 11. - 18. of February, 2007.

[15] C. Bourrely and J. Soffer, *Eur. Phys. J.* **C36** 371 (2004).

[16] I. Arsene *et al.* (BRAHMS collaboration), Phys. Rev. Lett. **93** 242303 (2004).

[17] B. Boimska (NA49 collaboration), PhD thesis, Warzaw (2004).

[18] D. Röhrich, Nucl. Phys. **A774** 297 (2006).

[19] D. Kharzeev, Y. V. Kovchegov and K. Tuchin, Phys. Lett. **B599** 23-31 (2004); D. Kharzeev, E. Levin and M. Nardi, Nucl. Phys. **A730** 448-459 (2004), erratum-ibid. **A743** 329-331 (2004).

[20] A. Dumitru, A. Hayashigaki and J. Jalilian-Marian, hep-ph/0506308.

[21] G. G. Barnafoldi, G. Papp and P. Levai, J. Phys. **G30** S1125-S1128 (2004).

[22] A. Arccadi and M. Gyulassy, J. Phys. **G30** S969-S974 (2004).

[23] R. Vogt, Phys. Rev. **C70** 064902 (2004).

[24] L. Frankfurt, V. Guzey and M. Strikman, Phys. Rev. **D71** 054001 (2005).

[25] J.W. Qiu and I. Vitev, hep-ph/0405068.

[26] K. Tywoniuk *et al.*, Acta Phys. Hung. **A27** 305 (2006).

[27] B. Kopeliovich et al., hep-ph/0501260.

[28] I. Vitev, 2005 RHIC&AGS Annual User's Meeting; T. Goldman, M. Johnson, J.W. Qiu, I. Vitev, in preparation.

[29] P. Staszel *et al.* (BRAHMS collaboration), Nucl. Phys. **A774** 77 (2006).

[30] S.S. Adler *et al.* (PHENIX Collaboration), Phys. Rev. Lett. **91** 072301 (2003).

[31] I. G. Bearden *et al.* (BRAHMS collaboration), Phys. Rev. Lett. **94** 162301 (2005).

[32] I. Arsene *et al.* (BRAHMS collaboration), Acta Phys. Slov. **56** 21 (2006).

[33] T. Hirano and Y. Nara, Nucl. Phys. **A743** 305 (2004); T. Hirano and Y. Nara, Phys. Rev. **C68** 064902 (2003).

[34] A. Dainese, C. Loizides and G. Paic, Eur. Phys. J. **C38** 461 (2005).

Manifestations of gluon saturation at RHIC

Javier L. Albacete
The Ohio State University

Abstract
The experimental results from RHIC provide accumulated evidence for the discovery of the Color Glass Condensate. I present a brief review of the saturation-based phenomenological works aimed at describing various aspects of heavy ion collisions. I discuss the success of such models in describing bulk features of multiparticle production in Au-Au collisions as well as the rapidity dependence of the nuclear modification factor in d-Au collisions as the most compelling indication for the presence of gluon saturation effects at RHIC.

1 Introduction

During the last years, the Relativistic Heavy Ion Collider (RHIC) has carried out an extensive experimental program in Au-Au, Cu-Cu, d-Au and p-p collisions over an broad range of collision energies, from 19.2 to 200 GeV per nucleon, with the ultimate goal of forming and studying the Quark Gluon Plasma (QGP). Besides the success of the RHIC program in this line of research [1–3], its discovery potential has reached other areas of QCD. Thus, the analyses of experimental data strongly suggest that RHIC collisions probe a novel regime of QCD governed by coherent non-linear phenomena and gluon saturation: the Color Glass Condensate (CGC). The CGC physics (for a review see, e.g. [4]) describes hadronic and nuclear wave functions at small values of the Bjorken-x variable. In such regime the gluon occupation numbers reach the maximal values allowed by unitarity i.e. they *saturate*. Further growth of the gluon densities is suppressed by gluon-gluon repulsive interactions. Very succinctly, the CGC comprises classical (the McLerran-Venugopalan model [5] and Glauber-Mueller rescatterings [6]) and quantum evolution (nonlinear JIMWLK [7] and BK [8] equations) effects both in small-x hadronic wave functions and in scattering process, leading to a universal description of high energy QCD scattering.

The presence of saturation effects in RHIC collisions could be argued a priori: At high energies, the colliding nuclei are highly Lorentz contracted along their direction of motion, leading to the spatial superposition of the gluon fields associated to their constituent nucleons or, equivalently, to large transverse gluon densities. Alternatively, the coherence length at small enough values of Bjorken-x is eventually larger than the nuclear radius, $l_c \sim 1/2m_N x > R_A$, so coherent phenomena may play an important role in the collision dynamics. Actually, the theoretical estimations for the saturation scale of the gold nucleus at RHIC were $Q_{sA}^2 \sim 1 \div 2$ GeV^2, in principle large enough for saturation effects to be important. However, the complicated dynamics of Au-Au collisions at the highest RHIC energies, including the QGP formation and its subsequent expansion, raises the question of whether such effects would have a clear experimental manifestation or whether they would be blurred by the strong final state effects induced by the presence

of the QGP. It turns out that some of the bulk features of multiparticle production in Au-Au collisions, such as the collision energy, rapidity and centrality dependence of particle multiplicities, seem to be mostly controlled by the initial state of the collision and, therefore, describable in terms of CGC physics.

The RHIC program also includes d-Au reactions at collision energy $\sqrt{s} = 200$ GeV. The d-Au program can be considered as an control experiment: the smaller energy densities involved in d-Au reactions do not suffice for the formation of a QGP. This reduces significantly the role of final state effects, allowing a clearer exploration of the initial state saturation effects. The situation is also more favourable on the theoretical side. The problem of calculating the evolution equations and production processes is better understood for dilute-dense scattering processes (i.e. proton-nucleus) than for dense-dense (nucleus-nucleus) scattering. Actually, one of the clearest signals of the presence of saturation effects at RHIC is given by suppression of the nuclear modification factor with increasing rapidity in d-Au collisions, which was predicted by CGC based calculations [9, 10].

2 Collision energy, rapidity and centrality dependence of hadron yields in d-Au and Au-Au collisions

CGC physics offers a natural explanation to the lower-than-predicted multiplicities measured at RHIC, namely the reduced flux of scattering centers, i.e. gluons, participating in the collision (for a review of predictions in the pre-RHIC era see, e.g. [11]). Thus, theoretical investigations [12] suggest a proportionality between the number of produced particles in A-A collisions and the number of partons in the wave function of the colliding nuclei, mostly dominated by semi-hard gluons with transverse momenta of the order of the saturation scale $k \sim Q_s$. Besides, the largeness of the saturation scale $Q_s >> \Lambda_{QCD}$ allows the use of weak coupling methods. The phenomenological implementation of these ideas was pioneered by Kharzeev, Levin and Nardi (KLN) [13–15], who extended the k_t-factorization formalism of [16] to describe multiparticle production at RHIC. In this approach primary gluon production in A-B collisions is given by the convolution of the unintegrated gluon distributions (udg's) of the projectile and target, $\varphi_{A(B)}$, according to

$$\frac{dN^{AB}}{d\eta\, d^2p_t\, d^2b} = \frac{4\pi N_c\, \alpha_s}{N_c^2 - 1} \int d^2k_t\, d^2s\, \varphi_A(x_1, \underline{k}, \underline{s})\, \varphi_B(x_2, \underline{p} - \underline{k}, \underline{b} - \underline{s})\,, \tag{1}$$

where $\underline{p}$ and η are the transverse momentum and pseudo-rapidity of the produced gluon and $\underline{b}$ is the impact parameter of the collision. The $\underline{s}$ integral in Eq. (1) extends over the collision area and $x_{1(2)} = |\underline{p}|/\sqrt{s}\, e^{\pm\eta}$, according to the $2 \to 1$ kinematics. Importantly, an analogous factorized formula holds exactly for p-A collisions. The udg's entering Eq. (1) present, at least, two distinct regimes: a *saturated* one and a dilute or perturbative one. Very schematically:

$$\varphi(x,k) \sim \begin{cases} Cte & \text{for} \quad k < Q_s(x) \\ \frac{Q_s^2(x)}{k^2} & \text{for} \quad k > Q_s(x) \end{cases} \tag{2}$$

The most important parameter in these calculations is the saturation scale, $Q_s(x)$, which provides the separation between the two regimes. Its energy/rapidity dependence is modelled as

$$Q_s^2(x) = Q_0^2\, (x_0/x)^{\lambda}\,, \tag{3}$$

where λ is often adjusted to the empirical value $\lambda = 0.288$ extracted from fits to small-x HERA data on deep inelastic lepton-hadron processes in the framework of saturation models [17, 18]. The phenomenological connection between HERA and RHIC is motivated by the property of *geometric scaling* displayed by small-x DIS data [19] and also exhibited by the solutions of the BK equation [20]. Additionally, local parton-hadron duality is assumed in order to compare Eq. (1), which describes primary gluon production, with the hadron spectra measured experimentally. Such assumption relies on the expectation that final state effects, including hadronization, do not modify substantially the angular distribution, and therefore the rapidity distribution of produced particles. This approach provides an excellent description of the collision energy and pseudo-rapidity dependence of the charged particle multiplicity data in d-Au and Au-Au collisions at energies $\sqrt{s} = 130$ and 200 GeV, as shown in Fig 1. Importantly, the recent calculation of running coupling corrections to the BK-JIMWLK kernel [21] allow to obtain a description of the nuclear udg's directly in terms of solutions of the BK equation which is in perfect agreement with the energy and rapidity dependence of RHIC data [22], thereby reducing the uncertainties associated to the parametrization of the nuclear udg's. Moreover, the combination of CGC calculations with subsequent hydrodynamic evolution of the system as carried out in [23] yields an equally successful comparison with RHIC multiplicity data, confirming the dominance of the initial state effects in this aspect of the collision.

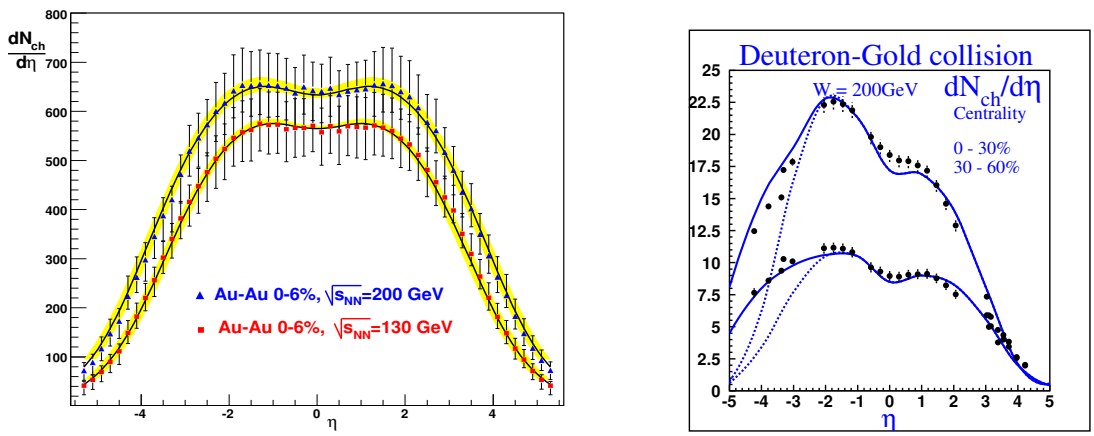


Fig. 1: Charged particle multiplicities in central Au-Au collisions at $\sqrt{s}=130$ and 200 GeV (left plot, figure from [22], data from [2]) and in d-Au collision at $\sqrt{s} = 200$ GeV for two centrality classes: 0-30 % and 30-60 % (right plot, figure taken from [24], Data from [25]).

The centrality dependence of RHIC multiplicities, normally discussed in terms of the number of participant nucleons in the collision area, N_{part}, is also naturally explained in saturation-based calculations [14], as seen in Fig 2. Under the assumption of *geometric scaling* of the nuclear udg's, the mid-rapidity multiplicity resulting from Eq. (1) rises proportional to the saturation scale which, as indicated by fits to DIS nuclear data, is roughly proportional to the number

of participants, yielding, from [26]:

$$\left.\frac{1}{N_{part}}\frac{dN^{AA}}{d^2b\,d\eta}\right|_{\eta=0} \propto \sqrt{s}^{\lambda}\, N_{part}^{\frac{1-\delta}{3\delta}}\,, \tag{4}$$

with $\delta \approx 0.8$. Eq. (4) shows two important features: First, it yields an exact factorization of the energy and centrality dependence of the mid-rapidity multiplicity. Second, it predicts an approximate scaling of the multiplicity densities with respect to N_{part}. This is a distinctive feature of saturation-based calculations with respect to the standard pQCD collinear approaches, which predict scaling with the number of binary collisions. In the original KLN approach the small violations of the N_{part} scaling rise as a consequence of running coupling corrections to Eq (1). Both features of Eq (1) are exhibited by experimental data, as seen in Fig 2.

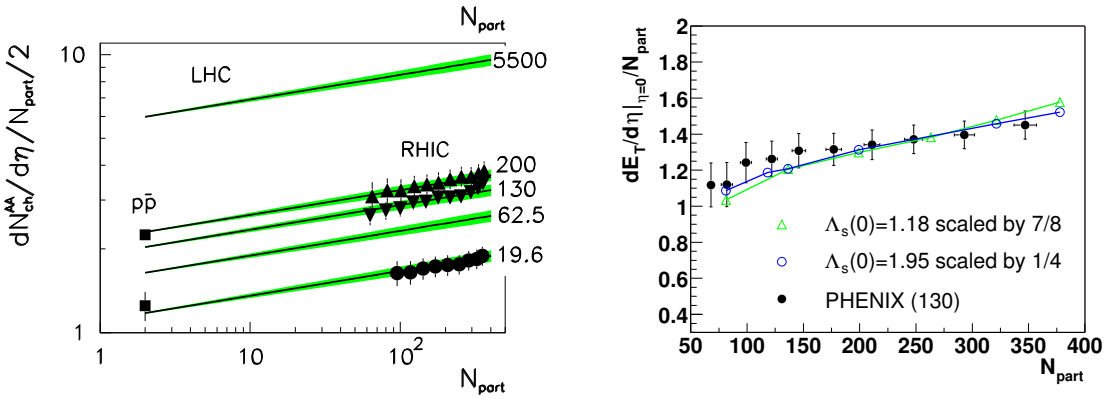


Fig. 2: Right plot: Centrality dependence of charged particle multiplicities in Au-Au collisions at $\sqrt{s} = 19.2$, 130 and 200 GeV calculated in [27]. Data from [28]. Left plot: Transverse energy of produced gluons in Au-Au collisions at $\sqrt{s} = 130$ GeV from the classical calculation in [29]. Data from [30].

An alternative approach to describe the multiplicities in Au-Au RHIC collisions was suggested in [31]: The gluon fields immediately after the collision can be calculated via the classical Yang-Mills equations of motion in the presence of a source term, given by the fast *valence* degrees of freedom of the colliding nuclei, $[D_\mu, F^{\mu,\nu}] = J^\nu$. Such approach has been intensively pursued in numerical calculations, see e.g. [29, 32]. The results of these calculations are also consistent with the bulk features of RHIC multiplicities discussed previously, as shown in in the right panel of Fig 2, where centrality dependence of the transverse energy of produced gluons in Au-Au collisions is compared to experimental data.

3 Nuclear modification factor in d-Au collisions

d-Au collisions are free of the highly distorting final state effects induced by the QGP, which permits a better exploration of saturation effects in more exclusive observables, such as particle spectra. The nuclear effects or, equivalently, the departure from superposition of incoherent

nucleon-nucleon scatterings, are normally discussed in terms of the nuclear modification factor, defined as

$$R_{AB} = \frac{\frac{dN^{AB}}{d^2b\,dp_t\,dy}}{N_{coll}\,\frac{dN^{pp}}{d^2b\,dp_t\,dy}}\,, \tag{5}$$

where N_{coll} is the number of binary collisions. R_{dAu} corresponding to charged particle spectra in d-Au collisions (and in central over peripheral Au-Au collisions) at mid-rapidity exceeds unity in an intermediate transverse momentum range of a few GeV, as seen in the left panel of Fig. 3. Such enhancement is commonly referred to as Cronin peak and admits a clear interpretation in the semi-classical MacLerran Venugopalan model: the produced parton acquires an average transverse momentum of the order of the saturation scale due to the multiple rescatterings in the gluon field of the nucleus, which explains enhancement in the region $p_t \sim Q_s$. At larger rapidities towards the deuteron fragmentation function the Cronin enhancement turns gradually into a uniform suppression in all the kinematic range accessible experimentally: $R_{pA} < 1$. As argued in [9, 10], such suppression is rooted in the shadowing built up by the non-linear small-x evolution of the nuclear gluon densities. Thus, the suppression is originated in the slower growth of nuclear densities with respect to those of the deuteron due to the relative enhancement of the non-linear effects in denser systems. Presently, the agreement between theory and data is of semi qualitative nature. Managing a more precise quantitative description of the suppression rate and of the particle species dependence of R_{pA}, which is different for e.g. pions and protons, remain nowadays as challenging issues.

An important step in that direction was made in [35], where an excellent description of data for charged particle production in d-Au collisions at different values of rapidity was achieved, see Fig 3. The new ingredients in that calculation are a *collinear* treatment of the dilute projectile, i.e. described by means of standard parton distribution functions and DGLAP evolution, plus an improved parametrization of the rapidity and transverse momentum dependence of the nuclear udg's, adjusted to reproduce HERA DIS data and some analytically known properties of the solutions of BK-JIMWLK equations. The recent developments in the determination of NLO corrections to the BK-JIMWLK equations also contribute largely to reduce the theoretical uncertainties associated to the determination of the nuclear udg's.

Contrary to d-Au collisions, the p_t spectra in Au-Au collisions at midrapity is uniformly suppressed, i.e. $R_{Au-Au} < 1$. The empiric observation that R_{pA} and R_{AA} follow opposite patterns with varying collision energy and centrality is crucial to interpret the suppression of the latter as a final state effect due to *jet quenching* induced by the presence of a QGP.

4 Others

Another experimental result which suggests the presence of saturation effects is the phenomenon of *limiting fragmentation*, the empirical observation that the rapidity distributions of produced particles at various collision energies tend to some universal curve in the fragmentation region. In the CGC framework, this property follows naturally from the unitarization of scattering amplitudes in the dense target, and the approximate Bjorken scaling in the fragmenting nucleus. The limiting curve then appears to be a reflection of the *valence*, large-x d.o.f of the projectile nucleus [37]. Additionally, the calculations of valence quark production in d-Au collisions of [38]

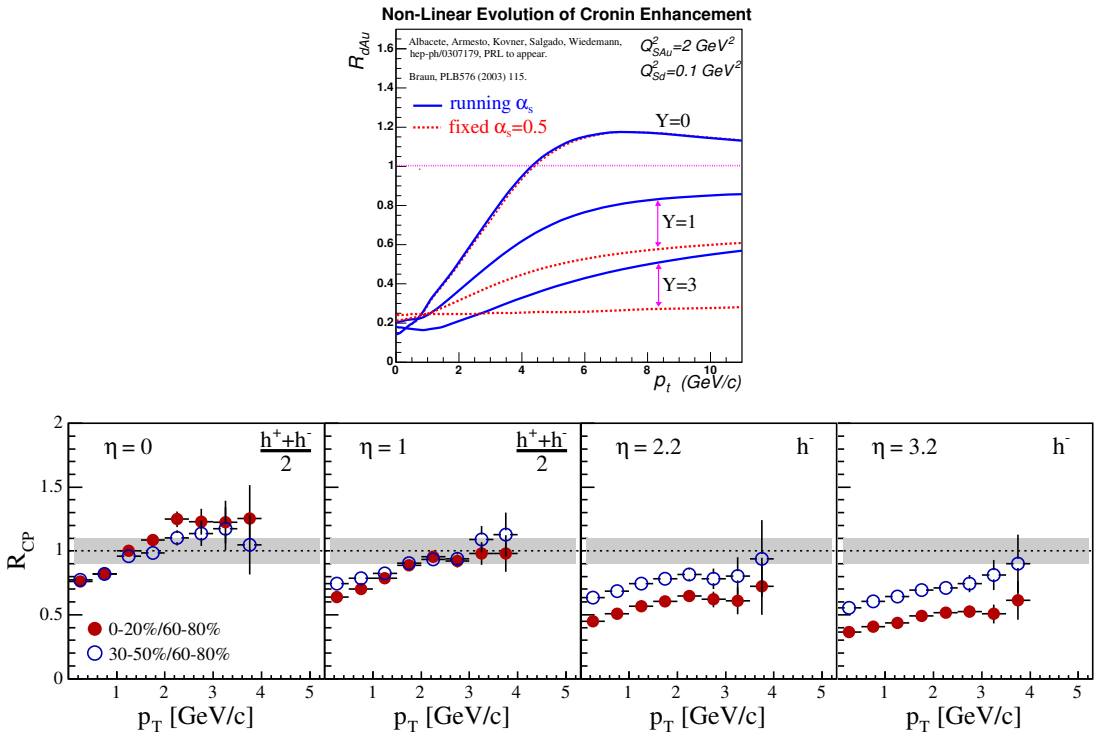


Fig. 3: Nuclear modificaton factor in d-Au collisions. Upper plot: theoretical results obtained with fixed (from [20]) and running coupling (udg's taken from [33]) evolution. Lower plot: Central over peripheral nuclear modification factor at pseudorapidity $\eta = 0$, 1, 2.2 and 3.2. Data from [34].

provide a qualitative explanation for the phenomenon of *baryon stopping*. The determination of heavy flavour production of [39] for d-Au collisions is in agreement with available experimental data. Other production processes have already been calculated in the framework of CGC (see [40] for an extensive review): Electromagnetic probes (lepton and photon production), long range in rapidity di-hadron correlations originated from di-gluon and gluon-valence quark production etc. However, the experimental test of the predictions stemming from these calculations is not yet possible due to the lack of the pertinent experimental data.

The definitive confirmation of the tentative conclusions drawn after the RHIC era awaits until the start of operation of the CERN LHC, which will operate at unprecedentedly large collision energies (5.5 TeV in Pb-Pb collisions and 7 TeV in p-Pb collisions). At such energies saturation effects are expected to manifest at their best and the applicability of a purely high energy formalism as the CGC is much better justified.

5 Acknowledgments

This work is sponsored in part by the U.S. Department of Energy under Grant No. DE-FG02-05ER41377. The author would like to thank the organizers for their invitation to such a nice and interesting meeting.

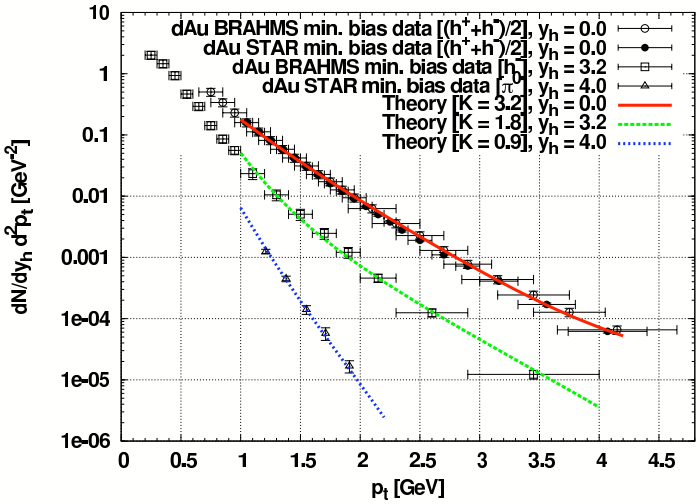


Fig. 4: Charged particle spectra in minimum bias d-Au collisions at rapidities 0, 3.2 and 4, from [35]. Data from [36].

References

[1] BRAHMS Collaboration, I. Arsene *et al.*, Nucl. Phys. **A757**, 1 (2005). nucl-ex/0410020;
PHENIX Collaboration, K. Adcox *et al.*, Nucl. Phys. **A757**, 184 (2005). nucl-ex/0410003;
STAR Collaboration, J. Adams *et al.*, Nucl. Phys. **A757**, 102 (2005). nucl-ex/0501009.

[2] B. B. Back *et al.*, Nucl. Phys. **A757**, 28 (2005). nucl-ex/0410022.

[3] M. Gyulassy and L. McLerran, Nucl. Phys. **A750**, 30 (2005). nucl-th/0405013.

[4] H. Weigert, Prog. Part. Nucl. Phys. **55**, 461 (2005). hep-ph/0501087;
E. Iancu and R. Venugopalan (2003). hep-ph/0303204.

[5] L. D. McLerran and R. Venugopalan, Phys. Rev. **D49**, 2233 (1994). hep-ph/9309289.

[6] A. H. Mueller, Nucl. Phys. **B335**, 115 (1990).

[7] J. Jalilian-Marian, A. Kovner, and H. Weigert, Phys. Rev. **D59**, 014015 (1999). hep-ph/9709432;
E. Iancu, A. Leonidov, and L. D. McLerran, Phys. Lett. **B510**, 133 (2001). hep-ph/0102009.

[8] I. Balitsky, Nucl. Phys. **B463**, 99 (1996). hep-ph/9509348;
Y. V. Kovchegov, Phys. Rev. **D60**, 034008 (1999). hep-ph/9901281.

[9] J. L. Albacete, N. Armesto, A. Kovner, C. A. Salgado, and U. A. Wiedemann, Phys. Rev. Lett. **92**, 082001 (2004). hep-ph/0307179.

[10] D. Kharzeev, Y. V. Kovchegov, and K. Tuchin, Phys. Rev. **D68**, 094013 (2003). hep-ph/0307037.

[11] N. Armesto and C. Pajares, Int. J. Mod. Phys. **A15**, 2019 (2000). hep-ph/0002163.

[12] Y. V. Kovchegov and A. H. Mueller, Nucl. Phys. **B529**, 451 (1998). hep-ph/9802440;
Y. V. Kovchegov, Nucl. Phys. **A692**, 557 (2001). hep-ph/0011252.

[13] D. Kharzeev and E. Levin, Phys. Lett. **B523**, 79 (2001). nucl-th/0108006.

[14] D. Kharzeev, E. Levin, and L. McLerran, Phys. Lett. **B561**, 93 (2003). hep-ph/0210332.

[15] D. Kharzeev, E. Levin, and M. Nardi, Phys. Rev. **C71**, 054903 (2005). hep-ph/0111315.

[16] L. V. Gribov, E. M. Levin, and M. G. Ryskin, Nucl. Phys. **B188**, 555 (1981).

[17] K. Golec-Biernat and M. Wüsthoff, Phys. Rev. **D59**, 014017 (1999). hep-ph/9807513.

[18] E. Iancu, K. Itakura, and S. Munier, Phys. Lett. **B590**, 199 (2004). hep-ph/0310338.

[19] A. M. Stasto, K. Golec-Biernat, and J. Kwiecinski, Phys. Rev. Lett. **86**, 596 (2001). hep-ph/0007192.

[20] J. L. Albacete, N. Armesto, J. G. Milhano, C. A. Salgado, and U. A. Wiedemann, Phys. Rev. **D71**, 014003 (2005). hep-ph/0408216.

[21] Y. V. Kovchegov and H. Weigert, Nucl. Phys. **A784**, 188 (2007). hep-ph/0609090;
I. Balitsky, Phys. Rev. **D75**, 014001 (2007). hep-ph/0609105;
E. Gardi, J. Kuokkanen, K. Rummukainen, and H. Weigert, Nucl. Phys. **A784**, 282 (2007). hep-ph/0609087;
J. L. Albacete and Y. V. Kovchegov, Phys. Rev. **D75**, 125021 (2007). arXiv:0704.0612 [hep-ph].

[22] J. L. Albacete (2007). arXiv:0707.2545 [hep-ph].

[23] T. Hirano and Y. Nara, Nucl. Phys. **A743**, 305 (2004). nucl-th/0404039.

[24] D. Kharzeev, E. Levin, and M. Nardi, Nucl. Phys. **A730**, 448 (2004). hep-ph/0212316.

[25] BRAHMS Collaboration, I. Arsene *et al.*, Phys. Rev. Lett. **94**, 032301 (2005). nucl-ex/0401025.

[26] J. L. Albacete, N. Armesto, J. G. Milhano, C. A. Salgado, and U. A. Wiedemann, Eur. Phys. J. **C43**, 353 (2005). hep-ph/0502167.

[27] N. Armesto, C. A. Salgado, and U. A. Wiedemann, Phys. Rev. Lett. **94**, 022002 (2005). hep-ph/0407018.

[28] PHOBOS Collaboration, B. B. Back *et al.*, Phys. Rev. **C70**, 021902 (2004). nucl-ex/0405027.

[29] A. Krasnitz, Y. Nara, and R. Venugopalan, Nucl. Phys. **A717**, 268 (2003). hep-ph/0209269.

[30] PHENIX Collaboration, K. Adcox *et al.*, Phys. Rev. Lett. **87**, 052301 (2001). nucl-ex/0104015.

[31] A. Kovner, L. D. McLerran, and H. Weigert, Phys. Rev. **D52**, 6231 (1995). hep-ph/9502289;
Y. V. Kovchegov and D. H. Rischke, Phys. Rev. **C56**, 1084 (1997). hep-ph/9704201.

[32] T. Lappi, Phys. Rev. **C67**, 054903 (2003). hep-ph/0303076.

[33] M. A. Braun, Phys. Lett. **B576**, 115 (2003). hep-ph/0308320.

[34] BRAHMS Collaboration, I. Arsene *et al.*, Phys. Rev. Lett. **93**, 242303 (2004). nucl-ex/0403005.

[35] A. Dumitru, A. Hayashigaki, and J. Jalilian-Marian, Nucl. Phys. **A770**, 57 (2006). hep-ph/0512129.

[36] BRAHMS Collaboration, I. Arsene *et al.*, Phys. Rev. Lett. **93**, 242303 (2004). nucl-ex/0403005;
STAR Collaboration, J. Adams *et al.*, Phys. Rev. Lett. **91**, 072304 (2003). nucl-ex/0306024;
STAR Collaboration, J. Adams *et al.*, Phys. Rev. **C70**, 064907 (2004). nucl-ex/0408016.

[37] J. Jalilian-Marian, Phys. Rev. **C70**, 027902 (2004). nucl-th/0212018;
F. Gelis, A. M. Stasto, and R. Venugopalan, Eur. Phys. J. **C48**, 489 (2006). hep-ph/0605087.

[38] K. Itakura, Y. V. Kovchegov, L. McLerran, and D. Teaney, Nucl. Phys. **A730**, 160 (2004). hep-ph/0305332;
J. L. Albacete and Y. V. Kovchegov, Nucl. Phys. **A781**, 122 (2007). hep-ph/0605053.

[39] H. Fujii, F. Gelis, and R. Venugopalan, Nucl. Phys. **A780**, 146 (2006). hep-ph/0603099.

[40] J. Jalilian-Marian and Y. V. Kovchegov, Prog. Part. Nucl. Phys. **56**, 104 (2006). hep-ph/0505052.

Measurement of the cross section and the single transverse spin asymmetry in very forward neutron production from polarized pp collisions at RHIC

Manabu Togawa (on behalf of the PHENIX collaboration)
RIKEN Nishina Center and RIKEN Brookhaven Research Center (RBRC)

Abstract
A large single transverse spin asymmetry of forward neutron production in polarized pp collision was discovered at RHIC. PHENIX experiment will provide new data to discuss the production mechanism with the polarized phenomenon. Results of the cross section and the single transverse spin asymmetry of the forward neutron at $\sqrt{s}$=200 GeV are presented. They may prefer the one pion exchange model which is successful in explaining forward neutron cross section of other experimental results.

1 Introduction

In 2001-2002, first polarized proton beams were accelerated to 100 GeV/c at the Relativistic Heavy Ion Collider (RHIC). The 12 o'clock interaction point experiment (IP12) was searching for single transverse spin asymmetries (A_N) which could be used as a monitor system for the spin direction of proton beams. The IP12 experiment was originally designed to detect photon and π^0 asymmetries based on the large pion asymmetry at $\sqrt{s}$=19.4 GeV [1]. Unfortunately their asymmetries had no significance in IP12 kinematics within the statistical error. However, unexpected large single transverse spin asymmetry in forward neutron production was discovered [2].

On the other hand, cross section measurements of the neutron production in such very forward angle have been reported as interesting results by the ISR and HERA (ZEUS, H1) experiments. ISR experiment performed unpolarized pp collision in $\sqrt{s}$ between 30.6 to 62.7 GeV [3]. The forward cross section has peak structure at high Feynman-x (x_F) and scales well with x_F, but not with center of mass energy. From the HERA, it is ep collision at $\sqrt{s}$ $\sim$300 GeV, the cross section of the forward neutron also has the peak structure [4].

These results are successfully described by One Pion Exchange (OPE) model [5]. According to this idea, one proton looks like meson-nucleon system and meson exchange is considered as shown in Fig1. Two important variables, common for pp and ep in very forward kinematics are,

$$x_F = p_L/p_{L(max)} = E_n \cos\theta_n / E_p \sim E_n/E_p \quad (1)$$

$$p_T = E_n \sin\theta_n \sim x_F E_p \theta_n \quad (2)$$

From these variables, the squared momentum transfer from proton to neutron can be written as,

$$t \sim -\frac{p_{\mathrm{T}}^2}{x_F} - t_0 \quad t_0 \equiv \frac{1-x_F}{x_F}(m_{\mathrm{n}}^2 - x_F m_{\mathrm{p}}^2) \quad (3)$$

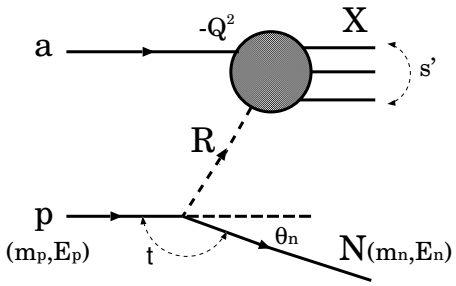


Fig. 1: A schematic diagram for forward neutron production with the Reggeon (meson) exchange model for $ap \rightarrow nX$ reaction showing with the Lorentz invariant variables s', Q^2, and t. a is proton or positron for pp or e^+p reaction. R indicates the Regge trajectory such as π, ρ, a_2 and Pomeron-π in the Regge theory. In case of the pion exchange model, R should be π (OPE model).

OPE model could also help to understand the neutron asymmetry since it must arise from an interference of spin-flip (g) and spin-nonflip (f) amplitudes,

$$A_N = \frac{2\mathrm{Im}(fg^*)}{|f|^2 + |g|^2} \tag{4}$$

and pion exchange is fully spin-flip interaction. This model was successfully applied to describe the polarization of inclusive Λ production in pp collision [6]. The neutron asymmetry would have the sensitivity for other Reggeon exchange which is spin-nonflip interaction even if it is small amplitude. More precise measurement is expected to give a new knowledge in forward physics.

PHENIX can make more precise measurements of neutron energy and position than that of IP12 experiment. With the improved energy resolution, the cross section and x_F dependence of asymmetry can be extracted.

2 Experimental setup

A plan view of the experiment for the forward neutron physics at PHENIX is shown in Fig.2.

The PHENIX experiment has measured the forward neutrons by Zero-Degree Calorimeter (ZDC) with position-sensitive Shower-Max Detector (SMD) which cover ± 2.8 mrad of forward and backward directions [7]. ZDC is composed of the W-Cu alloy plates and optical fibers. One ZDC module has 1.7 interaction length and 51 radiation length. It can achieve 21% energy resolution for the 100 GeV neutron with 3 ZDC modules in series (5.1 interaction length in total). SMD is arrays of the fifteen plastic scintillators (for y-position : 8, for x-position : 7). Neutron generates hadron-shower at the first ZDC module and position can be obtained by calculating the center of gravity of SMD hits. ZDCs are placed on a production angle of 0 $^{\circ}$ downstream of the RHIC Dx dipole magnets, which remove produced charged particles from pp collision. For the safe operation, a scintillator has been installed in front of the ZDC to remove charged particles from other sources. The correction values for taking cross section and asymmetry, signal identification, efficiency and so on, have been studied by Monte-Carlo simulations which are based on the GEANT3 with PYTHIA [8] and single-particle event generators.

In the OPE model frame work, it is interesting to study the other particles associated with the forward neutron since they will be generated by the proton-pion scattering (X in the Fig.1). For its study, we collected the data by not only the inclusive neutron trigger but also the coincidence with charged particles detected in Beam Beam Counter (BBC). BBC is composed

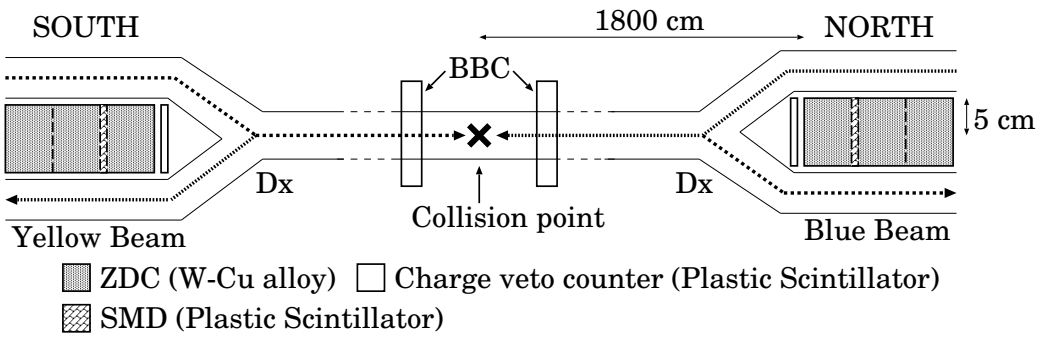


Fig. 2: A plan view of the experiment at PHENIX, not to scale. Shown are the principle components of the experiment.

of the 64 quartz radiators with photomultiplier tubes around beam pipe as a beehive structure. BBCs are placed in up- and down-stream and they are covering $\pm(3.0 \sim 3.9)$ and 2π in the pseudo-rapidity and azimuthal angle, respectively.

The RHIC polarized proton beams were vertically polarized and bunched. The 120 bunches in one beam had alternating spin directions, for example (↑,↓,↑,↓,..). We have collected the data for spin up and down at the same time and reduce the systematic errors for the asymmetry measurements by using these two spin patterns (square root formula, see equation (7)). The absolute polarization was evaluated by the measurements of single transverse spin asymmetries caused by Coulomb Nuclear Interference (CNI) in pC and pp scattering [9]. Average beam polarization is $\sim$48 % in this period.

We are using the data which were taken at SOUTH ZDC for neutron analysis. In this case, we can define "forward asymmetry" (positive x_F) with the polarization of yellow beam. When the measurement with the polarization of blue beam, asymmetry should be "backward asymmetry" (negative x_F).

3 Analysis formulas

Since we do not estimate $p_{\rm T}$ distribution from PHENIX data yet, the cross section was calculated as a differential cross section,

$$\frac{d\sigma}{dx_F} = \frac{1}{dx_F}\frac{N_{\rm neutron}}{L} \tag{5}$$

where, $N_{\rm neutron}$ is the neutron yield corrected for efficiency, background and energy unfolding. L is the integrated luminosity. $p_{\rm T}$ distribution of ISR result was used for Monte-Carlo simulation to estimate the efficiency with the assumption of the same $p_{\rm T}$ distribution in both experiments. To compare with ISR results, invariant cross section of ISR data were converted to the differential one with same $p_{\rm T}$ acceptance,

$$\frac{d\sigma}{dx_{\rm F}} = \frac{2\pi}{x_{\rm F}}\int E\frac{d^3\sigma}{d^3p}p_{\rm T}dp_{\rm T} \tag{6}$$

The single transverse spin asymmetry is defined as the differences over the sum of cross sections in left and right regions with respect to the beam polarization direction (it is so called left-right asymmetry). It can be calculated by square root formula which can cancel the detector and luminosity asymmetries in the first order.

$$A_N \equiv \frac{1}{P}\frac{\sigma_L - \sigma_R}{\sigma_L + \sigma_R} \approx \frac{1}{P}\frac{\sqrt{N_L^{\uparrow}N_R^{\downarrow}} - \sqrt{N_L^{\downarrow}N_R^{\uparrow}}}{\sqrt{N_L^{\uparrow}N_R^{\downarrow}} + \sqrt{N_L^{\downarrow}N_R^{\uparrow}}} \tag{7}$$

where, $N_L^{\uparrow}$ ($N_R^{\uparrow}$) is experimental yield of left (right) part detector with colliding particles with the up transverse spin. (Down transverse spin is assigned as $\downarrow$). P is beam polarization.

4 Results

4.1 Cross section

Obtained forward neutron cross section, $d\sigma/dx_F$, at $\sqrt{s}$=200 GeV is plotted with the ISR results in Fig.3. Acceptance cut is applied as radii from the center of the detector (r) less than 2 cm for the measurement of very forward region (0 to 1.1 mrad). By equation (2), it is equivalent $p_{\rm T}$ range as 0 to $0.11x_F$ GeV in each point and ISR invariant cross sections are converted to differential cross section by equation (6). The PHENIX result is consistent with the ISR data. There is no evidence for violation of the $x_{\rm F}$ scaling at higher energy.

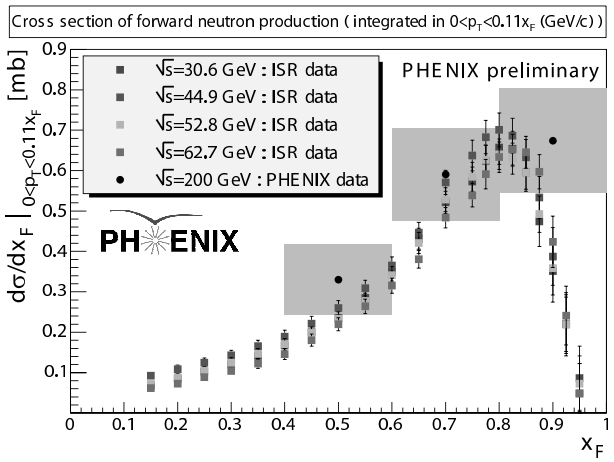


Fig. 3: Differential cross section of forward neutron production from pp collisions at $\sqrt{s}$=200 GeV (circle points). Square points show the results from ISR for various center of mass energies.

4.2 Azimuthal angle dependence of single transverse spin asymmetry

For the first step of asymmetry result, its ϕ-dependence is shown in Fig.4. To measure a left-right asymmetry, it is necessary to eliminate 0 $^{\rm o}$ production. For the acceptance cut, we required $0.5<r<4.5$ cm, or production angles 0.3 - 2.5 mrad. The ZDC hits are assigned coordinates (r,ϕ) about the 0 $^{\rm o}$ reference axis, and binned in ϕ counterclockwise, with ϕ=0 along the vertical axis. A vertical beam polarization would give a left-right asymmetry for ϕ=$\pm\pi$/2 and a radial beam polarization would give an asymmetry for ϕ = 0. Forward asymmetry is plotted in Fig.4 and there is no significance for backward asymmetry. Data can be fitted by sine curve well.

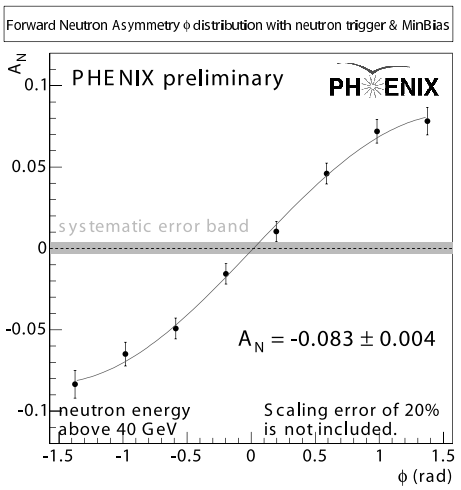


Fig. 4: ϕ-dependence of single transverse spin asymmetry for forward neutron production from pp collisions at $\sqrt{s}$=200 GeV. The sample was taken by the neutron trigger with charged particles detected in the BBC ($3.0 < |\eta| < 3.9$).

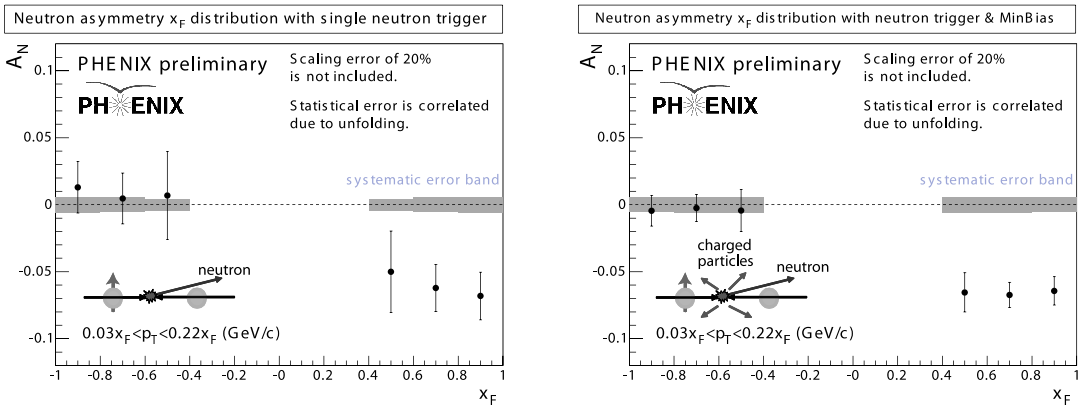


Fig. 5: x_F-dependence of single spin asymmetries for forward neutron production from pp collisions at $\sqrt{s}$=200 GeV. Left) Inclusive neutron trigger. Right) Neutron trigger with charged particles detected by the BBC ($3.0 < |\eta| < 3.9$).

4.3 x_F dependence of single transverse spin asymmetry

Figure 5 shows x_F dependence of neutron asymmetry for inclusive neutron with or without charged particles in the BBC. x_F is calculated using equation (1) after the energy unfold process and assigned positive and negative sign to x_F for the results from forward and backward asymmetries respectively.

Significant negative asymmetries can be seen in the forward region in both trigger sets and they look flat as a function of x_F within the correlated errors due to the unfolding. From this results, we can not see any differences between two trigger sets due to the large error bars.

4.4 Charged particles in the BBC tagged with the forward neutron

So far we investigated neutron measurement in forward kinematics. In addition, charged particles associated with the forward neutron indicates interesting behaviors.

First, we show the multiplicity distribution observed by the BBCs in Fig.6. In case of the

sample collected by requiring BBC self trigger, multiplicities of both BBCs are same distributions (Left figure). However their distributions are changed in the neutron tagged sample; multiplicity of forward BBC is lower than that of backward (Right figure).

This result may be explained by OPE model. In the OPE framework, charged particles will be generated by the proton-pion scattering. Since energy of pion is lower than that of proton, multiplicity of charged particles in the neutron direction may be lower.

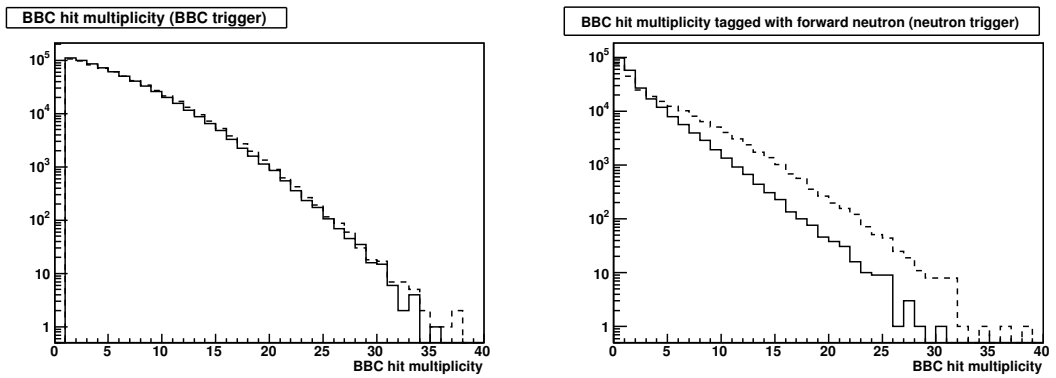


Fig. 6: The Multiplicity distributions of charged particles in BBC. Left) sample of the BBC self trigger (require at least 1 hit for both BBCs). Right) sample of the neutron tagged trigger by SOUTH ZDC. The solid line shows that for forward BBC in the neutron detection (SOUTH) and the dashed line shows that for backward BBC (NORTH).

The polarized phenomena were also observed in the charged particles for the sample of the neutron association; we can observe the significant left-right asymmetries, especially in same direction as neutron.

- Forward BBC (same direction as neutron) : -4.50 $\pm$ 0.50 $\pm$ 0.22 %
- Backward BBC (opposite direction as neutron) : 2.28 $\pm$ 0.55 $\pm$ 0.10 %

Without the neutron association, their asymmetries are consistent with 0.

In focus on the the asymmetry for same direction as neutron, its sign is negative as well as neutron asymmetry. One possibility of its origin is that the neutron is generated via the excited hadron state by the diffractive-like process, for example, $\Delta^+ \rightarrow n+\pi^+$. In this case, π^+ can have the same property of the neutron. Other consideration is that the information of polarization is delivered to the proton-pion scattering directly. In this case, charged particle from the scattering themselves can have asymmetry, but we may not know its sign. It is necessary to discuss with the theoretical calculation.

5 Summary

The cross section and the single transverse spin asymmetry of forward neutron production in $\sqrt{s}$=200 GeV polarized pp collision were measured at RHIC-PHENIX.

The cross section which is evaluated in 0-1.1 mrad is consistent with ISR results at very forward region. There is no evidence of violation of x_F scaling to higher energy. A significant

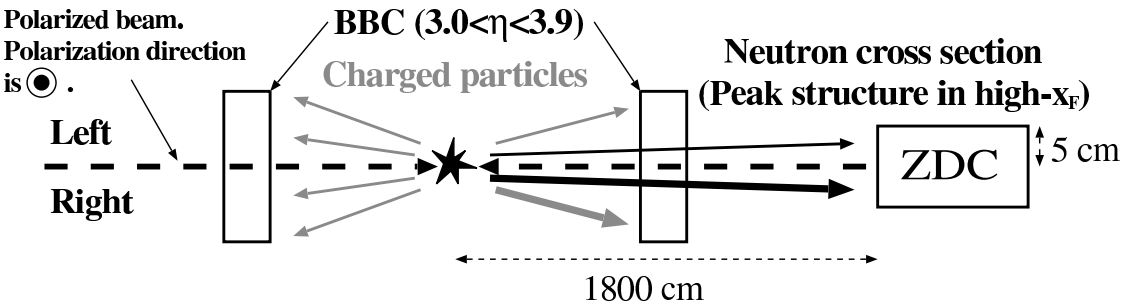


Fig. 7: Overall view of the observes for the forward neutron physics at PHENIX. The heavy lines for neutron and charged particles mean more hits than the thin lines. It indicates the particles have left-right asymmetry.

left-right asymmetry was seen in forward production, but not in backward. No x_F-dependence is found within the large correlated error due to unfolding. Charged particles which are detected by BBC associated with the forward newton have also interesting behaviors; asymmetric multiplicity distributions at forward and backward BBC in the neutron direction and its finite left-right asymmetries.

Let us summarize the phenomena for forward neutron production as follows.

1. Neutron cross section is scaled by x_F from ISR energy to RHIC energy ($\sqrt{s}$=200 GeV) and it has peak structure in high-x_F
2. Finite A_N of the forward neutron
3. Multiplicity of the charged particles associated with the forward neutron;
   Forward (Same direction as neutron) $<$ Backward (Opposite direction as neutron)
4. Finite A_N of the charged particles associated with the forward neutron

and their schematic view is shown in Fig.7. By comparing with the OPE model which can explain the previous experiments, it should also explain the cross section result, 1, as well as treatment for ISR. For phenomenon of 2, left-right asymmetry will be generated by the interference of spin-flip and spin-nonflip amplitudes, and pion exchange is fully spin flip interaction. Finite A_N can be explained by OPE. In case of 3, it will occur by the lower energy pion and proton scattering in the OPE frame work (Fig.1). Last phenomenon, 4, two probabilities are shown. One is the neutron production via the excited hadron state, for example, $\Delta^+ \to n + \pi^+$ and π^+ can have the same property as the neutron in this case. Other is the information of polarization which is delivered to the proton-pion scattering directly.

OPE model can explain most of our results qualitatively and it is necessary to discuss it quantitatively for the next step. Theoretical calculation is very welcome.

References

[1] FNAL E581/704 Collaboration, D. L. Adams *et al.*, Phys. Rett. **B261**, 201 (1991).

[2] Y. Fukao, M. Togawa, *et al.*, Phys. Rett. **B650**, 325 (2007).

[3] W. Flasher *et al.*, Nucl. Phys. **B109**, 347 (1976);
J. Engler *et al.*, Nucl. Phys. **B84**, 70 (1975).

[4] ZEUS Collaboration, S. Chekanov *et al.*, Nucl. Phys. **B637**, 3 (2002).

[5] N. N. Nikolaev, J. Speth, and B. G. Zakharov, [hep-ph/9708290];
B. P. B. Kopeliovich and I. Potashnikova, Z. Phys. **C73**, 125 (1996);
U. DAlesio and H. Pirner, Eur. Phys. J. **A7**, 109 (2000);
A. Bunyatyan and B. Povh, Eur. Phys. J. **A27**, 359 (2006);
A. B. Kaidalov *et al.*, Eur. Phys. J. **C47**, 385 (2006).

[6] J. Soffer and N. A. Törnqvist, Phys. Rev. Lett. **68**, 907 (1992).

[7] C. Adler *et al.*, Nucl. Instr. And Meth. **A470**, 488 (2001).

[8] T. Sjostrand, Comput. Phys. Commun. **135**, 238 (2001).

[9] J.Tojo *et al.*, Phys. Rev. Lett. **89**, 052302 (2002);
T. L. Trueman, hep-ph/0305085;
H. Okada *et al.*, Phys. Lett. **B638**, 450 (2006).

Gluon saturation: from pp to AA

A. Kovner
Physics Department, University of Connecticut

Abstract
I briefly review the status of our understanding of the physics of saturation as it is manifested in different scattering reactions.

1 Perturbative saturation - the basic approach

1.1 The setup

I start with a brief description of the basic perturbative approach to saturation physics. This line of reseaech started with the seminal paper of Gribov, Levin and Ryskin[1]. My exposition will however follow the logic stressed in the more recent developments of the last ten years or so. Our aim is to describe hadronic processes at high energy. The picture is that of two objects which we refer to as the "projectile" and "the target" colliding at large energy. The projectile moves to the right, while the target to the left. We use throughout the "projectile light cone gauge" $A^+ = 0$. In this gauge it is natural to think of the projectile as a bunch of color charges - partons. This may be a pretty big bunch, especially if the projectile itself is a nucleus, but it nevertheless is the natural light cone gauge perspective. The wave function of this bunch of charges is characterized by the color charge density in the transverse plane $\rho^a(x)$.

The interaction between the partons of the projectile and the target fields at high energy is eikonal, so that the second quantized S-matrix operator can written as

$$\hat{S} = e^{i\int_{x_\perp} \rho^a(x)\alpha^a(x)} \tag{1}$$

and the forward scattering amplitude

$$S = \langle T|\langle P|\, e^{i\int_{x_\perp} \rho^a(x)\alpha^a(x)}\, |P\rangle|T\rangle \tag{2}$$

1.2 Evolution

To discuss the evolution of the scattering amplitude with energy we boost the wave function of the projectile. In a gauge theory like QCD, the boost results in "materialization" of softer gluons from the "longitudinal field". Formally this is described by acting with the evolution operator Ω in the projectile state.

$$|P\rangle \;\rightarrow\; \Omega_Y[\rho, a, a^\dagger]|P\rangle \tag{3}$$

The color charge density increases due to presence of these soft gluons:

$$\rho^a \rightarrow \rho^a + \int_Y d\eta\, a^\dagger(\eta, x) T^a a(\eta, x) \tag{4}$$

This process has two important aspects, both of which must be understood. First, the evolution operator $\Omega[\rho]$ - has a nontrivial dependence on ρ. Thus the probability of emission of soft gluons in the boosted wave function depends nonlinearly on the valence color charge density. Secondly, emission of new gluons is associated with increased importance of multiple scattering contributions to the cross section. The factor $e^{i\int(\rho^a+a^\dagger T^a a)\alpha^a}$ - accounts for these multiple scatterings. All gluons are allowed to scatter independently of each other.

The "Holy Grail" of the perturbative saturation approach is to derive the evolution equation which takes into account both effects without further approximations beyond that of the eikonal nature of scattering. In the following I try to summarize how far are we from this goal at present, in relation to different processes.

2 Where do we think we are.

2.1 Scattering of "small" on "large": p-A scattering.

The situation when the projectile is a small object, and therefore its wave function can be treated perturbatively has been well studied and the evolution equation for the scattering matrix has been derived[2],[3],[4] In this case Ω turns out to be a coherent operator. It creates a "classical" Weizsacker-Williams field

$$\Omega = e^{i\int_{x,z}\left[\rho^a(x)\frac{(x-z)_i}{(x-z)^2}\left(a_i^a(z)+a_i^{\dagger a}(z)\right)\right]} \tag{5}$$

All multiple scattering effects in the evolution are taken into account: e.g. ALL soft gluons are allowed to scatter.

In this limit the color charge grows according to BFKL evolution

$$\rho_Y^2 \propto \rho_0^2 e^{\omega Y} \tag{6}$$

At large enough rapidity $Y \sim \frac{1}{\omega}$ almost all gluons in the wave function are soft, that is have rapidity closest to the target. Simultaneous scattering of these soft gluons is the leading effect beyond the simple perturbative picture.

The scattering amplitude unitarizes (does not exceed unity) due to these multiple scattering effects even though the color charge density in the wave function grows exponentially (BFKL type growth).

2.2 Large on small: A - p scattering.

Physically of course this is the same situation as before. Technically however the evolution now resides in the wave function of a large dense object. Thus we need to take into account nonperturbative effects in the wave function evolution.

The equation which describes the evolution is the so called JIMWLK equation [5]. Schematically:

$$\frac{d}{dY}S = \alpha H^{JIMWLK}[S]S \tag{7}$$

where H^{JIMWLK} is the evolution operator defined explicitly in [5].

What goes into the derivation of this equation? First of all, the evolution of $|P\rangle$ is fully nonlinear[6]. In other words all nonperturbative corrections which are due to large charge density have been resummed. On the other hand, since the target is assumed to be small, the multiple scatterings are less important. Thus produced soft gluons in the JIMWLK equation are allowed to scatter only via two gluon exchange. Thus only "long range" multiple scatterings - that is only processes in which particles at different rapidities scatter simultaneously are taken into account.

In fact it is the "long range" scatterings that dominate the multiple scattering contributions in the dense regime. To see this we note that in the saturated wave function the color charge density grows slowly with rapidity:

$$\rho_Y^2 \sim \rho_0^2 + \#Y \tag{8}$$

Gluons are distributed homogeneously in rapidity. Likely multiple scatterings are when the gluons sit far away from each other in rapidity, with "short range" multiple scattering being suppressed by powers of rapidity.

2.3 Small on small : p - p scattering.

This would seem to be the simplest of all possible situations, since both scattering objects are perturbatively small. However if we want to follow the evolution to very high energy, the situation is actually quite intricate. The point is that a small and dilute object when evolved to high rapidity becomes dense, and the perturbation theory breaks down even in this case.

At low enough rapidity, $Y < \frac{1}{\omega} \ln \alpha_s$, the evolution is indeed simple. It is just the BFKL equation. However for larger rapidity neither JIMWLK nor KLWMIJ evolutions are adequate.

It is obvious why KLWMIJ breaks down. At $Y \sim \frac{1}{\omega} \ln \alpha_s$ the density in the projectile becomes large and the "dilute" wave function evolution is not appropriate. It is a little less obvious why JIMWLK evolution is no good. The reason is that there is a range of rapidities (just before the saturation is reached) where ρ is not small but the evolution is still "BFKL type". The density is still growing exponentially and thus the "short range multiple scatterings" are important. Since those are not incorporated in the JIMWLK evolution, the error made is of the same order as the finite density corrections accounted for in the JIMWLK evolution.

So what do we do? We have to learn how to take into account properly both sets of corrections, if we want to describe the scattering of two small objects at very high energy, This has still not been achieved. There has been quite a bit of activity on this particular problem in the last couple of years. In particular there has been much work on what has been known as the "statistical model" approach [7]. In particular the recent paper [8] contains an inspiring analysis of the front propagation in stochastic FKKP equation.

However my understanding is that the connection of this approach to QCD is at best tenuous. If the conclusions of the "statistical approach" are taken literally, one would have to conclude that the BFKL equation does not hold even for small density (low energy) if the two scattering objects are very different in size (e.g. two dipoles of different sizes). This is not the case in QCD. In general the physics of this approach seems to be very different from the "finite density+multiple scatterings", and it is hard to see that QCD contains such additional physics. It would be very interesting to pinpoint the relation of this approach to QCD, and in this context

I would like to ask our colleagues who are working on the statistical models to try and provide a more concrete and precise relation to QCD. Time will tell if these models can teach us about QCD physics, but at the moment I am skeptical.

2.4 Large on large: A-A scattering.

This is obviously most complicated situation. The evolution must be accounted for in its full nonlinear glory. This is still work in progress, and not much can be said yet. Except, that calculating the scattering amplitude is kind of silly, since it is all saturated, $S \approx 0$, and small "preasymptotic" deviations from saturation are not really that interesting.

3 What should we calculate, and what can we calculate?

The total cross section is in fact not a good quantity to calculate in the perturbative saturation approach. The reason is that we know [9] that the Froissart bound is violated by this approach, since gluons are always massless. So peripheral events dominate the cross section and it grows as a power of energy.

We thus need to extend the approach to calculate more infrared safe observables. Recently there has been progress in this direction. The framework for calculation of semiinclusive observables has been developed in [10]. This includes various diffractive amplitudes and amplitudes at fixed transverse momentum transfer.

Inclusive gluon production has also been addressed. In particular the expression for double inclusive spectrum has been derived in [11]. This has been extended to an arbitrary number of gluons in [12].

This is a good beginning, but its only the beginning. First, all the expressions so far have been derived for the p-A scattering. And second, this program awaits numerical implementation if some numbers and/or plots are to be obtained.

3.1 Towards AA

Some progress has been made recently in approaching the general AA scattering problem. In particular [6] calculates the evolved wave function in the dense regime. The evolution operator turns out to have the form

$$\Omega = e^{i\int_x \left[b_i^a(x)\left(a_i^a(x)+a_i^{\dagger a}(x)\right)\right]} e^{\int_{x,y}(a_i^a(x)+a_i^{\dagger a}(x))M_{ij}^{ab}(x,y)(a_j^b(y)+a_j\dagger b(y))} \tag{9}$$

As opposed to the dilute case, the evolution produces many gluons in the wave function. It now has to be understood how to include all the relevant multiple scattering effects. One expects that the full evolution will incorporate the so called Pomeron loops. They must affect strongly the more exclusive observables. In particular we expect the number of produced gluons below the saturation momentum to grow with rapidity only very slowly:

$$\frac{dN}{dY} \propto Y \tag{10}$$

A very interesting program is being pursued in [13], where the problem of calculating inclusive gluon production is being attacked starting with scattering of classical fields.

3.2 Next to leading order.

Perhaps the most important set of corrections we need to calculate to be able to do sensible phenomenology based on the saturation theory, is that due to next to leading order in α_s. As is well known, the BFKL equation suffers from large next to leading order corrections. The same should be true in the present context.

The corrections due to quark-antiquark final states and the running of α_s have been analysed recently [14],[15]. The effect of these corrections is indeed very large. The evolution is slowed down considerably. Both the running of the coupling and the "genuine" NLO effects work in this direction. One can get a rough idea of the significance of the effect by looking at the numerical results of [15]. E.g. the saturation momentum dependence on rapidity for a fixed coupling case at $\alpha_s = 0.25$ is $\frac{dQ_s^2}{dY} \approx 0.4$, while for running coupling it is approximately $\frac{dQ_s^2}{dY} \approx 0.15$.

It is important to understand the effects due to gluons, which presumably will be even more significant.

References

[1] L.V. Gribov, E. Levin and M. Ryskin, *Phys. Rep.* **100**:1,1983.

[2] I. Balitsky, *Nucl. Phys.* **B463** 99 (1996); *Phys. Rev. Lett.* **81** 2024 (1998); *Phys. Rev.***D60** 014020 (1999).

[3] Y. V. Kovchegov, Phys. Rev. D **61**, 074018 (2000)

[4] A. Kovner and M. Lublinsky, Phys. Rev. D **71**, 085004 (2005).

[5] J. Jalilian Marian, A. Kovner, A.Leonidov and H. Weigert, *Nucl. Phys.***B504** 415 (1997); *Phys. Rev.* **D59** 014014 (1999); J. Jalilian Marian, A. Kovner and H. Weigert, *Phys. Rev.***D59** 014015 (1999); A. Kovner and J.G. Milhano, *Phys. Rev.* **D61** 014012 (2000) . A. Kovner, J.G. Milhano and H. Weigert, *Phys.Rev.* **D62** 114005 (2000); H. Weigert, *Nucl.Phys.* **A 703** (2002) 823; E.Iancu, A. Leonidov and L. McLerran, *Nucl. Phys.* **A 692** (2001) 583; Phys. Lett. **B 510** (2001) 133; E. Ferreiro, E. Iancu, A. Leonidov, L. McLerran; *Nucl. Phys.***A703** (2002) 489.

[6] A.Kovner, M.Lublinsky and U. Wiedemann; *JHEP* **0706**:075,2007;

[7] E. Iancu, A.H. Mueller and S. Munier; *Phys.Lett.* **B606**:342-350,2005;

[8] E. Brunet, B. Derrida, S. Munier and A.H. Mueller; *Europhys.Lett.* **76**:1-7,2006;

[9] A. Kovner and U. Wiedemann, *Phys.Rev.* **D66**:034031,2002;

[10] E. Levin and Y. Kovchegov, *Nucl.Phys.* **B577**:221-239,2000; H. Weigert, M. Hentschinski and A. Schäfer; *Phys.Rev.* **D73**:051501,2006; A. Kovner, M. Lublinsky and H. Weigert; *Phys.Rev.* **D74**:114023,2006.

[11] J. Jalilian Marian and Y. Kovchegov; *Phys.Rev.* **D70**:114017,2004, Erratum-ibid.D71:079901,2005.

[12] A. Kovner and M. Lublinsky; *JHEP* **0611**:083,2006.

[13] F. Gelis and R. Venugopalan; *Acta Phys.Polon.* **B37**:3253-3314,2006.

[14] I. Balitsky and A. Belitsky; *Nucl.Phys.* **B629**:290-322,2002; I. Balitsky, *Phys.Rev.* **D75**:014001,2007; E. Gardi, J. Kuokkanen , K. Rummukainen and H. Weigert; *Nucl.Phys.* **A784**:282-340,2007; Y. Kovchegov and H. Weigert; *Nucl.Phys.* **A784**:188-226,2007; *Nucl.Phys.* **A789**:260-284,2007.

[15] J. Albacete and Y. Kovchegov, *Phys.Rev.* **D75**:125021,2007.

Photoproduction in Ultra-Peripheral Heavy-Ion Collisions

Joakim Nystrand
Department of Physics and Technology, University of Bergen, Bergen, Norway

Abstract
This presentation summarizes the results on ultra-peripheral collisions obtained at RHIC. It also discusses some aspects of the corresponding electromagnetic interactions in pp and $p\overline{p}$ collisions.

Ultra-peripheral nucleus-nucleus collisions are defined as collisions in which the distance between the nuclei is large enough that no purely hadronic interactions can occur. This roughly means impact parameters larger than the sum of the nuclear radii. The interaction is then instead mediated by the electromagnetic field. For a recent review of ultra-peripheral collisions, see [1].

1 Ultra-peripheral collisions at RHIC

The Relativistic Heavy-Ion Collider (RHIC) at Brookhaven National Laboratory began operating in the year 2000. This meant an increase in the maximum center of mass energies for heavy-ion collisions by more than an order of magnitude compared with the earlier fixed-target experiments.

At very high collision energies, the electromagnetic field surrounding a nucleus contains photons energetic enough to produce new particles in ultra-peripheral collisions. This can happen in a purely electromagnetic process through a two-photon interactions or in an interaction between a photon from one of the nuclei and the other ("target") nucleus. The photon spectrum for a minimum impact parameter, b_{min}, extends to $\sim \gamma/b_{min}$, which corresponds to about 300 GeV in the rest frame of the target nucleus in a gold on gold collision at RHIC. These photon energies are thus far above the threshold for particle production. The coherent contribution from the Z protons in the nucleus, furthermore, enhances the number of equivalent photons by a factor Z^2.

The high photon energies and fluxes lead to large cross sections for several photon-induced reactions; some have cross sections much larger than the total hadronic cross section and are major sources of beam-loss at heavy-ion colliders [2]. For example, the cross section for breaking up one of the nuclei in an Au+Au collision at RHIC through a photonuclear interaction is 95 b. The cross section for exchanging two photons and thereby simultaneously breaking up both nuclei in the same event is also large, about 4 b. The dominating fragmentation mechanism is excitation to a Giant Dipole Resonance followed by emission of one or a few neutrons.

The mutual Coulomb dissociation has been studied at RHIC by detecting the forward going neutrons in Zero-Degree Calorimeters [3]. These are located 18 m downstream from the interaction point and have an angular acceptance of $\theta < 2$ mrad with respect to the beam axis. The relative contribution of the photon-induced fragmentation to the total cross section was found to be in good agreement with calculations based on the method of equivalent photons combined with measured γ+Au cross sections. The calculations also reproduced the neutron multiplicity distribution for photon-induced events reasonably well.

Another ultra-peripheral process with very high cross section is two-photon production of electron-positron pairs. Of particular interest is the sub-class of events where the produced electron binds to one of the beam nuclei. The captured electron changes the charge and thus the rigidity of the ion, leading to a different deflection by the guiding magnets in the accelerator ring and eventual loss. Under certain conditions, the ion with an attached electron will hit the wall of the beam-pipe enclosure at a well-defined spot down stream of the interaction point. At the Large Hadron Collider at CERN, because of the high beam flux and energy, this has the potential to heat and quench the superconducting magnets near this area. The phenomenon was recently observed for the first time at RHIC with Cu–beams [4]. The location of the point of incidence (≈140 m downstream from the interaction point) and the multiplicity of secondary particles resulting from the interaction of the 100 A GeV Cu beam with the beam-pipe and the surrounding magnets were found to be in good agreement with theoretical calculations, although the experimental uncertainties were large.

Particle production in ultra-peripheral collisions has been studied by both of the two large experiments at RHIC, STAR and PHENIX. Some of these results will be discussed in the following two sections.

2 Results from STAR

The first results on particle production in ultra-peripheral collisions at RHIC were studies of coherent production of ρ^0 mesons in Au+Au interaction by the STAR collaboration [5]. The cross section to produce a ρ^0 in an Au+Au collision at RHIC is about 10% of the total inelastic, hadronic cross section.

STAR has also published final results on two-photon production of free e^+e^-–pairs [6] and preliminary results on photo-production of ρ^0 in d+Au collisions [7] and coherent production of four pions in Au+Au collisions [8].

In d+Au collisions more than 90% of the photo-produced ρ^0 mesons come from events where the gold nucleus emitted the photon. The interactions can leave the deuteron intact $\gamma + d \rightarrow \rho^0 + d$ or lead to break-up $\gamma + d \rightarrow \rho^0 + n + p$. Two triggers were implemented to study the two cases. Both were based on triggering on low multiplicity combined with a "topology" cut to reject cosmic rays. The multiplicity was measured in the STAR Central Trigger Barrel, which consists of 240 scintillators covering the full azimuth in the pseudo-rapidity range $|\eta| < 1$. To trigger on interactions where the deuteron breaks up, it was in addition required that the forward going neutron should be detected in the Zero Degree Calorimeter. Examples of the $\pi^+\pi^-$ invariant mass distributions for the two samples are shown in Fig. 1.

The invariant mass distribution is well described by the sum of the amplitudes for a resonant ρ^0 term and a non-resonant (Söding) term:

$$\frac{d\sigma}{dm_{\pi\pi}} = \left| A\frac{\sqrt{m_{\pi\pi}m_\rho\Gamma_\rho}}{m_{\pi\pi}^2 - m_\rho^2 + im_\rho\Gamma_\rho} + B \right|^2 + f_p \qquad (1)$$

Here, $\Gamma_\rho = \Gamma_0 \cdot (m_\rho/m_{\pi\pi}) \cdot [(m_{\pi\pi}^2 - 4m_\pi^2)/(m_\rho^2 - 4m_\pi^2)]^{3/2}$ is the momentum dependent width, Γ_0 the natural width, and f_p is a second order polynomial describing the background (estimated from the like-sign yield). The mass and width of the ρ^0 are consistent with the Particle Data

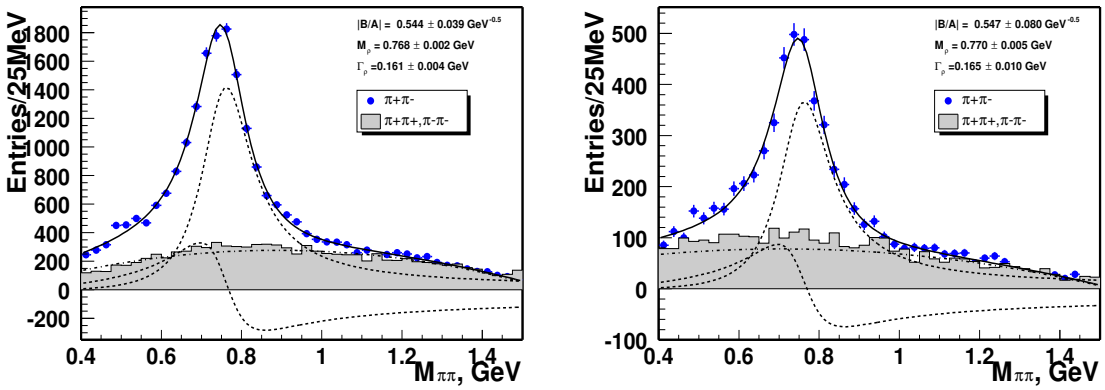


Fig. 1: Invariant mass distributions for photoproduction of $\pi^+\pi^-$–pairs in d+Au interactions at RHIC. The left (right) figure is for reactions where the deuteron remains intact (breaks up). From [7].

Group values. The ratio A/B is a measure of the relative resonant to non-resonant contribution. The values observed in d+Au interactions (0.544 and 0.547 GeV$^{-1/2}$) are consistent, within errors, with the value obtained in Au+Au interactions, $0.81 \pm 0.08 \pm 0.20$ GeV$^{-1/2}$ [5].

3 Results from PHENIX

The PHENIX experiment has studied the production of high-mass ($m_{inv} > 1.6$ GeV) e^+e^--pairs and J/Ψ mesons in ultra-peripheral Au+Au collisions [9]. A trigger was implemented for events where at least one of the nuclei break up through Coulomb dissociation. The trigger required a cluster with energy deposit $E > 0.8$ GeV in the Electromagnetic Calorimeter in coincidence with a signal in one of the Zero Degree Calorimeters and in anti-coincidence with a signal in the Beam-Beam Counters. The latter are Cherenkov counters covering $3.0 < |\eta| < 3.9$ and the absence of a signal corresponds to a rapidity gap on each side of the produced particles.

In the offline analysis, the electron and positron were identified by the Ring Imaging Cherenkov Counters and Electromagnetic Calorimeters. These detectors are part of the PHENIX mid-rapidity tracking arms and cover 2×90° in azimuth and $|\eta| < 0.35$ in pseudo-rapidity. Signal events were defined as those events with exactly one reconstructed e^+ and one reconstructed e^- in opposite tracking arms. Events with a like-sign pair were used to estimate the amount of background.

The transverse momentum and invariant mass distributions with the background from like-sign pairs subtracted are shown in Fig. 2. The transverse momentum is here the absolute value of the vector sum of the transverse momenta of the the e^+ and e^-.

The results show that exclusive production of high-mass e^+e^--pairs in Au+Au interactions at RHIC can be understood as a continuum contribution from two-photon production $\gamma + \gamma \rightarrow e^+e^-$ and a contribution from photoproduction of J/Ψs decaying into e^+e^--pairs.

The cross section to produce a J/Ψ in a coherent interaction is much larger than the cross

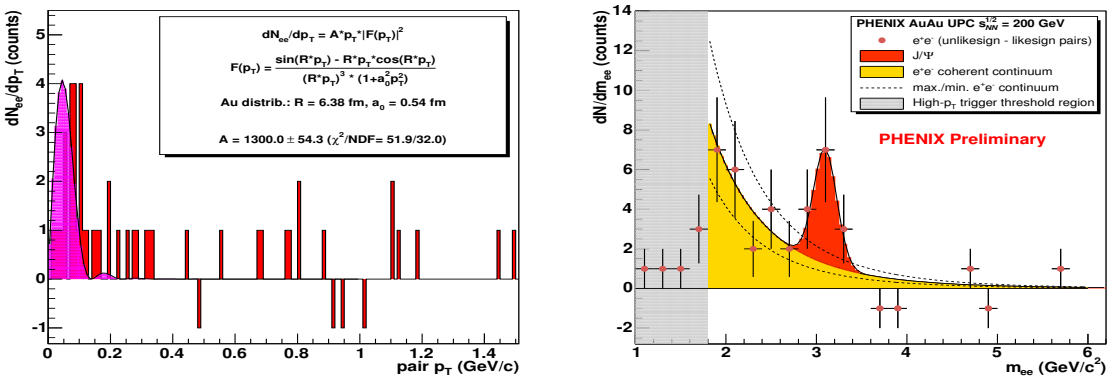


Fig. 2: Transverse momentum (left) and invariant mass (right) distributions for e^+e^--pairs produced in ultra-peripheral Au+Au collisions. The background estimated from events with like-sign pairs have been subtracted (hence the negative entries in some bins). The curve in the left figure corresponds to the nuclear form factor. The solid curve in the right figure is a fit to the sum of a continuum and J/Ψ distribution. The two additional dashed curves indicate the maximum and minimum continuum contributions. From [9].

section to produce a continuum pair in the corresponding mass range, but the branching ratio for $J/\Psi \rightarrow e^+e^-$ (5.94 %) and the broadening of the J/Ψ peak because of the limited experimental resolution make the rates comparable in the relevant mass range [10].

The transverse momentum distribution shows a clear peak at very low transverse momenta, which is expected for coherent events where the momentum transfer is restricted by the nuclear form factor. The signal events with $p_T > 100$ MeV/c are believed to come from quasi-elastic J/Ψ photoproduction, $\gamma + nucleon \rightarrow J/\Psi + nucleon$ [11].

The total net number of e^+e^--pairs in the sample (integrated luminosity $120 \pm 10\ \mu b^{-1}$) is about 40, of which ≈10 are estimated to come from decay of J/Ψs. The observed rates are in reasonable agreement with expectations for $\gamma\gamma \rightarrow e^+ + e^-$ and photoproduction of J/Ψ [10].

4 Ultra-peripheral proton-proton collisions

Electromagnetic interactions can of course also be studied with beams of protons or anti-protons, but there is then no enhancement ($\propto Z^2$) in the photon flux. Although evidence for electromagnetic particle production in pp collisions were observed at the ISR almost 30 years ago [12], electromagnetic interactions in pp collisions have so far attracted relatively little attention, much less than particle production in doubly diffractive interactions, for example. The CDF Collaboration has, however, recently published its first paper on two-photon production of e^+e^-–pairs with $m_{inv} > 10$ GeV in $p\overline{p}$ collisions at the Tevatron [13].

The choice of minimum invariant mass is unfortunate, since it falls right in the range of the $\Upsilon(1S)$, $\Upsilon(2S)$, and $\Upsilon(3S)$ vector mesons, and, as will be shown, these vector mesons are expected to give a significant contribution to the exclusive production of e^+e^-–pairs through the decay $\Upsilon \rightarrow e^+e^-$.

CDF is also analyzing the exclusive production of $\mu^+\mu^-$–pairs, $p\overline{p} \rightarrow p\overline{p} + \mu^+\mu^-$, at

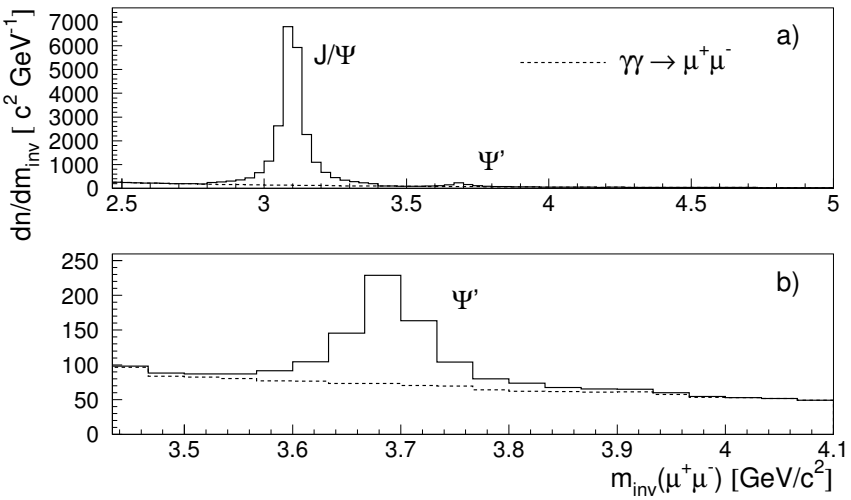


Fig. 3: Calculated invariant mass distributions for electromagnetic production of $\mu^+\mu^-$–pairs around mid-rapidity ($|\eta| < 2$) in $\sqrt{s}$ = 1.96 TeV $p\overline{p}$ collisions. Figure b) shows the same distribution as a) but restricted to a narrow intervall around the Ψ' mass. The widths of the J/Ψ and Ψ' have been set to roughly correspond to typical experimental widths.

lower invariant masses [14]. The two main contributions to these events are, as with heavy-ion beams, $\gamma\gamma \rightarrow \mu^+ + \mu^-$ and γ+Pomeron $\rightarrow J/\Psi$ or Ψ', followed by decay of the vector meson to a dilepton pair. There could also be a contribution from the elusive Odderon through the reaction Odderon+Pomeron $\rightarrow V \rightarrow \mu^+ + \mu^-$ [15, 16]. The size of this contribution is not very well known; it is possible that it is comparable to the other two processes.

There could also be a background to the J/Ψ production from Pomeron+Pomeron interactions producing a χ_c via the decay $\chi_c \rightarrow J/\Psi + \gamma$ where the photon escapes detection. This background is a problem only for the J/Ψ and not for the Ψ'.

Figure 3 shows the calculated yields for continuum $\mu^+\mu^-$–production and photoproduction of J/Ψ and Ψ' followed by decay to $\mu^+\mu^-$–pairs for $p\overline{p}$ collisions at the Tevatron ($\sqrt{s}$ = 1.96 TeV). It is required that both muons are within $|\eta| < 2$ to simulate the typical experimental acceptance at high-energy colliders. The vector meson production is calculated as in [17], but with a larger cut-off for the minimum impact parameter ($b > 1.4$ fm rather than 0.7 fm). This is believed to better reproduce the condition of no accompanying hadronic interactions. The input $\gamma + p \rightarrow p + \Psi'$ cross section is taken from [18]. The continuum $\gamma + \gamma \rightarrow \mu^+\mu^-$ is calculated under the same conditions as the vector mesons. The contribution from two-photon interactions is much smaller in pp or $p\overline{p}$ collisions compared with in heavy-ion collisions (cf. Fig. 2). The calculated cross sections are given in Table 1.

Table 1: Cross sections for photoproduction of vector mesons and $\mu^+\mu^-$–pairs in $p\overline{p}$ collisions at the Tevatron ($\sqrt{s}$ = 1.96 TeV). The rightmost column shows the cross section multiplied with the branching ratio for decay into $\mu^+\mu^-$.

	σ [nb]	$\sigma \cdot Br(\mu^+\mu^-)$ [nb]
$p + \overline{p} \rightarrow p + \overline{p} + J/\Psi$	15	0.87
$p + \overline{p} \rightarrow p + \overline{p} + \Psi'$	2.4	0.018
$p + \overline{p} \rightarrow p + \overline{p} + \mu^+\mu^-$ ($m_{inv} > 1.5$ GeV)	2.4	2.4

5 Summary

The fact that particles are produced in ultra-peripheral collisions and that the experiments that were designed to study central collisions can detect them have been shown by the STAR and PHENIX experiments at RHIC. Hopefully, the increase in the cross sections with energy and the extended trigger capabilities of future experiments will lead to an increased interest for ultra-peripheral collisions in proton-proton and heavy-ion collisions at the Large Hadron Collider.

References

[1] C. Bertulani, S. Klein, and J. Nystrand, Ann. Rev. Nucl. Part. Sci. **55**, 271 (2005).

[2] A. Baltz, M. Rhoades-Brown, and J. Weneser, Phys. Rev. E **54**, 4233 (1996).

[3] M. Chiu *et al.*, Phys. Rev. Lett. **89**, 012302 (2002).

[4] R. Bruce *et al.*, Phys. Rev. Lett. **99**, 144801 (2007).

[5] STAR Collaboration, C. Adler *et al.*, Phys. Rev. Lett. **89**, 272302 (2002).

[6] STAR Collaboration, J. Adams *et al.*, Phys. Rev. C **70**, 031902 (2004).

[7] STAR Collaboration, S. Timoshenko *et al.*, nucl-ex/0501010.

[8] STAR Collaboration, S. Klein *et al.*, nucl-ex/0506013.

[9] PHENIX Collaboration, D. d'Enterria *et al.*, nucl-ex/0601001 (Presentation at Quark Matter 2005).

[10] J. Nystrand, Nucl. Phys. A **752**, 470 (2005).

[11] M. Strikman, M. Tverskoy, and M. Zhalov, Phys. Lett. B **626**, 72 (2005).

[12] F. Vanucci *et al.*, CERN-EP/80-82, available from http://cdsweb.cern.ch/.

[13] CDF Collaboration, A. Abulencia *et al.*, Phys. Rev. Lett. **98**, 112001 (2007).

[14] A. Hamilton, private communication.

[15] L. Szymanowski, these proceedings.

[16] A. Schäfer, L. Mankiewicz, and O. Nachtmann, Phys. Lett. B **272**, 419 (1991).

[17] S. Klein and J. Nystrand, Phys. Rev. Lett. **92**, 142003 (2004).

[18] H1 Collaboration, C. Adloff *et al.*, Phys. Lett. B **541**, 251 (2002).

Fractional energy losses in the black disk regime and BRAHMS effect

L. Frankfurt[1]*, M. Strikman*[2†]
[1] School of Physics and Astronomy, Tel Aviv University, Tel Aviv, Israel
[2] Department of Physics, Pennsylvania State University, University Park, PA 16802, USA

Abstract
We argue that in the small x processes, in the black disc QCD regime (BDR) a very forward parton propagating through the nuclear matter should loose a significant and increasing with energy and atomic number fraction of its initial energy as a result of dominance of inelastic interactions, causality and energy-momentum conservation. We evaluate energy losses of forward partons in the kinematics close to BDR and find them to lead to the significant suppression of the forward jet production in the central NA collisions at collider energies with a moderate suppression of recoiling jet at central rapidities. We find our expectations to be in agreement with the recent RHIC data.

1 Introduction

It is well understood now that one of distinctive properties of hard processes in pQCD is the fast increase with energy of cross sections of hard inelastic processes and their significant value. Thus the interactions of the leading partons carrying finite fraction η of projectile momentum and produced in the sufficiently small x hard processes should be highly inelastic. Dominance of inelastic processes leads to the specific pattern of absorption for a parton propagating through the nuclear medium which is the main subject of this talk. For a more detailed discussion and extensive references see [1].

The difference between geometry of collisions dominated in the hard and soft QCD processes should disappear in the limit of complete absorption-black disc regime (BDR) i.e. at $x \leq x_{BDR}(Q^2)$ where Q^2 is the scale of hard processes and $x = (Q^2/\eta s)$. Decomposition of amplitude of DIS over powers of $1/Q^2$ disappears and therefore QCD factorization theorem is violated and at smaller $x \ll x_{BDR}$ hard partons are completely absorbed. With increase of Q leading partons leave kinematics of BDR and at sufficiently large Q conventional LT approximation will be restored. In this kinematics concept of fractional energy losses would become useful. Thus propagation of parton carrying significant fraction of projectile momentum differs strongly from that for the propagation of a parton in the center in rapidity where the elastic rescatterings of a parton dominates. Such a parton looses a finite energy [2] while propagating a distance L: $\Delta E \approx 0.02 GeV\, L^2/Fm^2$.

In contrast in the deep inelastic processes for example DIS off a proton the fraction of initial photon energy lost by incident parton is $\sim 10\%$ within DGLAP approximations, cf. dis-

[†] speaker

cussion in section 2. Numbers are probably similar within the NLO BFKL approximation corresponding to the rapidity interval between the leading particle and next rung in the ladder of about two. (It is equal to zero within the LO BFKL approximation which systematically neglects the loss of energy by energetic particles.)

In the regime where $x \approx x_{BDR}$ the contrast between the different patterns of energy losses becomes dramatic. A parton with energy E propagating sufficiently large distance L through the nuclear media should loose energy:

$$\Delta E/E = c(L/L_0) \tag{1}$$

with $c \approx 0.1$ in small x processes, and $L_0 \sim$ 3fm the mean free path for the interaction of a parton in BDR and $c(L/L_0) \to 1$ for $x \ll x_{BDR}$. This energy loss exceeds by orders of magnitude the losses in the large x regime.

Another subtle effect characteristic for a quantum field theory has been found long before the advent of QCD: eikonal interactions of energetic particle are cancelled out as the consequence of causality. This cancellation including additional suppression of eikonal diagrams due to energy-momentum conservation is valid for the exchanges by pQCD ladders with vacuum quantum numbers in the crossed channel. The cancellation of the contribution of eikonal diagrams has been demonstrated also for the exchanges by color octet ladders as the consequence of bootstrip condition for the reggeized gluon. Thus sufficiently energetic parton may experience only one inelastic collision. To produce n inelastic collisions wave function of energetic parton should develop component containing at least n constituents. This effect leads to the additional depletion of the spectrum of leading partons in the kinematics close to BDR where inelastic interactions of the energetic parton is important part of unitarization of amplitudes of hard processes.

Since the number of inelastic collisions is controlled by the number of scattering centres at given impact parameter the effect of the suppression of the yield of leading partons should be largest at the central impact parameters. We evaluate energy losses of leading parton in small x regime of QCD and show that blackening of pQCD interaction leads to dominance of peripheral collisions in the production of the leading hadrons/jets in high energy hadron - nucleus interactions and to a significant, increasing with energy and atomic number loss of finite fraction of leading parton energy in the central collisions. Inclusive cross section is $\propto A^{1/3}$ deep in the BDR region with suppression of the recoil jets depending on x of jet. One of characteristic features of BDR regime is that there is no suppression of recoil jet in the peripheral collisions. At moderately small x which are reached at RHIC, suppression of recoil jet should depend on its rapidity and be maximal if both jets carry a significant fraction of the projectile energy. We will show that this prediction is supported by the recent RHIC data on leading hadron production in dA collisions.

It is instructive to compare the kinematics of partons involved in the production of leading hadrons at RHIC with that for small x phenomena at HERA. Taking for example the STAR highest rapidity (y=4) and $\langle p_T \rangle = 1.3\,GeV/c$ bin [3] we find that $x_N \geq 0.7$ for the incoming parton. Hence, minimal x_g resolved by such a parton are $\sim 4p_T^2/(x_N s_{NN}) \sim (2 \div 3) \cdot 10^{-4}$. This is very close to the kinematics reached at HERA. The analyses of the HERA data within the dipole model approximation show that the partial amplitude for the quark interaction reaches at HERA strength up to 1/2 of the maximal strength, see review in Ref. [4]. In the case of heavy

nuclei one gets an enhancement factor $\sim 0.5A^{1/3}$ so the quark interaction with heavy nuclei should be close to BDR for $p_t^2 \leq 1.5GeV^2$ and $x_{projectile} \sim 0.5$. In the LHC kinematics BDR will cover much larger p_t^2 range, see for example Fig. 17 in Ref. [4].

Suppression of the forward spectra in the deuteron-gold collisions in the kinematics rather close to the BDR was reported by several RHIC experiments. The suppression factor is significantly larger than expected suppression due to the leading twist nuclear shadowing. Suppression was observed in the kinematics where the hadron production in pp collisions is in a reasonable agreement with the recent pQCD calculations based on the NLO DGLAP approximation [5]. Very recently STAR [3] has reported new results for the π^0 ratios for $y \sim 4$ and $p_t \leq 2.0\,GeV$. They observed a larger suppression factor $\sim 1/3$, which is consistent with a linear extrapolation of the suppression factor for negatively charged hadrons, h^- measured at smaller rapidities to $y = 4$ taking into account the 2/3 factor due to the isospin effects [6]. The STAR experiment also reported the first observation of the correlations between the forward π^0 production with the production of the hadrons at the central rapidities $|\eta_h| \leq 0.75$. Such correlations provide a new information about the mechanism of the suppression of the inclusive spectrum.

2 Energy losses of forward parton in the vicinity of black disk regime

The amplitude with color octet quantum numbers decreases with energy due to the gluon reggeization in pQCD as:

$$A_g \propto \alpha_s^2 s^{\beta(t)} \left(i + \tan(\pi\beta(t)/2)\right) \tag{2}$$

where $\beta(t)$ is the gluon Regge trajectory with $\beta(t=0) < 1$. Infrared divergences of $\beta(t)$ are regulated by hadron wave functions. At the same time the amplitude due to exchange by a ladder with the vacuum quantum numbers in the crossed channel rapidly grows with energy:

$$A \propto \alpha_s^2 s^{(1+\lambda(t))} \left(i + \tan((\pi/2)\lambda(t))\right) \tag{3}$$

where $\lambda(t=0) \approx 0.2$. (For the simplicity we restrict ourselves here by the phenomenological fit to the theoretical formulae and to the HERA data on structure functions of a proton.) Hence such amplitudes (modeled at moderately small x as the two gluon exchange ladder) fastly exceed single gluon exchange term and at larger energies achieve maximum values permitted by probability conservation.

Single inelastic collision of the parton produced in a hard high energy NN collision off another nucleon is described by the imaginary part of the two gluon ladder with the vacuum quantum numbers. By definition, the inelastic cross section is calculable in terms of the probability of inelastic interaction, $P_{inel}(b)$ of a parton with a target at a given impact parameter b:

$$\sigma_{inel} = \int d^2b P_{inel}(b, s, Q^2) \tag{4}$$

Since σ_{inel} is calculable in QCD above equation helps to calculate $P_{inel}(b, s, Q^2)$. The probability of inelastic interaction of a quark is cf. discussion in [4]:

$$P_{inel}(b, x, Q^2) = \frac{\pi^2}{3}\alpha_s(k_t^2)\frac{\Lambda}{k_t^2} x G_A(x, Q^2, b), \tag{5}$$

where $x \approx 4k_t^2/s_{qN}, Q^2 \approx 4k_t^2, \Lambda \sim 2\text{GeV}^2$ (for the gluon case $P_{inel}(b)$ is 9/4 times larger). We use gluon density of the nucleus in impact parameter space, $G_A(x,Q^2,b)$ ($\int d^2b G_A(x,Q^2,b) = G_A(x,Q^2)$) . Above equation for the probability of inelastic interaction is valid only for the onset of BDR when $P_{inel}(b,s,Q^2) < 1$ (which is the unitarity limit for $P_{inel}(b,s,Q^2)$).

If $P_{inel}(b,x,Q^2)$ as given by Eq.5 approaches one or exceeds one it means that average number of inelastic interactions, $N(b)$ becomes larger than one. Denoting as $G_{cr}(x,Q^2,b)$ for which $P_{inel}(b)$ reaches one we can evaluate $N(b,x,Q^2)$ as

$$N(b,x,Q^2) = G_A(x,Q^2,b)/G_{cr}(x,Q^2,b). \tag{6}$$

As soon as P_{inel} becomes close to one, we can easily evaluate lower boundary for the energy losses arising from the single inelastic interaction of a parton. This boundary follows from the general properties of the parton ladder. Really, the loss of finite fraction of incident parton energy ϵ arises from the processes of parton fragmentation into mass M which does not increase with energy. For binary collision $M^2 = \frac{k_t^2}{\epsilon(1-\epsilon)}$. For the contribution of small $\epsilon \leq 1/4$

$$\epsilon \approx k_t^2/M^2 \tag{7}$$

Here k_t is transverse momentum of incident parton after inelastic collision. The spectrum over the masses in the single ladder approximation (NLO DGLAP and BFKL approximations) is as follows

$$d\sigma \propto \int dM^2/M^2 (s/M^2)^\lambda \theta(M^2 - 4k_t^2), \tag{8}$$

where we accounted for the high energy behavior of the two gluon ladder amplitude Eq.(3). We effectively take into account the energy momentum conservation i.e. NLO effects. Consequently the *average* energy loss (for the contribution of relatively small energy losses ($\epsilon \leq \gamma \sim 1/4$) where approximation of Eq.(7) is valid):

$$\epsilon_N \equiv \langle \epsilon \rangle = \frac{\int_0^\gamma \epsilon d\epsilon/\epsilon^{1-\lambda}}{\int_0^\gamma d\epsilon/\epsilon^{1-\lambda}} = \gamma \frac{\lambda}{1-\lambda}. \tag{9}$$

For the realistic case $\gamma = 1/4, \lambda = 0.2$ this calculation gives the fractional energy loss of 6%. This is lower limit since we neglect here a significant contribution of larger ϵ (it will be calculated elsewhere).

In the kinematics of onset of BDR absorption at central impact parameters is due to $N(b) > 1$ inelastic collisions (interaction with several ladders). The energy of initial parton is shared before collisions at least between N constituents in the wave function of the incident parton to satisfy causality and energy-momentum conservation. This quantum field theory effect which is absent in the framework of eikonal approximation can be interpreted as an additional energy loss [4]:

$$\epsilon_A(b) \approx N(b)\epsilon_N. \tag{10}$$

Here ϵ_N is the energy lost due to exchange by one ladder - Eq. (9). Above we do not subtract scattering off nucleon since our interest in the paper is in energy losses specific for nuclear processes in the regime when interaction with a single nucleon is still far from the BDR. If collision

energies are far from BDR, the energy losses estimated above should be multiplied by small probability of secondary interactions. Inclusion of enhanced "pomeron" diagrams will not change our conclusions based on the necessity to account for the energy-momentum conservation law.

Yields of leading hadrons carrying fraction of projectile momentum $\geq x_F$ are rapidly decreasing with x_N as $\propto (1-x_F)^n$. For pion production $n \sim 5 \div 6$. Obviously for large x_F average values of x of the parton of the projectile involved in the production of the pion are even larger, leading to strong amplification of the suppression due to the energy losses. The spectrum of leading pions is given in pQCD by the convolution of the quark structure function, $\propto (1-x)^n, n \sim 3.5$ and the fragmentation function $\propto (1-z)^m, m \sim 1.5 \div 2$ leading to a very steep dependence on x_F, $\propto (1-x_F)^{n+m+1}$. As a result for the STAR kinematics $x \sim 0.7$ and $z \sim 0.8$ correspondingly energy losses of 10% lead to a suppression roughly by a factor $[(0.9-x_F)/(1-x_F)]^6$. For $x_F = 1/2$ this corresponds to suppression by a factor of four. In particular, introducing the energy loss of $\sim 6\%$ in the NLO calculation of the pion production is sufficient [6] to reproduce the suppression observed at y=3. Similar estimate shows that average losses of $\sim 8 \div 10\%$ reproduce the suppression of the inclusive yield observed by STAR [3]. This value is of the same magnitude as the above estimate. Also, Eq.(10) leads to much stronger suppression for production at central impact parameters than in peripheral collisions.

In the kinematics of LHC the same $k_t(BDR)$ would be reached at x_N which are smaller by a factor $s_{RHIC}/s_{LHC} \sim 10^{-3}$, while for the same x_N one expects much larger values of $k_t(BDR)$ (see e.g. Fig.17 in [4]). Thus in the kinematics of LHC the regime of large energy losses should extend to smaller x_N.

There are two effects associated with the interaction of partons in the BDR - one is an increase of the transverse momenta of the partons and another is the loss of the fraction of the longitudinal momentum [8]. The net result is that distribution of the leading hadrons should drop much stronger with x_F than in the Color Glass Condensate (CGC) models [9] where only k_t broadening, change of the resolution scale and suppression of coalescence of partons in the final state but not the absorption and related energy losses were taken into account. At the same time, the k_t distribution for fixed x_F should be broader. Note here that the leading particle yield due to the scattering with $k_t \gg k_{BDR}$ is not suppressed and may give a significant contribution at smaller k_t via fragmentation processes. This discussion shows that selection in the final state of the leading hadron ($x_F \geq 0.3 \div 0.5$ at RHIC) with moderately large k_t should strongly enhance the relative contribution of the peripheral collisions where BDR effects are much smaller. These expectations are consistent [1] with the STAR data [3].

At extremely high energies where kinematics of the BDR will be achieved for a broad range of the projectile's parton light-cone fractions and virtualities, QCD predicts dominance of scattering off the nuclear edge leading to inclusive pion production cross section $\propto A^{1/3}$for a large enough x_N and a wide range of p_t. With increase of incident energy the range of p_t for fixed x_N would increase. Also the suppression for a given p_t would be extended to smaller x_N.

3 Interaction of leading partons with opaque nuclear medium

At high energies leading partons with light cone momentum x_N, p_t are formed before nucleus and can be considered as plane wave if

$$(x_N s/m_N)(1/M^2) \gg 2R_A. \tag{11}$$

Here M is the mass of parton pair (and bremstrahlung gluon) produced in the hard collision. If sufficiently small x are resolved, the BDR regime would be reached:

$$4p_t^2/x_N s \leq x(BDR). \tag{12}$$

In the BDR interaction at impact parameters $b \leq R_A$ is strongly absorptive as the medium is opaque. As a result, interaction of leading parton lead to a hole of radius R_A in the wave function describing incident parton. Correspondingly, propagation of parton at large impact parameters leads to elastic scattering - an analogue of the Fraunhofer diffraction of light off the black screen. However since the parton belongs to a nucleon, the diffraction for impact parameters larger than $R_A + r_{str}$ (where r_{str} is the radius of the strong interaction) will lead to the proton in the final state - elastic p A scattering. Only for impact parameters $R_A + r_{str} > b > R_A$ the parton may survive to emerge in the final state and fragment into the leading hadron. Cross section of such diffraction is $2\pi R_A r_{str}$. Another contribution is due to the propagation of the parton through the media. This contribution is suppressed due to fractional energy losses which increase with the increase of energy, leading to gradual decrease of the relative contribution of the inelastic mechanism.

Thus we predict that in the kinematics when BDR is achieved in pA but not in pN scattering, the hadron inclusive cross section should be given by the sum of two terms - scattering from the nucleus edge which has the same momentum dependence as the elementary cross section and scattering off the opaque media which occurs with large energy losses:

$$\frac{d\sigma(d + A \to h + X)/dx_h d^2p_t}{d\sigma(d + p \to h + X)/dx_h d^2p_t} = c_1 A^{1/3} + c_2(A)A^{2/3} \tag{13}$$

The coefficient c_1 is essentially given by the geometry of the nucleus edge - cross section for a projectile nucleon to be involved in an inelastic interaction with a single nucleon of the target. Coefficient $c_2(A)$ includes a factor due to large energy losses and hence it decreases with increase of the incident energy for fixed x_h, p_t. Deep in the BDR the factor $c_2(A)$ would be small enough, so that the periphery term would dominate.

It is worth to compare outlined pattern of interaction in the BDR with the expectations of the CGC models for small x hard processes in the kinematics where transverse momenta of partons significantly larger than that characteristic for BDR. These models employ the LO BFKL approximation with saturation model used as initial condition of evolution in $\ln(x_o/x)$. In these models the dependence on atomic number is hidden in the "saturation scale" and in the blackness of interaction at this scale. In this model partons interact with maximal strength at small impact parameters without significant loss of energy. Note that leading parton looses significant fraction of incident energy in the NLO BFKL approximation but not in LO BFKL. As a result the cross section is dominated by the scattering at small impact parameters and depends on A at energies

of RHIC approximately as $A^{5/6}$ [7]. Also, the process which dominates in this model at central impact parameters is the scattering off the mean field leading (in difference from BDR where DGLAP approximation dominates in the peripheral processes in the kinematics of RHIC) to events without balancing jets. With increase of jet transverse momenta interaction becomes less opaque, leading to a graduate decrease of the probability of inelastic collisions and hence to the dominance of the volume term.

A natural way to distinguish between these possibilities is to study correlations between production of forward high p_t hadrons and production of hadrons at central rapidities. First such study was undertaken by the STAR experiment [3]. In the pp case the rate of recoiled jets at $y \sim 0$ was found to be compatible with pQCD calculations. This suggests that the mechanism for pion production in the STAR kinematics is predominantly perturbative so that it is legitimate to discuss the propagation of a parton through the nucleus leading to pion production.

Our analysis indicates that the dA correlation data [3] for production of the balancing hadron for the trigger with $\langle p_T \rangle \sim 1.3\, GeV/c$ occurs with the same strength as in pp scattering, corresponding to $< x_A > \sim 0.01$. Lack of the suppression of the pQCD mechanism for these x_A puts an upper limit on the x range where coherent effects may suppress the pQCD contribution. Since the analysis of [6] find that the pQCD contribution is dominated by $x_A \geq 0.01$, we can conclude that the main contribution both to inclusive and the correlated cross section originates from pQCD hard collisions at large impact parameters.

To ensure a suppression of the pion yield at central impact parameters for the discussed kinematics one needs a mechanism which is related to the propagation of the projectile parton which is generating a pion in a hard interaction with the $x \sim 0.01$ parton. For example, the rate of suppression observed by BRAHMS would require fractional energy losses $\sim 3\%$ both in the initial and final state [6]. Similar losses would produce a suppression of the pion yield in STAR kinematics comparable with the inclusive data. Modeling performed in [1] indicates that for the central impact parameters the fractional energy losses should be at least a factor of 1.5 larger. Note here that such losses are sufficient only because the kinematics of the elementary process is close to the limit of the phase space. At the same time, this estimate assumes that fluctuations in the energy losses should not be large. For example, processes with energy losses comparable to the initial energy (like in the case of high energy electron propagation through the media) would not generate necessary suppression provided overall losses are of the order of few percent. Note also that the second jet in the STAR kinematics has much smaller longitudinal momentum and hence is far from the BDR. Therefore in the STAR kinematics one does not expect the suppression of the correlation with production of the second jet. However a strong suppression is expected for production of two balancing forward jets since both of them are interacting in the BDR.

Hence the data are qualitatively consistent with the scenario described in the introduction that leading partons of the projectile (with $x \approx 0.7$) interact at central impact parameters with the small x nuclear gluon fields with the strength close to the BDR and do not contribute to the inclusive π^0 yield.

We also performed analysis of interplay of soft and hard QCD phenomena for correlations between forward and central hadron production based on the geometry of deuteron-gold collisions. This allowed us to determine average number of wounded nucleons, N_w, for the π^0 trigger. We find $N_w \sim 3$, which is much smaller than $N_w \sim 13$ for central impact parameters.

This strongly suggests dominance of the peripheral collisions in π^0 production rather than the central collisions as in the mechanism of [7]. The seeming suppression of the recoil reported by [3] is due to soft interactions and does not indicate suppression of the pQCD mechanism of the production of the recoil jets relative to other mechanisms.

Thus RHIC data are consistent with the pattern of energy losses in central collisions described above. Further analyses along the lines suggested in [1] would allow to diminish model dependence of comparison between the hard components of the interaction in pp and dAu cases, quantitative study of the suppression on the number of wounded nucleons, which also will provide a probe of the color transparency effects as well as effects of large gluon fields.

We want to stress that the discussed mechanism of energy losses is operational only for propagation of partons with transverse momenta $\leq$ than that typical for the BDR. At the same time pion production with transverse momenta significantly larger than that typical for BDR should be dominated by the scattering at central impact parameters. With increase of energy from RHIC to LHC energy losses at large x_N should strongly increase, while substantial losses $\geq 10\%$ should persist for rapidities $|y| \geq 2$. This effect should lead to suppression of the production of the recoil jets at the rapidity intervals where no suppression is present at RHIC. It may also lead to higher densities in the central collisions as compared to the current estimates. In the forward direction we expect a significantly larger suppression than already large suppression found in [9] where fractional energy losses were neglected. Fractional energy losses result in modification of the form of the QCD factorization theorem at LHC energies. Similar effects will be present in the central pp collisions at LHC. They would amplify the correlations between the hadron production in the fragmentation and central regions discussed in Ref. [4].

References

[1] L. Frankfurt and M. Strikman, Phys. Lett. B **645**, 412 (2007).

[2] R. Baier, Y. L. Dokshitzer, A. H. Mueller, S. Peigne and D. Schiff, Nucl. Phys. B **483**, 291 (1997).

[3] J. Adams *et al.* [STAR Collaboration], Phys. Rev. Lett. **97**, 152302 (2006).

[4] L. Frankfurt, M. Strikman and C. Weiss, Annu. Rev. Nucl. Part. Sci. **55**, 403 (2005).

[5] F. Aversa, P. Chiappetta, M. Greco and J. P. Guillet, Nucl. Phys. B **327**, 105 (1989); B. Jager, A. Schafer, M. Stratmann and W. Vogelsang, Phys. Rev. D **67**, 054005 (2003) Phys. Rev. D **67**, 054004 (2003)

[6] V. Guzey, M. Strikman, and W. Vogelsang, Phys. Lett. B **603**, 173 (2004).

[7] D. Kharzeev, E. Levin and L. McLerran, Phys. Lett. B **561**, 93 (2003)

D. Kharzeev, Y. V. Kovchegov and K. Tuchin, Phys. Rev. D **68**, 094013 (2003)

[8] L. Frankfurt, V. Guzey, M. McDermott and M. Strikman, Phys. Rev. Lett. **87**, 192301 (2001); L. Frankfurt and M. Strikman, Phys. Rev. Lett. **91**, 022301 (2003).

[9] A. Dumitru, L. Gerland and M. Strikman, Phys. Rev. Lett. **90**, 092301 (2003) [Erratum-ibid. **91**, 259901 (2003)]

The coherent inelastic processes on nuclei at ultrarelativistic energies

V.L. Lyuboshitz , V.V. Lyuboshitz [1] †
Joint Institute for Nuclear Research, 141980 Dubna, Moscow Region, Russia
[1] *E-mail: Valery.Lyuboshitz@jinr.ru*

Abstract
The coherent inelastic processes of the type $a \to b$, which may take place in the collisions of hadrons and γ-quanta with nuclei at very high energies (the nucleus remains the same), are theoretically investigated. The influence of matter inside the nucleus is taken into account by using the optical model based on the concept of refraction index. Analytical formulas for the effective cross-section $\sigma_{\rm coh}(a \to b)$ are obtained, taking into account that at ultrarelativistic energies the main contribution into $\sigma_{\rm coh}(a \to b)$ is provided by very small transferred momenta in the vicinity of the minimum longitudinal momentum transferred to the nucleus.

1 Momentum transfer at ultrarelativistic energies and coherent reactions on nuclei

In the present work we will investigate theoretically the processes of inelastic coherent scattering at collisions of particles with nuclei at very high energies. It is essential that at ultrarelativistic energies the minimum longitudinal momentum transferred to a nucleus tends to zero, and in connection with this the role of coherent processes increases.

Let $f_{a+N\to b+N}(\mathbf{q}) = [Zf_{a+p\to b+p}(\mathbf{q}) + (A-Z)f_{a+n\to b+n}(\mathbf{q})]/A$ be the average amplitude of an inelastic process $a + N \to b + N$ on a separate nucleon in the rest frame of the nucleus (laboratory frame). Here Z is the number of protons in the target nucleus, $(A - Z)$ is the number of neutrons in the target nucleus, $\mathbf{q} = \mathbf{k}_b - \mathbf{k}_a$ is the momentum transferred to the nucleon, $\mathbf{k}_a$ and $\mathbf{k}_b$ are the momenta of the particles a and b, respectively. In the framework of the impulse approximation [1], taking into account the interference phase shifts at the inelastic scattering of a particle a on the system of nucleons, the expression for the effective cross-section of the coherent inelastic process $a \to b$ on a nucleus can be presented in the following form:

$$\sigma_{\rm coh}(a \to b) = \int |f_{a+N\to b+N}(\mathbf{q})|^2 P(\mathbf{q}) d\Omega_b, \tag{1}$$

where $d\Omega_b$ is the element of the solid angle of flight of the particle b in the laboratory frame, and the magnitude $P(\mathbf{q})$ has the meaning of the probability of the event that at the collision with the particle a all the nucleons will remain in the nucleus and the quantum state of the nucleus will not change. Let us introduce the nucleon density $n(\mathbf{r})$ normalized by the total number of nucleons in the nucleus: $\int_V n(\mathbf{r}) d^3\mathbf{r} = A$, where the integration is performed over the volume of the nucleus. Then

$$P(\mathbf{q}) = \left| \int_V n(\boldsymbol{\rho}, z) \exp(-i\mathbf{q}_\perp \boldsymbol{\rho}) \exp(-iq_\parallel z) d^2\boldsymbol{\rho}\, dz \right|^2. \tag{2}$$

† speaker

Here the axis z is parallel to the initial momentum $\mathbf{k}_a$, $\mathbf{q}_\perp$ and $q_\parallel$ are the transverse and longitudinal components of the transferred momentum, respectively.

It is easy to see that the momenta $|\mathbf{q}| \lesssim 1/R$, transferred to a nucleon (R is the radius of a nucleus), give the main contribution to the effective cross-section of the coherent inelastic process $a \to b$ on the nucleus. At ultrarelativistic energies, when $E_a \gg 1/R$, $E_b \gg 1/R$, the recoil energy of the nucleon $E_{\rm rec} \approx |\mathbf{q}|^2/m_N \lesssim (m_N R^2)^{-1}$ and the much smaller recoil energy of the nucleus can be neglected. In doing so, the effective flight angles for the particle b are very small: $\theta \lesssim 1/kR \ll 1$, where $k = E_a \approx E_b$. Then it is possible to assume in Eqs. (1) and (2) that the transverse and longitudinal transferred momenta are as follows:

$$|\mathbf{q}_\perp| = k\theta, \qquad q_\parallel = q_{\rm min} = \frac{m_a^2 - m_b^2}{2k}, \tag{3}$$

where m_a and m_b are the masses of the particles a and b, respectively. Here $q_{\rm min}$ is the *minimum* transferred momentum corresponding to the "forward" direction.

In most cases the characteristic momentum transferred to the nucleus at the inelastic coherent scattering ($|\mathbf{q}| \sim 1/R$) is small as compared with the characteristic momentum transferred to the nucleon in the process $a+N \to b+N$. In connection with this, the amplitude $f_{a+N\to b+N}(\mathbf{q})$ in Eq.(1) can be replaced by its value $f_{a+N\to b+N}(0)$ corresponding to the flight of the particle b in the "forward" direction. Taking into account that at small angles θ the solid angle in Eq. (1) is $d\Omega_b = \sin\theta d\theta d\phi \approx d^2\mathbf{q}_\perp/k^2$ and using the properties of the two-dimensional δ-function, we obtain, as a result of integrating the expression (1) over the transverse transferred momenta and over the volume of the nucleus, the following equation:

$$\sigma_{\rm coh}(a \to b) = \frac{4\pi^2}{k^2}|f_{a+N\to b+N}(0)|^2 \times \int \left(\left| \int_{-\infty}^{\infty} n(\boldsymbol{\rho}, z) \exp(-iq_{\rm min}\, z)\, dz \right|^2 \right) d^2\boldsymbol{\rho}, \tag{4}$$

where $q_{\rm min}$ is determined by Eq. (3).

In the case of a spherical nucleus with the radius R and the constant density of nucleons $n_0 = 3A/4\pi R^3$, Eq. (4) gives at sufficiently high energies, when $q_{\rm min}R \ll 1$:

$$\sigma_{\rm coh}(a \to b) = \frac{8\pi^3}{k^2} n_0^2\, |f_{a+N\to b+N}(0)|^2 R^4 = \frac{9\pi}{2k^2R^2} A^2\, |f_{a+N\to b+N}(0)|^2. \tag{5}$$

In so doing, the magnitude $\Delta\Omega_b = 9\pi/2k^2R^2$ has the meaning of the "effective" solid angle of flight of the final particle b in the vicinity of the "forward" direction.

It should be noted that our consideration relates not only to binary reactions but also to multiparticle coherent processes $a \to b_1 + b_2 + ...b_i$ on nuclei at very high energies. In the general case vector $\mathbf{k}_b$ has the meaning of the total momentum of the system $b = \{b_1, b_2 ... b_i\}$ with the *effective mass* m_b. In so doing, the magnitude $|f_{a+N\to b+N}(0)|^2$ determines the cross section of the production of the system b, moving as a whole in the "forward" direction, at the collision of particle a with the separate nucleon.

2 Effect of matter inside the nucleus on coherent processes

In the relations obtained above the multiple scattering of the initial and final particles on nucleons of the nucleus was neglected. This is possible when the mean free paths of particles a and b inside the nucleus are much greater than the nuclear radius R. Actually, the role of matter inside the nucleus may be essential,- especially in the case of medium and heavy nuclei. For the analysis of the effects of matter inside the nucleus we will apply the optical model of the nucleus at high energy based on the concept of refraction index [1, 2].

Further we will consider the influence of matter inside the nucleus for *binary* reactions. According to the known formula for the refraction index, being close to unity, the renormalized momenta of ultrarelativistic particles a and b inside the nucleus can be presented in the form:

$$\widetilde{\mathbf{k}_a} = \mathbf{k}_a + \frac{\mathbf{k}_a}{|\mathbf{k}_a|}\chi_a(\mathbf{r}), \quad \widetilde{\mathbf{k}_b} = \mathbf{k}_b + \frac{\mathbf{k}_b}{|\mathbf{k}_b|}\chi_b(\mathbf{r}),$$

where

$$\chi_a(\mathbf{r}) = \frac{2\pi n(\mathbf{r})}{k} f_{a+N\to a+N}(0), \quad \chi_b(\mathbf{r}) = \frac{2\pi n(\mathbf{r})}{k} f_{b+N\to b+N}(0). \tag{6}$$

Here, as before, $n(\mathbf{r})$ is the density of nucleons inside the nucleus, $k = E_a$ is the initial energy in the rest frame of the nucleus (laboratory frame); $f_{a+N\to a+N}(0)$ and $f_{b+N\to b+N}(0)$ are the average amplitudes of elastic scattering of the particles a and b on a nucleon at the zero angle in the laboratory frame; the complex magnitudes χ_a and χ_b describe the phase shifts and the absorption of the particles a and b at their passage through the matter inside the nucleus, connected with the difference of the refraction indices from unity. The relations (6) hold at $|\chi_a|/k \ll 1$, $|\chi_b|/k \ll 1$.

Taking into account the refraction indices of the particles a and b, the influence of matter inside the nucleus on the coherent inelastic processes implies the introduction of the additional complex phase shift into Eq. (4): the exponential factor $\exp(-iq_{\min}z)$ is replaced by $Q = \exp[-iq_{\min}z + i\delta(\boldsymbol{\rho},\, z)]$. In the case of the spherical nucleus with the constant density $n(\rho,\, z) = n_0$ inside the interval $0 \le |z| \le \sqrt{R^2-\rho^2}$ ($\rho = |\boldsymbol{\rho}|$) and $n(\rho,\, z) = 0$ outside this interval, the additional phase inside the considered interval is described by the equation:

$$\begin{aligned}\delta(\rho, z) &= \chi_a\,(z + \sqrt{R^2-\rho^2}) + \chi_b\,(\sqrt{R^2-\rho^2} - z) = \\ &= (\chi_a - \chi_b)\,z \,+ (\chi_a + \chi_b)\,\sqrt{R^2-\rho^2}\,,\end{aligned} \tag{7}$$

where the magnitudes χ_a and χ_b are determined by Eq. (6) at $n(\mathbf{r}) = n_0$.

Using the optical theorem [3], we can rewrite the relations for χ_a, χ_b in the form:

$$\chi_a = i\,n_0(1 - i\,\alpha_a)\sigma_{aN}/2, \quad \chi_b = i\,n_0(1 - i\,\alpha_b)\sigma_{bN}/2,$$

where σ_{an} and σ_{bn} are the total cross-sections of interaction of the particles a and b with nucleons, averaged over the protons and neutrons of the nucleus, α_a and α_b are the ratios of the real parts of the amplitudes $f_{a+N\to a+N}(0)$ and $f_{b+N\to b+N}(0)$, respectively, to their imaginary parts. Let us note that the quantity $\mathrm{Re}\,(\chi_b - \chi_a)$ determines the additional longitudinal transferred momentum connected with the presence of the matter.

Taking into account Eq. (7), after the replacement $q_{\min}z \to q_{\min}z - \delta(\boldsymbol{\rho},\, z)$ in Eq. (4) and the integration over z, we obtain the following expression for the cross-section of the coherent reaction $a \to b$ on a nucleus:

$$\sigma_{\rm coh}(a \to b) = \frac{8\pi^3}{k^2} n_0^2 \, \frac{|f_{a+N\to b+N}(0)|^2}{|q_{\min} + \Delta\chi|^2} \times$$

$$\times \int_0^R \Big| \exp\Big[-2i\,(q_{\min} - \chi_a)\sqrt{R^2-\rho^2}\,\Big] - \exp\Big[2i\chi_b\sqrt{R^2-\rho^2}\,\Big]\Big|^2 \rho\, d\rho, \qquad (8)$$

where $\Delta\chi = \chi_b - \chi_a$.

3 Dependence of cross-sections of inelastic coherent processes on the nuclear radius

The results of the section 1 are valid when all effects connected with the rescattering of particles in the matter inside the nucleus are practically absent. In this situation the probabilities of absorption of the particles a and b and the additional phase shifts at their passage through the nucleus are close to zero. In the case of a spherical nucleus with the constant density of nucleons, this leads to the restrictions: $|\chi_a|R \ll 1$, $|\chi_b|R \ll 1$ or $L_a \gg R$, $L_b \gg R$, where

$$L_a = \frac{1}{n_0\sigma_{aN}}, \qquad L_b = \frac{1}{n_0\sigma_{bN}} \qquad (9)$$

are the mean free paths inside the nucleus.

In the case of medium and heavy nuclei the radius of the nucleus $R \approx 1.1 \cdot 10^{-13}\, A^{1/3}$ cm then the density of nucleons, incorporated in Eq. (8), amounts to $n_0 \approx 0.28 \cdot 10^{\,39}$ cm^{-3}.

It follows from Eq. (8) that when both the mean free paths are small as compared with the nuclear radius ($L_a \ll R$, $L_b \ll R$), the coherent processes are conditioned only by the peripheral collisions of the initial particle a with the nucleons located in the surface layer of the nucleus. In the considered case, neglecting in Eq. (8) the particle masses ($|q_{\min}| \ll |\Delta\chi|$), we obtain at $f_{b+N\to b+N}(0) \neq f_{a+N\to a+N}(0)$:

$$\sigma_{\rm coh}(a \to b) = \pi \, \frac{|f_{a+N\to b+N}(0)|^2}{|f_{b+N\to b+N}(0) - f_{a+N\to a+N}(0)|^2} \times$$

$$\times \Big[\, \frac{L_a^2}{2} + \frac{L_b^2}{2} \, + \, 4\, L_a^2 L_b^2\, {\rm Re}\left(\frac{1}{L_a + L_b + i(L_a\alpha_b - L_b\alpha_a)}\right)^2 \Big]. \qquad (10)$$

Let us consider now the situation when the total cross-section of the interaction of the initial particle a with nucleons is small, so that $\sigma_{aN} \ll \sigma_{bN}$, $L_a \gg R$, $L_b \lesssim R$; in doing so, the relation $|f_{a+N\to b+N}(0)| \ll |f_{b+N\to b+N}(0)|$ should hold. In particular, we can deal with the coherent production of vector mesons ρ^0, ω, ϕ at the interaction of very high energy photons with nuclei.

In the considered case Eq. (8) (without the terms, depending on the masses m_a and m_b) gives:

$$\sigma_{\rm coh}(a\to b)=\pi R^2\left|\frac{f_{a+N\to b+N}(0)}{f_{b+N\to b+N}(0)}\right|^2\times\Big\{1+\frac{1}{x^2}\Big[\frac{1}{2}(1-e^{-2x})-4\frac{1-\alpha^2}{(1+\alpha^2)^2}\,(1-e^{-x}\cos\alpha x)-$$

$$-\frac{8\alpha}{(1+\alpha^2)^2}\,e^{-x}\sin\alpha x\Big]+\frac{1}{x}\Big[\frac{4}{1+\alpha^2}\,e^{-x}\cos\alpha x\,-\,\frac{4\alpha}{1+\alpha^2}\,e^{-x}\sin\alpha x-e^{-2x}\Big]\Big\},\quad(11)$$

where $\alpha\equiv\alpha_b$, $x=n_0\sigma_{bN}R=R/L_b$. At $x\gg 1$ (large cross-sections σ_{bN}, heavy nuclei) we obtain the simple expression

$$\sigma_{\rm coh}(a\to b)=\pi R^2\left|\frac{f_{a+N\to b+N}(0)}{f_{b+N\to b+N}(0)}\right|^2.\quad(12)$$

Let us emphasize that, according to Eq. (12), the effective cross-section of the coherent process $a\to b$ on a nucleus at very high energies has the same dependence on the number of nucleons (proportional to $A^{2/3}$) as the cross-section of scattering of the final particle b on the "black" nucleus, despite the smallness of the cross-section of interaction of the initial particle a (for example, γ-quantum) with a separate nucleon (in connection with this, see [4,5]).

For the coherent process $\gamma\to\rho^0$ on the lead nucleus ($R=1.1\cdot 10^{-13}\,A^{1/3}$ cm ≈ 6.5 Fm, $L_\rho\sim 1.5$ Fm, $|f_{\gamma+N\to\rho+N}(0)/f_{\rho+N\to\rho+N}(0)|^2\sim 10^{-3}$), the formula (11) is applicable at the energies of γ-quanta above several tens of GeV in the nucleus rest frame ($k\gg m_\rho^2L_\rho\sim 4.5$ GeV). In doing so, $\sigma_{\rm coh}(\gamma+Pb\to\rho^0+Pb)\sim 1.3$ mb.

When, on the contrary, $\sigma_{aN}\gg\sigma_{bN}$, $L_b\gg R$, $L_a\sim R$, $|f_{a+N\to b+N}(0)|\ll|f_{a+N\to a+N}(0)|$, then the effective cross-section of the coherent production of the particle b is described by the same formulas (11), (12), in which one should take $x=R/L_a$, $\alpha\equiv\alpha_a$ and replace the amplitude $f_{b+N\to b+N}(0)$ by $f_{a+N\to a+N}(0)$.

It should be emphasized that at $L_a\gg R$, $L_b\ll R$ the coherent process $a\to b$ is conditioned by the interaction of particle a with nucleons located near the surface of the nucleus in the back hemisphere. On the contrary, at $L_a\ll R$, $L_b\gg R$ this coherent process is conditioned by the interaction of particle a with nucleons located in the vicinity of the nuclear surface in the front hemisphere.

Taking into account that

$$f_{b+N\to b+N}(0)=i\,k\,\sigma_{bN}(1-i\alpha_b)/4\pi,\quad(13)$$

it is easy to verify that the expansion of the expression (11) into the power series over the parameter x leads at $x\ll 1$ to the relation (5), just as one would expect at the conditions $L_a\gg R, L_b\gg R$. In this limit $\sigma_{\rm coh}(a\to b)$ is proportional to R^4 (or to $A^{4/3}$).

Let us note that the ratio of the values of the cross sections calculated according to the formulas (12) and (5), respectively, is the following, taking into account Eqs. (9), (13):

$$\eta_b=\frac{k^2}{8\pi^2|f_{b+N\to b+N}(0)|^2\,n_0^2\,R^2}=2\left(\frac{L_b}{R}\right)^2\frac{1}{1+|\alpha_b|^2}.\quad(14)$$

It is clear that the factor η_b has the magnitude of the order of the squared ratio of the "transparency" volume for particle b in the vicinity of the back hemisphere of the nuclear surface to the total volume of the nucleus. At $L_a \ll R$, $L_b \gg R$ the ratio of the corresponding cross sections $\eta_a \sim (L_a/R)^2$ has the analogous meaning with reference to particle a in the vicinity of the front hemisphere of the nuclear surface.

In the given paper we have performed the concrete calculations for the case of a spherical nucleus with the sharp boundary and the constant nucleon density. However, our general relations contain the nucleon density depending on coordinates (see Eqs. (4), (6)) and make it possible, in principle, to take into account the role of the nuclear surface. It is evident that when the thickness of the boundary layer is very small as compared with the radius of the nucleus core, then expression (5) at $L_a \gg R$, $L_b \gg R$ does not change practically. But, in the case of very small free paths, the "transparency" parameters η_b or η_a and, hence, the cross section of the coherent inelastic process can depend essentially on the concrete structure of the surface of the nucleus.

4 Summary

In the present work the coherent processes at the interaction of ultrarelativistic particles with atomic nuclei are investigated. The role of these processes essentially increases at very high energies due to the fact that the minimum momentum, transferred to a nucleon, tends to zero with increasing energy. For the purpose of the analysis of the influence of matter inside the nucleus on coherent reactions, the concept of refraction index is used. The relations, describing the dependence of the effective cross-sections of the inelastic processes on the nuclear radius and the mean free paths of the initial and final particles in the matter inside the nucleus, are obtained.

We did not consider the reverse transitions at the propagation of final particles in the matter inside the nucleus. In principle, the contribution of these transitions could be studied in the framework of the theory taking into account the distinction of the stationary states in the matter from the stationary states in the vacuum due to the mixing of the vacuum states. One may expect that really, with existing sizes of nuclei, the corresponding effects are relatively small.

This work is supported by Russian Foundation of Basic Research (Grant No. 05-02-16674).

References

[1] M. Goldberger, K. Watson, *Collision theory*. John Wiley & Sons, Inc., New York-London- Sydney, 1964, chapter 11.

[2] R. Jastrov, Phys. Rev. **82**, 261 (1951) .

[3] L.D. Landau, E.M. Lifshitz, *Quantum Mechanics. Nonrelativistic theory.* Moscow, Nauka, 1989 ; §125 [transl. Pergamon Press, New York, 1977].

[4] V.N. Gribov, Zh. Eksp. Teor. Fiz. **57**, 1307 (1969).

[5] L. Frankfurt, V. Guzey, M. McDermott and M. Strikman. Phys. Rev. Lett. **87**, 192301 (2001) .

Part IV

Opportunities at future colliders

Low-x and Diffractive Physics at Future Electron-Proton/Ion Colliders

Henri Kowalski
DESY
Notkestrasse 85, 22607 Hamburg, Germany

Abstract
In this talk we discuss the present and future low-x and diffractive physics. The main topics are nuclear tomography and the investigation of the different QCD evolution dynamics in the transverse plane.

1 HERA measurements

1.1 Introduction

Exclusive diffractive processes at HERA, such as exclusive vector meson production or deeply virtual Compton scattering (DVCS), are excellent probes of the evolution and the proton structure in the gluon dominated regime. Several investigations have already shown that these processes can be well described within a QCD dipole approach with the vector meson wave functions determined by educated guesses and the photon wave function computed within QED. For an overview and the complete set of references see [1].

We start with a short description of the HERA data in terms of the dipole model. The vector meson and DVCS processes are measured at HERA in the small-x regime where the behaviour of the inclusive deep-inelastic scattering (DIS) cross section, or the structure function F_2, is driven by the gluon density. The dipole model allows these processes to be calculated, through the optical theorem, from the gluon density determined by a fit to the total inclusive DIS cross sections.

We base this talk on the impact parameter dipole model developed by Kowalski, Teaney, Motyka and Watt [2], [1], since it takes the effects of the proton shape into account in a complete way. The observed t-distributions in the vector meson and DVCS processes show clearly that the proton has a Gaussian-like shape in the transverse plane. The gluon density is high in the center and low on the outskirts of the proton. Usually, it is assumed that the evolution of the gluon density is independent of the proton shape. The investigations of Ref. [2] and [1] show, however, that the transverse variation of the gluon density has implications on the emerging pattern of QCD evolution and saturation effects. The interplay of saturation and evolution effects was first investigated by Bartels, Golec-Biernat and Kowalski [3], leaving out the effects of transverse density variation. In this case the F_2 data can be described, as a function of x and Q^2, either by strong saturation and weak evolution or by strong evolution and weak saturation effects. The investigation of Ref. [1,2], which took into account also the proton shape in the transverse plane, concluded that only the second scenario is in agreement with data. The Gaussian form implies that a large contribution to the cross section has to come from the outskirts of the proton, where the gluon density is diluted. Hence, the evolution effects (DGLAP-like) are dominating the overall behaviour of the F_2 data whereas the saturation effects are limited to the center of the proton. In the center, however, saturation effects are substantial.

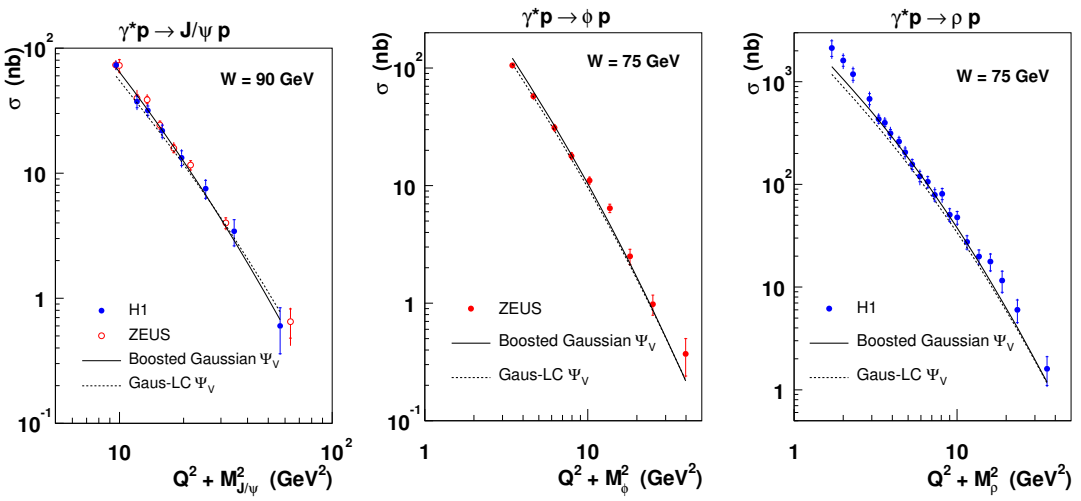


Fig. 1: Total cross section for $\gamma^* p \to Vp$ for different vector mesons compared to predictions from the b-Sat model.

1.2 Description of the HERA data

Various cross sections measured as a function of Q^2, W and t can be described by a model with a minimal number of free parameters, namely the parameters μ_0^2, A_g and λ_g of the initial gluon distribution, $xg(x,\mu_0^2) = A_g\, x^{-\lambda_g}\,(1-x)^{5.6}$, and the proton width B_G. The wave functions of the virtual photon are known from QED, while the vector meson wave functions are obtained by educated guesses. The long distance behaviour of the wave functions is also determined by the assumed values of the quark masses, see Ref. [1].

The observed cross sections are obtained from the overlap integral of the wave functions with the dipole cross section. The dipole cross section is assumed to be of the Glauber-Mueller form:

$$\frac{\mathrm{d}\sigma_{q\bar{q}}}{\mathrm{d}^2\vec{b}} = 2\left[1 - \exp\left(-\frac{\pi^2}{2N_c} r^2 \alpha_S(\mu^2) x g(x,\mu^2) T(b)\right)\right]. \qquad (1)$$

Here, the scale μ^2 is related to the dipole size r by $\mu^2 = 4/r^2 + \mu_0^2$. The gluon density, $xg(x,\mu^2)$, is evolved from a scale μ_0^2 up to μ^2 using LO DGLAP evolution, b denotes here the impact parameter. $T(b)$ is the proton shape. This assumption, together with the form of the dipole cross section defines the so called b-Sat model (called also KMW model on some plots below), described in detailed in Ref. [1]. Note, that in this type of model the dipole cross section determines the (unintegrated) gluon density [4]. The function $xg(x,\mu^2)$ coincides with the gluon density when the argument of the G-M exponent is small. The analysis of data in terms of the b-Sat model shows that this is not always the case. If the argument of the G-M exponent is substantial the gluon density saturates, with a strong impact parameter dependence.

The model parameters, which were fixed by the fit to the total inclusive DIS cross section and the vector meson t-distributions, describe the measured Q^2 and W dependence of vector meson production and DVCS very well, together with the absolute normalization, as shown in Figures 1 and 2. The data are compared to the results of the b-Sat model. Figures 3 shows the

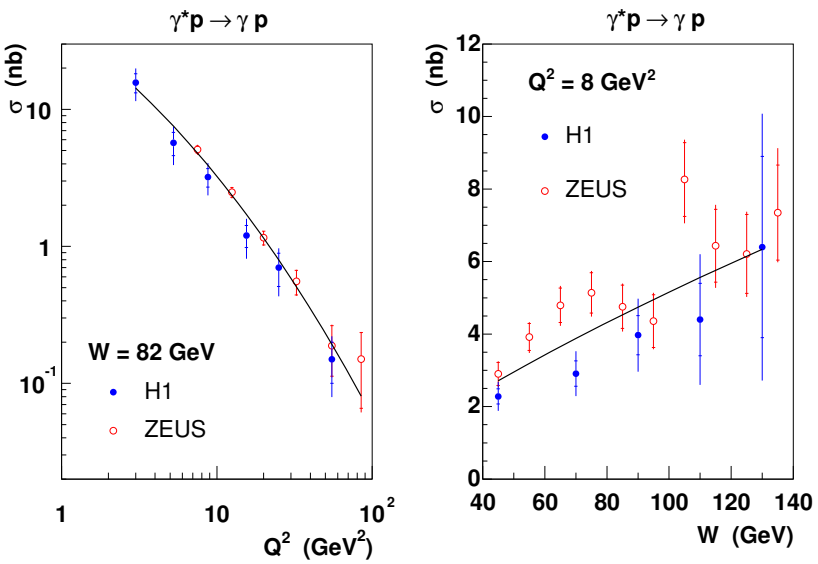


Fig. 2: Total DVCS cross sections σ vs. Q^2 (left) and σ vs. W (right) compared to predictions from the b-Sat model.

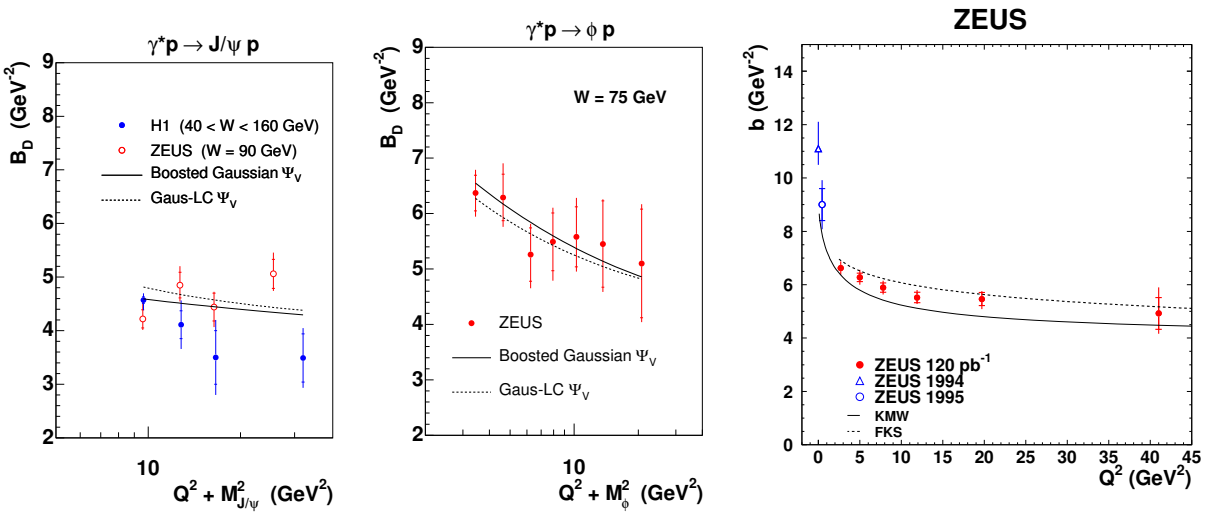


Fig. 3: The two left plots show the t-slope parameter B_D vs. $(Q^2 + M_V^2)$, where B_D is defined by fitting $\mathrm{d}\sigma/\mathrm{d}t \propto \exp(-B_D|t|)$, for the processes $\gamma^* p \to J/\Psi p$ and $\gamma^* p \to \phi p$. The right plot shows the same same parameter, called here b, determined in the process $\gamma^* p \to \rho p$.

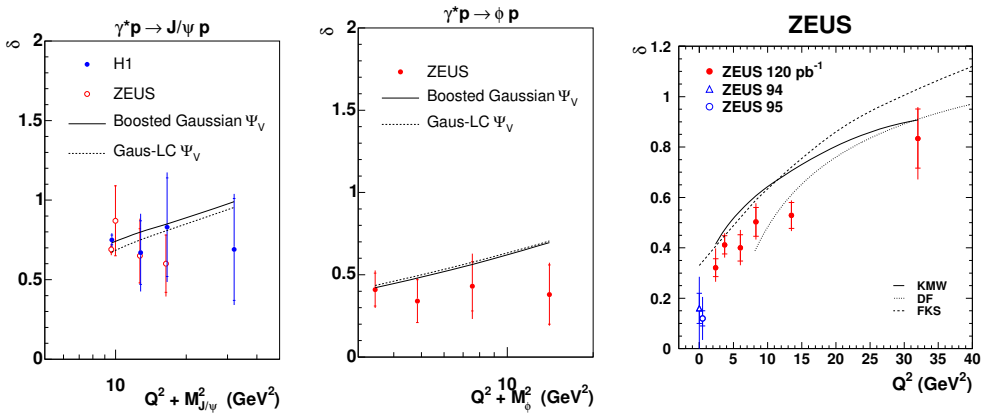


Fig. 4: The power δ vs. $(Q^2 + M_V^2)$ or Q^2, where δ is defined by fitting $\sigma \propto W^{\delta}$, compared to predictions from the dipole models. The left two plots show the $\gamma^* p \to J/\Psi p$ and $\gamma^* p \to \phi p$ processes , the right one shows the $\gamma^* p \to \rho p$ production.

t-slope parameter B_D vs. $(Q^2 + M_V^2)$. The plot for ρ mesons is taken from the recent ZEUS publication [5]. The parameter B_D is obtained by making a fit to the t-distributions of the form $\mathrm{d}\sigma/\mathrm{d}t \propto \exp(-B_D|t|)$. It has a physical interpretation as the size of the interaction region. For scattering of very small dipoles B_D is connected to the proton radius R_p via $B_D = R_p^2/3$. However, for larger dipoles the size of the interaction area depends not only on the proton radius but also on the size of the produced vector meson or real photon, which were taken into account following the work of Bartels, Golec-Biernat and Peters [4]. This allows the data for all vector mesons and DVCS to be described using a unique Gaussian proton shape, independent of the produced final state. The measured t-distributions agrees well with the model expectations. The slight underestimation of the parameter B_D by the model predictions for the ρ meson production is presumably due to the underestimation of the meson size by the assumed ρ wave function.

Although the vector meson wave functions are just guessed, the observed distributions for the J/Ψ and ϕ mesons are fairly insensitive to the particular assumptions and agrees well in all aspects with data. For the ρ meson the ratio σ_L/σ_T is not well described, see Ref. [5] for more details. This is presumably due to the lack of knowledge of the proper ρ meson wave function. A more precise measurement of the ratio σ_L/σ_T and of the spin density matrix elements would allow better constraints to be made on the form of the ρ wave function, as discussed in Ref. [1].

Figure 4 shows the power δ compared to the predictions from the b-Sat model. This power is a measure of the rate of rise of the cross sections with increasing W or diminishing x. The overall behaviour of data is well described by the b-Sat model which uses the Glauber–Mueller dipole cross section with DGLAP evolution of the gluon density. The gluon density is obtained from a fit to F_2. This plot is an important test on the universality of the gluon density and its evolution. The rate of rises are expected to depend on the sizes of the vector mesons, smaller size corresponds to the larger rate of rise, δ. The most precisely measured points, for J/Ψ photoproduction (the most left points with very small errors on the upper left plot), are very well reproduced by the dipole model. The ϕ data are also well reproduced but are not very precise.

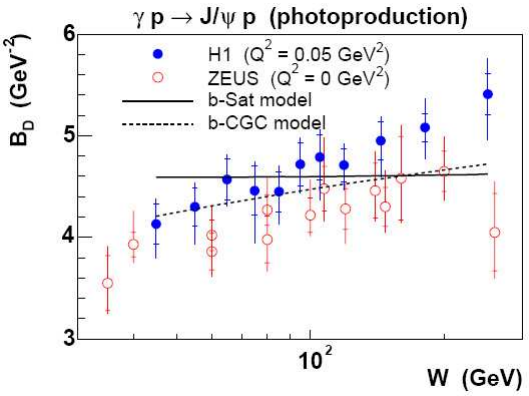


Fig. 5: The t-slope parameter B_D vs. W compared to predictions from the b-Sat and b-CGC models using the "boosted Gaussian" vector meson wave function.

In the ρ case we observe a small systematic deviation between data and model predictions which can be attributed to an underestimation of the size of ρ meson by the assumed wave function, as also seen, independently, in the plots of B_D, Fig. 3.

An important finding of this investigation is that the t-dependences of all three vector mesons and the DVCS process can be simultaneously described with one universal shape of the proton, see Figure 3. The parameter characterizing the size of the proton, $B_G = 4$ GeV^{-2}, determined in this investigation, corresponds to the proton radius of $R_p = \sqrt{3B_G} = 0.67$ fm. This is smaller than the proton charge radius of 0.870 ± 0.008 fm [6]. This leads to a rather surprising result that gluons are more concentrated in the center of the proton than quarks.

The b-Sat model, which gives the best description of data, uses the Glauber–Mueller dipole cross section with DGLAP evolution of the gluon density. Although the overall description of exclusive processes is very good, this approach has limitations, seen most clearly in the lack of W dependence of B_D in J/ψ photoproduction, see Fig.5. The measurement precision is sufficient to conclude that there is a coupling between the transverse and longitudinal evolution variables, that is, $\alpha'_{\mathbb{P}} \neq 0$. This indicates that DGLAP cannot be the only evolution schema in the low-x region. Such a coupling is more natural in the BFKL evolution which is a basis of the CGC evolution. The effect can be described by the impact parameter dependent CGC model. The "b-CGC" model gives a better description of the $\alpha'_{\mathbb{P}}$ effect but it provides a considerably poorer fit of F_2 than the b-Sat model and a worse overall description of exclusive processes.

The strong enhancement of gluon bremsstrahlung at small x leads to the specific nature of universal small-x dynamics in QCD. As x decreases, the occupation number of a transverse momentum mode $k_\perp$ in the hadron or nuclear wave-function grows rapidly. However, it can maximally be of order $1/\alpha_{\rm s}$ in QCD and it is saturated by the competing dynamics of bremsstrahlung and multi-parton recombination and screening contributions which deplete the gluon density at small x. In particular, the occupation number is maximal for modes with $k_\perp \lesssim Q_{\rm S}$, where $Q_{\rm S}(x)$, called the saturation scale, is a scale generated by the multi-parton dynamics. For a probe with transverse resolution $1/Q^2$, this scale is manifest in a universal scaling form of observables as a

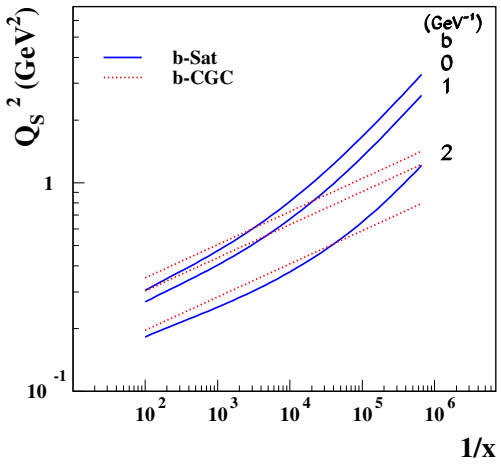


Fig. 6: The saturation scale $Q_S^2 \equiv 2/r_S^2$, where r_S is the dipole size and the scattering amplitude has the value $1 - \exp(-1/2) \simeq 0.4$.

function of $Q/Q_{\rm S}$ in a wide kinematical range in x and Q^2.

The saturation effects are best quantified by the value of the saturation scale $Q_S^2 \equiv 2/r_S^2$, where the saturation radius r_S is the dipole size and the scattering amplitude has the value $1 - \exp(-1/2) \simeq 0.4$. Figure 6 shows the saturation scale for the impact parameter dependent, b-Sat and b-CGC, models. The saturation scale is strongly dependent on the impact parameter b; in the center of the proton ($b \approx 0$), the b-Sat and b-CGC models have a similar saturation scale, comparable to the value in the GBW model. As b increases the value of the saturation scale drops quickly in both models. This is understandable since, in the b-Sat model with a Gaussian proton shape, at larger values of b the gluon density is diluted by the factor $T(b)$ and so the smaller gluon density leads to smaller saturation scales, as discussed in detail in [1].

Figure 7 shows the b-dependence of the total cross section, it gives a feeling for the relative contributions from the different impact parameters. The median value of this distribution is around $b = 2.6$ GeV^{-1}, that is, the majority of the cross section is determined by the dilute gluon region, where the saturation scale is small.

The investigation presented here demonstrates that a wide class of high-energy scattering processes measured at HERA may be understood within a simple and unified framework. The key ingredient is the gluon density which is probed in the longitudinal and transverse directions. The success of the description indicates the universality of the emerging gluon distribution.

2 Future possibilities

The vector meson and DVCS processes may be used to probe the properties of nuclear matter in a new way. As in the optical electromagnetic investigations, diffractive processes should allow the

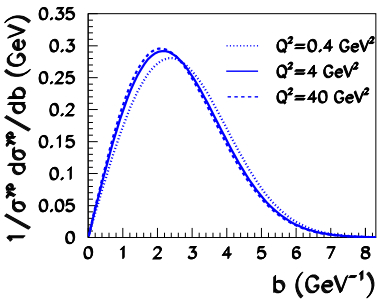


Fig. 7: The b-dependence of the total cross section, $\sigma_{\rm tot}^{\gamma^* p}$, for $Q^2 = 0.4$, 4 and 40 GeV^2 with $x = 10^{-4}$, 10^{-3} and 10^{-2} respectively, using a Gaussian $T(b)$ of width $B_G = 4$ GeV^{-2}.

detailed investigation of target properties. In measurements with polarized beams it is possible to achieve precision which would allow a tomographic picture of protons and nuclei to be obtained. The prerequisite of this type of measurement are detectors controlling particle production in the whole rapidity range [7].

The new facilities recently proposed are the ep and eA collider EIC and LHeC. EIC should have roughly a half of the HERA center-of-mass energy and a luminosity of a factor 100 to 1000 higher than HERA. The high luminosity should allow to improve substantially the measurement precision for low-x and diffractive processes. This would allow to reduce the errors on the measurement of the rate of rise of the exclusive diffractive process, shown in Fig. 4, by a large factor. This would allow to determine precisely the gluon density evolution and saturation effects also in the non-forward region, $t \neq 0$.

An important advantage of EIC is the possibility of electron-ion collisions. Because of the Lorentz contraction of the nuclear parton density, in the probe rest frame, the saturation scale $Q_{\rm S}$ has a strong A dependence, $\sim A^{1/3}$. In addition, since the density profile in a nucleus is more uniform than that of the proton, the saturation scale in nuclei decreases more slowly with b than in the proton. The dependence of the saturation scale on the impact parameter is plotted in Fig. 8. The saturation scale in Au nuclei at the median impact parameter for the total cross section $b_{\rm med.}$ is about 70% of the value at $b = 0$; in contrast, for proton, $Q_{\rm s,p}(b_{\rm med.})$ is only $\sim 35\%$ of the value at $b = 0$. Thus while the saturation scale in the center of the proton is a third of that in the center of the gold nucleus, the saturation scale at the median impact parameter is about a factor of six smaller. This leads to a significant enhancement of the saturation effects in nuclei as discussed in details in ref. [8].

The LHeC electron proton/ion collider would achieve a CMS energy of a factor 5 higher than HERA and can extend the x range by about a factor 25 over HERA. The largely extended x-range should give a new insight into QCD evolution dynamics. It is generally accepted that the evolution dynamics seen in HERA data is of the DGLAP type. The investigation of Ref. [1, 2] show that this is mainly due to a large contribution of the outskirts of the proton, in which gluon density is fairly diluted. The observed Gaussian shape of the proton implies a high, saturated

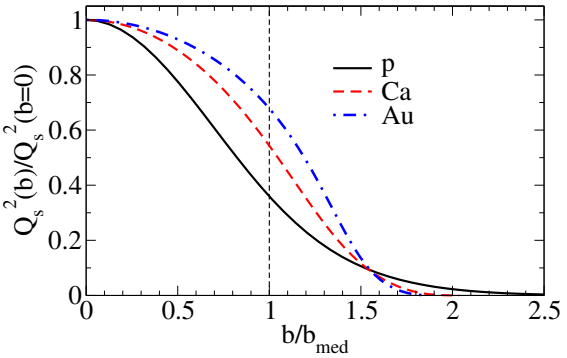


Fig. 8: Impact parameter dependence of the saturation scale for p, Ca and Au. The values are scaled by the median impact parameter b_{med} for the total cross section at $x = 0.001$ and $Q^2 = 1$ GeV^2.

gluon density in the center of the proton, irrespective of the particular assumption about the evolution dynamics. Therefore, the evolution dynamics depends on the impact parameter, and F_2 is determined by a mixture of different contributions. The vector meson diffractive measurement at LHeC (and also EIC) should have a potential to disentangle it. The main tools should be the dedicated detectors allowing the measurement of the t-dependence in the largely extended x range. A better understanding of the evolution is a fascinating theoretical and experimental problem. Somewhere in the mixture of the different evolution schema should be a region dominated by the properties determined by the pomeron-graviton correspondence [9], [10]. The largely extended x range of LHeC could be of crucial importance for this task.

Finally, let us note that in the pp scattering at LHC it is possible to measure processes with very small x values. In exclusive diffractive production of charmed or bottom mesons it is possible to reach x values which are three to four orders of magnitude lower than at HERA.

References

[1] H. Kowalski, L. Motyka, and G. Watt, Phys. Rev. **D74**, 074016 (2006).

[2] H. Kowalski and D. Teaney, Phys. Rev. **D68**, 114005 (2003).

[3] J. Bartels, K. Golec-Biernat, and H. Kowalski, Phys. Rev. **D66**, 014001 (2002).

[4] J. Bartels, K. Golec-Biernat, and K. Peters, Acta Phys. Polon. **B34**, 3051 (2003).

[5] ZEUS Collaboration, S. Chekanov *et al.*, PMC Phys. **A1**, 6 (2007). arXiv:0708.1478 [hep-ex].

[6] S. Eidelman *et al.* [Particle Data Group], Phys. Lett. **B592**, 1 (2004).

[7] I. Abt, A. Caldwell, X. Liu, and J. Sutiak (2004). hep-ex/0407053.

[8] H. Kowalski, T. Lappi, and R. Venugopalan (2007). arXiv:0705.3047 [hep-ph].

[9] R. C. Brower, J. Polchinski, M. J. Strassler, and C.-I. Tan (2006). hep-th/0603115.

[10] A. Kotikov, L. Lipatov, A. Onishchenko, and V. Velizhanin, Phys. Lett. **B632**, 754 (2006).

Low-x Physics at a Future Electron-Ion Collider (EIC) Facility

Bernd Surrow
Massachusetts Institute of Technology, Department of Physics, Laboratory for Nuclear Science
77 Massachusetts Avenue, Cambridge, MA 02139

Abstract
The proposed polarized electron-ion collider (EIC) facility will allow for precision exploration of various novel aspects of QCD including low-x phenomena and the spin structure of the proton. As this project gains momentum, it is increasingly important for the QCD community to understand quantitatively the kinematic reach and expected sensitivities for various measurements. We briefly summarize key accelerator design parameters and then focus on expected measurement sensitivities, thus exposing how the EIC will allow an extension of the successful HERA program into exciting new regimes.

1 Introduction

QCD is a spectacularly successful theory, yet it remains an active field of research in particle physics. While it has withstood over several decades of tests, we have yet to understand fully the mechanisms by which complex and rich phenomena emerge from a theory based solely on symmetry and local gauge invariance [1]. This quest is being pursued on many fronts: hadron structure, hadron spectroscopy, high temperature phenomena and high parton density systems. There is little doubt that our current understanding of QCD, in particular the role of gluons in QCD dynamics, has been greatly advanced by using electron-proton collisions at the HERA collider, which was the first facility to probe with high luminosity deep into the regime where gluons play a dominant role in hadron structure. In the following, we discuss how a high luminosity Electron-Ion Collider (EIC) facility will enable similar advances in the study of strong color fields, in particular many body gluon states probed at the saturation scale. The crucial element in these studies will be the use of heavy nuclei that, when probed at small Bjorken x, amplify such novel gluon states.

2 Opportunities in low-x physics at a future EIC facility

From deep inelastic scattering (DIS) we know that gluons carry half of the momentum of the proton, and from HERA we know that gluons dominate for $x < 0.01$ [2]. However, when probed at low-x, it is predicted that the gluon distribution within a proton will saturate. There are many quantitative arguments for this, but it is rather intuitive that at sufficiently high gluon density $2 \rightarrow 1$ gluon fusion (non-linear dynamics) will begin to dominate over $1 \rightarrow 2$ gluon splitting (linear dynamics). This transition occurs at a scale commonly referred to as the saturation scale (Q_s). Geometrical considerations [3] show that, in nuclei, $Q_s \propto A^{1/3} x^{-\delta}$, where $\delta \sim 1/3$ [4]. Thus, heavy nuclei can be used to amplify the scale at which gluon saturation sets in. Figure 1 shows the saturation scale in the Q^2 versus x plane for ions ranging from protons to Au [2]. Additionally,

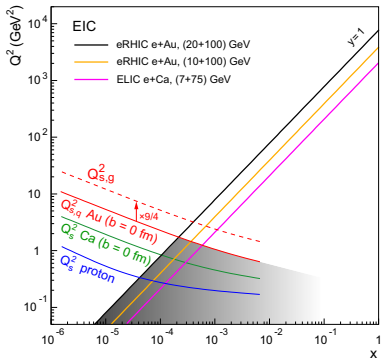


Fig. 1: The kinematic plane of DIS variables x and Q^2. The straight diagonal lines represent the kinematic boundaries of the EIC under various beam configurations. Regions below the lines are accessible. The curved/dashed lines indicate the saturation scale for various ions. Color online.

the colored diagonal lines show the kinematic limits of the EIC for various beam energies. The shaded band illustrates the accessible saturation region for 20 GeV electrons colliding with 100 GeV Au nuclei. The saturation scale for gluons in Au can be accessed at a factor of 10 larger x and Q^2 than Q_s for gluons in a proton. This has two significant impacts. First, by substituting heavy ions for protons, one can access the saturation regime at lower beam energies. Second, $Q^2_{s,g}(Au) > Q^2 > \Lambda^2_{QCD}$, thereby enabling use of perturbative methods for calculation. The saturation regime can be reached with reasonably modest beam energies, and it can be explored with the use of perturbative calculations.

In DIS the differential cross section $d^2\sigma/dx\ dQ^2$ can be decomposed in terms of two structure functions ($F_2(x,Q^2)$ and $F_L(x,Q^2)$), where F_2 is directly sensitive to quark and anti-quark distributions, and F_L is directly proportional to the gluon momentum distribution. These structure functions provide a direct means to quantitatively study saturation phenomena and we discuss them in more detail below. In the following we show the measurement prospects for various EIC configurations with a maximum center-of-mass energy of $\sqrt{s} = 14 \sim 140$ GeV/n and a maximum luminosity $L = 10^{33} \sim 10^{35}$ cm^{-2}s^{-1}, a factor of 100 higher than HERA. As the world's first electron-heavy-ion collider, the EIC would enable the high precision exploration of F_2 and F_L of heavy nuclei in the saturation regime, truly *terra incognita*. As we will show, the luminosity, energy and collider kinematics will be used to differentiate competing models of low-x QCD phenomena.

One of the first measurements at the EIC will be $F_2(x,Q^2)$ for both heavy (Au) and light (d) ions. The ratio, shown versus Q^2 for four x bins, is displayed in Figure 2 [2]. The points represent the anticipated statistical precision achievable with an integrated luminosity of 4/A fb^{-1}. The colored lines are predictions from competing models [2]. F_2 is directly sensitive to quark distributions, and is sensitive to gluons via scaling violations. nDS, EKS and FGS are pQCD models with differing treatment of parton shadowing, and they are compared to predictions from the Color Glass Condensate (CGC) model. Within the expected precision of the measurements, differentiation between the different models is clearly possible in the region $10^{-4} < x < 10^{-2}$.

With the ability to accelerate both light and heavy ions over a wide range of energies, the

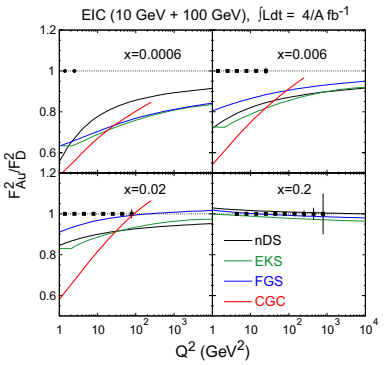


Fig. 2: The ratio of $F_2(Q^2)$ in Au to that in d nuclei, for four bins in x. The symbols represent the anticipated statistical precision achievable. The curves represent models with differing treatment of low-x phenomena. Color online.

EIC will be able to make significant contributions to the understanding of the gluon distribution in the proton. At low x, $F_L(x, Q^2) \propto \alpha_s\, x\, G(x, Q^2)$, where $G(x, Q^2)$ is the gluon distribution.

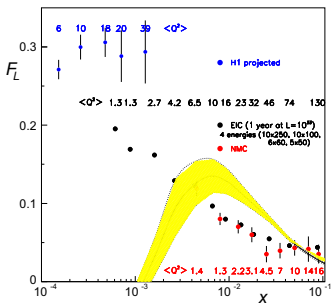


Fig. 3: $F_L(x)$ for protons from fixed target (red), projected H1 (blue) and projected EIC (black). Color online.

Extraction of F_L requires running at multiple beam energies, a task that highlights the flexibility of the EIC. Figure 3 shows $F_L(x)$ for a proton. The red points are from existing NMC fixed target data, and the blue H1 points show the expected precision (statistical and systematic uncertainties) achievable from the recent HERA energy scan [2]. The black points show the achievable precision from one year of running the EIC at four different energies (statistical uncertainties only) [2]. The EIC measurements will clearly compliment the HERA results, as well as bridge the region between HERA and fixed target results, contributing to a direct measurement of the gluon distribution for $10^{-4} < x < 10^{-1}$.

Finally, Figure 4 shows the ratio of gluon distributions in Pb to that in d ($R_g^{Pb} = F_L^{Pb}/F_L^d \sim G^{Pb}/G^d$) [2]. Current data on the gluon distribution at low-x in heavy nuclei is sparse. In turn, constraints on theoretical models are weak, as shown by the vast range of different theoretical predictions. The gluon distribution is critical for accurate calculations of cross sections at both

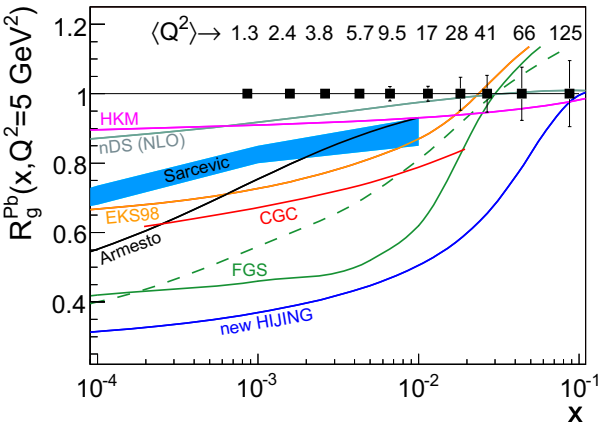


Fig. 4: The ratio of F_L in Pb to that in d. The black symbols represent anticipated statistical uncertainty from 10/A fb^{-1} of EIC data, compared to the large range of model predictions over this currently unexplored kinematic range. Color online.

RHIC and the LHC. With its high luminosity, the EIC can make significant contributions to the understanding of the gluon distribution in heavy nuclei over the relevant x range.

3 Summary

In conclusion, as the world's first high energy electron (heavy) ion collider, and with a luminosity approximately one hundred times that of HERA, the EIC will allow precision exploration of strong color fields. The use of heavy nuclei will amplify the scale at which saturation phenomena are predicted, placing it well within the accessibility of the EIC. There are many topics we have neglected to discuss, in particular diffraction, spin decomposition of the proton, and the study of partonic energy loss in cold nuclear matter. The physics program of the EIC is rich, diverse, and well targeted toward a unified understanding of strongly interacting matter. The project is gaining momentum on an international scale and will provide a continuation of the successful HERA program into exciting new regimes of QCD.

References

[1] F. Wilczek, Nucl. Phys. Proc. Suppl. **119**, 3 (2003).

[2] EIC-Collaboration, *A high luminosity, high energy electron-ion collider*. White paper prepared for the nuclear science advisory committee as input to the long range planning 2007.

[3] K. Golec-Biernat and M. Wustoff, Phys. Rev. **D59**, 014017 (1999).

[4] C. A. S. N. Armesto and U. A. Wiedemann, Phys. Rev. **94**, 0220002 (2005).

The LHeC and its low x Physics Potential

J. B. Dainton[1]†*, M. Klein*[2]*, P. R. Newman*[3]
[1] Cockcroft Institute of Accelerator Science and Technology,
[2] University of Liverpool
[3] University of Birmingham

Abstract
This contribution briefly recounts a talk given by one of us at the workshop on the potential and prospects for colliding electrons with protons or heavy ions at the LHC, as currently considered in the framework of the LHeC. Particular emphasis is placed on the opportunities which the LHeC offers for exploring low x physics.

1 The Large Hadron Electron Collider

Plans are being developed to build a Large Hadron Electron Collider (LHeC) as a complement to the LHC. The LHeC makes possible deep-inelastic lepton-hadron (ep, eD and eA) scattering for 4-momentum transfers squared Q^2 beyond $10^6\,\mathrm{GeV}^2$ and for Bjorken-x down to 10^{-6}, see Figure 1. New sensitivity to the existence of new states of matter, primarily in the lepton-quark sector and in dense Quantum Chromodynamics, is achieved. The precision possible with an electron-hadron experiment brings in addition crucial accuracy in the determination of hadron structure and of parton dynamics at the LHC energy scale.

Currently two versions of the LHeC are under consideration, a ring-ring collider [1], with high luminosity of the order of $10^{33}\mathrm{cm}^{-2}\mathrm{s}^{-1}$ and electron beam energies up to typically 70 GeV, and a linac-ring collider [2,3], with luminosity of the order of $5\cdot 10^{31}\mathrm{cm}^{-2}\mathrm{s}^{-1}$ but possibly much increased electron beam energies (up to perhaps 140 GeV). In the coming years the accelerator, the physics and the detector will be further investigated and, under the auspices of CERN and ECFA, a Conceptual Design Report is being worked out [3]. The LHeC could be operated simultaneously with pp collisions in a late phase of the LHC and would thus expand significantly the physics programme carried out at CERN in the future. Much more detailed information can be found at [4].

2 Low x Physics

The energies at the LHeC are so high that one expects parton densities at low x to reach the limits at which dynamical changes must occur in order to satisfy unitarity. This implies that definitive answers may be obtained to the questions raised by HERA as perhaps its most enduring legacy: namely its pioneering contribution to low x physics, stimulated by the strong rise of the proton quark ($\sim F_2$) and gluon ($\sim \partial F_2/\partial \ln Q^2$) densities with decreasing x. These observations have established a new field in Quantum Chromodynamics, its high density, low coupling limit, in which matter in a new state may be explored. Other striking HERA discoveries associated with

† speaker

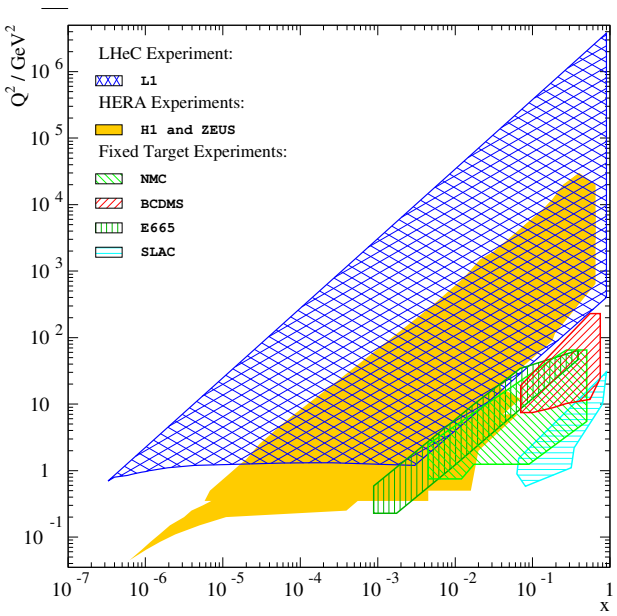


Fig. 1: Kinematic coverage of fixed target, HERA and LHeC deep inelastic lepton-proton scattering experiments (DIS). The LHeC, here assumed to be a $140x7000\,\mathrm{GeV}^2$ collider, is equivalent to a fixed target experiment with PeV beam energy and thus represents a huge extension of the kinematic range compared to the first DIS experiments. In the course of the work on the CDR, a detector, here called L1, will be designed and its measurement accuracy and kinematic coverage will be studied.

low x physics have been the process of hard diffraction in DIS and the Deeply Virtual Compton Scattering process (DVCS, $ep \to e\gamma p$), both of which have been now been investigated in some detail. The LHeC will allow these fields to be developed in much greater depth, both in electron-proton scattering, as can only be sketched below, and in electron-ion scattering. In the eA case the gain in kinematic coverage is astonishing, since the DIS lA experimental coverage is extended by 4 orders of magnitude in Q^2 and x and, moreover, since parton densities are expected to be amplified $\propto A^{1/3}$.

• **Inclusive Cross Sections and Parton Saturation:** It is expected that parton saturation effects could be conclusively established at the LHeC through the observation of deviations from expectations for one or more observable in the framework of perturbative QCD. In such studies at HERA, models based on colour dipole scattering [5–7] have been used in order to access the necessary very low Q^2 values.

In one example dipole study of HERA data [6], the inclusive structure function $F_2(x, Q^2)$ is subjected to fits in which the dipole cross section either does not exhibit saturation properties, or saturates as expected in two rather different models [6, 7]. All three dipole fits are able to describe the HERA data adequately in the perturbative region $Q^2 \geq 2\ \mathrm{GeV}^2$, whereas a clear preference for the models containing saturation effects becomes evident when data from the range $0.045 < Q^2 < 1\ \mathrm{GeV}^2$ are added [6]. Due to the non-perturbative nature of this kinematic

region, there is no clear interpretation in terms of parton dynamics (for example recombination effects, $gg \to g$). Similar conclusions are drawn when the same dipole cross sections are applied to various final state observables [8].

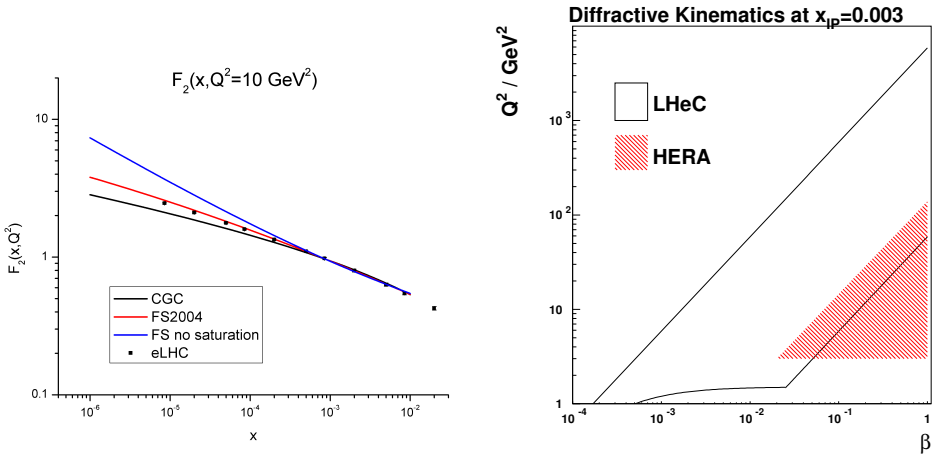


Fig. 2: Left: Example results from fits to HERA F_2 data with $10^{-4} \lesssim x < 10^{-2}$ using three different dipole models. The curves are extrapolated to lower x values [9] and compared with simulated LHeC data. Right: The $\beta - Q^2$ kinematic plane for diffractive DIS at HERA and the LHeC for an example $x_{I\!P} = 0.003$.

Figure 2 shows an extrapolation of the three dipole models [6] into the LHeC kinematic range at an example $Q^2 = 10\ \mathrm{GeV}^2$. The extrapolations are compared with a simulated LHeC measurement with $1\ \mathrm{fb}^{-1}$, where statistical errors are negligible and reasonable estimates of systematic errors are at the $1-3\%$ level. The LHeC data clearly distinguish between the extrapolated fits to HERA data without resorting to a region where perturbative methods are inapplicable. It remains to be shown whether this continues to be the case when the LHeC data are also included in the fits.

• **Diffractive DIS:** Statistical uncertainties should be insignificant for the measurement of a diffractive DIS cross section with $1\ \mathrm{fb}^{-1}$ at the LHeC. Systematic errors are estimated to be in the region of $5 - 10\%$, depending strongly on the design of the forward region of the detector. At an example $Q^2 = 10\ \mathrm{GeV}^2$, $x_{I\!P}$ values below 10^{-5} are accessible, allowing a very clean separation of the diffractive exchange from sub-leading contributions. The $\beta = x/x_{I\!P}$ and Q^2 kinematic plane at HERA and the LHeC is illustrated in Figure 2, for an example $x_{I\!P} = 0.003$. Accessing higher Q^2 at fixed β and $x_{I\!P}$ will test the factorisation properties of diffraction [10] in detail and will allow more precise constraints on diffractive parton distribution functions (DPDFs), including sensitivity to their flavour decomposition through W and Z exchange contributions. The low β region of the DPDFs, which, through the basic exchange of a pair of gluons, is particularly sensitive to parton saturation effects or other novel QCD dynamics, will be investigated for the first time.

• **Deeply Virtual Compton Scattering** As at HERA, measurements of DVCS could be made at the LHeC through the inclusive selection of $ep \to ep\gamma$ events and the statistical subtraction of the Bethe-Heitler background. A first simulation [11] has been performed assuming that final state photons with $p_\perp > 5$ GeV can be efficiently selected. With 10 fb^{-1}, a precision measurement becomes possible over an unprecedented range with, e.g. seven bins of W between 150 GeV and 750 GeV at $Q^2 = 30$ GeV^2, with $1 - 4\%$ statistical uncertainty. With the huge luminosity possible compared with HERA and the much extended kinematic range, the LHeC is likely to provide unique information on Generalised Parton Densities.

To summarize, with the LHeC the physics of deep inelastic scattering has a fascinating future, based on the powerful p and also A beams at the LHC. DIS physics will be led to new horizons at large scales, with sensitivity to eq masses up to 2 TeV. Correspondingly very low x values may be accessed in the DIS region, where a host of new and exciting measurements are possible, of which this report has barely scratched the surface. QCD is the richest theory of fundamental interactions and much is still to be done for its deep exploration!

Acknowledgement

We would like to thank Hannes Jung for his encouragement to submit this summary and his efforts to let the community share the excitements of QCD.

References

[1] J. Dainton et al., JINST 1 (2006) P10001.

[2] S. Chattopadhyay and F. Zimmermann, private communication.

[3] ECFA talk of M. Klein, November 2007, in [4].

[4] For more detailed information on the LHeC project, see $http://www.lhec.org.uk$.

[5] K. Golec-Biernat, M. Wüsthoff, Phys. Rev. D59 (1999) 014017.

[6] J. Forshaw, G. Shaw, JHEP 0412 (2004) 052.

[7] E. Iancu, K. Itakura, S. Munier, Phys. Lett. B590 (2004) 199;
H. Kowalski, L. Motyka, G. Watt, Phys.Rev. D74 (2006) 074016.

[8] J. Forshaw, R. Sandapen, G. Shaw, JHEP 0611 (2006) 025.

[9] J. Forshaw, private communication.

[10] For a HERA investigation, see e.g. H1 Collaboration, Eur. Phys. J. C48 (2006) 715, ibid 749.

[11] L. Favart, private communication.

Perturbative QCD in the Regge limit: Prospects at ILC

S. Wallon
LPT, Université Paris-Sud, CNRS, Orsay, France

Abstract
After recalling the theoretical and experimental status of QCD in the Regge limit and the requirement of high energy scattering process of onium-onium type for testing this limit, we show that the International Linear Collider would be a major step in this field.

1 QCD in the Regge limit: theoretical status

1.1 LL BFKL Pomeron

At high energy ($s \gg -t$), consider the elastic scattering amplitude of two *IR safe (hard) probes* (Fig.1). Small values of α_S (perturbation theory applies due to hard scales) are compensated by large values of $\ln s$, calling for a resummation of the $\sum_n (\alpha_S \ln s)^n$ series, resulting in the effective BFKL ladder [1], the Leading Log hard Pomeron (Fig.2). The optical theorem gives $\sigma_{tot} \sim s^{\alpha_P(0)-1}$ with $\alpha_P(0) - 1 = C\,\alpha_S$. Since $C > 0$, the Froissart bound is violated at perturbative order. The large N_c color dipole model [2, 3], based on perturbation theory on the light-cone, is equivalent to the BFKL approach at the level of diagrams and of the amplitude [4].

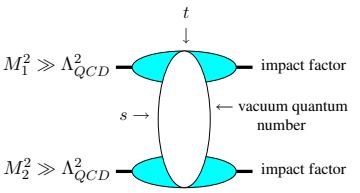


Figure 1: Scattering at $s \gg -t$.

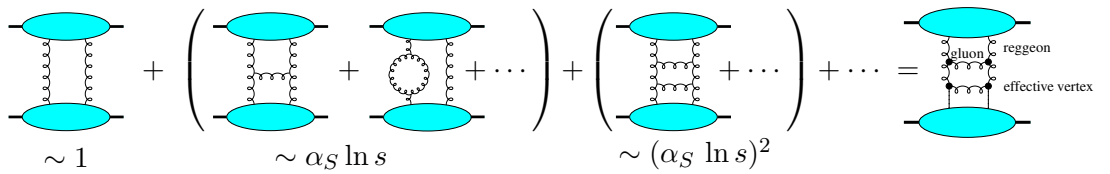


Figure 2: BFKL resummation.

1.2 k_T factorization ($\gamma^*\gamma^* \to \gamma^*\gamma^*$ case)

Using the Sudakov decomposition $k = \alpha p_1 + \beta p_2 + k_\perp$, the $d^4k = \frac{s}{2}\, d\alpha_k\, d\beta_k\, d^2k_\perp$ integration of Fig.3 reduces at large s in a 2-d integration, when setting $\alpha_k \simeq 0$ ($\beta_k \simeq 0$) in the upper (resp. lower) blob and integrating over β_k (resp. α_k). The tensor connecting upper and lower blob simplifies since only *non-sense* gluon polarizations propagates (along p_1 (p_2) in upper (lower) blob) at large s. This results in the representation (involving impact factors $\mathcal{J}$)

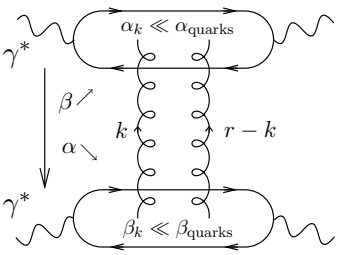


Figure 3: k_T factorization.

$$\mathcal{M} = is \int \frac{d^2\,\underline{k}}{(2\pi)^4 \underline{k}^2\,(\underline{r}-\underline{k})^2} \mathcal{J}^{\gamma^*\to\gamma^*}(\underline{k}, \underline{r}-\underline{k})\; \mathcal{J}^{\gamma^*\to\gamma^*}(-\underline{k}, -\underline{r}+\underline{k})\,.$$

1.3 LL BFKL Pomeron: limitations

First, at LL the scale s_0 entering in the $Y = \ln s/s_0$ resummation is not fixed. Running and scale

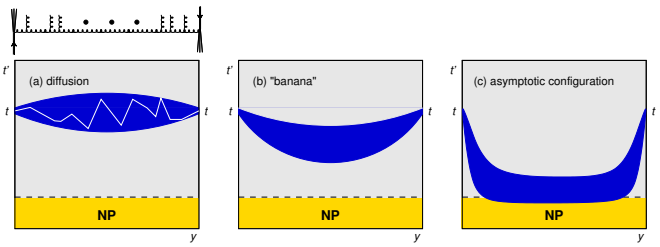


Figure 4: Diffusion along the BFKL ladder.

fixing of α_S are not prescribed at LL. Second, energy-momentum is not conserved in the BFKL approach (this remains at any order: NLL, NNLL, ...), but naturally implemented (vanishing of the first moment of the splitting functions) in the usual collinear renormalisation group approach (à la DGLAP [5]), since one starts with non local matrix elements. The energy-momentum tensor corresponds to their first moment, protected by radiative corrections. Third, diffusion along the ladder spoils the IR safeness of the BFKL Pomeron: at fixed α_S, there is a gaussian diffusion of k_T, with a cigar-like picture [6]. The more s increases, the larger is the broadness. Setting $t = \ln Q^2/\Lambda^2_{QCD}$ (fixed from the probes) and $t' = \ln k^2/\Lambda^2_{QCD}$ ($k^2 \sim -k_T^2$ = virtuality of an arbitrary exchanged gluon along the chain), the typical width of the cigar is $\Delta t' \sim \sqrt{\alpha_S Y}$ (Fig.4a). The Non-Perturbative domain is touched when $\Delta t' \sim \sqrt{\alpha_S Y} \sim t$. In a simple running implementation, the border of the cigar touches NP for $Y \sim bt^3$ ($b = 11/12$) while the center of the cigar approaches NP when $Y \sim bt^2$ ("banana structure" of Fig.4b). A more involved treatment of LL BFKL with running coupling [7] showed that the cigare is "swallowed" by NP in the middle of the ladder (Fig.4c): one faces tunneling when $Y \sim t$, meaning that IR safety is doubtful.

1.4 Higher order corrections

Higher order corrections to the BFKL kernel are known at NLL order ($\alpha_S \sum_n (\alpha_S \ln s)^n$ series) [8], now for arbitrary impact parameter. Impact factors are known in some cases at NLL ($\gamma^* \to \gamma^*$ at $t = 0$ [9], forward jet production [10], $\gamma^* \to \rho$ in forward limit [11]). This leads to *very large corrections with respect to LL*. The main part of these corrections can be obtained from a physical principle, based on a kinematical constraint along the gluon ladder (which is subleading with respect to LL BFKL) [12]. However this could have nothing to do with NLL correction: in principle this constraint would be satisfied when including LL+NLL+NNLL+NNNLL+... . This constraint is more related to improved collinear resummed approaches (see below) for which the vanishing of the first moment of the splitting function is natural. The above perturbative instabilities require an improved scheme. Either one can use a physical motivation to fix the scale of the coupling[1]: this is the basis of BLM scheme, applied for the $\gamma^*\gamma^* \to X$ total cross-section [13] and for the $\gamma^*\gamma^* \to \rho\rho$ exclusive process [14,15]. Or one can use a resummed approach inspired by compatibility with the usual renormalization group approach [16]. For example in $\gamma^*(Q_1)\gamma^*(Q_2) \to X$, one includes *both* full DGLAP LL for $Q_1 \gg Q_2$ and anti-DGLAP LL $Q_1 \ll Q_2$, fixes the relation between Y and s in a symmetric way compatible with DGLAP and implements the running of α_S. Coming back to the IR diffusion problem, this scheme enlarges the validity of perturbative QCD. A simplified version [17] at fixed α_S results in performing in the LL BFKL Green function

$$\frac{1}{\underline{k}^3 \underline{k}'^3} \int \frac{d\omega}{2\pi i} \int \frac{d\gamma}{2\pi i} \left(\frac{\underline{k}^2}{\underline{k}'^2}\right)^{\gamma - 1/2} \frac{e^{\omega Y}}{\omega - \omega(\gamma)}$$

[1] The running of the coupling constant should be implemented at NLL, while scale is fixed starting from NNLL.

the replacement $\omega - \omega(\gamma) \to \omega - \omega(\gamma, \omega)$. The ω integration is performed through contour closing around the pole at $\omega = \omega(\gamma, \omega)$, and the γ integration is made using the saddle point approximation at large Y. This takes into account the main NLL corrections (within 7 % accuracy).

1.5 Non-linear regime and saturation

The Froissart bound should be satisfied at asymptotically large s and for each impact parameter b, and amplitudes should fulfil $T(s, b) < 1$. Various unitarization and saturation models have been developed. First, the *Generalized Leading Log Approximation*, taking into account any *fixed* number n of t-channel exchanged reggeons, leads to the Bartels, Jaroszewicz, Kwiecinski, Praszalowicz equation [18], a 2-dimensional quantum mechanical problem (time $\sim \ln s$) with n sites. It is an *integrable model* in the large N_c limit [19], the XXX Heisenberg spin chain (its *non-compact* symmetry group $SL(2, C)$ makes the solution non-trivial). Solutions of BJKP (i.e. energy spectrum $\Rightarrow intercept$) exist for arbitrary n, describing both Pomeron $P = C = +1$ and Odderon $P = C = -1$ exchanges. For the Odderon, $\alpha_O < 1$ [20] but it decouples from the Born impact factors. A *critical* solution ($\alpha_O = 1$) coupled to Born impact factors can be obtained either from the perturbative Regge approach [21] or from the dipole model [22]. Second, the *Extended Generalized Leading Log Approximation* [23], in which the number of reggeons in the $t-$channel is non conserved, satisfies full unitarity (in all sub-channel) and is an *effective 2-d field theory* realizing the Gribov idea of Reggeon field theory in QCD. Its simplest version, leading to the Balitski-Kovchegov equation [24, 25], involves *fan-diagrams* (with singlet sub-channels). Loops (in terms of Pomerons) corrections are unknown, and obtaining them would be a major step. Another effective field theory approach has been developed separately [26]. Precise relationships between effective approaches remain to be clarified. Third, the multipomeron approach makes contact with AGK cutting rules of pre-QCD [27]. In the large N_c limit, this is the dominant contribution when coupling to Born impact factors (leading with respect to BJKP), and it leads to unitarization. Fourth, during the last decade, the Color Glass Condensate [28] and B-JIMWLK equation were elaborated. This effective field theory is based on the scattering picture of a probe off the field of a source, which is treated through a renormalisation group equation with respect to a longitudinal scale, with an explicit integration of modes below this scale. The approach of Balitski [25] relies on the scattering of Wilson loops and the computation of interaction of one loop with the field of the other (related to the eikonal phase approach à la Nachtmann). The mean field approximation of the B-JIMWLK equation leads to the BK equation. There is at the moment no clear one-to-one correspondence between EGLLA and CGC, except in the peculiar BK limiting case. Loops (in terms of Pomerons) corrections are also unknown. Toy models in 1+0 dimensions are under developement (Reggeon field theory) to understand these corrections. Very interesting links exist between saturation models and statistical physics (reaction-diffusion models of the FKPP class) [29]. These models provide a saturation scale $Q_s(Y)$ growing with Y: above this scale the scattering amplitude T is small (color transparency), and below it saturates. This reduces the contribution of gluons with $k^2 < Q_s^2$ and may solve the IR diffusion problem.

1.6 Onium-onium scattering as a gold plated experiment: $\gamma^{(*)}\gamma^{(*)}$ at colliders

Tests of perturbative QCD in the Regge limit require observables which are free of IR divergencies, by selecting external or internal probes with transverse sizes $\ll 1/\Lambda_{QCD}$ (*hard* γ^*, *heavy*

meson (J/Ψ, Υ), *energetic* forward jets) or by choosing large t. They should be governed by the *"soft"* perturbative dynamics of QCD (BFKL) and *not* by its *collinear* dynamics (DGLAP [5], ERBL [30]): probes should have comparable transverse sizes. They should allow control of k_T spreading, that is the transition from linear to non-linear (saturated regime), meaning the possibility of varying s for fixed transverse size of the probes. It should give access both to forward (i.e. inclusive) and non-forward (i.e. exclusive processes) dynamics, both testing linear and non-linear regimes. $\gamma^{(*)}\gamma^{(*)}$ scattering satisfies all these requirements.

2 Inclusive and Exclusive tests of BFKL dynamics

2.1 Hadron-hadron colliders

Mueller-Navelet jets

This test of BFKL at $t = 0$ is based on the measure for two jets at large p_T (hard scale) separated by a large rapidity $\Delta\eta$ (Fig.5). The signal is a decorrelation of relative azimutal angle between emitted jets when increasing $\Delta\eta$. Studies were made at LL [31], NLL [32] and resummed NLL [33]. Tevatron I data [34] agreed [35] with the modified BFKL approach [12] (see section 1.4). The measurement should be performed soon at CDF for $\Delta\eta$ up to 12, and presumably at LHC.

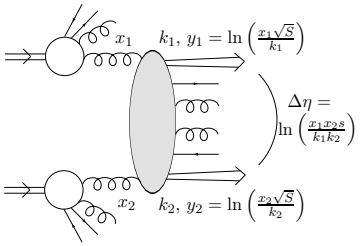


Figure 5: Mueller-Navelet jets.

Diffractive high energy double jet production

The idea is to measure two jets with a gap in rapidity (Fig.6), with hard scales provided by the energies E_T of the jets [36]. This tests BFKL at $t \neq 0$. Taking into account non perturbative gap survival rapidity [37], one can correctly describe the Tevatron data [38].

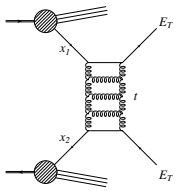


Figure 6: Diffractive high energy jet production.

High p_T jet production

This has been studied at LL and NLL [39]. It relies on computation of impact factors, kernel and Green function at LL and NLL order. The effective jet vertex requires a precise definition of the emitted jet (made of one or two $s-$channel emitted particle at NLL), and modeling of proton impact factor (the only hard scale is p_T^2).

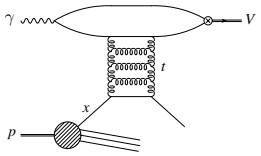


Figure 7: Exclusive vector meson production at large t.

2.2 HERA

DIS and diffractive DIS

Q^2 being the only hard scale for DIS, a model for the proton is needed [40]. BFKL (at $t = 0$) and DGLAP (NLL) both describe the data [41]. Diffractive DIS [43], corresponding experimentally to a gap in the detector between the proton remants and the jets [42], can be described both within collinear and BFKL approaches [44].

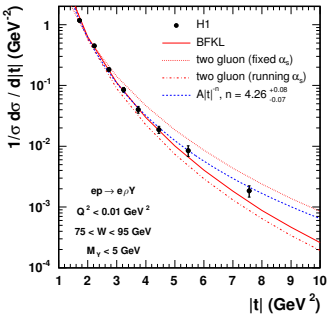


Figure 8: Exclusive vector meson production at HERA.

Energetic forward jet and π^0 production

It is a test of BFKL at $t = 0$, with hard scales given by the γ^* virtuality and the jet energy [45]. Data [46] favor BFKL but cannot exclude a partonic scenario [47].

Exclusive vector meson production at large t

This test of BFKL at large t, which provides the hard scale (Fig.7) [48], was made for H1, ZEUS data and favor BFKL (Fig.8). Problems with data remains for the spin density matrix.

2.3 $\gamma^*\gamma^*$ at LEP2

The LEP2 available energy ($\sqrt{s_{e^+e^-}}$ = 183 to 202 GeV) allowed tests of the total $\gamma^*\gamma^*$ cross-section. This process was studied with LL BFKL [49], dipole model [50,51], modified LL BFKL (based on kinematical constraints) [52] (Fig.9a), NLL BFKL [13] (Fig.9b). Fig.9c displays the comparison [52] between modified LL BFKL, including quark box (simulating usual DGLAP for $Q_1 \sim Q_2$), soft Pomeron and reggeon contributions, and OPAL data. Born 2 gluon exchange and quark exchange are too small in the large Y set of the data. LL BFKL is too high (even including quark mass effects [53]). Scenarios with modified BFKL or NLL BFKL with BLM scale fixing were plausible, but lack of statistics [54] (minimal detection angle of only 30 mrad, luminosity and energy limited) forbade any conclusion.

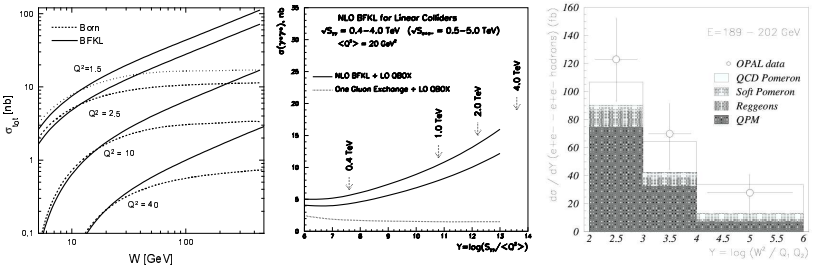


Figure 9: Modified LL BFKL (a) and BLM scale-fixed NLL BFKL (b) predictions versus Born. OPAL data versus modified LL (c).

3 Onium-onium scattering at ILC collider

3.1 Sources of photons

The direct $\gamma\gamma$ cross-section (box diagram) is out of reach experimentally. For example, $\sigma^{\gamma\gamma\to\gamma\gamma} \sim 10^{-64}(\omega_\gamma/\mathrm{eV})^6\mathrm{cm}^2$, that is $10^{-65}\mathrm{cm}^2$ for visible light ($\omega \sim 1$ eV)! Photons can be produced either, using the Fermi, Weizsäcker, Williams idea that the field of a charged particle is a flux of equivalent photon (which are almost real), from a high luminosity collider (Ap, pp, e^+p, e^+e^-) or from Compton backscattering to pump the energy of electrons of a storage ring or of a collider.

Photon colliders: hadron and nucleus colliders

To produce high energy $\omega = zE_{Ze}$ photons with high luminosity, the equivalent photon approximation

$$P_{\gamma/Ze}(z, Q^2) \sim Z^2\,\alpha_{em}/(z\,Q^2)$$

implies that one can use either a high energy (to compensate the $1/z$ pole) and high luminosity hadron collider (LHC, Tevatron), or a heavy nucleus collider (Z^2 then balances the lower luminosity) (RHIC, LHC) [2]. At LHC, both modes would give comparable fluxes of photons. However, $\gamma\gamma$ events are poluted by pure (soft) hadronic interactions between source of photons, since hadrons or nuclei are sensitive to strong interaction. One needs to select peculiar ultra-peripheral events for which the typical impact parameter b between hadrons (nucleus) exceeds

[2] see Nystrand's talk

$1/\Lambda_{QCD}$. This is possible experimentally with very forward detectors, with (anti)tagging protons: the forward detector at CDF (with coming data), LHC detectors (Roman pots) suggested at 420 m (FP420 at CMS and ATLAS) and 220 m (RP200 at ATLAS) from the Interaction Point at LHC. These last detectors are very promising for both $\gamma\gamma$ and hadronic diffractive physics (ex: Higgs exclusive production, MSSM, QCD), but they suffer from non trivial problems with fast time trigger (long distance from IP to the detector to be comparared with the rate of events at high luminosity). Combining both detectors would increase acceptance. Note that b is not directly reconstructed, and that the survival probability has to be taken into account (non-perturbative ingredient). The above situation should be contrasted with processes involving $e^{\pm}$, which are not directly affected by strong interaction. This is the key reason why e^+e^- *colliders are the cleanest solution in principle for* $\gamma^{(*)}\gamma^{(*)}$ *physics*, both from a theoretical and from an experimental point of view.

Photon colliders: $e \to \gamma$ *conversion*

At e^+e^- colliders, a small number of photons, of soft spectrum ($dn_\gamma \sim 0.03\, d\omega/\omega$), is produced:

$$L_{\gamma\gamma}(W_\gamma/(2E_e) > 0.1) \sim 10^{-2}\, L_{e^+e^-} \quad \text{and} \quad L_{\gamma\gamma}(W_\gamma/(2E_e) > 0.5) \sim 0.4\, 10^{-3}\, L_{e^+e^-}\,.$$

To produce a photon collider, the Novosibirsk group suggested [55] to reconsider the use of Compton backscattering of a laser on the high energy electron beam of a collider [56]. Due to the u-channel diagram of Fig.10, which has an almost vanishing propagator, the cross-section is peaked in the backward direction. In this direction, almost all the energy of the incoming electron is transfered to the outgoing photon (up to 82 % at ILC 500 GeV). The limit comes from the fact that one does not want to reconvert γ in e^+e^- pairs!). The corresponding number of equivalent photons is of the order of 1 if the beam has a small size, with laser flash energy of $1 - 10$ J. The photon beam follows the direction of the incoming electron beam with an opening angle of $1/\gamma_e$. Due to the very good focussing of electrons beams expected at ILC, this is the main effect limiting the luminosity in γ mode: the distance b between conversion region and Interaction Point is ~ 1.5 mm, making impossible to use a magnet to deflect the low energy outgoing electron beam. It has been suggested to use a non zero scattering angle between the two incoming beams to remove them (see Fig.11). In order to compensate the potential lost luminosity with non zero scattering angle, *crab-cross* scattering is studied (the paquet is not aligned with the direction of its propagation, like a crab). The luminosity could reach $0.17\, L_{e^+e^-}$, a very interesting value since the cross-sections in $\gamma\gamma$ are usually one order of magnitude higher than for e^+e^-. The matrix element of the Compton process is helicity-conserving except for the term proportional to the electron mass, which is helicity-flip, and *dominates in the backward region*. This provides a very elegant way of *producing quasi monochromatic photons of maximal energy and given polarization,* by using $2\lambda_e P_c = -1$ (λ_e = mean electron helicity and P_c = mean laser photon circular polarization), see Fig.12.

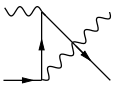


Figure 10: u-channel diagram for Compton scattering.

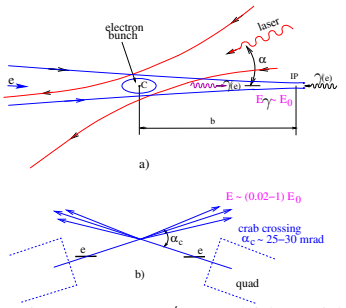


Figure 11: $\gamma\gamma/\gamma e$ collider with cross-crab angle.

Note that WW distribution is sharply peaked around almost on-shell and soft photons: in γe or $\gamma\gamma$ mode, in order to use perturbative QCD, one needs to provide hard scales, from the outgoing state (J/Ψ,...) or from large t. Ingoing γ^* hard states are provided only in e^+e^- mode with double tagged outgoing leptons.

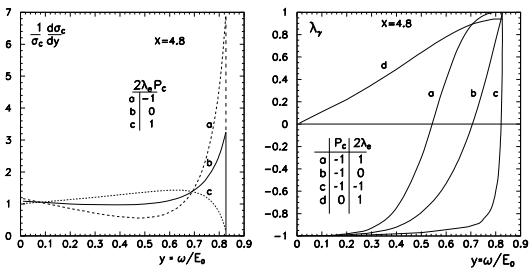


Figure 12: Spectrum (left) and average helicity (right) of the Compton-scattered photons.

3.2 ILC project

The ILC budget estimate is 6.65 G$, comparable to the cost of the LHC when including pre-existing facilities.

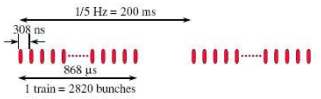


Figure 13: Paquet structure for ILC.

Reference Design Report for ILC

$\sqrt{s}_{e^+e^-}$ should be 500 GeV, with a luminosity of $125\,\mathrm{fb}^{-1}$ per year within 4 years of running, with a possible scan in energy between 200 GeV and 500 GeV. An upgrade at 1 TeV, with a luminosity of $1\,\mathrm{ab}^{-1}$ within 3 to 4 years is planned (see Fig.13 for the rather intricate structure needed for the paquets) [57]. There are non trivial technological problem for extracting the outgoing beam. At the moment, 3 options are considered for the scattering angle: 2 mrad, 14 mrad and 20 mrad, with in each case a hole in the detector at that angle to let the outgoing beam get through toward the beam dump (reducing the acceptance in the forward calorimeter). Crab-cross scattering is needed to get high luminosity. Two interaction regions are highly desirable: one which could be at low crossing-angle, and one compatible with $e\gamma$ and $\gamma\gamma$ physics (through single or double laser Compton backscattering). $\gamma\gamma$ mode leads to the severe constraint that $\alpha_c >$ 25 mrad [3]. The mirors could be placed either inside or outside the detector, depending on the chosen technology, with *almost no space for any forward detector in a cone of 95 mrad* (Fig.14). If the cheaper option suggested by Telnov (single detector + single interaction point + single extraction line, without displacement of the detector between 2 interaction points) would be chosen, diffractive physics could become very difficult.

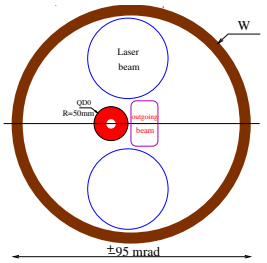


Figure 14: Quad, electron and laser beams.

Detectors at ILC

Each of the 4 detector concepts (GLD, LDC, Sid and 4th (sic)) involves a very forward electromagnetic calorimeter for luminosity measurement, with tagging angle for outgoing leptons down to 5 mrad (10 years ago, 20 mrad was almost impossible!). It is ideal for diffractive physics, which cross-sections are sharply peaked in the very forward region. The luminosity is enough to get high statistics, even for exclusive events. For example, LDC (Fig.15a) contains a BeamCal at 3.65 m from the vertex [58]. The main background is due to beamstrahlung photons, leading to

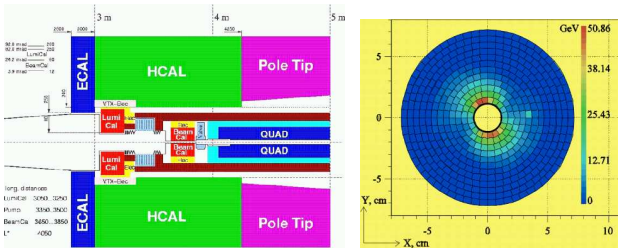


Figure 15: LDC (a). Beamstrahlung in BeamCal (b).

[3] last quadrupole (⌀ =5cm) at 4m from IP and horizontal disruption angle=12.5 mrad, thus 0125+5/400=25 mrad.

energy deposit in cells close from the beampipe (Fig.15b). This implies cutting-off the cells for lepton tagging with E_{min}=100 GeV, θ_{min} = 4 mrad (and to lower energies for large angles).

3.3 $\gamma^*\gamma^* \to hadrons$ total cross-section

In comparison to LEP, s would be higher, the luminosity would be much higher (a factor $\sim 10^3$), and detectors would give access to events closer to the beampipe (LEP: $\theta_{min} \geq 25$ to 30 mrad). One can thus hope to get a much better access to QCD in perturbative Regge limit. To have enough statistics in order to see a BFKL enhancement at TESLA, it was considered to be important to get access down to $\theta_{min} \simeq 25$ to 20 mrad [50]. Probably this could be extended up to 30 mrad due to the expected luminosity (a factor 2 to 3 of luminosity higher than TESLA project). With detection down to 4 mrad, this is thus not anymore a critical parameter[4]. In a modified LL BFKL scenario, one expects around 10^4 events per year with $\theta_{min} \simeq 10$ mrad.

3.4 $\gamma^{(*)}\gamma^{(*)}$ exclusive processes and other QCD studies

In the $\gamma\gamma$ case (e^+e^- without tagging or $\gamma\gamma$ collider option), one can consider any diffractive process of type $\gamma\gamma \to J/\Psi J/\Psi$ [59] (or other heavy produced state). The hard scale is provided by the charmed quark mass, with an expected number of events for ILC around $9\,10^4$. Due to the small detection angle offered by Beamcal, one could also investigate the process $\gamma^*\gamma^* \to \rho_L^0\ \rho_L^0$ [14, 60–63] from $e^+e^- \to e^+e^-\rho_L^0\ \rho_L^0$ with double tagged out-going leptons [64]. The channel $\gamma^*\gamma^*$ is also a gold place for production of C even resonances, such as π^0, η, η', f_2. It would be a good place to look for the elusive odderon, in processes like $\gamma^{(*)}\gamma^{(*)} \to \eta_c\,\eta_c$ [65]. Beside the regge limit, ILC would be also a nice place for finding exotic states like $q\bar{q}g$ with $J^{PC} = 1^{-+}$ [66]. Finally, it could have a great potential for photon structure studies [67].

References

[1] E.A. Kuraev, L.N. Lipatov and V.S. Fadin, Phys. Lett. B **60**, 50-52 (1975); Sov. Phys. JETP **44**, 443-451 (1976) ; Sov. Phys. JETP **45**, 199-204 (1977) ; Ya.Ya. Balitskii and L.N. Lipatov, Sov. J. Nucl. Phys. **28**, 822-829 (1978).

[2] N.N. Nikolaev and B.G. Zakharov, Zeit. für. Phys. C **49**, 607-618 (1991); Zeit. für Phys. C **53**, 331-346 (1992); N.N. Nikolaev, B.G. Zakharov and V.R. Zoller, Phys. Lett. B **328**, 486-494 (1994).

[3] A.H. Mueller, Nucl. Phys. B **415** (1994) 373-385. A.H. Mueller and B. Patel, Nucl. Phys. B **425**, 471-488 (1994); Nucl. Phys. B **437**, 107-126 (1995);

[4] Z. Chen and A.H. Mueller, Nucl. Phys. B **451** 579-604 (1995); H. Navelet and S. Wallon, Nucl. Phys. B **522**, 237 (1998).

[5] V. N. Gribov and L. N. Lipatov, Yad. Fiz. **15**, (1972) 781 [Sov. J. Nucl. Phys. **15**, 438 (1972)]; G. Altarelli and G. Parisi, Nucl. Phys. B **126**, 298 (1977); Y. L. Dokshitzer, Sov. Phys. JETP **46**, 641 (1977) [Zh. Eksp. Teor. Fiz. **73**, 1216 (1977)].

[6] J. Bartels and H. Lotter, Phys. Lett. B **309**, 400 (1993).

[7] M. Ciafaloni, D. Colferai, G. P. Salam and A. M. Stasto, Phys. Lett. B **541**, 314 (2002).

[8] G. Camici and M. Ciafaloni, Phys. Lett. B **412**, 396 (1997) [Erratum-ibid. B **417**, 390 (1998)]; Phys. Lett. B **430**, 349 (1998); V. S. Fadin and L. N. Lipatov, Phys. Lett. B **429**, 127 (1998).

[9] J. Bartels, S. Gieseke and C. F. Qiao, Phys. Rev. D **63**, 056014 (2001) [Erratum-ibid. D **65**, 079902 (2002)].

[10] J. Bartels, D. Colferai and G. P. Vacca, Eur. Phys. J. C **24**, 83 (2002); Eur. Phys. J. C **29**, 235 (2003).

[4]Note that within a γe and $\gamma\gamma$ option, the Telnov suggestion would forbid any forward detector bellow 100 mrad.

[11] D. Y. Ivanov, M. I. Kotsky and A. Papa, Eur. Phys. J. C **38**, 195 (2004).

[12] J. Kwiecinski, A. D. Martin and P. J. Sutton, Z. Phys. C **71**, 585 (1996); B. Andersson, G. Gustafson, H. Kharraziha and J. Samuelsson, Z. Phys. C **71**, 613 (1996); B. Andersson, G. Gustafson and J. Samuelsson, Nucl. Phys. B **467**, 443 (1996).

[13] S. J. Brodsky, V. S. Fadin, V. T. Kim, L. N. Lipatov and G. B. Pivovarov, JETP Lett. **70**, 155 (1999); JETP Lett. **76**, 249 (2002) [Pisma Zh. Eksp. Teor. Fiz. **76**, 306 (2002)].

[14] R. Enberg, B. Pire, L. Szymanowski and S. Wallon, Eur. Phys. J. C **45**, 759 (2006) [Erratum-ibid. C **51**, 1015 (2007)]; Acta Phys. Polon. B **37**, 847 (2006).

[15] D. Y. Ivanov and A. Papa, Nucl. Phys. B **732**, 183 (2006); Eur. Phys. J. C **49** 947 (2007).

[16] G. P. Salam, JHEP **9807**, 019 (1998); M. Ciafaloni and D. Colferai, Phys. Lett. B **452**, 372 (1999); M. Ciafaloni, D. Colferai and G. P. Salam, Phys. Rev. D **60**, 114036 (1999).

[17] V. A. Khoze, A. D. Martin, M. G. Ryskin and W. J. Stirling, Phys. Rev. D **70**, 074013 (2004).

[18] J. Bartels, Nucl. Phys. B **151** 293 (1979); Nucl. Phys. B **175**, 365-401 (1980); T. Jaroszewicz, Acta Phys. Pol. B **11**, 965-973 (1980); J. Kwiecinski and M. Praszalowicz, Phys. Lett. B **94**, 413-416 (1980);

[19] L. N. Lipatov, Phys. Lett. B **309**, 394 (1993); Padova preprint DFPD-93-TH-70, hep-th/9311037; JETP Lett. **59**, 596 (1994); L.D. Faddeev and G.P. Korchemsky, Phys. Lett. B **342**, 311 (1995); G.P. Korchemsky, Nucl. Phys. B **443**, 255 (1995).

[20] R. A. Janik and J. Wosiek, Phys. Rev. Lett. **82**, 1092 (1999); G. P. Korchemsky, J. Kotanski and A. N. Manashov, Phys. Rev. Lett. **88**, 122002 (2002); S. E. Derkachov, G. P. Korchemsky, J. Kotanski and A. N. Manashov, Nucl. Phys. B **645**, 237 (2002).

[21] J. Bartels, L. N. Lipatov and G. P. Vacca, Phys. Lett. B **477**, 178 (2000).

[22] Y. V. Kovchegov, L. Szymanowski and S. Wallon, Phys. Lett. B **586**, 267 (2004).

[23] J. Bartels, DESY 91-074 (unpublished); J. Bartels and M. Wüsthoff, Z. Phys. C **66**, 157 (1995); J. Bartels and C. Ewerz, JHEP **9909**, 026 (1999).

[24] Yu.V. Kovchegov, Phys. Rev. D **60**, 034008 (1999); Phys. Rev. D **61**, 074018 (1999).

[25] I. Balitsky, Nucl. Phys. D **463** (1996) 99; Phys. Rev. Lett. **81**, 2024 (1998); Phys. Rev. D **60**, 014021 (1999); Phys. Lett. B **518**, 235 (2001).

[26] R. Kirschner, L. N. Lipatov and L. Szymanowski, Nucl. Phys. B **425**, 579 (1994); Phys. Rev. D **51**, 838 (1995); L.N. Lipatov, Nucl. Phys. B **452**, 369 (1995); E. N. Antonov, L. N. Lipatov, E. A. Kuraev and I. O. Cherednikov, Nucl. Phys. B **721**, 111 (2005).

[27] J. Bartels and M. G. Ryskin, Z. Phys. C **76**, 241 (1997); J. Bartels, M. Salvadore and G. P. Vacca, Eur. Phys. J. C **42**, 53 (2005).

[28] J. Jalilian-Marian, A. Kovner, A. Leonidov and H. Weigert, Nucl. Phys. B **504**, 415 (1997); Phys. Rev. D **59**, 014014 (1999); J. Jalilian-Marian, A. Kovner and H. Weigert, Phys. Rev. D **59**, 014015 (1999); A. Kovner, J. G. Milhano and H. Weigert, Phys. Rev. D **62**, 114005 (2000); E. Iancu, A. Leonidov and L. McLerran, Nucl. Phys. A **692**, 583 (2001); Phys. Lett. B **510**, 133 (2001); E. Ferreiro, E. Iancu, A. Leonidov and L. McLerran, Nucl. Phys. A **703**, 489 (2002); H. Weigert, Nucl. Phys. A **703**, 823 (2002).

[29] S. Munier and R. Peschanski, Phys. Rev. Lett. **91**, 232001 (2003) Phys. Rev. D **69**, 034008 (2004); Phys. Rev. D **70**, 077503 (2004); E. Iancu, A. H. Mueller and S. Munier, Phys. Lett. B **606**, 342 (2005).

[30] G.P. Lepage and S.J. Brodsky, Phys. Lett. B **87**, 359 (1979); A.V. Efremov and A.V. Radyushkin, Phys. Lett. B **94**, 245 (1980).

[31] A. H. Mueller and H. Navelet, Nucl. Phys. B **282**, 727 (1987); V. Del Duca and C. R. Schmidt, Phys. Rev. D **51**, 2150 (1995).

[32] A. S. Vera, Nucl. Phys. B **746**, 1 (2006); A. S. Vera and F. Schwennsen, Nucl. Phys. B **776**, 170 (2007).

[33] C. Marquet and C. Royon, arXiv:0704.3409 [hep-ph].

[34] S. Abachi *et al.* [D0 Collaboration], Phys. Rev. Lett. **77**, 595 (1996).

[35] J. Kwiecinski, A. D. Martin, L. Motyka and J. Outhwaite, Phys. Lett. B **514**, 355 (2001).

[36] A. H. Mueller and W. K. Tang, Phys. Lett. B **284**, 123 (1992).

[37] R. Enberg, G. Ingelman and L. Motyka, Phys. Lett. B **524**, 273 (2002).

[38] B. Abbott *et al.* [D0 Collaboration], Phys. Lett. B **440**, 189 (1998); F. Abe *et al.* [CDF Collaboration], Phys. Rev. Lett. **80**, 1156 (1998).

[39] O. Kepka, C. Royon, C. Marquet and R. Peschanski, arXiv:hep-ph/0609299; arXiv:hep-ph/0612261; A. S. Vera and F. Schwennsen, arXiv:0708.0549 [hep-ph].

[40] A. J. Askew, K. J. Golec-Biernat, J. Kwiecinski, A. D. Martin and P. J. Sutton, Phys. Lett. B **325**, 212 (1994); H. Navelet, R. Peschanski, C. Royon and S. Wallon, Phys. Lett. B **385**, 357 (1996); S. Munier and R. Peschanski, Nucl. Phys. B **524**, 377 (1998).

[41] C. Adloff *et al.* [H1 Collaboration], Eur. Phys. J. C **21**, 33 (2001); S. Chekanov *et al.* [ZEUS Collaboration], Eur. Phys. J. C **21**, 443 (2001).

[42] A. Aktas *et al.* [H1 Collaboration], Eur. Phys. J. C **48**, 715 (2006); Eur. Phys. J. C **48**, 749 (2006); ZEUS Collab., S. Chekanov et al., Nucl. Phys. B **713**, 3 (2005); Eur. Phys. J. C **38**, 43 (2004).

[43] G. Ingelman, P. Schlein, Phys. Lett. B **152**, 256 (1985).

[44] S. Munier, R. Peschanski and C. Royon, Nucl. Phys. B **534**, 297 (1998); J.Bartels, J.Ellis, H.Kowalski, M.Wuesthoff, Eur. Phys. J. C **7**, 443 (1999); J.Bartels, C.Royon, Mod. Phys. Lett. A **14**, 1583 (1999); C. Royon, L. Schoeffel, S. Sapeta, R. Peschanski and E. Sauvan, Nucl. Phys. B **781**, 1 (2007).

[45] A. H. Mueller, J. Phys. G **17**, 1443 (1991); J. Bartels, A. de Roeck and M. Loewe, Z. Phys. C **54**, 635 (1992); J. Kwiecinski, A. D. Martin and P. J. Sutton, Phys. Rev. D **46**, 921 (1992); J. Bartels, V. Del Duca and M. Wusthoff, Z. Phys. C **76**, 75 (1997); J. Kwiecinski, A. D. Martin and J. J. Outhwaite, Eur. Phys. J. C **9**, 611 (1999).

[46] H1 Collab., S. Aid et al., Phys. Lett. B **356**, 118 (1995); J. Breitweg *et al.* [ZEUS Collaboration], Eur. Phys. J. C **6**, 239 (1999).

[47] P. Aurenche, R. Basu, M. Fontannaz and R. M. Godbole, Eur. Phys. J. C **42**, 43 (2005).

[48] J. R. Forshaw and M. G. Ryskin, Z. Phys. C **68**, 137 (1995); J. Bartels, J. R. Forshaw, H. Lotter and M. Wusthoff, Phys. Lett. B **375**, 301 (1996); R. Enberg, J. R. Forshaw, L. Motyka and G. Poludniowski, JHEP **0309**, 008 (2003); JHEP **0312**, 002 (2003).

[49] J. Bartels, A. De Roeck and H. Lotter, Phys. Lett. B **389**, 742 (1996); S. J. Brodsky, F. Hautmann and D. E. Soper, Phys. Rev. Lett. **78**, 803 (1997) [Erratum-ibid. **79**, 3544 (1997)], Phys. Rev. D **56**, 6957 (1997).

[50] M. Boonekamp, A. De Roeck, C. Royon and S. Wallon, Nucl. Phys. B **555**, 540 (1999).

[51] A. Bialas, W. Czyz and W. Florkowski, Eur. Phys. J. C **2**, 683 (1998).

[52] J. Kwiecinski and L. Motyka, Phys. Lett. B **462**, 203 (1999); Eur. Phys. J. C **18**, 343 (2000).

[53] J. Bartels, C. Ewerz and R. Staritzbichler, Phys. Lett. B **492**, 56 (2000).

[54] G. Abbiendi *et al.* [OPAL Collaboration], Eur. Phys. J. C **24**, 17 (2002); P. Achard *et al.* [L3 Collaboration], Phys. Lett. B **531**, 39 (2002); A. Heister *et al.* [ALEPH Collaboration], arXiv:hep-ex/0305107; J. Abdallah *et al.* [DELPHI Collaboration], Eur. Phys. J. C **46**, 559 (2006);

[55] I. F. Ginzburg, G. L. Kotkin, V. G. Serbo and V. I. Telnov, JETP Lett. **34**, 491 (1981) [Pisma Zh. Eksp. Teor. Fiz. **34**, 514 (1981)]; Nucl. Instrum. Meth. **205**, 47 (1983); I. F. Ginzburg, G. L. Kotkin, S. L. Panfil, V. G. Serbo and V. I. Telnov, Nucl. Instrum. Meth. A **219**, 5 (1984).

[56] F. R. Arutyunian and V. A. Tumanian, *Phys.Lett.* **4**, 176 (1963); F. R. Arutyunian I.I. Goldman and V. A. Tumanian, *Zh. Eksp. Teor. Fiz. (USSR)* **45**, 312 (1963); R. H. Milburn, *Phys. Rev. Lett.* **10**, 75 (1963).

[57] ILC, Basic Conceptual Design Report, http://www.linearcollider.org.

[58] LDC outline document, http://www.ilcldc.org.

[59] J. Kwiecinski and L. Motyka, Phys. Lett. B **438**, 203 (1998); J. Kwiecinski, L. Motyka and A. De Roeck, In *2nd ECFA/DESY Study 1998-2001* 556-564, [arXiv:hep-ph/0001180].

[60] B. Pire, L. Szymanowski and S. Wallon, Eur. Phys. J. C **44**, 545 (2005).

[61] B. Pire, M. Segond, L. Szymanowski and S. Wallon, Phys. Lett. B **39**, 642-651 (2006).

[62] M. Segond, L. Szymanowski and S. Wallon, Eur. Phys. J. C **52**, 93 (2007) [arXiv:hep-ph/0703166].

[63] F. Caporale, A. Papa and A. S. Vera, arXiv:0707.4100 [hep-ph].

[64] See talk "Studying QCD factorizations in exclusive $\gamma^*\gamma^* \to \rho_L^0\rho_L^0$", arXiv:0710.0838 [hep-ph], slides: https://indico.desy.de/conferenceDisplay.py?confId=372#9

[65] S. Braunewell and C. Ewerz, Phys. Rev. D **70**, 014021 (2004); for a review, see C. Ewerz, arXiv:hep-ph/0306137.

[66] I. V. Anikin, B. Pire, L. Szymanowski, O. V. Teryaev and S. Wallon, Eur. Phys. J. C **47**, 71 (2006).

[67] for a review, see M. Klasen, Rev. Mod. Phys. **74**, 1221 (2002).

[68] slides: https://indico.desy.de/conferenceDisplay.py?confId=372

Part V

Cosmic Rays and Astroparticle Physics

On the measurement of the proton-air cross section using cosmic ray data

Ralf Ulrich[1,*], *Johannes Blümer*[1,2], *Ralph Engel*[1], *Fabian Schüssler*[1], *Michael Unger*[1]
[1]Institut für Kernphysik, Forschungszentrum Karlsruhe, Karlsruhe, Germany
[2]Institut für Experimentelle Kernphysik, Universität Karlsruhe, Karlsruhe, Germany

Abstract
Cosmic ray data may allow the determination of the proton-air cross section at ultra-high energy. For example, the distribution of the first interaction point in air showers reflects the particle production cross section. As it is not possible to observe the point of the first interaction X_1 of a cosmic ray primary particle directly, other air shower observables must be linked to X_1. This introduces an inherent dependence of the derived cross section on the general understanding and modeling of air showers and, therfore, on the hadronic interaction model used for the Monte Carlo simulation. We quantify the uncertainties arising from the model dependence by varying some characteristic features of high-energy hadron production.

1 Introduction

The natural beam of cosmic ray particles extends to energies far beyond the reach of any earth-based accelerator. Therefore cosmic ray data provides an unique opportunity to study interactions at extreme energies. Unfortunately, the cosmic ray flux is extremely small making direct measurements of the particles and their interactions impossible above $\sim$ 100 TeV. One is forced to rely on indirect measurements such as extensive air shower studies, where the interpretation of the data is very difficult.

In this contribution we will briefly discuss different methods of measuring the proton-air cross section, focusing on methods that are based on extensive air shower (EAS) data. Figure 1 shows a compilation of proton-air cross section measurements and predictions of hadronic interaction models currently used in cosmic ray studies [1–11]

2 Methods of cross section measurements using cosmic ray data

2.1 Primary cosmic ray proton flux

Already in the 60's first estimates of the proton-air cross section $\sigma_{\mathrm{p-air}}$ were made using cosmic ray data [1]. These early measurements are relying on two independent observations of the flux of primary cosmic ray protons after different amounts of traversed atmospheric matter. Firstly the primary proton flux $\Phi(X_{\mathrm{top}})$ is measured at the top of the atmosphere with a satellite or at least very high up in the atmosphere on a balloon at $X_{\mathrm{top}} = 0 - 5$ gcm^{-2}. The second flux $\Phi(X_{\mathrm{bottom}})$ is measured with a ground based calorimeter at $X_{\mathrm{bottom}} = 600 - 1000$ gcm^{-2},

[*] speaker

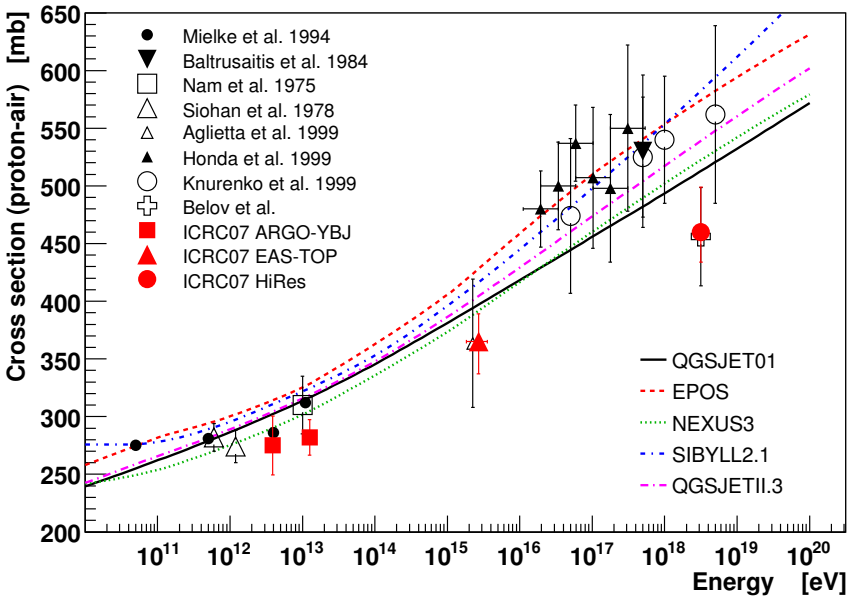


Fig. 1: Current data of proton-air production cross section measurements [1–11] and model predictions [12–18].

preferentially at high altitude and using efficient veto detectors to select unaccompanied hadrons. The effective attenuation length can then be calculated straightforwardly from

$$\lambda_{\mathrm{prod}} = (X_{\mathrm{bottom}} - X_{\mathrm{top}}) / \log(\Phi_{\mathrm{top}}/\Phi_{\mathrm{bottom}}). \tag{1}$$

As it is impossible to veto all hadronic interactions along the cosmic ray passage through the atmosphere, this attenuation length can only be used to obtain a lower bound to the high energy particle production cross section

$$\sigma_{\mathrm{p-air}} \geq \frac{\langle m \rangle}{\lambda_{\mathrm{prod}}}, \tag{2}$$

where $\langle m \rangle$ is the mean mass of air. The method is limited to proton energies lower than $\sim$TeV, since no sufficiently precise satellite or balloon borne data is available above this energy. By design the unaccompanied hadron flux is only sensitive to the particle production cross section, since primary protons with interactions without particle production cannot be separated from protons without any interaction.

2.2 Extensive air showers

In order to measure $\sigma_{\mathrm{p-air}}$ at even higher energies it is necessary to rely on EAS data [6–11]. The characteristics of the first few extremely high energy hadronic interactions during the startup of an EAS are paramount for the resulting air shower. Therefore it should be possible to relate EAS observations like the shower maximum X_{max}, or the total number of electrons $N_{\mathrm{e}}(X)|_{X=X_{\mathrm{obs}}} = N_{\mathrm{e}}^{\mathrm{rec}}$ and muons $N_{\mu}(X)|_{X=X_{\mathrm{obs}}} = N_{\mu}^{\mathrm{rec}}$ at a certain observation depth X_{obs}, to the depth of the

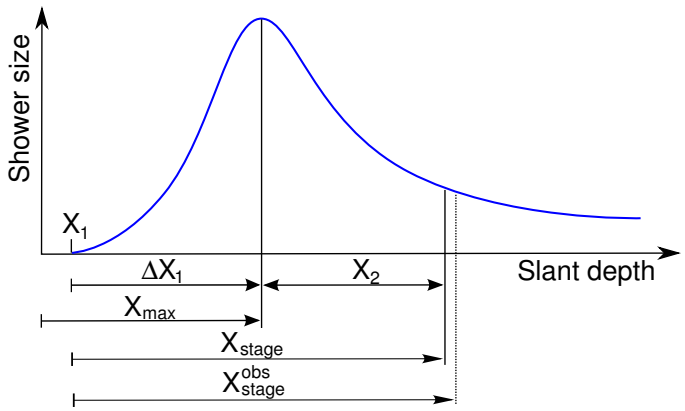


Fig. 2: Definition of variables to characterize EAS longitudinal profiles.

first interaction point and the characteristics of the high energy hadronic interactions.

Ground based observations

In case of ground based extensive air shower arrays, the frequency of observing EAS of the same energy at a given stage of their development is used for the cross section measurement. By selecting EAS of the same energy but different directions, the point of the first interaction has to vary with the angle to observe the EAS at the same development stage. The selection of showers of constant energy and stage depends on the particular detector setup, but the typical requirement is $\left(N_{\rm e}^{\rm rec},\ N_{\mu}^{\rm rec}\right) = \text{const}$ at observation level.

With the naming conventions given in Fig. 2, the probability of observing a shower of a given energy E_0 and shower stage at the zenith angle θ can be written as

$$\begin{aligned}\frac{1}{N}\,\frac{dN}{d\cos\theta}\bigg|_{N_{\rm e}^{\rm rec},N_{\mu}^{\rm rec}} &= \int dX_1 \int d\Delta X_1 \int d\Delta X_2\ \frac{e^{-X_1/\lambda_{\rm int}}}{\lambda_{\rm int}} \\ &\quad \times P_1(\Delta X_1) \times P_2(\Delta X_2) \\ &\quad \times P_{\rm res}(X_{\rm stage}^{\rm rec}, X_1 + \Delta X_1 + \Delta X_2). \end{aligned} \tag{3}$$

Here $X_{\rm stage}$ defines the distance between the first interaction point and the depth at which the shower reaches a given number of muons and electrons as defined by the selection criteria. The experimentally inferred shower stage at observation level $X_{\rm stage}^{\rm rec}$ does, in general, not coincide with the true stage due to the limited detector and shower reconstruction resolution. This effect is accounted for by the factor $P_{\rm res}$. The functions P_1 and P_2 describe the shower-to-shower fluctuations. The probability of a shower having its maximum at $X_{\rm max} = X_1 + \Delta X_1$ is expressed by P_1. The probability P_2 is defined correspondingly with $X_{\rm stage} = \Delta X_1 + \Delta X_2$.

In cross section analyses, Eq. (3) is approximated by an exponential function of $\sec\theta$. Assuming that the integration of Eq. (3) over the distributions P_1, P_2, and $P_{\rm res}$ does not yield any generally non-exponential tail at large $\sec\theta$, it can be written as

$$\frac{1}{N}\,\frac{dN}{d\cos\theta}\bigg|_{N_{\rm e}^{\rm rec},N_{\mu}^{\rm rec}} \propto\ e^{-X_{\rm obs}/\Lambda_{\rm obs}^{\rm S}} \propto\ e^{-\sec\theta/\Lambda_{\rm obs}^{\rm S}}. \tag{4}$$

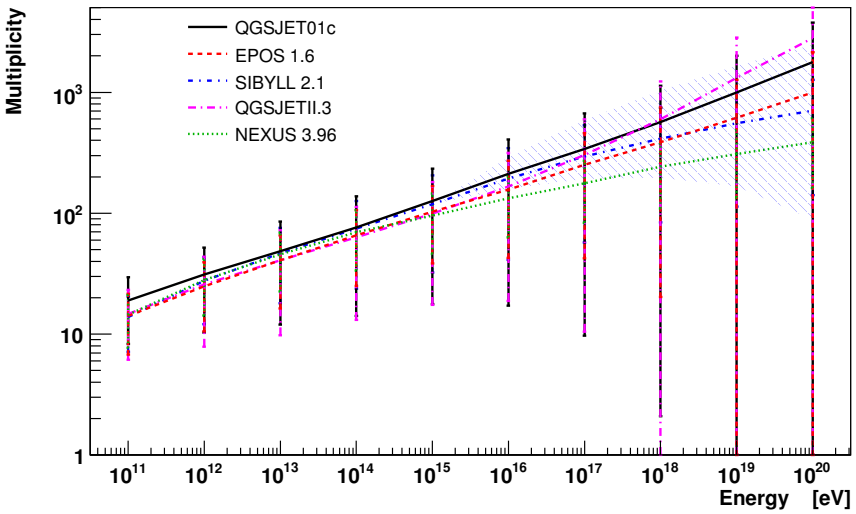


Fig. 3: Model predictions for the secondary particle multiplicity in high energy hadronic interactions. The lines denote the mean while the error bars indicate the RMS of the distributions. The shaded area is the range for SIBYLL using $0.3 \geq f_{10\mathrm{EeV}} \geq 3$.

However, the slope parameter $\Lambda^{\mathrm{S}}_{\mathrm{obs}}$ does not coincide with the interaction length λ_{int} due to non-Gaussian fluctuations and a possible angle-dependent experimental resolution. Therefore the measured attenuation length can be written as

$$\Lambda^{\mathrm{S}}_{\mathrm{obs}} = \lambda_{\mathrm{int}} \cdot k_{\Delta X_1} \cdot k_{\Delta X_2} \cdot k^{\mathrm{S}}_{\mathrm{resolution}} = \lambda_{\mathrm{int}} \cdot k_{\mathrm{S}}. \tag{5}$$

The k-factors $k_{\Delta X_1}$, $k_{\Delta X_2}$ and $k^{\mathrm{S}}_{\mathrm{resolution}}$ parametrize the contributions to $\Lambda^{\mathrm{S}}_{\mathrm{obs}}$ from the corresponding integrations. However, these integrations are difficult to perform separately and the individual k-factors are not known in most analyses (for a partial exception, see [10]).

Observations of the shower maximum $\mathbf{X}_{\mathrm{max}}$

Observing the position of the shower maximum directly allows one to simplify Eq. (3) by removing the term due to the shower development after the shower maximum P_2. Also the detector resolution P_{res} is much better under control for X_{max} and can be well approximated by a Gaussian distribution. The resulting distribution is

$$P(X^{\mathrm{rec}}_{\mathrm{max}}) \;=\; \int dX_1 \int d\Delta X_1 \; \frac{e^{-X_1/\lambda_{\mathrm{int}}}}{\lambda_{\mathrm{int}}} \times \; P_1(\Delta X_1) \times \; P_{res}(X^{\mathrm{rec}}_{\mathrm{max}} - X_{\mathrm{max}}), \tag{6}$$

with $X_1 + \Delta X_1 = X_{\mathrm{max}}$. In analogy to Eq. (4) only the tail of $P(X^{\mathrm{rec}}_{\mathrm{max}})$ at large $X^{\mathrm{rec}}_{\mathrm{max}}$ is approximated by an exponential distribution

$$P(X^{\mathrm{rec}}_{\mathrm{max}}) \;\propto\; e^{-X^{\mathrm{rec}}_{\mathrm{max}}/\Lambda^{\mathrm{X}}_{\mathrm{obs}}}, \tag{7}$$

whereas the exponential slope Λ_{obs} can be deduced from the convolution integral (6) as

$$\Lambda^{\mathrm{X}}_{\mathrm{obs}} = \lambda_{\mathrm{int}} \cdot k_{\Delta X_1} \cdot k^{\mathrm{X}}_{\mathrm{resolution}} = \lambda_{\mathrm{int}} \cdot k_{\mathrm{X}}. \tag{8}$$

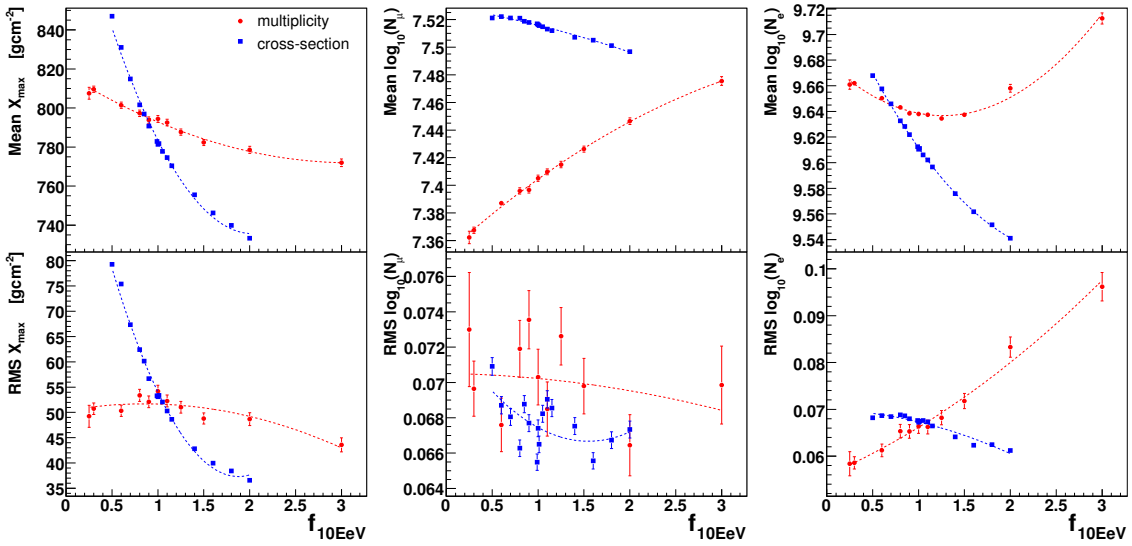


Fig. 4: Mean and RMS values for the resulting $X_{\max}$, $N_\mu(X)|_{X=1000\,\mathrm{gcm}^{-2}}$ and $N_\mathrm{e}(X)|_{X=1000\,\mathrm{gcm}^{-2}}$ distributions as a function of $f_{10\mathrm{EeV}}$ using SIBYLL 2.1. For each data point with changed *multiplicity*, 1000 air showers are simulated and 10000 for a changed *cross section*. The dashed lines are polynomial fits of 2nd order to guide the eye.

Again $k_{\Delta X_1}$ and $k^{\mathrm{X}}_{\mathrm{resolution}}$ are the contributions to $\Lambda^{\mathrm{X}}_{\mathrm{obs}}$ from the corresponding integrations of Eq. (6).
It was also recognized that Eq. (6) can be unfolded directly to retrieve the original X_1-distribution, if the ΔX_1-distribution is previously inferred by Monte-Carlo simulations [11]. Recently this triggered some discussion about the general shape and model dependence of the ΔX_1-distribution [19]. This directly implies a corresponding model dependence of the $k_{\Delta X_1}$-factors.

3 Impact of high energy interaction model characteristics on air shower development

To explore the impact of uncertainties of the present high energy hadronic interaction models on the interpretation of EAS observables, we modified the CONEX [20] program to change some of the interaction characteristics during EAS simulation. To achieve this, individual hadronic interaction characteristics are altered by the energy-dependent factor

$$f(E) = \begin{cases} 1 & E{\leq}1\ \mathrm{PeV} \\ 1 + (f_{10\mathrm{EeV}} - 1) \cdot \log_{10}(E/1\mathrm{PeV}) / \log_{10}(10\mathrm{EeV}/1\mathrm{PeV}) & E{>}1\ \mathrm{PeV} \end{cases} \quad (9)$$

which was chosen to be 1 below 1 PeV, because at these energies accelerator data is available (Tevatron corresponds to 1.8 PeV). Above 1 PeV, $f(E)$ increases logarithmically with energy, reaching the value of $f_{10\mathrm{EeV}}$ at 10 EeV.
The factor $f(E)$ is then used to re-scale specific characteristic properties of the high energy hadronic interactions such as the interaction cross section, secondary particle multiplicity or inelasticity. Obviously by doing this we may leave the parameter space allowed by the original model, but nevertheless one can get a clear impression of how the resulting EAS properties are

depending on the specific interaction characteristics.
We demonstrate the impact of a changing multiplicity $n_{\rm mult}$ and cross section σ on the following, important air shower observables: shower maximum $X_{\rm max}$, and the total number of electrons $N_{\rm e}^{\rm rec}$, as well as muons $N_{\mu}^{\rm rec}$ arriving at an observation level of $X_{\rm obs} = 1000$ gcm^{-2}. Figure 3 shows the range of extrapolations of $n_{\rm mult}$ used by the current hadronic interaction models and thus motivates the energy dependent re-scaling of $n_{\rm mult}$ by $0.3 \geq f_{\rm 10EeV} \geq 3$.
All simulations are performed for primary protons at 10 EeV using the SIBYLL 2.1 [17] interaction model. Figure 4 summarizes the results, which are discussed below.

Multiplicity of secondary particle production
The effect of a changed multiplicity on the $X_{\rm max}$-distribution is a shift to shallower $X_{\rm max}$ with increasing $n_{\rm mult}$. This is what is already predicted by the extended Heitler model [21]

$$X_{\rm max} \propto \lambda_r \cdot \ln \frac{E_0}{n_{\rm mult} \cdot E_{\rm crit}^{\rm e.m.}}, \tag{10}$$

where λ_r is the electromagnetic radiation length and $E_{\rm crit}^{\rm e.m.}$ the critical energy in air. This is a consequence of the distribution of the same energy onto a growing number of particles. The resulting lower energy electromagnetic sub-showers reach their maximum earlier. The impact on the RMS of the $X_{\rm max}$-distribution is small, but there is a trend to smaller fluctuations for an increasing number of secondaries.
The total muon number after 1000 gcm^{-2} of shower development is rising if the multiplicity increases. This reflects the overall increased number of particles. The fluctuations are not significantly affected.
More interesting is the impact on the electron number $N_{\rm e}^{\rm rec}$, which shows a minimum close to $f_{\rm 10EeV} = 1$. The rising trend in the direction of smaller $n_{\rm mult}$ can be explained by the increase of $X_{\rm max}$ and therefore the shower maximum coming closer to the observation level. On the other hand the rising trend in the direction of larger $n_{\rm mult}$ is again just the consequence of a generally growing number of particles. In contrary to the muon number the RMS does significantly change while $n_{\rm mult}$ gets larger. This can be explained by the strong dependence of fluctuations in $N_{\rm e}^{\rm rec}$ from the distance to the shower maximum.

Cross section
By construction, scaling the cross section does affect all hadronic interactions above 1 PeV, not only the first interaction.
The mean as well as the RMS of the $X_{\rm max}$-distribution are decreasing with an increasing cross section. The effect is very pronounced, since the depth of the first interaction X_1 is affected as well as the shower startup phase. Both effects are pointing to the same direction. This makes $X_{\rm max}$ a very sensitive observable for a cross section measurement.
The impact on the muon number $N_{\mu}^{\rm rec}$ is not very large. Since the shower maximum moves away from the observation level with increasing cross section, we just see the slow decrease of the muon number at late shower development stages, while the fluctuation of $N_{\mu}^{\rm rec}$ stay basically constant.
The mean electron number as well as its fluctuations depend strongly on the distance of $X_{\rm max}$ from the observation level. Combined with the influence of the modified cross section on $X_{\rm max}$ this explains well the strong decrease of the mean $N_{\rm e}^{\rm rec}$ as well as the RMS with increasing cross

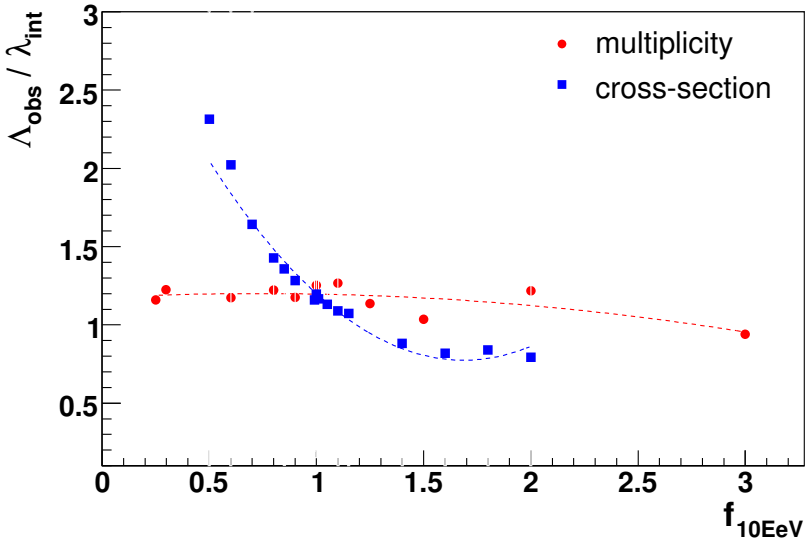


Fig. 5: Simulated k_{X}-factors ($k_{\mathrm{X}} = \Lambda^{\mathrm{X}}_{\mathrm{obs}}/\lambda_{\mathrm{int}}$) for SIBYLL at 10 EeV with modified cross section and multiplicity. $\Lambda^{\mathrm{X}}_{\mathrm{obs}}$ is obtained by an exponential fit to the tail of the resulting CONEX X_{max}-distribution. An ideal detector is assumed, hence $k_{\mathrm{X}} = k_{\Delta X_1}$. The polynomial fits of 2nd order are only plotted to guide the eye.

section. At very small cross sections the shower maximum comes very close to the observation level, which can be observed as a flattening in the mean $N_{\mathrm{e}}^{\mathrm{rec}}$ and the decrease of the fluctuations in $N_{\mathrm{e}}^{\mathrm{rec}}$ against the trend of increasing fluctuations of the position of the shower maximum itself.

4 Summary

All methods of EAS-based cross section measurements are very similar and thus suffer from the same limitations:

- The values of all k-factors must be retrieved from massive Monte-Carlo simulations. All analysis attempts so far have only calculated the combined factor of k_{S}, respectively k_{X}.
- k-factors depend on the resolution of the experiment and can therefore not be transferred simply to other experiments.
- k_{X}-factors are inherently different from k_{S}-factors and can therefore not be transferred from an X_{max}-tail analysis to that of ground based frequency attenuation or vice versa.
- It cannot be disentangled whether a measurement of Λ_{obs} can be attributed to λ_{int} entirely or at least partly to changed fluctuations in ΔX_1 and/or ΔX_2.
- Generally the P_1 and P_2 distributions have a complex shape and therefore the integrations of Eqs. (3) and (6) to yield the approximations Eqs. (5) and (8) are leading to non-exponential contributions.
- Any non-exponential contribution creates a strong dependence of the fitted Λ_{obs} on the chosen fitting range [22]. A strong non-exponential contribution makes the k-factor analysis unusable.

- It can be shown that the $P_1(\Delta X_1)$-distributions is very sensitive to changes of the high energy hadronic interaction characteristics and thus $P(\Delta X) = f(\sigma, n_{\rm mult}, ...)$ is a function of σ , $n_{\rm mult}$ and other high energy model parameters. Consequently this also makes the k-factors depending on the high energy interaction characteristics $k = f(\sigma, n_{\rm mult}, ...)$, which certainly must be considered for any cross section analysis.

In Fig. 5 we show how the here presented simulations can be used to quantify the uncertainty caused in the k-factors due to the dependence on $n_{\rm mult}$ to about $\pm \sim 0.1$ for a variation of the multiplicity by a factor from 0.3 up to 3. It is clear that even without considering the multiplicity as a possible source of uncertainty the σ-dependence of the k-factors certainly needs to be taken into account. Otherwise a systematic shift will be introduced into the resulting $\sigma_{\rm p-air}$, since part of the observed signal in $\Lambda_{\rm obs}$ is wrongly assigned to $\lambda_{\rm int}$, while in fact it must be attributed to $k(\sigma, n_{\rm mult}, \dots)$ [23]. This has not been considered in any EAS-based $\sigma_{\rm p-air}$ measurement so far.

References

[1] N. L. Grigorov *et al.* (1965). Proc. of 9th Int. Cosmic Ray Conf. (London), vol. 1, p. 860.

[2] G. B. Yodh, Y. Pal, and J. S. Trefil, Phys. Rev. Lett. **28**, 1005 (1972).

[3] R. A. Nam, S. I. Nikolsky, V. P. Pavluchenko, A. P. Chubenko, and V. I. Yakovlev (1975). In Proc. of 14th Int. Cosmic Ray Conf. (Munich), vol. 7, p. 2258.

[4] F. Siohan *et al.*, J. Phys. **G4**, 1169 (1978).

[5] H. H. Mielke, M. Föller, J. Engler, and J. Knapp, J. Phys. G **20**, 637 (1994).

[6] R. M. Baltrusaitis *et al.*, Phys. Rev. Lett. **52**, 1380 (1984).

[7] M. Honda *et al.*, Phys. Rev. Lett. **70**, 525 (1993).

[8] M. Aglietta *et al.* (1999). In Proc. of 26th International Cosmic Ray Conference (ICRC 99), Salt Lake City, Utah, 17-25 Aug 1999, vol. 1, p. 143.

[9] T. Hara *et al.*, Phys. Rev. Lett. **50**, 2058 (1983).

[10] S. P. Knurenko, V. R. Sleptsova, I. E. Sleptsov, N. N. Kalmykov, and S. S. Ostapchenko (1999). In Proc. of 26th International Cosmic Ray Conference (ICRC 99), Salt Lake City, Utah, 17-25 Aug 1999, vol. 1, p. 372-375.

[11] K. Belov, Nucl. Phys. Proc. Suppl. **151**, 197 (2006).

[12] J. Ranft, Phys. Rev. **D51**, 64 (1995).

[13] T. Pierog and K. Werner (2006). astro-ph/0611311.

[14] H. J. Drescher, M. Hladik, S. Ostapchenko, T. Pierog, and K. Werner, Phys. Rept. **350**, 93 (2001). hep-ph/0007198.

[15] N. N. Kalmykov, S. S. Ostapchenko, and A. I. Pavlov, Nucl. Phys. Proc. Suppl. **52B**, 17 (1997).

[16] S. Ostapchenko, Phys. Rev. **D74**, 014026 (2006). hep-ph/0505259.

[17] R. Engel, T. K. Gaisser, T. Stanev, and P. Lipari (1999). In Proc. of 26th International Cosmic Ray Conference (ICRC 99), Salt Lake City, Utah, 17-25 Aug 1999, p. 415-418.

[18] R. S. Fletcher, T. K. Gaisser, P. Lipari, and T. Stanev, Phys. Rev. **D50**, 5710 (1994).

[19] R. Ulrich, J. Blumer, R. Engel, F. Schussler, and M. Unger (2006). In Proc. of XIV ISVHECRI 2006, Weihai, China, 2006, astro-ph/0612205.

[20] T. Bergmann *et al.*, Astropart. Phys. **26**, 420 (2007). astro-ph/0606564.

[21] J. Matthews, Astropart. Phys. **22**, 387 (2005).

[22] J. Alvarez-Muniz, R. Engel, T. K. Gaisser, J. A. Ortiz, and T. Stanev, Phys. Rev. **D69**, 103003 (2004). astro-ph/0402092.

[23] R. Ulrich, J. Blumer, R. Engel, F. Schussler, and M. Unger (2007). In Proc. of 30th International Cosmic Ray Conference (ICRC 07), Merida, Mexico, 2007, 2007, vol. 1, p. 143, arXiv:0706.2086 [astro-ph].

EAS-TOP:The proton-air inelastic cross-section at $\sqrt{s} \approx 2$ TeV

G.C. Trinchero[1,2] *on behalf of the EAS-TOP Collaboration*
[1]Istituto di Fisica dello Spazio Interplanetario, INAF, Torino, Italy,
[2]Istituto Nazionale di Fisica Nucleare, Torino, Italy

Abstract
The proton-air inelastic cross section measurement at $\sqrt{s} \approx 2$ TeV from the EAS-TOP Extensive Air Shower experiment is reported. The technique exploits cosmic ray proton primaries in the energy region $E_0 = (1.5 \div 2.5) \cdot 10^{15}$ eV, studying the absorption length of their cascades when detected at maximum development. Primary energies are selected through the EAS muon number (N_μ), and proton originated cascades at maximum development by means of the shower size (N_e). The obtained value of the *p*-air inelastic cross section at $\sqrt{s} \approx 2$ TeV is $\sigma^{inel}_{p-\mathrm{air}}$=365$\pm$24(*stat*)-28(*sys*) mb. The statistical and systematic uncertainties, as well as the connections with the *pp* total cross section measurements are discussed.

1 Introduction

Hadronic cross section measurements at energies above the accelerators' limits have to be performed by exploiting the cosmic ray beam. This holds in particular for nucleus-nucleus interactions as the typical *p*-N, *p*-O ("*p*-air") ones, which rule the development of Extensive Air Showers (EAS).

The most relevant datum to which the EAS development is sensitive, is the *p*-air inelastic cross section ($\sigma^{inel}_{p-\mathrm{air}}$). In the present work we will address to its measurement. We will focus on primary energies $\sqrt{s} \approx 2$ TeV, which are of particular interest, as discussed in the following.

The *pp* total cross section, $\sigma^{tot}_{p\bar{p}}$, and $\sigma^{inel}_{p-\mathrm{air}}$ are related and can be inferred from each other by means of Glauber theory [1]. The whole procedure is model dependent, the results [2–7] differing of about 20% for $\sqrt{s}$ values in the TeV energy range. It is therefore of primary interest to have experimental measurements of $\sigma^{inel}_{p-\mathrm{air}}$ and $\sigma^{tot}_{p\bar{p}}$ at the same CM energies, i.e. around $\sqrt{s} \approx 2$ TeV, at which collider data are still available.

At the highest energies, the direct accelerator measurements themselves can be affected by systematic uncertainties of difficult evaluation, and, as a matter of fact, the available *pp* ($\bar{p}p$) cross section data at energies of $\sqrt{s} = 1.8$ TeV differ of about 10%, which exceeds the statistical uncertainties of the individual measurements [8–10] introducing further uncertanties in the *p*-nucleus cross section determination.

From the point of view of cosmic ray physics, the interpretation of Extensive Air Shower measurements (and therefore the energy determinations and the studies of primary composition) rely on simulations based on hadronic interaction models. Such models are based on theoretically guided extrapolations of the accelerator data obtained at lower energies (and usually restricted to limited kinematical regions).

A direct measurement of $\sigma^{inel}_{p-\mathrm{air}}$ and the comparison of basic quantities as obtained from measurements and model based simulations, in the same conditions, is therefore highly desirable for the validation of the methodology. This can be best performed at primary energies below the steepening (*knee*) of the primary spectrum (i.e. $\mathrm{E}_0 < 3 \cdot 10^{15}$ eV, $\sqrt{s} < 2.5$), where, in particular conditions, proton primaries can be reliably selected.

Following the particle array technique [11–13], the primary energy is first selected from the muon number (N_μ). Proton induced showers at maximum development are selected from the shower size (dominated by the electron number, N_e). The absorption in the atmosphere of such showers is related to the cross section of the primary. The observed absorption length (λ_{obs}), obtained through their angular distribution at observation level, is also affected by the fluctuations in the longitudinal development of the cascades and in the detector response. Such fluctuations can be studied through simulations, providing the conversion factor *k* between the observed absorption length and the interaction length of primary protons (k=$\lambda_{obs}/\lambda_{int}$).

2 The experiment and the simulation

The EAS-TOP array was located at Campo Imperatore, National Gran Sasso Laboratories, 2005 m a.s.l., 820 $\mathrm{g/cm^2}$ atmospheric depth.

The e.m. detector consisted of 35 modules $10\ \mathrm{m}^2$ each of plastic scintillators, 4 cm thick, distributed over an area of $10^5\ \mathrm{m}^2$. In the present work, events with at least six modules fired in a compact configuration, and the largest number of particles recorded by a module internal to the edges of the array are selected. Such triggering condition is fully efficient for $\mathrm{N}_e > 10^5$, i.e. for primary energies $E_0 > 3 \cdot 10^{14}$ eV for primary protons. Core location (X_c, Y_c), shower size (N_e), and slope of the lateral distribution function (s) are obtained by fitting the recorded number of particles in each module with the Nishimura-Kamata-Greisen (NKG) expression [14]. The resolutions of such measurements for $\mathrm{N}_e > 2 \cdot 10^5$ are: $\sigma_{N_e}/\mathrm{N}_e \simeq 0.1$; $\sigma_{X_c} = \sigma_{Y_c} \simeq 5$ m; $\sigma_s \simeq 0.1$. The arrival direction of the shower is measured from the times of flight among the modules with resolution $\sigma_\theta \simeq 0.9^o$. A detailed discussion of the performances of the e.m. detector is reported in Ref. [15].

The muon-hadron detector (MHD), located at an edge of the e.m. array, for the present analysis is used as a tracking module of 9 active planes. Each plane includes two layers of streamer tubes (12 m length, $3 \times 3\ \mathrm{cm}^2$ section) and is shielded by 13 cm of iron. The total height of the detector is 280 cm and the surface is $12 \times 12\ \mathrm{m}^2$. A muon track is defined by the alignment of at least 6 fired wires in different streamer tube layers defining an energy threshold of $E^{th}_\mu \approx 1$ GeV. The muon counting accuracy is $\Delta N_\mu < 1$ for $N_\mu < 15$ reaching $\Delta N_\mu < 2$ for $N_\mu < 30$.

Events with core distance from the muon detector 50 m $< r <$ 100 m, and up to zenith angle θ = 33.6^o are used (*"r−θ"* selection), for a total of 1.7·10^6 events.

Simulations are performed in order to obtain the event selection parameters (muon number for primary energy and shower size for proton shower at maximum development) and the k=$\lambda_{obs}/\lambda_{int}$ value, relating the observed absorption length to the interaction length, i.e. the contribution of fluctuations in the shower development and detector response.

In the present analysis we use the CORSIKA EAS simulation program [16] with the

QGSJET (QGSJET 01) high energy hadronic interaction model [17], that has shown to provide consistent descriptions of different shower parameters in the considered energy range both at sea level and mountain altitudes [18, 19]. Hadrons with energies below 80 GeV are treated with GHEISHA 2002 [20] interaction model.

The full response of the muon detector is included by means of simulations based on the GEANT code [21] taking into account the measured experimental efficiencies of the streamer tubes.

For the e.m. detector, parameterized expressions of the fluctuations and experimental uncertainties have been included, as well as trigger requirements. The muon contribution to N_e is added by using the average ldf (its overall contribution being anyway lower than 5%).
Poissonian fluctuations and parameterized expressions of experimental uncertainties have been included, as well as trigger requirements.

Simulated events have been treated following the same procedure as the experimental data. More than 10^6 proton showers have been simulated with energy threshold 10^{15} eV, spectral index $\gamma = 2.7$ (from which KASCADE spectra [22] have been afterward sampled), and uniform angular distribution. Every shower has been sampled over an area of $4.4{\cdot}10^5$ m^2 till the event fulfills the *"$r-\theta$"* and trigger requirements. The number of trials ($n_T(\theta)$) is recorded and used to obtain the angular acceptance.

3 The method and the analysis

The frequency of showers of given primary energy ($E_{0,1} < E_0 < E_{0,2}$) selected through their muon number N_μ ($N_{\mu,1} < N_\mu < N_{\mu,2}$) and shower size N_e corresponding to maximum development ($N_{e,1} < N_e < N_{e,2}$) is expected and observed to decrease exponentially with atmospheric depth through its zenith angle dependence:

$$f(\theta) = G(\theta) f(0) \exp[-x_0(\sec\theta - 1)/\lambda_{\rm obs}] \qquad (1)$$

where x_0 is the vertical atmospheric depth of the detector, and $G(\theta)$ the angular acceptance.

The observed absorption length $\lambda_{\rm obs}$, obtained from (1), is a combination of the interaction mean free path ($\lambda_{\rm int}$), and of the shower development and detector response fluctuations. Fluctuation effects are evaluated through simulations, by comparing the observed (λ_{obs}^{sim}) and interaction (λ_{int}^{sim}, which is known from the interaction model) lengths, and are expressed through the factor $k = \lambda_{obs}^{sim}/\lambda_{int}^{sim}$. Such factor is used to convert the observed experimental absorption length λ_{obs}^{exp} into the interaction one λ_{int}^{exp}.
The physical quantities required for the analysis are obtained through simulations as described in the following.
Events in the desired proton primary energy range ($E_0 = (1.5 \div 2.5) \cdot 10^{15}$ eV) are selected by means of a matrix of minimum ($N_{\mu,1}$) and maximum ($N_{\mu,2}$) detected muon numbers for each possible combination of zenith angle and core distance from the muon detector. The selection table is obtained from simulated data for 5 m bins in core distance (50 m $\leq$ r $\leq$ 100 m) and 0.025 $\sec\theta$ bins ($1.0 \leq \sec\theta \leq 1.2$) for zenith angle. $N_{\mu,1}$ and $N_{\mu,2}$ correspond respectively to the average muon numbers for $1.5{\cdot}10^{15}$ eV and $2.5{\cdot}10^{15}$ eV. The selection of proton initiated

cascades near maximum development is based on the simulated distribution of the shower size at maximum development N_e^{max} independently of the atmospheric depth at which it is reached. Choosing the shower size interval $\overline{LogN_e^{max}} \pm \sigma_{LogN_e^{max}}$ (i.e. 6.01< Log N_e < 6.16) provides the selection of the peak of the distribution and of about 65% of the events.
The effective energy distribution of the selected primaries, obtained following the KASCADE spectra, is shown in Fig. 1, the median value being $E_0^{median} = 2.3 \cdot 10^{15}$ eV with HWHM $0.7 \cdot 10^{15}$ eV and systematic uncertainty lower than 10%.

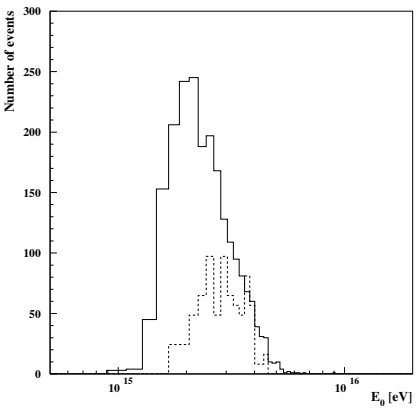


Fig. 1: Primary energy distribution of simulated proton events selected with the N_μ-N_e cuts (continuous line). The energy distribution of helium primaries satisfying the selection criteria is also shown (dashed line).

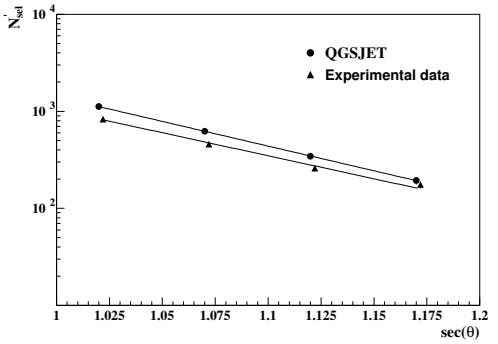


Fig. 2: Acceptance corrected event numbers vs. secθ for the simulated and experimental data selected with the N_μ-N_e cuts. The fits with expression (1) providing the λ_{obs} values are also shown (continuous lines).

The interaction length λ_{int}^{sim} is obtained as the average proton interaction depth in the selected energy range ($E_0 = (1.5 \div 2.5) \cdot 10^{15}$ eV), and results to be $\lambda_{int}^{sim} = 61.2 \pm 0.1$ g/cm^2.

The acceptance corrected numbers of selected events N'_{sel} vs. zenith angle are shown in Fig. 2. The fit with expression (1) provides $\lambda_{obs}^{sim} = 70.4 \pm 3.0$ g/cm^2, and therefore $k = \lambda_{obs}^{sim}/\lambda_{int}^{sim} = 1.15 \pm 0.05$.
The contamination due to heavier primary particles has been evaluated by simulating the helium contribution, assuming the KASCADE spectrum and composition, which accounts for a flux about twice the proton one in the energy range of interest (see Fig. 1).

4 Results and discussion

The same procedure as discussed for the simulation is applied to the experimental data. The corresponding event numbers as a function of sec(θ) are shown in Fig. 2, together with their fit providing $\lambda_{obs}^{exp} = 76.0 \pm 3.8$ g/cm^2. From $\lambda_{int}^{exp} = \lambda_{obs}^{exp}/k$, we obtain $\lambda_{int}^{exp} = \lambda_{p-\mathrm{air}} = 66.1 \pm 4.4$ g/cm^2 where the uncertainties are due to the statistics of the measurement and of the simulation (of the same order).

The *p*-air inelastic cross section is obtained from: $\sigma_{p-\mathrm{air}}^{\mathrm{inel}}(\mathrm{mb}) = 2.41 \cdot 10^4/\lambda_{p-\mathrm{air}}$, and

results to be $\sigma^{\rm inel}_{p-{\rm air}} = 365 \pm 24{\rm mb}$. Such value is plotted together with other experimental data and the values derived from the current hadronic interaction models in Fig. 3, resulting respectively about 10% and 15% smaller than QGSJET and SIBYLL [23] cross sections and in better agreement with the QGSJET modified version of Ref. [24].

Predicted $\sigma^{\rm inel}_{p-{\rm air}}$ values, that were obtained from different $\sigma^{tot}_{p\bar{p}}$ Tevatron measurements at $\sqrt{s} = 1.8$ TeV by using different calculations based on the Glauber theory, are reported in Fig. 4. The present measurement is in better agreement with the smaller values of the $\bar{p}p$ total cross section ($\sigma^{tot}_{p\bar{p}}$=72.8±3.1 mb [9], and $\sigma^{tot}_{p\bar{p}}$=71±2 mb [10]), and the *pp* to *p*-air cross section conversions of Refs. [3, 5, 6].

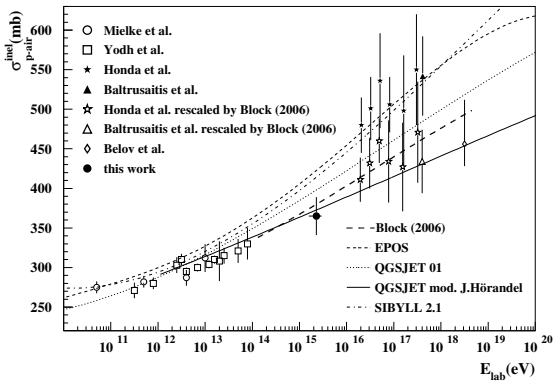


Fig. 3: *p*-air inelastic cross section data, including the present measurement, and values in use from hadronic interaction models.

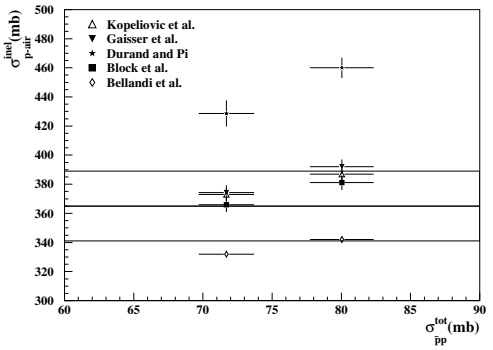


Fig. 4: Present measurement of the *p*-air inelastic cross section (± 1 s.d., solid lines) vs. the $\bar{p}p$ data reported at $\sqrt{s} = 1.8$ TeV. Results of different calculations are also shown.

Taking into account helium primaries, the overall simulated observed absorption length becomes $\lambda^{sim(p+He)}_{obs}$ = 65.2±3.6 g/cm^2, which implies k$^{(p+He)}$ = 1.07±0.06 , and $\lambda^{exp(p+He)}_{int}$ = 71.4 ±5.3 g/cm^2, i.e. increased of about 8%. Due to the uncertainty of the relative proton/helium flux we will not introduce such a correction, but rather consider it as a systematic uncertainty, possibly increasing the interaction length, and therefore leading to an overestimated cross section value expressed as:

$\sigma^{inel}_{p-{\rm air}}(\sqrt{s} \approx 2$ TeV)=365±24(*stat*)-28(*sys*)mb.

Independently from the cross-section analysis, the measured value of the absorption length ($\lambda^{exp}_{obs} = 76.0 \pm 3.8$ g/cm^2) can be directly compared with the analogous one obtained, for the same experimental conditions, from simulations based on QGSJET ($\lambda^{sim}_{obs} = 70.4 \pm 3.0$ g/cm^2). Inside the still large uncertainties, the measured value results nearly 10% larger than the simulated one (and it would be even larger including the helium contribution), showing a deeper penetration of showers in the atmosphere than predicted by the interaction model, as reflected in the corresponding smaller value of the *p*-air inelastic cross section (see also ref. [24]).

5 References

1. R. J. Glauber and G. Matthiae, Nucl. Phys. B., **21** (1970) 135.
2. R. Engel et al., Phys. Rev. D, **58** 014019 (1998).
3. T. K. Gaisser et al., Phys. Rev. D, **36** (1987) 1350.
4. L. Durand and H. Pi, Phys. Rev. D, **38** (1988) 78-84
5. B. Z. Kopeliovich, Phys. Rev. D, **39** (1989) 769-779.
6. M. M. Block, Phys. Rep., **436** (2006) 71-215.
7. J. Bellandi et al., Phys. Lett. B **343** (1995) 410.
8. F. Abe et al., Phys. Rev. D, **50** (1994) 5550.
9. N. A. Amos et al., Phys. Lett. B, **243** (1990) 158.
10. C. Avila et al., Phys. Lett. B, **445** (1999) 419.
11. T. Hara et al., Phys. Rev. Lett., **50** (1983) 2058.
12. M. Honda et al., Phys. Rev. Lett., **70** (1993) 525.
13. M. Aglietta et al., Nucl. Phys. B, **75A** (1999) 222.
14. K. Kamata and J. Nishimura, Prog. Theor. Pys. Suppl., **6** (1958) 93.
15. M. Aglietta et al., Nucl. Inst. Meth. Phys. Res. A, **336** (1993) 310.
16. D. Heck et al., Report **FZKA 6019**, Forschungszentrum Karlsruhe (1998).
17. N. N. Kalmykov, S. S. Ostapchenko and A. J. Pavlov, Nucl. Phys. B, **52** (1997) 17.
18. T. Antoni et al, J. Phys. G: Nucl. Part. Phys. **25** (1999) 1-15.
19. M. Aglietta et al. Astropart. Phys., **21** (2004) 583-596.
20. Fesefeldt H., PITHA-85/02 (RWTH, Aachen) (1985).
21. R. Brun and F. Carminati, CERN Program Library Long Writeup W5013, (1994).
22. T. Antoni et al, Astropart. Phys., **24** (2005) 1-25.
23. R. Engel et al. Proc. $26^{\rm th}$ Int. Cosmic Ray Conf., Salt Lake City (USA), **1** (1999) 415.
24. J.R. Hörandel, J. Phys. G: Nucl. Part. Phys. **29** (2002) 2439.
25. K. Werner, F.M. Liu and T. Pierog, Phys. Rev. C **74** (2006) 044902.

UHE Cosmic Rays above 10^{17} eV: The role of percolation

J. Alvarez-Muñiz[1] †, *P. Brogueira*[2], *R. Conceição*[3], *J. Dias de Deus*[2,4], *M.C. Espírito Santo*[2,3], *M. Pimenta*[2,3].
[1] Dept. Física Partículas & IGFAE, Univ. Santiago de Compostela, 15782 Santiago, SPAIN,
[2]Departamento de Física, IST, Av. Rovisco Pais, 1049-001 Lisboa, PORTUGAL,
[3]LIP, Av. Elias Garcia, 14-1, 1000-149 Lisboa, PORTUGAL,
[4]CENTRA, Av. Rovisco Pais, 1049-001 Lisboa, PORTUGAL

Abstract
We show that the string percolation hadronic model provides a consistent interpretation of the experimentally measured energy dependence of the depth of shower maximum as well as of the muon content in ultra high energy cosmic ray showers above 10^{17} eV. We discuss the importance of the inelasticity and of the particle multiplicity in the most energetic shower interactions, as well as the crucial role played by the nature of the leading primary.

1 Introduction

The composition of ultra high energy cosmic rays (UHECRs) is only determined indirectly through the observation of two shower variables that are used as experimental handles on composition, namely, the atmospheric depth of shower maximum $X_{\max}$, measured in fluorescence detectors, and the muon content of the shower on ground N_μ, measured in surface array detectors.

Fly's Eye/HiRes experimental data on the energy dependence of $X_{\max}$ show an increase in the slope around 10^{17} eV. Concerning the muon component, at the AGASA array the lateral distribution function of muons was measured above 10^{17} eV and combined with the Akeno array data. It was observed that the slope of the density of muons at 600 m from the shower core $\rho_\mu(600)$ vs E is flatter in data than predicted by hadronic models. Assuming $\rho_\mu \propto E^\beta$, data gives $\beta = 0.84 \pm 0.02$ [1, 2], while from simulation $\beta \sim 0.9$ ($\beta = 0.92$, 0.89 and 0.93 for protons with QGSJET-II.03, SIBYLL2.1 and EPOS 1.61 respectively). Both features have been interpreted as a change in composition, going from more Fe-like to more proton-like showers. An alternative interpretation is that these energy dependences are due to a change with energy of the features of the hadronic interactions. In this spirit, we show in this work that the string percolation model provides a consistent interpretation of the energy dependence of $X_{\max}$ and N_μ in cosmic ray data above 10^{17} eV.

2 The two interpretations of UHE Cosmic Ray data

2.1 The "change in composition" interpretation

In order to make the argument simple, we use the original Heitler model of shower development [3]. The average location of $X_{\max}$ in a shower initiated by a primary nucleus of energy E and

† speaker

mass A, is given by $\bar{X}_{\rm max} \simeq \bar{X}_1 + \bar{X}_0 \log(E/A)$, where $\bar{X}_1$ is the average depth of the first collision and $\bar{X}_0$ is the elongation rate. The muon content of the shower can be written as, $\bar{N}_\mu \simeq A(E/A)^\beta$. We then have,

$$\frac{d\bar{X}_{\rm max}}{d\log E} = \bar{X}_0 \left[1 - \frac{d\log A}{d\log E}\right], \tag{1}$$

and for the $\log N_\mu$ dependence on E,

$$\frac{d\log N_\mu}{d\log E} = (1-\beta)\frac{d\log A}{d\log E} + \beta\,. \tag{2}$$

As experimentally, above 10^{17} eV $d\bar{X}_{\rm max}/d\log E$ is larger and $d\log N_\mu/d\log E$ is slightly smaller, in comparison with lower energies, the conclusion is:

$$\frac{d\log A}{d\log E} < 0\,, \tag{3}$$

i.e., for $E \gtrsim 10^{17}$ eV the average mass number should, in this interpretation, decrease with E.

2.2 The "change in the features of hadronic interactions" interpretation

In this interpretation a key role is given to the variables characterising the first hadronic collisions. Among them the most relevant for shower development are the inelasticity K, defined as the fraction of energy distributed among the secondary particles except for the leading particle, the average (non-leading) multiplicity $\langle n\rangle$ at the collision energy and P_0, the probability of producing a leading π^0 in the collision.

Changing A has a similar effect on the behavior of $X_{\rm max}$ and N_μ with energy as changing K. The fastest particle in the collision, carrying an energy $(1-K)E$, will originate the shower branches that go deeper in the atmosphere. We can then write, $\bar{X}_{\rm max} \simeq \bar{X}_1 + \bar{X}_0 \log[(1-K)\frac{E}{E_0}]$, where E_0 is a low energy threshold. Regarding the muon content of the shower, a possible assumption is that while energy flows in the $(1-K)$ direction, the number of muons flows in the K direction and $N_\mu \sim N_\pi^\pm \propto KE$. We thus have,

$$\frac{d\bar{X}_{\rm max}}{d\log E} = \bar{X}_0 \left[\frac{d\log(1-K)}{d\log E} + 1\right]\,, \tag{4}$$

and

$$\frac{d\log N_\mu}{d\log E} = \frac{d\log K}{d\log E} + 1\,, \tag{5}$$

Since above 10^{17} eV, $d\bar{X}_{\rm max}/d\log E$ is larger and $d\log N_\mu/d\log E$ smaller than at lower E, we infer that:

$$\frac{d\log K}{d\log E} < 0\,, \tag{6}$$

i.e., some of the features in CR data can be alternatively explained by an inelasticity K decreasing with E.

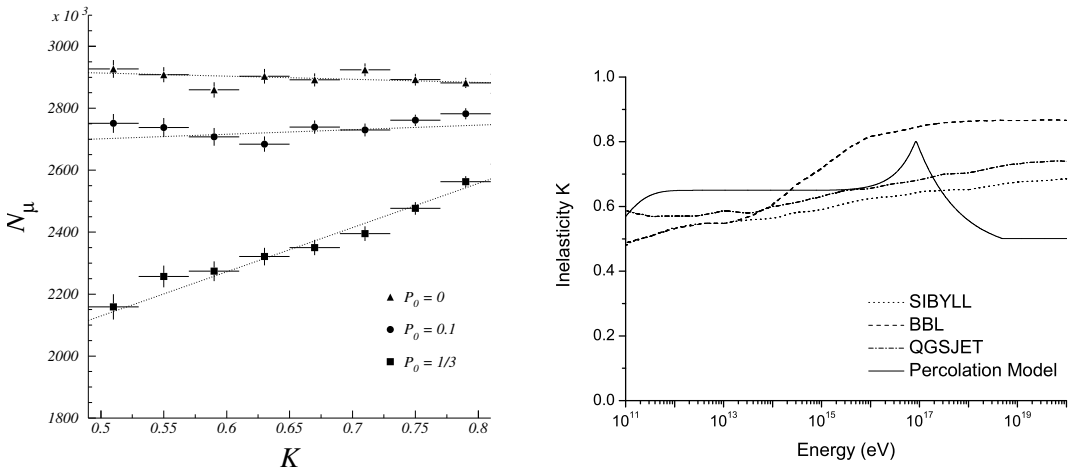


Fig. 1: Left: Hybrid Monte Carlo simulation prediction for the number of muons at ground as a function of inelasticity for different values of the probability P_0 of having a leading π^0 in a proton-induced shower of $E = 10^{18}$ eV. Right: Energy dependence of the average inelasticity K. The dotted curve is the SIBYLL simulation; the dashed-dotted curve corresponds to QGSJET simulations; and the dashed line is a model of [8]; the full line is our percolation model.

Moreover, the nature of the leading particle, plays a fundamental role in the interpretation of cosmic ray data, affecting the relation $N_\mu \propto K$. In fact, when the leading particle is a proton carrying an energy $(1-K)E$, the number of muons decreases with K due to the combination of two effects: on one hand the production of secondary π^0s, which decay into γs, carrying an energy $\sim 1/3\ KE$ that is lost for muon production, and on the other hand, the larger the K the smaller the energy carried by the leading particle, and hence the smaller the number of new charged pions and muons reaching ground it will produce. However, if π^0's are themselves leading particles - $P_0 > 0$, muons can only be produced in the K direction and N_μ is larger the larger the inelasticity. This can be seen in a very simplistic model in which the number of muons is proportional to the energy available for muon production in the first interaction $N_\mu \sim (1-P_0)\ (1-K)E + (2/3)\ KE$, where the factors $(1-P_0)$ and $2/3$ account for the energy lost into the electromagnetic branch. As a consequence,

$$\frac{dN_\mu}{dK} \sim (P_0 - \frac{1}{3})E, \tag{7}$$

showing that the behavior of N_μ with K depends on P_0. The fact that it inflects at the particular value $P_0 = 1/3$ comes from the very simplistic treatment and should not be taken seriously. This effect has been confirmed by a numerical implementation of P_0 in a full hybrid Monte Carlo simulation of shower development [4]. The crucial role played by P_0 on the dependence of N_μ with K is apparent in the left panel of Fig. 1.

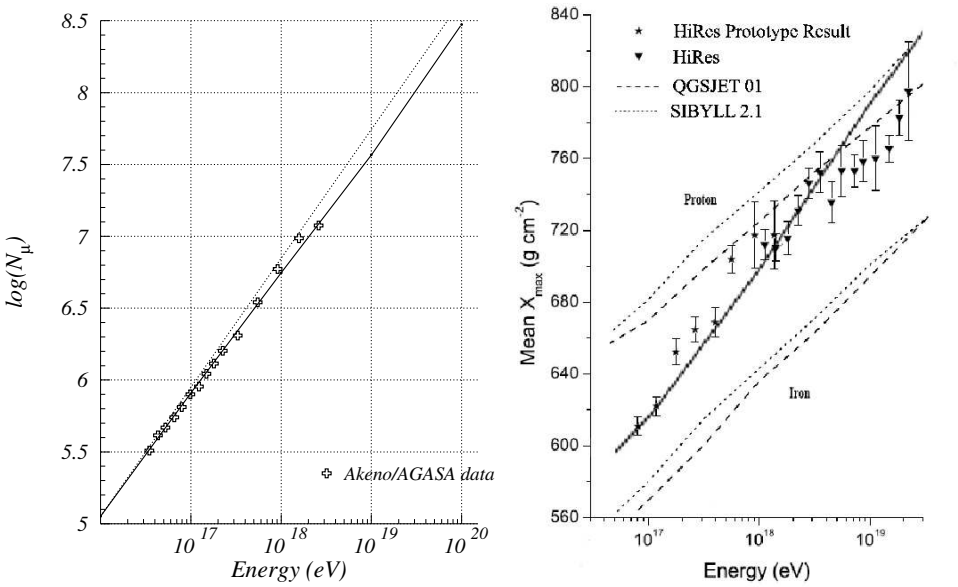


Fig. 2: Left: N_μ vs E. The results of the string percolation model (solid line) are compared to the Akeno/AGASA data (crosses). The dotted line corresponds to $N_\mu \propto E^{0.9}$ as predicted by most of the standard hadronic models. Right: $X_{\max}$ vs E in the percolation model (solid line) along with data (symbols) and the predictions of SIBYLL and QGSJET.

3 The role of the string percolation model

In string models of hadronic interactions, multiparticle production is described in terms of colour strings stretched between partons of the projectile and target particles. Colour strings might be viewed as small discs in the transverse space of radius $r_0 \sim 0.2$ fm, filled with the colour field. These strings fragment into new strings through $q - \bar{q}$ production and subsequently hadronize into particles. At low energy, valence strings are formed, forward and backward in the center of mass frame, containing most of the collision energy. As the energy increases additional sea strings, central in rapidity, are created carrying part of the energy of the valence strings. Softer secondaries are produced and the inelasticity increases with energy. With growing energy and/or atomic number of colliding particles, the number of strings increases further, and they begin to overlap forming clusters. A cumulative effect then occurs, the length in rapidity of fused strings is larger than that of individual strings and fast particles are produced. As a consequence, the inelasticity K starts to decrease with energy as can be seen in Fig. 1 [5]. The onset of this effect has been estimated in [5] to occur above $\sim 10^{17}$ eV for proton-proton collisions when the area occupied by the overlapping strings is ~ 1.13 times the area of the interaction region. Percolation also affects the multiplicity. Due to the fusion of strings less softer secondaries are produced and the multiplicity is reduced with respect to models in which strings decay independently. Moreover, and since fused strings are sea strings of the $q - \bar{q}$ type, the fast leading secondaries that are produced can be π^0s with a probability P_0 that tends to 0.3.

These predictions are in contrast with those of string models with no string fusion, in which the inelasticity and multiplicity increases monotonically with energy, and the probability

of π^0 being the leading particle is $P_0 \sim 0.1$ at most.

In order to test the effects of these predictions on the air shower observables, $X_{\max}$ and N_μ, we have implemented them into a hybrid and fast Monte Carlo simulation of shower development in the atmosphere described in [4]. In particular we have implemented an inelasticity K decreasing with energy [6] as shown in Fig. 1, a reduction of the multiplicity realized through a color summation factor [5], and a probability $P_0 = 0.3$ of the leading particle being a π^0, in all hadronic interactions above 10^{17} eV. In the left panel of Fig. 2 we show the prediction of percolation on the behavior of N_μ with E. A fit to our results yields $\beta = 0.83$ compatible with the experimental value measured by the Akeno/AGASA array $\beta = 0.84 \pm 0.02$. It is important to notice that in this study protons were used as primaries and the result in Fig. 2 corresponds to shifting the proton result to an intermediate and constant composition $A \sim 20$ using that $N_\mu \sim A(E/A)^\beta$. It is interesting to note that when $E > 10^{19}$ eV, the Lorentz boost factor of π^0s is large enough so that they begin to interact in the atmosphere instead of decaying, increasing the production of muons, steepening the slope of N_μ vs E line. A hint of this effect is clearly seen in the left panel of Fig. 2. This behaviour is consistent with observations of the total number of muons at the ground in inclined hybrid events collected at the Pierre Auger Observatory above 6.3×10^{18} eV [7].

In the right panel of Fig. 2 we show the prediction of the string percolation model on the behaviour of $X_{\max}$ with E along with the predictions of other models based on QCD taken from [8]. The prediction is reasonably consistent with data, following the tendency of the slope around 10^{17} eV. A slight overshoot of $X_{\max}$ can be seen at $E > 10^{18.5}$ eV which we believe might be due to the constant value of $P_0 = 0.3$ used in all interactions instead of a smoothly increasing function of the energy. The solid line in Fig. 2 corresponds to the prediction for proton primaries scaled by a constant composition of $A \sim$ 15-20, assuming $X_{\max} \sim \log(E/A)$. It is important to remark that the value of A is the same with which the N_μ vs E prediction was scaled.

4 Conclusions, discussion and outlook

We have shown that, in the interpretation of the energy dependence of the depth of the shower maximum and of the muon content in high energy cosmic ray showers ($E \gtrsim 10^{17}$ eV), other variables besides the composition may play an important role, in particular those characterising the first (high energy) hadronic collisions. The role of the inelasticity K, the probability P_0 of the leading particle being a π^0, and the particle multiplicity $< n >$ were discussed. Special emphasis has been put on the crucial role played by P_0 on the dependence of the number of muons with K.

For the first time the predictions of the behaviour of these variables in a string percolation model were included systematically and used to derive predictions on the behaviour of the depth of the shower maximum X_{max} and on the number of muons in the shower N_μ as a function of the energy. The model reasonably describes the trends seen in data.

The next step will be to create a full Monte Carlo simulation including percolation, adapted to the low and high energy regions and including proton-air and nuclei-air collisions where more complex effects may arise. Also we should account for the fact that the clusters of percolating

strings have a large colour content, and an increased production of baryons is likely and cannot be neglected since it affects the number of muons in the shower [9].

References

[1] M. Nagano *et al.*, Astropart. Phys. **13**, 277 (2000).

[2] N. Hayashida *et al.*, J. Phys. G **21**, 1101 (1995).

[3] M. Heitler, *The Quantum Theory of Radiation*. Oxford University Press, 1944.

[4] J. Alvarez-Muniz *et al.*, Phys. Rev. D **66**, 033011 (2002).

[5] J. D. de Deus *et al.*, Phys. Rev. Lett. **96**, 162001 (2006).

[6] J. Alvarez-Muniz *et al.*, Astropart. Phys. **27**, 271 (2007).

[7] The Pierre Auger Collaboration, P. Facal, Procs. of the XXX ICRC, Merida, Mexico, p. 319 (2007).

[8] H. Drescher, astro-ph/0411143.

[9] K. Werner *et al.*, these proceedings (2007).

Extended Air Shower Simulations Based on EPOS

Klaus Werner[1]†*and Tanguy Pierog*[2]
[1] SUBATECH, University of Nantes – IN2P3/CNRS– EMN, Nantes, France
[2]Forschungszentrum Karlsruhe, Institut für Kernphysik, Karlsruhe, Germany

Abstract
We discuss air shower simulations based on the EPOS hadronic interaction model. A remarkable feature is the fact that the number of produced muons is considerably larger compared to other interaction models. We show that this is due to an improved treatment of baryon-antibaryon production.

1 Introduction

Air shower simulations are a very powerful tool to interpret ground based cosmic ray experiments. However, most simulations are still based on hadronic interaction models being more than 15 years old. Much has been learned since, in particular due to new data available from the SPS and RHIC accelerators.

In this paper, we discuss air shower simulations based on EPOS, the latter one being a hadronic interaction model, which does very well compare to RHIC data [1, 2], and also all other available data from high energy particle physic experiments (ISR,CDF and especially SPS experiments at CERN).

EPOS is a consistent quantum mechanical multiple scattering approach based on partons and strings [3], where cross sections and the particle production are calculated consistently, taking into account energy conservation in both cases (unlike other models where energy conservation is not considered for cross section calculations [4]). A special feature is the explicit treatment of projectile and target remnants, leading to a very good description of baryon and antibaryon production as measured in proton-proton collisions at 158 GeV at CERN [5]. Nuclear effects related to CRONIN transverse momentum broadening, parton saturation, and screening have been introduced into EPOS [6]. Furthermore, high density effects leading to collective behavior in heavy ion collisions are also taken into account [7].

2 EPOS Basics

One may consider the simple parton model to be the basis of hadron-hadron interaction models at high energies. It is well known that the inclusive cross section is given as a convolution of two parton distribution functions with an elementary parton-parton interaction cross section. The latter one is obtained from perturbative QCD, the parton distributions are deduced from deep inelastic scattering. Although these distributions are taken as black boxes, one should not forget that they represent a dynamical process, namely the successive emission of partons (initial state space-like cascade), as shown in fig. 1(a). We refer to this whole structure as "parton ladder", with a corresponding simple symbol as shown in fig. 1(b), to simplify further discussion.

† speaker

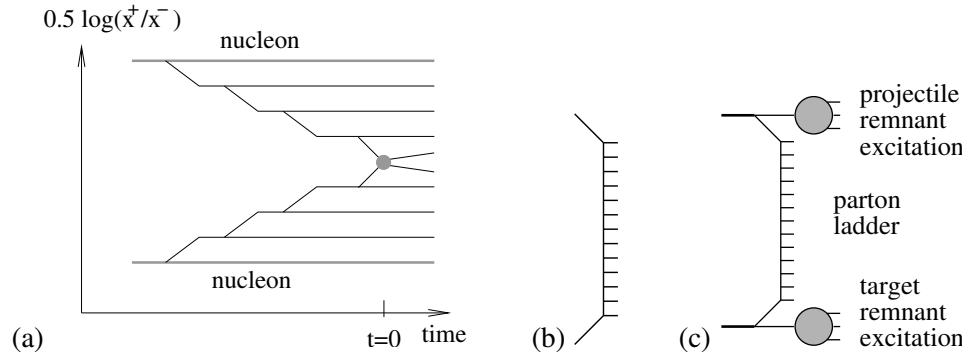


Fig. 1: (a) Elementary parton-parton scattering: the hard scattering in the middle is preceded by parton emissions (initial state space-like cascade). (b) Symbolic parton ladder, representing the structure shown left. (c) The complete picture, including remnants. The remnants are an important source of particle production at RHIC energies.

Actually our "parton ladder" is meant to contain two parts [3]: the hard one, as discussed above, and a soft one, which is a purely phenomenological object, parametrized in Regge pole fashion.

Still the picture is not complete, since so far we just considered two interacting partons, one from the projectile and one from the target. These partons leave behind a projectile and target remnant, colored, so it is more complicated than simply projectile/target deceleration. One may simply consider the remnants to be diquarks, providing a string end, but this simple picture seems to be excluded from strange antibaryon results at the SPS [8].

We therefore adopt the following picture, as indicated in fig. 1(c): not only a quark, but a two-fold object takes directly part in the interaction, being a quark-antiquark, or a quark-diquark, leaving behind a colorless remnant, which is, however, in general excited (off-shell). So we have finally three "objects", all being white: the two off-shell remnants, and the parton ladders between the two active "partons" on either side (by "parton" we mean quark, antiquark, diquark, or antidiquark). We showed in ref. [5] that the "three object picture" as discussed in this paper can solve the "multi-strange baryon problem" of ref. [8].

Even inclusive measurements require often more information than just inclusive cross sections, for example via trigger conditions. Anyhow, for detailed comparisons we need an event generator, which obviously requires information about exclusive cross sections (the widely used pQCD generators are not event generators in this sense, they are generators of inclusive spectra, and a Monte Carlo event is not a physical event). This problem is known since many years, the solution is Gribov's multiple scattering theory, employed since by many authors. This formulation is equivalent to using the eikonal formula to obtain exclusive cross sections from the knowledge of the inclusive one.

We indicated recently inconsistencies in this approach, proposing an "energy conserving multiple scattering treatment" [3]. The main idea is simple: in case of multiple scattering, when it comes to calculating partial cross sections for double, triple ... scattering, one has to explicitly care about the fact that the total energy has to be shared among the individual elementary

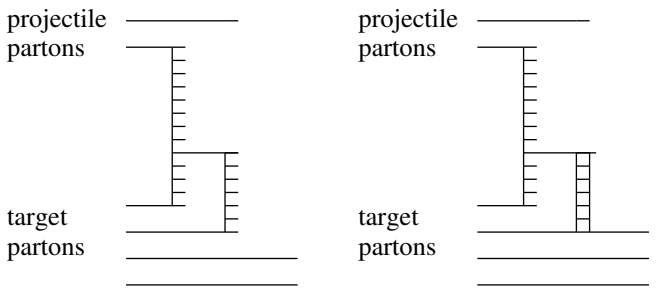


Fig. 2: Inelastic and elastic "rescattering" of a parton from the parton ladder with a second target parton. We talk about (inelastic and elastic) splitting of a parton ladder.

interactions.

A consistent quantum mechanical formulation of the multiple scattering requires not only the consideration of the (open) parton ladders, discussed so far, but also of closed ladders, representing elastic scattering. The closed ladders do not contribute to particle production, but they are crucial since they affect substantially the calculations of partial cross sections. Actually, the closed ladders simply lead to large numbers of interfering contributions for the same final state, all of which have to be summed up to obtain the corresponding partial cross sections. It is a unique feature of our approach to consider explicitly energy-momentum sharing at this level (the "E" in the name EPOS).

3 Splitting of Parton Ladders

Let us consider very asymmetric nucleus-nucleus collisions, like proton-nucleus or deuteron-nucleus. The formalism developed earlier for pp can be generalized to these nuclear collisions, as long as one assumes that a projectile parton always interacts with exactly one parton on the other side, elastically or inelastically (realized via closed or open parton ladders). We employ the same techniques as already developed in the previous section. The calculations are complicated and require sophisticated numerical techniques, but they can be done.

In case of protons (or deuterons) colliding with heavy nuclei (like gold), there is a complication, which has to be taken into account: suppose an inelastic interaction involving an open parton ladder, between a projectile and some target parton. The fact that these two partons interact implies that they are close in impact parameter (transverse coordinate). Since we have a heavy target, there are many target partons available, and among those there is a big chance to find one which is as well close in impact parameter to the two interacting partons. In this case it may be quite probable that a parton from the ladder interacts with this second target parton, inelastically or elastically, as shown in fig. 2.

The main effect of elastic splittingis suppression of small light cone momenta, which agrees qualitatively with the concept of saturation. But this is only a part of the whole story, several other aspects have to be considered [6]. Consider the example shown in figure 2(left). In the upper part, there is only an ordinary parton ladder, so we expect "normal" hadroniza-

tion. In the lower part, we have two ladders in parallel, which are in addition close in space, since they have a common upper end, and the lower ends are partons close in impact parameter, so the hadronization of the two ladders is certainly not independent, we expect some kind of a "collective" hadronization of two interacting ladders. Here, we only considered the most simple situation, one may also imagine three or more close ladders, hadronizing collectively.

The strength of the effects due to parton ladder splitting will depend on the target mass, via the number Z of partons available for additional legs. The number Z of available partons will also increase with energy, so at high enough energy the above-mentioned effects can already happen in pp collisions.

A quantitative discussion how the above-mentionned effects are realized may be found in [6].

4 Air Shower Simulations

In the following, we discuss air shower simulations, based on the shower programs CORSIKA [9] or CONEX [10, 11], using EPOS or QGSJET II-3 [12] (as a reference) as interaction model.

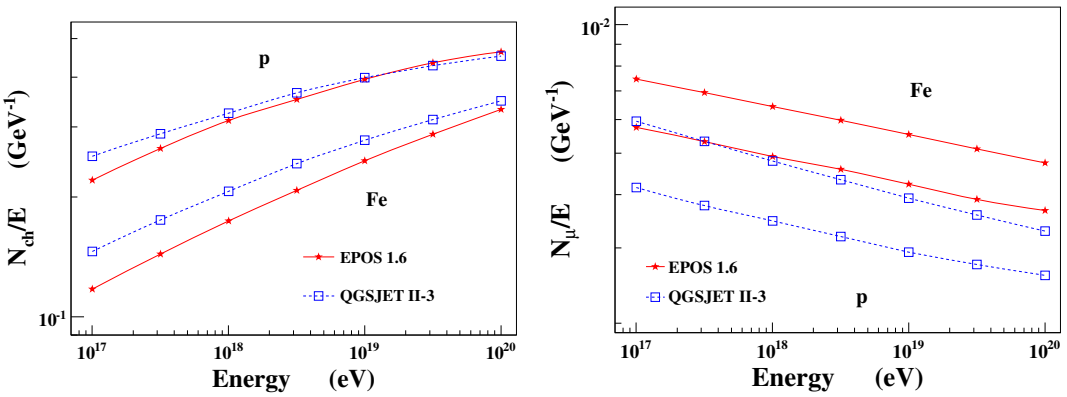


Fig. 3: Total number of charged particles (left plot) and muons (right plot) at ground divided by the primary energy as a function of the primary energy for proton and iron induced shower using EPOS (full lines) and QGSJET II-3 (dotted lines) as high energy hadronic interaction model.

Air shower simulations are very important to analyze the two most common types of high energy cosmic ray experiments: fluorescence telescopes and surface detectors. In the first ones, one observes directly the longitudinal shower development, from which the energy and the depth of shower maximum $\mathrm{X_{max}}$ can be extracted. Comparing the latter with models allows us to have informations on the mass of the primary. EPOS results concerning $\mathrm{X_{max}}$ are in good agreement with former models and experimental data.

Concerning particles measured at ground by air shower experiment, the situation is quite different. Whereas the number of charged particles is very similar for EPOS and QGSJET II-3 (see fig. 3), EPOS produces a much higher muon flux, in particular at high energy. At

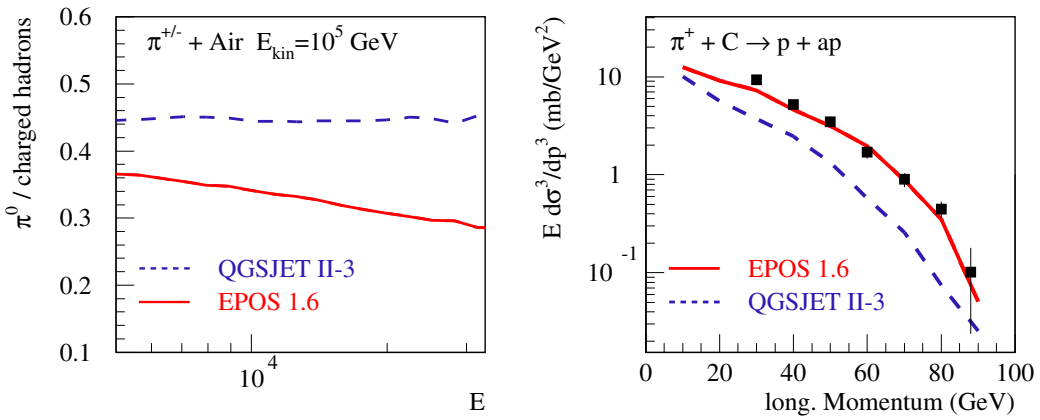


Fig. 4: Left: Ratio of the number of π^0 over the number of charged particles as a function of the energy of the secondary particles at 10^5 GeV kinetic energy with EPOS (full line) or QGSJET II-3 (dashed line) in pion-air. Right: Longitudinal momentum distributions of protons in pion carbon collisions at 100 GeV from EPOS (full) and QGSJET II-3 (dashed) compared to data.

10^{20} eV EPOS is more than 40% higher and gives even more muons with a primary proton than QGSJET II-3 for iron induced showers.

The muon excess from EPOS compared to other models will affect all experimental observables depending on simulated muon results. In the case of the Pierre Auger obervatory (PAO), this will affect mostly the results on inclined showers, for which the electromagnetic component is negligible at ground. It is interesting to notice that the PAO claims a possible lack of muons in air showers simulated with current hadronic interaction models.

5 The origin of the increased muon production

During the hadronic air shower development, the energy is shared between neutral pions which convert their energy into the electromagnetic component of the shower, and charged hadrons which continue the hadronic cascade producing muons. The ratio of the two (referred to as R) is a measure of the muon production.

Comparing EPOS to other models, this ratio R of neutral pions to charged hadrons produced in individual hadronic interactions is significantly lower, especially for pi-air reactions, as seen in fig. 4(left). This will increase the muon production, as discussed above.

Furthermore, the reduced ratio R is partly due to an enhanced baryon production, as shown in fig. 4(right) (data from [14]). This will increase the number of baryon initiated sub-showers. Since the ratio R is much softer in case of proton-air interactions compared to pion-air interactions, this will even more reduce R, providing a significant additional source of muons.

6 Summary

EPOS is a new interaction model constructed on a solid theoretical basis. It has been tested very carefully against all existing hadron-hadron and hadron nucleus data, also those usually not considered important for cosmic rays. In air shower simulations, EPOS provides more muons than other models, which was found to be linked to an increased baryon production.

References

[1] R. Bellwied (STAR Collaboration), arXiv:nucl-ex/0511006.

[2] B. Abelev (STAR Collaboration), arXiv:nucl-ex/0607033.

[3] H. J. Drescher, M. Hladik, S. Ostapchenko, T. Pierog, and K. Werner, Phys. Rept. 350, 93, 2001

[4] M. Hladik, H. J. Drescher, S. Ostapchenko, T. Pierog, and K. Werner *et al.*, Phys. Rev. Lett. **86**, 3506 (2001), arXiv:hep-ph/0102194.

[5] F.M. Liu, J.Aichelin, M.Bleicher, H.J. Drescher, S. Ostapchenko, T. Pierog, and K. Werner, Phys. Rev. D67, 034011, 2003

[6] K. Werner, F. M. Liu, and T. Pierog, Phys. Rev. C **74** (2006) 044902.

[7] K. Werner, Phys. Rev. Lett. 98, 152301 (2007), arXiv: 0704.1270.

[8] M. Bleicher, F. M. Liu, A. Kernen, J. Aichelin, S.A. Bass, F. Becattini, K. Redlich, and K. Werner, Phys.Rev.Lett.88, 202501, 2002.

[9] D. Heck *et al.*, Report **FZKA 6019**, and D. Heck, J. Knapp, Report **FZKA 6097**, Forschungszentrum Karlsruhe (1998).

[10] G. Bossard, H.J. Drescher, N.N. Kalmykov, S. Ostapchenko, A.I. Pavlov, T. Pierog, E.A. Vishnevskaya, and K. Werner, Phys.Rev. **D63**, 054030, (2001)

[11] T. Bergmann *et al.*, arXiv:astro-ph/0606564.

[12] S.Ostapchenko, Phys. Rev.D74, 014026 (2006)

[13] R. Engel, T.K. Gaisser, P. Lipari, T. Stanev, Proc. 26th Int. Cosmic Ray Conf., Salt Lake City, 415 (1999).

[14] D. S. Barton et al., Phys. Rev. D **27** (1983) 2580.

LHCf: a LHC Detector for Cosmic Ray Physics

Alessia Tricomi, on behalf of the LHCf Collaboration
University and INFN Catania, Italy

Abstract
The LHCf experiment has been designed to measure the very forward production of photons and neutral hadrons produced in proton-proton interaction at LHC. These measurements are of essential importance to calibrate the nuclear interaction models used in the Monte Carlo code of air showers, which are used to extract the energy spectra of incoming cosmic rays. Thanks to the unprecedented energy of LHC, LHCf will provide a calibration of nuclear interaction models with real data up to energies relevant to test the most debated region of the cosmic ray energy spectra.

1 Introduction

One of the most debated question in cosmic ray physics is related to the existence of events above the so called GZK cut-off. The existence of these events, if confirmed, poses some intruiguing questions to our understanding of astroparticle physics and, eventually, asks for New Physics in order to explain such a production. Indeed, evidence of Ultra High Energy Cosmic Rays, above the GZK cut-off, has been reported for the first time by the AGASA experiment [1]. On the contrary, the results of the HiRes [2] experiment are consistent with the existence of the cut-off. Recently the AUGER Collaboration [3, 4] reported results consistent with the HiRes ones. A key point which raises observing the cosmic ray energy spectra (Fig. 1) is the importance of the energy scale calibration between different experiments. It has been noted that with a shift by about 20% in the energy scale the disagreement between AGASA and HiRes results almost disappears. Indeed, many of the experimental procedures used to derive the energy spectra of the incoming cosmic rays depend strongly on the nuclear interaction models used in the Monte Carlo codes of the air showers, which amounts for the the main source of systematic uncertainties.

The derivation of the energy spectra is not the only item in cosmic ray physics in which we need to rely on Monte Carlo assumptions. Another open issue is the chemical composition of cosmic rays. Cosmic rays are not purely protons but they contain also heavy nuclei. Nuclear cascade showers initiated by the disintegration of heavy nuclei develop more rapidly in comparison with the showers initiated by protons. Fig. 2 shows the distribution of the shower maximum, X_{MAX}, as obtained by different collaborations around the knee region (10^{16} eV), compared with several different Monte Carlo models [5]. The position of the shower maximum cleary depends on the composition of the cosmic rays. As can be seen from the same Figure, different models predict different composition. Not being sure on which nuclear interaction model one should use, effectively reduces our ability to identify correctly the primary nucleon.

The importance of a correct choice of the nuclear interaction model is hence mandatory for a detailed study of cosmic ray physics. For this reason a detailed calibration of Monte Carlo codes

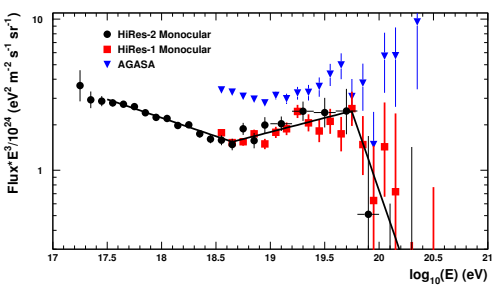


Fig. 1: Energy spectra of cosmic rays at the highest energies. Blue triangles represent the AGASA data, while red and black marks represent the new results from HiRes [2]. A clear discrepacy between AGASA and HiRes can be seen in the region above 10^{20} eV.

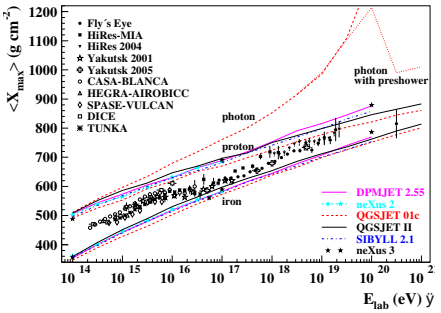


Fig. 2: The position of the shower maximum X_{MAX} is shown as a function of the primary cosmic ray energy. The various lines correspond to predictions made by different Monte Carlo models. Plot from Ref. [5]

with real data is clearly of extreme importance. In order to calibrate these codes and choose between different models it is very important to have a precise knowledge of the energy spectrum of foward emitted particles which are the main perpetrators of the air shower development. LHC with its unprecedent energy of 14 TeV in the center of mass system (equivalent to about 10^{17} eV in the laboratory system), gives us a unique opportunity to perform a complete calibration of Monte Carlo models in an energy range relevant to explore the already mentioned open questions of cosmic ray Physics.
The LHCf experiment [6] has been designed in order to measure the forward production spectra of photons and π^0's and the leading particle spectrum, thus providing all the essential tools needed to perform a detailed nuclear interaction model calibration.

2 The LHCf experiment

The main purpose of the LHCf experiment is to measure the neutral particle production in the very forward region at LHC: it should be able to identify photons, π^0 and neutrons, measure their energy spectra ($>$ 100 GeV) down to the high rapidity region and reconstruct the π^0 invariant mass thanks to the accurate measurement of the shower position and energy. In order to be compliant with these goals a double arm calorimeter design has been chosen. The two detectors are located on both side of the Interaction Point 1 ($\pm$ 140 m) at the Large Hadron Collider (LHC), at CERN. The two calorimeters are housed in a beam absorbing structure (TAN) in which the two proton beams are steered in the two separate beam lines which circulate in the LHC machine. Thus the flux of charged particles is swept away and only the neutral ones reach the calorimeter surface.
Each detector is a small sampling electromagnetic calorimeter arranged in a double tower geometry, each tower being made of plastic scintillators (16 layers) interleaved with tungsten layers as absorber (22 layers) and four layers of position sensitive detectors. The total dimensions of each detector (29 cm length, 9 cm width and 60 cm height) is constrained by the available slot in the

TAN region. The two detectors are very similar but not identical: the geometrical arrangment of the two towers is different and they also differ for the position sensitive layers. In detector #1 (ARM1) four layers of X-Y hodoscopes made with array of 1 mm $\times$ 1 mm scintillation fibers (SciFi) provide transverse position information of the showers. The position resolution for the shower center is expected to be 200 μm. A schematic of Detector #1 is shown in Fig. 3.

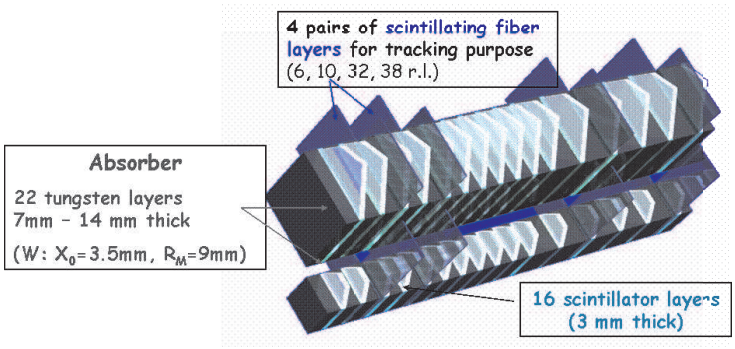


Fig. 3: A schematic drawing of the ARM1 LHCf calorimeter. The two towers have transverse dimensions of $2\times2\text{cm}^2$ and $4\times4\text{cm}^2$. The scintillator tiles are read out with phototubes. Four layers of scintillation fibers are used for tracking purpose.

The structure of Detector #2 (ARM2) is the same, but the two towers are stacked on their edges with an horizontal offset in order to maximize the effective aperture and the position sensitive layers are replaced by silicon microstrip detectors, as can bee seen in Fig. 4. The detector spatial resolution (i.e. the precision on the photon impact point measurement) is shown in Fig. 5 as a function of the depth for several photon energies ranging from 56 GeV to 1800 GeV.

The absorber lenght of the two calorimeters is enough to accurately measure the photon energy up to 2 TeV. The plastic scintillators provide both fine sampling of shower energy as well as a level 2 online trigger for data taking. Due to the smallness of the tower sizes, which are comparable to the Moliere radius of the electromagnetic showers, there is a certain amount of side leakage. However, this leakage can be corrected for by applying the position measurements of the silicon/scintillating fibre layers. Energy resolution is expected to be $3\%/\sqrt{E(TeV)}+1.2\%$. Also the capability to reconstruct separately the two showers from the 2 γs from π^0 decays allows for an excellent reconstruction of the invariant mass (5%) and thus provides an invaluable tool to calibrate the absolute energy scale, which is of crucial importance for the Physics program of LHCf (Fig. 6).

Good discrimination of hadron (neutron) showers from electromagnetic (γ) showers can be achieved by measuring the longitudinal shower distribution. Energy resolution of hadron showers is expected to be 30% at 6 TeV due to the longitudinal shower leakage through the back of the calorimeters.

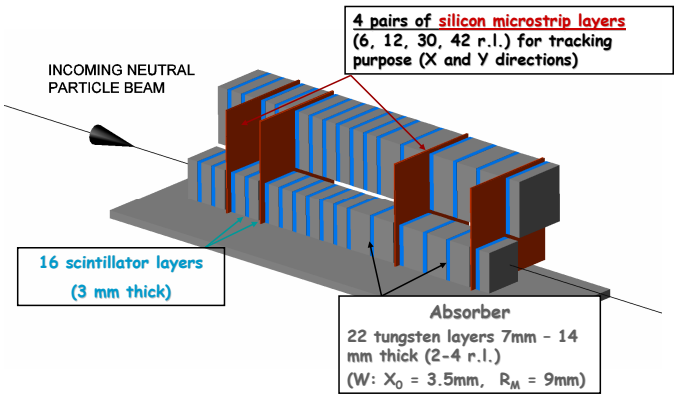


Fig. 4: A schematic drawing of the ARM2 LHCf calorimeter. The two towers have transverse dimensions of 2.5×2.5 cm^2 and 3.2×3.2 cm^2. The scintillator tiles are read out with phototubes while the silicon microstrip detectors have a redout pitch of 160 microns and provide a high precision measurement of the shower profile.

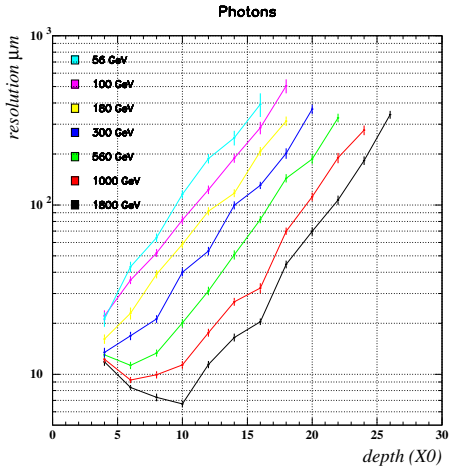


Fig. 5: Spatial resolution as a function of layer depth for the ARM2 calorimeter with silicon modules at various photon energies.

3 Monte Carlo Model Discrimination

The capability of LHCf to disentangle different interaction models is shown in Fig. 7 both for for the γ and neutron energy spectra. The models used are DPMJET3 [7], QGSJET-II [8] and SYBILL [9]. Depending on the nuclear interaction model used the energy spectra change more or less significantly. In the case of γ energy spectra, the discriminating power is already significant

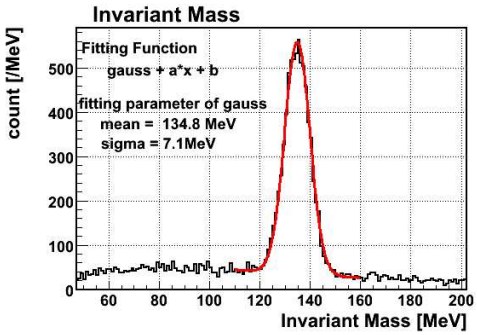


Fig. 6: Invariant mass resolution for π^0 for the ARM1 calorimeter.

at 1 TeV between SYBILL and the other codes, while discrimination between DPMJET3 and QGSJET-II can be achieved through a more sophisticated analysis, as described in Ref. [6].
The neutron sample gives more discrimination between different models. As it is shown in Fig. 7, even with a pessimistic 30% energy resolution, a very good disentangling of the different models is feasable.

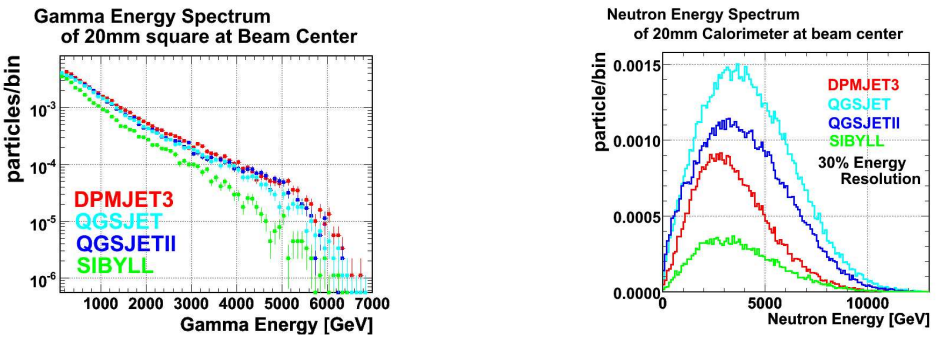


Fig. 7: Expected energy spectrum for γs and neutrons according to different interaction models. For neutrons a 30% energy resolution has been taken into account.

4 Status of the Experiment and Running scenario

The two LHCf calorimeters are fully assembled already since several months. Both were successfully pre-installed in the TAN region, to test all the connectivity, mechanics, cabling, etc. (Fig. 8) and the experiment is ready for the final installation into the LHC tunnel waiting to take data with LHC beams.

The LHCf detectors will take data in the first running period of LHC, already during the commissioning of the machine (mid 2008) till the LHC luminosity will not exceed 10^{31} cm^{-2}s^{-1}. Then the detector will be removed for reasons of radiation damage of the scintillator component. A successive phase, in which the detector will be re-installed at the next opportunity of a low luminosity run and during heavy ion runs is under discussion.



Fig. 8: ARM1 detector pre-installed in the TAN location in the LHC tunnel.

5 Conclusions

The LHCf experiment will take data at LHC in order to calibrate air shower Monte Carlo codes up to the energy of 10^{17} eV, thus providing invaluable input to questions posed since the first detection of UHECR. The two calorimeters are ready to take data and will be installed in the LHC tunnel at the beginning of 2008, while data taking will start at the beginning of LHC beam commissioning.

References

[1] M. Takeda *et al.*, Phys. Rev. Lett. **81**, 1163 (1998). astro-ph/9807193.

[2] HiRes Collaboration, R. Abbasi *et al.* (2007). astro-ph/0703099.

[3] Pierre Auger Collaboration, P. Sommers (2005). astro-ph/0507150.

[4] Pierre Auger Collaboration, T. Yamamoto (2007). arXiv:0707.2638 [astro-ph].

[5] M. Risse *et al.*, Czech. J. Phys. **56**, A327 (2006). astro-ph/0512434.

[6] LHCf Collaboration, O. Adriani *et al.* CERN-LHCC-2006-004.

[7] S. Roesler, R. Engel, and J. Ranft. Prepared for 27th International Cosmic Ray Conference (ICRC 2001), Hamburg, Germany, 7-15 Aug 2001.

[8] S. Ostapchenko, AIP Conf. Proc. **928**, 118 (2007). arXiv:0706.3784 [hep-ph].

[9] R. S. Fletcher, T. K. Gaisser, P. Lipari, and T. Stanev, Phys. Rev. **D50**, 5710 (1994).

Part VI

Theoretical Developments in High-Energy QCD

RHIC physics: short overview

Anna Staśto
Penn State University, 104 Davey Lab., University Park, 16802 PA, USA

Abstract
This talk gives a very short overview of some of the important physical phenomena observed at the Relativistic Heavy Ion Collider (RHIC). The emphasis is put on the multiplicities, hard probes and the properties of the initial state.

1 Introduction

The Relativistic Heavy Ion Collider (RHIC) is a unique machine designed to create a very high energy density over an extended region as a result of nuclei collisions. This process enables to investigate the collective phenomena in Quantum Chromodynamics. In particular, one hopes to create the quark-gluon plasma which is the state of deconfined quarks and gluons. According to cosmology such state existed at the very early Universe. RHIC machine is capable of accelerating and colliding different hadronic systems: proton-proton, nucleus-nucleus, deutron-nucleus at a wide range of centre-of-mass energies, from 19.6 to 200 GeV per nucleon pair. Just after the collision, a very high quantity of quarks and gluons is created. It is estimated that the formation time for the initial density is about 0.35 $\mathrm{fm/c}$. After that, the system thermalizes very quickly and reaches thermodynamic equillibrium. Estimates suggest that this happens rather quickly, with very short thermalization times of the order of 1 $\mathrm{fm/c}$. The assumption of thermalization is vital for the application of the hydrodynamics [1] which is used to describe the expansion of the system. When the system expands and cools down, the quarks and gluons form hadrons which finally reach the detectors. The phase transition from the quark-gluon plasma to hadrons occurs at rather large value of strong coupling which is beyond the applicability of the perturbative methods. Nevertheless, one can explore thermodynamic properties of QCD using lattice methods, see for example [2]. In Fig. 1 we show the result of the lattice calculations [2] for the energy density divided by T^4 as a function of temperature. The results clearly show the phase transition at the critical temperature T_c of about 173 MeV. The critical energy density corresponding to this temperature is about $\epsilon_c \simeq 0.7$ $\mathrm{GeV/fm^3}$. The energy density at RHIC [3] can be calculated from the transverse energy density at midrapidity via Bjorken formula: $\langle \epsilon \rangle \simeq \frac{1}{\tau A} \frac{dE_T}{dy}$, where A is the overlap area for the colliding nuclei. The average energy density depends crucially on the estimates of the time τ at which it is evaluated. For thermalization times in the range $0.6 - 1.0$ $\mathrm{fm/c}$ the average energy density is about $9.0 - 5.4$ $\mathrm{GeV/fm^3}$. This is well above the critical density obtained from lattice calculations, compare Fig. 1. It is interesting to note that the energy density of the cold nuclear matter is about 0.15 $\mathrm{GeV/fm^3}$. In Fig. 1 the energy densities probed by RHIC and LHC are also indicated. Notably, the calculations signal that already at SPS energies, the transition from hadron phase to quark-gluon plasma occured. Lattice calculations enable to probe the phase diagram of QCD, shown schematically in Fig. 2. The vertical axis is the temperature T and the horizontal one is the baryo-chemical potential.

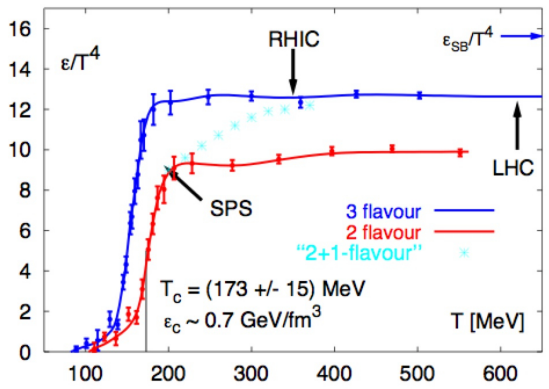


Fig. 1: Energy density $/T^4$ as a function of the temperature. The blue arrow with ϵ/T^4 is the Stefan-Boltzman limit. Figure by F. Karsch [4].

The region above the dashed-solid lines is the quark-gluon plasma phase, whereas the region below, at small temperatures and baryo-chemical potential, is the hadron phase. The transition between the two is a smooth crossover. Both RHIC and LHC probe the quark-gluon phase and the transition region at small values of the baryon chemical potential. Further to the right, for higher values of the baryo-chemical potential the critical endpoint is expected and the transition becomes of the 1st order. At high values of the baryo-chemical potential and smaller temperatures, new phase appears, the color superconductor. This phase is not accessible at the high energy colliders.

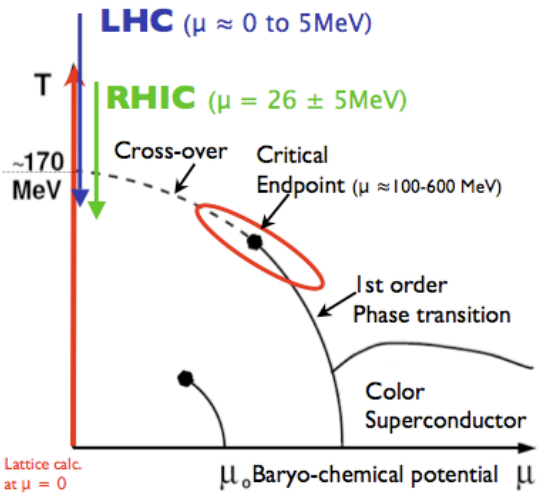


Fig. 2: Phase diagram of QCD.

The fact that RHIC reached quark-gluon plasma domain in the nucleus-nucleus collisions

suggests that, at least in some of the measured observables, one can expect to see dramatic effects as compared with proton-proton collisions. In reality the situation is quite complicated. Indeed, large differences are seen, for example the suppression of p_T distributions at large values of the transverse momenta with respect to the (scaled) proton-proton collisions. On the other hand, bulk properties, like total multiplicities and rapidity distributions, have quite similar shapes and energy dependences as compared with the scaled proton-proton measurements. We are going to review some of the observations performed at RHIC and discuss the phenomenological descriptions.

2 Multiplicities

In Fig. 3 from [3] the measurements of the total multiplicity in AA, $pp(p\bar{p})$, e^+e^- collisions, scaled by the number of participating nucleon pairs $N_{\rm part}/2$ are shown as a function of the increasing energy. The smooth rise with energy is well described by the $\ln^2 s$ behavior over wide range of the energies. What is striking, is the fact that the data for scaled multiplicity for nucleus-nucleus collisions lie on top of the data points for e^+e^- collisions. Proton-proton data lie lower, most probably due to the leading particle effect. In the $pp(p\bar{p})$ collisions, lots of the energy is taken by the quark spectators into the forward region, and only a fraction of the energy is used for the production of the secondary particles. The proton-proton data can be superimposed onto the nucleus-nucleus and e^+e^- data when the energy is rescaled by a factor of $1/2$. This universality of the multiplicites indicates that the bulk of the produced particles depends only on the total energy (and $N_{\rm part}$) and not the species of the colliding particles.

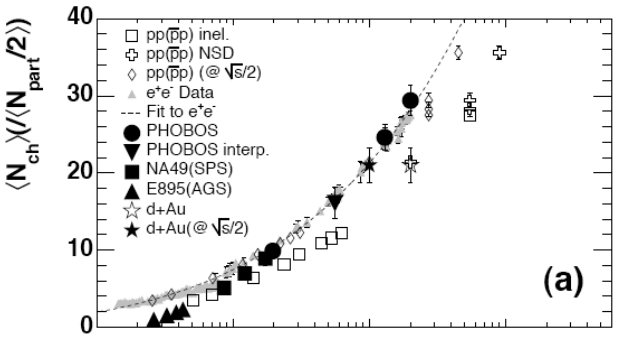


Fig. 3: Total multiplicity scaled by the number of participating pairs as a function of the energy. Compilation of data from e^+e^-, $pp(p\bar{p})$, AA and dA collisions. Figure by PHOBOS collaboration from [3].

The measured multiplicity at mid-(pseudo)rapidity in nucleus-nucleus collisions increases slower with energy , as $\ln s$. This simple linear in $\ln s$ extrapolation to the LHC energies predicts that $\frac{2}{N_{\rm part}}\frac{dN}{d\eta}|_{\eta=0} \simeq 6-7$. Various theoretical predictions for LHC energy are larger than this simple estimate and span a wide range, up to nearly 40 for the value at midrapidity. This is probably connected to the fact that in most of these calculations some semi-perturbative component is present which results in a power-like increase of the multiplicity rather than the logarithm. This large uncertainty of the phenomenological extrapolations reflects our rather limited theoretical understanding of the energy dependence of multiplicities.

2.1 Extended longitudinal scaling

The PHOBOS collaboration performed measurements of the rapidity distributions for various energies (and systems) and found that the distributions exhibit limiting fragmentation property which is also called extended longitudinal scaling [5]. This means that when viewed in the rest frame of one of the projectiles the (pseudo)rapidity distribution becomes a function of only $\eta' = \eta - Y_{\rm beam}$ where $Y_{\rm beam}$ is the rapidity of the beam. Therefore the rapidity distribution in the regime around $\eta' \sim 0$ is dominated by the fragments of the broken target whereas the fragments of the projectile move with increasing velocity as the energy is further increased (to study these fragments one has to go to the rest frame of the projectile $\eta + Y_{\rm beam}$). The limiting fragmentation also requires that the interaction between the target and the projectile does not depend appreciably on the energy. This scaling means that the rapidity distributions must be determined very early in the collision, most probably by the initial state.

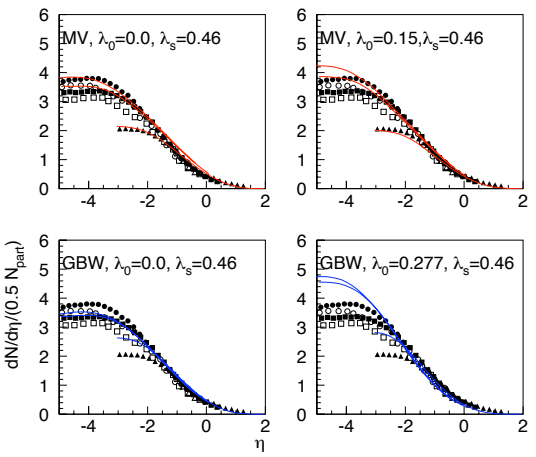


Fig. 4: Rapidity distributions for the nucleus-nucleus collisions as a function of the shifted variable $\eta' = \eta - Y_{\rm beam}$ for various center-of-mass energies. Curves are from calculation using the CGC nonlinear equations [6].

Fig. 4 illustrates this phenomenon. The curves shown in the figure are obtained from the calculation [6] based on the k_T-factorization approach together with the evolution via nonlinear equation for the gluon density. In this approach the rapidity distribution is evaluated as the convolution of two parton densities corresponding to the target and the projectile respectively. In the fragmentation region, the target parton density is evaluated at rather large values of Bjorken x whereas the projectile density is taken at rather small values of x. The essential part of this calculation, which enables to reproduce the observed scaling, is the fact that the rapidity distribution in the target fragmentation region is dominated by the initial state parton density of the target, probed at large values of the Bjorken variable x. At these values the parton density possesses Bjorken scaling,i.e. does not depend on the scale at which it is evaluated. The projectile density, which depends on rather small values of x and small scales, is saturated since it is evaluated from

the evolution equation which takes into account nonlinearities important at high parton densities. Therefore this density does not depend much on the x values and hence the center of mass energy. We see that even though the approach is semi-perturbative it does capture the essential physics features necessary to reproduce the limiting fragmentation phenomenon.

3 Hard probes

To explore the properties of the quark-gluon plasma created in the high energy nucleus-nucleus collisions experiments at RHIC measured the suppression of the production of high p_T particles and heavy quarks. These are excellent probes of the produced medium, and due to the large difference in scales (high p_T as compared to the bulk of low p_T particles), it should be in principle possible to employ the perturbative methods. One usually quantifies the effect of the medium by evaluating the ratio $R_{AA} = \frac{\sigma_{pp}^{inel}}{\langle N_{coll} \rangle} \frac{d^2 N_{AA}/d\eta dp_t}{d^2\sigma_{pp}/d\eta dp_t}$. As seen from Fig. 5 from [7] the R_{AA} ratio is significantly below 1 even at very high values of p_T. This phenomenon is called jet quenching which is interpreted as the interaction of the produced jet (or rather leading high p_T particle) with the produced medium. The interaction results in the significant energy loss of the leading high p_T particle. In fact the effect is so large that it indicates that the high p_T particles which reach the detectors are emitted from a relatively thin outer shell of the high density region.

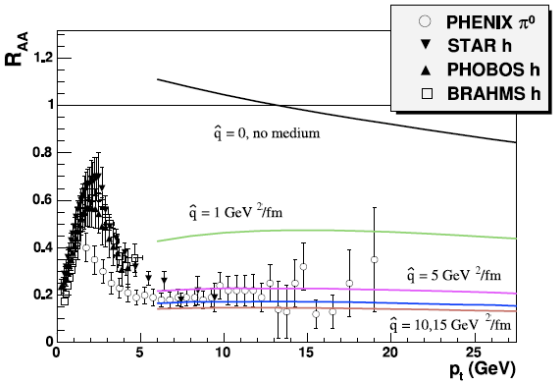


Fig. 5: R_{AA} for the produced hadrons as a function of their transverse momentum. Figure from [7].

To describe the jet quenching one usually starts from the standard collinear factorization formula for the exclusive hadron production in the vacuum

$$\sigma_{\rm vac}^{AB\to h} = f_A(x_1, Q^2) \otimes f_B(x_2, Q^2) \otimes \hat{\sigma}(x_1, x_2, Q^2) \otimes D^{f\to h} + \mathcal{O}(\Lambda/Q) \ , \qquad (1)$$

where f_A, f_B are parton distribution functions evaluated at scale Q^2 , $\hat{\sigma}$ is the partonic cross section and $D^{f\to h}$ is the fragmentation function from parton f to hadron h. To evaluate the production in the medium one convolutes the above expression with the so called quenching weight [8]

$$\sigma_{\rm med}^{AB\to h} = \sigma_{\rm vac}^{AB\to h} \otimes P(\Delta E, L, \hat{q}) \ , \qquad (2)$$

which depends on the length of the medium and the parameter $\hat{q}$ which acts as a transport coefficient for the medium. One has to emphasize that although in proton-proton collisions the factorization formula (1) is well established, (up to higher twist corrections) it is not proven to hold in form (2) for collisions which involve large nuclei. Final state interactions could in principle affect the partonic cross section $\hat{\sigma}$ in a non-factorizable way. It is therefore an assumption, that after the partons have been produced in the hard scattering process, one can further factorize their interactions into one universal function P. The curves in Fig. 5 are from [8] which is a calculation based on the theoretical framework described above. The quenching parameter $\hat{q}$ was fitted to get the best description of the data.

The production of the heavy quarks is another excellent process. In principle the calculation framework is the same as above. One does expect some differences due to the fact that in the vacuum the radiation pattern for heavy quarks is different from the light quarks. Due to their mass heavy quarks should radiate less than the light quarks at angles smaller than $\theta_0 = m/E$ where m is the mass of the heavy quark and E is its energy. This is called the dead cone effect [9]. Therefore the net effect would be less supression (larger R_{AA}) than for the light quarks. The measured suppression for the heavy quarks is of the same order as for the light quarks, and the theoretical predictions (for example [10]) do not quite predict such a large value. One has to emphasize that the heavy quark production in pp (from electrons emerging from semi-leptonic decays) is underestimated by the NLO perturbative QCD calculation by a factor of about 2 for PHENIX data and by about a factor 5 for the STAR data. Therefore the process with the heavy quarks calls for better understanding, possible taking into account various effects : collisional energy loss, bottom/charm ratio or factorization breaking.

We conclude our discussion of the hard probes with the description of the new calculational methods which employ the AdS/CFT correspondence to evaluate the jet quenching parameter. In this approach [11], the expectation value of the Wilson loop, as an average over the medium is evaluated using the string/gauge duality in the limit of the strong coupling constant. This expectation value is obtained as an exponential of the string action evaluated at the minimum

$$\langle W^F(C)\rangle = \exp(iS(C) - iS_0) \ ,$$

where S is the Nambu-Goto action with the metric on the $4+1$ dimensional AdS space. In the case of the finite temperature, the corresponding metric is that of the AdS Schwarzschild black hole. In the strong coupling and the multicolor limit the problem becomes classical, i.e. reduces to finding the extremum of the action. It is possible, using this method, to evaluate the value of the jet quenching parameter which in this case is $\hat{q}_{SYM} = 5 \ \mathrm{GeV}^2/\mathrm{fm}$. We note however, that all these results can be derived only for the case of the N=4 SYM theory.

4 Initial state

The processes described above clearly indicate the presence of the dense medium in the final state. The natural question arises whether one can also observe the effects coming from the initial state, namely the wave function of the colliding nuclei. BRAHMS collaboration performed a measurement of the high p_T suppression as a function of rapidity for dA collisions [12]. Whereas at midrapidity no suppression is observed for this process, the R_{CP} clearly shows a decreasing

trend when moving into forward rapidity. This phenomenon was quite successfully described by the models which involve saturation effects in the gluon density or in general by the Color Glass Condensate model [13]. In CGC the basic object is the wave function of the nucleus. Obviously the complete knowledge of such wave function requires methods which go beyond that known in preturbation theory. One can nevertheless calculate the variation of this wave function with energy. This is governed by the renormalization group equation which can be derived from the Feynman graphs in the leading logarithmic approximation. At very small values of Bjorken x one expects the fast growth of the gluon density within the nucleus. The CGC model together with the renormalization group equations predicts that this growth should be tamed whenever x becomes sufficiently small. The transition between the fast growth and the regime where the recombination effects for the gluons become important is governed by the saturation scale Q_s which is a function of the Bjorken x. Thus the saturation scale provides a dynamical cutoff at low values of x and at low scales. It is the prediction of the CGC model that the R_{CP} ratio should decrease at forward rapidities [14]. The CGC model has been successfully used to describe various observables in heavy ion collisions: multiplicites, rapidity distributions (mentioned already in the previous section) [15] and also R_{CP} ratio. One has to emphasize though that there are several questions concerning a strict applicability of this approach to the RHIC data. The values of x are not very small for the RHIC kinematics, the formalism correctly incorporates only gluons, and it has been so far only used at leading order whereas higher orders are known to be very large. Nevertheless, the CGC approach, mostly due to its interesting properties in the infrared regime, remains a very attractive approach both theoretically and phenomenologically and its predictions should be further confronted with the experimental data.

Conclusions

We have discussed a selection of the phenomena measured at the Relativistic Heavy Ion collider. Clearly, due to our space and time limitations the list presented here is by no means exhaustive. The bulk properties as shown in the measurements of the multiplicities are very similar to that measured in the simpler systems: proton-proton or even in e^+e^- collisions. The extended longitudinal scaling of rapidity distributions indicate the importance of the initial state. Hard probes in form of the high p_T particles or heavy quarks signify the presence of the strongly interacting medium. This is further corroborated by the observation of the strong elliptic flow in peripheral collisions. The theoretical descriptions based on hydrodynamics have been quite successful in describing the hadron spectra and the anisotropy. Also calculations which employ the perturbative methods supplemented by the rescattering or recombination(saturation) effects are able to describe the bulk of the data at large values of the transverse momenta. Nevertheless, despite these incontrovertible successes in phenomenology, the RHIC data still constitute a significant challenge for a theory and call for a more complete and coherent description within QCD.

Acknowledgments

I would like to thank the organizers of EDS2007 for the kind invitation to this very interesting workshop. This research was supported by the U.S. D.O.E. under grant number DE-FG02-90ER-40577 and by the Polish Committee for Scientific Research under grant No. KBN 1 P03B 028 28.

References

[1] U. W. Heinz, J. Phys. **G31**, S717 (2005). nucl-th/0412094.

[2] F. Karsch, Nucl. Phys. **A783**, 13 (2007). hep-ph/0610024.

[3] BRAHMS, PHENIX, PHOBOS, and STAR, Nucl.Phys. **A757**, 1 (2005).

[4] F. Karsch, *Lattice qcd: Present and future*, 2004. Talk given at Orsay, April 2004.

[5] B. B. Back *et al.*, Phys. Rev. Lett. **91**, 052303 (2003). nucl-ex/0210015.

[6] F. Gelis, A. M. Stasto, and R. Venugopalan, Eur. Phys. J. **C48**, 489 (2006). hep-ph/0605087.

[7] C. A. Salgado (2007). arXiv:0706.2264 [hep-ph].

[8] C. A. Salgado and U. A. Wiedemann, Phys. Rev. **D68**, 014008 (2003). hep-ph/0302184.

[9] Y. L. Dokshitzer and D. E. Kharzeev, Phys. Lett. **B519**, 199 (2001). hep-ph/0106202.

[10] N. Armesto, M. Cacciari, A. Dainese, C. A. Salgado, and U. A. Wiedemann, Phys. Lett. **B637**, 362 (2006). hep-ph/0511257.

[11] H. Liu, K. Rajagopal, and U. A. Wiedemann, JHEP **03**, 066 (2007). hep-ph/0612168.

[12] BRAHMS Collaboration, I. Arsene *et al.*, Phys. Rev. Lett. **93**, 242303 (2004). nucl-ex/0403005.

[13] E. Iancu and R. Venugopalan (2003). hep-ph/0303204.

[14] D. Kharzeev, Y. V. Kovchegov, and K. Tuchin, Phys. Lett. **B599**, 23 (2004). hep-ph/0405045.

[15] D. Kharzeev and E. Levin, Phys. Lett. **B523**, 79 (2001). nucl-th/0108006.

Nuclear shadowing and collisions of heavy ions

A.B.Kaidalov[1]
[1]Institute of Theoretical and Experimental Physics, Moscow

Abstract
Nuclear shadowing effects for quarks and gluons are calculated using information on diffractive DIS on a nucleon. The role of these effects in interactions of hadrons and nuclei with nuclei at high energies is investigated. A decrease in particle densities for heavy ion collisions in comparison with the Glauber model is predicted and nuclear modification factors are calculated. The situation in heavy quarkonia production on nuclei is discussed.

1 Introduction

Heavy ion collisions at high energies are usually considered as a tool to study hadronic matter at extreme conditions: high density quark-gluon systems in deconfined phase. It is very important to understand what are the relevant degrees of freedom in such situation. Investigation of DIS at very small x, and especially shadowing effects on nuclei, can give an important information on properties of dense quark-gluon systems.

It is worth to emphasize that hadrons and nuclei at very high energies can be considered as complicated fluctuations of quarks and gluons with long lifetimes (coherence length) proportional to energy. The structure of these Fock states is of primary importance for high-energy interactions. The space-time picture of hadron-nucleus hA (AB) interaction changes at energies E_c for which the coherence length becomes of the nuclear size R_A. For typical interactions $E_c \sim m_N^2 R_A$. At energies below E_c an elastic hA scattering amplitude can be considered as successive rescatterings of an initial hadron on nucleons of a nucleus (Glauber model [1]). For $E \gg E_c$ there is a coherent interaction of constituents of a hadron with nucleons of a nucleus. It was shown by V.N. Gribov [2] that, though the space-time picture changes, the hA elastic amplitude can be calculated as in the Glauber model, but with account of inelastic intermediate states.

Consider now the fast moving nucleus. Partons of a fast nucleus with small relative momenta $x < 1/(m_N R_A)$ overlap in the longitudinal space and can interact. For example two chains of partons from different nucleons can fuse into a single chain (for elastic amplitude this corresponds to the diagram with triple-pomeron interaction). From the point of view of Gribov approach such interactions correspond to diffractive production of large mass states. The corresponding couplings (g_{PPP},..) can be determined from experimental data on inclusive diffractive processes and turned out to be small (see for example [3]). This means that extra shadowing due to excitation of large masses in the intermediate states is not very important in hA-interactions. On the other hand for DIS on nuclei these effects play a dominant role in shadowing of partons.

This contribution contains a review of theoretical studies of shadowing effects for quarks

and gluons [4–6], based on the Gribov approach and HERA data on diffraction in DIS [1]. In the second part of the paper the results on partonic shadowing are applied to heavy ion collisions. It is shown that this shadowing leads to a suppression of particle densities in hadron-nucleus and nucleus-nucleus collisions. Suppression of particles with large transverse momenta and heavy quarkonia is discussed.

2 Shadowing effects for nuclear structure functions

Study of nuclear structure functions in the small-x region can provide an important information on mechanisms of shadowing. The total cross section of a virtual photon-nucleus interaction can be written as a series in number of rescattering on nucleons of a nucleus

$$\sigma^{(tot)}_{\gamma^*_A} = \sigma^{(1)}_{\gamma^*_A} + \sigma^{(2)}_{\gamma^*_A} + ... \tag{1}$$

The first term corresponds to a sum of incoherent interactions with nucleons of a nucleus

$$\sigma^{(1)}_{\gamma^*_A} = A\sigma_{\gamma^* N} \tag{2}$$

the second term describes the shadowing and according to Gribov theory [2] can be expressed in terms of cross section of diffraction dissociation of a virtual photon in $\gamma^* N$-interactions

$$\sigma^{(2)} = -4\pi \int d^2b\, T_A^2(b) \int dM^2 \frac{d\sigma^{DD}_{\gamma^* N}(t=0)}{dM^2 dt} F_A(t_{min}) \tag{3}$$

where $T(b) = \int dz \rho_A(r)$ is the nuclear profile function, and $\rho_A(r)$ - nuclear density $(\int \rho_A(r) d^3r = A)$, $F_A(q^2) = \int e^{iq\vec{r}} \rho(r)$ - nuclear form factor. The minimal value of momentum transfer to nucleons

$$t_{min} = -x_P^2 m_N^2 \text{ and } x_P = \frac{Q^2 + M^2}{S} = \frac{x}{\beta},$$

where $\beta = \frac{Q^2}{Q^2+M^2}$. It is important to emphasize that the shadowing effects are different from zero only in the region of very small x_P or x, where $(-t_{min}) << \frac{1}{R_A^2}$ (R_A is the nuclear radius). The same condition of coherence corresponds to lifetimes of the initial hadronic fluctuation $\tau_h \sim \frac{1}{m_N x}$ much larger than radius of a nucleus. It is also important for existence of shadowing in heavy ion collisions (see below).

Higher order rescatterings are model dependent. In papers [4–6] two types of models were used. The first one is the quasieikonal model, which was successfully used in hadronic interactions [7] and the second one is the generalized Schwimmer model [8], based on summation of fan-type diagrams of pomeron interactions. For the last model one can write

$$F_{2A}/F_{2N} = \int d^2b \frac{T_A(b)}{1 + F(x,Q^2) T_A(b)} \tag{4}$$

with $F(x,Q^2) = 4\pi \int dM^2 \left(d\sigma^{DD}_{\gamma^* N}(t=0)/dM^2 dt \right) \times (F_A(t_{min})/\sigma_{\gamma^* N}(x,Q^2))$. It was demonstrated in refs. [4–6], that predictions of two models indicated above for nuclear shadowing are

[1] for more references on this subject see [6]

not very different. HERA experiments provided rather complete information on diffractive dissociation in DIS, which can be used in eq.(4) to predict nuclear structure functions at very small x. Theoretical predictions do not contain free parameters and are in a good agreement with existing experimental data [4, 5]. Thus the shadowing effects for distributions of quarks in nuclei are predicted with a good accuracy. On the other hand shadowing for gluons until recently was not so well determined. This is connected with a difficulty of extraction of the gluonic distributions in diffractive DIS. In the paper [6] we used the most recent determinations of the diffractive gluonic distributions from HERA data [9] to calculate nuclear shadowing for gluons. Inclusion of the data on diffractive production of dijets and charm makes diffractive distributions of gluons much more reliable in the whole β region in comparison with previous determinations. Distributions of gluons in nuclei play an important role in many physical processes in nuclear collisions (see below).

3 Nuclear interactions at high energies and shadowing effects

An important consequence of the space–time structure of interactions of hadrons with nuclei is the theorem, based on AGK–cutting rules [10], that for inclusive cross sections all rescatterings cancel with each other and these cross sections are determined by the diagrams of impulse approximation. Note, however, that this result is valid asymptotically in the central rapidity region only for diagrams of the Glauber–type, i.e. when masses of diffractive intermediate states are limited and do not increase with energy. As a result, the inclusive cross section for the production of a hadron a is expressed, for a given impact parameter b, in terms of inclusive cross section for hN interactions

$$E\frac{d^3\sigma^a_{hA}(b)}{d^3p} = T_A(b)E\frac{d^3\sigma^a_{hN}}{d^3p} \tag{5}$$

where $T_A(b)$ is the nuclear profile function

For inclusive cross sections in nucleus-nucleus A_1A_2–collisions the result of the Glauber approximation is also very simple to formulate due to the AGK cancellation theorem. It is possible to prove, for an arbitrary number of interactions of nucleons of both nuclei , that all rescatterings cancel in the same way as for hA–interactions. Thus a natural generalization of eq. (5) for inclusive spectra of hadrons produced in the central rapidity region in nucleus–nucleus interactions takes place in the Glauber approximation

$$E\frac{d^3\sigma^a_{A_1A_2}(b)}{d^3p} = T_{A_1A_2}(b)\ E\frac{d^3\sigma^a_{NN}}{d^3p} \tag{6}$$

where $T_{A_1A_2}(b) = \int d^2sT_{A_1}(\vec{s})T_{A_2}(\vec{b}-\vec{s})$.

The densities of charged particles can be obtained from eq.(6) by dividing it by the total inelastic cross section of nucleus–nucleus interaction.

$$\frac{dn^{ch}_{A_1A_2}(b)}{dy} = \frac{T_{A_1A_2}(b)}{\sigma^{in}_{A_1A_2}}\sigma^{in}_{NN}\frac{dn^{ch}_{NN}}{dy} = n_{A_1A_2}(b)\frac{dn^{ch}_{NN}}{dy} \tag{7}$$

Equations (6),(7) are valid for $x_F \approx 0$ in the limit $s \to \infty$. For finite energies there are corrections due to energy-momentum conservation effects [11].

At very high energies the problem of shadowing of soft partons is very important in hadron-nucleus and nucleus-nucleus collisions. This phenomenon takes place only in the kinematic region where longitudinal momentum fractions of soft partons satisfy to the condition $x_i << 1/m_N R_A (i = 1, 2)$, discussed in the previous Section. Values of x_i can be determined from the conditions

$$x_1 \cdot x_2 = \frac{M_\perp^2}{s}; \;\; x_1 - x_2 = x_F$$

where $M_\perp$ is the transverse mass of the produced system and x_F is its Feynman x.

For example at RHIC energy $\sqrt{s} = 200\ GeV$ in the central rapidity region ($x_F \approx 0$) the shadowing for Au-Au collisions is possible only for transverse momenta less than several GeV.

In reggeon theory the shadowing effects discussed above are related to diagrams with interactions between pomerons. They lead to a substantial decrease of particle densities at high energies.

The same model, which has been used for description of shadowing effects for nuclear structure functions, was used to predict inclusive particle densities in heavy ion collisions [11]. In this approach the expression (7) for densities of particles in $A_1 A_2$ collisions is modified as follows [11].

$$\frac{dn_{A_1A_2}}{dy} = n_{A_1A_2}(b)\frac{dn_{NN}}{dy}\gamma_{A_1}\gamma_{A_2} \tag{8}$$

where

$$\gamma_A = \frac{1}{A}\int d^2b \frac{T_A(b)}{1 + F(x, Q^2)T_A(b)} \tag{9}$$

For LHC eqs.(8), (9) predict a decrease of particle densities by a factor ~ 4 compared to the Glauber model [11], while for RHIC the suppression is ≈ 2. Detailed predictions for shadowing suppressions are given in ref. [5]. This approach agrees [12] with experiments at RHIC [13, 14]. Dependence of number of produced particles on number of participant nucleons is also in agreement with the data [15].

The kinematic borders for shadowing discussed above correspond also to an essential change in the space–time picture of nuclear interactions and change [16] in AGK cutting rules. For example for $x_{A_2} << \frac{1}{m_N R_{A_2}}$ the lifetime for the initial state configuration of a nucleus A_1 is larger than the size of a nucleus A_2. In this case conditions for coherence are satisfied and usual AGK cutting rules [10] are valid . For $x_{A_2} \geq \frac{1}{m_N R_A}$ space–time picture is close to final state reinteractions of produced particles with formation time [16]. This situation is very general. For J/ψ production in hadron-nucleus interactions it was discussed in detail in ref. [17]. It has important implications for production of particles and jets with large $p_\perp$ and heavy quarkonia at RHIC.

Consider for example J/ψ production in D-Au-collisions. The transition from the picture of successive final state interactions to coherent interaction in this case for $x_F = 0$ happens in the RHIC energy region. At the highest RHIC energies the coherent interactions dominate and due

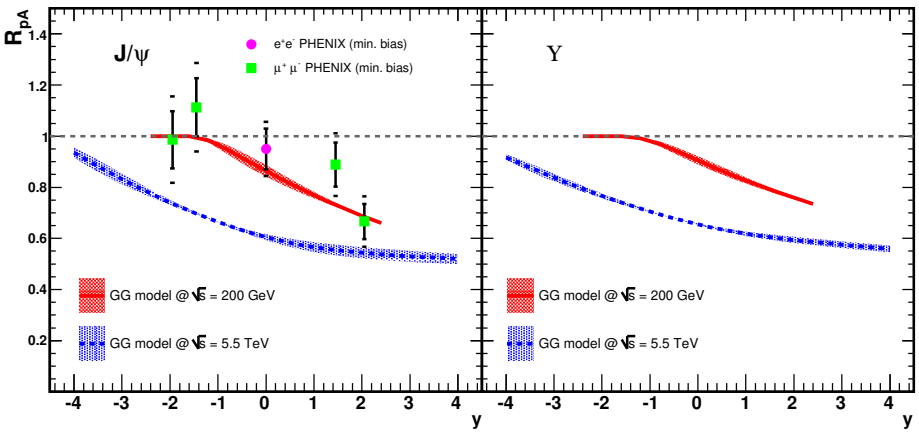


Fig. 1: Suppression of heavy quarkonia production in DAu (pPb)-collisions at RHIC and LHC

to AGK-cancellation only the diagrams with interactions between pomerons contribute. In other words only effects of shadowing for nuclear gluons can be taken into account. As was demonstrated above these effects are small for $x_A > 10^{-2}$ and experimental data on J/ψ production in d-Au-collisions [18] are well reproduced [19–21] (Fig.1). In this model it is possible to describe data on J/ψ production in hA-collisions in a broad energy region. The model predicts a substantial increase in J/ψ-suppression at LHC [21] (Fig.1). For heavy ion collisions there is an extra suppression of heavy quarkonia due to interactions with comoving particles and possible recombination of charm.

For pions with $p_\perp \geq 1 \div 2\ GeV$ the shadowing effects at $\sqrt{s} = 200\ GeV$ and $x_F = 0$ are small as was emphasized above and is demonstrated by the data on D-Au-collisions [22]. However for heavy ion collisions in this region of $x_{A_i} \geq \frac{1}{mR_A}$ the final state interactions with produced particles are important. In particular an account of Cronin effect and interaction of a particle (jet) with comovers allowed to describe [23] a suppression of particle production at large $p_\perp$ observed at RHIC [14] for Au-Au collisions.

The data in D-Au collisions [22] show that in the fragmentation region of D there is a suppression for production of particles with large $p_\perp$. At first sight this can be explained by a stronger shadowing at smaller values of $x_{Au} \sim 10^{-3}$. However with an account of correct two-jet kinematics the values of x_{Au} turned out to be not so small [24] and calculation of shadowing shows [20] that it is responsible for a small part of the effect. The rest can be explained by the energy-momentum conservation effects, which are important for $x_F \sim 1$. This is confirmed by the experimental observation of practically the same suppression of large $p_\perp$ hadrons in hA-collisions at SPS energies [25]. These observations make interpretations of the suppression, observed in the deutron fragmentation region, in terms of nuclear shadowing or "color glass condensate" highly unlikely.

4 Conclusions

The Gribov theory of high-energy interactions is able to describe a large class of physical processes including nuclear interactions. In this theory the Glauber approximation to nuclear dynamics is valid in the region of not too high energies and is modified already starting from RHIC energies.

The problem of "saturation" of parton densities is related in the Gribov theory to interactions between Pomerons. These effects are especially important for nuclear collisions. The shadowing effects are clearly seen in the RHIC data at small transverse momenta. A change in the space-time picture of particle production on nuclei with energy allows to understand the properties of heavy quarkonia production in D-Au collisions at RHIC.

Acknowledgments

This work was supported in part by grants: RFBR 06-02-17012, RFBR 06-02-72041-MNTI, SS-843.2006.2.

References

[1] R.J. Glauber, Lectures in Theoretical Physics. Ed. Britten W.E. N.Y.: Int.Publ. 1959, v.1, p.315.

[2] V.N. Gribov, *JETP* **56**, 892 (1969);
V.N. Gribov, *JETP* **57** 1306 (1969).

[3] A.B. Kaidalov, *Phys. Rep.* **50**, 157 (1979).

[4] A. Capella, A. Kaidalov, C. Merino, D. Pertermann, J. Tran Thanh Van, *Eur. Phys. J.* **C5**, 111 (1998).

[5] N. Armesto, A. Capella, A.B. Kaidalov, J. Lopez-Albacete, C.A. Salgado, *Eur. Phys. J.* **C29**, 531 (2003).

[6] K. Tywoniuk, I.C. Arsene, L. Bravina, A.B. Kaidalov and E. Zabrodin, arXiv: 0705, 1596 [hep-ph].

[7] A.B. Kaidalov, *Phys. Atom. Nucl.* **66**, 1994 (2003).

[8] A. Schwimmer, *Nucl. Phys.* **B94**, 445 (1975).

[9] H1 Collaboration, A. Aktas *et al.*, *Eur. Phys. J.* **C48**, 715, 749 (2006);
M.Kapishin, talk at the 23 International Conference on High Energy Physics, ICHEP 2006, Moscow.

[10] V.A. Abramovsky, V.N. Gribov and O.V. Kancheli, *Sov. J. Nucl. Phys.* **18**, 308 (1974).

[11] A. Capella, A. Kaidalov, J. Tran Thanh Van, *Heavy Ion Phys.* **9**, 169 (1999).

[12] A.B.Kaidalov, *Surveys in High Energy Physics* **16** 267 (2001).

[13] PHOBOS Collaboration, B.B.Back *et al.*, *Phys. Rev. Lett.* **87**, 102303 (2001)

[14] PHENIX Collaboration, S.S.Adler *et al.*, *Phys. Rev. Lett.* **91**, 072301 (2003).

[15] A. Capella and D. Sousa, *Phys. Lett.* **B511**, 185 (2001)

[16] K.G. Boreskov *et al*, *Yad. Fiz.* **53**, 569 (1991).

[17] K. Boreskov, A. Capella, A. Kaidalov and J. Tran Tranh Van, *Phys. Rev.* **D47**, 919 (1993).

[18] PHENIX Collaboration, S.S.Adler *et al.*, *Phys. Rev. Lett.* **96**, 012304 (2006).

[19] A. Capella, and E.G. Ferreiro, arXiv: 0610313 [hep-ph].

[20] K. Tywoniuk, I.C. Arsene, L. Bravina, A.B. Kaidalov and E. Zabrodin, Proc. of the Workshop on High p_T physics at LHC, Jyvaskyla, Finland, 2007.

[21] I.C. Arsene, L. Bravina, A.B. Kaidalov, K. Tywoniuk, E. Zabrodin, arXiv: 0708, 3801 [hep-ph].

[22] Brahms Collaboration, I.Arsene *et al.*, *Phys. Rev. Lett.* **93**, 242303 (2004).

[23] A. Capella, E.G. Ferreiro, A.B. Kaidalov, D. Sousa, *Eur. Phys. J.* **C40**, 129 (2005).

[24] V. Guzey, M. Strikman and W. Vogelsang, *Phys. Lett.* **B603**, 173 (2004)

[25] NA50 Collaboration, L. Ramallo *et al.*, *Nucl. Phys.* **D47**, 243c (2003).

NLO jet production in k_T factorization

J. Bartels[1], *A. Sabio Vera*[2], *F. Schwennsen*[1†]
[1]II. Institut für Theoretische Physik, Universität Hamburg, Luruper Chaussee 149,
D-22761 Hamburg, Germany,
[2]Physics Department, Theory Division, CERN, CH-1211 Geneva 23, Switzerland

Abstract
We discuss the inclusive production of jets in the central region of rapidity in the context of k_T–factorization at next–to–leading order (NLO). Calculations are performed in the Regge limit making use of the NLO BFKL results. We introduce a jet cone definition and carry out a proper phase–space separation into multi–Regge and quasi–multi–Regge kinematic regions. We discuss two situations: scattering of highly virtual photons, which requires a symmetric energy scale to separate impact factors from the gluon Green's function, and hadron–hadron collisions, where a non–symmetric scale choice is needed.

1 Introduction

An accurate knowledge of perturbative QCD is an essential ingredient in phenomenological studies at present and future colliders. At high center of mass energies the theoretical study of multijet events becomes an increasingly important task. In the context of collinear factorization the calculation of multijet production is complicated because of the large number of contributing diagrams. There is, however, a region of phase space where it is indeed possible to describe the production of a large number of jets: the Regge asymptotics (small–x region) of scattering amplitudes. If the jets are well separated in rapidity, the corresponding matrix element factorizes with effective vertices for the jet production connected by a chain of t-channel Reggeons. A perturbative analysis of these diagrams shows that it is possible to resum contributions of the form $(\alpha_s \ln s)^n$ to all orders, with α_s being the coupling constant for the strong interaction. This can be achieved by means of the Balitsky–Fadin–Kuraev–Lipatov (BFKL) equation [1].

The BFKL approach relies on the concept of the *Reggeized gluon* or *Reggeon*. In Regge asymptotics colour octet exchange can be effectively described by a t–channel gluon with its propagator being modified by a multiplicative factor depending on a power of s. This power corresponds to the *gluon Regge trajectory* which is a function of the transverse momenta and is divergent in the infrared. This divergence is removed when real emissions are included using gauge invariant Reggeon–Reggeon–gluon couplings. This allows us to describe scattering amplitudes with a large number of partons in the final state. The $(\alpha_s \ln s)^n$ terms correspond to the leading–order (LO) approximation and provide a simple picture of the underlying physics. This approximation has limitations: in leading order both α_s and the factor scaling the energy s in the resummed logarithms, s_0, are free parameters not determined by the theory. These free

[†] speaker

parameters can be fixed if next–to–leading terms $\alpha_s (\alpha_s \ln s)^n$ are included [2]. At this improved accuracy, diagrams contributing to the running of the coupling have to be included, and also s_0 is not longer undetermined. The phenomenological importance of the NLO effects has been recently shown in the scattering of virtual photons into vector mesons [3] as well as for azimuthal angle decorrelations in Mueller–Navelet jets in Refs. [4] and in Deep Inelastic Scattering in Ref. [5].

While at LO the only emission vertex – the Reggeon-Reggeon-gluon vertex – can be identified with the production of one jet, at NLO also Reggeon-Reggeon-gluon-gluon and Reggeon-Reggeon-quark-antiquark vertices enter the game. In this contribution we are interested in the description of the inclusive production of a single jet in the NLO BFKL formalism. The relevant events will be those with only one jet produced in the central rapidity region of the detector. Due to these new emission vertices at NLO we have to introduce a jet definition discriminating between the production of one or two jets by two particles. It is not sufficient to simply start from the fully integrated emission vertex available in the literature [2]. Rather, we have to carefully separate all the different contributions in its unintegrated form before we can combine them.

The present text is focused on describing the main elements of the analysis presented in Refs. [6]. There we show that this procedure enables us to determine the right choice of energy scales relevant for the process. Particular attention is given to the separation of multi-Regge and quasi-multi-Regge kinematics. There we also discuss similarities and discrepancies with the earlier work of Ref. [7].

As it turns out, the scale of the two projectiles in the scattering process has a large impact on the structure of the result. The jet vertex can not be constructed without properly defining the interface to the scattering objects. To show this, we will perform this study for two different cases: the jet production in the scattering of two photons with large and similar virtualities, and in hadron-hadron collisions. In the former case the cross section has a factorized form in terms of the photon impact factors and of the gluon Green's function which is valid in the Regge limit. In the latter case, since the momentum scale of the hadron is substantially lower than the typical k_T entering the production vertex, the gluon Green's function for hadron-hadron collisions has a slightly different BFKL kernel which, in particular, also incorporates some k_T-evolution from the nonperturbative, and model dependent, proton impact factor to the perturbative jet production vertex.

Our final expression for the cross section of the jet production in hadron-hadron scattering contains an *unintegrated gluon density*. This density depends on the longitudinal momentum fraction – as it also happens in the conventional collinear factorization – and on the transverse momentum k_T. As an important ingredient, the hard subprocesse (in our case, the production vertex) depends on the (off-shell) initial parton momenta. This scheme of k_T–factorization has been introduced by Catani et al. [8], and up to now it has been considered only at LO. Our results, valid in the small–x limit, show that it is possible to extend this scheme to NLO.

2 Inclusive jet production at LO

Let us start the discussion by considering the interaction between two photons with large virtualities $Q^2_{1,2}$ in the Regge limit $s \gg |t| \sim Q^2_1 \sim Q^2_2$. In this region the total cross section can be

written as a convolution of the photon impact factors with the gluon Green's function, *i.e.*

$$\sigma(s) = \int \frac{d^2\mathbf{k}_a}{2\pi\mathbf{k}_a^2} \int \frac{d^2\mathbf{k}_b}{2\pi\mathbf{k}_b^2}\, \Phi_A(\mathbf{k}_a)\, \Phi_B(\mathbf{k}_b) \int_{\delta-i\infty}^{\delta+i\infty} \frac{d\omega}{2\pi i} \left(\frac{s}{s_0}\right)^{\omega} f_\omega(\mathbf{k}_a, \mathbf{k}_b). \tag{1}$$

A convenient choice for the energy scale is $s_0 = |\mathbf{k}_a|\,|\mathbf{k}_b|$ which naturally introduces the rapidities $y_{\tilde{A}}$ and $y_{\tilde{B}}$ of the emitted particles with momenta $p_{\tilde{A}}$ and $p_{\tilde{B}}$ given that $\left(\frac{s}{s_0}\right)^{\omega} = e^{\omega(y_{\tilde{A}} - y_{\tilde{B}})}$.

The gluon Green's function f_ω corresponds to the solution of the BFKL equation

$$\omega f_\omega(\mathbf{k}_a, \mathbf{k}_b) \;=\; \delta^{(2)}(\mathbf{k}_a - \mathbf{k}_b) + \int d^2\mathbf{k}\, \mathcal{K}(\mathbf{k}_a, \mathbf{k}) f_\omega(\mathbf{k}, \mathbf{k}_b), \tag{2}$$

with kernel

$$\mathcal{K}(\mathbf{k}_a, \mathbf{k}) \;=\; 2\,\omega(\mathbf{k}_a^2)\,\delta^2(\mathbf{k}_a - \mathbf{k}) + \mathcal{K}_r(\mathbf{k}_a, \mathbf{k}), \tag{3}$$

where $\omega(\mathbf{k}_a^2)$ is the gluon Regge trajectory and $\mathcal{K}_r$ is the real emission contribution to the kernel which is of special interest in the following.

It is possible to single out one gluon emission by extracting its emission probability from the BFKL kernel. By selecting one emission to be exclusive we factorize the gluon Green's function into two components. Each of them connects one of the external particles to the jet vertex, and depends on the total energies of the subsystems $s_{AJ} = (p_A + q_b)^2$ and $s_{BJ} = (p_B + q_a)^2$, respectively. We have drawn a graph indicating this separation in Fig. 1. The symmetric situation suggests the choices $s_0^{(AJ)} = |\mathbf{k}_a|\,|\mathbf{k}_J|$ and $s_0^{(BJ)} = |\mathbf{k}_J|\,|\mathbf{k}_b|$, respectively, as the suitable energy scales for the subsystems. These choices can be related to the relative rapidity between the jet and the external particles. To set the ground for the NLO discussion of next section we introduce an additional integration over the rapidity η of the central system in the form

$$\begin{aligned}\frac{d\sigma}{d^2\mathbf{k}_J dy_J} = \int d^2\mathbf{q}_a \int d^2\mathbf{q}_b \int d\eta \left[\int \frac{d^2\mathbf{k}_a}{2\pi\mathbf{k}_a^2}\, \Phi_A(\mathbf{k}_a) \int_{\delta-i\infty}^{\delta+i\infty} \frac{d\omega}{2\pi i} e^{\omega(y_A-\eta)} f_\omega(\mathbf{k}_a, \mathbf{q}_a)\right] \\ \times\, \mathcal{V}(\mathbf{q}_a, \mathbf{q}_b, \eta; \mathbf{k}_J, y_J) \;\times \left[\int \frac{d^2\mathbf{k}_b}{2\pi\mathbf{k}_b^2}\, \Phi_B(\mathbf{k}_b) \int_{\delta-i\infty}^{\delta+i\infty} \frac{d\omega'}{2\pi i} e^{\omega'(\eta-y_B)} f_{\omega'}(-\mathbf{q}_b, -\mathbf{k}_b)\right]\end{aligned} \tag{4}$$

with the LO emission vertex being

$$\mathcal{V}(\mathbf{q}_a, \mathbf{q}_b, \eta; \mathbf{k}_J, y_J) = \mathcal{K}_r^{(\mathrm{Born})}(\mathbf{q}_a, -\mathbf{q}_b)\; \delta^{(2)}(\mathbf{q}_a + \mathbf{q}_b - \mathbf{k}_J)\; \delta(\eta - y_J). \tag{5}$$

In hadron–hadron collisions the colliding external particles do not provide a perturbative scale. There the jet is the only hard scale in the process and we have to deal with an asymmetric situation. In such a configuration the scales s_0 should be chosen as $\mathbf{k}_J^2$ alone. At LO accuracy s_0 is arbitrary and we are indeed free to make this choice. At this stage it is possible to introduce the concept of *unintegrated gluon density* in the hadron. This represents the probability of resolving

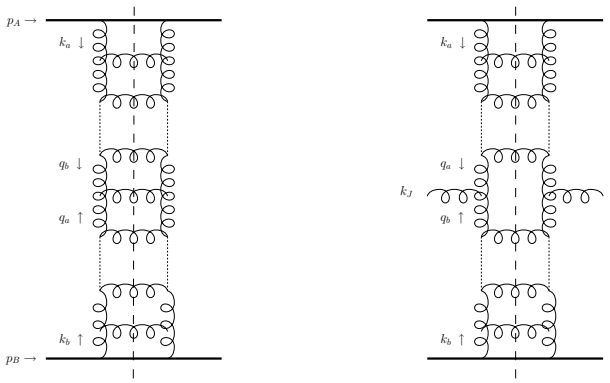


Fig. 1: Total cross section and inclusive one jet production in the BFKL approach.

a gluon carrying a longitudinal momentum fraction x from the incoming hadron, and with a certain transverse momentum k_T. Its relation to the gluon Green's function would be

$$g(x,\mathbf{k}) = \int \frac{d^2\mathbf{q}}{2\pi\mathbf{q}^2}\,\Phi_P(\mathbf{q})\int_{\delta-i\infty}^{\delta+i\infty}\frac{d\omega}{2\pi i}\,x^{-\omega}f_\omega(\mathbf{q},\mathbf{k}). \tag{6}$$

With this new interpretation we can then rewrite Eq. (4) as

$$\frac{d\sigma}{d^2\mathbf{k}_J dy_J} = \int d^2\mathbf{q}_a \int dx_1 \int d^2\mathbf{q}_b \int dx_2\; g(x_1,\mathbf{q}_a)g(x_2,\mathbf{q}_b)\mathcal{V}(\mathbf{q}_a,x_1,\mathbf{q}_b,x_2;\mathbf{k}_J,y_J), \tag{7}$$

with the LO jet vertex for the asymmetric situation being

$$\begin{aligned}\mathcal{V}(\mathbf{q}_a,x_1,\mathbf{q}_b,x_2;\mathbf{k}_J,y_J) &= \mathcal{K}_r^{(\mathrm{Born})}(\mathbf{q}_a,-\mathbf{q}_b)\\ &\times\delta^{(2)}(\mathbf{q}_a+\mathbf{q}_b-\mathbf{k}_J)\;\delta\left(x_1-\sqrt{\frac{\mathbf{k}_J^2}{s}}e^{y_J}\right)\delta\left(x_2-\sqrt{\frac{\mathbf{k}_J^2}{s}}e^{-y_J}\right).\end{aligned} \tag{8}$$

3 Inclusive jet production at NLO

It is possible to follow a similar approach when jet production is considered at NLO. The crucial step in this direction is to modify the LO jet vertex of Eq. (5) and Eq. (8) to include new configurations present at NLO. We show how this is done in the following first subsection. In the second subsection we implement this vertex in a scattering process. In case of hadron–hadron scattering we extend the concept of unintegrated gluon density of Eq. (6) to NLO accuracy. Most importantly, it is shown that a correct choice of intermediate energy scales in this case implies a modification of the impact factors, the jet vertex, and the evolution kernel.

3.1 The NLO jet vertex

For those parts of the NLO kernel responsible for one gluon production we proceed in exactly the same way as at LO. The treatment of those terms related to two particle production is more complicated since for them it is necessary to introduce a jet algorithm. In general terms, if the

two emissions generated by the kernel are nearby in phase space they will be considered as one single jet, otherwise one of them will be identified as the jet whereas the other will be absorbed as an untagged inclusive contribution. Hadronization effects in the final state are neglected and we simply define a cone of radius R_0 in the rapidity–azimuthal angle space such that two particles form a single jet if $R_{12} \equiv \sqrt{(\phi_1-\phi_2)^2+(y_1-y_2)^2} < R_0$. As long as only two emissions are involved this is equivalent to the k_T–clustering algorithm.

To introduce the jet definition in the $2 \to 2$ components of the kernel it is convenient to combine the gluon and quark matrix elements together with the MRK contribution:

$$\begin{aligned}
&\left(\mathcal{K}_{Q\bar{Q}}+\mathcal{K}_{GG}\right)(\mathbf{q}_a,-\mathbf{q}_b) \equiv \int d^{D-2}\mathbf{k}_2 \int dy_2\, \left|\mathcal{B}(\mathbf{q}_a,\mathbf{q}_b,\mathbf{k}_1,\mathbf{k}_2)\right|^2 \\
&= \int d^{D-2}\mathbf{k}_2 \int dy_2 \left\{ \left|\mathcal{A}_{2q}(\mathbf{q}_a,\mathbf{q}_b,\mathbf{k}_1,\mathbf{k}_2)\right|^2 + \left|\mathcal{A}_{2g}(\mathbf{q}_a,\mathbf{q}_b,\mathbf{k}_1,\mathbf{k}_2)\right|^2 \theta(s_\Lambda - s_{12}) \right. \\
&\left. - \mathcal{K}^{(\mathrm{Born})}(\mathbf{q}_a,\mathbf{q}_a-\mathbf{k}_1)\,\mathcal{K}^{(\mathrm{Born})}(\mathbf{q}_a-\mathbf{k}_1,-\mathbf{q}_b)\,\frac{1}{2}\,\theta\left(\ln\frac{s_\Lambda}{\mathbf{k}_2^2}-y_2\right)\theta\left(y_2-\ln\frac{\mathbf{k}_1^2}{s_\Lambda}\right)\right\}, \quad (9)
\end{aligned}$$

with $\mathcal{A}_{2P}$ being the two particle production amplitudes. At NLO it is necessary to separate multi-Regge kinematics (MRK) from quasi-multi-Regge kinematics (QMRK) in a distinct way. With this purpose we introduce an additional scale, s_Λ. The meaning of MRK is that the invariant mass of two emissions is considered larger than s_Λ while in QMRK the invariant mass of one pair of these emissions is below this scale.

The NLO version of Eq. (5) then reads

$$\begin{aligned}
\mathcal{V}(\mathbf{q}_a,\mathbf{q}_b,\eta;\mathbf{k}_J,y_J) &= \left(\mathcal{K}_r^{(\mathrm{Born})}+\mathcal{K}_r^{(\mathrm{virtual})}\right)(\mathbf{q}_a,-\mathbf{q}_b)\Big|_{(a)}^{[y]} \\
&+ \int d^{D-2}\mathbf{k}_2\; dy_2\, \left|\mathcal{B}(\mathbf{q}_a,\mathbf{q}_b,\mathbf{k}_J-\mathbf{k}_2,\mathbf{k}_2)\right|^2 \theta(R_0-R_{12})\Big|_{(b)}^{[y]} \\
&+ 2\int d^{D-2}\mathbf{k}_2\; dy_2\, \left|\mathcal{B}(\mathbf{q}_a,\mathbf{q}_b,\mathbf{k}_J,\mathbf{k}_2)\right|^2 \theta(R_{J2}-R_0)\Big|_{(c)}^{[y]}. \quad (10)
\end{aligned}$$

In this expression we have introduced the notation

$$\Big|_{(a,b)}^{[y]} = \delta^{(2)}\left(\mathbf{q}_a+\mathbf{q}_b-\mathbf{k}_J\right)\delta(\eta-y^{(a,b)}), \quad (11)$$

$$\Big|_{(c)}^{[y]} = \delta^{(2)}\left(\mathbf{q}_a+\mathbf{q}_b-\mathbf{k}_J-\mathbf{k}_2\right)\delta\left(\eta-y^{(c)}\right). \quad (12)$$

The various jet configurations demand several y and x configurations. These are related to the properties of the produced jet in different ways depending on the origin of the jet: if only one gluon was produced in MRK this corresponds to the configuration (a) in the table below, if two particles in QMRK form a jet then we have the case (b), and finally case (c) if the jet is produced out of one of the partons in QMRK. The factor of 2 in the last term of Eq. (10) accounts for the possibility that either emitted particle can form the jet. The vertex can be written in a similar way if one chooses to work in x configuration language. Just by kinematics we get the explicit expressions for the different x configurations listed in the following table:

JET	y configurations	x configurations	
a) $\vdash$	$y^{(a)} = y_J$	$x_1^{(a)} = \frac{\lvert\mathbf{k}_J\rvert}{\sqrt{s}} e^{y_J}$	$x_2^{(a)} = \frac{\lvert\mathbf{k}_J\rvert}{\sqrt{s}} e^{-y_J}$
b) $\lhd$	$y^{(b)} = y_J$	$x_1^{(b)} = \frac{\sqrt{\Sigma}}{\sqrt{s}} e^{y_J}$	$x_2^{(b)} = \frac{\sqrt{\Sigma}}{\sqrt{s}} e^{-y_J}$
c) $\lhd^{\times}$	$y^{(c)} = \frac{1}{2} \ln \frac{x_1^{(c)}}{x_2^{(c)}}$	$x_1^{(c)} = \frac{\lvert\mathbf{k}_J\rvert}{\sqrt{s}} e^{y_J} + \frac{\lvert\mathbf{k}_2\rvert}{\sqrt{s}} e^{y_2}$	$x_2^{(c)} = \frac{\lvert\mathbf{k}_J\rvert}{\sqrt{s}} e^{-y_J} + \frac{\lvert\mathbf{k}_2\rvert}{\sqrt{s}} e^{-y_2}$

The NLO virtual correction to the one–gluon emission kernel, $\mathcal{K}^{(v)}$, was originally calculated in Ref. [9]. It includes explicit infrared divergences which are canceled by the real contributions. The introduction of the jet definition divides the phase space into different sectors. Only if the divergent terms belong to the same configuration this cancellation can be shown analytically. With this in mind we add the singular parts of the two particle production $|\mathcal{B}_s|^2$ in the configuration (a) multiplied by $0 = 1 - \theta(R_0 - R_{12}) - \theta(R_{12} - R_0)$:

$$
\begin{aligned}
\mathcal{V} = & \left[\left(\mathcal{K}_r^{(\mathrm{Born})} + \mathcal{K}_r^{(\mathrm{virtual})} \right) (\mathbf{q}_a, -\mathbf{q}_b) + \int d^{D-2}\mathbf{k}_2 \, dy_2 \, |\mathcal{B}_s(\mathbf{q}_a, \mathbf{q}_b, \mathbf{k}_J - \mathbf{k}_2, \mathbf{k}_2)|^2 \right] \Big|_{(a)} \\
& + \int d^{D-2}\mathbf{k}_2 \, dy_2 \Big[\, |\mathcal{B}(\mathbf{q}_a, \mathbf{q}_b, \mathbf{k}_J - \mathbf{k}_2, \mathbf{k}_2)|^2 \Big|_{(b)} - |\mathcal{B}_s(\mathbf{q}_a, \mathbf{q}_b, \mathbf{k}_J - \mathbf{k}_2, \mathbf{k}_2)|^2 \Big|_{(a)} \Big] \\
& \times \theta(R_0 - R_{12}) + 2 \int d^{D-2}\mathbf{k}_2 \, dy_2 \Big[\, |\mathcal{B}(\mathbf{q}_a, \mathbf{q}_b, \mathbf{k}_J, \mathbf{k}_2)|^2 \, \theta(R_{J2} - R_0) \Big|_{(c)} \\
& - |\mathcal{B}_s(\mathbf{q}_a, \mathbf{q}_b, \mathbf{k}_J - \mathbf{k}_2, \mathbf{k}_2)|^2 \, \theta(R_{12} - R_0) \theta(|\mathbf{k}_1| - |\mathbf{k}_2|) \Big|_{(a)} \Big]. \qquad (13)
\end{aligned}
$$

The cancellation of divergences within the first line is now the same as in the calculation of the full NLO kernel. The remainder is explicitly free of divergences as well since these have been subtracted out.

3.2 Embedding of the jet vertex

The NLO corrections to the kernel have been derived in the situation of the scattering of two objects with an intrinsic hard scale. Hence in the case of $\gamma^*\gamma^*$ scattering the equation (4) is valid also at NLO if we replace the building blocks by their NLO counterparts. The most important piece being the jet vertex, which should be replaced by the one derived in the previous subsection.

We now turn to the case of hadron collisions where MRK has to be necessarily modified to include some evolution in the transverse momenta, since the momentum of the jet will be much larger than the typical transverse scale associated to the hadron. In the LO case we have already explained that, in order to move from the symmetric case to the asymmetric one, it is needed to change the energy scale. The independence of the result from this choice is guaranteed by a compensating modification of the impact factors

$$
\widetilde{\Phi}(\mathbf{k}_a) \;=\; \Phi(\mathbf{k}_a) - \frac{1}{2}\mathbf{k}_a^2 \int d^2\mathbf{q} \frac{\Phi^{(\mathrm{Born})}(\mathbf{q})}{\mathbf{q}^2} \mathcal{K}^{(\mathrm{Born})}(\mathbf{q}, \mathbf{k}_a) \ln \frac{\mathbf{q}^2}{\mathbf{k}_a^2} \qquad (14)
$$

and the evolution kernel

$$
\widetilde{\mathcal{K}}(\mathbf{q}_1, \mathbf{q}_2) \;=\; \mathcal{K}(\mathbf{q}_1, \mathbf{q}_2) - \frac{1}{2} \int d^2\mathbf{q} \, \mathcal{K}^{(\mathrm{Born})}(\mathbf{q}_1, \mathbf{q}) \, \mathcal{K}^{(\mathrm{Born})}(\mathbf{q}, \mathbf{q}_2) \ln \frac{\mathbf{q}^2}{\mathbf{q}_2^2}, \qquad (15)
$$

which corresponds to the first NLO term of a collinear resummation [10].

The emission vertex couples as a kind of impact factor to both Green's functions and receives two such modifications:

$$\begin{aligned}\widetilde{\mathcal{V}}(\mathbf{q}_a,\mathbf{q}_b) &= \mathcal{V}(\mathbf{q}_a,\mathbf{q}_b) - \frac{1}{2}\int d^2\mathbf{q}\,\mathcal{K}^{(\mathrm{Born})}(\mathbf{q}_a,\mathbf{q})\mathcal{V}^{(\mathrm{Born})}(\mathbf{q},\mathbf{q}_b)\ln\frac{\mathbf{q}^2}{(\mathbf{q}-\mathbf{q}_b)^2} \\ &\quad -\frac{1}{2}\int d^2\mathbf{q}\,\mathcal{V}^{(\mathrm{Born})}(\mathbf{q}_a,\mathbf{q})\,\mathcal{K}^{(\mathrm{Born})}(\mathbf{q},\mathbf{q}_b)\ln\frac{\mathbf{q}^2}{(\mathbf{q}_a-\mathbf{q})^2}. \qquad (16)\end{aligned}$$

4 Conclusions

We have extended the NLO BFKL calculations to derive a NLO jet production vertex in k_T–factorization. Our procedure was to 'open' the BFKL kernel to introduce a jet definition at NLO in a consistent way. As the central result, we have defined the off-shell jet production vertex and have shown how it can be used in the context of $\gamma^*\gamma^*$ or of hadron–hadron scattering to calculate inclusive single jet cross sections. For this purpose we have formulated, on the basis of the NLO BFKL equation, a NLO unintegrated gluon density valid in the small–x regime. More recently, a slightly different k_T–factorization scheme has been investigated [11]. A precise analysis of the connection between the two approaches is in progress.

Acknowledgments: F.S. is supported by the Graduiertenkolleg "Zukünftige Entwicklungen in der Teilchenphysik". Discussions with V. Fadin and L. Lipatov are gratefully acknowledged.

References

[1] L. N. Lipatov, Sov. J. Nucl. Phys. **23**, 338 (1976); V. S. Fadin, E. A. Kuraev, and L. N. Lipatov, Phys. Lett. **B60**, 50 (1975); E. A. Kuraev, L. N. Lipatov, and V. S. Fadin, Sov. Phys. JETP **44**, 443 (1976); E. A. Kuraev, L. N. Lipatov, and V. S. Fadin, Sov. Phys. JETP **45**, 199 (1977); I. I. Balitsky and L. N. Lipatov, Sov. J. Nucl. Phys. **28**, 822 (1978).

[2] V. S. Fadin and L. N. Lipatov, Phys. Lett. **B429**, 127 (1998). hep-ph/9802290; M. Ciafaloni and G. Camici, Phys. Lett. **B430**, 349 (1998). hep-ph/9803389.

[3] D. Y. Ivanov and A. Papa, Nucl. Phys. **B732**, 183 (2006). hep-ph/0508162; D. Y. Ivanov and A. Papa, Eur. Phys. J. **C49**, 947 (2007). hep-ph/0610042; F. Caporale, A. Papa and A. S. Vera, arXiv:0707.4100 [hep-ph] .

[4] A. Sabio Vera, Nucl. Phys. **B746**, 1 (2006). hep-ph/0602250; A. Sabio Vera and F. Schwennsen, Nucl. Phys. **B776**, 170 (2007). hep-ph/0702158; C. Marquet and C. Royon, arXiv:0704.3409 [hep-ph].

[5] A. Sabio Vera and F. Schwennsen (2007). arXiv:0708.0549 [hep-ph].

[6] J. Bartels, A. Sabio Vera, and F. Schwennsen, JHEP **11**, 051 (2006). hep-ph/0608154; F. Schwennsen. DESY-THESIS-2007-001, hep-ph/0703198.

[7] D. Ostrovsky, Phys. Rev. **D62**, 054028 (2000). hep-ph/9912258.

[8] S. Catani, M. Ciafaloni, and F. Hautmann. Nucl. Phys. **B366**, 135 (1991). .

[9] V. S. Fadin and L. N. Lipatov, Nucl. Phys. **B406**, 259 (1993); V. S. Fadin, R. Fiore, and A. Quartarolo, Phys. Rev. **D50**, 5893 (1994). hep-th/9405127; V. S. Fadin, R. Fiore, and M. I. Kotsky, Phys. Lett. **B389**, 737 (1996). hep-ph/9608229.

[10] G. P. Salam, JHEP **07**, 019 (1998). hep-ph/9806482; M. Ciafaloni and D. Colferai, Phys. Lett. **B452**, 372 (1999). hep-ph/9812366; M. Ciafaloni, D. Colferai, and G. P. Salam, Phys. Rev. **D60**, 114036 (1999). hep-ph/9905566; A. Sabio Vera, Nucl. Phys. **B722**, 65 (2005). hep-ph/0505128.

[11] J. C. Collins, T. C. Rogers and A. M. Staśto, arXiv:0708.2833 [hep-ph].

Connections between high energy QCD and statistical physics

Stéphane Munier
Centre de physique théorique, École polytechnique, CNRS, 91128 Palaiseau, France

Abstract
It has been proposed that the energy evolution of QCD amplitudes in the high-energy regime falls in the universality class of reaction-diffusion processes. We review the arguments for this correspondence, and we explain how it enables one to compute analytically asymptotic features of QCD amplitudes.

The high-energy regime of QCD has been intensively studied in deep-inelastic e-p scattering at HERA, in heavy-ion collisions at RHIC, and will be probed in proton and heavy-ion scattering at LHC. It is rich of interesting theoretical structures: Links have been found or conjectured with conformal field theory, string theory, and more recently, with a class of models known in statistical physics.

When hadrons scatter at very high energy, the color fields that are generated at the interaction point have a large strength. Perturbative methods qualify as soon as there is a large transverse momentum scale in the event: This property enables one, under certain conditions, to derive QCD evolution equations, in the form of partial differential equations (which can also be stochastic in particular formulations such as the dipole model [1]). On the other hand, strong fields cause the parton densities to saturate, which makes this evolution nonlinear.

Similar looking stochastic nonlinear partial differential equations also appear in problems of apparently different physical origin, such as reaction-diffusion, or population evolution. The goal of this short review is to explain that these similarities are not casual, and that once understood, they can help the derivation of new results for QCD cross sections. We refer the reader to the original papers [2, 3] for the details, and to Ref. [4] for a more extensive review.

In the following, we will consider the scattering of two hadrons, and we will aim at computing their cross section at very high energies. Their relative rapidity is denoted by Y. Since our discussion will rely on resummed perturbative QCD, we think of these hadrons as being small objects, such as color dipoles found, for example, as fluctuations of highly virtual photons. We will always be discussing a definite region of impact parameter.

1 High energy QCD and reaction-diffusion

Cross sections are measured by counting the number of events that are registered in a detector within a given interval of time. Each single event results from an interaction between the scattering hadrons *realized as definite quantum states*, that is, as particular Fock states. Let us go to the frame in which one hadron is almost at rest, while the other one carries most of the kinetic energy, and thus develops a highly-occupied Fock state. As long as saturation effects are negligible (i.e. far from the unitarity limit in which the hadrons appear black to each other), the probability of interaction is proportional to the number of partons in the fast hadron whose transverse momenta

k match the typical momentum scale of the slow hadron. Let us imagine that k is tunable (it is the case when the slow object is a virtual photon), and that one could actually measure the interaction probability of the slow hadron with *a particular Fock state* of the fast hadron. (In practice, it would require the replication of quantum Fock states, which is impossible). We call $T(k)$ this interaction probability (more precisely, it is the forward elastic scattering amplitude at a fixed impact parameter). T is an unphysical quantity, but it will be important to understand it theoretically. The physical amplitude $A(Y, k)$ is just the average of $T(k)$ over all possible Fock state realizations at the considered rapidity Y: $A = \langle T \rangle$, that is, A is the average over all events that may occur, appropriately weighted by their probabilities at a given rapidity.

Standard quantum field theory calculations, based on the evaluation of Feynman diagrams, would directly lead to the expression of A. However, it turns out that such calculations are extremely hard. Instead, understanding first the main analytical features of the scattering probability T off a single typical Fock state of the fast hadron and then averaging over events is a simpler approach, that has been successful in leading to analytical expressions for the asymptotics of the scattering cross sections.

What is precisely known about T is its evolution with rapidity (or energy), at least in the regime in which $T \ll 1$, that is, away from the unitarity limit. When one increases infinitesimally the rapidity of a hadron that has say n partons in its current Fock state, there is a transition rate to a $n+1$, $n+2$...–parton Fock state that is computable in perturbative QCD. It may be extracted from the BFKL equation. A direct formulation is the color dipole model [1], in which this transition probability is explicitely computed. When $T \ll 1$, T is a linear function of the number of partons. Roughly, it reads $T(k) \sim \alpha_s^2 n(k)$, where $n(k)$ is the number of gluons that have a transverse momentum of the order of k.

This transition to higher Fock states may be captured by a linear stochastic equation, of the form

$$\partial_{\bar{\alpha}Y} T = \chi(-\partial_{\ln k^2}) T + \alpha_s \sqrt{T}\, \nu, \tag{1}$$

where $\bar{\alpha} = \alpha_s N_c/\pi$. ν is an appropriate stochastic variable that has zero mean, and variations of order unity when $\bar{\alpha}Y$ is increased by one. $\chi(-\partial_{\ln k^2})$ is the usual BFKL kernel. It describes the branching diffusion of partons, at least in the regime of very high energy in which we are interested in. This means that, when acted on T, it roughly behaves like a diffusion term $\partial^2_{\ln k^2} T$ supplemented by a growth term T (with appropriate coefficients). The noise term is a consequence of discreteness: It implements the fact that we are considering the evolution of one single Fock state, that contains a definite (discrete) number of partons.

On the other hand, when T becomes of the order of 1, *saturation effects* have to enter in order to tame the growth of the number of partons, for unitarity to be preserved. From the work of Balitsky and Kovchegov (BK), we know that in the mean-field limit in which the noise can be neglected (that is, when $A = T$; this is realized when one of the interacting objects is a very large nucleus), the evolution equation for T reads

$$\partial_{\bar{\alpha}Y} T = \chi(-\partial_{\ln k^2}) T - T^2. \tag{2}$$

Hence we shall propose that the full evolution be described by the following stochastic equation:

$$\partial_{\bar{\alpha}Y} T = \chi(-\partial_{\ln k^2}) T - T^2 + \alpha_s \sqrt{T}\, \nu. \tag{3}$$

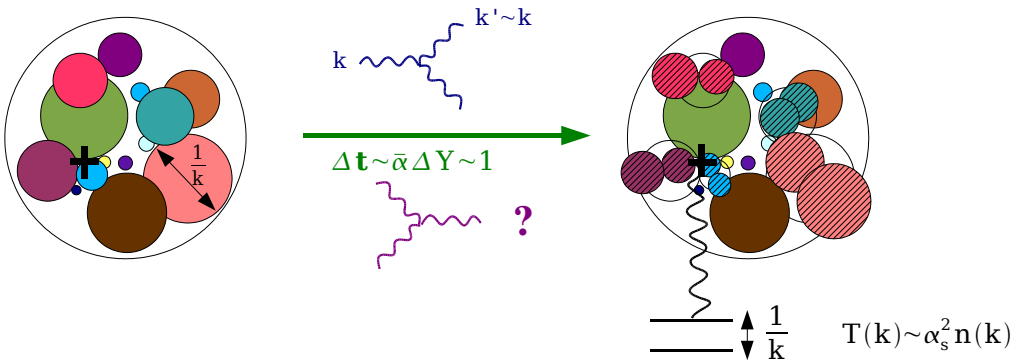


Fig. 1: *Sketch of the gluonic content (the gluons are represented by disks) of the hadron in the transverse plane.* In a little boost, each gluon can split, or nonlinear effects like recombination can take place. At the time of the interaction, the system is probed by a dipole of size $1/k$, which is sensitive to the number of gluons of similar size at a given impact parameter.

This equation is in the universality class of the stochastic version of the Fisher and Kolmogorov, Petrovsky, Piscounov (F-KPP) equation. (The latter would in fact be obtained by replacing $\chi(-\partial_{\ln k^2})T$ by $\partial_{\ln k^2}T + T$ and $\sqrt{T}$ by $\sqrt{T(1-T)}$; for a review and references, see [5].) A schematic picture of the evolution is presented in Fig. 1.

So far, no one has succeeded in formulating rigorously scattering in QCD in the form of a stochastic equation such as (3), in particular the way how saturation occurs is not yet fully understood. Is it gluon recombination, as was advocated in the early papers on saturation [6], or some more subtle process? So the best one can do at this stage is to set the noise term in such a way that the evolution of the hadron Fock state by gluon splittings is exactly reproduced away from the unitarity limit, where the nonlinear term may be neglected. A practical implementation of this process would be, for example, Salam's Monte-Carlo code of the dipole model [7] modified by the addition of a suitable saturation condition which makes sure that T (written in coordinate space) keeps always less than 1 and thus that unitarity is preserved. In this procedure, the expression for the noise is unambiguously fixed (it results from the splitting probability of the dipoles), and the BFKL limit is exactly taken into account. Such a procedure was suggested in Ref. [8], but has not been implemented so far for its technical awkwardness. Some other paths were followed: One may alternatively take ν to be a Gaussian white noise[1] [10]. This simple choice enables one to apply the Ito stochastic calculus, and to draw a link with equations established within QCD such as the B-JIMWLK equations (for a review and references, see Ref. [11], and A. Shoshi's talk at this conference [12].) One may also think of the whole process as a reaction-diffusion process, as we will implicitely do in the next section.

All this may look quite arbitrary: We have merely merged two known limits into a single equation, without much further justification. How can one be sure that A obtained from averaging realizations of Eq. (3) looks like the solution of a genuine QCD equation? Although it

[1] However, in this case, T should not exactly be the amplitude, but rather a kind of "dual amplitude" – see for example Ref. [9].

might sound strange a priori, the solution to the "arbitrary" equation that we have written down is very likely to contain the exact asymptotics of QCD. This fact is actually related to the universality of the solutions to such evolution equations. The statement is the following: For a large class of processes, i.e. for a number of stochastic functions ν and for a variety of forms of the nonlinearities, the asymptotics of the statistics of T (that is, the physical observables $A \equiv \langle T \rangle$, $\langle T^2 \rangle$...) for small α_s and large $\bar{\alpha} Y$ are identical. This is not a theorem, but a conjecture based on a general understanding of how noisy traveling waves propagate. (The propagation mechanism is described in the next section.) The whole point is that the details of the evolution equation do not matter for extracting the asymptotics of the QCD amplitudes.

Let us describe a typical process whose evolution is in the universality class described by the F-KPP equation: reaction-diffusion. This process involves particles on a lattice indexed by some variable x, that evolve by a set of rules of the following form: As time is increased, each particle has a probability either to jump to a nearby site, or to become two particles, or to recombine with another particle on the same lattice site. The balance between creation and recombination of particles determines the equilibrium number of particles on each site N. After a large evolution time, the number of particles on a given site oscillates about N (with an amplitude of the order of the typical statistical fluctuations $\sqrt{N}$). It is the number of particles per site normalized to N that obeys an equation in the universality class of the F-KPP equation.

At this point, we may establish a simple dictionary between reaction-diffusion and QCD. Time is the evolution variable, so is rapidity: $t \leftrightarrow \bar{\alpha} Y$. The variable in which diffusion takes place is $x \leftrightarrow \ln k^2$. The equilibrium number of particles is $N \leftrightarrow 1/\alpha_s^2$. (In QCD, it is fixed by the unitarity condition[2] $T \leq 1$.)

2 Statistical methods and application to QCD

In a first step, we ignore the stochastic term, that is, we address the simple BK equation (2), in order to gain intuition on the form of the solutions. A given localized initial condition ($T \sim \alpha_s^2$ in a region of order 1 around some initial scale $\ln k_0^2$: This would be the physical initial condition) will spread and grow under the action of the kernel $\chi(-\partial_{\ln k^2})$, which, as we wrote before, amounts to a branching diffusion. But as soon as T becomes of the order of 1, the nonlinear term enters to compensate the growth, making T saturate. Then further evolution necessarily has the form of two symmetric traveling waves, since the system can only escape to the right and to the left. Let us focus on the rightmoving wave, that travels towards larger values of $\ln k^2$. This wave front is represented schematically in Fig. 2. It turns out that the shape of this wave in its large-$\ln k^2$ tail is exponential, with a slope that is completely fixed by the linear kernel:

$$T \sim e^{-\gamma_0 \ln k^2}, \quad \gamma_0 \text{ being determined by } \frac{\chi(\gamma_0)}{\gamma_0} = \chi'(\gamma_0). \tag{4}$$

[2] This condition actually holds in coordinate space (when T is a function of transverse sizes). In momentum space, the growth of T with energy is also tamed as soon as the point $T = 1$ has been crossed, although $T(k)$ can take arbitrarily large values. This does not change the conclusions that we shall draw later: The only important feature of the evolution is that T changes behavior in the saturation region. One can see how it goes precisely in QCD e.g. in the numerical simulations presented in Ref. [13].

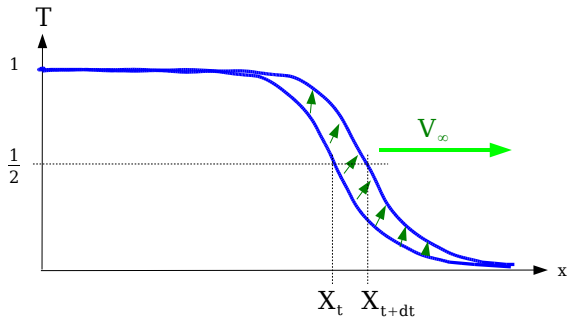


Fig. 2: *Deterministic F-KPP front and its evolution with time.* The arrows show where branching diffusion takes place to drive the motion towards larger values of x.

Since the wave front keeps its shape, it makes sense to characterize its motion by a single velocity V_∞. The latter is also completely determined by the kernel χ. It reads

$$V_\infty = \frac{\chi(\gamma_0)}{\gamma_0}. \tag{5}$$

In QCD, the position X_t of the wave is called the saturation scale $Q_s(Y)$. It characterizes the momentum below which nonlinear saturation effects (gluon recombination, multiple scattering...) become important. The velocity V_∞ defined above is simply the derivative of $\ln Q_s^2(Y)$ with respect to Y. (Recall that the x-variable is $\ln k^2$.)

Now that we have understood the deterministic limit, we may try to put back the noise. We do not know how to attack the problem directly. Instead, we shall stick to a physical approach, and view the evolution equation (3) as describing a reaction-diffusion process. In this framework, we recall that the origin of the noise was the discreteness of the number of particles on each site. Discreteness means in particular that the number of particles $n(k)$ cannot be a fraction of an integer. Consequently, coming back to the simple-minded relationship[3] $T(k) \sim \alpha_s^2 n(k)$, it means that T is either 0 are larger than α_s^2. Brunet and Derrida [15] proposed to replace the full stochastic equation by a deterministic one that takes into account this basic effect of discreteness, which can easily be done by not allowing any growth when $T < \alpha_s^2$. (It amounts to cutting off the tail of the front; to do this in practice, one may for example replace χ by a modified kernel obtained by subtracting its growth term in the region in which $T < \alpha_s^2$. Note that there is no unique prescription.) The solution to this modified equation is again a traveling wave, that exhibits the same overall exponential decay as given by Eq. (4) (except for an uninteresting additional prefactor). Its velocity now reads[4]

$$V_{\rm BD} = \frac{\chi(\gamma_0)}{\gamma_0} - \frac{\pi^2 \gamma_0 \chi''(\gamma_0)}{2\ln^2(1/\alpha_s^2)}. \tag{6}$$

[3] Again, this is not literally true: $T(k)$ is actually continuous, but the tails (below $T = \alpha_s^2$) are decaying exponentially with a characteristic length of one unit in the variable $\ln k^2$. This is steep enough for all our arguments to apply as if $T(k)$ itself were discrete.

[4] This result had already been obtained by Mueller and Shoshi [14]. Actually, the understanding of high-energy scattering as a peculiar reaction-diffusion process emerged from a reinterpretation of their work, in the light of the Brunet-Derrida analytical treatment of traveling waves with a cutoff [15].

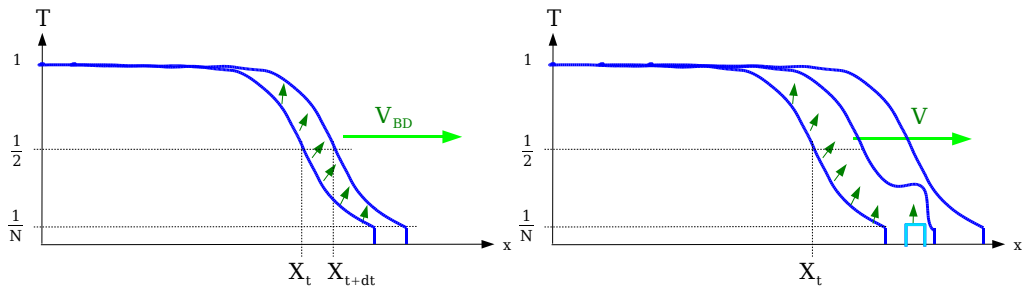


Fig. 3: *Traveling waves solution of the F-KPP equation with a cutoff that simulates discreteness.* In the left sketch, no stochasticity is taken into account while in the right one, particles may randomly be sent ahead of the deterministic front. Their further time/rapidity evolution is also represented.

It is thus less than the velocity of the front in the limit of an infinite number of particles (obtained by letting α_s go to 0), which had to be expected: Indeed, taking into account discreteness amounts to removing some "matter" from the front, which logically slows down its motion.

However, a deterministic solution can only reproduce approximately the realizations of a stochastic evolution. We can incorporate stochasticity back into the picture [16] by noting once again that the noise is only important in the forward tail of the front, where the number of particles is low on the average. From numerical simulations of simple reaction-diffusion models, we observed the following behavior: Most of the time, the motion of the front is almost deterministic, with a velocity given by the solution to the cutoff deterministic equation. From time to time, rarely, a large fluctuation causes a transitory acceleration of the front. This fluctuation consists in one or a few particles being sent far ahead of the deterministic tip of the front, which then evolve into a new front that later gets absorbed by the deterministic front. This behavior is represented in Fig. 3. We conjectured a probability distribution for these fluctuations, as well as the effect that they have on the position of the front after relaxation.

With these elements, we were able to deduce the full statistics of the saturation scale, that is to say not only the mean position (or velocity) of the front,

$$V = \frac{\langle \ln Q_s^2 \rangle}{\bar{\alpha} Y} = \frac{\chi(\gamma_0)}{\gamma_0} - \frac{\pi^2 \gamma_0 \chi''(\gamma_0)}{2 \ln^2(1/\alpha_s^2)} + \pi^2 \gamma_0^2 \chi''(\gamma_0) \frac{3 \ln \ln(1/\alpha_s^2)}{\gamma_0 \ln^3(1/\alpha_s^2)}, \tag{7}$$

but also all its cumulants:

$$\langle \ln^n Q_s^2 \rangle_{\text{cumulant}} = \pi^2 \gamma_0^2 \chi''(\gamma_0) \frac{n! \zeta(n)}{\gamma_0^n} \frac{\bar{\alpha} Y}{\ln^3(1/\alpha_s^2)}, \tag{8}$$

when $n \geq 2$.

Now we recall that the physical amplitude is obtained by averaging T over all possible realizations. Given that the fall off of the large-$\ln k^2$ tail of each single event is exponential, it is not difficult to get the scaling of the scattering amplitude with the help of Eq. (8):

$$A(Y,k) = A\left(\frac{\ln k^2 - \langle \ln Q_s^2(Y) \rangle}{\sqrt{\frac{\bar{\alpha} Y}{\ln^3(1/\alpha_s^2)}}} \right), \tag{9}$$

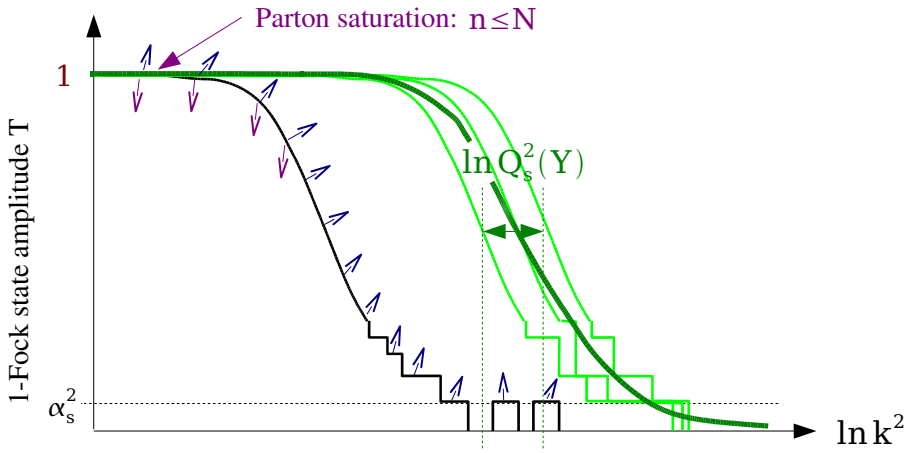


Fig. 4: *Time/rapidity evolution of a noisy traveling wave.* The noise is essentially concentrated at the tip of the front, where the occupation numbers are low. After some time (rapidity), the wave has moved to the right (3 realizations are shown with thin lines), roughly keeping its shape. However, stochasticity manifests itself macroscopically by inducing a dispersion in the positions of the fronts between different realizations. Since the physical amplitude A is the average of all realizations, its very shape is influenced by the noise. (A is represented by the thick line.)

where $\langle \ln Q_s^2(Y) \rangle$ is given by Eq. (7). This is the main analytical result for QCD that comes out of the statistical approach. Note that other results can be extracted on the statistics of the branchings of the gluons in the course of the evolution, but we cannot see a possible phenomenological application.

The emerging overall picture of front propagation is shown in Fig. 4.

3 Prospects

Clearly, the statistical interpretation of scattering processes has proved useful since it has led to both a new understanding and new asymptotical results for high energy QCD. Of course, it relies on a few conjectures that will eventually have to be proved in a more formal way, but we feel that we have so far provided robust physical arguments.

It has to be acknowledged that our new analytical results are not relevant for phenomenology yet, since they make sense for $\ln(1/\alpha_s^2) \gg 1$ only, which requires values of α_s so small that, of course, they are far beyond the experimentally attainable range. A number of authors have however taken seriously the extrapolation of these results to realistic values of α_s and have produced predictions, see e.g. Ref. [17]. On the other hand, numerics could give results valid for $\alpha_s < 0.1$ (optimistically), that is, not far from the phenomenological domain. (This point is discussed in Ref. [8]).

At this point, we have been able to extract properties that QCD shares with simple statistical models. We could claim that this was a correct procedure because asymptotic properties of the solutions do not depend on the details of how saturation occurs. So in some sense, we have done the "easy" part of the work. However, to go closer to phenomenology, one would

need to understand more deeply the details of saturation, which probably constrain the form of the noise ν in Eq. (3). Investigations of some possible models have been conducted, sometimes leading to pecularities in the interpretation, such as negative transition rates [18]. Building a complete picture, valid beyond asymptotics, remains a challenging open question, for which a further breakthrough may be needed.

Finally, our approach to the propagation of noisy traveling waves is not based on a field theory formulation, but is an event-by-event analysis of the shape of realizations, using methods more familiar to statistical physicists than to particle physicists. Being able to recover results such as Eqs. (7), (8), (9) within field theory, starting e.g. from an effective Lagrangian whose building blocks are Reggeon fields, would be a very interesting achievement. Some progress has been made recently, see e.g. Ref. [19].

References

[1] A. H. Mueller, Nucl. Phys. **B415**, 373 (1994).

[2] S. Munier and R. Peschanski, Phys. Rev. Lett. **91**, 232001 (2003);
S. Munier and R. Peschanski, Phys. Rev. **D69**, 034008 (2004);
S. Munier and R. Peschanski, Phys. Rev. **D70**, 077503 (2004).

[3] E. Iancu, A. H. Mueller, and S. Munier, Phys. Lett. **B606**, 342 (2005);
S. Munier, Nucl. Phys. **A755**, 622 (2005).

[4] S. Munier, Acta Phys. Polon. **B37**, 3451 (2006).

[5] D. Panja, Physics Reports **393**, 87.

[6] L. V. Gribov, E. M. Levin, and M. G. Ryskin, Nucl. Phys. **B188**, 555 (1981);
A. H. Mueller and J.-w. Qiu, Nucl. Phys. **B268**, 427 (1986).

[7] G. P. Salam, Comput. Phys. Commun. **105**, 62 (1997).

[8] S. Munier, Phys. Rev. **D75**, 034009 (2007).

[9] C. G. Gardiner, *Handbook of Stochastic Methods*. Springer, 2004.

[10] E. Iancu and D. N. Triantafyllopoulos, Nucl. Phys. **A756**, 419 (2005).

[11] H. Weigert, Prog. Part. Nucl. Phys. **55**, 461 (2005).

[12] A. I. Shoshi (2007). arXiv:0708.4322 [hep-ph].

[13] R. Enberg, K. J. Golec-Biernat, and S. Munier, Phys. Rev. **D72**, 074021 (2005).

[14] A. H. Mueller and A. I. Shoshi, Nucl. Phys. **B692**, 175 (2004).

[15] E. Brunet and B. Derrida, Physical Review E **57**, 2597.

[16] E. Brunet, B. Derrida, A. H. Mueller, and S. Munier, Phys. Rev. **E73**, 056126 (2006).

[17] Y. Hatta, E. Iancu, C. Marquet, G. Soyez, and D. N. Triantafyllopoulos, Nucl. Phys. **A773**, 95 (2006);
M. Kozlov, A. I. Shoshi, and B.-W. Xiao, Nucl. Phys. **A792**, 170 (2007);
M. Kozlov, A. Shoshi, and W. Xiang (2007). arXiv:0707.4142 [hep-ph].

[18] E. Iancu, G. Soyez, and D. N. Triantafyllopoulos, Nucl. Phys. **A768**, 194 (2006);
S. Bondarenko, L. Motyka, A. H. Mueller, A. I. Shoshi, and B. W. Xiao, Eur. Phys. J. **C50**, 593 (2007).

[19] E. Levin, J. Miller, and A. Prygarin (2007). arXiv:0706.2944 [hep-ph].

High energy QCD beyond the mean field approximation

Arif I. Shoshi[*]
Fakultät für Physik, Universität Bielefeld, D-33501 Bielefeld, Germany

Abstract
It has been recently understood how to deal with high-energy scattering beyond the mean field approximation. We review some of the main steps of this theoretical progress, like the role of Lorentz invariance and unitarity requirements, the importance of discreteness and fluctuations of gluon numbers (Pomeron loops), the high-energy QCD/statistical physics correspondence and the consequences for the saturation scale, the scattering amplitude and other, also measurable, quantities.

1 Introduction

The high-energy scattering of a dipole off a nucleus/hadron in the *mean field approximation* is decribed by the BK-equation [1]. The main results following from the BK-equation are the so-called geometric scaling behaviour of the scattering amplitude [2–4] and the, roughly, powerlike energy dependence of the saturation scale [3, 4] which are supported by the HERA data [5, 6].

Over the last few years, we have had real breakthroughs in our understanding of high-energy scattering near the unitarity limit. Namely, we have understood how to deal with small-x dynamics at high energy *beyond the mean field approximation*, i.e., beyond the BK-equation. In this work, after briefly introducing the known dynamics in the mean-field case, we discuss the main steps of the recent theoretical progress as follows: We start with a discussion of the first step beyond the mean field approximation, which was done in Ref. [7] by enforcing the BFKL evolution in the scattering process to satisfy natural requirements as unitarity limits and Lorentz invariance. The consequence was a correction to the saturation scale and the breaking of the geometric scaling at high energies. Then, we explain the relation between high-energy QCD and statistical physics found in Ref. [8] which has clarified the physical picture of, and the way to deal with, the dynamics beyond the BK-equation. We explain that *gluon number fluctuations* from one scattering event to another and the *discreteness* of gluon numbers, both ignored in the BK evolution and also in the Balitsky-JIMWLK equations [9], lead to the breaking of the geometric scaling and to the correction to the saturation scale, respectively. In a next step we show the new evolution equations, the so-called Pomeron loop equations [10–12], which include a new element in the evolution, the Pomeron loop. Finally, we discuss the possibility of phenomenological implications [13–17] of the recent theoretical advances. (For further studies on the recent theoretical advances (not discussed here) see also [17–27].)

1.1 Mean field approximation

Consider the high-energy scattering of a dipole of transverse size $\mathbf{r} = (\mathbf{x} - \mathbf{y})$ off a target (hadron, nucleus) at rapidity $Y = \ln(1/x)$. The Y-dependence of the T-matrix in the mean field

[*]The author acknowledges financial support by the Deutsche Forschungsgemeinschaft under contract 92/2-1.

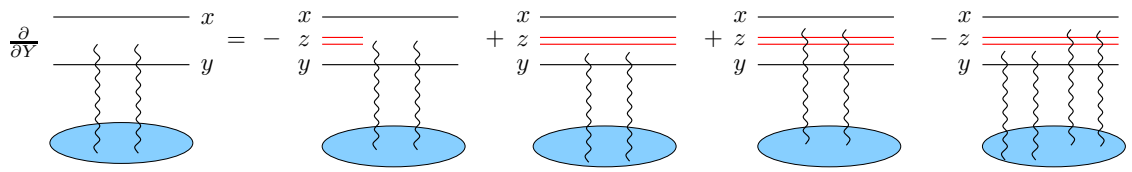


Fig. 1: The diagrammatic representation of the BK-equation for dipole-hadron scattering.

approximation is given by the BK-equation (Y-dependence is suppressed for simplicity)

$$\frac{\partial T_{\mathbf{xy}}}{\partial Y} = \frac{\alpha_s N_c}{2\pi^2} \int d^2\mathbf{z}\, M_{\mathbf{xyz}}\, \left[-T_{\mathbf{xy}} + T_{\mathbf{xz}} + T_{\mathbf{zy}} - T_{\mathbf{xz}}\, T_{\mathbf{zy}}\right] . \tag{1}$$

This equation can be interpreted as follows; If increasing the rapidity of the dipole by dY while keeping the rapidity of the target fixed, the probability for the dipole to emit a gluon increases. In the large-N_c limit the initial quark-antiquark state plus the emitted gluon can be viewed as two dipoles - one of the dipoles consists of the inital quark and the antiquark part of the gluon while the other dipole is given by the quark part of the gluon and the inital antiquark. The probability for the spliting of the inital dipole $(\mathbf{x}-\mathbf{y})$ into two daughter dipoles with transverse sizes $(\mathbf{x}-\mathbf{z})$ and $(\mathbf{z}-\mathbf{y})$ is given by the weight in Eq.(1), $\alpha_s N_c M_{\mathbf{xyz}}/(2\pi^2) d^2\mathbf{z} dY$, where $\mathbf{z}$ is the transverse size of the emitted gluon and $M_{\mathbf{xyz}} = (\mathbf{x}-\mathbf{y})^2/[(\mathbf{x}-\mathbf{z})^2\,(\mathbf{x}-\mathbf{z})^2]$ [28]. On the right-hand side of Eq.(1), the first three terms (first one is virtual) describe the scattering of a single dipole with the target whereas the last term gives the simultanous scattering of the two daughter dipoles with the target, as shown in Fig. 1. Without the last term, the BK-equation reduces to a linear equation, the BFKL equation, which gives the growth of $T_{\mathbf{xy}}$ with rapidity, while the nonlinaer term, $T_{xz}\, T_{zy}$, tames the growth of $T_{\mathbf{xy}}$ such that the unitarity limit, $T_{\mathbf{xy}} \leq 1$, is satisfied.

One of the main results following from the BK-equation is the *geometric scaling* behaviour of the T-matrix [2–4] in a large kinematical window

$$T(r, Y) = T(r^2\, Q_s^2(Y)) , \tag{2}$$

where $Q_s(Y)$ is the so-called *saturation momentum* defined such that $T(r \simeq 1/Q_s, Y)$ be of $\mathcal{O}(1)$. Eq. (2) means that the T-matrix scales with a single quantity $r^2\, Q_s^2(Y)$ rather than depending on r and Y separatelly. This behaviour implies a similar scaling for the DIS cross section, $\sigma^{\gamma^* p}(Y, Q^2) = \sigma^{\gamma^* p}(Q^2/Q_s^2(Y))$, which is supported by the HERA data [5].

Another important result that can be extracted from the BK-equation is the rapidity dependence of the saturation momentum (leading-Y contribution) [3, 4],

$$Q_s^2(Y) = Q_0^2\, \mathrm{Exp}\left[\frac{2\alpha_s N_c}{\pi} \frac{\chi(\lambda_0)}{1-\lambda_0} Y\right] , \tag{3}$$

where $\chi(\lambda)$ is the BFKL kernel and $\lambda_0 = 0.372$.

The shape of the T-matrix resulting from the BK-equation is preserved in the transition region from weak ($T \simeq \alpha_s^2$) to strong ($T \simeq 1$) scattering with increasing Y, showing a "travelling wave" behaviour as sketched in Fig.2, on the left hand side. With increasing Y, the saturation

region at $r \gg 1/Q_s(Y)$ where $T \simeq 1$ however widens up, including smaller and smaller dipoles, due to the growth of the saturation momentum. As we will see in the next sections, the situation changes a lot once gluon number fluctuations are taken into account.

2 Beyond the mean field approximation

2.0.1 Lorentz invariance and unitarity requirements

Let's start with an elementary dipole of size r_1 at rapidity $y = 0$ and evolve it using the BFKL evolution up to $y = Y$. The number density of dipoles of size r_2 at Y in this dipole, $n(r_1, r_2, Y)$, obeys a completeness relation

$$n(r_1, r_2, Y) = \int \frac{d^2r}{2\pi r^2}\, n(r_1, r, Y/2)\, n(r, r_2, Y/2) \tag{4}$$

where on the right hand side the rapidity evolution is separated in two successive steps, $y = 0 \to y = Y/2 \to y = Y$. With

$$T(r_1, r_2, Y) \simeq c\, \alpha_s^2\, r_2^2\, n(r_1, r_2, Y) \tag{5}$$

eq.(4) can be approximately rewritten in terms of the T-matrix as

$$\left(\frac{1}{r_2^2}\, T(r_1, r_2, Y)\right) \simeq \frac{1}{2c\alpha_s^2} \int d\rho \ \left(\frac{1}{r^2}\, T(r_1, r, Y/2)\right) \left(\frac{1}{r_2^2}\, T(r, r_2, Y/2)\right) \tag{6}$$

where $\rho = \ln(r_0^2/r^2)$. In Ref. [7] it was realized that the above completeness relations, or, equivalently, the Lorentz invariance, is satisfied by the BK evolution only by violating unitarity limits. This can be illustrated as follows: Suppose that r_2 is close to the saturation line, $r_2 \simeq 1/Q_s(Y)$, so that the left hand side of Eq.(6) is large. On the right hand side of Eq.(6) it turns out that $T(r_1, r, Y/2)/r^2$ is typically very small in the region of ρ which dominates the integral. This means that $T(r, r_2, Y/2)/r_2^2$ must be typically very large and must violate unitarity, $T(r, r_2, Y/2) \gg 1$, in order to satisfy (6).

The simple procedure used in Ref. [7] to solve the above problem was to limit the region of the ρ-integration in Eq.(6) by a boundary $\rho_2(Y/2)$ so that $T(r, r_2, Y/2)/r_2^2$ would never violate unitarity, or $T(r_1, r, Y/2)/r^2$ would always be larger than α_s^2. The main consequence of this procedure, i.e., BK evolution plus boundary correcting it in the weak scattering region, is the following scaling behaviour of the T-matrix near the unitarity limit

$$T(r, Y) = T\left(\frac{\ln(r^2 Q_s^2(Y))}{\alpha_s Y/(\Delta\rho)^3}\right) \tag{7}$$

and the following energy dependence of the saturation momentum

$$Q_s^2(Y) = Q_0^2\, \mathrm{Exp}\left[\frac{2\alpha_s N_c}{\pi} \frac{\chi(\lambda_0)}{1-\lambda_0} Y \left(1 - \frac{\pi^2 \chi''(\lambda_0)}{2(\Delta\rho)^2 \chi(\lambda_0)}\right)\right] \tag{8}$$

with

$$\Delta\rho = \frac{1}{1-\lambda_0} \ln \frac{1}{\alpha_s^2} + \frac{3}{1-\lambda_0} \ln\ln \frac{1}{\alpha_s^2} + \text{const.}\,. \tag{9}$$

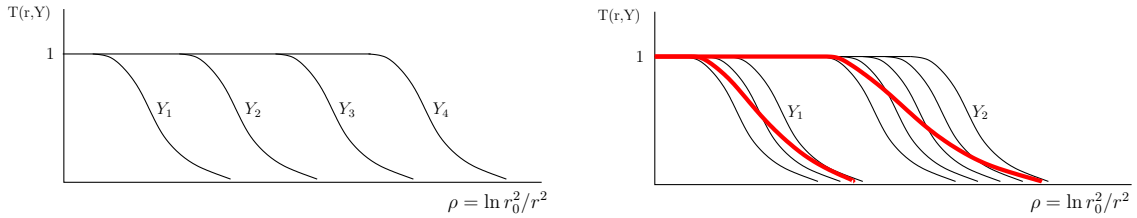


Fig. 2: Left-hand side: The "travelling wave" behaviour of the solution to the BK-equation. Right-hand side: The T-matrix at two different rapidities, Y_1 and Y_2, for different events (thin lines). The thick lines represent the average over the events, $\langle T \rangle$, at the two rapidities, respectivelly. The shape of $\langle T \rangle$ becomes flatter with rising rapidity.

Eq.(7) shows the breaking of the geometric scaling, which was the hallmark of the BK-equation shown in Eq.(2), and Eq.(8) shows the correction to the saturation momentum (cf. Eq.(3)), both emerging as a consequence of the evolution beyond the mean field approximation.

2.0.2 Statistical physics - high density QCD correspondence

The high energy evolution can be viewed also in another way which is inspired by dynamics of reaction-diffusion processes in statistical physics [8]. To show it, let's consider an elementary target dipole of size r_1 which evolves from $y = 0$ up to $y = Y$ and is then probed by an elementary dipole of size r, giving the amplitude $\bar{T}(r_1, r, Y)$. It has become clear that the evolution of the target dipole is *stochastic* leading to random dipole number realizations inside the target dipole at Y, corresponding to different events in an experiment. The physical amplitude, $\bar{T}(r_1, r, Y)$, is then given by averaging over all possible dipole number realizations/events, $\bar{T}(r_1, r, Y) = \langle T(r_1, r, Y) \rangle$, where $T(r_1, r, Y)$ is the amplitude for dipole r scattering off a particular realization of the evolved target dipole at Y. An illustration is shown in Fig.2, the right-hand side plot, where the T-matrix for different events (thin lines) and the average over all events (thick lines), $\langle T \rangle$, are shown at two different rapidities, respectivelly.

The mean field description breaks down at low target dipole occupancy due to the *discreteness and the fluctuations of dipole numbers*. Because of discreteness the dipole occupancy can not be less than one for any dipole size. Taking this fact into account by using the BK equation with a cutoff when T becomes of order α_s^2 [8], or the occupancy of order one (see Eq.(5)), leads exactly to the same correction for the saturation momentum as given in Eq.(3). The latter cutoff is essentially the same as, and gives a natural explanation of, the boundary used in Ref. [7] and briefly explained in the previous section.

The dipole number fluctuations in the low dipole occupancy region result in fluctuations of the saturation momentum from event to event, with the strength

$$\sigma^2 = \langle \rho_s^2 \rangle - \langle \rho_s \rangle^2 \propto \frac{\alpha_s Y}{(\Delta\rho)^3} \tag{10}$$

extracted from numerical simulations of statistical models. The averaging over all events with random saturation momenta, in order to get the physical amplitude, causes the breaking of the geometric scaling and replaces it by a new scaling law, the so-called *diffusive scaling*, in which

case the scattering amplitude is a function of another variable,

$$\langle T(r,Y)\rangle = f\left(\frac{\ln(r^2Q_s^2(Y))}{\sqrt{\alpha_s Y/(\Delta\rho)^3}}\right) . \tag{11}$$

This equation differs from Eq.(7) since Eq.(7) misses dipole number fluctuations. Note that because of the geometric scaling violation, the result in Eq.(11) changes the shape as the rapidity increases, as illustrated in Fig. 2 (right-hand side) by the decreasing slope of the thick line with growing rapidity, in contrast to the solution to the BK-equation in Eq.(2).

The statistical physics/high-density QCD correspondence suggests the following picture for the wavefunction of a highly evolved hadron which is probed by a dipole of transverse size r: As the hadron is boosted to high rapidities the density of gluons inside the hadron grows. Also the fluctuation in gluon numbers, which is characterized by the dispersion in Eq. (10), grows with rising rapidity. However, as long as $\sigma^2 \ll 1$, which means $Y \ll Y_{DS} \simeq (\Delta\rho)^3/\alpha_s$, the effects of fluctuations can be neglected and the evolution of the hadron is described to a good approximation by the BK-equation. Thus, for $Y \ll Y_{DS}$, as shown in Fig.3, to the left of the saturation line, $\rho \ll \langle\rho_s(Y)\rangle = \langle\ln(Q_s^2(Y)\, r_0^2)\rangle$, is the "saturation region" with the "large-size" (small momentum) gluons at a large density, of order $1/\alpha_s$ or the $T \simeq 1$, while the shadowed region is the transition region from high to low gluon density, or the front of the T-matrix (geometric scaling regime). At higher rapidities, $Y \gg Y_{DS}$, where the fluctuations become important, the geometric scaling regime is replaced by the diffusive scaling given in Eq. (11).

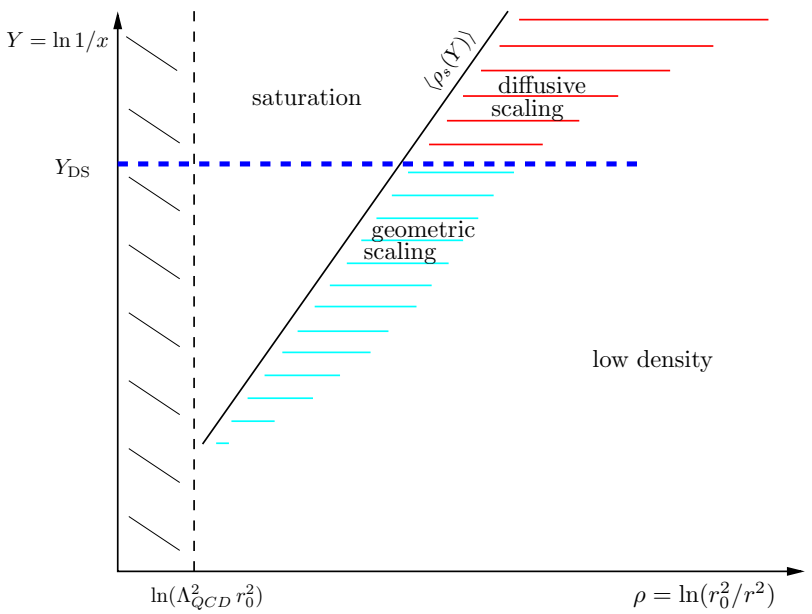


Fig. 3: The phase diagram of the wavefunction of a highly evolved hadron.

2.0.3 Pomeron loop equations

It was always clear that the BK equation does not include fluctuations. However, it took some time to realize that also the Balitsky-JIMWLK equations do miss them. It turned out (see first Reference in [11]) that the Balitsky-JIMWLK equations do include BFKL evolution, "pomeron mergings" but not also "pomeron splittings", which are represented by the three graphs in Fig. 4 for two dipoles scattering off a target, respectivelly. After this insight, the so-called Pomeron loop equations [10, 11] have been constructed to account for "pomeron splittings" or dipole number fluctuations.

The Pomeron loop equations can be expressed in a Hamiltonian language, in which case one extends the JIMWLK-equation [10], or in terms of scattering amplitudes [11], in which case the Balitsky equations are extended. In order to be close to the BK-equation discussed in sec. 1.1, we show the Pomeron loops using the scattering amplitude. In the large-N_c limit, they can be written either as a stochastic equation of Langevin-type,

$$\begin{aligned}\frac{\partial T_{\mathbf{xy}}}{\partial Y} &= \frac{\alpha_s N_c}{2\pi^2}\int\limits_{\mathbf{z}} M_{\mathbf{xyz}}\,\left[-T_{\mathbf{xy}}+T_{\mathbf{xz}}+T_{\mathbf{zy}}-T_{\mathbf{xz}}\,T_{\mathbf{zy}}\right]\\ &+ \frac{\alpha_s}{2\pi}\sqrt{\frac{\alpha_s N_c}{2\pi^2}}\int\limits_{\mathbf{u},\mathbf{v},\mathbf{z}}\mathcal{A}(\mathbf{x},\mathbf{y}|\mathbf{u},\mathbf{z})\frac{|\mathbf{u}-\mathbf{v}|}{(\mathbf{u}-\mathbf{z})^2}\sqrt{\nabla^2_{\mathbf{u}}\nabla^2_{\mathbf{v}}\,T_{\mathbf{uv}}}\,\nu(\mathbf{u},\mathbf{v},\mathbf{z};Y)\end{aligned}\tag{12}$$

or, equivalently, as a hierarchy of coupled equations of averaged amplitudes, where for simplicity we show only the first two of them, which read

$$\begin{aligned}\frac{\partial\langle T_{\mathbf{xy}}\rangle}{\partial Y} &= \frac{\alpha_s N_c}{2\pi^2}\int\limits_{\mathbf{z}} M_{\mathbf{xyz}}\,\left[-\langle T_{\mathbf{xy}}\rangle+\langle T_{\mathbf{xz}}\rangle+\langle T_{\mathbf{zy}}\rangle-\langle T_{\mathbf{xz}}\,T_{\mathbf{zy}}\rangle\right]\\ \frac{\partial\langle T_{\mathbf{xz}}T_{\mathbf{zy}}\rangle}{\partial Y} &= \frac{\alpha_s N_c}{2\pi^2}\int\limits_{\mathbf{t}} M_{\mathbf{xzt}}\,\left[-\langle T_{\mathbf{xz}}T_{\mathbf{zy}}\rangle+\langle T_{\mathbf{xt}}T_{\mathbf{zy}}\rangle+\langle T_{\mathbf{tz}}T_{\mathbf{zy}}\rangle-\langle T_{\mathbf{xt}}\,T_{\mathbf{tz}}T_{\mathbf{zy}}\rangle\right]\\ &+ \frac{\alpha_s N_c}{2\pi^2}\int\limits_{\mathbf{t}} M_{\mathbf{zyt}}\,\left[-\langle T_{\mathbf{xz}}T_{\mathbf{zy}}\rangle+\langle T_{\mathbf{xz}}T_{\mathbf{zt}}\rangle+\langle T_{\mathbf{xz}}T_{\mathbf{ty}}\rangle-\langle T_{\mathbf{xz}}\,T_{\mathbf{zt}}T_{\mathbf{ty}}\rangle\right]\\ &+ \left(\frac{\alpha_s}{2\pi}\right)^2\frac{\alpha_s N_c}{2\pi^2}\int\limits_{\mathbf{u},\mathbf{v}}\mathcal{R}(\mathbf{x},\mathbf{z},\mathbf{z},\mathbf{y}|\mathbf{u},\mathbf{v})\,\langle T_{\mathbf{uv}}\rangle\end{aligned}\tag{13}$$

where the noise is non-diagonal (non-Gaussian) in the first two arguments

$$\langle\nu(\mathbf{u}_1,\mathbf{v}_1,\mathbf{z}_1;Y)\nu(\mathbf{u}_2,\mathbf{v}_2,\mathbf{z}_2;Y')\rangle=\delta_{\mathbf{u}_1\mathbf{v}_2}\,\delta_{\mathbf{u}_2\mathbf{v}_1}\,\delta_{\mathbf{z}_1\mathbf{z}_2}\,\delta_{YY'}\tag{14}$$

the triple Pomeron kernel [29] reads

$$\mathcal{R}(\mathbf{x}_1,\mathbf{y}_1,\mathbf{x}_2,\mathbf{y}_2|\mathbf{u},\mathbf{v})=\int\limits_{\mathbf{z}}\nabla^2_{\mathbf{u}}\nabla^2_{\mathbf{v}}\,\left[M_{\mathbf{uvz}}\,\mathcal{A}(\mathbf{x}_1,\mathbf{y}_1|\mathbf{u},\mathbf{z})\,\mathcal{A}(\mathbf{x}_2,\mathbf{y}_2|\mathbf{z},\mathbf{v})\right],\tag{15}$$

and $\alpha_s^2\mathcal{A}$ is the amplitude for dipole-dipole scattering in the two-gluon exchange approximation and for large-N_c, with

$$\mathcal{A}(\mathbf{x},\mathbf{y}|\mathbf{u},\mathbf{v})=\frac{1}{8}\,\ln^2\left[\frac{(\mathbf{x}-\mathbf{v})^2\,(\mathbf{y}-\mathbf{u})^2}{(\mathbf{x}-\mathbf{u})^2\,(\mathbf{y}-\mathbf{v})^2}\right]\,.\tag{16}$$

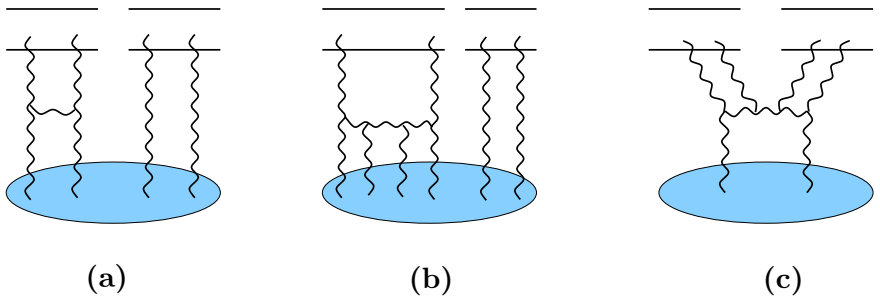


Fig. 4: Two dipoles scattering off a hadron: (a) BFKL interaction, (b) "pomeron mergings", (c) "pomeron splittings".

In above equations the integrations are always over transverse sizes, $\int_{\mathbf{x},y} = d^2x\, d^2y$.

The last term in Eq.(12), containing the non-Gaussian noise ν, is new as compared with the BK-equation and accounts for fluctuations in the dipole numbers or the stochastic nature of the evolution in small-x physics. The hierarchy in Eq.(13) reduces to the BK-equation only in the mean field approximation, i.e., when $\langle T\, T\rangle = \langle T\rangle\langle T\rangle$. The hierarchy in Eq.(13), as compared with the Balitsky-JIMWLK hierarchy, involves in addition to linear BFKL evolution (Fig.4(a)) and pomeron mergings (Fig.4(b)), also pomeron splittings (Fig.4(c)), and therefore, in the course of the evolution, also *pomeron loops*. The three pieces of evolution are represented by the linear terms, nonlinear terms and the last term on the right-hand side of the second equation in Eq.(13), respectivelly, which describes the scattering of two dipoles off a target.

2.0.4 Phenomenology

It isn't yet clear at which energy fluctuation/Pomeron loop effects start becoming important. The results shown in the previous sections, Eq.(8) and Eq.(11), are valid at asymptotic energies. A solution to the evolution equations, which is not yet available because of their complexity, would have helped to better understand the subasymptotics.

Using the statistical physics/high density QCD correspondence, phenomenological consequences of fluctuations in the fixed coupling case have been studied, for example for DIS and diffractive cross sections [15], forward gluon production in hadron-hadron collisions [16] and for the nuclear modification factor R_pA [13], in case fluctuations become important in the range of LHC energies. Recently, in the fixed coupling case, it has been shown that dipole-proton scattering amplitudes which include fluctuation effects seem to describe better the HERA data. Also the parameters turn out reasonable: The diffusion coefficient $D \simeq 0.35$ ($\sigma^2 = D\,Y$) is in agreement with numerical simulations of approximations to Pomeron loop equations [19, 24], and the saturation exponent $\lambda \simeq 0.2$ ($Q_s^2 = (x_0/x)^\lambda$) is decreased as expected theoretically. On the other hand, allowing the coupling to run, however, within a toy model [24] which is supposed to mimic the QCD evolution equations with Pomeron loops, it has been argued that gluon number fluctuations/pomeron loops can be neglected in the range of HERA and LHC energies.

References

[1] Y. V. Kovchegov, Phys. Rev. **D60**, 034008 (1999);
I. Balitsky, Nucl. Phys. **B463**, 99 (1996).

[2] E. Iancu, K. Itakura, and L. McLerran, Nucl. Phys. **A708**, 327 (2002).

[3] A. H. Mueller and D. N. Triantafyllopoulos, Nucl. Phys. **B640**, 331 (2002).

[4] S. Munier and R. Peschanski, Phys. Rev. Lett. **91**, 232001 (2003);
S. Munier and R. Peschanski, Phys. Rev. **D69**, 034008 (2004).

[5] A. M. Stasto, K. J. Golec-Biernat, and J. Kwiecinski, Phys. Rev. Lett. **86**, 596 (2001). hep-ph/0007192.

[6] D. N. Triantafyllopoulos, Nucl. Phys. **B648**, 293 (2003).

[7] A. H. Mueller and A. I. Shoshi, Nucl. Phys. **B692**, 175 (2004).

[8] E. Iancu, A. H. Mueller, and S. Munier, Phys. Lett. **B606**, 342 (2005).

[9] E. Iancu and R. Venugopalan (2003). hep-ph/0303204;
H. Weigert, Prog. Part. Nucl. Phys. **55**, 461 (2005).

[10] A. H. Mueller, A. I. Shoshi, and S. M. H. Wong, Nucl. Phys. **B715**, 440 (2005).

[11] E. Iancu and D. N. Triantafyllopoulos, Nucl. Phys. **A756**, 419 (2005);
E. Iancu and D. N. Triantafyllopoulos, Phys. Lett. **B610**, 253 (2005).

[12] A. Kovner and M. Lublinsky, Phys. Rev. **D71**, 085004 (2005).

[13] M. Kozlov, A. I. Shoshi, and B.-W. Xiao, Nucl. Phys. **A792**, 170 (2007);
M. Kozlov, A. I. Shoshi, and B.-W. Xiao (2007). arXiv:0706.3998 [hep-ph].

[14] M. Kozlov, A. Shoshi, and W. Xiang (2007). arXiv:0707.4142 [hep-ph].

[15] Y. Hatta, E. Iancu, C. Marquet, G. Soyez, and D. N. Triantafyllopoulos, Nucl. Phys. **A773**, 95 (2006).

[16] E. Iancu, C. Marquet, and G. Soyez, Nucl. Phys. **A780**, 52 (2006).

[17] A. Dumitru, E. Iancu, L. Portugal, G. Soyez, and D. N. Triantafyllopoulos (2007). arXiv:0706.2540 [hep-ph].

[18] A. Kovner and M. Lublinsky, Phys. Rev. Lett. **94**, 181603 (2005);
A. Kovner and M. Lublinsky, Phys. Rev. **D72**, 074023 (2005);
C. Marquet, A. H. Mueller, A. I. Shoshi, and S. M. H. Wong, Nucl. Phys. **A762**, 252 (2005);
J. P. Blaizot, E. Iancu, K. Itakura, and D. N. Triantafyllopoulos, Phys. Lett. **B615**, 221 (2005).

[19] G. Soyez, Phys. Rev. **D72**, 016007 (2005);
R. Enberg, K. J. Golec-Biernat, and S. Munier, Phys. Rev. **D72**, 074021 (2005).

[20] E. Brunet, B. Derrida, A. H. Mueller, and S. Munier, Europhys. Lett. **76**, 1 (2006);
E. Brunet, B. Derrida, A. H. Mueller, and S. Munier, Phys. Rev. **E73**, 056126 (2006);
C. Marquet, G. Soyez, and B.-W. Xiao, Phys. Lett. **B639**, 635 (2006).

[21] A. I. Shoshi and B.-W. Xiao, Phys. Rev. **D73**, 094014 (2006);
A. I. Shoshi and B.-W. Xiao, Phys. Rev. **D75**, 054002 (2007).

[22] S. Bondarenko, L. Motyka, A. H. Mueller, A. I. Shoshi, and B. W. Xiao, Eur. Phys. J. **C50**, 593 (2007).

[23] J. P. Blaizot, E. Iancu, and D. N. Triantafyllopoulos, Nucl. Phys. **A784**, 227 (2007).

[24] E. Iancu, J. T. de Santana Amaral, G. Soyez, and D. N. Triantafyllopoulos, Nucl. Phys. **A786**, 131 (2007).

[25] S. Munier, Phys. Rev. **D75**, 034009 (2007).

[26] M. Kozlov and E. Levin, Nucl. Phys. **A779**, 142 (2006);
M. Kozlov, E. Levin, V. Khachatryan, and J. Miller, Nucl. Phys. **A791**, 382 (2007);
E. Levin and A. Prygarin (2007). hep-ph/0701178.

[27] M. A. Braun and G. P. Vacca, Eur. Phys. J. **C50**, 857 (2007).

[28] A. H. Mueller, Nucl. Phys. **B415**, 373 (1994).

[29] M. A. Braun and G. P. Vacca, Eur. Phys. J. **C6**, 147 (1999).

High–energy scattering and Euclidean–Minkowskian duality

Enrico Meggiolaro
Dipartimento di Fisica, Università di Pisa, and INFN, Sezione di Pisa,
Largo Pontecorvo 3, I–56127 Pisa, Italy.

Abstract
We shall discuss how some relevant analyticity and crossing-symmetry properties of the "eikonal scattering amplitudes" of two Wilson loops in QCD, when going from Euclidean to Minkowskian theory, can be related to the still unsolved problem of the asymptotic s–dependence of the hadron–hadron total cross–sections. In particular, we critically discuss the question if (and how) a *pomeron*–like behaviour can be derived from this Euclidean–Minkowskian duality.

1 Loop–loop and meson–meson scattering amplitudes

It was shown in Refs. [1, 2] (for a review see Refs. [3–5] and references therein) that the high–energy meson–meson elastic scattering amplitude can be approximately reconstructed in two steps: i) one first evaluates, in the functional–integral approach, the high–energy elastic scattering amplitude of two $q\bar{q}$ pairs (usually called *dipoles*), of given transverse sizes $\vec{R}_{1\perp}$ and $\vec{R}_{2\perp}$ and given longitudinal–momentum fractions f_1 and f_2 of the two quarks in the two dipoles respectively; ii) one then averages this amplitude over all possible values of $\vec{R}_{1\perp}, f_1$ and $\vec{R}_{2\perp}, f_2$ with two proper squared wave functions $|\psi_1(\vec{R}_{1\perp}, f_1)|^2$ and $|\psi_2(\vec{R}_{2\perp}, f_2)|^2$, describing the two interacting mesons.

The high–energy elastic scattering amplitude of two dipoles (defined in Eq. (8) below) is governed by the following (properly normalized) connected correlation function of two Wilson loops forming an hyperbolic angle χ in the longitudinal plane (see Eq. (4) below) and separated by a distance $\vec{z}_\perp = (z^2, z^3)$ in the transverse plane (impact parameter):

$$\mathcal{C}_M(\chi, \vec{z}_\perp; 1, 2) \equiv \lim_{T\to\infty} \left[\frac{\langle \mathcal{W}_1^{(T)} \mathcal{W}_2^{(T)} \rangle}{\langle \mathcal{W}_1^{(T)} \rangle \langle \mathcal{W}_2^{(T)} \rangle} - 1 \right], \tag{1}$$

where the arguments "1" and "2" in the function $\mathcal{C}_M$ stand for "$\vec{R}_{1\perp}, f_1$" and "$\vec{R}_{2\perp}, f_2$" respectively and the expectation values $\langle \ldots \rangle$ are averages in the sense of the QCD functional integrals. The two (infrared regularized) Wilson loops $\mathcal{W}_1^{(T)}$ and $\mathcal{W}_2^{(T)}$ are defined as:

$$\mathcal{W}_{1,2}^{(T)} \equiv \frac{1}{N_c} \mathrm{Tr} \left\{ \mathcal{P} \exp \left[-ig \oint_{\mathcal{C}_{1,2}} A_\mu(x) dx^\mu \right] \right\}, \tag{2}$$

where $\mathcal{C}_1$ and $\mathcal{C}_2$ are two rectangular paths which follow the classical straight lines for quark $[X_q(\tau)$, forward in proper time $\tau]$ and antiquark $[X_{\bar{q}}(\tau)$, backward in $\tau]$ trajectories, i.e.,

$$\begin{aligned} \mathcal{C}_1 \quad &: \quad X_{1q}^\mu(\tau) = z^\mu + \frac{p_1^\mu}{m}\tau + (1-f_1)R_1^\mu, \quad X_{1\bar{q}}^\mu(\tau) = z^\mu + \frac{p_1^\mu}{m}\tau - f_1 R_1^\mu, \\ \mathcal{C}_2 \quad &: \quad X_{2q}^\mu(\tau) = \frac{p_2^\mu}{m}\tau + (1-f_2)R_2^\mu, \quad X_{2\bar{q}}^\mu(\tau) = \frac{p_2^\mu}{m}\tau - f_2 R_2^\mu, \end{aligned} \tag{3}$$

and are closed by straight–line paths at proper times $\tau = \pm T$, where T plays the role of an infrared cutoff, which can and must be removed in the end ($T \to \infty$). Here p_1 and p_2 are the four–momenta of the two dipoles, taken for simplicity with the same mass m, moving (in the center–of–mass system) with speed V and $-V$ along, for example, the x^1–direction:

$$p_1 = m\left(\cosh\frac{\chi}{2}, \sinh\frac{\chi}{2}, \vec{0}_\perp\right), \quad p_2 = m\left(\cosh\frac{\chi}{2}, -\sinh\frac{\chi}{2}, \vec{0}_\perp\right), \tag{4}$$

$\chi = 2\,\mathrm{arctanh} V$ being the hyperbolic angle between the two trajectories $1q$ and $2q$, i.e., $p_1 \cdot p_2 = m^2 \cosh\chi$. Therefore, in terms of the usual Mandelstam variable s:

$$s \equiv (p_1 + p_2)^2 = 2m^2\,(\cosh\chi + 1)\ , \quad \text{i.e.}: \ \chi \underset{s\to\infty}{\sim} \log\left(\frac{s}{m^2}\right). \tag{5}$$

It is convenient to consider also the correlation function $\mathcal{C}_E(\theta, \vec{z}_\perp; 1, 2)$ in the Euclidean theory of two Euclidean Wilson loops running along two rectangular paths $\widetilde{\mathcal{C}}_1$ and $\widetilde{\mathcal{C}}_2$, defined analogously to (3), with the same $\vec{R}_{1\perp}$, $\vec{R}_{2\perp}$, $\vec{z}_\perp$ and with the Minkowskian four–momenta p_1, p_2 replaced by the following Euclidean four–vectors:

$$p_{1E} = m\left(\sin\frac{\theta}{2}, \vec{0}_\perp, \cos\frac{\theta}{2}\right), \quad p_{2E} = m\left(-\sin\frac{\theta}{2}, \vec{0}_\perp, \cos\frac{\theta}{2}\right), \tag{6}$$

θ being the angle formed by the two trajectories $1q$ and $2q$ in Euclidean four–space, i.e., $p_{1E} \cdot p_{2E} = m^2 \cos\theta$. It has been proved in Ref. [6] that the Minkowskian quantity $\mathcal{C}_M$ with $\chi \in \mathbb{R}^+$ can be reconstructed from the corresponding Euclidean quantity $\mathcal{C}_E$, with $\theta \in (0, \pi)$, by an analytic continuation in the angular variables $\theta \to -i\chi$, exactly as in the case of Wilson lines [7–9]. This result is derived under certain hypotheses of analyticity in the angular variables [10]. In particular, one makes the assumption that the function $\mathcal{C}_E$, as a function of the *complex* variable θ, can be *analytically extended* from the real segment $(0 < \mathrm{Re}\theta < \pi, \mathrm{Im}\theta = 0)$ to a domain $\mathcal{D}_E$, which also includes the negative imaginary axis $(\mathrm{Re}\theta = 0+, \mathrm{Im}\theta < 0)$; and, therefore, the function $\mathcal{C}_M$, as a function of the *complex* variable χ, can be *analytically extended* from the positive real axis $(\mathrm{Re}\chi > 0, \mathrm{Im}\chi = 0+)$ to a domain $\mathcal{D}_M = \{\chi \in \mathbb{C} \mid -i\chi \in \mathcal{D}_E\}$, which also includes the imaginary segment $(\mathrm{Re}\chi = 0, 0 < \mathrm{Im}\chi < \pi)$. The validity of this assumption is confirmed by explicit calculations in perturbation theory [6, 7, 11]. Denoting with $\overline{\mathcal{C}}_M$ and $\overline{\mathcal{C}}_E$ such analytic extensions, we then have the following *analytic–continuation relations* [6, 10]:

$$\begin{aligned} \overline{\mathcal{C}}_E(\theta, \vec{z}_\perp; 1, 2) &= \overline{\mathcal{C}}_M(i\theta, \vec{z}_\perp; 1, 2), \qquad \forall \theta \in \mathcal{D}_E; \\ \overline{\mathcal{C}}_M(\chi, \vec{z}_\perp; 1, 2) &= \overline{\mathcal{C}}_E(-i\chi, \vec{z}_\perp; 1, 2), \qquad \forall \chi \in \mathcal{D}_M. \end{aligned} \tag{7}$$

The validity of the relation (7) for the loop–loop correlators in QCD has been also recently verified in Ref. [11] by an explicit calculation up to the order $\mathcal{O}(g^6)$ in perturbation theory. However we want to stress that the analytic continuation (7) is expected to be an *exact* result, i.e., not restricted to some order in perturbation theory or to some other approximation, and is valid both for the Abelian and the non–Abelian case.

The relation (7) allows the derivation of the *loop–loop scattering amplitude*, which is defined as

$$\mathcal{M}_{(ll)}(s, t; \vec{R}_{1\perp}, f_1, \vec{R}_{2\perp}, f_2) = -i\,2s\,\widetilde{\mathcal{C}}_M\left(\chi \underset{s\to\infty}{\sim} \log\left(\frac{s}{m^2}\right), t; 1, 2\right), \tag{8}$$

$\widetilde{\mathcal{C}}_M$ being the two–dimensional Fourier transform of $\mathcal{C}_M$, with respect to the impact parameter $\vec{z}_\perp$, at transferred momentum $\vec{q}_\perp$ (with $t = -|\vec{q}_\perp|^2$), i.e.,

$$\widetilde{\mathcal{C}}_M(\chi, t; 1, 2) \equiv \int d^2\vec{z}_\perp e^{i\vec{q}_\perp \cdot \vec{z}_\perp} \mathcal{C}_M(\chi, \vec{z}_\perp; 1, 2), \tag{9}$$

from the analytic continuation $\theta \to -i\chi$ of the corresponding Euclidean quantity:

$$\widetilde{\mathcal{C}}_E(\theta, t; 1, 2) \equiv \int d^2\vec{z}_\perp e^{i\vec{q}_\perp \cdot \vec{z}_\perp} \mathcal{C}_E(\theta, \vec{z}_\perp; 1, 2), \tag{10}$$

which can be evaluated non-perturbatively by well–known and well–established techniques available in the Euclidean theory. This approach has been extensively used in the literature [12–16] in order to tackle, from a theoretical point of view, the still unsolved problem of the asymptotic s–dependence of hadron–hadron elastic scattering amplitudes and total cross sections. As we have already said in the beginning, the *hadron–hadron elastic scattering amplitude* $\mathcal{M}_{(hh)}$ can be obtained by averaging the loop–loop scattering amplitude (8) over all possible dipole transverse separations $\vec{R}_{1\perp}$ and $\vec{R}_{2\perp}$ and longitudinal–momentum fractions f_1 and f_2 with two proper squared hadron wave functions [1–5]:

$$\begin{aligned} \mathcal{M}_{(hh)}(s,t) &= \int d^2\vec{R}_{1\perp} \int_0^1 df_1 \, |\psi_1(\vec{R}_{1\perp}, f_1)|^2 \int d^2\vec{R}_{2\perp} \int_0^1 df_2 \, |\psi_2(\vec{R}_{2\perp}, f_2)|^2 \\ &\times \mathcal{M}_{(ll)}(s, t; \vec{R}_{1\perp}, f_1, \vec{R}_{2\perp}, f_2). \end{aligned} \tag{11}$$

Denoting with $\mathcal{C}_M^{(hh)}$ and $\mathcal{C}_E^{(hh)}$ the quantities obtained by averaging the corresponding loop–loop correlation functions $\mathcal{C}_M$ and $\mathcal{C}_E$ over all possible dipole transverse separations $\vec{R}_{1\perp}$ and $\vec{R}_{2\perp}$ and longitudinal–momentum fractions f_1 and f_2, in the same sense as in Eq. (11), we can write:

$$\mathcal{M}_{(hh)}(s,t) = -i\, 2s\, \widetilde{\mathcal{C}}_M^{(hh)} \left(\chi \underset{s\to\infty}{\sim} \log\left(\frac{s}{m^2}\right), t \right). \tag{12}$$

Clearly, by virtue of the relation (7), we also have that:

$$\overline{\widetilde{\mathcal{C}}_M^{(hh)}}(\chi, t) = \overline{\widetilde{\mathcal{C}}_E^{(hh)}}(-i\chi, t), \qquad \forall \chi \in \mathcal{D}_M. \tag{13}$$

By virtue of the optical theorem, the hadron–hadron total cross section can be derived from the imaginary part of the forward hadron–hadron elastic scattering amplitude. Experimental observations at the present time seem to be well described by a *pomeron*–like high–energy behaviour (see, for example, Ref. [4] and references therein):

$$\sigma_{\text{tot}}^{(hh)}(s) \underset{s\to\infty}{\sim} \frac{1}{s} \text{Im}\mathcal{M}_{(hh)}(s, t=0) \sim \sigma_0^{(hh)} \left(\frac{s}{s_0}\right)^{\epsilon_P}, \quad \text{with } \epsilon_P \simeq 0.08. \tag{14}$$

A behaviour like the one of Eq. (14) seems to emerge directly (apart from possible undetermined $\log s$ prefactors) when applying the Euclidean–to–Minkowskian analytic–continuation approach to the study of the line–line/loop–loop scattering amplitudes in strongly coupled (confining) gauge theories using the AdS/CFT correspondence [15, 16].

Moreover, it has been found in Ref. [11] that the dipole–dipole cross section, evaluated from the loop–loop correlator up to the order $\mathcal{O}(g^6)$, reproduces the first iteration of the BFKL *kernel* in the leading–log approximation, the so–called BFKL–*pomeron* behaviour, i.e., $\sim s^{\frac{12\alpha_s}{\pi}\log 2}$, with $\alpha_s = g^2/4\pi$ [17].

2 How a pomeron–like behaviour can be derived

The way in which a *pomeron*–like behaviour can emerge, using the Euclidean–to–Minkowskian analytic continuation, was first shown in Ref. [7] in the case of the line–line (i.e., parton–parton) scattering amplitudes. Here we shall readapt that analysis to the case of the loop–loop scattering amplitudes, with more technical developments, new interesting insights and critical considerations [18]. We start by writing the Euclidean hadronic correlation function in a partial–wave expansion:

$$\widetilde{\mathcal{C}}_E^{(hh)}(\theta,t)=\sum_{l=0}^{\infty}(2l+1)A_l(t)P_l(\cos\theta). \tag{15}$$

As shown in Ref. [10], the loop–antiloop correlator at angle θ in the Euclidean theory (or at hyperbolic angle χ in the Minkowskian theory) can be derived from the corresponding loop–loop correlator by the substitution $\theta\to\pi-\theta$ (or $\chi\to i\pi-\chi$ in the Minkowskian theory). Because of these *crossing–symmetry relations*, it is natural to decompose also our hadronic correlation function $\widetilde{\mathcal{C}}_E^{(hh)}(\theta,t)$ as a sum of a *crossing–symmetric* function $\widetilde{\mathcal{C}}_E^{+}(\theta,t)$ and of a *crossing–antisymmetric* function $\widetilde{\mathcal{C}}_E^{-}(\theta,t)$:

$$\widetilde{\mathcal{C}}_E^{(hh)}(\theta,t)=\widetilde{\mathcal{C}}_E^{+}(\theta,t)+\widetilde{\mathcal{C}}_E^{-}(\theta,t),\quad \widetilde{\mathcal{C}}_E^{\pm}(\theta,t)\equiv\frac{\widetilde{\mathcal{C}}_E^{(hh)}(\theta,t)\pm\widetilde{\mathcal{C}}_E^{(hh)}(\pi-\theta,t)}{2}. \tag{16}$$

Using Eq. (15), we can find the partial–wave expansions of these two functions as follows:

$$\widetilde{\mathcal{C}}_E^{\pm}(\theta,t)=\frac{1}{2}\sum_{l=0}^{\infty}(2l+1)A_l(t)[P_l(\cos\theta)\pm P_l(-\cos\theta)]. \tag{17}$$

Because of the relation $P_l(-\cos\theta)=(-1)^lP_l(\cos\theta)$, valid for non–negative integer values of l, we immediately see that $\widetilde{\mathcal{C}}_E^{+}(\theta,t)$ gets contributions only from even l, while $\widetilde{\mathcal{C}}_E^{-}(\theta,t)$ gets contributions only from odd l. For this reason the functions $\widetilde{\mathcal{C}}_E^{\pm}(\theta,t)$ can also be called *even–signatured* and *odd–signatured* correlation functions respectively and we can replace $A_l(t)$ in Eq. (17) respectively with $A_l^{\pm}(t)\equiv\frac{1}{2}[1\pm(-1)^l]A_l(t)$. However, if we write the hadronic correlation function $\widetilde{\mathcal{C}}_E^{(hh)}(\theta,t)$ in terms of the loop–loop correlation function, averaged over all possible dipole transverse separations $\vec{R}_{1\perp}$ and $\vec{R}_{2\perp}$ and longitudinal–momentum fractions f_1 and f_2 with two proper squared hadron wave functions $|\psi_1(\vec{R}_{1\perp},f_1)|^2$ and $|\psi_2(\vec{R}_{2\perp},f_2)|^2$, and we make use: i) of the so–called *crossing–symmetry relations* for loop–loop correlators [10]:

$$\begin{aligned}&\mathcal{C}_E(\pi-\theta,\vec{z}_\perp;\vec{R}_{1\perp},f_1,\vec{R}_{2\perp},f_2)\\&\quad=\mathcal{C}_E(\theta,\vec{z}_\perp;\vec{R}_{1\perp},f_1,-\vec{R}_{2\perp},1-f_2)=\mathcal{C}_E(\theta,\vec{z}_\perp;-\vec{R}_{1\perp},1-f_1,\vec{R}_{2\perp},f_2),\quad\forall\theta\in\mathbb{R};\end{aligned} \tag{18}$$

and ii) of the rotational– and C–invariance of the squared hadron wave functions, that is:

$$|\psi_i(\vec{R}_{i\perp},f_i)|^2=|\psi_i(-\vec{R}_{i\perp},f_i)|^2=|\psi_i(\vec{R}_{i\perp},1-f_i)|^2=|\psi_i(-\vec{R}_{i\perp},1-f_i)|^2 \tag{19}$$

(see Refs. [3, 5] and also [4], chapter 8.6, and references therein), then we immediately conclude that the hadronic correlation function $\widetilde{\mathcal{C}}_E^{(hh)}(\theta,t)$ is automatically crossing symmetric and

so it coincides with the even–signatured function $\widetilde{\mathcal{C}}_E^+(\theta,t)$, the odd–signatured function $\widetilde{\mathcal{C}}_E^-(\theta,t)$ being identically equal to zero. Upon analytic continuation from the Euclidean to the Minkowskian theory (see again Ref. [10]), this means that the Minkowskian hadronic correlation function $\widetilde{\mathcal{C}}_M^{(hh)}(\chi,t)$, and therefore also the scattering amplitude $\mathcal{M}_{(hh)}$ written in Eq. (12), turns out to be automatically crossing symmetric, i.e., invariant under the exchange $\chi \to i\pi - \chi$: $\widetilde{\mathcal{C}}_M^{(hh)}(\chi,t) = \widetilde{\mathcal{C}}_M^+(\chi,t)$, $\widetilde{\mathcal{C}}_M^-(\chi,t) = 0$. In other words, our formalism naturally leads to a high–energy meson–meson scattering amplitude which, being crossing symmetric, automatically satisfies the Pomeranchuk theorem. An *odderon* (i.e., $C=-1$) exchange seems to be excluded for high–energy meson–meson scattering, while a *pomeron* (i.e., $C=+1$) exchange is possible [19].

Let us therefore proceed by considering our *crossing–symmetric* Euclidean correlation function:

$$\widetilde{\mathcal{C}}_E^{(hh)}(\theta,t) = \widetilde{\mathcal{C}}_E^+(\theta,t) = \frac{1}{2}\sum_{l=0}^{\infty}(2l+1)A_l^+(t)[P_l(\cos\theta)+P_l(-\cos\theta)]. \tag{20}$$

We can now use Cauchy's theorem to rewrite this partial–wave expansion as an integral over l, the so–called *Sommerfeld–Watson transform*:

$$\widetilde{\mathcal{C}}_E^{(hh)}(\theta,t) = \widetilde{\mathcal{C}}_E^+(\theta,t) = -\frac{1}{4i}\int_C \frac{(2l+1)A_l^+(t)[P_l(-\cos\theta)+P_l(\cos\theta)]}{\sin(\pi l)}dl, \tag{21}$$

where "C" is a contour in the complex l–plane, running clockwise around the real positive l–axis and enclosing all non–negative integers, while excluding all the singularities of A_l^+. Here (as in the original derivation: see, e.g., Ref. [4] and references therein) we make the fundamental *assumption* that the singularities of $A_l^+(t)$ in the complex l–plane (at a given t) are only *simple poles*. (However, we want to remark that our *partial–wave amplitudes* $A_l^+(t)$ are *not* the same partial–wave amplitudes considered in the original derivation.) Then we can use again Cauchy's theorem to reshape the contour C into the straight line $\mathrm{Re}(l) = -\frac{1}{2}$ and rewrite the integral (21) as follows:

$$\begin{aligned}\widetilde{\mathcal{C}}_E^{(hh)}(\theta,t) = \widetilde{\mathcal{C}}_E^+(\theta,t) = \\ -\frac{\pi}{2}\sum_{\mathrm{Re}(\sigma_n^+)>-\frac{1}{2}} \frac{(2\sigma_n^+(t)+1)r_n^+(t)[P_{\sigma_n^+(t)}(-\cos\theta)+P_{\sigma_n^+(t)}(\cos\theta)]}{\sin(\pi\sigma_n^+(t))} \\ -\frac{1}{4i}\int_{-\frac{1}{2}-i\infty}^{-\frac{1}{2}+i\infty} \frac{(2l+1)A_l^+(t)[P_l(-\cos\theta)+P_l(\cos\theta)]}{\sin(\pi l)}dl,\end{aligned} \tag{22}$$

where $\sigma_n^+(t)$ is a pole of $A_l^+(t)$ in the complex l–plane and $r_n^+(t)$ is the corresponding residue. We have also assumed that the large–l behaviour of A_l^+ is such that the integrand function in Eq. (21) vanishes enough rapidly (faster than $1/l$) as $|l| \to \infty$ in the right half–plane, so that the contribution from the infinite contour is zero.

Eq. (22) immediately leads to the asymptotic behaviour of the scattering amplitude in the limit $s \to \infty$, with a fixed t ($|t| \ll s$). In fact, making use of the analytic extension (13) when

continuing the angular variable, $\theta \to -i\chi$, we derive that for every $\chi \in \mathbb{R}^+$:

$$\widetilde{\mathcal{C}}_M^{(hh)}(\chi,t) = \overline{\widetilde{\mathcal{C}}_E^{(hh)}}(-i\chi,t) = \\ -\frac{\pi}{2}\sum_{\mathrm{Re}(\sigma_n^+)>-\frac{1}{2}} \frac{(2\sigma_n^+(t)+1)r_n^+(t)[P_{\sigma_n^+(t)}(-\cosh\chi)+P_{\sigma_n^+(t)}(\cosh\chi)]}{\sin(\pi\sigma_n^+(t))} \\ -\frac{1}{4i}\int_{-\frac{1}{2}-i\infty}^{-\frac{1}{2}+i\infty} \frac{(2l+1)A_l^+(t)[P_l(-\cosh\chi)+P_l(\cosh\chi)]}{\sin(\pi l)}dl. \tag{23}$$

Now we must take the large–χ (large–s) limit of this expression, with the hyperbolic angle χ expressed in terms of s by the relation (5), i.e., $\cosh\chi = \frac{s}{2m^2} - 1$. The asymptotic form of $P_\nu(z)$ when $z \to \infty$ is known to be a linear combination of z^ν and of $z^{-\nu-1}$. When $\mathrm{Re}(\nu) > -1/2$, the last term can be neglected and thus, in the limit $s \to \infty$, with a fixed t ($|t| \ll s$), we obtain, from the sum in Eq. (23) (see Ref. [18] for more details):

$$\widetilde{\mathcal{C}}_M^{(hh)}\left(\chi \underset{s\to\infty}{\sim} \log\left(\frac{s}{m^2}\right), t\right) \sim \sum_{\mathrm{Re}(\sigma_n^+)>-\frac{1}{2}} \beta_n^+(t) s^{\sigma_n^+(t)}. \tag{24}$$

The integral in Eq. (23), usually called the *background term*, vanishes at least as $1/\sqrt{s}$ and therefore can be neglected. From eqs. (12) and (24) we can extract the elastic scattering amplitude:

$$\mathcal{M}_{(hh)}(s,t) \underset{s\to\infty}{\sim} -2i \sum_{\mathrm{Re}(\sigma_n^+)>-\frac{1}{2}} \beta_n^+(t) s^{1+\sigma_n^+(t)}. \tag{25}$$

This equation gives the explicit s–dependence of the scattering amplitude at very high energy ($s \to \infty$) and small transferred momentum ($|t| \ll s$). As we can see, this amplitude comes out to be a sum of powers of s. This sort of behaviour for the scattering amplitude is known in the literature as a *Regge behaviour* and $1 + \sigma_n^+(t) \equiv \alpha_n^+(t)$ is the so–called *Regge trajectory*. In the original derivation (see, e.g., Ref. [4] and references therein) the asymptotic behaviour (25) is recovered by analytically continuing the t–channel scattering amplitude to very large imaginary values of the angle between the trajectories of the two exiting particles in the t–channel scattering process. Instead, in our derivation (see Ref. [18]), we have used the Euclidean–to–Minkowskian analytic continuation (13) and we have analytically continued the Euclidean loop–loop correlator to very large (negative) imaginary values of the angle θ between the two Euclidean Wilson loops.

Denoting with $\sigma_P(t)$ the pole with the largest real part (at that given t) and with $\beta_P(t)$ the corresponding coefficient $\beta_n^+(t)$ in Eq. (24), we thus find that:

$$\widetilde{\mathcal{C}}_M^{(hh)}\left(\chi \underset{s\to\infty}{\sim} \log\left(\frac{s}{m^2}\right), t\right) \sim \beta_P(t) s^{\sigma_P(t)} \Longrightarrow \mathcal{M}_{(hh)}(s,t) \underset{s\to\infty}{\sim} -2i\,\beta_P(t)\,s^{\alpha_P(t)}, \tag{26}$$

where $\alpha_P(t) \equiv 1 + \sigma_P(t)$ is the *pomeron trajectory*. Therefore, by virtue of the optical theorem:

$$\sigma_{\mathrm{tot}}^{(hh)}(s) \underset{s\to\infty}{\sim} \frac{1}{s}\mathrm{Im}\mathcal{M}_{(hh)}(s,t=0) \sim \sigma_0^{(hh)}\left(\frac{s}{s_0}\right)^{\epsilon_P}, \quad \text{with } \epsilon_P = \mathrm{Re}[\alpha_P(0)] - 1. \tag{27}$$

We want to stress two important issues which clarify under which conditions we have been able to derive this *pomeron*–like behaviour for the elastic amplitudes and the total cross sections.

i) We have ignored a possible energy dependence of hadron wave functions and we have thus ascribed the high–energy behaviour of the Minkowskian hadronic correlation function exclusively to the *fundamental* loop–loop correlation function (9). With this hypothesis, the coefficients A_l^+ in the partial–wave expansion (15) and, as a consequence, the coefficients β_n^+ and σ_n^+ in the Regge expansion (24) do not depend on s, but they only depend on the variable t.

ii) However, this is not enough to guarantee the experimentally–observed *universality* (i.e., independence on the specific type of hadrons involved in the reaction) of the *pomeron* trajectory $\alpha_P(t)$ in Eq. (26) and, therefore, of the *pomeron* intercept $1+\epsilon_P$ in Eq. (27). In fact, the partial–wave expansion (15) of the hadronic correlation function can also be considered as a result of a partial–wave expansion of the loop–loop Euclidean correlation function (10), i.e.,

$$\widetilde{\mathcal{C}}_E(\theta,t;1,2)=\sum_{l=0}^{\infty}(2l+1)\mathcal{A}_l(t;1,2)P_l(\cos\theta), \tag{28}$$

which is then averaged with two proper squared hadron wave functions, in the same sense as in Eq. (11), so giving the Euclidean hadronic correlation function (15). If we now repeat for the partial–wave expansion (28) the same manipulations that have led us from Eq. (15) to Eq. (24), we arrive at the following Regge expansion for the (even–signatured) loop–loop Minkowskian correlator:

$$\widetilde{\mathcal{C}}_M^+\left(\chi\underset{s\to\infty}{\sim}\log\left(\frac{s}{m^2}\right),t;1,2\right)\sim\sum_{\mathrm{Re}(a_n^+)>-\frac{1}{2}}b_n^+(t;1,2)s^{a_n^+(t;1,2)}, \tag{29}$$

where $a_n^+(t;1,2)$ is a pole of $\mathcal{A}_l^+(t;1,2)$ in the complex l–plane. After inserting the expansion (29) into the expression for the Minkowskian hadronic correlation function:

$$\begin{aligned}\widetilde{\mathcal{C}}_M^{(hh)}(\chi,t) &= \int d^2\vec{R}_{1\perp}\int_0^1 df_1\,|\psi_1(\vec{R}_{1\perp},f_1)|^2\int d^2\vec{R}_{2\perp}\int_0^1 df_2\,|\psi_2(\vec{R}_{2\perp},f_2)|^2\\ &\times\ \widetilde{\mathcal{C}}_M^+(\chi,t;1,2),\end{aligned} \tag{30}$$

one in general finds a high–energy behaviour which hardly fits with that reported in Eq. (26) with a universal *pomeron* trajectory $\alpha_P(t)$, *unless* one assumes that, for each given loop–loop correlation function with transverse separations $\vec{R}_{1\perp}$ and $\vec{R}_{2\perp}$ and longitudinal–momentum fractions f_1 and f_2, (at least) the location of the pole $a_n^+(t;1,2)$ with the largest real part does not depend on $\vec{R}_{1\perp}, f_1$ and $\vec{R}_{2\perp}, f_2$, but only depends on t. If we denote this common pole with $\sigma_P(t)$, we then immediately recover the high–energy behaviour (26), where the coefficient $\beta_P(t)$ in front, differently from the universal function $\alpha_P(t)=1+\sigma_P(t)$, explicitly depends on the specific type of hadrons involved in the process.

3 Conclusions and outlook

In conclusion, we have shown that the Euclidean–to–Minkowskian analytic–continuation approach can, with the inclusion of some extra (more or less plausible) *assumptions*, easily reproduce a *pomeron*–like behaviour for the high–energy total cross sections, in apparent agreement with the present–time experimental observations. However, we should also keep in mind that

the *pomeron*–like behaviour (14) is, strictly speaking, theoretically forbidden (at least if considered as a true *asymptotic* behaviour) by the well–known Froissart–Lukaszuk–Martin (FLM) theorem [20]. In this respect, the *pomeron*–like behaviour (14) can at most be regarded as a sort of *pre–asymptotic* (but not really *asymptotic*) behaviour of the high–energy total cross sections, valid in a certain high–energy range.
Immediately the following question arises: why our approach, which was formulated so to give the really asymptotic large–s behaviour of scattering amplitudes and total cross sections, is also able to reproduce pre–asymptotic behaviours (violating the FLM bound) like the one in (14)?
The answer is clearly that the extra *assumptions*, i.e., the *models*, which one implicitly or explicitly uses in the calculation of the Euclidean correlation function $\widetilde{C}_E$, play a fundamental role in this respect. Of course, every model has its own *limitations*, which reflect in the variety of answers in the literature. Unfortunately these *limitations* are often out of control, in the sense that no one knows exactly how much infromation is lost due to these approximations. This is surely a crucial point which, in our opinion, should be further investigated in the future, also with the help of direct lattice calculations of the loop–loop Euclidean correlation function.

References

[1] H.G. Dosch, E. Ferreira and A. Krämer, Phys. Rev. **D50**, 1992 (1994).

[2] O. Nachtmann, in *Perturbative and Nonperturbative aspects of Quantum Field Theory*, edited by H. Latal and W. Schweiger, Springer–Verlag, Berlin, Heidelberg, 1997.

[3] H.G. Dosch, in *At the frontier of Particle Physics – Handbook of QCD (Boris Ioffe Festschrift)*, vol. 2, edited by M. Shifman, World Scientific, Singapore, 2001, pp. 1195–1236.

[4] S. Donnachie, G. Dosch, P. Landshoff and O. Nachtmann, *Pomeron Physics and QCD*, Cambridge University Press, Cambridge, 2002.

[5] A.I. Shoshi, F.D. Steffen and H.J. Pirner, Nucl. Phys. **A709**, 131 (2002).

[6] E. Meggiolaro, Nucl. Phys. **B707**, 199 (2005).

[7] E. Meggiolaro, Z. Phys. **C76**, 523 (1997).

[8] E. Meggiolaro, Eur. Phys. J. **C4**, 101 (1998).

[9] E. Meggiolaro, Nucl. Phys. **B625**, 312 (2002).

[10] M. Giordano and E. Meggiolaro, Phys. Rev. **D74**, 016003 (2006).

[11] A. Babansky and I. Balitsky, Phys. Rev. **D67**, 054026 (2003).

[12] A.I. Shoshi, F.D. Steffen, H.G. Dosch and H.J. Pirner, Phys. Rev. **D68**, 074004 (2003).

[13] E. Shuryak and I. Zahed, Phys. Rev. **D62**, 085014 (2000).

[14] A.E. Dorokhov and I.O. Cherednikov, Ann. Phys. **314**, 321 (2004).

[15] R.A. Janik and R. Peschanski, Nucl. Phys. **B586**, 163 (2000).

[16] R.A. Janik, Phys. Lett. **B500**, 118 (2001).

[17] V.S. Fadin, E.A. Kuraev and L.N. Lipatov, Phys. Lett. **B60**, 50 (1975);
L.N. Lipatov, Sov. J. Nucl. Phys. **23**, 338 (1976);
E.A. Kuraev, L.N. Lipatov and V.S. Fadin, Sov. Phys. JETP **45**, 199 (1977);
I.I. Balitsky and L.N. Lipatov, Sov. J. Nucl. Phys. **28**, 822 (1978).

[18] E. Meggiolaro, Phys. Lett. **B651**, 177 (2007).

[19] H.G. Dosch and M. Rueter, Phys. Lett. **B380**, 177 (1996).

[20] M. Froissart, Phys. Rev. **123**, 1053 (1961);
A. Martin, Il Nuovo Cimento **42A**, 930 (1966);
L. Lukaszuk and A. Martin, Il Nuovo Cimento **47A**, 265 (1967).

Insight into New Physics with Tagged Forward Protons at the LHC

V.A. Khoze[1,2]†*, A.D. Martin*[1] *and M.G. Ryskin*[1,2]
[1] Department of Physics and Institute for Particle Physics Phenomenology,
University of Durham, DH1 3LE, UK
[2] St. Petersburg Nuclear Physics Institute, Gatchina, St. Petersburg, 188300, Russia

Abstract
The addition of forward proton detectors to LHC experiments will significantly enlarge the potential for studying New Physics. We discuss a topical example of Higgs production by the central exclusive diffractive process, $pp \to p + H + p$. Special attention is paid to the backgrounds to the $H \to b\bar{b}$ signal.

1 Introduction

The use of diffractive processes to study the Standard Model (SM) and New Physics at the LHC has only been fully appreciated within the last few years; see, for example [1–6]. By detecting protons that have lost only about 1-3% of their longitudinal momentum [7], a rich QCD, electroweak and BSM programme becomes accessible experimentally, with the potential to study phenomena which are unique to the LHC, and difficult even at a future linear collider. Particularly interesting are the so-called central exclusive production (CEP) processes which provide an extremely favourable environment to search for, and identify the nature of, new particles at the LHC. The first that comes to mind are the Higgs bosons, but there is also a rich, more exotic, physics menu including (light) gluino and squark production, searches for extra dimensions, gluinonia, radions, and indeed any new object which has 0^{++} (or 2^{++}) quantum numbers and couples strongly to gluons. By "central exclusive" we mean a process of the type $pp \to p+X+p$, where the + signs denote the absence of hadronic activity (that is, the presence of rapidity gaps) between the outgoing protons and the decay products of the centrally produced system X. The basic mechanism driving the process is shown in Fig. 1. There are several reasons why CEP is

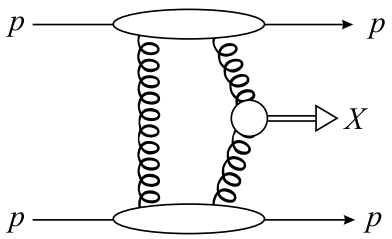


Fig. 1: The basic mechanism for the exclusive process $pp \to p + X + p$. The system X is produced by the fusion of two active gluons, with a screening gluon exchanged to neutralize the colour.

especially attractive for searches for new heavy objects. *First*, if the outgoing protons remain

† speaker

intact and scatter through small angles then, to a very good approximation, the primary active di-gluon system obeys a $J_z = 0$, C-even, P-even, selection rule [8]. Here J_z is the projection of the total angular momentum along the proton beam axis. This selection rule readily permits a clean determination of the quantum numbers of the observed new (for example, Higgs-like) resonance, when the dominant production is a scalar state. *Secondly*, because the process is exclusive, the energy loss of the outgoing protons is directly related to the mass of the central system, allowing a potentially excellent mass resolution, irrespective of the decay mode of the centrally produced system. *Thirdly*, in many topical cases, in particular, for Higgs boson production, a signal-to-background ratio of order 1 (or even better) is achievable [3, 9–11]. In particular, due to $J_z = 0$ selection, leading-order QCD $b\bar{b}$ production is suppressed by a factor $(m_b/E_T)^2$, where E_T is the transverse energy of the $b, \bar{b}$ jets. Therefore, for a low mass Higgs, $M_H \lesssim 150$ GeV, there is a possibility to observe the main $b\bar{b}$ decay mode and to directly measure the $H \to b\bar{b}$ Yukawa coupling constant. The signal-to-background ratio may become significantly larger for a Higgs boson in certain regions of the MSSM parameter space.

It is worth mentioning that, by tagging both of the outgoing protons, the LHC is effectively turned into a gluon-gluon collider. This will open up a rich, QCD physics menu, which will allow the study of the skewed, unintegrated gluon densities, as well as the details of rapidity gap survival. Note that CEP provides a source of practically pure gluon jets; that is we effectively have a 'gluon factory' [8]. The forward-proton-tagging approach also offers a unique programme of high-energy photon-interaction physics at the LHC.

2 Central Exclusive Higgs production

The 'benchmark' CEP new physics process is Higgs production. Studies of the Higgs sector are at the heart of the recent proposal [7] to complement the LHC central detectors with proton taggers placed at 420 m either side of the interaction point.

Our current understanding is, that if a SM-like Higgs boson exists in Nature, it will be detected at the LHC. However, various extended models predict a large diversity of Higgs-like bosons with different masses, couplings and CP-parities. The best studied extension of the SM up to now is the MSSM, in which there are three neutral Higgs bosons, the scalars h and H, and the pseudoscalar A.

The forward proton tagging mode is especially advantageous for the study of the MSSM sector. Note that when using the "standard" non-diffractive production mechanisms, there is usually an important region of MSSM parameter region, where the LHC can detect only the Higgs boson with SM-like properties. To check that a discovered state is indeed a scalar Higgs boson, and to distinguish between the Higgs boson(s) of the SM or the MSSM and those from of extended Higgs theories will be highly non-trivial task. Without forward proton tagging, it would require interplay with observations at the Next Linear Collider. Moreover, within the MSSM, the weak-boson-fusion channel becomes of no practical use for the production of the heavier scalar H or the pseudoscalar A boson. On the other hand, in the forward proton mode the pseudoscalar A is practically filtered out, and the detection of the H boson should be achievable [9, 10]. In addition, in some MSSM scenarios, CEP provides an excellent opportunity for probing the CP-structure of the Higgs sector by measuring directly the azimuthal asymmetry of the outgoing protons [12]. In Fig. 2 we show, for reference purposes, the total CEP cross section for the SM Higgs boson

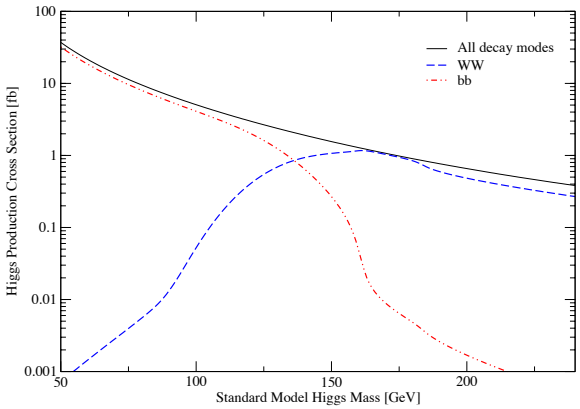


Fig. 2: The cross section times branching ratio for CEP of the SM Higgs [13].

times branching ratio for the WW and $b\bar{b}$ channels, as a function of the Higgs mass. We see that the expected total cross section for the CEP of a SM Higgs, with mass 120 GeV, is 3 fb, falling to just less than 1 fb for a mass of 200 GeV. With a good understanding of the detectors and favourable experimental conditions, the rate for the SM Higgs of mass 120 GeV for the integrated LHC luminosity of $\mathcal{L} = 60\ \mathrm{fb}^{-1}$ would be quite sizeable (around 100 events). However, with the presently envisaged LHC detectors, there are various experimental problems. First of all, trigger signals from protons detected at 420 m cannot reach the central detector in time to be used in the Level 1 trigger. For this, we have to rely on the central detector. Other factors may also strongly reduce the current expectations for the detected signal rate, in particular, the b-tagging efficiency, the jet energy resolution etc. At high luminosities there is also a potentially dangerous problem of backgrounds due to the overlapping events in the same bunch crossing (the so-called "pile-up" events). In summary, with the current hardware, the expectation is that there will be not more than a dozen SM Higgs signal events for an integrated LHC luminosity of $\mathcal{L} = 60\ \mathrm{fb}^{-1}$. Whether experimental ingenuity will increase this number remains to be seen. Indeed, it is quite possible that "clever" hardware and the use of optimized cuts will increase the rate.

As we already mentioned, in the MSSM, the CEP cross sections can be an order-of-magnitude or more higher. This is illustrated in Fig. 3, which shows the contours for the ratio R of signal events in the MSSM over those in the SM in the CEP of $H \to b\bar{b}$ in the M_A–$\tan\beta$ plane, see [10].

As discussed above, the exclusive Higgs signal is particularly clean, and the signal-to-background ratio is quite favourable, at least, at an instantaneous luminosity $L \sim 2 \times 10^{33}\,\mathrm{cm}^{-2}\,\mathrm{s}^{-1}$, when the effect of pile-up can be kept under full control, see [10, 11] and references therein. However, without improving the LHC hardware, the expected event rate in the SM case is quite limited, and so it is important to test various ingredients of the adopted theoretical scheme [1,2,8] by studying the related processes at HERA and the Tevatron. Various such tests have been performed so far,

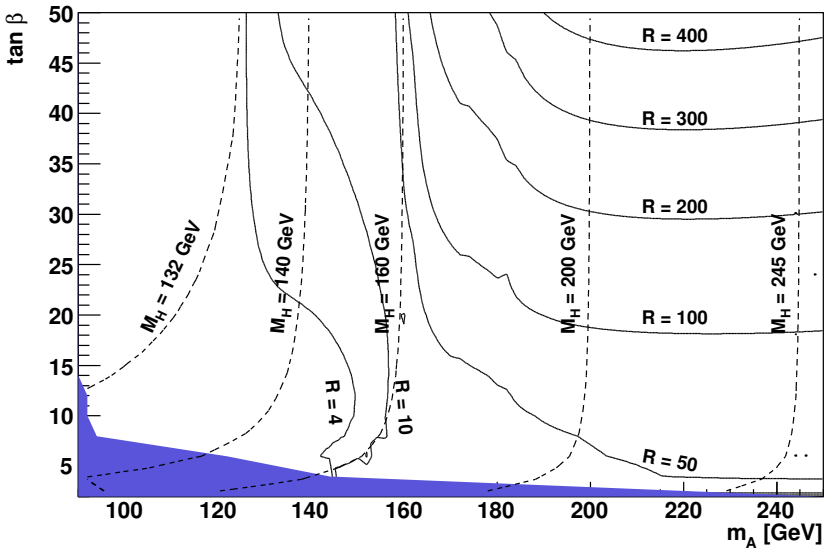


Fig. 3: Contours for the ratio R of the $H \to b\bar{b}$ signal events in the MSSM over those in the SM in CED process in the M_A–$\tan\beta$ plane. The ratio is shown for the $M_h^{\max}$ benchmark scenario (with $\mu = +200$ GeV). The values of the mass of the Higgs boson are indicated by dashed contour lines. The dark shaded region is excluded by the LEP Higgs searches.

see for example, [14, 15] and references therein.

The straightforward checks come from the study of processes which are mediated by the same mechanism as CEP of the Higgs boson, but with rates which are sufficiently high, so that they may be observed already at the Tevatron. The most obvious examples are those in which the Higgs is replaced by either a dijet system, or a χ_c meson, or a $\gamma\gamma$ pair. The reported preliminary CDF data on these CEP processes (see for example, [16]) show a good agreement with the theoretical expectations by Durham group.

Especially impressive are the recent CDF data [16] on exclusive production of a pair of high E_T jets, $p\bar{p} \to p + jj + \bar{p}$. The corresponding cross section was evaluated to be about 10^4 times larger than that for the production of a SM Higgs boson. Since the dijet CEP cross section is rather large, this process appears to be an ideal 'standard candle'. A comparison of the data with analytical predictions [1, 2] is given in Fig. 4. It shows the $E_T^{\min}$ dependence for the dijet events with $R_{jj} \equiv M_{\rm dijet}/M_{\rm PP} > 0.8$, where $M_{\rm PP}$ is the invariant energy of the incoming Pomeron-Pomeron system. The agreement with the theoretical expectations [1, 2] lends credence to the predictions for the CED Higgs production [16].

3 The backgrounds to the $p + (h, H \to b\bar{b}) + p$ signal

The importance of the $p + (h, H \to b\bar{b}) + p$ process means that the physical backgrounds to this reaction must be thoroughly addressed. Recall that the unique advantage of the $b\bar{b}$ CEP process

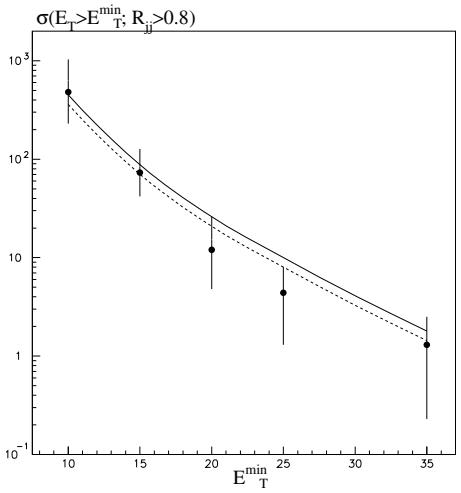


Fig. 4: The cross section for 'exclusive' dijet production as a function $E_T^{\rm min}$ as measured by CDF [16]. The data correspond to the cross section integrated over the domain $R_{jj} \equiv M_{\rm dijet}/M_{\rm PP} > 0.8$ and $E_T > E_T^{\rm min}$. A jet cone of $R < 0.7$ is used. The curves are the exclusive cross section calculated [2] using the CDF event selection. The solid curve is obtained by rescaling the parton transverse momentum p_T to the measured jet transverse energy E_T by $E_T = 0.8 p_T$. The dashed curve assumes $E_T = 0.75 p_T$. The rescaling procedure effectively accounts for the hadronization and radiative effects, and for jet energy losses outside the jet cone.

is the $J_z = 0$ selection rule, which requires the LO $gg^{PP} \to b\bar{b}$ background to vanish in the limit of massless quarks and forward going protons. However, there are still four main sources of background [3, 17].

(i) The prolific (LO) $gg^{PP} \to gg$ subprocess can mimic $b\bar{b}$ production since we may misidentify the gluons as b and $\bar{b}$ jets.

(ii) An admixture of $|J_z| = 2$ production, arising from non-forward going protons, which contributes to the LO $gg^{PP} \to b\bar{b}$ background.

(iii) Because of non-zero mass of the quark there is a contribution to the $J_z = 0$ cross section of order m_b^2/E_T^2. This term currently raises the main concern. The problem is that the result is strongly affected by the large higher-order QCD effects. In particular, the one-loop double logarithmic contribution exceeds the Born term, and the final result becomes strongly dependent on the NNLO effects. There is no complete calculation of these effects for the $gg^{PP} \to b\bar{b}$ process. The validity of estimates given in [17] has an accuracy not better than a factor of 2-4. The good news is that this contribution decreases with increasing E_T much faster than the other backgrounds.

(iv) Finally, there is a possibility of NLO $gg^{PP} \to b\bar{b}g$ background contributions, which for large angle, hard gluon radiation do not obey the selection rules. In particular, the extra gluon may go unobserved in the direction of a forward proton. This background is reduced by requiring the approximate equality $M_{\rm missing} = M_{b\bar{b}}$. Calculations [18] show that this

background may be safely neglected. The remaining danger is large-angle hard gluon emission which is collinear with either the b or $\bar{b}$ jet, and, therefore, unobservable. This background source results in a sizeable contribution, see [17].

There are also other (potentially worrying) background sources, which after a thorough investigation [17, 18], have been neglected. This is either because their contributions are numerically small from the very beginning, or because they can be reduced to an acceptable level by straightforward experimental cuts.
Next, a potential background source can arise from the collision of two soft Pomerons. Such backgrounds were carefully evaluated in [18], and it was found that they are quite small.
In summary, the main background contributions come from exclusive dijet production as listed in the items (i)-(iv) above. Within the accuracy of the existing calculations [3, 8, 17], the overall background to the 0^+ Higgs signal in the $b\bar{b}$ mode can be approximated by the following formula, see [10]

$$\frac{\mathrm{d}\sigma^B}{\mathrm{d}M} \approx 0.5\,\mathrm{fb/GeV}\left[0.92\left(\frac{120}{M}\right)^6 + \frac{1}{2}\left(\frac{120}{M}\right)^8\right]. \qquad (1)$$

Note that this approximate expression may be used only for the purposes of making quick estimates of the background, since no detector simulation has been performed.

4 Conclusion

The installation of proton-tagging detectors in the distant forward regions around the ATLAS and/or CMS central detectors would add unique capabilities to the existing LHC experimental programme. The calculation of the rates of CEP processes show that there is a good chance that new heavy particle production could be observed in this mode. For a Higgs boson this would amount to a direct determination of its quantum numbers. For certain MSSM scenarios, the tagged-proton channel may even be the Higgs discovery channel. Moreover, with sufficient luminosity, proton tagging may provide direct evidence of CP-violation within the Higgs sector. There is also a rich QCD, electroweak, and more exotic physics, menu.

Here we focused on the unique advantages of CEP Higgs production. The events are clean, but the predicted yield for the SM Higgs for an integrated luminosity of $\mathcal{L} = 60\ \mathrm{fb}^{-1}$ is comparatively low, after experimental cuts and acceptances. Further efforts to optimize the event selection and cut procedure are very desirable. In the MSSM there are certain regions of parameter space which can be especially 'proton tagging friendly' [9–11]. Here the signal-to-background ratios in the $b\bar{b}$ channel can exceed the SM by up to two orders of magnitude. Moreover, the observation of the decay of Higgs to $b\bar{b}$ would allow a direct determination of the $H \to b\bar{b}$ Yukawa coupling. From the experimental perspective, the simplest exclusive channel in which to observe a SM Higgs boson with mass between 140 GeV and 200 GeV is the WW decay mode. However, contrary to the $b\bar{b}$ case, no dramatic rise in the rate is expected within the MSSM [10].

References

[1] V.A. Khoze, A.D. Martin and M.G. Ryskin, *Eur. Phys. J.* **C14** (2000) 525.

[2] V.A. Khoze, A.D. Martin and M.G. Ryskin, *Eur. Phys. J.* **C23** (2002) 311.

[3] A. De Roeck, V.A. Khoze, A.D. Martin, R. Orava and M. Ryskin, *Eur. Phys. J.* **C25** (2002) 391,

[4] A. De Roeck, these proceedings.

[5] J. Forshaw, these proceedings.

[6] M. Tasevsky, these proceedings.

[7] FP420 R & D proposal, M.G. Albrow *et al.*, CERN-LHCC-2005-025.

[8] V.A. Khoze, A.D. Martin and M. Ryskin, *Eur. Phys. J.* **C19** (2001) 477.

[9] A.B. Kaidalov, V.A. Khoze, A.D. Martin and M.G. Ryskin, *Eur. Phys. J.* **C33** (2004) 261.

[10] S. Heinemeyer, V.A. Khoze, M.G. Ryskin, W.J. Stirling, M. Tasevsky and G. Weiglein, arXiv:0708.3052 [hep-ph].

[11] B. Cox, F. Loebinger and A. Pilkington, arXiv:0709.3035 [hep-ph].

[12] V.A. Khoze, A.D. Martin and M. Ryskin, *Eur. Phys. J.* **C34** (2004) 327.

[13] B. Cox et al., *Eur. Phys. J.* **C45** (2006) 401.

[14] A. D. Martin, V. A. Khoze and M. G. Ryskin, hep-ph/0605189.

[15] A.B. Kaidalov, V.A. Khoze, A.D. Martin and M.G. Ryskin, *Eur. Phys. J.* **C47** (2006) 385.

[16] K. Goulianos, these proceedings.

[17] V.A. Khoze, M. Ryskin and W.J. Stirling, *Eur. Phys. J.* **C48** (2006) 797.

[18] V.A. Khoze, A.D. Martin and M. Ryskin, Phys. Lett. B **650**, 41 (2007).

BFKL at NNLO

S. Marzani [1†]*, R.D. Ball* [1]*, P. Falgari* [2]*, S. Forte* [3]
[1] School of Physics, University of Edinburgh,
[2] Institut für Theoretische Physik E, RWTH Aachen,
[3] Dipartimento di Fisica, Università di Milano and
INFN, Sezione di Milano.

Abstract
We present a recent determination of an approximate expression for the $O(\alpha_s^3)$ contribution χ_2 to the kernel of the BFKL equation. This includes all collinear and anticollinear singular contributions and is derived using duality relations between the GLAP and BFKL kernels.

1 QCD at small-x

Reducing the theoretical uncertainties in cross-sections for hadron colliders requires the computation of higher order contributions in perturbative QCD, both at fixed order and at the resummed level. In particular at high energy colliders such as the LHC, we must be able to control both the logarithms of Q^2 and x as given by GLAP and BFKL evolution. Fixed–order BFKL kernels, which resum only logs of x, have been widely used in many studies (such as saturation and BFKL Monte Carlos for final states). The BFKL kernel has been computed explicitly at the next-to-leading order accuracy [1]; here we present an approximation of the NNLO contribution. The fixed–order expansion of the kernel is known to be slowly convergent, hence the NNLO contribution is important for an accurate assessment of the NLO uncertainty at any particular scale.

Let us consider the GLAP and the BFKL equations:

$$\frac{d}{dt}G(N,t) = \gamma(N,\alpha_s)G(N,t)\,, \tag{1}$$

$$\frac{d}{d\xi}G(\xi,M) = \chi(M,\alpha_s)G(\xi,M)\,, \tag{2}$$

They describe, respectively, the evolution with respect to $t = ln\frac{Q^2}{\mu^2}$ and $\xi = ln\frac{s}{Q^2} = ln\frac{1}{x}$ of the singlet parton density. The complex variables N and M are the Mellin moments with respect to x and Q^2 respectively: upon taking moments the integro-differential evolution equations become ordinary differential equations. Note that the GLAP evolved parton density G is integrated over the transverse momenta, while the BFKL equation is usually written in terms of the unintegrated quantity $\mathcal{G}$. We shall return to this issue in the next section.

Eq. (2) is written in the fixed coupling approximation; the introduction of the running of the coupling is nontrivial because upon Mellin transform $\alpha_s(t)$ becomes a differential operator:

$$\alpha_s(t) = \frac{\alpha_s}{1+\alpha_s\beta_0 t} \quad \Longrightarrow \quad \hat{\alpha}_s = \frac{\alpha_s}{1-\alpha_s\beta_0\frac{\partial}{\partial M}}\,.$$

[†] speaker

As a consequence the BFKL kernel $\chi(\hat{\alpha}_s, M)$ becomes an operator beyond leading order. It is useful to notice that different arguments for the running coupling correspond to different orderings of the operators.

The fixed-order expansion of the BFKL kernel is:

$$\chi(M, \hat{\alpha}_s) = \hat{\alpha}_s \chi_0(M) + \hat{\alpha}_s^2 \chi_1(M) + \hat{\alpha}_s^3 \chi_2(M) + \dots \tag{3}$$

It is well known that the NLO order term χ_1 is large and has a qualitatively different shape to the leading order kernel χ_0. The determination of the NNLO contribution χ_2 is motivated not only by the slow convergence of the perturbative expansion but also by the expectation that the NNLO approximation will have the same qualitative shape as the LO thus having better stability proprieties than the NLO. We compute an approximation to the NNLO kernel which includes all the collinear $(M \sim 0)$ and anticollinear $(M \sim 1)$ singularities: this computation is based on so called duality relations between the BFKL kernel and the GLAP anomalous dimension.

2 The collinear approximation of the BFKL kernel

At fixed coupling, the two evolution equations (1) and (2) admit the same leading twist solution when the kernels are related by:

$$\chi(\gamma(N, \alpha_s), \alpha_s) = N, \qquad \gamma(\chi(M, \alpha_s), \alpha_s) = M, \tag{4}$$

and the boundary conditions are suitably matched [2], [3].

The GLAP anomalous dimension $\gamma(N, \alpha_s)$ has been computed up to NNLO, i.e. $O\left(\alpha_s^3\right)$ [4]. Using duality it is thus possible to determine the first three coefficients of the Laurent expansion about $M = 0$ of the BFKL kernel. This means that we can compute *all* the collinear singularities of the $O\left(\alpha_s^3\right)$ contribution: writing

$$\chi_2(M) = \frac{c_{2,-3}}{M^3} + \frac{c_{2,-2}}{M^2} + \frac{c_{2,-1}}{M} + \dots . \tag{5}$$

the determination of the coefficients $c_{2,-3}$, $c_{2,-2}$ and $c_{2,-1}$ requires the knowledge of the LO, NLO and NNLO anomalous dimension respectively.

At LO the calculation is straightforward because it only involves the inversion of eq. (4), but beyond that several other contributions must be taken into account. More precisely we have to address the following complications:

- The inclusion of running coupling effects.
- The relation between kernels for the integrated and the unintegrated parton density.
- The dependence of the kernel on the factorisation scheme.
- The choice of kinematic variables.

All these issues were well understood at NLO [5], but only recently under control at NNLO.

The frozen coupling hypothesis is no longer valid beyond leading order: duality relations still hold but they receive running coupling contributions [6], [7]. Running coupling duality has been proved to all orders using an operator method. As we already noticed the running coupling in M-space is a differential operator; duality states that the BFKL and GLAP solutions coincide

if the respective operator kernels are the inverse of each other when acting on physical states. Because of non-vanishing commutation relations the inversions of the kernels is not trivial; the operator formalism enables us to compute the running coupling corrections in an algebraic way, calculating commutators of the relevant operators, e.g.

$$[\hat{\alpha}_s^{-1}, M] = -\beta_0 + \alpha_s \beta_0 \beta_1 + \dots \tag{6}$$

and express the result in terms of the fixed coupling duals as described extensively in [8].

The BFKL equation describes the evolution of a parton density $\mathcal{G}$ unintegrated over the transverse momenta, while GLAP of the integrated one G. The relation between $\mathcal{G}$ and G is given by:

$$\mathcal{G}(N,t) = \frac{d}{dt} G(N,t)\,.$$

This gives the following NNLO relation between unintegrated kernel and the integrated one χ^i derived from duality:

$$\chi_2 = \chi_2^i - \beta_0 \beta_1 \frac{\chi_0^i}{M} - 2\beta_0 \frac{\chi_1^i}{M}\,. \tag{7}$$

The direct computation of the BFKL kernel is based on determination of the gluon Green's function in the high energy limit in the framework of the $k_\perp$- factorisation theorem. This is compatible with the usual factorisation theorem of collinear singularities but it differs from it by a computable scheme change. This arises from a difference in normalisation between the gluon Green's functions which enter the BFKL equation and GLAP equations. The usual computation of the BFKL kernel using gluon Reggeization [1] is performed in the so called Q_0 scheme [9]. The gluon normalisation factor relating conventional $\overline{MS}$ to the Q_0 scheme can be factorised as [10]

$$R(N,t) = \mathcal{N}(N,t)\mathcal{R}(N,t)\,, \tag{8}$$

where $\mathcal{N}$ contains readily calculable running coupling and integrated/unintegrated contributions, while $\mathcal{R}$ is related to the $\overline{MS}$ definition of the anomalous dimension. The leading log-x contribution to the $\mathcal{R}$ scheme change was computed in [11]. We discuss the collinear approximation of the NLLx scheme change in [12], where we show that it can be derived from the analytic continuation of the GLAP anomalous dimension to $d = 4 - 2\varepsilon$ space-time dimensions. However although the $O(\alpha_s \varepsilon)$ and $O(\alpha_s \varepsilon^2)$ contributions are known the $O(\alpha_s^2 \varepsilon)$ contribution is not. We assess the uncertainty in our calculation due to this unknown contribution to the scheme change in fig. 2 below.

Once we have all the possible contributions with correct duality relations at NNLO under control, we can compute the collinear approximation of the BFKL kernel in the Q_0 scheme. In such scheme the result can be extend in the anticollinear region $M \sim 1$ because the kernel is symmetric upon the exchange:

$$M \leftrightarrow 1 - M \tag{9}$$

as a consequence of the symmetry of the diagrams for BFKL processes upon the exchange of the virtualities at the top and the bottom [1], [13]. Before we can exploit this symmetry we must make sure that all sources of symmetry breaking have been removed. The symmetry may be broken by the choice of kinematic variables (e.g. in DIS we choose $x = \frac{Q^2}{s}$), and by the argument of

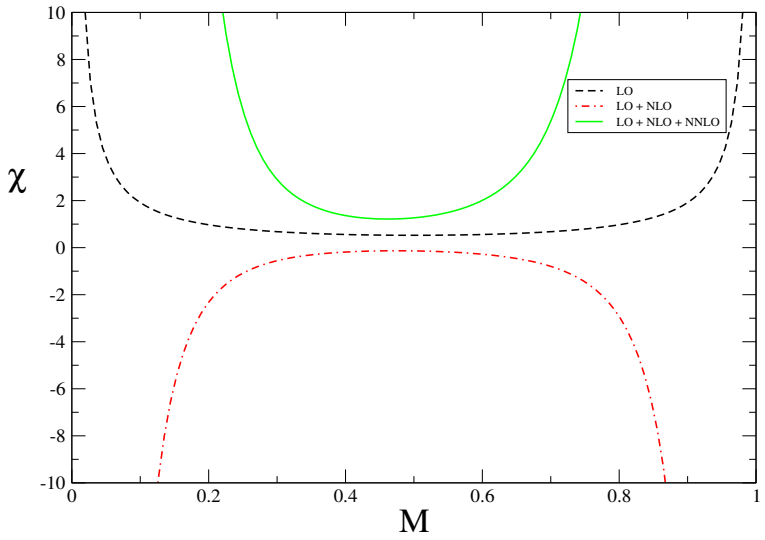


Fig. 1: This plot shows the LO, NLO and NNLO approximations to the BFKL kernel in Q_0-scheme for $\alpha_s = 0.2$.

the running coupling ($\alpha_s(Q^2)$ in DIS). The BFKL kernel can be written in symmetric variables ($x_{sym} = \sqrt{Q^2 k^2}/s$) thanks to the relation:

$$\chi^{sym}(\hat{\alpha}_s, M) = \chi^{DIS}(\hat{\alpha}_s, M + \frac{1}{2}\chi^{sym}(\hat{\alpha}_s, M))\,. \tag{10}$$

The kernel in symmetric variables can be extended to the anticollinear region:

$$\chi_2^{sym}(\hat{\alpha}_s, M) = \sum_{j=1,5} c_{2,-j} \left[\hat{\alpha}_s^3 \frac{1}{M^j} + \frac{1}{(1-M)^j}\hat{\alpha}_s^3\right] + O(M^0)\,. \tag{11}$$

The different order of the operators in the collinear and anticollinear regions corresponds to a symmetric choice for the running coupling. After the symmetrisation one can express the results canonically ordered with all the powers of $\hat{\alpha}_s$ on the left. This choice will, of course, break the symmetry of the kernel.

The results are plotted in figure 1. It is clear that the expansion of BFKL kernel is not well behaved (due to the collinear and anticollinear poles at $M = 0$ and $M = 1$ of increasing order and alternating sign). However, as expected because of the sign of the dominant pole, the BFKL kernel at NNLO has a minimum for every value of the coupling. In figure 2 we plot the intercept, defined as the value of the kernel in its minimum, as a function of the coupling constant. The inclusion of the NNLO contribution improves the convergence of the perturbative expansion, however for values of the coupling constants relevant for phenomenology (say $\alpha_s \gtrsim 0.1$) the series has yet to converge.

3 Discussion

We have seen that thanks to duality relations and the computation of the anomalous dimension at NNLO, the calculation of the collinear approximation of the BFKL kernel at $O(\alpha_s^3)$ can be performed. Here we discuss the accuracy and the limitations of our result.

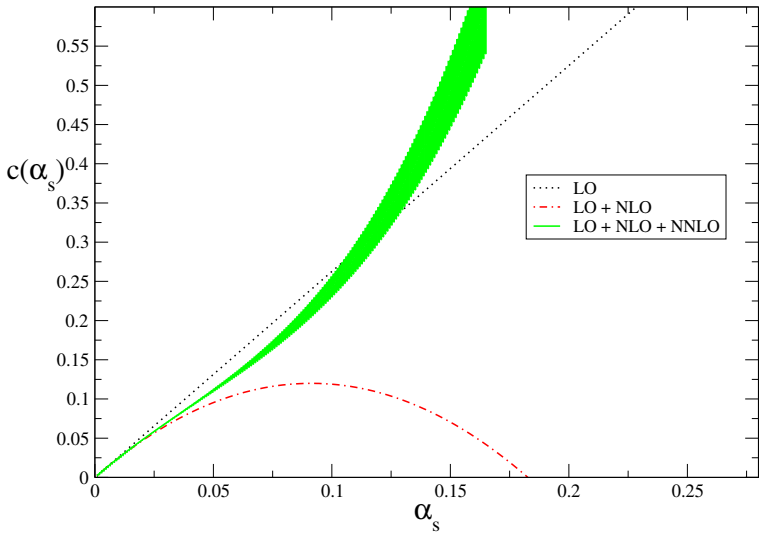


Fig. 2: This plot shows the intercept as a function of the coupling, at LO, NLO and NNLO. The error band is due to the unknown term in the scheme change.

We have computed an approximation to the forward BFKL kernel, which has been azimuthal averaged over the transverse momenta. The collinear approximation is based on the computation of coefficients of the Laurent series in $M \sim 0$ of the BFKL kernel. Because of the singularities at $M = \pm 1$ this series has radius of convergence one. Similarly the Laurent series for the anticollinear singularities around $M = 1$ also has radius of convergence one. Thus we expect the approximate calculations to do well over the central region $0 \leq M \leq 1$, but to break down as $M \to -1$, $M \to 2$. In figure 3 we show how well the approximation actually performs at LO and NLO, where the exact result is known. As expected the agreement is excellent close to $M = 0$ and $M = 1$, and even in the central region the difference between the collinear approximation and the full result is at the percent level. Hence we can conclude that at leading twist the collinear kernel is a very good approximation to the full LO and NLO ones. For this reason we also expect our result for χ_2 to be a good approximation, within a few per cent, for calculations performed at leading twist. A reasonable variation of the unknown contribution to the NLLx scheme change in our calculation changes the kernel χ_2 by $\sim 5\%$, hence well within the accuracy we expect for our approximation.

It is well known that beyond NLO BFKL evolution presents various unsolved problems. A direct computation shows that the universality of the pomeron exchange is broken at NNLO [14]. Furthermore a new class of contributions involving the t-channel exchange of four gluons enters at NNLO (see [15] and references therein). These are twist-four contributions which can mix with the twist-four part of the two-gluon operators. The form of the full BFKL equation at NNLO is thus different from that at LO and NLO, in contrast to the GLAP equation which has the same form to all orders in perturbation theory. Nevertheless collinear factorisation and running coupling duality guarantee the existence of a universal and factorised leading twist kernel for small-x evolution [8], valid in the approximation where all higher twist contributions are suppressed.

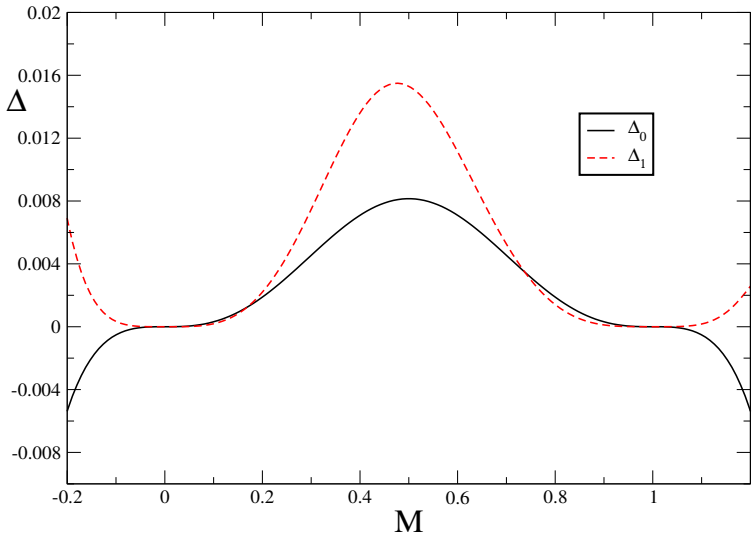


Fig. 3: This plot shows the relative differences $\Delta =$ (exact-approximate)/exact for the leading order kernel (Δ_0) and the next-to-leading kernel (Δ_1).

4 Conclusions

We have discussed the collinear approximation of the BFKL kernel. Results on duality relations and factorisation schemes, with the inclusion of the running coupling enable us to construct an approximation of the BFKL kernel at NNLO, which contains all the singular contributions at $M = 0$ and $M = 1$. The collinear approximation of χ_0 and χ_1 are in excellent agreement with the full results and so our result for χ_2 is also likely to be close to the true result for the NNLO kernel in the region relevant at leading twist.

References

[1] V. S. Fadin and L. N. Lipatov, Phys. Lett. **B429**, 127 (1998). hep-ph/9802290.
[2] R. D. Ball and S. Forte, Phys. Lett. **B405**, 317 (1997). hep-ph/9703417.
[3] G. Altarelli, R. D. Ball, and S. Forte, Nucl. Phys. **B575**, 313 (2000). hep-ph/9911273.
[4] A. Vogt, S. Moch, and J. A. M. Vermaseren, Nucl. Phys. **B691**, 129 (2004). hep-ph/0404111.
[5] G. P. Salam, Acta Phys. Polon. **B30**, 3679 (1999). hep-ph/9910492.
[6] R. D. Ball and p. Forte, Phys. Lett. **B465**, 271 (1999). hep-ph/9906222.
[7] G. Altarelli, R. D. Ball, and S. Forte, Nucl. Phys. **B621**, 359 (2002). hep-ph/0109178.
[8] R. D. Ball and S. Forte, Nucl. Phys. **B742**, 158 (2006). hep-ph/0601049.
[9] M. Ciafaloni, Phys. Lett. **B356**, 74 (1995). hep-ph/9507307.
[10] M. Ciafaloni and D. Colferai, JHEP **09**, 069 (2005). hep-ph/0507106.
[11] S. Catani and F. Hautmann, Nucl. Phys. **B427**, 475 (1994). hep-ph/9405388.
[12] S. Marzani, R. D. Ball, P. Falgari, and S. Forte (2007). arXiv:0704.2404 [hep-ph].
[13] M. Ciafaloni, D. Colferai, and G. P. Salam, JHEP **10** (1999).
[14] V. Del Duca and E. W. N. Glover, JHEP **10**, 035 (2001). hep-ph/0109028.
[15] J. Bartels and C. Bontus, Phys. Rev. **D61**, 034009 (2000). hep-ph/9906308.

Unintegrated parton distributions and correlation functions

Anna Staśto
Penn State University, 104 Davey Lab., University Park, 16802 PA, USA

Abstract
We discuss the limitations of the standard collinear approach. The kinematical approximations necessary to derive the collinear factorization are insufficient for the description of the exclusive final states. We argue that for a proper treatment of the final states one needs to use fully unintegrated parton correlation functions. We introduce the gauge invariant definitions of these objects and the factorization theorem for one jet production in deep inelastic scattering.

1 Introduction: factorization and integrated parton distribution functions

The leading twist formalism based on the collinear factorization [1] has been proved widely successful in a variety of processes in QCD. The collinear factorization allows for the separation of the short and long distance contributions in the processes which involve hadrons. The short distance part is the partonic cross section, which can be systematically calculated order by order in the strong coupling within the perturbation theory. The long distance parts are parton distribution and fragmentation functions which contain all the non-perturbative information. Thanks to the factorization theorem these quantities are universal and once determined in one process can be taken over to the other process to determine the corresponding cross section. These standard parton distribution functions are often referred as the integrated parton distribution functions (PDFs) since they depend only on the fraction of the longitudinal momentum x and the hard scale μ. Problems arise when one tries to address more exclusive processes with final states. Then, the details of the kinematics are essential and standard kinematic approximation can be insufficient for these purposes. This is where the formalism with the parton distributions unintegrated over the other components of the momenta is necessary. One also needs to prove more general factorization theorems which incorporate these unintegrated parton distribution/fragmentation functions.

To start with, let us first recall the standard definition of the integrated quark parton density:

$$f(x_{Bj},\mu) \;=\; \int \frac{dy^-}{4\pi} e^{-ix_{Bj}p^+y^-} \langle P|\bar{\psi}(0,y^-,0_T)V_y^\dagger(n)V_0(n)\gamma^+\psi(0)|P\rangle_R \,. \qquad (1)$$

Here, ψ is the quark field and $|P\rangle$ is the proton state in which the operator above is evaluated. Subscript R means that we are considering renormalized operators and μ is the renormalization scale. The object inserted between the quark fields is the Wilson line

$$V_y^\dagger(n)V_0(n) \;=\; \mathrm{P}\exp\left(-ig\int_0^{y^-} d\lambda\, n\cdot A(\lambda n)\right) \,. \qquad (2)$$

in the lightlike direction $n = (0, 1, 0_T)$. This ensures the gauge invariance and can be shown to arise from graphs with arbitrarily many gluon exchanges which appropriately factorize into this path-ordered exponential.

To illustrate some issues related with the kinematical approximations used in the standard collinear approach let us consider the parton model of the deep inelastic scattering. The lowest order graph is pictured in Fig. 1 and we can write down formally its contribution to the hadronic tensor as

$$W^{\mu\nu}(q,P) \;=\; \sum_j \frac{e_j^2}{4\pi} \int \frac{d^4k}{(2\pi)^4} \mathrm{Tr}[\gamma^\mu J_j(k+q)\gamma^\nu F_j(k,P)] \;, \tag{3}$$

with the sum over j as a sum over the quark flavors.

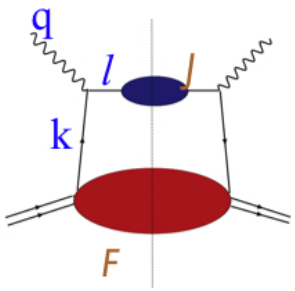


Fig. 1: Parton model in deep inelastic scattering.

The kinematic approximations needed to obtain the factorized form set the quarks on-shell and massless

$$\begin{aligned} k \simeq \hat{k} \;&\equiv\; (x_{Bj}P^+, 0, 0_T) \;, \\ l \simeq \hat{l} \;&\equiv\; (0, \frac{Q^2}{2x_{Bj}P^+}, 0_T) \;. \end{aligned} \tag{4}$$

These approximations give the familiar expression for the hadronic tensor

$$W^{\mu\nu}(q,P) \;\simeq\; \sum_j \frac{e_j^2}{4\pi} \left\{ \int \frac{dk^- d^2k_T}{(2\pi)^4} F_j^+(x_{Bj}P^+, k^-, k_T) \right\} \mathrm{Tr}[\gamma^\mu \gamma^+ \gamma^\nu \hat{\not{k}}] \;. \tag{5}$$

The expression in the curly brackets corresponds to the parton density and the expression with the trace is the partonic cross section. Note, that the approximations are good when the momentum components k_T and k^- are small with respect to k^+. This is sufficient when the momenta are integrated over in the inclusive cross section but might lead to large errors when we look at some more exclusive processes. Indeed the parton model approximation makes the following replacement

$$\delta^{(4)}(k+q-l) \longrightarrow \delta(k^+ + q^+)\delta(q^- - l^-)\delta^{(2)}(l_T) \;.$$

These two delta functions can lead to similar results when integrated over all momenta (inclusive processes) but can lead to very different results in the exclusive cases. If we allow for the invariant

mass of the outgoing parton $l^2 = M^2$ we see that the parton model value $k^+ = xP^+$ becomes significantly modified

$$k^+ = xP^+ + \frac{M^2 + k_T^2}{2(k^- + q^-)} \, .$$

As shown in [2] on the example of the $c\bar{c}$ production in DIS there are huge differences between standard parton model, unintegrated partons and exact kinematics. In particular the p_T distributions of the produced charmed quarks depend heavily whether integrated or unintegrated formalism is used. The general conclusion [2] is that conventional formalism with integrated parton densities is not suitable for the analysis of the final states. In the next sections we discuss the general factorization framework which makes use of the unintegrated parton correlation functions. All the details, including the derivation of the factorization and the definitions of the unintegrated parton correlation functions can be found in [3].

2 Integrated, unintegrated, fully unintegrated parton correlation functions

We have learned from the discussion in the introduction that the description of the exclusive processes requires a new formalism with new parton densities and fragmentation functions. We distinguish three types of objects:

- Conventional integrated parton distributions and fragmentation functions. These depend on the fraction of the longitudinal momentum and the scale

$$\mathcal{F}(x, \mu)$$

- Unintegrated parton distribution functions (and FFs) which depend on the transverse momentum

$$\mathcal{F}(x, k_t, \mu)$$

- Fully unintegrated parton correlation functions which depend on all components of the momenta: longitudinal, transverse, and virtuality

$$\mathcal{F}(x, k_T, k^2, \mu)$$

The unintegrated (over k_T) parton distribution functions have been introduced in the context of small x physics, (see for example [4]). There, as a result of the high-energy approximation, the 4-point gluon Green's function emerges as a fundamental object. It depends on the transverse momenta of 4-off shell gluons. Its evolution with rapidity is then governed by the BFKL equation. There have been numerous efforts [5–7] to construct the unintegrated parton densities outside the small x limit, many of them using the angular ordered CCFM equation. However, theses approaches do not provide the operator definitions of the unintegrated parton distribution functions. Therefore, it is desirable to have a unique and consistent approach which demonstrates factorization using the properly defined unintegrated parton correlation functions. Then, hopefully, different approaches developed so far will be reproduced as a particular limit or approximation to a more general case.

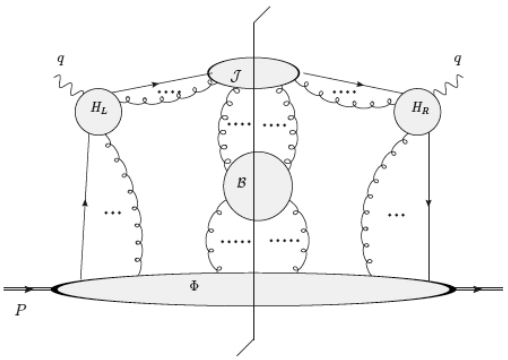


Fig. 2: Most general graph with one jet production in deep inelastic scattering.

3 General strategy

The general formalism for use in the case of the deep inelastic scattering is introduced in detail in [3]. The main points are

- Retain the exact kinematics in initial and final states.
- Keep the explicit factors (bubbles) representing final states.
- Retain on-shell matrix elements.
- Define projections from exact to approximate momenta.
- Construct definitions of the gauge invariant parton correlation factors and the soft factor.
- Use eikonal lines and Ward identities to prove factorization.
- Use non-light-like eikonal Wilson lines to regularize light-cone divergences in the unintegrated parton distributions (this introduces a cutoff in rapidity, similarly to what is done at small x).

One starts with the most general graph in the case of the deep inelastic scattering which is illustrated in Fig. 3. This graphs differs from the ordinary parton model due to several distinctive features. First of all, the final state quark has a jet subgraph. This is a minimal required assumption since we know that the quark has to hadronize. A second important point is that we need to allow for the non-perturbative (or soft) interactions between the outgoing jet and the target remnant. These are obviously necessary to neutralize the color. Therefore we need to allow for arbitrarily many gluon connections between the soft bubble and the target and jet subgraphs. So graph in Fig. 3 constitutes a necessary extension to a simple parton model.

In order to prove the factorization one needs first to identify all the leading regions: collinear to jet, collinear to the target and soft. On also needs to perform subtractions to ensure that the smaller regions are appropriately suppressed. Then the Ward identities are used to disentangle the gluons between the different subgraphs (for example collinear to soft subgraphs). In particular one has to prove that the Ward identities work properly in the presence of the subtractions. After the application of Ward identities the gluons factorize into the Wilson lines in the

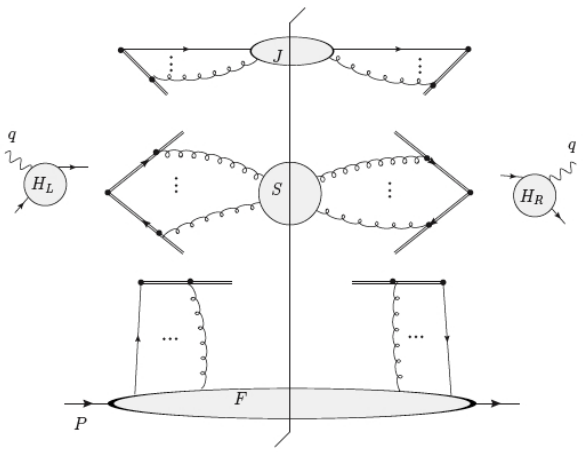


Fig. 3: Most general graph with one jet production in deep inelastic scattering in the factorized form. Double lines denote the eikonal lines.

appropriate objects. The final factorization formula proven in [3] reads

$$P_{\mu\nu}W^{\mu\nu} = \int \frac{d^4k_{\rm T}}{(2\pi)^4}\frac{d^4k_{\rm J}}{(2\pi)^4}\frac{d^4k_S}{(2\pi)^4}(2\pi)^4\delta^{(4)}(q+P-k_{\rm T}-k_{\rm J}-k_S)\times \\ \times\,|H(Q,\mu)|^2\,\mathcal{S}(k_S,y_{\rm T},y_{\rm J},\mu)\,\mathcal{F}(k_{\rm T},y_p,y_{\rm T},y_s,\mu)\,\mathcal{J}(k_{\rm J},y_{\rm J},y_s,\mu), \quad (6)$$

where $\mathcal{S},\mathcal{F},\mathcal{J},H$ denote the soft factor, parton distribution, jet factor and hard scattering cross section respectively. $P^{\mu\nu}$ denotes the projection onto the apropriate structure function. All the non-perturbative factors depend on the all components of the 4-momenta k_i. Note the appearance of the rapidity variables y_i. These are necessary to suppress the contributions from the regions where the rapidities are very large (rapidity divergencies). It has been demonstrated that this can be regularized by changing the direction of the Wilson lines from the light-like directions to slightly non-light-like [3]. The parton distribution, fragmentation functions and soft factors acquire then additional parameters. Appropriate evolution equations give the prescription on the variation of these quantities with the rapidity. The final factorized graph is shown in Fig. 3 where by double lines we denote the Wilson lines.

4 Gauge invariant definitions of PCFs

The analysis of the single gluon attachment allows to construct the gauge invariant definitions of the parton correlation functions (PCFs) and the soft factor. As already discussed in a previous section critical to these are the directions of the Wilson lines. Soft gluons couple to the target jet, with its large plus component of momentum, and to the outgoing jet with its large minus component of momentum. This means that in coordinate space the soft factor is the vacuum expectation value of Wilson lines that are nearly light-like in the plus and minus directions [3]

$$\tilde{\mathcal{S}}(w,y_{\rm T},y_{\rm J},\mu) \quad = \quad \langle 0|I^\dagger_{n_{\rm T};w,0}V_w(n_{\rm T})V_w^\dagger(n_{\rm J})I_{n_{\rm J};w,0}V_0(n_{\rm J})V_0^\dagger(n_{\rm T})|0\rangle_R \quad . \quad (7)$$

Note that we have replaced in this expression the light-like Wilson lines with the non-light-like ones in the directions denoted by the vectors $n_T = (1, -e^{-2y_{\rm T}}, \mathbf{0}_T)$, and $n_J = (-e^{-|2y_{\rm J}|}, 1, \mathbf{0}_T)$ where $y_T \gg 1$ and $|y_J| \gg 1,\ y_J < 0$. As mentioned above, the reason for their presence is that they provide cutoffs on rapidity divergences. The factors I are the transverse links at infinity which are needed to ensure strict gauge invariance [8]. With these included, the soft factor (7) is the expectation value of the closed Wilson loop.

The target PCF is defined as the gauge invariant expectation value of two quark fields. Its definition reads [3]

$$\tilde{F}(w, y_p, y_{\rm T}, y_s, \mu) \qquad = \qquad \frac{\langle p|\bar{\psi}(w)V_w^\dagger(n_s)I_{n_s;w,0}\dfrac{\gamma^+}{2}V_0(n_s)\psi(0)|p\rangle_R}{\langle 0|I^\dagger_{n_{\rm T};w,0}V_w(n_{\rm T})V_w^\dagger(n_s)I_{n_s;w,0}V_0(n_s)V_0^\dagger(n_{\rm T})|0\rangle_R}. \quad (8)$$

where w is a reference point in space-time. The two quark fields are connected via three Wilson lines, two of them going into the direction $n_s = (-e^{y_s}, e^{-y_s}, \mathbf{0}_T)$ which corresponds to the rapidity close to zero in the center-of-mass system. This expectation value is divided by the soft factor, in order to ensure the proper cancellation of the double counting contributions. Note that the soft factor has now n_J replaced by the n_s vector. This guarantees that the definition (8) gives a good approximation for the gluons close to the target region. Similar definition can be constructed for the jet factor with vector n_T replaced by n_J

$$\tilde{\mathcal{J}}(w, \text{argument like } y_J, y_{\rm J}, y_s, \mu) = \frac{\langle 0|\bar{\psi}(w)V_w^\dagger(-n_s)I_{-n_s;w,0}\gamma^- V_0(-n_s)\psi(0)|0\rangle_R}{\langle 0|I^\dagger_{-n_s;w,0}V_w(-n_s)V_w^\dagger(n_{\rm J})I_{n_{\rm J};w,0}V_0(n_{\rm J})V_0^\dagger(-n_s)|0\rangle_R}. \quad (9)$$

Acknowledgments

The work presented in this talk was performed in collaboration with John Collins and Ted Rogers [3]. I would like to thank the organizers of EDS2007 for the kind invitation to this very interesting workshop. This research was supported by the U.S. D.O.E. under grant number DE-FG02-90ER-40577 and by the Polish Committee for Scientific Research under grant No. KBN 1 P03B 028 28.

References

[1] J. C. Collins, D. E. Soper, and G. Sterman, Adv. Ser. Direct. High Energy Phys. **5**, 1 (1988). hep-ph/0409313.

[2] J. Collins and H. Jung (2005). hep-ph/0508280.

[3] J. C. Collins, T. C. Rogers, and A. M. Stasto (2007). arXiv:0708.2833 [hep-ph].

[4] L. N. Lipatov, Phys. Rept. **286**, 131 (1997). hep-ph/9610276.

[5] M. A. Kimber, J. Kwiecinski, A. D. Martin, and A. M. Stasto, Phys. Rev. **D62**, 094006 (2000). hep-ph/0006184.

[6] M. A. Kimber, A. D. Martin, and M. G. Ryskin, Phys. Rev. **D63**, 114027 (2001). hep-ph/0101348.

[7] G. Watt, A. D. Martin, and M. G. Ryskin, Eur. Phys. J. **C31**, 73 (2003). hep-ph/0306169.

[8] A. V. Belitsky, X. Ji, and F. Yuan, Nucl. Phys. **B656**, 165 (2003). hep-ph/0208038.

Non-linear QCD at high energies

E. Levin
Department of Particle Physics, School of Physics and Astronomy, Raymond and Beverly Sackler Faculty of Exact Science Tel Aviv University, Tel Aviv, 69978, Israel

Abstract
In this talk I give a mini-review on recent development in the non-linear QCD (at low x).

This year is a jubilee year: 25 years ago Leonid Gribov, Michael Ryskin and me published our GLR paper [1] in which we set a new field, so called, high parton density QCD or non-linear QCD. In this paper we formulate the main physical question that we need to answer: what happens with the system of partons when their density becomes so large that the partons start to interact. This interaction was omitted in linear evolution but has to be important to suppress the power like growth of the deep inelastic cross section which follows from linear evolution and contradicts the Froissart theorem. The non-linear evolution equation which nowadays goes under the name Balitsky-Kovchegov equation [2] was suggested; the new scale: saturation momentum (Q_s), was introduced and the equation for this scale was derived; as well as the phenomenon of the saturation of the parton densities was foreseen.

During the quarter of century we have understood a lot: the role of the large number of colours in the approach [3], a geometrical scaling behaviour of the scattering amplitude [4,5], the equation for the diffractive dissociation processes [6] and many other results. However, I think, we have had two major breakthroughs: the dipole approach [7] and the colour glas condensate approach(CGC) [8, 9]. The dipole approach leads to a new understanding what we calculate (dipole scattering amplitude), considerably simplified all calculations and gives rise to statistical treatment of the problem. CGC reduces the problem of saturation to the theory of classical field in QCD giving the explanation of this phenomenon and developing a new theoretical method for the solution. I firmly believe that we are now in the middle of the third breakthrough since we have started to attack the most difficult and challenging problem: the dynamical correlations in the QCD cascade which is known under slang name of summing Pomeron loops. Therefore, the largest part of this talk I will spend on the discussion of this theoretical problem but I would like to start with more practical question: are we ready for the LHC.

1. Practical impact on the LHC physics. The honest answer to the above question is firm no. I see two reasons for this sad fact: first the saturation physics is not the hottest problem that the LHC hopes to resolve in spite of having ALICE collaboration for ion-ion collisions where the saturation effect will be more pronounced. Second, is a kind of contradiction between the theoretical approach and the reality. Let me repeat what we are doing in hd QCD in more formal language. In the kinematic region where $\alpha_S \ln s \approx 1$ the asymptotical behaviour of QCD ampltude is known [10] to be power-like as $A \propto \alpha_S^2 s^{\Delta}$(BFKL Pomeron) where s is the energy and Δ can be expanded as $\Delta = C_1\alpha_S + C_2\alpha_S^2$ with known coefficient C_1. The calculation of C_2 has been performed [11] but these corrections will be important only for $\alpha_S \ln s \geq 1/\alpha_S$.

However, for lower energy , another type of interaction turns to be essential, namely, the exchange of two and more BFKL Pomerons. Such exchange leads to the contribution which is of the order of $\left(\alpha_S^2 s^{\Delta_{LO}}\right)^n$. Therefore when $\alpha_S^2 s^{\Delta_{LO}} \approx 1$ we need to sum all contributions due to BFKL Pomeron exchanges. In terms of energy this is the range $1 \leq \alpha_S \ln s \leq \ln(1/\alpha_S^2)$. In simple words, theoreticaly first we need to solve the problem of high parton density QCD and only for higher energies we should take care about next-to-leading order corrections to Δ. However, the life turns out to be more complicated and these corrections numerically are so huge that for any practical applications we have to account for them. The sad truth is we have not learned how to do this. As far as I know there is only one attempt to include them in non-linear evolution [12] which is still very approximate. It means that, frankly speaking, we cannot guarantee the value of the possible high parton density effects at the LHC.

At the moment we can give some estimates to illustrate how essential can be the high density collective effects at the LHC. The most important result has been achieved during the past year. It turns out that the contribution of the semi-hard processes (with the typical transverse momenta of the order of the saturation scale) to the survival probability of the diffractive Higgs boson production is large and it could lead to a substantial suppression of the QCD calculated cross section (see Refs. [13, 14]. The estimates were obtained for different contributions: the fan diagrams in Ref. [13] and the enhanced diagrams in Ref. [14] with the same results. Namely, all diagrams of these types should be summed. The model attempt to perform such a summation with the result that the survival probability is as small as 0.4%. This is a good example that we need to concentrate our efforts on LHC physics even in the case of the first wave of experiments, in particular in Higgs search.

2. Statistical approach: its beauty and problems. Based on the probability interpretation of the non-linear equation in the dipole approach [7] we have tried to develop the more general statistical-like scheme that would include the Pomeron loops (see review [15] and references therein). The hope is to rewrite the QCD evolution equations including Pomeron loops in the form of Langevin equation ($\bigotimes$ stands for all needed integrations):

$$\frac{dN}{d\ln s} \;=\; \alpha_S K \bigotimes \left(N - N^2\right) + \zeta \quad \text{with} \quad \langle|\zeta|\rangle = 0,\ \langle|\zeta\ \zeta|\rangle \;\neq\; 0 \tag{1}$$

In Ref. [17] it was proven that in QCD we can obtain Eq. (1) but the form of $\langle|\zeta\ \zeta|\rangle$ is so complicated that , I think, there is no chance of solving Eq. (1). The attempts to solve Eq. (1) were made in the QCD motivated models with a lot of assumptions. All these assumptions (especially that impact parameter is much larger than the dipole sizes) are such that we are losing the possibility to calculate the Pomeron loops. The main physical result from these models and statistical like approach is the violation of the geometrical scaling behaviour [16]. I do not think we can trust this prediction.

3. BFKL Pomeron calculus: overlapping singularities. The important news is the fact that everything that has been done during the past three years is nothing more than understanding of the BFKL Pomeron calculus [17]. Therefore we have to return back to this calculus to re-examine how to include the Pomeron loops in our approach. In doing so, Refs. [18, 19] found that the Pomeron interaction generates a new state with the intercept large than intercept of two BFKL Pomerons. In spite of the lack of room I will try to illustrate this result calculating the first

fan diagram (see Fig. 1).

The expression for this diagram includes the integral over anomalous dimensions, dipole sizes in the triple Pomeron vertices which leads to δ - function , shown in Fig. 1, and the integral over ω which has the form:

$$A \;\propto\; \frac{1}{2\pi i}\int_{\epsilon-i\infty}^{\epsilon+i\infty} d\omega e^{\omega\, Y}\,\frac{1}{\omega-\omega(\gamma)}\,\frac{1}{\omega-\omega(\gamma_1)-\omega(\gamma_2)}$$

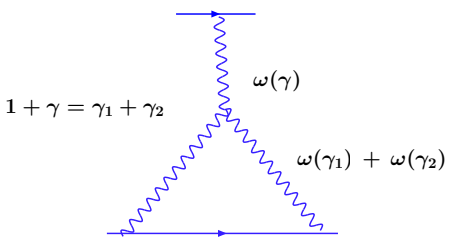


Fig. 1: The first fan diagram.

One can see that we can close the contour over ω on two poles: $\omega(\gamma)$ and $\omega(\gamma_1)\,+\,\omega(\gamma_2)$, which lead to contribution $\exp\left(\omega(1/2)Y\right)$ and $\exp\left(2\omega(1/2)Y\right)$. However, in the integral over γ there exists $\gamma\,=\,\gamma_0$ which is a solution to the equation: $\omega(2\gamma_0\,-\,1)\,=\,2\,\omega(\gamma_0)$. For γ_0 we have a double pole and the amplitude behaves as $A\;\propto\;Y\,e^{2\,\omega(\gamma_0)\,Y}\;\gg\;\exp\left(\omega(1/2)Y\right)$. This new singularity we call overlapping singularity. Its appearance is kind of disaster since it means that even in 'fan' diagrams the partons from different parton showers, which are described by exchange of two Pomerons, interacts. In particular, overlapping singularities destroy the non-linear Balitsky-Kovchegov equation even for the scattering with nucleus, preserving nevertheless the Balitsky chain of equations [2, 20]. So, the truth is that we have to start from the beginning not only in summing the Pomeron loops but also in the mean field approximation.

4. BFKL Pomeron calculus: solution for $\alpha_S\, lns\,<\,1/\alpha_S$. Therefore, the first thing that we need to do is to suggest our way to overcome the difficulties related to the overlapping singularities.

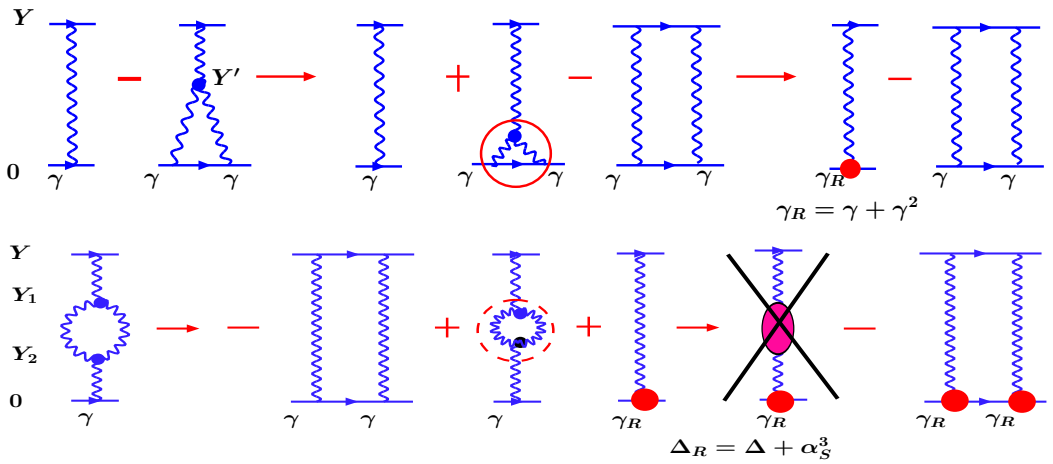


Fig. 2: The calculation of the first fan and enhanced diagrams.

Our observation is the following: $\gamma_0\;>\;\gamma_{cr}$ therefore, two Pomerons (γ_1 and γ_2) are inside the saturation region while one upper Pomeron is outside. Inside the saturation region we cannot use the BFKL kernel to determine $\omega(\gamma)$ but we need to use the expression found in Ref. [4], namely, $\omega_{sat}(\gamma)\;=\;\frac{\omega(\gamma_{cr})}{1-\gamma_{cr}}\,(1-\gamma)$. Noticing that equation $2\omega_{sat}(\gamma_0)\;=\;\omega_{pert}(2\gamma_0-1)$

has no solution, we can conclude that as the first try we can neglect the overlapping singularities. However, we have to check the self consistency of our approach, namely, obtaining a solution to calculate back the diagrams and show that they indeed give a small contribution.

Our main idea [19] that in this case and for the kinematic region $\alpha_S\, lns\, <\, 1/\alpha_S$ we are dealing with the system of non-interacting Pomerons, Fig. 2, in which we present the calculation of the first fan and the first enhanced diagrams, illustrates this idea. One can see in Fig. 2 that these diagrams can be reduced to the system of non-inetracting Pomerons since in the kinematic region under consideration the corrections to the Pomeron intercept turn out to be small. (see Fig. 2). Having this fact in mind we can use for summing Pomeron loops the Iancu-Mueller-Patel -Salam approximation [21], improved by the renormalization of the scattering amplitude at low energies. This approach is nothing more than the t-channel unitarity constraint adjusted to the dipole approach.

However, the first part of the problem: to find the sum of fan diagrams we need to solve using a different method. We were able to do this for the simplified BFKL kernel in which we took into account only the leading twist part of the full BFKL kernel. We heavily use the fact that in Ref. [22] the solution for this kernel has been found. The simplified kernel looks as follows

$$\omega(\gamma)\; =\; \bar{\alpha}_S\; \begin{cases} \frac{1}{\gamma} & \text{for } r^2\, Q_s^2\, \ll\, 1 \;\text{ summing }\; (\bar{\alpha}_S \ln(1/(r^2\, Q_s^2)))^n; \\ \\ \frac{1}{1-\gamma} & \text{for } r^2\, Q_s^2\, \gg\, 1 \;\text{ summing }\; (\bar{\alpha}_S \ln(r^2\, Q_s^2))^n; \end{cases} \tag{2}$$

For this kernel we obtain: the solution that icludes the Pomeron loops, with the following main properties: ,geometrical scaling behaviour and rather slow approaching the asymptotic value, namely $1 - N\; \propto\; \exp(-z)$ where $z\; =\; \ln(r^2 Q_s^2)$.

Resume. One my friend, a good experimentalist, told me, that what I am doing, is the same as string theorists are doing : the approach is complicated and a lot of promises but no delivery (no connection with the reality) . I agree with him that the problem is not simple and during the last 25 years we learned how difficult it is. However, the main difference with the string theory is that we are solving a well formulated theoretical problem about the nature while string theory is dealing with the imaginary world without any chance to approach reality and in attempts to include the principle property of the nature they have to build models for each well established phenomenon: running α_S; confinement of quarks and gluons; and the violation of chiral symmetry. Accepting the fact that we have not prepared yet the experimental program for the LHC for measuring saturation effect we are developing fast in this direction and I firmly believe that I will report very soon to my friend about such program beating his second claim.

References

[1] L. V. Gribov, E. M. Levin and M. G. Ryskin, *Phys. Rep.* **100**, 1 (1983).

[2] I. Balitsky, [arXiv:hep-ph/9509348]; *Phys. Rev.* **D60**, 014020 (1999) [arXiv:hep-ph/9812311] Y. V. Kovchegov, *Phys. Rev.* **D60**, 034008 (1999), [arXiv:hep-ph/9901281].

[3] J. Bartels, Z. Phys. C **60** (1993) 471; Phys. Lett. B **298** (1993) 204; E. M. Levin, M. G. Ryskin and A. G. Shuvaev, Nucl. Phys. B **387** (1992) 589.

[4] J. Bartels and E. Levin, Nucl. Phys. **B387** (1992) 617.

[5] E. Iancu, K. Itakura and L. McLerran, *Nucl. Phys.* **A708** (2002) 327 [arXiv:hep-ph/0203137].

[6] Y. V. Kovchegov and E. Levin, Nucl. Phys. B **577** (2000) 221 [arXiv:hep-ph/9911523].

[7] A. H. Mueller, *Nucl. Phys.* **B415**, 373 (1994); *ibid* **B437**, 107 (1995).

[8] L. McLerran and R. Venugopalan, *Phys. Rev.* **D 49**,2233, 3352 (1994); **D 50**,2225 (1994); **D 53**,458 (1996); **D 59**,09400 (1999).

[9] J. Jalilian-Marian, A. Kovner, A. Leonidov and H. Weigert, *Phys. Rev.* **D59**, 014014 (1999), [arXiv:hep-ph/9706377]; *Nucl. Phys.* **B504**, 415 (1997), [arXiv:hep-ph/9701284]; J. Jalilian-Marian, A. Kovner and H. Weigert, *Phys. Rev.* **D59**, 014015 (1999), [arXiv:hep-ph/9709432]; A. Kovner, J. G. Milhano and H. Weigert, *Phys. Rev.* **D62**, 114005 (2000), [arXiv:hep-ph/0004014] ; E. Iancu, A. Leonidov and L. D. McLerran, *Phys. Lett.* **B510**, 133 (2001); [arXiv:hep-ph/0102009]; *Nucl. Phys.* **A692**, 583 (2001), [arXiv:hep-ph/0011241]; E. Ferreiro, E. Iancu, A. Leonidov and L. McLerran, *Nucl. Phys.* **A703**, 489 (2002), [arXiv:hep-ph/0109115]; H. Weigert, *Nucl. Phys.* **A703**, 823 (2002), [arXiv:hep-ph/0004044].

[10] E. A. Kuraev, L. N. Lipatov, and F. S. Fadin, *Sov. Phys. JETP* **45**, 199 (1977); Ya. Ya. Balitsky and L. N. Lipatov, *Sov. J. Nucl. Phys.* **28**, 22 (1978).

[11] V.S. Fadin and L. N. Lipatov, *Phys. Lett.* **429** (1998) 127; G. Camici and M. Ciafaloni, *Phys. Lett.* **B430** (1998) 349.

[12] E. Gotsman, E. Levin, U. Maor and E. Naftali, Nucl. Phys. A **750** (2005) 391 [arXiv:hep-ph/0411242].

[13] J. Bartels, S. Bondarenko, K. Kutak and L. Motyka, Phys. Rev. D **73** (2006) 093004 [arXiv:hep-ph/0601128].

[14] J. S. Miller, arXiv:hep-ph/0610427.

[15] S. Munier, *"Connections between high energy QCD and statistical physics,"* arXiv:0709.0784 [hep-ph] Acta Phys. Polon. B **37** (2006) 3451 [arXiv:hep-ph/0609161].

[16] E. Iancu, A. H. Mueller and S. Munier, Phys. Lett. B **606** (2005) 342 [arXiv:hep-ph/0410018].

[17] M. Kozlov, E. Levin and A. Prygarin, Nucl. Phys. A **792** (2007) 122 [arXiv:0704.2124 [hep-ph]].

[18] Y. Hatta and A. H. Mueller, Nucl. Phys. A **789** (2007) 285, arXiv:hep-ph/0702023.

[19] E. Levin, J. Miller and A. Prygarin, *"Summing Pomeron loops in the dipole approach,"* arXiv:0706.2944 [hep-ph].

[20] E. Levin and M. Lublinsky, Phys. Lett. B **607** (2005) 131 [arXiv:hep-ph/0411121].

[21] A. H. Mueller and B. Patel, *Nucl. Phys.* **B425**, 471 (1994); A. H. Mueller and G. P. Salam, *Nucl. Phys.* **B475**, 293 (1996), [arXiv:hep-ph/9605302]; G. P. Salam, *Nucl. Phys.* **B461**, 512 (1996); E. Iancu and A. H. Mueller, *Nucl. Phys.* **A730** (2004) 460, 494, [arXiv:hep-ph/0308315],[arXiv:hep-ph/0309276].

[22] E. Levin and K. Tuchin, Nucl. Phys. A **693** (2001) 787 [arXiv:hep-ph/0101275] ; Nucl. Phys. A **691** (2001) 779 [arXiv:hep-ph/0012167], Nucl. Phys. B **573** (2000) 833 [arXiv:hep-ph/9908317] .

Small x QCD and Multigluon States: a Color Toy Model

G.P. Vacca[1]†*and P. L. Iafelice*
[1] INFN - Sez. di Bologna and Univ. of Bologna, Physics Depart., Via Irnerio 46, 40126 Bologna

Abstract
We introduce and study a toy model with a finite number of degrees of freedom whose Hamiltonian presents the same color strucure of the BKP system appearing in the studies of QCD in the Regge limit. We address within this toy model the question of the inportance of finite N_c corrections with respect to the planar limit case.

1 Introduction

The large N_c expansion [1] is a widely popular framework of approximations which has been succefully applied to gauge theories and has given at leading order some analytical results otherwise impossible to obtain. Within the Regge limit of QCD scattering amplitudes, L.N. Lipatov found [2] that systems of reggeized gluons evolving in rapidity in the leading logarithmic approximation (LLA) were showing the emergence of an integrable structure in the planar limit. Similar feature were found later in other kinematical regimes for other QCD observables. Moreover the $N = 4$ SYM theory has been investigated at different orders in perturbation theory and is now believed to be integrable at all orders.

But if one considers some QCD observables at the physical point $N_c = 3$ the situation is much more complicated and even the order of the corrections with respect to the planar limit are not really known. This is the situation, for example, for the spectrum of the BKP kernel [3, 4] at one loop, which describes the high energy behavior in the Regge limit of a system of reggeized gluons.

It is the pourpose of this talk to discuss a toy model [5] which has a color structure similar to the BKP system but a different "configuration" dynamics with a finite number of d.o.f., constrained only by the fact that the two Hamiltonians must have the same leading eigenvalues in the large N_c limit for both one and two cylinder topologies. The main motivation to study this model is to understand in a simpler case how much the large N_c approximation fails to reproduce the dynamics at finite N_c. In order to understand this we shall study the spectrum of such a model as a function of N_c.

2 Small x QCD: the LLA BKP kernel

Let us start by giving a brief overview of the LLA kernels encoding the evolution in rapidity of systems of interacting reggeized gluons, which provide a convenient perturbative description of some relevant QCD degrees of freedom in the Regge limit (small x). Their dynamics determine the high energy behavior of the cross sections, typically associated to the so called BFKL (perturbative) pomeron [6, 7]. In the simplest form, the BFKL pomeron turns out to be a composite

† speaker

state of two interacting reggeized gluons "living" in the transverse configuration plane in the colorless configuration. Its kernel or Hamiltonian is infrared finite and in LLA is constructed summing the perturbative contributions of different Feynman diagrams: in particular the virtual ones (reggeized one loop gluon trajectories) ω and the real ones (associated to an effective real gluon emission vertex) V. One writes formally $H = \omega_1 + \omega_2 + \vec{T}_1\vec{T}_2 V_{12}$ where $\vec{T}_i$ are the generators of the color group in adjoint representation . In the colorless case one has $\vec{T}_1\vec{T}_2 = -N_c$ and finally one obtains:

$$H_{12} = \ln\,|p_1|^2 + \ln\,|p_2|^2 + \frac{1}{p_1 p_2^*}\ln\,|\rho_{12}|^2\; p_1 p_2^* + \frac{1}{p_1^* p_2}\ln\,|\rho_{12}|^2\; p_1^* p_2 - 4\Psi(1)\,, \qquad (1)$$

where $\Psi(x) = d\ln\Gamma(x)/dx$, a factor $\bar{\alpha}_s = \alpha_s N_c/\pi$ has been omitted and the gluon holomorphic momenta and coordinates have been introduced. One has the freedom, because of gauge invariance to choose a description within the Möbius space [8–10]. Then the BFKL hamiltonian has the property of the holomorphic separability ($H_{12} = h_{12} + \bar{h}_{12}$) and is invariant under the Möbius group $SL(2,C)$ transformations, whose generators for the holomorphic sector in the Möbius space for the principal series of unitary representations are given by $M_r^3 = \rho_r\partial_r\,,\; M_r^+ = \partial_r\,,\; M_r^- = -\rho_r^2\partial_r$. The associated Casimir operator for two gluons is $M^2 = |\vec{M}|^2 = -\rho_{12}^2\,\partial_1\,\partial_2$ where $\vec{M} = \sum_{r=1}^2 \vec{M}_r$ and $\vec{M}_r \equiv (M_r^+, M_r^-, M_r^3)$. Note that, after defining formally $J(J-1) = M^2$, one may write $h_{12} = \psi(J) + \psi(1-J) - 2\psi(1)$.

The eigenstates and eigenvalues of the full hamiltonian in eq. (1), $H_{12}E_{h,\bar{h}} = 2\chi_h E_{h,\bar{h}}$ are labelled by the conformal weights $h = \frac{1+n}{2} + i\nu\,,\; \bar{h} = \frac{1-n}{2} + i\nu$. The leading eigenvalue, at the point $n = \nu = 0$, has a value $\chi_{max} = 4\ln 2 \approx 2.77259$, responsible for the rise of the total cross section as $s^{\bar{\alpha}_s\chi_{max}}$, which corresponds to a strong violation of unitarity.

Let us now consider the evolution in rapidity of composite states of more than 2 reggeized gluons [3, 4]. The BKP Hamiltonian in LLA, acting on a colorless state, can be written in terms of the BFKL pomeron Hamiltonian and has the form (see [2])

$$H_n = -\frac{1}{N_c}\sum_{1\le k<l\le n}\vec{T}_k\vec{T}_l H_{kl}\,. \qquad (2)$$

This Hamiltonian is conformal invariant but can be solved only for 3 reggeized gluons, since the color structure factorizes, leaving an integrable dynamics [2]. Different families of odderon solutions were found [11, 12]. The family of solutions given in [12] are the leading ones corresponding to intercept up to 1 and have a non null coupling to photon-meson impact factors [13].

The case of more than three reggeized gluons is in general not solvable, but in the large N_c limit, taking the one cylinder topology (1CT), one obtains the integrable Hamiltonian

$$H_n^\infty = \frac{1}{2}\left[H_{12} + H_{23} + \cdots + H_{n1}\right] = h_n + \bar{h}_n\,, \qquad (3)$$

i.e. there exists a set of other $n-1$ operators q_r, which commute with it and are in involution. This integrable model is a non compact generalization of the Heisenberg XXX spin chains [2, 14] and has been intensively studied with different techniques in the last decade [15–20].

Here we remind the value of the highest eigenvalue of a system of 4 reggeized gluons: $H_4^\infty\psi_4 = 2E_4^{1\mathrm{CT}}\psi_4$. The maximum value found, for zero conformal spin, is

$$E_4^{1\mathrm{CT}} = 0.67416\,. \qquad (4)$$

How to go beyond the large N_c approximation is not an easy question to answer. One may be tempted to apply variational or perturbative techniques to the spectral problem, which nevertheless appears to be quite involved.

3 Color structure for the 4 gluon case

Let us analyze the color structure of the BKP kernel H_4 for four gluons, given in eq. (2). It is acting on 4-gluon states, which may be represented as functions of the transverse plane coordinates and of the gluon colors, $v(\{\boldsymbol{\rho}_i\})^{a_1a_2a_3a_4}$. Since the four gluons are in a total color singlet the color vector $v^{a_1a_2a_3a_4}$ can be described in terms of the color state of a two gluon subchannel. On such a subspace, introducing the projectors $P[R_i]^{a_1'a_2'}_{a_1a_2}$ onto irreducible representations of $SU(N_c)$, one has $1 = P_1 + P_{8A} + P_{8S} + P_{10+\bar{10}} + P_{27} + P_0 = \sum_i P[R_i]$, where $TrP[R_i] = d_i$ is the dimension of the corresponding representation and we consider a unique subspace for the 10 and $\bar{10}$ representations. This is convenient for our purposes and we shall therefore work with 6 different projectors to span the color space of two gluons.

On considering gluons $(1,2)$ to be the reference channel we introduce as the base for the color vector space the set $\{P[R_i]^{a_3a_4}_{a_1a_2}\}$ of projectors and write

$$v^{a_1a_2a_3a_4} = \sum_i v^i \left(P[R_i]^{a_3a_4}_{a_1a_2}\right) \quad \text{or} \quad v = \sum_i v^i P_{12}[R_i]\,. \tag{5}$$

Having chosen a color basis, the next step is to write the BKP kernel with respect to it. Since $\sum_i \vec{T}_i v = 0$ one may finally obtain:

$$H_4 = -\frac{1}{N_c}\left[\vec{T}_1\vec{T}_2\,(H_{12}+H_{34}) + \vec{T}_1\vec{T}_3\,(H_{13}+H_{24}) + \vec{T}_1\vec{T}_4\,(H_{14}+H_{23})\right]. \tag{6}$$

Let us now write explicitely the action of the color operators $\vec{T}_i\vec{T}_j = \sum_a T_i^a T_j^a$ which are associated to the interaction between the gluons labelled i and j. We start from the simple "diagonal channel" for which we have relation $\vec{T}_i\vec{T}_j = -\sum_k a_k P_{ij}[R_k]$ with coefficients $a_k = (N_c, \frac{N_c}{2}, \frac{N_c}{2}, 0, -1, 1)$. Consequently we can write in the $(1,2)$ reference base

$$\left(\vec{T}_1\vec{T}_2 v\right)^j = -a_j v^j = -\left(A\,v\right)^j\,, \tag{7}$$

where $A = diag(a_k)$. The action on v of the $\vec{T}_1\vec{T}_3$ and $\vec{T}_1\vec{T}_4$ operators is less trivial and is constructed in terms of the $6j$ symbols of the adjoint representation of $SU(N_c)$ group:

$$\left(\vec{T}_1\vec{T}_3\,v\right)^j = -\sum_i\left(\sum_k C_k^j a_k C_i^k\right)v^i = -\left(CA\,C\,v\right)^j \tag{8}$$

and

$$\left(\vec{T}_1\vec{T}_4\,v\right)^j = -\sum_i\left(\sum_k s_j C_k^j a_k C_i^k s_i\right)v^i = -\left(SCA\,CS\,v\right)^j\,. \tag{9}$$

The matrix C is the symmetric crossing matrix build on the $6j$ symbols and $S = diag(s_j)$ is constructed on the parities $s_j = \pm 1$ of the different representations R_j.

We can therefore write the general BKP kernel for a four gluon state, given in eq. (6), as

$$H_4 = \frac{1}{N_c}\left[A\left(H_{12}+H_{34}\right)+CAC\left(H_{13}+H_{24}\right)+SCACS\left(H_{14}+H_{23}\right)\right] \qquad (10)$$

One can check that if we make trivial the transverse space dynamics, replacing the H_{ij} operators by a unit operators, the general BKP kernel in eq. (2) becomes $H_n = \frac{n}{2}\hat{1}$ and indeed one can verify that $A + CAC + SCACS = N_c\hat{1}$.

Let us make a few comments on the large N_c limit approximation. As we have already discussed, in the Regge limit one faces the factorization of an amplidute in impact factors and a Green's function which exponentiates the kernel. The topologies resulting from the large N_c limit depend on the impact factor structure. In particular one expects the realization of two cases: the one and two cylinder topologies. The former corresponds to the case, well studied, of the integrable kernel, Heisenberg XXX spin chain-like. It is encoded in the relation: $\vec{T}_i\vec{T}_j \to -\frac{N_c}{2}\delta_{i+1,j}$ which leads to $H_4 = \frac{1}{2}\left(H_{12}+H_{23}+H_{34}+H_{41}\right)$. It is characterized by eigenvalues corresponding to an intercept less then a pomeron. The latter case instead is expected to have a leading intercept, corresponding to an energy dependence given by two pomeron exchange. Consequently one expects at finite N_c a contribution with an energy dependence even stronger. In the two cylinder topology the color structure is associated to two singlets ($\delta_{a_1a_2}\delta_{a_3a_4}$, together with the other two possible permutations). Such a structure is indeed present in the analysis, within the framework of extended generalized LLA, of unitarity corrections to the BFKL pomeron exchange [21] and diffractive dissociation in DIS [22], where the perturbative triple pomeron vertex (see also [23, 24]) was discovered and shown to couple exactly to the four gluon BKP kernel.

It is therefore of great importance to understand how much the picture derived in the planar $N_c = \infty$ case is far from the real situation with $N_c = 3$. One clearly expects, for example, that the first corrections to the eigenvalues of the BKP kernel are proportional to $1/N_c^2$, but what is unknown is the multiplicative coefficient as well as the higher order terms.

4 A BKP toy model

In this section we shall consider a toy model [5], different from the BKP system, but sharing several features with it. Analysing it may help to understand the large N_c approximation might be more or less satisfactory.

Besides the color space, a state of n reggeized gluons undergoing the BKP evolution belongs to the configuration space R^{2n}, associated to the position or momenta in the transverse plane of the n gluons. The operators H_{kl} act (see eq. (10)) on such a state and, in the Möbius space, can be written in terms of the Casimir of the Möbius group, i.e. in terms of the scalar product of the generators of the non compact spin group $SL(2,C)$: $H_{kl} = H_{kl}(\vec{M}_k \cdot \vec{M}_l)$.

We are therefore led to consider a class of toy models where the BKP configuration space R^{2n} is subsituted by the space V_s^n where V_s is the finite space spanned by spin states belonging to the irreducible representation of $SU(2)$ with spin s. In particular we shall consider quantum

systems with an Hamiltonian:

$$\mathcal{H}_n = -\frac{1}{N_c} \sum_{1\le k<l\le n} \vec{T}_k \vec{T}_l \, f(\vec{S}_k \vec{S}_l)\,, \tag{11}$$

where $\vec{S}_i$ are $SU(2)$ generators associated to the particle i in any chosen representation and f is a generic function. A particular toy model is therefore specified by giving the spin s of each particle ("gluons") and the function f. Our BKP toy model is built choosing the spin $s = 1$ case in a global singlet state v ($\sum_i \vec{S}_i \, v = 0$) and the family of functions f

$$f_\alpha(x) = 2\mathrm{Re}\left[\psi\left(\frac{1}{2} + \sqrt{-\alpha(4+2x)}\right)\right] - 2\psi(1)\,. \tag{12}$$

This form is suggested by the conformal spin $n = 0$ BFKL Hamiltonian with the substitution $\frac{1}{4} + L_{ij}^2 \to -\alpha\, S_{ij}^2$ which assures to have the same leading eigenvalue for any α, since both expressions have the value zero as upper bound. The parameter α will be chosen in order to constrain the full 4-particle Hamiltonian (11) to have the same leading eigenvalue as the QCD BKP system in the large N_c limit an one cylinder topology (at zero conformal spin), given in eq. (4). This "BKP toy model" will be used to investigate finite N_c effects.

Since we have chosen to work with states singlet under $SU(2)_{spin\ conf}$, also for the spin part we employ the 2 particle subchannel decomposition in irreducible representations, in a way similarly adopted for the color part. After that one is left with the problem of diagonalizing an Hamiltonian which is a 18×18 matrix. Therefore we proceed by introducing, for 2 particle spin 1 states the resolution of unity $1 = Q_1 + Q_3 + Q_5 = \sum_i Q[R_i]$ which let us write $f(\vec{S}_i\vec{S}_j) = \sum_k f(-b_k) Q_{ij}[R_k]$ with $b_k = (2, 1, -1)$, using for f a power series representation ($Q_{ij}[R_k]$ are projectors). Introducing the crossing matrices D and the parity matrix S' we obtain the relations $\left(f\left(\vec{S}_1\vec{S}_2\right) v\right)^j = (B\,v)^j$, $\left(f\left(\vec{T}_1\vec{T}_3\right) v\right)^j = (DB\,D\,v)^j$ and $\left(f\left(\vec{T}_1\vec{T}_4\right) v\right)^j = (S'DB\,DS'\,v)^j$. It is then straightforward to derive a matrix form for the Hamiltonian of this toy model

$$\mathcal{H}_{4a} = \frac{2}{N_c}\left(A \otimes B + CA\,C \otimes DB\,D + SCA\,CS \otimes S'DB\,DS'\right) \tag{13}$$

which depends on N_c and on the parameter α through the function f_α given in eq. (12).

In the large N_c limit one faces for the Hamiltonian two possible cases (see [5] for more detais): the one cylinder topology (1CT) which corresponds to the simpler Hamiltonian $\mathcal{H}_{4a}^{1CT} = B + S'DBDS'$ and the two cylinder topology (2CT) corresponding to the even simpler Hamiltonian $\mathcal{H}_{4a}^{2CT} = 2B$. Let us remark that while in the case of $N_c > 3$ we consider a basis for the vector states made of $P[R_i]Q[R_j]$ with 18 elements since in the color sector there is also the P_0 projector, the case $N_c = 3$ is characterized by a basis of 15 elements.

The last step to obtain the BKP toy model is to fix the parameter α by requiring $\mathcal{H}_{4a}^{1CT}$ to have the value of eq. (4) so we obtain $\alpha = 2.80665$. We are therefore left with an Hamiltonian which is just a function of the number of colors N_c.

Let us now consider its spectrum for the cases $N_c = 3$ and $N_c = \infty$. Here we report just the leading eigenvalues of $\mathcal{H}_{4a}$ with their multiplicities: $(7.042, 2\times 5.519, 2\times 1.123, \cdots)$. Changing N_c from 3 to ∞ we observe that the first three move to the 2CT leading eigenvalue 5.545

while the next two move to the 1CT leading eigenvalue 0.674. With very good approximation one finds that the N_c dependence of the leading eigenvalue E_0 is given by

$$E_0(N_c) = E_0(\infty)\left(1 + \frac{2.465}{N_c^2}\right), \tag{14}$$

One can see that for this toy model the large N_c approximation corresponds to an error of about 27%, an error which is not negligible because the coefficient of the leading correction to the asymptotic value, proportional to $1/N_c^2$, is a large number. The color- "spin" configuration mixing which is encoded in the eigenvectors has been also studied.

5 Conclusions

We have introduced a family of dynamical models describing interacting particles with color and spin degrees of freedom in order to see how much the large N_c approximation is significant when one is trying to extract the spectrum of these quantum systems. In particular we have investigated a toy model, constructed to mimic some features of the 4 gluon BKP system. We have determined the N_c dependence of the spectrum and discussed the $N_c = \infty$ limit finding for the leading eigenvalue corrections of about 30% at $N_c = 3$.

References

[1] G. 't Hooft, Nucl. Phys. **B72**, 461 (1974).

[2] L. N. Lipatov (1993). hep-th/9311037.

[3] J. Bartels, Nucl. Phys. **B175**, 365 (1980).

[4] J. Kwiecinski and M. Praszalowicz, Phys. Lett. **B94**, 413 (1980).

[5] P. L. Iafelice and G. P. Vacca (2007). arXiv:0709.0655 [hep-th].

[6] E. A. Kuraev, L. N. Lipatov, and V. S. Fadin, Sov. Phys. JETP **44**, 443 (1976).

[7] I. I. Balitsky and L. N. Lipatov, Sov. J. Nucl. Phys. **28**, 822 (1978).

[8] L. N. Lipatov, Sov. Phys. JETP **63**, 904 (1986).

[9] J. Bartels, L. N. Lipatov, and G. P. Vacca, Nucl. Phys. **B706**, 391 (2005). hep-ph/0404110.

[10] J. Bartels, L. N. Lipatov, M. Salvadore, and G. P. Vacca, Nucl. Phys. **B726**, 53 (2005). hep-ph/0506235.

[11] R. A. Janik and J. Wosiek, Phys. Rev. Lett. **82**, 1092 (1999). hep-th/9802100.

[12] J. Bartels, L. N. Lipatov, and G. P. Vacca, Phys. Lett. **B477**, 178 (2000). hep-ph/9912423.

[13] J. Bartels, M. A. Braun, D. Colferai, and G. P. Vacca, Eur. Phys. J. **C20**, 323 (2001). hep-ph/0102221.

[14] L. D. Faddeev and G. P. Korchemsky, Phys. Lett. **B342**, 311 (1995). hep-th/9404173.

[15] S. E. Derkachov, G. P. Korchemsky, and A. N. Manashov, Nucl. Phys. **B617**, 375 (2001). hep-th/0107193.

[16] H. J. De Vega and L. N. Lipatov, Phys. Rev. **D64**, 114019 (2001). hep-ph/0107225.

[17] S. E. Derkachov, G. P. Korchemsky, J. Kotanski, and A. N. Manashov, Nucl. Phys. **B645**, 237 (2002). hep-th/0204124.

[18] H. J. de Vega and L. N. Lipatov, Phys. Rev. **D66**, 074013 (2002). hep-ph/0204245.

[19] G. P. Vacca, Phys. Lett. **B489**, 337 (2000). hep-ph/0007067.

[20] J. Kotanski (2005). hep-th/0511279.

[21] J. Bartels, Z. Phys. **C60**, 471 (1993).

[22] J. Bartels and M. Wusthoff, Z. Phys. **C66**, 157 (1995).

[23] M. A. Braun and G. P. Vacca, Eur. Phys. J. **C6**, 147 (1999). hep-ph/9711486.

[24] G. P. Vacca (1998). hep-ph/9803283.

The Reggeon → 2 Reggeons + Particle vertex in the Lipatov effective action formalism

M.A.Braun[†] *M.I.Vyazovsky*
Dept. of High Energy Physics, University of St. Petersburg,
198904 St. Petersburg, Russia

Abstract
The Reggeon→ 2 Reggeons+Particle vertex is constructed in the framework of Lipatov effective action formalism. Its reduction to a pure transverse form for the diffractive amplitude gives the standard Bartels vertex plus an additional contribution given by a longitudinal integral divergent both in the ultraviolet and infrared. A certain specific recipe for this part, including the principal value prescription for the integration, allows to eliminate this unwanted contribution.

1 Introduction

Particle interaction in the Regge kinematics and QCD perturbative region , $\Lambda^2_{QCD} << |t| << s$, is described by exchange of reggeized gluons ('reggeons') accompanied by emission of real gluons ('particles'). To automatically calculate all relevant diagrams in a systematic and self-consistent way a potentially powerful formalism of an effective action has been proposed by L.N.Lipatov [1], in which the longidudinal and transverse variables are separated from the start and one arrives at a theory of interaction of reggeized gluons and particles described by independent fields. However the resulting vertices are 4-dimensional and reduction of them to the 2-dimensional transverse form still has to be done.

Up to the present, several application of this formalism have been done and a number of interaction vertices have been calculated [2]. In this paper we study a vertex for the transition of a reggeon into a pair of reggeons and a particle (the RRRP vertex). The 2-dimensional form of this vertex (the 'Bartels' vertex) is well-known [3,4]. The found 4-dimensional vertex resembles the Bartels vertex, although it contains a new structure absent in the latter and of course longitudinal variables. Unlike the vertices obtained so far in the effective action formalism, reduction of the RRRP vertex to the 2-dimensional form involves a non-trivial integration in the loop formed by the two reggeons and the target. For a simple diffractive diagram, in which both the projectile and target are quarks, a literal integration over the longitudinal variables proves to be impossible (divergent). The Bartels vertex is obtained only if certain *ad hoc* rules are followed, which reduce to neglecting all small longitudinal momenta in the target factor and subsequent integration over the minus component of the loop momentum according to the principal value prescription.

2 Calculation of the vertex

In the effective action formalism, calculation of the RRRP vertex is straightforward. The relevant Feyman rules were presented in [2] and we only recapitulate them here for convenience and to

[†] speaker

fix our notations. We write $D_\mu = \partial_\mu + gV_\mu$ where $V_\mu = -iV_\mu^a T^a$ is the gluon field and T^a are the $SU(N)$ generators in the adjoint representation. The reggeon field $A_\pm = -iA_\pm^a T^a$ satisfies the kinematical condition

$$\partial_+ A_- = \partial_- A_+ = 0. \tag{1}$$

The field A_+ comes from the region with a higher rapidity, its momentum q_- is small, the field A_- comes from the region with a smaller rapidity, its q_+ is small. The QCD Lagrangian for the particle (gluon) field V is standard and so are the Feynman rules. The effective action is

$$\mathcal{L}_{eff} = \mathcal{L}_{QCD}(V_\mu + A_\mu) + \mathrm{Tr}\left(\mathcal{A}_+(V_+ + A_+) - A_+)\partial_\perp^2 A_- + \mathcal{A}_-(V_- + A_-) - A_-)\partial_\perp^2 A_+\right), \tag{2}$$

where

$$\mathcal{A}_\pm(V_\pm) = -\frac{1}{g}\partial_\pm \frac{1}{D_\pm}\partial_\pm * 1 = \sum_{n=0}(-g)^n V_\pm(\partial_\pm^{-1}V_\pm)^n$$
$$= V_\pm - gV_\pm\partial_\pm^{-1}V_\pm + g^2 V_\pm\partial_\pm^{-1}V_\pm\partial_\pm^{-1}V_\pm + -... \tag{3}$$

The reggeon propagator in the momentum space is

$$< A_+^a A_-^b >= -i\frac{2\delta_{ab}}{q_\perp^2}. \tag{4}$$

The well-known R→RP ('Lipatov') vertex is

$$\frac{gf^{ab_2d}}{2}\Big[q_\sigma + q_{2\sigma} + \Big(\frac{q_2^2}{q_+} - q_{2-}\Big)n_\sigma^+ + \Big(\frac{q^2}{q_{2-}} - q_+\Big)n_\sigma^-\Big]. \tag{5}$$

In the convenient gauge $V_+ = 0$ the polarization vector has the form

$$\epsilon_\mu(k) = \epsilon_\mu^\perp(k) - \frac{k\epsilon^\perp}{k_+}n_\mu^+. \tag{6}$$

Convolutiong the vertex (5) with this polarization vector we find

$$gf^{ab_2d}q_\perp^2\Big(\frac{q\epsilon_\perp}{q_\perp^2} - \frac{k\epsilon_\perp}{k_\perp^2}\Big), \tag{7}$$

which form of the Lipatov vertex is widely used in literature.

Our aim is to calculate the vertex R→RRP. The total contribution to it is represented by four diagrams shown in Fig. 1, in which particles are shown by solid lines and reggeons by wavy lines.

Of these diagrams the one described by Fig. 1.3 vanishes due to condition (1). Diagram 1.4 gives

$$V_4 = \frac{ig^2}{4}\Big[f^{b_1cd}f^{ab_2d}\Big(2\frac{q_\perp^2 n_\mu^-}{p_-q_{2-}} - n_\mu^+\Big) + f^{ab_1d}f^{b_2cd}\Big(2\frac{q_\perp^2 n_\mu^-}{p_-q_{1-}} - n_\mu^+\Big)\Big]. \tag{8}$$

Diagram Fig. 1.1 gives

$$V_{1.1} = \frac{-ig^2 f^{b_1cd}f^{ab_2d}}{4k^2}\Big(-2p_+g_{\mu\sigma} + (p+2q_1)_\mu n_\sigma^+ + (p-q_1)_\sigma n_\mu^+ + \frac{q_1^2}{p_+}n_\mu^+ n_\sigma^+\Big)$$

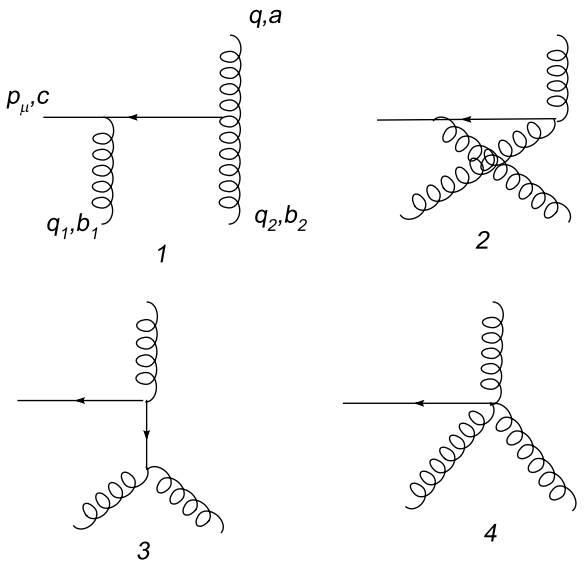


Fig. 1: Reggeon diagrams for the vertex R→RRP

$$\Big[q_\sigma + q_{2\sigma} + \Big(\frac{q_2^2}{q_+} - q_{2-}\Big)n_\sigma^+ + \Big(\frac{q^2}{q_{2-}} - q_+\Big)n_\sigma^-\Big]. \tag{9}$$

The contribution from diagram Fig. 1.2 is obtained by the interchange of the outgoing gluons 1 and 2.

The total vertex obtained as a sum of the contributions from diagrams shown in Fig. 1 is found to be transversal (convolution with p_μ is zero) as it should be.

To find the transition amplitude one has to convolute the sum of diagrams Fig. 2.1+2+4 with the polarization vector $\epsilon_\mu^*(p)$. In the gauge $V_+ = 0$ the result of the convolution is

$$g^2\frac{f^{b_1cd}f^{ab_2d}}{(q-q_2)^2}\Big[q_+(q\epsilon_\perp^*) + \frac{q^2}{q_{2-}}\Big(-(q-q_2)\epsilon_\perp^* + \frac{(q-q_2)^2}{p_\perp^2}(p\epsilon_\perp^*)\Big)\Big]$$

$$+g^2\frac{f^{b_2cd}f^{ab_1d}}{(q-q_1)^2}\Big[q_+(q\epsilon_\perp^*) + \frac{q^2}{q_{1-}}\Big(-(q-q_1)\epsilon_\perp^* + \frac{(q-q_1)^2}{p_\perp^2}(p\epsilon_\perp^*)\Big)\Big]. \tag{10}$$

3 The diffractive amplitude

The obtained R→RRP vertex (10) has a 4-dimensional form. To reduce it to the transverse vertex we have to study a concrete amplitude which involves this vertex. We choose the simplest amplitude possible: production of a real gluon in collision of two quarks, the target quark interacting with the two final reggeized gluons in the colourless state (Fig. 2). Note that there are additional diagrams for this process which involve two reggeon exchange between projectile and target with the gluon emitted by the Lipatov vertex. However, as is known, for them integration over longitudinal variables in the loop presents no difficulties, so that all the problem is concentrated in the diagram with the found R→RRP vertex.

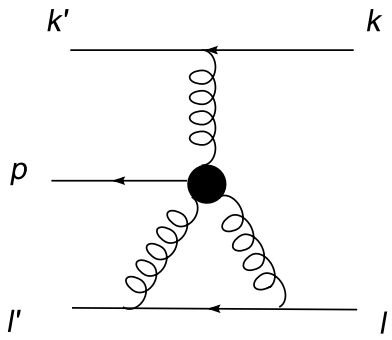


Fig. 2: The difractive diagram with a R→RPP vertex

The two terms in the vertex (10), which differ by the permutation $1 \leftrightarrow 2$, evidently give the same contribution after integration over the loop momentum and summation over colour indices. So it is sufficient to study only one of them. We choose the second term.

Reduction to the 2-dimensional form requires integration over the longitudinal variables. We first integrate over q_{1+} and then over q_{1-}.

The first term in the second part of (10), proportional to $(q\epsilon)_\perp$ has two denominators depending on the longitudinal variables:

$$[2q_{1-}(q_{1+}-q_+)+(q-q_1)\perp^2+i0][2q_{1+}(l_-+q_{1-})+q_{1\perp}^2+i0] \tag{11}$$

in the direct term and

$$[2q_{1-}(q_{1+}-q_+)+(q-q_1)\perp^2+i0][-2(q_{1+}-l'_+)(l'_--q_{1-})+(l'-q_1)^2_\perp+i0]. \tag{12}$$

in the crossed term. A non-zero result is obtained only when the two poles in q_{1+} are on the opposite sides from the real axis. This limits the integration over q_{1-}: $-l_- < q_{1-} < 0$ and $0 < q_{1-} < l'_- \simeq l_-$ in the direct and crossed terms respectively. Calculation of integrals is straightforward, meets no trouble and can be done separately in the direct and crossed term. In their sum the real parts cancel and only the imaginary part remains, given exclusively by the direct term.

Taking into account the colour factor and momentum factors coming from the two impact factors we find the contribution from the first term in the second part of (10) as

$$\int \frac{dq_{1+}dq_{1-}}{2\pi i}T_1 = 4\pi i(pl)\delta_{ac}u't^a u\cdot\frac{1}{q_{1\perp}^2 q_{2\perp}^2}\frac{q\epsilon_\perp}{q_\perp^2}. \tag{13}$$

It coincides with the first term in the contribution from the Bartels vertex to the diffractive amplitude.

Note that the same result is obtained if one introduces energies squared $s_1=(q-q_1)^2$ and $s_2=(l+q_1)^2$ for the amplitudes R+R→ P+R and q+R→ q+R and then deforms the Feynman integration contour to close on the unitarity cuts of both amplitudes. The contribution from the intermediate quark+gluon state will immediately give (13).

The situation is a bit more complicated with the second term in the second part of (10), proportional to $(q-q_1)\epsilon_\perp$. In both the direct and crossed term an extra factor $1/q_{1-}$ appears. The integration over q_{1+} is done exactly as before. However the subsequent integration over q_{1-} cannot be done separately for the direct and crossed term because of the singularity at $q_{1-}=0$. However in their sum this singularity cancels and integration becomes trivial. Adding all the rest factors we get for the second term in the second part of (10)

$$\int \frac{dq_{1+}dq_{1-}}{2\pi i} T_2 = -4\pi i (pl)\delta_{ac} u' t^a u \cdot \frac{1}{q_{1\perp}^2 q_{2\perp}^2} \frac{(q-q_1)\epsilon_\perp}{(q-q_1)_\perp^2}. \tag{14}$$

This coincides with the second part of the contribution corresponding to the Bartels vertex.

Note that if one tries to use here the method of integration over energies of the R+R$\to$R+P and q+R$\to$ q+P amplitudes by closing the contour around the unitarity cuts, then one encounters the singularity at $q_{1-}=0$ with an unknown way of integration around it. If one just neglects this singularity, that is takes into account only the unitarity contribution to the dicontinuities of the amplitudes, then one gets a result which is twice larger than (14) and hence incorrect.

We are left with the third term in the second part of (10) with a structure which has no counterpart in the Bartels vertex. For the 4 dimensional and 2-dimensional pictures to coincide this contribution has to disappear.

The only denominator in the direct term is

$$(l+q_1)^2 + i0 = 2q_{1+}(l_- + q_{1-}) + q_{1\perp}^2 + i0 \tag{15}$$

and in the crossed term

$$(l'-q_1)^2 + i0 = -2(q_{1+} - l'_+)(l'_- - q_{1-}) + (l'-q_1)_\perp^2 + i0. \tag{16}$$

Integration over q_{1+} gives

$$-\frac{i\pi}{2}\Big(\frac{\mathrm{sign}\,(l_- + q_{1-})}{l_- + q_{1-}} + \frac{\mathrm{sign}\,(l'_- - q_{1-})}{l'_- - q_{1-}}\Big). \tag{17}$$

This expression does not vanish at $q_{1-}=0$, so that the subsequent integration with the denominator q_{1-} is meaningless.

To give some sense to this integration we may assume that in the target denominators one may neglect minus components of all momenta except for the incoming target momentum l_-. This means that in (15) and (16) we take $l'_- = l_-$ and $q_{1-}=0$. Then the result of integration over q_{1+} becomes independent of q_{1-}. After that we find the integral over q_{1-} of the form

$$\int_{-\infty}^{\infty} \frac{dq_{1-}}{q_{1-}}. \tag{18}$$

If we assume that this integral should be taken according to the principal value prescription then it vanishes, the third term in (10) disappears and the obtained transverse vertex coincides with the Bartels one.

4 Conclusions

We have found that the longitudinal integration of the 4-dimensional vertex constructed by the effective action technique requires certain caution. One finds a piece, for which a strict integration is divergent. To overcome this diffculty one has to neglect the small minus components in the target impact factor (and then do the q_{1+} integration in the trival manner closing the contour around the unitarity cut of the reggeon-target amplitude) and afterwards do the remaining q_{1-} integration by the principal value recipe. This result has been derived only for the diffractive amplitude. It remains an open question if it has a wider validity and applies also to other cases, which correspond to double and single cuts of the general triple pomeron amplitude.

5 Acknowledgements

The authors have benefited from constructive discussions with J.Bartels, L.Lipatov and G.P.Vacca, whose comments they highly appreciate. This work has been supported by grants RNP 2.1.1.1112 and RFFI 06-02-16115a of Russia.

References

[1] L.N.Lipatov, Phys. Rep. **286** (1997) 131.

[2] E.N.Antonov, L.N.Lipatov, E.A.Kuraev and I.O. Cherednikov, Nucl. Phys. **B 721** (2005) 111.

[3] J.Bartels, Nucl. Phys. **B175** (1980) 365.

[4] J.Bartels and M.Wšthoff, Z.Phys. **C 66** (1995) 157.

On the behaviour of R_{pA} at high energy

Misha Kozlov [1†], *Arif I. Shoshi* [1], *Bo-Wen Xiao* [2]
[1] Fakultät für Physik, Universität Bielefeld, D-33501 Bielefeld, Germany
[2] Department of Physics, Columbia University, New York, NY, 10027, USA

Abstract
We discuss the behaviour of R_{pA}, the ratio of the unintegrated gluon distribution of a nucleus over the unintegrated gluon distribution of a proton scaled up by $A^{1/3}$, at high energy and fixed coupling. We show that R_{pA} exhibits a rising gluon shadowing with growing rapidity, approaching $1/A^{1/3}$ at asymptotic rapidity, which means total gluon shadowing due to gluon number fluctuations or Pomeron loops.

1 Introduction

We study the ratio of the unintegrated gluon distribution of a nucleus $\varphi_A(k_\perp, Y)$ over the unintegrated gluon distribution of a proton $\varphi_p(k_\perp, Y)$ scaled up by $A^{1/3}$

$$R_{pA} = \frac{\varphi_A\left(k_\perp, Y\right)}{A^{\frac{1}{3}}\,\varphi_p\left(k_\perp, Y\right)}\,. \tag{1}$$

This ratio is a measure of the number of particles produced in a proton-nucleus collision versus the number of particles in proton-proton collisions times the number of collisions. The transverse momentum of gluons is denoted by $k_\perp$ and the rapidity variable by $Y = \ln(1/x)$.

The ratio R_{pA} has been widely studied [1] in the framework of the BK-equation [2] which describes the small-x physics in the *mean field approximation*. Using the BK-equation one finds in the geometric scaling regime (transition from high to low gluon density, see Fig.1) in the fixed coupling case that the shape of the unintegrated gluon distribution of the nucleus and proton as a function of $k_\perp$ is preserved with increasing Y, see Fig.2(a), because of the geometric scaling behaviour $\varphi_{p,A}(k_\perp, Y) = \varphi_{p,A}(k_\perp^2/Q_s^2(Y))$, and therefore the leading contribution to the ratio R_{pA} is basically $k_\perp$ and Y independent, scaling with the atomic number A as [3, 4]

$$R_{pA} \simeq \frac{1}{A^{\frac{1}{3}(1-\gamma_0)}}\,, \tag{2}$$

where $\gamma_0 = 0.6275$. This means that gluons inside the nucleus and proton are somewhat shadowed since $\varphi_A/\varphi_p = A^{\gamma_0/3}$ lies between total ($\varphi_A/\varphi_p = 1$) and zero ($\varphi_A/\varphi_p = A^{1/3}$) gluon shadowing. The *partial gluon shadowing* comes from the anomalous behaviour of the unintegrated gluon distributions which stems from the BFKL evolution. The partial gluon shadowing may explain why particle production in heavy ion collisions scales, roughly, like N_{part} [5].

Over the last few years, it has been understood how to deal with small-x physics at high energy *beyond the mean field approximation*, i.e., beyond the BK [2] and JIMWLK [6] equations. We have learned how to account for the elements missed in the mean field evolution,

† speaker

such as the discreteness and fluctuations of gluon numbers [7, 8] or the Pomeron loops [9]. The main result as a consequence of the above is the emerging of a new scaling behaviour for the dipole-hadron/nucleus scattering amplitude at high rapidities [7, 8], the so-called diffusive scaling. This is different from the geometric scaling behaviour which is the hallmark of the "mean-field" evolution equations (JIMWLK and BK equations). The effects of fluctuations on the scattering amplitude [10], the diffractive scattering processes [11, 12] and forward gluon production in hadronic scattering processes [13, 14] has been studied so far. In this work we show how the behaviour of R_{pA} as a function of $k_\perp$ and Y in the fixed coupling case is completely changed due the effects of gluon number fluctuations or Pomeron loops at high rapidity [15].

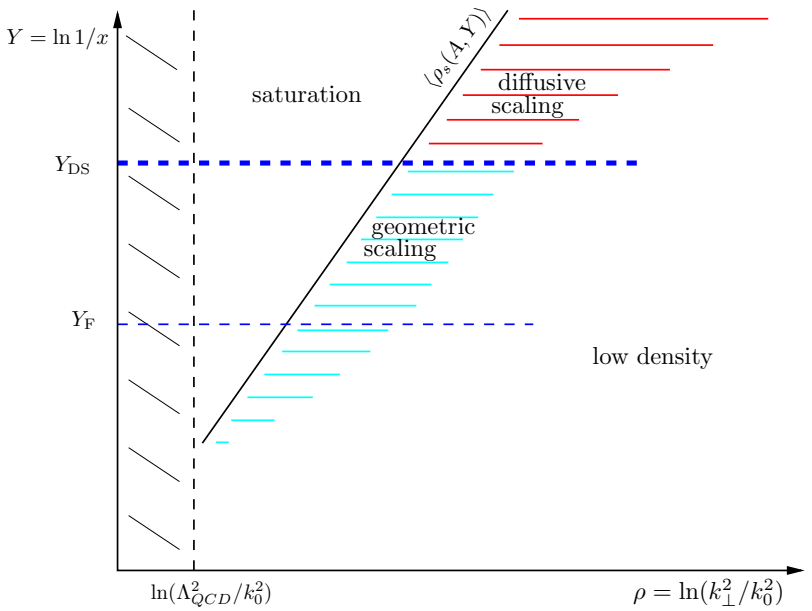


Fig. 1: Phase diagram of a highly evolved nucleus/proton.

2 R_{pA} ratio in the diffusive scaling regime

According to the statistical physics/high energy QCD correspondence [8] the influence of fluctuations on the unintegrated gluon distribution of a nucleus/proton is as follows: Starting with an intial gluon distribution of the nucleus/proton at zero rapidity, the stochastic evolution generates an ensemble of distributions at rapidity Y, where the individual distributions seen by a probe typically have different saturation momenta and correspond to different events in an experiment. To include gluon number fluctuations one has to average over all individual events,

$$\langle \varphi_{p,A}(\rho - \rho_s) \rangle = \int d\rho_s \; \varphi_{p,A}(\rho - \rho_s) \; P(\rho_s - \langle \rho_s \rangle) \; , \tag{3}$$

where $\varphi_{p,A}(\rho - \rho_s)$ is the distribution for a single event with $\rho = \ln(k_\perp^2/k_0^2)$ and $P(\rho_s - \langle \rho_s \rangle)$ the probability distribution of the logarithm of the saturation momentum, $\rho_s(Y) = \ln(Q_s^2(Y)/k_0^2)$,

which is argued to have a Gaussian form [16],

$$P(\rho_s) \simeq \frac{1}{\sqrt{2\pi\sigma^2}} \exp\left[-\frac{(\rho_s - \langle\rho_s\rangle)^2}{2\sigma^2}\right] \quad \text{for} \quad \rho - \rho_s \ll \gamma_c^2\sigma^2 \,, \tag{4}$$

with the dispersion

$$\sigma^2 = \langle\rho_s^2\rangle - \langle\rho_s\rangle^2 = DY. \tag{5}$$

The main consequence of fluctuations is the replacement of the geometric scaling, $\varphi_{p,A}(k_\perp, Y) = \varphi_{p,A}(k_\perp^2/Q_s^2(Y))$, by a new scaling, the diffusive scaling [7,8], namely, $\langle\varphi_{p,A}(k_\perp, Y)\rangle$ is a function of another scaling variable ($\langle Q_s\rangle$ is the average saturation momentum),

$$\langle\varphi_{p,A}(k_\perp, Y)\rangle = F_{p,A}\left(\frac{\ln(k_\perp^2/\langle Q_s(Y)\rangle^2)}{DY}\right) . \tag{6}$$

The diffusive scaling, see Fig. 1, sets in when the dispersion of the different events is large, $\sigma^2 = \langle\rho_s^2\rangle - \langle\rho_s\rangle^2 = DY \gg 1$, i.e., $Y \gg Y_{DS} = 1/D$ where D is the diffusion coefficient, and is valid in the region $\sigma \ll \ln(k_\perp^2/\langle Q_s(Y)\rangle^2) \ll \gamma_0\,\sigma^2$.

The diffusive scaling means that the shape of the unintegrated gluon distribution of the nucleus/proton changes with increasing Y because of the additional DY dependence as compared with the geometric scaling. The shape becomes flatter and flatter with increasing rapidity Y, as shown in Fig.2(b), in contrast to the preserved shape in the geometric scaling regime shown in Fig.2(a). This flattening will lead to a new phenomenon for R_{pA} as discussed below.

Using Eq.(3) for the averaging over all events and the result from the BK-equation for the single event distribution one obtains [15] for the ratio

$$R_{pA} \simeq \frac{1}{A^{\frac{1}{3}(1-\frac{\Delta\rho_s}{2\sigma^2})}} \left[\frac{k_\perp^2}{\langle Q_s^2(A,y)\rangle}\right]^{\frac{\Delta\rho_s}{\sigma^2}} \tag{7}$$

with the difference between the average saturation lines of the nucleus and the proton

$$\Delta\rho_s \;\equiv\; \langle\rho_s(A,Y)\rangle - \langle\rho_s(p,Y)\rangle \;=\; \ln\frac{\langle Q_s(A,Y)\rangle^2}{\langle Q_s(p,Y)\rangle^2} \tag{8}$$

where $\langle Q_s(A,Y)\rangle$ ($\langle Q_s(p,Y)\rangle$) is the average saturation momentum of the nucleus (proton). The difference $\Delta\rho_s$ is fixed by the inital conditions for the average saturation momenta of the nucleus and proton and is Y-indipendent in the fixed coupling case. For example, using the known assumption $\langle Q_s(A)\rangle^2 = A^{1/3}\,\langle Q_s(p)\rangle^2$ one obtains $\Delta\rho_s = \ln A^{1/3}$.

The ratio R_{pA} in Eq. (7) shows the following very different features as compared with the ratio in the geometric scaling regime given in Eq. (2):

- In the diffusive scaling regime where $k_\perp^2$ is close to $\langle Q_s^2(A,Y)\rangle$, the gluon shadowing characterized by $A^{\frac{1}{3}(\frac{\Delta\rho_s}{2\sigma^2}-1)}$ increases as the rapidity grows (at fixed A or $\Delta\rho_s$) because of $\sigma^2 = DY$. At asymptotic rapidity one obtains *total gluon shadowing*, $R_{pA} = A^{1/3}$, which means that the unintegrated gluon distribution of the nucleus and that of the proton

become the same in the diffusive scaling regime at $Y \to \infty$. The phenomenon of total gluon shadowing is universal since it does not depend on the initial conditions ($\Delta\rho_s$).

Total gluon shadowing is an effect of gluon number fluctuations (or Pomeron loops) since fluctuations make the unintegrated gluon distributions of the nucleus and of the proton flatter and flatter [8] and their ratio closer and closer to 1 (at fixed $\Delta\rho_s$) with rising rapidity, as shown in Fig.2(b). Total gluon shadowing is not possible in the geometric scaling regime in the fixed coupling case since the shapes of the gluon distributions of the nucleus and of the proton remain the same with increasing Y giving a constant ratio unequal one, as shown in Fig.2(a). In the absence of fluctuations one can expect only partial gluon shadowing, see Eq. (2), in the fixed coupling case.

- The ratio R_{pA} increases with rising $k_\perp^2$ within the diffusive scaling region. Since the exponent $\Delta\rho_s/\sigma^2$ decreases with rapidity, the slope of R_{pA} as a function of $k_\perp^2$ becomes smaller with growing Y. The result for R_{pA} in the diffusive scaling regime in Eq.(3) is very different from the result obtained in the mean field approximation given in Eq. (2), where gluon number fluctuations are not included, which is basically $k_\perp$ and Y-independent.

The qualitative behaviour of R_{pA} as a function of $k_\perp$ at four different rapidities, $Y_1 \leq Y_2 \leq Y_3 \leq Y_4$, in the diffusive scaling regime and for a fixed coupling is shown in Fig. 3. Note that R_{pA} is always smaller than one for values of $k_\perp$ in the diffusive scaling regime.

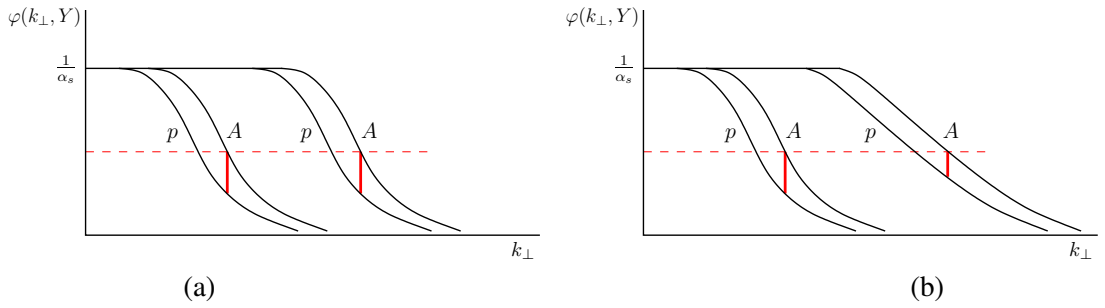


Fig. 2: The qualitative behaviour of the unintegrated gluon distribution of a nucleus (A) and a proton (p) at two different rapidities in the geometric scaling regime (a) and diffusive scaling regime (b).

The above effects of fluctuations on R_{pA} are valid in the fixed coupling case and at very large energy. It isn't clear yet whether the energy at LHC is high enough for them to become important. Recently, while in Ref. [17] a possible evidence of gluon number fluctuations in the HERA data has been found, in Ref. [18], using a toy model, it has been argued that in case of a running coupling fluctuations can be neglected in the range of HERA and LHC energies. See also Refs. [7, 19] for more studies on running coupling plus fluctuation effects.

Moreover, the running of the coupling [20] may become more important than the effect of gluon number fluctuations [18]. In case of a running coupling, the gluon shadowing increases with rising rapidity in the geometric scaling regime [1], as opposed to the (roughly) fixed value (partial shadowing) in the fixed-coupling case, and would lead to total gluon shadowing [4]

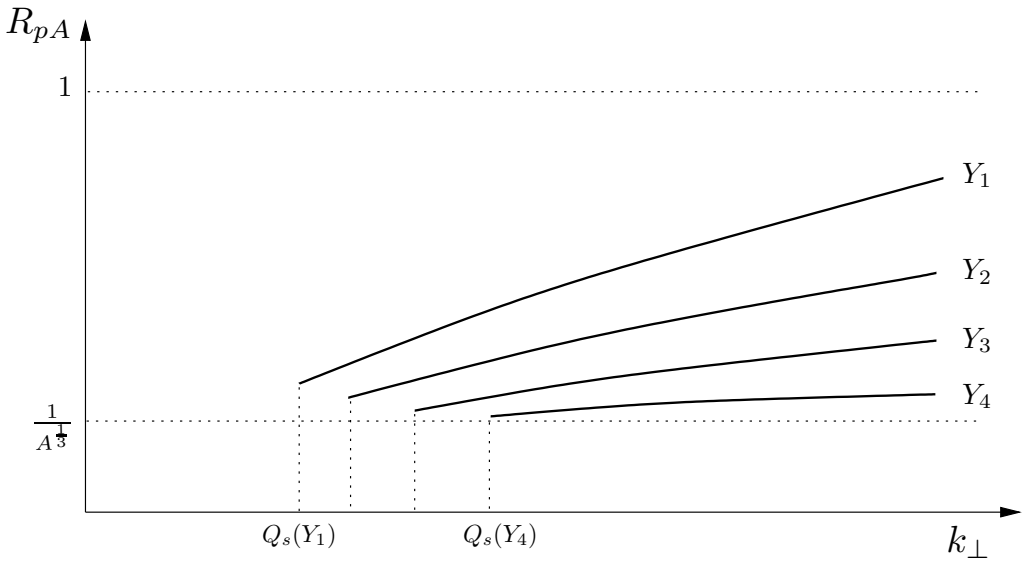


Fig. 3: The qualitative behaviour of the ratio R_{pA} as a function of $k_\perp$ at four different rapidities, $Y_1 \leq Y_2 \leq Y_3 \leq Y_4$, in the diffusive scaling regime. R_{pA} is always smaller than one for values of $k_\perp$ in the diffusive scaling regime.

at very high rapidities even if fluctuations were absent. In case fluctuations are important at LHC energy, in addition to the theoretically interesting consequences of fluctuations on R_{pA}, the features of R_{pA} worked out here, as the increase of the gluon shadowing and the decrease as a function of the gluon momentum with rising rapidity, may be viewed as signatures for fluctuation effects in the LHC data. More work remains to be done in order to clarify how important fluctuation or running coupling effects are at given energy, e.g., at LHC energy. An extension of this work by the running coupling may help to clarify some of the open questions.

Acknowledgments

A. Sh. and M. K. acknowledge financial support by the Deutsche Forschungsgemeinschaft under contract Sh 92/2-1.

References

[1] E. Iancu, K. Itakura, and D. N. Triantafyllopoulos, Nucl. Phys. **A742**, 182 (2004). hep-ph/0403103;
A. H. Mueller, Nucl. Phys. **A724**, 223 (2003). hep-ph/0301109;
J. L. Albacete, N. Armesto, A. Kovner, C. A. Salgado, and U. A. Wiedemann, Phys. Rev. Lett. **92**, 082001 (2004). hep-ph/0307179;
R. Baier, A. H. Mueller, and D. Schiff, Nucl. Phys. **A741**, 358 (2004). hep-ph/0403201;
R. Baier, A. Kovner, and U. A. Wiedemann, Phys. Rev. **D68**, 054009 (2003). hep-ph/0305265;
D. Kharzeev, Y. V. Kovchegov, and K. Tuchin, Phys. Rev. **D68**, 094013 (2003). hep-ph/0307037;
J. Jalilian-Marian, Y. Nara, and R. Venugopalan, Phys. Lett. **B577**, 54 (2003). nucl-th/0307022;
F. Gelis, A. M. Stasto, and R. Venugopalan, Eur. Phys. J. **C48**, 489 (2006). hep-ph/0605087.

[2] I. Balitsky, Nucl. Phys. **B463**, 99 (1996). hep-ph/9509348;
I. Balitsky, Phys. Lett. **B518**, 235 (2001). hep-ph/0105334;

Y. V. Kovchegov, Phys. Rev. **D60**, 034008 (1999). hep-ph/9901281;
Y. V. Kovchegov, Phys. Rev. **D61**, 074018 (2000). hep-ph/9905214.

[3] A. H. Mueller, Nucl. Phys. **A724**, 223 (2003). hep-ph/0301109.

[4] E. Iancu, K. Itakura, and D. N. Triantafyllopoulos, Nucl. Phys. **A742**, 182 (2004). hep-ph/0403103.

[5] D. Kharzeev, E. Levin, and L. McLerran, Phys. Lett. **B561**, 93 (2003). hep-ph/0210332.

[6] J. Jalilian-Marian, A. Kovner, A. Leonidov, and H. Weigert, Nucl. Phys. **B504**, 415 (1997). hep-ph/9701284;
J. Jalilian-Marian, A. Kovner, A. Leonidov, and H. Weigert, Phys. Rev. **D59**, 014014 (1999). hep-ph/9706377;
J. Jalilian-Marian, A. Kovner, and H. Weigert, Phys. Rev. **D59**, 014015 (1999). hep-ph/9709432;
E. Iancu, A. Leonidov, and L. D. McLerran, Phys. Lett. **B510**, 133 (2001). hep-ph/0102009;
E. Ferreiro, E. Iancu, A. Leonidov, and L. McLerran, Nucl. Phys. **A703**, 489 (2002). hep-ph/0109115.

[7] A. H. Mueller and A. I. Shoshi, Nucl. Phys. **B692**, 175 (2004). hep-ph/0402193.

[8] E. Iancu, A. H. Mueller, and S. Munier, Phys. Lett. **B606**, 342 (2005). hep-ph/0410018.

[9] A. H. Mueller, A. I. Shoshi, and S. M. H. Wong, Nucl. Phys. **B715**, 440 (2005). hep-ph/0501088;
E. Iancu and D. N. Triantafyllopoulos, Phys. Lett. **B610**, 253 (2005). hep-ph/0501193;
A. Kovner and M. Lublinsky, Phys. Rev. **D71**, 085004 (2005). hep-ph/0501198;
E. Levin and M. Lublinsky, Nucl. Phys. **A763**, 172 (2005). hep-ph/0501173;
Y. Hatta, E. Iancu, L. McLerran, A. Stasto, and D. N. Triantafyllopoulos, Nucl. Phys. **A764**, 423 (2006). hep-ph/0504182.

[10] E. Brunet, B. Derrida, A. H. Mueller, and S. Munier, Phys. Rev. **E73**, 056126 (2006). cond-mat/0512021;
S. Munier, Phys. Rev. **D75**, 034009 (2007). hep-ph/0608036;
Y. Hatta and A. H. Mueller, Nucl. Phys. **A789**, 285 (2007). hep-ph/0702023;
M. Kozlov, E. Levin, and A. Prygarin (2006). hep-ph/0606260;
M. Kozlov, E. Levin, and A. Prygarin, Nucl. Phys. **A792**, 122 (2007). arXiv:0704.2124 [hep-ph];
E. Levin, J. Miller, and A. Prygarin (2007). arXiv:0706.2944;
A. I. Shoshi and B.-W. Xiao, Phys. Rev. **D73**, 094014 (2006). hep-ph/0512206;
M. Kozlov and E. Levin, Nucl. Phys. **A779**, 142 (2006). hep-ph/0604039;
S. Bondarenko, L. Motyka, A. H. Mueller, A. I. Shoshi, and B. W. Xiao, Eur. Phys. J. **C50**, 593 (2007). hep-ph/0609213;
E. Levin and A. Prygarin (2007). hep-ph/0701178;
M. A. Braun and G. P. Vacca, Eur. Phys. J. **C50**, 857 (2007). hep-ph/0612162;
J. P. Blaizot, E. Iancu, and D. N. Triantafyllopoulos, Nucl. Phys. **A784**, 227 (2007). hep-ph/0606253;
E. Iancu, J. T. de Santana Amaral, G. Soyez, and D. N. Triantafyllopoulos, Nucl. Phys. **A786**, 131 (2007). hep-ph/0611105;
G. Soyez, Phys. Rev. **D72**, 016007 (2005). hep-ph/0504129.

[11] Y. Hatta, E. Iancu, C. Marquet, G. Soyez, and D. N. Triantafyllopoulos, Nucl. Phys. **A773**, 95 (2006). hep-ph/0601150.

[12] A. Kovner, M. Lublinsky, and H. Weigert, Phys. Rev. **D74**, 114023 (2006). hep-ph/0608258;
A. I. Shoshi and B.-W. Xiao, Phys. Rev. **D75**, 054002 (2007). hep-ph/0605282;
M. Kozlov, E. Levin, V. Khachatryan, and J. Miller, Nucl. Phys. **A791**, 382 (2007). hep-ph/0610084.

[13] E. Iancu, C. Marquet, and G. Soyez, Nucl. Phys. **A780**, 52 (2006). hep-ph/0605174.

[14] A. Kovner and M. Lublinsky, JHEP **11**, 083 (2006). hep-ph/0609227.

[15] M. Kozlov, A. I. Shoshi, and B.-W. Xiao, Nucl. Phys. **A792**, 170 (2007). hep-ph/0612053;
M. Kozlov, A. I. Shoshi, and B.-W. Xiao (2007). arXiv:0706.3998 [hep-ph].

[16] C. Marquet, G. Soyez, and B.-W. Xiao, Phys. Lett. **B639**, 635 (2006). hep-ph/0606233.

[17] M. Kozlov, A. Shoshi, and W. Xiang (2007). arXiv:0707.4142.

[18] A. Dumitru, E. Iancu, L. Portugal, G. Soyez, and D. N. Triantafyllopoulos (2007). arXiv:0706.2540.

[19] G. Beuf (2007). arXiv:0708.3659 [hep-ph].

[20] J. L. Albacete and Y. V. Kovchegov, Phys. Rev. **D75**, 125021 (2007). arXiv:0704.0612 [hep-ph];
Y. V. Kovchegov and H. Weigert, Nucl. Phys. **A789**, 260 (2007). hep-ph/0612071;
I. Balitsky, Phys. Rev. **D75**, 014001 (2007). hep-ph/0609105;
M. A. Braun, Eur. Phys. J. **C51**, 625 (2007). hep-ph/0703006;
M. A. Braun (2007). arXiv:0707.2314;
J. L. Albacete (2007). arXiv:0707.2545 [hep-ph].

The coordinate representation of NLO BFKL and the dipole picture

Fadin V.S.
Institute of Nuclear Physics and Novosibirsk State University, 630090, Novosibirsk, Russia

Abstract
For scattering of colourless objects, the freedom in definition of the BFKL kernel resulting from invariance of scattering amplitudes under simultaneous transformations of the kernel and impact factors permits to present the kernel in the dipole form. This form is found in the next-to-leading order (NLO) by direct transfer from the momentum space to the coordinate one.

1 Introduction

The BFKL approach [1] gives the most common basis for theoretical description of small-x processes. Usually the approach is formulated in the momentum space. Scattering amplitudes $\mathcal{A}_{AB}^{A'B'}$ are presented in the form of convolution $\Phi_{A'A} \otimes G \otimes \Phi_{B'B}$ of impact factors Φ and Green's function G for two interacting Reggeized gluons (see Fig.1). All dependence from properties of scattering particles is contained in the impact factors $\Phi_{A'A}$ and $\Phi_{B'B}$ describing transitions $A \to A'$ and $B \to B'$. The Green's function G holds all energy dependence. The impact factors and the kernel of the BFKL equation for the Green function are defined in the transverse momentum space. The kernel is known now in the NLO for arbitrary momentum transfer t and all possible colour states in the t – channel [2–4]. The most important for phenomenological applications is the colour singlet state – Pomeron channel. In the following only this channel is considered. A distinctive feature of the colour singlet kernel is the cancellation of the infrared divergencies.

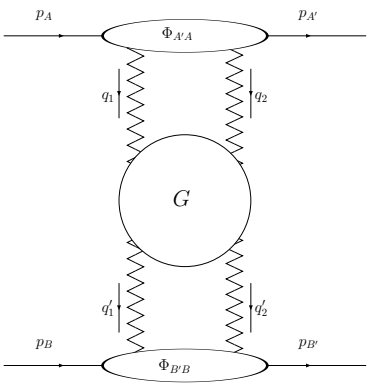


Fig.1

For scattering of colourless objects, in the leading order (LO), a remarkable property of the BFKL equation is its Möbius invariance [5]. In this case the BFKL kernel can be taken in a special representation, which we call dipole form. The Möbius invariance of the kernel in this representation can be made evident by transformation from the transverse momentum to the transverse coordinate space. Moreover, in the coordinate space the dipole form coincides with the kernel of the colour dipole approach [6]. It makes very interesting the finding of the dipole form of the BFKL kernel in the NLO. Of course, the conformal invariance is violated by renormalization. One may wonder, however, whether the renormalization is the only source of the violation. If so, one can expect the conformal invariance of the NLO BFKL kernel in supersymmetric extensions of QCD.

The dipole form of the BFKL kernel is very useful also for a better understanding of the relation between the BFKL and colour dipole approaches. It should help in further development of the theoretical description of small-x processes.

An additional reason is the complexity of the NLO BFKL kernel in the momentum space for $t \neq 0$. It is found in the form of intricate two-dimensional integrals. Its simplification is extremely desirable.

2 The dipole form in the LO

In the operator notations (see e.g. [7]) s–channel discontinuities of scattering amplitudes are presented in the form

$$\delta(\vec{q}_A - \vec{q}_B) disc_s \mathcal{A}_{AB}^{A'B'} = \frac{i}{4(2\pi)^{D-2}} \langle A'\bar{A}| e^{Y\widehat{\mathcal{K}}} \frac{1}{\hat{\vec{q}}_1^{\,2}\hat{\vec{q}}_2^{\,2}} |\bar{B}'B\rangle \,, \tag{1}$$

where $\langle A'\bar{A}|$ and $|\bar{B}'B\rangle$ are t–channel states related to the impact factors, $Y = \ln(s/s_0)$, $\widehat{\mathcal{K}}$ is the BFKL kernel, $\widehat{\mathcal{K}} = \widehat{\Omega} + \widehat{\mathcal{K}}_r$, $\widehat{\Omega} = \omega(\hat{\vec{q}}_1) + \omega(\hat{\vec{q}}_2)$ is the "virtual" part, $\langle \vec{q}_i|\hat{\omega}_i|\vec{q}_i{}'\rangle = \delta(\vec{q}_i - \vec{q}_i{}')\omega(\vec{q}_i)$, $\omega(\vec{q})$ is the gluon Regge trajectory; $\widehat{\mathcal{K}}_r$ is the "real" part;

$$\langle \vec{q}_1, \vec{q}_2|\hat{\mathcal{K}}_r|\vec{q}_1{}', \vec{q}_2{}'\rangle = \delta(\vec{q} - \vec{q}\,') \frac{1}{\vec{q}_1^{\,2}\vec{q}_2^{\,2}} \mathcal{K}_r(\vec{q}_1, \vec{q}_1{}'; \vec{q}), \ \vec{q} = \vec{q}_1 + \vec{q}_1{}' = \vec{q}_2 + \vec{q}_2{}',$$

$\widehat{\mathcal{K}}_r(\vec{q}_1, \vec{q}_1{}'; \vec{q})$ is the usually used expression for it. In the leading order at $D = 4 + 2\epsilon$

$$\omega^{(1)}(\vec{q}) = -\frac{g^2 N_c \Gamma(1-\epsilon)}{(4\pi)^{2+\epsilon}} \frac{2}{\epsilon} (\vec{q}\,)^{\epsilon}, \quad \mathcal{K}_r^B(\vec{q}_1, \vec{q}_2; \vec{q}) = \frac{g^2 N_c}{(2\pi)^{D-1}} \left(\frac{\vec{q}_1^{\,2}\vec{q}_2^{\,\prime 2} + \vec{q}_2^{\,2}\vec{q}_1^{\,\prime 2}}{(\vec{q}_1 - \vec{q}_1^{\,\prime})^2} - \vec{q}^{\,2} \right). \tag{2}$$

The direct Fourier transform of the LO kernel gives [7]

$$\langle \vec{r}_1\vec{r}_2|\widehat{\mathcal{K}}|\vec{r}_1{}'\vec{r}_2{}'\rangle = \langle \vec{r}_1\vec{r}_2|\widehat{\mathcal{K}}_{dip}|\vec{r}_1{}'\vec{r}_2{}'\rangle$$

$$-\frac{g^2 N_c \Gamma^2(1+\epsilon)}{8\pi^{3+2\epsilon}} \left[\frac{\delta(\vec{r}_{11'})}{\vec{r}_{12'}^{\,2(1+2\epsilon)}} + \frac{\delta(\vec{r}_{22'})}{\vec{r}_{21'}^{\,2(1+2\epsilon)}} - 2\frac{\delta(\vec{r}_{1'2'})\vec{r}_{11'}\vec{r}_{22'}}{\vec{r}_{11'}^{\,2(1+\epsilon)}\vec{r}_{22'}^{\,2(1+\epsilon)}} \right], \tag{3}$$

where

$$\langle \vec{r}_1\vec{r}_2|\hat{\mathcal{K}}_{dip}|\vec{r}_1{}'\vec{r}_2{}'\rangle = \frac{g^2 N_c \Gamma^2(1+\epsilon)}{8\pi^{3+2\epsilon}} \int d^{2+2\epsilon}\rho \left(\frac{\vec{r}_{1\rho}}{\vec{r}_{1\rho}^{\,2(1+\epsilon)}} - \frac{\vec{r}_{2\rho}}{\vec{r}_{2\rho}^{\,2(1+\epsilon)}} \right)^2$$

$$\times (\delta(\vec{r}_{11'})\delta(\vec{r}_{2\rho}) + \delta(\vec{r}_{22'})\delta(\vec{r}_{1\rho}) - \delta(\vec{r}_{11'})\delta(\vec{r}_{22'})) \tag{4}$$

is the dipole kernel in the $(D-2)$-dimensional space. Here and below $\vec{r}_{ij} = \vec{r}_i - \vec{r}_j$, $\vec{r}_{i'j'} = \vec{r}_{i'} - \vec{r}_{j'}$, $\vec{r}_{ij'} = \vec{r}_i - \vec{r}_{j'}$, $\vec{r}_{i\rho} = \vec{r}_i - \vec{\rho}$. At $D = 4$ $\langle \vec{r}_1\vec{r}_2|\hat{\mathcal{K}}_{dip}|\vec{r}_1{}'\vec{r}_2{}'\rangle$ acquires well known form:

$$\langle \vec{r}_1\vec{r}_2|\hat{\mathcal{K}}_{dip}|\vec{r}_1{}'\vec{r}_2{}'\rangle = \frac{\alpha_s N_c}{2\pi^2} \int d^2\rho \frac{\vec{r}_{12}^{\,2}}{\vec{r}_{1\rho}^{\,2}\vec{r}_{2\rho}^{\,2}} (\delta(\vec{r}_{11'})\delta(\vec{r}_{2\rho}) + \delta(\vec{r}_{22'})\delta(\vec{r}_{1\rho}) - \delta(\vec{r}_{11'})\delta(\vec{r}_{22'})) \,. \tag{5}$$

It is seen that the BFKL kernel is not equivalent to the dipole one. Actually the first is more general than the second. This is clear, because the BFKL kernel can be applied not only in the case of scattering of colourless objects.

However, when it is applied to the latter case, one can use the "dipole" and "gauge invariance" properties of targets and projectiles [5] and omit the terms in the kernel proportional to $\delta(\vec{r}_{1'2'})$, as well as change the terms independent either of $\vec{r}_1$ or of $\vec{r}_2$ in such a way that the resulting kernel becomes conserving the "dipole" property.

Indeed, for colourless objects the impact factors in the representation (1) are "gauge invariant":

$$\langle A'\bar{A}|\vec{q},0\rangle = \langle A'\bar{A}|0,\vec{q}\rangle = 0\ .$$

Therefore $\langle A'\bar{A}|\Psi\rangle = 0$ if $\langle\vec{r}_1,\vec{r}_2|\Psi\rangle$ does not depend either on $\vec{r}_1$ or on $\vec{r}_2$. Since $\langle\vec{q}_1,\vec{q}_2|\hat{\mathcal{K}}_r|\vec{q}_1^{\,'},\vec{q}_2^{\,'}\rangle$ vanishes at $\vec{q}_1^{\,'}=0$ or $\vec{q}_2^{\,'}=0$, $\langle A'\bar{A}|\hat{\mathcal{K}}$ is "gauge invariant" as well. It means that we can change $|In\rangle \equiv (\hat{\vec{q}}_1^{\,2}\hat{\vec{q}}_2^{\,2})^{-1}|\bar{B}'B\rangle$ for $|In_d\rangle$, where $|In_d\rangle$ has the "dipole " property $\langle\vec{r},\vec{r}|In_d\rangle = 0$. After this the terms proportional to $\delta(\vec{r}_{1'2'})$ can be omitted, and independent either of $\vec{r}_1$ or of $\vec{r}_2$ terms can be changed so that $\hat{\mathcal{K}} \to \hat{\mathcal{K}}_{dip}$ with the property $\langle\vec{r},\vec{r}|\hat{\mathcal{K}}_{dip}|\vec{r}_1'\vec{r}_2'\rangle = 0$. The coordinate representation of the kernel obtained in such a way is what we call the dipole form of the BFKL kernel.

3 A general structure of the dipole form of the NLO kernel and its ambiguity

In the NLO the dipole form can be written as

$$\langle\vec{r}_1\vec{r}_2|\hat{\mathcal{K}}_d^{NLO}|\vec{r}_1'\vec{r}_2'\rangle = \frac{\alpha_s^2(\mu)N_c^2}{4\pi^3}\left[\delta(\vec{r}_{11'})\delta(\vec{r}_{22'})\int d\vec{\rho}\, g^0(\vec{r}_1,\vec{r}_2;\vec{\rho})\right.$$

$$\left.+\delta(\vec{r}_{11'})g(\vec{r}_1,\vec{r}_2;\vec{r}_2')+\delta(\vec{r}_{22'})g(\vec{r}_2,\vec{r}_1;\vec{r}_1')+\frac{1}{\pi}g(\vec{r}_1,\vec{r}_2;\vec{r}_1',\vec{r}_2')\right] \qquad (6)$$

with the functions g turning into zero when their first two arguments coincide. The first three terms contain ultraviolet singularities which cancel in their sum, as well as in the LO, with account of the "dipole" property of the "target" impact factors. The coefficient of $\delta(\vec{r}_{11'})\delta(\vec{r}_{22'})$ is written in the integral form in order to make the cancellation evident. The term $g(\vec{r}_1,\vec{r}_2;\vec{r}_1',\vec{r}_2')$ is absent in the LO because the LO kernel in the momentum space does not contain terms depending on all three independent momenta simultaneously.

The discontinuities (1) are invariant under the operator transformation

$$\hat{\mathcal{K}} \to \hat{\mathcal{O}}^{-1}\hat{\mathcal{K}}\hat{\mathcal{O}},\ \langle A'\bar{A}| \to \langle A'\bar{A}|\hat{\mathcal{O}},\ \frac{1}{\hat{\vec{q}}_1^{\,2}\hat{\vec{q}}_2^{\,2}}|\bar{B}'B\rangle \to \hat{\mathcal{O}}^{-1}\frac{1}{\hat{\vec{q}}_1^{\,2}\hat{\vec{q}}_2^{\,2}}|\bar{B}'B\rangle\ . \qquad (7)$$

In the LO the kernel can be fixed by the requirement of the Möbius invariance of its dipole form. But even after this transformations with $\hat{\mathcal{O}} = 1+\hat{O}$, where $\hat{O}\sim g^2$, are still possible. At that

$$\hat{\mathcal{K}} \to \hat{\mathcal{K}} - [\hat{\mathcal{K}}^B\hat{O}]. \qquad (8)$$

These transformations rearrange NLO corrections to the kernel and impact factors. They can be used for simplification of the dipole form.

4 The quark contribution

The simplest piece of the NLO BFKL kernel is the "non-Abelian" (leading in N_c) part of the quark contribution. It is known at arbitrary D [2]. Its dipole form is found [7] at arbitrary D as well. However, it is rather complicated. In the physical space-time dimension $D = 4$ the dipole form can be obtained in a much easier way, starting from the renormalized BFKL kernel at $D = 4$ in a specific form [7]. It occurs that the dipole form of the original "non-Abelian" part [7] contains the term $g(\vec{r}_1, \vec{r}_2; \vec{r}_1\,', \vec{r}_2\,')$ and is not very simple. But the operator transformation (8) with

$$\hat{O}_Q = \frac{\alpha_s(\mu)}{8\pi}\frac{2}{3} n_f \ln\left(\hat{\vec{q}}_1^{\,2}\hat{\vec{q}}_2^{\,2}\right) \tag{9}$$

removes this term and simplifies the dipole form considerably. After this transformation we remain with

$$g_Q(\vec{r}_1, \vec{r}_2; \vec{\rho}) = -g_Q^0(\vec{r}_1, \vec{r}_2; \vec{\rho}) = \frac{n_f}{3N_c}\left(\frac{\vec{r}_{12}^{\,2}}{\vec{r}_{1\rho}^{\,2}\vec{r}_{2\rho}^{\,2}}\ln\frac{\vec{r}_Q^{\,2}}{\vec{r}_{12}^{\,2}} + \frac{\vec{r}_{1\rho}^{\,2} - \vec{r}_{2\rho}^{\,2}}{\vec{r}_{1\rho}^{\,2}\vec{r}_{2\rho}^{\,2}}\ln\frac{\vec{r}_{1\rho}^{\,2}}{\vec{r}_{2\rho}^{\,2}}\right), \tag{10}$$

where

$$\ln \vec{r}_Q^{\,2} = -\frac{5}{3} + 2\psi(1) - \ln\frac{\mu^2}{4}. \tag{11}$$

The result agrees with the quark contribution to the small-x evolution of color dipoles [8].

The "Abelian" contribution was calculated in the momentum representation many years ago in the framework of QED [9] and is extremely complicated. It turns out, however, that the dipole form of the Abelian" part of the quark contribution is quite simple. This part contributes only to $g_(\vec{r}_1, \vec{r}_2; \vec{r}_1\,', \vec{r}_2\,')$:

$$g_Q(\vec{r}_1, \vec{r}_2; \vec{r}_1\,', \vec{r}_2\,') = \frac{n_f}{N_c^3}\frac{1}{\vec{r}_{1'2'}^{\,4}}\left[\left(\frac{\vec{r}_{12'}^{\,2}\vec{r}_{1'2}^{\,2} + \vec{r}_{11'}^{\,2}\vec{r}_{22'}^{\,2} - \vec{r}_{12}^{\,2}\vec{r}_{1'2'}^{\,2}}{2(\vec{r}_{12'}^{\,2}\vec{r}_{1'2}^{\,2} - \vec{r}_{11'}^{\,2}\vec{r}_{22'}^{\,2})}\ln\frac{\vec{r}_{12'}^{\,2}\vec{r}_{1'2}^{\,2}}{\vec{r}_{11'}^{\,2}\vec{r}_{22'}^{\,2}} - 1\right)\right]. \tag{12}$$

It coincides with the corresponding part of the quark contribution to the dipole kernel [8]. Moreover, it is conformal invariant. It could be especially interesting for the QED Pomeron.

5 The gluon contribution

Note that the transformation of the kernel (8) must be accompanied by a corresponding transformation of the impact factors. The transformation (8) with $\hat{O} = \hat{O}_Q$ (9) removes quark parts of NLO corrections to impact factors, so that all related to quarks corrections turn out to be included in the kernel. The reason is the simplicity of the quark corrections. They are related to the charge renormalization only. For the gluon contribution transformations which include all corrections to the kernel are not known. It would be a miracle if they existed at all.

It seems reasonable to perform the transformation related to the charge renormalization, i.e. the transformation (8) with

$$\hat{O}_G = \frac{\alpha_s(\mu)}{8\pi}(-\frac{11}{3}N_c)\ln\left(\hat{\vec{q}}_1^{\,2}\hat{\vec{q}}_2^{\,2}\right). \tag{13}$$

With this tranformation the result [11] is the following.

$$g_G^0(\vec{r}_1,\vec{r}_2;\rho)=\frac{3}{2}\frac{\vec{r}_{12}^{\,2}}{\vec{r}_{1\rho}^{\,2}\vec{r}_{2\rho}^{\,2}}\ln\left(\frac{\vec{r}_{1\rho}^{\,2}}{\vec{r}_{12}^{\,2}}\right)\ln\left(\frac{\vec{r}_{2\rho}^{\,2}}{\vec{r}_{12}^{\,2}}\right)-\frac{11}{12}\left[\frac{\vec{r}_{12}^{\,2}}{\vec{r}_{1\rho}^{\,2}\vec{r}_{2\rho}^{\,2}}\ln\left(\frac{\vec{r}_{1\rho}^{\,2}\vec{r}_{2\rho}^{\,2}}{r_G^4}\right)\right.$$
$$\left.+\left(\frac{1}{\vec{r}_{2\rho}^{\,2}}-\frac{1}{\vec{r}_{1\rho}^{\,2}}\right)\ln\left(\frac{\vec{r}_{2\rho}^{\,2}}{\vec{r}_{1\rho}^{\,2}}\right)\right]\,, \tag{14}$$

$$g_G(\vec{r}_1,\vec{r}_2;\vec{r}_2')\;=\frac{11}{6}\frac{\vec{r}_{12}^{\,2}}{\vec{r}_{22'}^{\,2}\vec{r}_{12'}^{\,2}}\ln\left(\frac{\vec{r}_{12}^{\,2}}{r_G^2}\right)+\frac{11}{6}\left(\frac{1}{\vec{r}_{22'}^{\,2}}-\frac{1}{\vec{r}_{12'}^{\,2}}\right)\ln\left(\frac{\vec{r}_{22'}^{\,2}}{\vec{r}_{12'}^{\,2}}\right)$$
$$+\frac{1}{2\vec{r}_{22'}^{\,2}}\ln\left(\frac{\vec{r}_{12'}^{\,2}}{\vec{r}_{22'}^{\,2}}\right)\ln\left(\frac{\vec{r}_{12}^{\,2}}{\vec{r}_{12'}^{\,2}}\right)-\frac{\vec{r}_{12}^{\,2}}{2\,\vec{r}_{22'}^{\,2}\vec{r}_{12'}^{\,2}}\ln\left(\frac{\vec{r}_{12}^{\,2}}{\vec{r}_{22'}^{\,2}}\right)\ln\left(\frac{\vec{r}_{12}^{\,2}}{\vec{r}_{12'}^{\,2}}\right), \tag{15}$$

where

$$\ln r_G^2=2\psi(1)-\ln\frac{\mu^2}{4}-\frac{3}{11}\left(\frac{67}{9}-2\zeta(2)\right). \tag{16}$$

Both $g_G^0(\vec{r}_1,\vec{r}_2;\vec{\rho})$ and $g_G(\vec{r}_1,\vec{r}_2;\vec{\rho})$ vanish at $\vec{r}_1=\vec{r}_2$. Then, these functions turn into zero for $\vec{\rho}^{\,2}\to\infty$ faster than $(\vec{\rho}^{\,2})^{-1}$ to provide the infrared safety. The ultraviolet singularities of these functions at $\vec{\rho}=\vec{r}_2$ and $\vec{\rho}=\vec{r}_1$ cancel on account of the "dipole" property of the "target" impact factors.

The most complicated is the structure which is absent in the LO:

$$g_G(\vec{r}_1,\vec{r}_2;\vec{r}_1',\vec{r}_2')=\left[\frac{(\vec{r}_{22'}\,\vec{r}_{12})}{\vec{r}_{11'}^{\,2}\vec{r}_{22'}^{\,2}\vec{r}_{1'2'}^{\,2}}-\frac{2\,(\vec{r}_{22'}\,\vec{r}_{11'})}{\vec{r}_{11'}^{\,2}\vec{r}_{22'}^{\,2}\vec{r}_{1'2'}^{\,2}}+\frac{2\,(\vec{r}_{22'}\,\vec{r}_{12'})\,(\vec{r}_{11'}\,\vec{r}_{12'})}{\vec{r}_{11'}^{\,2}\vec{r}_{22'}^{\,2}\vec{r}_{1'2'}^{\,2}\vec{r}_{12'}^{\,2}}\right]\ln\left(\frac{\vec{r}_{12'}^{\,2}}{\vec{r}_{1'2'}^{\,2}}\right)$$
$$+\frac{1}{2\vec{r}_{1'2'}^{\,2}}\left[\frac{(\vec{r}_{11'}\,\vec{r}_{22'})}{\vec{r}_{11'}^{\,2}\,\vec{r}_{22'}^{\,2}}+\frac{(\vec{r}_{21'}\,\vec{r}_{12'})}{\vec{r}_{21'}^{\,2}\,\vec{r}_{12'}^{\,2}}-\frac{2(\vec{r}_{22'}\,\vec{r}_{21'})}{\vec{r}_{22'}^{\,2}\vec{r}_{21'}^{\,2}}\right]\ln\left(\frac{\vec{r}_{11'}^{\,2}\,\vec{r}_{22'}^{\,2}}{\vec{r}_{1'2'}^{\,2}\vec{r}_{12}^{\,2}}\right)+\frac{(\vec{r}_{11'}\,\vec{r}_{22'})}{2\vec{r}_{11'}^{\,2}\,\vec{r}_{22'}^{\,2}\vec{r}_{1'2'}^{\,2}}\ln\left(\frac{\vec{r}_{21'}^{\,2}\,\vec{r}_{12'}^{\,2}}{\vec{r}_{11'}^{\,2}\,\vec{r}_{22'}^{\,2}}\right)$$
$$+\frac{1}{d\,\vec{r}_{1'2'}^{\,2}}\left[\frac{(\vec{r}_{1'2'}\,\vec{r}_{12'})\vec{r}_{12}^{\,2}}{\vec{r}_{11'}^{\,2}}+\frac{2(\vec{r}_{22'}\,\vec{r}_{21'})(\vec{r}_{12}\,\vec{r}_{21'})}{\vec{r}_{21'}^{\,2}}+\frac{(\vec{r}_{22'}\,\vec{r}_{12'})(\vec{r}_{11'}\,\vec{r}_{21'})}{\vec{r}_{11'}^{\,2}\,\vec{r}_{22'}^{\,2}}\vec{r}_{1'2'}^{\,2}-\vec{r}_{1'2'}^{\,2}\right]\ln\left(\frac{\vec{r}_{12'}^{\,2}\,\vec{r}_{21'}^{\,2}}{\vec{r}_{11'}^{\,2}\,\vec{r}_{22'}^{\,2}}\right)$$
$$+\frac{1}{2\vec{r}_{1'2'}^{\,4}}\left(\frac{\vec{r}_{11'}^{\,2}\,\vec{r}_{22'}^{\,2}}{d}\ln\left(\frac{\vec{r}_{12'}^{\,2}\,\vec{r}_{21'}^{\,2}}{\vec{r}_{11'}^{\,2}\vec{r}_{22'}^{\,2}}\right)-1\right)+\frac{1}{\vec{r}_{11'}^{\,2}}\left(\frac{(\vec{r}_{12}\,\vec{r}_{21'})}{\vec{r}_{1'2'}^{\,2}\vec{r}_{21'}^{\,2}}-\frac{(\vec{r}_{11'}\,\vec{r}_{12})}{\vec{r}_{1'2'}^{\,2}\vec{r}_{22'}^{\,2}}-\frac{(\vec{r}_{11'}\,\vec{r}_{21'})}{\vec{r}_{22'}^{\,2}\vec{r}_{21'}^{\,2}}\right)\ln\left(\frac{\vec{r}_{12'}^{\,2}}{\vec{r}_{11'}^{\,2}}\right)$$
$$-\frac{(\vec{r}_{12}\,\vec{r}_{22'})}{\vec{r}_{1'2'}^{\,2}\vec{r}_{22'}^{\,2}\vec{r}_{12'}^{\,2}}\ln\left(\frac{\vec{r}_{11'}^{\,2}}{\vec{r}_{1'2'}^{\,2}}\right)+(1\leftrightarrow 2), \tag{17}$$

where

$$d=\vec{r}_{12'}^{\,2}\vec{r}_{21'}^{\,2}-\vec{r}_{11'}^{\,2}\vec{r}_{22'}^{\,2}. \tag{18}$$

This term also vanishes at $\vec{r}_1=\vec{r}_2$, so that it possesses the "dipole" property. It has ultraviolet singularity only at $\vec{r}_{1'2'}=0$ and tends to zero at large $\vec{r}_1'^{\,2}$ and $\vec{r}_2'^{\,2}$ sufficiently quickly in order to provide the infrared safety.

The term (17) violates conformal invariance, although it has no relation to the charge renormalization. Remind, however, the ambiguity of the NLO kernel discussed in Section (3). The transformation (8) can change non-invariant contributions. It is not yet clear, if it is possible to find such transformation which makes $g(\vec{r}_1,\vec{r}_2;\vec{r}_1',\vec{r}_2')$ conformal invariant.

6 Summary

The colour singlet BFKL kernel is more general than the dipole one. However, in the case of scattering of colourless objects the BFKL kernel can be written in the dipole form (Möbius representation). In the NLO the dipole form is greatly simplified in comparison with the BFKL kernel in the momentum space. The quark contribution to the dipole form agrees with the corresponding contribution to the kernel of the colour dipole approach. It would be extremely interesting to compare corresponding gluon contributions. Unfortunately, such contribution to the kernel of the colour dipole approach is not yet known. The "Abelian" part of the quark contribution is conformal invariant. The ambiguity of the NLO kernel reserves a hope for conformal invariance of the dipole form of the colour singlet NLO BFKL kernel at $N = 4$ SUSY.

References

[1] V.S. Fadin, E.A. Kuraev and L.N. Lipatov, Phys. Lett. **B60** (1975) 50; E.A. Kuraev, L.N. Lipatov and V.S. Fadin, Zh. Eksp. Teor. Fiz. **71** (1976) 840 [Sov. Phys. JETP **44** (1976) 443]; **72** (1977) 377 [**45** (1977) 199]; Ya.Ya. Balitskii and L.N. Lipatov, Sov. J. Nucl. Phys. **28** (1978) 822.

[2] V.S. Fadin, R. Fiore and A. Papa, Phys. Rev. **D60** (1999) 074025.

[3] V. S. Fadin and D. A. Gorbachev, JETP Lett. **71** (2000) 222 [Pisma Zh. Eksp. Teor. Fiz. **71** (2000) 322].

[4] V.S. Fadin and R. Fiore, Phys. Lett. **B610** (2005) 61 [*Erratum-ibid.* **B621** (2005) 61]; Phys. Rev. **D72** (2005) 014018.

[5] L.N. Lipatov, Sov. Phys. JETP **63** (1986) 904 [Zh. Eksp. Teor. Fiz. **90** (1986) 1536].

[6] N.N. Nikolaev and B.G. Zakharov, Z. Phys. **C64** (1994) 631;
N.N. Nikolaev, B.G. Zakharov and V.R. Zoller, JETP Lett. **59** (1994) 6;
A.H. Mueller, Nucl. Phys. **B415** (1994) 373;
A.H. Mueller and B. Patel, Nucl. Phys. **B425** (1994) 471.

[7] V. S. Fadin, R. Fiore and A. Papa, Nucl. Phys. **B769** (2007) 108 [arXiv:hep-ph/0612284].

[8] I. Balitsky, Phys. Rev. **D75** (2007) 014001 [arXiv:hep-ph/0609105].

[9] H. Cheng, T.T. Wu, Phys. Rev. **D10** (1970) 2775; V.N. Gribov, L.N. Lipatov and G.V. Frolov, Sov. J. Nucl. Phys. **12** (1971) 543 [Yad. Fiz. **12** (1970) 994].

[10] V.S. Fadin, R. Fiore and A. Papa, Phys. Lett. **B647** (2007) 179 [arXiv:hep-ph/0701075].

[11] V. S. Fadin, R. Fiore, A. V. Grabovsky and A. Papa, arXiv:0705.1885 [hep-ph].

Angular decorrelations in Mueller-Navelet jets and DIS

Agustín Sabio Vera[1]†, *Florian Schwennsen*[2]
[1] Physics Department, Theory Division, CERN, CH–1211 Geneva 23, Switzerland,
[2] II. Institut für Theoretische Physik, Universität Hamburg, Luruper Chaussee 149 D–22761 Hamburg, Germany.

Abstract
We discuss the azimuthal angle decorrelation of Mueller–Navelet jets at hadron colliders and forward jets in Deep Inelastic Scattering within the BFKL framework with a NLO kernel. We stress the need of collinear improvements to obtain good perturbative convergence. We provide estimates of these decorrelations for large rapidity differences at the Tevatron, LHC and HERA.

1 BFKL cross sections

In this contribution we discuss the results recently obtained in [1] where azimuthal angle correlations in Mueller–Navelet jets [2] and forward jets at HERA using the Balitsky–Fadin–Kuraev–Lipatov (BFKL) equation in the next–to–leading (NLO) approximation [3] were investigated (related works can be found in [4]). In this section we focus on normalized differential cross sections for Mueller–Navelet jets, which are quite insensitive to parton distribution functions. This justifies the use of partonic cross sections which can be written as

$$\frac{d\hat{\sigma}}{d^2\vec{q}_1 d^2\vec{q}_2} = \frac{\pi^2\bar{\alpha}_s^2}{2}\frac{1}{q_1^2 q_2^2}\int\frac{d\omega}{2\pi i}e^{\omega \mathrm{Y}} f_\omega\left(\vec{q}_1,\vec{q}_2\right), \tag{1}$$

where $\bar{\alpha}_s = \alpha_s N_c/\pi$, $\vec{q}_{1,2}$ are the transverse momenta of the tagged jets, and Y their relative rapidity. The Green's function carries the bulk of the Y dependence and is the solution to the NLO BFKL equation,

$$\left(\omega - \bar{\alpha}_s\hat{K}_0 - \bar{\alpha}_s^2\hat{K}_1\right)\hat{f}_\omega = \hat{1}, \tag{2}$$

which acts on the basis including the azimuthal angle, *i.e.*,

$$\langle\vec{q}|\,\nu,n\rangle = \frac{1}{\pi\sqrt{2}}\left(q^2\right)^{i\nu-\frac{1}{2}}\,e^{in\theta}. \tag{3}$$

As Y increases the azimuthal dependence is mainly driven by the kernel and therefore we use LO jet vertices which are simpler than the NLO ones [5]. The differential cross section in the azimuthal angle $\phi = \theta_1 - \theta_2 - \pi$, with θ_i being the angles of the two tagged jets, reads

$$\frac{d\hat{\sigma}\left(\alpha_s,\mathrm{Y},p_{1,2}^2\right)}{d\phi} = \frac{\pi^2\bar{\alpha}_s^2}{4\sqrt{p_1^2 p_2^2}}\sum_{n=-\infty}^{\infty}e^{in\phi}\,\mathcal{C}_n\left(\mathrm{Y}\right), \tag{4}$$

† speaker

where

$$\mathcal{C}_n\left(\mathrm{Y}\right) \;=\; \frac{1}{2\pi}\int_{-\infty}^{\infty}\frac{d\nu}{\left(\frac{1}{4}+\nu^2\right)}\left(\frac{p_1^2}{p_2^2}\right)^{i\nu} e^{\chi\left(|n|,\frac{1}{2}+i\nu,\bar{\alpha}_s(p_1p_2)\right)\mathrm{Y}}, \tag{5}$$

and the NLO kernel can be written as

$$\chi\left(n,\gamma,\bar{\alpha}_s\right) \;=\; \bar{\alpha}_s\chi_0\left(n,\gamma\right)+\bar{\alpha}_s^2\left(\chi_1\left(n,\gamma\right)-\frac{\beta_0}{8N_c}\frac{\chi_0\left(n,\gamma\right)}{\gamma\left(1-\gamma\right)}\right). \tag{6}$$

The eigenvalue of the LO kernel is $\chi_0\left(n,\gamma\right)=2\psi\left(1\right)-\psi\left(\gamma+\frac{n}{2}\right)-\psi\left(1-\gamma+\frac{n}{2}\right)$, with ψ being the logarithmic derivative of the Euler function. The action of $\hat{K}_1$, in $\overline{\mathrm{MS}}$ scheme, can be found in [6]. The full cross section only depends on the $n=0$ component,

$$\hat{\sigma}=\frac{\pi^3\bar{\alpha}_s^2}{2\sqrt{p_1^2p_2^2}}\,\mathcal{C}_0\left(\mathrm{Y}\right). \tag{7}$$

The average of the cosine of the azimuthal angle times an integer projects out the contribution from each of these angular components:

$$\frac{\left\langle\cos\left(m\phi\right)\right\rangle}{\left\langle\cos\left(n\phi\right)\right\rangle} \;=\; \frac{\mathcal{C}_m\left(\mathrm{Y}\right)}{\mathcal{C}_n\left(\mathrm{Y}\right)}. \tag{8}$$

The normalized differential cross section is

$$\frac{1}{\hat{\sigma}}\frac{d\hat{\sigma}}{d\phi} \;=\; \frac{1}{2\pi}\sum_{n=-\infty}^{\infty}e^{in\phi}\frac{\mathcal{C}_n\left(\mathrm{Y}\right)}{\mathcal{C}_0\left(\mathrm{Y}\right)} \;=\; \frac{1}{2\pi}\left\{1+2\sum_{n=1}^{\infty}\cos\left(n\phi\right)\left\langle\cos\left(n\phi\right)\right\rangle\right\}. \tag{9}$$

The BFKL resummation is not stable at NLO for zero conformal spin. A manifestation of this lack of convergence is what we found in the gluon–bremsstrahlung scheme where our NLO distributions have an unphysical behavior whenever the $n=0$ conformal spin appears in the calculation. To solve this problem we imposed compatibility with renormalization group evolution in the DIS limit following [7] for all conformal spins. The new kernel with improvements to all orders reads [1]

$$\begin{aligned}\omega \;=\;& \bar{\alpha}_s\left(1+\mathcal{A}_n\bar{\alpha}_s\right)\left\{2\,\psi\left(1\right)-\psi\left(\gamma+\frac{|n|}{2}+\frac{\omega}{2}+\mathcal{B}_n\bar{\alpha}_s\right)\right.\\ &\left.-\,\psi\left(1-\gamma+\frac{|n|}{2}+\frac{\omega}{2}+\mathcal{B}_n\bar{\alpha}_s\right)\right\}+\bar{\alpha}_s^2\left\{\chi_1\left(|n|,\gamma\right)-\frac{\beta_0}{8N_c}\frac{\chi_0\left(n,\gamma\right)}{\gamma\left(1-\gamma\right)}\right.\\ &\left.-\mathcal{A}_n\chi_0\left(|n|,\gamma\right)\right)+\left(\psi'\left(\gamma+\frac{|n|}{2}\right)+\psi'\left(1-\gamma+\frac{|n|}{2}\right)\right)\left(\frac{\chi_0\left(|n|,\gamma\right)}{2}+\mathcal{B}_n\right)\Bigg\},\end{aligned} \tag{10}$$

where $\mathcal{A}_n$ and $\mathcal{B}_n$ are collinear coefficients [1]. After this collinear resummation our observables have a good physical behavior and are independent of the renormalization scheme. It is very important to remark that the asymptotic behavior of the BFKL resummation is convergent for non zero conformal spins. In this sense the ideal distributions to investigate experimentally are those of the form $\langle cos(m\phi)\rangle\,/\,\langle cos(n\phi)\rangle$ with $m,n\neq 0$, we will see that in this case the difference between the LO and higher orders results is small.

2 Phenomenology for Mueller–Navelet jets

The DØ [8] collaboration analyzed data for Mueller–Navelet jets at $\sqrt{s} = 630$ and 1800 GeV. For the angular correlation LO BFKL predictions were first obtained in [9] and failed to describe the data estimating too much decorrelation. An exact fixed NLO analysis using JETRAD underestimated the decorrelation, while HERWIG was in agreement with the data.

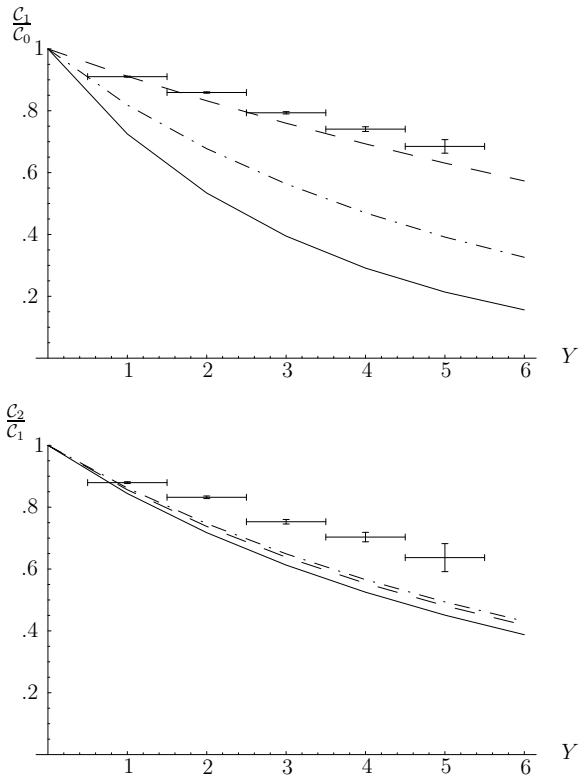


Fig. 1: Top: $\langle \cos\phi \rangle = \mathcal{C}_1/\mathcal{C}_0$ and Bottom: $\frac{<\cos 2\phi>}{<\cos\phi>} = \frac{\mathcal{C}_2}{\mathcal{C}_1}$, at a $p\bar{p}$ collider with $\sqrt{s}$ = 1.8 TeV for BFKL at LO (solid) and NLO (dashed). The results from the resummation presented in the text are shown as well (dash–dotted).

In Fig. 1 we compare the Tevatron data for $\langle \cos\phi \rangle = \mathcal{C}_1/\mathcal{C}_0$ with our LO, NLO and resummed predictions. For Tevatron's cuts, where the transverse momentum for one jet is 20 GeV and for the other 50 GeV, the NLO calculation is instable under renormalization scheme changes. The convergence of our observables is poor whenever the coefficient associated to zero conformal spin, $\mathcal{C}_0$, is involved. If we eliminate this coefficient by calculating the ratios defined in Eq. (8) then the predictions are very stable, see Fig. 1.

The full angular dependence studied at the Tevatron by the DØ collaboration was published in [8]. In Fig. 2 we compare this measurement with the predictions obtained in our approach. For the differential cross section we also make predictions for the LHC at larger Y in Fig. 3. We estimated several uncertainties in our approach which are represented by gray bands.

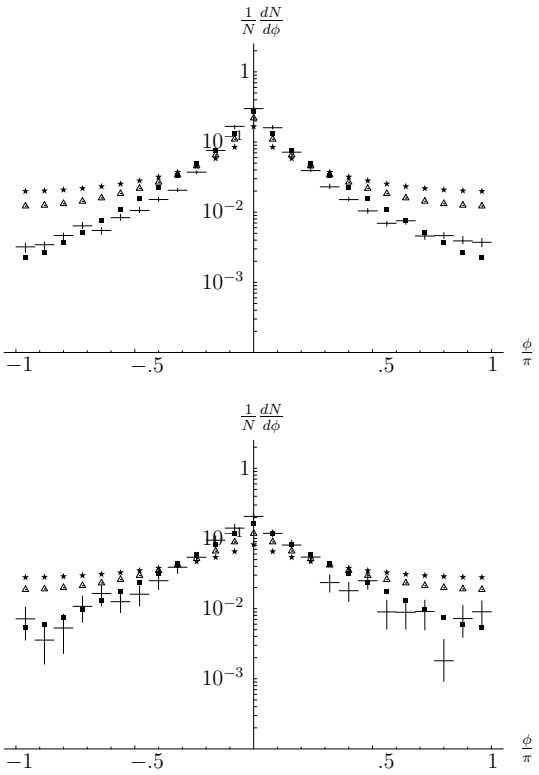


Fig. 2: $\frac{1}{N}\frac{dN}{d\phi}$ in a $p\bar{p}$ collider at $\sqrt{s}$=1.8 TeV using a LO (stars), NLO (squares) and resummed (triangles) BFKL kernel. Plots are shown for Y = 3 (top) and Y = 5 (bottom).

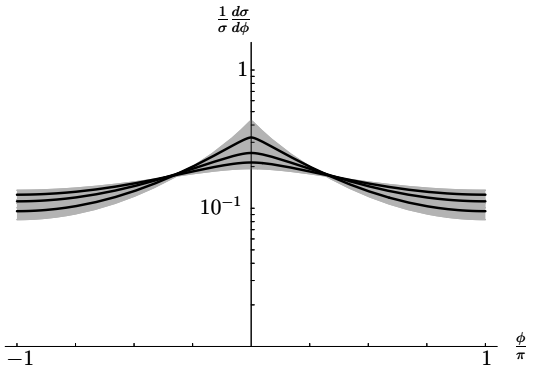


Fig. 3: $\frac{1}{\sigma}\frac{d\sigma}{d\phi}$ in our resummation scheme for rapidities Y = 7, 9, 11 from top to bottom. The gray band reflects the uncertainty in s_0 and in the renormalization scale μ.

3 Forward jets at HERA

In this section we apply the BFKL formalism to predict the decorrelation in azimuthal angle between the electron and a forward jet associated to the proton in Deep Inelastic Scattering (DIS). When the separation in rapidity space between the scattered electron and the forward jet is large and the transverse momentum of the jet is similar to the virtuality of the photon resolving the hadron, then the dominant terms are of BFKL type. This process is similar to that of Mueller–Navelet jets, the only difference being the substitution of one jet vertex by the electron vertex describing the coupling of the electron to the BFKL gluon Green's function via a quark–antiquark pair. Azimuthal angles in forward jets were studied at LO in [10]. We improved their calculation by considering the NLO BFKL kernel.

In the production of a forward jet in DIS it is necessary to extract a parton with a large longitudinal momentum fraction $x_{\rm FJ}$ from the proton. When the jet is characterized by a hard scale it is possible to use conventional collinear factorization to describe the process, and the jet production rate may be written as

$$\sigma(s) \;\; = \;\; \int dx_{\rm FJ}\; f_{\rm eff}(x_{\rm FJ},\mu_F^2)\hat{\sigma}(\hat{s}), \tag{11}$$

with $\hat{\sigma}(\hat{s})$ denoting the partonic cross section, and the effective parton density [11] being

$$f_{\rm eff}(x,\mu_F^2) \;\; = \;\; G(x,\mu_F^2) + \frac{4}{9}\sum_f \left[Q_f(x,\mu_F^2) + \bar{Q}_f(x,\mu_F^2)\right], \tag{12}$$

where the sum runs over all quark flavors, and μ_F stands for the factorization scale.

The final expression for the cross section at hadronic level is of the form

$$\frac{d\sigma}{dY\; d\phi} \;\; = \;\; C_0(Y) + C_2(Y)\cos 2\phi, \tag{13}$$

with

$$C_n(Y) \;\; = \;\; \frac{\pi^2\bar{\alpha}_s^2}{2}\int_{\rm cuts} dx_{\rm FJ}\, dQ^2\, dy\, f_{\rm eff}(x_{\rm FJ},Q^2)B^{(n)}(y,Q^2,Y)\delta\left(x_{\rm FJ} - \frac{Q^2e^Y}{ys}\right), \tag{14}$$

where the index in the integral sign refers to the cuts

$$20\ {\rm GeV}^2 < Q^2 < 100\ {\rm GeV}^2, \quad 0.05 < y < 0.7, \quad 5\cdot 10^{-3} > x_{\rm Bj} > 4\cdot 10^{-4}. \tag{15}$$

The integration over the longitudinal momentum fraction $x_{\rm FJ}$ of the forward jet involves a delta function fixing the rapidity $Y = \ln x_{\rm FJ}/x_{\rm Bj}$, and $B^{(n)}$ is a complicated function which can be found in [1].

Since the structure of the electron vertex singles out the components with conformal spin 0 and 2, the number of observables related to the azimuthal angle dependence is limited when compared to the Mueller–Navelet case. The most relevant observable is the dependence of the average $< \cos 2\phi >= C_2/C_0$ with the rapidity difference between the forward jet and the outgoing lepton. It is natural to expect that the forward jet will be more decorrelated from the

leptonic system as the rapidity difference is larger since the phase space for further gluon emission opens up. This is indeed what we observe in our numerical results shown in Fig. 4. We find results similar to the Mueller–Navelet jets case where the most reliable calculation is that with a collinearly–improved kernel. The main effect of the higher order corrections is to increase the azimuthal angle correlation for a given rapidity difference, while keeping the decrease of the correlation as Y grows.

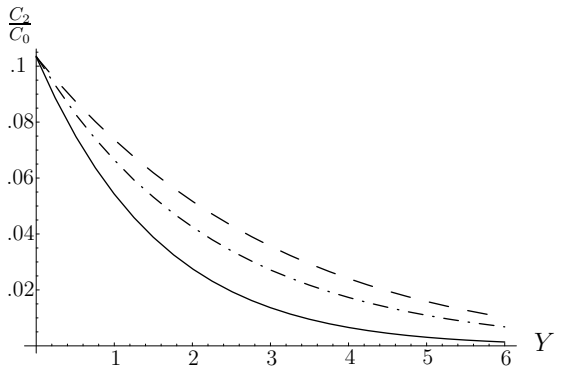


Fig. 4: $< \cos 2\phi >$ at the ep collider HERA at leading (solid), next to leading order (dashed), and for resummed kernel (dash-dotted).

References

[1] A. Sabio Vera, Nucl. Phys. **B746**, 1 (2006). hep-ph/0602250;
A. Sabio Vera and F. Schwennsen, Nucl. Phys. **B776**, 170 (2007). hep-ph/0702158;
F. Schwennsen (2007). hep-ph/0703198;
A. Sabio Vera and F. Schwennsen (2007). arXiv:0708.0549 [hep-ph].

[2] A. H. Mueller and H. Navelet, Nucl. Phys. **B282**, 727 (1987).

[3] V. S. Fadin and L. N. Lipatov, Phys. Lett. **B429**, 127 (1998). hep-ph/9802290;
M. Ciafaloni and G. Camici, Phys. Lett. **B430**, 349 (1998). hep-ph/9803389.

[4] C. Marquet and C. Royon, Nucl. Phys. **B739**, 131 (2006). hep-ph/0510266;
O. Kepka, C. Royon, C. Marquet, and R. Peschanski (2006). hep-ph/0609299;
O. Kepka, C. Royon, C. Marquet, and R. Peschanski (2006). hep-ph/0612261;
C. Marquet and C. Royon (2007). arXiv:0704.3409 [hep-ph].

[5] J. Bartels, D. Colferai, and G. P. Vacca, Eur. Phys. J. **C24**, 83 (2002). hep-ph/0112283;
J. Bartels, D. Colferai, and G. P. Vacca, Eur. Phys. J. **C29**, 235 (2003). hep-ph/0206290.

[6] A. V. Kotikov and L. N. Lipatov, Nucl. Phys. **B582**, 19 (2000). hep-ph/0004008.

[7] G. P. Salam, JHEP **07**, 019 (1998). hep-ph/9806482;
M. Ciafaloni, D. Colferai, G. P. Salam, and A. M. Stasto, Phys. Rev. **D68**, 114003 (2003). hep-ph/0307188;
A. Sabio Vera, Nucl. Phys. **B722**, 65 (2005). hep-ph/0505128.

[8] D0 Collaboration, S. Abachi *et al.*, Phys. Rev. Lett. **77**, 595 (1996). hep-ex/9603010.

[9] V. Del Duca and C. R. Schmidt, Phys. Rev. **D49**, 4510 (1994). hep-ph/9311290;
W. J. Stirling, Nucl. Phys. **B423**, 56 (1994). hep-ph/9401266.

[10] J. Bartels, V. Del Duca, and M. Wusthoff, Z. Phys. **C76**, 75 (1997). hep-ph/9610450.

[11] B. L. Combridge and C. J. Maxwell, Nucl. Phys. **B239**, 429 (1984).

Breakdown of Coherence ?

Michael H. Seymour[1,2]
[1]Physics Department, CERN, CH-1211 Geneva 23, Switzerland,
[2]School of Physics & Astronomy, University of Manchester, Manchester, M13 9PL, U.K.

Abstract
In a recent paper [1], Albrecht Kyrieleis, Jeff Forshaw and I discovered a new tower of *super-leading* logarithms in gaps between jets cross sections. After discussions with the referee of our paper and further investigation, we have come to view this as a breakdown of naïve coherence for initial state radiation. In this talk I illustrate this statement in a simple way, and show how it results in the super-leading logarithms.

1 Introduction and The Bottom Line

I begin by illustrating, in a simple pictorial way, what I mean by naïve coherence. Consider an arbitrary hard process that produces a hard parton, which then fragments into a system of hard collinear partons, as shown in Fig. 1a. To be precise, by hard collinear I mean that the plus components of all the partons are of the same order as that of the originating parton, and all their transverse momenta are much smaller, with the originating parton defining the plus direction. Consider calculating the first correction to this amplitude coming from a soft wide-angle gluon. Again, to be precise, by soft wide-angle, I mean that its transverse momentum is much smaller than the relative transverse momenta of all collinear partons in the jet, and that its plus momentum is at most of order its transverse momentum. As illustrated in Fig. 1b, this amplitude is obtained from the first one by inserting the soft wide-angle gluon onto each of the external partons, summing over those partons. Studying the integral over the momentum of the soft wide-angle gluon, it is straightforward to see that the momentum-dependent parts of all these insertions are identical and they only differ by colour algebra. It is also straightforward to show, for example using the diagrammatic technique of [2], that the contributions are simply additive in colour space. The final result is therefore, as illustrated in Fig. 1c, that the amplitude can be calculated *as if* the soft wide angle gluon was emitted by an *on-shell* parton with the same plus momentum and colour as the initiating parton. This is the usual statement of naïve colour coherence: soft wide angle gluons are emitted by the jet as a whole, imagined to be on shell.

Now I turn to the case of an initial-state parton, Fig. 2. Consider an arbitrary hard process initiated by a hard parton, which fragments into a system of hard collinear partons and its correction coming from a soft wide-angle gluon, as shown in Figs. 2a and c. At first sight it looks the same as the final-state case and, in fact, if the soft wide-angle gluon is real, it is, so it is as if the soft wide-angle gluon was emitted by the internal line, imagined to be on shell, Fig. 2b. However, if the soft wide-angle gluon is virtual, one has to consider the momentum structure of the loop integral more carefully. Performing one integration by contour, we generally pick up poles from either the soft gluon propagator or the hard parton propagators. The former gives a real part that has an identical form in all cases. The problem then reduces to colour algebra again and, just like

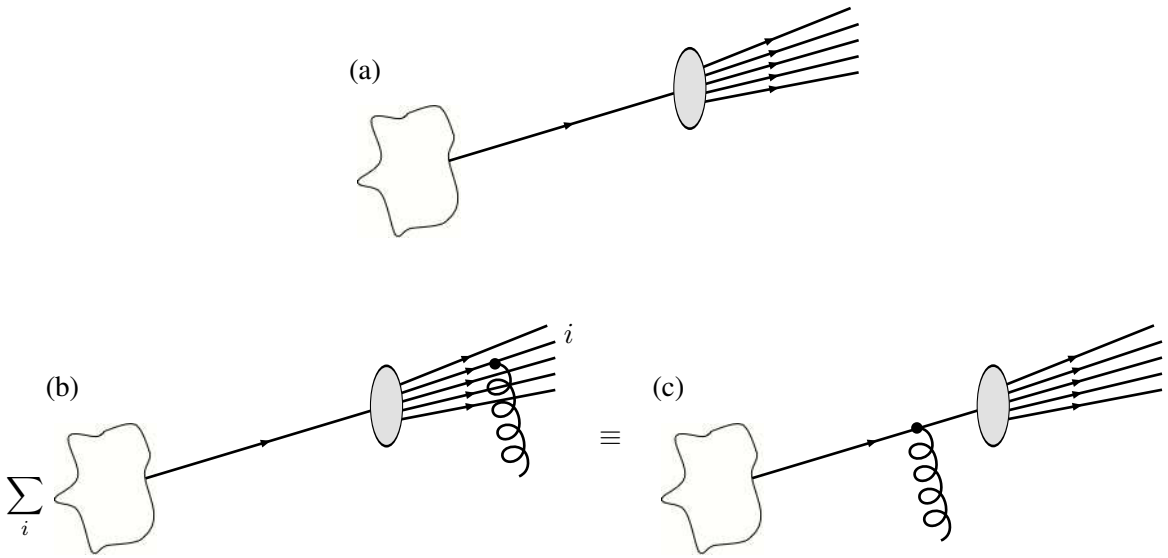


Fig. 1: Illustration of naïve coherence in final-state radiation. A hard parton produced in the hard process fragments into a system of hard collinear partons (a). The amplitude for this system to emit a soft, wide-angle, real or virtual gluon should be calculated from the insertion of the soft gluon onto each of the external hard partons, summed over these partons (b). Colour coherence implies that this can be calculated *as if* the soft gluon were emitted by the original hard parton, i.e. by the total colour charge of the jet (c).

for real emission, it is as if the soft wide-angle gluon was emitted by the internal line, imagined to be on shell, Fig. 2b. However, for the other pole, coming from hard parton propagators, its causal structure depends on whether the hard partons the gluon is attached to are in the final state or the initial state. In particular, the imaginary part is zero if the gluon connects an initial-state parton to a final-state parton[1], and non-zero for initial-initial and final-final connections. Therefore there is a mismatch between the different diagrams in Fig. 2c and they do not correspond to the contribution from a single on-shell parton, Fig. 2d. It is this statement that we describe as a *breakdown of naïve coherence for initial-state radiation*.

We 'discovered' this breakdown of coherence in calculating corrections to the conventional calculations of gaps-between-jets cross sections from one gluon emitted outside the gap accompanied by any number of soft wide-angle gluons. It was a great surprise to us, but we soon learnt that it was actually well known to the early pioneers of QCD. In particular, there are lengthy discussions in the literature of whether or not these known effects (coming from "Coulomb gluons") lead to violations of the Bloch–Nordsiek theorem (see for example Ref. [3]). These issues were eventually settled, at least for massless partons, by Collins, Soper and Sterman's proof of factorization [4]. The hard collinear, and soft real, corrections are quickly dealt with in their paper, and most of the subtlety of their proof is related to gluons with plus and minus momenta much smaller than their transverse momenta (the "Glauber region"), which are exactly the ones that give the imaginary parts we are discussing. They showed that these do lead to violations of

[1] I am working in Feynman gauge.

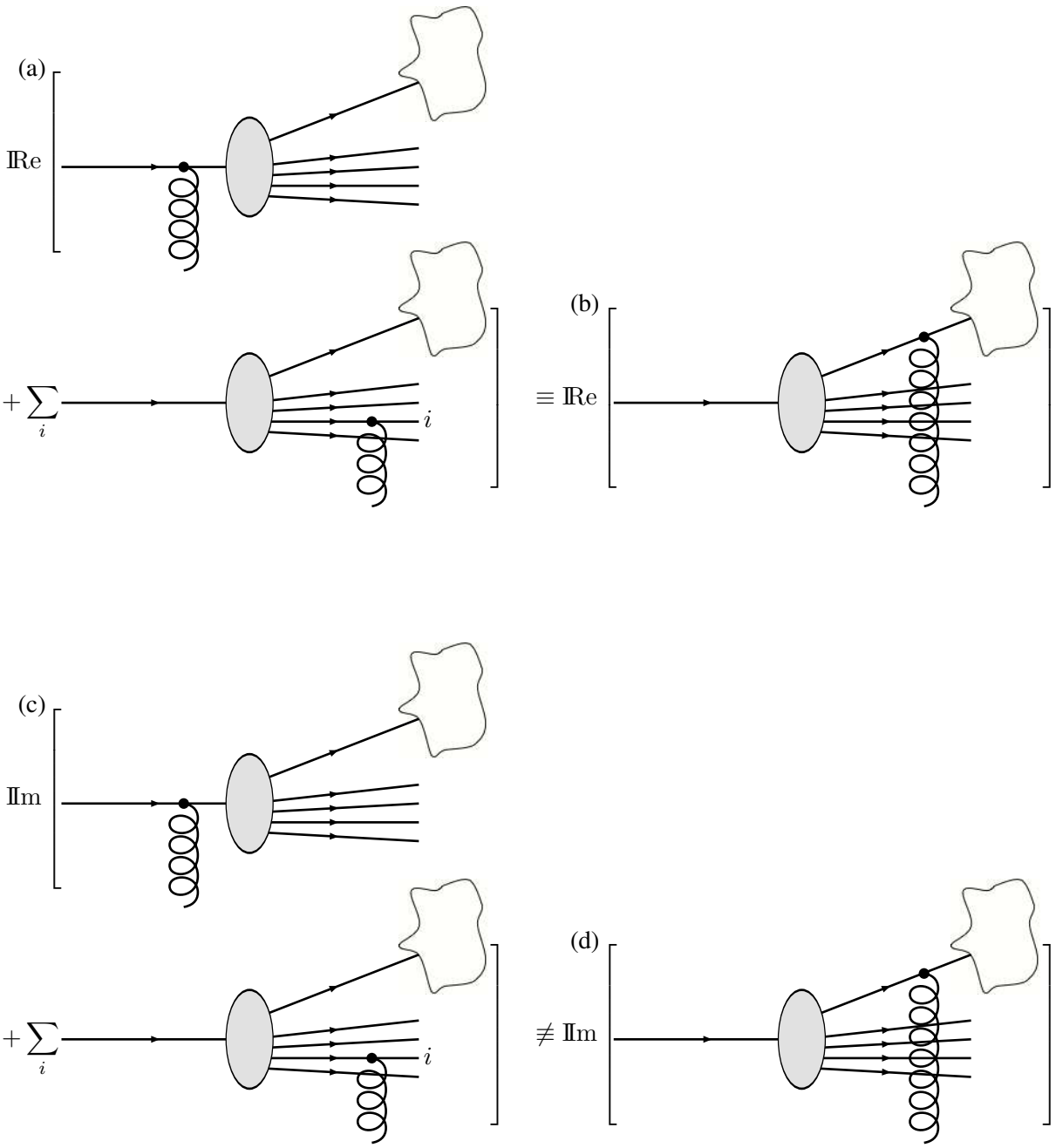


Fig. 2: The analogue of Fig. 1 for initial-state radiation. A hard initial-state parton entering the hard process fragments into a system of hard final-state collinear partons. The amplitude for this system to emit a soft, wide-angle, real or virtual gluon should again be calculated from the insertion of the soft gluon onto each of the external hard partons, summed over these partons (a,c). Because when the soft gluon is virtual the imaginary part of the loop correction is sensitive to the direction of the momentum flow, the colour coherence argument can only be used for real emission and the real part of the loop (b) but not for the imaginary part (d).

factorization in individual diagrams, but that, eventually, these violations cancel each other after summing over all diagrams *for the scattering of colour-singlet incoming hadrons*. Diagrams in which the gluons are attached to the outgoing hadron remnants are essential for this cancelation.

However, in calculating perturbatively-exclusive cross sections, for example the gaps-between-jets cross section defined below, one can perform factorization at the perturbative scale defined by the scale below which the observable is inclusive, and one can calculate the cross section perturbatively using incoming partons defined at this scale. Therefore one cannot appeal to the hadron remnants, and these effects really remain in the cross section.

2 Consequences: Super-Leading Logarithms in Gaps Between Jets Cross Sections

In the remainder of the talk, I discuss the consequences of this breakdown of naïve coherence and, in particular, the appearance of super-leading logarithms in the gaps-between-jets cross section. Here I am simply recapping the results of Ref. [1], so I can be brief.

To define the gap cross section, and the kinematic variables I use to describe it, consider two-jet production at lowest order in hadron collisions. Since I am interested in the soft or collinear corrections, the lowest-order kinematics are sufficient. I define the jets to have transverse momenta Q and to be separated by a (reasonably large) rapidity interval Δy. I define a 'gap' event sample by summing up the total scalar transverse momentum in a rapidity interval of length $Y < \Delta y$ in the region between the two jets and only accepting events in which this summed transverse momentum is less than $Q_0 \leq Q$. Provided Q_0 is well above the confinement scale, this gap cross section is perturbatively calculable. For $Q_0 \ll Q$ it develops large logarithmic corrections at every order that must be summed to all orders to yield a reliable result.

The conventional wisdom for such calculations is that the logarithmic series is $\alpha_s^n \log^n$, which define the leading logs for this process, that these leading logs can be calculated by considering only soft wide-angle virtual gluons stretched between the hard external partons, and that for every real emission outside the gap there is an equal and opposite virtual correction. Our findings contradict all of these points: we find super-leading[2] logarithms $\alpha_s^n \log^{n+1}$. We already expected, based on the work of Dasgupta and Salam [5] contributions from emission from gluons outside the gap, but in distinction to their result which is an edge effect: emission just outside the gap produces radiation just inside, the effect we find comes from emission arbitrarily far outside the gap. These results are directly related to a real–virtual mis-cancellation due to Coulomb gluon effects and ultimately due to the breakdown of naïve coherence for initial-state radiation.

To illustrate how these effects ultimately give rise to the super-leading logarithms, I briefly recap the ingredients of the 'conventional' calculations for gaps-between-jets developed by Sterman and others over many years [6], first in the simpler setting of e^+e^- annihilation.

[2] I should clear up one possible point of confusion: by super-leading we do not mean that there are more than the two logarithms per order expected from QCD, but only that this observable, which is expected to have only soft contributions, so one logarithm per power of α_s, actually develops additional collinear logarithms at high orders, which we call super-leading since they are beyond the expected soft-only tower. More precisely, one power of Y that appears in the coefficient of the leading logarithm, and is the remnant of the collinear logarithm, gets promoted to become a logarithm of Q/Q_0.

2.1 Gaps in e^+e^- annihilation

The lowest order process produces a quark of momentum p_1 and an antiquark of momentum p_2. Its amplitude is defined to be $\mathcal{A}$. The one-loop correction in the Feynman gauge is given by the single diagram with a gluon of momentum k stretched between p_1 and p_2. In order to extract the leading logarithms, the eikonal approximation is sufficient. Performing the loop integral over k by contour, one picks up poles at $k^2 = 0$ and at $p_1^2 = p_2^2 = 0$. The former gives a contribution that has exactly the form of a phase-space integral for a real gluon emission and leads to a term in the cross section that is exactly equal and opposite to the real-emission cross section. The conventional calculation uses this fact, by assuming that the real–virtual cancellation is perfect for transverse momenta below Q_0 and rapidities outside the gap, so that the entire first-order correction can be calculated from the loop diagram integrated over the disallowed region of phase space,

$$\mathcal{A}_1 = -\frac{2\alpha_s}{\pi}\int_{Q_0}^{Q}\frac{dk_t}{k_t}C_F\,(Y - i\pi)\,\mathcal{A}_0, \tag{1}$$

where the Y term is the integral of the $k^2 = 0$ pole over the gap region and the $i\pi$ term comes from the $p_1^2 = p_2^2 = 0$ pole. To obtain the leading logarithmic contribution at nth order, one can simply nest the k_t integral n times and obtain

$$\mathcal{A} = e^{-\frac{2\alpha_s}{\pi}\int_{Q_0}^{Q}\frac{dk_t}{k_t}C_F(Y-i\pi)}\mathcal{A}_0. \tag{2}$$

The gap cross section is then given by

$$\sigma = \mathcal{A}^\star\mathcal{A} = \mathcal{A}_0^\star e^{-\frac{2\alpha_s}{\pi}\int_{Q_0}^{Q}\frac{dk_t}{k_t}C_F(Y+i\pi)}e^{-\frac{2\alpha_s}{\pi}\int_{Q_0}^{Q}\frac{dk_t}{k_t}C_F(Y-i\pi)}\mathcal{A}_0. \tag{3}$$

It is easy to see that the Coulomb phase terms in the amplitude and its conjugate cancel, having no physical effect.

2.2 Gaps in $2 \longrightarrow 2$ scattering

In $2 \to 2$ scattering, one can make an exactly analogous calculation, with the one-loop result nesting and exponentiating to give the all-order result. The only difference is that for a hard process involving more than three partons there can be more than one colour structure, so the amplitude becomes a vector in colour space and the loop correction (the $C_F(Y - i\pi)$ in the e^+e^- case) becomes a matrix,

$$\sigma = \mathcal{A}_0^\dagger e^{-\frac{2\alpha_s}{\pi}\int_{Q_0}^{Q}\frac{dk_t}{k_t}\Gamma^\dagger}S\,e^{-\frac{2\alpha_s}{\pi}\int_{Q_0}^{Q}\frac{dk_t}{k_t}\Gamma}\mathcal{A}_0, \tag{4}$$

where S is the metric of the colour space. The simplest case is quark scattering, in which the colour space is 2 dimensional, and the anomalous dimension matrix Γ is given by[3]

$$\Gamma = \begin{pmatrix} 0 & \frac{N_c^2-1}{4N_c^2}i\pi \\ i\pi & \frac{N_c}{2}Y - \frac{1}{N_c}i\pi \end{pmatrix}. \tag{5}$$

The important point is that Γ and $\Gamma^\dagger$ do not commute, so the Coulomb phase terms do not cancel. Instead, they are responsible for important physical effects, giving rise to the 'BFKL'-type logarithms in the limit of large Y [8].

[3] I am grateful to Lev Lipatov for pointing out that this matrix was first calculated in Ref. [7].

2.3 Emission outside the gap

The main point of Ref. [1] was to check whether emission outside the gap really cancels to all orders, as is observed in the lowest order case, and as is assumed in the structure of the all-order calculation. To do this, we explicitly calculated the cross section for one (real or virtual) gluon outside the gap, summed over any number of soft virtual gluons integrated inside the gap and any number of Coulomb gluons. The result is simply the sum of the all-order corrected virtual and real terms, integrated over the out-of-gap phase space,

$$\sigma_1 = -\frac{2\alpha_s}{\pi}\int_{Q_0}^{Q}\frac{dk_t}{k_t}\int_{out}\frac{dy\,d\phi}{2\pi}\left(\Omega_V+\Omega_R\right). \tag{6}$$

Ω_V corresponds to one virtual emission outside the gap and its all-order evolution. It has a very similar structure to the conventional gap cross section,

$$\Omega_V = \mathcal{A}_0^\dagger e^{-\frac{2\alpha_s}{\pi}\int_{Q_0}^{Q}\frac{dk_t'}{k_t'}\Gamma^\dagger} S_V e^{-\frac{2\alpha_s}{\pi}\int_{Q_0}^{k_t}\frac{dk_t'}{k_t'}\Gamma}\,\gamma\, e^{-\frac{2\alpha_s}{\pi}\int_{k_t}^{Q}\frac{dk_t'}{k_t'}\Gamma}\mathcal{A}_0 + c.c., \tag{7}$$

where γ describes the virtual emission (roughly speaking it is the differential of Γ) and I have just renamed S to S_V for a reason that will be seen shortly. The real part has a more complicated structure, because it involves the evolution of a five-parton system at scales below k_t (the soft wide-angle gluon can be attached to the real out-of-gap gluon, in addition to the original four partons). The five-parton colour structure has a different (higher) dimensionality (four for the simplest case, $qq \to qqg$ for which the anomalous dimension matrix, Λ, was calculated in Ref. [9]) so the real emission matrix element, D^μ, is a rectangular matrix acting on the colour space of the four-parton process on the right and of the five-parton process on the left. The structure is then

$$\Omega_R = \mathcal{A}_0^\dagger e^{-\frac{2\alpha_s}{\pi}\int_{k_t}^{Q}\frac{dk_t'}{k_t'}\Gamma^\dagger} D_\mu^\dagger e^{-\frac{2\alpha_s}{\pi}\int_{Q_0}^{k_t}\frac{dk_t'}{k_t'}\Lambda^\dagger} S_R e^{-\frac{2\alpha_s}{\pi}\int_{Q_0}^{k_t}\frac{dk_t'}{k_t'}\Lambda} D^\mu\, e^{-\frac{2\alpha_s}{\pi}\int_{k_t}^{Q}\frac{dk_t'}{k_t'}\Gamma}\mathcal{A}_0, \tag{8}$$

where S_R is the metric of the five-parton colour space.

The out-of-gap gluon must be integrated everywhere outside the gap, including right into the collinear regions, in which Ω_V and Ω_R are separately divergent. It is easy to check that in the final-state collinear region, they indeed become equal and opposite and the singularities cancel. In the initial-state collinear limit[4] however, one finds

$$\Omega_V + \Omega_R \overset{|y|\to\infty}{\longrightarrow} \text{const.} \tag{9}$$

This means that in the pure eikonal theory the cross section is not well-behaved, because the contribution from hard collinear configurations becomes significant. This non-cancellation can be traced to the Coulomb phase terms in the evolution matrices, and ultimately to the breakdown of naïve coherence discussed earlier.

Having made this discovery, it is easy to see how this behaviour leads to the superleading logarithms we observed. To leading approximation, the effect of incorporating the correct splitting functions, energy conservation, etc, in the collinear limit is to introduce an effective cutoff on

[4]This means the rapidity tending to infinity, but at fixed k_t, so the emission never becomes truly collinear.

the rapidity range over which the eikonal result should be integrated, $y_{max} \sim \ln \frac{Q}{k_t}$. The nested integrals over k_t then have one additional log of k_t, leading to one additional log of Q/Q_0,

$$\sigma_1 \sim \sigma_0 \left(\frac{2\alpha_s}{\pi}\right)^4 \pi^2 Y \, \ln^5 \frac{Q}{Q_0} + \mathcal{O}\left(\alpha_s^n \ln^{n+1} \frac{Q}{Q_0}\right). \tag{10}$$

3 Open Issues

I end this talk by briefly mentioning some of the many open issues that remain.

I stated that we do not need to consider soft gluons attached to the hadron remnants. A simple estimate shows that this has to be the case. Since we are only interested in gluons with transverse momenta above Q_0, even in the Glauber region, and we assume that Q_0 is large relative to the hadronic scale, any such corrections should be suppressed by powers of Q_0. Nevertheless, since a number of objections have been made in this direction, it would be worth working through the first such correction, to shore up this argument.

Once we accept the breakdown of naïve coherence, the choice of ordering variable becomes relevant. Our calculation is based on transverse momentum ordering and different ordering variables might give different coefficients for the super-leading logarithms. Further work, for example by developing a full diagrammatic approach, is needed to be sure that transverse momentum ordering leads to the correct physical results.

Once we have found that one gluon outside the gap gives a tower of terms enhanced by one additional logarithm, it is natural to speculate that n gluons outside the gap will give n additional logarithms [1]. If this is right it would mean that at each order, the leading term is actually $\alpha_s^n \log^{2n-3}$ and it would be imperative to organize and sum these terms to all orders. Performing such a resummation is a daunting task, since, like an exact calculation of non-global logarithms, it would depend on the full colour structure of multi-parton ensembles.

I close by mentioning that I look forward to a critical appraisal of this work. The result came as such a surprise to us that we felt sure it was wrong. Two years of checking has not diminished this feeling. However we have certainly ruled out simple error, since, in addition to the two independent calculations we made, James Keates recently succeeded in constructing an algorithm that generates all possible cut diagrams order by order and evaluates them [10]. Within the same strongly-ordered-in-k_t approximation that we use, his calculation reproduces ours up to fourth order, and confirms the coefficient of the first super-leading logarithm. Once issues of calculational speed have been solved, he will be able to run at fifth order and beyond and check our speculation about the rôle of multiple gluons outside the gap.

In the meantime we are trying to obtain a deeper understanding of our findings, and I welcome any comments that help us in this direction.

Acknowledgements

I am grateful to my collaborators Jeff Forshaw and Albrecht Kyrieleis, and also to George Sterman, for fruitful discussions of these and related points.

References

[1] J. R. Forshaw, A. Kyrieleis, and M. H. Seymour, JHEP **08**, 059 (2006). hep-ph/0604094.

[2] Y. L. Dokshitzer and S. I. Manaenkov. LENINGRAD-85-1103;
J. Hakkinen and H. Kharraziha, Comput. Phys. Commun. **100**, 311 (1997). hep-ph/9603229.

[3] R. Doria, J. Frenkel, and J. C. Taylor, Nucl. Phys. **B168**, 93 (1980).

[4] J. C. Collins, D. E. Soper, and G. Sterman, Nucl. Phys. **B261**, 104 (1985);
J. C. Collins, D. E. Soper, and G. Sterman, Nucl. Phys. **B308**, 833 (1988).

[5] M. Dasgupta and G. P. Salam, JHEP **03**, 017 (2002). hep-ph/0203009.

[6] M. G. Sotiropoulos and G. Sterman, Nucl. Phys. **B419**, 59 (1994). hep-ph/9310279;
G. Oderda and G. Sterman, Phys. Rev. Lett. **81**, 3591 (1998). hep-ph/9806530;
C. F. Berger, T. Kucs, and G. Sterman, Phys. Rev. **D65**, 094031 (2002). hep-ph/0110004.

[7] L. N. Lipatov, Nucl. Phys. **B309**, 379 (1988).

[8] J. R. Forshaw, A. Kyrieleis, and M. H. Seymour, JHEP **06**, 034 (2005). hep-ph/0502086.

[9] A. Kyrieleis and M. H. Seymour, JHEP **01**, 085 (2006). hep-ph/0510089.

[10] J. Keates. Work in progress.

BFKL equation and anomalous dimensions in $N = 4$ SUSY

L.N. Lipatov
Universität Hamburg, Germany
Petersburg Nuclear Physics Institute, Russia

Abstract
The BFKL approach to the Regge processes in QCD is reviewed. It is shown, that in the multi-colour QCD the BKP equations for composite states of several Reggeized gluons are integrable. We discuss the relation between Pomeron and Graviton in N=4 SUSY. The property of the maximal transcendentality is formulated. It gives us a possibility to calculate the three-loop anomalous dimension. With the use of the asymptotic Bethe ansatz and a model for wrapping effects the anomalous dimension is calculated in four loops in an agreement with the BFKL and double-logarithmic predictions.

1 Introduction

It is known [1], that the QCD scattering amplitude in the leading logarithmic approximation (LLA) has the Regge-type asymptotics

$$M_{AB}^{A'B'}(s,t) = M_{AB}^{A'B'}(s,t)|_{Born}\, s^{\omega(t)}\,, \tag{1}$$

where $M_{AB}^{A'B'}(s,t)|_{Born}$ is the Born amplitude and the gluon Regge trajectory is given below

$$\omega(-|q|^2) = -\frac{\alpha_c}{4\pi^2}\, N_c \int d^2k\, \frac{|q|^2}{|k|^2|q-k|^2} \approx -\frac{\alpha_c}{2\pi}\, \ln\frac{|q^2|}{\lambda^2}\,. \tag{2}$$

At high energies the gluons are produced in the multi-Regge kinematics. The elastic amplitude with the vacuum quantum numbers in the t-channel can be obtained with the use of the s-channel unitarity by summing over multi-gluon intermediate states [1]. It is convenient to introduce the complex variables for the gluon transverse coordinates and momenta

$$\rho_k = x_k + iy_k\,,\ \rho_k^* = x_k - iy_k\,,\ p_k = i\frac{\partial}{\partial\rho_k}\,,\ p_k^* = i\frac{\partial}{\partial\rho_k^*}\,. \tag{3}$$

In the coordinate representation the Balitsky-Fadin-Kuraev-Lipatov (BFKL) equation for the Pomeron wave function can be written as follows [1]

$$E\,\Psi(\vec\rho_1,\vec\rho_2) = H_{12}\,\Psi(\vec\rho_1,\vec\rho_2)\,,\ \Delta = -\frac{\alpha_s N_c}{2\pi}\,\min\,E\,, \tag{4}$$

where Δ is the Pomeron intercept. The BFKL Hamiltonian is presented below [2]

$$H_{12} = \ln\,|p_1p_2|^2 + \frac{1}{p_1p_2^*}\ln\,|\rho_{12}|^2 p_1p_2^* + \frac{1}{p_1^*p_2}\ln\,|\rho_{12}|^2 p_1^*p_2 - 4\psi(1)\,, \tag{5}$$

where $\rho_{12} = \rho_1 - \rho_2$. The kinetic energy is proportional to the gluon Regge trajectories, and the potential energy $\sim \ln |\rho_{12}|^2$ is related to the gluon production effective vertices.

The Hamiltonian is invariant under the Möbius transformation [3]

$$\rho_k \to \frac{a\rho_k + b}{c\rho_k + d}\,, \tag{6}$$

where a, b, c and d are complex numbers. The eigenvalues of the Casimir operators

$$M^2 = \left(\sum_{r=1}^{2} \vec{M}^{(r)}\right)^2 = \rho_{12}^2\, p_1\, p_2\,,\ M^{*2} = (M^2)^* \tag{7}$$

are related with the conformal weights

$$m = 1/2 + i\nu + n/2\,,\ \widetilde{m} = 1/2 + i\nu - n/2 \tag{8}$$

for the principal series of unitary representations.

2 Integrability of the BFKL dynamics at $N_c \to \infty$

The Bartels-Kwiecinskii-Praszalowicz (BKP) equation [5] for the n-gluon composite state is simple at $N_c \to \infty$, where its Hamiltonian has the property of the holomorphic separability [4]

$$H = \frac{1}{2}\sum_k H_{k,k+1} = \frac{1}{2}(h + h*)\,,\ [h, h*] = 0\,. \tag{9}$$

The holomorphic Hamiltonian can be written as follows

$$h = \sum_k h_{k,k+1}\,,\ h_{12} = \ln(p_1 p_2) + \frac{1}{p_1}\,\ln\rho_{12}\ p_1 + \frac{1}{p_2}\,\ln\rho_{12}\ p_2 - 2\psi(1)\,, \tag{10}$$

where $\psi(x) = (\ln\Gamma(x))'$. As a result, we obtain for Ψ the holomorphic factorization [4]

$$\Psi(\vec{\rho}_1, \vec{\rho}_2, ..., \vec{\rho}_n) = \sum_{r,s} a_{r,s}\,\Psi_r(\rho_1, ..., \rho_n)\,\Psi_s(\rho_1^*, ..., \rho_n^*) \tag{11}$$

and the duality symmetry [6]

$$\rho_{r,r+1} \to p_r \to \rho_{r-1,r}\,. \tag{12}$$

Moreover, there are integrals of motion commuting among themselves and with h [2,7]

$$q_r = \sum_{k_1<k_2<...<k_r} \rho_{k_1k_2}\rho_{k_2k_3}...\rho_{k_rk_1}\,p_{k_1}p_{k_2}...p_{k_r}\,,\ [q_r, h] = 0\,. \tag{13}$$

The integrability of the BFKL dynamics [7] is related to the fact, that H coincides with the local Hamiltonian of the Heisenberg spin model [8].

In particular the Pomeron intercept Δ is positive [1]

$$\Delta = 4\,\frac{\alpha_s}{\pi} N_c\,\ln 2 \tag{14}$$

and the Froissart bound for the total cross-section is violated. To restore the s-channel unitarity of scattering amplitudes one can use the effective field theory for Reggeized gluons [9]- [11].

3 DGLAP and BFKL dynamics in $N = 4$ SUSY

The momenta $f_a(j, Q^2)$ of parton distributions satisfy the renormalization group equation with the anomalous dimension matrix γ_{ab}

$$\frac{d}{d\ln Q^2} f_a(j, Q^2) = \sum_b \gamma_{ab}(j) f_b(j, Q^2)\,. \tag{15}$$

They are proportional to matrix elements of the light-cone components of twist-2 operators

$$O^a = \tilde{n}^{\mu_1}...\tilde{n}^{\mu_j}\, O^a_{\mu_1,...,\mu_j}\ ,\ \tilde{\mathcal{O}}^a = \tilde{n}^{\mu_1}...\tilde{n}^{\mu_j}\tilde{\mathcal{O}}^a_{\mu_1,...,\mu_j}\,. \tag{16}$$

The anomalous dimensions do not depend on other possible tensor projections

$$\tilde{n}^{\mu_1}...\tilde{n}^{\mu_{1+\omega}}\, O^a_{\mu_1,...,\mu_{1+\omega},\sigma_1,...,\sigma_{|n|}}\, l_\perp^{\sigma_1}...l_\perp^{\sigma_{|n|}}. \tag{17}$$

The solution of the BFKL equation due to its Möbius invariance is classified by the anomalous dimension $\gamma = \frac{1}{2} + i\nu$ and the conformal spin $|n|$ coinciding with the number of transverse indices of O. The eigenvalue of the BFKL kernel in the next-to-leading approximation is

$$\omega = \omega_0(n,\,\gamma) + 4\,\hat{a}^2\,\Delta(n,\gamma)\,,\ \hat{a} = g^2 N_c/(16\pi^2)\,. \tag{18}$$

In QCD $\Delta(n,\gamma)$ is a non-analytic function of the conformal spin $|n|$ [12, 13]

$$\Delta_{QCD}(n,\gamma) = c_0\delta_{n,0} + c_2\delta_{n,2} + analytic\ terms\,,$$

but in $N = 4$ SUSY the Kroniker symbols are cancelled [13].

Moreover, in this model we obtain for $\Delta(n,\gamma)$ the Hermitian separability

$$\Delta(n,\gamma) = \phi(M) + \phi(M^*) - \frac{\rho(M) + \rho(M^*)}{2\hat{a}/\omega}\,,\ M = \gamma + \frac{|n|}{2}\,, \tag{19}$$

$$\rho(M) = \beta'(M) + \frac{1}{2}\zeta(2)\,,\ \beta'(z) = \frac{1}{4}\left[\Psi'\Big(\frac{z+1}{2}\Big) - \Psi'\Big(\frac{z}{2}\Big)\right]. \tag{20}$$

It is important, that here all special functions have the maximal trancendentality property [13].

$$\phi(M) = 3\zeta(3) + \Psi''(M) - 2\Phi(M) + 2\beta'(M)\Big(\Psi(1) - \Psi(M)\Big), \tag{21}$$

where

$$\Phi(M) = \sum_{k=0}^{\infty}\frac{\beta'(k+1)}{k+M} + \sum_{k=0}^{\infty}\frac{(-1)^k}{k+M}\left(\Psi'(k+1)\ -\ \frac{\Psi(k+1) - \Psi(1)}{k+M}\right). \tag{22}$$

For the one loop anomalous dimension matrix of the twist-2 operators in the case $N = 4$ the calculations were performed in Ref. [14]. The eigenvalues of this matrix are expressed in terms of the universal anomalous dimension for the super-multiplet unifying all twist-2 operators

$$\gamma^{(0)}_{uni}(j) = -4S_1(j-2)\,,\ S_r(j) = \sum_{i=1}^{j}\frac{1}{i^r}\,. \tag{23}$$

Note, that $\gamma^{(0)}_{uni}(j)$ has the maximal transcendentality property, which leads to an integrability of evolution equations for matrix elements of quasi-partonic operators in $N = 4$ SUSY [14].

4 Relation between Pomeron and Graviton

The Pomeron intercept in the $N = 4$ supersymmetric gauge theory was calculated recently at large coupling constants [17]. Here we shall review the basic arguments. To begin with, one can simplify the eigenvalue for the BFKL kernel in the diffusion approximation as follows (see [12])

$$j = 2 - \Delta - D\nu^2\,,\ \gamma_{uni} = \frac{j}{2} + i\nu\,, \tag{24}$$

assuming, that the parameter Δ is small at large $z = \alpha N_c/\pi$. Due to the energy-momentum conservation we have $\gamma|_{j=2} = 0$ and therefore γ can be expressed in terms of the parameter Δ

$$\gamma = (j-2)\left(\frac{1}{2} - \frac{1/\Delta}{1+\sqrt{1+(j-2)/\Delta}}\right). \tag{25}$$

On the other hand with the use of the AdS/CFT correspondence [18] the above BFKL equation can be written as the graviton Regge trajectory

$$j = 2 + \frac{\alpha'}{2}\,t\,,\ t = E^2/R^2\,,\ \alpha' = \frac{R^2}{2}\,\Delta\,. \tag{26}$$

The behaviour of γ at $g \to \infty$, $j \to \infty$ was predicted earlier [19]

$$\gamma_{|z\to\infty} = -\sqrt{j-2}\,\Delta^{-1/2}_{|j\to\infty} = \sqrt{\pi j}\,z^{1/4}\,. \tag{27}$$

Therefore one can calculate the Pomeron intercept at large coplings [17] (see also Ref. [23])

$$j = 2 - \Delta\,,\ \Delta = \frac{1}{\pi}\,z^{-1/2}\,. \tag{28}$$

5 Two and three loops anomalous dimensions in $N = 4$

One can argue [13], that the perturbative expansion of the universal anomalous dimension

$$\gamma_{uni}(j) = \hat{a}\gamma^{(0)}_{uni}(j) + \hat{a}^2\gamma^{(1)}_{uni}(j) + \hat{a}^3\gamma^{(2)}_{uni}(j) + ... \tag{29}$$

contains in each order of the perturbation theory only special functions with the highest trancendentality. With such assumption one can obtain [13]

$$\frac{1}{8}\,\gamma^{(1)}_{uni}(j+2) = 2S_1(j)\,(S_2(j) + S_{-2}(j)) - 2S_{-2,1}(j) + S_3(j) + S_{-3}(j)\,, \tag{30}$$

where the corresponding harmonic sums are given below

$$S_a(j) = \sum_{m=1}^{j}\frac{1}{m^a}\,,\ S_{a,b,c,\cdots}(j) = \sum_{m=1}^{j}\frac{1}{m^a}\,S_{b,c,\cdots}(m)\,, \tag{31}$$

$$S_{-a}(j) = \sum_{m=1}^{j}\frac{(-1)^m}{m^a},\ S_{-a,b,\cdots}(j) = \sum_{m=1}^{j}\frac{(-1)^m}{m^a}\,S_{b,\cdots}(m), \tag{32}$$

$$\overline{S}_{-a,b,c\cdots}(j) = (-1)^j S_{-a,b,\ldots}(j) + S_{-a,b,\cdots}(\infty)\Big(1 - (-1)^j\Big). \tag{33}$$

This result was verified by direct calculations of the anomalous dimension matrix in two loops [15].

Later the three-loop anomalous dimension matrix for QCD was calculated [16], which allowed us to find the universal anomalous dimension in three loops for $N = 4$ SUSY [17]

$$\begin{aligned}\frac{1}{32}\,\gamma^{(2)}_{uni}(j+2) = {} & 24\,S_{-2,1,1,1} - 12\,\left(S_{-3,1,1} + S_{-2,1,2} + S_{-2,2,1}\right)\\ & +6\,\left(S_{-4,1} + S_{-3,2} + S_{-2,3}\right) - 3\,S_{-5}\\ & -2\,S_1^2\,\left(3\,S_{-3} + S_3 - 2\,S_{-2,1}\right) - S_2\,\left(S_{-3} + S_3 - 2\,S_{-2,1}\right)\\ & -S_1\left(8\bar{S}_{-4} + \bar{S}^2_{-2} + 4S_2\bar{S}_{-2} + 2S_2^2\right)\\ & -S_1\left(3S_4 - 12\bar{S}_{-3,1} - 10\bar{S}_{-2,2} + 16\bar{S}_{-2,1,1}\right)\,.\end{aligned} \tag{34}$$

6 Relations between weak and strong coupling regimes

The asymptotics of γ_{uni} for $N = 4$ SUSY at $j - 1 = \omega \to 0$

$$\gamma^{N=4}_{uni}(j) = \hat{a}\frac{4}{\omega} - 32\zeta_3\,\hat{a}^2 + 32\zeta_3\,\hat{a}^3\frac{1}{\omega} - \frac{16\hat{a}^4}{\omega^4}\left(32\zeta_3 + \frac{\pi^4}{9}\omega\right) + ... \tag{35}$$

is in an agreement with the predictions from the BFKL equation [13].

Near the negative even points $j + 2r = \omega \to 0$ the anomalous dimension satisfy the equation

$$\begin{aligned}\omega\gamma_{uni} = {} & \gamma^2_{uni} + 16\hat{a}^2(S_2 + \zeta_2 - S_1^2)\\ & +4\,\hat{a}\left(1 - \omega S_1 - \omega^2(S_2 + \zeta_2) + \gamma^2(S_2 + S_{-2})\right)\end{aligned}$$

resumming the double logarithmic terms $\sim \alpha/\omega^2$ and corrections to them.

Further, the universal anomalous dimension at large j

$$\gamma^{N=4}_{uni} = a(z)\,\ln j\,,\;\; z = \frac{\alpha N_c}{\pi} = 4\hat{a} \tag{36}$$

can be found from our results up to three loops

$$a(z) = -z + \frac{\pi^2}{12}\,z^2 - \frac{11}{720}\pi^4 z^3 + \ldots\,. \tag{37}$$

It is remarkable, that using the AdS/CFT correspondence [18] between the superstring model on the anti-de-Sitter space and the $N = 4$ supersymmetric Yang-Mills theory A. Polyakov with collaborators found the coefficient $a(z)$ in the strong coupling limit [19]

$$\lim_{z\to\infty} a(z) = -z^{1/2} + \frac{3\ln 2}{4\pi} + \ldots\,. \tag{38}$$

In Ref. [15] the resummation of $a(z)$ in the form

$$\widetilde{a} = -z + \frac{\pi^2}{12}\,\widetilde{a}^2. \tag{39}$$

was suggested. The prediction of this equation

$$\widetilde{a} = -z + \frac{\pi^2}{12}\,z^2 - \frac{1}{72}\pi^4 z^3 + ... \tag{40}$$

is in a rather good agreement with $a(z)$ in three loops and the strong coupling asymptotics.

7 Beisert-Eden-Staudacher equation

Our results agree also with the recent papers [20, 21], where $a(z)$ is constructed in all orders. One can rewrite the Eden-Staudacher integral equation [20] as a set of linear equations [22]

$$a_{n,\epsilon} = \sum_{n'=1}^{\infty} K_{n,n'}(\epsilon)\,\left(\delta_{n',1} - a_{n',\epsilon}\right)\,,\;\; K_{n,n'}(\epsilon) =$$

$$2n\sum_{R=0}^{\infty}(-1)^R\,\frac{2^{-2R-n-n'}}{\epsilon^{2R+n+n'}}\zeta(2R+n+n')\,\frac{(2R+n+n'-1)!\,(2R+n+n')!}{R!\,(R+n)!\,(R+n')!\,(R+n+n')!}\,, \tag{41}$$

where the function $a(z)$ is expressed in terms of $a_{1,\epsilon}$

$$a(z) = \frac{2(1-a_{1,\epsilon})}{\epsilon^2}\,,\;\; \epsilon = \frac{1}{g\sqrt{2}}\,. \tag{42}$$

We can easiliy prove, that the maximal transcendentality property for $a(z)$ is valid in all orders of perturbation theory and the coefficients in front of the products of the corresponding ζ-functions are integer numbers [22]. Also $a(z)$ has an essential singularity in the point $g = \infty$.

It is possibly to show [22], that the asymptotic behaviour of $a(z)$ in the case of the Beisert-Eden-Staudacher equation [20] is in an agreement with the AdS/CFT prediction [19]

$$\lim_{g\to\infty}\gamma_{sing} = \frac{2}{\epsilon}\,\frac{I_1(2\epsilon^{-1})}{I_0(2\epsilon^{-1})} \approx 2\sqrt{2}\,g\;-\frac{1}{2}\,. \tag{43}$$

8 Universal anomalous dimension in 4 loops

With the use of the asymptotic Bethe ansatz and the maximal transcendentality hypothesis the anomalous dimension in four loops was calculated [24]

$$\frac{\gamma_4}{256} = \mathbf{4S_{-7}} + \mathbf{6S_7} + 2(S_{-3,1,3} + S_{-3,2,2} + S_{-3,3,1} + S_{-2,4,1})$$

$$+3(-S_{-2,5} + S_{-2,3,-2}) + 4(S_{-2,1,4} - S_{-2,-2,-2,1} - S_{-2,1,2,-2}$$

$$-S_{-2,2,1,-2} - S_{1,-2,1,3} - S_{1,-2,2,2} - S_{1,-2,3,1}) + ...$$

$$-72S_{1,1,1,-4} - 80S_{1,1,-4,1} - \zeta(\mathbf{3})\mathbf{S_1}(\mathbf{S_3} - \mathbf{S_{-3}} + \mathbf{2S_{-2,1}})\,,$$

where the dots mean the dropped terms. The harmonic sums here depend on the parameter $M = j - 2$. They can be analytically continued to the complex values of M. It turns out, that the first two terms lead to the singularity of γ_4 at $\omega = M + 1 \to 0$

$$\lim_{M\to -1} \gamma_4(M) = -\frac{512}{\omega^7}\,,$$

which contradicts to the above BFKL prediction

Therefore the asymptotic Bethe ansatz is not correct and it is needed to take into account the so-called wrapping effects. As an attempt to find the contribution of these effects we can modify the last term in the expression for γ_4 corresponding to the so-called dressing phase, which was found in Ref. [21] for the cusp anomalous dimension. The simplest modification conserving the transcendentality property and reproducing the BFKL prediction is given by the substitution of the factor $\zeta(3)$ in the dressing phase by the following linear combination of the harmonic sums

$$\zeta_3 \to \frac{47\zeta_3}{24} - \frac{S_{-3}}{4} + \frac{3S_{-2}S_1}{4} + \frac{3S_1S_2}{8} + \frac{3S_3}{8} + \frac{S_{-2,1}}{6} - \frac{17S_{2,1}}{24}\,.$$

It turns out, that after this substitution the anomalous dimension has the correct singularity at even negative points M predicted by the double-logarithmic resummation

$$\frac{1}{256}\,\gamma_4|_{j\to -2k+\omega} = \frac{5}{\omega^7} - 20\frac{S_1}{\omega^6} + \frac{24\,S_1^2 - 14(S_2+\zeta_2) + 4(S_2+S_{-2})}{\omega^5} + \dots\,.$$

Therefore it is plausible, that this substitutions leads to the correct expression for γ_4.

9 Discussion

The high energy theory in QCD is based on the fact, that the gluons and quarks are reggeized. To solve the unitarization problem for the BFKL Pomeron one should use the effective action local in the particle rapidities. The Reggeon calculus in the form of a 2+1 field theory can be derived from this action. In particular next-to-leading corrections to the BFKL kernel are calculated in QCD and in N=4 SUSY. In N=4 SUSY the eigenvalue of the kernel is expressed as a sum of the most complicated functions which could appear in this order. Using the hypothesis of the maximal transcendentality for the universal anomalous dimension of the twist-2 operators we calculated it up to the third order. Our resummation procedure is in an agreement with the strong coupling predictions obtained from the AdS/CFT correspondence. In particular, we calculated the intercept of the BFKL pomeron in $N = 4$ SUSY and the cusp anomalous dimension at strong couplings. The anomalous dimension in 4-loops was also found with the use of the asymptotic Bethe ansatz, maximal transcendentality and predictions obtained from the BFKL and double-logarithmic resummation.

References

[1] V.S. Fadin, E.A. Kuraev, L.N. Lipatov, *Phys. Lett.* B **60** (1975) 50;
Ya.Ya. Balitsky, L.N. Lipatov, *Yad. Fiz.* **28** (1978) 1597.

[2] L.N. Lipatov, *Phys.Lett.* B **309** (1993) 394.

[3] L.N. Lipatov *JETP* **90** (1986) 1536.

[4] L.N. Lipatov *Phys.Lett.* B **251** (1990) 284.

[5] J. Bartels, *Nucl.Phys* B **175** (1980) 365;
J. Kwiecinski, M. Praszalowicz, *Phys.Lett.*B **94** (1980) 413.

[6] L.N. Lipatov,*Nucl.Phys.*B **548** (1999) 328.

[7] L.N. Lipatov *High energy asymptotics of multi-colour QCD and exactly solvable lattice models*, Padova preprint DFPD/93/TH/70, hep-th/9311037, unpublished.

[8] L.N. Lipatov, *JETP Lett.* **59** (1994) 596;
L.D. Faddeev, G.P. Korchemsky, *Phys. Lett.*B **342** (1995) 311.

[9] L.N. Lipatov, *Nucl.Phys.* B **365** (1991) 614.

[10] L.N. Lipatov, *Nucl.Phys.* B **452** (1995) 369.

[11] E. Antonov, I. Cherednikov, E. Kuraev, L. Lipatov, *Nucl.Phys.* B **721** (2005) 111.

[12] V. Fadin, L. Lipatov,*Phys. Lett* B **429** (1998) 127;
M. Ciafaloni, G. Camici,*Phys. Lett* B **430** (1998) 349.

[13] A. Kotikov, L. Lipatov, *Nucl.Phys.* B **582** 19 (2000), *Nucl.Phys.* B **661** (2003) 19.

[14] L. Lipatov, talk at "Perspectives in Hadronic Physics", Proc. of Conf. ICTP. Triest, Italy, May 1997.

[15] A. Kotikov, L. Lipatov, V. Velizhanin, *Phys. Lett.*B **557** (2003) 114.

[16] S. Moch, J.A.M. Vermaseren, A. Vogt, *Nucl.Phys.* B **688** (2004) 101.

[17] A. Kotikov, L. Lipatov, A. Onishchenko, V. Velizhanin, *Phys. Lett.*B **595** (2004) 521;
*Phys. Lett.*B **632** (2006) 754.

[18] J.M. Maldacena, *Adv. Theor. Math. Phys.* **2** (1998) 231.

[19] S.S. Gubser, I.R. Klebanov, A.M. Polyakov, *Nucl.Phys.*B **636** (2002) 99.

[20] B. Eden, M. Staudacher, *J. Stat. Mech.* **0611** (2006) P014.

[21] N. Beisert, B. Eden, M. Staudacher, *J. Stat. Mech.* **0701** (2007) P021.

[22] A. V. Kotikov, L. N. Lipatov, Nucl. Phys. *Nucl.Phys.*B **769** (2007) 217.

[23] R.C. Brower, J. Polchinski, M.J. Strassler, C-I Tan, preprint hep-th/0603115.

[24] A.V. Kotikov, L.N. Lipatov, A. Rej, M. Staudacher, V.N. Velizhanin, preprint hep-th/0704.3586.

Gluon Saturation and Black Hole Criticality

L. Álvarez-Gaumé[1], *C. Gómez*[2]†, *A. Sabio Vera*[1], *A. Tavanfar*[1,3], *M. A. Vázquez-Mozo*[4]
[1]Theory Group, Physics Department, CERN, CH-1211 Geneva 23, Switzerland,
[2]Instituto de Física Teórica UAM/CSIC, Universidad Autónoma de Madrid, E-28049 Madrid, Spain,
[3]Institute for Studies in Theoretical Physics and Mathematics (IPM) P.O. Box 19395-5531, Tehran, Iran,
[4]Departamento de Física Fundamental, Universidad de Salamanca, Plaza de la Merced s/n, E-37008 Salamanca, Spain and Instituto Universitario de Física Fundamental y Matemáticas (IUFFyM), Universidad de Salamanca, Spain.

Abstract
We discuss the recent proposal [1] where it was shown that the critical anomalous dimension associated to the onset of non–linear effects in the high energy limit of QCD coincides with the critical exponent governing the radius of the black hole formed in the spherically symmetric collapse of a massless scalar field. We argue that a new essential ingredient in this mapping between gauge theory and gravity is continuous self-similarity, not present in the scalar field case but in the spherical collapse of a perfect fluid with barotropic equation of state. We identify this property with geometric scaling, present in DIS data at small values of Bjorken x. We also show that the Choptuik exponent in dimension five tends to the QCD critical value in the traceless limit of the energy momentum tensor.

1 Criticality in high energy QCD and black hole formation

One of the major insights of string theory is the unexpected connection between black hole physics and confinement in QCD. This connection is realized on the basis of the deep holographic [2] duality between gravity and gauge theories [3, 4]. A particularly interesting connection between black holes and gauge theories is the dual interpretation [4] of the Hawking–Page phase transition [5] in gravity as the confinement / deconfinement transition in gauge theory at finite temperature. Holography is based on a very concrete set of rules for computing quantum

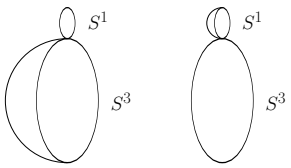


Fig. 1: The two relevant bulk geometries for confinement / deconfinement transition.

† speaker

field theory expectation values in terms of classical solutions to SUGRA equations with concrete boundary conditions. A further important ingredient of holography is the generalization of the gauge–gravity correspondence to non local observables such as Wilson or Polyakov loops. In this 'non local' version of the correspondence expectation values of Wilson loops are defined as sums of string world sheets in the bulk geometry with boundary determined by the loop.

Wilson loops are natural candidates to define the order parameter of QCD phases. This is the case not only for confinement but also for the transition from a dilute gas of partons to the so–called 'color glass condensate' [6] of hadronic parton distributions. In the same way as there exists a geometrical qualitative picture of the transition to confinement, illustrated in Fig. 1, it is natural to search for the corresponding holographic description of the saturation phenomena present in the high energy limit of QCD [7]. A very important experimental discovery in HERA data was the rise of the gluon distribution function $x\,G(x,Q^2)$ (which is related to the number of gluons in the target proton wave function with effective transverse size of order $1/Q^2$ carrying a fraction x of the hadron longitudinal momentum) when, for fixed Q^2, the value of x becomes small. This can be seen, *e.g.*, in Fig. 2. In the 'dipole frame' the total cross section for

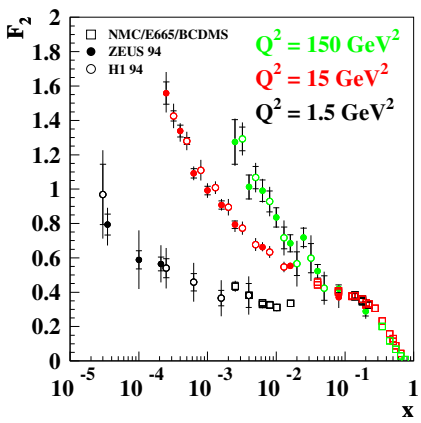


Fig. 2: The dependence on x of the proton structure function F_2 for different values of Q^2.

the scattering of the virtual photon off the hadron can be expressed in terms of the probability amplitude for the photon to decay into a quark–antiquark pair, creating a colour dipole of size $r = 1/Q$, which then scatters off the proton's effective colour field. The forward scattering amplitude for the dipole depends on r and the rapidity variable $Y = \log(1/x)$. In the leading order approximation this scattering amplitude depends linearly on $x\,G(x,Q^2)$. Since unitarity requires the forward scattering amplitude not to be larger than one this indicates that the rise of the gluon distribution should reach a saturation point, leading to the kinematic diagram shown in Fig. 3, where the saturation line indicates the critical value $x_c(Q^2)$ such that for $x < x_c$ and fixed Q^2 the gluon distribution function becomes effectively constant in x.

The two main theoretical problems associated with the previous picture are to identify $i)$ the dynamical origin of the rise of $x\,G(x,Q^2)$ with decreasing x and $ii)$ the nature of the non–

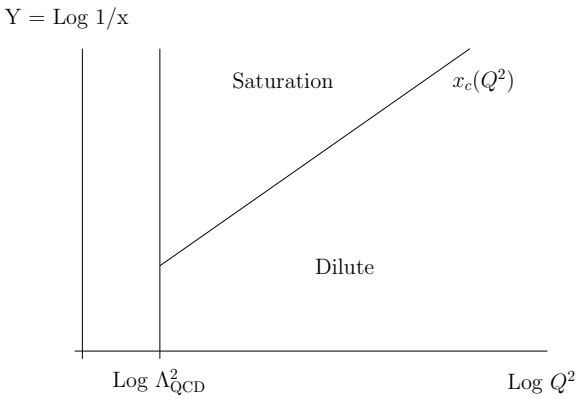


Fig. 3: QCD kinematic space in DIS

linear dynamics responsible for saturation and restoration of unitarity. The current understanding is that the dynamical origin of the rise of the gluon distribution function is due to the dominance of BFKL dynamics [8] while the non–linear BK equation [9] is responsible for the onset of saturation effects in the high energy limit of scattering amplitudes. In the eikonal approximation the exponential rise in Y for the forward scattering amplitude can be computed as the Wilson loop for the quark–antiquark pair propagating in the effective colour field of the proton which, in the proton infinite momentum frame and large center–of–mass energies, is dominated by soft gluon emissions in multi–Regge kinematics, with strong ordering in longitudinal components but not in transverse ones. These configurations, shown in Fig. 4, build up the BFKL hard pomeron.

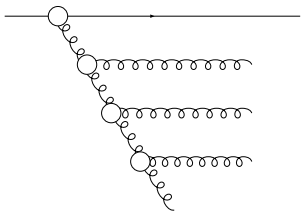


Fig. 4: BFKL gluon cascade in multi–Regge kinematics

In this framework the rapidity Y acts as a cutoff in the effective integration over longitudinal momenta and the BFKL equation controlling the evolution in Y plays the conceptual rôle of a renormalization group equation with a 'fixed point', generated by non–linear effects, at the saturation line. This line, of the form $Q_s(x) \sim x^{-\lambda}$, is characterized by the 'saturation exponent', which, in the limit of a very small coupling, reads $\lambda \simeq \alpha_s N_c 2.44/\pi$. A direct consequence of the onset of non–linear effects is that asymptotic amplitudes only depend on the variable $\sqrt{\tau} \simeq Q x^{\lambda}$ nearby the saturation region, *i.e.*, in the $(Y, \log Q^2)$ plane this implies that physical observables only depend on lines of constant τ as it is shown in Fig. 5. Along those lines any continuous boost in longitudinal components can be compensated by an equivalent one in the transverse directions to leave physical quantities invariant. The 'geometric scaling' on this variable has been

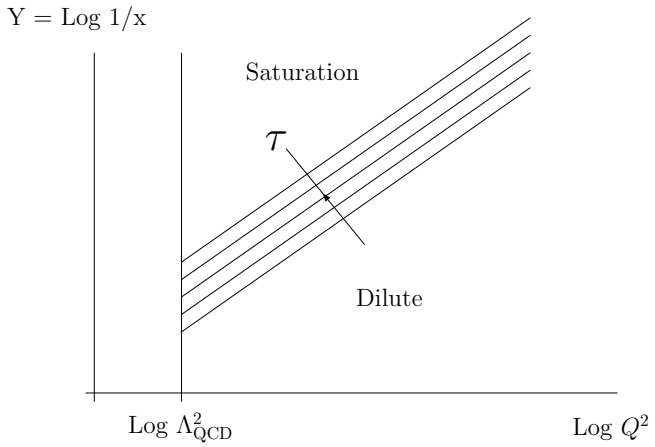


Fig. 5: Continuous self–similarity on the $(Y, \log Q^2)$ plane.

experimentally observed in HERA data [7] for the $\gamma^* p$ cross sections in the region $x < 0.01$ over a large range in Q^2, see Fig.6.

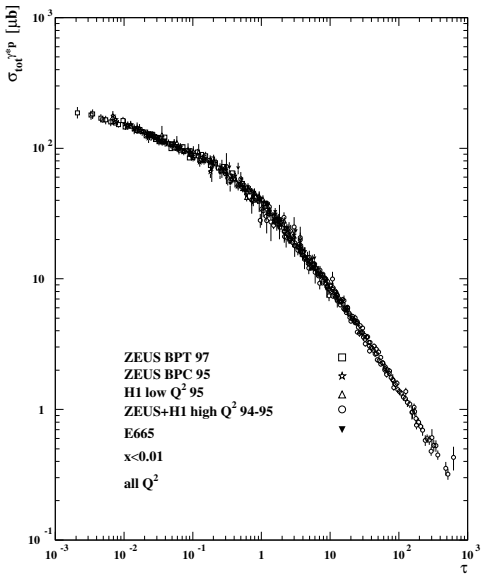


Fig. 6: HERA data for $\sigma_{\gamma^* p}$ with $x < 0.01$ versus the variable τ.

Our target is to find the holographic dual of the saturation line [10]. Taking into account the Wilson loop picture of the forward scattering amplitude for the dipole, the holographic representation of this quantity leads us to sum over world sheet amplitudes for a certain bulk geometry [11]. Since the dynamics we want to describe in gravity dual terms is the rapidity dependence of the amplitude, we will formally consider a background metric depending on the dual variable to Y in such a way that in the transition from the dilute to the dense or saturated regime it man-

ifests some sort of 'geometric scaling' in terms of properly chosen holographic variables. To establish the correspondence correctly this scaling must be characterized by a critical quantity related to the saturation exponent λ.

A first hint in this direction was shown in [1]. There it was argued that in the numerical studies of black hole formation for the spherically symmetric collapse of a massless scalar field carried out by Choptuik [12] (see [13] for a review) there appears a critical exponent very similar to λ. In particular, if we denote by p a generic parameter describing the initial radial density for imploding scalar waves, Choptuik found that there are critical lines in p, $p = p^*$, such that, if $p < p^*$ the scalar wave packet implodes through $r = 0$ and then disperses into flat space–time. But if $p > p*$, *i.e.*, the 'supercritical' case, then after the implosion there is a fraction of field which forms a small black hole. The interesting point is that its radius scales as $r_{\rm BH} \simeq |p-p^*|^{\frac{1}{\lambda_c}}$, and it turns out that precisely in dimension five $\lambda_c \simeq 2.44$.

Nonetheless, there is a difficulty to map the collapse of a scalar field with QCD, namely, the metric and field components obtained in this case manifest 'discrete self–similarity'. This means that a similar variable as the above–mentioned τ leaves physical observables invariant under the transformation $\tau \to \tau + \Delta$, with Δ a constant which has no analogue in four dimensional high energy scattering. We have investigated in detail a different type of gravitational collapse which has self–similarity, in this case 'continuous self–similarity' (CSS): the spherical collapse of a perfect fluid with a barotropic equation of state. The Einstein's equations together with matter's equations of motion in d dimensions can be solved assuming a unique dependence on the variable $\tau = -r/t$. As an example we discuss the function $y(r,t)$ which is proportional to the ratio of the mean density inside the sphere of radius r to the local density at r. In Fig. 7 it can be seen how $y(r,t)$ maintains a constant r–profile for different values of t. This implies that the solution is CSS since any change in the time coordinate can be compensated by a change in r keeping y unchanged. This CSS property is what we associate with 'geometric scaling' in QCD, with t and r being, respectively, the holographic duals of $\alpha_s N_c Y$ and $\log Q^2$ in QCD. The Choptuik exponent characterizing the black hole radius can be obtained by searching for

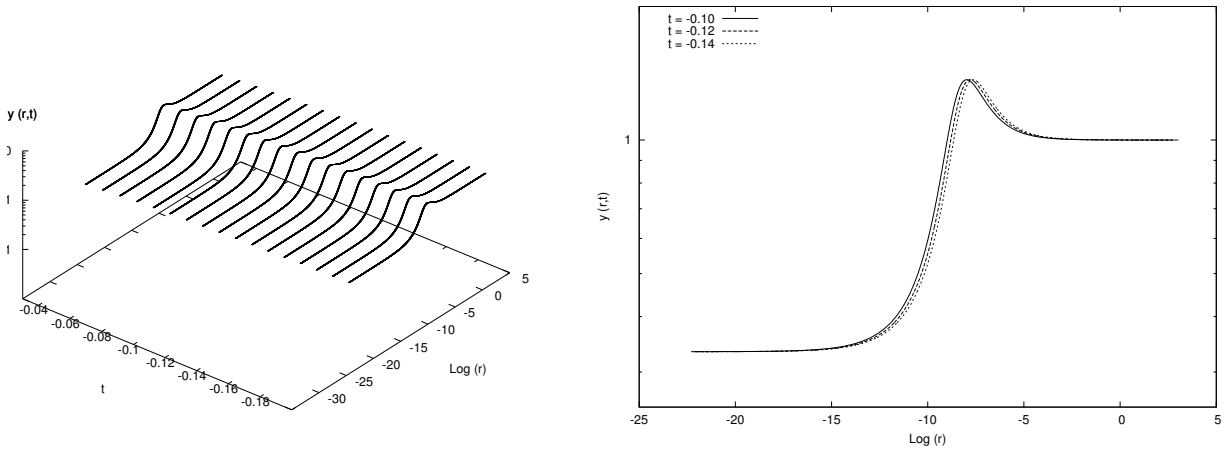


Fig. 7: A typical solution to gravitational collapse of a perfect fluid with continuous self–similarity.

Liapunov modes of instability of the CSS solution. In Fig. 8 we show how the exponentially

growing mode removes CSS from the solution to the collapse. The rate of growth of this mode is given by a coefficient which coincides with Choptuik's exponent. We have numerically extracted this coefficient in the five dimensional case and proven that it is very close to the QCD saturation exponent in the limit of traceless energy–momentum tensor for the fluid [10].

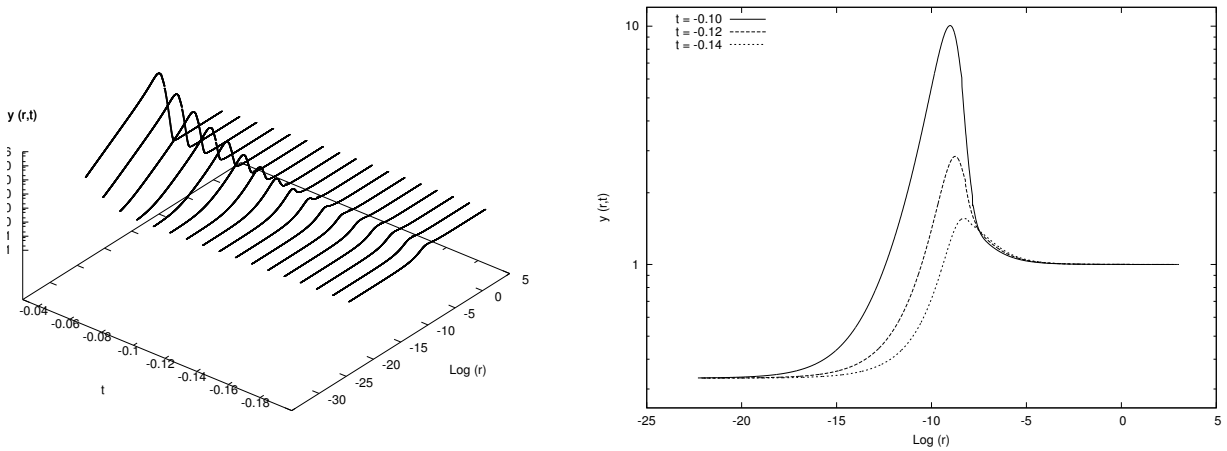


Fig. 8: Continuous self–similarity is lost by an exponentially growing mode in t.

References

[1] L. Álvarez-Gaumé, C. Gómez, and M. A. Vázquez-Mozo, Phys. Lett. **B649**, 478 (2007). hep-th/0611312.

[2] G. 't Hooft (1993). gr-qc/9310026;
L. Susskind, J. Math. Phys. **36**, 6377 (1995). hep-th/9409089.

[3] J. M. Maldacena, Adv. Theor. Math. Phys. **2**, 231 (1998). hep-th/9711200;
S. S. Gubser, I. R. Klebanov, and A. M. Polyakov, Phys. Lett. **B428**, 105 (1998). hep-th/9802109;
O. Aharony, S. S. Gubser, J. M. Maldacena, H. Ooguri, and Y. Oz, Phys. Rept. **323**, 183 (2000). hep-th/9905111.

[4] E. Witten, Adv. Theor. Math. Phys. **2**, 253 (1998). hep-th/9802150.

[5] S. W. Hawking and D. N. Page, Commun. Math. Phys. **87**, 577 (1983).

[6] E. Iancu, A. Leonidov, and L. D. McLerran, Nucl. Phys. **A692**, 583 (2001). hep-ph/0011241;
E. Iancu, A. Leonidov, and L. D. McLerran, Phys. Lett. **B510**, 133 (2001). hep-ph/0102009.

[7] A. M. Stasto, K. J. Golec-Biernat, and J. Kwiecinski, Phys. Rev. Lett. **86**, 596 (2001). hep-ph/0007192.

[8] V. S. Fadin, E. A. Kuraev, and L. N. Lipatov, Phys. Lett. **B60**, 50 (1975);
E. A. Kuraev, L. N. Lipatov, and V. S. Fadin, Sov. Phys. JETP **44**, 443 (1976);
E. A. Kuraev, L. N. Lipatov, and V. S. Fadin, Sov. Phys. JETP **45**, 199 (1977);
I. I. Balitsky and L. N. Lipatov, Sov. J. Nucl. Phys. **28**, 822 (1978).

[9] I. Balitsky, Nucl. Phys. **B463**, 99 (1996). hep-ph/9509348;
Y. V. Kovchegov, Phys. Rev. **D60**, 034008 (1999). hep-ph/9901281.

[10] L. Álvarez-Gaumé, C. Gómez, A. Sabio Vera, A. Tavanfar, and M. A. Vázquez-Mozo, work in progress.

[11] H. Liu, K. Rajagopal, and U. A. Wiedemann, Phys. Rev. Lett. **97**, 182301 (2006). hep-ph/0605178;
H. Liu, K. Rajagopal, and U. A. Wiedemann, Phys. Rev. Lett. **98**, 182301 (2007). hep-ph/0607062;
H. Liu, K. Rajagopal, and U. A. Wiedemann, JHEP **03**, 066 (2007). hep-ph/0612168.

[12] M. W. Choptuik, Phys. Rev. Lett. **70**, 9 (1993).

[13] C. Gundlach, Phys. Rept. **376**, 339 (2003). gr-qc/0210101.

Part VII

Summary

Experimental summary

Halina Abramowicz
DESY and Tel Aviv University

Abstract

A summary of the experimental results presented at this conference is discussed together with an attempt to point out the links between the various areas of research, affected by the understanding of elastic and diffractive scattering.

1 Introduction

As demonstrated at this conference, elastic and diffractive scattering affect many areas of research in high energy physics. While the definition of elastic scattering in hadron-hadron collisions is unique, both theoretically and experimentally, the definition of diffractive scattering is less precise. In elastic scattering, the interacting particles preserve their identity in the final state and carry out of the scattering all the available energy. In single diffraction, one of the incoming particles remains unscathed and is expected to carry out most of its initial momentum. Typical of diffractive scattering at high energy is a large rapidity gap separating the diffracted system from the 'unscathed' particle. In double diffractive scattering, both incoming particles loose their identity, however the respective final states, again well separated in rapidity, preserve the quantum numbers of the colliding particles.

In soft hadron-hadron interactions, elastic and diffractive scattering are described by Regge theory and understood as due to the exchange of the Pomeron trajectory [1,2]. The appearance of diffractive scattering with associated large transverse momentum jets in $p\bar{p}$ collisions observed by the UA8 experiment [3], have prompted Ingelman and Schlein [4] to propose the concept of a partonic structure of the Pomeron. Today, more than a decade after the discovery of diffractive interactions in deep inelastic ep scattering (DIS) at HERA [5, 6], it is clear that the Pomeron is predominantly a gluonic object [7]. This is consistent with expectations of perturbative QCD where, in leading order, diffractive scattering is mediated by two-gluon exchange [8, 9]. The appearance of diffraction is therefore closely related to the structure function of the proton and its large gluon component at low x, where x is the fraction of the proton momentum carried by a parton.

At high energy, elastic and diffractive scattering constitute a large fraction of the total scattering cross section. However, in spite of a large theoretical effort vested in understanding the dynamics of diffractive scattering (see summary by K. Golec-Biernat in these proceedings), there is as yet no consistent theoretical framework able to describe all the aspects of experimental observations. Various theoretical frameworks, based on different degrees of freedom (partons, color dipoles, color glass condensates, Regge trajectories), achieve different level of success, weakening therefore their predictive power and making the present and future experimental program that much more interesting and important.

The various aspects of diffractive scattering (large gluon density at low x, leading particle effect, factorization breaking) correlate many research programs, at HERA, at FNAL, at RHIC, at LHC and even in cosmic ray physics with extensive air showers (EAS). Some of it will be pointed out in this summary.

2 Inclusive diffraction and rescattering

In DIS at HERA, the diffractive structure function of the proton, F_2^D, can be parameterised in terms of diffractive parton distributions (dPDF) which can then be used to test the diffractive QCD factorisation theorem, expected to hold at large Q^2 [10]. Factorisation in diffractive scattering has been successfully tested in dijet [11, 12] and in charm [13, 14] production in DIS , as well as in diffractive charm photoproduction [14, 15].

As expected, factorisation fails in $p\bar{p}$ interactions [18], where typically rates for diffractive production in the presence of a hard scale are a factor 10 lower than expected from the HERA dPDF. This rate reduction may be explained as the result of multiple interactions, whereby the remnant partons of the diffracted proton rescatter off the leading proton and the products of the rescatter destroy the large rapidity gap (gap survival probability) [19]. A similar effect, albeit at a lower rate because of the size of the photon, is expected in dijet production in γp interactions [20], in the regime in which the photon interacts with the proton through its partonic component. A factor two suppression of dijet photoproduction has been observed by the H1 experiment [16] independent of whether the reaction proceeds through the resolved or direct photon component (see Fig. 1), though for the latter one expects factorisation to hold. A much weaker suppression,

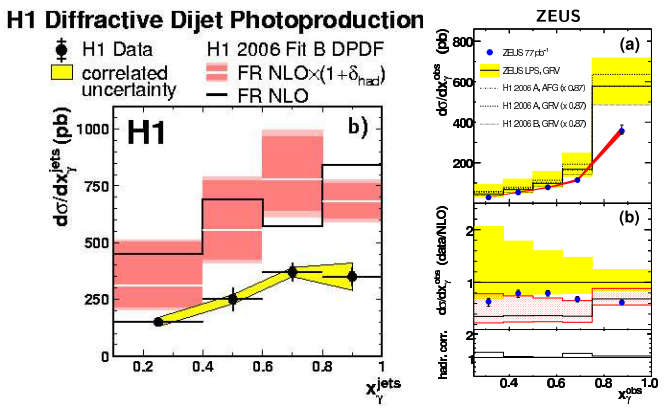


Fig. 1: The differential cross section for diffractive dijet production in γp scattering as a function of the fraction of the photon momentum involved in the interaction, x_γ^{jets} or x_γ^{obs}, as measured by H1 (left) and by ZEUS (right).

if at all, has been reported by the ZEUS experiment [17] (see Fig. 1). This apparent discrepancy requires further studies. What might be significant is that the transverse momenta of jets probed by ZEUS are higher than those of H1, possibly squeezing the photon into a smaller transverse configuration, in which case a smaller suppression would be expected. Gap survival and its dependence on the projectile size may turn out to be important in understanding and modeling multiple interactions.

3 Exclusive reactions in hard diffraction

The sensitivity of diffractive scattering to the size of interacting objects may be directly probed in exclusive reactions, such as vector meson production or deeply virtual Compton scattering (DVCS), in ep interactions at HERA. The size of the interacting photon may be controlled either by its virtuality Q^2, or the mass of the vector meson (J/ψ, Υ), or the momentum transferred squared at the proton vertex. Indeed, as discussed by A. Levy at this conference, when the photon is squeezed into a small size $q\bar{q}$ fluctuation, a bare proton emerges from the interaction and the measurements are consistent with a picture in which the exclusive processes proceed via the exchange of a two-gluon ladder.

In a larger picture, exclusive processes in ep scattering become a source of knowledge of generalized parton distribution (GPD) functions [21] from which one can extract not only the standard one-dimensional, longitudinal, parton distributions in the proton, but also the transversal distributions and various correlations.

3.1 DVCS and GPDs

The various GPDs, which contribute to DVCS, $H,\ E,\ \tilde{H},\ \tilde{E}$, may be extracted from exclusive photon production, $ep \to ep\gamma$, from the interference terms between the DVCS (QCD) and the Bethe-Heitler amplitude. The interference terms distort the distribution of the azimuthal angle, ϕ, and lead to beam-charge, beam-spin, longitudinal target-spin asymmetries. The measurements reported by the HERMES experiment at this conference clearly demonstrate the presence of these asymmetries (see talk by R. Fabbri). These data will be invaluable in constraining GPDs, for which the QCD evolution is known.

An attempt to extract GPDs in NLO and the ensuing three dimensional view of the proton structure has been presented at this conference (see talk by K. Passek-Kumericki). As x decreases, the number of partons increases as expected, and the radial coverage in the transverse plane increases (see Fig. 2). This is an important correlation which will affect the probability of

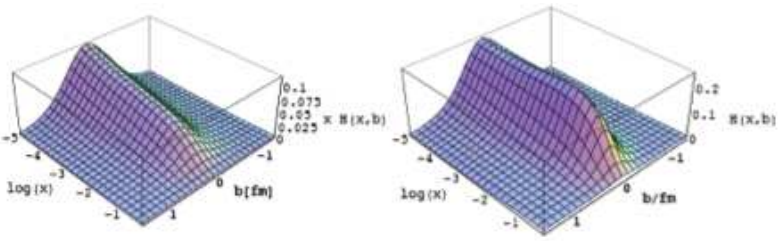


Fig. 2: Three dimensional extraction of the quark (left) and gluon (right) GPD (H).

multiple interactions in pp collisions as a function of x and the scale of the interaction [22].

3.2 Exclusive diffraction in $p\bar{p}$

An analogue of the two-gluon exchange reaction in $p\bar{p}$ (pp) is shown in Fig. 3(left). The same

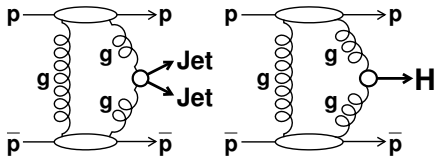


Fig. 3: Exclusive dijet (left) or Higgs (right) production in $p\bar{p}$ interactions.

diagram, as shown in Fig. 3(right,) may lead to exclusive Higgs production, which may yet turn out to be the cleanest way to measure the Higgs properties at the LHC [23], as massless quark production in $gg \to q\bar{q}$ is suppressed in leading order QCD by the $J_z = 0$ selection rule (for a discussion see contribution by A. De Roeck in this proceedings).

CDF has searched for diffractive exclusive dijets production in their RunII data. A significant excess of events in which the invariant mass of the two jets, M_{jj} saturates the total diffractive mass measured, M_X, is observed over MC expectations for diffractive, inclusive dijet production. As shown by K. Goulianos at this conference, the excess, in shape and rate, agrees well with the expectations of the model by Khoze et al. [23]. Moreover, as expected by the $J_z = 0$ selection rule, the fraction of dijets containing either charm or beauty decreases for large values of M_{jj}/M_X.

This is certainly good news for the LHC forward physics program as indeed diffractive Higgs production may be observed, although the expected rates are not very encouraging. In the best case scenario of the SM, about 100 events are expected (acceptance included) for an integrated luminosity of 30 fb^{-1} (see talk by J. Forshaw). The rates could turn out to be much larger in some scenarios of the MSSM, where the channel $h, H \to b\bar{b}$ is enhanced.

4 Forward physics at LHC

Both the ATLAS and the CMS experiments have instrumented forward regions to study the energy flow of particles in the very forward region, and to tag elastic and diffractive scattering (see contributions by M. Tasevsky, M. Deile, A. Hamilton, A. De Roeck, L. Fano, C. Sbarra) . The ATLAS forward detectors include LUCID, ALFA and ZDC. The first two, located at $\pm$17 m and $\pm$220 m from the interaction point (IP), were originally designed for precise luminosity measurement, while ZDC, located at $\pm$140 m is sensitive to neutral particles emitted at 0°. In addition, the LHCf experiment has its calorimeters and trackers located at 140 m from the IP of ATLAS. As an example, the pseudo-rapidity coverage provided by these detectors is shown in Fig. 4. The CMS forward detectors include HF, CASTOR, and CMS-ZDC. The HF calorimeters, for forward jet tagging is located $\pm$11 m from the IP. The CASTOR calorimeters are located at $\pm$14 m from the IP. As in the case of ATLAS, the ZDC in CMS is located at $\pm$140 m from the IP. In addition, the TOTEM experiment has its two tracking telescopes (at about $\pm$10 and $\pm$14.5 m from the IP) and its Roman-pot stations (at $\pm$147 and $\pm$220 m from the IP) included in the read-out of CMS, making the pseudo-rapidity coverage of CMS the largest ever achieved at colliders.

For precise measurements of the Higgs mass from exclusive diffraction, the detectors lo-

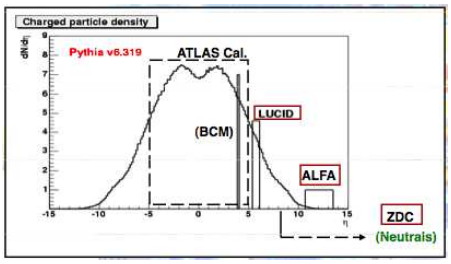


Fig. 4: The η coverage in the ATLAS experiment.

cated at 220 m from IP will have to be complemented by detectors at 420 m.

The forward coverage may provide a substantial extension of the low x range probed at large scales, as to be sensitive to the expected saturation (unitarity) effects in QCD. In any event, measurements of the very forward energy flow, be it in a restricted phase space, will provide invaluable information for tuning MC programs which model the development of EAS and which at present may differ by as much as factor two (see talk by A. Hamilton).

5 Underlying event and MPIs

Hard collisions in hadron-hadron interactions are accompanied by the so-called underlying event, which is the result of fragmentation of hadron remnants after their color coherence is broken by the hard parton-parton scattering. This part of the underlying event is usually assumed to have the characteristics typical of soft interactions (cylindrical phase space). In addition, because parton-parton scattering has an unphysically large cross section for low transverse momenta jets, multiple hard scatters are expected. The added activity in the event obscures the properties of hard physics, to be confronted with theory, and it is essential to model the underlying event properly.

The pp and $p\bar{p}$ data indicate that the presence of one subcollision enhances the probability of another one (for a review and discussion see contribution by G. Gustafson in these proceedings) . Moreover the harder the collision, the larger the probability of another collision. Multiple interactions are also needed to describe jet production in ep collisions at HERA at moderate Q^2, which is interpreted as due to the presence of resolved virtual photons (see presentation by T. Namsoo). This adds yet another dimension to the multiparton interactions, which may well depend on the size of interacting objects.

An extensive study of the underlying event has been made by R. Field at the Tevatron (see for example [24]) and he managed to tune the underlying event model of Sjoestrand and van Zijl [25] in PYTHIA to essentially describe all the data. However the correlation between the transverse energy and hadron multiplicity is not properly reproduced. An important ingredient of the model is the non-uniform distribution of partons inside the proton and the dependence of the cross section on the impact parameter. The studies of GPDs may help in modeling this aspect of multiple interactions.

The experiments at the LHC, where the analysis will be complicated by the added presence

of multiple collisions between two protons, are gearing themselves towards the direct measurement of the properties of the underlying events. For that purpose both the forward and central detectors will be used with special triggers, in particular for minimum bias events, as discussed by L. Fano at this conference. It will be very interesting to observe what happens when at the LHC the high density of gluons will be probed. Surprises may be expected, as diffraction is not part of the modeling of multiple interactions.

6 Forward physics in heavy ion collisions

The complexity of the physics of forward particle production is exemplified by the results from RHIC (see talk by D. Roehrich). Forward produced particles, with high transverse momenta, originate from interactions of low x partons, predominantly from gq and gg interactions as derived from NLO QCD calculations, which provide a reasonable description of the data. Therefore, sensitivity to effects due to gluon saturation is expected on nuclear targets, where the gluon density is enhanced by the presence of many nucleons, and in particular in central collisions.The pattern of particle production and suppression (see Fig. 5) strongly suggest that collisions in-

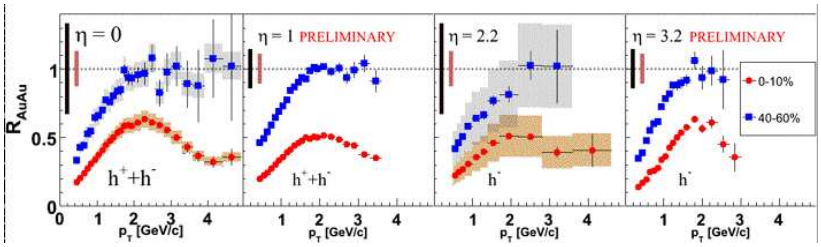


Fig. 5: Nuclear modification factor R_{AuAu} as a function of transverse momentum p_T for different values of pseudo rapidity η, for central (dots) and peripheral (squares) $AuAu$ collisions.

volving nuclear targets at RHIC probe a novel regime of QCD governed by coherent non-linear phenomena and gluon saturation - the color glass condensate. These effects are expected to be amplified in heavy ion collisions at LHC.

7 Total cross section measurements and luminosity at the LHC

The energy dependence of the total pp cross section as well as the t dependence of elastic cross cross section constitute a reference for the properties of soft interactions at high energy. Both measurements are notoriously difficult at colliders. At present, the model dependent extrapolation of the total cross section to be expected at the LHC is anywhere between 90 and 130 mb [26].

The LHC community has set a goal to measure both the total cross section and the t dependence of the elastic cross section to high precision. The TOTEM experiment (see talk by M. Deile), with the $3.1 < |\eta| < 6.5$ region of phase space instrumented with trackers and Roman pots, close to the CMS IP, aims at measuring the total pp cross section to a precision of 4% in the early stages of LHC running, to be improved to a 1% level at a later stage. This will be

achieved by determining the $d\sigma_{el}/dt$ at $t = 0$ and by measuring the elastic and inelastic rates. The detector acceptance for inelastic events is close to 95%, where most of the loss is due to low mass diffraction. A byproduct of these measurements is luminosity. Dedicated beam conditions will be needed to achieve these goals.

The results of TOTEM will be used by the ATLAS experiment to calibrate its luminosity monitor (LUCID) and later will be cross checked when the very forward ALPHA detectors will be installed (see talk by C. Sbarra).

8 Cosmic rays

Cosmic ray energy spectrum extends far beyond 10^{17} eV, the LHC energy reach. Cosmic rays are therefore a unique source of high energy particles and could be important in providing information on total cross section behavior beyond accelerator energies. The interaction length is extracted from properties of EAS, such as the shower maximum, and the total number of muons and electrons at the observation depth, as explained by R. Ulrich in this conference. The translation of these properties into cross section requires simulations of shower development in air, which are based on extrapolating our understanding of particle production to very high energies. These simulations are particularly sensitive to the inelastic cross section and to particle production spectra, which as shown in Fig. 6, vary substantially from model to model (see talks by G. G. Trinchero and A. Tricomi). New constraints on these models are expected from the LHCf

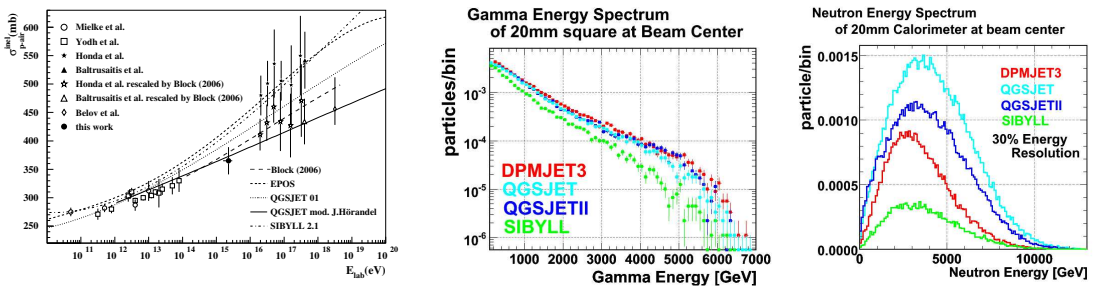


Fig. 6: Comparison of various shower development models: for inelastic p-air cross sections as a function of energy (left), for expected γ spectrum (middle) and neutron spectrum (right).

detector whose purpose is to measure the forward spectra of neutral particles, π^0 and neutrons, at the LHC (see talk by A. Tricomi).

9 Conclusions

The area of high energy physics, which encompasses total, elastic and diffractive cross sections, is far from being understood from first principles, yet it impacts many other aspects of high energy physics. There is a steady influx of new experimental results to guide the theoretical concepts. New results are expected at the LHC, though the experimental environment is very difficult and requires great ingenuity of experimentalists.

References

[1] P. D. Collins, "An Introduction To Regge Theory And High-Energy Physics," *Cambridge University Press, 1977*.

[2] V. N. Gribov, JETP Lett. **41** (1961) 667.

[3] R. Bonino *et al.* [UA8 Collab.], Phys. Lett. **B211** (1988) 239 .

[4] G. Ingelman and P. E. Schlein, Phys. Lett. **B152** (1985) 256 .

[5] M. Derrick *et al.* [ZEUS Collab.], Phys. Lett. **B315** (1993) 481 .

[6] T. Ahmed *et al.* [H1 Collab.], Nucl. Phys. **B429** (1994) 477.

[7] A. Aktas *et al.* [H1 Collab.], Eur. Phys. J. **C48** (2006) 715,[arXiv:hep-ex/0606004]

[8] F. E. Low, Phys. Rev. **D12** (1975) 163.

[9] S. Nussinov, Phys. Rev. Lett. **34** (1975) 1286.

[10] J. C. Collins, Phys. Rev. **D57** (1998) 3051, [arXiv:hep-ph/9709499]; erratum Phys. Rev. **D61** (1998) 2000.

[11] A. Aktas *et al.* [H1 Collaboration], JHEP **0710** (2007) 042, [arXiv:0708.3217 [hep-ex]].

[12] S. Chekanov *et al.* [ZEUS Collaboration], Eur. Phys. J. **C52** (2007) 813, arXiv:0708.1415 [hep-ex].

[13] S. Chekanov *et al.* [ZEUS Collaboration], Nucl. Phys. B **672** (2003) 3, [arXiv:hep-ex/0307068].

[14] A. Aktas *et al.* [H1 Collaboration], Eur. Phys. J. **C50** (2007) 1, [arXiv:hep-ex/0610076].

[15] S. Chekanov *et al.* [ZEUS Collaboration], Eur. Phys. J. **C51** (2007) 301, [arXiv:hep-ex/0703046].

[16] A. Aktas *et al.* [H1 Collaboration], Eur. Phys. J. **C51** (2007) 549, [arXiv:hep-ex/0703022].

[17] S. Chekanov [ZEUS Collaboration], arXiv:0710.1498 [hep-ex].

[18] A. A. Affolder *et al.* [CDF Collaboration], Phys. Rev. Lett. **84** (2000) 5043.

[19] A.B. Kaidalov *et al.*, Eur. Phys. J. **C21** (2001) 521,[arXiv:hep-ph/0105145];
E. Gotsman, E. Levin and U. Maor, Phys. Lett. **B438** (1998) 229, [arXiv:hep-ph/9804404];
B. Cox, J. Forshaw and L. Lönnblad, JHEP **9910** (1999) 023, [arXiv:hep-ph/9908464].

[20] A.B. Kaidalov *et al.*, Phys. Lett. **B567** (2003) 61, [arXiv:hep-ph/0306134].

[21] D. Mueller *et al.*, Fortsch. Phys. **42** (1994) 101, [arXiv:hep-ph/9812448];
A. V. Radyushkin, Phys. Rev. **D56** (1997) 5524, [arXiv:hep-ph/9704207];
X. Ji, J. Phys. **G24** (1998) 1181, [arXiv:hep-ph/9807358].

[22] L. Frankfurt, M. Strikman and C. Weiss, Ann. Rev. Nucl. Part. Sci. **55** (2005) 403, [arXiv:hep-ph/0507286].

[23] V. A. Khoze, A. D. Martin and M. G. Ryskin, Eur. Phys. J. **C23** (2002) 311, [arXiv:hep-ph/0111078].

[24] R. D. Field [CDF Collaboration], FERMILAB-CONF-06-409-E,presented at 33rd International Conference on High Energy Physics (ICHEP 06), Moscow, Russia, 26 Jul - 2 Aug 2006.

[25] T. Sjoestrand and M. van Zijl, Phys. Rev. **D36** (1987) 2019.

[26] J. R. Cudell *et al.* [COMPETE Collaboration], Phys. Rev. Lett. **89** (2002) 201801, [arXiv:hep-ph/0206172].

Theoretical summary

Krzysztof Golec-Biernat[1,2]
[1]Institute of Nuclear Physics Polish Academy of Sciences, Cracow, Poland
[2]Institute of Physics, University of Rzeszów, Rzeszów, Poland

Abstract
A summary of the theoretical talks given at 12th International Conference on Elastic and Diffractive Scattering – Forward Physics and QCD (EDS07) is presented.

1 Forward physics at the LHC

The subtitle of the EDS07 conference is "Forward physics and QCD" with an obvious relation to the forward physics program at the LHC. The program is impressive. Albert De Roeck in his talk [1] gave the following examples (see also [2]):

- soft and hard diffraction
- exclusive production of new mass states
- low-x dynamics
- new forward physics phenomena
- forward physics in heavy ion collisions.

All these topics were covered in the talks at this conference. In my summary, I will mostly concentrate on their theoretical side, leaving the experimental aspects, which are crucial for the final success, to the complementary talk by Halina Abramowicz [3]

2 Diffractive Higgs production

I start with a discussion of a particularly interesting processes which allow to search for new particles at the LHC in a very clean experimental environment [4, 5]. This is central exclusive production (CEP), $pp \to p + X + p$, where the protons lost only a few percent of their initial momenta, see Fig. 1. Thus, we deal with diffractive processes with large rapidity gaps between the central system X and the scattered protons. By measuring them, the mass of X will be determined as well as its quantum numbers.

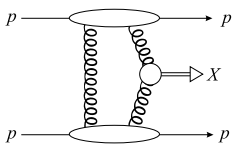


Fig. 1: Central exclusive production in pp scattering.

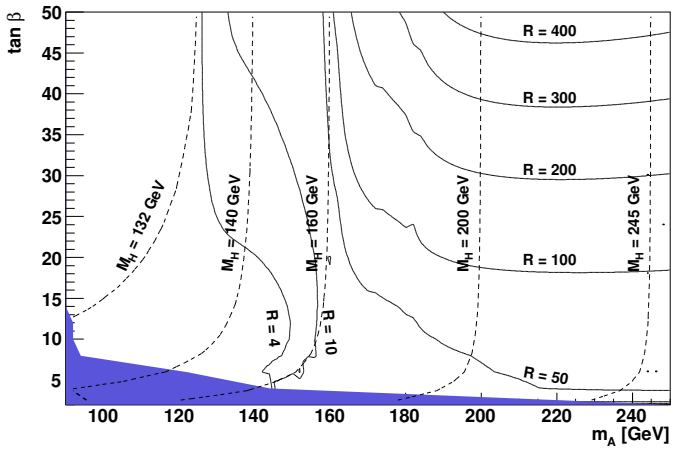


Fig. 2: The ratio of Higgs signals, $R = MSSM/SM$, for the decay mode $H \to b\bar{b}$.

The gold-plated CEP is a SM Higgs boson production. For Higgs masses in the range $140 - 200$ GeV, it is possible to measure Higgs through its decay to WW bosons with a background which can be safely eliminated. However, for low Higgs mass, $M_H < 150$ GeV, the dominant decay mode to $b\bar{b}$ quarks is more difficult to measure. Mostly because the trigger signals from protons detected at 420 meters (where forward detectors are placed) cannot reach the central detector on time to register Higgs decay [1, 5]. Summarising the current estimates, there will be only a dozen of Higgs events from CEP at the LHC for an integrated luminosity $60\,\mathrm{mb}^{-1}$. This estimation can be lowered if unitarity corrections to the two gluon exchange are considered, e.g. in the form of the black disk limit, as discussed in [6].

The situation is more optimistic in the MSSM. There are three neutral Higgs bosons in this case, the scalars h and H and the pseudoscalar A. In the forward proton mode, the pseudoscalar boson is filtered out and the heavier scalar bosons can be measured through the decay to $b\bar{b}$ quarks with the rate for large $\tan\beta$ of one or two orders of magnitude bigger than for the SM Higgs, see Fig. 2 [5]. The prospects to detect Higgs in the NMSSM are discussed in detail in [4].

The centrally produced system can also be formed by more exotic particles like supersymmetric light gluino or squark. In fact, any new object can be detected which has 0^{++} or 2^{++} quantum numbers and strongly couples to gluons. The latter aspect is related to the dominant mechanism of CEP with a fusion of two gluons to produce the central system and the exchange of an additional gluon which neutralises color. Thus, effectively, the LHC is turned into a gluon–gluon collider which allows QCD studies of different aspects of gluon densities, as well as the details of rapidity gap survival [5].

3 Total and elastic cross sections

The precise measurement of the total, σ_{tot}, and elastic, $d\sigma_{el}/dt$, cross sections for pp scattering at the LHC is very important for various reasons. First, it allows to test different models of soft

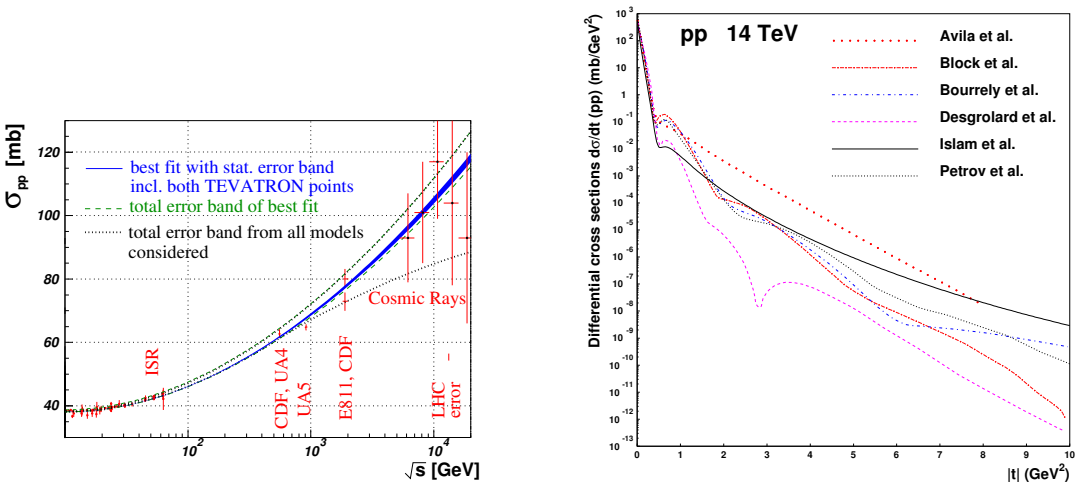


Fig. 3: Predictions for σ_{tot} (left) and $d\sigma_{el}/dt$ (right) cross sections from different models.

interactions between nucleons, as well as their large distance structure. QCD, the underlying theory of strong interactions, cannot say much at about soft interactions and their modelling is necessary. Secondly, there is also a practical reason. From the elastic and inelastic rates, N_{el} and N_{inel}, the luminosity $\mathcal{L}$ can be measured:

$$\mathcal{L} = \frac{1+\rho^2}{16\pi} \frac{(N_{el}+N_{inel})^2}{dN_{el}/dt|_{t=0}} . \tag{1}$$

Here ρ is the ratio of the real to imaginary parts of the forward elastic scattering amplitude. The measurement needs extrapolation to $t = 0$ and assumptions on the value of ρ, see [7] for details. Current predictions for σ_{tot} at the LHC energy 14 TeV stay in a wide range between 85 mb and 130 mb, see Fig. 3 (left) [7]. A broad range of predictions exists also for $d\sigma_{el}/dt$ at $|t| > 0.3$ GeV, see Fig. 3 (right) [8]. The LHC measurements should bring order to the ideas encoded in the above curves.

There were several talks presenting these ideas during the conference. The authors of [9] analyse the behaviour of the elastic scattering amplitude at small t, assuming a contribution from the hard pomeron. They link the strong energy growth of this component to the saturation regime, called the black disk limit, which manifests itself in a non-exponential behaviour of the scattering amplitude at small t. Whether this can be connected to parton saturation remains an open question, but the possibility of a new behaviour of the hadronic amplitude has to be taken into account while extracting σ_{tot} from data.

The behaviour of σ_{tot} and $d\sigma_{el}/dt$ at the LHC energy is strongly dependent on unitarity conditions imposed on elastic scattering amplitudes with a simple pomeron singularity. In [10], models with the unitarized pomeron are fitted to the existing data and after that the predictions for the LHC are made. The problem of unitarization of the soft or hard pomeron, reflected in the behaviour of the total and elastic cross sections, is also studied in a multi-component nucleon-structure model in [8]. The result for $d\sigma_{el}/dt$ in this case is shown as the solid line in Fig. 3.

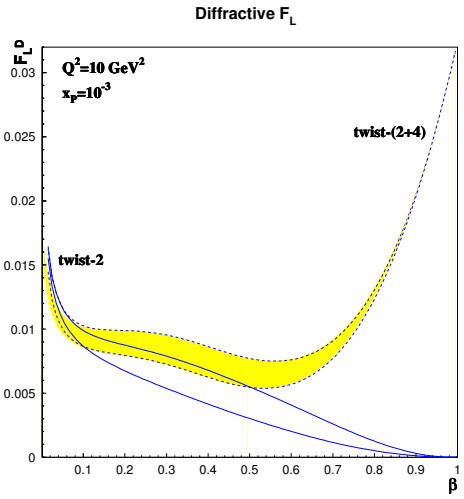


Fig. 4: Predictions for the longitudinal diffractive structure function from the analysis with higher twist (dashed lines).

4 Diffraction at ep and pp colliders

A wealth of diffractive data from HERA and the Tevatron raises important questions about the nature of diffractive interactions. In hard diffraction, when a large scale is present, QCD plays an important role. The hard part of diffractive scattering is described by perturbative QCD but softer aspects, like the energy dependence, have to resort to modelling.

It has been proven that the diffractive cross sections in DIS can be factorised into process-dependent coefficient functions, computed in perturbative QCD (pQCD), and diffractive parton distribution functions (DPDFs) which can be extracted from fits to data. The natural question is whether the DPDFs are universal objects like inclusive PDFs. It seems to be the case for DIS processes. However, the DPDFs from HERA overestimate the Tevatron data on the diffractive jet production in the $p\bar{p}$ scattering by a factor of ten or so. This effect can be understood on theoretical ground by taking into account soft interactions between spectator partons which spoil large rapidity gaps between the diffractive system and the scattered protons. It is interesting to know whether a similar effect occurs for the γp scattering at HERA with low virtuality photons, which resemble hadrons in the range of phase space where the resolved photon contribution dominates ($x_\gamma \ll 1$). The experimental studies of this problem are reported in [11] with the conclusion that the H1 measurement gives a global suppression of the diffractive cross section by a factor of 2, while the ZEUS measurement agrees with the calculations based on QCD factorisation. The difference between these measurements can be partially attributed to the kinematic region of the ZEUS analysis in which the resolved photon contribution might be suppressed.

The problem of proper theoretical schemes used to determine the DPDFs is discussed in [12, 13]. In the standard procedure, based on the leading twist–2 formulas, the DPDFs are fitted to the diffractive data from HERA, using the DGLAP equations to evolve them in Q^2. As emphasised in [12], it is also necessary to consider a higher twist contribution. In DIS, it

describes diffractive production of a $q\bar{q}$ pair from longitudinally polarised virtual photons and dominates for small diffractive masses, $M^2 \ll Q^2$ ($\beta \to 1$). The biggest impact of such an analysis is on the diffractive gluon distribution and longitudinal structure function, see Fig. 4.

The role of the perturbative pomeron in the determination of the DPDFs is discussed in [13]. One typically assumes Regge factorisation of the DPDFs with a pomeron flux describing the colorless exchange responsible for the rapidity gap formation. In [13], the direct and resolved perturbative Pomeron exchange is introduced. The latter exchange leads to an inhomogeneous term in the DGLAP equations which is very important for the DPDFs determination.

Exclusive diffractive processes at HERA, such as vector meson production or deeply virtual compton scattering (DVCS), were analysed in [14] using a dipole approach. An important role in this case is played by the dipole scattering amplitude which describes the interaction of a $q\bar{q}$ dipole from the virtual photon, which later forms a meson, with the proton. The measured t-distributions of the vector meson or DVCS cross sections allow to determine the shape of the proton in the impact parameter space b, through the b-dependence of the dipole scattering amplitude. An impressive agreement with the data is found in this comprehensive analysis, showing universality of the dipole approach in the description of diffractive processes at HERA.

Various diffractive processes, measured in the $p\bar{p}$ scattering at the Tevatron by the CDF collaboration, are reported in [15] with the aim to elucidate the QCD nature of diffractive interactions. Most important from this point of view is the central dijet production which is described within the same QCD framework as the exclusive Higgs production in Sec. 2. The good news is that the measured dijet rates support calculations which lead to the predictions for the diffractive Higgs production.

5 Multiple interactions

There is a growing experimental evidence, reported in [16], that multiple parton interactions will play a very important role in the interpretation of the LHC results. The necessity to include multiple interactions into Monte Carlo models of hadronic scattering is discussed in [17]. The minijet cross section, which describes parton-parton subcollisions, is divergent when parton's $p_\perp \to 0$. Introducing a lower cutoff such that the minijet cross section equals the total cross section, it is found that $p_{\perp min} \approx 2.5$ GeV at the Tevatron and 5 GeV at the LHC. These large values mean that on average there must be several hard subcollisions in one event, which tame the minijet cross section.

Multiple scattering at high energy can be modelled by multipomeron exchanges. In QCD, the pomeron is represented by a gluon ladder. *Assuming* the AGK cutting rules, the multiplicity in a multiple collision event can be calculated by cutting gluonic ladders. In particular, two cuts double the multiplicity. However, the analysis of the CDF data shows that two subcollisions do not give doubled multiplicity. Thus neglected pomeron interactions, given by pomeron loops or multipomeron vertices, are very important.

A first Monte Carlo realization of such effects, given in a dipole cascade model, is presented in [17]. In this model, pomeron loops are formed due to a "dipole swing" in color space, see Fig. 5. The multiple scattering Monte Carlo for hadron-hadron and nucleus-nucleus collisions is also discussed in [18].

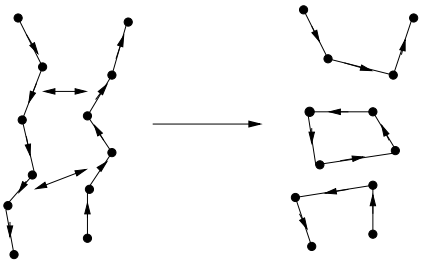


Fig. 5: Pomeron loop from "dipole swing" in a dipole cascade model.

The validity of the Abramowski-Gribov-Kancheli (AGK) cutting rules in QCD is discussed in [19]. Multiple parton interactions are necessary in this context for unitarization of the perturbative QCD (BFKL) pomeron. In this analysis, the multipomeron amplitude is built from reggeized gluons and two important conditions are fomulated in order for the AGK cutting rules to be valid in QCD.

6 BFKL pomeron

The vacuum quantum number exchange responsible for diffractive processes, called traditionally the pomeron, is modelled in pQCD with the help of gluon exchanges projected into a color singlet state. The Balitsky-Fadin-Lipatov-Kuraev (BFKL) pomeron is found in the Regge limit after summing an infinite class of virtual corrections to the lowest order exchange with two gluons. In the leading logarithmic order (LO), these corrections are proportional to the powers of large logarithm of energy multiplied by the strong coupling constant, $(\alpha_s \log s)^n$. There are two related problems with the BFKL pomeron. First, the question of the next-to-leading order corrections (NLO) proportional to the powers $\alpha_s(\alpha_s \log s)^n$. Secondly, the problem of unitarity corrections since the BFKL pomeron gives the power like dependence on energy, which *violates* the Froissart bound for the total cross sections.

The NLO corrections to the BFKL pomeron equation were computed almost ten years ago but they are still subjected to intensive studies. The BFKL kernel in the NLO is quite complicated and a simpler form is desirable. This is achieved in [20], where a real part of the kernel is computed in the transverse coordinate (dipole) representation. The new form, computed for the scattering of colourless objects, is much simpler than the original one in the transverse momentum space representation.

In the NNLO, the pomeron is no longer described by the equation in the BFKL form since more than two (reggeized) gluons have to be exchanged. Nevertheless, the NNLO corrections to the BFKL kernel are estimated in [21] for a better stability of the BFKL based results.

Various phenomenological applications of the NLO BFKL corrections were presented during the conference. In [22], the azimuthal angle decorrelation between two jets separated by large rapidity in hadronic scattering is studied within the NLO framework. The decorrelation between the scattered electron and a forward jet in DIS is also presented there. The jet production in

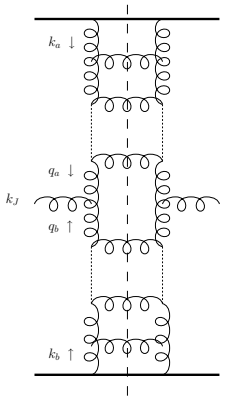


Fig. 6: Central inclusive jet production in the BFKL approach.

the central region of rapidity with two BFKL pomerons and the NLO jet vertex, see Fig. 6, is analysed in [23]. This problem is discussed in the context of a proper choice of the energy scale s_0 for the dimensional quantity s/s_0, which has to be used in the calculations. Finally, the exclusive vector meson electroproduction, calculated with the BFKL corrections in hard scattering amplitudes, is reported in [24]. These are preliminary studies with the LO BFKL resummation which are already important for the data analysis.

The central role in the computational scheme (called k_T-factorisation) of the presented analyses play *unintegrated parton distributions*. A comprehensive discussion of these important objects, concerning their proper definition in QCD, is presented in [25].

The calculation of unitarity corrections to the BFKL pomeron can be attempted with the Lipatov effective action, which defines the theory of interaction of reggeized gluons (R) and particles (P) described by independent fields. An interaction vertex for these fields (the RRRP vertex) is studied in [26] in connection with the basic calculation done by Bartels.

Some years ago Lipatov showed that the theory of reggeized gluons in the leading logarithmic approximation is *integrable* in the large N_c limit. It is now believed that this might be true to all orders for the $N = 4$ supersymmetric Yang–Mills theory. Important aspects of this theory, studied with the help of the asymptotic Bethe ansatz, are discussed by Lipatov in [27]. The role of the finite N_c corrections to the theory of reggeized gluons is discussed in [28].

7 Odderon

The odderon is a counterpart of the pomeron with $C = -1$ parity. In the lowest order QCD approach, the odderon is the color singlet exchange of three perturbative gluons. In the Regge limit of QCD, the pomeron is modelled by three interacting reggeized gluons. In this case, the Bartels-Kwiecinski-Praszalowicz (BKP) equation is obtained, which gives to the odderon energy dependence.

The odderon exchange is very elusive since it has not been experimentally identified yet. Thus, it is very important to study processes involving the odderon at the LHC. One of them

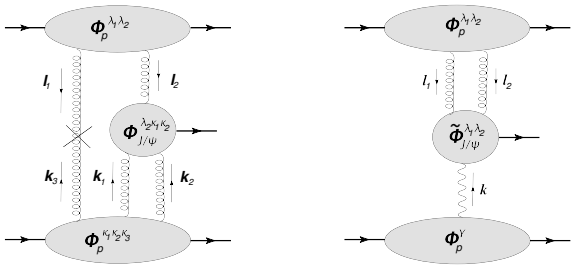


Fig. 7: The lowest order diagrams for the pomeron-odderon (-photon) fusion in exclusive vector meson production.

is exclusive hadroproduction of vector mesons with C odd parity, like J/ψ or Υ, is discussed in [29]. Such a production occurs as a result of the pomeron–odderon (or pomeron–photon) fusion, see Fig. 7. The predictions for the cross sections from this analysis are at the nb level, but special care is needed to filter out the pomeron–photon fusion background. Careful studies of the exclusive J/ψ hadroproduction with absorptive corrections is also performed in [30].

In DIS at HERA, the odderon searches were concentrated on the diffractive photoproduction of neutral pion, $\gamma p \to \pi^o N^*$, with no positive result. The experimental upper limit for the corresponding cross section equals $49\ \mathrm{nb}$, while the theoretical estimations, based on the Heidelberg model of the QCD vacuum, predicts $300\ \mathrm{nb}$. The experimental suppression of this process is explained in [31] as a consequence of chiral symmetry since the amplitude for the π^0 production, proportional to the pion mass, vanishes in the chiral limit. A new process with the odderon is proposed in [31] for peripheral collisions at the LHC: $\gamma\gamma \to \pi^0\pi^0$ scattering. This process could also be measured at the future ILC.

A nonperturbative odderon is discussed within the Regge theory in [32]. It seems that the only experimental evidence for such a odderon is the difference between the elastic cross sections for $p\bar{p}$ and pp scattering at ISR in the first dip region. According to [32], the nonperturbative odderon will manifest itself in oscillations in t of the difference between the pp and $p\bar{p}$ elastic cross sections. The LHC does not offer $p\bar{p}$ beams, thus the best way to look for such an effect is the combination of RHIC and UA4/2 data.

8 High density QCD

High density (or high energy) QCD arises from a question: what happens with the system of partons in the nucleon when their density becomes so large that they start to interact [33]. It is believed that parton densities saturate in such a case and the power-like growth with energy of the DIS cross sections, violating the Froissart bound, is tamed by nonlinear evolution equations.

The dipole picture of DIS at small x (large energy) is particularly useful in the discussion of saturation. It considerably simplifies the understanding of unitarity conditions which have to be imposed and provides interesting links to statistical physics [34]. In this picture, a $q\bar{q}$ pair from the virtual photon is viewed as a color dipole of a transverse size r, which scatters off the proton. The limitations on the validity of this picture are presented in [35].

The basic quantity to discuss is the dipole scattering amplitude, T, which obeys the non-

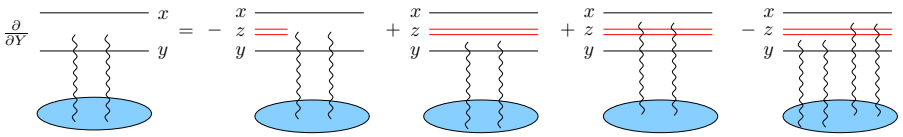


Fig. 8: The BK equation for the dipole-proton scattering amplitude T.

linear Balitsky-Kovchegov (BK) evolution equation in rapidity Y, shown in the pictorial form in Fig. 8 [36]. The nonlinearity sits in the last term to the right which involves the amplitude squared. The main property of the asymptotic solutions to the BK equation is *geometric scaling*, when T becomes a function of only one variable, rQ_s, with the energy dependent saturation momentum Q_s. This behaviour implies a similar scaling for the DIS cross section $\sigma_{tot}^{\gamma^* p}$, observed in the HERA data. It is very important that the local unitarity condition, $T \leq 1$, is satisfied for fixed impact parameter of the dipole. However, the Froissart bound is still violated because of the long range perturbative gluons.

The BK equation was derived in the so-called mean field approximation in which important effects were neglected. The most important ones are: confinement (which is beyond the reach of pQCD) and fluctuations in the number of dipoles in the proton target, computed on the event-by-event basis. Despite the fact that these fluctuations are important in the low density regime, they lead to observable effects in the saturation region. In particular, geometric scaling is replaced by *diffusive scaling*, when the averaged scattering amplitude becomes a function of $\ln(rQ_s)/\sqrt{Y}$ [34, 36]. It has not been fully understood yet how saturation occurs beyond the mean field approximation in the high density region. It is proposed in [34] that the corresponding QCD evolution equation should belong to the universality class of the stochastic Fisher-Kolmogorov-Petrovski-Piscounov (sFKKP) equation, known from statistical physics. Unfortunately, nobody has proven this rigorously.

In [37], parton saturation in perturbative QCD is discussed from a general perspective in which hadron or nucleus scattering can be accommodated. Depending on the relation between two colliding objects, called the projectile and the target, different pictures of the unitarity limit are achieved through the BK, JIMWLK or KLWMIJ equations. The most challenging is the situation when two large high density objects scatter, e.g. in the nucleus-nucleus collisions. In this case, both the nonlinear evolution of partons and subsequent multiple scattering are important. The theory of such collisions is not fully developed, nevertheless, promissing attempts exist.

The properties of dense quark-gluon systems are also studied in [38], using the Gribov approach to the description of DIS. In this approach, an overlap of small x partons in longitudinal momentum space leads to saturation, e.g. in the form of fusion of two chains of partons which give large mass diffractive production. This size of this effect is estimated in [38] from the HERA data and after that predictions for nuclear collisions are made.

Experimental aspects of parton saturation in hadron and nucleus scattering were intensively discussed during the conference. They concern the gluon density saturation in nucleus [39], hot spots in the proton [40] and the search for color glass condensate at RHIC [41]. A comprehensive review of RHIC physics is also presented in [42].

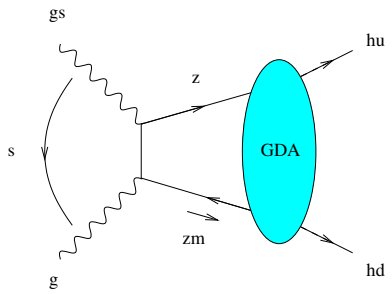


Fig. 9: The GDA in $e^+e^- \to e^+e^-\rho_L^0\rho_L^0$ scattering

The transition to saturation is a source of inspirations for more exotic analyses. Based on some numerical coincidence and following the idea of duality between gauge theory and gravity, it is proposed in [43] that this phenomenon can be linked to the critical behaviour in the black hole formation.

9 Exclusive reactions with photons

I finish my summary describing talks which are not directly related to the forward physics program of the LHC, but are equally important for the QCD based understanding of high energy scattering processes.

Various amplitudes involving QCD partonic operators can be studied in exclusive processes with virtual or quasi-real photons. In the collinear factorisation approach with two quark operators, these are: generalised parton distributions (GPD), distribution amplitudes (DA), generalised distribution amplitudes (GDA) and transition distribution amplitudes (TDA). They are all nonperturbative objects which undergo pQCD evolution in the DGLAP or BFKL form. Thus, the BFKL pomeron can be studied in the high energy $\gamma^*\gamma^* \to \rho_L^0\rho_L^0$ scattering at the future ILC [44]. For moderate energies, however, the standard GDA is relevant for this process, see Fig. 9.

In ep scattering at HERA, the generalised parton distributions are determined through vector meson electroduction [45] or DVCS [46]. The theoretical analysis of these processes has reached the state of maturity in which the NLO evolution equations are applied. In addition, the transverse structure of the proton is being determined through the t-dependence of the GPDs [46]. The transition between the soft and hard t domains in DVCS can be analysed with the Regge model proposed in [47].

Different approaches to exclusive electroproduction from those based on the collinear factorisation of hard scattering amplitudes were also presented. They emphasise nonperturbative aspects of these processes like the QCD vacuum [48] or the meson cloud of the proton [49].

10 Conclusions

Diffractive physics is very challenging since its experimental and theoretical aspects are pushed into their boundaries. On the theory side, QCD is studied in most difficult limits touching con-

finement or the transition between soft and hard regimes. The experience accumulated up till now, combined with the excitement of a younger generation of physicists working in this area, guarantees success in the years to come. At the dawn of the LHC era, the EDS07 conference has shown that diffractive physics is in a good shape.

ACKNOWLEDGEMENTS

I would like to thank the organizers for perfect organization of the conference. The support by the MEiN research grant 1 P03B 028 28 (2005-08), the Research Training Network HEPTools (MRTN-2006-CT-035505) and the Polish-German Joint Project "Hadronic final states and parton distribution functions" is acknowledged.

References

[1] A. De Roeck, *Prospects for Diffraction at the LHC*, in these proceedings.

[2] A. Hamilton, *Prospects of Forward Energy Flow and Low-x Physics at the LHC* , in these proceedings.

[3] H. Abramowicz, *Experimental summary*, in these proceedings.

[4] J. Forshaw and A. Pilkington, *Central Production of New Physics*, in these proceedings.

[5] V.A. Khoze, A.D. Martin and M.G. Ryskin, *Insight into New Physics with Tagged Forward Protons at the LHC*, in these proceedings.

[6] L. Frankfurt, C.E. Hyde, M. Strikman and C. Weiss, *Rapidity gap survival in the black-disk regime*, in these proceedings.

[7] M. Deile, *Total Cross-Section Measurement and Diffractive Physics with TOTEM*, in these proceedings.

[8] M.M. Islam, *pp Elastic Scattering at LHC in a Nucleon-Structure Model*, in these proceedings.

[9] O.V. Selyugin and J.-R. Cudell, *Saturation effects in elastic scattering at the LHC*, in these proceedings.

[10] E. Martynov, *Elastic pp and $p\bar{p}$ scattering in the models of unitarized pomeron*, in these proceedings.

[11] A. Bonato, *Factorisation breaking in diffraction*, in these proceedings.

[12] K. Golec-Biernat and A. Luszczak, *Diffractive structure function F_L^D from fits with higher twist*, in these proceedings.

[13] G. Watt, A.D. Martin and M.G. Ryskin, *Diffractive parton distributions: the role of the perturbative Pomeron*, in these proceedings.

[14] H. Kowalski, *Low-x and Diffractive Physics at Future Electron-Proton/Ion Colliders*, in these proceedings.

[15] K. Goulianos, *Diffraction at CDF*, in these proceedings.

[16] L. Fano, *Multiple Parton Interactions, Underlying Event and Forward Physics at LHC*, in these proceedings.

[17] G. Gustafson, *Multiple Scattering, Underlying Event and Minimum Bias*, in these proceedings.

[18] K. Werner and T. Pierog, *Extended Air Shower Simulations Based on EPOS*, in these proceedings.

[19] M. Savadore, J. Bartels and G.P. Vacca, *Multiple interactions and AGK rules i pQCD*, in these proceedings.

[20] V.S. Fadin, *The coordinate representation of NLO BFKL and the dipole picture*, in these proceedings.

[21] S. Marzani, R.D. Ball, P. Falgari and S. Forte, *BFKL at NNLO*, in these proceedings.

[22] A. Sabio Vera and F. Schwennsen, *Angular decorrelations in Mueller Navelet jets in DIS*, in these proceedings.

[23] J. Bartels, A. Sabio Vera and F. Schwennsen, *NLO jet production in k_T factorization*, in these proceedings.

[24] D. Yu. Ivanov, *Exclusive vector meson production*, in these proceedings.

[25] A. Staśto, *Unitegrated parton distributions and correlation functions*, in these proceedings.

[26] M.A. Braun and M.I. Vyazovsky, *The Reggeon → 2 Reggeon + Particle vertex in the Lipatov effective action*, in these proceedings.

[27] L.N. Lipatov, *BFKL equation and anomalous dimensions in $N = 4$ SUSY*, in these proceedings.

[28] G.P. Vacca and P.L. Iafelice, *Small x QCD and Multigluon States: a Color Toy Model*, in these proceedings.

[29] L. Szymanowski, *Exclusive J/psi and Υ hadroproduction as a probe of the QCD Odderon*, in these proceedings.

[30] A. Szczurek, *Diffractive production of quarkonia*, in these proceedings.

[31] C. Ewerz and O. Nachtmann, *Diffractive Neutral Pion Production, Chiral Symmetry and the Odderon*, in these proceedings.

[32] B. Nicolescu, *The Odderon at RHIC and LHC*, in these proceedings.

[33] E. Levin, *Non-linear QCD at high energies*, in these proceedings.

[34] S. Munier, *Connections between high energy QCD and statistical physics*, in these proceedings.

[35] C. Ewerz, A. von Matheuffel and O. Nachtmann, *On the Limitations of the Color Dipole Picture*, in these proceedings.

[36] A.I. Shoshi, *High energy QCD beyond the mean field approximation*, in these proceedings.

[37] A. Kovner, *Gluon saturation: from pp to AA*, in these proceedings.

[38] A. Kaidalov, *Nuclear shadowing and collisions of heavy ions*, in these proceedings.

[39] M. Kozlov, A.I. Shoshi and Bo-Wen Xiao, *On the behaviour of R_{pA} at high energy*, in these proceedings.

[40] B.Z. Kopeliovich, B. Povh and I. Schmidt, *Gluon drops inside hadrons*, in these proceedings.

[41] J.L. Albacete, *Manifestation of gluon saturation at RHIC*, in these proceedings.

[42] A. Staśto, *RHIC physics: short overview*, in these proceedings.

[43] L. Álvarez-Gaumé, C. Gómez, A. Sabio Vera, A. Tavanfar, M.A. Vázquez-Mozo, *Gluon saturation and Black Hole Criticality*, in these proceedings.

[44] S. Wallon, B. Pire, M. Segond and L. Szymanowski, *Studying QCD factorizations in exclusive $\gamma^*\gamma^* \to \rho^0_L\rho^0_L$*, in these proceedings.

[45] S.V. Goloskokov, *Vector meson electroduction within GPD approach*, in these proceedings.

[46] K. Kumericki, D. Müller and K. Passek-Kumericki, *Fitting DVCS at NLO and beyond*, in these proceedings.

[47] L.L. Jenkovshky, *A Regge-pole model for DVCS*, in these proceedings.

[48] E. Ferreira and H.G. Dosch, *Photo and electroproduction of vector mesons: a unified nonperturbative treatment*, in these proceedings.

[49] J.T. Londergan and A.P. Szczepaniak, *What is Measured in Hard Exclusive Electroproduction*, in these proceedings.